

**NASA
Reference
Publication
1257**

1991

Transport Methods and Interactions for Space Radiations

John W. Wilson and Lawrence W. Townsend
*Langley Research Center
Hampton, Virginia*

Walter Schimmerling
*Lawrence Berkeley Laboratory
University of California
Berkeley, California*

Govind S. Khandelwal and Ferdous Khan
*Old Dominion University
Norfolk, Virginia*

John E. Nealy, Francis A. Cucinotta,
Lisa C. Simonsen, and Judy L. Shinn
*Langley Research Center
Hampton, Virginia*

John W. Norbury
*Rider College
Lawrenceville, New Jersey*



National Aeronautics and
Space Administration
Office of Management
Scientific and Technical
Information Program

1

2



Contents

Preface	xi
Chapter 1—Introduction	1
1.1. Pre-NASA History	1
1.2. History of Langley Program	5
1.3. Overview of Space-Radiation Interactions	11
1.4. References	20
Chapter 2—Coulomb Interactions in Atoms and Molecules	27
2.1. Introduction	27
2.2. Extremely Rarefied Gas Interactions	31
2.2.1. Stopping at low energies	32
2.2.2. Bethe stopping theory	32
2.2.3. Optical oscillator strengths within screened hydrogenic model	36
2.3. Stopping in Molecular Gases	39
2.3.1. Historical perspective	39
2.3.2. Excitation spectra of one- and two-electron systems	46
2.3.3. Stopping and straggling parameters of atoms	49
2.3.4. Covalent-bond effects	50
2.3.5. Ionic-bond effects	54
2.3.6. Metallic-bond effects	56
2.3.7. Discussion of results	60
2.4. Molecular Stopping Cross Sections	61
2.5. Stopping Cross Sections of Liquid Water	67
2.6. Semiempirical Methods	73
2.7. References	76
Chapter 3—High-Energy Interactions	85
3.1. Introduction	85
3.2. Multiple-Scattering Theory	87
3.2.1. Glauber theory	87
3.2.2. Multiple-scattering series	88
3.2.3. Optical potential	90
3.3. Heavy Ion Dynamical Equations	91
3.3.1. Coupled-channel equations	91
3.3.2. Born approximation	92
3.3.3. Perturbation expansion and distorted-wave Born approximation	95
3.4. Coupled-Channel Amplitudes	98
3.5. The Elastic Channel	100
3.6. Abrasion Theory	102

3.6.1. Abrasion cross section	103
3.6.2. Generalized abrasion theory	104
3.6.3. Isotope production cross section	105
3.6.4. Results	105
3.7. Abrasion-Ablation Model	106
3.8. Electromagnetic Interactions	110
3.9. References	111
Chapter 4—Elastic Channel Data Base	117
4.1. Introduction	117
4.2. Optical Model Cross Sections	120
4.2.1. Nuclear density distributions	120
4.2.2. Nucleon-nucleon scattering parameters	123
4.2.3. Results	124
4.3. Coupled-Channel Formalism	127
4.4. Parametric Cross Sections	133
4.4.1. Total nuclear cross sections	134
4.4.2. Nuclear-absorption cross sections	141
4.5. Parametric Differential Cross Sections	149
4.5.1. Nucleon-nucleon spectrum	149
4.5.2. Nucleon-nucleus spectrum	150
4.6. Summary	154
4.7. References	154
Chapter 5—Reaction Channel Data Base	161
5.1. Introduction	161
5.2. Nuclear Abrasion Model	161
5.2.1. Optical potential	161
5.2.2. Abrasion theory	162
5.2.3. Collision parameters	164
5.2.4. Results	165
5.3. Simple Ablation Model	167
5.3.1. Prefragment charge distributions	168
5.3.2. Prefragment excitation energies	170
5.3.3. Ablation factors (EVAP-4)	172
5.3.4. Fragmentation results	172
5.4. Abrasion Dynamics	177
5.4.1. Method of calculation	177
5.4.2. Results	180
5.4.3. Estimating collision impact parameters	182
5.4.4. Remarks	183
5.5. Direct Reaction Processes	184

5.5.1. Exclusive inelastic scattering	184
5.5.2. Physical inputs	185
5.5.3. Results and discussion	187
5.5.4. Inclusive inelastic scattering	194
5.5.5. Correlations and inclusive scattering	195
5.5.6. Model calculations	197
5.6. Coulomb Dissociation	199
5.6.1. Electric dipole transitions	199
5.6.2. Results	201
5.6.3. Electric quadrupole transitions	201
5.6.4. Nuclear versus coulomb contributions	204
5.7. Semiempirical Data Base	204
5.7.1. Nucleon nonelastic spectrum	204
5.7.2. Light-fragment spectrum	208
5.7.3. Fragmentation cross sections	208
5.7.4. Heavy-fragment spectrum	215
5.7.5. Energy-transfer cross section	217
5.7.6. Heavy ion fragmentation model	222
5.8. Summary	231
5.9. References	231
Chapter 6—Transport Theory	239
6.1. Introduction	239
6.2. Transport Formalism	241
6.3. Approximation Procedures	244
6.3.1. Neglect of target fragmentation	244
6.3.2. Space radiations	245
6.3.3. Velocity conserving interaction	246
6.3.4. Decoupling of target and projectile flux	247
6.3.5. Back-substitution and perturbation theory	249
6.4. References	250
Chapter 7—Dose Approximation in Arbitrary Convex Geometry	255
7.1. Introduction	255
7.2. High-Energy Transport	256
7.3. Properties of the Dose Response Function	257
7.4. Expansion for Two-Dimensional Transport	260
7.5. References	265
Chapter 8—Nucleon Transport Methods	267
8.1. Introduction	267
8.2. Charged-Particle Transport	268
8.2.1. Energy-independent cross sections	268

8.2.2. Discrete spectrum	269
8.2.3. Continuous spectrum	273
8.3. Buildup Factors	275
8.3.1. Simplified theory of proton buildup factors	276
8.3.2. Buildup in an external shield	278
8.3.3. Tissue buildup factors	280
8.4. Numerical Methods	284
8.4.1. Energy-independent proton model	285
8.4.2. First-order explicit methods	285
8.4.3. "Linearized" methods	286
8.4.4. Unconditionally stable numerical methods	287
8.5. Error Analysis of Unconditionally Stable Methods	288
8.5.1. Local relative error	288
8.5.2. Error propagation	291
8.5.3. Numerical procedure	292
8.6. Coupled Baryon Transport Methods	293
8.7. Results and Discussion	297
8.8. Concluding Remarks	305
8.9. References	305
Chapter 9—High Charge and Energy (HZE) Transport	309
9.1. Introduction	309
9.2. Energy-Independent Flux	311
9.2.1. Neon beam transport	311
9.2.2. Iron beam transport	312
9.3. Monoenergetic Ion Beams	312
9.3.1. Total flux comparisons	321
9.3.2. Monoenergetic beam results	321
9.4. Realistic Ion Beams	324
9.5. Approximate Spectral Solutions	328
9.5.1. Approximate monoenergetic beams	328
9.5.2. Approximate realistic beams	331
9.6. Recommended Methods	333
9.7. Impulse Response	335
9.8. Galactic Ion Transport	339
9.8.1. Galactic cosmic-ray propagation	341
9.8.2. Discussion of results	342
9.9. Analytic Benchmarks	343
9.9.1. Benchmark results	345
9.9.2. Remarks	346
9.10. Methods for Energy-Dependent Cross Sections	346

9.10.1. Depth-dose relations	347
9.10.2. Nuclear absorption	349
9.10.3. Nuclear-fragmentation parameters	352
9.11. Laboratory Validation	354
9.12. References	359
Chapter 10—Target Fragment and Nuclear Recoil Transports	363
10.1. Introduction	363
10.2. Target Fragment Transport	364
10.3. Neutron KERMA	366
10.4. Effects in Conventional Risk Assessment	368
10.4.1. Theoretical considerations	368
10.4.2. Results and discussion	369
10.5. Bone-Tissue Interface Effects	372
10.5.1. Fragment transport	373
10.5.2. Results and discussion	375
10.5.3. Conclusions	382
10.6. Effects on Harderian Tumorigenesis	383
10.6.1. Radiation response of Harderian gland	383
10.6.2. Ion reactions in tissue	387
10.6.3. Results	388
10.7. Effects on Cellular Track Models	390
10.7.1. Katz model and target fragments	392
10.7.2. Results and discussion	393
10.8. Effects on Fluence-Related Risk Coefficients	393
10.9. Effects on Hit-Size Effectiveness Spectrum	396
10.9.1. Microdosimetric quantities	396
10.9.2. Response to an internal volumetric source	398
10.9.3. Response to a surface source	401
10.9.4. Response to an external volumetric source	401
10.9.5. Remarks	403
10.10. References	404
Chapter 11—Space-Radiation Exposure Issues	409
11.1. Introduction	409
11.2. Galactic Cosmic-Ray Exposure	410
11.2.1. Results	411
11.2.2. Discussion	420
11.3. GCR Component Breakdown	421
11.4. Quality Factors	425
11.4.1. Katz model	426
11.4.2. Remarks	431

11.5. Other Biological Effect Modifications	432
11.6. Nuclear Models, Materials, and LET Spectra	436
11.7. Human Geometry Factors	438
11.7.1. Equivalent sphere model	438
11.7.2. Results	439
11.8. August 1972 Solar Particle Event Risk Assessment	441
11.9. Hypothetical, Worst-Case SPE Scenario Results	445
11.10. Exposure of Female Breast	448
11.10.1. Simplified breast geometry	448
11.10.2. Results	450
11.11. References	452
Chapter 12—Application to Space Exploration	459
12.1. Introduction	459
12.2. Space-Radiation Environment	461
12.2.1. Galactic cosmic rays	464
12.2.2. Solar activity	464
12.2.3. Solar cosmic rays	465
12.2.4. Geomagnetic effects on orbital environment	474
12.2.5. Dose estimation	480
12.2.6. Method for Shuttle geometry	481
12.2.7. Results	482
12.2.8. Geomagnetically trapped radiations	485
12.3. Analysis for Deep Space Missions	486
12.3.1. Transport codes	486
12.3.2. Propagation data	488
12.4. Description of Shield Assessment Results	494
12.4.1. Transportation vehicles	494
12.4.2. Lunar surface habitation	500
12.4.3. Martian surface habitation	503
12.5. Issues and Concerns	508
12.5.1. Environment	508
12.5.2. Transport codes	509
12.5.3. Radiobiology	509
12.5.4. Dosimetric measurement	510
12.5.5. Flare prediction	510
12.5.6. Alternate shielding concepts	510
12.6. Concluding Remarks	511
12.7. References	511
Chapter 13—Radiation Safety in the Earth's Atmosphere	519
13.1. Introduction	519

13.2. Solar Effects on Atmospheric Radiations	520
13.3. Background Radiation Data Base	521
13.3.1. Radiation levels at high latitude	521
13.3.2. Radiation levels within the geomagnetic field	530
13.3.3. Comparison with other methods	535
13.4. Global Dose Rate Estimates	537
13.4.1. ICRP 26 quality factors	538
13.4.2. Revised quality factors	539
13.5. Analysis for Selected Flight Paths	552
13.6. References	556
Chapter 14—Radiation Effects in Electronic Materials	561
14.1. Introduction	561
14.2. Gallium Arsenide Solar Cells	561
14.2.1. Proton defect formation	562
14.2.2. Electron defect formation	566
14.2.3. Minority-carrier recombination	568
14.2.4. Evaluation of defect spatial distribution	570
14.2.5. Comparison with experiment	570
14.2.6. Equivalent electron-fluence concept	571
14.2.7. Angular isotropy effects	573
14.2.8. Effects of space-radiation environment	574
14.3. Microscopic Defect Structures and Equivalent Electron- Fluence Concepts	575
14.3.1. Theory	577
14.3.2. Conclusions	580
14.4. GaAs Model Refinements	580
14.5. Microelectronic Applications	585
14.5.1. Microelectronic upsets	586
14.5.2. Nuclear-fragmentation cross sections	589
14.5.3. Nuclear recoil transport	590
14.5.4. Fragmentation energy-loss spectra	592
14.5.5. Results	595
14.6. References	599
Chapter 15—Concluding Remarks	605
15.1. Current Status	605
15.2. Future Goals	605
Acknowledgments	606

11

12

13

14



Preface

This report presents a brief history leading to the involvement of the Langley Research Center of the National Aeronautics and Space Administration (NASA) in space-radiation physics and protection. Indeed, a relatively complete summary of technical capability as of the summer of 1990 is given. The Boltzmann equations for coupled ionic and neutronic fields are presented and inversion techniques for the Boltzmann operator are discussed. Errors generated by the straight ahead approximation are derived and are shown to be negligible for most problems of space-radiation protection. A decoupling of projectile propagation from the target fields greatly simplifies the Boltzmann equations and allows an analytic solution of the target fragment transport. Analytic and numerical methods of solving the projectile transport equations are discussed. The study shows that explicit numerical techniques can develop unstable roots that require some care in applying discrete numerical methods. A second class of numerical methods is derived by first inverting the Boltzmann operator to form a Volterra equation from which an unconditionally stable numerical marching procedure is derived. Error propagation in the marching procedure is studied. Local relative errors must be on the order of h^2 for adequate control of propagated errors, where h is the step size.

The nuclear physics underlying the coefficients in the Boltzmann equation is discussed. A coupled-channel optical model is found as a consequence of the loose binding of nuclear matter and closure of the nuclear states in high-energy reactions. An abrasion optical model is derived that agrees well with experiment if the two-body interaction matrix is properly symmetrized. The optical model is found to be a good approximation to the elastic channel in the coherent approximation. Noncoherent effects are explicitly evaluated in a bordered matrix approximation. A complete elastic channel data base is presented. Inelastic and nonelastic processes are treated in the bordered matrix approximation with encouraging comparisons with experiment. The theory of electromagnetic dissociation is reviewed, and a model for single-nucleon and two-nucleon knockouts is presented and compared with experimental data. A semiempirical nuclear-fragmentation model is presented for the generation of a nuclear reaction data base and compared with experimental data. A relatively complete nuclear reaction data base is presented.

Transport solutions with the developed data base are used with laboratory experiments to validate both the transport code and the data base. Numerical benchmarks and comparison with Monte Carlo calculations are also used for code validation.

The analytic methods and data base are used to study coupling of the local radiation fields to electronic devices, dosimeters, and biological systems. Energy deposition fluctuations in thin silicon detectors caused by target fragmentation in the silicon device are shown and compared with experiment. Energy fluctuation in microscopic volumes is studied and the relation to tissue equivalent microdosimeters is described. The bone-tissue interface is examined for possible damage enhancement effects in the transition region near the interface. Target fragmentation corrections to damage coefficients of biological experimental data are discussed. Comparisons are made with results obtained by others using different nuclear data bases.

Approximate solutions to the Boltzmann equation in arbitrary convex geometry are found in preparation for application to space radiations. A buildup factor formalism is derived for space use, and example calculations for the human geometry in a space vehicle or on the surface of the Moon and Mars are given. The heavy ion transport code is used to study the shielding requirements for lunar or martian missions. Future needs of the NASA radiation physics program are discussed.

Chapter 1

Introduction

1.1. Pre-NASA History

The panel meeting (Armstrong, 1949) on "Aero Medical Problems of Space Travel," sponsored by the School of Aviation Medicine, Wright Field, Ohio, was held in 1949, the year following the first published account of the existence of heavy ions in the galactic cosmic rays (GCR) observed at high altitude in the Earth's atmosphere (Freier et al., 1948). It was C. F. Gell, a member of the panel, who suggested that space radiation may be life threatening despite stratospheric radiation studies indicating the contrary. He gave two reasons for this possibility: (1) The cosmic radiation that is unable to penetrate to the stratosphere may be important and (2) the geomagnetic field deflects many of the particles away from the Earth; therefore, they are not observed in current stratospheric flight experiments. He proposed the need to further investigate space-radiation protection and the subject plunged into immediate controversy. In the following year, H. J. Schaefer (1950), of the Naval School of Aviation Medicine, provided a review of atmospheric radiations. He reported that cosmic rays are greatly diminished at the Earth's surface (0.1 mR/day (1 R corresponds to the exposure unit of formation of 1 esu/cm³ of dry air at standard conditions)), increase to a maximum of 15 mR/day at 70 000 ft, and decrease beyond the transition maximum formed by the well-known transition effect (fig. 1.1). The transition effect results from interactions of the most penetrating radiations producing secondary particles in sufficient numbers to increase the dose. A belief that the ionization rates would decline to the free space values, where only the primary particles were present, had been generally accepted. However, as Schaefer notes, the discovery of "heavy nuclei rays" with their low penetrating power leads one to expect the decline beyond 70 000 ft to reach a minimum followed by a rise in ionization at higher altitudes. He credits C. F. Gell for first suggesting this possibility. Schaefer further suggests that the unusually high specific ionization of these energetic heavy nuclei indicates they may pose a significant health hazard and stresses the importance of further study.

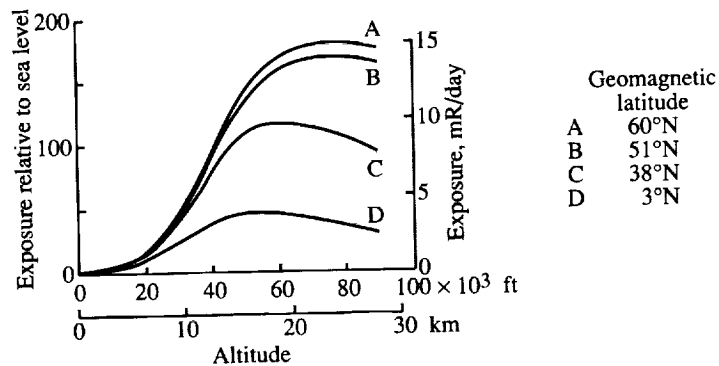
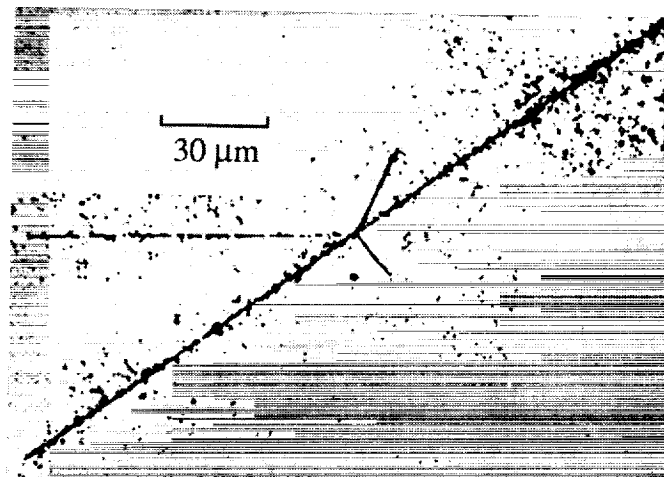
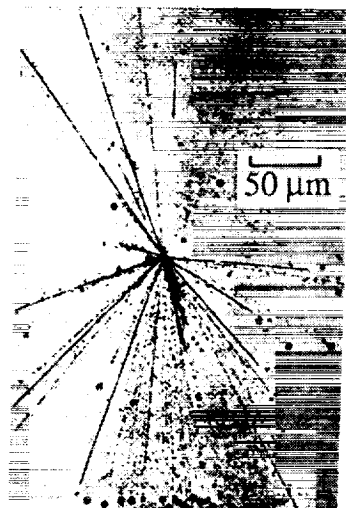


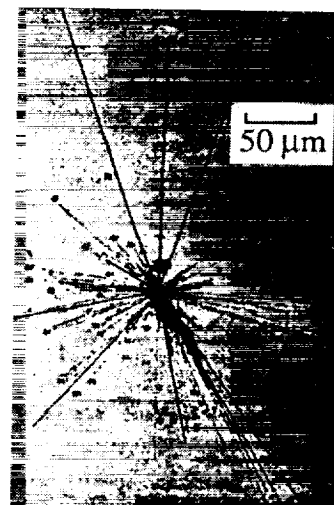
Figure 1.1. Altitude dependence of ionization in tissue from cosmic radiation (from Schaefer, 1950).



(a) $Z \approx 20$ projectile, low-energy transfer event.



(b) Neutral primary, 27 relativistic charged prongs.



(c) $Z \approx 17$ projectile, high-energy transfer event.

Figure 1.2. Nuclear-star events observed in nuclear emulsion (from Krebs, 1950).

After the publication of the findings of the panel, Krebs (1950) at the Field Research Laboratory of the Army Medical Service, Fort Knox, Kentucky, described his work on biological experiments with cosmic air showers by emphasizing the importance of nuclear-star contributions. Krebs suggests in particular that the "explosive (or 'nuclear') stars," assumed to be created by "heavy nuclei coming from outside of the atmosphere," are a novel physical process (fig. 1.2) with potential for biological effects that "cannot be overemphasized." Clearly, Krebs'

emphasis on the nuclear-star contribution is to be distinguished from Schaefer's concern over the direct ionization of cosmic heavy nuclei. Although nuclear-star effects in tissue remains an important biological issue (see chapter 11), it was the insight of Schaefer on the nature of high energy and charge (HZE) ions 40 years ago that is having a lasting impact on radiation physics and biology.

The Symposium on Space Medicine at the 23rd Annual Meeting of the Aero Medical Association, held in March of 1952, was a watershed for space-radiation biology and protection. Schaefer (1952) argued eloquently that delayed effects are the likely consequence of cosmic heavy nuclei exposure and that we cannot extrapolate from well-established dose response curves for common radiations. The nature of atmospheric ionization exposure was discussed as was the problem of extrapolation to free space (fig. 1.3) with the limiting effects of geomagnetic cutoff, solar modulation, and the uncertainty in the radiobiology. Schaefer then looked at the issue of track structure (fig. 1.4) and described a model of injury near the end of the heavy nuclei tracks (microbeams), which was a small linear lesion somewhat

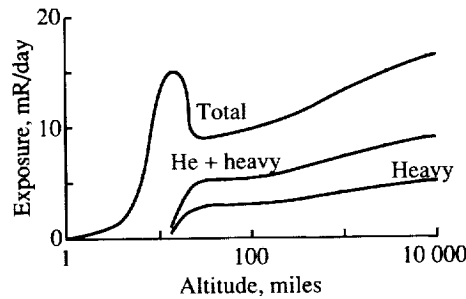


Figure 1.3. Ionization dosage from cosmic radiation for distances from 1 to 10 000 miles from Earth at higher latitudes (from Schaefer, 1952).

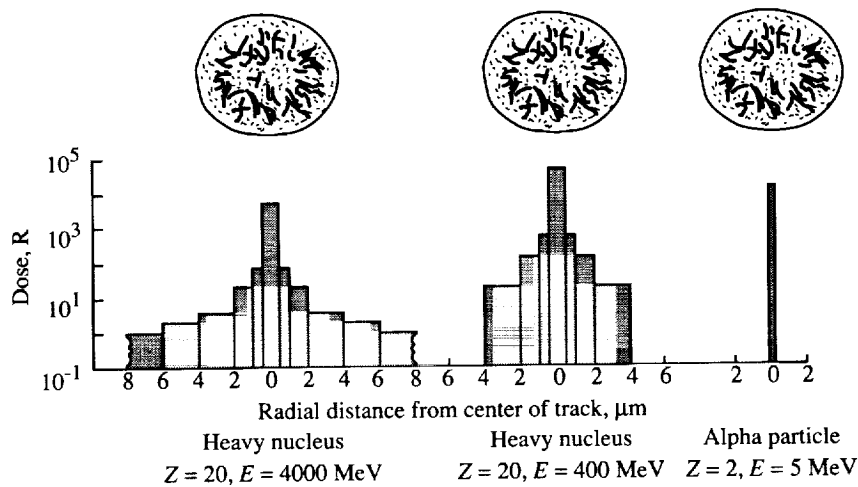


Figure 1.4. Radial spread of ionization about heavy nucleus and alpha tracks to be compared with size of human cell at top (from Schaefer, 1952).

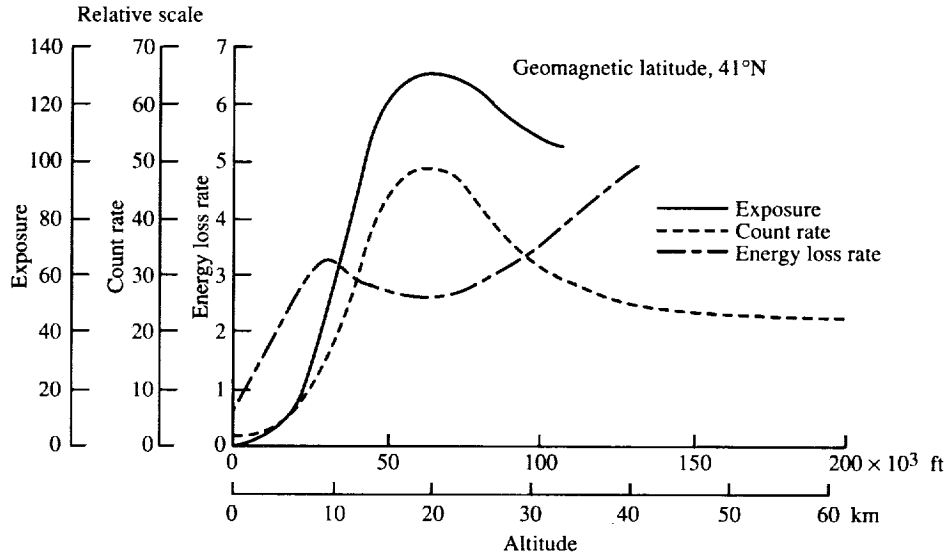


Figure 1.5. Ionization, counting rate, and average rate of energy loss (proportional to specific ionization) (from Tobias, 1952).

similar to Todd's microlesion but without the carcinogenic interpretation Todd (1983) suggests. It was Schaefer (1952) who first suggested that linear energy transfer (LET) may not be a good predictor of biological response because the track width also controls the biochemistry.

Also presented at the Symposium on Space Medicine was a particularly lucid paper by C. A. Tobias (1952), of the Donner Laboratory, on the radiation hazards in high-altitude aviation. Like Schaefer, Tobias argued that a rapid change in GCR composition is expected in the upper atmosphere where particles of high specific ionization are absorbed (fig. 1.5) and are converted partly to particles of lesser charge. He estimated the neutron-biological exposure to be 10 mrem/day (1 rem (= 0.01 Sv) is an older unit of dose equivalent) at 45 000 ft from the measurements of Yuan (1951), with the assumption of a Relative Biological Effectiveness (RBE) of 10, and stressed the need to look for low-energy, cosmic nuclei near the North Pole where geomagnetic effects are minimal. Because primary iron nuclei will undergo nuclear fragmentation in a few grams per centimeter², he suggested that less ionizing secondaries produced by fragmentation of heavy ions may pose a reduced hazard. One can observe the rapid decline of the high-energy pulse events in gas-filled proportional counters (fig. 1.6) used by McClure and Pomerantz (1950). Tobias argued that the RBE for cosmic-ray nuclei may be as high as 100 but that the values are unknown because no such ground-based facilities are able to accelerate iron nuclei to high energy (Tobias and Segrè, 1946) and biological flight experiments are impractical because of the low flux and limited exposure time. He estimated the exposure to be 26 rem per year at the top of the atmosphere or about 50 rem per year in free space. He then surveyed the biological data available and proposed a radiobiological program that would be the mold for the

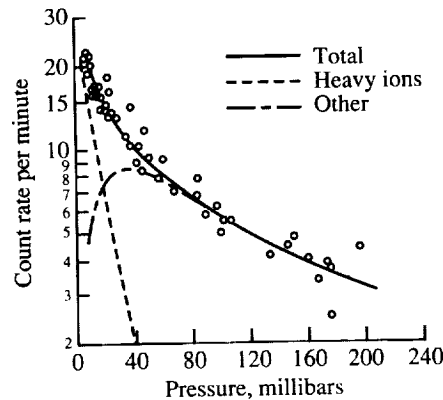


Figure 1.6. Bursts produced by protons, neutrons, α -particles, and heavy ions (from McClure and Pomerantz, 1950).

next 40 years of heavy ion, space-radiation biology. He predicted the possible direct observations of light flashes from heavy ion exposure in dark-adapted eyes, which were observed by Apollo astronauts nearly 20 years later.

New emphasis was given to space radiation after the occurrence of an enormous solar flare on February 23, 1956, which was summarized by Schaefer (1957) and further detailed in 1958 (Schaefer, 1958). After the successful launch of an unmanned satellite by the USSR, NASA was formed out of the older civil aeronautical agency (National Advisory Committee for Aeronautics (NACA)) and elements of the military space effort in 1958. In this same year, Van Allen discovered the trapped radiation belts. In July 1959, Schaefer (1959) began to explore the possibilities of space travel despite the presence of the Van Allen belts.

1.2. History of Langley Program

In June 1960, a conference on radiation problems in manned space flight, organized by the Office of Life Science Programs, NASA (Jacobs, 1960), was convened to address the problem of potential acute and chronic radiation damage. A background paper on space radiation was presented by J. A. Winckler of the University of Minnesota in which the 1956 solar flare and subsequent events through 1959 were discussed. We now know that an even bigger solar flare event occurred on November 12–13, 1960, 5 months after the June 1960 conference. Nearly all factors important to solar flare events were identified at the NASA conference: important locations on the Sun for active regions to affect the Earth, propagation and storage effects, geomagnetic effects including magnetic disturbances, the significance of type-IV radio noise as a signature of particle events, importance of riometer and ground-level neutron monitors, and an estimate of the required shielding thickness. Winckler suggested that GCR exposures were probably unimportant for short-duration missions. Winckler's review noted that the inner Van Allen zone was reasonably stable with dose rates of 30 R/hr compared with the dynamic outer zone with peak rates near 10 R/hr. (Shielding of the ion chambers was not specified.) An attempt was made to establish a rationale to define

acceptable risk. J. E. Pickering, of the Air Force School of Aviation Medicine, Wright Field, Ohio, suggested radiation risk should be in line with other mission risks; this then became a dominant theme in NASA's exposure-limits assessments. The main conclusions to be drawn were that the Mercury program, which flew at 100 n.mi. at low inclination, was not expected to have a radiation problem, but a vigorous radiation program would be required for future NASA missions. This is the historical context of the beginning of space-radiation protection at NASA Langley Research Center which continues at present and is the main focus of the rest of this report.

The Langley effort began in 1958 with Trutz Foelsche (1959) evaluating specific ionization caused by cosmic-ray primaries in water or tissue. Aware of the high altitudes projected by the U.S. Supersonic Transport (SST) Program, the potential impact on commercial operations was brought to the forefront (Foelsche, 1961). A major concern in Foelsche's estimates was uncertainty in neutron and target-recoil contributions (Foelsche, 1962a and 1962b) which would be a dominant issue at Langley for the next decade. His estimates of space-radiation doses were a prime contribution to the Conference on Environmental Problems of Space Flight Structures, convened under the Advisory Committee on Missile and Space Vehicle Structures (Vosteen, 1962).

The first Symposium on the Protection Against Radiation Hazards in Space, held in Gatlinburg, Tennessee (first Gatlinburg Conference, Anon., 1962), was a coming together of the diverse elements working on various aspects of the space-radiation problem. At the conference, plans for the Space Radiation Effects Laboratory (SREL) at Langley were unveiled with its central 600-MeV synchrocyclotron and various other low-energy machines. (The site is the current location of the Continuous Electron Beam Acceleration Facility (CEBAF).) The main experimental thrust of the radiation-protection group was secondary particle production from collisions of energetic protons and α -particles (Orr, 1972; Beck and Powell, 1976). Also presented at the conference by Kinney, Coveyou, and Zerby (1962) were the beginnings of the High-Energy Transport Code (HETC). The most surprising feature of the conference in retrospect was the lack of papers on energetic heavy ions, except for the biological experiments of H. J. Curtis, who used deuteron microbeams to simulate the high-energy, heavy ion microlesions suggested by Schaefer (1952) as a potential biological hazard a decade before.

The second Gatlinburg conference, held in Gatlinburg, Tennessee, 2 years later (Reetz, 1965), showed considerable maturation. Foelsche identified major uncertainties in neutron-exposure rates that justified an atmospheric-measurements program starting in 1965, which ran out of funds just 7 months before the now-famous solar event of August 1972 (Korff et al., 1979). Unlike the earlier conference, there were three papers in reference to high-energy heavy ions. One was written by P. Todd (1965) presenting a host of cell survival data for heavy ion beams measured at the Donner Laboratory of the Lawrence Radiation Laboratory at Berkeley (LRLB) and the other was written by S. B. Curtis (Curtis, Dye, and Sheldon, 1965), who later joined the staff at the Donner Laboratory. Several fundamental papers appeared using HETC, including one by R. G. Alsmiller, Jr., et al. (1965), showing the validity of the straight ahead approximation for high-energy nucleon transport as applied to space radiations. This paper had an important impact on transport theory development at Langley. Probably the

most surprising paper in retrospect was the four-part paper written by J. Billingham, D. E. Robbins, J. L. Modisette, and P. W. Higgins (1965). This paper described the dose limits for design purposes in the Apollo mission as 200 rem (blood-forming organ, ocular lens), 700 rem (skin), and 980 rem (hands and feet), which were adequate to return the astronauts to Earth for proper medical attention (Reetz, 1965). A clear balance was established between radiation risk and other mission risks for this exploratory high-risk mission.

In December 1964, the FAA requested that NASA resolve the issue of radiation exposure for the commercial supersonic transport as had been so elegantly discussed by Foelsche at the second Gatlinburg conference. A detailed measurements program began the following year by combining efforts at Langley with the work of the Korff group at New York University (NYU). The flight experiment package included tissue-equivalent ion chambers, a fast neutron spectrometer (1–10 MeV), and nuclear emulsion. Over the next several years, there were hundreds of high-altitude balloon and airplane flights, a world latitude survey on a Boeing 707 airplane, and high-altitude studies, especially for solar flare events, in U2 and RB-57F flights. (See fig. 1.7.) The main limitation of the Langley experimental effort was the lack of neutron spectrum measurements outside the fast region. The year after the Langley measurements program began, the International Commission for Radiological Protection (ICRP) Task Group (1966) for SST exposure published their conclusion that the biological exposure from atmospheric neutrons was nearly negligible.

The Langley effort was to extend the measured neutron spectrum to both lower and especially to higher energies by using the Monte Carlo work at the Oak Ridge National Laboratory (ORNL), namely, the HETC. The importance of

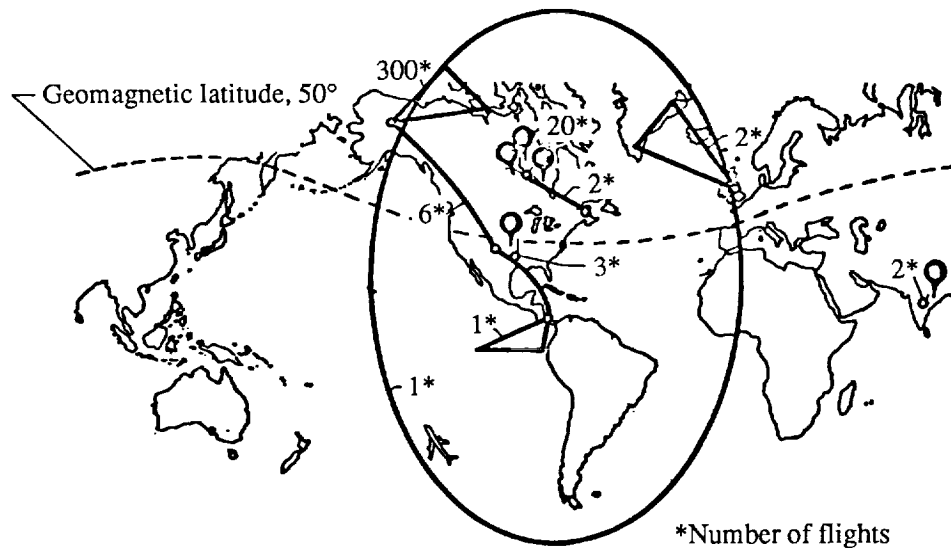


Figure 1.7. High-altitude radiation measurements from 1965 to 1971.

the development of the Bertini (1967) nuclear reaction code and the associated shielding code (HETC) cannot be overemphasized. An outstanding feature of the code is the inclusion of the intranuclear cascade code (Bertini, 1967) as part of the internuclear cascade calculation (HETC) reducing the reliance on external nuclear data bases. At the same time, this feature made the complete code computationally inefficient in the midst of demands and requests for results for various disciplines. The Langley atmospheric program found itself standing in line with accelerator, biomedical, dosimetry, and space programs waiting to be serviced by the HETC code. The decision was made at Langley to develop an in-house capability.

Code development was undertaken by physicists within the computational division at Langley with great vigor; for after all, when the supply of nuclear data is exhausted, a real opportunity to develop nuclear theory exists. The code (PROPER-C) chosen for Langley development was written by Leimdorfer and Crawford (1968) for applications at energies below pion-production threshold. This code was extended to high energies (PROPER-3C) by incorporating the recently published Bertini (1967) data (Wilson, 1972b) and making a high-energy extrapolation (Lambiotte, Wilson, and Filippas, 1971). There were critical meetings concerning the SST in early 1969, and results from the Langley code were the only available results to fill the gap (Foelsche et al., 1969; Foelsche and Wilson, 1969; Wilson, Lambiotte, and Foelsche, 1969). The Langley code was extremely fast because the intranuclear nucleon cascade was represented by a numerical data set and yet required over \$80,000 of computer time (1968 dollars) to make the extension of the fast neutron spectrum to high energies. The results predicted the transition curve (fig. 1.8) measured for fast neutrons (Foelsche et al., 1969; Foelsche and Wilson, 1969), the importance of high-energy neutrons (Foelsche and Wilson, 1969; Wilson, 1969) in contributing to biological dose (fig. 1.9), and an interesting structure in the atmospheric neutron spectrum (Wilson, Lambiotte, and Foelsche, 1969). These results were confirmed by later calculations at NYU (Korff et al., 1979) and ORNL (Foelsche et al., 1974). A summary of the atmospheric radiation program is given by Foelsche et al. (1974) and Korff et al. (1979). From these studies, the background radiation levels were still uncertain, since the transition curves of the other heavier primary ions were not known, and these heavier ions may make important contributions to the dose equivalent for some solar flare events. Therefore, preliminary studies for heavy ion reactions were begun (Foelsche et al., 1974; Skoski, Merker, and Shen, 1973) at the Princeton Particle Accelerator (PPA). As further justification for heavy ion experiments, a simple model of visual impairment by heavy ion exposure revealed required shield uncertainties for a 3-year Mars mission of 4.5 to 29 g/cm² of aluminum (fig. 1.10) and further emphasized the value of a vigorous heavy ion physics and radiobiology program (memorandum to the Langley director concerning continuation and modification of the Princeton Particle Accelerator by NASA in 1970). Experiments began at a meager level and were later moved to the Lawrence Berkeley Laboratory (Schimmerling, Kast, and Ortendahl, 1979), where they continue to this day at a very modest funding level (Schimmerling, Curtis, and Vosburgh, 1977; Schimmerling et al., 1987 and 1989).

Two accomplishments resulted from the PROPER-3C code (Lambiotte, Wilson, and Filippas, 1971): The available nuclear data were exhausted, laying the

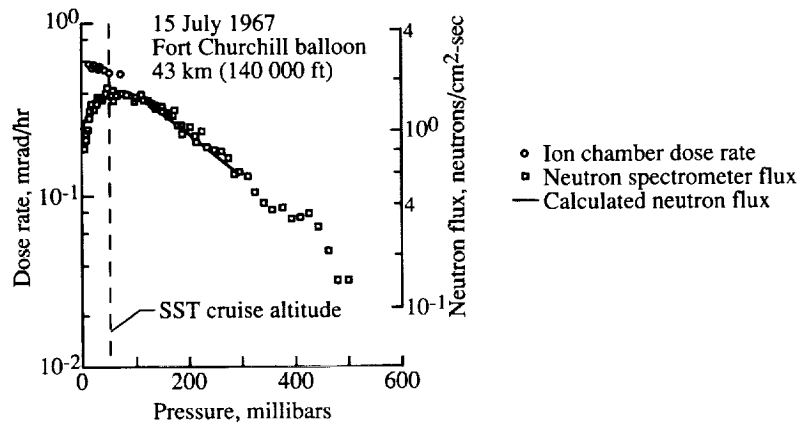


Figure 1.8. Galactic cosmic rays 2 years after galactic cosmic-ray maximum (July 1967, Fort Churchill, geomagnetic latitude $\approx 69^\circ$). The neutron flux and ion chamber dose rate have both decreased about 25 to 30 percent at SST altitudes (solar modulation). (From Foelsche et al., 1974.)

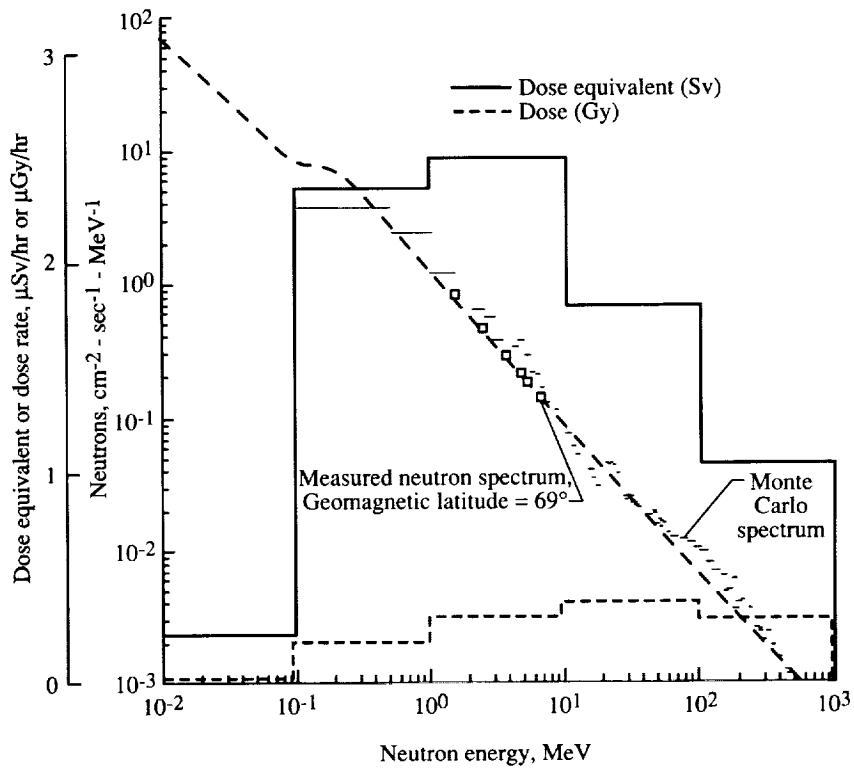


Figure 1.9. The high-latitude (geomagnetic latitude $\approx 69^\circ$) neutron spectrum measured at SST altitudes ($\approx 50 \text{ g/cm}^2$) on August 3, 1965, by Korff et al. (1979), with its extension to lower and higher energies compared with the shape of the Monte Carlo spectrum. (From Foelsche et al., 1974.)

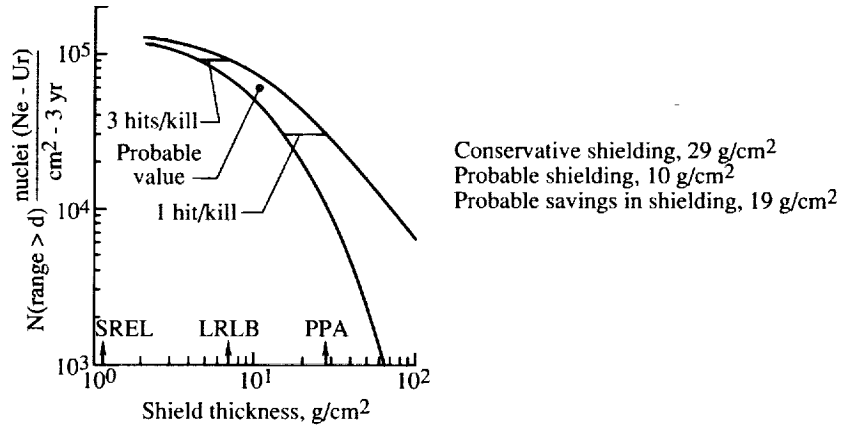


Figure 1.10. Shield analysis of Wilson.

groundwork for a theoretical nuclear program, and an appreciation of the tedious details of the Monte Carlo method, not to mention the intense computer requirements. Consequently, the first fruits of a nuclear theory program produced new skills in multiple scattering theory (Wilson, 1972a, 1973, and 1974b), a fundamental theory of heavy ion reactions (Wilson, 1974a), and the first Langley-developed data base for heavy ion cross sections (Wilson and Costner, 1975). These theories provided the framework for nuclear model development for the next 15 years and continue to provide the core of the Langley nuclear program. The greater appreciation of the limitations of the Monte Carlo methods in radiation shielding led to the development of a series of deterministic codes beginning with nucleon transport (Wilson and Lamkin, 1975; Lamkin, 1974; Wilson and Khandelwal, 1976b) and moving onward toward the development of heavy ion transport theory (Wilson, 1977a, 1977b, and 1978). The deterministic approach at Langley was seen as the necessary means of obtaining codes useful for an engineering design environment. A more detailed overview of the Langley program was given by Wilson (1978) at the workshop on the satellite power system, held at Lawrence Berkeley Laboratory (Schimmerling and Curtis, 1978).

The third Gatlinburg conference was held in Las Vegas in March 1971 (Warman, 1972). Reported at this conference were the light flashes in the Apollo missions that Tobias (1952) had predicted 20 years earlier. A great deal of the symposium was concerned with space nuclear power. Two important papers by Wilkinson and Curtis (1972) and Curtis and Wilkinson (1972) showed that there were major uncertainties in shield requirements caused by current uncertainty in heavy ion fragmentation parameters. The importance of galactic cosmic-ray exposure was a concern for long-duration missions in view of unknown but potentially large biological effects. The emphasis in the conference was still the proton shielding aspects of the Apollo mission and the successful conclusion of the Man on the Moon Program. Although this conference provided important documentation of the previous decade of work, it also marked the rapid decline in radiation research funding within NASA. In spite of the total lack of funding from 1973 to 1980, Langley maintained its files on radiation interaction and managed to perform radiation related tasks on a time-available basis. Fundamental work on dosimetry (Khandelwal, Costner, and Wilson, 1974; Khandelwal and Wilson, 1974; Wilson,

1975b), new methods in radiation transport (Wilson and Khandelwal, 1976a and 1976b; Wilson, 1975a; Wilson and Denn, 1977b and 1977c), and analysis of space-radiation-protection issues (Wilson and Denn, 1976 and 1977a; Wilson, 1981) were completed.

It was natural in these intermediate years to work in closely related disciplines. The first such area was nuclear-induced plasmas and nuclear pumped lasers (Wilson and De Young, 1978a and 1978b; Harries and Wilson, 1979; De Young and Wilson, 1979; Wilson, De Young, and Harries, 1979; Wilson and Shapiro, 1980; Wilson, 1980). The nuclear flash-lamp-pumped laser work (Wilson, 1980) was a natural lead into direct solar-pumped laser systems (Wilson and Lee, 1980; Harries and Wilson, 1981; Wilson, Raju, and Shiu, 1983; Wilson et al., 1984). With new skills in nuclear-induced plasma chemistry, nuclear interactions in materials became a natural work area more closely akin to space radiations. A small amount of funds was available allowing work on structural materials (Wilson and Kamaratos, 1981; Wilson and Xu, 1982; Wilson et al., 1982; Kamaratos et al., 1982; Xu, Khandelwal, and Wilson, 1984a and 1984b; Rustgi et al., 1988) and electronic materials (Wilson, Stith, and Stock, 1983; Wilson and Stock, 1984). The space-radiation-protection research was restored under a proposal to the Life Sciences Division entitled "Space Radiation Protection Methods," submitted July 31, 1979, by John Wilson. The proposal contained a local theoretical effort at Langley and experiments at the Lawrence Berkeley Laboratory as an augmentation of experiments funded by the National Cancer Institute conducted by Walter Schimmerling.

The present report gives an account of the methods and underlying data bases currently in use at the Langley Research Center. It is the goal of the Langley program to go beyond progress in fundamental methods to provide analysis tools that can be easily used by the nonexpert in engineering and experimental design applications. Such tools are not only to be convenient to use but are also to have been validated by laboratory experiments so that their domain of applicability is clearly delineated. Although such a goal was barely conceivable 20 years ago when we embarked on this course, this report demonstrates great progress toward this goal. We look forward to its successful completion in the coming decades.

1.3. Overview of Space-Radiation Interactions

An overview of the space environment and its interaction with materials was given by Wilson (1978). A number of details could be added but very little change in the basic protection requirements would result, and considerable uncertainty in radiation-protection practice remains even today. Here, we present a pedestrian view of space-radiation interaction and refer to the earlier review (Wilson, 1978) for somewhat expanded detail. The present document contains the interaction description in greater detail and our aim in this section is to give an overview to the processes described herein.

The energetic particles in space consist mainly of atomic constituents covering a very broad energy spectrum and flux values as shown in figure 1.11 (Wilson, 1978). The particles themselves are small ($\approx 10^{-13}$ cm) but are electrically charged

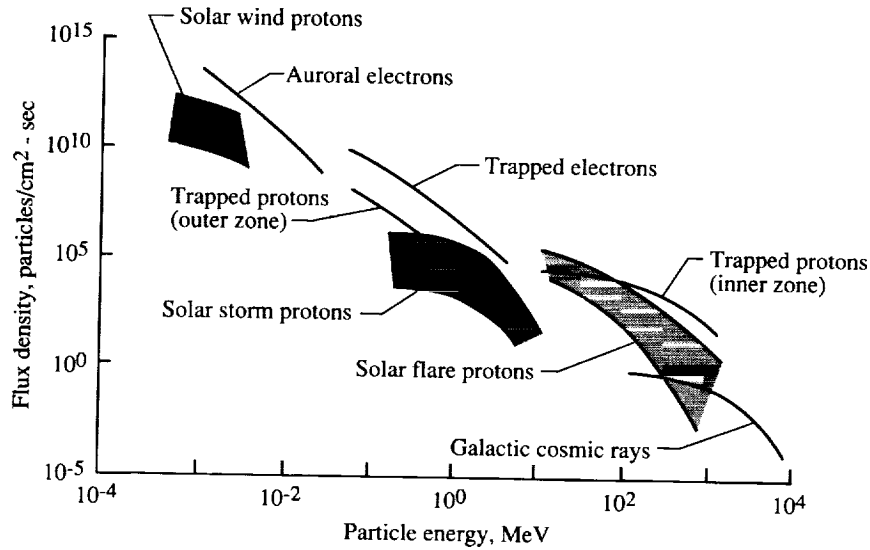


Figure 1.11. Space-radiation environment.

resulting in a long-range force component. A casual look at condensed matter reveals mostly the structure of the electron clouds which contain only 0.05 percent of the mass but occupy virtually all the space within the material. Embedded within these electron clouds are the atomic nuclei whose dimensions are 10^{-5} times smaller than the complete atom but contain 99.95 percent of the mass of the atom. Clearly, an energetic particle passing through such a material will mainly interact with the electrons in the cloud and seldom strike a nucleus.

We now discuss some of the physical parameters related to shielding calculations using elementary concepts. The dominant term in a shielding calculation is energy loss through ionization, that is, a collision between the incoming charged particle (whether it is a proton, electron, or heavy ion) and the orbital electrons of the shielding material (fig. 1.12). They interact through coulomb scattering, and the energy transferred from an ion of energy E and charge Z_P to a target particle of charge Z_T is labeled Q . The cross section σ has an inverse Q^2 dependence, and therefore the energy transfer is usually quite small. In the figure, μ is reduced mass for the projectile target system of masses M_P and M_T .

When the target is an electron bound in an atomic orbital, there are two options of either producing excitation when specific energy transfers ($\epsilon_i - \epsilon_j$, where ϵ_i and ϵ_j denote atomic energy levels) are made or ionization where the energy transferred must be greater than the ionization potential (fig. 1.13). The cross section is related to this energy transfer and goes like the inverse of Q^2 . Another process that is extremely important, especially for incident electrons, is coulomb interaction with the atomic nucleus which results in multiple-scattering effects. These multiple-scattering effects are important for electron shielding or for laboratory ion experiments.

The cross sections for secondary electrons produced from impacts of ions with atoms as described in figures 1.12 and 1.13 are shown in figure 1.14. This

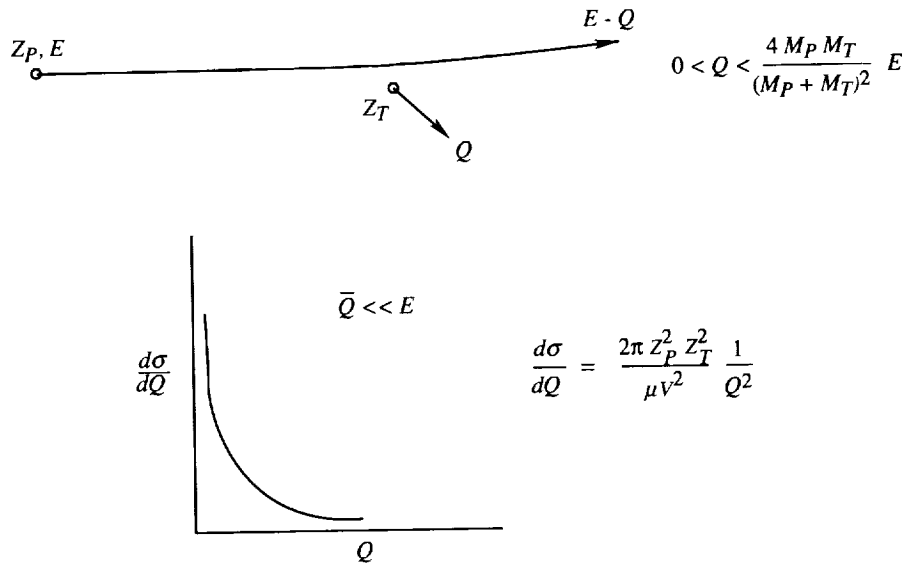


Figure 1.12. Coulomb scattering.

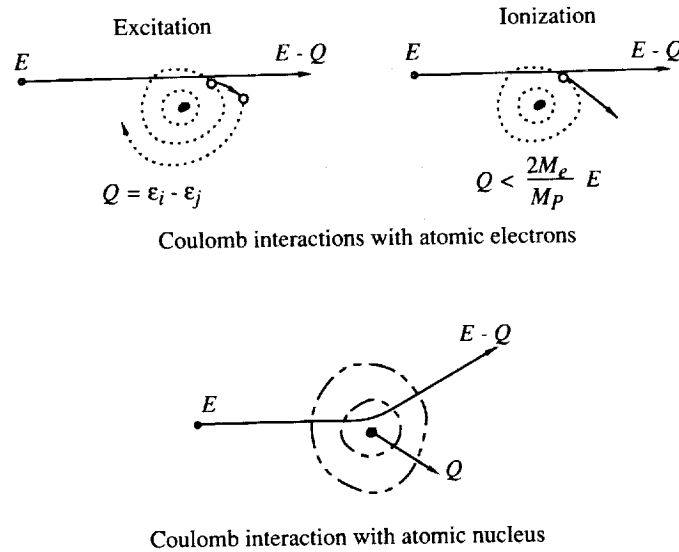


Figure 1.13. Schematic of coulomb interactions with atomic electrons and atomic nucleus.

figure shows curve fits to the experimental data (Manson et al., 1975) at 1 and 5-MeV proton impacts, and the inverse Q^2 dependence above about 20 eV for the secondary electron energy is again evident. The corrections below 20 eV are due to binding effects which can only be treated quantum mechanically. The electron is actually bound in an atom, and these binding effects become important when the energy transfer is on the order of the binding energy. These types of data are important in giving the lateral spread of the energy from the track as the particle passes through a material.

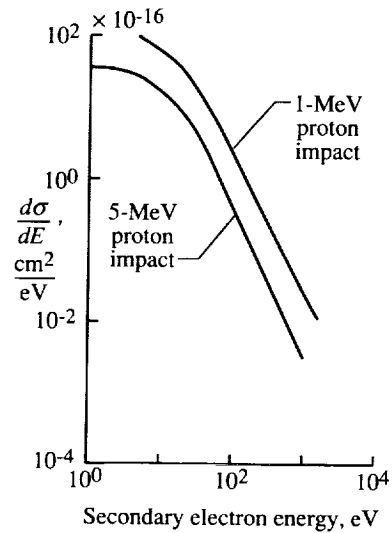


Figure 1.14. Secondary electron production spectra from proton impact with helium.

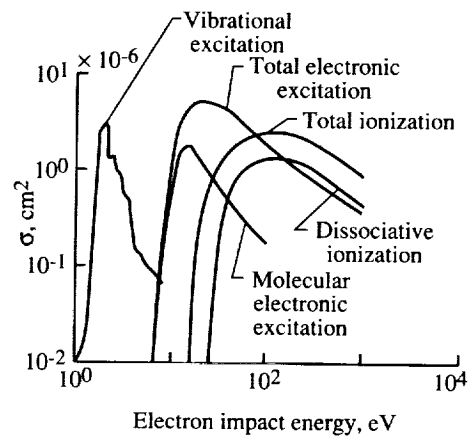


Figure 1.15. Electron impact cross section with N_2 molecules.

There are a number of other degrees of freedom that one contends with when looking at molecular systems. Shown in figure 1.15 is a collection of data for N_2 molecules, which we chose as a typical molecule mainly because we could find the most data for it. Vibrational excitation is important for electron energies below about 10 eV. Once the electronic excitation or ionization threshold is exceeded, everything becomes heavily dominated by those two processes alone. In about one half the cases, ionization results in dissociation; and according to the data we have been able to collect, most molecules undergoing electronic excitation result in dissociation. There are, however, considerable differences in the dissociation cross section for the two processes as seen in figure 1.15. Those differences are probably due to the small number of molecular states observed in the experiments. The dissociative excitation cross section will probably change as future experiments are performed, and total dissociative cross section will probably show the same energy dependence as the ionization cross section at high energy. The data are taken from Schulz (1976), Cartwright et al. (1977), Köllmann (1975), and Wight, Van der Wiel, and Brion (1976). The problem of molecular binding effects is difficult to treat using quantum theory but local plasma models have shown some success in treating both the molecular binding problem (Wilson and Kamaratos, 1981; Kamaratos, 1982; Xu, Khandelwal, and Wilson, 1984a and 1984b) and condensed phase effects (Wilson et al., 1984; Xu, Khandelwal, and Wilson, 1985).

Although most collisions in the material are with orbital electrons, the rare nuclear collisions are of importance because of the large energy transferred in the collision and the generation of new energetic particles. This process of transferring kinetic energy into new secondary radiations occurs through several different processes, such as direct knockout of nuclear constituents, resonant excitation followed by particle emission, pair production, and possible coherent effects within the nucleus. Through these processes, a single-particle incident on the shield

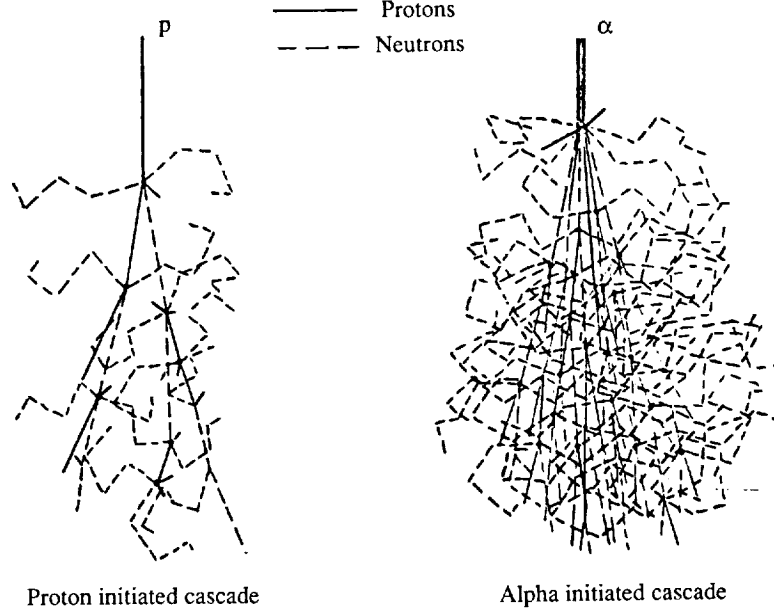


Figure 1.16. Cascade development in matter.

may attenuate through energy transfer to electrons of the media or generate a multitude of secondaries causing an increase in exposure (transition effect). The process that dominates depends on energy, particle type, and material composition. This development of cascading particles is depicted in figure 1.16 as a relative comparison between high-energy proton and α -particle cascades in the Earth's atmosphere. Note the similarities displayed in figure 1.16 for individual reaction events and the nuclear-star events shown in figure 1.2 for nuclear emulsion.

The relevant transport equations are derived on the basis of conservation principles. Consider a region of space filled by matter described by appropriate atomic and nuclear cross sections. In figure 1.17, we show a small portion of the region enclosed by a sphere of radius δ . The number of particles of type j leaving a surface element $\delta^2 d\bar{\Omega}$ is given as $\phi_j(\vec{x} + \delta\bar{\Omega}, \bar{\Omega}, E)\delta^2 d\bar{\Omega}$, where $\phi_j(\vec{x}, \bar{\Omega}, E)$ is the particle flux density, \vec{x} is a vector to the center of the sphere, $\bar{\Omega}$ is normal to the surface element, and E is the particle energy. The projection of the surface element through the sphere center to the opposite side of the sphere defines a flux tube through which pass a number of particles of type j given as $\phi_j(\vec{x} - \delta\bar{\Omega}, \bar{\Omega}, E)\delta^2 d\bar{\Omega}$, which would equal the number leaving the opposite face if the tube defined by the projection were a vacuum. The two numbers of particles, in fact, differ by the gains and the losses created by atomic and nuclear collisions as follows:

$$\begin{aligned}
 & \phi_j(\vec{x} + \delta\bar{\Omega}, \bar{\Omega}, E)\delta^2 d\bar{\Omega} \\
 &= \phi_j(\vec{x} - \delta\bar{\Omega}, \bar{\Omega}, E)\delta^2 d\bar{\Omega} \\
 &+ \delta^2 d\bar{\Omega} \int_{-\delta}^{\delta} dl \sum_k \int \sigma_{jk}(\bar{\Omega}, \bar{\Omega}', E, E') \phi_k(\vec{x} + l\bar{\Omega}, \bar{\Omega}', E') d\bar{\Omega}' dE' \\
 &- \delta^2 d\bar{\Omega} \int_{-\delta}^{\delta} dl \sigma_j(E) \phi_j(\vec{x} + l\bar{\Omega}, \bar{\Omega}, E)
 \end{aligned} \tag{1.1}$$

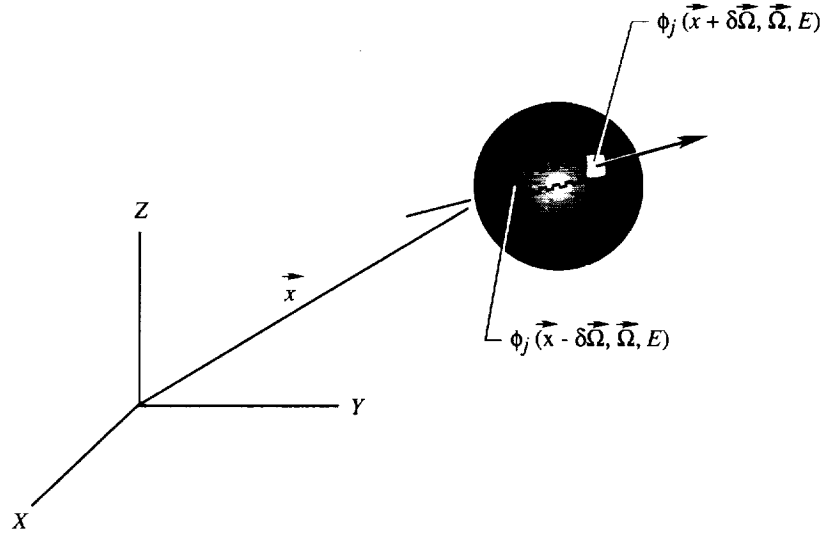


Figure 1.17. Transport of particles through spherical region.

where $\sigma_j(E)$ and $\sigma_{jk}(\vec{\Omega}, \vec{\Omega}', E, E')$ are the media macroscopic cross sections. The cross section $\sigma_{jk}(\vec{\Omega}, \vec{\Omega}', E, E')$ represents all those processes by which type k particles moving in direction $\vec{\Omega}'$ with energy E' produce a type j particle in direction $\vec{\Omega}$ with energy E . Note, there may be several reactions which may accomplish this result and the appropriate cross sections of equation (1.1) are the inclusive ones. Note that the second term on the right-hand side of equation (1.1) is the source of secondary particles integrated over the total volume $2\delta^3 d\vec{\Omega}$ and the third term is the loss through nuclear reaction integrated over the same volume. We expand the terms of each side and retain terms to order δ^3 explicitly as

$$\begin{aligned} & \delta^2 d\vec{\Omega} \left[\phi_j(\vec{x}, \vec{\Omega}, E) + \delta\vec{\Omega} \cdot \nabla \phi_j(\vec{x}, \vec{\Omega}, E) \right] \\ &= \delta^2 d\vec{\Omega} \left[\phi_j(\vec{x}, \vec{\Omega}, E) - \delta\vec{\Omega} \cdot \nabla \phi_j(\vec{x}, \vec{\Omega}, E) \right. \\ & \quad + 2\delta \sum_k \int \sigma_{jk}(\vec{\Omega}, \vec{\Omega}', E, E') \phi_k(\vec{x}, \vec{\Omega}', E') d\vec{\Omega}' dE' \\ & \quad \left. - 2\delta \sigma_j(E) \phi_j(\vec{x}, \vec{\Omega}, E) \right] + O(\delta^4) \end{aligned} \quad (1.2)$$

which may be divided by the cylindrical volume $2\delta(\delta^2 d\vec{\Omega})$ and written as

$$\begin{aligned} \vec{\Omega} \cdot \nabla \phi_j(\vec{x}, \vec{\Omega}, E) &= \sum_k \int \sigma_{jk}(\vec{\Omega}, \vec{\Omega}', E, E') \phi_k(\vec{x}, \vec{\Omega}', E') d\vec{\Omega}' dE' \\ & \quad - \sigma_j(E) \phi_j(\vec{x}, \vec{\Omega}, E) + O(\delta) \end{aligned} \quad (1.3)$$

for which the last term $O(\delta)$ approaches zero in the limit as $\delta \rightarrow 0$. Equation (1.3) is recognized as a time independent form of the Boltzmann equation for a tenuous

gas. Atomic collisions (i.e., collisions with atomic electrons) preserve the identity of the particle and two terms of the right-hand side of equation (1.3) contribute. The differential cross sections have the approximate form for atomic processes

$$\sigma_{jk}^{at}(\vec{\Omega}, \vec{\Omega}', E, E') = \sum_n \sigma_{jn}^{at}(E) \delta(\vec{\Omega} \cdot \vec{\Omega}' - 1) \delta_{jk} \delta(E + \varepsilon_n - E') \quad (1.4)$$

where n labels the electronic excitation levels and ε_n are the corresponding excitation energies which are small (1–100 eV in most cases) compared with the particle energy E . The atomic terms may then be written as

$$\begin{aligned} & \sum_k \int \sigma_{jk}^{at}(\vec{\Omega}, \vec{\Omega}', E, E') \phi_k(\vec{x}, \vec{\Omega}', E') d\vec{\Omega}' dE' - \sigma_j^{at}(E) \phi_j(\vec{x}, \vec{\Omega}, E) \\ &= \sum_n \sigma_{jn}^{at}(E) \phi_j(\vec{x}, \vec{\Omega}, E + \varepsilon_n) - \sigma_j^{at}(E) \phi_j(\vec{x}, \vec{\Omega}, E) \\ &\approx \sum_n \sigma_{jn}^{at}(E) \left[\phi_j(\vec{x}, \vec{\Omega}, E) + \sum_n \varepsilon_n \frac{\partial}{\partial E} \sigma_{jn}^{at}(E) \phi_j(\vec{x}, \vec{\Omega}, E) \right] \\ &\quad - \sigma_j^{at}(E) \phi_j(\vec{x}, \vec{\Omega}, E) \\ &= \frac{\partial}{\partial E} \left[S_j(E) \phi_j(\vec{x}, \vec{\Omega}, E) \right] \end{aligned} \quad (1.5)$$

since the stopping power is

$$S_j(E) = \sum_n \sigma_{jn}(E) \varepsilon_n \quad (1.6)$$

and the total atomic cross section is

$$\sigma_j^{at}(E) = \sum_n \sigma_{jn}^{at}(E) \quad (1.7)$$

Equations (1.5) to (1.7) allow us to rewrite equation (1.3) in the usual continuous slowing down approximation as

$$\begin{aligned} & \vec{\Omega} \cdot \nabla \phi_j(\vec{x}, \vec{\Omega}, E) - \frac{\partial}{\partial E} \left[S_j(E) \phi_j(\vec{x}, \vec{\Omega}, E) \right] + \sigma_j(E) \phi_j(\vec{x}, \vec{\Omega}, E) \\ &= \int \sum_k \sigma_{jk}(\vec{\Omega}, \vec{\Omega}', E, E') \phi_k(\vec{x}, \vec{\Omega}', E') d\vec{\Omega}' dE' \end{aligned} \quad (1.8)$$

where the cross sections of equation (1.8) now contain only the nuclear contributions.

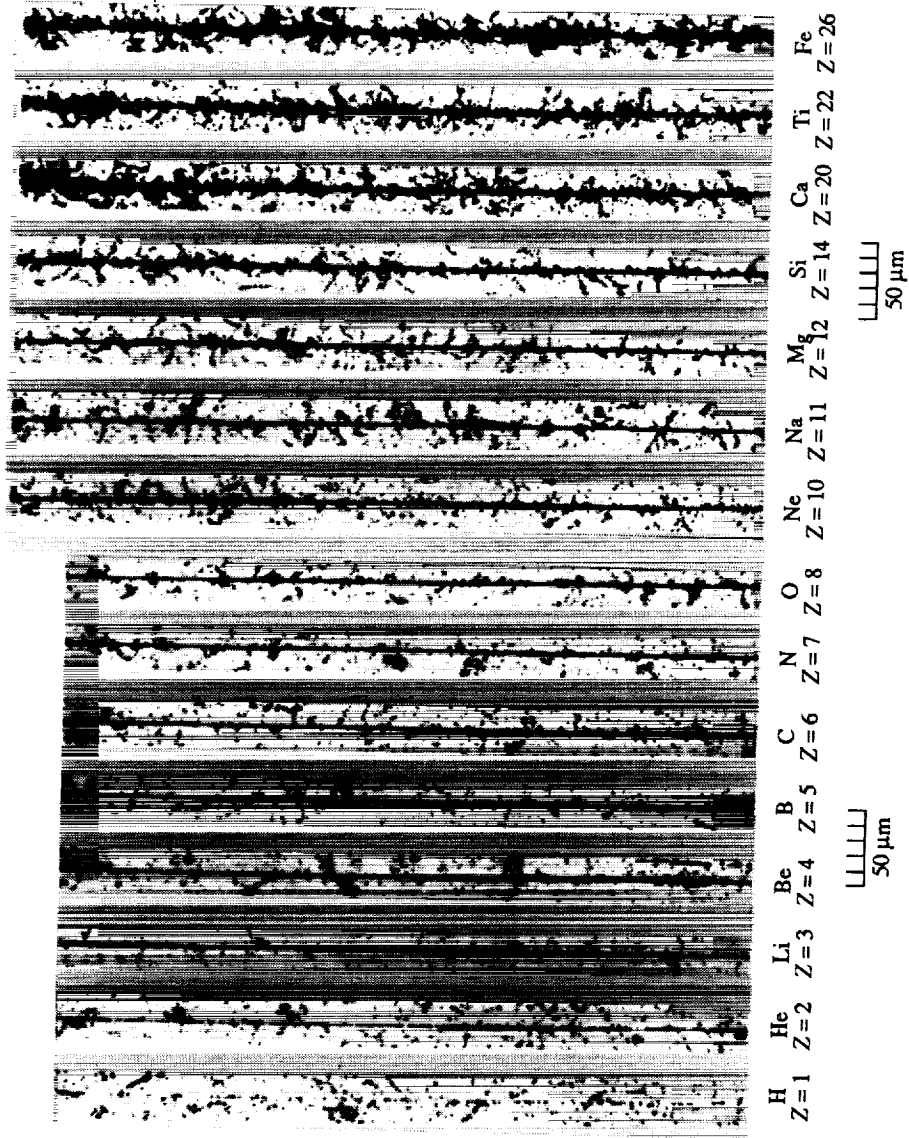


Figure 1.18. Cosmic-ray ion tracks in nuclear emulsion. (Taken from McDonald, 1965.)

ORIGINAL PAGE
BLACK AND WHITE PHOTOGRAPH

The rest of this report concerns finding values for the atomic and nuclear cross sections, evaluating solutions to equation (1.8) for various boundary conditions, and making application to various radiation-protection issues.

The response of materials to ionizing radiation is related to the amount of local energy deposited and the manner in which that energy is deposited. The energy given up to nuclear emulsion (McDonald, 1965) is shown for several ions in figure 1.18. The figure registers developable crystals caused by the passage of the particle directly by ionization or indirectly by the ionization of secondary electrons (δ -rays). These δ -rays appear as hairs emanating from the particle track. Note that the scale of the δ -ray track is on the order of biological cell dimensions ($2\text{--}10\ \mu\text{m}$). Many of the modern large integrated circuits are even of the $0.5\text{-}\mu\text{m}$ scale. For this scale, track structure effects become important as interruptive events as a particle passes through active elements of such circuits.

From the radiation-protection perspective, the issues of shielding are somewhat clearly drawn. Given the complex external environment, the shield properties alter the internal environment within the spacecraft structure as shown in figure 1.19. The internal environment interacts with onboard personnel or equipment. If sufficient knowledge is known about specific devices and biological responses, then the shield properties can be altered to minimize adverse effects. Since the shield is intimately connected to the overall engineering systems and often impacts launch cost, the minimization of radiation risk is not independent of other risk factors and mission costs. Even mission objectives are at times impacted by radiation-protection requirements (e.g., Viking solar cell design to ensure sufficient solar

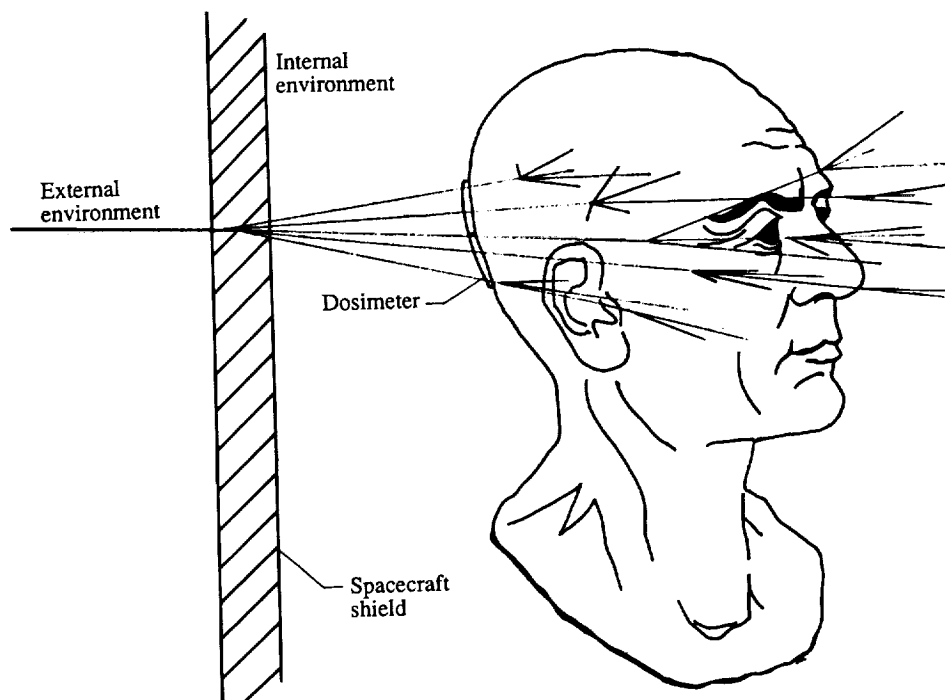


Figure 1.19. Schematic of space-radiation-protection problem.

Transport Methods and Interactions for Space Radiations

power in the event of decreased performance caused by a large solar flare during the mission affected the weight allowed the experiments package). Clearly, the uncertainty in shield specification is an important factor when such critical issues are being addressed. There is uncertainty in subsystem response which can be easily (more or less) obtained for electronic or structural devices. The uncertainty in response of biological systems is complicated by the long delay times (up to 30 years) before system response occurs and the unusually small signal-to-noise ratio in biological response. Clearly, a difficult task remains before risk assignments can be made for long-duration deep space missions.

1.4. References

- Alsmiller, R. G., Jr.; Irving, D. C.; Kinney, W. E.; and Moran, H. S., 1965: The Validity of the Straightahead Approximation in Space Vehicle Shielding Studies. *Second Symposium on Protection Against Radiations in Space*, Arthur Reetz, Jr., ed., NASA SP-71, pp. 177-181.
- Anon., 1962: *Proceedings of the Symposium on the Protection Against Radiation Hazards in Space*, Books 1 and 2. TID-7652, U.S. Atomic Energy Commission.
- Armstrong, Harry; Haber, Heinz; and Strughold, Hubertus, 1949: Aero Medical Problems of Space Travel—Panel Meeting, School of Aviation Medicine. *J. Aviation Med.*, vol. 20, no. 6, pp. 383-417.
- Beck, Sherwin M.; and Powell, Clemans A., 1976: *Proton and Deuteron Double Differential Cross Sections at Angles From 10° to 60° From Be, C, Al, Fe, Cu, Ge, W, and Pb Under 558-MeV-Proton Irradiation*. NASA TN D-8119.
- Bertini, Hugo W., 1967: *Preliminary Data From Intranuclear-Cascade Calculations of 0.75-, 1-, and 2-GeV Protons on Oxygen, Aluminum, and Lead, and 1-GeV Neutrons on the Same Elements*. ORNL-TM-1996, U.S. Atomic Energy Commission.
- Billingham, John; Robbins, Donald E.; Modisette, Jerry L.; and Higgins, Peter W., 1965: Status Report on the Space Radiation Effects on the Apollo Mission. *Second Symposium on Protection Against Radiations in Space*, Arthur Reetz, Jr., ed., NASA SP-71, pp. 139-156.
- Cartwright, D. C.; Trajmar, S.; Chutjian, A.; and Williams, W., 1977: Electron Impact Excitation of the Electronic States of N₂. II. Integral Cross Sections at Incident Energies From 10 to 50 eV. *Phys. Review A*, vol. 16, no. 3, pp. 1041-1051.
- Curtis, S. B.; Dye, D. L.; and Sheldon, W. R., 1965: Fractional Cell Lethality Approach to Space Radiation Hazards. *Second Symposium on Protection Against Radiations in Space*, Arthur Reetz, Jr., ed., NASA SP-71, pp. 219-223.
- Curtis, S. B.; and Wilkinson, M. C., 1972: The Heavy Particle Hazard—What Physical Data Are Needed? *Proceedings of the National Symposium on Natural and Manmade Radiation in Space*, E. A. Warman, ed., NASA TM X-2440, pp. 1007-1015.
- DeYoung, R. J.; and Wilson, J. W., 1979: Population Inversion Mechanisms Producing Nuclear Lasing in He-3-Ar, Xe, Kr, Cl, and UF₆. *Proceedings of the 1st International Symposium on Nuclear Induced Plasmas and Nuclear Pumped Lasers*, Les Editions de Physique Z. I. de Courtaboeuf (Orsay, Essonne, France), pp. 25-32.

- Foelsche, T., 1959: Estimate of the Specific Ionization Caused by Heavy Cosmic Ray Primaries in Tissue or Water. *J. Astronaut. Sci.*, vol. VI, no. 4, pp. 57-62.
- Foelsche, T., 1961: Radiation Exposure in Supersonic Transports. *Symposium on Supersonic Air Transport*, Conf. 14/WP-SYMP/49, International Air Transportation Assoc.
- Foelsche, Trutz, 1962a: Protection Against Solar Flare Protons. *Advances in the Astronautical Sciences*, Volume 8, Plenum Press, Inc., pp. 357-374.
- Foelsche, Trutz, 1962b: *Radiation Exposure in Supersonic Transports*. NASA TN D-1383.
- Foelsche, Trutz; and Wilson, John W., 1969: Results of NASA SST-Radiation Studies Including Experimental Results on Solar Flare Events. Minutes of the Standing Committee on Radiobiology Aspects of the SST, Federal Aviation Adm.
- Foelsche, T.; Mendell, Rosalind; Adams, Richard R.; and Wilson, John W., 1969: Measured and Calculated Radiation Levels Produced by Galactic and Solar Cosmic Rays in SST Altitudes and Precaution Measures To Minimize Implications at Commercial SST-Operations. NASA paper presented at French-Anglo United States Supersonic Transport Meeting (Paris, France).
- Foelsche, Trutz; Mendell, Rosalind B.; Wilson, John W.; and Adams, Richard R., 1974: *Measured and Calculated Neutron Spectra and Dose Equivalent Rates at High Altitudes; Relevance to SST Operations and Space Research*. NASA TN D-7715.
- Freier, Phyllis; Lofgren, E. J.; Ney, E. P.; and Oppenheimer, F., 1948: The Heavy Component of Primary Cosmic Rays. *Phys. Review*, vol. 74, second ser., no. 12, pp. 1818-1827.
- Harries, W. L.; and Wilson, J. W., 1979: Simplified Model of a Volumetric Direct Nuclear Pumped He-3-Ar Laser. *Proceedings of the 1st International Symposium on Nuclear Induced Plasmas and Nuclear Pumped Lasers*, Les Editions de Physique Z. I. de Courtaboeuf (Orsay, Essonne, France), pp. 33-42.
- Harries, W. L.; and Wilson, J. W., 1981: Solar-Pumped Electronic-to-Vibrational Energy Transfer Lasers. *Space Sol. Power Review*, vol. 2, no. 4, pp. 367-381.
- ICRP Task Group, 1966: Radiobiological Aspects of the Supersonic Transport. *Health Phys.*, vol. 12, no. 2, pp. 209-226.
- Jacobs, George J., ed. (appendix A by J. R. Winckler), 1960: *Proceedings of Conference on Radiation Problems in Manned Space Flight*. NASA TN D-588.
- Kamaratos, E.; Chang, C. K.; Wilson, J. W.; and Xu, Y. J., 1982: Valence Bond Effects on Mean Excitation Energies for Stopping Power in Metals. *Phys. Lett.*, vol. 92A, no. 7, pp. 363-365.
- Khandelwal, G. S.; Costner, C. M.; and Wilson, J. W., 1974: Geometric Correction for Spherical Ion Chambers. *Trans. American Nuclear Soc.*, vol. 19, p. 481.
- Khandelwal, G. S.; and Wilson, John W., 1974: *Proton Tissue Dose for the Blood Forming Organ in Human Geometry: Isotropic Radiation*. NASA TM X-3089.

Transport Methods and Interactions for Space Radiations

- Kinney, W. E.; Coveyou, R. R.; and Zerby, C. D., 1962: A Series of Monte Carlo Codes To Transport Nucleons Through Matter. *Proceedings of the Symposium on the Protection Against Radiation Hazards in Space*, Book 2, TID-7652, U.S. Atomic Energy Commission, pp. 608-618.
- Köllmann, K., 1975: Dissociative Ionization of H₂, N₂ and CO by Electron Impact—Measurement of Kinetic Energy, Angular Distributions, and Appearance Potentials. *Int. J. Mass Spectrom. & Ion Phys.*, vol. 17, pp. 261-285.
- Korff, Serge A.; Mendell, Rosalind B.; Merker, Milton; Light, Edward S.; Verschell, Howard J.; and Sandie, William S., 1979: *Atmospheric Neutrons*. NASA CR-3126.
- Krebs, A. T., 1950: Possibility of Biological Effects of Cosmic Rays in High Altitudes, Stratosphere and Space. *J. Aviation Med.*, vol. 21, no. 6, pp. 481-494.
- Lambiotte, Jules J., Jr.; Wilson, John W.; and Filippas, Tassos A., 1971: Proper 3C: A Nucleon-Pion Transport Code. NASA TM X-2158.
- Lamkin, Stanley Lee, 1974: A Theory for High-Energy Nucleon Transport in One Dimension. M.S. Thesis, Old Dominion Univ.
- Leimdorfer, Martin; and Crawford, George W., eds., 1968: *Penetration and Interaction of Protons With Matter—Part I. Theoretical Studies Using Monte Carlo Techniques*. NASA CR-108228.
- Manson, Steven T.; Toburen, L. H.; Madison, D. H.; and Stolterfoht, N., 1975: Energy and Angular Distribution of Electrons Ejected From Helium by Fast Protons and Electrons: Theory and Experiment. *Phys. Review A*, vol. 12, third ser., no. 1, pp. 60-79.
- McClure, G. W.; and Pomerantz, M. A., 1950: Ionization Chamber Bursts at Very High Altitudes. *Phys. Review*, vol. 79, second ser., no. 5, pp. 911-912.
- McDonald, F. B., 1965: Review of Galactic and Solar Cosmic Rays. *Second Symposium on Protection Against Radiations in Space*, Arthur Reetz, Jr., ed., NASA SP-71, pp. 19-29.
- Orr, Harry D., III, 1972: Low Energy Protons From C, AL, NI, CU, and AU Under 600 MeV Proton Bombardment. Ph.D. Thesis, Univ. of South Carolina.
- Reetz, Arthur, Jr., ed., 1965: *Second Symposium on Protection Against Radiations in Space*. NASA SP-71.
- Rustgi, M. L.; Pandey, L. N.; Wilson, J. W.; Long, S. A. T.; and Zhu, G., 1988: Distribution of Energy in Polymers Due to Incident Electrons and Protons. *Radiat. Eff.*, vol. 105, pp. 303-311.
- Schaefer, Hermann J., 1950: Evaluation of Present-Day Knowledge of Cosmic Radiation at Extreme Altitude in Terms of the Hazard to Health. *J. Aviation Med.*, vol. 21, no. 5, pp. 375-394, 418.
- Schaefer, Hermann J., 1952: Exposure Hazards From Cosmic Radiation Beyond the Stratosphere and in Free Space. *J. Aviation Med.*, vol. 23, no. 4, pp. 334-344.

- Schaefer, Hermann J., 1957: Cosmic Ray Dosage During the Giant Solar Flare of February 26, 1956. *J. Aviation Med.*, vol. 28, no. 4, pp. 387-396.
- Schaefer, Hermann J., 1958: New Knowledge of the Extra-Atmospheric Radiation Field. *J. Aviation Med.*, vol. 29, no. 7, pp. 492-500.
- Schaefer, Hermann J., 1959: Radiation Dosage in Flight Through the Van Allen Belt. *Aerosp. Med.*, vol. 30, no. 9, pp. 631-639.
- Schimmerling, Walter; Curtis, Stanley B.; and Vosburgh, Kirby G., 1977: Velocity Spectrometry of 3.5-GeV Nitrogen Ions. *Radiat. Res.*, vol. 72, no. 1, pp. 1-17.
- Schimmerling, Walter; and Curtis, Stanley B., eds., 1978: *Workshop on the Radiation Environment of the Satellite Power System*. LBL-8581 (Contract W-7405-ENG-48), Lawrence Berkeley Lab., Univ. of California.
- Schimmerling, Walter; Kast, John W.; and Ortendahl, Douglas, 1979: Measurement of the Inclusive Neutron Production by Relativistic Neon Ions on Uranium. *Phys. Review Lett.*, vol. 43, no. 27, pp. 1985-1987.
- Schimmerling, Walter; Alpen, Edward L.; Powers-Risius, Patricia; Wong, Mervyn; DeGuzman, Randy J.; and Rapkin, Marwin, 1987: The Relative Biological Effectiveness of 670 MeV/A Neon as a Function of Depth in Water for a Tissue Model. *Radiat. Res.*, vol. 112, pp. 436-448.
- Schimmerling, Walter; Miller, Jack; Wong, Mervyn; Rapkin, Marwin; Howard, Jerry; Spieler, Helmut G.; and Jarret, Blair V., 1989: The Fragmentation of 670A MeV Neon-20 as a Function of Depth in Water. *Radiat. Res.*, vol. 120, pp. 36-71.
- Schulz, George J., 1976: A Review of Vibrational Excitation of Molecules by Electron Impact at Low Energies. *Principles of Laser Plasmas*, George Bekefi, ed., John Wiley & Sons, Inc., pp. 33-88.
- Skoski, L.; Merker, M.; and Shen, B. S. P., 1973: Absolute Cross Section for Producing ^{11}C From Carbon by 270-MeV/Nucleon ^{14}N Ions. *Phys. Review Lett.*, vol. 30, no. 2, pp. 51-54.
- Tobias, Cornelius; and Segrè, Emilio, 1946: High Energy Carbon Nuclei. *Phys. Review*, vol. 70, second ser., nos. 1 and 2, p. 89.
- Tobias, Cornelius A., 1952: Radiation Hazards in High Altitude Aviation. *J. Aviation Med.*, vol. 23, no. 4, pp. 345-372.
- Todd, Paul, 1965: Biological Effects of Heavy Ions. *Second Symposium on Protection Against Radiations in Space*, Arthur Reetz, Jr., ed., NASA SP-71, pp. 105-114.
- Todd, Paul, 1983: Unique Biological Aspects of Radiation Hazards—An Overview. *Adv. Space Res.*, vol. 3, no. 8, pp. 187-194.
- Vosteen, Louis F., 1962: *Environmental Problems of Space Flight Structures—I. Ionizing Radiation in Space and Its Influence on Spacecraft Design*. NASA TN D-1474.
- Warman, E. A., ed., 1972: *Proceedings of the National Symposium on Natural and Manmade Radiation in Space*. NASA TM X-2440.

Transport Methods and Interactions for Space Radiations

- Wight, G. R.; Van der Wiel, M. J.; and Brion, C. E., 1976: Dipole Excitation, Ionization and Fragmentation of N₂ and CO in the 10-60 eV Region. *J. Phys. B: At. Mol. Phys.*, vol. 9, no. 4, pp. 675-689.
- Wilkinson, M. C.; and Curtis, S. B., 1972: Galactic Cosmic Ray Heavy Primary Secondary Doses. *Proceedings of the National Symposium on Natural and Manmade Radiation in Space*, E. A. Warman, ed., NASA TM X-2440, pp. 104-107.
- Wilson, John W., 1969: Description of Transport Calculations. Minutes of the Standing Committee on Radiobiology Aspects of the SST, Federal Aviation Adm.
- Wilson, John W.; Lambiotte, Jules J.; and Foelsche, T., 1969: Structure in the Fast Spectra of Atmospheric Neutrons. *J. Geophys. Res.*, vol. 74, no. 26, pp. 6494-6496.
- Wilson, John W., 1972a: *Comparison of Exact and Approximate Evaluations of the Single-Scattering Integral in Nucleon-Deuteron Elastic Scattering*. NASA TN D-6884.
- Wilson, John W., 1972b: *Isosinglet Approximation for Nonelastic Reactions*. NASA TN D-6942.
- Wilson, John W., 1973: Intermediate Energy Nucleon-Deuteron Elastic Scattering. *Nuclear Phys.*, vol. B66, pp. 221-244.
- Wilson, John W., 1974a: Multiple Scattering of Heavy Ions, Glauber Theory, and Optical Model. *Phys. Lett.*, vol. B52, no. 2, pp. 149-152.
- Wilson, John W., 1974b: Proton-Deuteron Double Scattering. *Phys. Review C*, vol. 10, no. 1, pp. 369-376.
- Wilson, John W., 1975a: Composite Particle Reaction Theory. Ph.D. Diss., College of William and Mary in Virginia.
- Wilson, John W., 1975b: Weight Optimization Methods in Space Radiation Shield Design. *J. Spacecr. & Rockets*, vol. 12, no. 12, pp. 770-773.
- Wilson, John W.; and Costner, Christopher M., 1975: *Nucleon and Heavy-Ion Total and Absorption Cross Section for Selected Nuclei*. NASA TN D-8107.
- Wilson, John W.; and Lamkin, Stanley L., 1975: Perturbation Theory for Charged-Particle Transport in One Dimension. *Nuclear Sci. & Eng.*, vol. 57, no. 4, pp. 292-299.
- Wilson, John W.; and Denn, Fred M., 1976: *Preliminary Analysis of the Implications of Natural Radiations on Geostationary Operations*. NASA TN D-8290.
- Wilson, John W.; and Khandelwal, G. S., 1976a: *Computer Subroutines for the Estimation of Nuclear Reaction Effects in Proton-Tissue-Dose Calculations*. NASA TM X-3388.
- Wilson, John W.; and Khandelwal, Govind S., 1976b: Proton-Tissue Dose Buildup Factors. *Health Phys.*, vol. 31, no. 2, pp. 115-118.
- Wilson, John W., 1977a: *Analysis of the Theory of High-Energy Ion Transport*. NASA TN D-8381.

- Wilson, J. W., 1977b: Depth-Dose Relations for Heavy Ion Beams. *Virginia J. Sci.*, vol. 28, no. 3, pp. 136-138.
- Wilson, John W.; and Denn, Fred M., 1977a: *Implications of Outer-Zone Radiations on Operations in the Geostationary Region Utilizing the AE4 Environmental Model*. NASA TN D-8416.
- Wilson, John W.; and Denn, Fred M., 1977b: *Improved Analysis of Electron Penetration and Numerical Procedures for Space Radiation Shielding*. NASA TN D-8526.
- Wilson, John W.; and Denn, Fred M., 1977c: Methods of Shield Analysis for Protection Against Electrons in Space. *Nuclear Technol.*, vol. 35, no. 1, pp. 178-183.
- Wilson, John W., 1978: Environmental Geophysics and SPS Shielding. *Workshop on the Radiation Environment of the Satellite Power System*, Walter Schimmerling and Stanley B. Curtis, eds., LBL-8581, UC-41 (Contract W-7405-ENG-48), Univ. of California, pp. 33-116.
- Wilson, J. W.; and DeYoung, R. J., 1978a: Power Density in Direct Nuclear-Pumped ^3He Lasers. *J. Appl. Phys.*, vol. 49, no. 3, pt. I, pp. 980-988.
- Wilson, John W.; and DeYoung, R. J., 1978b: Power Deposition in Volumetric $^{235}\text{UF}_6$ -He Fission-Pumped Nuclear Lasers. *J. Appl. Phys.*, vol. 49, no. 3, pt. I, pp. 989-993.
- Wilson, J. W.; DeYoung, R. J.; and Harries, W. L., 1979: Nuclear-Pumped ^3He -Ar Laser Modeling. *J. Appl. Phys.*, vol. 50, no. 3, pt. I, pp. 1226-1235.
- Wilson, J. W., 1980: Nuclear-Induced Xe-Br* Photolytic Laser Model. *Appl. Phys. Lett.*, vol. 37, no. 8, pp. 695-697.
- Wilson, J. W.; and Lee, J. H., 1980: Modeling of a Solar-Pumped Iodine Laser. *Virginia J. Sci.*, vol. 31, pp. 34-38.
- Wilson, J. W.; and Shapiro, A., 1980: Nuclear-Induced Excimer Fluorescence. *J. Appl. Phys.*, vol. 51, no. 5, pp. 2387-2393.
- Wilson, J. W., 1981: Solar Radiation Monitoring for High Altitude Aircraft. *Health Phys.*, vol. 41, no. 4, pp. 607-617.
- Wilson, J. W.; and Kamaratos, E., 1981: Mean Excitation Energy for Molecules of Hydrogen and Carbon. *Phys. Lett.*, vol. 85A, no. 1, pp. 27-29.
- Wilson, J. W.; Chang, C. K.; Xu, Y. J.; and Kamaratos, E., 1982: Ionic Bond Effects on the Mean Excitation Energy for Stopping Power. *J. Appl. Phys.*, vol. 53, no. 2, pp. 828-830.
- Wilson, J. W.; and Xu, Y. J., 1982: Metallic Bond Effects on Mean Excitation Energies for Stopping Powers. *Phys. Lett.*, vol. 90A, no. 5, pp. 253-255.
- Wilson, John W.; Stith, John J.; and Stock, L., 1983: *A Simple Model of Space Radiation Damage in GaAs Solar Cells*. NASA TP-2242.
- Wilson, John W.; Raju, S.; and Shiu, Y. J., 1983: *Solar-Simulator-Pumped Atomic Iodine Laser Kinetics*. NASA TP-2182.

Transport Methods and Interactions for Space Radiations

- Wilson, John W.; and Stock, L. V., 1984: Equivalent Electron Fluence for Space Qualification of Shallow Junction Heteroface GaAs Solar Cells. *IEEE Trans. Electron Devices*, vol. ED-31, no. 5, pp. 622-625.
- Wilson, John W.; Lee, Yeunggil; Weaver, Willard R.; Humes, Donald H.; and Lee, Ja H., 1984: *Threshold Kinetics of a Solar-Simulator-Pumped Iodine Laser*. NASA TP-2241.
- Xu, Y. J.; Khandelwal, G. S.; and Wilson, J. W., 1984a: Intermediate Energy Proton Stopping Power for Hydrogen Molecules and Monoatomic Helium Gas. *Phys. Lett.*, vol. 100A, no. 3, pp. 137-140.
- Xu, Y. J.; Khandelwal, G. S.; and Wilson, J. W., 1984b: Low-Energy Proton Stopping Power of N₂, O₂, and Water Vapor, and Deviations From Bragg's Rule. *Phys. Review A*, vol. 29, third ser., no. 6, pp. 3419-3422.
- Xu, Y. J.; Khandelwal, G. S.; and Wilson, J. W., 1985: Proton Stopping Cross Sections of Liquid Water. *Phys. Review A*, vol. 32, third ser., no. 1, pp. 629-636.
- Yuan, Luke C. L., 1951: Distribution of Slow Neutrons in Free Atmosphere up to 100,000 Feet. *Phys. Review*, vol. 81, second ser., no. 2, pp. 175-184.

Chapter 2

Coulomb Interactions in Atoms and Molecules

2.1. Introduction

In deriving the Boltzmann equation in chapter 1, we included atomic/molecular and nuclear collision processes. The total cross section $\sigma_j(E)$ with the medium for each particle type of energy E may be expanded as

$$\sigma_j(E) = \sigma_j^{at}(E) + \sigma_j^{el}(E) + \sigma_j^r(E) \quad (2.1)$$

where the first term refers to collision with atomic electrons, the second term is for elastic nuclear scattering, and the third term describes nuclear reactions. The microscopic cross sections are ordered as follows:

$$\sigma_j^{at}(E) \sim 10^{-16} \text{ cm}^2 \quad (2.2)$$

$$\sigma_j^{el}(E) \sim 10^{-19} \text{ cm}^2 \quad (2.3)$$

$$\sigma_j^r(E) \sim 10^{-24} \text{ cm}^2 \quad (2.4)$$

to allow flexibility in expanding solutions to the Boltzmann equation as a sequence of perturbative approximations, for example, the continuous slowing down approximation is one such approach. It is clear that many atomic collisions ($\sim 10^6$) occur in a cm of ordinary matter, whereas $\sim 10^3$ nuclear elastic collisions occur per cm. In distinction, nuclear reactions are separated by many cm. We shall further elaborate this point of view and indicate important atomic and molecular quantities required for transport theory development. In particular, we will examine a more general formulation than that presented in equation (1.5).

The Boltzmann equation, ignoring terms associated with equations (2.3) and (2.4), can be written with the aid of equation (1.4) as

$$\vec{\Omega} \cdot \nabla \phi_j(\vec{x}, \vec{\Omega}, E) = \sum_n \sigma_n^{at}(E + \epsilon_n) \phi_j(\vec{x}, \vec{\Omega}, E + \epsilon_n) - \sigma_j^{at}(E) \phi_j(\vec{x}, \vec{\Omega}, E) \quad (2.5)$$

where ϵ_n is the atomic/molecular excitation energy. Equation (2.5) is equivalent to one-dimensional transport along the ray directed by $\vec{\Omega}$. For simplicity of notation we use a one-dimensional equation as

$$\frac{\partial}{\partial z} \phi_j(z, E) = \sum_n \sigma_n^{at}(E + \epsilon_n) \phi_j(z, E + \epsilon_n) - \sigma_j^{at}(E) \phi_j(z, E) \quad (2.6)$$

where we drop the superscript *at* and subscript *j* in the rest of this section. The boundary condition is taken as

$$\phi(0, E) = \delta(E - E_0) \quad (2.7)$$

The solution can be written with perturbation theory as

$$\phi^{(0)}(z, E) = \exp(-\sigma z) \delta(E - E_0) \quad (2.8)$$

$$\phi^{(1)}(z, E) = \sigma z \exp(-\sigma z) \sum_n g_n \delta(E + \epsilon_n - E_0) \quad (2.9)$$

$$\phi^{(2)}(z, E) = \frac{(\sigma z)^2}{2!} \exp(-\sigma z) \sum_n g_m g_n \delta(E + \epsilon_n + \epsilon_m - E_0) \quad (2.10)$$

and similarly for higher order terms, where $\delta(\cdot)$ is the Dirac delta function, and $E_0 \gg \epsilon_n$ has been assumed so that σ and $g_n = \sigma_n/\sigma$ are evaluated at E_0 . The average energy after penetration to a distance z is given by

$$\langle E \rangle = E_0 - \bar{\epsilon} \sigma z \quad (2.11)$$

where the average excitation energy is

$$\bar{\epsilon} = \sum_n g_n \epsilon_n \quad (2.12)$$

and the sum over n contains both discrete and continuous terms. The standard deviation about the average energy is similarly found to be

$$s^2 \equiv \langle (E - \langle E \rangle)^2 \rangle = \bar{\epsilon}^2 \sigma z \quad (2.13)$$

where

$$\bar{\epsilon}^2 = \sum_n g_n \epsilon_n^2 \quad (2.14)$$

Similar results can be derived for the higher moments of the energy distribution, which depend on atomic quantities through the g_n terms. Considering the nonlinear dependence of the transported spectrum on the atomic cross sections σ_n , it is somewhat surprising that the transported spectral parameters depend linearly on g_n . Equations (2.11) and (2.13) apply when $\bar{\epsilon} \sigma z \ll E_0$ so that the energy variations in the cross sections can be ignored. The expressions are easily generalized to deep penetrations as

$$\bar{E}(z) = E_0 - \int_0^z S[\bar{E}(y)] dy \quad (2.15)$$

and

$$\bar{E}^2(z) = \bar{E}^2(0) + \int_0^z \frac{S_1[\bar{E}(y)]}{S[\bar{E}(y)]} dy \quad (2.16)$$

where the stopping power is given by

$$S(E) = \sum_n \sigma_n(E) \epsilon_n \quad (2.17)$$

and the straggling is related to

$$S_1(E) = \sum_n \sigma_n(E) \epsilon_n^2 \quad (2.18)$$

The degrading particle energy $\bar{E}(y)$ is found through the usual range-energy relations

$$R(E) = \int_0^E \frac{dE'}{S(E')} \quad (2.19)$$

It is clear that $R(E)$ is the average stopping path length for the ions. The corresponding spectrum is taken as

$$\phi(z, E) = \frac{1}{\sqrt{2\pi}s} \exp \left[\frac{-(E - \bar{E})^2}{2s^2} \right] \quad (2.20)$$

where the standard deviation s is given by equation (2.13). The usual continuous slowing down approximation is found in the limit as $s \rightarrow 0$. The evaluation requires knowledge of the appropriate atomic cross sections σ_n .

The atomic collisions occur quite frequently in ordinary matter (10^6 – 10^7 per cm). Less frequent are the elastic nuclear collisions, the largest contribution of which is coulomb scattering. The elastic cross section for scattering from the nucleus is represented as $\sigma_s(\theta)$ with expansion in terms of Legendre polynomials $P_n(x)$ as

$$\sigma_s(\theta) = \sum a_n P_n(\cos \theta) \quad (2.21)$$

where the coefficients are given as

$$a_n = \frac{2n+1}{2} \int_{-1}^1 \sigma_s(\theta) P_n(\cos \theta) d \cos \theta \quad (2.22)$$

and the corresponding equation for transport through a slab

$$\begin{aligned} \cos \theta \frac{\partial}{\partial z} \phi(z, \theta) + \sigma \phi(z, \theta) &= \int \sigma_s(\gamma) \phi(z, \theta') d \cos \theta' d \varphi' \\ &= 2\pi \sum a_n P_n(\cos \theta) \int P_n(\cos \theta') \phi(z, \theta') d \cos \theta' \end{aligned} \quad (2.23)$$

where

$$\cos \gamma = \cos \theta \cos \theta' + \sin \theta \sin \theta' \cos(\varphi - \varphi') \quad (2.24)$$

and we have used the addition theorem

$$P_n(\cos \gamma) = P_n(\cos \theta) P_n(\cos \theta') + 2 \sum_l P_n^l(\cos \theta) P_n^l(\cos \theta') \cos l(\varphi - \varphi') \quad (2.25)$$

The differential operator can be inverted in equation (2.23) to obtain

$$\begin{aligned} \phi(z, \theta) &= \exp \left(\frac{-\sigma z}{\cos \theta} \right) \phi(0, \theta) \\ &+ \sum_n 2\pi \int_0^z \exp \left[\frac{-\sigma(z-\tau)}{\cos \theta} \right] a_n P_n(\cos \theta) \int P_n(\cos \theta') \phi(\tau, \theta') d \cos \theta' d \tau \end{aligned} \quad (2.26)$$

Transport Methods and Interactions for Space Radiations

The scattering is strongly peaked in the forward direction and the integral kernel varies slowly for forward propagation along off-axis rays (Breitenberger, 1959). The attenuation kernel $\exp[-\sigma(z - \tau)/\cos \theta]$ is shown in figure 2.1. We simplify the propagation equation as

$$\begin{aligned} \phi(z, \theta) = & \exp(-\sigma z) \phi(0, \theta) \\ & + 2\pi \sum_n \int_0^z \exp[-\sigma(z - \tau)] a_n P_n(\cos \theta) P_n(\cos \theta') \phi(\tau, \theta') d \cos \theta' d\tau \end{aligned} \quad (2.27)$$

The approximate multiple-scattering equation may be solved by expanding the flux as

$$\phi(z, \theta) = \sum A_n(z) P_n(\cos \theta) \quad (2.28)$$

where

$$A_n(z) = \frac{2n + 1}{2} \int \phi(z, \theta) P_n(\cos \theta) d \cos \theta \quad (2.29)$$

The coefficients then satisfy

$$A_n(z) = \exp(-\sigma z) A_n(0) + \frac{4\pi}{2n + 1} a_n \int_0^z \exp[-\sigma(z - \tau)] A_n(\tau) d\tau \quad (2.30)$$

Let the boundary condition be

$$\phi(0, \theta) = \frac{1}{2\pi} \delta(\cos \theta - 1) \quad (2.31)$$

where $\delta(\)$ is the Dirac delta function. Then $A_n(0) = (2n + 1)/4\pi$. The iterated solution of equation (2.30) may be written as

$$A_n(z) = \frac{2n + 1}{4\pi} \exp \left[- \left(\sigma - \frac{4\pi}{2n + 1} a_n \right) z \right] \quad (2.32)$$

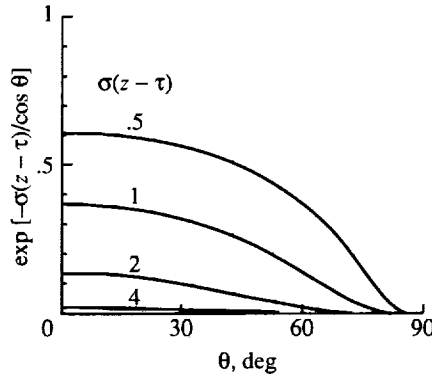


Figure 2.1. Transport kernel as a function of angle of propagation.

In the absence of absorptive processes, the forward isotropic term ($n = 0$) shows no spatial dependence. In distinction, the higher order ($n > 0$) terms display

spatial attenuation at greater depths of penetration. The angular distribution is now characterized in terms of the mean cosine of the zenith angle as

$$\begin{aligned}\langle \cos \theta \rangle &= \int \cos \theta \phi(z, \theta) d\Omega \\ &= \frac{2}{3} A_1(z) \\ &= \exp \left[- \left(\sigma - \frac{4}{3} \pi a_1 \right) z \right]\end{aligned}\quad (2.33)$$

and is related to the average angular deflection as

$$\begin{aligned}\langle \theta^2 \rangle &\approx 2[1 - \langle \cos \theta \rangle] \\ &= 2 \left\{ 1 - \exp \left[- \left(\sigma - \frac{4}{3} \pi a_1 \right) z \right] \right\}\end{aligned}\quad (2.34)$$

Initially the root-mean-square angle is zero as expected for the unidirectional boundary condition (eq. (2.31)) and increases to a value approaching 90° at very large depths. In cases of interest to us, we find that the asymptotic value is never reached since energy loss due to atomic collision or nuclear reaction processes limits the beam propagation before this occurs (e.g., see Janni, 1982a and 1982b).

2.2. Extremely Rarefied Gas Interactions

In passing through matter, an ion loses a large fraction of its energy to atomic/molecular excitation of the material. Although a satisfactory theory of high-energy interaction exists in the form of Bethe's theory (Bethe, 1950) using the Born approximation or more exact calculations using transitions from specific atomic shells (Merzbacher and Lewis, 1958; Khandelwal, 1968), an equally satisfactory theory for low-energy collisions is not available. In the rest of this chapter, we give a brief overview of the theory of stopping power and the formalism used in our transport calculations. Future directions of research to allow more accurate evaluation of these transport parameters are discussed.

In an extremely rarefied gas, we may assume that the passing ion interacts singly with the media molecules. This is an extreme simplification but is an idealization which still leaves many challenges to theoretical treatment. Even so, our aim is to treat the noble gases in fair detail, but even the interaction for the extremely rarefied noble gases cannot as yet be fully calculated with great confidence.

The gas atom can, for practical purposes, be taken as in the ground state before interacting with the passing particle. At the lowest energies, the gas molecule or atom interacts through adiabatic processes for which the Born-Oppenheimer approximation is appropriate. The electronic portion of the total Hamiltonian appears as part of the potential through which the massive nuclei move. The exchange of electrons between the moving particle and target molecule or atom

can change the charge state of the projectile as it passes through the media. The exchange of electrons leads to potential curve crossing which is usually treated in the Landau-Zener model (Landau and Lifshitz, 1958; Zener, 1932) or by a molecular orbital approximation (Suzuki, Nakamura, and Ishiguro, 1984; Xu, Khandelwal, and Wilson, 1989). In the media, the projectile state is not well-defined and changes randomly in charge state and excitation level. The charge state is usually described by some equilibrium distribution with some mean charge that depends on both the kinetic energy of the projectile and the character of the media. These charge changing cross sections are quite large, and equilibrium values are achieved over relatively short distances (less than 1 mg/cm² of material).

2.2.1. Stopping at low energies. At the lowest energies, the projectile is hardly able to penetrate the atomic orbitals of the media, and the media atoms or molecules recoil in tack. The stopping cross section has been calculated by Firsov with the Thomas-Fermi model (Martynenko, 1970) to be

$$S_n(E) = \left(\frac{2\alpha NC}{E} \right) \ln \left(1 + \sqrt{\lambda} \frac{E}{C} \right) \quad (2.35)$$

where

$$\alpha = \frac{\pi^2 Z_P Z_T C^2 0.8853 a_0}{8 (Z_P^{1/2} + Z_T^{1/2})^{2/3}} \left(\frac{M_P}{M_T} \right)^{1/2} \quad (2.36)$$

$$C = \frac{8e^2 Z_P Z_T (Z_P^{1/2} + Z_T^{1/2})^{2/3} (M_P/M_T)^{1/2}}{\pi 0.8853 a_0} \quad (2.37)$$

$$\lambda = \frac{4M_P M_T}{(M_P + M_T)^2} \quad (2.38)$$

where Z_P and Z_T are projectile and target atomic numbers and M_P and M_T are their atomic weights, a_0 is the Bohr radius, e is the electron charge, and N is the number of target atoms per unit volume.

At somewhat higher kinetic energy, the outer electron cloud is penetrated and the nuclear electric repulsion becomes more effective giving rise to Rutherford scattering described by

$$S_n(E) \approx \frac{C'}{E} \ln E \quad (2.39)$$

where C' is a constant and the raising of electrons to higher orbitals is possible.

2.2.2. Bethe stopping theory. At sufficiently high energies, the Born approximation is applicable, which may be used for both molecules and atoms. In practice, the molecular electronic wave functions are not known, and such calculations are limited to interaction with atoms (noble gases in practice). The differential cross section for the nonrelativistic case in lowest order (Born) approximation is given by the formula

$$\frac{d\sigma_n}{dQ} = \frac{2\pi Z_P^2 e^4}{mv^2} Z_T \frac{|F_n(\vec{q})|^2}{Q^2} \quad (2.40)$$

and the mean energy loss (see eq. (2.17))

$$-\frac{dE}{dx} = \frac{2\pi Z_P^2 e^4 N Z_T}{mv^2} \sum_n (E_n - E_o) \int_{\frac{(E_n - E_o)^2}{2mv^2}}^{2mv^2} |F_n(\vec{q})|^2 \frac{dQ}{Q^2} \quad (2.41)$$

In equations (2.40) and (2.41), \vec{q} is the momentum transferred to the electron, and $Q = q^2/2m$, the energy absorbed by a free electron of mass m at rest (Xu, Khandelwal, and Wilson, 1986), Z_T is the target atomic number, and N is the number of target atoms per unit volume. The quantity $(E_n - E_o)$ is the excitation energy, and the form factor $F_n(\vec{q})$ is defined as

$$F_n(\vec{q}) = \sum_{j=1}^{Z_T} \left\langle \Psi_n \left| \exp\left(\frac{i\vec{q} \cdot \vec{r}_j}{\hbar}\right) \right| \Psi_o \right\rangle \quad (2.42)$$

in which \vec{r}_j denotes the position of the j th atomic electron relative to the nucleus, and Ψ_n and Ψ_o are the final- and the initial-state wave functions of the target.

The Bethe method (Fano, 1963; Bethe, 1933; Livingston and Bethe, 1937; Bethe and Ashkin, 1953) depends on rewriting equation (2.41) by dividing the integration over Q into two parts: low Q and high Q in which the intermediate value is Q_o . Thus consider the following term of equation (2.41):

$$\begin{aligned} & \sum_n (E_n - E_o) \int_{Q_{\min}}^{Q_{\max}} |F_n(\vec{q})|^2 \frac{dQ}{Q^2} \\ &= \sum_n (E_n - E_o) \int_{\frac{(E_n - E_o)^2}{2mv^2}}^{Q_o} |F_n(\vec{q})|^2 \frac{dQ}{Q^2} \\ &+ \sum_n (E_n - E_o) \int_{Q_o}^{2mv^2} |F_n(\vec{q})|^2 \frac{dQ}{Q^2} \end{aligned} \quad (2.43)$$

Consider the first term in equation (2.43). Expanding $|F_n(q)|^2$ for low q in equation (2.42) and retaining only the first nonvanishing term give:

$$|F_n(\vec{q})|^2 \approx \frac{q^2}{\hbar^2} \left| \left\langle \Psi_n \left| \sum_j x_j \right| \Psi_o \right\rangle \right|^2 \quad (2.44)$$

Notice that the other higher order terms are neglected in this approximation. Thus, the first term in equation (2.43) becomes

$$\sum_n (E_n - E_o) \int_{\frac{(E_n - E_o)^2}{2mv^2}}^{Q_o} |F_n(\vec{q})|^2 \frac{dQ}{Q^2} = \ln \left(\frac{Q_o 2mv^2}{I_T^2} \right) \quad (2.45)$$

where

$$\ln I_T = \sum_n f_n \ln(E_n - E_o) \quad (2.46)$$

and

$$f_n = \frac{2m}{\hbar^2} (E_n - E_o) \left| \sum_j \langle n|x_j|0\rangle \right|^2 \quad (2.47)$$

In equations (2.46) and (2.47), I_T is known as mean excitation energy of the medium and f_n is the optical oscillator strength.

The second term in equation (2.43) can be written as

$$\sum_n (E_n - E_o) \int_{Q_o}^{2mv^2} |F_n(\vec{q})|^2 \frac{dQ}{Q^2} \approx \ln Q \Big|_{Q_o}^{2mv^2} \quad (2.48)$$

where the Bethe sum rule

$$\sum_n (E_n - E_o) |F_n(\vec{q})|^2 = Q \quad (2.49)$$

has been used. Equation (2.41) with equations (2.43), (2.45), and (2.48) becomes

$$-\frac{dE}{dx} = \frac{4\pi Z_P^2 e^4 N Z_T}{mv^2} \ln \frac{2mv^2}{I_T} \quad (2.50)$$

which is the celebrated Bethe stopping power equation.

The derivation of equation (2.50) from equation (2.41) depends on the sum rule (eq. (2.49)), the upper limit $2mv^2$ in equation (2.41), and the intermediate value Q_o . The main thrust of these assumptions is to treat all the electrons as essentially free electrons. This assumption fails for innershell electrons which are tightly bound to the atom. To incorporate the correct treatment of these innershell electrons, one introduces a "shell correction" term C in equation (2.50). Basically, the treatment of the correction involves the exact evaluation of the form factor $|F_n|^2$ of equation (2.42). The equation for energy loss per unit path length then reads as

$$-\frac{dE}{dx} = \frac{4\pi Z_P^2 e^4 N Z_T}{mv^2} \left[\ln \frac{2mv^2}{I_T} - \frac{C}{Z_T} \right] \quad (2.51)$$

The evaluation of mean excitation energy I_T from equations (2.46) and (2.47) has been studied intently for the last several decades. Extensive calculations for many atoms using the Hartree-Slater potential model have been performed recently by many authors (Dehmer, Inokuti, and Saxon, 1975; Inokuti, Baer, and Dehmer, 1978; Inokuti and Turner, 1978; Inokuti et al., 1981). These are later compared with the values obtained with the local plasma model.

Similarly, shell corrections have been studied by various authors (Bethe, 1933; Livingston and Bethe, 1937; Bethe, Brown, and Walske, 1950; Brown, 1950; Walske, 1952 and 1956; Khandelwal, 1968 and 1982; Janni, 1966; Merzbacher and Lewis, 1958; Bichsel, 1966¹) for the last 60 years. Basically, one employs

¹ Research on the L -shell correction in stopping power done by Hans Bichsel at the Nuclear Physics Laboratory, University of Southern California, and supported by the National Cancer Institute and the U.S. Atomic Energy Commission.

the screened hydrogenic approximation (only one parameter for screened nuclear charge Z_i for both the initial- and final-state electron is used) and calculations are made for a particular shell. The total shell correction C , in principle, can be obtained by summing the contributions shell by shell.

As noted in section 2.1, the fluctuation in energy loss is also related to the atomic cross sections as (see eq. (2.18))

$$S_1(E) = \frac{2\pi Z_P^2 e^4 N Z_T}{mv^2} \sum_n (E_n - E_o)^2 \int_{Q_{\min}}^{Q_{\max}} |F_n(q)|^2 \frac{dQ}{Q^2} \quad (2.52)$$

where the limits on Q are those discussed in connection with equation (2.41). By arguments similar to those leading to equation (2.50), one finds

$$S_1(E) \approx \frac{4\pi Z_P^2 e^4 N Z_T}{mv^2} \ln \frac{2mv^2}{\Delta} \quad (2.53)$$

where Δ is given as

$$\ln \Delta = \sum_n f_n(E_n - E_o) \ln(E_n - E_o) \quad (2.54)$$

These quantities are important in calculating the energy spectra of slowing ions within a medium. (See eq. (2.20).)

As is evident from equation (2.51), the determination of the energy loss per unit path length depends upon the accurate knowledge of the mean excitation energy I and the shell corrections C . In practice one invokes some sort of parameter fitting involving the experimental data on stopping power and the quantities I and C . Quite often (Bichsel, 1963; Janni, 1966) the theoretical values are used in conjunction with the experimental values for parameter fitting. It would thus be desirable to obtain stopping power without the need to have access to the parameters I and C .

We have initiated such an attempt which is described as follows. The main thrust of the approach is to calculate exactly the one-electron form factor within a screened hydrogenic model. As is known for an atom with more than one electron, the form factor given by equation (2.41) within the one-electron model can be approximated as

$$F_{n'n}(q) \approx \left\langle \psi_{n'}(\vec{r}) \left| \exp(i\vec{q} \cdot \vec{r}) \right| \psi_n(\vec{r}) \right\rangle \quad (2.55)$$

where ψ_n and $\psi_{n'}$ are wave functions with a single electron (henceforth, we use natural units in which \hbar and c are unity). Historically, equation (2.55) has been justified on the basis of Hartree-Fock approximation. The knowledge of the form factor of equation (2.55) thus depends on knowing the radial integrals for the process of excitation as well as ionization when a projectile passes through matter. We have recently calculated the radial integral for the optically allowed transitions in He atoms and helium-like ions under the screened hydrogenic model. The model

describes the atom by single-particle hydrogenic wave functions and treats the initial state and the final state by two different effective charge parameters Z_i and Z_f , respectively. The generalized radial integral (corresponding to the expansion of eq. (2.55) in a power series in q) is presented in the following section and the dipole term is discussed.

2.2.3. Optical oscillator strengths within screened hydrogenic model. The generalized radial integral $R_\beta(n'l' - kl)$ of concern is the following:

$$R_\beta(n'l' - kl) = \int_0^\infty [R(n', l'; r)] r^{\beta+1} R(k, l; r) r^2 dr \quad (2.56)$$

where $R(n', l'; r)$ and $R(k, l; r)$ are the bound and the free-state radial wave functions, respectively. These wave functions in terms of Z_i and Z_f are

$$\begin{aligned} R(n', l'; r) = & \frac{(-1)^{n'+l'+1} 2^n Z_i^{n+1/2}}{[(n'+1)!]^{1/2} [(n'-l'-1)!]^{1/2} n'^{n'+1}} \\ & \times \left[\sum_{j=0}^{n'-l'-1} \frac{1}{j!} \left[-\frac{n'}{2Z_i} \right]^j \prod_{i=0}^j (n'+l'-i)(n'-l'-1-i) \right. \\ & \left. \times \exp\left(\frac{-Z_i r}{n'}\right) r^{n'-1-j} \right] \end{aligned} \quad (2.57)$$

$$\begin{aligned} R(k, l; r) = & \frac{(-1)^{l+1} (2\sqrt{Z_f})}{\left[1 - \exp\left(-2\frac{\pi Z_f}{k}\right)\right]^{1/2}} \prod_{s=0}^l \left(s^2 + \frac{Z_f^2}{k^2}\right)^{1/2} \left(\frac{1}{2k}\right)^{l+1} \\ & \times \frac{r^{-(l+1)}}{2\pi} \oint \exp(-2ikr\xi) \left(\xi + \frac{1}{2}\right)^{-i\frac{Z_f}{k} - l - 1} \\ & \times \left(\xi - \frac{1}{2}\right)^{i\frac{Z_f}{k} - l - 1} d\xi \end{aligned} \quad (2.58)$$

When equations (2.57) and (2.58) are substituted into equation (2.56), one obtains (Khandelwal et al., 1989)

$$R_\beta(n'l' - kl) = F_1 \frac{\sqrt{k} \exp\{-2(Z_f/k) \tan^{-1}[k(n'/Z_i)]\}}{(1 - \exp(-2\pi Z_f/k))^{1/2} \left[k^2(n')^2 / Z_i^2 + 1\right]^{(\beta+n'+2)}} \left[\prod_{s=1}^l \left(\frac{k^2}{Z_f^2} s^2 + 1\right)^{1/2} \right] G_1 \quad (2.59)$$

where the quantities F_1 and G_1 are defined by

$$F_1 \equiv \frac{Z_f^{l+1/2} 2^{n'+l+1} (n')^{\beta+l+2} (-1)^{l+l'-\beta}}{Z_i^{\beta+l+5/2} i^{\beta+n'-l+1} [(n'+l)!]^{1/2} [(n'-l'-1)!]^{1/2}} \quad (2.60)$$

$$G_1 \equiv \sum_{j=0}^{n'-l'-1} \left\{ (i/2)^j (k/Z_f)^{j-n'-1-\beta+1} \left[1 + \frac{k^2(n')^2}{Z_i^2} \right]^j \frac{(p-1)!}{j!} \right. \\ \times \prod_{i=0}^{j-1} (n'+l'-i)(n'-l'-1-i) \left. \sum_{m=1}^p \left\{ \left(i + \frac{kn'}{Z_i} \right)^{p-m} \left(i - \frac{kn'}{Z_i} \right)^{m-1} \right. \right. \\ \left. \left. \times \prod_{\gamma=1}^{m-1} \left(-i - l \frac{k}{Z_f} - \gamma \frac{k}{Z_f} \right) [(p-m)! (m-1)!]^{-1} \prod_{\kappa=1}^{p-m} \left(i - l \frac{k}{Z_f} - \kappa \frac{k}{Z_f} \right) \right\} \right\} \quad (2.61)$$

with

$$p = \beta + n' - l - j + 2 \quad (2.62)$$

The square of the radial matrix element is given by

$$R_{\beta}^2(n'l' - kl) dk = |F_1|^2 \frac{k \exp[(-4Z_f/k) \tan^{-1}(kn'/Z_i)]}{[1 - \exp(-2\pi Z_f/k)] [(k^2 n'^2 / Z_i^2) + 1]^{2(\beta+n'+2)}} \\ \times \prod_{s=1}^l \left(\frac{k^2}{Z_f^2} s^2 + 1 \right) |G_1|^2 dk \quad (2.63)$$

The radial integral for bound-bound transitions can be obtained by substituting the bound wave functions into equation (2.56). However, it is easy to accomplish the same task if one recognizes the fact that a continuous spectrum of positive eigenvalues adjoins the discrete levels of negative energy (Bethe and Salpeter, 1957). This implies the calculations of the residue of the bound-free matrix element at

$$k = i \frac{Z_f}{n} \quad (2.64)$$

Furthermore, $[1 - \exp(-2\pi Z_f/k)] \rightarrow 1$. Such a prescription has been tested by various authors (Khandelwal et al., 1989). Thus from equation (2.63), one obtains

$$R_{\beta}^2(n'l' - nl) dn = \frac{Z_f^2 |F_1|^2}{n^3 \left\{ 1 - [(n')^2/n^2] \left(Z_f^2/Z_i^2 \right) \right\}^{2(\beta+n'+2)}} \\ \times \left(\frac{nZ_i - n'Z_f}{nZ_i + n'Z_f} \right)^{2n} \left[\prod_{s=1}^l \left(1 - \frac{s^2}{n^2} \right) \right] |G_2|^2 dn \quad (2.65)$$

where the quantity G_2 stands for the following:

$$\begin{aligned}
 G_2 \equiv & \sum_{j=0}^{n'-l'-1} \left\{ \left(\frac{1}{2}\right)^j (i)^{j+p-1} \left(\frac{1}{n}\right)^{j-n'-1-\beta+l} \left[1 - \frac{Z_f^2 (n')^2}{Z_i^2 n^2}\right]^j \frac{(p-1)!}{j!} \right. \\
 & \times \prod_{i=0}^{j-1} (n' + l' - i)(n' - l' - 1 - i) \left. \right\} \\
 & \times \sum_{m=1}^p \left\{ \frac{[1 + (Z_f/Z_i)(n'/n)]^{p-m} [1 - (Z_f/Z_i)(n'/n)]^{m-1}}{(p-m)! (m-1)!} \right. \\
 & \times \prod_{\gamma=1}^{m-1} \left(-1 - \frac{l}{n} - \frac{\gamma}{n}\right) \prod_{\kappa=1}^{p-m} \left(1 - \frac{l}{n} - \frac{\kappa}{n}\right) \left. \right\} \quad (2.66)
 \end{aligned}$$

with $p = \beta + n' - l - j + 2$.

The discrete dipole oscillator strength f_n and the differential oscillator strength $df/d\epsilon$ for ejected energy ϵ are important in various physical applications (Khandelwal, Khan, and Wilson, 1989; Khan, Khandelwal, and Wilson, 1988a, 1988b, and 1990). These can be obtained from equations (2.66) and (2.63) for $1s - np$ or k transitions for $\beta = 0$ as:

$$f_n = E_n \frac{2^9}{3} n^7 (n^2 - 1) Z_i^3 Z_f^5 (2Z_i - Z_f)^2 \frac{(nZ_i - Z_f)^{2n-6}}{(nZ_i + Z_f)^{2n+6}} \quad (2.67)$$

and

$$\frac{df}{d\epsilon} = (\epsilon + 2Z_i^2 - Z^2) \left(\frac{Z_f}{Z-1}\right)^2 \frac{1}{3k} R^2 (1s - k) \quad (2.68)$$

where

$$k^2 = \frac{Z_f^2 \epsilon}{(Z-1)^2} \quad (2.69)$$

$$E_n = 2Z_i^2 - Z^2 - \frac{Z_f^2}{n^2} \quad (2.70)$$

and

$$R^2 (1s - k) dk = \frac{2^8 k Z_i^3 Z_f (Z_f^2 + k^2) (2Z_i - Z_f)^2 \exp[-4(Z_f/k) \tan^{-1}(k/Z_i)]}{(Z_i^2 + k^2)^6 [1 - \exp(2\pi Z_f/k)]} dk \quad (2.71)$$

Recently, we have applied equations (2.67) and (2.68) to helium atoms and to helium-like ions (Khandelwal, Khan, and Wilson, 1989; Khan, Khandelwal, and Wilson, 1988a, 1988b, and 1990). We find that the screened hydrogenic model reasonably reproduces the existing dipole oscillator-strength values with

little effort, and nonrelativistic numerical values for bound-bound and for bound-continuum transitions are available for many target He-like ions. The model has also been successful in reproducing the known dipole polarizability values and in predicting the other unknown values. Moments of dipole oscillator-strength distribution (Khan, Khandelwal, and Wilson, 1990) for the helium sequence have also recently been calculated under the screened hydrogenic model. This approach has resulted in values which are in reasonable agreement with the various moment values of other authors (including the mean excitation energy parameter I_T).

In order to obtain the stopping power, one has to include all momentum transfers in the form factor. Khandelwal and coworkers at Old Dominion University, Norfolk, Virginia, under sponsorship of the NASA Langley Research Center, have recently calculated the related radial integral (generalized oscillator strength) for the $1s$ to nl transitions. Thus, it would be an easy matter to obtain stopping power of a helium atom for a projectile such as a proton or a heavy ion. This work is currently underway. This is an ambitious undertaking but is more satisfying in that the calculations are done directly for each atom from first principles, thereby avoiding the inherent approximations such as the underlying Bethe energy loss formula (involving I_T and C).

2.3. Stopping in Molecular Gases

In an extremely rarefied atomic gas, charge particle interactions can occur singly with individual gas constituents leading to great simplification in theoretical treatment. Two physical effects occur as the gas density increases: (1) The projectile no longer reaches asymptotic states in subsequent reactions and (2) the interaction is modified by the presence of the surrounding medium. In addition, for low-energy collisions, the charge state of the projectile is likewise altered by these same physical effects and new states of the partially charged projectile states become important since radiative and Auger transition times become on the order of or greater than the mean free time between collisions. Although Bethe's theory for ordinary matter has questionable applicability it has been shown to be useful in estimating stopping powers provided empirical mean excitation energies are used. This is further discussed in section 2.6.

2.3.1. Historical perspective. Early in the classical treatment of charged particle slowing down it was recognized that the free-electron, long-range coulomb interaction leads to divergencies in the energy-loss rate. These divergencies indicate that there is a need for a long-range saturation effect. The saturation in gases was discussed by Bohr (1915) in terms of Ehrenfest's principle. Bohr proposed that the saturation in gases is caused by the bonding of the electrons. To effect energy transfer, the interaction time $\tau = b/v$ (where b is the impact parameter and v is the ion velocity) must be short compared with the oscillating period of the bonded electron. Hence, the adiabatic long-range collisions provide the necessary saturation, and an upper limit is established for the effective impact parameters. Most of our modern understanding stems from Bethe's detailed quantum theory (1930) based on the Born approximation. Stopping power for

gaseous media with this approximation is given by

$$S = \frac{4\pi N Z_P^2 Z_T e^4}{mv^2} \left\{ \ln \left[\frac{2mv^2}{(1-\beta^2)I_T} \right] - \beta^2 - \frac{C}{Z_T} \right\} \quad (2.72)$$

where Z_P is the projectile charge, N is the number of targets per unit volume, Z_T is the number of electrons per target, m is the electron mass, v is the projectile velocity, $\beta = v/c$, c is the velocity of light, C is the velocity-dependent shell-correction term (Walske and Bethe, 1951), and I_T is the mean excitation energy given by solving

$$Z_T \ln I_T = \sum_n f_n \ln E_n \quad (2.73)$$

where f_n is the electric dipole oscillator strength of the target and E_n is the corresponding excitation energy. The sum in equation (2.73) includes discrete and continuum levels. Empirically, it was observed that molecular stopping power is reasonably approximated by the sum of the corresponding empirically derived "atomic" stopping powers (Bragg and Kleeman, 1905). Equations (2.72) and (2.73) imply

$$Z_T \ln I_T = \sum_j n_j Z_j \ln I_j \quad (2.74)$$

where Z_T and I_T pertain to the molecule, Z_j and I_j are the corresponding atomic values, and n_j represents the stoichiometric coefficients. This additivity rule, given by equation (2.74), is called Bragg's rule.

Sources of deviations from Bragg's additivity rule for molecules and the condensed phase are discussed by Platzman (1952a and 1952b). Aside from shifts in excitation energies and adjustments in line strengths as a result of molecular bonding, new terms in the stopping power are caused by the coupling of vibrational and rotational modes. Additionally, in the condensed phase, some discrete transitions are moved into the continuum, and collective modes among valence electrons in adjacent atoms produce new terms to be dealt with in the absorption spectrum. Platzman proposed that the experimentally observed additivity rule may not show that molecular stopping power is the sum of atomic processes but rather it demonstrates that molecular bond shifts for covalent-bonded molecules are relatively independent of the molecular combination. On the basis of such arguments, Platzman suggested that ionic-bonded substances should be studied as a rigid test of the additivity rule because of the radical difference in bonding type. He further estimated that ionic-bond shifts could change the stopping power by as much as 50 percent.

Among the early indicators of the violation of the Bragg rule was the calculation of 15 eV for the mean excitation energy of atomic hydrogen (using eq. (2.72) with the exactly known oscillator strengths and excitation levels) compared with a rather firmly established experimental value for molecular hydrogen of about 18 eV. Since accurate values of atomic mean excitation energies have been calculated for numerous elements by Inokuti and coworkers (Dehmer, Inokuti, and Saxon, 1975; Inokuti, et al., 1981) for the purpose of evaluating chemical bonding effects in molecules, empirical values have been substantially perturbed by effects

of the chemical bonds. Although the mean excitation energy for gas molecules could be evaluated in principle from equation (2.72), the lack of knowledge of the excitation levels and corresponding oscillator strengths is the main hindrance.

It was suggested by Dalgarno (1960) that the oscillator strength distributions could be determined empirically from the photoabsorption spectra (aside from experimental uncertainty). Much of these data are obtained by energy-loss experiments by electron impact scattering at forward angles. Values of mean excitation energy for a number of simple molecules have in this way been estimated and demonstrate the shift in atomic values caused by chemical bonding (Zeiss and Meath, 1975; Zeiss et al., 1977).

Theoretical calculation of mean excitation energies is hindered by the difficulty of solving for the complete excitation spectrum of complex quantum systems. Dalgarno (1963) was able to simplify the calculation by introducing a generalized function, which is related to the excitation spectrum as follows:

$$F_D(\omega) = \sum_n \frac{f_n}{E_n + \omega} \quad (2.75)$$

However, this function can be evaluated without explicitly forming the indicated sum. Thus, Dalgarno was able to reduce equation (2.75) to

$$F_D(\omega) = \frac{2}{3} \left(\vec{X}, \sum_{i=1}^{Z_T} \nabla_i \psi_o \right) \quad (2.76)$$

with

$$(H - E_o + \omega)\vec{X} + \sum_{i=1}^{Z_T} \vec{r}_i \psi_o = 0 \quad (2.77)$$

where ψ_o is the ground-state wave function, E_o is the corresponding energy, ω is an energy eigenvalue, and \vec{X} is the corresponding eigenvector. Chan and Dalgarno (1965) calculated I as 42 eV for helium and Kamikawai, Watanabe, and Amemiya (1969) calculated 18.2 eV for molecular hydrogen by the same method. These values are in excellent agreement with experiments.

Simultaneous with the development of the microscopic theory of stopping power was the macroscopic electrodynamic description of energy loss as required for the description of the long-range part of the interaction in the condensed phase. This is because the interaction is simultaneous among many constituents. The slowing down is through the force exerted on the passing particle by the electric field induced in the medium by the passage (Landau and Lifshitz, 1960). It is customary to assume that the electric displacement vector is linearly related to the time-varying electric field as

$$\vec{D}(t) = \vec{E}(t) + \int_0^t g(\tau) \vec{E}(t - \tau) d\tau \quad (2.78)$$

for which the dielectric constant is

$$\epsilon(\omega) = 1 + \int_0^\infty g(\tau) \exp(i\omega\tau) d\tau \quad (2.79)$$

The short-range collisions are still treated by Bethe theory with the result for total stopping power (see Ahlen (1980) for details) of

$$S = \frac{4\pi N Z_P^2 Z_T e^4}{mv^2} \left\{ \ln \left[\frac{2mv^2}{(1-\beta^2)I_T} \right] - \beta^2 - \frac{\delta}{2} \right\} \quad (2.80)$$

where δ is a density-effect correction applicable at high energies ($\beta^2 > 1/\epsilon(0)$). Also,

$$Z_T \ln I_T = \frac{m}{2\pi^2 N e^2} \int_0^\infty \omega \operatorname{Im} \left[\frac{-1}{\epsilon(\omega)} \right] \ln(\hbar\omega) d\omega \quad (2.81)$$

where $\operatorname{Im}(Z)$ denotes the imaginary part of Z and \hbar is Planck's constant. A result of dispersion theory is

$$\frac{m}{2\pi^2 N e^2} \omega \operatorname{Im}[\epsilon(\omega)] = f(\omega) \quad (2.82)$$

where $f(\omega)$ is the dipole oscillator strength per unit cell of the medium, and

$$Z_T \ln I_T = \int_0^\infty \frac{f(\omega)}{|\epsilon(\omega)|^2} \ln(\hbar\omega) d\omega \quad (2.83)$$

which reduces to the usual Bethe expression (eq. (2.73)) in a sparse gas for which $\epsilon(\omega) \approx 1$.

If the long-range saturation effect is in terms of adiabatic limits for a gas and in terms of the medium polarization response for condensed dielectrics, the saturation effect for a free-electron gas is related to the tendency of a neutral plasma to screen a local charge imbalance at large distances (Kramers, 1947). The dielectric function of a free-electron gas is derived by Lindhard (1954) and applied to the stopping power problem for a classical electron gas and for the interaction-free Sommerfeld electron gas model. For a free-electron gas at rest, Lindhard arrives at the equation

$$S = \frac{4\pi Z_P^2 e^4 \rho}{mv^2} \ln \left(\frac{2mv^2}{\hbar\omega_p} \right) \quad (2.84)$$

where ρ is the electron density and ω_p is the classical plasma frequency given by

$$\omega_p^2 = \frac{4\pi e^2}{m} \rho \quad (2.85)$$

Strictly speaking, equation (2.84) applies only when the electron gas is at rest, but it also applies in the limit of high projectile velocity compared with the average motion of the electrons.

A discovery which paralleled the Lindhard investigations was made by Bohm and Pines (Bohm and Pines, 1951 and 1953; Pines and Bohm, 1952), in which collective long-range interactions in a quantum electron gas were separated from individual electron motion through a canonical transformation, after which the normal coordinates of collective oscillation appear. This separation of the Hamiltonian into collective and individual electron motions is accomplished because of the effective screening of the coulomb fields of individual electrons for distances greater than the screening distance λ_c . For collective motion to give a major contribution to the Hamiltonian, the individual electron wavelength must be greater than λ_c . Bohm and Pines (1953) found the average collective plasma frequency to be

$$\langle\omega\rangle = \left[1 + \frac{3}{2} \frac{\chi^2}{\lambda_s} \left(1 + \frac{3}{10} \chi^2\right)\right] \omega_p \quad (2.86)$$

where λ_s is the average electron separation and χ is the ratio of the average electron wavelength to the screening distance. Pines (1953) suggests that the screening parameter χ should be chosen to minimize the electron long-range correlation energy (that is, the electronic coulomb energy), which, for plane-wave states appropriate to their degenerate electron gas model, is given by

$$E_{lr,corr} = \frac{0.866\chi^3}{\lambda_s^{1.5}} - \frac{0.458\chi^2}{\lambda_s} + \frac{0.019\chi^4}{\lambda_s} \quad (2.87)$$

Pines (1953) derived the stopping power in this degenerate electron gas and showed that the usual classical plasma frequency ω_p is replaced by $\langle\omega\rangle$, which includes corrections for individual electron motion.

A rather bold suggestion was made by Lindhard and Scharff (1960) that equation (2.84) could be applied on the atomic scale if the appropriate average over the atomic electron density was made. They further suggested that the effects of individual bonding of the electrons in their atomic orbitals could be incorporated through the added factor $\gamma \approx \sqrt{2}$ as

$$S = \frac{4\pi e^4 Z_p^2 N}{mv^2} \int d^3r \rho(\vec{r}) \ln \left(\frac{2mv^2}{\gamma \hbar \omega_p} \right) \quad (2.88)$$

From equation (2.88), the mean excitation energy is given by

$$Z_T \ln I_T = \int d^3r \rho(\vec{r}) \ln(\gamma \hbar \omega_p) \quad (2.89)$$

Lindhard and Scharff estimated the mean excitation energy for atomic Hg as 768 eV compared with ≈ 800 eV from experiment. For He, they got 37 eV compared with 35 eV from quoted experiments (more modern experiments yield 42 eV). They further approximated molecular hydrogen by taking the effective charge to be $Z = 1.2$ and obtained 16 eV.

Following this initial success of treating atoms as localized electron plasmas, Lindhard and Winther (1964) extended equation (2.88) by using the more general

velocity-dependent dielectric function derived by Lindhard (1954), and demonstrated the ability of the Lindhard theory to predict tight bonding corrections of similar character to those of Walske (1952) in connection with the Bethe theory.

Chu and Powers (1972) made extensive use of the work of Lindhard and Scharff (1960) to demonstrate Z_2 oscillations in the mean excitation energy. This work gave rise to corresponding Z_2 oscillations in stopping power from which periodic variations are associated with the atomic shell structure (Chu and Powers, 1972). The more detailed calculations of Rousseau, Chu, and Powers (1971) utilized the velocity-dependent Lindhard-Winther theory and Bonderup's (1967) simplified form of the Lindhard theory and showed good agreement with 2-MeV α -particle stopping power data (Chu and Powers, 1969). Throughout these efforts, the parameter γ is taken as the square root of 2, as suggested by Lindhard and Scharff (1960).

Chu, Moruzzi, and Ziegler (1975), using the theory of Lindhard and Winther in which individual electron corrections to the local collective excitation were treated empirically by taking γ as an adjustable parameter, evaluated the aggregation effects for condensed noble gases and metals. The condensed-gas calculations determined electron densities according to atomic Hartree-Fock densities, including overlap from the nearest neighbors in the condensed phase. Metallic wave functions were taken from the muffin-tin model calculations of Moruzzi, Janak, and Williams (1978). In most cases, the empirically determined γ was in the range from 1.2 to 1.3. (See Ziegler, 1980.)

As noted by Dehmer, Inokuti, and Saxon (1975), equation (2.89) may be rewritten as

$$Z_T \ln I_T = \int d\omega \left[\int d^3r \delta(\omega - \gamma\omega_p) \rho(r) \right] \ln(\hbar\omega) \quad (2.90)$$

from which can be obtained

$$f(\omega) = \int d^3r \delta(\omega - \gamma\omega_p) \rho(r) \quad (2.91)$$

where $\delta(x)$ is the Dirac delta function. It is seen from equation (2.91) that, in the local plasma approximation, the volume of plasma with cutoff frequency $\gamma\omega_p = \omega$ approximates the total oscillator strength of the system at frequency ω . No exact equivalence is implied between the oscillator frequency distribution given by equation (2.91) and the oscillator frequency distribution of a quantum system. (This is true because equation (2.91) exhibits a continuous spectrum, although quantum systems generally exhibit a series of poles associated with the discrete quantum levels as well as a continuum at higher frequencies.) Some insight may be gained by comparing dispersion relations for atomic systems with those for a related plasma. The dispersion relation for a classical plasma is given by the dielectric constant $\epsilon(\omega)$ as

$$\epsilon(\omega) = 1 - \frac{\omega_p^2}{\omega^2} \quad (2.92)$$

where ω_p is the usual plasma frequency and equation (2.92) results from the plasma conductivity (Hubbard, 1955). Indeed, the same pole term in $\epsilon(\omega)^{-1}$ appears in metals as the result of the conduction electrons that give metals their characteristic optical properties (Hubbard, 1955; Fröhlich and Pelzer, 1955). The more general dispersion relation, derived from equations (2.78) and (2.81), is

$$\epsilon(\omega) = 1 - \frac{4\pi Z_T e^2}{m} P \int_0^\infty \frac{f(x)}{x^2 - \omega^2} dx \quad (2.93)$$

where P denotes the principal value at the singularity. In atomic systems, the oscillator strengths are broadly separated in frequencies according to shells; the outer shells appear at the lowest frequencies, and the innermost shell appears at the highest frequencies. The lack of oscillator strength at frequencies between shells results in large gaps in the spectrum. Let ω be a frequency in the broad gap between two successive shells—the first centered at ω_1 and the second at ω_2 . Then the dispersion relation (eq. (2.93)) becomes

$$\epsilon(\omega) \approx 1 - \frac{\omega_{p,1}^2}{\omega^2} \quad (2.94)$$

where

$$\omega_{p,1}^2 \approx \frac{4\pi Z_T e^2}{m} \int_0^{\omega_1} f(x) dx \quad (2.95)$$

so that $\omega_{p,1}$ is the plasma frequency associated with the electrons of the outermost shell. Although equations (2.94) and (2.95) provide motivation (Wilson et al., 1984b) for using the local plasma approximation (eq. (2.91)), there is plenty of room for a more complete understanding as to why the model works as well as it does in practical calculations (Wilson and Kamaratos, 1981; Wilson et al., 1984b).

In previous investigations, we considered the use of the local plasma model to evaluate molecular bonding effects on the mean excitation energy of molecules of covalent-bonded hydrogen and carbon (Wilson and Kamaratos, 1981) as well as ionic crystals and gases (Wilson et al., 1982), in which quite sensible corrections to the usual Bragg's rule were obtained. The chemical-bond shifts were unambiguously defined in terms of atomic integrals and molecular parameters. In the usual implementation of the local plasma model (eq. (2.89)), γ corrects for a shift in the local plasma frequency caused by individual electron effects. Lindhard and Scharff (1960) suggest $\gamma = \sqrt{2}$; however, $\gamma \approx 1.2$ yields atomic mean excitation energies from the local plasma model in better agreement with the accurate atomic values calculated by Dehmer, Inokuti, and Saxon (1975). The fact that the larger value ($\gamma = \sqrt{2}$) gives better agreement with empirical data suggests that this larger value corrects (in addition to individual electron shifts) for the chemical shifts as well. Such chemical shifts were estimated separately for covalent and ionic bonds by Wilson and Kamaratos (1981) and Wilson et al. (1982).

Encouraged by the smallness (<30 percent) of the empirical individual electron corrections to the collective plasma frequency (Ziegler, 1980; Wilson and Kamaratos, 1981; Wilson et al., 1982), a calculation (Wilson and Xu, 1982) in which individual electron shifts were estimated according to the theory for plane-wave

states in an extended plasma, as calculated by Pines (1953), yields results that are in good agreement with Dehmer, Inokuti, and Saxon (1975). Consequently, the local plasma model is placed on a parameter-free basis (Wilson et al., 1984a and 1984b) in which chemical shifts are determined from atomic/molecular parameters alone, and effects of individual electron motion are evaluated in terms of the Pines correction, the combined effects of which are on the order of the plasma frequency shift of $\gamma \approx \sqrt{2}$ suggested by Lindhard and Scharff.

The Pines correction makes a remarkable improvement in the prediction of the local plasma model, and further adjustments in the theory to account for the plasma frequency shifts resulting from the atomic shell structure should bring the model into predictive capability. To further elucidate the relationship between the local plasma model and the more exact quantum treatment of bonded systems, related quantities of both theories in the case of one- and two-electron systems are examined in section 2.3.2. Atomic mean excitation energies and straggling parameters, based on the local plasma model, are compared with accurate calculations of Inokuti et al. (Dehmer, Inokuti, and Saxon, 1975; Inokuti, Baer, and Dehmer, 1978; Inokuti et al., 1981) in section 2.3.3. The use of the Gordon-Kim electron gas model of molecular bonding (Gordon and Kim, 1972) to determine the effects of covalent chemical-bond shifts of mean excitation energy for elements of the first two rows is presented in section 2.3.4. Calculations of mean excitation energies of ionic-bonded substances are discussed in section 2.3.5, and the mean excitation energies of metals are discussed in section 2.3.6.

2.3.2. Excitation spectra of one- and two-electron systems. The hydrogen atomic excitation spectrum in the dipole approximation is well-known as

$$f_H(\omega) = \left\{ \begin{array}{ll} \sum_{n=2}^{\infty} \frac{2^8}{3} \left(1 - \frac{1}{n^2}\right) n^7 \frac{(n-1)^{2n-5}}{(n+1)^{2n+5}} \delta(\omega - \omega_n) & (\hbar\omega < R) \\ \frac{1}{2} \sqrt{\frac{\hbar}{R\omega}} \frac{2^8}{3} \hbar\omega \frac{k}{(1+k^2)^5} \frac{\exp[(-4/k) \tan^{-1} k]}{1 - \exp(-2\pi/k)} & (\hbar\omega > R) \end{array} \right\} \quad (2.96)$$

where n is the principal quantum number, R is the Rydberg constant, ω_n is given by

$$\hbar\omega_n = R \left(1 - \frac{1}{n^2}\right) \quad (2.97)$$

and

$$Rk^2 = \hbar\omega - R \quad (2.98)$$

The corresponding spectrum for the local plasma model (eq. (2.91)) is given as

$$f_p(\omega) = \left\{ \begin{array}{ll} 4\omega\omega_0^{-2} \ln^2(\omega/\omega_0) & (\omega < \omega_0) \\ 0 & (\omega > \omega_0) \end{array} \right\} \quad (2.99)$$

where $\omega_0 = 55.12$ eV. The cumulative oscillator strength

$$F(\omega) = \int_0^\omega f(\omega') d\omega' \quad (2.100)$$

is shown in figure 2.2 for each of the two models. Similarly, the excitation spectrum of the helium atom has been evaluated for screened wave functions and is shown in figure 2.2. The fractional excitations of the two models never differ by more than ≈ 15 percent above the excitation threshold. As noted by Dehmer, Inokuti, and Saxon (1975), the main error in the local plasma model is the contribution to absorption below excitation threshold all the way down to zero. This error is also evident in the energy moments of the plasma model. The moments of the energy spectrum for the hydrogen atom are shown in figure 2.3, where

$$\langle\langle E/R \rangle\rangle^m = \int_0^\infty \left(\frac{\hbar\omega}{R}\right)^m f(\omega) d\omega \quad (2.101)$$

and m is a continuous parameter. The low-frequency contributions associated with the local plasma model cause a divergence in equation (2.101) at $m \approx -2$ which is not present in the quantum system. Atomic polarizability and the low-frequency refractive index are affected the most. Other atomic properties, such as the total inelastic cross section, the mean excitation energy, the straggling parameter, and the mean electronic kinetic energy, are reasonably presented by the plasma model. Also shown in figure 2.3 are results, including the Pines (1953) correction to the plasma frequency, which indicate substantial improvement in the prediction of atomic properties, although low-energy atomic properties are still beyond the scope of the model.

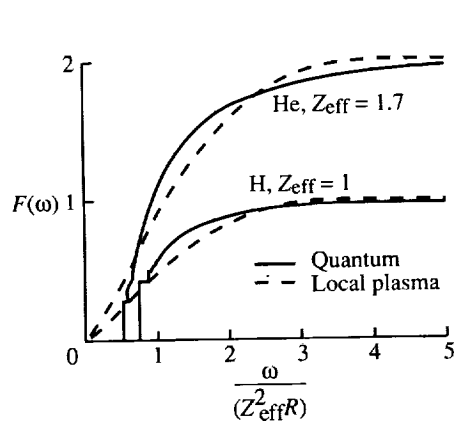


Figure 2.2. Cumulative oscillator strength distribution for atomic hydrogen and helium.

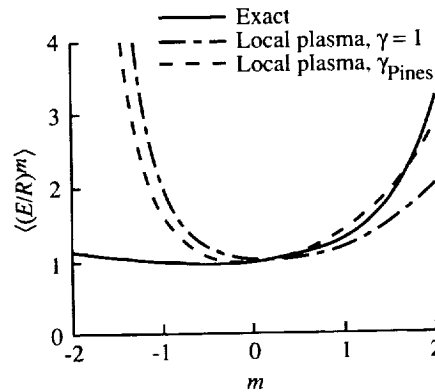


Figure 2.3. Moments of oscillator strengths of hydrogen atom.

The plasma model is expected to be more accurate as more electrons are added to the system. This occurs in two ways, as seen in figure 2.2. First, a greater contribution comes from the continuum, which is most like the plasma. Second, the excitation thresholds shift to relatively lower energies and fill in the low-frequency region, for which the plasma model normally tends to err. A considerable improvement in the energy moments of helium for the local plasma approximation is clearly shown in figure 2.4.

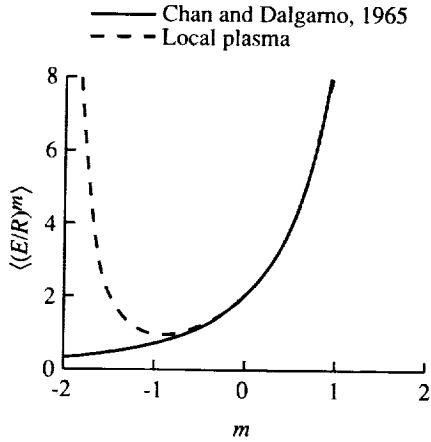


Figure 2.4. Moments of oscillator strengths of helium atom according to quantum oscillator strengths using screened wave functions. $Z_{\text{eff}} = 1.7$.

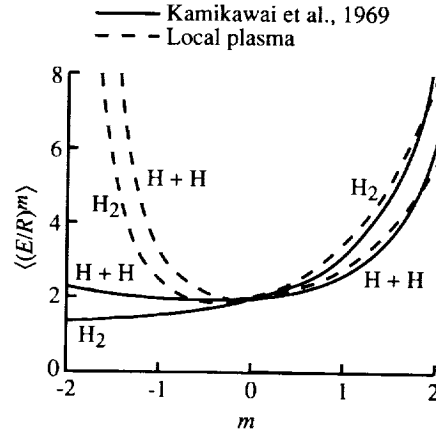


Figure 2.5. Moments of oscillator strengths of hydrogen molecule for several models.

The moments of the excitation spectrum of H_2 have been evaluated empirically by using experimental oscillator strengths (Dalgarno and Williams, 1965) and theoretically (Kamikawai, Watanabe, and Amemiya, 1969) using the Dalgarno (1963) sum rules (eqs. (2.75) and (2.76)). These are compared in figure 2.5 with an "atomic" approximation to H_2 taken as a generalization of Bragg's rule (Zeiss et al., 1977). Also shown in figure 2.5 are values for H_2 calculated by using the local plasma model with the Pines correction and with the Gordon-Kim model of the molecular wave functions given as

$$\rho_{H_2}(\vec{r}) = \rho_H(\vec{r}) + \rho_H(\vec{r} - \vec{R}) \quad (2.102)$$

where $\rho_H(\vec{r})$ is the atomic hydrogen electron density and \vec{R} is the displacement vector of length $1.4a_0$ between the two centers. It is clear from figure 2.5 that, even with the simple Gordon-Kim approximation, the plasma model is a considerable improvement over the Bragg rule, except for the lowest-energy molecular properties (i.e., $m < -0.5$). Figure 2.5 also shows that the Gordon-Kim approximation introduces minor errors compared with the inherent limitations of the local plasma model.

The mean excitation energy for stopping power may likewise be evaluated. Atomic hydrogen and molecular hydrogen are presented in table 2.1 along with a recent compilation of experimental data (Seltzer and Berger, 1982). Quite reasonable estimates of atomic and molecular properties of importance to ionizing radiation are obtained by this local plasma model if the Pines correction is included. Optical and other low-frequency properties, however, are poorly represented. The plasma model should become more accurate for more complex many-electron systems, especially those in which the optical properties are more in line with those predicted by the plasma model.

Table 2.1. Hydrogen Mean Excitation Energy for Stopping Power

Chemical species	Hydrogen mean excitation energy, eV, for stopping power for—			
	Quantum model	Oscillator strength distribution	Local plasma model (a)	Experiment
H	^b 14.99	^d 18.4	14.69	^e 18.5 ± 0.5
H ₂	^c 18.2		18.9	

^aWith Pines correction.

^bWith oscillator strengths of equation (2.96).

^cKamikawai, Watanabe, and Amemiya, 1969.

^dDalgarno and Williams, 1965.

^eSeltzer and Berger, 1982.

With the present results, it is now clear what approach should be taken to improve the plasma model applications. Clearly, a correction factor similar to that of Pines should be introduced to suppress absorption below excitation threshold and, correspondingly, to enhance frequencies just above threshold. A number of possibilities are open to implement such a correction, which would appear as a first-order quantum correction for the discrete spectrum. Preliminary work by Walecka (1976) on the study of collective atomic oscillations may be a starting point for further development.

2.3.3. Stopping and straggling parameters of atoms. In this section, parameters are considered for atoms associated with the stopping of charged particles and fluctuations in their energy transfer. The energy moment is

$$S(m) = \langle (E/R)^m \rangle \quad (2.103)$$

and the related quantity is

$$L(m) = \frac{dS(m)}{dm} \quad (2.104)$$

In terms of these quantities, the mean excitation energy is

$$\ln I = \frac{L(0)}{S(0)} \quad (2.105)$$

and the straggling parameter related to fluctuations in energy loss is

$$\ln \Delta = \frac{L(1)}{S(1)} \quad (2.106)$$

The mean excitation energy (eq. (2.105)) has been evaluated in the context of the local plasma model and is presented in figure 2.6 along with the values computed by Inokuti and coworkers for atoms through krypton and the compilation of experimental data by Seltzer and Berger (1982). Hartree-Fock wave functions (Clementi and Roetti, 1974) have been used for elements helium through neon

and sodium through krypton are represented by screened wave functions (Clementi and Raimondi, 1963).

The values for the straggling parameter were similarly evaluated and are presented in figure 2.7 with the values obtained by Inokuti and coworkers. Also shown are values for noble gases compiled by Inokuti et al. (1981) and values obtained by Zeiss et al. (1977). The present values tend to be about 25 percent low at $Z \approx 36$, with improvements at lower values of Z , which may be caused by the lack of shell structure corrections in the plasma frequencies of the K and L shells.

It is clear from these atomic calculations that the plasma model with the Pines correction generally provides good results for mean excitation energy and reasonable estimates for the straggling parameter. Although the Hartree-Fock wave functions are required for low atomic numbers, reasonable results are obtained using screened wave functions for atoms heavier than argon. The low-energy atomic properties mainly require improvements beyond the Pines correction. These properties emphasize the need for a first-order quantum correction to the atomic structure.

2.3.4. Covalent-bond effects. Early experimental work with ionization energy loss was conducted in covalent-bonded gases (also noble gases) from which Bragg's rule was derived. Although more recent experimental work, beginning with Thompson (1952), has shown systematic variation from Bragg's rule, such rules still seem appropriate for fixed molecular structures (Lodhi and Powers, 1974; Neuwirth, Pietsch, and Kreutz, 1978). As a result of the theoretical efforts of Inokuti and coworkers, it is clear that chemical-bond shifts in the mean excitation energy have occurred, and as suggested by Platzman (1952a), all covalent shifts are of similar magnitude.

In any molecular dynamic calculation, there is a trade-off between model accuracy and computation efficiency. As pertains to the radiolysis of large molecular structures, the most useful model is the lowest order possible. It is clear that the use of self-consistent field methods to determine molecular wave functions would seriously limit the ability to study systems of practical interest. Considering the relative success of the Gordon-Kim electron gas model of molecular bonding (Gordon and Kim, 1972; Tossell, 1979; Waldman and Gordon, 1979), a simple method for the calculation of chemical-bond effects on the mean excitation energies is suggested. As suggested by Gordon and Kim, the molecular electron density as a superposition of the unperturbed atomic states is given by

$$\rho(\vec{r}) = \rho_1(\vec{r}) + \rho_2(\vec{r} - \vec{R}_{12}) \quad (2.107)$$

for diatomic molecules. There is an obvious generalization of equation (2.107) for the polyatomic case. Whereas Gordon and Kim used equation (2.107) to calculate the molecular potential (see Tossell, 1979; Waldman and Gordon, 1979, for ionic and covalent applications) from which R_{12} is theoretically obtained, here R_{12} is taken from observed experimental bond distances. Substituting equation (2.107)

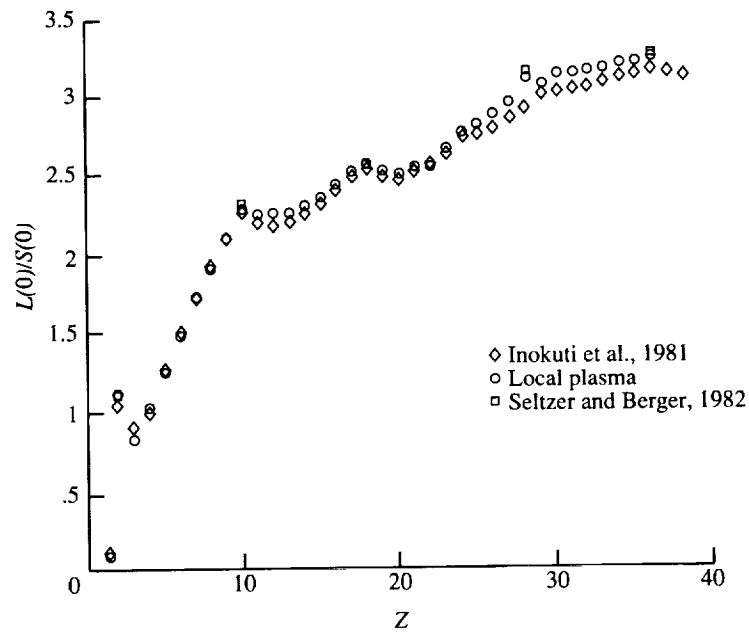


Figure 2.6. Atomic mean excitation energies from quantum calculations of Inokuti et al., 1981, and local plasma model. Empirical values are from Seltzer and Berger, 1982.

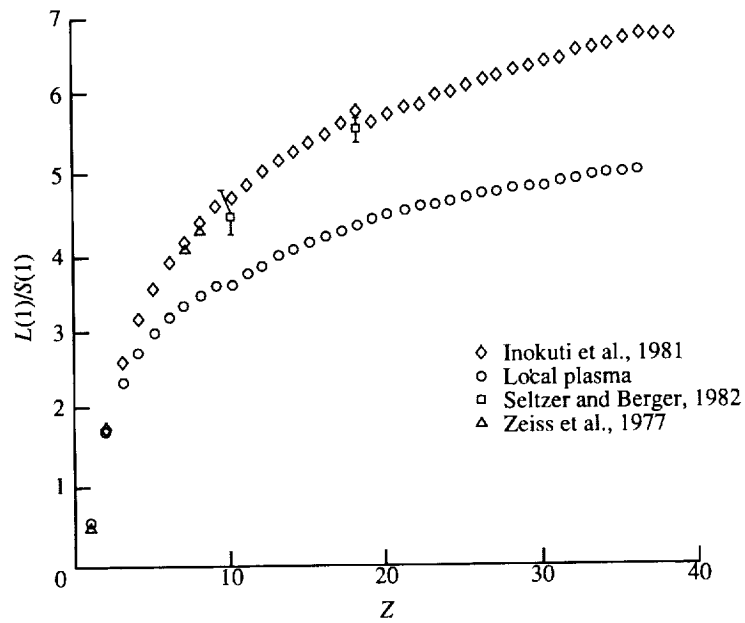


Figure 2.7. Atomic straggling parameters from quantum calculations of Inokuti et al., 1981, and local plasma model along with various experimental results.

into equations (2.85) and (2.89) and reducing results in

$$\begin{aligned}
 Z \ln(I) = & Z_1 \ln(I_1) + \int \rho_1(\vec{r}) \ln \left[1 + \frac{\rho_2(\vec{r} - \vec{R}_{12})}{\rho_1(\vec{r})} \right]^{1/2} d^3r \\
 & + Z_2 \ln(I_2) + \int \rho_2(\vec{r}) \ln \left[1 + \frac{\rho_1(\vec{r} - \vec{R}_{21})}{\rho_2(\vec{r})} \right]^{1/2} d^3r \quad (2.108)
 \end{aligned}$$

where I_1 and I_2 are the corresponding atomic values, which are accurately known (Inokuti, Baer, and Dehmer, 1978; Inokuti et al., 1981). The chemical-bonding correction is generally

$$\ln(1 + \delta_{ij}) = \frac{1}{Z_i} \int \rho_i(\vec{r}) \ln \left[1 + \frac{\rho_i(\vec{r} - \vec{R}_{ij})}{\rho_i(\vec{r})} \right]^{1/2} d^3r \quad (2.109)$$

Equation (2.108) for diatomic molecules is generalized for polyatomic systems as

$$Z \ln(I) = \sum_i Z_i \ln \left[\left(1 + \sum_j \delta_{ij} \right) I_i \right] \quad (2.110)$$

where the sum over j includes every bond in which Z is attached in the molecule. Correction factors have been calculated (Wilson and Kamaratos, 1981) for hydrogen and carbon molecules with the bond parameters in table 2.2. Carbon sp^3 hybrid orbital wave functions were used in these calculations, although s^2p^2 values were only slightly different. The tetrahedral orbitals were spherically symmetrical in their electron densities. Therefore, spherical symmetry was assumed throughout subsequent calculations.

Recommended values of mean excitation energies (Seltzer and Berger, 1982) are presented in table 2.3 along with theoretical values calculated by using atomic mean excitation energies from Dehmer, Inokuti, and Saxon (1975) with the bond corrections in table 2.2. Bragg's rule is also used with the atomic values of Dehmer, Inokuti, and Saxon for comparison. Although the theoretical values are within 4 percent of the experimental and empirical values, Bragg's rule values are from 17 to 21 percent low, indicating a substantial adjustment as the result of chemical bonding.

Mean excitation energies have been calculated for covalent gases of the first two rows using the local plasma model and the Pines correction. Results of this calculation and the empirical values of Seltzer and Berger (1982) are given in table 2.4. Corresponding values for covalent solids are shown in table 2.5.

Table 2.2. Hydrogen and Carbon Molecular Parameters

Molecular parameter	H-H	H-C	C-H	C-C	C=C	C≡C	H-C benzene	C-H benzene	CC benzene	CC graphite
R_{AB} , bohrs	1.40	2.08	2.08	2.94	2.52	2.28	2.02	2.02	2.64	2.68
δ	0.261	0.432	0.044	0.062	0.087	0.105	0.453	0.045	0.079	0.076

Table 2.3. Molecular Mean Excitation Energy

Chemical species	Molecular mean excitation energy, eV, for—		
	Present theory	Seltzer and Berger, 1982	Bragg's rule
CH ₄	44.7	42.8	35.1
(CH ₂) _x	55.0	53.4	43.5
C ₆ H ₆	60.6	61.4 ± 1.9	50.6
H ₂	18.9	18.5 ± 0.5	15.0
Graphite	76.1	78.5 ± 1.5	62.0

Table 2.4. Molecular Mean Excitation Energies for Covalent Gases

Chemical species	R_{AB} , bohrs	I , eV	
		Local plasma model	Seltzer and Berger, 1982
H ₂	1.40	18.9	^a 19.2 ± 0.4
N ₂	2.08	85.0	^a 82 ± 1.6
O ₂	2.34	99.6	^a 95 ± 1.9
F ₂	2.67	114.2	115 ± 10
Cl ₂	3.76	170.8	171 ± 14

^a These values are strongly influenced by Zeiss et al. (1977).

Table 2.5. Mean Excitation Energies for Covalent-Bonded Crystals

Chemical species	R_{AB} , bohrs	I , eV	
		Local plasma model	Seltzer and Berger, 1982
B (tetragonal)	3.06	67.3	76 ± 7.6
C (diamond)	2.94	75.3	
C (graphite)	2.68	76.1	78 ± 2.3
Si (diamond)	4.42	151.0	173 ± 4
P (black)	4.16	155.7	^a 181 ± 14
S (rhombohedral)	3.85	162.7	^a 190 ± 15

^aUnspecified allotropic form.

Moments for the N₂ molecule using the plasma model are presented in figure 2.8 with values calculated from the oscillator strengths compiled by Dalgarno, Degges, and Williams (1967). As can be seen, good agreement between the present simple plasma model calculations and the oscillator strength distribution of Dalgarno, Degges, and Williams is obtained except for the lowest frequency phenomena.

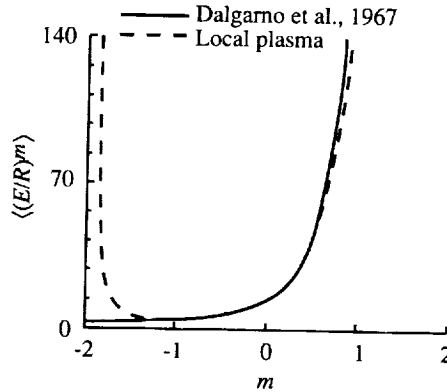


Figure 2.8. Moments of N₂ oscillator strengths from empirical values of Dalgarno, Degges, and Williams (1967) and local plasma model using Gordon-Kim molecular model densities.

2.3.5. Ionic-bond effects. Although covalent-bond shifts were found to be relatively small corrections to atomic values, such a separation as in equation (2.108) in terms of neutral atomic values is not possible for ionic bonds. Using the Gordon-Kim model electron density of the partial ionic (diatomic) system,

$$\rho_p(\vec{r}) = \rho_{A^{(\pm p)}}(\vec{r}) + \rho_{B^{(-p)}}(\vec{r} - \vec{R}_{AB}) \quad (2.111)$$

where $A^{(+p)}$ and $B^{(-p)}$ refer to partially ionic states of the two constituents, \vec{R}_{AB} is their nuclear separation, and p is the partial ionic fraction. The electron density of a partial ionic atom in equation (2.110) is

$$\rho_{A^{(\pm p)}}(\vec{r}) = (1 - p)\rho_A(\vec{r}) + p\rho_{A^\pm}(\vec{r}) \quad (2.112)$$

where $\rho_A(\vec{r})$ is the electron density of the neutral atom and $\rho_{A^\pm}(\vec{r})$ is the electron density of the atomic ion. With the aid of equations (2.111) and (2.112), shifts in the mean excitation energy caused by ionic and covalent effects can be evaluated. As shown by Wilson et al. (1982),

$$\begin{aligned}
Z \ln(I) = & Z_{A(+p)} \ln [I_{A(+p)}] + \int \rho_{A(+p)}(\vec{r}) \ln \left[1 + \frac{\rho_{B(-p)}(\vec{r} - \vec{R}_{AB})}{\rho_{A(+p)}(\vec{r})} \right]^{1/2} d^3r \\
& + Z_{B(-p)} \ln [I_{B(-p)}] + \int \rho_{B(-p)}(\vec{r}) \ln \left[1 + \frac{\rho_{A(+p)}(\vec{r} - \vec{R}_{AB})}{\rho_{B(-p)}(\vec{r})} \right]^{1/2} d^3r \quad (2.113)
\end{aligned}$$

with

$$Z_{A(+p)} \ln [I_{A(+p)}] = \int \rho_{A(+p)}(\vec{r}) \ln [\gamma \hbar \omega_{A(+p)}(\vec{r})] d^3r \quad (2.114)$$

where γ is the Pines correction given by equation (2.85) or estimated empirically as given by Neuwirth, Pietsch, and Kreutz (1978). Mean excitation energies for various stages of ionization calculated with the Pines correction and the atomic wave functions of Clementi and Roetti (1974) are shown in figure 2.9. In addition to the ionic-bond shifts, there are shifts caused by covalent-like character, as given by

$$\ln [1 + \delta_{A(+p), B(-p)}] = \frac{1}{Z_{A(+p)}} \int \rho_{A(+p)}(\vec{r}) \ln \left[1 + \frac{\rho_{B(-p)}(\vec{r} - \vec{R})}{\rho_{A(+p)}(\vec{r})} \right]^{1/2} d^3r \quad (2.115)$$

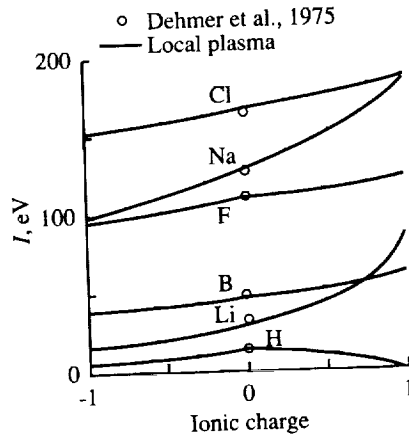


Figure 2.9. Mean excitation energies for partially ionic atoms.

Mean excitation energies for partial ionic-bonded substances are shown in table 2.6 with the corresponding bond parameters used in the model. Also shown are values for a pure covalent bond and Bragg's values using the neutral atomic mean excitation energies of Dehmer, Inokuti, and Saxon (1975), as well as Bragg's values of the corresponding partial ionic states. The ionic-bond fractions are taken from Pauling (1967) as experimental data for HF and LiH. Bond lengths are for ionic crystals except for the HF gas. Atomic mean excitation energies are shown for partial ionic states in figure 2.9 and differ from values of Wilson et al. (1982) because of the Pines correction.

Table 2.6. Ionic-Bond Parameters

Chemical species	R_{AB} , bohrs	p	I_c , eV	I_{IB} , eV	I_B , eV	I , eV
HF	1.72	0.50	97.6	91.7	91.0	96.4
LiH	3.85	0.25	27.8	25.2	25.9	26.7
LiF	3.85	0.90	83.4	92.6	81.6	93.6

It is clear from table 2.6 that the main contribution to corrections to the Bragg rule is the adjustment from atomic neutral to atomic ion mean excitation energies as proposed by Platzman (1952a). Indeed, when there is little difference between the usual Bragg value and the partially ionic Bragg value, the covalent value is in near agreement with the predicted value of I for HF and LiH in the table. For LiF, the relatively large adjustment from the usual Bragg value (81.6) to the partially ionic Bragg value (92.6) leaves a large difference between the covalent value (83.4) and the predicted value of I (93.6). The adjustment of the ionic-bond shift caused by the covalent-like character for LiF is 1 eV compared with adjustments of the neutral states caused by the pure covalent bond of 1.8 eV. This comparison shows the greater role of the coulomb attraction in forming the bond of the ionic molecules relative to the two-electron interaction in forming the covalent bond.

Calculated mean excitation energies for ionic crystals using the Pines correction are shown in table 2.7, along with recommended values of Seltzer and Berger (1982). The crystal parameter and fractional ionic charge have been taken from Pauling (1967). The LiF value is the only one with an experimental basis (Wilson et al., 1982).

Table 2.7. Mean Excitation Energies of Ionic Crystals

Chemical species	R_{AB} , bohrs	p	I , eV	
			Local plasma model	Seltzer and Berger, 1982
LiF	3.80	0.90	92.8	94 ± 8
LiCl	4.86	0.73	139.1	144 ± 12
NaF	4.37	^a 0.91	131.5	147 ± 12
NaCl	5.31	0.75	159.1	181 ± 14

^aPauling partial ionic character function.

2.3.6. Metallic-bond effects. Our first approach to metals is similar to that taken by Chu, Moruzzi, and Ziegler (1975), in which they employed the

muffin-tin wave functions (Moruzzi, Janak, and Williams, 1978) and stopping power theory according to Lindhard and Winther (1964). Individual electron corrections to the local plasma frequency are treated empirically through an adjustable parameter γ . (See table I of Ziegler (1980) and related discussion.) Unlike this previous work, the present work includes estimates of shifts in the plasma frequency according to the Pines correction in equation (2.86) and is in that sense completely deterministic.

The metallic wave functions for lithium metal approximated by the Wigner-Seitz model (Wigner and Seitz, 1934) are considered first. In deriving these wave functions, the lithium ion core potential was taken from the screened wave functions of Clementi and Raimondi (1963), and the calculated crystal-valence wave functions (aside from normalization) were found to be a slight perturbation (mainly due to boundary conditions) of the free hydrogenic ($2s$) orbital inside the Wigner-Seitz sphere (Wigner and Seitz, 1934). The final crystal wave functions used were constructed from unperturbed Hartree-Fock orbitals (Clementi and Roetti, 1974) in the core region with a small perturbation outside the core. This perturbation matched the boundary conditions on the surface of the Wigner-Seitz sphere. This was followed by normalization of the valence-shell wave functions (to make the valence electron density add up to give the correct number of valence electrons). These wave functions are quite similar to the muffin-tin model and yield mean excitation energies in substantial agreement with Ziegler (1980) when γ is taken as his empirical value. The mean excitation energies for metals of the second and third rows using Wigner-Seitz wave functions (treating all valence electrons as spatially equivalent) and the Pines correction are presented in table 2.8 along with empirical values from Seltzer and Berger (1982).

Table 2.8. Metallic Parameters for Selected Metal of First Two Rows

Chemical species	I_{at} , eV Dehmer, Inokuti, and Saxon, 1975	r_s , bohrs	I , eV	
			Wigner-Seitz model	Seltzer and Berger, 1982
Lithium	34.0	3.260	45	41.5 ± 3.7
Beryllium	38.6	2.375	60	63.7 ± 3.2
Sodium	123.6	3.99	140	162 ± 8
Magnesium	121.2	3.34	144	164 ± 8
Aluminum	124.3	2.991	149	166 ± 3

The present results clearly demonstrate that the effects of the metallic bond in lithium and beryllium are large and are mainly the result of collective oscillations in the free-electron gas formed by the valence electrons. Although similar good agreement should be expected for sodium and magnesium, it is emphasized here only that these empirical values are interpolations without an experimental basis, and smaller empirical values more in line with the present results should not be eliminated. The small value predicted for aluminum (149 eV) is in doubt, as the

empirical value (166 ± 3 eV) is based on one of the most experimentally studied quantities since aluminum served as a standard in stopping power experiments for many years. The fault could well lie in the use of the Wigner-Seitz model for group III metals. It is well-known that the success of the Wigner-Seitz theory rests mainly on application to alkali metals. Although some hope for application to group II metals exists, treating the three valence electrons of group III as spatially equivalent is clearly in error. Correction to metals from an alternate model, proposed by Pauling (1967) for metallic orbitals and implemented here in simplified fashion, is considered next.

In X-ray diffraction experiments, even beryllium metal shows a considerable degree of covalent quality, as suspected from bulk material properties (Brown, 1972). In this view, a model is considered in which the valence-bond effects can be included explicitly. In the spirit of the Pauling valence-bond theory and the Gordon-Kim model of valence bonding, the electron density about the ion cores is assumed to be a superposition of partial ionic core states among nearest core neighbors. Additional contributions from the next nearest neighbors are assumed to add to the electron continuum states in a manner analogous to the Pauling unsynchronized resonances in lithium crystals (Pauling, 1967). The electron density of the partially ionic core of charge p is

$$\rho_{A(+p)}(\vec{r}) = \left(\frac{v-p}{v} \right) \rho_A(\vec{r}) + \frac{p}{v} \rho_{A(+v)}(\vec{r}) \quad (2.116)$$

where v is the number of valence electrons, $\rho_A(\vec{r})$ is the electron density of the atomic neutral state, and $\rho_{A(+v)}(\vec{r})$ is the electron density of the valence-stripped ion cores. We have used the observation by Slater that radial wave functions of the L shell are nearly the same for both values of l as a result of exchange interaction between the ($2s$) and ($1s$) orbitals. The same is true for the M shell. In the present calculation, each metal ion core has been placed into a Wigner-Seitz cell, and the electron density from nearest neighbors has been approximated by reflecting the exterior core density function across the cell boundary. The continuum electron density is then taken as

$$\rho_e = [p + (v-p)\delta] \frac{3}{4\pi r_s^3} \quad (2.117)$$

where δ is the next nearest neighbor contribution to the continuum. The value of δ is determined by requiring a full complement of v valence electrons per cell. The resultant electron density $\rho(r)$ was used to calculate the local plasma frequency and mean excitation energy per cell. The Pines correction was used for individual particle shifts. The radii r_s for the Wigner-Seitz cell are given in table 2.8. The ion-core wave functions were calculated from the Hartree-Fock wave functions of Clementi and Roetti. A slight dependence on the ion-core charge appears (Kamaratos et al., 1982) in which there is some increase in mean excitation to $I = 155$ eV for aluminum. However, there are some unresolved questions concerning periodicity at the cell boundaries, which leave the value of this model somewhat in doubt.

The mean excitation energy for aluminum requires the reconsideration of the data on which it is based and the corresponding analysis. In an analysis by Andersen and Ziegler (1977), 162 eV was assumed as the mean excitation energy for aluminum. A reduction in I to 150 eV results in a 3-percent increase in

stopping power at 1 MeV, which leaves it within the stated uncertainty limits of the Andersen and Ziegler parametric curves. These curves correspond to the uncertainty in the experimental data used in the analysis. (See fig. 2.10.) Indeed, a number of authors have reported mean excitation energies for aluminum in line with the present results (Bakker and Segrè, 1951; Simmons, 1952; Mather and Segrè, 1951; Sachs and Richardson, 1953; Bogaardt and Koudijs, 1952; Vasilevskii and Prokoshkin, 1960), although more recent analyses are higher. A recent study of aluminum optical properties indicates that a value of I several electron volts lower than 166 is not inconsistent with the empirical dielectric function (Shiles et al., 1980). The shift of several electron volts is associated with polarization of the Al^{3+} core by the valence electrons in their metallic orbitals. Such core polarization effects are not calculated in the present model. Furthermore, quantum corrections to K - and L -shell discrete spectra may cause further small adjustments. In any case, the apparent discrepancy is due to the electronic wave functions used in the present calculation, to the inadequate treatment of corrections to the Bethe formula, from which I is extracted from the experimental data (see, for example, Andersen et al. (1977) and Khandelwal (1982)), to quantum corrections, or to a combination of these.

To further clarify the relationship between the mean excitation energy for aluminum and experimental data, a band is shown in figure 2.10 which brackets the experimental data of Andersen et al. (1977), Kahn (1953), Neilsen (1961), Leminen, Fontell, and Bister (1968), Nakata (1971), and Sorensen and Andersen (1973) for proton energies between 0.5 and 10 MeV. These energies are compared with the reduced stopping power calculated from the Andersen and Ziegler (1977) empirical shell corrections. The older data of Kahn (1953), which would have lowered the band considerably, were excluded from the figure. The mean excitation energies exhibited in the figure are 167 eV used as input to Shiles et al. (1980), 162 eV determined by Andersen and Ziegler (1977), 155 eV estimated using one form of valence-bond theory, and 149 eV calculated according to the present (simplified) Wigner-Seitz model. Although it is not clear that the curve for 167 eV is superior to the curve for 149 eV, a modest shift in the empirical shell corrections can bring any of the four curves into an equally good fit to the data. It is further emphasized that shell corrections are not exactly known, and, in empirical analysis, shell corrections are not usually differentiated from other corrections to the Bethe formula (eq. (2.72)).

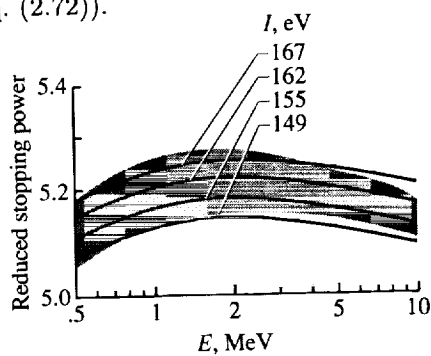


Figure 2.10. Reduced stopping power for aluminum for several mean excitation energies and range of experimental data. Shaded area is band of experimental data.

2.3.7. Discussion of results. The present results are combined in figure 2.11 with the evaluated data of Seltzer and Berger (1982). Care is taken when possible to model the same physical chemical state. (See specific tables for details.) Results for free atoms (Hartree-Fock wave functions for $Z \leq 10$ and screened wave functions elsewhere) and the accurate atomic values of Dehmer, Inokuti, and Saxon (1975) are presented in figure 2.11. It is clear that the trends in the first- and second-period elements are well approximated by the present application of the local plasma model, especially when the Pines correction is applied. The present results are generally in fair agreement with the compilation and recommendations of Seltzer and Berger (1982), although small discrepancies in the third period remain to be resolved.

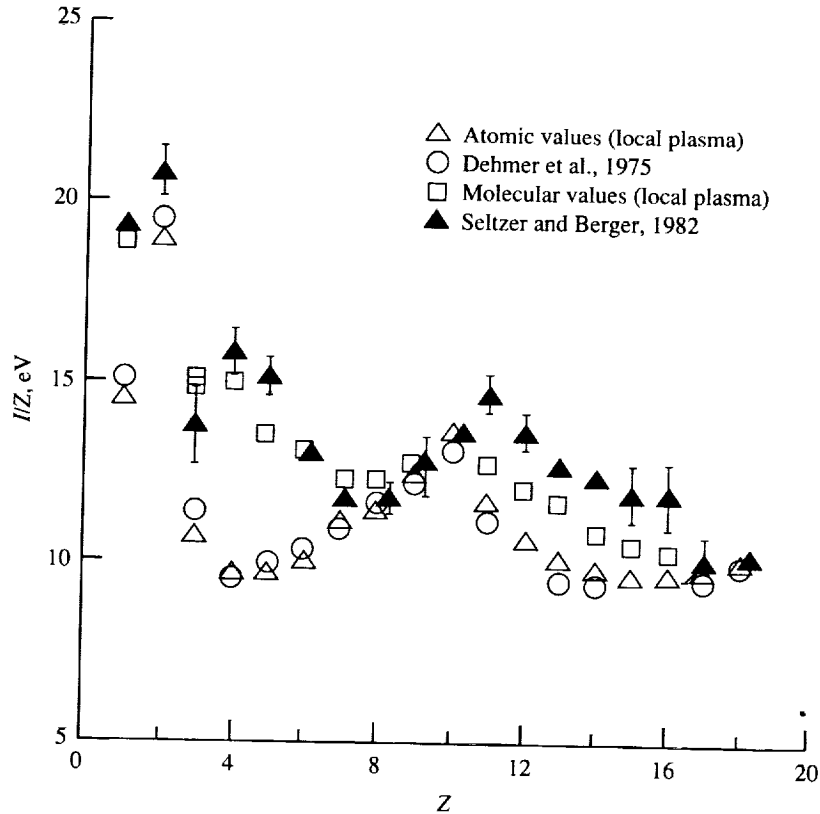


Figure 2.11. Mean excitation energies for atoms, molecules, solids, and metals. Specific data taken from tables 2.3, 2.4, 2.5, and 2.8.

Perhaps the greatest criticism of the present application of the local plasma model calculations is the use of the Gordon-Kim approximation to the covalent-bonded wave functions. When the moments of the energy spectrum are considered, it is clear that the Gordon-Kim model approximately adjusts the excitation spectrum in the region of greatest importance to ionizing radiation and appears no more in error than the basic plasma model in which it is used. (See fig. 2.5.) Of course, accurate use of the local plasma model implies the necessary use of the Pines correction, as demonstrated for the hydrogen atom in figure 2.3 and

used throughout the present calculations. Although the Pines correction produces marked improvements in the predictive capability of the model, further quantum corrections for the discrete spectrum would produce additional corrections and would hopefully remove most of the remaining error in the plasma model. Further improvement in electronic wave functions would be helpful in identifying the remaining corrections required for the plasma model.

2.4. Molecular Stopping Cross Sections

In section 2.3, departures from Bragg's rule have been noticed in the theoretical calculations of the mean excitation energies of various molecular systems. Analysis of the experimental data on energy loss of low-energy α -particles in gases also indicates deviations from Bragg's rule (Bourland and Powers, 1971; Lodhi and Powers, 1974). In this section, the stopping power theory of Lindhard and Winther (1964) and the local plasma theory of Lindhard and Scharff (1960) are used to perform calculations in the low-energy region. Modifications are introduced through a simplifying model which incorporates the effects of the shell corrections and of the screening of the projectile (Xu, Khandelwal, and Wilson, 1984a and 1984b). The model is justified on the basis of fulfilling the more ambitious aim of obtaining the molecular stopping power. The Gordon-Kim electron density model of molecular wave functions (Gordon and Kim, 1972) is utilized in the calculations. As shown, such a model allows a successful method of calculating chemical-bond effects. Calculations done on N_2 , O_2 , and water vapor are found to be in fair agreement with experiments (Xu, Khandelwal, and Wilson, 1984b). Furthermore, departures from Bragg's rule are noticed for all these systems.

The celebrated stopping power formula for an energetic charged particle of charge Z_P and velocity v traversing matter of charge number Z_T is given by

$$-\frac{dE}{dx} = \frac{4\pi Z_P^2 e^4}{mv^2} N Z_T L \quad (2.118)$$

where m is the mass of an electron and N the number of atoms per unit volume of the medium.

The stopping number L of equation (2.118) has been a topic of considerable study. For instance, Lindhard and Winther (1964) have investigated the function L for a free-electron gas in the regions of low- and high-energy incident charged particles. For the high-energy case, these authors give the expression for L to order $1/v^2$ as

$$L = Z_T \ln Y - \frac{\langle T \rangle}{\frac{1}{2}mv^2} \quad (2.119)$$

where $Y = 2mv^2/\hbar\omega_p$, the classical plasma frequency $\omega_p = (4\pi\rho e^2/m)^{1/2}$, ρ is the electron density, and $\langle T \rangle$, the average kinetic electron energy, is given by

$$\langle T \rangle = \left(\frac{3}{10} \right) mv_F^2$$

where v_F is the Fermi velocity.

For the low-energy case, they give

$$L = \left(\frac{\chi^2}{3}\right)^{3/4} Y^{3/2} C_1(\chi) \quad (2.120)$$

where

$$C_1(\chi) = \frac{1}{2[1 - (\chi^2/3)]^2} \left(\ln \frac{1 + \frac{2}{3}\chi^2}{\chi^2} - \frac{1 - \frac{1}{3}\chi^2}{1 + \frac{2}{3}\chi^2} \right) \quad (2.121)$$

with

$$\chi^2 = \frac{e^2}{\pi \hbar v_F} \quad (2.122)$$

$$\hbar = \frac{h}{2\pi} \quad (2.123)$$

Equation (2.119) for the L function warrants some discussion. First, one notes that the L function of equations (2.119) and (2.120) is derived by Lindhard and Winther for a free-electron system. Transition to an atomic system of the first term of equation (2.119), as studied widely, is accomplished under the so-called local plasma model in which density $\rho(\vec{r})$ is evaluated by using quantum mechanical wave functions. The local plasma model is equivalent to replacing the molecular dipole oscillator strengths by the corresponding classical plasma absorption spectrum. The adequacy of such a replacement was recently shown by Johnson and Inokuti (1983) to be most accurate for evaluating atomic quantities associated with stopping power in spite of differences between the plasma spectrum and the actual oscillator strength distribution. A quantum mechanical analog of the second term of equation (2.119) would be of interest. In this context, a result first derived by Brown would prove to be useful. Brown (1950) studied the K -shell asymptotic stopping power of a hydrogenic system (with two K electrons) for a fast projectile, taking the maximum momentum transfer equal to $2mv$ as if the electron was free. (See Xu, Khandelwal, and Wilson, 1986.) The asymptotic stopping power equation obtained by Brown can be expressed in a form similar to equation (2.119). The first terms of both these equations, since they involve the mean excitation energy, can be assumed essentially equivalent within the local-plasma approximation. For the second term in equation (2.119) for a hydrogenic system, he obtained $1/\eta_s$, where $\eta_s = \frac{1}{2}mv^2/Z_s^2R$, Z_s is the effective nuclear charge for the s shell ($s = K, L, \dots$), and R is the Rydberg constant. Walske (1952), on the other hand, taking the upper limit for momentum transfer as infinity, overestimated the nuclear momentum recoiling and obtained $2/\eta_s$ instead. In reality, however, because of the recoiling of the nucleus, the result should be expected to fall somewhere between $1/\eta_s$ and $2/\eta_s$. This fact is incorporated into equation (2.126) as a parameter which we later estimate. At the present, however, for the sake of simplicity, combining Brown's result for the K shell with Walske's result for the L shell, but retaining the consistency with the free-electron model, we write the analogous second term (known as shell correction C) for a hydrogenic system with Z_T electrons as

$$C = C_{K,\text{total}} + C_L = \frac{1}{\eta_K} + \frac{1}{\eta_L} \left(\frac{Z_T - 2}{8} \right) \quad (2.124)$$

which can be rewritten for a real atom as

$$C = \frac{1}{2} \frac{\langle T \rangle}{\frac{1}{2} m v^2} \phi(Z_T) \quad (2.125)$$

where

$$\phi(Z_T) = Z_T f(Z_T) g \quad (2.126)$$

and

$$\langle T \rangle = \frac{1}{Z_T} \left[Z_K^2 R + (Z_T - 2) \frac{1}{4} Z_L^2 R \right] \quad (2.127)$$

In equation (2.126), a coefficient $f(Z_T)$ has been introduced to distinguish a real atom from a hydrogenic atom. The coefficient $f(Z_T)$ is known to be less than unity for L shells for targets with low atomic number. The coefficient g is introduced to incorporate the effect due to the recoiling of the nucleus.

At this stage, it is appropriate to discuss various features associated with the low-energy projectiles and the targets with low atomic number. First, in the low-energy region, the projectile's full charge Z_P will not be operational in the stopping process due to electron capture that is influenced mainly by the outer shell electrons of the medium. Second, Walske has pointed out that the coefficient $f(Z_T)$ is unreliable for the low atomic number $Z_T \leq 30$ due to use of the hydrogenic wave functions.

It is evident from the above observations that some sort of crude estimate of the quantity C is in order. This is justified since the usual incorporation of these effects involves fitting with experimental data. The inclusion of the effect of the projectile's effective charge should decrease the stopping number of all elements. The decrease should be the most for Li and the least for Ne. In order to incorporate this effect and the other problem of the need for an accurate value of the coefficient $f(Z_T)$, it is reasonable as a first approximation to assume a semiempirical constant value of the quantity $\phi(Z_T)$ equal to one half the total number of electrons in noble-gas atoms. Such a division should overestimate shell corrections for lithium and beryllium in decreasing fashion and underestimate that for helium, neon, carbon, nitrogen, oxygen, and fluorine also in a decreasing manner. Such a change in shell corrections is indeed needed to compensate for the effect of the effective charge of the projectile on the stopping power. In this paper since we are interested in the atoms with atomic number below 10, this assumption implies that

$$\phi(Z_T) = \begin{cases} 1 & (Z_T \leq 2) \\ 5 & (3 \leq Z_T \leq 10) \end{cases} \quad (2.128)$$

Implicit in the above partition of ϕ (eq. (2.128)) is the fact that the quantity C no longer represents the so-called shell corrections only but presumably also some other effects including those of the projectile's effective charge and the neglect of the higher order terms in equation (2.119). One can now write equation (2.125)

as

$$\frac{C}{Z_T} = \begin{cases} \frac{1}{2} \frac{\langle T \rangle}{\frac{1}{2} m v^2} \frac{1}{Z_T} & (Z_T \leq 2) \\ \frac{1}{2} \frac{\langle T \rangle}{\frac{1}{2} m v^2} \frac{5}{Z_T} & (3 \leq Z_T \leq 10) \end{cases} \quad (2.129)$$

where $\langle T \rangle$ by virial theorem is just the average kinetic energy of the electron and should be averaged over all the Z_T electrons in the atom.

In order to make a transition to an atomic system, we assume the above results and accordingly replace equation (2.119) with

$$L = \begin{cases} \ln Y - \frac{3^{1.5}}{10\chi Z_T} \frac{1}{Y} & (Z_T \leq 2) \\ \ln Y - \frac{3^{1.5}}{2\chi Z_T} \frac{1}{Y} & (3 \leq Z_T \leq 10) \end{cases} \quad (2.130)$$

The low- and high-energy L functions should now be combined to determine the appropriate dependence of the stopping power on energy. To do this, we used equations (2.120) and (2.130) for our desired results after replacing ω_p by $\gamma\omega_p$, where nonconstant values of γ were obtained from Wilson and Xu (1982). Bonderup (1967) had combined equations (2.119) and (2.120) and assumed a constant value of γ equal to $\sqrt{2}$. Unlike Bonderup, we tried to preserve the continuity between the low-energy stopping number function given by equation (2.120) and the high-energy function given by equation (2.130). In this way, stopping number values for a system can be obtained given the velocity of the projectile and the density $\rho(\vec{r})$.

For a diatomic molecule, the Gordon-Kim model gives the density as

$$\rho_{\text{molecule}} = \rho_a(\vec{r}) + \rho_b(\vec{r} - \vec{R}_{ab}) \quad (2.131)$$

where $\rho_a(\vec{r})$ is the atomic ground-state density and \vec{R}_{ab} is the distance between the two atoms, which is known to be 1.094 Å for N₂ and 1.207 Å for the O₂ molecule. Equation (2.131) was generalized for water vapor including its partial ionic-bond nature and neglecting the overlap between the two H atoms. The distance between the O and H nuclei was taken as 0.958 Å. The molecular stopping power for protons was obtained by averaging the stopping number over \vec{r} for N₂, O₂, and water vapor molecules. Hartree-Fock wave functions were employed in these calculations. Tables 2.9 and 2.10 list the results of the present work, together with curve-fitted results of Andersen and Ziegler (1977), and two sets of experimental data for the O₂ and N₂ molecules, respectively, (Reynolds et al., 1953; Langley, 1975). In table 2.11, the results for water vapor from the present work and experimental data for energies ranging from 40 to 500 keV are presented. Good agreement, within 10 percent, is found between the two sets of data.

Table 2.9. Proton Stopping Cross Sections for Oxygen Molecule

<i>E</i> , keV	Proton stopping cross section, eV-cm ² /10 ¹⁵ atoms			
	Theoretical (a)	Curve fitted (b)	Experimental	
			Reynolds et al., 1953	Langley, 1975
40	15.89	14.6	15.2 ± 2.6	
80	17.48	17.0	17.25 ± 2.6	
100	17.43	17.0	17.17 ± 2.6	
300	11.84	11.9	11.99 ± 1.7	
500	8.92	8.8	8.84 ± 1.7	
1037	5.64			5.25
2591	2.97			2.85

^aPresent paper.^bAndersen and Ziegler, 1977.

Table 2.10. Proton Stopping Cross Sections for Nitrogen Molecule

<i>E</i> , keV	Proton stopping cross section, eV-cm ² /10 ¹⁵ atoms			
	Theoretical (a)	Curve fitted (b)	Experimental	
			Reynolds et al., 1953	Langley, 1975
40	17.20	16.0	17.1 ± 2.6	
80	18.41	17.9	18.5 ± 2.6	
100	17.79	17.7	17.9 ± 2.6	
300	10.85	11.2	11.2 ± 1.7	
500	8.10	8.1	8.08 ± 1.7	
1037	5.20			4.78
2591	2.71			2.56

^aPresent paper.^bAndersen and Ziegler, 1977.

In order to discuss the departures from Bragg's rule, it would be relevant to cite a systematic study carried out in a series of experiments at Baylor University (Bourland and Powers, 1971; Powers et al., 1972; Lodhi and Powers, 1974). The study revealed that for low-energy projectiles there may exist a deviation from Bragg's rule depending on the physical state, but most importantly, on the chemical structure of the compounds. The confusing status of the dependence on the chemical structure can best be described by citing these studies in chronological order. First, in 1971 the Baylor group (Bourland and Powers, 1971)

theorized that the compounds with single and double bonds should obey Bragg's rule. The compounds containing triple-bond structures were found to deviate from Bragg's rule by as much as 12.8 percent (α -particles of energy between 0.3 and 2.0 MeV often were the projectiles). In particular, these authors indicated that the molecular hydrogen (single-bonded molecule) should obey Bragg's rule. Later in 1972, the Baylor group (Powers et al., 1972) critically looked again at their previous conclusions. They indicated that perhaps the hydrogen atomic stopping cross section may be considerably different than one half the molecular stopping cross section and thus should cause considerable deviations. However, the Baylor group in 1974 (Lodhi and Powers, 1974) recognized the difficulty of obtaining atomic cross sections experimentally and based their analysis on the existence of some modified, but unique, atomic stopping cross sections.

Table 2.11. Proton Stopping Cross Sections for Water Vapor

Source	Proton stopping cross section, eV-cm ² /10 ¹⁵ molecules, at <i>E</i> , keV, of—				
	40	80	100	300	500
Present paper	28.81	27.8	26.8	17.1	12.6
Reynolds et al., 1953	25.0 ± 2.6	27.6 ± 2.6	27.3 ± 2.6	17.9 ± 1.7	13.0 ± 1.7

It is therefore imperative that in order to discuss the deviations from Bragg's rule, one must have access to the atomic and molecular stopping cross sections. We calculated both the atomic and the molecular stopping cross sections as a function of projectile energy of the O₂, N₂, and H₂ molecules. These results, together with the deviations from Bragg's rule, are exhibited in tables 2.12 through 2.14. One sees that the deviations from Bragg's rule become small as incident energy increases—in agreement with observations made by many workers including those at Baylor University. It is to be noted that N₂ is a triple-bonded molecule, O₂ is an approximately double-bonded molecule (from the bond energy point of view), and H₂ is a single-bonded molecule. The maximum deviations from Bragg's rule for energy of 100 keV and above are 6.1, 2.6, and 10 percent, respectively, for these molecules. Thus, the deviation depends on the chemical structure. When the Gordon-Kim model is used, the overlap of electron density determines the deviation or molecular bond effects. For instance, for the hydrogen molecule, the distance between nucleons is very small, 0.74 Å. It is expected that the overlap of electron density is large, thus explaining the considerable deviation from Bragg's rule. The stronger the bond energy, the shorter the distance will be. It is interesting to note that single-, double-, and triple-bonded carbon molecules have internuclear distances equal to 2.94, 2.52, and 2.24 bohrs, respectively. We may thus expect that the triple-bonded carbon will have more deviation from Bragg's rule than the single-bonded carbon.

Table 2.12. Deviations From Bragg's Rule for Oxygen Molecule

Stopping cross section	E , keV, of—						
	40	100	200	300	500	1037	100 000
ϵ (atomic) ^a , eV-cm ² /10 ¹⁵ atoms . . .	17.44	17.48	14.65	12.15	9.1	5.72	0.1492
ϵ (molecule), eV-cm ² /10 ¹⁵ atoms . . .	15.89	17.43	14.36	11.84	8.92	5.64	0.1476
Deviation, percent	8.9	0.3	2	2.6	2	1.4	1.1

^aObtained from equations (2.116) and (2.126).

Table 2.13. Deviations From Bragg's Rule for Nitrogen Molecule

Stopping cross section	E , keV, of—						
	40	100	200	300	500	1037	100 000
ϵ (atomic) ^a , eV-cm ² /10 ¹⁵ atoms . . .	19.33	18.57	14.32	11.46	8.53	5.30	0.1340
ϵ (molecule), eV-cm ² /10 ¹⁵ atoms . . .	17.20	17.79	13.75	10.85	8.10	5.20	0.1319
Deviation, percent	11	4.2	4.00	6.1	5.0	1.9	1.3

^aObtained from equations (2.116) and (2.126).

Table 2.14. Deviations From Bragg's Rule for Hydrogen Molecule

Stopping cross section	E , keV, of—						
	100	200	300	500	800	1037	2591
ϵ (atomic) ^a , eV-cm ² /10 ¹⁵ molecules . .	12.7	8.13	6.1	4.17	2.89	2.36	1.11
ϵ (molecule), eV-cm ² /10 ¹⁵ molecules .	11.43	7.53	5.71	3.93	2.75	2.24	1.07
Deviation, percent	10	7.4	6.4	5.8	4.8	5.1	3.6

^aObtained from equations (2.116) and (2.126).

2.5. Stopping Cross Sections of Liquid Water. The stopping cross section of water is of interest in many fields but especially in radiation protection. Since the living tissues are basically composed of liquid water, a simple theoretical model for the calculation of the stopping power of water is of great practical interest. The importance of such a direct calculation has increased since various authors (Bourland and Powers, 1971; Powers et al., 1972; Lodhi and Powers, 1974) found that deviations from Bragg's rule may exist in the low-energy regime; meanwhile, the physical-state effect has also been observed in many experiments.

In previous work (Xu, Khandelwal, and Wilson, 1984a), we have established a modified local plasma model, based on the works of Lindhard and Winther (1964),

Brown (1950), and Walske (1952 and 1956). The model, applied to molecules using the Gordon-Kim molecular wave function (Gordon and Kim, 1972), has shown reasonable predictive capability for molecular bond effects as well as for atomic targets and covers a rather wide energy region.

In this section the modified local plasma model is applied to liquid water by employing a simple model of water molecules (Xu, Khandelwal, and Wilson, 1985). The calculated stopping cross section of liquid water is found to be about 5.5 to 14 percent lower than the calculated gas-state results for energies from 80 to 500 keV and is about 8.5 to 13.4 percent lower than gas-state results in the same energy range measured by Reynolds et al. (1953). The calculated liquid-water stopping power is within 2.5 percent of experimental values for ice in the energy range of 60 to 500 keV. It is proposed that for liquid water, this physical effect is due to interactions with neighbor molecules which confine each molecule to an effective close-packed sphere, thus causing the electrons to be more bonded and confined. Hence, the momentum transfer between projectile and electrons is reduced; this reduction decreases stopping power.

As is well-known, the structure of liquid water is complicated and far from completely known. As Pauling (1960) pointed out, "the structure for water that has received serious consideration for many years is the one proposed by Bernal and Fowler." Bernal and Fowler (1933) suggested that liquid water retains in part a hydrogen-bonded structure, similar to that of ice. They pointed out that as more and more hydrogen bonds are broken with increase in temperature, the oxygen atoms rearrange themselves into an approximately more and more close-packed structure. The rigidity of the hydrogen-bonded crystal structure is lost, allowing the motion between liquid molecules to be more flexible than that in the ice. A simple model of the close-packed structure of liquids was considered by Lennard-Jones and Devonshire (1937 and 1938) who derived the potential of the molecule in the liquid state from the interaction of all neighbors (fig. 2.12). Figure 2.12 shows clearly the effective volume to which the molecule is confined.

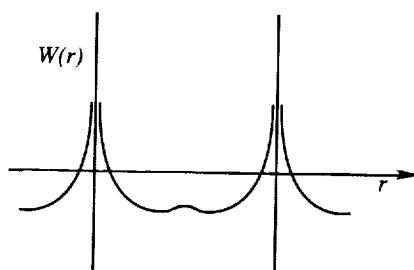


Figure 2.12. Intermolecular potential of molecule in liquid phase (Lennard-Jones and Devonshire, 1937 and 1938).

The hydrogen bond of the ice structure is rather weak compared with the molecular O-H bond. When ice melts, these hydrogen bonds of ice are distorted, and finally many are broken. Therefore, as a first-order approximation in the stopping power calculation, we can ignore the electronic overlap between

molecules. As was pointed out by Xu, Khandelwal, and Wilson (1984a), the overlap of the electronic density in some sense expresses the bond energy or molecular bonding effect. The simplest model of this picture is to confine each molecule inside its close-packed sphere. Hence, the electronic density of this water molecule vanishes at distances exceeding the sphere radius, as shown in figure 2.13.

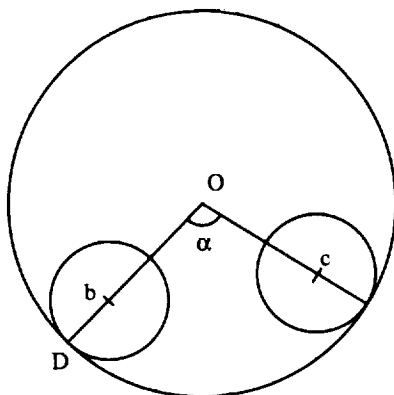


Figure 2.13. Liquid-water molecule in its close-packed spherical configuration.

In figure 2.13, O is the center of an oxygen atom, b and c are centers of two hydrogen atoms, α is the angle between two O-H bonds, and Ob is the distance between the center of the oxygen and the center of the hydrogen atom ($Ob = 1.01 \text{ \AA}$) obtained by neutron diffraction of deuterium oxide ice (Peterson and Levy, 1957). The radius OD is obtained from the effective volume per molecule V_{eff} as $R = (3V_{\text{eff}}/4\pi)^{1/3} = 2.992$ bohrs. Inside the sphere, the Gordon-Kim model is employed; this model assumes that the molecular electronic density to first-order approximation is simply the algebraic sum of corresponding atomic electron densities. The molecular density for H_2O can be expressed as follows:

$$\rho_{\text{mol}} = \rho_{\text{O}}(\vec{r}) + \rho_{\text{H}}(\vec{r} - \vec{R}_{\text{Ob}}) + \rho_{\text{H}}(\vec{r} - \vec{R}_{\text{Oc}}) \quad (2.132)$$

where \vec{R}_{Ob} and \vec{R}_{Oc} are displacement vectors of the nuclei at b and c, respectively (fig. 2.13). Since the radius of the hydrogen atom is much smaller than that of oxygen, the internuclear distance between the hydrogen atoms is large compared with their radii and the H-H interaction may be neglected within the H_2O molecule. Thus,

$$\rho_{\text{mol}} = \rho_{\text{O}}(\vec{r}) + 2\rho_{\text{H}}(\vec{r} - \vec{R}) \quad (2.133)$$

The partial ionic-bond effects are considered through

$$\rho_{\text{mol}} = \rho_{\text{O}}^+(\vec{r}) + 2\rho_{\text{H}}^-(\vec{r} - \vec{R}) \quad (2.134)$$

with $\rho^{\pm} = (1-p)\rho(\vec{r}) + p\rho^{\pm}(\vec{r})$, where p is the partial ionic fraction with $\rho(\vec{r})$ the neutral-atom electron density and $\rho^{\pm}(\vec{r})$ the ionic electron density. In the water molecule, according to Pauling (1960), p equals 0.33. The wave functions are obtained from Clementi and Roetti (1974). These wave functions are renormalized

within the close-packed sphere according to

$$\int_{V_{\text{eff}}} \rho_{\text{mol}} d^3\vec{r} = 10 \quad (2.135)$$

The above electronic density is to be used with the formula for stopping power given by

$$-\frac{dE}{dx} = \frac{4\pi Z_P^2 e^4}{mv^2} N Z_T L \quad (2.136)$$

where m is the mass of an electron, N is the number of atoms per unit volume of the medium, Z_P is the charge of the projectile, and Z_T is the charge number of target; L is given elsewhere (Xu, Khandelwal, and Wilson, 1984a and 1984b). For the low projectile energies,

$$L = \left(\frac{\chi^2}{3}\right)^{3/4} Y^{3/2} C_1(\chi) \quad (2.137)$$

where

$$C_1(\chi) = \frac{1}{2(1 - \frac{\chi^2}{3})^2} \left(\ln \frac{1 + \frac{2\chi^2}{3}}{\chi^2} - \frac{1 - \frac{\chi^2}{3}}{1 + \frac{2\chi^2}{3}} \right) \quad (2.138)$$

where $\chi^2 = e^2/\pi\hbar v_F$, $\hbar = h/2\pi$, v_F is the Fermi velocity, $Y = 2mv^2/\gamma\hbar\omega_p$, $\omega_p^2 = 4\pi e^2\rho/m$ is the classical plasma frequency, and ρ is the electronic density. For high projectile energies

$$L = \begin{cases} \ln Y - \frac{3\sqrt{3}}{10\chi} \frac{1}{Y} & (Z_T \leq 2) \\ \ln Y - \frac{3\sqrt{3}}{2\chi Z_T} \frac{1}{Y} & (3 \leq Z_T \leq 10) \end{cases} \quad (2.139)$$

The low- and high-energy L functions should be combined by joining them continuously (Xu, Khandelwal, and Wilson, 1984a and 1984b).

Table 2.15 shows the proton stopping cross section values of water vapor and liquid water together with the experimental results of water vapor measured by Reynolds et al. (1953). As can be seen, the agreement between the experiments and the theory is very good. There is a marked reduction in stopping power in the liquid phase by a few percent even at the highest energies shown. As noted by Thwaites (1981), there appears to be little difference between the stopping power of water in the liquid phase and of ice. (See, in particular, fig. 2 of Thwaites (1981).) The experimental data of Wenzel and Whaling (1952) for ice are shown in comparison with the calculated values for liquid water. The results given in table 2.15 are shown graphically in figure 2.14.

Table 2.15. Proton Stopping Cross Sections for Water

E , keV	Proton stopping cross section, $\text{eV}\cdot\text{cm}^2/10^{15}$ molecules			
	Theoretical ^a		Experimental	
	Water vapor	Liquid water	Vapor ^b	D ₂ O ice ^c
40	28.7	21.6	25.0 ± 2.6	22.6
60	28.6	23.5	26.9 ± 2.6	24.0
80	27.8	23.9	27.6 ± 2.6	24.0
100	26.8	23.7	27.3 ± 2.6	23.7
200	21.1	19.5	22.0 ± 1.7	20.1
300	17.1	16.0	17.9 ± 1.7	16.0
400	14.4	13.6	15.0 ± 1.7	13.3
500	12.6	11.9	13.0 ± 1.7	11.6
600	11.2	10.7		
700	10.1	9.7		
800	9.3	8.9		
900	8.6	8.2		
1 000	8.0	7.6		
10 000	1.37	1.34		

^aPresent theory with partial ionic fraction of $p = 0.33$.

^bReynolds et al., 1953.

^cWenzel and Whaling, 1952.

We see from table 2.15 that the calculated stopping cross section of liquid water is about 5.6 to 14 percent lower than calculated gas-state results from 80 to 500 keV and is about 8.5 to 13.4 percent lower than measured gas-state results. In the same energy regime, Matteson, Powers, and Chau (1977) reported that in their experimental results for 0.3- to 2.0-MeV α -particles, the stopping cross section of H₂O vapor was found to be 4 to 12 percent higher than that of *ice*. This difference is less than that found previously for protons (10 to 14 percent) in the same velocity interval. Thwaites (1981) reported that for α -particles down to 1.8 MeV, the stopping cross section of H₂O vapor was found to be ~ 4 percent higher than that of *liquid water*. In the same velocity interval, our calculated results show that the proton stopping cross section of water vapor is about 5.6 percent higher than that of liquid water. The work of De Carvalho and Yagoda (1952) and Ellis, Rossi, and Failla (1955) found that the stopping cross section of 5- to 8-MeV α -particles in H₂O was the same in the vapor and condensed states. Wenzel and Whaling (1952) and Reynolds et al. (1953) found a greater stopping cross section for protons in the vapor states of H₂O than in the solid state, and Palmer (1966) observed the stopping cross section for α -particles to be less in the liquid than in the vapor state of H₂O. This physical-state effect is observed by most experimental physicists. The results of De Carvalho and Yagoda (1952) and Ellis, Rossi, and Failla (1955) may be explained since, in the high-energy regime, this effect becomes less important. This tendency is also exhibited in our calculated results. Palmer (1966) tried to explain this effect as a low-energy polarization screen effect. Matteson, Powers, and Chau (1977) explained it as an aggregation effect.

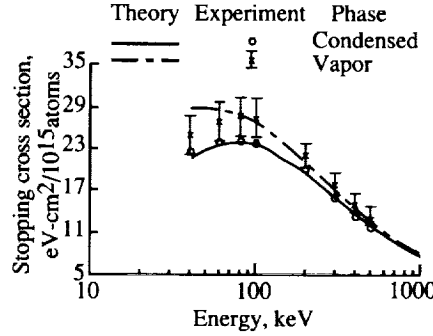


Figure 2.14. Proton stopping cross section of water molecules in vapor and condensed phases.

We now consider the effect according to the local plasma model. We will first explain the molecular effect or deviation from Bragg's rule. It is found that in the low-energy regime, the molecular stopping power may be lower than the atomic stopping power calculated by employing Bragg's rule. This is due to the fact that when an electron in a molecular gas is more bonded than in an atomic gas caused by the chemical bond, the momentum transfer between projectile and the electron becomes harder, causing decreased energy loss or stopping power of the projectile. In the formula

$$L = \ln Y - \frac{3\sqrt{3}}{10\chi Z_T} \frac{1}{Y} = \ln \left(\frac{2mv^2}{\gamma\hbar\omega_\rho} \right) - \frac{1}{Z_T} \frac{\langle T \rangle}{mv^2} \quad (Z_T \leq 2) \quad (2.140)$$

where $\omega_\rho \approx \sqrt{\rho}$ and the average kinetic energy of electron $\langle T \rangle = \frac{3}{10}mv_F^2\rho^{2/3}$ are functions of electronic density. The chemical bond causes an increased electron density in the interatomic space and, hence, increased mean excitation energy and average kinetic energy. Physically, when an electron is more bonded, it is harder to excite, resulting in increased mean excitation energy. When an electron is more bonded, the magnitude of the total energy is increased (in bonded states), since $\langle T \rangle = |\langle E \rangle|$, the average kinetic energy is increased. Both effects tend to decrease the stopping power. In the low-energy regime, this effect becomes more important, mainly due to the contribution of the $\langle T \rangle$ term. In the high-energy regime, this term vanishes. The mean excitation term also becomes less important due to the influence of the factor $1/v^2$. Meanwhile, in liquid water, many of these hydrogen bonds between molecules are broken; also, compared with the partial ionic bond, the hydrogen bond is weaker. With this picture of molecular bond effects, how are we to understand the considerable difference of stopping cross section due to the physical state?

Matteson, Powers, and Chau (1977) correctly pointed out that the physical-state effects are due to the effects of aggregation upon the molecules. As mentioned previously, in liquid water these hydrogen bonds are not the main reason for this physical effect. Rather, it is a collective effect of the whole liquid-water molecule, since liquid molecules are more mobile than those in ice. Because of the interactions with all its neighbors each molecule is confined in an effective volume. This can be seen from figure 2.12, where we show $W(r)$ as the average

potential of each molecule due to the interactions of all neighbors, according to the well-known Lennard-Jones and Devonshire theory (1937 and 1938). Thus, as a part of the molecule, electrons are more difficult to remove from this volume or more difficult to be excited. Simply said, the electrons are more bound because of the neighborhood interactions. This confinement of the electron causes less momentum transfer between the projectile and the electrons and decreases the stopping power. Our local plasma model describes this picture because the electronic density is more concentrated so that both the mean excitation energy and average kinetic energy terms are increased and cause a decrease in the stopping power. Moreover, we notice that the structure of ice is more open than that of liquid water. It is reasonable to expect a slight difference of stopping cross section between ice and liquid water.

2.6. Semiempirical Methods

In passing through an ordinary material, an ion loses the larger fraction of its energy to electronic excitation of the material. Although a satisfactory theory of high-energy ion-electron interaction is available in the form of Bethe's theory utilizing the Born approximation, an equally satisfactory theory for low energies is not available. Bethe's high-energy approximation to the energy loss per unit path (that is, stopping power) is given as

$$S_e = \frac{4\pi N Z_P^2 Z_T e^4}{mv^2} \left\{ \ln \left[\frac{2mv^2}{(1-\beta^2)I_T} \right] - \beta^2 - \frac{C}{Z_T} \right\} \quad (2.141)$$

where Z_P is the projectile charge, N is the number of target molecules per unit volume, Z_T is the number of electrons per target molecule, m is the electron mass, v is the projectile velocity, $\beta = v/c$, c is the velocity of light, C is the velocity-dependent shell correction term (Walske and Bethe, 1951), and I_T is the mean excitation energy given by

$$Z_T \ln(I_T) = \sum_n f_n \ln(E_n) \quad (2.142)$$

where f_n represents the electric dipole oscillator strengths of the target and E_n represents the corresponding excitation energies. Note that the sum in equation (2.142) includes discrete and continuum levels. Empirically it has been observed that molecular stopping power is reasonably approximated by the sum of the corresponding empirically derived atomic stopping powers for which equations (2.141) and (2.142) imply that

$$Z_T \ln(I_T) = \sum_j n_j Z_j \ln(I_j) \quad (2.143)$$

where Z_T and I_T pertain to the molecule, Z_j and I_j are the corresponding atomic values, and n_j is the stoichiometric coefficient. This additive rule (eq. (2.143)), usually called Bragg's rule (Bragg and Kleeman, 1905), is the basis for providing stopping cross sections for arbitrary material compositions.

Sources of deviations from Bragg's additive rule for molecules and for the condensed phase are discussed. Aside from shifts in excitation energies and

adjustments in line strengths as a result of molecular bonding, new terms in the stopping power appear due to coupling between vibrational and rotational modes. Additionally, in the condensed phase, some discrete transitions are moved into the continuum, and collective modes among valence electrons in adjacent atoms produce new terms in the absorption spectrum that needs to be dealt with. Platzman (1952a and 1952b) proposed that the experimentally observed additive rule may not show that molecular stopping power is the sum of atomic processes but rather demonstrates that molecular bond shifts for covalent-bonded molecules are relatively independent of the molecular combination as was theoretically demonstrated in section 2.3.4. On the basis of such arguments, Platzman suggested that ionic-bonded substances should be studied as a rigid test of the additive rule because of the radical difference in bonding type. He further estimated that ionic-bond shifts could change the stopping power by as much as 50 percent. Recent results on molecular bond shifts and condensed phase effects on mean excitation energies were discussed in section 2.5 (Wilson and Kamaratos, 1981; Wilson and Xu, 1982; Wilson et al., 1982).

The electron stopping power for protons is adequately described by equation (2.141) for energies above 500 keV for which the shell or "tight binding" correction C makes an important contribution below 10 MeV (Andersen and Ziegler, 1977; Janni, 1982a and 1982b). For proton energies below 500 keV, charge exchange (electron transfer) reactions alter the proton charge over much of its path; therefore, equation (2.141) is to be understood in terms of an average over the proton charge states. Normally an average over the charge states is introduced into equation (2.141) so that the effective charge is the root-mean-square ion charge and not the average ion charge. At any ion energy, charge equilibrium is established very quickly in all materials. Utilizing the effective charge in equation (2.141) appears to make only modest improvement below 500 keV, presumably an indication of the failure of this theory based on an empirical basis (Andersen et al., 1977; Janni, 1966, 1982a, and 1982b). The resultant stopping power for protons in water is shown along with the evaluated data of Bichsel (1963) in figure 2.15.

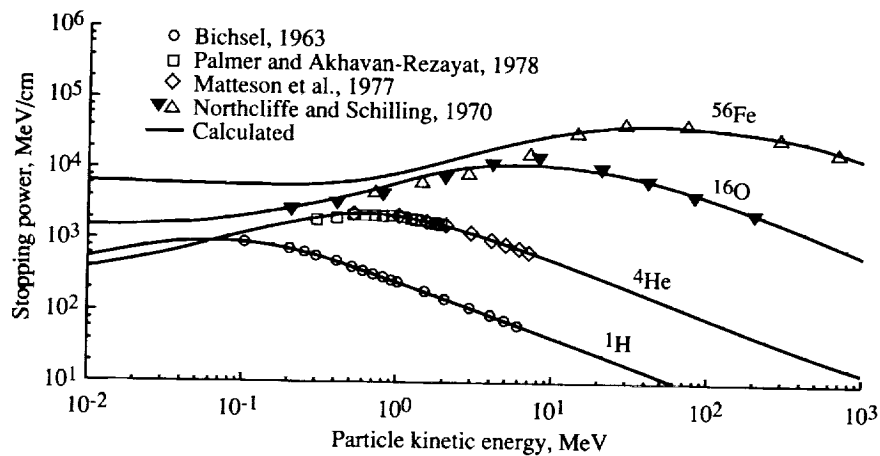


Figure 2.15. Calculated and experimental stopping powers in water for typical cosmic-ray ions as function of particle kinetic energy.

The electronic stopping power for α -particles requires terms in equation (2.141) of higher order in the projectile charge Z_P resulting from corrections to the Born approximation. The alpha and proton stopping powers cannot be related through their effective charges. Parametric fits to experimental data are given by Ziegler (1977) for all elements in both the gaseous and condensed phases.

The electronic stopping powers for heavier ions are related to the alpha stopping power through their corresponding effective charges. The effective charge suggested by Barkas (1963) is used:

$$Z^* = Z_P \left[1 - \exp \left(\frac{-125\beta}{Z_P^{2/3}} \right) \right] \quad (2.144)$$

where Z_P is the atomic number of the ion.

At sufficiently low energies, the energy lost by an ion in a nuclear collision becomes important. The nuclear stopping theory used in this report is a modification of the theory of Lindhard, Scharff, and Schiott (1963). The reduced energy is given as

$$\epsilon = \frac{32.53 A_P A_T E}{Z_P Z_T (A_P + A_T) (Z_P^{2/3} + Z_T^{2/3})^{1/2}} \quad (2.145)$$

where E is in units of keV/nucleon and A_P and A_T are the atomic masses of the projectile and target. The nuclear stopping power in reduced units (Ziegler, 1977) is

$$S_n = \left\{ \begin{array}{ll} 1.59\epsilon^{1/2} & (\epsilon < 0.01) \\ \frac{1.7\epsilon^{1/2} \ln[\epsilon + \exp(1)]}{1 + 6.8\epsilon + 3.4\epsilon^{3/2}} & (0.01 < \epsilon < 10) \\ \frac{\ln(0.47\epsilon)}{2\epsilon} & (10 < \epsilon) \end{array} \right\} \quad (2.146)$$

and the conversion factor to units of eV-cm²/10¹⁵ atoms is

$$f = \frac{8.426 Z_P A_T A_P}{(A_P + A_T) (Z_P^{2/3} + Z_T^{2/3})^{1/2}} \quad (2.147)$$

The total stopping power S_j is obtained by summing the electronic and nuclear contributions. Other processes of energy transfer such as Bremsstrahlung and pair production are unimportant.

For energies above a few MeV per nucleon, Bethe's equation is adequate provided that appropriate corrections to Bragg's rule (Wilson et al., 1984a and 1984b), shell corrections (Janni, 1982a and 1982b), and an effective charge are included. Electronic stopping power for protons is calculated from the parametric formulas of Andersen and Ziegler (1977). The calculated stopping power for

protons above a few MeV in water is shown in figure 2.15 along with data given by Bichsel (1963).

Because alpha stopping power is not derivable from the proton stopping power formula using the effective charge at low energy, the parametric fits to empirical alpha stopping powers given by Ziegler (1977) are used. Applying his results for condensed phase, water poorly represented the data of Matteson, Powers, and Chau (1977) and Palmer and Akhavan-Rezayat (1978). Considering that the physical-state and molecular binding effects are most important for hydrogen (Wilson and Kamaratos, 1981), the water stopping power was approximated by using the condensed phase parameters for hydrogen and the gas phase parameters for oxygen (which are known experimentally). These results are presented along with experimental data for condensed phase water in figure 2.15. It appears that Ziegler overestimated the condensed phase effects for oxygen since the gas phase oxygen data give satisfactory results as seen in figure 2.15.

Electronic stopping powers for ions with a charge greater than 2 are related to the alpha stopping power through the effective charge given by equation (2.144). For water, the condensed phase formula of Ziegler for α -particles probably gives the best stopping powers for heavier ions. Calculated results for ^{16}O and ^{56}Fe ions in water, shown in figure 2.15 along with the Northcliffe and Schilling (1970) results for ^{56}Fe ions, are especially important, since their data seem to agree with the range measured in General Electric Lexan plastic by J. H. Chan (Fleischer, Price, and Walker, 1975).

2.7. References

- Ahlen, Steven P., 1980: Theoretical and Experimental Aspects of the Energy Loss of Relativistic Heavily Ionizing Particles. *Reviews Modern Phys.*, vol. 52, no. 1, pp. 121-173.
- Andersen, H. H.; Bak, J. F.; Knudsen, H.; and Nielsen, B. R., 1977: Stopping Power of Al, Cu, Ag, and Au for MeV Hydrogen, Helium, and Lithium Ions Z_1^3 and Z_1^4 Proportional Deviations From the Bethe Formula. *Phys. Review A*, vol. 16, no. 5, pp. 1929-1940.
- Andersen, H. H.; and Ziegler, J. F., 1977: *Hydrogen—Stopping Powers and Ranges in All Elements*. Volume 3 of *The Stopping and Ranges of Ions in Matter*, J. F. Ziegler, organizer, Pergamon Press, Inc.
- Bakker, C. J.; and Segrè, E., 1951: Stopping Power and Energy Loss for Ion Pair Production for 340-Mev Protons. *Phys. Review*, vol. 81, second ser., no. 4, pp. 489-492.
- Barkas, Walter H., 1963: *Nuclear Research Emulsion—I. Techniques and Theory*. Academic Press, Inc.
- Bernal, J. D.; and Fowler, R. H., 1933: A Theory of Water and Ionic Solution, With Particular Reference to Hydrogen and Hydroxyl Ions. *J. Chem. Phys.*, vol. 1, no. 8, pp. 515-548.
- Bethe, H., 1930: Zur Theorie des Durchgangs schneller Korpuskularstrahlen durch Materie. *Ann. Phys.*, 5 Folge, Bd. 5, pp. 325-400.
- Bethe, H., 1933: Quantenmechanik der Ein- und Zwei-Elektronenprobleme. *Handbook of Physics*, Bd. XXIV, Kap. 3, Julius Springer (Berlin), pp. 273-560.

- Bethe, H. A., 1950: The Range-Energy Relation for Slow Alpha-Particles and Protons in Air. *Reviews Modern Phys.*, vol. 22, no. 2, pp. 213-219.
- Bethe, H. A.; Brown, L. M.; and Walske, M. C., 1950: Stopping Power of *K*-Electrons. *Phys. Review*, vol. 79, second ser., no. 2, p. 413.
- Bethe, Hans A.; and Ashkin, Julius, 1953: Passage of Radiations Through Matter. *Experimental Nuclear Physics*, Volume I, E. Segrè, ed., John Wiley & Sons, Inc., pp. 166-357.
- Bethe, Hans A.; and Salpeter, Edwin E., 1957: *Quantum Mechanics of One- and Two-Electron Atoms*. Academic Press.
- Bichsel, Hans, 1963: Passage of Charged Particles Through Matter. *American Institute of Physics Handbook*, Second ed., Dwight E. Gray, ed., McGraw-Hill Book Co., Inc., pp. 8-20-8-47.
- Bogaardt, M.; and Koudijs, B., 1952: On the Average Excitation Potentials and the Range-Energy Relations in Light Elements. *Physica*, vol. 18, pp. 249-264.
- Bohm, David; and Pines, David, 1951: A Collective Description of Electron Interactions. I. Magnetic Interactions. *Phys. Review*, vol. 82, second ser., no. 5, pp. 625-634.
- Bohm, David; and Pines, David, 1953: A Collective Description of Electron Interactions. III. Coulomb Interactions in a Degenerate Electron Gas. *Phys. Review*, vol. 92, second ser., no. 3, pp. 609-625.
- Bohr, N., 1915: On the Decrease of Velocity of Swiftly Moving Electrified Particles in Passing Through Matter. *Philos. Mag. & J. Sci.*, ser. 6, vol. 30, no. 175, pp. 581-612.
- Bonderup, E., 1967: Stopping of Swift Protons Evaluated From Statistical Atomic Model. *Mat.-Fys. Medd.—K. Dan. Vidensk. Selsk.*, vol. 35, no. 17.
- Bourland, P. D.; and Powers, D., 1971: Bragg-Rule Applicability to Stopping Cross Sections of Gases for α Particles of Energy 0.3-2.0 MeV. *Phys. Review B*, vol. 3, third ser., no. 11, pp. 3635-3641.
- Bragg, W. H.; and Kleeman, R., 1905: On the α Particles of Radium, and Their Loss of Range in Passing Through Various Atoms and Molecules. *Philos. Mag. & J. Sci.*, ser. 6, vol. 10, no. 57, pp. 318-340.
- Breitenberger, E., 1959: Theory of Multiple Scattering. *Proc. Royal Soc. (London)*, ser. A, vol. 250, no. 1263, pp. 514-523.
- Brown, L. M., 1950: Asymptotic Expression for the Stopping Power of *K*-Electrons. *Phys. Review*, vol. 79, second ser., no. 2, pp. 297-303.
- Brown, P. J., 1972: A Study of Charge Density in Beryllium. *Philos. Mag.*, vol. 26, no. 6, pp. 1377-1394.
- Chan, Y. M.; and Dalgarno, A., 1965: The Stopping Powers of Atoms and Molecules. *Proc. Phys. Soc. (London)*, vol. 85, pp. 457-459.

Transport Methods and Interactions for Space Radiations

- Chu, W. K.; and Powers, D., 1969: Alpha-Particle Stopping Cross Section in Solids From 400 KeV to 2 MeV. *Phys. Review*, vol. 187, second ser., no. 2, pp. 478-490.
- Chu, W. K.; and Powers, D., 1972: Calculations of Mean Excitaton Energy for All Elements. *Phys. Lett.*, vol. 40A, no. 1, pp. 23-24.
- Chu, W. K.; Moruzzi, V. L.; and Ziegler, J. F., 1975: Calculations of the Energy Loss of ^4He Ions in Solid Elements. *J. Appl. Phys.*, vol. 46, no. 7, pp. 2817-2820.
- Clementi, E.; and Raimondi, D. L., 1963: Atomic Screening Constants From SCF Functions. *J. Chem. Phys.*, vol. 38, no. 11, pp. 2686-2689.
- Clementi, Enrico; and Roetti, Carla, 1974: Roothaan-Hartree-Fock Atomic Wavefunctions. *At. Data & Nuclear Data Tables*, vol. 14, nos. 3-4, pp. 177-478.
- Dalgarno, A., 1960: The Stopping Powers of Atoms. *Proc. Phys. Soc. (London)*, vol. 76, pt. 3, no. 489, pp. 422-424.
- Dalgarno, A., 1963: Sum Rules and Atomic Structure. *Reviews Modern Phys.*, vol. 35, no. 3, pp. 522-524.
- Dalgarno, A.; and Williams, D. A., 1965: Properties of the Hydrogen Molecule. *Proc. Phys. Soc. (London)*, vol. 85, pt. 4, no. 546, pp. 685-689.
- Dalgarno, A.; Degges, T.; and Williams, D. A., 1967: Dipole Properties of Molecular Nitrogen. *Proc. Phys. Soc. (London)*, vol. 92, pt. 2, no. 576, pp. 291-295.
- De Carvalho, Hervasio G.; and Yagoda, Herman, 1952: The Range of Alpha-Particles in Water. *Phys. Review*, vol. 88, no. 2, pp. 273-278.
- Dehmer, J. L.; Inokuti, Mitio; and Saxon, R. P., 1975: Systematics of Moments of Dipole Oscillator-Strength Distributions for Atoms of the First and Second Row. *Phys. Review A*, vol. 12, third ser., no. 1, pp. 102-121.
- Ellis, R. Hobart, Jr.; Rossi, H. H.; and Failla, G., 1955: Stopping Power of Water Films. *Phys. Review*, vol. 97, no. 4, pp. 1043-1047.
- Fano, U., 1963: Penetration of Protons, Alpha Particles, and Mesons. *Annual Review of Nuclear Science*, Volume 13, Emilio Segrè, ed., Annual Reviews, Inc., pp. 1-66.
- Fleischer, Robert L.; Price, P. Buford; and Walker, Robert M., 1975: *Nuclear Tracks in Solids—Principles and Applications*. Univ. of California Press.
- Fröhlich, H.; and Pelzer, H., 1955: Plasma Oscillations and Energy Loss of Charged Particles in Solids. *Proc. Phys. Soc. (London)*, vol. 68, pt. 6, no. 426A, pp. 525-529.
- Gordon, Roy G.; and Kim, Yung Sik, 1972: Theory for the Forces Between Closed-Shell Atoms and Molecules. *J. Chem. Phys.*, vol. 56, no. 6, pp. 3122-3133.
- Hubbard, J., 1955: The Dielectric Theory of Electronic Interactions in Solids. *Proc. Phys. Soc. (London)*, vol. 68, pt. 11, no. 431A, pp. 976-986.

- Inokuti, Mitio; Baer, T.; and Dehmer, J. L., 1978: Addendum: Systematics of Moments of Dipole Oscillator-Strength Distributions for Atoms in the First and Second Row. *Phys. Review A*, vol. 17, no. 3, pp. 1229–1231.
- Inokuti, Mitio; and Turner, James E., 1978: Mean Excitation Energies for Stopping Power as Derived From Oscillator-Strength Distributions. *Sixth Symposium on Microdosimetry*, Volume I, J. Booz and H. G. Ebert, eds., Harwood Academic Publ., Ltd. (London), pp. 675–687.
- Inokuti, M.; Dehmer, J. L.; Baer, T.; and Hanson, J. D., 1981: Oscillator-Strength Moments, Stopping Powers, and Total Inelastic-Scattering Cross Sections of All Atoms Through Strontium. *Phys. Review A*, vol. 23, no. 1, pp. 95–109.
- Janni, Joseph F.; 1966: *Calculations of Energy Loss, Range, Pathlength, Stragglng, Multiple Scattering, and the Probability of Inelastic Nuclear Collisions for 0.1- to 1000-Mev Protons*. AFWL-TR-65-150, U.S. Air Force. (Available from DTIC as AD 643 837.)
- Janni, Joseph F., 1982a: Proton Range-Energy Tables 1 keV–10 GeV—Energy Loss, Range, Path Length, Time-of-Flight, Stragglng, Multiple Scattering, and Nuclear Interaction Probability. Part 1. For 63 Compounds. *At. Data & Nuclear Data Tables*, vol. 27, nos. 2/3, pp. 147–339.
- Janni, Joseph F., 1982b: Proton Range-Energy Tables, 1 keV–10 GeV—Energy Loss, Range, Path Length, Time-of-Flight, Stragglng, Multiple Scattering, and Nuclear Interaction Probability. Part 2. For Elements $1 \leq Z \leq 92$. *At. Data & Nuclear Data Tables*, vol. 27, nos. 4/5, pp. 341–529.
- Johnson, R. E.; and Inokuti, Mitio, 1983: The Local-Plasma Approximation to the Oscillator-Strength Spectrum: How Good Is it and Why? *Comments At. Mol. Phys.*, vol. 14, nos. 1 & 2, pp. 19–31.
- Kahn, David, 1953: The Energy Loss of Protons in Metallic Foils and Mica. *Phys. Review*, vol. 90, second ser., no. 4, pp. 503–509.
- Kamaratos, E.; Chang, C. K.; Wilson, J. W.; and Xu, Y. J., 1982: Valence Bond Effects on Mean Excitation Energies for Stopping Power in Metals. *Phys. Lett.*, vol. 92A, no. 7, pp. 363–365.
- Kamikawai, Ryotaro; Watanabe, Tsutomu; and Amemiya, Ayao, 1969: Mean Excitation Energy for Stopping Power of Molecular Hydrogen. *Phys. Review*, vol. 184, second ser., no. 2, pp. 303–311.
- Khan, F.; Khandelwal, G. S.; and Wilson, J. W., 1988a: Differential Oscillator Strengths and Dipole Polarizabilities for Transitions of the Helium Sequence. *Phys. Review A*, vol. 38, third ser., no. 12, pp. 6159–6164.
- Khan, F.; Khandelwal, G. S.; and Wilson, J. W., 1988b: $1s^2 \ ^1S$ - $1s \ nP$ Transitions of the Helium Isoelectronic Sequence Members up to $Z = 30$. *Astrophys. J.*, vol. 329, no. 1, pt. 1, pp. 493–497.
- Khan, F.; Khandelwal, G. S.; and Wilson, J. W., 1990: Moments of Dipole Oscillator-Strength Distribution for the Helium Sequence. *J. Phys. B.: At., Mol. & Opt. Phys.*, vol. 23, no. 16, pp. 2717–2726.

Transport Methods and Interactions for Space Radiations

- Khandelwal, Govind S., 1968: Shell Corrections for *K*- and *L*-Electrons. *Nuclear Phys.*, vol. A116, no. 1, pp. 97-111.
- Khandelwal, Govind S., 1982: Stopping Power of *K* and *L* Electrons. *Phys. Review A*, vol. 26, third ser., no. 5, pp. 2983-2986.
- Khandelwal, G. S.; Khan, F.; and Wilson, J. W., 1989: An Asymptotic Expression for the Dipole Oscillator Strength for Transition of the He Sequence. *Astrophys. J.*, vol. 336, no. 1, pt. 1, pp. 504-506.
- Khandelwal, G. S.; Pritchard, W. M.; Grubb, G.; and Khan, F., 1989: Screened Hydrogenic Radial Integrals. *Phys. Review A*, vol. 39, third ser., no. 8, pp. 3960-3963.
- Kramers, H. A., 1947: The Stopping Power of a Metal for α -Particles. *Physica*, vol. 13, pp. 401-412.
- Landau, L. D.; and Lifshitz, E. M. (J. B. Sykes and J. S. Bell, transl.), 1958: *Quantum Mechanics—Non-Relativistic Theory*. Addison-Wesley Publ. Co., Inc.
- Landau, L. D.; and Lifshitz, E. M., 1960: *Electrodynamics of Continuous Media*. Addison-Wesley Publ. Co., Inc.
- Langley, Robert A., 1975: Stopping Cross Sections for Helium and Hydrogen in H₂, N₂, O₂, and H₂S (0.3-2.5 MeV). *Phys. Review B*, vol. 12, no. 9, pp. 3575-3583.
- Leminen, E.; Fontell, A.; and Bister, M., 1968: Stopping Power of Al, Zn, and In for 0.6-2.4 MeV Protons. *Ann. Acad. Sci. Fenn.*, ser. A, no. 281, pp. 4-12.
- Lennard-Jones, J. E.; and Devonshire, A. F., 1937: Critical Phenomena in Gases—I. *Proc. Royal Soc. (London)*, ser. A, vol. CLXIII, pp. 53-70.
- Lennard-Jones, J. E.; and Devonshire, A. F., 1938: Critical Phenomena in Gases—II. Vapour Pressures and Boiling Points. *Proc. Royal Soc. (London)*, ser. A, vol. CLXV, pp. 1-11.
- Lindhard, J., 1954: On the Properties of a Gas of Charged Particles. *Mat.-Fys. Medd.—K. Dan. Vidensk. Selsk.*, vol. 28, no. 8, pp. 1-58.
- Lindhard, Jens; and Scharff, Morten, 1960: Recent Developments in the Theory of Stopping Power. 1. Principles of the Statistical Method. *Penetration of Charged Particles in Matter*, Edwin Albrecht Uehling, ed., Nuclear Sci. Ser. Rep. No. 29 (Publ. 752), National Academy of Sciences, National Research Council, pp. 49-55.
- Lindhard, J.; Scharff, M.; and Schiott, H. E., 1963: Range Concepts and Heavy Ion Ranges (Notes on Atomic Collisions, II). *Mat.-Fys. Medd.—K. Dan. Vidensk. Selsk.*, vol. 33, no. 14, pp. 1-42.
- Lindhard, Jens; and Winther, Aage, 1964: Stopping Power of Electron Gas and Equipartition Rule. *Mat.-Fys. Medd.—K. Dan. Vidensk. Selsk.*, vol. 34, no. 4, pp. 3-22.
- Livingston, M. Stanley; and Bethe, H. A., 1937: Nuclear Physics—C. Nuclear Dynamics, Experimental. *Reviews Modern Phys.*, vol. 9, no. 3, pp. 245-390.

- Lodhi, A. S.; and Powers, D., 1974: Energy Loss of α Particles in Gaseous C-H and C-H-F Compounds. *Phys. Review A*, vol. 10, no. 6, pp. 2131-2140.
- Martynenko, Yu. V., 1970: Radiation Damage of Crystals Irradiated by Atomic Particles. *Sov. Phys.—Solid State*, vol. 11, no. 7, pp. 1582-1585.
- Mather, R.; and Segrè, E., 1951: Range Energy Relation for 340-Mev Protons. *Phys. Review*, vol. 84, second ser., no. 2, pp. 191-193.
- Matteson, S.; Powers, D.; and Chau, E. K. L., 1977: Physical-State Effect in the Stopping Cross Section of H₂O Ice and Vapor for 0.3 to 2.0 MeV α Particles. *Phys. Review A*, vol. 15, ser. A, no. 3, pp. 856-864.
- Merzbacher, E.; and Lewis, H. W., 1958: X-ray Production by Heavy Charged Particles. *Encyclopedia of Physics*, Volume XXXIV, S. Flugge, ed., Springer-Verlag, pp. 166-192.
- Moruzzi, V. L.; Janak, J. F.; and Williams, A. R., 1978: *Calculated Electronic Properties of Metals*. Pergamon Press, Inc.
- Nakata, Hiroshi, 1971: Analysis of Energy-Loss Data for 0.2-0.5 MeV/amu p , α , and N in Se. *Phys. Review B*, vol. 3, no. 9, pp. 2847-2851.
- Neilsen, L. P., 1961: Energy Loss and Straggling of Protons and Deuterons. *Mat.-Fys. Medd.—K. Dan. Vidensk. Selsk.*, vol. 33, no. 6.
- Neuwirth, Wolfgang; Pietsch, Werner; and Kreutz, Ronald, 1978: Chemical Influences on the Stopping Power. *Nuclear Instrum. & Methods*, vol. 149, nos. 1-3, pp. 105-113.
- Northcliffe, L. C.; and Schilling, R. F., 1970: Range and Stopping-Power Tables for Heavy Ions. *Nuclear Data*, Sect. A, vol. 7, no. 3-4, pp. 233-463.
- Palmer, Rita B. J., 1966: The Stopping Power of Hydrogen and Hydrocarbon Vapours for Alpha Particles Over the Energy Range 1 to 8 MeV. *Proc. Phys. Soc.*, vol. 87, pp. 681-688.
- Palmer, Rita B. J.; and Akhavan-Rezayat, Ahmad, 1978: Range-Energy Relations and Stopping Power of Water, Water Vapour and Tissue Equivalent Liquid for α Particles Over the Energy Range 0.5 to 8 MeV. *Sixth Symposium on Microdosimetry*, Volume II, J. Booz and H. G. Ebert, eds., Harwood Academic Publ., Ltd. (London), pp. 739-748.
- Pauling, Linus, 1960: *The Nature of the Chemical Bond*, Third ed. Cornell Univ. Press.
- Pauling, Linus, 1967: *The Chemical Bond*. Cornell Univ. Press.
- Peterson, S. W.; and Levy, Henri A., 1957: A Single-Crystal Neutron Diffraction Study of Heavy Ice. *Acta Crystallogr.*, vol. 10, pp. 70-76.
- Pines, David; and Bohm, David, 1952: A Collective Description of Electron Interactions: II. Collective vs Individual Particle Aspects of the Interactions. *Phys. Review*, vol. 85, second ser., no. 2, pp. 338-353.
- Pines, David, 1953: A Collective Description of Electron Interactions: IV. Electron Interaction in Metals. *Phys. Review*, vol. 92, second ser., no. 3, pp. 626-636.

Transport Methods and Interactions for Space Radiations

- Platzman, Robert L., 1952a: Influences on Details of Electronic Binding on Penetration Phenomena, and the Penetration of Energetic Charged Particles Through Liquid Water. *Symposium on Radiobiology—The Basic Aspects of Radiation Effects on Living Systems*, James J. Nickson, ed., John Wiley & Sons, Inc., pp. 139–176.
- Platzman, Robert L., 1952b: On the Primary Processes in Radiation Chemistry and Biology. *Symposium on Radiobiology—The Basic Aspects of Radiation Effects on Living Systems*, James J. Nickson, ed., John Wiley & Sons, Inc., pp. 97–116.
- Powers, D.; Chu, W. K.; Robinson, R. J.; and Lodhi, A. S., 1972: Measurement of Molecular Stopping Cross Sections of Halogen-Carbon Compounds and Calculation of Atomic Stopping Cross Sections of Halogens. *Phys. Review A*, vol. 6, no. 4, pp. 1425–1435.
- Reynolds, H. K.; Dunbar, D. N. F.; Wenzel, W. A.; and Whaling, W., 1953: The Stopping Cross Section of Gases for Protons, 30–600 keV. *Phys. Review*, vol. 92, no. 3, pp. 742–748.
- Rousseau, C. C.; Chu, W. K.; and Powers, D., 1971: Calculations of Stopping Cross Sections for 0.8- to 2.0-MeV Alpha Particles. *Phys. Review A*, vol. 4, third ser., no. 3, pp. 1066–1070.
- Sachs, Donald C.; and Richardson, J. Reginald, 1953: Mean Excitation Potentials. *Phys. Review*, vol. 89, second ser., no. 6, pp. 1163–1164.
- Seltzer, S. M.; and Berger, M. J., 1982: Evaluation of the Collision Stopping Power of Elements and Compounds for Electrons and Positrons. *Int. J. Appl. Radiat. & Isot.*, vol. 33, no. 11, pp. 1189–1218.
- Shiles, E.; Sasaki, Taizo; Inokuti, Mitio; and Smith, D. Y., 1980: Self-Consistency and Sum-Rule Tests in the Kramers-Kronig Analysis of Optical Data: Applications to Aluminum. *Phys. Review B*, vol. 22, no. 4, pp. 1612–1628.
- Simmons, D. H., 1952: The Range-Energy Relation for Protons in Aluminum. *Proc. Phys. Soc. (London)*, vol. 65, pt. A, pp. 454–456.
- Sorensen, H.; and Andersen, H. H., 1973: Stopping Power of Al, Cu, Ag, Au, Pb, and U for 5–18-MeV Protons and Deuterons. *Phys. Review B*, vol. 8, no. 5, pp. 1854–1863.
- Suzuki, Reiko; Nakamura, Hiroki; and Ishiguro, Eiichi, 1984: Semiclassical Scattering Theory Based on the Dynamical-State Representation: Application to the $\text{Li}^+ + \text{Na}$ and $\text{Li}^+ + \text{Na}^+$ Collisions. *Phys. Review A*, vol. 29, third ser., no. 6, pp. 3060–3070.
- Thompson, Theos Jardin, 1952: Effect of Chemical Structure on Stopping Powers for High-Energy Protons. UCRL-1910, Univ. of California.
- Thwaites, D. I., 1981: Stopping Cross-Sections of Liquid Water and Water Vapour for Alpha Particles Within the Energy Region 0.3 to 5.5 MeV. *Phys. Med. & Biol.*, vol. 26, no. 1, pp. 71–80.
- Tossell, J. A., 1979: Calculation of Bond Distances and Cohesive Energies for Gaseous Halides Using the Modified Electron Gas Ionic Model. *Chem. Phys. Lett.*, vol. 67, no. 2–3, pp. 359–364.
- Vasilevskii, I. M.; and Prokoshkin, Yu. D., 1960: *Ionizatsionnye Potentsialy Atomov (Ionization Potentials of Atoms)*. Dubna: Ob'edinen. Inst. of Yadernykh Issledovaniy.

- Waldman, Marvin; and Gordon, Roy G., 1979: Scaled Electron Gas Approximation for Intermolecular Forces. *J. Chem. Phys.*, vol. 71, no. 3, pp. 1325-1339.
- Walecka, J. D., 1976: Collective Excitations in Atoms. *Phys. Lett.*, vol. 58A, no. 2, pp. 83-86.
- Walske, M. C.; and Bethe, H. A., 1951: Asymptotic Formula for Stopping Power of *K*-Electrons. *Phys. Review*, vol. 83, pp. 457-458.
- Walske, M. C., 1952: The Stopping Power of *K*-Electrons. *Phys. Review*, vol. 88, second ser., no. 6, pp. 1283-1289.
- Walske, M. C., 1956: Stopping Power of *L*-Electrons. *Phys. Review*, vol. 101, second ser., no. 3, pp. 940-944.
- Wenzel, W. A.; and Whaling, Ward, 1952: The Stopping Cross Section of D₂O Ice. *Phys. Review*, vol. 87, no. 3, pp. 499-503.
- Wigner, E. P.; and Seitz, F., 1934: On the Constitution of Metallic Sodium. II. *Phys. Review*, vol. 46, second ser., no. 6, pp. 509-524.
- Wilson, J. W.; and Kamaratos, E., 1981: Mean Excitation Energy for Molecules of Hydrogen and Carbon. *Phys. Lett.*, vol. 85A, no. 1, pp. 27-29.
- Wilson, J. W.; Chang, C. K.; Xu, Y. J.; and Kamaratos, E., 1982: Ionic Bond Effects on the Mean Excitation Energy for Stopping Power. *J. Appl. Phys.*, vol. 53, no. 2, pp. 828-830.
- Wilson, J. W.; and Xu, Y. J., 1982: Metallic Bond Effects on Mean Excitation Energies for Stopping Powers. *Phys. Lett.*, vol. 90A, no. 5, pp. 253-255.
- Wilson, J. W.; Xu, Y. J.; Chang, C. K.; and Kamaratos, E., 1984a: Atomic Mean Excitation Energies for Stopping Powers From Local Plasma Oscillator Strengths. *J. Appl. Phys.*, vol. 56, no. 3, pp. 860-861.
- Wilson, J. W.; Xu, Y. J.; Kamaratos, E.; and Chang, C. K., 1984b: Mean Excitation Energies for Stopping Powers in Various Materials Composed of Elements Hydrogen Through Argon. *Canadian J. Phys.*, vol. 62, no. 7, pp. 646-660.
- Xu, Y. J.; Khandelwal, G. S.; and Wilson, J. W., 1984a: Intermediate Energy Proton Stopping Power for Hydrogen Molecules and Monoatomic Helium Gas. *Phys. Lett.*, vol. 100A, no. 3, pp. 137-140.
- Xu, Y. J.; Khandelwal, G. S.; and Wilson, J. W., 1984b: Low-Energy Proton Stopping Power of N₂, O₂, and Water Vapor, and Deviations From Bragg's Rule. *Phys. Review A*, vol. 29, third ser., no. 6, pp. 3419-3422.
- Xu, Y. J.; Khandelwal, G. S.; and Wilson, J. W., 1985: Proton Stopping Cross Sections of Liquid Water. *Phys. Review A*, vol. 32, third ser., no. 1, pp. 629-632.
- Xu, Y. J.; Khandelwal, G. S.; and Wilson, J. W., 1986: The Maximum Momentum Transfer in Proton-Hydrogen Collisions. *Phys. Lett. A*, vol. 115, no. 1, 2, pp. 37-38.

Transport Methods and Interactions for Space Radiations

- Xu, Y. J.; Khandelwal, G. S.; and Wilson, J. W., 1989: *Charge Exchange Transition Probability for Collisions Between Unlike Ions and Atoms Within the Adiabatic Approximation*. NASA TM-101559.
- Zeiss, G. D.; and Meath, W. J., 1975: The H₂O-H₂O Dispersion Energy Constant and the Dispersion of the Specific Refractivity of Dilute Water Vapour. *Mol. Phys.*, vol. 30, no. 1, pp. 161-169.
- Zeiss, G. D.; Meath, William J.; MacDonald, J. C. F.; and Dawson, D. J., 1977: Accurate Evaluation of Stopping and Straggling Mean Excitation Energies for N, O, H₂, N₂, O₂, NO, NH₃, H₂O, and N₂O Using Dipole Oscillator Strength Distributions—A Test of the Validity of Bragg's Rule. *Radiat. Res.*, vol. 70, no. 2, pp. 284-303.
- Zener, Clarence, 1932: Non-Adiabatic Crossing of Energy Levels. *Proc. Royal Soc. (London)*, ser. A, vol. CXXXVII, pp. 696-702.
- Ziegler, J. F., 1977: *Helium—Stopping Powers and Ranges in All Elemental Matter*. Volume 4 of *The Stopping and Ranges of Ions in Matter*, J. F. Ziegler, organizer, Pergamon Press, Inc.
- Ziegler, J. F., 1980: The Stopping of Energetic Ions in Solids. *Nuclear Instrum. & Methods*, vol. 168, nos. 1-3, pp. 17-24.

Chapter 3

High-Energy Interactions

3.1. Introduction

We will not attempt to give any comprehensive review of nuclear physics but will touch only on the highlights of work directly related to the development of nuclear models at the Langley Research Center. We will attempt to place the Langley work into a cohesive framework and relate it to the early work on reaction model development.

Following the discovery of cosmic rays through air ionization phenomena, the development of the cloud chamber and nuclear emulsion began to reveal the details of cosmic-ray interactions. These observations showed the production of fast particles in the forward direction and isotropic slow particles.

Serber (1947) suggested that the fast particles produced in high-energy proton and neutron reactions are direct knockout products of scattering with individual nuclear constituents followed by the emission of slow particles in the evaporation decay of the residual excited nucleus. This two-step Serber model was implemented through the first step by Goldberger (1948) at the University of Chicago using semiclassical methods and Monte Carlo techniques whereby the importance of the Pauli exclusion principle is demonstrated. G. F. Chew (1951) who performed the Monte Carlo calculation as a student for Goldberger introduced a corresponding quantum mechanical model in the so-called impulse approximation. Watson (1953) derived a complete quantum description of the first Serber step as a multiple-scattering series in which the impulse approximation of Chew is the first term in the series. A great simplification in the quantum theory came with the introduction of the eikonal by Glauber (1955) for which a successful, yet simple, scattering theory was derived including the multiple-scattering series (Franco and Glauber, 1966). Remler (1968) later derived a formal relation between the Glauber multiple-scattering theory and the Watson multiple-scattering theory.

The second step of the Serber model assumed that the level density within a nucleus is large and that the high excitation energy is distributed in thermal equilibrium among the many states. The excitation energy is then given up to the most energetic nuclear particles that can escape the nuclear potential region. Such a model was based on low-energy reaction studies in which reactions proceed through a compound nuclear state. The formation of the compound nuclear state at low energies was taken as the absorption of the passing plane wave by the nucleus which was assumed to act like a "cloudy crystal ball." This crystal ball is referred to as the optical model (Fernbach, Serber, and Taylor, 1949) in which the nuclear interior is treated as a medium with a complex index of refraction. The relationship between multiple scattering and the optical model was given by Watson (1953).

There was rapid progress in the development of intranuclear cascade models with compound nuclear de-excitation after the introduction of large-scale scientific computers (Metropolis, et al., 1958; Bertini, 1969). These intranuclear cascade

codes had a large impact on the Apollo mission and continue to be used even to this day (Santoro et al., 1986). The primary data base for shielding against high-energy protons and neutrons remains to be that derived from intranuclear cascade codes. An effort to extend the intranuclear cascade codes to include complex projectiles has met with some success but is computationally inefficient (Gabriel, Bishop, and Lillie, 1984).

The Langley program began with computations using the multiple-scattering formalism (Wilson, 1973a and 1973b) derived from the work of Mandelstam (1955). In accordance with Mandelstam, the transition amplitude is related to the residue at the pole of the propagator of the particles appearing in the asymptotic states. The propagator is fully symmetrized and can be formed into a multiple-scattering series by neglecting three-body terms and by projecting only the positive energy states. As Gross (1965) noted, the nuclear vertex can be related to nonrelativistic nuclear wave functions. The two-body scattering amplitudes were reconstructed from phase shift analysis and extrapolated to off-shell values by evaluating the one-pion exchange contributions directly and extrapolating the remaining contributions by assuming a two-pion exchange pole (Wilson, 1972). The S-state and D-state wave functions were taken from Humberston and Wallace (1970). The final calculation performed by Wilson (1973a, 1973b, and 1974a) was very successful (fig. 3.1) at describing the measured angular distributions of cross section and polarization measured for 146 MeV protons by Postma and Wilson (1961). With this success at applying the multiple-scattering theory to the three-body nuclear problem, we were encouraged to see these new skills help solve problems closer to NASA's interest.

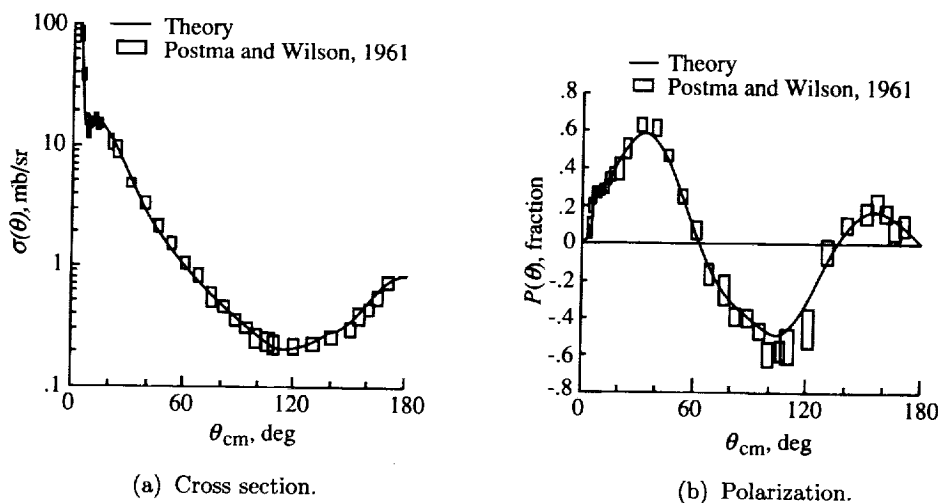


Figure 3.1. Comparison of S-wave plus P-wave fits using numerical integration for single scattering. D-state restricted to 6.93 ± 1 percent in search procedures and 5.93 at minimum $E = 146$ MeV.

3.2. Multiple-Scattering Theory

3.2.1. Glauber theory. The content of the Glauber (1955) theory is contained in the profile operator

$$\Gamma(\vec{b}) = 1 - \exp[-i\chi(\vec{b})] \quad (3.1)$$

where \vec{b} is the impact parameter vector and the phase shift operator is

$$\chi(\vec{b}) = \frac{1}{\hbar v} \int_{-\infty}^{\infty} V(\vec{b} + \vec{z}) dz \quad (3.2)$$

where v is the projectile velocity, V is the interaction potential, and z is the space variable in the direction of motion. The interaction potential for scattering an elementary projectile from a composite system (assuming only two-body potentials between projectile and constituents) is taken as

$$V(\vec{r}) = \sum_{\alpha} V_{\alpha}(\vec{r} - \vec{r}_{\alpha}) \quad (3.3)$$

which leads to the usual Glauber result. The usual extension to the scattering for composite systems is to take (Czyż and Maximon, 1969)

$$V(\vec{r}) = \sum_{j\alpha} V_{j\alpha}(\vec{r}_j - \vec{r}_{\alpha}) \quad (3.4)$$

where α constituents are located in the target of atomic weight A_T , and j constituents are located in the projectile of atomic weight A_P . The multiple-scattering form of the profile function is then (assuming that the potentials are commutative)

$$\Gamma(\vec{b}) = 1 - \prod_j \prod_{\alpha} [1 - \gamma_{j\alpha}(\vec{b})] \quad (3.5)$$

where $\gamma_{j\alpha}$ is the profile of the (j, α) colliding pair given as

$$\gamma_{j\alpha}(\vec{b}) = 1 - \exp\left[-i \frac{1}{\hbar v} \int_{-\infty}^{\infty} V_{j\alpha}(\vec{r}_j - \vec{r}_{\alpha}) dz\right] \quad (3.6)$$

Equation (3.5) is expanded as

$$\Gamma(\vec{b}) = \sum_{j\alpha} \gamma_{j\alpha}(\vec{b}) - \sum_{\substack{(j,\alpha) \neq (k,\beta) \\ j > k}} \gamma_{j\alpha}(\vec{b}) \gamma_{k\beta}(\vec{b}) + \dots \quad (3.7)$$

The graphical representation of the single-scattering term of equation (3.7) is shown in figure 3.2. The double-scattering term contains two distinct types of graphs illustrated in figure 3.3. Note that the series in equation (3.7) ends after $(A_P \cdot A_T)$ terms.

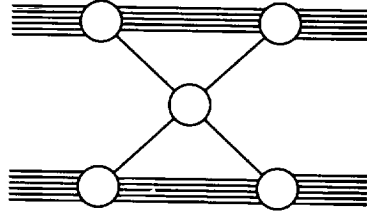


Figure 3.2. Single-scattering graph.

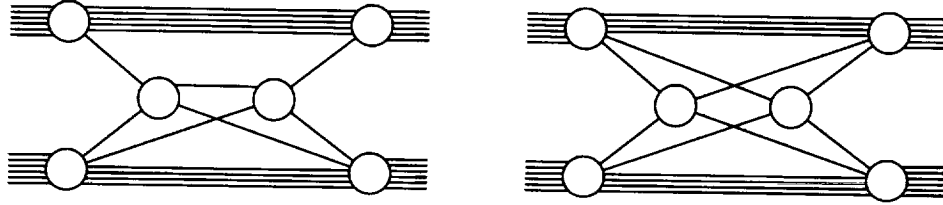


Figure 3.3. Rescattering graphs.

3.2.2. Multiple-scattering series. The free projectile and target Hamiltonians, H_P and H_T , respectively, are taken together with the interaction potential V (assumed to be sums of two-body potentials between constituents) to form the full Hamiltonian

$$H = H_P + H_T + \sum_{\alpha j} V_{\alpha j} \quad (3.8)$$

The wave function in a remote region of space after the scattering satisfies

$$H\Psi = E\Psi \quad (3.9)$$

and consists of the superposition of the incident plane wave and the asymptotically scattered wave

$$\Psi = \varphi + \Psi_{sc} \quad (3.10)$$

where

$$(H_P + H_T)\varphi = E\varphi \quad (3.11)$$

and

$$\Psi_{sc} = GT\varphi \quad (3.12)$$

with Green's function given by

$$\lim_{\eta \rightarrow 0_+} (E - H_P - H_T + i\eta)G = 1 \quad (3.13)$$

and the transition operator by

$$T = V + VGT \quad (3.14)$$

In future equations we will assume that η is set to zero in the sense of the limit in equation (3.13). The usual wave operator Ω that transforms plane wave entering states to final scattered states

$$\Psi = \Omega\varphi \quad (3.15)$$

is given as

$$\Omega = 1 + GV\Omega \quad (3.16)$$

so that \mathcal{T} is formally given as

$$\mathcal{T} = V\Omega \quad (3.17)$$

Our purpose is to find a series for \mathcal{T} that is in terms of simpler functions. The development closely follows the original work of Watson (1953). The present derivation for heavy ions was made by Wilson (1974b).

To proceed with this purpose, the transition operator is defined for scattering the α constituent of the target with the j constituent of the projectile as

$$t_{\alpha j} = V_{\alpha j} + V_{\alpha j}Gt_{\alpha j} \quad (3.18)$$

The wave operator that transforms the entering free state up to the collision of the α and j constituents is given by

$$\omega_{\alpha j} = 1 + \sum_{(\beta,k) \neq (\alpha,j)} Gt_{\beta k}\omega_{\beta k} \quad (3.19)$$

Equation (3.19) is interpreted in the following way. The propagation to the time just before the α and j constituents scatter is the sum of an operator that brings the initial free state plus the scattered part from the scattering of all other β and k constituents. Clearly, the full wave operator consists of the wave operator that transforms the system to the α and j collision, plus the additional contribution caused by the scattering of the α and j constituents; that is,

$$\Omega = \omega_{\alpha j} + Gt_{\alpha j}\omega_{\alpha j} \quad (3.20)$$

which, written symmetrically using equation (3.19), is

$$\Omega = 1 + \sum_{\alpha j} Gt_{\alpha j}\omega_{\alpha j} \quad (3.21)$$

The series given by equations (3.18) through (3.21) constitutes an exact representation of the scattering process defined by equations (3.8) through (3.17). Consider the product

$$\begin{aligned} V_{\alpha j}\Omega &= V_{\alpha j}\omega_{\alpha j} + V_{\alpha j}Gt_{\alpha j}\omega_{\alpha j} \\ &= (V_{\alpha j} + V_{\alpha j}Gt_{\alpha j})\omega_{\alpha j} = t_{\alpha j}\omega_{\alpha j} \end{aligned} \quad (3.22)$$

Summing the α and j constituents gives

$$\mathcal{T} = \sum_{\alpha j} V_{\alpha j}\Omega = \sum_{\alpha j} t_{\alpha j}\omega_{\alpha j} \quad (3.23)$$

which shows equations (3.18), (3.19), and (3.21) as a solution to (3.16). By iteration of equations (3.23) and (3.19), the multiple-scattering series

$$\mathcal{T} = \sum_{\alpha j} t_{\alpha j} + \sum_{(\beta,k) \neq (\alpha,j)} t_{\alpha j}Gt_{\beta k} + \dots \quad (3.24)$$

is obtained, which constitutes a formal solution to the exact scattering problem (Wilson, 1974b). If the usual replacement (Watson, 1953; Wilson, 1974b) is made, that is,

$$G \rightarrow G_0 \equiv \frac{1}{E - \sum_j T_j - \sum_\alpha T_\alpha}$$

where G_0 is the free n -body Green's function given in terms of total energy and constituent kinetic energy operators, then $t_{\alpha j}$ becomes essentially two-body operators and equation (3.24) becomes a series of sequential two-body operators. The graphical representations of the terms of the series of equation (3.24) are the same as those shown in figures 3.2 and 3.3. The series (eq. (3.24)) reduces to the usual Watson series when the projectile consists of a single particle. When equation (3.24) is evaluated using the eikonal approximation, the Glauber theory is obtained, implying cancellation of an infinity of terms of equation (3.24) in the eikonal context. This type of cancellation was first noted by Remler (1968) and Harrington (1969).

3.2.3. Optical potential. A potential operator V_{opt} must be found whose corresponding Born series for the \mathbf{T} -matrix is equivalent to the multiple-scattering expansion (eq. (3.24)). Such an operator is closely related to the so-called optical potential (Úlehla, Gomolčák, and Pluhař, 1964; Foldy and Walecka, 1969), which will be referred to as V_{opt} . The transition operator

$$\mathcal{T}_{\text{opt}} = V_{\text{opt}} + V_{\text{opt}} G \mathcal{T}_{\text{opt}} \quad (3.25)$$

will be defined by

$$V_{\text{opt}} = \sum_{\alpha j} t_{\alpha j} \quad (3.26)$$

from which

$$\mathcal{T} = \mathcal{T}_{\text{opt}} + \sum_{\alpha j} t_{\alpha j} G t_{\alpha j} + \dots \quad (3.27)$$

The optical model is obtained by retaining the first term in equation (3.27), and the order of approximation is

$$\mathcal{T} - \mathcal{T}_{\text{opt}} \approx \frac{V_{\text{opt}} G V_{\text{opt}}}{A_T A_P} \quad (3.28)$$

because $t_{\alpha j} \approx V_{\text{opt}} / (A_T A_P)$ where A_T and A_P are the atomic weights of the target and projectile, respectively. The amplitude in equation (3.25) is a rather good approximation to the exact amplitude for light as well as heavy nuclei.

In summary, a multiple-scattering series for heavy ion scattering has been derived that appears as a natural extension to the Watson formalism. The structure of this series indicates that it reduces to the Glauber result within the eikonal context. A potential operator is found which shows that an optical model for heavy ion scattering is a good approximation for even rather light nuclei.

3.3. Heavy Ion Dynamical Equations

In the previous section, an optical potential equation was derived for use in the scattering of heavy ions. In this section, the coupled-channel equations for composite particle scattering are examined. Our method will be similar to that of Foldy and Walecka (1969) and has been presented elsewhere (Wilson, 1975). Particular attention will be given to the relation between the coherent elastic-scattered wave, the Born approximation, Chew's (1951) form of impulse approximation, the distorted-wave Born approximation (DWBA), and various approximation procedures to the coupled equations. Finally, the coupled equations will be solved by using the eikonal approximation. A simplified expression for the scattering amplitude is derived from that approximation, which includes the elastic- and all the inelastic-scattered amplitudes for small scattering angles. A discussion about the customary use of the optical theorem to estimate total cross sections from the coherent elastic-scattered wave will shed some light on the reasons that this estimate of total cross sections is successful.

3.3.1. Coupled-channel equations. The starting point for the present discussion is the coupled-channel (Schrödinger) equation relating the entrance channel to all excited states of the target and projectile. This equation was derived by Wilson (1974b and 1975) by assuming the kinetic energy to be large compared with the excitation energy of the target and projectile and closure for the accessible internal eigenstates. These coupled equations are given as

$$\left(\nabla_{\vec{x}}^2 + \vec{k}^2\right) \psi_{m\mu}(\vec{x}) = \frac{2mA_P A_T}{N} \sum_{m'\mu'} V_{m\mu, m'\mu'}(\vec{x}) \psi_{m'\mu'}(\vec{x}) \quad (3.29)$$

where subscripts m and μ label the eigenstates of the projectile and target; A_P and A_T are projectile and target mass number, respectively; m is constituent mass; \vec{k} is projectile momentum relative to the center of mass; and \vec{x} is the projectile position vector relative to the target, with

$$V_{m\mu, m'\mu'}(\vec{x}) = \left\langle g_{P,m}(\vec{\xi}_P) g_{T,\mu}(\vec{\xi}_T) \left| V_{\text{opt}}(\vec{\xi}_P, \vec{\xi}_T, \vec{x}) \right| g_{P,m'}(\vec{\xi}_P) g_{T,\mu'}(\vec{\xi}_T) \right\rangle \quad (3.30)$$

The quantities $g_{P,m}(\vec{\xi}_P)$ and $g_{T,\mu}(\vec{\xi}_T)$ are the projectile and target internal wave functions, respectively; $\vec{\xi}_P$ and $\vec{\xi}_T$ are collections of internal coordinates of the projectile and target constituents, respectively; and $V_{\text{opt}}(\vec{\xi}_P, \vec{\xi}_T, \vec{x})$ is the effective potential operator derived in the previous section and is given by

$$V_{\text{opt}}(\vec{\xi}_P, \vec{\xi}_T, \vec{x}) = \sum_{\alpha j} t_{\alpha j}(\vec{x}_\alpha, \vec{x}_j) \quad (3.31)$$

Here, $t_{\alpha j}(\vec{x}_\alpha, \vec{x}_j)$ is the two-body transition operator for the j constituent of the projectile at position \vec{x}_j and the α constituent of the target at \vec{x}_α . The total

constituent number N is defined as

$$N = A_P + A_T \quad (3.32)$$

The notation is simplified by introducing the wave vector

$$\psi(\vec{x}) = \begin{bmatrix} \psi_{00}(\vec{x}) \\ \psi_{01}(\vec{x}) \\ \psi_{10}(\vec{x}) \\ \psi_{11}(\vec{x}) \\ \vdots \end{bmatrix} \quad (3.33)$$

and the potential matrix

$$U(\vec{x}) = \frac{2m A_T A_P}{N} \begin{bmatrix} V_{00,00}(\vec{x}) & V_{00,01}(\vec{x}) & V_{00,10}(\vec{x}) & \dots \\ V_{01,00}(\vec{x}) & V_{01,01}(\vec{x}) & V_{01,10}(\vec{x}) & \dots \\ V_{10,00}(\vec{x}) & V_{10,01}(\vec{x}) & V_{10,10}(\vec{x}) & \dots \\ V_{11,00}(\vec{x}) & V_{11,01}(\vec{x}) & V_{11,10}(\vec{x}) & \dots \\ \vdots & \vdots & \vdots & \vdots \end{bmatrix} \quad (3.34)$$

The coupled equations are then written in matrix form as

$$\left(\nabla_{\vec{x}}^2 + \vec{k}^2 \right) \psi(\vec{x}) = U(\vec{x}) \psi(\vec{x}) \quad (3.35)$$

for which the approximate solution is considered.

The object of the solution of equation (3.35) is the calculation of the scattering amplitude given by

$$f(\vec{q}) = -\sqrt{\frac{\pi}{2}} \int \exp(-i\vec{k}_f \cdot \vec{x}) U(\vec{x}) \psi(\vec{x}) d^3\vec{x} \quad (3.36)$$

where \vec{k}_f is the final projectile momentum and \vec{q} is the momentum transfer vector

$$\vec{q} = \vec{k}_f - \vec{k} \quad (3.37)$$

Because equation (3.35) cannot be solved in general, the rest of this chapter is devoted to the study of approximation procedures for the evaluation of equation (3.36). To gain insight, the simplest approximations are examined first and provide a basis for more accurate and complex procedures.

3.3.2. Born approximation. The Born approximation is obtained by approximating $\psi(\vec{x})$ by the incident plane wave. The coupled amplitude is then written as

$$f^B(\vec{q}) = -\frac{1}{4\pi} \int \exp(-i\vec{q} \cdot \vec{x}) U(\vec{x}) d^3\vec{x} \quad (3.38)$$

which is a matrix of approximate scattering amplitudes relating all possible entrance channels to all possible final channels. For example, diagonal elements

relate to all possible elastic scatterings of the system where the elastic channel is defined by the entrance channel. Using the definition of the potential given in equations (3.30) and (3.31) results in

$$\begin{aligned} V_{m\mu, m'\mu'}(\vec{x}) &= \sum_{\alpha j} \left\langle g_{P,m}(\vec{\xi}_P) g_{T,\mu}(\vec{\xi}_T) \left| t_{\alpha j}(\vec{x}_\alpha, \vec{x}_j) \right| g_{P,m'}(\vec{\xi}_P) g_{T,\mu'}(\vec{\xi}_T) \right\rangle \\ &= \sum_{\alpha j} \int \rho_{T,\mu\mu'}(\vec{r}_\alpha) t_{\alpha j}(\vec{x}_\alpha, \vec{x}_j) \rho_{P,mm'}(\vec{r}_j) d^3\vec{r}_\alpha d^3\vec{r}_j \end{aligned} \quad (3.39)$$

where

$$\rho_{P,mm'}(\vec{r}_j) = \int g_{P,m}^*(\vec{\xi}_P) \delta^3(\vec{r}_j - \vec{\xi}_{P,j}) g_{P,m'}(\vec{\xi}_P) d^3\vec{\xi}_P \quad (3.40)$$

and

$$\rho_{T,\mu\mu'}(\vec{r}_\alpha) = \int g_{T,\mu}^*(\vec{\xi}_T) \delta^3(\vec{r}_\alpha - \vec{\xi}_{T,\alpha}) g_{T,\mu'}(\vec{\xi}_T) d^3\vec{\xi}_T \quad (3.41)$$

where an asterisk denotes complex conjugation. The Fourier transform of equation (3.39) yields

$$\begin{aligned} &\int V_{m\mu, m'\mu'}(\vec{x}) \exp(-i\vec{q} \cdot \vec{x}) d^3\vec{x} \\ &= \sum_{\alpha j} \int \exp(-i\vec{q} \cdot \vec{x}) \left[\int \rho_{T,\mu\mu'}(\vec{r}_\alpha) \rho_{P,mm'}(\vec{r}_j) t_{\alpha j}(\vec{x}_\alpha, \vec{x}_j) d^3\vec{r}_\alpha d^3\vec{r}_j \right] d^3\vec{x} \\ &= \sum_{\alpha j} t_{\alpha j}(k, \vec{q}) F_{T,\mu\mu'}(\vec{q}) F_{P,mm'}(-\vec{q}) \end{aligned} \quad (3.42)$$

where the transition amplitudes $t_{\alpha j}(\vec{x}_\alpha, \vec{x}_j)$ used depend only on the relative position vector of the α and j constituents relative to one another. The form factors $F_{P,mm'}(-\vec{q})$ and $F_{T,\mu\mu'}(\vec{q})$ are the Fourier transforms of their corresponding single-particle transition densities given in equations (3.40) and (3.41), respectively. Using equations (3.34) and (3.42) in equation (3.38) results in the following form for the Born approximation:

$$f_{m'\mu', m\mu}^B(\vec{q}) = -\frac{1}{4\pi} \left(\frac{2mA_P^2 A_T^2}{N} \right) F_{T,\mu'\mu}(\vec{q}) F_{P,m'm}(-\vec{q}) \bar{t}(k, \vec{q}) \quad (3.43)$$

where

$$\bar{t}(k, \vec{q}) = \frac{1}{A_P A_T} \sum_{\alpha j} t_{\alpha j}(k, \vec{q}) \quad (3.44)$$

is the transition amplitude averaged over nuclear constituents.

Consider now the projectile form factor given by the Fourier transform of the single-particle densities as

$$\begin{aligned}
 F_{P,m'm}(\vec{q}) &= \int \exp(i\vec{q} \cdot \vec{r}_\alpha) \rho_{P,m'm}(\vec{r}_\alpha) d^3\vec{r}_\alpha \\
 &= \int g_{P,m'}^*(\vec{\xi}_P) \exp(i\vec{q} \cdot \vec{\xi}_{P,\alpha}) g_{P,m}(\vec{\xi}_P) d^3\vec{\xi}_P \quad (3.45)
 \end{aligned}$$

Expanding the exponential factor as a power series results in

$$F_{P,m'm}(\vec{q}) = \delta_{m'm} + i\vec{a}_{P,1} \cdot \vec{q} - \frac{1}{2} \vec{q} \cdot \overleftrightarrow{a}_{P,2} \cdot \vec{q} + \dots \quad (3.46)$$

where the first term in equation (3.46) corresponds to the normalization condition of the eigenstates; the second term contains the dipole transition moment given by

$$\vec{a}_{P,1} = \left\langle g_{P,m'}(\vec{\xi}_P) \left| \vec{\xi}_{P,\alpha} \right| g_{P,m}(\vec{\xi}_P) \right\rangle \quad (3.47)$$

and the third term contains the dyadic quadrupole transition moment

$$\overleftrightarrow{a}_{P,2} = \left\langle g_{P,m'}(\vec{\xi}_P) \left| \vec{\xi}_{P,\alpha} \vec{\xi}_{P,\alpha} \right| g_{P,m}(\vec{\xi}_P) \right\rangle \quad (3.48)$$

The higher order multipole transitions are indicated by dots in equation (3.46). The lowest order nonzero term in equation (3.46) depends on the properties of the internal wave functions involved. In general, the ℓ th transition moment with magnitude given by

$$a_{P,\ell} = \left| \left\langle g_{P,m'}(\vec{\xi}_P) \left| (\vec{\xi}_{P,\alpha})^\ell \right| g_{P,m}(\vec{\xi}_P) \right\rangle \right| \quad (3.49)$$

is zero unless

$$\left| J_{m'} - J_m \right| \leq \ell \leq \left| J_{m'} + J_m \right| \quad (3.50)$$

as a result of the Wigner-Eckart theorem where J_m and $J_{m'}$ are the projectile internal angular-momentum quantum numbers in the entering and final states, respectively. Because of the orthogonality, equation (3.49) reduces to

$$a_{P,0} = \delta_{m'm} \quad (3.51)$$

for $\ell = 0$. It follows from relations (3.50) and (3.51) and for small momentum transfer that

$$F_{P,m'm}(\vec{q}) \approx \delta_{m'm} + \frac{a_{P,\ell_P} |\vec{q}|^{\ell_P}}{\ell_P!} \quad (3.52)$$

where

$$\ell_P = \max \left\{ \left| J_{m'} - J_m \right|, 1 \right\} \quad (3.53)$$

is the angular momentum associated with the lowest order transition moment. Similarly, for the target one obtains

$$F_{T,\mu'\mu}(\vec{q}) \approx \delta_{\mu'\mu} + \frac{a_{T,\ell_T} |\vec{q}|^{\ell_T}}{\ell_T!} \quad (3.54)$$

where

$$\ell_T = \max \left\{ \left| J_{\mu'} - J_{\mu} \right|, 1 \right\} \quad (3.55)$$

It follows from relations (3.43), (3.52), and (3.54) that the Born amplitude has proportionality given by

$$f_{m'\mu',m\mu}^B(\vec{q}) \propto \left(\delta_{m'm} + \frac{a_{P,\ell_P} |\vec{q}|^{\ell_P}}{\ell_P!} \right) \left(\delta_{\mu'\mu} + \frac{a_{T,\ell_T} |\vec{q}|^{\ell_T}}{\ell_T!} \right) \tilde{t}(k, \vec{q}) \quad (3.56)$$

where a_{P,ℓ_P} and a_{T,ℓ_T} are the lowest order nonvanishing transition moments of the projectile and target corresponding to equations (3.53) and (3.55).

On the basis of the Born approximation, a very strong threshold effect on the various excitation processes is observed. This effect causes an ordering in the contribution of specific excitation channels in going from small to large momentum transfer. At zero momentum transfer, only the elastic channel is open. As the momentum transfer increases, the single dipole transitions for either the target or the projectile, but not both, are displayed first. Note that this condition severely restricts the accessible angular momentum states in the excitation process. At slightly higher momentum transfer, coincident dipole transitions in projectile and target and single quadrupole transitions are in competition with and may eventually dominate the single dipole transitions at sufficiently high momentum transfer. Similarly, at higher momentum transfer, transitions to higher angular-momentum states are possible.

3.3.3. Perturbation expansion and distorted-wave Born approximation. According to the previous discussion, for a restricted range of momentum transfer, the off-diagonal elements of the "Born" matrix of scattering amplitudes are small compared with the elastic-scattering amplitudes for the various channels found along the diagonal. By noting that these amplitudes are proportional to the potential, a decomposition of the potential into large and small components (Wilson, 1975) may be made as

$$U(\vec{x}) = U_d(\vec{x}) + U_o(\vec{x}) \quad (3.57)$$

where $U_d(\vec{x})$ denotes the diagonal parts of $U(\vec{x})$ and $U_o(\vec{x})$ denotes the corresponding off-diagonal parts. Clearly,

$$U_d(\vec{x}) \gg U_o(\vec{x}) \quad (3.58)$$

which is in accordance with the preceding discussion. Treating the off-diagonal contribution as a perturbation and considering the iterated solution will lead to substantial simplification (Wilson, 1975).

Rewriting equation (3.35) as

$$\left[\nabla_x^2 + \vec{k}^2 - U_d(\vec{x}) \right] \psi(\vec{x}) = U_o(\vec{x}) \psi(\vec{x}) \quad (3.59)$$

and taking as a first approximation

$$\left[\nabla_x^2 + \vec{k}^2 - U_d(\vec{x}) \right] \psi_0(\vec{x}) = 0 \quad (3.60)$$

leads to a solvable problem. The only nonzero component of $\psi_0(\vec{x})$ is the elastic coherent scattered wave. If the initial prepared nuclei are in their ground states, then the solution for the coherent elastic wave is obtained from

$$\left(\nabla_x^2 + \vec{k}^2 \right) \psi_c(\vec{x}) = U_{00,00}(\vec{x}) \psi_c(\vec{x}) \quad (3.61)$$

and the first approximation to the coupled-channel problem is

$$\psi_0(\vec{x}) = \begin{bmatrix} \psi_c(\vec{x}) \\ 0 \\ 0 \\ 0 \\ \vdots \end{bmatrix} \quad (3.62)$$

Estimating the perturbation by using equation (3.62) yields the lowest order correction as

$$\left[\nabla_x^2 + \vec{k}^2 - U_d(\vec{x}) \right] \psi^{(1)}(\vec{x}) = U_o(\vec{x}) \psi_0(\vec{x}) \quad (3.63)$$

The right-hand side is a term describing the source of excitation caused by the interaction of the coherent amplitude and is of the form

$$U_o(\vec{x}) \psi_0(\vec{x}) = \begin{bmatrix} 0 \\ U_{01,00} \\ U_{10,00} \\ U_{11,00} \\ \vdots \end{bmatrix} \psi_c(\vec{x}) \quad (3.64)$$

Because the first component of the source of excitation is zero, the equation for the first component of equation (3.35) is

$$\left[\nabla_x^2 + \vec{k}^2 - U_{00,00}(\vec{x}) \right] \psi_{00}^{(1)}(\vec{x}) = 0 \quad (3.65)$$

and reveals that the iteration of the elastic channel yields again the coherent elastic amplitude

$$\psi_{00}^{(1)}(\vec{x}) = \psi_c(\vec{x}) \quad (3.66)$$

The remaining components of equation (3.63) are

$$\left[\nabla_x^2 + \vec{k}^2 - U_{m\mu,m\mu}(\vec{x}) \right] \psi_{m\mu}^{(1)}(\vec{x}) = U_{m\mu,00}(\vec{x}) \psi_c(\vec{x}) \quad (3.67)$$

This process of successive iteration is equivalent to the series approximation

$$\psi(\vec{x}) = \psi_0(\vec{x}) + \psi_1(\vec{x}) + \psi_2(\vec{x}) + \dots \quad (3.68)$$

where

$$\left[\nabla_{\vec{x}}^2 + \vec{k}^2 - U_d(\vec{x}) \right] \psi_0(\vec{x}) = 0 \quad (3.69)$$

and

$$\left[\nabla_{\vec{x}}^2 + \vec{k}^2 - U_d(\vec{x}) \right] \psi_i(\vec{x}) = U_o(\vec{x}) \psi_{i-1}(\vec{x}) \quad (3.70)$$

The iterated solution and series solution are related as

$$\left. \begin{aligned} \psi_i(\vec{x}) &= \psi^{(i)}(\vec{x}) - \psi^{(i-1)}(\vec{x}) \\ \psi^{(-1)}(\vec{x}) &\equiv 0 \end{aligned} \right\} \quad (3.71)$$

and the i th iterate $\psi^{(i)}(\vec{x})$ is the i th partial sum of the series.

Further insight can be gained by considering the formal solution to the coupled equations (3.69) and (3.70). Introducing the diagonal coherent propagator

$$G_c = \left[\nabla_{\vec{x}}^2 + \vec{k}^2 - U_d(\vec{x}) \right]^{-1} \quad (3.72)$$

and the coherent wave operator

$$\Omega_c = 1 + \left(\nabla_{\vec{x}}^2 + \vec{k}^2 \right)^{-1} U_d(\vec{x}) \quad (3.73)$$

produces the solution to equation (3.70) as

$$\psi_i(\vec{x}) = G_c U_o(\vec{x}) \psi_{i-1}(\vec{x}) \quad (3.74)$$

with

$$\psi_0 = \Omega_c \psi_p \quad (3.75)$$

where ψ_p is the entering plane-wave state. The series (eq. (3.68)) may now be written as

$$\psi = \Omega_c \psi_p + G_c U_o \Omega_c \psi_p + G_c U_o G_c U_o \Omega_c \psi_p + \dots \equiv \Omega \psi_p \quad (3.76)$$

The first term is the coherent elastic-scattered wave as noted in equation (3.75) and represents attenuation and propagation of the incident plane wave in matter. Since Ω_c is diagonal, this propagation is in undisturbed matter. The second term of equation (3.76) relates to the excitation caused by the presence of the coherent elastic wave followed by coherent propagation in disturbed matter. Note that the second term has no contribution in the elastic channel. The third term of equation (3.76) relates to further excitation caused by the presence of the scattered waves formed exclusively by coherent excitation and the first correction to the elastic channel caused by incoherent processes. Hence, the coherent elastic wave is correct up to second-order terms in off-diagonal elements of the potential matrix. These off-diagonal elements show considerable damping or suppression at small

momentum transfer as shown in connection with equation (3.56). This may well be the reason that the coherent elastic amplitude has been so successful in nuclear applications (Wilson, 1975; Wilson and Costner, 1975; Best, 1972).

The structure of the second term in the series (eq. (3.76)) is either the usual distorted-wave Born approximation (Austern, 1963) or the single inelastic scattering approximation (Goldberger and Watson, 1964). The entire series could be aptly referred to as the distorted-wave Born series. However, recalling that the terms of the series correspond to a successively larger number of changes in states of excitation (that is, the first term contains no excitation, the second term transforms the coherent elastic wave to the excited states, the third term transforms the excited states of the second term to new excitation levels, and so on), a more appropriate name for the series would be the "multiple-excitation series."

3.4. Coupled-Channel Amplitudes

The coupled equations (3.35) are now solved within a small-angle approximation. This solution in effect sums the multiple-excitation series to all orders and, as a final result, gives expressions for the scattering amplitudes connecting all possible entrance channels to all possible final channels. By making the forward-scattering assumption, the boundary condition is given by

$$\lim_{z \rightarrow -\infty} \psi(\vec{x}) = \left(\frac{1}{2\pi} \right)^{3/2} \exp(i\vec{k} \cdot \vec{x}) \hat{\delta} \quad (3.77)$$

where $-\hat{z}$ is the direction to the beam source and $\hat{\delta}$ is a constant vector with a unit entry at the entrance channel element but zero elsewhere. Equation (3.77) simply states that no particles are scattered backward. Physically, this assumption is justified because the backward-scattered component for most high-energy scattering is many orders of magnitude less than the forward-scattered component. The form of the solution to equation (3.35) is taken as

$$\psi(\vec{x}) = \left(\frac{1}{2\pi} \right)^{3/2} \exp[i\phi(\vec{x})] \exp(i\vec{k} \cdot \vec{x}) \hat{\delta} \quad (3.78)$$

where the boundary condition (3.77) implies that

$$\lim_{z \rightarrow -\infty} \phi(\vec{x}) = 0 \quad (3.79)$$

as a boundary condition on $\phi(\vec{x})$. By using equation (3.78), one may write an equation for $\phi(\vec{x})$ as

$$i\nabla_x^2 \phi(\vec{x}) - [\nabla_x \phi(\vec{x})]^2 - 2\vec{k} \cdot \nabla_x \phi(\vec{x}) - U(\vec{x}) = 0 \quad (3.80)$$

If $U(\vec{x})$ is small compared with the kinetic energy

$$U(\vec{x}) \ll k^2 \quad (3.81)$$

and if the change in $U(\vec{x})$ is small over one oscillation of the incident wave, that is,

$$\nabla_x U(\vec{x}) \ll \vec{k} U(\vec{x}) \quad (3.82)$$

where inequalities refer to magnitudes of elements on each side of equations (3.81) and (3.82), then equation (3.80) may be approximated by

$$2k \frac{\partial}{\partial z} \phi(\vec{x}) = -U(\vec{x}) \quad (3.83)$$

which has the solution

$$\phi(\vec{x}) = -\frac{1}{2k} \int_a^z U(\vec{x}') d\vec{z}' \quad (3.84)$$

where the value of a is fixed by the boundary condition (eq. (3.79)) to be $-\infty$. The scattered wave (eq. (3.78)) may now be written as

$$\psi(\vec{x}) = \left(\frac{1}{2\pi}\right)^{3/2} \exp\left[-\frac{i}{2k} \int_{-\infty}^z U(\vec{x}') d\vec{z}'\right] \exp(i\vec{k} \cdot \vec{x}) \hat{\delta} \quad (3.85)$$

Note that the wave operator is approximated by

$$\Omega \approx \exp\left[-\frac{i}{2k} \int_{-\infty}^z U(\vec{x}') d\vec{z}'\right] \quad (3.86)$$

The eikonal result for the scattering amplitudes is given by

$$\begin{aligned} f(\vec{q}) \hat{\delta} &= -\sqrt{\frac{\pi}{2}} \int \exp(-i\vec{k}_f \cdot \vec{x}) U(\vec{x}) \psi(\vec{x}) d^3\vec{x} \\ &= -\frac{1}{4\pi} \int \exp(-i\vec{q} \cdot \vec{x}) U(\vec{x}) \exp\left[-\frac{i}{2k} \int_{-\infty}^z U(\vec{x}') d\vec{z}'\right] \hat{\delta} d^3\vec{x} \end{aligned} \quad (3.87)$$

where \vec{k}_f is the final projectile momentum and \vec{q} the momentum transfer given by

$$\vec{q} = \vec{k}_f - \vec{k} \quad (3.88)$$

The eikonal approximation to the coupled-channel amplitude (eq. (3.87)) can be further simplified by making an additional small-angle approximation as follows. By using a cylindrical coordinate system with cylinder axis along the beam direction and writing

$$\vec{x} = \vec{b} + \vec{z} \quad (3.89)$$

where \vec{b} is the impact parameter vector, the product of \vec{q} and \vec{x} may be written as

$$\vec{q} \cdot \vec{x} = \vec{q} \cdot \vec{b} + O(\theta^2) \quad (3.90)$$

where θ is the scattering angle which is assumed to be small. This small-angle approximation allows equation (3.87) to be written as

$$f(\vec{q}) = -\frac{1}{4\pi} \int \exp(-i\vec{q} \cdot \vec{b}) U(\vec{b} + \vec{z}) \exp\left[-\frac{i}{2k} \int_{-\infty}^z U(\vec{b} + \vec{z}') d\vec{z}'\right] d^2\vec{b} d\vec{z} \quad (3.91)$$

where the integral over \vec{z} can be performed exactly. Performing the integral over \vec{z} in equation (3.91) yields the final simplified expression for the scattering amplitude as

$$f(\vec{q}) = -\frac{ik}{2\pi} \int \exp(-i\vec{q} \cdot \vec{b}) \left\{ \exp \left[i \chi(\vec{b}) \right] - 1 \right\} d^2\vec{b} \quad (3.92)$$

where

$$\chi(\vec{b}) = -\frac{1}{2k} \int_{-\infty}^{\infty} U(\vec{b} + \vec{z}) d\vec{z} \quad (3.93)$$

Equation (3.92) gives the matrix of scattering amplitudes of all possible entrance channels to all possible final channels of the system.

The relation between the eikonal result for the full scattering amplitude (eq. (3.92)) and the various approximate results discussed earlier in this section is now derived. First, consider the expansion in powers of χ of the integrand of equation (3.92):

$$f(\vec{q}) = \frac{ik}{2\pi} \int \exp(-i\vec{q} \cdot \vec{b}) \left(i\chi - \frac{1}{2!}\chi^2 - \frac{1}{3!}i\chi^3 + \dots \right) d^2\vec{b} \quad (3.94)$$

The first term is the Born approximation at small angles. Higher order terms are multiple-scattering corrections to the Born result. Recall that the Born approximation for the optical potential is equivalent to Chew's impulse approximation. A more interesting result is obtained by separating the χ matrix into its diagonal and off-diagonal parts as

$$\chi(\vec{b}) = \chi_d(\vec{b}) + \chi_o(\vec{b}) \quad (3.95)$$

which correspond to the diagonal and off-diagonal parts of the matrix potential $U(\vec{x})$. An expansion in powers of the off-diagonal part of χ in equation (3.92) yields

$$f(\vec{q}) = -\frac{ik}{2\pi} \int \exp(-i\vec{q} \cdot \vec{b}) \left\{ \exp \left[i \chi_d(\vec{b}) \right] - 1 \right\} d^2\vec{b} \\ - \frac{ik}{2\pi} \int \exp(-i\vec{q} \cdot \vec{b}) \exp \left[i \chi_d(\vec{b}) \right] \left(i\chi_o - \frac{1}{2!}\chi_o^2 - \frac{1}{3!}i\chi_o^3 + \dots \right) d^2\vec{b} \quad (3.96)$$

The first integral is the elastic coherent amplitude, the first term of the second integral is the distorted-wave Born approximation, and the remaining terms are multiple-excitation corrections.

3.5. The Elastic Channel

Section 3.4 showed that within a small-angle approximation, the coupled-channel equations could be solved. The principal difficulty in calculating the full coupled-channel amplitude lies in the almost complete lack of knowledge of the internal wave functions for the colliding nuclei for all orders of excitation. On the very general principles for near forward scattering, transitions to the excited states are kinematically suppressed. This was the main motivation for expanding the solution in terms of off-diagonal matrix elements of the potential. Near forward scattering, the scattering amplitude is dominated by the diagonal elements. If elastic scattering is strongly forward, then a reasonable approximation to the

elastic amplitude is obtained by neglecting the off-diagonal contribution (coherent approximation), and, in addition, the eikonal small-angle approximation should be accurate. In this vein, the elastic-channel amplitude is approximated by retaining only the first term in equation (3.96). Detailed comparisons with experimental data are made to justify this approximation.

Wilson (1975) showed that the elastic-channel potential (actually the coherent potential) can be reduced to

$$U_c(\vec{x}) = \frac{2mA_T^2 A_P^2}{N} \int d^3\vec{z} \rho_T(\vec{z}) \int d^3\vec{y} \rho_P(\vec{x} + \vec{y} + \vec{z}) \tilde{t}(k, \vec{y}) \quad (3.97)$$

where $\rho_T(\vec{z})$ and $\rho_P(\vec{z})$ are the target and projectile ground-state single-particle densities, respectively, and $\tilde{t}(k, \vec{y})$ is the energy- and space-dependent two-body transition amplitudes averaged over the projectile and target constituent types as

$$\tilde{t} = \frac{1}{A_P A_T} [N_P N_T t_{nn} + Z_P Z_T t_{pp} + (N_P Z_T + Z_P N_T) t_{np}] \quad (3.98)$$

with N_P and N_T being the projectile and target neutron numbers, respectively, and Z_P and Z_T being the corresponding proton numbers. The normalization of the \tilde{t} amplitude is given by

$$\tilde{t}(k, \vec{y}) = - \frac{1}{(2\pi)^2 \mu} \int \exp(i\vec{q} \cdot \vec{y}) f(e, \vec{q}) d^3\vec{q} \quad (3.99)$$

with the usual expression for the spin-independent two-nucleon transition amplitudes as

$$f(e, \vec{q}) = \frac{\sigma(e)\sqrt{me}}{4\pi} [\alpha(e) + i] \exp\left[-\frac{1}{2} B(e) \vec{q}^2\right] \quad (3.100)$$

where e is the kinetic energy in the two-body center-of-mass frame, $\mu = m/2$ is the two-body reduced mass, $\sigma(e)$ is the energy-dependent total two-body cross section, $\alpha(e)$ is the ratio of real to imaginary parts, and $B(e)$ is the slope parameter. The elastic-channel phase function may now be approximated by

$$\chi(\vec{b}) = -\frac{1}{2k} \int_{-\infty}^{\infty} U_c(\vec{b} + \vec{z}) d\vec{z} \quad (3.101)$$

from which the elastic-channel (coherent) amplitude may be calculated by

$$f_c(\vec{q}) = -ik \int_0^{\infty} b db J_0\left(2kb \sin \frac{\theta}{2}\right) \left\{ \exp[i\chi(\vec{b})] - 1 \right\} \quad (3.102)$$

where the property that the phase function is cylindrically symmetric about the \hat{z} -direction has been used and $J_0(\)$ is the zeroth-order Bessel function. Applying now the optical theorem

$$\sigma_{\text{tot}} = \frac{4\pi}{k} \text{Im} [f_c(\vec{0})] \quad (3.103)$$

yields

$$\sigma_{\text{tot}} \approx 4\pi \int_0^{\infty} b db \left\{ 1 - \exp[-\chi_i(\vec{b})] \cos[\chi_r(\vec{b})] \right\} \quad (3.104)$$

where χ_r and χ_i are the real and imaginary parts, respectively, of χ . Since the scattering is strongly forward, the total elastic cross section may be calculated by using the eikonal expression by

$$\begin{aligned} \sigma_s &= \int |f(\vec{q})|^2 d\hat{q} \\ &\approx 4\pi \int_0^\infty b db \left\{ 1 - \exp \left[-\chi_i(\vec{b}) \right] \cos \left[\chi_r(\vec{b}) \right] \right\} \\ &\quad - 2\pi \int_0^\infty b db \left\{ 1 - \exp \left[-2 \chi_i(\vec{b}) \right] \right\} \end{aligned} \quad (3.105)$$

from which it follows that

$$\sigma_{\text{abs}} = \sigma_{\text{tot}} - \sigma_s \approx 2\pi \int_0^\infty b db \left\{ 1 - \exp \left[-2 \chi_i(\vec{b}) \right] \right\} \quad (3.106)$$

The use of the coherent wave as an approximation to the elastic channel has, at least in part, been justified by comparison with experiment (Wilson, 1975; Wilson and Costner, 1975). The formalism gave good agreement with the experiments of Schimmerling et al. (1971 and 1973), as shown in figures 3.4 and 3.5, and predicted oscillations in cross sections for nuclei corresponding to the shell structure of nuclei (Wilson, 1975) as shown in figures 3.4 to 3.6.

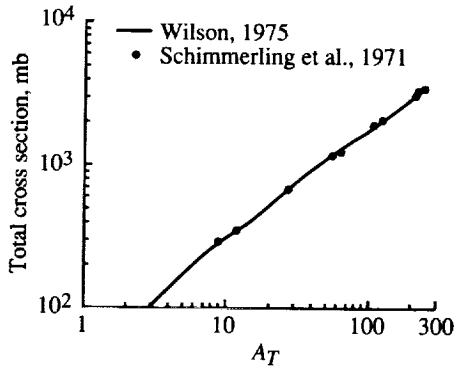


Figure 3.4. Total nucleon-nucleus cross section as a function of a nuclear mass number at 1.064 GeV.

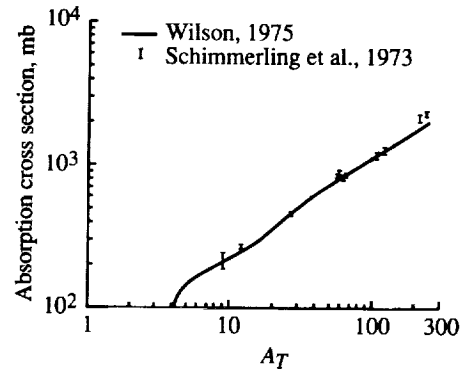


Figure 3.5. Nucleon-nucleus absorption cross section as a function of nuclear mass number at about 1 GeV.

3.6. Abrasion Theory

Abrasion theories developed in recent years have relied on Glauber theory as the basic formalism for the evaluation of probabilistic collision factors. Consequently, the inherent restrictions of Glauber theory are also limitations in these models. With the more powerful theoretical methods now available (Wilson, 1975), the development of a new abrasion theory is appropriate based on these more general results from current abrasion theories. The present development follows closely the work of Townsend (1983 and 1984).

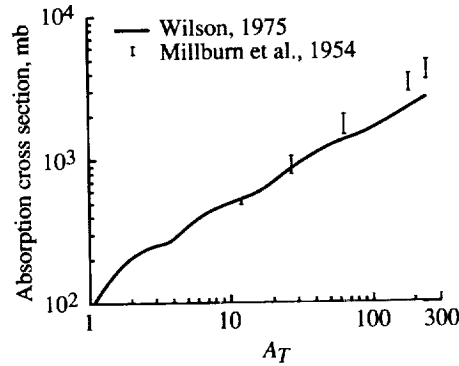


Figure 3.6. Triton-nucleus absorption cross section as a function of target mass at 100 MeV/nucleon.

In the abrasion-ablation collision model, projectile fragmentation is a three-step process. In the first step (abrasion), m nucleons are knocked out of the projectile nucleus of mass number A_P , leaving an excited prefragment nucleus of mass number

$$A_F = A_P - m \quad (3.107)$$

In the next step, the prefragment is ablated by gamma emission, particle emission (usually nucleons or α -particles), or a combination of the two. The third and final phase involves interactions between the particles in the final state. These final-state interactions, although not unique to this collision formalism, are nevertheless significant experimentally and must be included in any complete theory.

3.6.1. Abrasion cross section. From Bleszynski and Sander (1979), the cross section for abrading m projectile nucleons is given by

$$\sigma_m = \binom{A_P}{m} 2\pi \int [1 - P(\vec{b})]^m P(\vec{b})^{A_F} b db \quad (3.108)$$

where $\binom{A_P}{m}$ is the binomial coefficient that reflects the number of possible combinations of m nucleons taken from an ensemble of A_P identical nucleons. The total absorption cross section

$$\sigma_{\text{abs}} = 2\pi \int [1 - P(\vec{b})^{A_P}] b db \quad (3.109)$$

is obtained by summing over all values of m according to

$$\sigma_{\text{abs}} = \sum_{m=1}^{A_P} \sigma_m \quad (3.110)$$

In equations (3.108) and (3.109), $P(\vec{b})$ is the probability as a function of impact parameter for not removing a single projectile nucleon in the abrasion process. Hence, $1 - P(\vec{b})$ is the probability for the removal of a nucleon.

The probability in Glauber theory is given by (Bleszynski and Sander, 1979)

$$P(\vec{b}) = 2\pi \int D_P(\vec{s}) \exp \left[-A_T \sigma_{NN} D_T(\vec{s} + \vec{b}) \right] s ds \quad (3.111)$$

where A_T is the mass number of the target and $D(\vec{s})$ denotes the single-particle densities summed along the beam direction (thickness functions)

$$D(\vec{s}) = \int_{-\infty}^{\infty} \rho(\vec{s} + \vec{z}) dz \quad (3.112)$$

The abrasion theory is now extended to a more general collision theory that does not exhibit the convergence problems inherent with Glauber theory (Wilson, 1975; Wilson and Costner, 1975; Wilson and Townsend, 1981). An added feature of the extended abrasion theory, which gives symmetry to the final result, is that the projectile and target nuclei are treated on an equal basis.

3.6.2. Generalized abrasion theory. From the optical model derived in a previous section, the absorption cross section is expressed using the eikonal approximation

$$\sigma_{\text{abs}} = 2\pi \int_0^{\infty} \left\{ 1 - \exp \left[-2 \text{Im} \chi(\vec{b}) \right] \right\} b db \quad (3.113)$$

where the eikonal phase function $\chi(\vec{b})$, with the optical-model potential approximation from Wilson and Costner (1975) incorporated, is written as

$$\chi(\vec{b}) = \frac{1}{2} A_P A_T \sigma(e) [\alpha(e) + i] I(\vec{b}) \quad (3.114)$$

where

$$I(\vec{b}) = [2\pi B(e)]^{-3/2} \int d\vec{z} \int d^3\vec{\xi}_T \rho_T(\vec{\xi}_T) \times \int d^3\vec{y} \rho_P(\vec{b} + \vec{z} + \vec{y} + \vec{\xi}_T) \exp \left[\frac{-\vec{y}^2}{2 B(e)} \right] \quad (3.115)$$

In equations (3.114) and (3.115), $\sigma(e)$ is the energy-dependent nucleon-nucleon cross section, $\alpha(e)$ is the energy-dependent ratio of the real part to the imaginary part of the scattering amplitudes, $B(e)$ is the energy-dependent slope parameter, and ρ_P and ρ_T are the projectile and target single-particle nuclear densities, respectively. Townsend (1983) uses equations (3.109) and (3.113) to imply that

$$P(\vec{b})^{A_P} = \exp \left[-2 \text{Im} \chi(\vec{b}) \right] \quad (3.116)$$

Substitution of equation (3.114) into equation (3.116) yields

$$P(\vec{b}) = \exp \left[-A_T \sigma(e) I(\vec{b}) \right] \quad (3.117)$$

Finally, the cross section for abrading any m nucleons (eq. (3.108)) is written as

$$\sigma_m = \binom{A_P}{m} 2\pi \int \left\{ 1 - \exp \left[-A_T \sigma(e) I(\vec{b}) \right] \right\}^m \exp \left[-A_T A_F \sigma(e) I(\vec{b}) \right] b db \quad (3.118)$$

In evaluating equation (3.118), values for $\sigma(e)$ and $B(e)$ were taken from the compilations of Hellwege (1973) and Benary, Price, and Alexander (1970). The nuclear single-particle densities in equation (3.115) were extracted from the charge density data in De Jager, De Vries, and De Vries (1974) using the detailed procedure of Wilson and Costner (1975).

3.6.3. Isotope production cross section. Up to this point, all nucleons have been treated as identical objects. To differentiate between protons and neutrons, equation (3.111) is replaced by (Hüfner, Schäfer, and Schürmann, 1975)

$$\sigma_{nz} = \binom{N_P}{n} \binom{Z_P}{z} 2\pi \int \left[1 - P(\vec{b}) \right]^{n+z} P(\vec{b})^{A_P - n - z} b db \quad (3.119)$$

where $P(\vec{b})$ is again given by equation (3.117). In equation (3.119), σ_{nz} is the cross section for abrading n out of N_P neutrons and z out of Z_P protons from the projectile nucleus. Implicit in this expression is the assumption that the neutron and proton distributions in the projectile nucleus are completely uncorrelated. This oversimplification of the actual complex nature of nucleon correlations in nuclei provides an analytically simple and convenient starting point for computing cross sections for specific fragment species.

3.6.4. Results. Figure 3.7 displays results obtained from equation (3.118) for ^{16}O projectile nuclei colliding with various stationary target nuclei. The incident kinetic energy is 2.1 GeV/nucleon. The shapes of the curves are largely determined by the $2\pi b$ factor and the effect of the spatial variations of ρ_T and ρ_P on $P(\vec{b})$ in the integrand of equation (3.118). The comparatively large cross sections for abrading 1 or 2 nucleons are indicative of the dominance at large impact parameters of the $2\pi b$ factor. Were it not for the large degree of nuclear-matter transparency in this very low density region, these cross sections would be even larger in magnitude. Physically, these theoretical results are not unexpected. In peripheral interactions, the nucleons near the surface are the least tightly bound and are more easily removed than those in the nuclear interior. Because of the short finite range of the nuclear force, abrasion is possible even if the projectile and target densities do not physically overlap.

As the number of abraded nucleons increases, overlap between the projectile and target must occur. This increases the overlapping densities that do not, however, offset the initial decrease in the impact parameter. As a result, the cross sections initially decrease with increasing values of m . Between $m = 5$ and $m = 11$, the cross-section curves flatten as the increasing nuclear densities tend to balance the decrease in the $2\pi b$ factor. For $m \geq 11$, the curves display a marked dependence on the size of the target nucleus. The rapid decrease in σ_m for the ^9Be target indicates that abrasion of all, or nearly all, projectile nucleons

by the smaller target is likely to occur only for very small impact parameters. If the target is pure hydrogen (curve not shown), the cross section for abrading all projectile nucleons in one collision, from equation (3.118), is less than 5 nanobarns (nb)—approximately a million times smaller than for the Be target. As target size increases, the abrasion cross sections increase as m increases. This results from the larger geometric area for which the projectile and target volumes completely overlap.

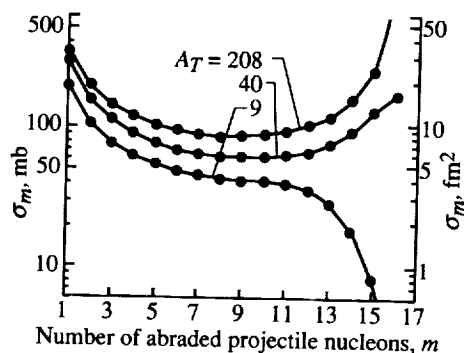


Figure 3.7. Oxygen-target abrasion cross sections σ_m as a function of the number of abraded projectile nucleons m . The lines are merely to guide the eye. Incident kinetic energy is 2.1 GeV/nucleon.

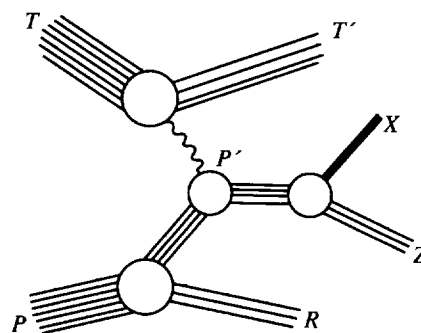


Figure 3.8. Equivalent Feynman diagram (lowest order; no time reversal) of projectile prefragmentation used in this work.

3.7. Abrasion-Ablation Model

In previous work (Townsend, 1984; Townsend et al., 1984b; Townsend, 1983), abrasion-ablation cross sections have been determined by calculating abrasion cross sections that are then multiplied by an ablation probability obtained from compound nucleus decay probabilities. This study demonstrates (Norbury, Townsend, and Deutchman, 1985) that the method of determining abrasion-ablation cross sections arises solely from particular approximations to the general formalism developed herein, and it is therefore only a special case of this more general formalism.

In terms of the transition rate, the total cross section is written as

$$\sigma = \frac{\nu}{v} w \quad (3.120)$$

where ν is the normalization volume and v is the incident velocity of the projectile. The transition rate is given as

$$w = \frac{2\pi}{\hbar} |T_{ki}^{AA}|^2 \rho(\epsilon_k) \quad (3.121)$$

where Planck's constant is denoted by \hbar and the transition amplitude is given by

$$T_{ki}^{AA} = \sum_n T_{kn}^{abl} G_{ni} T_{ni}^{abr} \quad (3.122)$$

where T_{kn}^{abl} is the ablation amplitude, G_{ni} is the propagator, and T_{ni}^{abr} is the abrasion amplitude. The total abrasion-ablation cross section for the phase space associated with figure 3.8 is

$$\sigma(Z) = \frac{2\pi\nu}{\hbar\nu} \frac{\nu^3}{(2\pi\hbar)^9} \frac{d}{d\epsilon_{ZXRT'}} \times \int \int \int |T_{ki}^{AA}|^2 d^3p_X d^3p_{T'} d^3p_Z \quad (3.123)$$

Using a phase space recurrence relation

$$\rho_4(\epsilon_{ZXRT}) = \int \int \int \rho_2(\epsilon_{ZXRT}) \times \rho_2(\epsilon_{ZX R}) \rho_2(\epsilon_{ZX}) d\epsilon_{ZX} d\epsilon_{ZX R} \quad (3.124)$$

demonstrates that d^3p_X can be replaced by $d^3p_{P'}$ in equation (3.123) where

$$d^3p_{P'} \equiv d^3p_{ZX} \quad (3.125)$$

This, together with equation (3.122), allows the cross section in equation (3.123) to be written as

$$\sigma(Z) = \frac{2\pi\nu}{\hbar\nu} \frac{\nu^3}{(2\pi\hbar)^9} \frac{d}{d\epsilon_{ZXRT'}} \int \int \int \left| \sum_n T_{kn}^{abl} G_{ni} T_{ni}^{abr} \right|^2 \times d^3p_{P'} d^3p_{T'} d^3p_Z \quad (3.126)$$

A major approximation is now introduced as

$$\left| \sum_n T_{kn}^{abl} G_{ni} T_{ni}^{abr} \right|^2 \approx \sum_n \left| T_{kn}^{abl} \right|^2 \left| G_{ni} \right|^2 \left| T_{ni}^{abr} \right|^2 \quad (3.127)$$

which will henceforth be referred to as the ‘‘classical probability approximation’’ because it involves the classical addition of probabilities (right-hand side) rather than the quantum mechanical addition of amplitudes (left-hand side). In essence, it involves ignoring the interference terms of the left-hand side of equation (3.127). We believe that the famous Bohr assumption for compound nucleus decay (Blatt and Weisskopf, 1959), which justifies the separation of a two-step cross section (such as compound nucleus formation and decay or abrasion-ablation) into a product of formation and decay (partial width) cross sections, is based upon this classical probability approximation. The Bohr assumption is so widely used because of the reasonableness of the classical argument. Equation (3.127) is sometimes justified quantum mechanically, especially when dealing with angular-momentum matrix elements (Brink and Satchler, 1968) where theorems on Clebsch-Gordan coefficients are available (Norbury, 1983). This is especially true, for example, for a single (one-level) resonant state involving several different angular-momentum projections M where the summation over n simply becomes a summation over M for the single resonance of a particular energy (Brink

and Satchler, 1968). This was also the case for the pion production work of Townsend and Deutchman (1981); Deutchman and Townsend (1980 and 1982); Deutchman et al. (1983); Townsend et al. (1984a); and Norbury, Deutchman, and Townsend (1984) where there was only the single intermediate isobar Δ resonance at a fixed energy but with various spin and isotopic spin projections. Norbury (1983) has shown that equation (3.127) results from the spin-isospin Clebsch-Gordan algebra. Another example is the photonuclear excitation of a compound nucleus where the formation of a resonant state of a single energy, but with different spin projections (Norbury et al., 1978), justifies the use of the Bohr assumption when calculating (γ, n) cross sections via compound nucleus formation and decay. In general, however, the preceding simplifications that justify the classical probability assumption do not hold for the abrasion-ablation process. For example, a particular final projectile fragment could result from the ablation of numerous different prefragments, each with a quite different excitation energy.

The partial width, which is simply a transition rate multiplied by Planck's constant, is

$$\Gamma_n = 2\pi \frac{\nu}{(2\pi\hbar)^3} \frac{d}{d\epsilon_{P'}} \int |T_{kn}^{abl}|^2 d^3 p_Z \quad (3.128)$$

Substituting equations (3.127) and (3.128) into equation (3.126) yields

$$\begin{aligned} \sigma(Z) = \sum_n \frac{\nu}{\hbar\nu} \frac{\nu^2}{(2\pi\hbar)^6} \frac{d}{d\epsilon_{ZXRT'}} \int \int \int \Gamma_n |G_{ni}|^2 |T_{ni}^{abr}|^2 \\ \times d^3 p_{P'} d^3 p_{T'} d\epsilon_{P'} \end{aligned} \quad (3.129)$$

which can be rewritten as

$$\begin{aligned} \sigma(Z) = \sum_n \frac{\nu}{\hbar\nu} \int \int \Gamma_n |G_{ni}|^2 |T_{ni}^{abr}|^2 \\ \times d \text{Nips}(\epsilon_{P'RT'}; p_{P'}, p_{R'}, p_{T'}) d\epsilon_{P'} \end{aligned} \quad (3.130)$$

where $d \text{Nips}$ is the noninvariant phase space factor. The abrasion cross section is

$$\begin{aligned} \sigma_n(A) = \frac{2\pi\nu}{\hbar\nu} \int |T_{ni}^{abr}|^2 \\ \times d \text{Nips}(\epsilon_{P'RT'}; p_{P'}, p_R, p_{T'}) \end{aligned} \quad (3.131)$$

where P' is approximated by the on-shell value. Equation (3.131) yields

$$\sigma(Z) = \frac{1}{2\pi} \sum_n \int \Gamma_n |G_{ni}|^2 \sigma_n(A) d\epsilon_{P'} \quad (3.132)$$

Inserting Green's function, the abrasion-ablation cross section is

$$\sigma(Z) = \frac{1}{2\pi} \sum_n \int \frac{\Gamma_n}{(\epsilon_n - \epsilon_i)^2 + (\Gamma/2)^2} \sigma_n(A) d\epsilon_{P'} \quad (3.133)$$

where the total Γ and partial widths are related by

$$\Gamma = \sum_n \Gamma_n \quad (3.134)$$

To evaluate the integral in equation (3.133), the zero-width approximation (Pilkuhn, 1967)

$$\lim_{\Gamma \rightarrow 0} \frac{\Gamma/2\pi}{(\epsilon_n - \epsilon_i)^2 + (\Gamma/2)^2} = \delta(\epsilon_n - \epsilon_i) \quad (3.135)$$

is introduced. If we write the energies explicitly as

$$\epsilon_n = \epsilon_{P'} + \epsilon_{T'} + \epsilon_R \quad (3.136)$$

with an initial-state energy given by

$$\epsilon_i = \epsilon_P + \epsilon_T \quad (3.137)$$

and the final-state energy as

$$\epsilon_k = \epsilon_X + \epsilon_Z + \epsilon_{T'} + \epsilon_R \quad (3.138)$$

then conservation of energy

$$\epsilon_k = \epsilon_i \quad (3.139)$$

yields

$$\epsilon_n - \epsilon_i = \epsilon_{P'} - (\epsilon_X + \epsilon_Z) \quad (3.140)$$

Inserting equation (3.140) into equation (3.133) indicates a variable, intermediate, virtual resonance energy $\epsilon_{P'}$ centered about $\epsilon_X + \epsilon_Z$, which is integrated over. The nature of the delta function in equation (3.135), however, destroys this quantum mechanical feature of virtual energy in the integral. The zero-width approximation, then, can be considered as another classical approximation. Inserting equations (3.135) and (3.140) into equation (3.133) yields

$$\sigma(Z) = \sum_n \frac{\Gamma_n}{\Gamma} \sigma_n(A) \quad (3.141)$$

If the branching ratio is defined as

$$g_n \equiv \frac{\Gamma_n}{\Gamma} \quad (3.142)$$

and is recognized as the usual ablation probability factor (Townsend et al., 1984b; Townsend, 1983)

$$\sigma(Z) = \sum_n g_n \sigma_n(A) \quad (3.143)$$

which is the standard abrasion-ablation cross-section result (Bleszynski and Sander, 1979; Hüfner, Schäfer, and Schürmann, 1975; Townsend et al., 1984b; Townsend, 1983; Bowman, Swiatecki, and Tsang, 1973).

This result (eq. (3.143)) can also be obtained from equation (3.133) by an alternative method. Since $\sigma_n(A)$ is obtained by integrating over all impact parameters, it is independent of $\epsilon_{P'}$. Taking it outside the integral enables equation (3.133) to be written as

$$\sigma(Z) = \frac{1}{2\pi} \sum_n \sigma_n(A) \int \frac{\Gamma_n}{(\epsilon_n - \epsilon_i)^2 + (\Gamma/2)^2} d\epsilon_{P'} \quad (3.144)$$

Inserting

$$\frac{\Gamma}{\Gamma} = 1 \quad (3.145)$$

inside the integral in equation (3.144) and substituting equation (3.142) yields

$$\sigma(Z) = \frac{1}{2\pi} \sum_n \sigma_n(A) \int g_n \frac{\Gamma}{(\epsilon_n - \epsilon_i)^2 + (\Gamma/2)^2} d\epsilon_{P'} \quad (3.146)$$

If g_n is independent of $\epsilon_{P'}$ (which merely requires Γ_n and Γ to possess the same energy dependence), then it can be taken outside the integral to yield

$$\sigma(Z) = \frac{1}{2\pi} \sum_n g_n \sigma_n(A) \int \frac{\Gamma}{(\epsilon_n - \epsilon_i)^2 + (\Gamma/2)^2} d\epsilon_{P'} \quad (3.147)$$

In principle, if the dependence of Γ on $\epsilon_{P'}$ is known, then the integral can be calculated numerically if not analytically. If the zero-width approximation is inserted from equation (3.135), equation (3.143) is again obtained.

Equation (3.143) is one of the central results of the present work. It represents a first-principles derivation of the usual abrasion-ablation cross section and results directly from the following: (1) the time-ordering approximation, (2) the classical probability approximation, and (3) the zero-width approximation. Clearly, then, the most obvious improvements to the abrasion-ablation theory would be to remove these assumptions. (The time-ordering approximation is the least important.)

3.8. Electromagnetic Interactions

So far we have discussed specifically nuclear interaction processes that dominate whenever the impact parameter is less than or equal to the sum of the nuclear radii. At larger impact parameters, the electromagnetic processes dominate because of the long-range interaction of the coulomb field. The elastic coulomb scattering contributes to the beam divergence with negligible energy loss (Rossi and Greisen, 1941; Highland, 1975). The inelastic coulomb scattering contributes to fragmentation of the projectile and target nuclei (Norbury and Townsend, 1990).

The ejection of the particles X from a nucleus by coulomb dissociation is given by

$$\sigma_{EM}(X) = \sum_{\pi\ell} \int_{E_0(x)}^{\infty} \sigma_{\gamma}^{\pi\ell}(E, X) N^{\pi\ell}(E) dE \quad (3.148)$$

where $\pi\ell$ indicates the active electromagnetic moment of the transition ($\pi = E$ or $M, \ell = 1, 2, \dots$), $N^{\pi\ell}(E)$ is the virtual photon density distribution generated by the passing heavy ion, and $\sigma_{\gamma}^{\pi\ell}(E, X)$ is the usual photonuclear cross section. The electric dipole (E1) contribution is related to the giant dipole resonance absorption cross section and the Weizsäcker-Williams virtual photon density function (Norbury and Townsend, 1986 and 1990; Norbury, Townsend, and Badavi, 1988; Norbury et al., 1988; Norbury, 1989a and 1989b; Cucinotta, Norbury, and Townsend, 1988). The electric quadrupole (E2) contributions are considered by Norbury (1990) and Norbury and Townsend (1990).

3.9. References

- Austern, N., 1963: Direct Reaction Theories. *Fast Neutron Physics. Part II: Experiments and Theory*, J. B. Marion and J. L. Fowler, eds., Interscience Publ., pp. 1113–1216.
- Benary, Odette; Price, Leroy R.; and Alexander, Gideon, 1970: *NN and ND Interactions (Above 0.5 GeV/c)—A Compilation*. UCRL-20000 NN, Lawrence Radiation Lab., Univ. of California.
- Bertini, Hugo W., 1969: Intranuclear-Cascade Calculation of the Secondary Nucleon Spectra From Nucleon-Nucleus Interactions in the Energy Range 340 to 2900 MeV and Comparisons With Experiment. *Phys. Review*, vol. 188, second ser., no. 4, pp. 1711–1730.
- Best, Melvyn E., 1972: Particle-Nucleus Scattering at Intermediate Energies. *Canadian J. Phys.*, vol. 50, no. 14, pp. 1609–1613.
- Blatt, John M.; and Weisskopf, Victor F., 1959: *Theoretical Nuclear Physics*. Springer-Verlag.
- Bleszynski, M.; and Sander, C., 1979: Geometrical Aspects of High-Energy Peripheral Nucleus-Nucleus Collisions. *Nuclear Phys. A*, vol. 326, nos. 2–3, pp. 525–535.
- Bowman, J. D.; Swiatecki, W. J.; and Tsang, C. F., 1973: *Abrasion and Ablation of Heavy Ions*. LBL-2908, Lawrence Berkeley Lab., Univ. of California.
- Brink, D. M.; and Satchler, G. R., 1968: *Angular Momentum, Second ed.* Clarendon Press.
- Chew, Geoffrey F., 1951: High Energy Elastic Proton-Deuteron Scattering. *Phys. Review*, vol. 84, second ser., no. 5, pp. 1057–1058.
- Cucinotta, Francis A.; Norbury, John W.; and Townsend, Lawrence W., 1988: *Multiple Nucleon Knockout by Coulomb Dissociation in Relativistic Heavy-Ion Collisions*. NASA TM-4070.
- Czyż, W.; and Maximon, L. C., 1969: High Energy, Small Angle Elastic Scattering of Strongly Interacting Composite Particles. *Ann. Phys. (N.Y.)*, vol. 52, no. 1, pp. 59–121.
- De Jager, C. W.; De Vries, H.; and De Vries, C., 1974: Nuclear Charge- and Magnetization-Density-Distribution Parameters From Elastic Electron Scattering. *At. Data & Nuclear Data Tables*, vol. 14, no. 5/6, pp. 479–508.
- Deutchman, P. A.; and Townsend, L. W., 1980: Coherent Isobar Production in Peripheral Relativistic Heavy-Ion Collisions. *Phys. Review Lett.*, vol. 45, no. 20, pp. 1622–1625.

Transport Methods and Interactions for Space Radiations

- Deutchman, P. A.; and Townsend, L. W., 1982: Isobars and Isobaric Analog States. *Phys. Review*, vol. 25, ser. C, no. 2, pp. 1105-1107.
- Deutchman, P. A.; Madigan, R. L.; Norbury, J. W.; and Townsend, L. W., 1983: Pion Production Through Coherent Isobar Formation in Heavy-Ion Collisions. *Phys. Lett.*, ser. B, vol. 132, no. 1, 2, 3, pp. 44-46.
- Fernbach, S.; Serber, R.; and Taylor, T. B., 1949: The Scattering of High Energy Neutrons by Nuclei. *Phys. Review*, vol. 75, second ser., no. 9, pp. 1352-1355.
- Foldy, L. L.; and Walecka, J. D., 1969: On the Theory of the Optical Potential. *Ann. Phys.*, vol. 54, no. 3, pp. 447-504.
- Franco, V.; and Glauber, R. J., 1966: High-Energy Deuteron Cross Sections. *Phys. Review*, vol. 142, second ser., no. 4, pp. 1195-1214.
- Gabriel, T. A.; Bishop, B. L.; and Lillie, R. A., 1984: *Shielding Considerations for Multi-GeV/Nucleon Heavy Ion Accelerators: The Introduction of a New Heavy Ion Transport Code*, HIT. ORNL/TM-8952 (Contract No. W-7405-eng-26), Oak Ridge National Lab.
- Glauber, R. J., 1955: Cross Sections in Deuterium at High Energies. *Phys. Review*, vol. 100, second ser., no. 1, pp. 242-248.
- Goldberger, M. L., 1948: The Interaction of High Energy Neutrons and Heavy Nuclei. *Phys. Review*, vol. 74, no. 10, pp. 1269-1277.
- Goldberger, Marvin L.; and Watson, Kenneth M., 1964: *Collision Theory*. John Wiley & Sons, Inc.
- Gross, Franz, 1965: Relativistic Treatment of Loosely Bound Systems in Scattering Theory. *Phys. Review*, vol. 140, second ser., no. 2B, pp. B410-B421.
- Harrington, David R., 1969: Multiple Scattering, the Glauber Approximation, and the Off-Shell Eikonal Approximation. *Phys. Review*, vol. 184, second ser., no. 5, pp. 1745-1749.
- Hellwege, K.-H., ed., 1973: *Landolt-Börnstein Numerical Data and Functional Relationships in Science and Technology—Group I: Nuclear and Particle Physics*, Volume 7, *Elastic and Charge Exchange Scattering of Elementary Particles*. Springer-Verlag.
- Highland, Virgil L., 1975: Some Practical Remarks on Multiple Scattering. *Nuclear Instrum. & Methods*, vol. 129, no. 2, pp. 497-499.
- Hüfner, J.; Schäfer, K.; and Schürmann, B., 1975: Abrasion-Ablation in Reactions Between Relativistic Heavy Ions. *Phys. Review*, vol. 12, ser. C, no. 6, pp. 1888-1898.
- Humberston, J. W.; and Wallace, J. B. G., 1970: Deuteron Wave Functions for the Hamada-Johnston Potential. *Nuclear Phys.*, vol. A141, no. 2, pp. 362-368.
- Mandelstam, S., 1955: Dynamical Variables in the Bethe-Salpeter Formalism. *Proc. Royal Soc. (London)*, ser. A, vol. 233, no. 1193, pp. 248-266.

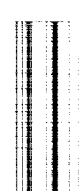
- Metropolis, N.; Bivins, R.; Storm, M.; Turkevich, Anthony; Miller, J. M.; and Friedlander, G., 1958: Monte Carlo Calculations on Intranuclear Cascades. I. Low-Energy Studies. *Phys. Review*, vol. 110, second ser., no. 1, pp. 185–203.
- Millburn, G. P.; Birnbaum, W.; Crandall, W. E.; and Schecter, L., 1954: Nuclear Radii From Inelastic Cross-Section Measurements. *Phys. Review*, vol. 95, second ser., no. 1, pp. 1268–1278.
- Norbury, J. W.; Thompson, M. N.; Shoda, K.; and Tsubota, H., 1978: Photoneutron Cross Sections of ^{54}Fe . *Australian J. Phys.*, vol. 31, no. 6, pp. 471–475.
- Norbury, John William, 1983: *Pion Production in Relativistic Heavy Ion Collisions*. Ph.D. Diss., Univ. of Idaho Graduate School.
- Norbury, J. W.; Deutchman, P. A.; and Townsend, L. W., 1984: A Particle-Hole Formalism for Pion Production From Isobar Formation and Decay in Peripheral Heavy Ion Collisions. *Bull. American Phys. Soc.*, vol. 29, no. 4, p. 688.
- Norbury, John W.; Townsend, Lawrence W.; and Deutchman, Philip A., 1985: *A T-Matrix Theory of Galactic Heavy-Ion Fragmentation*. NASA TP-2363.
- Norbury, John W.; and Townsend, Lawrence W., 1986: *Electromagnetic Dissociation Effects in Galactic Heavy-Ion Fragmentation*. NASA TP-2527.
- Norbury, John W.; Cucinotta, F. A.; Townsend, L. W.; and Badavi, F. F., 1988: Parameterized Cross Section for Coulomb Dissociation in Heavy-Ion Collisions. *Nuclear Instrum. & Methods Phys. Res.*, vol. B31, no. 4, pp. 535–537.
- Norbury, John W.; Townsend, Lawrence W.; and Badavi, Forooz F., 1988: *Computer Program for Parameterization of Nucleus-Nucleus Electromagnetic Dissociation Cross Sections*. NASA TM-4038.
- Norbury, John W., 1989a: Comment on “Electromagnetic Dissociation of ^{59}Co and ^{197}Au Targets by Relativistic ^{139}La Projectiles.” *Phys. Review C*, vol. 39, third ser., no. 6, pp. 2472–2473.
- Norbury, John W., 1989b: Nucleon Emission Via Electromagnetic Excitation in Relativistic Nucleus-Nucleus Collisions: Reanalysis of the Weizsäcker-Williams Method. *Phys. Review C*, vol. 40, third ser., no. 6, pp. 2621–2628.
- Norbury, John W., 1990: Electric Quadrupole Excitations in the Interactions of ^{89}Y With Relativistic Nuclei. *Phys. Review C*, vol. 41, third ser., no. 1, pp. 372–373.
- Norbury, John W.; and Townsend, Lawrence W., 1990: *Calculation of Two-Neutron Multiplicity in Photonuclear Reactions*. NASA TP-2968.
- Pilkuhn, Hartmut, 1967: *The Interactions of Hadrons*. John Wiley & Sons, Inc.
- Postma, Herman; and Wilson, Richard, 1961: Elastic Scattering of 146-MeV Polarized Protons by Deuterons. *Phys. Review*, vol. 121, second ser., no. 4, pp. 1229–1244.
- Remler, Edward A., 1968: High-Energy Scattering by Nuclei. *Phys. Review*, vol. 176, second ser., no. 5, pp. 2108–2112.

Transport Methods and Interactions for Space Radiations

- Rossi, Bruno; and Greisen, Kenneth, 1941: Cosmic-Ray Theory. *Reviews Modern Phys.*, vol. 13, no. 4, pp. 240–309.
- Santoro, R. T.; Alsmiller, R. G.; Barnes, J. M.; and Corbin, J. M., 1986: *Shielding of Manned Space Stations Against Van Allen Belt Protons: A Preliminary Scoping Study*. ORNL/TM-10040 (Contract No. IDOD3070-0000), Oak Ridge National Lab.
- Schimmerling, W.; Devlin, T. J.; Johnson, W.; Vosburgh, K. G.; and Mischke, R. E., 1971: Neutron-Nucleus Total Cross Sections From 900 to 2600 MeV/c. *Phys. Lett.*, vol. 37B, no. 2, pp. 177–180.
- Schimmerling, Walter; Devlin, Thomas J.; Johnson, Warren W.; Vosburgh, Kirby G.; and Mischke, Richard E., 1973: Neutron-Nucleus Total and Inelastic Cross Sections: 900 to 2600 MeV/c. *Phys. Review C*, vol. 7, third ser., no.1, pp. 248–262.
- Serber, R., 1947: Nuclear Reactions at High Energies. *Phys. Review*, vol. 72, no. 11, pp. 1114–1115.
- Townsend, L. W.; and Deutchman, P. A., 1981: Isobar Giant Resonance Formation in Self-Conjugate Nuclei. *Nuclear Phys.*, vol. A355, pp. 505–532.
- Townsend, L. W., 1983: Abrasion Cross Sections for ^{20}Ne Projectiles at 2.1 GeV/Nucleon. *Canadian J. Phys.*, vol. 61, no. 1, pp. 93–98.
- Townsend, Lawrence W., 1984: *Ablation Effects in Oxygen-Lead Fragmentation at 2.1 GeV/Nucleon*. NASA TM-85704.
- Townsend, L. W.; Deutchman, P. A.; Madigan, R. L.; and Norbury, J. W., 1984a: Pion Production Via Isobar Giant Resonance Formation and Decay. *Nuclear Phys. A*, vol. 415, pp. 520–529.
- Townsend, Lawrence W.; Wilson, John W.; Norbury, John W.; and Bidasaria, Hari B., 1984b: *An Abrasion-Ablation Model Description of Galactic Heavy-Ion Fragmentation*. NASA TP-2305.
- Ůlehla, Ivan; Gomolčák, Ladislav; and Pluhař, Zdeněk (G. Alter, transl.), 1964: *Optical Model of the Atomic Nucleus*. Academic Press Inc.
- Watson, Kenneth M., 1953: Multiple Scattering and the Many-Body Problem—Applications to Photomeson Production in Complex Nuclei. *Phys. Review*, vol. 89, second ser., no. 3, pp. 575–587.
- Wilson, John W., 1972: *Comparison of Exact and Approximate Evaluations of the Single-Scattering Integral in Nucleon-Deuteron Elastic Scattering*. NASA TN D-6884.
- Wilson, J. W., 1973a: Intermediate Energy Nucleon-Deuteron Scattering Theory. *Phys. Lett.*, vol. 44B, no. 2, pp. 125–126.
- Wilson, John W., 1973b: Intermediate Energy Nucleon-Deuteron Elastic Scattering. *Nuclear Phys.*, vol. B66, pp. 221–244.
- Wilson, John W., 1974a: Proton-Deuteron Double Scattering. *Phys. Review C*, vol. 10, no. 1, pp. 369–376.

- Wilson, J. W., 1974b: Multiple Scattering of Heavy Ions, Glauber Theory, and Optical Model. *Phys. Lett.*, vol. B52, no. 2, pp. 149–152.
- Wilson, John W., 1975: Composite Particle Reaction Theory. Ph.D. Diss., College of William and Mary in Virginia.
- Wilson, John W.; and Costner, Christopher M., 1975: *Nucleon and Heavy-Ion Total and Absorption Cross Section for Selected Nuclei*. NASA TN D-8107.
- Wilson, J. W.; and Townsend, L. W., 1981: An Optical Model for Composite Nuclear Scattering. *Canadian J. Phys.*, vol. 59, no. 11, pp. 1569–1576.

1
2
3
4
5
6
7
8
9
10
11
12
13
14
15
16
17
18
19
20
21
22
23
24
25
26
27
28
29
30
31
32
33
34
35
36
37
38
39
40
41
42
43
44
45
46
47
48
49
50
51
52
53
54
55
56
57
58
59
60
61
62
63
64
65
66
67
68
69
70
71
72
73
74
75
76
77
78
79
80
81
82
83
84
85
86
87
88
89
90
91
92
93
94
95
96
97
98
99
100



Chapter 4

Elastic Channel Data Base

4.1. Introduction

The development of the multiple-scattering theory and the corresponding optical model described in chapter 3 had a tremendous unifying effect on the Langley approach to nuclear scattering. The elastic channel amplitude could be reasonably represented by the free two-body scattering amplitudes and the ground state nuclear matter densities. From the elastic channel amplitude, one obtains the values of elastic differential cross sections, total elastic cross sections, and (by the optical theorem) the total cross sections. Armed with these new methods, a search for adequate nuclear matter density functions was undertaken (Wilson, 1975). Matter densities were derived from charge density distributions, and the Woods-Saxon distributions gave the best overall agreement with the neutron experiments of Schimmerling et al. (1971, 1973) and Palevsky et al. (1967) as seen in figures 4.1 and 4.2. Energy dependence was introduced through the usual analytic form for the two-body amplitudes, which is

$$f_{NN}(\vec{q}) = \frac{1}{4\pi} \sigma(e) k_{NN} [\alpha(e) + i] \exp \left[-\frac{1}{2} B(e) \vec{q}^2 \right] \quad (4.1)$$

where \vec{q} is the momentum transfer, $\sigma(e)$ is the total cross section at kinetic energy e , k_{NN} is the wave number, $\alpha(e)$ is the ratio of real to imaginary part, and $B(e)$ is the slope parameter. In the first data base derived by Wilson and Costner (1975), the nuclear matter densities below $A_T = 17$ were taken as Gaussian and densities above $A_T = 16$ as Woods-Saxon. Results for copper targets are shown in figures 4.3 and 4.4. Calculated absorption cross sections for various projectiles and targets are shown in figures 4.5 through 4.8 with experimental results (Lindstrom et al., 1975; Cheshire et al., 1974; Jakobsson and Kullberg, 1976; Antonchik et al., 1981). (See Wilson and Townsend (1981) for details.) The matter densities for light nuclei ($3 \leq Z \leq 8$) were subsequently replaced by Townsend (1982) with harmonic well functions, and Pauli correlations were added to modify the free two-body

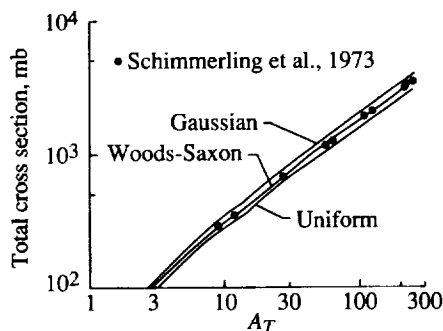


Figure 4.1. Total nucleon-nucleus cross section at ≈ 1 GeV as function of nuclear mass number for three model single-particle densities.

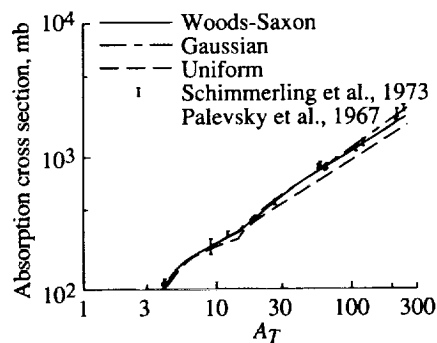


Figure 4.2. Nucleon-nucleus absorption cross section at ≈ 1 GeV function of nuclear mass number for three model single-particle densities.

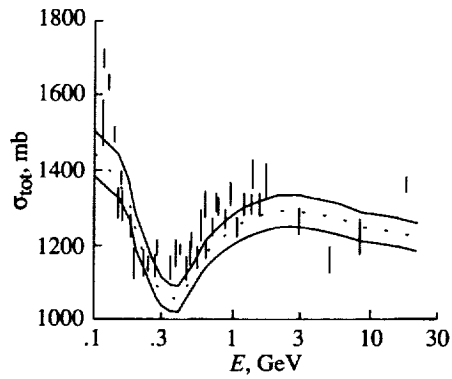


Figure 4.3. Nucleon-copper total cross section as function of laboratory energy. Curves give range of uncertainty.

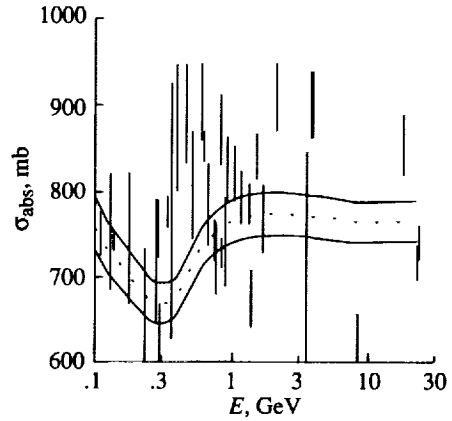


Figure 4.4. Nucleon-copper absorption cross section as function of laboratory energy. Curves give range of uncertainty.

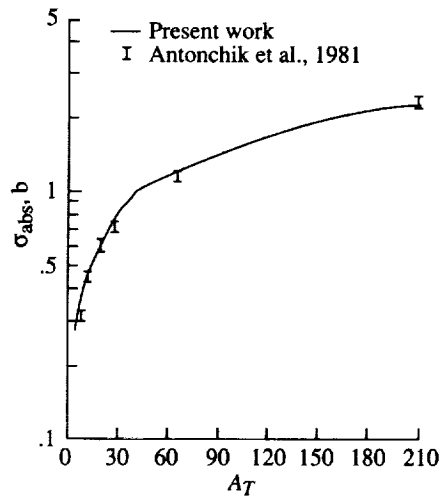


Figure 4.5. ${}^4\text{He}$ -nucleus absorption cross sections at 3.6 GeV/nucleon.

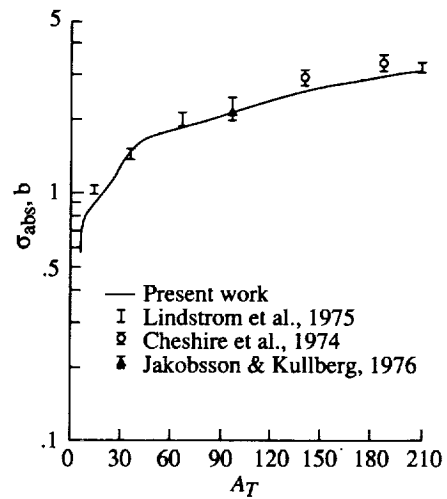


Figure 4.6. ${}^{16}\text{O}$ -nucleus absorption cross sections at 2.1 GeV/nucleon.

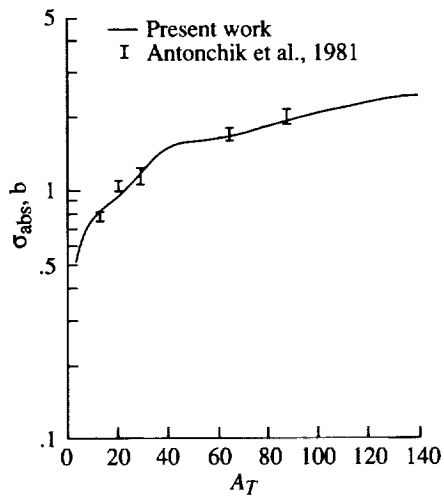


Figure 4.7. ^{12}C -nucleus absorption cross sections at 3.6 GeV/nucleon.

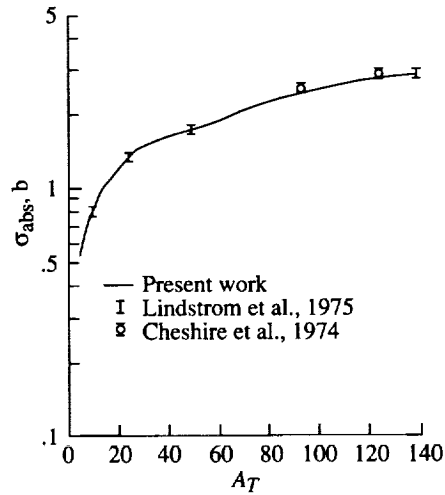


Figure 4.8. ^{12}C -nucleus absorption cross sections at 2.1 GeV/nucleon.

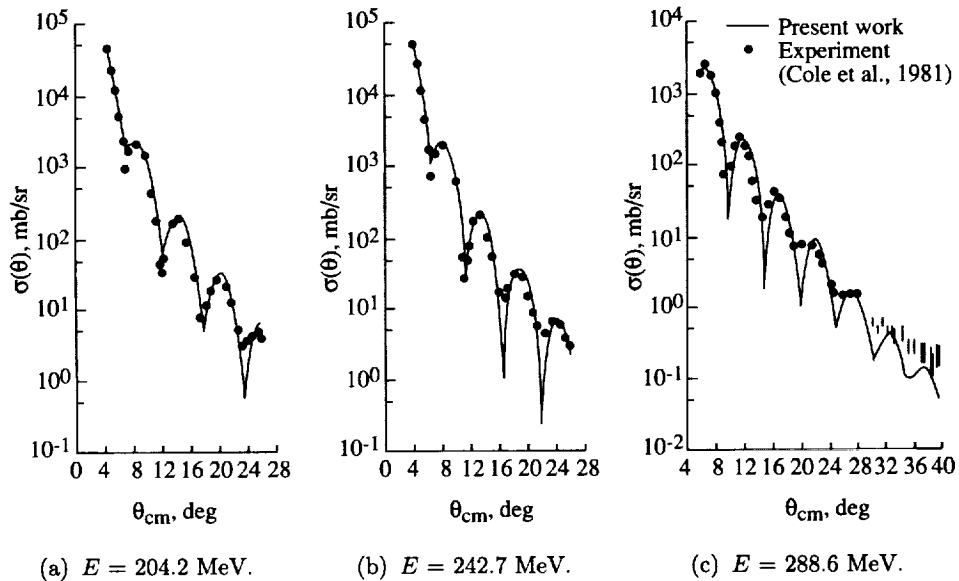


Figure 4.9. ^{12}C - ^{12}C elastic differential cross sections as function of center-of-mass scattering angle.

amplitudes. The low-energy elastic scattering required a partial wave analysis after which Bidasaria, Townsend, and Wilson (1983) found good agreement with scattering experiments (Cole et al., 1981) as shown in figure 4.9. The final data base uses the charge form factor data compiled by De Jager, De Vries, and De Vries (1974).

Although model developments for meson (Hong et al., 1989) and antinucleon (Buck et al., 1986 and 1987) data bases are underway, we will only discuss the nucleonic and heavy ion data as they now exist for space-radiation shielding.

4.2. Optical Model Cross Sections

The nucleus-nucleus potential (Wilson, 1975; Wilson and Townsend, 1981) including Pauli correlation effects (Townsend, 1982) is

$$W(\vec{x}) = A_P A_T \int d^3 \vec{\xi}_T \rho_T(\vec{\xi}_T) \int d^3 \vec{y} \rho_P(\vec{x} + \vec{y} + \vec{\xi}_T) \times \tilde{t}(e, \vec{y}) [1 - \tilde{C}(\vec{y})] \quad (4.2)$$

This potential was derived from an optical model potential approximation to the exact composite-particle multiple-scattering series.

The collision absorption (incoherent) cross sections are given by

$$\sigma_{\text{abs}} = 2\pi \int_0^\infty (1 - \exp\{-2 \text{Im}[\chi(\vec{b})]\}) b \, db \quad (4.3)$$

where the complex phase function, in terms of the reduced potential U , is

$$\chi(\vec{b}) = -\frac{1}{2k} \int_{-\infty}^\infty U(\vec{b}, z) \, dz \quad (4.4)$$

and the reduced (coherent) potential is

$$U(\vec{x}) = 2m A_P A_T (A_P + A_T)^{-1} W(\vec{x}) \quad (4.5)$$

where m is the nucleon mass, A_P is the nuclear mass number of the projectile, and A_T is the nuclear mass number of the target.

In equation (4.2), \tilde{t} is the constituent-averaged, energy-dependent, two-body transition amplitude

$$\tilde{t}(e, \vec{y}) = -\left(\frac{e}{m}\right)^{1/2} \sigma(e) [\alpha(e) + i] [2\pi B(e)]^{-3/2} \exp\left[\frac{-\vec{y}^2}{2B(e)}\right] \quad (4.6)$$

and the correlation function is taken to be

$$\tilde{C}(\vec{y}) = 0.25 \exp\left(\frac{-k_F^2 \vec{y}^2}{10}\right) \quad (4.7)$$

For the analyses of this work, the Fermi momentum is assumed to be that of infinite nuclear matter, $k_F = 1.36 \text{ fm}^{-1}$.

4.2.1. Nuclear density distributions. The correct nuclear density distributions ρ_j ($j = P, T$) to use in equation (4.2) are the nuclear ground state,

single-particle number densities for the collision pair. Since these are not experimentally known, the number densities are obtained from their experimental charge density distributions by assuming that

$$\rho_c(\vec{r}) = \int \rho_p(\vec{r}') \rho_A(\vec{r} + \vec{r}') d^3\vec{r}' \quad (4.8)$$

where ρ_c is the nuclear charge distribution, ρ_p is the proton charge distribution, and ρ_A is the desired nuclear single-particle density. All density distributions in equation (4.8) are normalized to unity. The proton charge distribution is taken to be the usual Gaussian form and is

$$\rho_p(\vec{r}) = \left(\frac{3}{2\pi r_p^2} \right)^{3/2} \exp\left(\frac{-3r^2}{2r_p^2} \right) \quad (4.9)$$

where $r_p = 0.87$ fm is the proton root-mean-square charge radius (Borkowski et al., 1975).

When the projectile is a nucleon, equation (4.8) yields a delta function for ρ_A :

$$\rho_A(\vec{r} + \vec{r}') = \delta(\vec{r} + \vec{r}') \quad (4.10)$$

because ρ_c and ρ_p are identical.

For nuclei lighter than neon ($A < 20$), the nuclear charge distribution is the harmonic well (HW) form given by De Jager, De Vries, and De Vries (1974) as

$$\rho_c(\vec{r}) = \rho_o \left[1 + \gamma \left(\frac{r}{a} \right)^2 \right] \exp\left(\frac{-r^2}{a^2} \right) \quad (4.11)$$

where ρ_o is the normalization constant, r is the radial coordinate, and a and γ are charge parameters. Values for a and γ used herein are given in table 4.1. Substituting equations (4.9) and (4.11) into equation (4.8) yields (Townsend, 1982)

$$\rho_A(\vec{r}) = \frac{\rho_o a^3}{8s^3} \left(1 + \frac{3\gamma}{2} - \frac{3\gamma a^2}{8s^2} + \frac{\gamma a^2 r^2}{16s^4} \right) \exp\left(\frac{-r^2}{4s^2} \right) \quad (4.12)$$

where

$$s^2 = \frac{a^2}{4} - \frac{r_p^2}{6} \quad (4.13)$$

For neon and heavier nuclei ($A > 20$), the nuclear charge distribution is taken to be the Woods-Saxon (WS) form

$$\rho_c(\vec{r}) = \frac{\rho_o}{1 + \exp[(r - R)/c]} \quad (4.14)$$

where R is the radius at half-density, and the surface diffuseness c is related to the nuclear skin thickness t through

$$c = \frac{t}{4.4} \quad (4.15)$$

Transport Methods and Interactions for Space Radiations

Values for R and t used herein are given in table 4.1. Most values in table 4.1 are taken from De Jager, De Vries, and De Vries (1974). Inserting equations (4.9) and (4.14) into equation (4.8) yields, after some simplification (Wilson and Costner, 1975), a number density ρ_A that is of the WS form (see eq. (4.14)) with the same R , but different overall normalization factor ρ_o and surface thickness. The latter is given by

$$t_A = \frac{8.8r_p}{3^{1/2}} \left[\ln \left(\frac{3\beta - 1}{3 - \beta} \right) \right]^{-1} \quad (4.16)$$

where

$$\beta = \exp \left(\frac{4.4r_p}{t_c 3^{1/2}} \right) \quad (4.17)$$

with t_c noting the charge skin thickness obtained by using equation (4.15) and the charge distribution surface diffuseness values listed by De Jager, De Vries, and De Vries (1974).

Table 4.1. Nuclear Charge Distribution Parameters
From Electron Scattering Data

Nucleus	Distribution (a)	γ	a , fm
		or t , fm (b)	or R , fm (b)
² H	HW	0	1.71
⁴ He	HW	0	1.33
⁷ Li	HW	0.327	1.77
⁹ Be	HW	0.611	1.791
¹¹ B	HW	0.811	1.69
¹² C	HW	1.247	1.649
¹⁴ N	HW	1.291	1.729
¹⁶ O	HW	1.544	1.833
²⁰ Ne	WS	2.517	2.74
²⁷ Al	WS	2.504	3.05
⁴⁰ Ar	WS	2.693	3.47
⁵⁶ Fe	WS	2.611	3.971
⁶⁴ Cu	WS	2.504	4.20
⁸⁰ Br	WS	2.306	4.604
¹³⁸ Ba	WS	2.621	5.517
¹⁰⁸ Ag	WS	2.354	5.139
²⁰⁸ Pb	WS	2.416	6.624

^aThe harmonic well (HW) distribution (eq. (4.11)) is used for $A < 20$ and the Woods-Saxon (WS) distribution (eq. (4.14)) for $A \geq 20$.

^b γ and a are for HW distributions and t and R are for WS distributions.

4.2.2. Nucleon-nucleon scattering parameters. The nucleon-nucleon cross sections $\sigma(e)$ used in the energy-dependent, two-body transition amplitude (eq. (4.6)) are obtained by performing a spline interpolation of values taken from various compilations (Benary, Price, and Alexander, 1970; Schopper, 1973 and 1980; Binstock, 1974). The results are displayed in figures 4.10 and 4.11 as a function of incident kinetic energy. No curve for neutron-neutron cross sections is displayed because only limited quantities of experimental data exist for these collisions. For computation purposes, we assumed that the proton-proton values for each energy listed adequately represented the neutron-neutron cross sections. Details of the constituent averaging for $\sigma(e)$ are given by Wilson and Costner (1975).

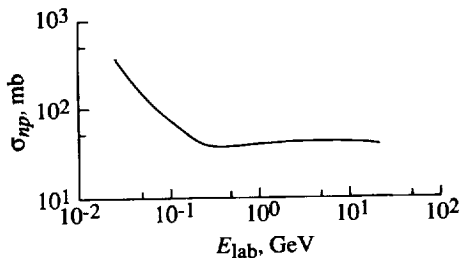


Figure 4.10. Neutron-proton total cross section as function of incident kinetic energy.

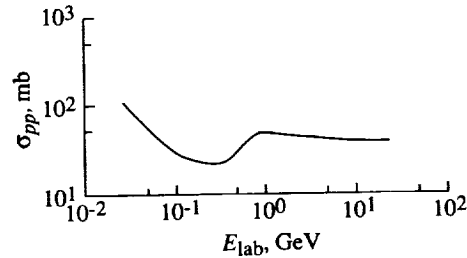


Figure 4.11. Proton-proton total cross section as function of incident kinetic energy.

Since scattering at these energies is mainly diffractive, the nucleon-nucleon slope parameters $B(e)$ are those appropriate to purely diffractive scattering. From Ringia et al. (1972) these are given by

$$B(e) = 10 + 0.5 \ln \left(\frac{s'}{s_0} \right) \quad (4.18)$$

where s' is the square of the nucleon-nucleon center-of-mass energy and $s_0 = 1 \text{ (GeV}/c)^{-2}$. Typical values from equation (4.18), displayed in figure 4.12, differ markedly from the nondiffractive compilation values of $B \approx 5 \text{ (GeV}/c)^{-2}$ used previously by Townsend, Wilson, and Bidasaria (1983a and 1983b). The improved agreement between theory and experiment obtained with equation (4.18) is clearly demonstrated by Bidasaria and Townsend (1983). Values of the parameter $\alpha(e)$ are not required for these analyses, because only the imaginary part of equation (4.6) is used in equations (4.3) and (4.4).

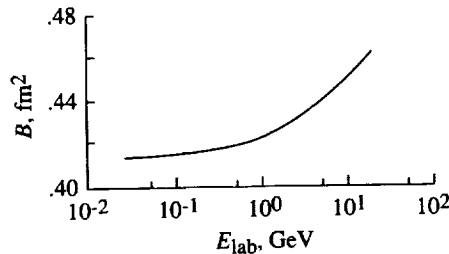


Figure 4.12. Nucleon-nucleon scattering slope parameter as function of incident kinetic energy.

4.2.3. Results. With the formalism described in sections 4.2.1 and 4.2.2, absorption cross sections for nucleons, deuterons, and selected heavy ions colliding with various target nuclei have been calculated.

Theoretical predictions for nucleon-nucleus scattering and representative experimental results of Schimmerling et al. (1973); Renberg et al. (1972); and Barashenkov, Gudima, and Toneev (1969) are presented in figures 4.13 through 4.18. Also displayed are the predictions using the empirical parameterization of Letaw, Silberberg, and Tsao (1983). The agreement between theory, empirical predictions, and experimental data is good.

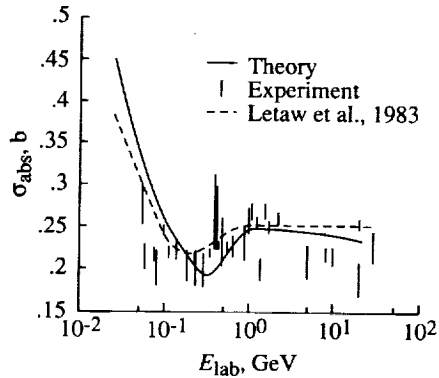


Figure 4.13. Nucleon-carbon absorption cross sections as function of incident nucleon kinetic energy.

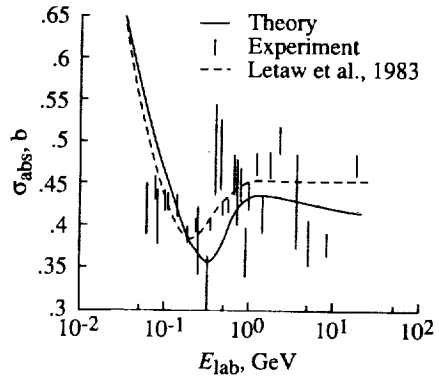


Figure 4.14. Nucleon-aluminum absorption cross sections as function of incident nucleon kinetic energy.

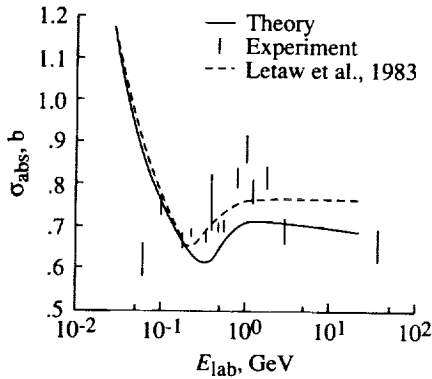


Figure 4.15. Neutron-iron absorption cross sections as function of incident nucleon kinetic energy.

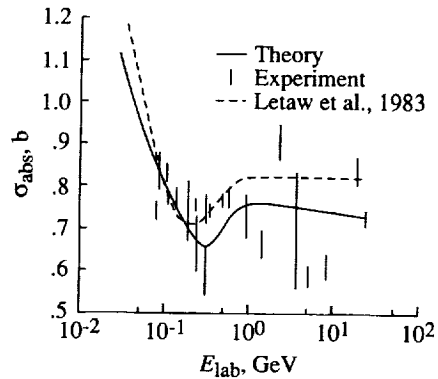


Figure 4.16. Nucleon-copper absorption cross sections as function of incident nucleon kinetic energy.

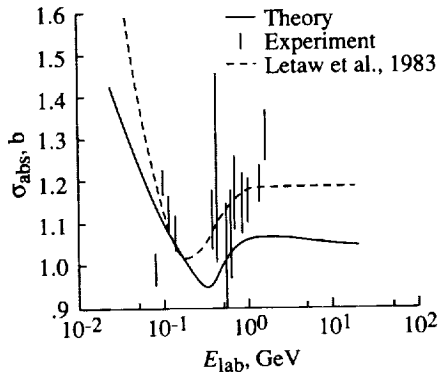


Figure 4.17. Nucleon-silver absorption cross sections as function of incident nucleon kinetic energy.

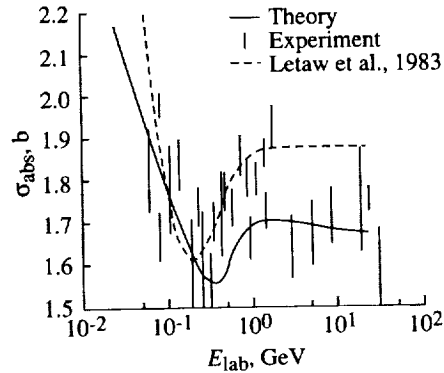


Figure 4.18. Nucleon-lead absorption cross sections as function of incident nucleon kinetic energy.

Figures 4.19 and 4.20 compare the theoretical predictions for deuteron-helium and deuteron-carbon scattering with experimental results from Jaros et al. (1978). For the helium target, theory and experiment agree to within 1 percent of the quoted cross sections, and the theory is well within the uncertainty in the experiment. For the carbon target, the disagreement between theory and experiment is less than 3 percent.

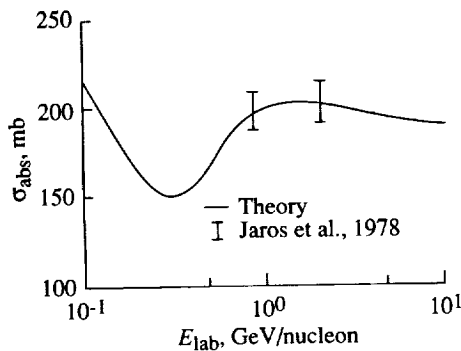


Figure 4.19. Absorption cross sections for deuteron-helium scattering as function of incident kinetic energy.

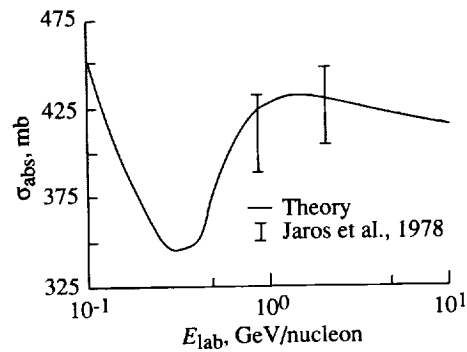


Figure 4.20. Absorption cross sections for deuteron-carbon scattering as function of incident kinetic energy.

Heavy ion absorption cross sections are presented along with experimental data (Jaros et al., 1978; Heckman et al., 1978; Cheshire et al., 1974; Skrzypczak, 1980; Jakobsson and Kullberg, 1976; Cole et al., 1981; Kox et al., 1984; Buenerd et al., 1984; Kullberg et al., 1977; Perrin et al., 1982; Antonchik et al., 1981; Westfall et al., 1979) in figures 4.21 through 4.30. The agreement between theory and experiment is excellent, even for energies lower than 100 MeV/nucleon, where the validity of the eikonal formalism is questionable (Vary and Dover, 1974). Further details are given by Townsend and Wilson (1985).

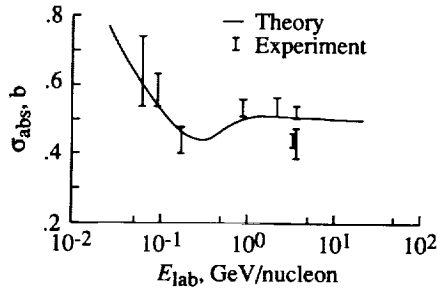


Figure 4.21. Absorption cross sections for helium-carbon scattering as function of incident kinetic energy.

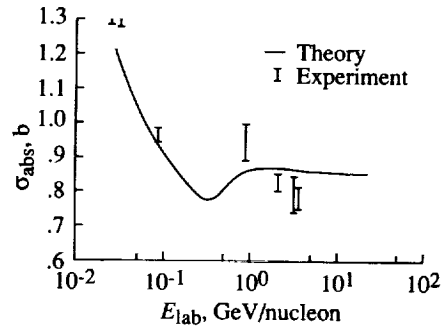


Figure 4.22. Absorption cross sections for carbon-carbon scattering as function of incident kinetic energy.

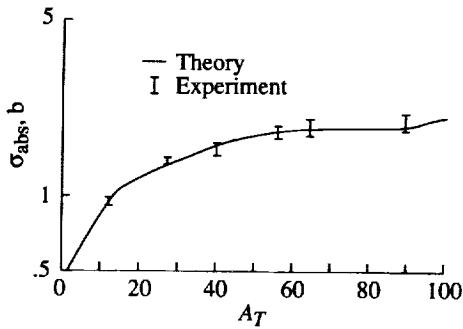


Figure 4.23. Absorption cross sections for carbon projectiles at 83 MeV/nucleon as function of target mass number.

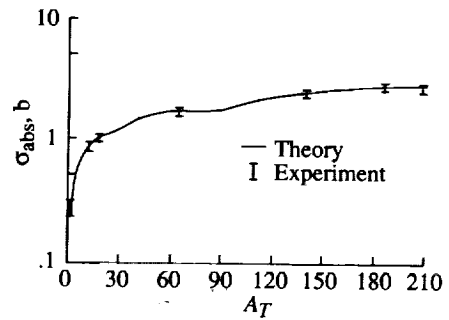


Figure 4.24. Absorption cross sections for carbon projectiles at 2.1 GeV/nucleon as function of target mass number.

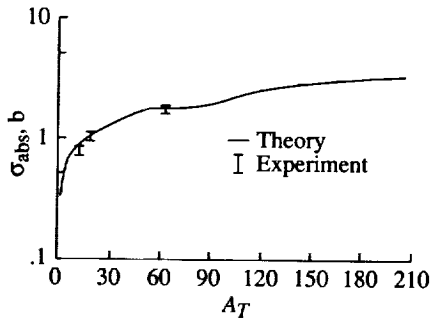


Figure 4.25. Absorption cross sections for carbon projectiles at 3.6 GeV/nucleon as function of target mass number.

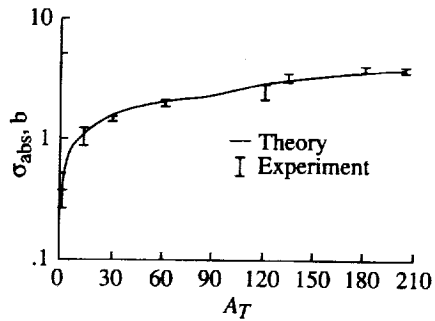


Figure 4.26. Absorption cross sections for oxygen projectiles at 2.1 GeV/nucleon as function of target mass number.

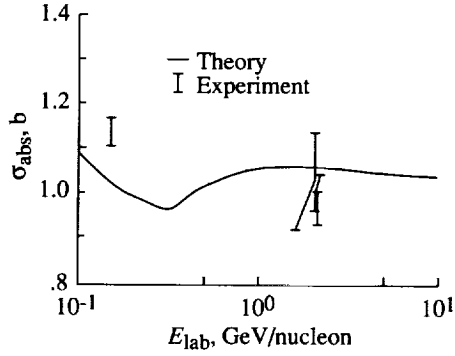


Figure 4.27. Absorption cross sections for oxygen-emulsion scattering as function of energy.

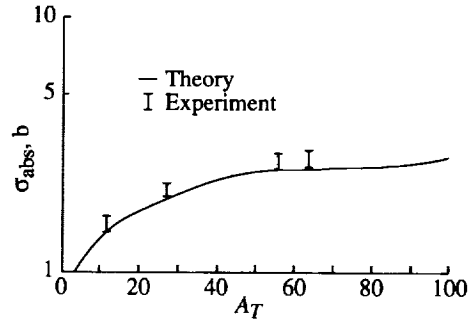


Figure 4.28. Absorption cross sections for neon projectiles at 30 MeV/nucleon as function of target mass number.

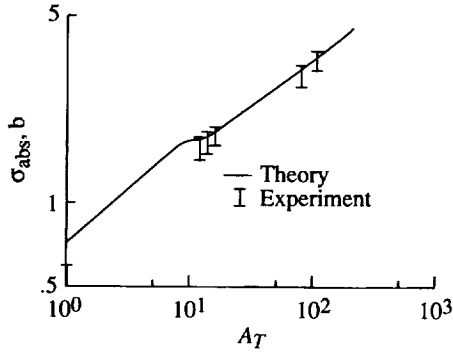


Figure 4.29. Absorption cross sections for iron projectiles at 1.88 GeV/nucleon as function of target mass number with experimental data obtained with emulsion target.

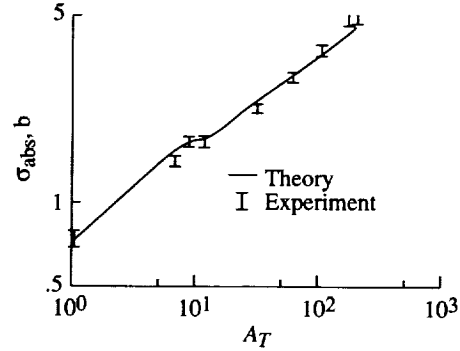


Figure 4.30. Absorption cross sections for iron projectiles at 1.88 GeV/nucleon as function of target mass number with experimental data obtained for removal of one or more nucleons.

4.3. Coupled-Channel Formalism

The optical model is extremely successful in describing the elastic scattering amplitude for many combinations of interacting systems. Section 4.2 used the optical model in the coherent amplitude approximation (Wilson, 1975; Wilson and Costner, 1975). This section represents the work of Cucinotta et al., 1989, and evaluates noncoherent contributions to the elastic scattering amplitude.

The coupled-channel (CC) Schrödinger equation for heavy ion scattering can be solved in the eikonal approximation (Wilson, 1975; Feshbach and Hüfner, 1970; Dadić, Martinis, and Pisk, 1971) resulting in the following matrix of scattering amplitudes

$$f(\vec{q}) = \frac{-ik}{2\pi} \int \exp(-i\vec{q} \cdot \vec{b}) \{ \exp[i\chi(\vec{b})] - 1 \} d^2b \quad (4.19)$$

where the boldface quantities represent matrices, k is the projectile momentum relative to the center of mass, \vec{b} is the projectile impact-parameter vector, \vec{q} is the momentum transfer, and $\chi(\vec{b})$ is the eikonal phase matrix. For a projectile transition from quantum states n to n' and target transition from ν to ν' , we write

$$\chi_{n\nu, n'\nu'}(\vec{b}, z) = \sum_{\alpha j}^{A_P, A_T} \frac{-\mu}{2k} \int_{-\infty}^z dz' \langle n\nu | t_{\alpha j} | n'\nu' \rangle \quad (4.20)$$

where $t_{\alpha j}$ is the free-particle, two-body amplitude in the overall center-of-mass frame and μ is the projectile-target reduced mass. The matrix elements of χ are given by equation (4.20) with $z \rightarrow \infty$. Equation (4.19) holds only if the commutator (Feshbach and Hufner, 1970)

$$\left[\chi(\vec{b}, z), \frac{d\chi(\vec{b}, z)}{dz} \right] = 0 \quad (4.21)$$

Assuming this commutation relation will hold effectively eliminates all reflection terms and reduces the optical potential solution to Watson's form of the nucleus-nucleus multiple-scattering series (within small-angle and high-energy approximations) to the Glauber series (Wilson and Townsend, 1981). This can be seen by considering an element of f and expanding the exponential in equation (4.19):

$$\begin{aligned} f_{n\nu, n'\nu'}(\vec{q}) &= \frac{-ik}{2\pi} \int \exp(-i\vec{q} \cdot \vec{b}) \left(i \langle n\nu | \hat{\chi} | n'\nu' \rangle \right. \\ &\quad \left. - \frac{1}{2} \sum_{m, \mu} \langle n\nu | \hat{\chi} | m\mu \rangle \langle m\mu | \hat{\chi} | n'\nu' \rangle + \dots \right) d^2b \end{aligned} \quad (4.22)$$

which is equivalent to

$$f_{n\nu, n'\nu'}(\vec{q}) = \frac{ik}{2\pi} \int \exp(-i\vec{q} \cdot \vec{b}) \langle n\nu | [1 - \exp(i\hat{\chi})] | n'\nu' \rangle d^2b \quad (4.23)$$

Upon introduction of the two-body profile function, we arrive at the Glauber form for the nucleus-nucleus scattering amplitude (Franco and Nutt, 1978)

$$f_{n\nu, n'\nu'}(\vec{q}) = \frac{ik}{2\pi} \int \exp(-i\vec{q} \cdot \vec{b}) \langle n\nu | \left(1 - \prod_{\alpha j} [1 - \Gamma_{\alpha j}(\vec{b} - \vec{s}_\alpha - \vec{s}_j)] \right) | n'\nu' \rangle d^2b \quad (4.24)$$

We note that we have not considered the question of noncommuting interactions. Also, the eikonal CC approach is based on an ansatz for the optical-model CC equation wave function; therefore, we have not rigorously considered the connection between Watson's form of the nucleus-nucleus multiple-scattering series and the Glauber approximation. Such considerations can be found in Wallace (1975). Having shown the equivalence of the CC approach to the Glauber approximation, we next consider the second-order solution to equation (4.19) for the elastic channel, which we will compare with the second-order optical phase shift approximation to the Glauber amplitude.

The second-order approximation to the elastic amplitude is obtained by including all transitions between the ground and excited states and assuming that transitions between excited states are negligible. Furthermore, the densities of all excited states are approximated by an average excited-state density. The phase matrix is then of the bordered form

$$\chi(\vec{b}) = \begin{pmatrix} \chi_{el} & \chi_{00,01} & \chi_{00,10} & \chi_{00,11} & \cdots \\ \chi_{01,00} & \chi_{exc} & 0 & 0 & \cdots \\ \chi_{10,00} & 0 & \chi_{exc} & 0 & \cdots \\ \chi_{11,00} & 0 & 0 & \chi_{exc} & \cdots \\ \vdots & \vdots & \vdots & \vdots & \vdots \end{pmatrix} \quad (4.25)$$

where $\chi_{el} = \chi_{00,00}$. The characteristic equation of this bordered matrix is

$$(\chi_{exc} - \lambda)^{N-2} [(\chi_{el} - \lambda)(\chi_{exc} - \lambda) - \Upsilon^2] = 0, \quad (4.26)$$

where N is the rank of χ , λ is the eigenvalue, and Υ^2 is defined by

$$\Upsilon^2(\vec{b}) = \sum_{n \text{ or } \nu \neq 0} \chi_{00,n\nu} \chi_{n\nu,00} \quad (4.27)$$

The eigenvalues are then given by

$$\lambda_{1,2} = \frac{1}{2}(\chi_{el} + \chi_{exc}) \pm \left\{ \left[\frac{1}{2}(\chi_{el} - \chi_{exc}) \right]^2 + \Upsilon^2 \right\}^{1/2} \quad (4.28)$$

with all others taking the value χ_{exc} . The form of the eigenvalues allows us to treat the scattering system as an effective two-channel problem with

$$\chi = \begin{pmatrix} \chi_{el} & \Upsilon \\ \Upsilon & \chi_{exc} \end{pmatrix} \quad (4.29)$$

Then using Sylvester's theorem (Merzbacher, 1970), we find

$$f_{CC}^{(2)}(\vec{q}) = \frac{-ik}{2\pi} \int \exp(-i\vec{q} \cdot \vec{b}) \left\{ \exp \left[\frac{1}{2}i(\chi_{el} + \chi_{exc}) \right] \left[\cos(\chi_{dif}^2 + \Upsilon^2)^{1/2} + i\chi_{dif} \frac{\sin(\chi_{dif}^2 + \Upsilon^2)^{1/2}}{(\chi_{dif}^2 + \Upsilon^2)^{1/2}} \right] - 1 \right\} d^2b \quad (4.30)$$

where $\chi_{dif} = \frac{1}{2}(\chi_{el} - \chi_{exc})$. An examination of equation (4.30) reveals, as expected, that χ_{exc} appears only in third-order and higher order terms in $f_{NN}(\vec{q})$.

As discussed by Feshbach and Hüfner (1970) a reasonable approximation to χ_{exc} is to assume the ground-state density for the excited states. If χ_{exc} is set equal to χ_{el} , we find

$$f_{CC}^{(2)}(\vec{q}) \approx \frac{-ik}{2\pi} \int \exp(-i\vec{q} \cdot \vec{b}) [\exp(i\chi_{\text{el}}) \cos \Upsilon - 1] d^2b \quad (4.31)$$

The coherent approximation (Wilson, 1975; Wilson and Townsend, 1981) is recovered in the limit of small Υ .

Using closure to perform the summations in equation (4.27) and transforming from the overall center-of-mass (CM) frame to the nucleon-nucleon (NN) CM frame using nonrelativistic kinematics, Υ^2 is

$$\begin{aligned} \Upsilon^2(\vec{b}) = & A_P A_T \left(\frac{1}{2\pi k_{\text{NN}}} \right)^2 \int d^2q d^2q' \exp(-i\vec{q} \cdot \vec{b}) \exp(-i\vec{q}' \cdot \vec{b}) \\ & \times f_{\text{NN}}(\vec{q}) f_{\text{NN}}(\vec{q}') \left[-A_P A_T F^{(1)}(\vec{q}) F^{(1)}(\vec{q}') G^{(1)}(-\vec{q}) G^{(1)}(-\vec{q}') \right. \\ & + (A_P - 1)(A_T - 1) F^{(2)}(\vec{q}, \vec{q}') G^{(2)}(-\vec{q}, -\vec{q}') \\ & + (A_T - 1) F^{(1)}(\vec{q} + \vec{q}') G^{(2)}(-\vec{q}, -\vec{q}') \\ & + (A_P - 1) F^{(2)}(\vec{q}, \vec{q}') G^{(1)}(-\vec{q} - \vec{q}') \\ & \left. + F^{(1)}(\vec{q} + \vec{q}') G^{(1)}(-\vec{q} - \vec{q}') \right] \end{aligned} \quad (4.32)$$

where $F^{(1)}$ and $F^{(2)}$ ($G^{(1)}$ and $G^{(2)}$) are one- and two-body ground-state form factors, respectively, for the projectile (target). The last term on the right-hand side of equation (4.32) is a self-correlation term that appears through the use of closure. The physical meanings of the other terms in equation (4.32) have been discussed by Franco and Nutt (1978).

The optical phase shift expansion given by Franco and Nutt (1978) to the Glauber approximation is written

$$f_{\text{Glauber}}(\vec{q}) = \frac{-ik}{2\pi} \int \exp(-i\vec{q} \cdot \vec{b}) [\exp(i\chi_{\text{opt}}) - 1] d^2b \quad (4.33)$$

with

$$\chi_{\text{opt}} = \chi_1 + \chi_2 \dots \quad (4.34)$$

In comparison, we note that $\chi_1 = \chi_{\text{el}}$, and dropping the last term in Υ^2 yields $i\chi_2 = -\frac{1}{2}\Upsilon^2$. Approximating the density of all excited states by the ground-state density yields almost the same results for the coupled-channel and Glauber optical models:

$$f_{CC}^{(2)}(\vec{q}) = \frac{-ik}{2\pi} \int \exp(-i\vec{q} \cdot \vec{b}) \left[\exp(i\chi_{\text{el}}) \left(1 - \frac{1}{2}\Upsilon^2 + \frac{1}{24}\Upsilon^4 - \dots \right) - 1 \right] d^2b \quad (4.35)$$

and

$$f_{\text{Glauber}}^{(2)}(\vec{q}) = \frac{-ik}{2\pi} \int \exp(-i\vec{q} \cdot \vec{b}) \left[\exp(i\chi_{\text{el}}) \left(1 - \frac{1}{2}\Upsilon^2 + \frac{1}{8}\Upsilon^4 - \dots \right) - 1 \right] d^2b \quad (4.36)$$

if $\frac{1}{2}\Upsilon^2 \ll 1$. Note that $\frac{1}{2}\Upsilon^2 \ll 1$ is found to be true for light collision pairs, whereas for large mass number nuclei, this condition should at least hold at large impact parameters, where most of the scattering occurs but may give rise to differences and should be further studied.

We now consider the evaluation of the elastic amplitude for α - α scattering. At high energies, only the central piece of the NN amplitude will be important in spin-0-spin-0 scattering. Therefore, we use the following parameterization:

$$f_{\text{NN}}(\vec{q}) = \frac{1}{4\pi} k_{\text{NN}} \sigma (\alpha + i) \exp\left(-\frac{1}{2}Bq^2\right) \quad (4.37)$$

The isospin-averaged values for the parameters σ , B , and α at the energies considered in this paper are listed in table 4.2. For the calculation of χ_{el} , we use the following parameterization for the ${}^4\text{He}$ charge form factor (McCarthy, Sick, and Whitney, 1977):

$$F_{\text{ch}}(\vec{q}) = [1 - (aq)^2] \exp(-bq^2) \quad (4.38)$$

with $a = 0.316$ fm and $b = 0.681$ fm². The charge form factor F_{ch} is related to the matter form factor F by $F = F_{\text{ch}}/F_P$ with $F_P = \exp\left(-\frac{1}{6}r_P^2q^2\right)$, where $r_P = 0.86$ fm. We also include coulomb effects in the usual way, assuming just the first term in equation (4.38).

Table 4.2. Nucleon-Nucleon Parameters

E , MeV	σ , mb	B , fm ⁻²	α
635	3.93	0.132	-0.39
1050	4.4	0.25	-0.28

The ${}^4\text{He}$ correlations caused by CM recoil are important. It is well-known that the CM motion can only be treated exactly for shell-model, harmonic-oscillator wave functions. Therefore, we use the harmonic-oscillator CM correction factor in our calculations such that the intrinsic one- and two-body form factors that appear in equation (4.32) are written in terms of model form factors F_M such as

$$F^{(1)}(\vec{q}) = \frac{F_M^{(1)}(\vec{q})}{F_{\text{CM}}(\vec{q})} \quad (4.39)$$

and

$$F^{(2)}(\vec{q}, \vec{q}') = \frac{F_M^{(2)}(\vec{q}, \vec{q}')}{F_{CM}(\vec{q} + \vec{q}')} \quad (4.40)$$

with $F_{CM}(\vec{q}) = \exp\left[-\left(R^2/4A\right)q^2\right]$. For ${}^4\text{He}$, we use $R^2 = 1.94 \text{ fm}^2$. The model two-particle density described below will be integrated to obtain these form factors.

In the Jastrow (1955) method (see Frullani and Mougey, 1984), if three-particle and higher particle correlations are ignored, we write

$$\rho_M^{(2)}(\vec{r}, \vec{r}') = N_n \rho_s^{(1)}(\vec{r}) \rho_s^{(1)}(\vec{r}') |g(\vec{r}, \vec{r}')|^2 \quad (4.41)$$

where $\rho_s^{(1)}$ is the uncorrelated single-particle density, $\rho_s \propto \exp(-r^2/R^2)$, and N_n is the normalization constant. The correlation factor can be written in terms of the nucleon-nucleon relative momentum distribution as (Frullani and Mougey, 1984)

$$g(\vec{r}, \vec{r}') = 1 - \int \exp[i\vec{p}_r \cdot (\vec{r} - \vec{r}')] N(\vec{p}_r) d\vec{p}_r \quad (4.42)$$

where \vec{p}_r is the NN relative momentum vector. We parameterize $N(\vec{p}_r)$ according to Akaishi (1984) as

$$N(\vec{p}_r) = C \left[\exp\left(\frac{-p_r^2}{a_1}\right) + S \exp\left(\frac{-p_r^2}{a_2}\right) \right] \quad (4.43)$$

with $a_1 = 5.4 \text{ fm}^{-2}$, $a_2 = 4a_1$, $S = 0.015$, and C as the normalization. The first term on the right-hand side of equation (4.43) can be attributed to a Hartree-Fock-type correlation with the value of a_1 , leading to a correlation length of about 0.8 fm, upon comparison with the usual Gaussian parameterization of the correlation factor. The higher momentum component in equation (4.43) should reflect the true dynamical correlations (Akaishi, 1984).

An average excited-state phase can be a complicated quantity to calculate. ${}^4\text{He}$ has many resonance states lying below an excitation of 40 MeV that should contribute. Some calculations are available (Liu, Zamick, and Jaqaman, 1985), but states higher in the continuum should be more dominant. Because this phase element only appears at third order in f_{NN} , a simple model will suffice to show that significant deviations from the ground-state phase are of negligible importance in the double scattering region. Since the form factor for this state must approach unity as $\vec{q} \rightarrow 0$, we choose a Gaussian and consider deviations from the ground state through

$$R_{\text{exc}} = R(1 + \delta R) \quad (4.44)$$

In figures 4.31 and 4.32, we show our predictions compared with 635 MeV/nucleon (Berger et al., 1980) and 1050 MeV/nucleon (Satta et al., 1984) α - α scattering data. As can be seen, the Glauber and CC calculations, with excited-state phase approximated by the ground-state phase, are virtually indistinguishable at all momentum transfers. We find no appreciable differences between the results for

$\chi_{\text{exc}} = \chi_{\text{el}}$ and $\delta R = 0.5$ until the second minima at both energies. The effect of this phase on the double scattering region appears to have been overestimated by Feshbach and Hüfner (1970). No conclusions can be made at larger angles because three-body correlations should become important there. As noted by previous authors (Franco and Nutt, 1978) and as can be seen in figures 4.31 and 4.32, the differences between first- and second-order calculations become significant for increasing angles in α - α scattering. The second-order effects should be large enough to distinguish between models for the two-body density, for example, the Jastrow method used here and the more phenomenological Gaussian parameterization of the correlation factor that is used by Franco and Nutt (1978).

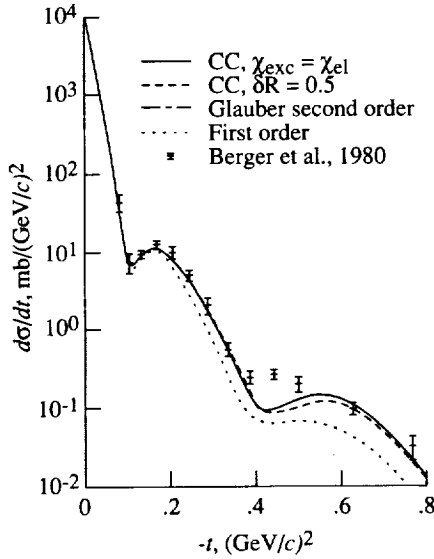


Figure 4.31. The α - α elastic differential cross section at 5.05 GeV/c.

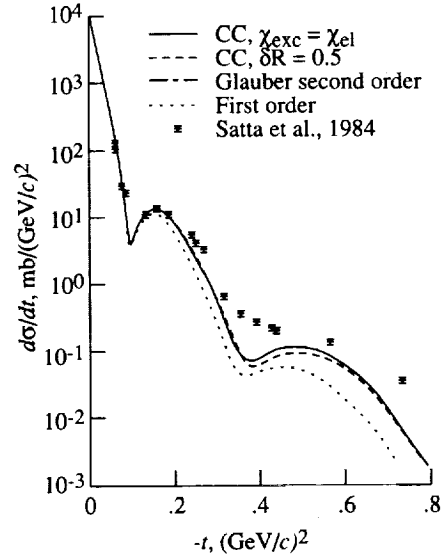


Figure 4.32. The α - α elastic differential cross section at 7 GeV/c.

In conclusion, the coupled-channels, semiclassical approximation of an optical-model solution to Watson's form of the nucleus-nucleus multiple-scattering series has been shown to be equivalent to the Glauber approximation. A second-order solution to the elastic channel obtained by neglecting all transitions between nuclear-excited states was found to be almost identical to the second-order optical phase shift expansion of the Glauber series. An average excited-state phase was seen to be of minor importance in studying the role of correlations in α - α scattering. The α - α scattering data studied is expected to be sensitive to how the two-body density is modeled and should warrant further study.

4.4. Parametric Cross Sections

In sections 4.2 and 4.3, we discussed basic theoretical issues required for an accurate understanding of the interaction process. This understanding is necessary to fill in gaps in experimental data and to further develop reactive theories. The rest of this chapter is a review of parametric representation of results for transport code input.

4.4.1. Total nuclear cross sections. After many decades of experimental activity at various accelerators with ever increasing energies, the cross sections for two-nucleon interactions are reasonably well-defined. Although recent advances in the theory of the two-nucleon interaction in terms of phenomenological meson exchange models (Gross, 1974) show considerable success, a simple parameterization of the experimental data is sufficient for our purposes. For $E \geq 25$ MeV, the proton-proton (pp) total cross section (mb) is found to be reasonably approximated by

$$\sigma_{pp}(E) = \left(1 + \frac{5}{E}\right) \left\{40 + 109 \cos(0.199\sqrt{E}) \exp\left[-0.451(E - 25)^{0.258}\right]\right\} \quad (4.45)$$

and for lower energies, by

$$\sigma_{pp}(E) = \exp\left\{6.51 \left[\exp\left(-\frac{E}{134}\right)^{0.7}\right]\right\} \quad (4.46)$$

These forms are compared with experiments above 50 MeV (Lock and Measday, 1970) shown in figure 4.33. For $E \geq 0.1$ MeV, the neutron-proton (np) cross section is taken as

$$\sigma_{np}(E) = 38 + 12\,500 \exp\left[-1.187(E - 0.1)^{0.35}\right] \quad (4.47)$$

and at lower energies, by

$$\sigma_{np}(E) = 26\,000 \exp\left[-\frac{E}{0.282}\right]^{0.3} \quad (4.48)$$

These forms are compared with experiments above 25 MeV (Lock and Measday, 1970) in figure 4.34.

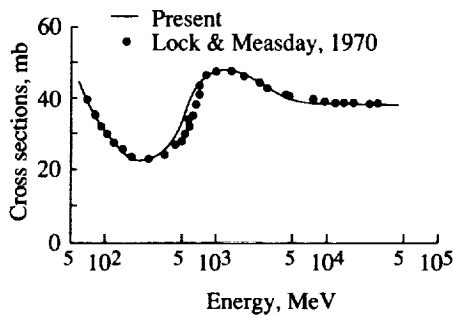


Figure 4.33. Total proton-proton cross sections.

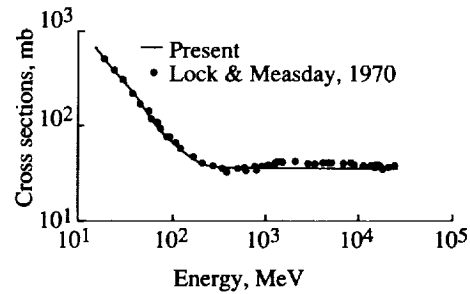


Figure 4.34. Total neutron-proton cross sections.

The low-energy, neutron-nucleus total cross sections exhibit a complicated fine resonance structure over a broad, slowly varying background. This background is marked by very broad Ramsauer resonances that persist even to neutron energies of 100 MeV. Although a simple fundamental theory for the Ramsauer resonances

is not available, a semiempirical formalism is given by Angeli and Csikai (1970 and 1971). Their formalism starts with the usual partial wave expansion as

$$\sigma_{\text{tot}} = 2\pi\lambda^2 \sum_{\ell} (2\ell + 1) [1 - \text{Re}(\eta_{\ell})] \quad (4.49)$$

with

$$\eta_{\ell} = \exp(i\delta_{\ell}) \quad (4.50)$$

where δ_{ℓ} is the complex phase shift for the ℓ th partial wave and $\text{Re}(Z)$ denotes the real part of Z . In the opaque nucleus model, the fact that $n_{\ell} \approx 1$ for all values of $\ell > R/\lambda$, where R is the nuclear radius, leads Angeli and Csikai to assume that

$$\sigma_{\text{tot}} \approx 2\pi(R + \lambda)^2 [1 - \text{Re}(\eta)] \quad (4.51)$$

where $\eta = 0$ gives the usual opaque nucleus result such that

$$\begin{aligned} \text{Re}(\eta) &= \exp[-\text{Im}(\delta)] \cos[\text{Re}(\delta)] \\ &\equiv p \cos\left(qA_T^{1/3} - r\right) \end{aligned} \quad (4.52)$$

is a reasonable starting point to parameterize the total cross sections, where $\text{Im}(\delta)$ denotes the imaginary part of δ . Their complete parameterization is

$$\sigma_{\text{tot}} = 2\pi \left(r_0 A_T^{1/3} + \lambda\right)^2 \left[a - p \cos\left(qA_T^{1/3} - r\right)\right] \quad (4.53)$$

where $r_0 = 1.4$ fm, and the neutron wavelength is

$$\lambda = \frac{4.55}{\sqrt{E}} \frac{A_t + 1}{A_t} \quad (4.54)$$

The parameters of Angeli and Csikai (1970 and 1971) are adequately approximated by

$$a = \frac{1}{1 + \left[2/(3.8E + 0.1E\sqrt{E} + 0.1E^3\sqrt{E})\right]} \quad (4.55)$$

$$p = 0.15 - 0.0066\sqrt{E} \quad (4.56)$$

$$q = 2.72 - 0.203\sqrt{E} \quad (4.57)$$

$$r = \min\left\{-5.3 + 1.66\sqrt{E}; 1.3\right\} \quad (4.58)$$

Strictly speaking, equations (4.53) to (4.58) apply only to $A_T \geq 40$ and $0.5 \leq E \leq 40$ MeV. A simple extension to all values of A_T and $0.1 \leq E \leq 100$ MeV gives qualitatively similar results to the experimental data and provides a starting point to representing the total cross section. The cross sections given by equations (4.53) through (4.58) are shown in figure 4.35. These should be compared with the experimental data (Hughes and Schwartz, 1958) shown in figure 4.36. Note that

the data in figure 4.36 have only the broad resonances shown. The very narrow resonances have been averaged. We now seek some pure empirical modification to the Angeli-Csikai cross sections to better approximate the total cross sections.

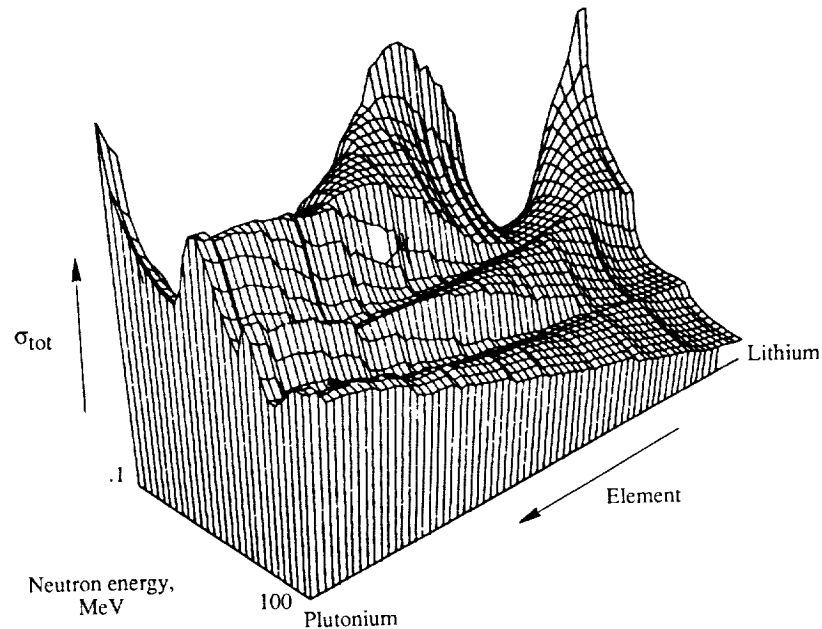


Figure 4.35. Total neutron-nucleus cross section according to Ramsauer resonance formalism.

Our modifications to the Angeli-Csikai formalism are as follows:

1. If $A_T > 75$, then a is taken as 0.18 for values of equation (4.55) less than 0.18
2. The value of p is taken to be greater than $0.4a$ unless $A_T > 76$ for which p can be as small as $0.3a$
3. A modifying factor of $1 + D \exp(-\alpha E)$ is used with

$$D = \begin{cases} 0.5 & (145 < A_T < 235) \\ 1.0 & (\text{Otherwise}) \end{cases}$$

and

$$\alpha = \begin{cases} 1.0 & (205 < A_T < 235) \\ 2.0 & (\text{Otherwise}) \end{cases}$$

4. An additional modifying factor is applied as

$$F_1 \left\{ 1 - 0.5 \exp \left[\frac{-(A_T - 63.54)^2}{20} \right] - 0.45 \exp \left[\frac{-(A_T - 58.71)^2}{4} \right] \exp(-2E) + F_2 \right\}$$

where

$$F_1 = \begin{cases} 0.7 & (A_T \leq 63; E \leq 0.8) \\ 1.0 & (\text{Otherwise}) \end{cases}$$

$$F_2 = \begin{cases} 0 & (E > 0.5) \\ -4.95 \exp(-18E) & (40 \leq A_T < 42) \\ -1.79 \exp(-15E) & (32 \leq A_T < 34) \end{cases}$$

5. If $A_T < 30$, then numerical interpolation between experimental values is used

The final cross sections as modified above are shown in figure 4.37 and should be compared with figure 4.36

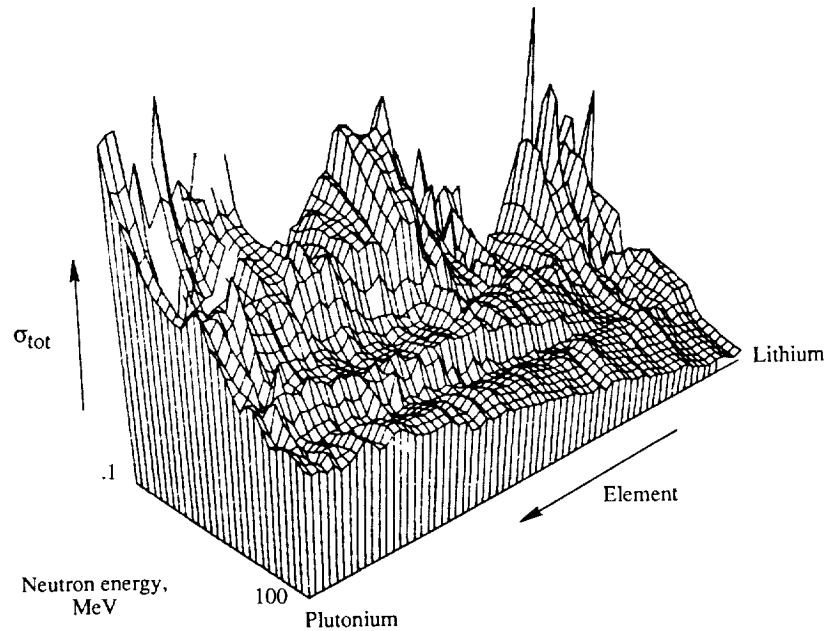


Figure 4.36. Total neutron cross section according to Hughes and Schwartz (1958).

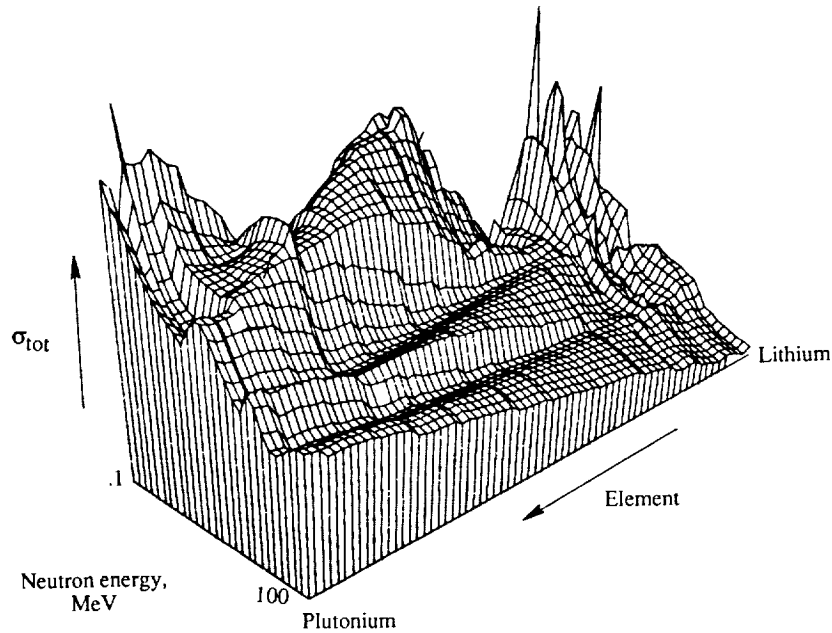


Figure 4.37. Total neutron-nucleus cross section according to present formalism.

The total cross sections above 100 MeV have been taken from Townsend, Wilson, and Bidasaria (1983b). The high-energy cross sections of Townsend, Wilson, and Bidasaria (1983b) have been approximated by

$$\sigma_{\text{tot}}(A_T, E) = 52.5 A_T^{0.758} \left[1 + \left[0.8 + 2.4 \exp\left(\frac{-A_T}{30}\right) \right] \exp\left(\frac{-E}{135}\right) \sin \Theta_E \right] \quad (4.59)$$

where the phase angle is given by

$$\Theta_E = \begin{cases} 14.41 & (E \leq 40 \text{ MeV}) \\ 1.29 \ln^2(E) - \pi & (E > 40 \text{ MeV}) \end{cases} \quad (4.60)$$

The expressions (4.59) and (4.60) are shown along with the theory of Townsend, Wilson, and Bidasaria (1983b) and a compilation of experiments in figures 4.38 through 4.41. Equations (4.53) through (4.58) are connected smoothly at 70 MeV to the results of equations (4.59) and (4.60) at 130 MeV with an assumed exponential dependence on energy. The total cross section is used to calculate the scattering cross section as

$$\sigma_s(E) = \sigma_{\text{tot}}(E) - \sigma_{\text{abs}}(E) \quad (4.61)$$

The total (tot) neutron-nucleus cross section is shown with experimental data (Hughes and Schwartz, 1958) in figures 4.42 through 4.45.

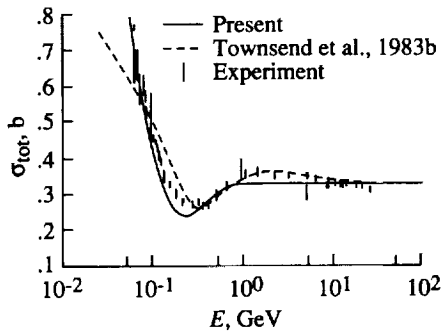


Figure 4.38. Total nucleon-carbon cross sections.

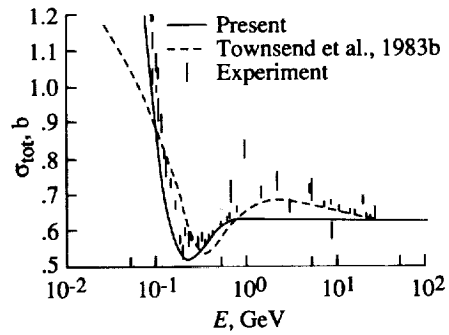


Figure 4.39. Total nucleon-aluminum cross sections.

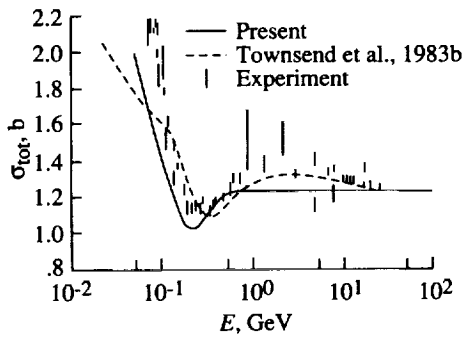


Figure 4.40. Total nucleon-copper cross sections.

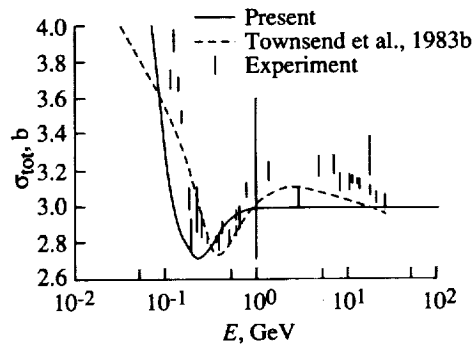


Figure 4.41. Total nucleon-lead cross sections.

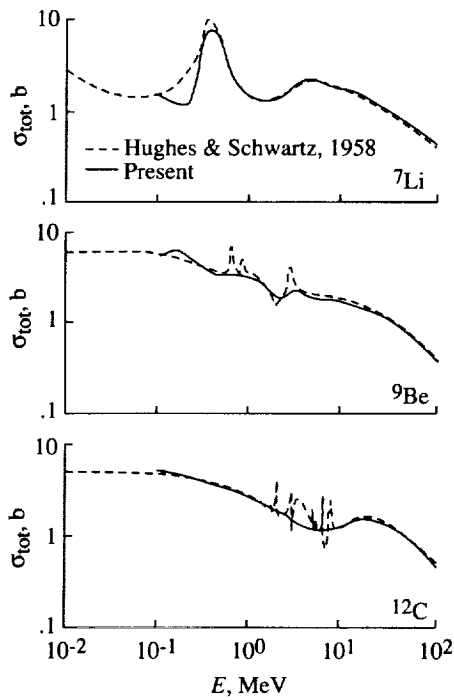


Figure 4.42. Total neutron-nucleus cross sections of ${}^7\text{Li}$, ${}^9\text{Be}$, and ${}^{12}\text{C}$.

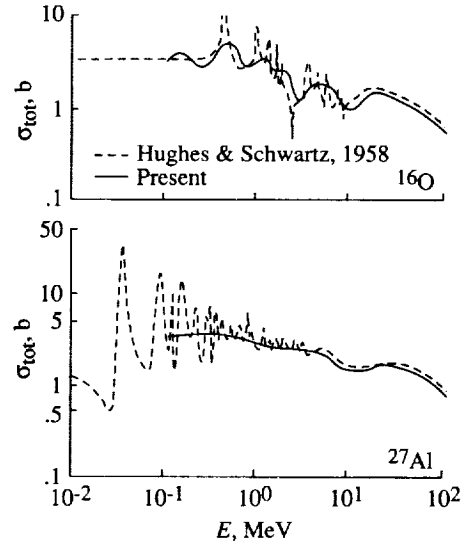


Figure 4.43. Total neutron-nucleus cross sections of ${}^{16}\text{O}$ and ${}^{27}\text{Al}$.

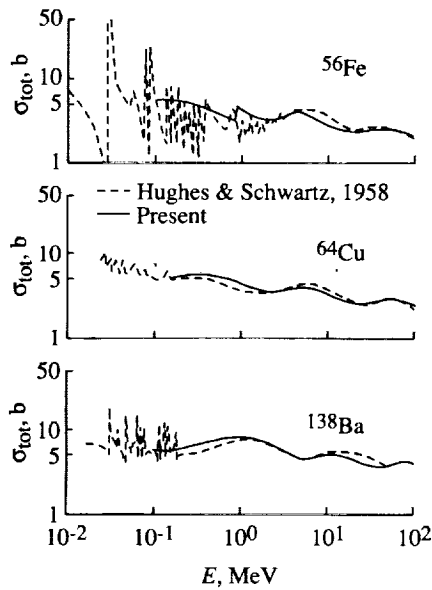


Figure 4.44. Total neutron-nucleus cross sections of ${}^{56}\text{Fe}$, ${}^{64}\text{Cu}$, and ${}^{138}\text{Ba}$.

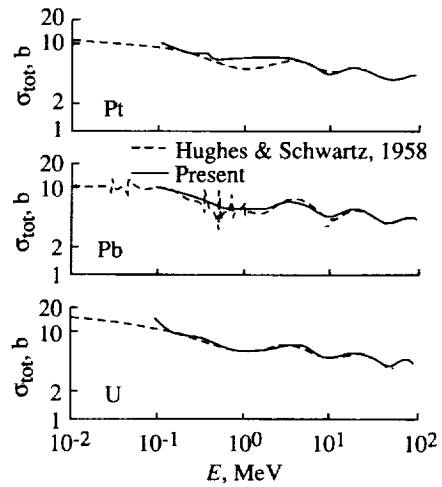


Figure 4.45. Total neutron-nucleus cross sections of Pt, Pb, and U.

4.4.2. Nuclear-absorption cross sections. Qualitatively, the nuclear-absorption cross sections show an energy dependence similar to that observed for the total nuclear cross sections. An analytic formula for protons was derived by Letaw, Silberberg, and Tsao (1983) by first fitting the cross sections of Bobchenko et al. (1979) with the formula

$$\sigma_{\text{abs}} = 45A_T^{0.7} \{1 + 0.016 \sin[5.3 - 2.63 \ln(A_T)]\} \quad (4.62)$$

where A_T is the mass number of the target nucleus. Equation (4.62) reproduces the Bobchenko data to within ± 2 percent. A somewhat better fit to the Bobchenko data is given by

$$\sigma_{\text{abs}} = 45A_T^{0.7} (1 - 0.018 \sin \Theta_A) \quad (4.63)$$

where the angle Θ_A is

$$\Theta_A = 2.94 \ln(A_T) + 0.63 \sin[3.92 \ln(A_T) - 2.329] - 0.176 \quad (4.64)$$

Equation (4.63) fits the Bobchenko data to within the 1.2-percent difference, which is on the order of the quoted experimental uncertainty. Although the Bobchenko data represent a consistent set of measurements for many different targets and probably well define the A -dependence of the high-energy cross sections, they may nonetheless be in error in absolute value as suggested by many other independent experiments (Townsend and Wilson, 1985).

Letaw, Silberberg, and Tsao (1983) assume the energy dependence for all nuclei to be the same and to be approximated by

$$f(E) = 1 - 0.62 \exp\left(\frac{-E}{200}\right) \sin(10.9E^{-0.28}) \quad (4.65)$$

where the nucleon kinetic energy is in units of MeV. We observe oscillations according to the quantum mechanical calculations of Townsend, Wilson, and Bidasaria (1983b) with phase angle

$$\Theta_E = \begin{cases} 1.44 & (E < 25 \text{ MeV}) \\ 1.33 \ln(E) - 2.84 & (\text{Otherwise}) \end{cases} \quad (4.66)$$

but with an A -dependent amplitude given by

$$f(E) = 1 - \left[0.3E^{-0.22} + 0.76 \exp\left(\frac{-E}{135}\right)\right] \left[0.4 + 0.9 \exp\left(\frac{-A_t}{30}\right)\right] \sin \Theta_E \quad (4.67)$$

The absorption cross section as given by equations (4.64), (4.66), and (4.67), the fit of Letaw, Silberberg, and Tsao, and various experimental results are given in figures 4.46 through 4.50. As one can see from the figures, a figure of merit is difficult to assign to the fit because great scatter in the data obscures the result. Generally, above 20 MeV the results are on the order of ± 10 percent accurate as estimated from the scatter in the experiments.

Below 20 MeV, the neutron cross sections are represented by numerical data sets at discrete energies of 1, 3, 5, 10, 14, and 20 MeV as taken from Hughes and Schwartz (1958), Stehn et al. (1964), and Brodsky (1978). Interpolated values

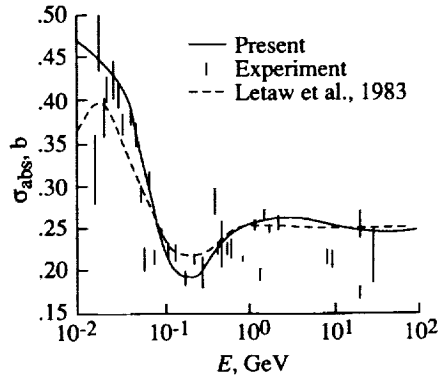


Figure 4.46. Neutron-carbon absorption cross sections.

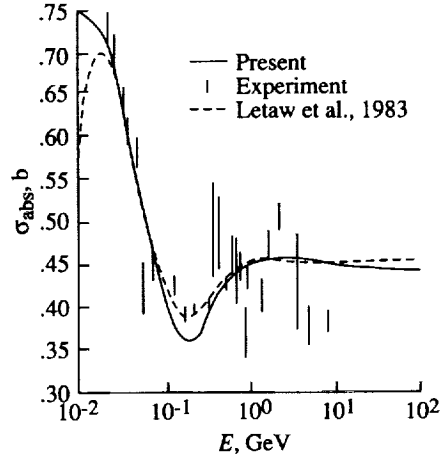


Figure 4.47. Neutron-aluminum absorption cross sections.

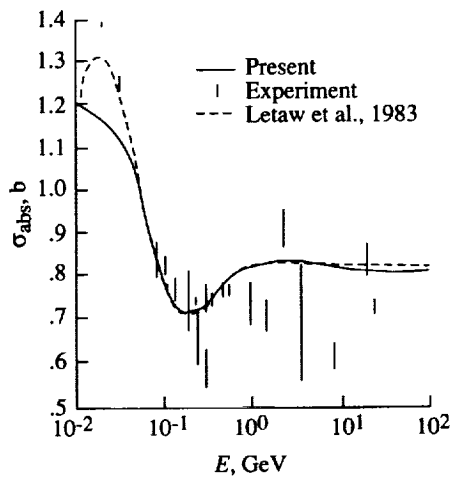


Figure 4.48. Neutron-copper absorption cross sections.

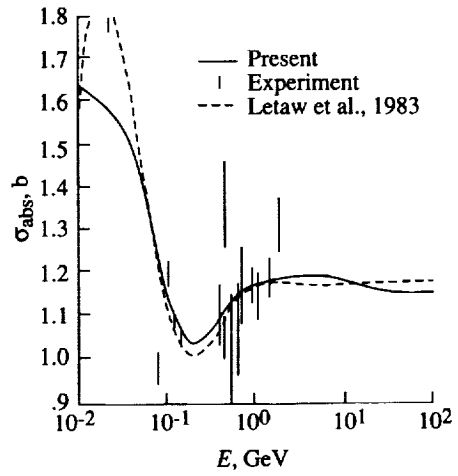


Figure 4.49. Neutron-silver absorption cross sections.

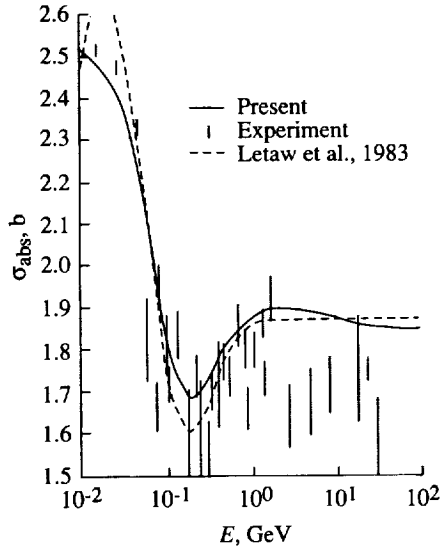


Figure 4.50. Neutron-lead absorption cross sections.

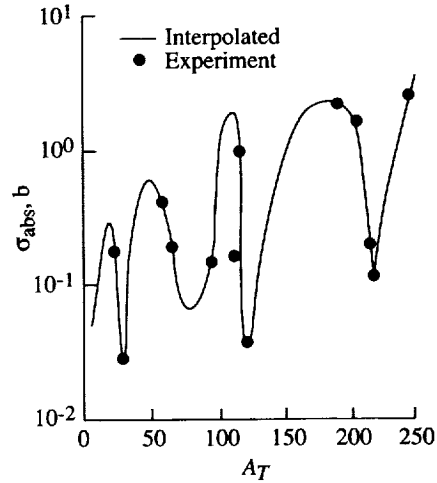


Figure 4.51. Interpolated neutron-nucleus absorption cross sections at 1 MeV.

between data points at the available target masses are shown in figures 4.51 through 4.56. Intermediate energy values are found according to

$$\sigma(A_T, E) = \sigma(A_T, E_i) \exp[-a(E - E_i)] \quad (4.68)$$

where E_i and a are taken according to the appropriate subinterval. The cross sections are assumed to be zero at energies below 0.5 MeV. The absorption cross sections for elements from lithium to plutonium for energies between 1 and 100 MeV are displayed in figure 4.57.

The cross sections presented in this section are probably sufficiently accurate for most applications. Because of their special importance in evaluating radiation quantities in tissue systems, the low-energy neutron cross sections for carbon, nitrogen, and oxygen are treated on a special basis. These neutron cross sections are represented by a data table that was compared with the ENDF/B-V data file compiled by Brookhaven National Laboratory (1982) in figures 4.58 through 4.60.

In section 4.2, we formulated a fully energy-dependent optical model potential approximation to the exact composite particle, multiple-scattering series. The formulation includes the effects of the finite nuclear force, treats Pauli correlations in an approximate way, and has no arbitrarily adjusted parameters. It is applicable to any projectile nucleus of mass number A_P colliding with any target nucleus of mass number A_T at any energy above 25 MeV/nucleon. When used within the context of eikonal scattering theory, which has been shown to be valid (Townsend, Bidasaria, and Wilson, 1983) even at energies as low as 25 MeV/nucleon, the absorption cross sections can be calculated from

$$\sigma_{\text{abs}} = \int d^2\vec{b} (1 - \exp\{-2 \text{Im} [\chi(\vec{b})]\}) \quad (4.69)$$

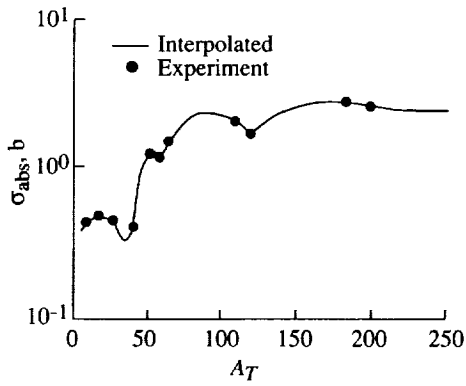


Figure 4.52. Interpolated neutron-nucleus absorption cross sections at 3 MeV.

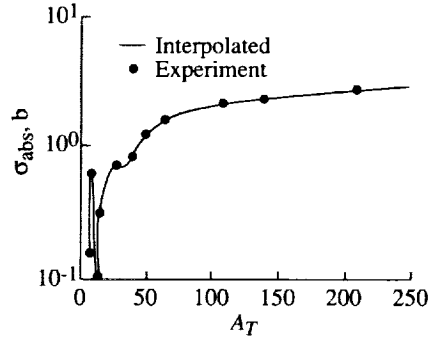


Figure 4.53. Interpolated neutron-nucleus absorption cross sections at 5 MeV.

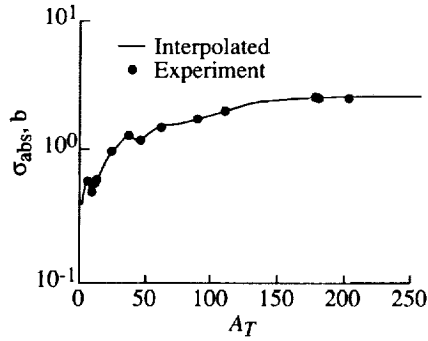


Figure 4.54. Interpolated neutron-nucleus absorption cross sections at 10 MeV.

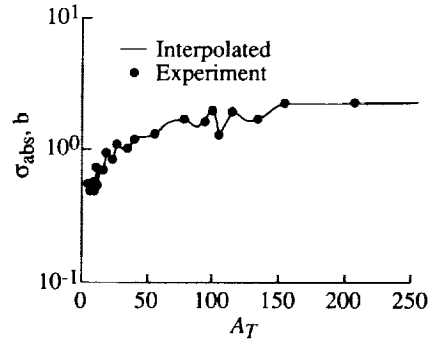


Figure 4.55. Interpolated neutron-nucleus absorption cross sections at 14 MeV.

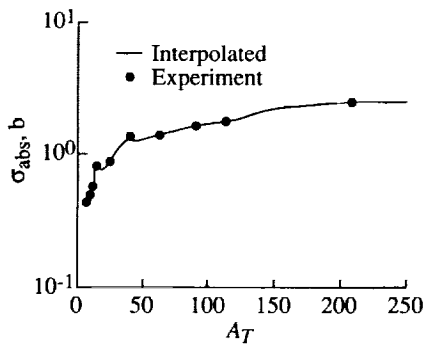


Figure 4.56. Interpolated neutron-nucleus absorption cross sections at 20 MeV.

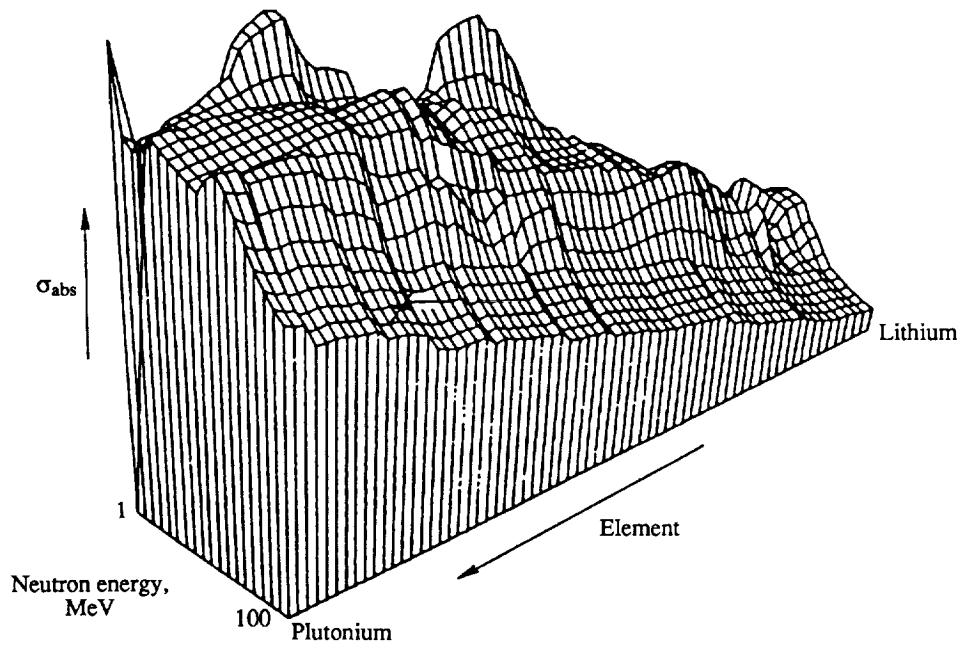


Figure 4.57. Neutron-nucleus absorption cross section.

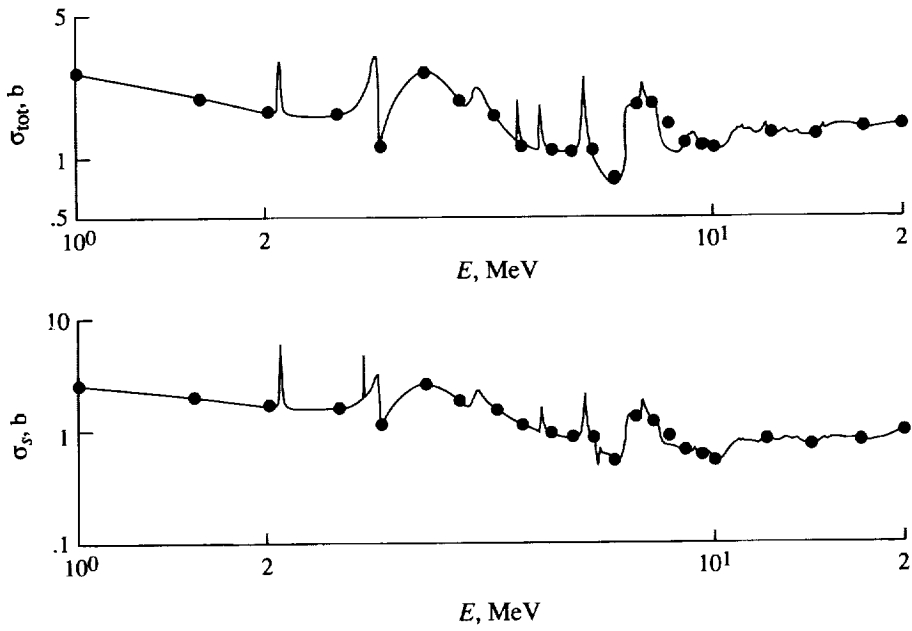


Figure 4.58. Nuclear cross sections for neutron projectiles onto carbon targets.

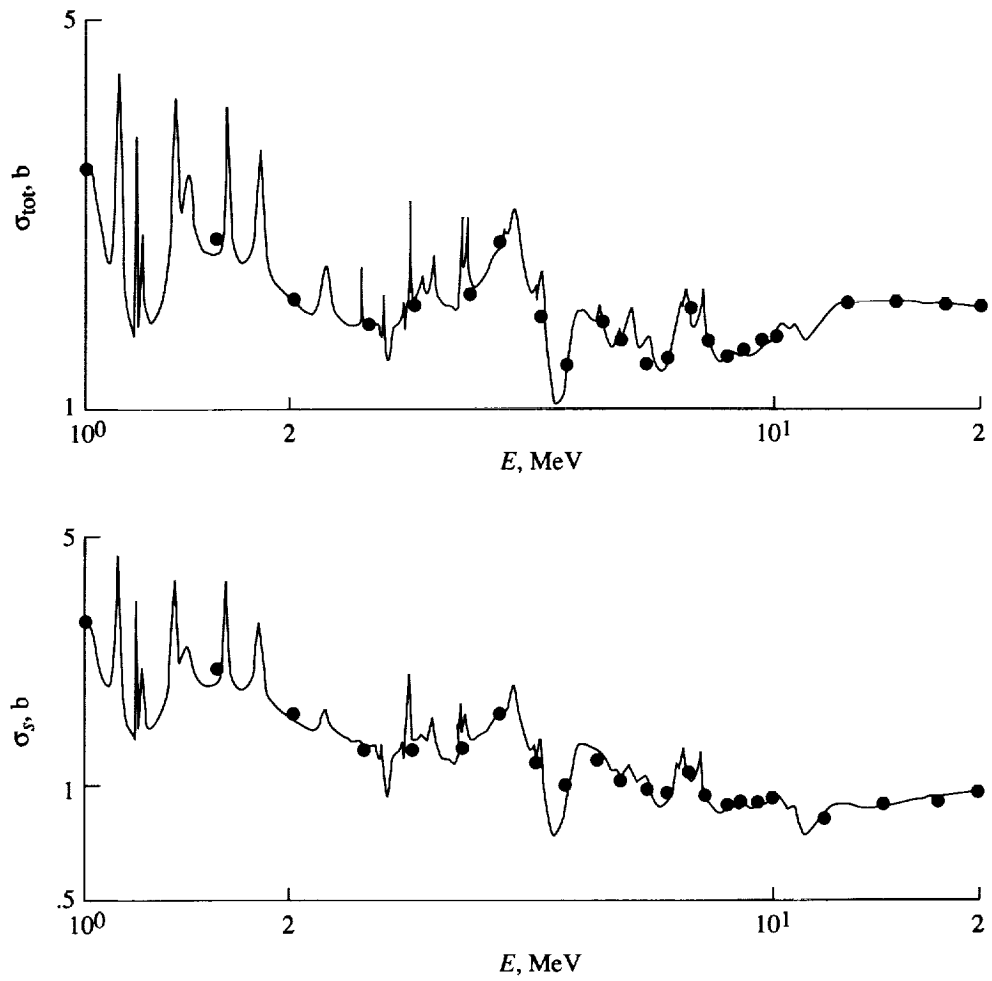


Figure 4.59. Nuclear cross sections for neutron projectiles onto nitrogen targets.

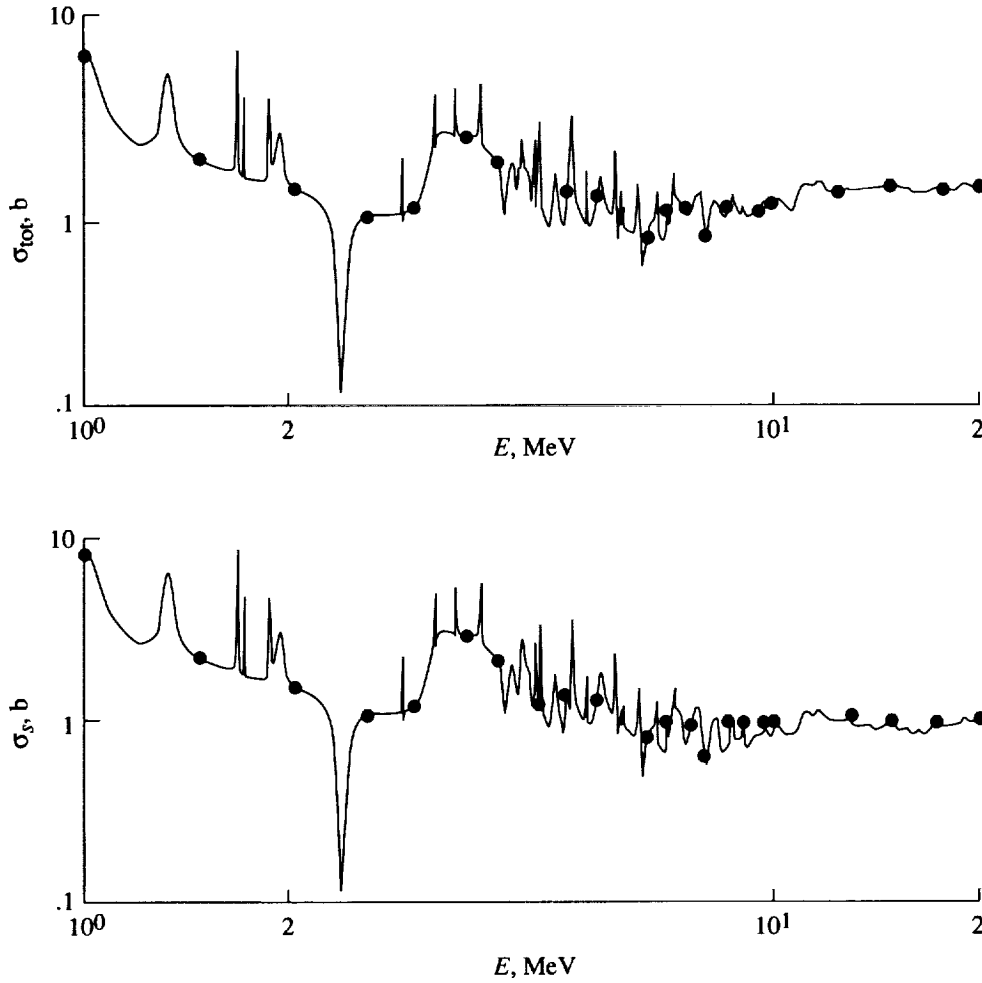


Figure 4.60. Nuclear cross sections for neutron projectiles onto oxygen targets.

where the complex phase function as a function of impact parameter \vec{b} is

$$\chi(\vec{b}) = -mA_P A_T k^{-1} (A_P + A_T)^{-1} \int V(\vec{b}, z) dz \quad (4.70)$$

and the optical potential is

$$V(\vec{b}, z) = A_P A_T \int d^3\vec{r} d^3\vec{y} \rho_P(\vec{b} + \vec{z} + \vec{r} + \vec{y}) \rho_T(\vec{r}) \tilde{t}(e, \vec{y}) \quad (4.71)$$

In equations (4.69) and (4.70), m is the nucleon mass, k is the momentum wave number, and ρ_i ($i = P, T$) is the respective number density distribution for the projectile and target nuclei. The constituent-averaged, two-nucleon transition amplitude \tilde{t} is used to describe high-energy nucleon-nucleon scattering. Details can be found in Wilson and Townsend (1981) and Townsend and Wilson (1985). Typical results for carbon projectiles are displayed in figure 4.61 along with recent experimental data of Kox et al. (1984). Because these calculations are too complex

to be repeatedly performed within a transport calculation, extensive tables, which can be easily stored on disk or magnetic tape for access as needed, have been published (Townsend and Wilson, 1985). Typical agreement between theory and experiment is within 10 percent for energies as low as 25 MeV/nucleon and within 3 percent for energies above 80 MeV/nucleon.

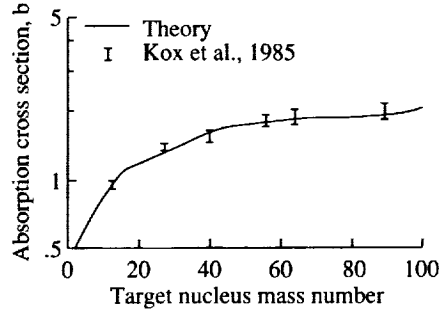


Figure 4.61. Absorption cross sections for carbon beams at 83 MeV/nucleon.

As an alternative to these tables, an energy-dependent parameterization of these tables has been formulated (Townsend and Wilson, 1986)

$$\sigma_{\text{abs}} = \pi r_o^2 \beta(E) \left(A_P^{1/3} + A_T^{1/3} - \delta \right)^2 \quad (4.72)$$

where

$$\delta = 0.200 + A_P^{-1} + A_T^{-1} - 0.292 \exp\left(\frac{-E}{792}\right) \cos(0.229E^{0.453}) \quad (4.73)$$

with

$$\beta(E) = 1 + 5E^{-1} \quad (4.74)$$

$r_o = 1.26$ fm, and E expressed in units of MeV/nucleon. Note that for large values of E , $\beta(E) \rightarrow 1$ and δ becomes energy independent, so that a typical form from Bradt and Peters (1950) is reproduced. Nominal differences between the cross sections obtained with equations (4.69) and (4.72) are less than 5 percent for $A > 4$ and $E > 50$ MeV/nucleon. For $E < 50$ MeV/nucleon, the differences are less than 10 percent. For helium-helium collisions, differences of approximately 20 percent exist at all energies. Representative predictions for carbon-carbon scattering as a function of energy are displayed in figure 4.62 along with experimental results (Kox et al., 1984; Jaros et al., 1978; Aksinenko et al., 1980; Heckman et al., 1978; Kox et al., 1985) and estimates obtained from a recently proposed energy-independent parameterization (Silberberg et al., 1984). The agreement with experimental data is quite good for the energy-dependent predictions, whereas the energy-independent parameterization clearly breaks down at low energies.

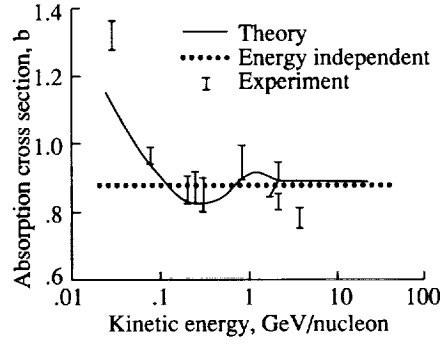


Figure 4.62. Absorption cross sections estimated by energy-dependent and energy-independent parameterizations and experiment for carbon-carbon scattering.

4.5. Parametric Differential Cross Sections

After the angular distribution in elastic scattering is sufficiently known, then the energy transferred to the target nucleus may be found as well as the new energy spectrum of the projectile. The differential energy and angle distributions are discussed in this section and simple parametric forms are given.

4.5.1. Nucleon-nucleon spectrum. The forward scattered nucleon differential cross section (Schopper, 1973) is well represented by

$$f_f(E, E') = B \frac{\exp[-B(E' - E)]}{1 - \exp(-BE')} \quad (4.75)$$

where

$$B = \frac{2mc^2b}{10^6} \quad (4.76)$$

In equation (4.76), mc^2 is the nucleon rest energy (938 MeV), and b is the usual slope parameter given by (in units of GeV^{-2})

$$b = \begin{cases} 3 + 14 \exp\left(\frac{-E'}{200}\right) & \text{(For } pp\text{)} \\ 3.5 + 30 \exp\left(\frac{-E'}{200}\right) & \text{(For } pn\text{)} \end{cases} \quad (4.77)$$

where E' (MeV) is the initial nucleon energy in the rest frame of the target. The backward scattering spectrum is similar in form

$$f_b(E, E') = \frac{B \exp(-BE)}{1 - \exp(-BE')} \quad (4.78)$$

where we assume the backward scatter slope parameter is the same as the forward value. This is strictly true for pp scattering, but the slope parameter for pn charge exchange scattering (Bertini, Guthrie, and Culkowski, 1972) would be more correct. The forward-to-backward ratio for np scattering is well represented by

$$F_B(E') = 0.12 - 0.015E' + \frac{0.41}{1 + \exp[4(E' - 1.2)]} \quad (4.79)$$

where E' in equation (4.79) has units of GeV. The full differential spectrum is then

$$f(E, E') = \frac{B \exp[-B(E' - E)] + F_B(E')B \exp(-BE)}{[1 - \exp(-BE')][1 + F_B(E')]} \quad (4.80)$$

where $F_B(E') = 1$ for pp scattering. The differential cross sections are normalized such that

$$\frac{d\sigma}{dE} = \sigma(E')f(E, E') \quad (4.81)$$

where $\sigma(E')$ is the appropriate nucleon-nucleon total cross section. Obviously, we have neglected the inelastic processes that must yet be included so that $\sigma(E')$ in equation (4.81) is currently set equal to total cross section to ensure conservation of energy, mass, and charge. The distribution of the center-of-mass angle θ_{cm} is related to the energy change in the laboratory frame of reference (relativistic kinematics are not yet included) by

$$\frac{d\sigma}{d\Omega} = \frac{E'}{4\pi} \frac{d\sigma}{dE} \quad (4.82)$$

where Ω denotes the solid angle element in the center-of-mass frame of reference. The center-of-mass angular distributions are compared with the compilation of experimental data (Hess, 1958) in figures 4.63 and 4.64.

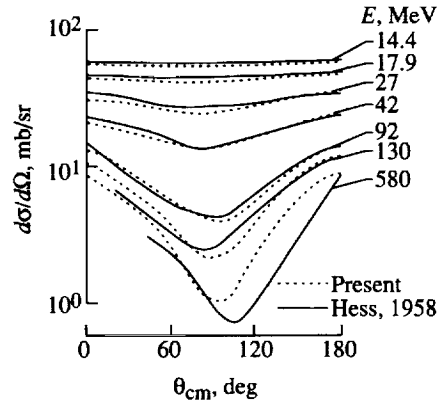


Figure 4.63. Neutron-proton differential elastic scattering cross section of present model and experiment.

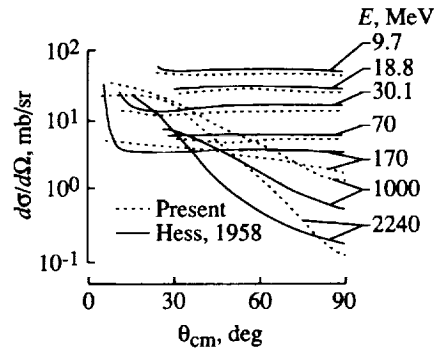


Figure 4.64. Proton-proton differential elastic scattering cross sections.

4.5.2. Nucleon-nucleus spectrum. The nucleon-nucleus differential cross section in Chew's form of the impulse approximation (note that this is just the Born term of the optical model) is given by

$$\begin{aligned} \frac{d\sigma_I}{dq^2} &= c \exp(-2bq^2) \left| F_A(q^2) \right|^2 \\ &\approx c \exp(-2bq^2) \exp\left(\frac{-2a^2q^2}{3}\right) \end{aligned} \quad (4.83)$$

where b is the slope parameter of equation (4.77) averaged among nuclear constituents, q is the magnitude of momentum transfer, and a is the nuclear root-mean-square (rms) radius. The nuclear rms radius (Wilson, 1975) in terms of the rms charge radius (in fermi) is given as

$$a = \left(\sqrt{a_c^2 - 0.64} \right)^{1/2} \quad (4.84)$$

where the rms charge radius (in fermi) is

$$a_c = \begin{cases} 0.84 & (A_T = 1) \\ 2.17 & (A_T = 2) \\ 1.78 & (A_T = 3) \\ 1.63 & (A_T = 4) \\ 2.4 & (6 \leq A_T \leq 14) \\ 0.82A_T^{1/3} + 0.58 & (A_T \geq 16) \end{cases} \quad (4.85)$$

the nuclear form factor is the Fourier transform of the nuclear-matter distribution. Note that the above equation assumes that the nuclear-matter distribution is a Gaussian function. Such an approximation is reasonable for the light-mass nuclei but is less valid for $A_T \gg 20$.

The energy transferred to the nucleus E_T is restricted by kinematics to

$$0 \leq E_T \leq (1 - \alpha)E' \quad (4.86)$$

where

$$\alpha = \frac{(A_T - 1)^2}{(A_T + 1)^2} \quad (4.87)$$

The energy-transfer spectrum is given as

$$f_I(E_T, E') = \frac{4A_T mc^2 \left(B + \frac{a^2}{3} \right) \exp \left[-4A_T mc^2 \left(B + \frac{a^2}{3} \right) E_t \right]}{1 - \exp \left[-4A_t mc^2 (1 - \alpha) \left(B + \frac{a^2}{3} \right) E' \right]} \quad (4.88)$$

Similarly, the scattered nucleon energy E is restricted to

$$\alpha E' \leq E \leq E' \quad (4.89)$$

The nucleon spectrum is given by

$$f(E, E') = \frac{4A_T mc^2 \left(B + \frac{a^2}{3} \right) \exp \left[-4A_T mc^2 \left(B + \frac{a^2}{3} \right) (E' - E) \right]}{1 - \exp \left[-4A_T mc^2 (1 - \alpha) \left(B + \frac{a^2}{3} \right) E' \right]} \quad (4.90)$$

One should note that both equations (4.88) and (4.90) reduce to the usual isotropic scattering results at low incident energy. The differential spectrum is normalized as

$$\frac{d\sigma}{dE} = \sigma_s(E') f(E, E') \quad (4.91)$$

where $\sigma_s(E')$ is the total scattering cross section obtained from equation (4.61).

The angular distribution of scattered nucleons is rather well-defined by equation (4.83) near the forward direction (Wilson et al., 1989). To approximate the cross section at large angles, we evaluate the $\ell = 0$ phase shift (Merzbacher, 1970) and introduce an energy-dependent parameter as follows. The S-wave phase shift δ_0 is related to the optical potential as

$$\tan \delta_0 \approx -k \int_0^\infty [j_0(kr')]^2 U(r')(r')^2 dr' \quad (4.92)$$

where

$$U(\vec{x}) = \frac{2mA_T^2 A_P^2}{(A_T + A_P)} \int d^3z d^3y \rho_T(\vec{z}) \rho_P(\vec{x} + \vec{z} + \vec{y}) \tilde{i}(k, \vec{y}) \quad (4.93)$$

as given in chapter 3. Because we assume that $\rho_T(\vec{z})$, $\rho_P(\vec{z})$, and $\tilde{i}(k, \vec{y})$ are Gaussian in coordinate space, the integrals are easily evaluated. The S-wave cross section is given as

$$\sigma_0 = \sqrt{\frac{mE'}{2}} \sin \delta_0 \quad (4.94)$$

with the corresponding differential contribution

$$\frac{d\sigma_0}{dE} = \frac{(A_P + A_T)^2 \sigma_0}{A_P A_T E'} \frac{1}{4\pi} \quad (4.95)$$

where $A_P = 1$ for neutron scattering.

The S-wave contribution is combined with the impulse approximation, with the interference terms neglected, as follows

$$\frac{d\sigma_s}{dE} = \left[\frac{d\sigma_I}{dE} + b_s(E') \frac{d\sigma_0}{dE} \right] N_s \quad (4.96)$$

where the renormalization factor N_s is chosen to preserve the relation

$$\sigma_s = \int_0^{(1-\alpha)E'} \frac{d\sigma_s}{dE} dE \quad (4.97)$$

for which N_s is found to be

$$N_s = \frac{\sigma_s(E')}{\sigma_s(E') + b_s(E')\sigma_0(E')} \quad (4.98)$$

The parameter $b_s(E')$ is taken as a function of energy

$$b_s(E') = \frac{1}{2} + \frac{3}{32} E' \quad (4.99)$$

The results are compared with the work of others (Fernbach, 1958; Goldberg, May, and Stehn, 1962) in figures 4.65 through 4.68. The scaled S-wave contribution used to represent the large angle scattering of neutrons shows improvement for most nuclei and gives satisfactory KERMA values as shown in chapter 10.

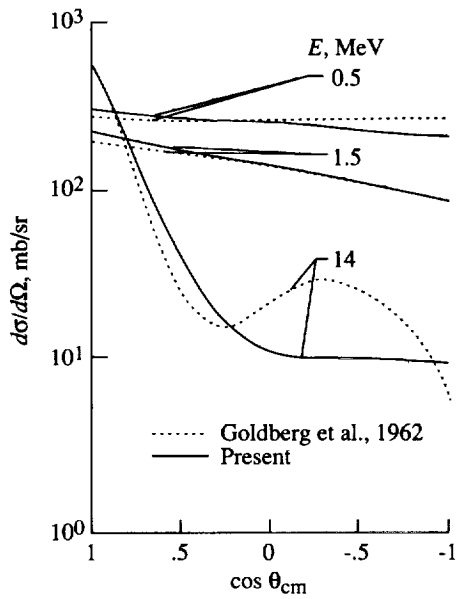


Figure 4.65. Neutron-carbon differential elastic scattering cross sections.

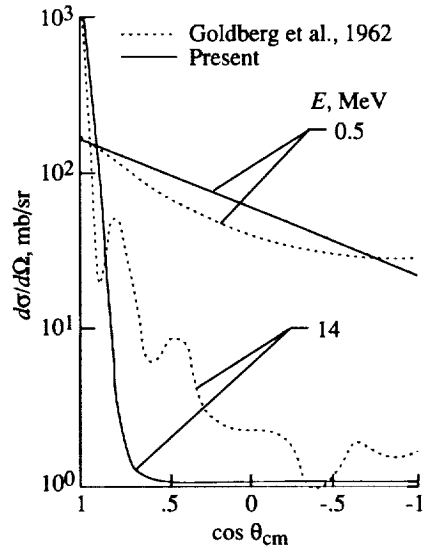


Figure 4.66. Neutron-uranium differential elastic scattering cross sections.

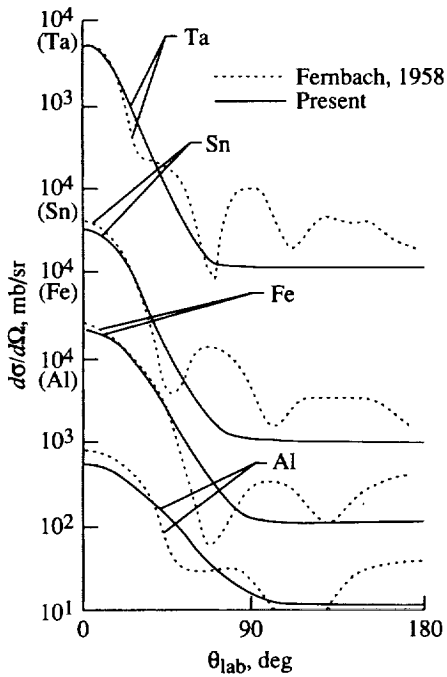


Figure 4.67. Neutron scattering cross section for several elements for 7-MeV neutrons.

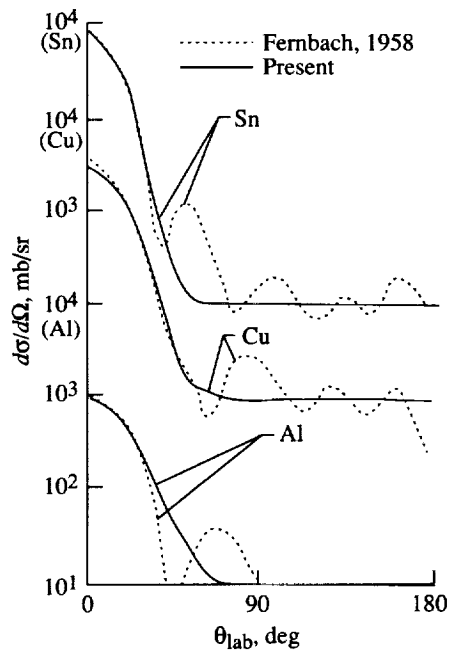


Figure 4.68. Neutron scattering cross section for several elements for 14-MeV neutrons.

4.6. Summary

A reasonably accurate data base is available to describe the elastic channel of nucleon and nucleus interactions. Future activity should concentrate on generating a meson and antinucleon data base.

4.7. References

- Akaishi, Yoshinori, 1984: Random Number Method in Few Body Calculation. *Nuclear Phys.*, vol. A416, pp. 409c-419c.
- Aksinenko, V. D.; Anikina, M. Kh.; Buttsev, V. S.; Chkaidze, L. V.; Glagoleva, N. S.; Golokhvastov, A. I.; Grachov, R. G.; Gudima, K. K.; Dementjev, E. A.; Kadikova, S. V.; Kaminski, N. I.; Khorozov, S. A.; Kuznetsova, E. S.; Lukstins, J.; Matyushin, A. T.; Matyushin, V. T.; Mescherjakov, M. G.; Musulmanbekov, Zh. Zh.; Nurgozhin, N. N.; Okonov, E. O.; Ostanovich, T. G.; Peisert, A.; Skrzypczak, E.; Szwed, R.; Shevchenko, E. A.; Sidorin, S. S.; Khusainov, E. K.; Toneev, V. D.; Vardenga, G. L.; Volodin, V. D.; Zakrzewski, J. A.; and Zuravleva, M. S., 1980: Streamer Chamber Study of the Cross Sections and Multiplicities in Nucleus-Nucleus Interactions at the Incident Momentum of 4.5 GeV/c per Nucleon. *Nuclear Phys.*, vol. A348, nos. 4,5, pp. 518-534.
- Angeli, I.; and Csikai, J., 1970: Total Neutron Cross Sections and the Nuclear Ramsauer Effect. *Nuclear Phys.*, vol. A158, no. 2, pp. 389-392.
- Angeli, I.; and Csikai, J., 1971: Total Neutron Cross Sections and the Nuclear Ramsauer Effect. (II). $E_n = 0.5-42$ MeV. *Nuclear Phys.*, vol. A170, no. 3, pp. 577-583.
- Antonchik, V. A.; Bakaev, V. A.; Bogdanov, S. D.; Vikhrov, A. I.; Dudkin, V. E.; Nefedov, N. A.; Ostroumov, V. I.; and Potapov, Yu. V., 1981: Interaction of ^{56}Fe at 1.8 GeV Nucleon With the Nuclei C, N, and O and With Ag and Br. *Sov. J. Nuclear Phys.*, vol. 33, no. 4, pp. 558-560.
- Barashenkov, V. S.; Gudima, K. K.; and Toneev, V. D., 1969: Cross Sections for Fast Particles and Atomic Nuclei. *Prog. Phys.*, vol. 17, no. 10, pp. 683-725.
- Benary, Odette; Price, Leroy R.; and Alexander, Gideon, 1970: *NN and ND Interactions (Above 0.5 GeV/c)—A Compilation*. UCRL-20000 NN, Lawrence Radiation Lab., Univ. of California.
- Berger, J.; Dufflo, J.; Goldzahl, L.; Oostens, J.; Plouin, F.; Fabbri, F. L.; Picozza, P.; Satta, L.; Bizard, G.; Lefebvres, F.; Steckmeyer, J. C.; and Legrand, D., 1980: $\alpha\alpha$ Elastic Scattering at 4.32 GeV/c and 5.07 GeV/c. *Nuclear Phys.*, vol. A338, no. 2, pp. 421-428.
- Bertini, Hugo W.; Guthrie, Miriam P.; and Culkowski, Arline H., 1972: *Nonelastic Interactions of Nucleons and π -Mesons With Complex Nuclei at Energies Below 3 GeV*. ORNL-TM-3148, U.S. Atomic Energy Commission.
- Bidasaria, H. B.; and Townsend, L. W., 1983: Microscopic Optical Potential Analyses of Carbon-Carbon Elastic Scattering. *Canadian J. Phys.*, vol. 61, no. 12, pp. 1660-1662.
- Bidasaria, H. B.; Townsend, L. W.; and Wilson, J. W., 1983: Theory of Carbon-Carbon Scattering From 200 to 290 MeV. *J. Phys. G: Nuclear Phys.*, vol. 9, no. 1, pp. L17-L20.

- Binstock, Judith, 1974: Parameterization of σ_{tot} , $\sigma(\Theta)$, $P(\Theta)$ for 25–100 MeV np Elastic Scattering. *Phys. Review*, vol. 10, ser. C, no. 1, pp. 19–23.
- Bobchenko, B. M.; Buklei, A. E.; Viasov, A. V.; Vorob'ev, I. I.; Vorob'ev, L. S.; Goryainov, N. A.; Grishuk, Yu. G.; Gushchin, O. B.; Druzhinin, B. L.; Zhurkin, V. V.; Zavrazhnov, G. N.; Kosov, M. V.; Leksin, G. A.; Stolin, V. L.; Surin, V. P.; Fedorov, V. B.; Fominykh, B. A.; Shvartsman, B. B.; Shevchenko, S. V.; and Shuvalov, S. M., 1979: Measurement of Total Inelastic Cross Sections for Interaction of Protons With Nuclei in the Momentum Range From 5 to 9 GeV/c and for Interaction of π^- Mesons With Nuclei in the Momentum Range From 1.75 to 6.5 GeV/c. *Sov. J. Nuclear Phys.*, vol. 30, no. 6, pp. 805–813.
- Borkowski, F.; Simon, G. G.; Walther, V. H.; and Wendling, R. D., 1975: On the Determination of the Proton RMS-Radius From Electron Scattering Data. *Z. Phys. A.*, vol. 275, no. 1, pp. 29–31.
- Bradt, H. L.; and Peters, B., 1950: The Heavy Nuclei of the Primary Cosmic Radiation. *Phys. Review*, vol. 77, second ser., no. 1, pp. 54–70.
- Brodsky, Allen, ed., 1978: *CRC Handbook of Radiation Measurement and Protection—General Scientific and Engineering Information, Volume I: Physical Science and Engineering Data*. CRC Press, Inc.
- Brookhaven National Lab., 1982: *Guidebook for the ENDF/B-V Nuclear Data Files*. EPRI NP-2510 (Res. Proj. 975-1. BNL-NCS-31451, ENDF-328).
- Buck, W. W.; Norbury, J. W.; Townsend, L. W.; and Wilson, J. W., 1986: Theoretical Antideuteron-Nucleus Absorptive Cross Sections. *Phys. Review*, vol. 33, third ser., no. 1, pp. 234–238.
- Buck, Warren W.; Wilson, John W.; Townsend, Lawrence W.; and Norbury, John W., 1987: *Possible Complementary Cosmic-Ray Systems: Nuclei and Antinuclei*. NASA TP-2741.
- Buenerd, M.; Lounis, A.; Chauvin, J.; Lebrun, D.; Martin, P.; Duhamel, G.; Gondrand, J. C.; and De Saintignon, P., 1984: Elastic and Inelastic Scattering of Carbon Ions at Intermediate Energies. *Nuclear Phys.*, vol. A424, no. 2, pp. 313–334.
- Cheshire, D. L.; Huggett, R. W.; Johnson, D. P.; Jones, W. V.; Rountree, S. P.; Verma, S. D.; Schmidt, W. K. H.; Kurz, R. J.; Bowen, T.; and Krider, E. P., 1974: Fragmentation Cross Sections of 2.1-GeV/Nucleon ^{12}C and ^{16}O Ions. *Phys. Review*, vol. 10, ser. D, no. 1, pp. 25–31.
- Cole, A. J.; Rae, W. D. M.; Brandan, M. E.; Dacal, A.; Harvey, B. G.; Legrain, R.; Murphy, M. J.; and Stokstad, R. G., 1981: $^{12}\text{C} + ^{12}\text{C}$ Reaction Cross Section Between 70 and 290 MeV Obtained From Elastic Scattering. *Phys. Review Lett.*, vol. 47, no. 24, pp. 1705–1708.
- Cucinotta, F. A.; Khandelwal, G. S.; Townsend, L. W.; and Wilson, J. W., 1989: Correlations in α - α Scattering and Semi-Classical Optical Models. *Phys. Lett.*, vol. B223, no. 2, pp. 127–132.
- Dadić, I.; Martinis, M.; and Pisk, K., 1971: Inelastic Processes and Backward Scattering in a Model of Multiple Scattering. *Ann. Phys.*, vol. 64, no. 2, pp. 647–671.

Transport Methods and Interactions for Space Radiations

- De Jager, C. W.; De Vries, H.; and De Vries, C., 1974: Nuclear Charge- and Magnetization-Density-Distribution Parameters From Elastic Electron Scattering. *At. Data & Nuclear Data Tables*, vol. 14, no. 5/6, pp. 479-508.
- Fernbach, S., 1958: Nuclear Radii as Determined by Scattering of Neutrons. *Reviews Modern Phys.*, vol. 30, no. 2, pt. 1, pp. 414-418.
- Feshbach, H.; and Hüfner, J., 1970: On Scattering by Nuclei at High Energies. *Ann. Phys.*, vol. 56, no. 1, pp. 268-294.
- Franco, Victor; and Nutt, W. T., 1978: Short Range Correlations in High Energy Heavy Ion Collisions. *Phys. Review C*, vol. 17, third ser., no. 4, pp. 1347-1358.
- Frullani, Salvatore; and Mougey, Jean, 1984: Single-Particle Properties of Nuclei Through ($e, e'p$) Reactions. *Advances in Nuclear Physics*, Volume 14, J. W. Negele and Erich Vogt, eds., Plenum Press, pp. 1-289.
- Goldberg, Murrey D.; May, Victoria M.; and Stehn, John R., 1962: *Angular Distributions in Neutron-Induced Reactions. Volume I, Z = 1 to 22*. BNL 400, Second ed., Vol. I, Sigma Center, Brookhaven National Lab.
- Gross, Franz, 1974: New Theory of Nuclear Forces. Relativistic Origin of the Repulsive Core. *Phys. Review D*, vol. 10, no. 1, pp. 223-242.
- Heckman, H. H.; Greiner, D. E.; Lindstrom, P. J.; and Shwe, H., 1978: Fragmentation of ^4He , ^{12}C , ^{14}N , and ^{16}O Nuclei in Nuclear Emulsion at 2.1 GeV/Nucleon. *Phys. Review*, vol. 17, ser. C, no. 5, pp. 1735-1747.
- Hess, Wilmot N., 1958: Summary of High-Energy Nucleon-Nucleon Cross-Section Data. *Reviews Modern Phys.*, vol. 30, no. 2, pt. I, pp. 368-401.
- Hong, Byungsik; Maung, Khin Maung; Wilson, John W.; and Buck, Warren W., 1989: *Kaon-Nucleus Scattering*. NASA TP-2920.
- Hughes, Donald, J.; and Schwartz, Robert B., 1958: *Neutron Cross Sections*. BNL 325, Second ed., Brookhaven National Lab.
- Jakobsson, B.; and Kullberg, R., 1976: Interactions of 2 GeV/Nucleon ^{16}O With Light and Heavy Emulsion Nuclei. *Phys. Scr.*, vol. 13, no. 6, pp. 327-338.
- Jaros, J.; Wagner A.; Anderson, L.; Chamberlain, O.; Fuzesy, R. Z.; Gallup, J.; Gorn, U; Schroeder, L.; Shannon, S.; Shapiro, G.; and Steiner, H., 1978: Nucleus-Nucleus Total Cross Sections for Light Nuclei at 1.55 and 2.89 GeV/c per Nucleon. *Phys. Review*, vol. 18, ser. C, no. 5, pp. 2273-2292.
- Jastrow, Robert, 1955: Many-Body Problem With Strong Forces. *Phys. Review*, vol. 98, second ser., no. 5, pp. 1479-1484.
- Kox, S.; Gamp, A.; Cherkaoui, R.; Cole, A. J.; Longequeue, N.; Menet, J.; Perrin, C.; and Viano, J. B., 1984: Direct Measurements of Heavy-Ion Total Reaction Cross Sections at 30 and 83 MeV/Nucleon. *Nuclear Phys.*, vol. A420, no. 1, pp. 162-172.

- Kox, S.; Gamp, A.; Perrin, C.; Arvieux, J.; Bertholet, R.; Barundet, J. F.; Buenerd, M.; El Masri, Y.; Longequeue, N.; and Merchez, F., 1985: Transparency Effects in Heavy-Ion Collisions Over the Energy Range 100–300 MeV/Nucleon. *Phys. Lett.*, vol. 159B, no. 1, pp. 15–18.
- Kullberg, R.; Kristiansson, K.; Lindkvist, B.; and Otterlund, I., 1977: Production Cross Sections of Multiply Charged Fragments in Heavy Ion Interactions at 150–200 MeV/Nucleon. *Nuclear Phys.*, vol. A280, no. 2, pp. 491–497.
- Letaw, John R.; Silberberg, R.; and Tsao, C. H., 1983: Proton-Nucleus Total Inelastic Cross Sections: An Empirical Formula for $E > 10$ MeV. *Astrophys. J.*, Suppl. ser., vol. 51, no. 3, pp. 271–276.
- Lindstrom, P. J.; Greiner, D. E.; Heckman, H. H.; Cork, B.; and Bieser, F. S., 1975: *Isotope Production Cross Sections From the Fragmentation of ^{16}O and ^{12}C at Relativistic Energies*. LBL-3650 (NGR-05-003-513), Lawrence Berkeley Lab., Univ. of California.
- Liu, H.; Zamick, L.; and Jaqaman, H., 1985: Excited States of ^4He . *Phys. Review C*, vol. 31, third ser., no. 6, pp. 2251–2255.
- Lock, W. O.; and Measday, D. F., 1970: *Intermediate Energy Nuclear Physics*. Methuen & Co. Ltd. (London).
- McCarthy, J. S.; Sick, I.; and Whitney, R. R., 1977: Electromagnetic Structure of the Helium Isotopes. *Phys. Review C*, vol. 15, third ser., no. 4, pp. 1396–1414.
- Merzbacher, Eugen, 1970: *Quantum Mechanics*, Second ed. John Wiley & Sons, Inc.
- Palevsky, H.; Friedes, J. L.; Sutter, R. J.; Bennett, G. W.; Igo, G. J.; Simpson, W. D.; Phillips, G. C.; Corley, D. M.; Wall, N. S.; Stearns, R. L.; and Gottschalk, B., 1967: Elastic Scattering of 1-BeV Protons From Hydrogen, Helium, Carbon, and Oxygen Nuclei. *Phys. Review Lett.*, vol. 18, no. 26, pp. 1200–1204.
- Perrin, C.; Kox, S.; Longequeue, N.; Viano, J. B.; Buenerd, M.; Cherkaoui, R.; Cole, A. J.; Gamp, A.; Menet, J.; Ost, R.; Bertholet, R.; Guet, C.; and Pinston, J., 1982: Direct Measurement of the $^{12}\text{C} + ^{12}\text{C}$ Reaction Cross Section Between 10 and 83 MeV/Nucleon. *Phys. Review Lett.*, vol. 49, no. 26, pp. 1905–1909.
- Renberg, P. U.; Measday, D. F.; Pepin, M.; Schwaller, P.; Favier, B.; and Richard-Serre, C., 1972: Reaction Cross Sections for Protons in the Energy Range 220–570 MeV. *Nuclear Phys.*, vol. A183, no. 1, pp. 81–104.
- Ringia, F. E.; Dobrowolski, T.; Gustafson, H. R.; Jones, L. W.; Longo, M. J.; Parker, E. F.; and Cork, Bruce, 1972: Differential Cross Sections for Small-Angle Neutron-Proton and Neutron-Nucleus Elastic Scattering at 4.8 GeV/c. *Phys. Review Lett.*, vol. 28, no. 3, pp. 185–188.
- Satta, L.; Duflo, J.; Plouin, F.; Picozza, P.; Goldzahl, L.; Banaigs, J.; Frascaria, R.; Fabbri, F. L.; Codino, A.; Berger, J.; Boivin, M.; and Berthet, P., 1984: Elastic Scattering of α Particles on Light Nuclei at $P_\alpha = 7$ GeV/c. *Phys. Lett.*, vol. 139B, no. 4, pp. 263–266.

Transport Methods and Interactions for Space Radiations

- Schimmerling, W.; Devlin, T. J.; Johnson, W.; Vosburgh, K. G.; and Mischke, R. E., 1971: Neutron-Nucleus Total and Inelastic Cross Sections From 900 to 2600 MeV/c. *Phys. Lett.*, vol. 37B, no. 2, pp. 177-180.
- Schimmerling, Walter; Devlin, Thomas J.; Johnson, Warren W.; Vosburgh, Kirby G.; and Mischke, Richard E., 1973: Neutron-Nucleus Total and Inelastic Cross Sections: 900 to 2600 MeV/c. *Phys. Review*, vol. 7, no. 1, pp. 248-262.
- Schopper, H., ed., 1973: *Elastic and Charge Exchange Scattering of Elementary Particles. Landolt-Börnstein Numerical Data and Functional Relationships in Science and Technology, Group I, Volume 7*, Springer-Verlag.
- Schopper, H., ed., 1980: *Elastic and Charge Exchange Scattering of Elementary Particles. Landolt-Börnstein Numerical Data and Functional Relationships in Science and Technology, Group I, Volume 9*, Springer-Verlag.
- Silberberg, R.; Tsao, C. H.; Adams, J. H., Jr.; and Letaw, J. R., 1984: Radiation Doses and LET Distributions of Cosmic Rays. *Radiat. Res.*, vol. 98, pp. 209-226.
- Skrzypczak, E., 1980: Cross-Sections for Inelastic ^4He and ^{12}C -Nucleus Collisions at 4.5 GeV/c/N Incident Momentum. *Proceedings of the International Conference on Nuclear Physics, Volume 1, Abstracts*, LBL-11118 (Contract No. W-7405-ENG-48), Lawrence Berkeley Lab., Univ. of California, p. 575.
- Stehn, John R.; Goldberg, Murrey D.; Magurno, Benjamin A.; and Wiener-Chasman, Renate, 1964: *Neutron Cross Sections. Volume 1, Z = 1 to 20*. BNL 325, Second ed., Suppl. No. 2 (Physics—TID-4500, 32nd ed.), Sigma Center, Brookhaven National Lab. Associated Univ., Inc.
- Townsend, Lawrence W., 1982: *Harmonic Well Matter Densities and Pauli Correlation Effects in Heavy Ion Collisions*. NASA TP-2003.
- Townsend, L. W.; Bidasaria, H. B.; and Wilson, J. W., 1983: Eikonal Phase Shift Analyses of Carbon-Carbon Scattering. *Canadian J. Phys.*, vol. 61, no. 6, pp. 867-871.
- Townsend, Lawrence W.; Wilson, John W.; and Bidasaria, Hari B.; 1983a: *Heavy-Ion Total and Absorption Cross Sections Above 25 MeV/Nucleon*. NASA TP-2138.
- Townsend, Lawrence W.; Wilson, John W.; and Bidasaria, Hari B., 1983b: *Nucleon and Deuteron Scattering Cross Sections From 25 MeV/Nucleon to 22.5 GeV/Nucleon*. NASA TM-84636.
- Townsend, Lawrence W.; and Wilson, John W., 1985: *Tables of Nuclear Cross Sections for Galactic Cosmic Rays—Absorption Cross Sections*. NASA RP-1134.
- Townsend, L. W.; and Wilson, J. W., 1986: Energy-Dependent Parameterization of Heavy-Ion Absorption Cross Sections. *Radiat. Res.*, vol. 106, pp. 283-287.
- Vary, J. P.; and Dover, C. B., 1974: Microscopic Models for Heavy Ion Scattering at Low, Intermediate and High Energies. *2nd High Energy Heavy Ion Summer Study—July 15-26, 1974 at the Lawrence Berkeley Laboratory*, LBL-3675, Lawrence Berkeley Lab., Univ. of California, pp. 197-259.

- Wallace, Stephen J., 1975: High-Energy Expansion for Nuclear Multiple Scattering. *Phys. Review C*, vol. 12, third ser., no. 1, pp. 179–193.
- Westfall, G. D.; Wilson, Lance W.; Lindstrom, P. J.; Crawford, H. J.; Greiner, D. E.; and Heckman, H. H., 1979: Fragmentation of Relativistic ^{56}Fe . *Phys. Review*, vol. 19, ser. C, no. 4, pp. 1309–1323.
- Wilson, John W., 1975: Composite Particle Reaction Theory. Ph.D. Diss., College of William and Mary in Virginia.
- Wilson, John W.; and Costner, Christopher M., 1975: *Nucleon and Heavy-Ion Total and Absorption Cross Section for Selected Nuclei*. NASA TN D-8107.
- Wilson, J. W.; and Townsend, L. W., 1981: An Optical Model for Composite Nuclear Scattering. *Canadian J. Phys.*, vol. 59, no. 11, pp. 1569–1576.
- Wilson, John W.; Townsend, Lawrence W.; Nealy, John E.; Chun, Sang Y.; Hong, B. S.; Buck, Warren W.; Lamkin, S. L.; Ganapol, Barry D.; Khan, Ferdous; and Cucinotta, Francis A., 1989: BRYNTRN: *A Baryon Transport Model*. NASA-TP-2887.

1

2

3

4

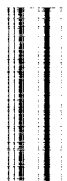
5

6

7

8

9



Chapter 5

Reaction Channel Data Base

5.1. Introduction

After substantial improvements had been made to the description of the elastic channel (Wilson and Townsend, 1981), Townsend (1981) began the development of an abrasion reaction model for the absorptive processes observed in the elastic amplitude, Cucinotta (1988) began a theory for α -particle breakup and Khan et al. (1988) investigated heavy ion abrasion dynamics by using the optical model. It was in this development that the need for inclusion of Pauli correlation and more accurate density functions for light nuclei became apparent (Townsend, 1982). Development of abrasion theory was greatly encouraged by the work of Stevenson, Martinis, and Price (1981) (whose experiments measured directly the abrasion event). The α breakup model is required to further extend the nucleon transport code to light fragments. The first semiempirical code was also developed by Wilson, Townsend, and Badavi (1987a and 1987b) and Badavi et al. (1987) to provide the data base for heavy ion reactions.

5.2. Nuclear Abrasion Model

We now discuss the work of Townsend (1981) in deriving a nuclear abrasion model for the optical potential formalism.

5.2.1. Optical potential. The optical model potential operator (Wilson, 1974a) is

$$V_{\text{opt}} = \sum_{\alpha j} t_{\alpha j} \quad (5.1)$$

where $t_{\alpha j}$ is the transition operator for scattering between the α constituent of the target and the j constituent of the projectile. The optical potential was derived as

$$W(\vec{x}) = A_P A_T \int d^3 \vec{\xi}_T \rho_T(\vec{\xi}_T) \int d^3 \vec{y} \rho_P(\vec{x} + \vec{y} + \vec{\xi}_T) t(e, \vec{y}) \quad (5.2)$$

when couplings to various excited internal states were neglected. The development of equation (5.2) was made independent of the eikonal approximation (Wilson, 1975) and then subsequently used within that context. Note that Franco and Varma (1978) use this same expression to represent their single-scattering term. Differences between Wilson's and Glauber's approximations occur in the higher order terms. For example, unlike the Glauber theory, the Wilson (1974b) propagator includes target recoil and terms to order k^2 . In equation (5.2), t is the two-body transition amplitude averaged over the constituent types, and ρ_T and ρ_P are the target and projectile single-particle matter densities. Equation (5.2) does not include the correlation effects of the Pauli exclusion principle because only simple unsymmetrized product wave functions were used by Wilson and Townsend

(1981). The accuracy of the results of Wilson and Townsend (1981) supports the idea that exchange correlation effects were unimportant when determining total and absorption cross sections. This section confirms this idea. For abrasion predictions, however, correlation effects of Pauli are found to be important when there is a large overlap between the colliding nuclear volumes (i.e., for small residual mass fragments of the projectile nucleus).

Because equation (5.1) was derived independent of any assumptions regarding nuclear wave functions, it is the starting point. When rewriting equation (5.1) in second quantization notations, we have

$$V_{\text{opt}} = \sum_{\beta k} \sum_{\alpha j} (\beta k | t | \alpha j) a_k^\dagger a_\beta^\dagger a_\alpha a_j \quad (5.3)$$

where the a_i^\dagger and a_i are the usual creation and annihilation operators for the single-particle state i . After the usual operator manipulations, the optical potential reduces to

$$W(x) = \sum_{\alpha}^{A_T} \sum_j^{A_P} [(\alpha j | t | \alpha j) - (\alpha j | t | j \alpha)] \quad (5.4)$$

When assuming a correlation function C , which depends only upon the relative separation of the α - and j -constituents, Townsend (1982) derives

$$W(\vec{x}) = A_P A_T \int d^3 \vec{\xi}_T \rho_T(\xi_T) \int d^3 \vec{y} \rho_P(\vec{x} + \vec{y} + \vec{\xi}_T) t(e, \vec{y}) [1 - C(\vec{y})] \quad (5.5)$$

Note that equation (5.5) reduces to equation (5.2) if there are no correlation effects ($C = 0$).

5.2.2. Abrasion theory. From Bleszynski and Sander (1979), the cross section for abrading n -projectile nucleons is

$$\sigma_n = \binom{A_P}{n} \int d^2 \vec{b} [1 - P(\vec{b})]^n P(\vec{b})^{A_P} \quad (5.6)$$

where $P(\vec{b})$ is the probability for not removing a nucleon in the collision and A_F , the residual fragment mass number, is

$$A_F = A_P - n \quad (5.7)$$

The total absorption cross section

$$\sigma_{\text{abs}} = \int d^2 \vec{b} [1 - P(\vec{b})^{A_P}] \quad (5.8)$$

is obtained by summing σ_n over all values of n . In the eikonal approximation, the absorption cross section is

$$\sigma_{\text{abs}} = \int d^2\vec{b} \left(1 - \exp \left\{ -2 \operatorname{Im} \left[\chi(\vec{b}) \right] \right\} \right) \quad (5.9)$$

where $\operatorname{Im}(\chi)$ denotes the imaginary part of χ . Comparing equation (5.8) and equation (5.9) gives

$$P(\vec{b}) = \exp \left\{ \frac{-2 \operatorname{Im} \left[\chi(\vec{b}) \right]}{A_P} \right\} \quad (5.10)$$

Substituting for the eikonal phase function gives

$$P(\vec{b}) = \exp \left[-A_T \sigma(e) I(\vec{b}) \right] \quad (5.11)$$

with

$$\begin{aligned} I(\vec{b}) &= [2\pi B(e)]^{-3/2} \int dz \int d^3\vec{\xi}_T \rho_T(\vec{\xi}_T) \\ &\quad \times \int d^3\vec{y} \rho_P(\vec{b} + \vec{z} + \vec{y} + \vec{\xi}_T) \exp \left[\frac{-y^2}{2B(e)} \right] \\ &\quad \times [1 - C(\vec{y})] \end{aligned} \quad (5.12)$$

Values for $\sigma(e)$ and $B(e)$, the nucleon-nucleon cross section and slope parameter, were taken from compilations.

The Glauber theory result (Bleszynski and Sander, 1979) is

$$P(\vec{b}) = 2\pi \int D_P(\vec{s}) \exp \left[-A_T \sigma_{NN} D_T(\vec{s} + \vec{b}) \right] s ds \quad (5.13)$$

where $D(\vec{s})$, the single-particle densities summed along the beam direction, is given by

$$D(\vec{s}) = \int_{-\infty}^{\infty} \rho(\vec{s} + \vec{z}) dz \quad (5.14)$$

The main advantages of equation (5.11) over equation (5.13) are its improved convergence and the added symmetry feature that the projectile and target are treated on an equal basis.

Substituting equation (5.11) into equation (5.6) gives

$$\begin{aligned} \sigma_n &= \binom{A_P}{n} \int d^2\vec{b} \left\{ 1 - \exp \left[-A_T \sigma(e) I(\vec{b}) \right] \right\}^n \\ &\quad \times \exp \left[-A_T A_F \sigma(e) I(\vec{b}) \right] \end{aligned} \quad (5.15)$$

5.2.3. Collision parameters. From Bohr and Mottelson (1969), the correlation function in the Fermi gas model is

$$C(y) = \frac{1}{4} \frac{3j_1^2(k_F y)}{k_F y} \quad (5.16)$$

where $k_F = 1.36 \text{ fm}^{-1}$. For analytic simplicity, equation (5.16) is replaced by a simple Gaussian function. Expanding equation (5.16) in a power series gives

$$\frac{3j_1^2(k_F y)}{k_F y} = 1 - \left(\frac{k_F^2 y^2}{10} \right) + 0(k_F^4 y^4) \quad (5.17)$$

For small values of $k_F y$, where correlations are most important in actual nuclei, we note that

$$\exp \left(\frac{-k_F^2 y^2}{10} \right) \approx 1 - \left(\frac{k_F^2 y^2}{10} \right) \quad (5.18)$$

Thus, for computations in this work, we use

$$C(y) \approx \frac{1}{4} \exp \left(\frac{-k_F^2 y^2}{10} \right) \quad (5.19)$$

Determinations of σ_n require the use of nuclear single-particle matter densities ρ for the nuclei in the collision. For the ^{20}Ne projectiles, matter densities are extracted from Woods-Saxon charge data of Knight et al. (1981) as described by Wilson and Townsend (1981). For the ^{96}Mo target, the matter density was found from the three-parameter Gaussian charge density data (De Jager, De Vries, and De Vries, 1974) by assuming that the charge density is given by the folded integral of a Gaussian proton charge density ρ_p , with the unknown nuclear matter density ρ_m according to

$$\rho_c(\vec{r}) = \int \rho_p(\vec{r}') \rho_m(\vec{r} + \vec{r}') d^3 r' \quad (5.20)$$

Inserting the Gaussian for $\rho_p(\vec{r})$, simplifying the ensuing expression (Wilson and Costner, 1975), and using a two-point Gauss-Hermite quadrature formula to evaluate the result yield

$$\rho_c(r) \approx \frac{1}{2} \left[\rho_m \left(r + \frac{r_p}{3^{1/2}} \right) + \rho_m \left(r - \frac{r_p}{3^{1/2}} \right) \right] \quad (5.21)$$

for determining the ^{96}Mo matter density. In equation (5.21), $r_p \approx 0.87 \text{ fm}$ is the proton rms radius (Borkowski et al., 1975). For the ^{12}C target, which has a harmonic well charge density, a matter density expression can be analytically extracted. Taking the Fourier transform of equation (5.20) and using the convolution theorem yield the following well-known result:

$$F_c(q) = F_p(q) F_m(q) \quad (5.22)$$

where for a Gaussian proton charge density,

$$F_p(q) = \exp\left(\frac{-q^2 r_p^2}{6}\right) \quad (5.23)$$

The ^{12}C harmonic well charge density (De Jager, De Vries, and De Vries, 1974)

$$\rho_c(r) = \rho_0 \left[1 + \alpha \left(\frac{r}{a}\right)^2\right] \exp\left(\frac{-r^2}{a^2}\right) \quad (5.24)$$

has a form factor (Townsend, 1982)

$$F_c(q) = \rho_0 \pi^{3/2} a^3 \left(1 + \frac{3\alpha}{2} - \frac{\alpha q^2 a^2}{4}\right) \exp\left(\frac{-q^2 a^2}{4}\right) \quad (5.25)$$

Values for parameters α and a are also given by De Jager, De Vries, and De Vries (1974).

Using equations (5.23) and (5.25) in equation (5.22) gives the matter density form factor $F_m(q)$. Taking the inverse transform of this $F_m(q)$ gives a ^{12}C harmonic well matter density

$$\rho_m(r) = \left(\frac{\rho_0 a^3}{8s^3}\right) \left(1 + \frac{3\alpha}{2} - \frac{3\alpha a^2}{8s^2} + \frac{\alpha a^2 r^2}{16s^4}\right) \exp\left(\frac{-r^2}{4s^2}\right) \quad (5.26)$$

with

$$s^2 = \frac{a^2}{4} - \frac{r_p^2}{6} \quad (5.27)$$

These density results are displayed in figures 5.1 through 5.3.

5.2.4. Results. Abrasion cross sections for ^{20}Ne - ^{12}C collisions at 2.1 GeV/nucleon obtained from equation (5.15) are given in table 5.1. Also listed are predicted cross sections when the Pauli correlation effects are ignored. From these results, the correlation effects have little or no effect on the abrasion cross sections for $n \leq 12$ because peripheral processes are the greatest contributors to

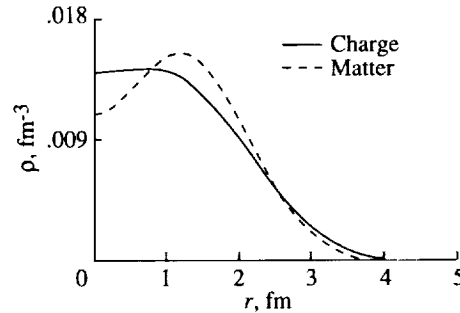


Figure 5.1. Harmonic well charge and matter density distributions for ^{12}C .

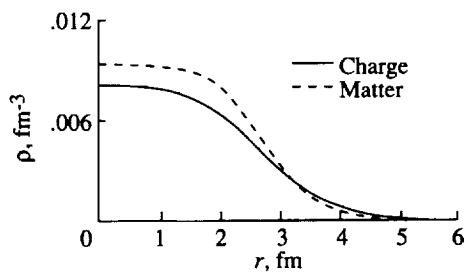


Figure 5.2. Woods-Saxon charge and matter density distribution for ^{20}Ne .

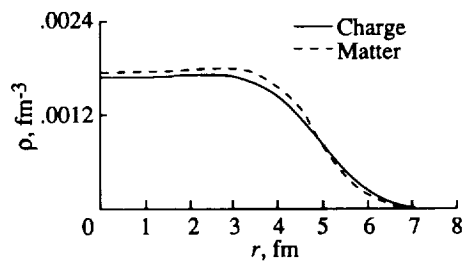


Figure 5.3. Three-parameter Gaussian charge and matter density distributions for ^{96}Mo .

Table 5.1. Optical Model Abrasion Cross Sections for ^{20}Ne - ^{12}C Collisions at 2.1 GeV/Nucleon

n	σ_n, mb	
	Pauli correlations	No Pauli correlations
1	248	248
2	134	134
3	95	95
4	76	75
5	64	64
6	57	56
7	52	51
8	48	48
9	45	45
10	43	43
11	42	42
12	40	42
13	38	42
14	33	41
15	27	39
16	18	33
17	10	25
18	4	14
19	1	6
20	0.1	1

these abrasions. As n increases, greater overlap between the colliding nuclear volumes is required, and the importance of correlation effects increases. They are most important when there is complete overlap between the colliding volumes ($n = 20$). On the other hand, summing the abrasion cross sections to give a total absorption cross section demonstrates that correlation effects only reduce σ_{abs} by ≈ 6 percent (1076 mb versus 1144 mb) for this collision. These abrasion results are also displayed in figure 5.4 with the recent experimental results of Stevenson, Martinis, and Price (1981). Because the experimental results are given in relative probabilities (RP) rather than cross sections, theoretical relative probabilities were calculated from

$$\text{RP} = \frac{\sigma_n}{\sigma_{\text{abs}} - 0.5\sigma_1} \quad (5.28)$$

where the denominator correction $0.5\sigma_1$ accounts for the missing ^{19}Ne fragments that were discriminated out experimentally as discussed by Stevenson, Martinis, and Price (1981). Additionally, for $n = 1$, the relative probabilities were determined by setting the numerator in equation (5.28) equal to $0.5\sigma_1$ to again account for the missing ^{19}Ne fragments. Finally, the theoretical RP, which are discrete numbers, were folded with the finite detector resolution ($\sigma \approx 1.5$ amu) to yield the displayed curves. As shown, the agreement between theory and experiment when correlation effects are included is excellent. The slight disagreement for small residual fragment masses may be caused by the approximations used in the correlation function.

To test the sensitivity of the abrasion results to the shape of the nuclear density distributions, relative probabilities were determined for the Ne + C collision by using a Woods-Saxon density for the neon projectile and two different distributions for the carbon target: a Woods-Saxon and a harmonic well. Correlation effects were not included. The superiority of the more exact harmonic well density is obvious in figure 5.5, where the theoretical predictions and the experimental results are presented.

Table 5.2 lists abrasion cross sections for $^{20}\text{Ne}-^{96}\text{Mo}$ collisions, at 2.1 GeV/nucleon, obtained from equation (5.15). Pauli correlation effects are included in the results. The relative probabilities, obtained from equation (5.28), are plotted in figure 5.6 with the experimental results of Stevenson, Martinis, and Price (1981). The agreement between theory and experiment for this collision pair is good but not as good as was obtained in the Ne-C collision. The discrepancy may be caused by inaccuracies in the correlation function approximation and/or the ^{96}Mo matter density distribution approximation because the theoretical RP clearly overshoot the experimental values for small residual mass fragments ($A_F < 6$).

5.3. Simple Ablation Model

The quantum mechanical abrasion model using the optical model approximation was so successful that further development (Townsend et al., 1984) seems warranted. The obvious starting point is to use a simple compound nuclear evaporation decay model. Such calculations require specification of the initial compound nuclear state defined by the mass, charge, and excitation energy.

Table 5.2. Optical Model Abrasion Cross Sections
for ^{20}Ne - ^{96}Mo Collisions at 2.1 GeV/Nucleon

n	σ_n , mb
1	380
2	207
3	148
4	119
5	101
6	90
7	82
8	77
9	73
10	71
11	70
12	71
13	72
14	75
15	81
16	90
17	105
18	135
19	201
20	294

5.3.1. Prefragment charge distributions. Since the abraded nucleons consist of protons and neutrons, which are not identical, a prescription for calculating the charge dispersions of the prefragments is needed to calculate final, isotope, and/or elemental production cross sections caused by the fragmentation process. Two such methods are used in the fragmentation theory described in this work. The method of Oliveira, Donangelo, and Rasmussen (1979) treats the neutron and proton distributions as completely uncorrelated. The cross section for forming a particular prefragment of mass A_j and charge Z_j is then given in terms of the

$$\sigma_{\text{abr}}(Z_j, A_j) = \frac{\binom{N}{n} \binom{Z}{z}}{\binom{A_P}{m}} \sigma_m \quad (5.29)$$

where z out of the original Z projectile nucleus protons is abraded along with n out of the original N projectile neutrons. Note that

$$A_P = N + Z \quad (5.30)$$

and

$$m = n + z \quad (5.31)$$

with

$$Z_j = Z - z \quad (5.32)$$

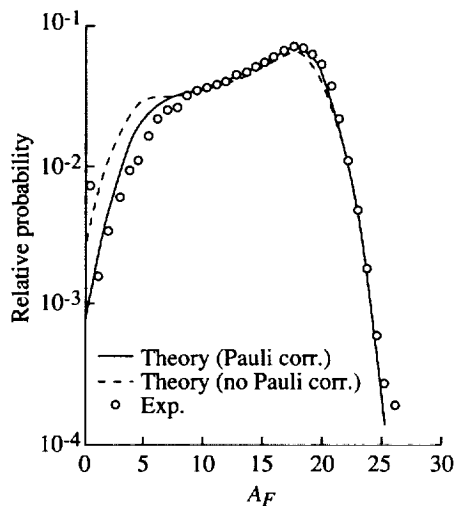


Figure 5.4. Ne-C abrasion results. Experimental results are from Stevenson, Martinis, and Price (1981).

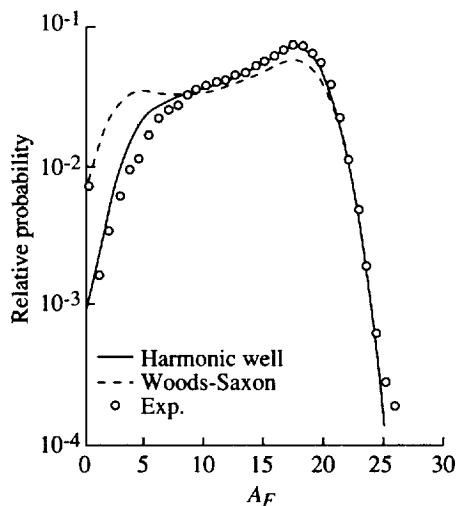


Figure 5.5. Theoretical Ne-C abrasion predictions. Experimental results are from Stevenson, Martinis, and Price (1981).

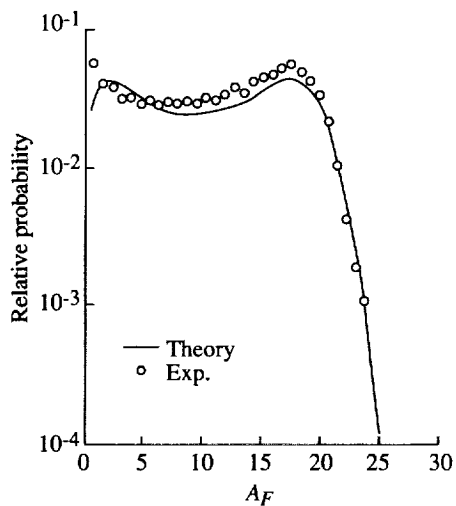


Figure 5.6. Ne-Mo abrasion results. Experimental results are from Stevenson, Martinis, and Price (1981).

and

$$A_j = A_P - m \quad (5.33)$$

This hypergeometric distribution is based on the assumption that there is no correlation at all between neutron and proton distributions. Therefore, unphysical results such as abrading all neutrons or protons from a nucleus while leaving the remaining fragment intact could occur.

As an alternative to the hypergeometric distribution, Morrissey et al. (1978) proposed a charge dispersion model based upon the zero-point vibrations of the giant dipole resonance of the projectile nucleus. In this model, equation (5.29) becomes

$$\sigma_{\text{abr}}(Z_j, A_j) = N_j (2\pi\alpha_Z^2)^{-1/2} \exp \left\{ \frac{-(Z_j - A_j(Z/A_P))^2}{2\alpha_Z^2} \right\} \sigma_m \quad (5.34)$$

where the variance (dispersion) is

$$\alpha_Z = 2.619 \left(\frac{u}{A_P} \right)^{1/2} \frac{Z}{A_P} \frac{dm}{db} (1+u)^{-3/4} \quad (5.35)$$

with

$$u = \frac{3J}{Q(A_P)^{1/3}} \quad (5.36)$$

In the droplet model of the nucleus, the coefficients J and Q have the nominal values of 25.76 and 11.9 MeV, respectively. The rate of change of the number of nucleons removed as a function of impact parameter (dm/db) is calculated numerically by using the geometric abrasion model of Bowman, Swiatecki, and Tsang (1973). The normalization factor N_j ensures that a given value of A_j , the discrete sum over all allowed values of Z_j , yields unity for the dispersion probabilities. This overall normalization is a new feature of this work and is not included in the original model of Morrissey et al. (1978).

5.3.2. Prefragment excitation energies. The excitation energy of the projectile prefragment following abrasion of m nucleons is calculated from the clean-cut abrasion formalism of Bowman, Swiatecki, and Tsang (1973) and Gosset et al. (1977). For this model, the colliding nuclei are assumed to be uniform spheres of radii R_i ($i = P, T$). In collision, the overlapping volumes shear off so that the resultant projectile prefragment is a sphere with a cylindrical hole gouged out of it. The excitation energy is then determined by calculating the difference in surface area between the misshapen sphere and a perfect sphere of equal volume. This excess surface area Δ is given by Gosset et al. (1977) as

$$\Delta = 4\pi R_P^2 \left[1 + P - (1 - F)^{2/3} \right] \quad (5.37)$$

where the expressions for P and F differ, depending upon the nature of the collision (peripheral versus central) and the relative sizes of the colliding nuclei.

For the case where $R_T > R_P$, we have

$$P = 0.125(\mu\nu)^{1/2} \left(\frac{1}{\mu} - 2 \right) \left(\frac{1-\beta}{\nu} \right)^2 - 0.125 \left[0.5(\mu\nu)^{1/2} \left(\frac{1}{\mu} - 2 \right) + 1 \right] \left(\frac{1-\beta}{\nu} \right)^3 \quad (5.38)$$

and

$$F = 0.75(1-\nu)^{1/2} \left(\frac{1-\beta}{\nu} \right)^2 - 0.125 \left[3(1-\nu)^{1/2} - 1 \right] \left(\frac{1-\beta}{\nu} \right)^3 \quad (5.39)$$

with

$$\nu = \frac{R_P}{R_P + R_T} \quad (5.40)$$

$$\beta = \frac{b}{R_P + R_T} \quad (5.41)$$

and

$$\mu = \frac{1}{\nu} - 1 = \frac{R_T}{R_P} \quad (5.42)$$

Equations (5.38) and (5.39) are valid when the collision is peripheral (i.e., the two nuclear volumes do not completely overlap). In this case, the impact parameter b is restricted such that

$$R_T - R_P \leq b \leq R_T + R_P \quad (5.43)$$

If the collision is central, then the projectile nucleus volume completely overlaps the target nucleus volume ($b < R_T - R_P$), and all the projectile nucleons are abraded. In this case, equations (5.38) and (5.39) are replaced by

$$P = -1 \quad (5.44)$$

and

$$F = 1 \quad (5.45)$$

and there is no ablation of the projectile because it was destroyed by the abrasion.

For the case where $R_P > R_T$ and the collision is peripheral, equations (5.38) and (5.39) become (Morrissey et al., 1978)

$$P = 0.125(\mu\nu)^{1/2} \left(\frac{1}{\mu} - 2 \right) \left(\frac{1-\beta}{\nu} \right)^2 - 0.125 \left\{ 0.5 \left(\frac{\nu}{\mu} \right)^{1/2} \left(\frac{1}{\mu} - 2 \right) - \frac{[(1/\nu)(1-\mu^2)^{1/2} - 1][(2-\mu)\mu]^{1/2}}{\mu^3} \right\} \left(\frac{1-\beta}{\nu} \right)^3 \quad (5.46)$$

and

$$F = 0.75(1 - \nu)^{1/2} \left(\frac{1 - \beta}{\nu} \right)^2 - 0.125 \left\{ \frac{3(1 - \nu)^{1/2}}{\mu} - \frac{[1 - (1 - \mu^2)^{3/2}][1 - (1 - \mu)^2]^{1/2}}{\mu^3} \right\} \left(\frac{1 - \beta}{\nu} \right)^3 \quad (5.47)$$

where the impact parameter is restricted such that

$$R_P - R_T \leq b \leq R_P + R_T \quad (5.48)$$

For a central collision ($b < R_P - R_T$) with $R_P > R_T$, equations (5.46) and (5.47) become

$$P = \left[\frac{1}{\nu}(1 - \mu^2)^{1/2} - 1 \right] \left[1 - \left(\frac{\beta}{\nu} \right)^2 \right]^{1/2} \quad (5.49)$$

and

$$F = [1 - (1 - \mu^2)^{3/2}] \left[1 - \left(\frac{\beta}{\nu} \right)^2 \right]^{1/2} \quad (5.50)$$

For the excess surface area obtained from equation (5.37), the excitation energy is given by

$$E_{\text{exc}} = \Delta E_s \quad (5.51)$$

where E_s , the nuclear surface energy coefficient (Bowman, Swiatecki, and Tsang, 1973; Gosset et al., 1977) obtained from the liquid drop model of the nucleus, is 0.95 MeV/fm².

5.3.3. Ablation factors (EVAP-4). Depending upon the excitation energy, the excited prefragment may decay by emitting one or more nucleons (protons or neutrons), composites (deuterons, tritons, ³He, or α -particles), or gamma rays. The probability α_{ij} for formation of a particular final fragment of type i as a result of the de-excitation of a prefragment of type j is obtained from the EVAP-4 computer code (Guthrie, 1970) by treating the prefragment as a compound nucleus with an excitation energy given by equation (5.51). The final fragmentation cross section for projectile of the type i isotope is then given by

$$\sigma_F(Z_i, A_i) = \sum_j \alpha_{ij} \sigma_{\text{abr}}(Z_j, A_j) \quad (5.52)$$

where $\sigma_{\text{abr}}(Z_j, A_j)$ is obtained from equation (5.29) or equation (5.34). The elemental production cross sections are obtained by summing over all isotope contributions as

$$\sigma_F(Z) = \sum_A \sigma_F(Z, A) \quad (5.53)$$

5.3.4. Fragmentation results. As an illustrative application of the theory, element production cross sections for fragments of calcium ($Z = 20$) and heavier

Table 5.3. Elemental Production Cross Sections for
 Reaction $^{56}\text{Fe} + ^{12}\text{C} \rightarrow Z + X$
 [Incident kinetic energy, 1.88 GeV/nucleon]

Element produced	Elemental production cross sections, mb		
	Hypergeometric	Giant dipole resonance	Westfall et al., 1979
Fe	161	209	
Mn	321	308	181 ± 27
Cr	156	142	124 ± 13
V	126	124	100 ± 11
Ti	90	88	87 ± 11
Sc	69	69	54 ± 9
Ca	77	78	78 ± 11

Table 5.4. Elemental Production Cross Sections for
 Reaction $^{56}\text{Fe} + ^{108}\text{Ag} \rightarrow Z + X$
 [Incident kinetic energy, 1.88 GeV/nucleon]

Element produced	Elemental production cross sections, mb		
	Hypergeometric	Giant dipole resonance	Westfall et al., 1979
Fe	296	262	
Mn	381	446	280 ± 23
Cr	226	230	218 ± 21
V	150	149	117 ± 15
Ti	126	128	124 ± 15
Sc	101	100	104 ± 13
Ca	102	112	118 ± 14

elements were calculated for ^{56}Fe projectiles at an incident kinetic energy of 1.88 GeV/nucleon and collided with stationary target nuclei of ^{12}C , ^{108}Ag , and ^{208}Pb . These reactions were chosen for analysis because of the availability of experimental data for comparison purposes (Westfall et al., 1979) and because relativistic ^{56}Fe nuclei are among the dominant high charge and energy (HZE) particles of radiobiological significance for manned spaceflight.

Tables 5.3 through 5.5 display the elemental production cross sections obtained for carbon, silver, and lead targets by using both the hypergeometric (eq. (5.29)) and giant dipole resonance (eq. (5.34)) dispersion expressions. Also displayed are the experimental results of Westfall et al. (1979). Except for the cross section

for Mn production (carbon and silver targets) and V production (silver and lead targets), the agreement between theory and experiment is quite good. When compared with the predictions obtained with the hypergeometric distribution assumption of equation (5.29), the use of the giant dipole resonance expression for charge dispersion (eq. (5.34)) appears to yield slightly improved overall agreement between theory and experiment.

Figures 5.7 through 5.9 display the elemental production cross sections obtained from equation (5.34), for the giant dipole resonance dispersion (GDR) along with the experimental data from Westfall et al. (1979). Also displayed, for comparison, are the predictions from the semiempirical relations of Silberberg, Tsao, and Shapiro (1976). For the semiempirical relations, the unmodified predictions are displayed. Also displayed are the fragmentation cross sections obtained by renormalizing to ensure mass and charge conservation. Details of the renormalization can be found in Wilson et al. (1984). For the carbon target (Bevington, 1969), χ^2 for the giant dipole resonance predictions is 31.6, which is larger than the 19.4 obtained using the Silberberg-Tsao (ST) methods. For the GDR, most of the χ^2 comes from the Mn overestimate. If that point is excluded, χ^2 is reduced from 31.6 to 9.4. The comparative results for Ca, Sc, Ti, V, and Cr are in better agreement with the experiment for the silver target; the χ^2 for GDR is 57.3 (5.2 if the Mn datum is excluded), whereas the χ^2 for ST is 32.4 (9.5 if the Mn datum is excluded). For the lead target, the χ^2 for GDR is 4.4 (1.9 if the V datum is excluded), compared with the χ^2 for ST of 52.4 (2.3 if the Mn underestimate is excluded). In general, the overall agreement between theory and experiment for the abrasion-ablation model is satisfactory when considering its simple nature.

To illustrate further the results of the model, cross sections for the production of sulfur, phosphorous, silicon, and aluminum isotopes caused by the fragmentation of ^{40}Ar projectiles at 213 MeV/nucleon by carbon targets are shown in figure 5.10. These theoretical predictions were obtained with the hypergeometric distribution.

Also shown are the experimental data from Viyogi et al. (1979). In general, the agreement is surprisingly good, considering the simple nature of the calculations. Partial production cross sections for these same isotopes were also calculated with the GDR distribution. In general, those cross sections were less accurate when compared with the experiment than the ones obtained from the hypergeometric distribution. Typical results are shown as dashed lines in figure 5.10 for the sulfur and silicon isotopes.

In previous heavy ion transport work (Wilson, 1983; Wilson et al., 1984), the improved agreement between theory and experiment for Bragg (depth-dose) curves was obtained by using ST fragmentation parameters modified to scale by velocity (rather than total kinetic energy) and renormalized to conserve fragment charge and mass. As shown in figures 5.7 through 5.9, the modifications (labeled VR) do improve the ST predictions for the predominant, near-projectile mass fragments (in this case, Mn) but yield substantial overestimates for the fragmentation cross sections for the lighter mass fragments. Simple corrections to the ST parameters,

Table 5.5. Elemental Production Cross Sections for
Reaction $^{56}\text{Fe} + ^{208}\text{Pb} \rightarrow Z + X$

[Incident kinetic energy, 1.88 GeV/nucleon]

Element produced	Elemental production cross sections, mb		
	Hypergeometric	Giant dipole resonance	Westfall et al., 1979
Fe	345	302	
Mn	445	521	509 ± 40
Cr	267	268	242 ± 25
V	175	174	142 ± 20
Ti	152	151	148 ± 22
Sc	121	119	111 ± 17
Ca	116	129	144 ± 22

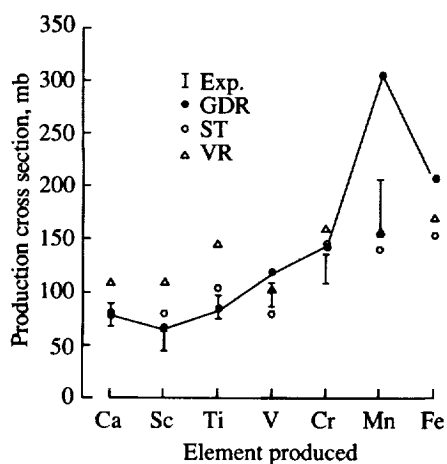


Figure 5.7. Elemental production cross sections for iron projectile nuclei fragmenting in carbon targets.

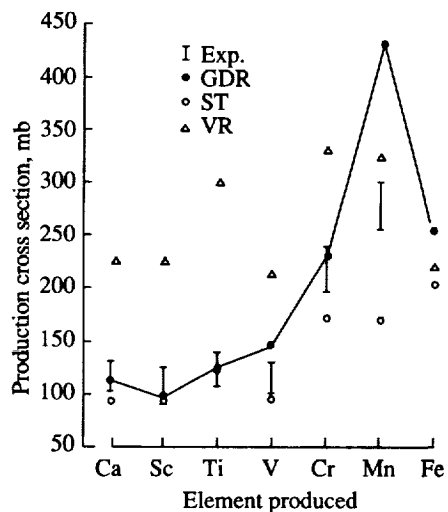


Figure 5.8. Elemental production cross sections for iron projectile nuclei fragmenting in silver targets.

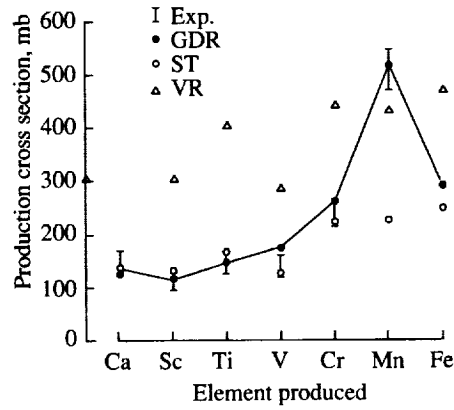


Figure 5.9. Elemental production cross sections for iron projectile nuclei fragmenting in lead targets.

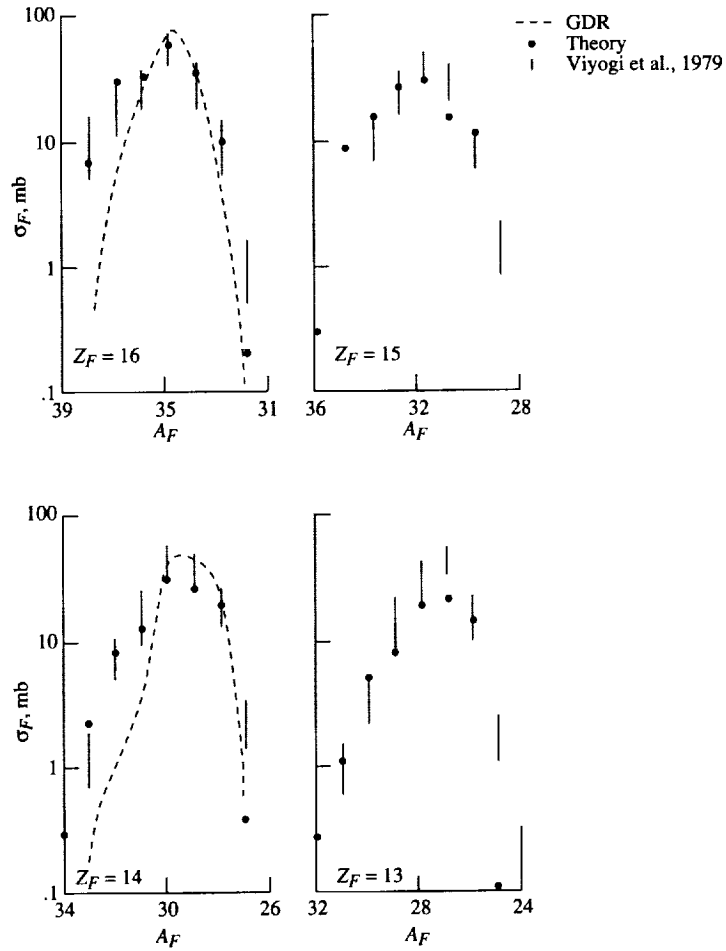


Figure 5.10. Production cross sections for isotopes of sulfur, phosphorous, silicon, and aluminum produced by the fragmentations of ^{40}Ar projectiles at 213 MeV/nucleon in carbon targets.

such as renormalization, are apparently adequate for gross total-dose comparisons (Wilson et al., 1984). However, only certain fragments may be biologically significant. Therefore, these corrections may be inadequate for the more pertinent shielding problems such as the accurate predictions of individual fragment species production. Clearly, the need remains for a comprehensive and accurate HZE particle fragmentation theory, of which the work just described is a beginning.

Improvements to this simple abrasion-ablation model should center on extending the GDR charge dispersion method to incorporate the actual quantum mechanical abrasion formalism rather than using the geometric model approximation of Bowman, Swiatecki, and Tsang (1973). Improved methods for estimating the prefragment excitation energy spectrum should also be developed (Khan, 1989). Finally, an alternative to the EVAP-4 ablation code should be tried, such as an intranuclear cascade code (Morrissett et al., 1979); or the development of other methods to describe the ablation step should be undertaken (Townsend et al., 1986a and 1986b; Cucinotta et al., 1987).

5.4. Abrasion Dynamics

One possible limitation of the abrasion-ablation model described in sections 5.2 and 5.3 is the use of the geometric model in estimating the prefragment excitation energies. We now look at an alternative method (Khan, 1989) of estimating the prefragment system parameters closely related to the work of Fricke (1985).

5.4.1. Method of calculation. The coupled-channel Schrödinger equation for composite particle scattering, which relates the entrance channel to all the excited states of the target and projectile, was derived by assuming large, incident projectile kinetic energies and closure of the accessible eigenstates (Wilson, 1975 and chapter 3). The equation is written as

$$(\nabla^2 + k^2) \psi_{n\mu}(\vec{x}) = 2m A_P A_T (A_P + A_T)^{-1} \sum_{n'\mu'} V_{n\mu, n'\mu'}(\vec{x}) \psi_{n'\mu'}(\vec{x}) \quad (5.54)$$

where the subscripts n and μ (with and without primes) label the projectile and target eigenstates; m is the nucleon mass; A_P and A_T are the mass numbers of the projectile and target; \vec{k} is the incident projectile momentum relative to the center of mass; and \vec{x} is the projectile position vector relative to the target. As for the nucleon-nucleon scattering t -matrix $t_{\alpha j}$ and the internal state vectors of the projectile $g_n^P(\vec{\xi}_P)$ and target $g_\mu^T(\vec{\xi}_T)$, the potential matrix can be expressed as

$$V_{n\mu, n'\mu'}(\vec{x}) = \left\langle g_n^P, g_\mu^T \left| V_{\text{opt}}(\vec{\xi}_P, \vec{\xi}_T, \vec{x}) \right| g_{n'}^P, g_{\mu'}^T \right\rangle \quad (5.55)$$

where

$$V_{\text{opt}}(\vec{\xi}_P, \vec{\xi}_T, \vec{x}) = \sum_{\alpha j} t_{\alpha j} \quad (5.56)$$

This same formalism can be used to investigate relativistic heavy ion collision momentum transfers. Within the context of eikonal scattering, the solution to the

Schrödinger equation

$$H \psi(\vec{x}, \vec{\xi}_P, \vec{\xi}_T) = E \psi(\vec{x}, \vec{\xi}_P, \vec{\xi}_T) \quad (5.57)$$

at high energies is

$$\begin{aligned} \psi(\vec{x}, \vec{\xi}_P, \vec{\xi}_T) &= (2\pi)^{-3/2} \exp\left[-\frac{i}{v} \int_{-\infty}^z V_{\text{opt}}(\vec{x}, \vec{\xi}_P, \vec{\xi}_T) dz'\right] \\ &\times g_n^P(\vec{\xi}_P) g_\mu^T(\vec{\xi}_T) \exp(i\vec{k} \cdot \vec{x}) \end{aligned} \quad (5.58)$$

where v is the velocity. The total momentum of the projectile is then given by the matrix element involving the sum of the projectile single-nucleon momentum operators as

$$\vec{P}_{\text{tot}} = \left\langle \psi \left| -i \sum_{\alpha=1}^{A_P} \vec{\nabla}_{P,\alpha} \right| \psi \right\rangle \quad (5.59)$$

where the subscript P on the gradient operator denotes that the gradient is to be taken with regard to the projectile internal coordinates $\vec{\xi}_P$. Equation (5.59) actually denotes a momentum matrix $\vec{P}_{n\mu, n'\mu'}$ in analogy with equation (5.55). Therefore, substituting equation (5.58) into equation (5.59) yields

$$\vec{P}_{n\mu, n'\mu'} = \left\langle g_n^P(\vec{\xi}_P) g_\mu^T(\vec{\xi}_T) \left| \exp(-iS) \left(-i \sum_{\alpha=1}^{A_P} \vec{\nabla}_{P,\alpha} \right) \exp(iS) \right| g_{n'}^P(\vec{\xi}_P) g_{\mu'}^T(\vec{\xi}_T) \right\rangle \quad (5.60)$$

where

$$S = \frac{1}{v} \int_{-\infty}^z V_{\text{opt}}(\vec{x}', \vec{\xi}_P, \vec{\xi}_T) dz' \quad (5.61)$$

With the chain rule for differentiation, equation (5.60) can be further expressed as

$$\vec{P}_{n\mu, n'\mu'} = \vec{P}_o + \left\langle g_n^P g_\mu^T \left| \left(-\sum_{\alpha}^{A_P} \vec{\nabla}_{P,\alpha} S \right) \right| g_{n'}^P g_{\mu'}^T \right\rangle \quad (5.62)$$

where the incident projectile momentum before the collision is

$$\vec{P}_o = \left\langle g_n^P g_\mu^T \left| \left(-i \sum_{\alpha=1}^{A_P} \vec{\nabla}_{P,\alpha} \right) \right| g_{n'}^P g_{\mu'}^T \right\rangle \quad (5.63)$$

The total momentum transfer to the projectile is then given by

$$\vec{Q}_{n\mu, n'\mu'} = \vec{P}_{n\mu, n'\mu'} - \vec{P}_o = \left\langle g_n^P g_\mu^T \left| \left(-\sum_{\alpha} \vec{\nabla}_{P,\alpha} S \right) \right| g_{n'}^P g_{\mu'}^T \right\rangle \quad (5.64)$$

For high-energy collisions, dominant scattering processes occur near the forward directions, because the momentum transferred is small when compared with the

incident momentum of the projectile; hence, couplings between excited states are small and can be neglected (Wilson 1975). The total momentum transfer to the projectile is then approximated by

$$\vec{Q} = \vec{Q}_{00,00} = \left\langle g_o^P g_o^T \left| \left(- \sum_{\alpha} \vec{\nabla}_{P,\alpha} S \right) \right| g_o^P g_o^T \right\rangle \quad (5.65)$$

In terms of projectile and target number densities and the constituent-averaged two-nucleon transition amplitude \bar{t} , equation (5.65) becomes

$$\begin{aligned} \vec{Q}(\vec{b}) = & -A_P A_T \int d^3 \vec{\xi}_P \rho_P(\vec{\xi}_P) \int d^3 \vec{\xi}_T \rho_T(\vec{\xi}_T) \\ & \times \left[\vec{\nabla}_P \int_{-\infty}^{\infty} \bar{t}(\vec{b} + \vec{z}' + \vec{\xi}_P - \vec{\xi}_T) \frac{dz'}{v} \right] \end{aligned} \quad (5.66)$$

where the integration limit in the longitudinal direction has been extended to infinity. The momentum transfer in equation (5.66) is therefore only a function of the impact parameter of the collision. The projectile and target number densities (ρ_P and ρ_T) are normalized to unity as

$$\int \rho(\vec{x}) d^3 \vec{x} = 1 \quad (5.67)$$

The constituent-averaged, two-nucleon transition amplitude is obtained from the impulsive, first-order t -matrix used in our previous studies (Wilson 1975; Wilson and Townsend, 1981; Townsend, 1981 and 1982; Townsend et al., 1986a and 1986b) of nucleus-nucleus collisions as

$$\bar{t}(e, \vec{x}) = - \left(\frac{e}{m} \right)^{1/2} \sigma(e) [\alpha(e) + i] [2\pi B(e)]^{-3/2} \exp \left[\frac{-x^2}{2B(e)} \right] \quad (5.68)$$

where e is the two-nucleon kinetic energy in its center-of-mass frame, $\sigma(e)$ is the nucleon-nucleon total cross section, $\alpha(e)$ is the ratio of the real-to-imaginary part of the forward-scattering amplitude, and $B(e)$ is the nucleon-nucleon slope parameter. Values for these parameters taken from various compilations are given in Wilson and Townsend (1981) and Townsend (1982).

The dynamic momentum transfer to the projectile, given by equation (5.66), results from interactions with the target. Note that it is a complex quantity that is consistent with the use of a complex optical potential (Rodberg and Thaler, 1967). The real part of the momentum transfer, which comes from the real part of the complex optical potential, is the contribution arising from elastic scattering. It is purely transverse. The imaginary component, which comes from the absorptive part of the complex optical potential, arises mainly from absorption and inelastic scattering processes. At high energies, the latter are mainly breakup (fragmentation) reactions because these account for over 95 percent of the total reaction cross section. Physically, this imaginary component represents attenuation of the incident wave front in analogy with the usual discussions for a complex index of refraction in an absorptive medium (Rodberg and Thaler,

1967). Concomitant with this attenuation of the incident wave by these absorptive processes, there is a loss of momentum from the wave front in the beam direction. This longitudinal momentum transfer (loss) is interpreted as arising from the imaginary component of \vec{Q} . From equation (5.66), the transverse component is

$$Q_{\perp} = -A_P A_T \int d^3 \vec{\xi}_P \rho_P(\vec{\xi}_P) \int d^3 \vec{\xi}_T \rho_T(\vec{\xi}_T) \times \vec{\nabla}_P \int_{-\infty}^{\infty} \text{Re} \left[i(\vec{b} + \vec{z}' + \vec{\xi}_P - \vec{\xi}_T) \right] \frac{dz'}{v} \quad (5.69)$$

and the longitudinal component is

$$Q_{\parallel} = -A_P A_T \int d^3 \vec{\xi}_P \rho_P(\vec{\xi}_P) \int d^3 \vec{\xi}_T \rho_T(\vec{\xi}_T) \times \left\{ \vec{\nabla}_P \int_{-\infty}^{\infty} \text{Im} \left[i(\vec{b} + \vec{z}' + \vec{\xi}_P - \vec{\xi}_T) \right] \frac{dz'}{v} \right\} \quad (5.70)$$

Calculated momentum transfers obtained with equations (5.69) and (5.70) are displayed in figure 5.11 for ^{16}O at 2.1 GeV/nucleon colliding with a beryllium target. These calculations use the harmonic well nuclear densities from our previous work (Townsend, 1982 and 1983; Townsend et al., 1984). From the figure, two features are readily apparent. First, the longitudinal momentum transfer is larger than the transverse; this indicates the primarily absorptive nature of the nuclear collision at this energy. Second, the predicted momentum transfer decreases rapidly with increasing impact parameter. This decrease is discussed further in sections 5.4.3 and 5.4.4, but its occurrence is not surprising because the nuclear optical potential decreases rapidly with increasing separation of the colliding nuclei.

5.4.2. Results. The collisional momentum transfers computed with the model described in section 5.4.1 can be related to experimentally measured, heavy ion fragment momentum downshifts/widths through considerations of energy and momentum conservation. As has been formulated by Goldhaber (1974) and Wong (1981), a momentum transfer in any direction Q_j modifies the width h_j of the fragment momentum distribution in that direction by

$$(h'_j)^2 = h_j^2 + \frac{F^2 Q_j^2}{A^2} \quad (5.71)$$

and the mean by

$$\vec{P}'_j = \vec{P}_j + \frac{F}{A} \vec{Q}_j \quad (5.72)$$

From equation (5.72), the longitudinal momentum downshift is given by

$$\Delta P_{\parallel} = P'_{\parallel} - P_{\parallel} = \frac{F}{A} Q_{\parallel}, \quad (5.73)$$

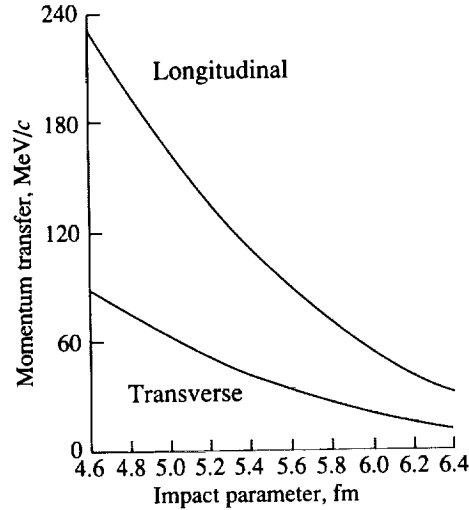


Figure 5.11. Momentum transfer to ^{16}O projectile as function of impact parameter for oxygen colliding with beryllium target at 2.1 GeV/nucleon.

where Q_{\parallel} is the magnitude of the longitudinal momentum transfer (obtained from eq. (5.70)), F is the fragment mass number, and A is the initial mass number of the fragmenting nucleus. Recalling that Q_{\parallel} is a function of impact parameter, an appropriate method for choosing the impact parameter for each fragmentation channel is necessary. Recently, a semiempirical abrasion-ablation fragmentation model (NUCFRAG) was proposed by Wilson, Townsend, and Badavi (1987b). Although it assumes simple uniform density distributions for the colliding ions and a zero-range (delta function) interaction, it does include frictional spectator interactions (FSI) and agrees with experimental cross-section data to the extent that they agree among themselves. Also, and most importantly for this work, it is easily modified to yield impact parameters for each fragmentation channel. Hence, the procedure for evaluation of equations (5.71) and (5.73) is to extract impact parameters from NUCFRAG for each nucleon removal corresponding exactly to $\Delta A = 1, 2, 3, \dots$. These most probable impact parameters are then inserted in equations (5.69) and (5.70) to obtain the corresponding momentum transfers for use in evaluating equations (5.71) and (5.73) because NUCFRAG uses uniform densities; uniform densities are also used in evaluating equations (5.69) and (5.70). In addition, the zero-range interaction in NUCFRAG is simulated for numerical integration purposes in equations (5.69) and (5.70) through the use of a very narrow Gaussian form for the t -matrix given by equation (5.68). This narrow Gaussian is the same width for all collision pairs and therefore is not an arbitrarily adjusted parameter. We have checked the validity of using the “most probable” impact parameter in the calculations by actually computing the momentum transfers averaged over a range of impact parameters from NUCFRAG corresponding to $\Delta A - 0.5$ to $\Delta A + 0.5$. The differences between the estimates using averaged and most probable values are negligible (Khan, 1989).

Representative calculations for momentum downshifts as a function of fragment mass number are displayed in figure 5.12 for ^{16}O projectiles colliding with

targets of Be, C, Al, Cu, Ag, and Pb at 2.1 GeV/nucleon. These momentum downshifts are target averaged by using simple arithmetic averaging. For comparison, the target-averaged experimental data of Greiner et al. (1975) are also displayed. For display and comparison purposes, the theory is also averaged over all isotopes contributing to each fragment mass number using

$$(\Delta P_{\parallel})_{\text{av}} = \frac{\sum_i \sigma_i (\Delta P_{\parallel}^i)}{\sum_i \sigma_i} \quad (5.74)$$

where σ_i is the experimental production cross section for the i th fragment isotope. Reasonable agreement is obtained for the heavier fragments when comparing the theoretical estimates to the experimental data. When considering the simplified form of the nuclear fragmentation model used in these calculations and the overall sensitivity of the calculated momentum transfer to the choice of impact parameter, the agreement is rather good. Improved agreement is expected if impact parameters from a fragmentation model using realistic nuclear densities and interactions were used. This is especially true for collisions involving lighter ions, such as carbon, oxygen, and beryllium, which are poorly represented by simple uniform nuclear distributions.

Figure 5.13 displays transverse momentum widths as a function of fragment mass number for ^{139}La fragmenting in carbon targets at 1.2 GeV/nucleon. The experimental data are taken from Brady et al. (1988). Again, impact parameters from NUCFRAG are used as inputs into the momentum transfer expressions (eqs. (5.69) and (5.70)). For consistency with the use of these impact parameters, a narrow Gaussian t -matrix and uniform nuclear densities were again used in the momentum transfer calculations. From figure 5.13, the agreement is much better than in figure 5.12 and probably reflects that a uniform nuclear density distribution is a more reasonable approximation for a heavy nucleus like lanthanum than for light nuclei such as oxygen.

5.4.3. Estimating collision impact parameters. So far in this work, we have used collision impact parameters as inputs into a momentum transfer computational model, which in turn, has yielded estimates of heavy ion fragment momentum downshifts/widths for comparison with experimental data. However, this procedure can be reversed and the model used to estimate collision impact parameters from measured momentum downshifts for relativistic collisions. Let F be the fragment mass number with measured longitudinal momentum downshift ΔP_{\parallel} produced in a relativistic collision between a projectile nucleus (mass number A) and some target. Then, from equation (5.73), the longitudinal momentum transfer to the projectile from the target is

$$Q_{\parallel} = \frac{A}{F} \Delta P_{\parallel} \quad (5.75)$$

The collision impact parameter can then be estimated from equation (5.70) by computing Q_{\parallel} as a function of impact parameter (e.g., in fig. 5.11) and using Q_{\parallel} from equation (5.75) as the entry. To illustrate, consider a collision involving

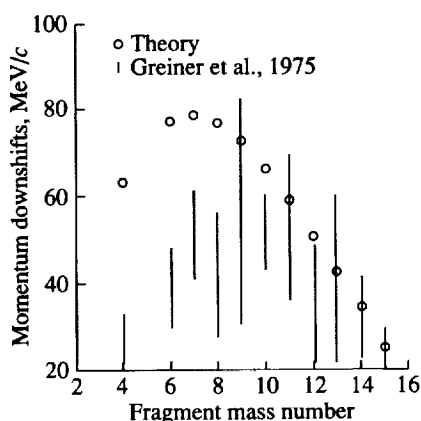


Figure 5.12. Target-averaged longitudinal momentum downshifts as function of projectile fragment mass number for ^{16}O colliding with Be, C, Al, Cu, Ag, and Pb targets at 2.1 GeV/nucleon.

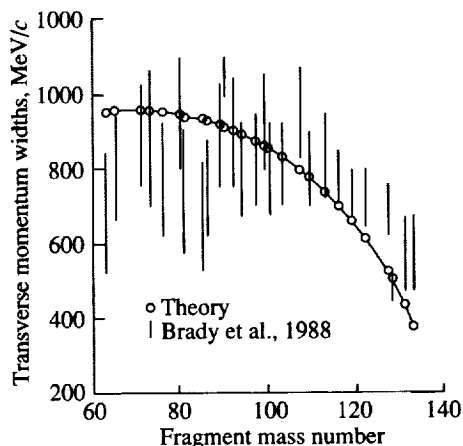


Figure 5.13. Transverse momentum widths as function of projectile fragment mass number for ^{139}La colliding with a carbon target at 1.2 GeV/nucleon.

oxygen colliding with a beryllium target at 2.1 GeV/nucleon. The calculated momentum transfer using realistic nuclear densities is displayed in figure 5.11. If the measured (hypothetical) momentum downshift for the ^{14}N fragment is 35 ± 7 MeV/c, then equation (5.75) yields a longitudinal momentum transfer of 40 ± 8 MeV/c. From figure 5.11, the corresponding range of impact parameters is 6.1–6.4 fm. A similar procedure incorporating measured momentum distribution widths and equations (5.71) and (5.69) or (5.70) could also be used to estimate collision impact parameters. These proposed methods for estimating collision impact parameters are similar in concept to the use of heavy fragment yields in the quantum molecular dynamics approach of Aichelin and collaborators (Aichelin et al., 1988).

5.4.4. Remarks. Beginning with composite particle multiple-scattering theory, an optical model description of collision momentum transfer in relativistic heavy ion collisions was derived. General expressions for transverse and longitudinal momentum transfers, which use a finite-range, two-nucleon interaction and realistic nuclear densities, were presented. The theory was used as input into the Goldhaber (1974) formalism to estimate heavy ion fragment momentum downshifts for relativistic oxygen and transverse momentum widths for relativistic lanthanum projectiles. The main new feature of this work was the interpretation of the imaginary component of the momentum transfer as the longitudinal collision momentum transfer. Finally, the use of the model as a mechanism for estimating collision impact parameters was described.

The present theory is mainly applicable at intermediate or high energies because of the use of eikonal wave functions and the impulse approximation. At lower energies (below several hundred MeV/nucleon), the validity of straight-line trajectories and the assumption of a constant projectile velocity are questionable. Therefore, revisions to the model are necessary to compare theory

with experiment at lower energies. In particular, deceleration corrections to the constant velocity assumption are being developed. For incident energies greater than 1 GeV/nucleon, first-order deceleration corrections are small (<1 percent). As the incident energy decreases, however, the first-order corrections increase significantly (over 50 percent) at 100 MeV/nucleon; this indicates that higher order terms must be included (Khan, 1989). Work on this is in progress.

In addition to the described work on abrasion-ablation models, Khan et al. (1988) have examined contributions of direct knockout and excitation decay contributions in ^{12}C fragmentation (Webb et al., 1987). The t -matrix formulation of Norbury, Townsend, and Deutchman (1985) has received additional analysis (Cucinotta et al., 1987) but requires more fundamental development.

5.5. Direct Reaction Processes

Reaction mechanisms discussed in sections 5.2 through 5.4 have dealt with the outcome for spectator constituents in the reaction. In this section we look at collision participants and the direct breakup and knockout of particles from the projectile or target nucleus including transitions to excited nuclear states. The calculations follow closely the work of Cucinotta (1988) and Cucinotta et al. (1988).

5.5.1. Exclusive inelastic scattering. The scattering amplitude matrix in the eikonal approximation is given by Wilson (1975) as

$$f(\vec{q}) = -\frac{ik}{2\pi} \int \exp(-i\vec{q} \cdot \vec{b}) \left\{ \exp[i\chi(\vec{b})] - 1 \right\} d^2b \quad (5.76)$$

where the eikonal phase shift matrix is related to the coupled-channel optical potential

$$\chi(\vec{b}) = \frac{-i}{2k} \int_{-\infty}^{\infty} \mathbf{U}(\vec{b}, z) dz \quad (5.77)$$

where \mathbf{U} is the optical potential relating all the states of the interacting systems. The elastic scattering amplitude is found to be (Cucinotta et al., 1988)

$$f_{\text{elas}}(\vec{q}) = \frac{-ik}{2\pi} \int \exp(-i\vec{q} \cdot \vec{b}) [\exp(i\chi_{\text{opt}}) \cos \Upsilon - 1] d^2b \quad (5.78)$$

where the inelastic amplitudes are

$$f_{00,n\mu}(q) = \frac{k}{2\pi} \int \exp(-i\vec{q} \cdot \vec{b}) \exp(i\chi_{\text{opt}}) \frac{\sin \Upsilon}{\Upsilon} \chi_{00,n\mu} d^2b \quad (5.79)$$

where

$$\Upsilon^2 = \sum_{(n,\mu) \neq (0,0)} \chi_{00,n\mu} \chi_{n\mu,00} \quad (5.80)$$

The usual coherent approximation and the DWBA (distorted-wave Born approximation) are found for $\Upsilon \rightarrow 0$ in equations (5.78) and (5.79), respectively.

The function Υ as given in equation (5.80) is directly related to the pair correlation function. This can be seen as follows (Cucinotta et al., 1988):

$$\begin{aligned} \Upsilon^2 &= \left(\frac{\mu_r}{2k}\right)^2 \left(\frac{1}{2\pi}\right)^4 \int d^2q d^2q' \exp(-i\vec{q} \cdot \vec{b}) \exp(-i\vec{q}' \cdot \vec{b}) \\ &\times \sum_{\mu \text{ or } n \neq 0}^{\infty} F_{0n}(\vec{q}) F_{0n}(\vec{q}') F_{0\mu}(-\vec{q}) F_{\mu 0}(-\vec{q}') \\ &\times t(\vec{q}) t(\vec{q}') \end{aligned} \quad (5.81)$$

From Kerman, McManus, and Thaler (1959), we have the following sum rule on the form factors

$$\begin{aligned} \sum_{n \neq 0}^{\infty} F_{0n}(\vec{q}) F_{n0}(\vec{q}') &= \frac{-1}{A} F_{00}(q) F_{00}(q') \\ &+ \frac{1}{A} F_{00}(\vec{q} + \vec{q}') + \left(1 - \frac{1}{A}\right) C_{00}(\vec{q}, \vec{q}') \end{aligned} \quad (5.82)$$

where A is the mass number of the nucleus in question, and $C_{00}(\vec{q}, \vec{q}')$ is the Fourier transform of the pair correlation function. Analytic models for $C_{00}(\vec{q}, \vec{q}')$ are under investigation. In section 5.5.3, we consider a numerical study of long-range correlations involving partial summation of the infinite sum that appears in equation (5.81) for ^{12}C .

Finally, the first- and second-order solutions to the eikonal coupled-channel scattering amplitudes were found by approximating the form of χ . We expect that higher order solutions, though more difficult, could be found by approximating the form of higher powers of χ .

5.5.2. Physical inputs. As a numerical study, we compare the first- and second-order eikonal coupled-channel solutions of p for ^{12}C and ^4He on ^{12}C scattering. The 2^+ at 4.65 MeV, 0^+ at 7.66 MeV, 3^- at 9.65 MeV, and 4^+ at 14.1 MeV excited states of ^{12}C are considered. An advantage of the bordered interaction matrix is that the eikonal phase matrix elements may be obtained through knowledge of form factors measured in electron scattering experiments, so that no excited-state wave function is needed as inputs. This would not be true for couplings between the off-diagonal elements. The charge form factors for the ground and first three excited states have been parameterized by Saudinos and Wilkin (1974) and Viollier (1975) in the form

$$F_{\text{charge}}(q) = Bq^m(1 - Cq^2) \exp(-dq^2) \quad (5.83)$$

where the parameters B, C, d , and m are listed in table 5.6. Table 5.6 also lists the form factor for excitation of the 4^+ state at 14.1 MeV of ^{12}C , which we have parameterized to the data of Nakada, Torizuka, and Horikawa (1971).

Table 5.6. Form Factors

(a) ^{12}C

$E, \text{ MeV}$	J^P	m	B	C	$d, \text{ fm}^{-2}$
0	0^+	0	1.0	0.296	0.7
4.43	2^+	2	0.24	0.13	0.57
7.65	0^+	2	0.167	0	0.99
9.67	3^-	3	0.134	0	0.77
14.1	4^+	4	0.00392	0	0.64

(b) ^4He

$$C_1 = 1.098$$

$$C_2 = 0.098$$

$$d_1 = 0.72$$

$$d_2 = 3.6$$

The matter form factors are obtained from the charge form factors in the following equation (Überall, 1971):

$$F_A(q) = \frac{F_{\text{charge}}(q)}{F_p(q)F_{cm}(q)} \quad (5.84)$$

where $F_p(q)$ is the proton charge form factor given by

$$F_p(q) = \exp\left(\frac{-r_p^2 q^2}{6}\right) \quad (5.85)$$

where $r_p = 0.87 \text{ fm}$, and $F_{cm}(q)$ is a center-of-mass correction of the form

$$F_{cm}(q) = \exp\left(\frac{q^2 a_0^2}{4A}\right) \quad (5.86)$$

with

$$a_0^2 = \frac{\langle r^2 \rangle - r_p^2}{\frac{Z-2}{Z} + \frac{3(A-1)}{2A}} \quad (5.87)$$

where $\langle r^2 \rangle$ is the root-mean-square radius of the nucleus. For the ground state of ^4He , we use the parameterization of Auger, Gillespie, and Lombard (1976),

$$F_{4\text{He}} = C_1 \exp(-d_1 q^2) - C_2 \exp(-d_2 q^2) \quad (5.88)$$

where C_1, C_2, d_1 , and d_2 are listed in table 5.6.

The two-body amplitude is assumed to contain only a central piece of the usual form

$$t(\bar{q}) = -\sqrt{\frac{e}{m}} \sigma(e) [\alpha(e) + i] \exp\left(-\frac{1}{2} B(e) q^2\right) \quad (5.89)$$

Table 5.7. Two-Body Amplitude Parameters
 [Isospin-averaged parameters of Ray (1979)]

$T_{\text{lab}}, \text{MeV}$	$B(e), \text{fm}^2$	$\sigma(e), \text{fm}^2$	$\alpha(e)$
340	0.62	3.03	0.28
800	0.20	4.3	-0.056
1000	0.21	4.3	-0.26

where the energy-dependent parameters $\sigma(e)$, $\alpha(e)$, and $B(e)$ are taken from Ray (1979) and given in table 5.7. The Gaussian forms for the form factors and two-body amplitude assumed in the calculations allow us to obtain analytic solutions for all eikonal phase matrix elements needed as inputs for our calculations.

5.5.3. Results and discussion. The first- and second-order scattering solutions and experimental data (Blanpied et al., 1981; Bertini et al., 1973; Chaumeaux et al., 1976) for elastic and inelastic scattering of p on ^{12}C at 800 MeV and 1000 MeV and for ^4He on ^{12}C at 340 MeV/nucleon are shown in figures 5.14 through 5.24. For p - ^{12}C elastic scattering (figs. 5.14 and 5.18), the coherent approximation (dashed line, first-order) and bordered matrix (solid line, second-order) results are nearly the same in the region of the forward peak where single scattering dominates. This was implied by Wilson (1975) on theoretical arguments

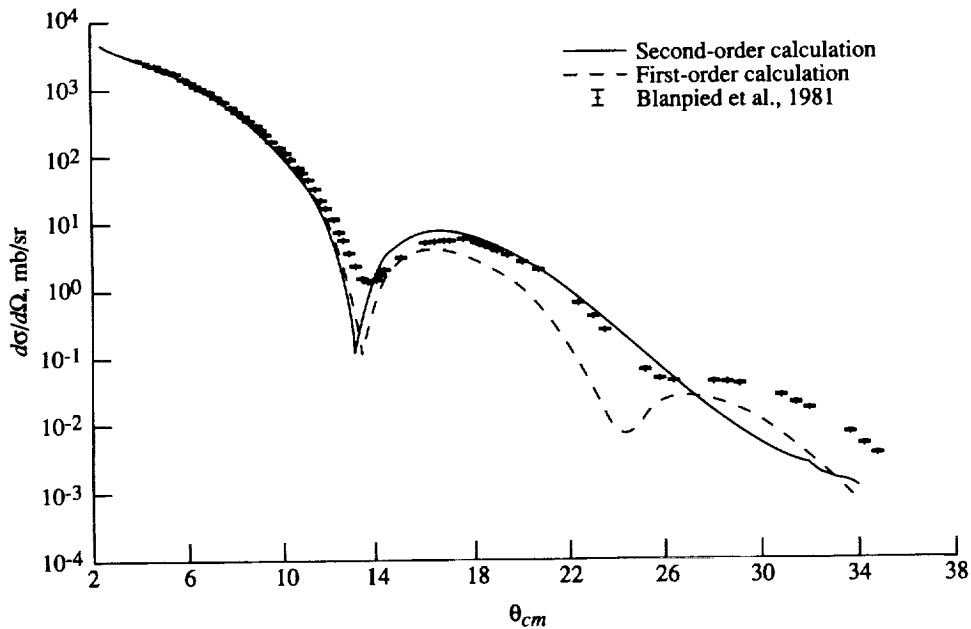


Figure 5.14. Theoretical and experimental elastic angular distributions for p - ^{12}C scattering at 800 MeV.

repeated in chapter 3. We include coulomb effects only in an approximate way assuming a point coulomb interaction. A more exact treatment is needed to completely fill in the first minimum. (See, for example, Chaumeaux et al., 1976; Glauber and Matthiae, 1970.) Here, spin effects may also be important as noted by Saudinos and Wilkin (1974) and Ahmad (1975). The effect of coupling the elastic channel to low-lying excited states is seen in the second maximum (figs. 5.14 and 5.18) where the bordered matrix agrees well, whereas the coherent approximation underestimates the data both at 800 and 1000 MeV. The sensitivity to the number of channels included in the second-order calculations can be seen in figure 5.19, where the dashed line includes only the 2^+ state; the long-dash-short-dash line, the 2^+ and 0^+ states; and the solid line, the 2^+ , 0^+ , 3^- , and 4^+ states. At larger angles, agreement with the data is poor. Here, the validity of the eikonal approximation is suspect, and the momentum transfers being probed are beyond the region where the phenomenological fits to the form factors and two-body amplitudes are made. For the second-order solutions, the effects of channel truncation, including the neglect of short-range correlations in the Υ -function, may be more important at larger angles.

Calculations of the excitation of the 2^+ , 0^+ , and 3^- states in ^{12}C by 800 and 1040 MeV protons are shown in figures 5.15 through 5.17 and 5.20 through 5.22, respectively. The dashed line is the DWBA, and the solid line is the bordered matrix (second-order) solution. For all excited states, the DWBA and bordered matrix give similar results in the region of the first and second maxima. Although the bordered matrix contains all couplings to second order for the elastic channel, the cascades between excited states, which are neglected, should be considered a second-order effect for inelastic transitions. These cascades would be more important in the region of the second maximum. In the region of the third maximum, we do see better agreement for the bordered matrix solutions as compared with the DWBA for all transitions considered.

In figures 5.23 and 5.24 we show calculations for elastic scattering and excitation of the 0^+ state of ^{12}C for ^4He on ^{12}C collisions at 340 MeV/nucleon. The experimental results of Chaumeaux et al. (1976) do not report the forward peak with the data beginning at approximately 5° . No correlation effect is included for ^4He in the calculations. The importance of correlations is expected to increase for the lightest nuclei (Feshbach, Gal, and Hüfner, 1971).

In table 5.8, total cross sections are given for all channels considered for p - ^{12}C scattering at 340, 800, and 1000 MeV. The total of the cross sections $\sigma(\text{tot})$ is calculated by the optical theorem, and the reaction cross section $\sigma(\text{re})$ is taken as the difference between the total and total elastic cross sections $\sigma(\text{el})$. The first- and second-order results are nearly the same for all channels. This agreement is expected because our angular distributions show almost complete agreement between the two solutions in the forward angles where most of the cross section occurs. In table 5.8, we also sum the excited-state cross sections $\sigma(2^+)$, $\sigma(0^+)$, $\sigma(3^-)$, $\sigma(4^+)$ for the bound-excited (BE) states calculated, $\sigma(\text{be})$. We note that $\sigma(\text{be})$ represents only a small fraction (<5 percent) of the total reaction cross section. This is an indication that the neglect of the bound-excited states in the abrasion model is a good approximation, although the importance of the giant dipole resonance state should be estimated.

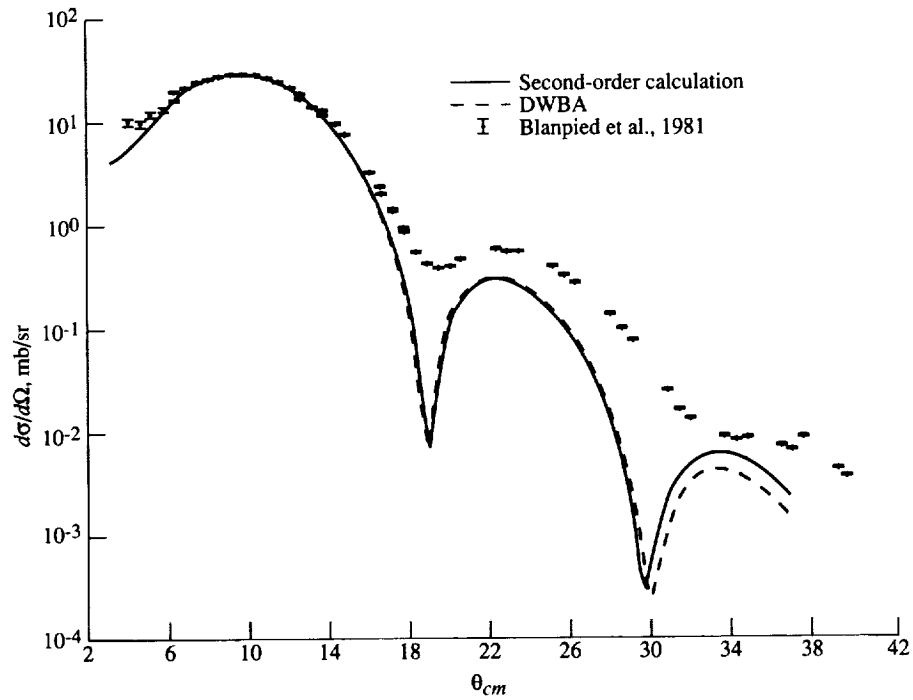


Figure 5.15. Theoretical and experimental inelastic angular distributions for excitation of 2^+ state in ^{12}C by 800-MeV protons.

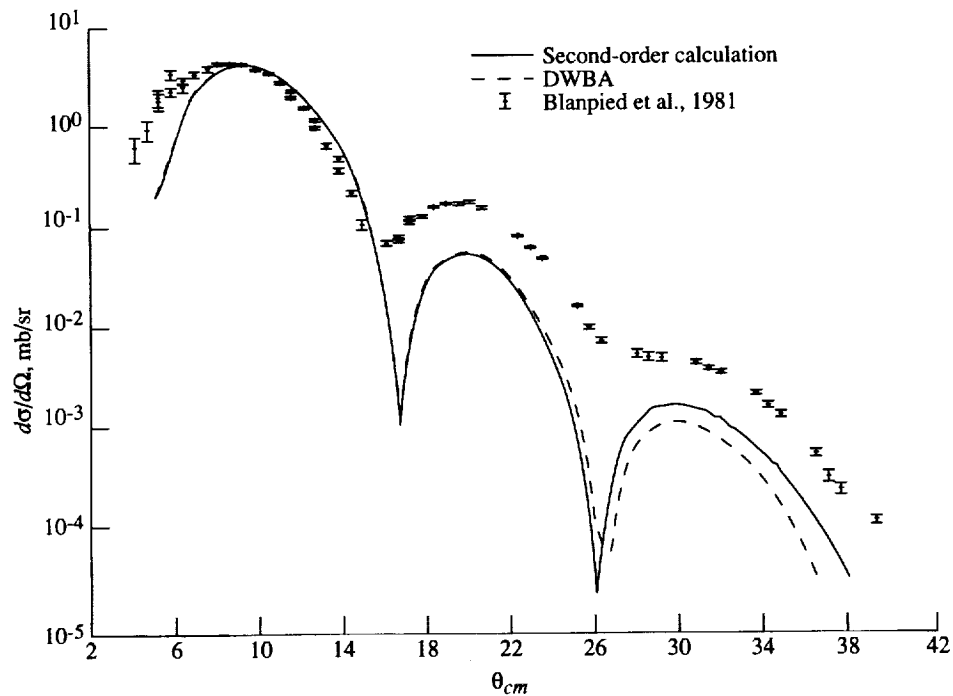


Figure 5.16. Theoretical and experimental inelastic angular distributions for excitation of 0^+ state in ^{12}C by 800-MeV protons.

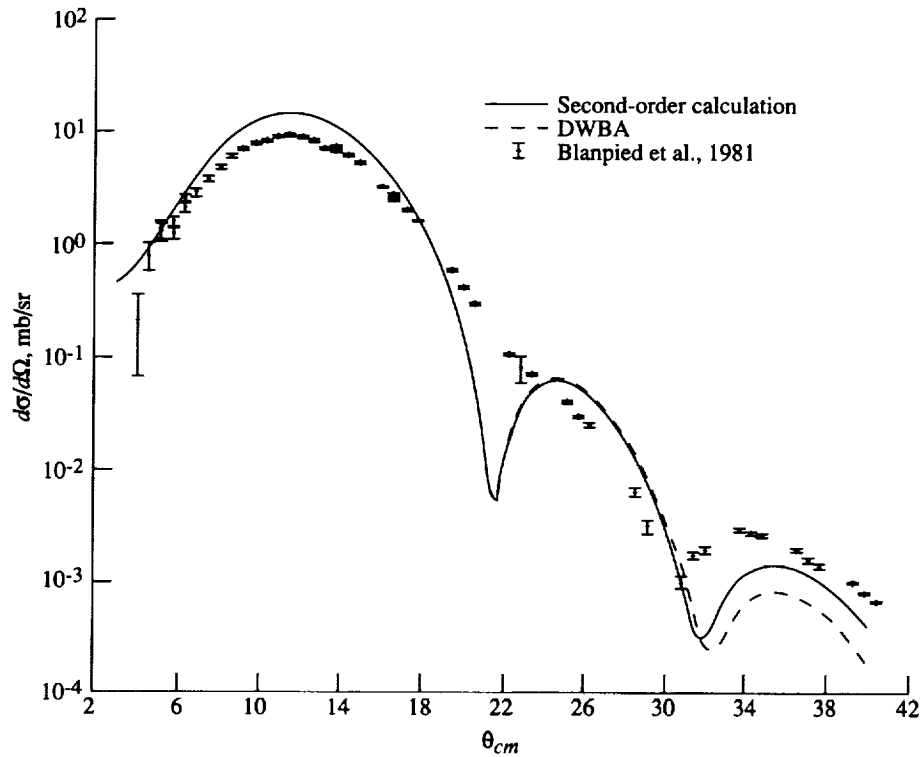


Figure 5.17. Theoretical and experimental inelastic angular distributions for excitation of 3^- state in ^{12}C by 800-MeV protons.

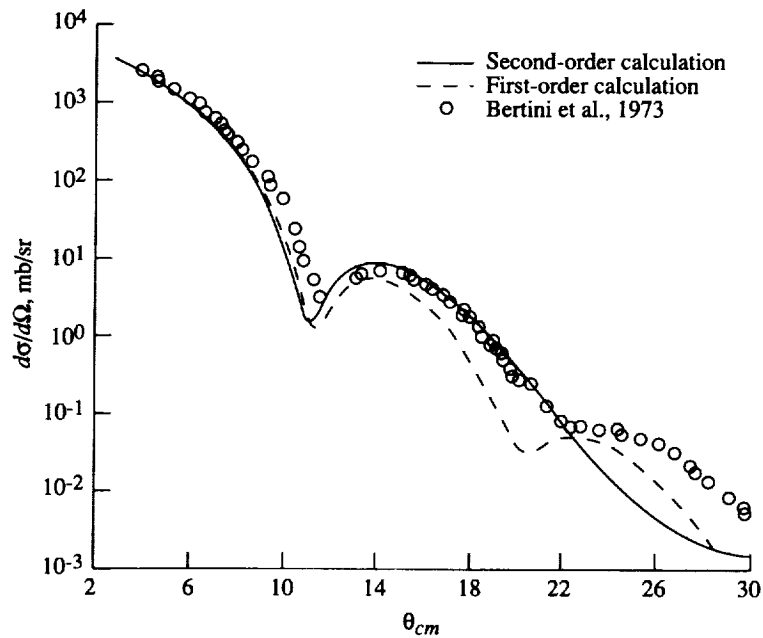


Figure 5.18. Theoretical and experimental elastic angular distributions for excitation for p - ^{12}C scattering at 1040 MeV.

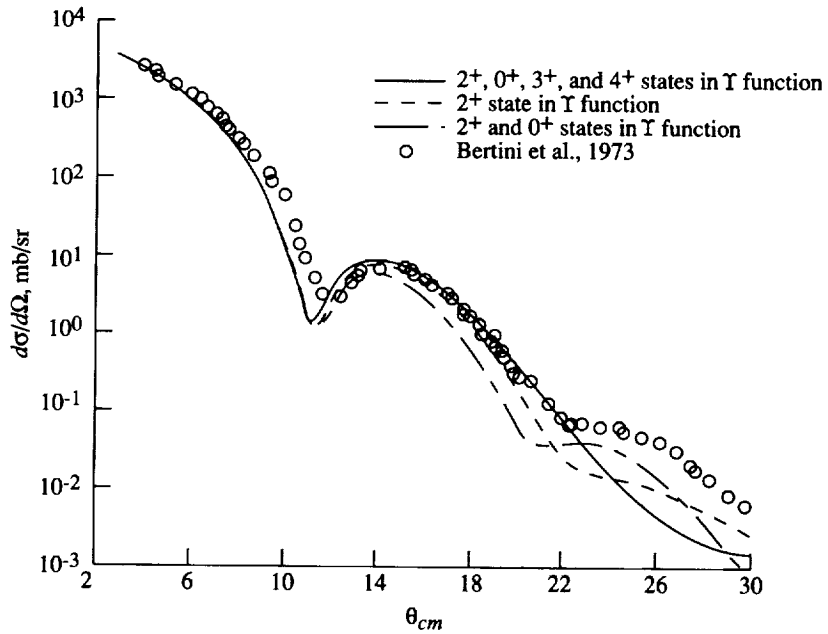


Figure 5.19. Effects of channel truncation in second-order calculations for p - ^{12}C elastic scattering at 1040 MeV.

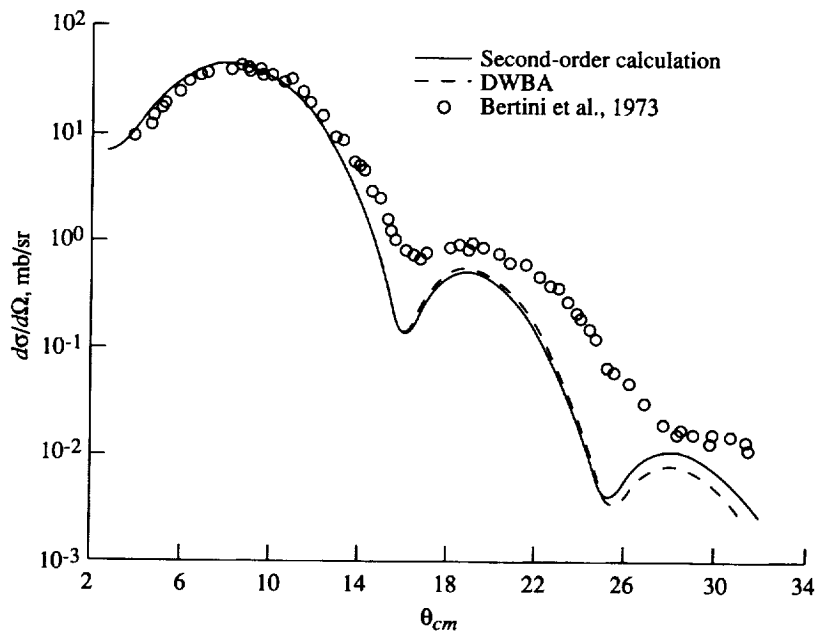


Figure 5.20. Theoretical and experimental inelastic angular distributions for excitation of 2^+ state in ^{12}C by 1040-MeV protons.

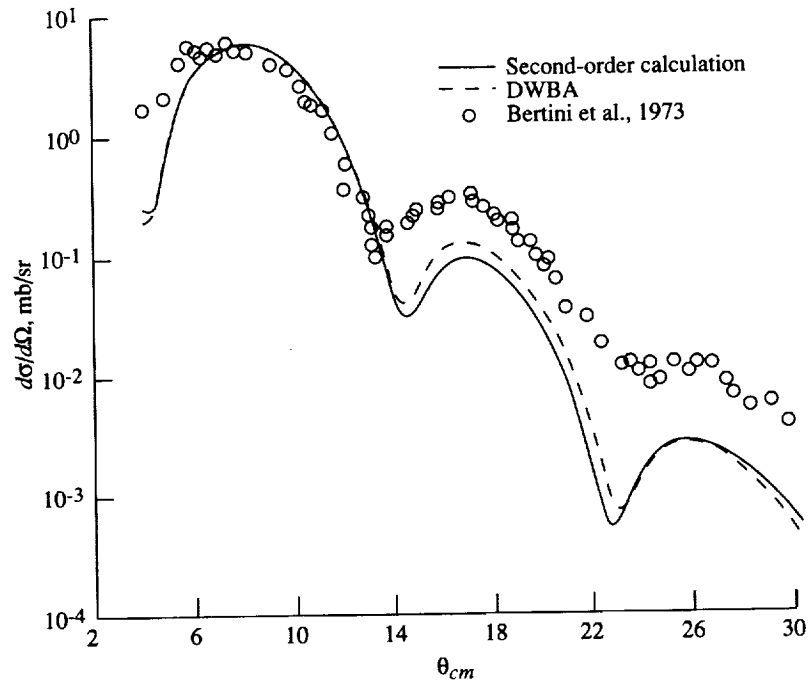


Figure 5.21. Theoretical and experimental inelastic angular distributions for excitation of 0^+ state in ^{12}C by 1040-MeV protons.

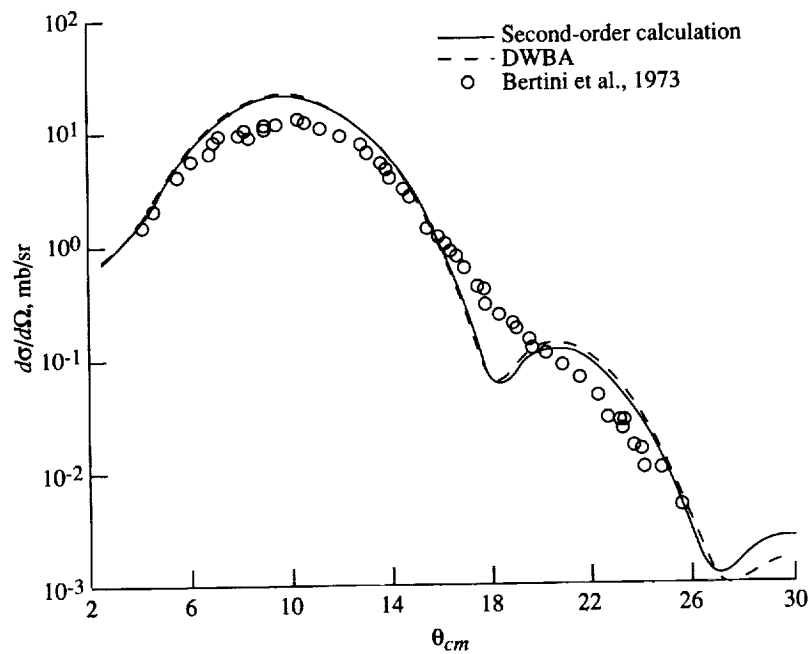


Figure 5.22. Theoretical and experimental inelastic angular distributions for excitation of 3^- state in ^{12}C by 1040-MeV protons.

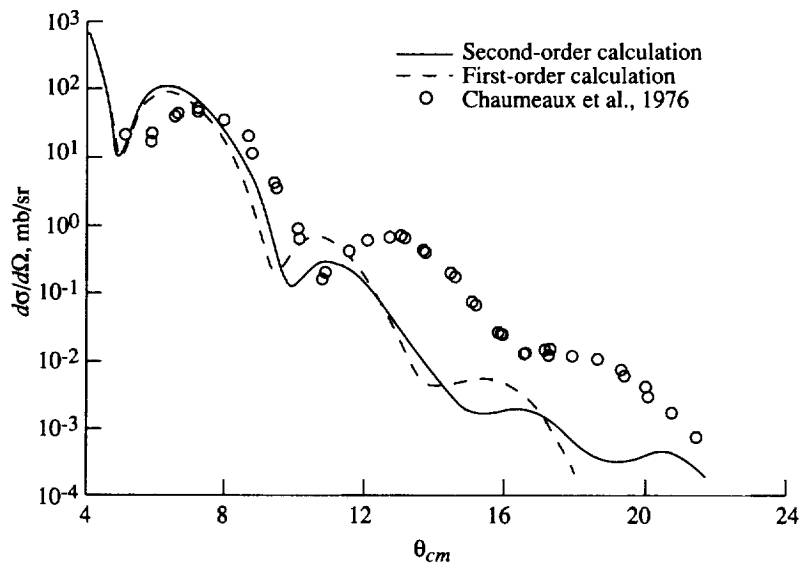


Figure 5.23. Theoretical and experimental elastic angular distributions for α - ^{12}C scattering at 340 MeV.

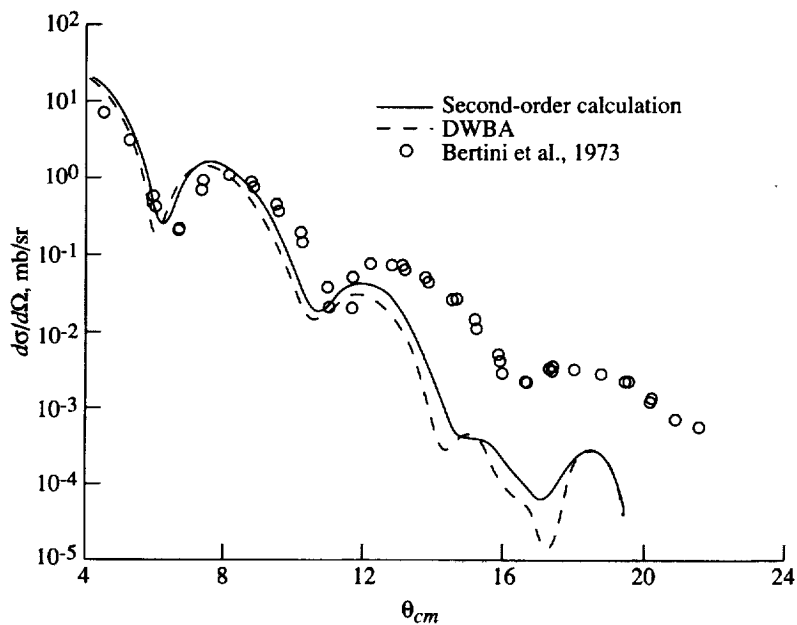


Figure 5.24. Theoretical and experimental inelastic angular distributions for excitation of 0^+ state in α - ^{12}C scattering at 340 MeV/nucleon.

Table 5.8. Total Channel Cross Sections for p on ^{12}C

Cross section	$T_{\text{lab}} = 340 \text{ MeV}$		$T_{\text{lab}} = 800 \text{ MeV}$		$T_{\text{lab}} = 1000 \text{ MeV}$	
	Coherent	Bordered	Coherent	Bordered	Coherent	Bordered
$\sigma_{\text{el}}, \text{mb}$	54.1	53.5	92.5	91.3	103.5	102.1
$\sigma(\text{be}), \text{mb}$	3.5	3.5	7.1	7.1	7.5	7.5
$\sigma(2^+), \text{mb}$	2.2	2.2	4.1	4.1	4.3	4.3
$\sigma(0^+), \text{mb}$	0.3	0.3	0.4	0.4	0.4	0.4
$\sigma(3^-), \text{mb}$	1.0	1.0	2.5	2.5	2.6	2.6
$\sigma(4^+), \text{mb}$	0.03	0.03	0.1	0.1	0.1	0.1
$\sigma(\text{re}), \text{mb}$	220.9	220.3	238.3	237.2	223.8	223.0
$\sigma(\text{tot}), \text{mb}$	275.0	273.8	330.8	328.5	327.3	325.1

5.5.4. Inclusive inelastic scattering. Cucinotta et al. (1990) consider nucleus-nucleus scattering at high energies for the case where an inclusive measurement of the projectile final state is made,

$$P + T \rightarrow P + X \quad (5.90)$$

with P and T labeling the projectile and target, respectively, and X being some final state of the target that is not measured. In equation (5.90), the projectile scatters without fragmenting, and meson production is not considered. In the overall center-of-mass (CM) frame, with the projectile and target states denoted by $|m_P\rangle$ and $|\nu_T\rangle$, respectively, the angular distribution for equation (5.90) is found by summing the nuclear-scattering operator over all final states of the target,

$$\left. \frac{d\sigma^P}{d\Omega} \right)_{\text{tot}} = \sum_{\nu_T} |\langle \nu_T 0_P | \hat{f}(\vec{q}) | 0_T 0_P \rangle|^2 \quad (5.91)$$

where \hat{f} is the scattering operator and \vec{q} is the momentum transfer to the projectile defined by

$$\vec{q} \equiv \vec{k} - \vec{k}_F \quad (5.92)$$

In equation (5.92), \vec{k} and \vec{k}_F are the initial and final projectile wave vectors, respectively. In equation (5.91), the phase space is approximated by a two-body phase space that is expected to be accurate at high energies. Equation (5.91) can be separated into elastic and inelastic contributions given by

$$\left. \frac{d\sigma}{d\Omega} \right)_{\text{el}} = |\langle 0_P 0_T | \hat{f}(\vec{q}) | 0_P 0_T \rangle|^2 \quad (5.93)$$

and

$$\left. \frac{d\sigma^P}{d\Omega} \right)_{\text{in}} = \sum_{\nu_T \neq 0} |\langle 0_P \nu_T | \hat{f}(\vec{q}) | 0_P 0_T \rangle|^2 \quad (5.94)$$

The summation in equation (5.94) includes all excited states, bound and continuum, of the target. This infinite summation can be reduced to a single matrix element through the use of closure on the target states:

$$\sum_{\nu_T \neq 0} |\nu_T\rangle \langle \nu_T| = 1 - |0_T\rangle \langle 0_T| \quad (5.95)$$

Inserting equation (5.95) into equation (5.94), we find

$$\left. \frac{d\sigma^P}{d\Omega} \right)_{\text{in}} = \left. \frac{d\sigma^P}{d\Omega} \right)_{\text{tot}} - \left. \frac{d\sigma}{d\Omega} \right)_{\text{el}} \quad (5.96)$$

where

$$\left. \frac{d\sigma^P}{d\Omega} \right)_{\text{tot}} = \langle 0_T | \langle 0_P | \hat{f}(\vec{q}) | 0_P \rangle \langle 0_P | \hat{f}^+(\vec{q}) | 0_P \rangle | 0_T \rangle \quad (5.97)$$

The great advantage of equation (5.96) over equation (5.94) is that only the ground-state wave function of the target is required.

A second reaction that we consider is complete inelastic scattering



where the projectile and target are both left in excited states. The angular distribution for equation (5.98) is given by

$$\left. \frac{d\sigma^{PT}}{d\Omega} \right)_{\text{in}} = \sum_{\nu_T \neq 0} \sum_{n_P \neq 0} |\langle \nu_T n_P | \hat{f}(\vec{q}) | 0_P 0_T \rangle|^2 \quad (5.99)$$

which is written, using closure on both the target and projectile states, as

$$\left. \frac{d\sigma^{PT}}{d\Omega} \right)_{\text{in}} = \left. \frac{d\sigma}{d\Omega} \right)_{\text{tot}} + \left. \frac{d\sigma}{d\Omega} \right)_{\text{el}} - \left. \frac{d\sigma^P}{d\Omega} \right)_{\text{tot}} - \left. \frac{d\sigma^T}{d\Omega} \right)_{\text{tot}} \quad (5.100)$$

where

$$\left. \frac{d\sigma}{d\Omega} \right)_{\text{tot}} = \langle 0_P 0_T | (|\hat{f}(\vec{q})|^2) | 0_P 0_T \rangle \quad (5.101)$$

Equation (5.100) may be written as

$$\left. \frac{d\sigma^{PT}}{d\Omega} \right)_{\text{in}} = \left. \frac{d\sigma}{d\Omega} \right)_{\text{tot}} - \left. \frac{d\sigma}{d\Omega} \right)_{\text{el}} - \left. \frac{d\sigma^P}{d\Omega} \right)_{\text{in}} - \left. \frac{d\sigma^T}{d\Omega} \right)_{\text{in}} \quad (5.102)$$

The distributions given by equations (5.96) through (5.102) are evaluated when models for the nuclear-scattering operator and ground-state wave functions are introduced.

5.5.5. Correlations and inclusive scattering. The effects of short-range dynamical correlations and Pauli blocking in the nuclear wave function will be

most pronounced in the inelastic distribution at small and medium momentum transfers. In order to include these effects in the inelastic scattering distributions, we consider the eikonal coupled-channel (ECC) model. Assuming correct or equivalent kinematics, the ECC can be considered the matrix representation of the Glauber amplitude. In the ECC, the matrix of scattering amplitudes for all possible projectile-target transitions is given by Cucinotta et al. (1989) as

$$\mathbf{f}(\vec{q}) = \frac{ik}{2\pi} \int d^2b \exp(i\vec{q} \cdot \vec{b}) \left\{ \exp \left[i\chi(\vec{b}) \right] - \mathbf{1} \right\} \quad (5.103)$$

where bold-faced quantities represent matrices and the elements of χ are written as

$$\begin{aligned} \langle m_P \mu_T | \hat{\chi}(\vec{b}) | n_P \nu_T \rangle &= \frac{1}{2\pi k_{NN}} \sum_{\alpha_j} \int d^2q \exp(i\vec{q} \cdot \vec{b}) \\ &\times F_{m_p n_p}^{(1)}(-\vec{q}) G_{\mu_T \nu_T}^{(1)}(\vec{q}) f_{NN}(\vec{q}) \end{aligned} \quad (5.104)$$

where F and G are projectile and target form factors. Assuming that the off-diagonal terms in χ are small compared with the diagonal terms (see chapter 3 and Wilson, 1975), we separate χ into diagonal (χ_D) and off-diagonal, χ_O terms as

$$\chi(\vec{b}) = \chi_D(\vec{b}) + \chi_O(\vec{b}) \quad (5.105)$$

We further assume that the nuclear density in the excited states is approximately the same as the ground state, such that the elements of the diagonal matrix χ_D are all taken as the elastic element,

$$\chi(\vec{b}) = \frac{A_P A_T}{(2\pi k_{NN})} \int d^2q F^{(1)}(-\vec{q}) G^{(1)}(\vec{q}) \exp(i\vec{q} \cdot \vec{b}) \quad (5.106)$$

To treat off-diagonal scattering, we expand \mathbf{f} in powers of χ_O

$$\mathbf{f}(\vec{q}) = \frac{-ik}{2\pi} \int d^2b \exp \left[i\vec{q} \cdot \vec{b} + i\chi_D(\vec{b}) \right] \sum_{m=1} \frac{[i\chi_O(\vec{b})]^m}{m!} \quad (5.107)$$

The inclusive distribution for the projectile then follows as:

$$\begin{aligned} \left. \frac{d\sigma^P}{d\Omega} \right)_{\text{in}} &= \left| \frac{ik}{2\pi} \right|^2 \int d^2b d^2b' \exp \left[i\vec{q} \cdot (\vec{b} - \vec{b}') \right] \exp \left\{ i \left[\chi(\vec{b}) - \chi^+(\vec{b}') \right] \right\} \\ &\times \sum_{\nu_T \neq 0} \left[T_S(\vec{b}, \vec{b}') + T_D(\vec{b}, \vec{b}') + \dots \right] \end{aligned} \quad (5.108)$$

where the single inelastic scattering terms are

$$T_S(\vec{b}, \vec{b}') = \langle 0_P 0_T | \hat{\chi}(\vec{b}) | 0_P \nu_T \rangle \langle \nu_T 0_P | \hat{\chi}^+(\vec{b}') | 0_P 0_T \rangle \quad (5.109)$$

and the double inelastic scattering terms are

$$\begin{aligned}
T_D(\vec{b}, \vec{b}') &= -\frac{1}{4} \sum_{\mu_T \neq 0} \sum_{n_p=0} \left\langle 0_P 0_T \left| \hat{\chi}(\vec{b}) \right| \mu_T n_p \right\rangle \left\langle \mu_T n_p \left| \hat{\chi}(\vec{b}) \right| 0_P \nu_T \right\rangle \\
&\times \sum_{\mu'_T \neq 0} \sum_{n'_p=0} \left\langle \nu_T 0_P \left| \hat{\chi}^+(\vec{b}') \right| \mu'_T n'_p \right\rangle \left\langle \mu'_T n'_p \left| \hat{\chi}^+(\vec{b}') \right| 0_P 0_T \right\rangle \quad (5.110)
\end{aligned}$$

Each term in the inelastic scattering expansion of equation (5.108) can be reduced through use of closure to terms involving matrix elements of one-, two-, ..., n -body operators over the ground state and thus includes the effects of two or more particle correlations. Details are given by Cucinotta et al. (1990).

5.5.6. Model calculations. We now consider the evaluation of the inelastic distributions in equation (5.106). Ignoring spin effects, we use an isospin-averaged, two-body amplitude given by

$$f_{NN}(\vec{q}) = \frac{\sigma(\alpha + i)k_{NN}}{4\pi} \exp\left(\frac{-Bq^2}{2}\right) \quad (5.111)$$

where the energy dependent parameters σ , B , and α are listed in table 5.9. For the projectile, we use a one-body form factor

$$F^{(1)}(\vec{q}) = \exp\left(\frac{-R_P^2 q^2}{4}\right) \quad (5.112)$$

where R_P is the matter radius of the projectile. For the target one-body form factor, we use the harmonic well form of Townsend and Wilson (1985)

$$G^{(1)}(\vec{q}) = (1 - C_T q^2) \exp\left(\frac{-R_T^2 q^2}{4}\right) \quad (5.113)$$

where R_T is the target matter radius and

$$C_T = \frac{\gamma_T R_T^2}{4(1 + \frac{3}{2}\gamma_T)} \quad (5.114)$$

where values of γ_T are given by Townsend and Wilson (1985)

Correlation effects are included in the two-particle density through the approximate form given by Moniz and Nixon (1971) as

$$\rho^{(2)}(\vec{x}, \vec{y}) = \rho^{(1)}(\vec{x})\rho^{(1)}(\vec{y}) \left\{ 1 - \exp\left[\frac{-(\vec{x} - \vec{y})^2}{2\ell_c^2}\right] \right\} \quad (5.115)$$

Table 5.9. Parameters For Nucleon-Nucleon Scattering Amplitude

Reaction	σ, fm^2	B, fm^2	α
α - α at 642 MeV/nucleon	3.93	0.13	-0.39
α - ^{12}C at 3.64 GeV/nucleon	4.2	0.28	-0.43
p - ^{16}O at 1 GeV/nucleon	4.3	0.26	-0.22
$\bar{\alpha}$ - A_T at 1 GeV/nucleon	4.3	0.26	-0.23

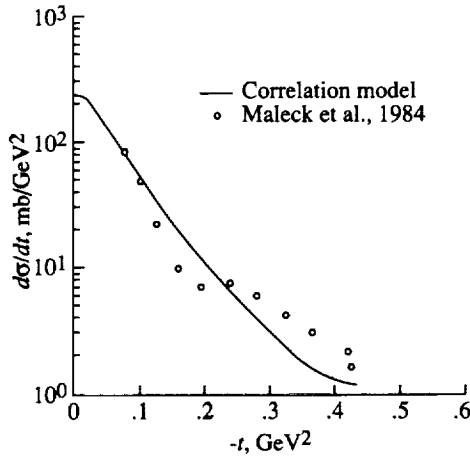


Figure 5.25. Inclusive α cross section on helium target.

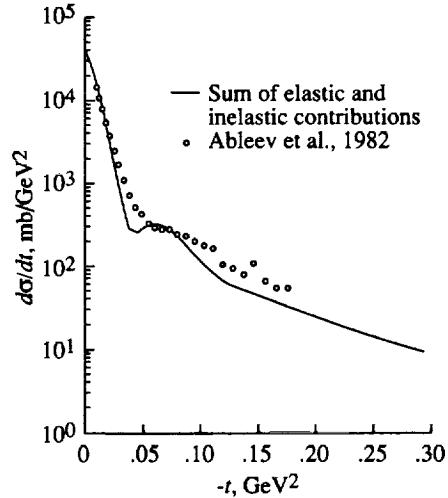


Figure 5.26. Inclusive α cross section on carbon target.

where ℓ_c is an effective correlation length, $\ell_c = 0.7 \text{ fm}$. For comparison with experimental results, the inclusive invariant distribution is written as

$$\left. \frac{d\sigma^P}{dt} \right)_{\text{in}} \approx \frac{\pi}{k^2} \left. \frac{d\sigma^P}{d\Omega} \right)_{\text{in}} \quad (5.116)$$

with

$$t \approx -q^2 \quad (5.117)$$

In figure 5.25, we show the correlation model and the experimental results of Maleck, Picozza, and Satta (1984) for α - α scattering at 642 MeV/nucleon. The correlation model produces good agreement over the region of momentum transfers studied.

Experimental results of Ableev et al. (1982) for total inclusive scattering of α -particles on ^{12}C at 3.64 GeV/nucleon are shown in figure 5.26. The solid line represents the sum of inelastic and elastic contributions. Agreement with the data is fair, whereas calculations underestimate the data at larger values of t . Correlation effects in elastic scattering have been shown to increase the cross

section in this region by a substantial amount (Cucinotta et al., 1989; Cucinotta, 1988) such that a second-order elastic scattering model should lead to improved agreement. The dominance of elastic scattering at small values of t , as seen in figure 5.26, indicates that the model is sufficient when total scattering distributions are considered.

5.6. Coulomb Dissociation

The coulomb cross section for producing state X was given as a multipole series as

$$\sigma_{\text{em}}(X) = \sum_{\pi\ell} \int_{E_0(X)}^{\infty} \sigma_{\gamma}^{\pi\ell}(E, X) N^{\pi\ell}(E) dE \quad (5.118)$$

where $\sigma_{\gamma}^{\pi\ell}(E, X)$ is the photonuclear cross section and $N^{\pi\ell}(E)$ is the virtual photon density produced by the passing ion. The virtual photon densities $N^{\pi\ell}(E)$ are known, and the corresponding photonuclear cross sections are the primary uncertainties.

5.6.1. Electric dipole transitions. The $E1$ virtual photon density experienced by a passing ion is (Norbury and Townsend, 1990a)

$$N^{E1}(E) = \frac{1}{E} \frac{2}{\pi} Z_t^2 \alpha \frac{1}{\beta^2} \left\{ x K_0(x) K_1(x) - \frac{1}{2} x^2 \beta^2 [K_1^2(x) - K_0^2(x)] \right\} \quad (5.119)$$

where E is the photon energy, Z_t the nuclear charge of the target, β is the velocity in units of c , α the fine structure constant, and $K_0(x)$ and $K_1(x)$ are the modified Bessel functions of the second kind.

The parameter x is given as

$$x = \frac{Eb_{\text{min}}}{\gamma\beta\hbar c} \quad (5.120)$$

where γ is the usual relativistic factor and b_{min} is the minimum impact parameter taken as (Norbury et al., 1988)

$$b_{\text{min}} = R_{0.1}(A_T) + R_{0.1}(A_P) \quad (5.121)$$

where the 10-percent charge density radius measured in fm is given by (Norbury et al., 1988)

$$R_{0.1}(A) = (1.18A^{1/3} + 0.75) \quad (5.122)$$

The photonuclear cross sections are assumed to be of the form

$$\sigma_{\gamma}^{E1}(E, X) = g_X^{E1}(E) \sigma_{\text{abs}}^{E1} \quad (5.123)$$

with $g_X^{E1}(E)$ assumed to be energy independent. The $E1$ absorption cross section is taken to be the giant electric dipole resonance (GDR), which is

$$\sigma_{\text{abs}}^{E1}(E) = \frac{\sigma_m}{1 + [(E^2 - E_{\text{GDR}}^2)/E^2\Gamma^2]} \quad (5.124)$$

where E_{GDR} is the resonance energy, Γ is the resonance width, and σ_m is given by (Levinger, 1960)

$$\sigma_m = \frac{\sigma_{\text{TRK}}}{\pi(\Gamma/2)} \quad (5.125)$$

with the Thomas-Reiche-Kuhn cross section in MeV-mb given by

$$\sigma_{\text{TRK}} = \frac{60NZ}{A} \quad (5.126)$$

where N , Z , and A are neutron numbers, proton numbers, and nucleon numbers, respectively. The resonance energy is given by (Westfall et al., 1979)

$$E_{\text{GDR}} = \hbar c \left[\frac{m^* R_o^2}{8J} \left(1 + u - \frac{1 + \epsilon + 3u}{1 + \epsilon + u} \epsilon \right) \right]^{-1/2} \quad (5.127)$$

with

$$u = \frac{3J}{Q'A^{1/3}} \quad (5.128)$$

and

$$R_o = r_o A^{1/3} \quad (5.129)$$

where $\epsilon = 0.0768$, $Q' = 17$ MeV, $J = 36.8$ MeV, $r_o = 1.18$ fm, and m^* is 0.7 times the nucleon rest mass. The resonance width in MeV is approximately

$$\Gamma = \left\{ \begin{array}{ll} 10 & (A < 50) \\ 4.5 & (A \geq 50) \end{array} \right\} \quad (5.130)$$

The branching ratios g_x satisfy

$$\sum_x g_x(E) = 1 \quad (5.131)$$

The proton branching ratio was found by Westfall et al. (1979) to be

$$g_p = \min \left[\frac{Z}{A}, 1.95 \exp(-0.075Z) \right] \quad (5.132)$$

If all other processes are assumed to emit neutrons, we may write

$$\begin{aligned} \sum_s \sigma_\gamma(E, sn) &= \sigma_\gamma(E, n) + \sigma_\gamma(E, 2n) + \dots \\ &= (1 - g_p) \sigma_{\text{abs}}^{E1}(E) \end{aligned} \quad (5.133)$$

with the total photoneutron production cross section as

$$\begin{aligned} M(E) \sum_s \sigma_\gamma(E, sn) &= \sum_s s \sigma_\gamma(E, sn) \\ &= \sum_s s g_{sn} \sigma_{\text{abs}}^{E1}(E) \end{aligned} \quad (5.134)$$

and further assume that the processes emitting more than two neutrons are negligible yields

$$M(E) (1 - g_p) \approx g_n + 2g_{2n} \quad (5.135)$$

which yields

$$g_{2n} = [M(E) - 1](1 - g_p) \quad (5.136)$$

and

$$g_n = 1 - g_p - g_{2n} \quad (5.137)$$

The average multiplicity was shown to be

$$M(E) = 1 + (1 - f_d) \left[1 - \left(1 + \frac{E_{\text{sec}}}{\Theta} \right) \exp \left(-\frac{E_{\text{sec}}}{\Theta} \right) \right] \quad (5.138)$$

where

$$E_{\text{sec}} = E - E_o(\gamma, 2n) \quad (5.139)$$

and the nuclear temperature (Blatt and Weisskopf, 1952) is

$$\Theta = \left[\left(\frac{A}{8E^*} \right)^{1/2} - \frac{5}{4E^*} \right]^{-1} \quad (5.140)$$

where the excitation energy

$$E^* = E - E_o(\gamma, n) \quad (5.141)$$

See Norbury and Townsend (1990a) for details.

5.6.2. Results. Reasonable values of coulomb dissociation are obtained with experiments (Heckman and Lindstrom, 1976; Mercier et al., 1984) by neglecting the $2n$ channel (Norbury, Townsend, and Badavi, 1988) by setting $M(E) = 1$ as shown in tables 5.10 and 5.11. Further analysis is given by Norbury (1989). A fully parameterized computer program is available for generating one nucleon removal cross section (Norbury, Townsend, and Badavi, 1988). Preliminary work on evaluating the $2n$ photonuclear cross sections is hopeful but not complete (Norbury and Townsend, 1990a; Cucinotta, Norbury, and Townsend, 1988).

5.6.3. Electric quadrupole transitions. The $E2$ virtual photon density experienced by a passing ion is (Bertulani and Baur, 1988)

$$N^{E2}(E) = \frac{1}{E} \frac{2}{\pi} Z_T^2 \alpha \frac{1}{\beta^4} \left\{ 2(1 - \beta^2) K_1^2(x) + x(2 - \beta^2) K_0(x) K_1(x) - \frac{x^2}{2\beta^4} [K_1^2(x) - K_0^2(x)] \right\} \quad (5.142)$$

where E is the photon energy, Z_T is the nuclear charge of the target, β is the velocity of the projectile in units of c , α is the fine structure constant, and $K_0(x)$

Table 5.10. Calculated Total Electromagnetic Reaction Cross Sections for ^{12}C And ^{16}O Incident Upon Various Targets

Projectile	Energy, GeV/nucleon	Target	Final state	σ_{EM} , mb (a)	σ_{EM} , mb (present work)	
^{12}C	2.1	^{208}Pb	$^{11}\text{C} + \text{n}$	50 + 18	68	
			$^{11}\text{B} + \text{p}$	50 ± 25	68	
	1.05		$^{11}\text{C} + \text{n}$	38 ± 24	43	
			$^{11}\text{B} + \text{p}$	50 ± 26	43	
^{16}O	2.1		$^{15}\text{O} + \text{n}$	50 + 25	99	
			$^{15}\text{N} + \text{p}$	97 ± 17	99	
^{12}C	2.1		^{108}Ag	$^{11}\text{C} + \text{n}$	22 ± 12	26
				$^{11}\text{B} + \text{p}$	20 ± 12	26
	1.05	$^{11}\text{C} + \text{n}$		22 ± 12	17	
		$^{11}\text{B} + \text{p}$		25 ± 20	17	
^{16}O	2.1	$^{15}\text{O} + \text{n}$		26 ± 13	37	
		$^{15}\text{N} + \text{p}$		29 ± 19	37	
^{12}C	2.1	^{64}Cu		$^{11}\text{C} + \text{n}$	10 ± 6	11
				$^{11}\text{B} + \text{p}$	4 ± 8	11
	1.05		$^{11}\text{C} + \text{n}$	10 ± 7	7.4	
			$^{11}\text{B} + \text{p}$	5 ± 8	7.4	
^{16}O	2.1		$^{15}\text{O} + \text{n}$	10 ± 7	16	
			$^{15}\text{N} + \text{p}$	14 ± 9	16	
^{12}C	2.1		^{27}Al	$^{11}\text{C} + \text{n}$	0 ± 3	2.5
				$^{11}\text{B} + \text{p}$	0 ± 3	2.5
	1.05	$^{11}\text{C} + \text{n}$		1 ± 3	1.8	
		$^{11}\text{B} + \text{p}$		1 ± 3	1.8	
^{16}O	2.1	$^{15}\text{O} + \text{n}$		0 ± 3	3.6	
		$^{15}\text{N} + \text{p}$		0 ± 0	3.6	
^{12}C	2.1	^{12}C		$^{11}\text{C} + \text{n}$	0 ± 1	0.58
				$^{11}\text{B} + \text{n}$	0 ± 3	0.58
	1.05		$^{11}\text{C} + \text{n}$	0 ± 2	0.43	
			$^{11}\text{B} + \text{p}$	0 ± 1	0.43	
^{16}O	2.1		$^{15}\text{O} + \text{n}$	0 ± 2	0.83	
			$^{15}\text{N} + \text{p}$	0 ± 3	0.83	

^aThis column represents the measurements (isotope averaged) of Heckman and Lindstrom (1976). See Mercier et al. (1984).

Table 5.11. Calculated Total Electromagnetic Reaction Cross Sections for Various Projectiles Incident Upon ^{197}Au

Projectile	Energy, GeV/nucleon	Final state	σ_{EM} , mb (a)	σ_{EM} , mb (present work)
^{12}C	2.1	$^{196}\text{Au} + \text{n}$	66 ± 20	39
^{20}Ne	2.1		136 ± 21	104
^{40}Ar	1.8		420 ± 120	299
^{56}Fe	1.7		680 ± 160	588

^a This column represents the data of Mercier et al. (1984).

Table 5.12. EM Cross Sections for Reaction $^{89}\text{Y}(\text{projectile}, X)^{88}\text{Y}$

Projectile	$R_{0.1}(P)$ fm	Energy, GeV/nucleon	σ_{expt} , mb (a)	σ_{ww} , mb	σ_{E1} , mb	σ_{E2} , mb	$\sigma_{E1} + \sigma_{E2}$, mb
^{12}C	3.30	2.1	9 ± 12	12	12	1	13
^{20}Ne	4.00	2.1	43 ± 12	32	31	3	34
^{40}Ar	4.72	1.8	132 ± 17	90	88	9	97
^{56}Fe	5.24	1.7	217 ± 20	175	171	16	187

^a This column represents the data of Mercier et al. (1984).

and $K_1(x)$ are the modified Bessel functions of the second kind. The parameter x is given as

$$x = \frac{Eb_{\text{min}}}{\gamma\beta\hbar c} \quad (5.143)$$

where γ is the usual Lorentz factor and b_{min} is the minimum impact parameter taken herein as the sum of the 10-percent radii of the target and projectile. The photonuclear cross section is assumed to be the isoscalar component of the electric giant quadrupole resonance (GQR) given by Norbury (1990b) as

$$\sigma_{E2}(E) = \frac{\sigma_{\text{EWSR}} E_{\text{GQR}}^2}{1 + (E^2 - E_{\text{GQR}}^2)^2 / \Gamma^2 E^2} \quad (5.144)$$

where the energy-weighted sum rule (EWSR) cross section in $\mu\text{b}/\text{MeV}$ is

$$\sigma_{\text{EWSR}} = f \frac{0.22ZA^{2/3}}{\pi\Gamma/2} \quad (5.145)$$

The data of Mercier et al. (1986) were analyzed by Norbury (1990a) with results shown in table 5.12. In this table, the 10-percent charge radius used for ^{89}Y is 6.02 fm and the GQR parameters are $f = 0.55$, $\Gamma = 3.2$ MeV, and

$E_{\text{GQR}} = 13.8$ MeV. The $^{89}\text{Y}(\gamma, n)$ threshold is at 11.0 MeV. Calculations are made for Weizsäcker-Williams theory (σ_{WW}), and individual $E1$ and $E2$ multipole cross sections are calculated. The cross section $\sigma_{E1} + \sigma_{E2}$ is in reasonable agreement with experiment. All calculations use the minimum impact parameter given by $b_{\text{min}} = R_{0.1}(A_P) + R_{0.1}(A_T)$.

5.6.4. Nuclear versus coulomb contributions. An extensive comparison of the electromagnetic theory (Norbury, 1989, 1990a, 1990b, and 1990c) with experiment (Hill et al., 1988) showed that significant discrepancies still remained at higher energies. These have been attributed to an incorrect subtraction of the nuclear contribution to the total experimental cross section; thus an incorrect experimental electromagnetic cross section (Benesh, Cook, and Vary, 1989) resulted. Calculations were then performed (Benesh, Cook, and Vary, 1989; Norbury and Townsend, 1990b) of both the nuclear and electromagnetic cross sections and were compared with the total measured cross sections. Much more satisfactory agreement was then obtained. Thus, the electromagnetic and nuclear contributions to single-nucleon removal seem reasonably well understood; however, recent comparisons with exclusive data for nucleon removal from ^{28}Si indicate that some work remains to be done in understanding how to calculate excitation energies relevant to single-nucleon removal at higher energies (14 GeV/nucleon).

Future work should be directed to understanding nuclear and coulomb contributions to the removal of a few nucleons.

5.7. Semiempirical Data Base

Even though the accuracy of the data for specific reactions improves, a reasonable means of representing data in computational procedures is still a challenge. We have avoided a point representation of the data since large multidimensional arrays will eventually rival computer storage. Mostly, we use empirical methods built on some theoretical base which describes approximately the systematic variation of reaction cross sections and add a few adjustable parameters or interpolation and extrapolation procedures.

5.7.1. Nucleon nonelastic spectrum. The nonelastic differential cross sections (the inelastic process in which the nucleus is raised to an excited level is ignored) use the results of Bertini's MECC-7 (Anon., 1968) program. The nucleon multiplicities are given in tables 5.13 and 5.14. We have required the multiplicities to be monotonic in energy, and thus the values in parentheses, which were obtained by scaling from lower and higher energies, are correct values and are used in the calculations. The results below 400 MeV were taken from Alsmiller, Barish, and Leimdorfer (1968), and the results for carbon, calcium, bromine, cesium, and holmium above 400 MeV are obtained by interpolation. The nonelastic spectra are represented as

$$f(E, E') = \sum_{i=1}^3 \frac{N_i}{\alpha_i} \frac{\exp(-E'/\alpha_i)}{1 - \exp(-E'/\alpha_i)} + \frac{N_Q}{E'} \{1 + \exp[-20(1 - E/E')]\} \quad (5.146)$$

The first term of the summation represents the evaporation peak so that N_1 (the number of evaporation nucleons) is taken from table 5.13 and the spectral parameter α_1 (in GeV) is taken from Ranft (1980)

$$\alpha_{1p} = \begin{cases} (0.019 + 0.0017E')(1 - 0.001A_T) & (E' < 5 \text{ GeV}) \\ 0.027(1 - 0.001A_T) & (E' \geq 5 \text{ GeV}) \end{cases}$$

$$\alpha_{1n} = \begin{cases} (0.017 + 0.0017E')(1 - 0.001A_T) & (E' < 5 \text{ GeV}) \\ 0.023(1 - 0.001A_T) & (E' \geq 5 \text{ GeV}) \end{cases} \quad (5.148)$$

The second term is taken from Ranft (1980) to represent the low-energy cascade particles as

$$n_{2p} = \begin{cases} 0.0035\sqrt{A_T} & (E' \leq 0.1 \text{ GeV}) \\ 0.007\sqrt{A_T}[0.5 + 1(1 + \log_{10} E')^2] & (0.1 < E' < 5 \text{ GeV}) \\ 0.0245\sqrt{A_T} & (E' \leq 5 \text{ GeV}) \end{cases} \quad (5.149)$$

$$n_{2n} = \begin{cases} 0.0042\sqrt{A_T} & (E' \leq 0.1 \text{ GeV}) \\ 0.007\sqrt{A_T}[0.6 + 1.3(1 + \log_{10} E')^2] & (0.1 < E' < 5 \text{ GeV}) \\ 0.032\sqrt{A_T} & (E' \leq 5 \text{ GeV}) \end{cases} \quad (5.150)$$

with the corresponding spectral parameters

$$\alpha_{2p} = \begin{cases} (0.11 + 0.01E')(1 - 0.001A_T) & (E' < 5 \text{ GeV}) \\ 0.16(1 - 0.001A_T) & (E' \geq 5 \text{ GeV}) \end{cases} \quad (5.151a)$$

$$\alpha_{1n} = \begin{cases} (0.1 + 0.01E')(1 - 0.001A_T) & (E' < 5 \text{ GeV}) \\ 0.15(1 - 0.001A_T) & (E' \geq 5 \text{ GeV}) \end{cases} \quad (5.151b)$$

The third term in the summation is the balance of cascade particles after the inclusion of the quasi-elastic contribution.

The quasi-elastic contribution is estimated by including the nuclear attenuation following the quasi-elastic event. The proton quasi-elastic cross section is

$$\left. \begin{aligned} \sigma_{Q,pp} &= Z_T\sigma_{pp} + (A_T - Z_T)\sigma_{np} \\ \sigma_{Q,pn} &= (A_T - Z_T)\sigma_{np} \end{aligned} \right\} \quad (5.152)$$

and similarly for neutrons

$$\left. \begin{aligned} \sigma_{Q,nn} &= (A_T - Z_T)\sigma_{nn} + Z_T\sigma_{np} \\ \sigma_{Q,np} &= Z_T\sigma_{np} \end{aligned} \right\} \quad (5.153)$$

Transport Methods and Interactions for Space Radiations

Table 5.13. Number of Evaporation Nucleons Produced in Nuclear Collisions
[Values in parentheses are modified and used in the code]

	Number of nucleons produced at—					
	25 MeV	200 MeV	400 MeV	1000 MeV	2000 MeV	3000 MeV
$A_T = 12:$						
$p \rightarrow p$	0.51	0.54	0.50	0.72	0.75	0.84
$p \rightarrow n$	0.026	0.32	0.35	0.79	0.79	0.79
$n \rightarrow p$	0.052	0.30	0.35	0.73	0.73	0.80
$n \rightarrow n$	0.43	0.57	0.52	0.77 (0.71)	0.71 (0.71)	0.73
$A_T = 16:$						
$p \rightarrow p$	0.62	0.73	0.71	0.84	0.89	0.98 (0.93)
$p \rightarrow n$	0.87	0.36	0.441	0.11 (0.87)	0.93 (0.87)	0.82 (0.87)
$n \rightarrow p$	0.12	0.47	0.53	0.86	0.86	0.89
$n \rightarrow n$	0.55	0.60	0.59	0.79	0.79	0.81
$A_T = 27:$						
$p \rightarrow p$	0.54	0.99	1.03	1.36	1.49	1.86
$p \rightarrow n$	0.37	0.61	0.62	1.29	2.03 (1.92)	1.52 (1.92)
$n \rightarrow p$	0.14	0.78	0.82	1.29	1.60	1.74
$n \rightarrow n$	0.75	0.76	0.71	1.34	1.51	1.60
$A_T = 40:$						
$p \rightarrow p$	0.50	1.03	1.06	1.74	2.32	2.93
$p \rightarrow n$	0.53	1.12	1.24	2.63	3.36	3.64
$n \rightarrow p$	0.12	0.74	0.84	1.60	2.29	2.67
$n \rightarrow n$	0.89	1.39	1.44	2.76	3.25	3.54
$A_T = 65:$						
$p \rightarrow p$	0.18	0.75	0.91	2.11	3.15	4.00
$p \rightarrow n$	1.04	2.33	2.65	3.97	4.79	5.37
$n \rightarrow p$	0.03	0.49	0.66	1.90	2.98	3.61
$n \rightarrow n$	1.46	2.77	2.90	4.17	4.99	5.49
$A_T = 80:$						
$p \rightarrow p$	0.10	0.60	1.07	2.2	3.18	4.89
$p \rightarrow n$	1.29	2.20	3.18	3.72	5.07	6.77
$n \rightarrow p$	0.02	0.53	0.79	1.87	2.91	4.53
$n \rightarrow n$	1.58	3.19	3.43	4.07	5.35	6.91
$A_T = 100:$						
$p \rightarrow p$	0.03	0.46	1.28	2.96	4.56	5.78
$p \rightarrow n$	1.53	1.97	3.72	5.46	7.04	8.17
$n \rightarrow p$	0.004	0.59	0.96	2.71	4.27	5.44
$n \rightarrow n$	1.67	3.60	3.97	5.63	7.31	8.33
$A_T = 132:$						
$p \rightarrow p$	0.01	0.61	1.03	2.68	4.51	6.32
$p \rightarrow n$	1.91	4.11	5.25	8.76	11.34	12.31
$n \rightarrow p$	0.001	0.47	0.81	2.51	4.47	5.98
$n \rightarrow n$	1.96	4.73	5.59	8.93	10.6	12.42
$A_T = 164:$						
$p \rightarrow p$	0.003	0.42	0.76	2.38	4.68	6.86
$p \rightarrow n$	2.17	5.79	7.07	12.09	15.7	16.45
$n \rightarrow p$	0.003	0.28	0.58	2.30	4.68	6.52
$n \rightarrow n$	2.26	5.96	7.07	12.3	14.6	16.51
$A_T = 207:$						
$p \rightarrow p$	0.001	0.21	0.44	2.23	5.19	7.39
$p \rightarrow n$	2.29	7.22	9.24	15.3	17.81	20.6
$n \rightarrow p$	0.00	0.10	0.30	2.10	4.88	7.05
$n \rightarrow n$	2.29	7.38	9.53	15.6	18.2	20.6

Table 5.14. Number of Cascade Nucleons Produced in Nuclear Collisions

	Number of nucleons produced at—					
	25 MeV	200 MeV	400 MeV	1000 MeV	2000 MeV	3000 MeV
$A_T = 12:$						
$p \rightarrow p$	0.58	1.43	1.63	1.95	2.15	2.48
$p \rightarrow n$	0.41	0.86	0.93	1.42	1.66	2.08
$n \rightarrow p$	0.42	0.90	0.92	1.43	1.65	1.91
$n \rightarrow n$	0.56	1.42	1.69	1.95	2.27	2.57
$A_T = 16:$						
$p \rightarrow p$	0.56	1.41	1.72	2.05	2.39	2.60
$p \rightarrow n$	0.38	0.90	0.98	1.47	1.86	2.19
$n \rightarrow p$	0.38	0.91	0.96	1.49	1.85	2.01
$n \rightarrow n$	0.54	1.43	1.70	2.05	2.52	2.70
$A_T = 27:$						
$p \rightarrow p$	0.46	1.38	1.67	2.29	2.86	3.19
$p \rightarrow n$	0.34	0.97	1.16	1.86	2.54	3.25
$n \rightarrow p$	0.32	0.93	1.01	1.69	2.28	2.71
$n \rightarrow n$	0.49	1.48	1.81	2.42	3.22	3.71
$A_T = 40:$						
$p \rightarrow p$	0.40	1.33	1.69	2.32	3.01	3.53
$p \rightarrow n$	0.30	1.04	1.24	2.46	3.52	4.48
$n \rightarrow p$	0.28	0.89	1.08	1.79	2.51	3.06
$n \rightarrow n$	0.45	1.49	1.88	2.99	4.13	4.83
$A_T = 65:$						
$p \rightarrow p$	0.30	1.21	1.69	2.35	3.16	3.87
$p \rightarrow n$	0.28	1.09	1.46	3.06	4.49	5.72
$n \rightarrow p$	0.21	0.86	1.08	1.88	2.75	3.41
$n \rightarrow n$	0.40	1.53	2.00	3.55	5.03	5.95
$A_T = 80:$						
$p \rightarrow p$	0.27	1.18	1.57	2.32	3.18	3.95
$p \rightarrow n$	0.25	1.08	1.45	3.27	4.92	6.35
$n \rightarrow p$	0.19	0.81	1.04	1.86	2.78	3.54
$n \rightarrow n$	0.36	1.51	1.98	3.78	5.40	6.64
$A_T = 100:$						
$p \rightarrow p$	0.25	1.15	1.55	2.29	3.20	4.04
$p \rightarrow n$	0.22	1.06	1.52	3.47	5.35	6.98
$n \rightarrow p$	0.17	0.78	1.08	1.84	2.44	3.67
$n \rightarrow n$	0.31	1.47	2.03	3.96	5.76	7.33
$A_T = 132:$						
$p \rightarrow p$	0.20	1.00	1.46	2.21	3.17	3.87
$p \rightarrow n$	0.20	1.11	1.57	3.31	5.20	7.91
$n \rightarrow p$	0.13	0.70	1.00	1.79	2.69	3.52
$n \rightarrow n$	0.28	1.45	2.10	3.86	6.86	8.29
$A_T = 164:$						
$p \rightarrow p$	0.16	0.90	1.36	2.13	3.15	3.69
$p \rightarrow n$	0.18	1.11	1.60	3.16	5.06	8.86
$n \rightarrow p$	0.11	0.63	0.88	1.72	2.55	3.39
$n \rightarrow n$	0.26	1.42	2.11	3.56	7.94	9.25
$A_T = 208:$						
$p \rightarrow p$	0.14	0.82	1.27	2.05	7.74	3.51
$p \rightarrow n$	0.16	1.03	1.71	2.97	7.23	9.77
$n \rightarrow p$	0.09	0.58	0.87	1.67	2.41	3.24
$n \rightarrow n$	0.23	1.36	2.10	3.36	7.63	10.21

The corresponding multiplicities are taken as

$$N_{Q,jk} = \frac{\exp(-0.05\sqrt{A_T}) \sigma_{Q,jk}}{\sum_{\ell} \sigma_{Q,j\ell}} \quad (5.154)$$

where the exponential factor accounts for the attenuation of the quasi-elastic particles before they escape the nucleus. The balance of the cascade particles is contained in N_3 as

$$N_3 = N_c - N_2 - N_Q \quad (5.155)$$

with an assumed spectral coefficient given by

$$\alpha_3 = \frac{\alpha_2}{0.7} \quad (5.156)$$

Results of the present formalism and the calculations of Bertini, Guthrie, and Culkowski (1972) are shown in figures 5.27 to 5.40. Some further improvements in this parameterization need to be made.

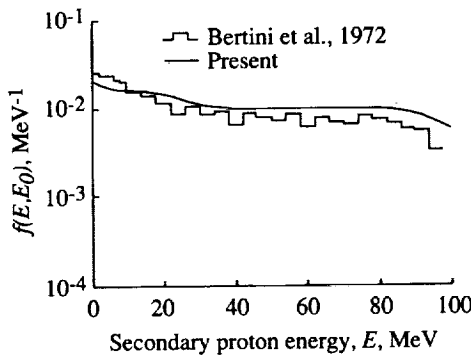


Figure 5.27. Nucleon cascade spectrum for protons produced by 100-MeV protons on oxygen.

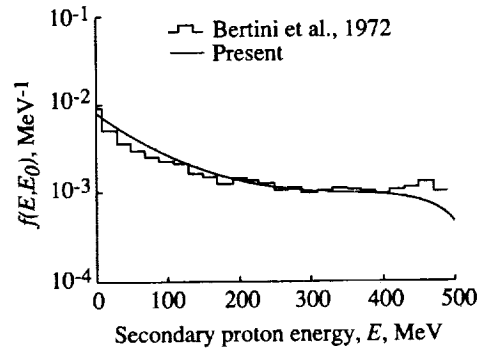


Figure 5.28. Nucleon cascade spectrum for protons produced by 500-MeV protons on oxygen.

5.7.2. Light-fragment spectrum. The light-fragment yields per event are given in table 5.15 as obtained from Bertini's MECC-7 (Anon., 1968) calculations. These results are extrapolated and interpolated in energy and mass number. The corresponding mean energies are given in table 5.16. The mean energies are used in Ranft's formula for nucleons and are similarly used for the light ions.

5.7.3. Fragmentation cross sections. The local distribution of ions and radicals produced in ionizing radiation events is known to be an indicator of biological response. Such distributions for high-energy nuclear radiation vastly altered by local nuclear-reaction events have been studied in nuclear emulsion (Van Allen, 1952; Lord, 1951) and are regular components in risk assessments in high-energy neutron and proton radiation fields (Alsmiller, Armstrong, and Coleman, 1970; Foelsche et al., 1974). Risk assessments have generally depended on the results of calculational models of these reactions because the detailed study of such reactions was largely inaccessible to experimental study until the advent of high-energy heavy ion beams.

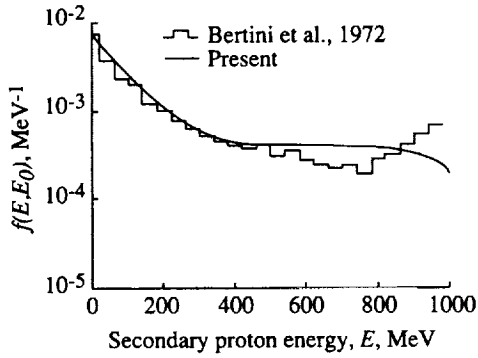


Figure 5.29. Nucleon cascade spectrum for protons produced by 1000-MeV protons on oxygen.

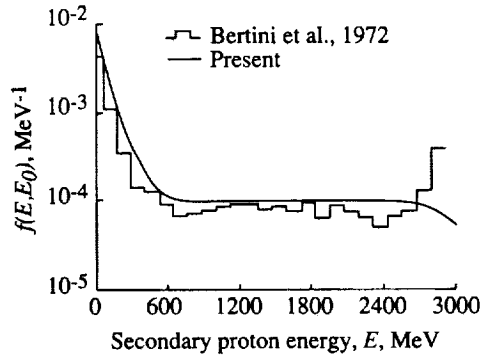


Figure 5.30. Nucleon cascade spectrum for protons produced by 3000-MeV protons on oxygen.

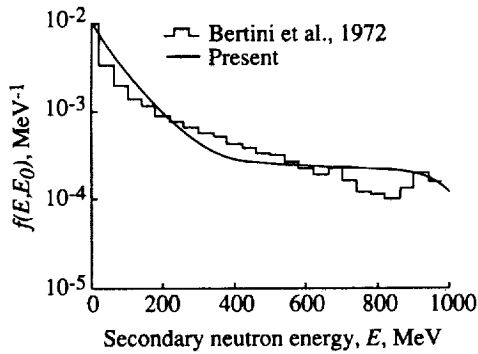


Figure 5.31. Nucleon cascade spectrum for neutrons produced by 1000-MeV protons on oxygen.

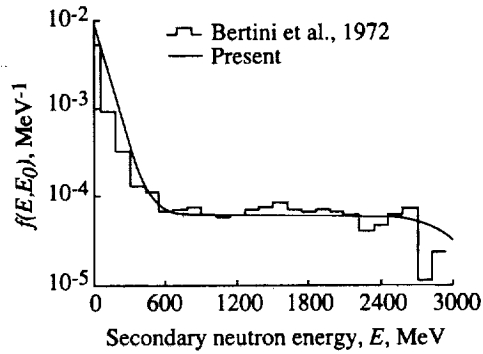


Figure 5.32. Nucleon cascade spectrum for neutrons produced by 3000-MeV protons on oxygen.

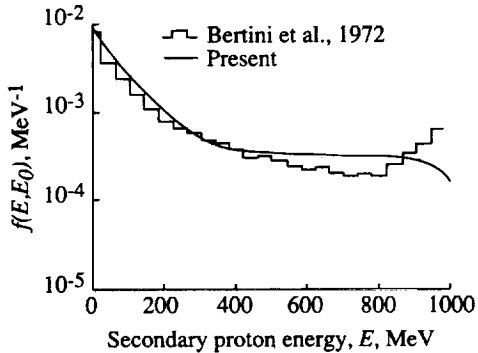


Figure 5.33. Nucleon cascade spectrum for protons produced by 1000-MeV protons on aluminum.

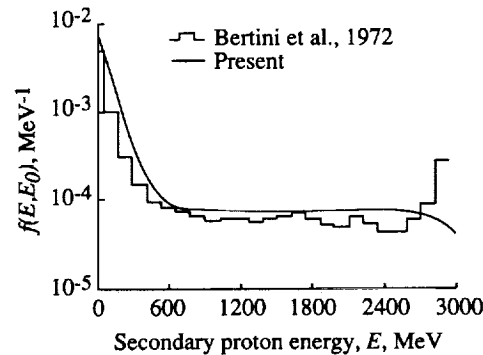


Figure 5.34. Nucleon cascade spectrum for protons produced by 3000-MeV protons on aluminum.

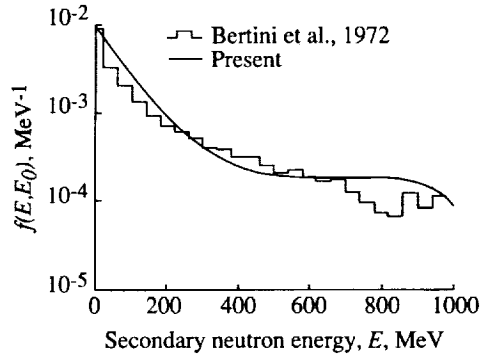


Figure 5.35. Nucleon cascade spectrum for neutrons produced by 1000-MeV protons on aluminum.

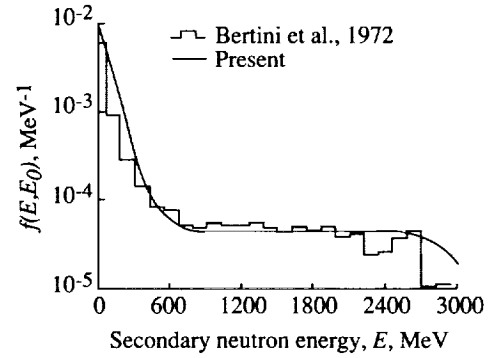


Figure 5.36. Nucleon cascade spectrum for neutrons produced by 3000-MeV protons on aluminum.

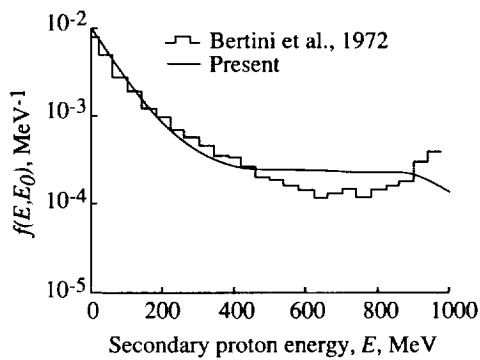


Figure 5.37. Nucleon cascade spectrum for protons produced by 1000-MeV protons on lead.

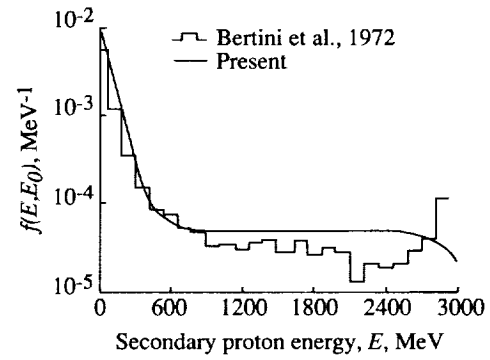


Figure 5.38. Nucleon cascade spectrum for protons produced by 3000-MeV protons on lead.

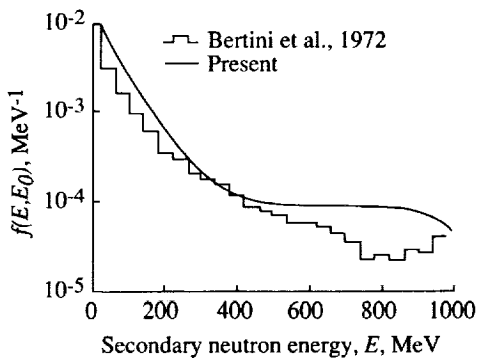


Figure 5.39. Nucleon cascade spectrum for neutrons produced by 1000-MeV protons on lead.

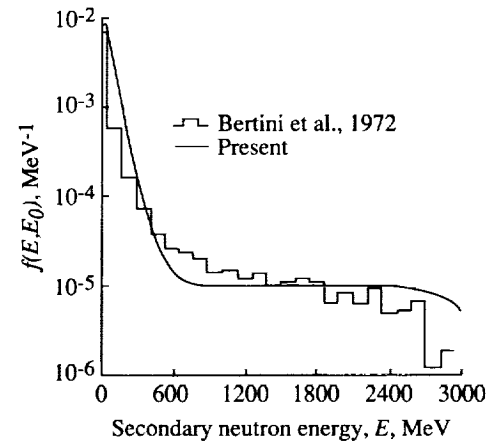


Figure 5.40. Nucleon cascade spectrum for neutrons produced by 3000-MeV protons on lead.

Table 5.15. Evaporated Ion Yields From Nucleon-Nucleus Collisions

[Values in parentheses are for proton reactions]

	Ion yields at—			
	500 MeV	1000 MeV	2000 MeV	3000 MeV
$A_T = 16:$				
d	0.111 (0.094)	0.199 (0.237)	0.257 (0.265)	0.304 (0.311)
t	0.022 (0.029)	0.024 (0.025)	0.033 (0.025)	0.029 (0.029)
he	0.018 (0.034)	0.035 (0.043)	0.037 (0.052)	0.037 (0.048)
α	0.664 (0.400)	0.720 (0.696)	0.666 (0.624)	0.640 (0.667)
$A_T = 27:$				
d	0.126 (0.130)	0.245 (0.269)	0.380 (0.396)	0.442 (0.433)
t	0.028 (0.023)	0.048 (0.052)	0.063 (0.065)	0.072 (0.069)
he	0.042 (0.035)	0.067 (0.074)	0.073 (0.091)	0.083 (0.092)
α	0.370 (0.400)	0.550 (0.566)	0.597 (0.582)	0.577 (0.577)
$A_T = 65:$				
d	0.150 (0.171)	0.379 (0.390)	0.748 (0.766)	0.935 (0.087)
t	0.031 (0.035)	0.075 (0.068)	0.145 (0.145)	0.177 (0.191)
he	0.013 (0.014)	0.039 (0.056)	0.112 (0.124)	0.166 (0.177)
α	0.124 (0.137)	0.231 (0.231)	0.373 (0.377)	0.431 (0.441)
$A_T = 100:$				
d	0.174 (0.183)	0.456 (0.475)	1.01 (1.02)	1.44 (1.48)
t	0.028 (0.029)	0.080 (0.081)	0.207 (0.192)	0.269 (0.273)
he	0.012 (0.017)	0.055 (0.060)	0.162 (0.185)	0.249 (0.262)
α	0.158 (0.156)	0.320 (0.339)	0.490 (0.467)	0.549 (0.540)
$A_T = 207:$				
d	0.131 (0.152)	0.536 (0.565)	1.51 (1.57)	2.54 (2.54)
t	0.038 (0.037)	0.152 (0.163)	0.415 (0.424)	0.641 (0.644)
he	0.001 (0.002)	0.017 (0.017)	0.112 (0.106)	0.211 (0.239)
α	0.053 (0.063)	0.195 (0.210)	0.527 (0.515)	0.751 (0.746)

The first detailed relativistic heavy ion beam experiments were performed by the Heckman group (Heckman, 1975; Greiner et al., 1975; Lindstrom et al., 1975) at the Lawrence Berkeley Laboratory (LBL), in which beams of carbon and oxygen were fragmented on a series of targets ranging from hydrogen to lead. The momentum distribution of the projectile fragments relative to the projectile rest frame was measured for all the isotopes produced. These results will be analyzed to ascertain relevant biological factors with their corresponding implications on radiation risk assessment in high-energy nucleonic radiation fields. An ion fragmentation model will be recommended for use in radiological protection and studies.

Individual nuclear constituents are ejected in the collision of high-energy neutrons and protons by direct collision (Serber, 1947). The remaining nuclear structure is left in an excited state that seeks an equilibrium minimum-energy configuration through particle emission (Rudstam, 1966). This is the basis of Rudstam's study of the systematics of spallation products produced in such collisions in which he assumes that the resultant isotopes are distributed in a bell-shaped distribution near the nuclear stability line. The total change in nuclear mass and the dependence on the incident projectile energy are treated empirically in Rudstam's formalism.

The fragment charge distribution for a given fragment mass A_F is given as

$$f(Z_F) = \exp\left(\rho A_F - r \left| Z_F - s A_F + v A_F^2 \right| \right) \quad (5.157)$$

Table 5.16. Mean Energies of Light Nuclear Fragments Produced in Nucleon-Nucleus Collisions

[Values in parentheses are for proton reactions]

	Mean energies at—			
	500 MeV	1000 MeV	2000 MeV	3000 MeV
$A_T = 16:$				
<i>n</i>	5.55 (6.19)	7.91 (7.89)	9.55 (9.81)	11.1 (9.80)
<i>p</i>	6.10 (6.40)	8.33 (8.69)	9.71 (10.2)	10.3 (11.2)
<i>d</i>	8.53 (7.64)	12.2 (10.7)	14.9 (14.8)	16.3 (13.08)
<i>t</i>	6.40 (7.83)	10.6 (10.4)	12.5 (9.74)	13.7 (10.1)
<i>he</i>	12.1 (8.76)	11.8 (11.2)	11.1 (13.1)	12.9 (10.3)
α	9.36 (6.24)	12.6 (12.3)	13.1 (14.6)	13.6 (13.8)
$A_T = 27:$				
<i>n</i>	5.08 (5.09)	7.34 (7.48)	9.91 (10.5)	11.6 (12.0)
<i>p</i>	6.87 (6.90)	8.61 (8.92)	11.1 (11.9)	13.5 (13.7)
<i>d</i>	9.57 (9.42)	10.8 (11.2)	14.3 (14.8)	17.2 (17.4)
<i>t</i>	9.16 (9.54)	10.8 (11.1)	13.0 (13.9)	16.6 (13.7)
<i>he</i>	10.5 (10.8)	12.5 (12.8)	13.4 (14.1)	14.4 (14.5)
α	12.7 (13.4)	13.2 (13.6)	13.8 (13.8)	14.5 (14.6)
$A_T = 65:$				
<i>n</i>	4.24 (4.32)	5.67 (5.70)	7.92 (7.91)	9.67 (9.58)
<i>p</i>	8.25 (8.30)	9.66 (9.76)	12.1 (12.3)	14.4 (14.2)
<i>d</i>	9.88 (10.1)	13.5 (11.8)	13.8 (14.2)	15.6 (15.9)
<i>t</i>	10.0 (10.5)	11.7 (11.6)	13.7 (13.8)	15.1 (15.9)
<i>he</i>	14.6 (14.1)	16.4 (16.2)	17.5 (19.3)	19.5 (19.2)
α	12.7 (13.4)	13.2 (13.6)	13.8 (13.8)	14.5 (14.6)
$A_T = 100:$				
<i>n</i>	3.90 (3.90)	5.13 (5.16)	7.11 (7.04)	8.61 (8.74)
<i>p</i>	9.63 (9.62)	11.0 (11.0)	12.9 (13.2)	14.6 (14.7)
<i>d</i>	11.0 (11.1)	12.5 (12.6)	14.4 (15.0)	16.1 (16.0)
<i>t</i>	11.3 (11.7)	12.6 (13.0)	14.7 (14.3)	15.5 (16.5)
<i>he</i>	17.8 (18.7)	13.2 (13.6)	13.8 (13.8)	14.5 (14.6)
α	16.5 (16.5)	16.8 (16.9)	17.5 (17.5)	17.6 (17.6)
$A_T = 107:$				
<i>n</i>	3.28 (3.27)	4.37 (4.33)	5.83 (5.78)	6.90 (6.95)
<i>p</i>	12.5 (12.5)	12.2 (13.4)	14.9 (14.9)	16.2 (16.3)
<i>d</i>	13.2 (13.2)	14.4 (14.2)	16.0 (16.8)	17.4 (17.8)
<i>t</i>	13.6 (13.8)	5.0 (15.3)	16.6 (16.8)	17.4 (17.8)
<i>he</i>	24.1 (27.0)	26.2 (26.5)	28.0 (27.8)	29.1 (28.5)
α	25.3 (25.7)	26.0 (26.3)	26.4 (26.3)	25.9 (26.4)

where the coefficients show a slight energy and fragment-mass dependence as

$$\tau = 11.8A_F^{-0.45} \tag{5.158}$$

$$s = 0.486 \tag{5.159}$$

$$\nu = 3.8 \times 10^{-4} \tag{5.160}$$

$$\rho = \begin{cases} 20E^{-0.77} & (E < 2100 \text{ MeV}) \\ 0.056 & (E \geq 2100 \text{ MeV}) \end{cases} \tag{5.161}$$

where E is the nucleon energy. The complete Rudstam cross section is given by

$$\sigma(A_F, Z_F) = \frac{F_1 F_2 \rho A_T^{-0.3} f(Z_F)}{D} \tag{5.162}$$

Table 5.17. Present Correction Factors
for Rudstam's Formula

ΔA	Correction factor for—	
	^{12}C	^{16}O
1	1.3	1.5
2	0.5	1.0
3	0.3	1.0
4	0.1	1.0
5	1.0	1.5
6	0.35	0.5
7		0.5
8		0.1
9		2.5
10		1.0

where

$$D = 1.79 \left[\exp(\rho A_T) \left(1 - \frac{0.3}{\rho A_T} \right) - \frac{0.3}{A_T} + \frac{0.3}{\rho A_T} \right] \quad (5.163)$$

$$F_1 = 5.18 \exp(-0.25 + 0.0074 A_T) \quad (5.164)$$

$$F_2 = \begin{cases} \exp(1.73 - 0.0071 E) & (E < 240 \text{ MeV}) \\ 1 & (E \geq 240 \text{ MeV}) \end{cases} \quad (5.165)$$

We have applied a simple mass-dependent correction factor to Rudstam's formula as shown in table 5.17 and renormalized his cross sections to the total absorption cross section. Many corrective factors have been added to Rudstam's formalism by Silberberg, Tsao, and Shapiro (1976). Estimates have also been made by Guzik (1981) for some of the isotopes produced in connection with cosmic-ray propagation studies with some attempts at experimental verification (Guzik et al., 1985).

From a nuclear model point of view, isotope production at low energy results from the formation of a compound nuclear state that decays through particle emission. At higher energies, the direct ejection of particles from the nucleus becomes important, and intranuclear cascades represented as sequences of two-body scatterings within the nucleus with Pauli blocking are the usual means of evaluation. Subsequent to the cascade, the residual nucleus is assumed to be in thermal equilibrium and seeks to minimize its internal energy through particle emission.

The measurement of isotope production cross sections at proton accelerators does not allow the direct observation of the fragment products. Customary

measurements used γ or β counting techniques to identify the isotopes produced. Stable and short-lived isotopes produced in the reactions were either not observed or their number was greatly distorted by loss through decay.

This is particularly true for light-mass targets such as those that are important to biological health considerations. Consequently, the fragmentation of carbon and oxygen nuclei by protons remained shrouded in experimental obscurity until the advent of heavy ion accelerators.

One of the earliest experiments performed at the Lawrence Berkeley Laboratory Bevatron, when the ions of carbon and oxygen could be accelerated to relativistic energies, used detectors able to measure the energy and charge of an ion beam in conjunction with a bending magnet for momentum analysis (Heckman, 1975). In this way, the density in phase space was measured for each isotope produced in collision with a fixed target.

The isobar cross section (σ_{LBL}) measured by Lindstrom et al. (1975) for 2.1 GeV/nucleon oxygen fragmentation on hydrogen targets is given in table 5.18 along with the results of the Bertini MECC-7 code (Anon., 1968), Rudstam (1966), and Silberberg, Tsao, and Shapiro (1976). Note that the Rudstam results contain the correction factors from table 5.17 and are renormalized as described previously.

The oxygen-fragmentation cross sections represented by three parametric forms are shown in figures 5.41 to 5.45 along with the Bertini results and various experiments. The baryon-15 isobaric cross sections in figure 5.41 show that experiments favor the curve of Silberberg, Tsao, and Shapiro, 1976. Although the Bertini model provides an overestimate, the other parametric curves provide improved estimates compared with the Bertini code. The baryon-14 isobaric experimental cross sections are in reasonable agreement with the three parametric curves as well as with the Bertini model as seen in figure 5.42. Again, the experiments show no clear advantage of one parametric curve over another for the baryon-13 cross section as seen in figure 5.43, although the Bertini results appear somewhat low. We show experimental results for baryon numbers between 9 and 14 of the LBL Group (Lindstrom et al., 1975) in table 5.18. Clearly, the equally good agreement for the Rudstam parameterization and the parameterization of Silberberg, Tsao, and Shapiro is obtained for baryon numbers 12, 11, and 10. The Bertini cross section is far too low to represent the cross section for baryon-11. The baryon-9 cross sections are shown in figure 5.44. (The results of Yiu are reported in Guzik, 1981.) The cross sections of Silberberg, Tsao, and Shapiro are favored. The baryon-7 cross sections are shown in figure 5.45. At energies below 300 MeV, the baryon-7 results of Silberberg, Tsao, and Shapiro are favored.

The measurements of Lindstrom et al. (1975) for relativistic carbon beams are shown along with the results from Rudstam and Silberberg, Tsao, and Shapiro in table 5.19 for two beam energies. The good agreement with the results of Silberberg, Tsao, and Shapiro is no surprise, because their parameterization was fit to these experimental data sets.

Table 5.18. Oxygen Fragmentation Cross Sections

A_F	Fragmentation cross section, σ , mb, from—			
	Bertini (a)	LBL (b)	Present	NRL (c)
16	7.0	0.02	8.7	
15	85.1	61.5	61.0	59.4
14	39.0	35.4	32.6	32.2
13	13.9	22.8	29.7	17.7
12	28.1	34.1	27.9	36.0
11	5.0	24.4	31.4	19.9
10	9.1	12.7	12.0	11.0
9	1.0	5.2	7.1	12.1
8	0.2	1.23	2.1	14.7
7	1.1	22.2	27.8	19.4
6	3.8	13.9	18.0	16.7
Total	193.3	235.5	258.3	239.1

^a Anon., 1968.

^b Heckman et al., 1975.

^c Silberberg, Tsao, and Shapiro, 1976.

5.7.4. Heavy-fragment spectrum. Following the direct ejection of nucleons in nuclear collision, the nucleus is left in a highly excited state that decays through particle emission. From a sudden approximation point of view, as proposed by Serber (1947), the momentum distribution of the decay particles is governed by the Fermi distribution before collision. The collective momentum of decay products and nuclear fragments is thus derived on the basis of combinatorial rules on the random ways in which a given fragment mass can be formed from the nucleon distributions before collision. The formulation of Goldhaber (1974) is physically meaningful and simplistic. The momentum distribution is Gaussian in momentum space with a momentum width parameter given by

$$\sigma_p = \sigma_0 \left[\frac{A_F(A_T - A_F)}{(A_T - 1)} \right]^{1/2} \quad (5.166)$$

where σ_0 is the usual mean fermi momentum of the struck nucleus. However, the σ_0 of nuclear fragmentation is found to be about 25-percent smaller than that observed in electron scattering experiments (Greiner et al., 1975). The mean Fermi momentum is a slowly varying function of nuclear mass.

A slight modification of Goldhaber's results is found to adequately represent the experimental results of Greiner et al. (1975) given by

$$\sigma_p = 0.8b \left[\frac{4\delta_A}{20(A_T - 1)} \right]^{1/2} \quad (5.167)$$

Table 5.19. Carbon Fragmentation Cross Sections
(a) ^{12}C at 1000 MeV/nucleon

A_F	Fragmentation cross section, σ , mb, from—		
	LBL (a)	Present	NRL (b)
12	0.1	6.7	0
11	55.3	63.2	69.0
10	22.7	28.0	22.0
9	5.8	10.0	15.2
8	1.4	4.8	26.0
7	18.9	21.7	20.7
6	12.4	14.7	16.9
Total	116.6	149.1	169.8

^a Heckman et al., 1975.

^b Silberberg, Tsao, and Shapiro, 1976.

(b) ^{12}C at 2000 MeV/nucleon

A_F	Fragmentation cross section, σ , mb, from—		
	LBL (a)	Present	NRL (b)
12	0.09	6.2	0
11	57.0	60.4	58.5
10	22.7	27.8	20.5
9	6.20	10.4	14.2
8	1.6	5.2	24.1
7	20.49	24.4	19.9
6	14.8	17.2	16.7
Total	122.9	151.6	153.9

^a Heckman et al., 1975.

^b Silberberg, Tsao, and Shapiro, 1976.

where the parameters b and δ_A are given, respectively, by

$$b = \min(112A_T^{1/2}, 260) \quad (5.168)$$

and

$$\delta_A = \begin{cases} 0.45 & (A_T = A_F) \\ A_T - A_F & (\text{Otherwise}) \end{cases} \quad (5.169)$$

A comparison of formulas (5.167) through (5.169) with experiments and the parameterization of Greiner et al. is given in table 5.20. Clearly, the present formulas are quite accurate.

The spectral distributions of the nuclear fragments in the rest frame of the struck nucleus before collision are given by

$$\frac{d\sigma_f}{dE} = \frac{\sigma_f}{(2\pi E_0^3)^{1/2}} E^{1/2} \exp\left(\frac{-E}{2E_0}\right) \quad (5.170)$$

where σ_f is the fragmentation cross section and the energy parameter is

$$E_0 = \frac{3\sigma_p^2}{2A_F} \quad (5.171)$$

The average energies $\bar{E}(= 3E_0)$ of various fragments obtained by equations (5.167) through (5.171) and the results of the Bertini model are presented in table 5.21. Generally, the average energies predicted by the Bertini model are reasonably accurate, although some specific isotopes differ by a factor of 2 or more.

5.7.5. Energy-transfer cross section. The energy-loss spectrum $\psi_j(\vec{x}, \vec{\Omega}, E)$ of the ion fragment j may be written as (Wilson, 1977)

$$\psi_j(\vec{x}, \vec{\Omega}, E) \approx A_j \zeta_j(\vec{x}) \int_E^{E_\gamma} \left(\frac{m}{2\pi\sigma_p^2}\right)^{3/2} \sqrt{2E'} \exp\left(\frac{-mE'}{\sigma_p^2}\right) dE' \quad (5.172)$$

where A_j is the fragment mass number, $\zeta_j(\vec{x})$ is the fragment source, and E_γ is related to the distance to the boundary along the direction $\vec{\Omega}$ as given elsewhere by Wilson (1977). For distances far from the boundary, one may take $E_\gamma = \infty$. The cumulative energy-loss spectrum far from the boundary ($E_\gamma = \infty$) is

$$D_j(\vec{x}, E) = 4\pi \int_E^\infty \psi_j(\vec{x}, \vec{\Omega}, E') dE' \quad (5.173)$$

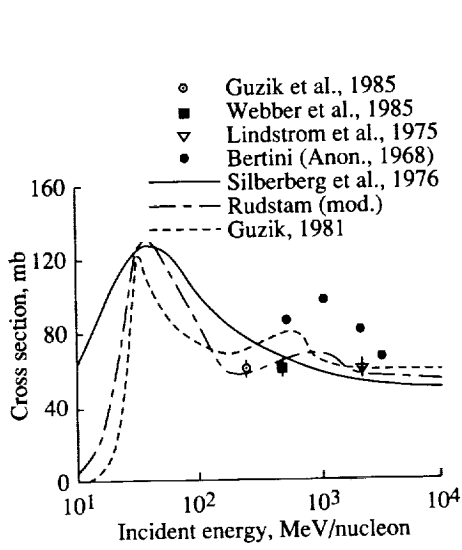


Figure 5.41. Oxygen fragmentation cross sections for baryon-15 isobars in proton collisions.

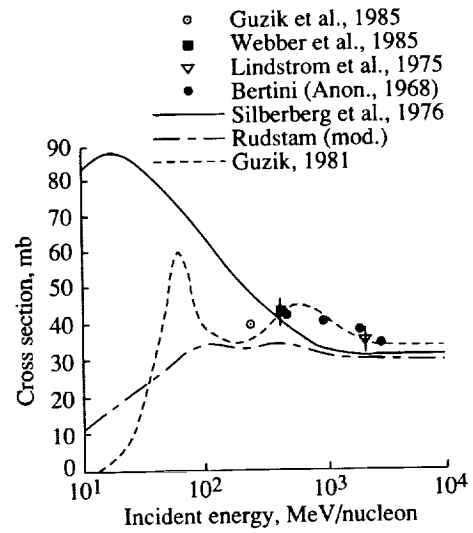


Figure 5.42. Oxygen fragmentation cross sections for baryon-14 isobars in proton collisions.

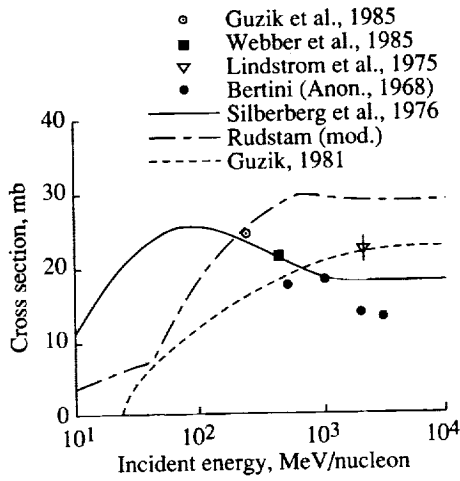


Figure 5.43. Oxygen fragmentation cross sections for baryon-13 isobars in proton collisions.

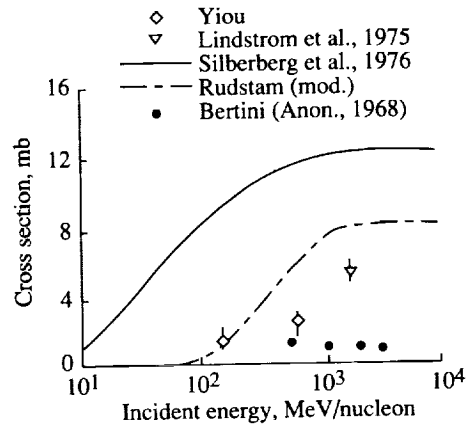


Figure 5.44. Oxygen fragmentation cross sections for baryon-9 isobars in proton collisions.

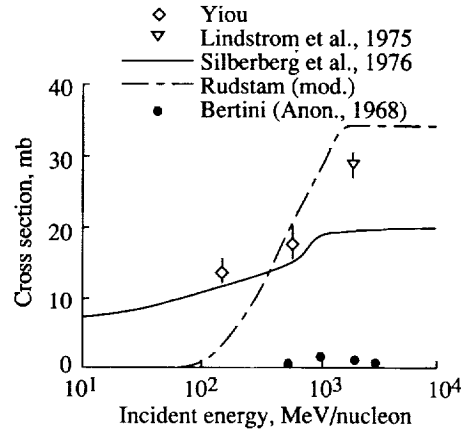


Figure 5.45. Oxygen fragmentation cross sections for baryon-7 isobars in proton collisions.

Table 5.20. σ_p for ^{16}O Fragments Produced by 2.1-GeV Protons

Fragment	σ_p , MeV/c, from—		
	Experiments	Present work	Greiner et al., 1975
^{15}O	94 ± 3	80.0	83.8
^{14}O	99 ± 6	109.5	113.1
^{13}O	143 ± 14	129.2	133.5
^{16}N	54 ± 11	55.0	
^{15}N	95 ± 3	80.0	
^{14}N	112 ± 3	109.5	113.0
^{13}N	134 ± 2	129.2	133.5
^{12}N	153 ± 11	143.4	148.1
^{15}C	125 ± 19	80.0	82.8
^{14}C	125 ± 3	109.5	113.10
^{13}C	130 ± 3	129.2	133.5
^{12}C	120 ± 4	143.36	148.09
^{11}C	162 ± 5	153.45	158.5
^{10}C	190 ± 9	160.3	165.6
^{13}B	166 ± 10	129.2	133.5
^{12}B	163 ± 8	143.4	148.1
^{11}B	160 ± 2	153.5	158.5
^{10}B	175 ± 7	160.3	165.6
^8B	175 ± 22	165.5	171.0
^{11}Be	197 ± 20	153.5	158.5
^{10}Be	159 ± 6	160.0	165.0
^9Be	166 ± 7	164.24	169.66
^7Be	166 ± 2	164.24	169.66
^9Li	188 ± 15	164.24	169.66
^8Li	170 ± 13	165.4	171.0
^7Li	163 ± 4	164.24	169.66
^6Li	141 ± 7	160.0	169.66
^6He	167 ± 20	160.0	165.0

Table 5.21. Average Recoil Energy \bar{E} of ^{16}O Fragments
Produced by 2.1-GeV Protons

Fragment	Average energy, \bar{E} , MeV, from—		
	Bertini (Anon., 1968)	Present results	Experiments
^{16}F	2.65	1.01	
^{15}F	4.19	.69	
^{16}O	1.05	1.012	1.01
^{15}O	.52	.69	.88
^{14}O	1.82	1.37	1.12
^{13}O	4.24	2.05	2.51
^{16}N	1.11	1.01	.30
^{15}N	.63	.69	.96
^{14}N	1.12	1.37	1.42
^{13}N	1.84	2.05	2.20
^{12}N	3.85	2.74	3.11
^{11}N	5.95	3.42	3.64
^{14}C	1.62	1.34	1.78
^{13}C	1.97	2.05	2.07
^{12}C	2.64	2.74	1.91
^{11}C	4.70	3.42	3.81
^{10}C	5.58	4.11	5.76
^9C	4.41	4.79	5.10
^{13}B	2.35	2.05	3.38
^{12}B	3.43	2.74	3.53
^{11}B	4.33	3.71	3.42
^{10}B	4.79	4.11	4.89
^9B	1.19	4.79	
^{10}Be	4.53	4.11	4.03
^9Be	8.76	4.79	4.89
^{10}Li	4.61	4.11	
^9Li	2.26	4.79	6.27
^8Li	4.41	5.48	5.76
^7Li	4.75	6.16	6.06
^6Li	5.76	6.85	5.29

Table 5.22. Fragment Energy-Transfer Cross Sections

A_F	Energy-transfer cross sections, $\bar{E}\sigma$, MeV-mb, from—		
	Bertini	Greiner et al., 1975	Present
16	5.04	0.0006	0.26
15	60.6	56.9	56.4
14	48.8	48.3	62.9
13	37.6	48.3	62.9
12	85.8	68.2	55.8
11	37.9	99.1	117.9
10	52.8	62.0	58.6
9	6.5	25.7	35.1
8	2.5	7.1	12.1
7	6.11	121.7	152.4
6	31.4	73.4	95.1
Total	375.1	614.1	694.2

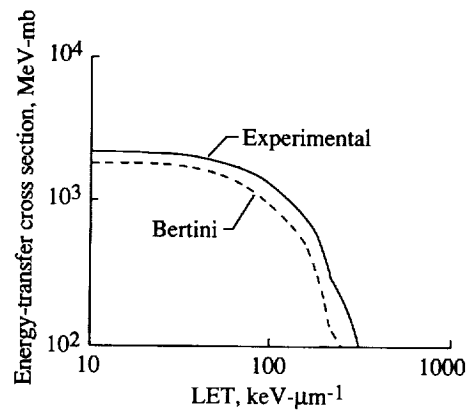


Figure 5.46. Linear energy-transfer (LET) cross section for fragmenting oxygen nucleus in water.

for which the distribution in linear energy transfer (LET) of energy deposit can be found. The total energy absorbed is given by

$$\begin{aligned}
 D(\vec{x}) &= \sum_j D_j(\vec{x}, 0) \\
 &\approx \sum_j E_j \sigma_j \rho \phi
 \end{aligned}
 \tag{5.174}$$

where E_j is the average energy of the fragment j , σ_j is the fragmentation cross section, ρ is the target density, and ϕ is the effective nucleon flux initiating the fragmentation events. The energy-transfer cross section of the various fragment components is $E_j \sigma_j$ and is shown in table 5.22 for the Rudstam parameterization (present results), Bertini data, and experiments of the Heckman group (Greiner et al., 1975) for comparison. Equations (5.172) through (5.174) also provide a basis for resolving the energy-transfer cross section into its various LET components. The LET components of equation (5.173) are shown in figure 5.46 for $\rho = \phi = 1$ for all contributions with a fragment charge greater than 1. The two curves shown in the figure are for the Bertini data and the experiments of the Heckman group. Results obtained with our modified Rudstam formalism and the parameterized momentum distributions are virtually indistinguishable from the curve based on the LBL experiments. The results shown in figure 5.46 clearly show that estimates of exposure from heavy ion recoil nuclei in tissue based on Bertini cross sections are generally low.

5.7.6. Heavy ion fragmentation model. In the abrasion-ablation fragmentation model, the projectile nuclei, moving at relativistic speeds, collide with stationary target nuclei. In the abrasion step, those portions of the nuclear volumes that overlap are sheared away by the collision. The remaining projectile piece, called a prefragment or primary residue, continues its trajectory with essentially its precollision velocity. As a result of the dynamics of the abrasion process, the prefragment is highly excited and subsequently decays by the emission of gamma radiation and/or nuclear particles. This step is the ablation stage. The resultant isotope, sometimes referred to as a secondary product, is the nuclear fragment whose cross section is measured. The abrasion process can be analyzed with classical geometric arguments (Bowman, Swiatecki, and Tsang, 1973) or methods obtained from formal quantum scattering theory (Townsend et al., 1986a and 1986b). The ablation stage can be analyzed from geometric arguments (Bowman, Swiatecki, and Tsang, 1973) or more sophisticated methods based upon Monte Carlo or intranuclear cascade techniques (Gosset et al., 1977; Hüfner, Schäfer, and Schürmann, 1975; Morrissey et al., 1978; Guthrie, 1970). Predictions of fragmentation cross sections can also be made with the approximate semiempirical parameterization formulas of Silberberg, Tsao, and Shapiro (1976). The present data base uses the method of Wilson, Townsend, and Badavi (1987b).

The amount of nuclear material stripped away in the collision of two nuclei is taken as the volume of overlap region times an average attenuation factor. The relevant formula for the constituents in the overlap volume in the projectile is

given by the following formula:

$$\Delta_{\text{abr}} = FA_P \left[1 - \frac{1}{2} \exp\left(\frac{-C_P}{\lambda}\right) - \frac{1}{2} \exp\left(\frac{-C_T}{\lambda}\right) \right] \quad (5.175)$$

where C_P and C_T are the maximum chord lengths of the intersecting surface in the projectile and the target, respectively, and the expressions for F differ depending on the nature of the collision (peripheral versus central) and the relative sizes of the colliding nuclei. The value for F is given by equations (5.38) through (5.50). The charge ratio of removed nuclear matter is assumed to be that of the parent nucleus.

The surface distortion excitation energy of the projectile prefragment following abrasion of m nucleons is calculated from the clean-cut abrasion formalism of Bowman, Swiatecki, and Tsang (1973). For this model, the colliding nuclei are assumed to be uniform spheres of radii R_i ($i = P, T$). In the collision, the overlapping volumes shear off so that the resultant projectile prefragment is a sphere with a cylindrical hole gouged out of it. The excitation energy is then determined by calculating the difference in surface area between the misshapen sphere and a perfect sphere of equal volume. This excess surface area ΔS is given by Gosset et al. (1977) as

$$\Delta S = 4\pi R_p^2 \left[1 + P - (1 - F)^{2/3} \right] \quad (5.176)$$

where the expressions for P and F differ depending upon the nature of the collision (peripheral versus central) and the relative sizes of the colliding nuclei which were given in section 5.3.2. (See eqs. (5.38) through (5.50).)

The excitation energy associated with surface energy is well-known to be 0.95 MeV/fm² for near equilibrium nuclei so that

$$E'_s = 0.95\Delta S \quad (5.177)$$

for small surface distortions. When large numbers of nucleons are removed in the abrasion process, equation (5.177) is expected to be an underestimate to the actual excitation. We therefore introduce an excess excitation factor in terms of the number of abraded nucleons Δ_{abr} as

$$f = 1 + \frac{10\Delta_{\text{abr}}}{A_P} + \frac{25\Delta_{\text{abr}}^2}{A_P^2} \quad (5.178)$$

which approaches 1 when the impact parameter is large but increases the excess excitation when large portions of the nuclei are removed in the collisions and when grossly misshapened nuclei are formed. The total excitation energy is then

$$E_s = E'_s f \quad (5.179)$$

which reduces to equation (5.177) for small Δ_{abr} . We assume that all fragments with a mass of 5 are unbound, that 90 percent of the fragments with a mass of 8

are unbound, and that 50 percent of the fragments with a mass of 9 (^9B) are unbound.

A secondary contribution to the excitation energy is the transfer of kinetic energy of relative motion across the intersecting boundary of the two ions. The rate of energy loss of a nucleon when it passes through nuclear matter (Westfall et al., 1979) is taken at 13 MeV/fm, and the energy deposit is assumed to be symmetrically dispersed about the azimuth so that 6.5 MeV/nucleon-fm at the interface is the average rate of energy transfer into excitation energy. This energy is transferred in single particle collision processes, and on half of the events, the energy is transferred to excitation energy of the projectile and the remaining half of the events leaves the projectile excitation energy unchanged. The first estimate of this contribution is to use the length of the longest chord C_1 in the projectile surface interface. This chord length is the maximum distance traveled by any target constituent through the projectile interior. The number of other target constituents in the interface region may be found by estimating the maximum chord C_t transverse to the projectile velocity which spans the projectile surface interface. The total excitation energy from excess surface and spectator interaction is then

$$E'_x = 13C_1 + \frac{1}{3} 13C_1(C_t - 1.5) \quad (5.180)$$

where the second term only contributes if $C_t > 1.5$ fm. We further assume that the effective longitudinal chord length for these remaining nucleons is one third the maximum chord length.

The decay of highly excited nuclear states is dominated by heavy particle emission. In the present model, we assume that a nucleon is removed for every 10 MeV of excitation energy as

$$\Delta_{\text{abl}} = \frac{(E_s + E_x)}{10 \text{ MeV}} \quad (5.181)$$

In accordance with the previously discussed directionality of the energy transfer, E_x is double valued as

$$E_x = \left\{ \begin{array}{ll} E'_x & (P_x = \frac{1}{2}) \\ 0 & (P_{\bar{x}} = \frac{1}{2}) \end{array} \right\} \quad (5.182)$$

where P_j is the corresponding probability of occurrence of each value in collisions.

The number of nucleons removed through the abrasion-ablation process is given as a function of impact parameter as

$$\Delta A = \Delta_{\text{abr}}(b) + \Delta_{\text{abl}}(b) \quad (5.183)$$

The values of ΔA for carbon projectiles on a copper target and for copper projectiles on a carbon target are shown in figure 5.47. In each case, the dashed curve corresponds to $E_x = 0$, whereas the solid curve corresponds to $E_x = E'_x$ as given by equation (5.180). A real collision would be given by a statistical distribution between the limits shown by these two curves. The average event

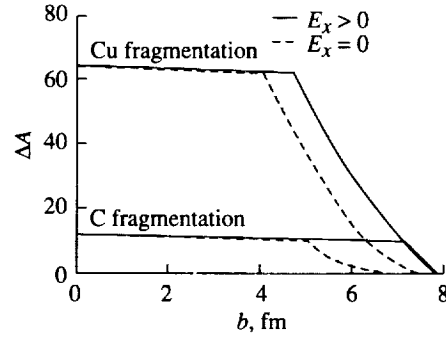


Figure 5.47. Nucleon removal number as function of impact parameter in carbon-copper collisions.

is calculated as if the two extremes occurred with equal probability, as noted in equation (5.182).

The nuclear fragmentation parameters herein are approximated according to the abrasion-ablation model of Bowman, Swiatecki, and Tsang (1973). The cross section for removal of ΔA nucleons is estimated as

$$\sigma(\Delta A) = \pi b_2^2 - \pi b_1^2 \quad (5.184)$$

where b_2 is the impact parameter for which the volume of intersection of the projectile contains Δ_{abr} nucleons and the resulting excitation energies release an additional Δ_{abl} nucleons at the rate of 1 nucleon for every 10 MeV of excitation such that

$$\Delta_{\text{abr}}(b_2) + \Delta_{\text{abl}}(b_2) = \Delta A - \frac{1}{2} \quad (5.185)$$

and similarly for b_1

$$\Delta_{\text{abr}}(b_1) + \Delta_{\text{abl}}(b_1) = \Delta A + \frac{1}{2} \quad (5.186)$$

The charge distributions of the final projectile fragments are strongly affected by nuclear stability. We expect that the Rudstam (1966) charge distribution for a given $\sigma(\Delta A)$ to be reasonably correct as

$$\sigma(A_F, Z_F) = F_1 \exp \left[-R \left| Z_F - S A_F + T A_F^2 \right|^{3/2} \right] \sigma(\Delta A) \quad (5.187)$$

where $R = 11.8/A_F^D$, $D = 0.45$, $S = 0.486$, and $T = 3.8 \times 10^{-4}$ according to Rudstam and F_1 is a normalizing factor such that

$$\sum_{Z_F} \sigma(A_F, Z_F) = \sigma(\Delta A) \quad (5.188)$$

The Rudstam formula for $\sigma(\Delta A)$ was not used because the ΔA dependence is too simple and breaks down for heavy targets (Townsend et al., 1984; Townsend, Wilson, and Norbury, 1985).

The charge of the removed nucleons ΔZ is calculated according to charge conservation

$$Z_P = Z_F + \Delta Z \quad (5.189)$$

and is divided among the nucleons and α -particles according to the following rules. The abraded nucleons are those removed from that portion of projectile in the overlap region with the target. Therefore, the abraded nucleon charge is assumed to be proportional to the charge fraction of the projectile nucleus as

$$Z_{abr} = \frac{Z_P \Delta_{abr}}{A_P} \quad (5.190)$$

This, of course, ignores the charge separation caused by the giant dipole resonance model of Morrissey et al. (1978). The charge release in the ablation is then given as

$$Z_{abl} = \Delta Z - Z_{abr} \quad (5.191)$$

which simply conserves the remaining charge.

The α -particle is known to be unusually tightly bound in comparison with other arrangements of nucleons. Because of this unusually tight binding of the α -particle, the helium production is maximized in the ablation process

$$N_\alpha = \text{int} \left(\frac{Z_{abl}}{2} \right) \quad (5.192)$$

where $\text{int}(x)$ denotes the integer part of x . The number of protons produced is given by charge conservation as

$$N_P = \Delta Z - 2N_\alpha \quad (5.193)$$

Similarly, neutral conservation requires the number of neutrons produced to be

$$N_n = \Delta A - N_P - 4N_\alpha \quad (5.194)$$

The fragments with masses of 2 and 3 are ignored.

The calculation is performed for $\Delta A = 1$ to $\Delta A = A_P - 1$, for which the cross section associated with $\Delta A > A_P - 0.5$ is missed. These are, of course, the central collisions for which it is assumed that the projectile disintegrates into single nucleons if $R_P < R_T$ as

$$N_P = Z_P \quad (5.195)$$

$$N_n = A_P - Z_P \quad (5.196)$$

and is ignored otherwise. The energetic target fragments as well as the mesonic components are being ignored. The peripheral collisions with $\Delta A < 0.5$ are also missing. Most important in these near collisions will be the coulomb dissociation process studied by Norbury and Townsend (1986).

Only the nuclear radius for use in the model is yet undefined. The nuclear absorption cross sections are taken as energy independent and are approximated by Townsend and Wilson (1986) as

$$\sigma(A_1, A_2) = \pi r_0^2 \left(A_1^{1/3} + A_2^{1/3} - 0.2 - A_1^{-1} - A_2^{-1} \right)^2 \quad (5.197)$$

where $r_0 = 1.26$ fm. Equation (5.197) is an accurate representation of the high-energy cross sections. The choice of nuclear radius as

$$R = 1.26A^{1/3} \quad (5.198)$$

is consistent with equation (5.197) when the peripheral collisions ($\Delta A < 0.5$) are taken into account. This completes the description of the basic fragmentation model in present use.

In the present evaluation, we look only to elemental fragmentation cross sections for which most of the experimental data have been obtained. This is also motivated by the crudeness of the present model which is not expected to be completely accurate. Even so, the quality of the experimental data base is uncertain with experiments of different groups differing by a factor of 2, in general, and differing even more for specific isotopes.

The first comparison is with the experiments of Heckman (1975) with ^{12}C ion beams at 1.05 GeV/nucleon on the series of targets extending from hydrogen to lead as shown in table 5.23. The present calculations are shown as values in parentheses. The calculated values for hydrogen targets are those of Rudstam. Note that all values are within 20 percent of the experiments with few exceptions (namely, fragments from hydrogen targets and the neutron removal cross section in copper and lead targets).

The charge removal cross sections for several projectiles on carbon targets are given in table 5.24. The agreement between the present model and the Lawrence Berkeley Laboratory groups (Heckman, 1975; Westfall et al., 1979) is quite good. Our results tend to be low compared with the experiments of Webber et al. (1983a and 1983b) and Guerreau et al. (1983). The model can be adjusted once experimental differences are resolved.

The elemental fragmentation cross section of iron projectiles on several targets is shown in table 5.25. Again, reasonable agreement is found generally with a few examples of relatively large errors. The bracketed quantities at the bottom of the table are the coulomb dissociation cross sections for forming manganese. These are to be added to the nuclear fragmentation cross sections for manganese in parentheses before comparing with experimental values.

Comparing the model cross sections with the experimental data set reveals that 92 percent of the calculated cross sections are within 50 percent of the measured values. If we reduce the error band to 30 percent, we will find 81 percent of the cross sections are in agreement to within this level. Among the least accurate are the iron on hydrogen target data which again is Rudstam's theory and the cross

Table 5.23. Fragmentation Cross Sections of Carbon Beams at 1.05 GeV/nucleon in Various Targets

[Quantities in parentheses are present theory]

Fragment	Carbon cross section, ^a mb, in target of—				
	H (b)	Be	C	Cu	Pb
Li	23 ± 2 (34)	51 ± 2 (54)	52 ± 3 (61)	71 ± 5 (81)	103 ± 14 (113)
Be	17 ± 1 (22)	35 ± 1 (32)	35 ± 1 (33)	47 ± 2 (48)	71 ± 6 (63)
B	50 ± 4 (42)	81 ± 4 (86)	78 ± 3 (100)	119 ± 8 (138)	203 ± 32 (185)
C	28 ± 3 (10)	49 ± 3 (39)	50 ± 4 (44)	86 ± 8 (57)	139 ± 22 (79)

^a Heckman, 1975.

^b Values in parentheses in this column are those of modified Rudstam (1966).

Table 5.24. Charge Removal Cross Sections of Various Projectiles on Carbon Targets

[Quantities in parentheses are present theory; number in brackets is energy in GeV/nucleon]

ΔZ	Charge removal cross section, mb, of projectile of—					
	C [2.1] (a)	O [2.1] (a)	O [0.9] (b)	Ne [0.47] (b)	Ar [0.21] (c)	Fe [1.88] (d)
0	50 ± 4 (40)	45 ± 2 (45)	-----	----- (40)	----- (132)	----- (64)
1	78 ± 3 (100)	105 ± 4 (101)	176 ± 5	129 ± 3 (90)	----- (151)	181 ± 27 (157)
2	35 ± 1 (33)	116 ± 6 (93)	164 ± 5	214 ± 3 (98)	154 ± 26 (85)	124 ± 13 (110)
3	52 ± 2 (61)	50 ± 2 (65)	55 ± 3	155 ± 3 (75)	122 ± 16 (72)	100 ± 11 (87)
4		36 ± 1 (24)	27 ± 2	140 ± 3 (65)	144 ± 19 (64)	87 ± 11 (76)
5		65 ± 3 (47)	-----	74 ± 2 (54)	81 ± 15 (59)	54 ± 9 (62)
6				33 ± 1 (19)	112 ± 15 (51)	78 ± 11 (67)
7				----- (40)	90 ± 3 (50)	52 ± 7 (57)
8					92 ± 13 (44)	55 ± 9 (52)
9					65 ± 11 (42)	53 ± 7 (49)
10					83 ± 13 (37)	54 ± 10 (45)
11					----- (35)	59 ± 10 (42)
12						57 ± 10 (39)
13						83 ± 11 (36)
14						----- (35)

^a Heckman, 1975.

^b Webber et al., 1983a and 1983b.

^c Guerreau et al., 1983.

^d Westfall et al., 1979.

sections of Webber et al. Note that our model agrees with experiments to the extent that the experimentalists agree among themselves for the same projectile-target combinations. From this point of view, little progress can be made in

Table 5.25. Fragmentation Cross Section of Iron Projectiles at 1.88 GeV/nucleon in Various Targets

[Quantities in parentheses are values from present model; values in square brackets are coulomb dissociation cross sections for forming manganese]

		Cross section, mb, of iron projectiles in—										
Z_F	H	Li	Be	C	S	Cu	Ag	Ta	Pb	U		
13	25±10 (19)	50±5 (33)	50±7 (34)	83±11 (36)	78±18 (45)	179±27 (57)	112±19 (64)	81±14 (72)	191±34 (74)	307±79 (77)		
14	31±9 (22)	54±5 (36)	75±8 (37)	57±10 (39)	106±14 (47)	72±11 (61)	158±20 (67)	115±20 (75)	119±22 (77)	169±28 (80)		
15	22±10 (26)	57±6 (39)	57±8 (38)	59±10 (42)	50±8 (51)	88±15 (63)	64±13 (70)	133±20 (79)	78±16 (81)	176±34 (84)		
16	37±24 (30)	56±6 (43)	63±8 (45)	54±10 (45)	74±12 (54)	56±11 (67)	96±13 (74)	109±17 (82)	116±19 (85)	116±22 (88)		
17	36±18 (36)	38±4 (44)	54±7 (48)	53±7 (49)	66±14 (58)	86±13 (71)	79±14 (79)	101±18 (87)	90±19 (90)	133±22 (93)		
18	31±9 (41)	55±6 (49)	54±7 (51)	55±9 (52)	74±13 (62)	95±15 (76)	84±14 (83)	100±18 (94)	73±15 (95)	113±19 (98)		
19	36±9 (47)	56±5 (53)	65±7 (55)	52±7 (57)	55±21 (66)	88±14 (81)	79±11 (89)	111±20 (98)	90±19 (101)	105±15 (104)		
20	47±11 (55)	64±6 (59)	68±7 (60)	78±11 (67)	97±14 (72)	98±14 (87)	118±14 (96)	107±17 (106)	144±22 (109)	143±19 (112)		
21	62±11 (65)	67±6 (64)	77±8 (66)	54±9 (62)	91±13 (79)	100±15 (95)	104±13 (104)	129±18 (116)	111±17 (118)	153±21 (122)		
22	22±13 (77)	75±6 (71)	83±9 (74)	87±11 (76)	64±10 (89)	101±14 (106)	124±16 (116)	152±19 (129)	148±22 (132)	95±16 (136)		
23	60±11 (88)	88±7 (83)	88±9 (84)	100±11 (87)	86±12 (103)	121±15 (121)	117±15 (132)	150±19 (146)	142±20 (151)	181±27 (156)		
24	80±13 (101)	98±7 (101)	111±9 (105)	124±13 (110)	128±16 (126)	149±16 (146)	218±21 (161)	206±22 (176)	242±25 (181)	208±22 (190)		
25	127±24 (119)	141±18 (147)	156±21 (154)	181±27 (157)	250±22 (182)	219±20 (208)	280±23 (228)	457±34 (250)	509±40 (256)	646±43 (260)		
	[0]	[1]	[1]	[3]	[15]	[42]	[97]	[211]	[258]	[316]		

^a Values in parentheses in this column are those of Rudstam (1966).

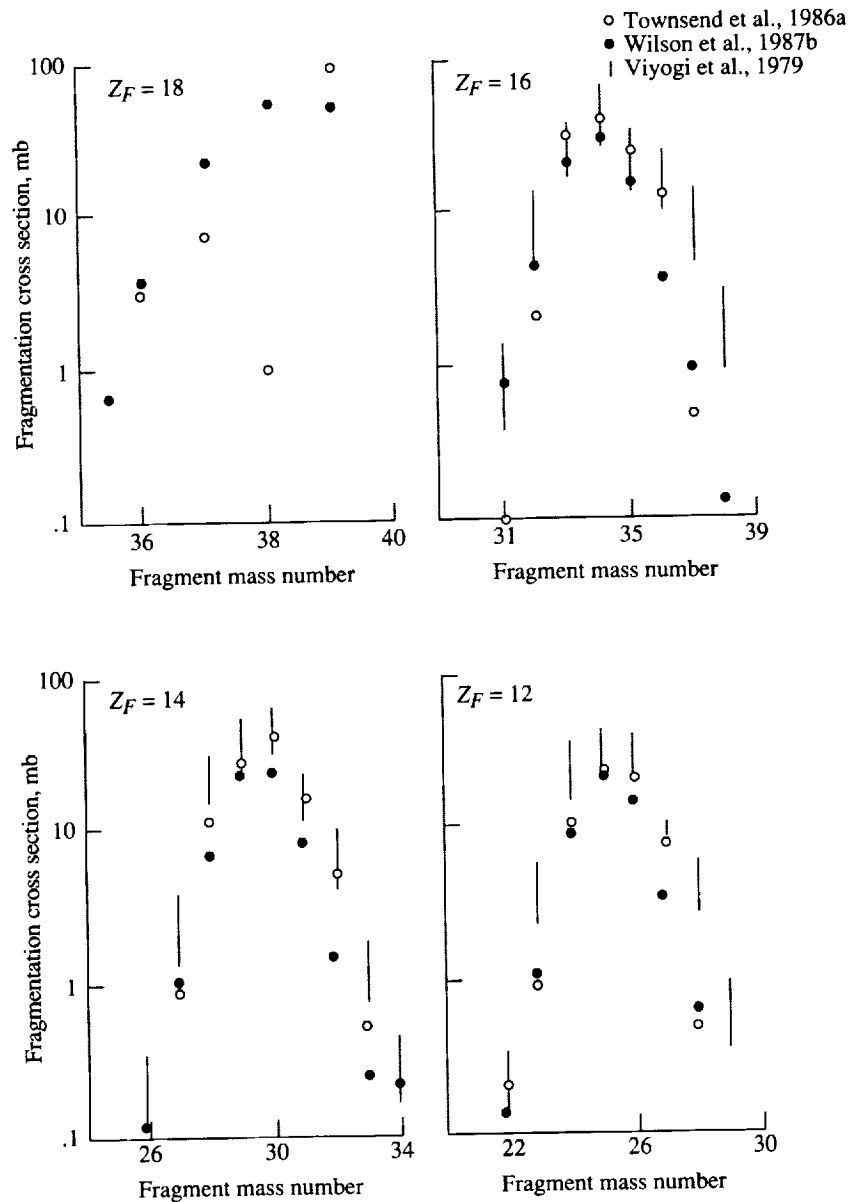


Figure 5.48. Representative argon-carbon fragmentation cross sections.

improving the model until the experimental situation is clarified. Clearly, the model of Silberberg, Tsao, and Shapiro (1976), which includes many corrections to Rudstam's formulas, is preferred for hydrogen targets.

The semiempirical model for argon fragmentation on carbon is shown with the quantum mechanical optical model calculation in figure 5.48. Also shown are experimental data of Viyogi et al. (1979). Reasonable agreements are seen between the two models except for neutron removal where there are no data yet to resolve the difference (Townsend and Wilson, 1989).

5.8. Summary

The current empirical data base represented in this chapter constitutes the nuclear data over which the current radiation transport codes are written. The adequacy of the data base depends on whether the important transport quantities are accurately represented. This issue is further addressed in chapters 8 and 9.

5.9. References

- Anon., 1968: MECC-7 *Intranuclear Cascade Code, 500-MeV Protons on O-16*. I4C Analysis Codes (Programmed for H. W. Bertini). Available from Radiation Shielding Information Center, Oak Ridge National Lab.
- Ableev, V. G.; Bodyagin, V. A.; Vorob'ev, G. G.; Zaporozhets, S. A.; Nomofilov, A. A.; Piskunov, N. M.; Sitnik, I. M.; Stokovskii, E. A.; Strunov, L. N.; Tarasóv, A. V.; Filipkovski, A.; Khristova, I. U.; and Sharov, V. I., 1982: Scattering of 17.9-GeV/c α Particles by C, Al, and Cu Nuclei. *Sov. J. Nuclear Phys.*, vol. 36, no. 5, pp. 698-703.
- Ahmad, I., 1975: An Analysis of Some Proton-Nucleus Scattering Data at 1 GeV. *Nuclear Phys.*, vol. A247, no. 3, pp. 418-440.
- Aichelin, J.; Peilert, G.; Bohnet, A.; Rosenhauer, A.; Stöcker, H.; and Greiner, W., 1988: Quantum Molecular Dynamics Approach to Heavy Ion Collisions: Description of the Model, Comparison With Fragmentation Data, and the Mechanism of Fragment Formation. *Phys. Review C*, vol. 37, no. 6, pp. 2451-2468.
- Alsmiller, R. G., Jr.; Barish, J.; and Leimdorfer, M., 1968: Analytic Representation of Nonelastic Cross Sections and Particle-Emission Spectra From Nucleon-Nucleus Collisions in the Energy Range 25 to 400 MeV. *Protection Against Space Radiation*, NASA SP-169, pp. 495-515.
- Alsmiller, R. G., Jr.; Armstrong, T. W.; and Coleman, W. A., 1970: The Absorbed Dose and Dose Equivalent From Neutrons in the Energy Range 60 to 3000 MeV and Protons in the Energy Range 400 to 3000 MeV. *Nuclear Sci. & Eng.*, vol. 42, no. 3, pp. 367-381.
- Auger, J. P.; Gillespie, J.; and Lombard, R. J., 1976: Proton- ^4He Elastic Scattering at Intermediate Energies. *Nuclear Phys.*, vol. A262, no. 3, pp. 372-388.
- Badavi, Forooz F.; Townsend, Lawrence W.; Wilson, John W.; and Norbury, John W., 1987: An Algorithm for a Semiempirical Nuclear Fragmentation Model. *Comput. Phys. Commun.*, vol. 47, pp. 281-294.
- Benesh, C. J.; Cook, B. C.; and Vary, J. P., 1989: Single Nucleon Removal in Relativistic Nuclear Collisions. *Phys. Review C*, vol. 40, third ser., no. 3, pp. 1198-1206.
- Bertini, Hugo W.; Guthrie, Miriam P.; and Culkowski, Arline H., 1972: *Nonelastic Interactions of Nucleons and π -Mesons With Complex Nuclei at Energies Below 3 GeV*. ORNL-TM-3148, U.S. Atomic Energy Commission.
- Bertini, R.; Beurtey, R.; Brochard, F.; Bruge, G.; Catz, H.; Chaumeaux, A.; Durand, J. M.; Faivre, J. C.; Fontaine, J. M.; Garreta, D.; Gustafsson, C.; Hendrie, D.; Hibou, F.; Legrand, D.; Saudinos, J.; and Thiron, J., 1973: Angular Distribution of 1.04 GeV Protons Scattered by ^{12}C , ^{58}Ni , ^{208}Pb . *Phys. Lett.*, vol. 45B, no. 2, pp. 119-122.

Transport Methods and Interactions for Space Radiations

- Bertulani, Carlos A.; and Baur, Gerhard, 1988: Electromagnetic Processes in Relativistic Heavy Ion Collisions. *Phys. Rep.*, vol. 163, nos. 5 & 6, pp. 299-408.
- Bevington, Philip R., 1969: *Data Reduction and Error Analysis for the Physical Sciences*. McGraw-Hill Book Co., Inc.
- Blanpied, G. S.; Hoffmann, G. W.; Barlett, M. L.; McGill, J. A.; Greene, S. J.; Ray, L.; Van Dyck, O. B.; Amann, J.; and Thiessen, H. A., 1981: Large Angle Scattering of 0.8 GeV Protons From ^{12}C . *Phys. Review C*, vol. 23, third ser., no. 6, pp. 2599-2605.
- Blatt, John M.; and Weisskopf, Victor F., 1952: *Theoretical Nuclear Physics*. John Wiley & Sons, Inc.
- Bleszynski, M.; and Sander, C., 1979: Geometrical Aspects of High-Energy Peripheral Nucleus-Nucleus Collisions. *Nuclear Phys. A*, vol. 326, nos. 2-3, pp. 525-535.
- Bohr, Aage; and Mottelson, Ben R., 1969: *Nuclear Structure. Volume I—Single-Particle Motion*. W. A. Benjamin, Inc.
- Borkowski, F.; Simon, G. G.; Walther, V. H.; and Wendling, R. D., 1975: On the Determination of the Proton RMS-Radius From Electron Scattering Data. *Z. Phys. A*, vol. 275, no. 1, pp. 29-31.
- Bowman, J. D.; Swiatecki, W. J.; and Tsang, C. F., 1973: *Abrasion and Ablation of Heavy Ions*. LBL-2908, Lawrence Berkeley Lab., Univ. of California.
- Brady, F. P.; Christie, W. B.; Romero, J. L.; Tull, C. E.; McEachern, B.; Webb, M. L.; Young, J. C.; Crawford, H. J.; Greiner, D. E.; Lindstrom, P. J.; and Sann, H., 1988: Large p_T From the Fragmentation of 1.2-GeV/Nucleon ^{139}La Nuclei. *Phys. Review Lett.*, vol. 60, no. 17, pp. 1699-1702.
- Chaumeaux, A.; Bruge, G.; Bauer, T.; Bertini, R.; Boudard, A.; Catz, H.; Couvert, P.; Duhm, H. H.; Fontaine, J. M.; Garreta, D.; Lugol, J. C.; Layly, V.; and Schaeffer, R., 1976: Scattering of 1.37 GeV α -Particles by ^{12}C . *Nuclear Phys.*, vol. A267, no. 3, pp. 413-424.
- Cucinotta, Francis A.; Norbury, John W.; Khandelwal, Govind S.; and Townsend, Lawrence W., 1987: *Doubly Differential Cross Sections for Galactic Heavy-Ion Fragmentation*. NASA TP-2659.
- Cucinotta, Francis A., 1988: Theory of Alpha-Nucleus Collisions at High Energies. Ph.D. Thesis, Old Dominion Univ.
- Cucinotta, Francis A.; Khandelwal, Govind S.; Maung, Khin M.; Townsend, Lawrence W.; and Wilson, John W., 1988: *Eikonal Solutions to Optical Model Coupled-Channel Equations*. NASA TP-2830.
- Cucinotta, Francis A.; Norbury, John W.; and Townsend, Lawrence W., 1988: *Multiple Nucleon Knockout by Coulomb Dissociation in Relativistic Heavy-Ion Collisions*. NASA TM-4070.
- Cucinotta, F. A.; Khandelwal, G. S.; Townsend, L. W.; and Wilson, J. W., 1989: Correlations in α - α Scattering and Semi-Classical Optical Models. *Phys. Lett.*, vol. B223, no. 2, pp. 127-132.

- Cucinotta, Francis A.; Townsend, Lawrence W.; Wilson, John W.; and Khandelwal, Govind S., 1990: *Inclusive Inelastic Scattering of Heavy Ions and Nuclear Correlations*. NASA TP-3026.
- De Jager, C. W.; De Vries, H.; and De Vries, C., 1974: Nuclear Charge- and Magnetization-Density-Distribution Parameters From Elastic Electron Scattering. *At. Data & Nuclear Data Tables*, vol. 14, no. 5/6, pp. 479-508.
- Feshbach, Herman; Gal, Avraham; and Hüfner, Jörg, 1971: On High-Energy Scattering by Nuclei—II. *Ann. Phys.*, vol. 66, no. 1, pp. 20-59.
- Foelsche, Trutz; Mendell, Rosalind B.; Wilson, John W.; and Adams, Richard R., 1974: *Measured and Calculated Neutron Spectra and Dose Equivalent Rates at High Altitudes; Relevance to SST Operations and Space Research*. NASA TN D-7715.
- Franco, Victor; and Varma, Girish K., 1978: Collisions Between Composite Particles at Medium and High Energies. *Phys. Review C*, vol. 18, no. 1, pp. 349-370.
- Fricke, Scott Herbert, 1985: A Theoretical Study of Anomalous Projectile Fragments Produced in Relativistic Heavy Ion Interactions. Ph.D. Thesis, Univ. of Minnesota.
- Glauber, R. J.; and Matthiae, G., 1970: High-Energy Scattering of Protons by Nuclei. *Nuclear Phys.*, vol. B21, no. 1, pp. 135-157.
- Goldhaber, A. S., 1974: Statistical Models of Fragmentation Processes. *Phys. Lett.*, vol. 53B, no. 4, pp. 306-308.
- Gosset, J.; Gutbrod, H. H.; Meyer, W. G.; Poskanzer, A. M.; Sandoval, A.; Stock, R.; and Westfall, G. D., 1977: Central Collisions of Relativistic Heavy Ions. *Phys. Review*, vol. 16, ser. C, no. 2, pp. 629-657.
- Greiner, D. E.; Lindstrom, P. J.; Heckman, H. H.; Cork, Bruce; and Bieser, F. S., 1975: Momentum Distributions of Isotopes Produced by Fragmentation of Relativistic ^{12}C and ^{16}O Projectiles. *Phys. Review Lett.*, vol. 35, no. 3, pp. 152-155.
- Guerreau, D.; Borrel, V.; Jacquet, D.; Galin, J.; Gatty, B.; and Tarrago, X., 1983: Isotopic Distributions of Projectile-Like Fragments in 44 MeV/u ^{40}Ar Induced Reactions. *Phys. Lett.*, vol. 131B, no. 4,5,6, pp. 293-296.
- Guthrie, Miriam P., 1970: *EVAP-4: Another Modification of a Code To Calculate Particle Evaporation From Excited Compound Nuclei*. ORNL-TM-3119, U.S. Atomic Energy Commission.
- Guzik, T. Gregory, 1981: The Low-Energy Galactic Cosmic Ray Carbon, Nitrogen, and Oxygen Isotopic Composition. *Astrophys. J.*, no. 2, pt. 1, pp. 695-710.
- Guzik, T. G.; Wefel, J. P.; Crawford, H. J.; Greiner, D. E.; Lindstrom, P. J.; Schimmerling, W.; and Symons, T. J. M., 1985: Implications of New Measurements of $^{16}\text{O} + p \rightarrow ^{12,13}\text{C}, ^{14,15}\text{N}$ for the Abundances of C, N Isotopes at the Cosmic Ray Source. *19th International Cosmic Ray Conference*, OG Sessions, Volume 2, NASA CP-2376, pp. 80-83.
- Heckman, H. H., 1975: *Heavy Ion Fragmentation Experiments at the Bevatron*. NASA CR-142589.

Transport Methods and Interactions for Space Radiations

- Heckman, Harry H.; and Lindstrom, Peter J., 1976: Coulomb Dissociation of Relativistic ^{12}C and ^{16}O Nuclei. *Phys. Review Lett.*, vol. 37, no. 1, pp. 56-59.
- Hill, John C.; Wohn, F. K.; Winger, J. A.; and Smith, A. R., 1988: Electromagnetic Dissociation for High-Z Projectiles at Ultrarelativistic Energies. *Phys. Review Lett.*, vol. 60, no. 11, pp. 999-1001.
- Hüfner, J.; Schäfer, K.; and Schürmann, B., 1975: Abrasion-Ablation in Reactions Between Relativistic Heavy Ions. *Phys. Review*, vol. 12, ser. C, no. 6, pp. 1888-1898.
- Kerman, A. K.; McManus, H.; and Thaler, R. M., 1959: The Scattering of Fast Nucleons From Nuclei. *Ann. Phys. (N.Y.)*, vol. 8, no. 4, pp. 551-635.
- Khan, Ferdous; Khandelwal, Govind S.; Wilson, John W.; Townsend, Lawrence W.; and Norbury, John W., 1988: Excitation Decay Contribution of Projectile and Projectile Fragments to (^{12}C , $^{11}\text{B}+\text{P}$) Cross Section at 2.1 A GeV With ^{12}C Targets. *Proceedings of the 8th High Energy Heavy Ion Study*, J. W. Harris and G. J. Wozniak, eds., LBL-24580, Lawrence Berkeley Lab., pp. 440-449.
- Khan, Ferdous, 1989: Nuclear Fragmentation Energy and Momentum Transfer Distributions in Relativistic Heavy Ion Collisions. Ph.D. Thesis, Old Dominion Univ.
- Knight, E. A.; Singhal, R. P.; Arthur, R. G.; and Macauley, M. W. S., 1981: Elastic Scattering of Electrons From $^{20,22}\text{Ne}$. *J. Phys. G: Nuclear Phys.*, vol. 7, no. 8, pp. 1115-1121.
- Levinger, Joseph S., 1960: *Nuclear Photo-Disintegration*. Oxford Univ. Press.
- Lindstrom, P. J.; Greiner, D. E.; Heckman, H. H.; Cork, Bruce; and Bieser, F. S., 1975: *Isotope Production Cross Sections From the Fragmentation of ^{16}O and ^{12}C at Relativistic Energies*. LBL-3650 (NGR-05-003-513), Lawrence Berkeley Lab., Univ. of California.
- Lord, J. J., 1951: The Altitude and Latitude Variation in the Rate of Occurrence of Nuclear Disintegrations Produced in the Stratosphere by Cosmic Rays. *Phys. Review*, vol. 81, second ser., no. 6, pp. 901-909.
- Maleck, A.; Picozza, P.; and Satta, L., 1984: Inclusive Inelastic Cross Section for α - α Scattering at High Energies. *Phys. Lett.*, vol. 136B, no. 5/6, pp. 319-321.
- Mercier, M. T.; Hill, J. C.; Wohn, F. K.; and Smith, A. R., 1984: Electromagnetic Dissociation of ^{197}Au by Relativistic Heavy Ions. *Phys. Review Lett.*, vol. 52, no. 11, pp. 898-901.
- Mercier, M. T.; Hill, John C.; Wohn, F. K.; McCullough, C. M.; Nieland, M. E.; Winger, J. A.; Howard, C. B.; Renwick, S.; Matheis, D. K.; and Smith, A. R., 1986: Electromagnetic Dissociation of ^{59}Co , ^{89}Y , and ^{197}Au Targets by Relativistic Heavy Ions to $Z = 26$. *Phys. Review C*, vol. 33, third ser., no. 5, pp. 1655-1667.
- Moniz, E. J.; and Nixon, G. D., 1971: High Energy Coherent Processes With Nuclear Targets. *Ann. Phys. (N.Y.)*, vol. 67, no. 1, pp. 58-97.
- Morrissey, D. J.; Marsh, W. R.; Otto, R. J.; Loveland, W.; and Seaborg, G. T., 1978: Target Residue Mass and Charge Distributions in Relativistic Heavy Ion Reactions. *Phys. Review*, vol. 18, ser. C, no. 3, pp. 1267-1274.

- Morrissey, D. J.; Oliveira, L. F.; Rasmussen, J. O.; Seaborg, G. T.; Yariv, Y.; and Fraenkel, Z., 1979: Microscopic and Macroscopic Model Calculations of Relativistic Heavy-Ion Fragmentation Reactions. *Phys. Review Lett.*, vol. 43, no. 16, pp. 1139-1142.
- Nakada, A.; Torizuka, Y.; and Horikawa, Y., 1971: Determination of the Deformation in ^{12}C From Electron Scattering. *Phys. Review Lett.*, vol. 27, no. 11, pp. 745-748.
- Norbury, John W.; Townsend, Lawrence W.; and Deutchman, Philip A., 1985: *A T-Matrix Theory of Galactic Heavy-Ion Fragmentation*. NASA TP-2363.
- Norbury, John W.; and Townsend, Lawrence W., 1986: *Electromagnetic Dissociation Effects in Galactic Heavy-Ion Fragmentation*. NASA TP-2527.
- Norbury, John W.; Cucinotta, F. A.; Townsend, L. W.; and Badavi, F. F., 1988: Parameterized Cross Sections for Coulomb Dissociation in Heavy-Ion Collisions. *Nuclear Instrum. & Methods Phys. Res.*, vol. B31, no. 4, pp. 535-537.
- Norbury, John W.; Townsend, Lawrence W.; and Badavi, Forooz F., 1988: *Computer Program for Parameterization of Nucleus-Nucleus Electromagnetic Dissociation Cross Sections*. NASA TM-4038.
- Norbury, John W., 1989: Nucleon Emission Via Electromagnetic Excitation in Relativistic Nucleus-Nucleus Collisions: Reanalysis of the Weizsäcker-Williams Method. *Phys. Review C*, vol. 40, third ser., no. 6, pp. 2621-2628.
- Norbury, John W., 1990a: Charge Dependence and Electric Quadrupole Effects on Single-Nucleon Removal in Relativistic and Intermediate Energy Nuclear Collisions. *Phys. Review C*, vol. 42, third ser., no. 5, pp. 2259-2262.
- Norbury, John W., 1990b: Electric Quadrupole Excitations in the Interactions of ^{89}Y With Relativistic Nuclei. *Phys. Review C*, vol. 41, third ser., no. 1, pp. 372-373.
- Norbury, John W., 1990c: Electric Quadrupole Excitations in Relativistic Nucleus-Nucleus Collisions. *Phys. Review C*, vol. 42, third ser., no. 2, pp. 711-715.
- Norbury, John W.; and Townsend, Lawrence W., 1990a: *Calculation of Two-Neutron Multiplicity in Photonuclear Reactions*. NASA TP-2968.
- Norbury, John W.; and Townsend, Lawrence W., 1990b: Single Nucleon Emission in Relativistic Nucleus-Nucleus Reactions. *Phys. Review C*, vol. 42, third ser., no. 4, pp. 1775-1777.
- Oliveira, Luiz F.; Donangelo, Raul; and Rasmussen, John O., 1979: Abrasion-Ablation Calculations of Large Fragment Yields From Relativistic Heavy Ion Reactions. *Phys. Review C*, vol. 19, ser. C, no. 3, pp. 826-833.
- Ranft, J., 1980: The FLUKA and KASPRO Hadronic Cascade Codes. *Computer Techniques in Radiation Transport and Dosimetry*, Walter R. Nelson and Theodore M. Jenkins, eds., Plenum Press, pp. 339-371.
- Ray, L., 1979: Proton-Nucleus Total Cross Sections in the Intermediate Energy Range. *Phys. Review C*, vol. 20, third ser., no. 5, pp. 1857-1872.

Transport Methods and Interactions for Space Radiations

- Rodberg, Leonard S.; and Thaler, R. M., 1967: *Introduction to the Quantum Theory of Scattering*. Academic Press Inc.
- Rudstam, G., 1966: Systematics of Spallation Yields. *Zeitschrift fur Naturforschung*, vol. 21a, no. 7, pp. 1027-1041.
- Saudinos, Jean; and Wilkin, Colin, 1974: Proton-Nucleus Scattering at Medium Energies. *Annual Review of Nuclear Science*, Volume 24, Emilio Segrè, J. Robb Grover, and H. Pierre Noyes, eds., Annual Reviews, Inc., pp. 341-377.
- Serber, R., 1947: Nuclear Reactions at High Energies. *Phys. Review*, vol. 72, no. 11, pp. 1114-1115.
- Silberberg, R.; Tsao, C. H.; and Shapiro, M. M., 1976: Semiempirical Cross Sections, and Applications to Nuclear Interactions of Cosmic Rays. *Spallation Nuclear Reactions and Their Applications*, B. S. P. Shen and M. Merker, eds., D. Reidel Publ. Co., pp. 49-81.
- Stevenson, J. D.; Martinis, J.; and Price, P. B., 1981: Measurement of the Summed Residual Projectile Mass in Relativistic Heavy-Ion Collisions. *Phys. Review Lett.*, vol. 47, no. 14, pp. 990-993.
- Townsend, Lawrence W., 1981: *Optical-Model Abrasion Cross Sections for High-Energy Heavy Ions*. NASA TP-1893.
- Townsend, Lawrence W., 1982: *Harmonic Well Matter Densities and Pauli Correlation Effects in Heavy-Ion Collisions*. NASA TP-2003.
- Townsend, L. W., 1983: Abrasion Cross Sections for ^{20}Ne Projectiles at 2.1 GeV/Nucleon. *Canadian J. Phys.*, vol. 61, no. 1, pp. 93-98.
- Townsend, Lawrence W.; Wilson, John W.; Norbury, John W.; and Bidasaria, Hari B., 1984: *An Abrasion-Ablation Model Description of Galactic Heavy-Ion Fragmentation*. NASA TP-2305.
- Townsend, Lawrence W.; and Wilson, John W., 1985: *Tables of Nuclear Cross Sections for Galactic Cosmic Rays—Absorption Cross Sections*. NASA RP-1134.
- Townsend, L. W.; Wilson, J. W.; and Norbury, J. W., 1985: A Simplified Optical Model Description of Heavy Ion Fragmentation. *Canadian J. Phys.*, vol. 63, no. 2, pp. 135-138.
- Townsend, L. W.; and Wilson, J. W., 1986: Energy-Dependent Parameterization of Heavy-Ion Absorption Cross Sections. *Radiat. Res.*, vol. 106, pp. 283-287.
- Townsend, L. W.; Wilson, J. W.; Cucinotta, F. A.; and Norbury, J. W., 1986a: Comparison of Abrasion Model Differences in Heavy Ion Fragmentation: Optical Versus Geometric Models. *Phys. Review*, vol. 34, ser. C, no. 4, pp. 1491-1494.
- Townsend, Lawrence W.; Wilson, John W.; Cucinotta, Francis A.; and Norbury, John W., 1986b: *Optical Model Calculations of Heavy-Ion Target Fragmentation*. NASA TM-87692.
- Townsend, L. W.; and Wilson, J. W., 1989: Nuclear Cross Sections for Estimating Secondary Radiations Produced in Spacecraft. *High-Energy Radiation Background in Space*, American Inst. of Physics, pp. 177-191.

- Überall, Herbert, 1971: *Electron Scattering From Complex Nuclei*, Part A. Academic Press, Inc.
- Van Allen, James A., 1952: The Nature and Intensity of the Cosmic Radiation. Chapter XIV of *Physics and Medicine of the Upper Atmosphere*, Clayton S. White and Otis O. Benson, Jr., eds., Univ. of New Mexico Press (Albuquerque), pp. 239-266.
- Viollier, R. D., 1975: High-Energy Proton-Nucleus Scattering and Correlations. *Ann. Phys.*, vol. 93, no. 1-2, pp. 335-368.
- Viyogi, Y. P.; Symons, T. J. M.; Doll, P.; Greiner, D. E.; Heckman, H. H.; Hendrie, D. L.; Lindstrom, P. J.; Mahoney, J.; Scott, D. K.; Van Bibber, K.; Westfall, G. D.; Wieman, H.; Crawford, H. J.; McParland, C.; and Gelbke, C. K., 1979: Fragmentations of ^{40}Ar at 213 MeV/Nucleon. *Phys. Review Lett.*, vol. 42, no. 1, pp. 33-36.
- Webb, M. L.; Crawford, H. J.; Engelage, J.; Baumgartner, M. E.; Greiner, D. E.; Lindstrom, P. J.; Olson, D. L.; and Wada, R., 1987: Probing the Direct Step of Relativistic Heavy Ion Fragmentation: (^{12}C , $^{11}\text{B} + p$) at 2.1 GeV/Nucleon With C and CH_2 Targets. *Phys. Review C*, vol. 36, third ser., no. 1, pp. 193-202.
- Webber, W. R.; Brautigam, D. A.; Kish, J. C.; and Schrier, D., 1983a: Fragmentation of ~ 500 MeV/nuc Ne and O Nuclei in CH_2 , C and H Targets—Charge and Isotopic Cross Sections. *18th International Cosmic Ray Conference—Conference Papers*, OG Sessions, Vol. 2, Tata Inst. of Fundamental Research (Colaba, Bombay), pp. 202-205.
- Webber, W. R.; Brautigam, D. A.; Kish, J. C.; and Schrier, D., 1983b: Fragmentation of 710 and 1050 MeV/nuc Fe Nuclei in CH_2 and C Targets—Isotopic Cross Sections for H Targets. *18th International Cosmic Ray Conference—Conference Papers*, OG Sessions, Vol. 2, Tata Inst. of Fundamental Research (Colaba, Bombay), pp. 198-201.
- Westfall, G. D.; Wilson, Lance W.; Lindstrom, P. J.; Crawford, H. J.; Greiner, D. E.; and Heckman, H. H., 1979: Fragmentation of Relativistic ^{56}Fe . *Phys. Review*, vol. 19, ser. C, no. 4, pp. 1309-1323.
- Wilson, J. W., 1974a: Multiple Scattering of Heavy Ions, Glauber Theory, and Optical Model. *Phys. Lett.*, vol. B52, no. 2, pp. 149-152.
- Wilson, John W., 1974b: Proton-Deuteron Double Scattering. *Phys. Review C*, vol. 10, no. 1, pp. 369-376.
- Wilson, John W., 1975: Composite Particle Reaction Theory. Ph.D. Diss., College of William and Mary in Virginia.
- Wilson, John W.; and Costner, Christopher M., 1975: *Nucleon and Heavy-Ion Total and Absorption Cross Section for Selected Nuclei*. NASA TN D-8107.
- Wilson, John W., 1977: *Analysis of the Theory of High-Energy Ion Transport*. NASA TN D-8381.
- Wilson, J. W.; and Townsend, L. W., 1981: An Optical Model for Composite Nuclear Scattering. *Canadian J. Phys.*, vol. 59, no. 11, pp. 1569-1576.

Transport Methods and Interactions for Space Radiations

Wilson, John W., 1983: *Heavy-Ion Transport in the Straight Ahead Approximation*. NASA TP-2178.

Wilson, John W.; Townsend, L. W.; Bidasaria, H. B.; Schimmerling, Walter; Wong, Mervyn; and Howard, Jerry, 1984: ^{20}Ne Depth-Dose Relations in Water. *Health Phys.*, vol. 46, no. 5, pp. 1101-1111.

Wilson, J. W.; Townsend, L. W.; and Badavi, F. F., 1987a: Galactic HZE Propagation Through the Earth's Atmosphere. *Radiat. Res.*, vol. 109, no. 2, pp. 173-183.

Wilson, John W.; Townsend, Lawrence W.; and Badavi, F. F., 1987b: A Semiempirical Nuclear Fragmentation Model. *Nuclear Instrum. & Methods Phys. Res.*, vol. B18, no. 3, pp. 225-231.

Wong, Cheuk-Yin, 1981: Peripheral and Central Collisions at Around 100 MeV per Nucleon. *5th High Energy Heavy Ion Study*, LBL-12652 (Contract W-7405-ENG-48), Lawrence Berkeley Lab., Univ. of California, pp. 61-86.

Chapter 6

Transport Theory

6.1. Introduction

The 1912 experiments of V. Hess to study the decline of terrestrial radiation in the atmosphere led to the discovery of cosmic rays (Hess and Eugster, 1949). The next two decades saw the study of the increase of cosmic rays with altitude and decreasing atmospheric shielding. Even after 30 years of study, a meaningful theory of the propagation of the nucleonic component came only after sufficient understanding of the nuclear force and nuclear theory. Thus, development began with the historic paper of Bethe, Korff, and Placzek (1940), which concerned atmospheric neutrons; these results, although incomplete, remain substantially correct today. The detection several years later of neutrons in coincidence with atmospheric air showers (Cocconi, Cocconi-Tongiorgi, and Greisen, 1948) and cloud chamber data with evaporation stars leads one to suspect that moderate energy neutrons are part of a normal air shower event as assumed by Bethe, Korff, and Placzek (1940). The subsequent work of Cocconi, Cocconi Tongiorgi, and Widgoff (1950) on atmospheric cascades begins to place the whole subject of air showers on firm ground. Yet to be added to the understanding of air showers is the discovery of the heavy ion component (Freier et al., 1948) and the related propagation equations.

Early works in setting up the galactic ion transport equations ignored energy loss by ionization of the medium. Peters (1958) used a one-dimensional equilibrium solution ignoring ionization energy loss and radioactive decay to show that the light ions of the galactic cosmic rays have their origin in the breakup of heavy particles in interstellar space. Davis (1960) showed that one-dimensional propagation is simplistic and that leakage at the galactic boundary must be included. Ginzburg and Syrovatskii (1964) argued that the leakage can be approximated as a superposition of nonequilibrium one-dimensional solutions.

In distinction to cosmic-ray studies that accentuated the nuclear reactions and ignored ionization energy loss, the early space shielding studies (mainly concerned with solar proton events and trapped radiation) ignored nuclear reaction effects and treated only the ionization energy loss (Shaefer, 1959; Foelsche, 1959; Dye and Noyes, 1960). Such studies were mainly limited by the available nuclear data. The hope for comprehensive nuclear data began with a study by M. L. Goldberger (1948) in which a two-dimensional, intranuclear cascade calculation by a young student named G. F. Chew was made with random number tables and a mechanical calculator. (G. F. Chew cast his vote for nuclear democracy at the first heavy ion conference at Lawrence Berkeley Laboratory 25 years later.) Detailed development of the intranuclear cascade method awaited the introduction of large-scale scientific computers (Metropolis et al., 1958) which, when developed, had a tremendous impact on the space-radiation program (Bertini, 1962; Alsmiller, 1967). A series of Monte Carlo and deterministic transport codes began to emerge using the new nuclear models (Alsmiller, 1967; Dye, 1962; Lambiotte, Wilson, and Filippas, 1971; Wilson and Lamkin, 1975). A relatively complete set of shielding

codes was then available for determining shield requirements for protection from space protons. Now heavy ion transport required future development.

Heavy ion transport was important for understanding the origin of galactic cosmic rays as in the early works of Peters (1958), Davis (1960), and Ginzburg and Syrovatskii (1964). In these early works, the complications introduced by ionization energy loss were ignored. Even later papers would ignore or simplify the energy loss term. The "solution" to the steady-state equations is given as a Volterra equation by Gloeckler and Jokipii (1969) which is solved to first order in the fragmentation cross sections ignoring energy loss. They provide an approximation to the first-order solution with ionization energy loss included but are valid only at relativistic energies. Lezniak (1979) gives an overview to cosmic-ray propagation and derives a Volterra equation including the ionization energy loss, which he refers to as a solution "only in the iterative sense," and evaluates only the unperturbed term. No attempt is made to evaluate the first-order perturbation term or higher order terms. The main interest among cosmic-ray physicists has been in solution to, at most, first order in the fragmentation cross sections since path lengths in interstellar space are on the order of 3 to 4 g/cm². Clearly, higher order terms cannot be ignored in accelerator or space shielding transport problems (Wilson, 1977a and 1983; Wilson et al., 1984). Aside from this simplification, the cosmic-ray studies discussed previously have neglected the complicated three-dimensional nature of the fragmentation process.

Several approaches to the solution of high-energy, heavy ion propagation, including the ionization energy loss, have been developed over the last 20 years. All but one (Wilson, 1977a) have assumed the straight ahead approximation and velocity conserving fragmentation interactions. Only two (Wilson, 1977a; Wilson et al., 1984) have incorporated energy-dependent nuclear cross sections. The approach by Curtis, Doherty, and Wilkinson (1969) for a primary ion beam represented the first-generation secondary fragments as a quadrature over the collision density of the primary beam. Allkofer and Heinrich (1974) used an energy multigroup method in which an energy-independent fragment transport approximation was applied within each energy group after which the energy group boundaries were moved according to continuous slowing-down theory ($-dE/dx$). Chatterjee, Tobias, and Lyman (1976) solved the energy-independent fragment transport equation with primary collision density as a source and neglected higher order fragmentation. The primary source term extended only to the primary ion range from the boundary. The energy-independent transport solution was modified to account for the finite range of the secondary fragment ions. Wilson (1977b) derived an expression for the ion transport problem to first order (first-collision term) and gave an analytic solution for the depth-dose relation. Wilson (1977a) further examined the more common approximations used in solving the heavy ion transport problem. The effects of conservation of velocity on fragmentation and the straight ahead approximation are found to be negligible for cosmic-ray applications. Solution methods for representing the energy-dependent nuclear cross sections are developed (Wilson, 1977a). Letaw, Tsao, and Silberberg (1983) approximate the energy-loss term and ion spectra by simple forms for which energy derivatives are evaluated explicitly (even if approximately). The resulting ordinary differential equations in position are solved analytically in a manner that is similar to the method of Allkofer and Heinrich (1974). This approximation

assumes a separable solution and results in a decoupling of motion in space and a change in energy. In Letaw's formalism, the energy shift is replaced by an effective attenuation (separable) factor. Wilson (1983) adds the next higher order (second collision) term to his previous analytic expansion (Wilson, 1977b). This term was found to be very important in describing 670 MeV/nucleon ^{20}Ne beams. The three-term expansion of Wilson (1983) was modified to include the effects of energy variation of the nuclear cross sections (Wilson et al., 1984). The integral form of the transport equation was further used to derive a numerical marching procedure to solve the cosmic-ray transport problem (Wilson and Badavi, 1986). This method can easily include the energy-dependent nuclear cross sections within the numerical procedure. Comparison of the numerical procedure (Wilson and Badavi, 1986) with an analytical solution to a simplified problem (Wilson and Townsend, 1988) validates the numerical procedure to about 1-percent accuracy. Several solution techniques and analytic methods have been developed for testing future numerical solutions to the transport equations (Ganapol, Townsend, and Wilson, 1989; Ganapol et al., 1991). More recently, an analytic solution for the laboratory ion-beam transport problem has been derived assuming a straight ahead approximation, velocity conservation at the interaction site, and an energy-independent nuclear cross section (Wilson et al., 1989a and 1989b).

In the above overview of past developments, the applications were split into two separate categories: a single-ion species with a single energy at the boundary versus a broad host of elemental types with a broad, continuous energy spectrum. Techniques requiring a representation of the spectrum over an array of energy values require vast computer storage and computation speed for the laboratory beam problem to maintain sufficient energy resolution. On the other hand, analytic methods (Wilson, 1977a; Wilson and Badavi, 1986) are probably best applied in a marching procedure, which again has within it a similar energy resolution problem. This is a serious limitation, because we require a final code for cosmic-ray shielding that has been validated by laboratory experiments. In this chapter, we examine past developments and new methods in an attempt to overcome these difficulties. Our final objective, as always, is to develop a set of self-contained codes for use in an engineering design environment.

6.2. Transport Formalism

A massive ion, after entering a region filled with ordinary matter, interacts with orbital electrons, thus causing ionization and excitation of the medium. Because of the large mass difference between the ion and these orbital electrons, only a small amount of the ion energy can be transferred in a collision with a single electron. Because of the long range of the coulomb force and the large percentage of the material volume being occupied by electrons, the electron interactions can, to a good approximation, be treated as a continuous slowing-down process over any finite path length. Although the energy lost by an ion over some fixed path length fluctuates about a mean value, this fluctuation amounts to no more than a few percent (Janni, 1982a and 1982b; Schimmerling et al., 1986) and is of no importance in the study of space radiation (Alsmiller, Barish, and Scott, 1969). In the following paragraphs, continuous slowing-down theory will be assumed throughout, and the relevant quantity is the average energy loss per unit path length, denoted by $S_j(E)$, where E is the ion energy and j denotes the ion type.

The mean-free path for nuclear collisions is large (more than a centimeter); by comparison, the mean-free path for collision of the ion with electrons is small. Although collisions with electrons result only in a small transfer of energy compared with the total ion kinetic energy, the nuclear collision generally alters (loss of mass and charge) the ion and the struck nucleus, with many secondary particles being produced. The secondary particles produced as fragments of the primary heavy ion will have longer ranges and free paths causing much greater penetration. As the secondaries undergo additional nuclear reactions, more secondaries, which penetrate deeper into the material, are produced. This process produces the transition effect observed for cosmic rays. The purpose here is to develop the theoretical understanding of the transport of such radiations in extended materials.

The massive particle transport equations are derived by balancing the change in particle flux as it crosses a small volume of material with the gains and losses caused by nuclear collision (Wilson and Lamkin, 1975; see also chapters 1 and 2 for details). The resulting equations for a homogeneous material are given by

$$\begin{aligned} \left[\vec{\Omega} \cdot \nabla - \frac{1}{A_j} \frac{\partial}{\partial E} S_j(E) + \sigma_j(E) \right] \phi_j(\vec{x}, \vec{\Omega}, E) \\ = \sum_k \int dE' d\vec{\Omega}' \sigma_{jk}(E, E', \vec{\Omega}, \vec{\Omega}') \phi_k(\vec{x}, \vec{\Omega}', E') \end{aligned} \quad (6.1)$$

where $\phi_j(\vec{x}, \vec{\Omega}, E)$ is the flux of ions of type j with atomic mass A_j at \vec{x} with motion along $\vec{\Omega}$ and energy E in units of MeV/nucleon, $\sigma_j(E)$ is the corresponding macroscopic cross section, $S_j(E)$ is the linear energy transfer (LET), and $\sigma_{jk}(E, E', \vec{\Omega}, \vec{\Omega}')$ is the production cross section for type j particles with energy E and direction $\vec{\Omega}$ by the collision of a type k particle of energy E' and direction $\vec{\Omega}'$. The term on the left side of equation (6.1) containing $S_j(E)$ is a result of the continuous slowing-down approximation, whereas the remaining terms of equation (6.1) are seen to be the usual Boltzmann terms. The solutions to equation (6.1) exist and are unique in any convex region for which the inbound flux of each particle type is specified everywhere on the bounding surface. If the boundary is given as the loci of the two-parameter vector function $\vec{\gamma}(s, t)$ for which a generic point on the boundary is given by $\vec{\Gamma}$, then the boundary condition is specified by requiring the solution of equation (6.1) to meet

$$\phi_j(\vec{\Gamma}, \vec{\Omega}, E) = \psi_j(\vec{\Gamma}, \vec{\Omega}, E) \quad (6.2)$$

for each value of $\vec{\Omega}$ such that

$$\vec{\Omega} \cdot \vec{n}(\vec{\Gamma}) < 0 \quad (6.3)$$

where $\vec{n}(\vec{\Gamma})$ is the outward-directed unit normal vector to the boundary surface at the point $\vec{\Gamma}$ and ψ_j is a specified boundary function.

The fragmentation of the projectile and target nuclei is represented by the quantities $\sigma_{jk}(E, E', \vec{\Omega}, \vec{\Omega}')$, which are composed of three functions:

$$\sigma_{jk}(E, E', \vec{\Omega}, \vec{\Omega}') = \sigma_k(E') \nu_{jk}(E') f_{jk}(E, E', \vec{\Omega}, \vec{\Omega}') \quad (6.4)$$

where $\nu_{jk}(E')$ is the average number (which we loosely refer to as multiplicity) of type j particles being produced by a collision of a type k of energy E' , and $f_{jk}(E, E', \vec{\Omega}, \vec{\Omega}')$ is the probability density distribution for producing particles of type j of energy E into direction $\vec{\Omega}$ from the collision of a type k particle with energy E' moving in direction $\vec{\Omega}'$. For an unpolarized source of projectiles and unpolarized targets, the energy-angle distribution of reaction products is a function of the energies and cosine of the production angle relative to the incident projectile direction. The secondary multiplicities $\nu_{jk}(E')$ and secondary energy-angle distributions are the major unknowns in ion transport theory.

Information on the multiplicity $\nu_{jk}(E')$ was obtained in the past through experiments with galactic cosmic rays as an ion source, and the fragmentation of the ions on target nuclei was observed in nuclear emulsion (Cleghorn, Freier, and Waddington, 1968). Such data are mainly limited by not knowing the identity of the initial or secondary ions precisely and by relatively low counting rates of each ion type. The heavy ion acceleration by machine makes a reduction in the uncertainty possible because large count rates can be obtained with known ion types. In addition, the target nuclei in accelerator experiments can conveniently be other than nuclear emulsion, and accurate detector techniques with modern electronic processing are greatly improving the experimental data base. (See chapter 5.) In addition, the accelerator experiments are providing information on the spectral distribution $f_{jk}(E, E', \vec{\Omega}, \vec{\Omega}')$ which has not been available before (Heckman et al., 1972).

The spectral distribution function is found to consist of two terms that describe the fragmentation of the projectile and the fragmentation of the struck nucleus as follows (Heckman, 1975; Raisbeck and Yiou, 1975):

$$\begin{aligned} \sigma_{jk}(E, E', \vec{\Omega}, \vec{\Omega}') = \sigma_k(E') \left[\nu_{jk}^P(E') f_{jk}^P(E, E', \vec{\Omega}, \vec{\Omega}') \right. \\ \left. + \nu_{jk}^T(E') f_{jk}^T(E, E', \vec{\Omega}, \vec{\Omega}') \right] \end{aligned} \quad (6.5)$$

where ν_{jk}^P and f_{jk}^P depend only weakly on the target and ν_{jk}^T and f_{jk}^T depend only weakly on the projectile. Although the average secondary velocities associated with f^P are nearly equal to the projectile velocity, the average velocities associated

with f^T are near zero. During experiments, Heckman (1975) observed that

$$f_{jk}^P(E, E', \vec{\Omega}, \vec{\Omega}') \approx \left[\frac{m}{2\pi (\sigma_{jk}^P)^2} \right]^{3/2} \sqrt{2E} \exp \left[-\frac{(\vec{p} - \vec{p}')^2}{2 (\sigma_{jk}^P)^2} \right] \\ \approx \left[\frac{m}{2\pi (\sigma_{jk}^P)^2} \right]^{3/2} \sqrt{2E} \exp \left[-\frac{(\vec{\Omega} \sqrt{2mE} - \vec{\Omega}' \sqrt{2mE'})^2}{2 (\sigma_{jk}^P)^2} \right] \quad (6.6)$$

where \vec{p} and \vec{p}' are the momenta per unit mass of j and k ions, respectively, and

$$f_{jk}^T(E, E', \vec{\Omega}, \vec{\Omega}') \approx \left[\frac{m}{2\pi (\sigma_{jk}^T)^2} \right]^{3/2} \sqrt{2E} \exp \left[-\frac{\vec{p}^2}{2 (\sigma_{jk}^T)^2} \right] \quad (6.7)$$

where σ_{jk}^P and σ_{jk}^T are related to the root-mean-square (rms) momentum spread of secondary products. These parameters depend only on the fragmenting nucleus. Feshbach and Huang (1973) suggested that the parameters σ_{jk}^P and σ_{jk}^T depend on the average square momentum of the nuclear fragments as allowed by Fermi motion. A precise formulation of these ideas in terms of a statistical model was obtained by Goldhaber (1974).

6.3. Approximation Procedures

6.3.1. Neglect of target fragmentation. Using equations (6.5), (6.6), and (6.7) in the evaluation of the source term $\zeta_j(\vec{x}, \vec{\Omega}, E)$ of equation (6.1) results in

$$\zeta_j(\vec{x}, \vec{\Omega}, E) = \sum_k \int dE' d\vec{\Omega}' \sigma_k(E') \phi_k(\vec{x}, \vec{\Omega}', E') \\ \times \left[\nu_{jk}^P(E') f_{jk}^P(E, E', \vec{\Omega}, \vec{\Omega}') + \nu_{jk}^T f_{jk}^T(E, E', \vec{\Omega}, \vec{\Omega}') \right] \\ \equiv \zeta_j^P(\vec{x}, \vec{\Omega}, E) + \zeta_j^T(\vec{x}, \vec{\Omega}, E) \quad (6.8)$$

where, as before, the superscripts P and T refer to fragmentation of the projectile and target, respectively. The target term is seen to be

$$\zeta_j^T(\vec{x}, \vec{\Omega}, E) = \sum_k \left[\frac{m}{2\pi (\sigma_{jk}^T)^2} \right]^{3/2} \sqrt{2E} \exp \left[\frac{-mE}{(\sigma_{jk}^T)^2} \right] \\ \times \int d\vec{\Omega}' \int_E^\infty dE' \nu_{jk}^T(E') \sigma_k(E') \phi_k(\vec{x}, \vec{\Omega}', E') \quad (6.9)$$

which is negligibly small for

$$E \gg \frac{(\sigma_{jk}^T)^2}{m} \quad (6.10)$$

Thus, for calculating the flux at high energy,

$$\zeta_j(\vec{x}, \vec{\Omega}, E) \approx \zeta_j^P(\vec{x}, \vec{\Omega}, E) \quad (6.11)$$

6.3.2. Space radiations. A convenient property of space radiations is that they are nearly isotropic. This fact, coupled with the forward peaked spectral distribution, leads to substantial reductions in the source term as follows:

$$\begin{aligned} \zeta_j^P(\vec{x}, \vec{\Omega}, E) \approx \sum_k \int dE' d\vec{\Omega}' \sigma_k(E') \nu_{jk}^P(E') \left[\frac{m}{2\pi (\sigma_{jk}^P)^2} \right]^{3/2} \sqrt{2E'} \\ \times \exp \left[-\frac{(\vec{\Omega} \sqrt{2mE} - \vec{\Omega}' \sqrt{2mE'})^2}{2 (\sigma_{jk}^P)^2} \right] \phi_k(\vec{x}, \vec{\Omega}', E') \end{aligned} \quad (6.12)$$

Assuming that $\phi_k(\vec{x}, \vec{\Omega}', E')$ is a slowly varying function of $\vec{\Omega}'$, one may seek an expansion about the sharply peaked maximum of the exponential function. Such an expansion is made by letting

$$\vec{\Omega}' = \vec{\Omega} + (\cos \theta - 1)\vec{\Omega} + \vec{e}_\phi \sin \theta \quad (6.13)$$

where

$$\cos \theta = \vec{\Omega} \cdot \vec{\Omega}' \quad (6.14)$$

and

$$\vec{e}_\phi = \frac{\vec{\Omega} \times \vec{\Omega}'}{|\vec{\Omega} \times \vec{\Omega}'|} \quad (6.15)$$

with which the flux may be expanded as

$$\begin{aligned} \phi_k(\vec{x}, \vec{\Omega}', E') &= \phi_k(\vec{x}, \vec{\Omega}, E') \\ &+ \left[\frac{\partial}{\partial \Omega} \phi_k(\vec{x}, \vec{\Omega}, E') \right] \cdot [(\cos \theta - 1)\vec{\Omega} + \vec{e}_\phi \sin \theta] + \dots \end{aligned} \quad (6.16)$$

Substituting equation (6.16) into equation (6.12) and simplifying results in

$$\begin{aligned} \zeta_j^P(\vec{x}, \vec{\Omega}, E) &\approx \sum_k \int dE' \sigma_k(E') \nu_{jk}^P(E') \\ &\times \left[\frac{m}{2\pi (\sigma_{jk}^P)^2} \right]^{3/2} \frac{\sqrt{2}}{\sqrt{E'}} \exp \left[-\frac{(\sqrt{2mE} - \sqrt{2mE'})^2}{2(\sigma_{jk}^P)^2} \right] \\ &\times \left\{ \phi_k(\vec{x}, \vec{\Omega}, E') - \left[\vec{\Omega} \cdot \frac{\partial}{\partial \vec{\Omega}} \phi_k(\vec{x}, \vec{\Omega}, E') \right] \left[\frac{(\sigma_{jk}^P)^2}{2m\sqrt{EE'}} \right] + \dots \right\} \end{aligned} \quad (6.17)$$

The leading term of equation (6.17) is clearly a good approximation to the source term whenever

$$\frac{2mE}{(\sigma_{jk}^P)^2} \gg \frac{\vec{\Omega} \cdot \frac{\partial}{\partial \vec{\Omega}} \phi_k(\vec{x}, \vec{\Omega}, E')}{\phi_k(\vec{x}, \vec{\Omega}, E')} \quad (6.18)$$

Note that the leading term is equivalent to assuming that secondary ions are produced only in the direction of motion of the primary ions. In the case of space radiations that are nearly isotropic, relation (6.18) is easily met, and neglect of higher order terms in equation (6.17) results in the usual straight ahead approximation. If the radiation is highly anisotropic, then relation (6.18) is not likely to apply. Validity of the straight ahead approximation was discovered empirically by Alsmiller et al. (1965) and Alsmiller, Irving, and Moran (1968) for the case of proton transport and is discussed further in the next chapter.

6.3.3. Velocity conserving interaction. Customarily, in cosmic ion transport studies (Curtis and Wilkinson, 1972), the fragment velocities are assumed to be equal to the fragmenting ion velocity before collision. Derived below is the order of approximation resulting from such an assumption. Assuming that the projectile energy E' is equal to the secondary energy plus a positive quantity ϵ ,

$$E' = E + \epsilon \quad (6.19)$$

and that ϵ will contribute to equation (6.17) only over a small range above zero energy, substituting equation (6.19) into equation (6.17) and expanding the

integrand results in

$$\begin{aligned} \zeta_j^P(\vec{x}, \vec{\Omega}, E) = \sum_k \sigma_k(E) \nu_{jk}^P(E) \left\{ \phi_k(\vec{x}, \vec{\Omega}, E) \left[1 - \sqrt{\frac{(\sigma_{jk}^P)^2}{\pi m E}} \right] \right. \\ \left. + \left[E \frac{\partial}{\partial E} \phi_k(\vec{x}, \vec{\Omega}, E) \right] \sqrt{\frac{(\sigma_{jk}^P)^2}{\pi m E}} \right. \\ \left. - \left[\vec{\Omega} \cdot \frac{\partial}{\partial \vec{\Omega}} \phi_k(\vec{x}, \vec{\Omega}, E) \right] \frac{(\sigma_{jk}^P)^2}{2mE} + \dots \right\} \end{aligned} \quad (6.20)$$

Because $\sqrt{\frac{(\sigma_{jk}^P)^2}{\pi m E}} \ll 1$ at those energies at which most nuclear reactions occur, the assumption of velocity conservation is clearly inferior to a straight ahead approximation but may be adequate for space radiations where the variation of $\phi_k(\vec{x}, \vec{\Omega}, E)$ with energy is sufficiently smooth. That is,

$$E \frac{\partial}{\partial E} \phi_k(\vec{x}, \vec{\Omega}, E) \approx \phi_k(\vec{x}, \vec{\Omega}, E)$$

Although the validity of the velocity conserving approximation is usually accepted without question in transport applications, it is clearly an inferior approximation to the straight ahead approximation which is often held suspect.

6.3.4. Decoupling of target and projectile flux. Equation (6.1) with the use of equation (6.8) may be rewritten as

$$B_j \phi_j(\vec{x}, \vec{\Omega}, E) = \sum_k F_{jk}^T \phi_k(\vec{x}, \vec{\Omega}, E) + \sum_k F_{jk}^P \phi_k(\vec{x}, \vec{\Omega}, E) \quad (6.21)$$

where the differential operator is given by

$$B_j = \left[\vec{\Omega} \cdot \nabla - \frac{1}{A_j} \frac{\partial}{\partial E} S_j(E) + \sigma_j(E) \right] \quad (6.22)$$

and the integral operator ($F_{jk} = F_{jk}^T + F_{jk}^P$) is given by

$$F_{jk} \phi_k(\vec{x}, \vec{\Omega}, E) = \int dE' d\vec{\Omega}' \sigma_{jk}(E, E', \vec{\Omega}, \vec{\Omega}') \phi_k(\vec{x}, \vec{\Omega}', E') \quad (6.23)$$

Defining the flux as a sum of two terms

$$\phi_j(\vec{x}, \vec{\Omega}, E) = \phi_j^T(\vec{x}, \vec{\Omega}, E) + \phi_j^P(\vec{x}, \vec{\Omega}, E) \quad (6.24)$$

allows the following separation:

$$B_j \phi_j^P(\vec{x}, \vec{\Omega}, E) = \sum_k F_{jk}^P \phi_k^P(\vec{x}, \vec{\Omega}, E) + \sum_k F_{jk}^P \phi_k^T(\vec{x}, \vec{\Omega}, E) \quad (6.25)$$

$$B_j \phi_j^T(\vec{x}, \vec{\Omega}, E) = \sum_k F_{jk}^T \phi_k^P(\vec{x}, \vec{\Omega}, E) + \sum_k F_{jk}^T \phi_k^T(\vec{x}, \vec{\Omega}, E) \quad (6.26)$$

As noted in connection with equations (6.8) through (6.11), the source term on the right-hand side of equation (6.26) is small at high energies and one may assume that

$$\phi_j^T(\vec{x}, \vec{\Omega}, E) \approx 0 \quad (6.27)$$

for $E \gg (\sigma_{jk}^T)^2/m$. As a result of equation (6.27) and the fact that the ion range is small compared with its mean-free path at low energy, one obtains

$$B_j \phi_j^P(\vec{x}, \vec{\Omega}, E) \approx \sum_k F_{jk}^P \phi_k^P(\vec{x}, \vec{\Omega}, E) \quad (6.28)$$

$$B_j \phi_j^T(\vec{x}, \vec{\Omega}, E) \approx \sum_k F_{jk}^T \phi_k^P(\vec{x}, \vec{\Omega}, E) \quad (6.29)$$

The advantage of this separation is that once equation (6.28) is solved by whatever means necessary, then equation (6.29) can be solved in closed form. The solution of equation (6.29) is accomplished by noting that the inwardly directed flux ϕ_j^T must vanish on the boundary, with the result that

$$\begin{aligned} \phi_j^T(\vec{x}, \vec{\Omega}, E) &\approx \sum_k \int_E^{E_\gamma} dE' \frac{A_j P_j(E')}{P_j(E) S_j(E)} \int dE'' d\vec{\Omega}' \sigma_{jk}^T(E', E'', \vec{\Omega}, \vec{\Omega}') \\ &\times \phi_k^P\left\{\vec{x} + [R_j(E) - R_j(E')] \vec{\Omega}, \vec{\Omega}', E''\right\} \end{aligned} \quad (6.30)$$

where $E_\gamma = R_j^{-1}[d + R_j(E)]$, with d denoting the projected distance to the boundary.

Using equations (6.5) and (6.7) in equation (6.30) yields

$$\begin{aligned} \phi_j^T(\vec{x}, \vec{\Omega}, E) &\approx \int_E^{E_\gamma} dE' \frac{A_j P_j(E')}{P_j(E) S_j(E)} \left[\frac{m}{2\pi (\sigma_{jk}^T)^2} \right]^{3/2} \sqrt{2E'} \exp \left[\frac{-mE'}{(\sigma_{jk}^T)^2} \right] \\ &\times \zeta_j^T\left\{\vec{x} + [R_j(E) - R_j(E')] \vec{\Omega}\right\} \end{aligned} \quad (6.31)$$

where

$$\zeta_j^T(\vec{x}) = \sum_k \int dE' d\vec{\Omega}' \sigma_k(E') \nu_{jk}^T(E') \phi_k^P(\vec{x}, \vec{\Omega}', E') \quad (6.32)$$

and σ_{jk}^T has been assumed to be a slowly varying function of projectile type k and projectile energy E . If the range of secondary type j ions is small compared with

their mean-free path lengths and the mean-free paths of the fragmenting parent ions ℓ_k , that is,

$$R_j \left[\frac{(\sigma_{jk}^T)^2}{m} \right] \ll \ell_k \quad (6.33)$$

then the integral of equation (6.31) may be simplified as

$$\phi_j^T(\vec{x}, \vec{\Omega}, E) \approx \frac{A_j}{S_j(E)} \zeta_j^T(\vec{x}) \int_E^{E_\gamma} \left[\frac{m}{2\pi(\sigma_{jk}^T)^2} \right]^{3/2} \sqrt{2E'} \exp \left[\frac{-mE'}{(\sigma_{jk}^T)^2} \right] dE' \quad (6.34)$$

which may be reduced into terms of known functions. Thus,

$$\phi_j^T(\vec{x}, \vec{\Omega}, E) \approx \frac{A_j}{S_j(E)} \zeta_j^T(\vec{x}) \frac{1}{2\pi\sqrt{\pi}} \left\{ \Gamma \left[\frac{3}{2}, \frac{mE}{(\sigma_{jk}^T)^2} \right] - \Gamma \left[\frac{3}{2}, \frac{mE_\gamma}{(\sigma_{jk}^T)^2} \right] \right\} \quad (6.35)$$

in terms of the incomplete gamma function. One can show that equation (6.35) is equivalent to

$$\begin{aligned} \phi_j^T(\vec{x}, \vec{\Omega}, E) \approx \frac{A_j}{S_j(E)} \zeta_j^T(\vec{x}) \frac{1}{2\pi} \left\{ \frac{1}{2} \operatorname{erfc} \left[\sqrt{\frac{mE}{(\sigma_{jk}^T)^2}} \right] - \frac{1}{2} \operatorname{erfc} \left[\sqrt{\frac{mE_\gamma}{(\sigma_{jk}^T)^2}} \right] \right. \\ \left. + \sqrt{\frac{mE}{\pi(\sigma_{jk}^T)^2}} \exp \left[\frac{-mE}{(\sigma_{jk}^T)^2} \right] - \sqrt{\frac{mE_\gamma}{\pi(\sigma_{jk}^T)^2}} \exp \left[\frac{-mE_\gamma}{(\sigma_{jk}^T)^2} \right] \right\} \quad (6.36) \end{aligned}$$

At points sufficiently removed from the boundary such that

$$R_j^{-1}(d) \gg \frac{(\sigma_{jk}^T)^2}{m} \quad (6.37)$$

equation (6.36) may be reduced to

$$\phi_j^T(\vec{x}, \vec{\Omega}, E) \approx \frac{A_j}{S_j(E)} \zeta_j^T(\vec{x}) \frac{1}{2\pi} \left\{ \frac{1}{2} \operatorname{erfc} \left[\sqrt{\frac{mE}{(\sigma_{jk}^T)^2}} \right] + \sqrt{\frac{mE}{\pi(\sigma_{jk}^T)^2}} \exp \left[\frac{-mE}{(\sigma_{jk}^T)^2} \right] \right\} \quad (6.38)$$

The solution of equation (6.28) will now be further examined.

6.3.5. Back-substitution and perturbation theory. One approach to the solution of equation (6.28) results from the tendency of the multiple-charged ions

to be destroyed in nuclear reactions. Thus,

$$F_{jk}^P \equiv 0 \quad (j \geq k) \quad (6.39)$$

This means that there is a maximum j such that

$$B_J \phi_J^P(\vec{x}, \vec{\Omega}, E) = 0 \quad (6.40)$$

where J is the largest j . Furthermore,

$$B_{J-1} \phi_{J-1}^P(\vec{x}, \vec{\Omega}, E) = F_{J-1, J}^P \phi_J^P(\vec{x}, \vec{\Omega}, E) \quad (6.41)$$

and, in general,

$$B_{J-N} \phi_{J-N}^P(\vec{x}, \vec{\Omega}, E) = \sum_{k=1}^{N-1} F_{J-N, J-k}^P \phi_{J-k}^P(\vec{x}, \vec{\Omega}, E) \quad (6.42)$$

for $N < J-1$. Note that equations (6.41) and (6.42) constitute solvable problems. The singly charged ions satisfy

$$B_1 \phi_1^P(\vec{x}, \vec{\Omega}, E) = F_{1,1}^P \phi_1^P(\vec{x}, \vec{\Omega}, E) + \sum_{k=2}^J F_{1,k}^P \phi_k^P(\vec{x}, \vec{\Omega}, E) \quad (6.43)$$

which, unlike equations (6.40) to (6.42), is an integral-differential equation that is difficult to solve directly. Equation (6.43) is solvable by perturbation theory, and the resultant series is known to converge rapidly for intermediate and low energies (Wilson and Lamkin, 1975; Wilson et al., 1989a and 1989b; Wilson and Townsend 1988). Note that equations (6.40) and (6.42) are also obtained from perturbation theory as applied to equation (6.28) at the outset. Thus, the perturbation series is expected to converge after the first J plus a few terms.

6.4. References

- Allkofer, O. C.; and Heinrich, W., 1974: Attenuation of Cosmic Ray Heavy Nuclei Fluxes in the Upper Atmosphere by Fragmentation. *Nuclear Phys. B*, vol. B71, no. 3, pp. 429-438.
- Alsmiller, R. G., Jr.; Irving, D. C.; Kinney, W. E.; and Moran, H. S., 1965: The Validity of the Straightahead Approximation in Space Vehicle Shielding Studies. *Second Symposium on Protection Against Radiations in Space*, Arthur Reetz, Jr., ed., NASA SP-71, pp. 177-181.
- Alsmiller, R. G., 1967: High-Energy Nucleon Transport and Space Vehicle Shielding. *Nuclear Sci. & Eng.*, vol. 27, no. 2, pp. 158-189.
- Alsmiller, R. G., Jr.; Irving, D. C.; and Moran, H. S., 1968: Validity of the Straightahead Approximation in Space-Vehicle Shielding Studies, Part II. *Nuclear Sci. & Eng.*, vol. 32, no. 1, pp. 56-61.
- Alsmiller, R. G., Jr.; Barish, J.; and Scott, W. W., 1969: The Effects of Multiple Coulomb Scattering and Range Straggling in Shielding Against Solar-Flare Protons. *Nuclear Sci. & Eng.*, vol. 35, no. 3, pp. 405-406.

- Bertini, H. W., 1962: Monte Carlo Calculations for Intranuclear Cascades. *Proceedings of the Symposium on the Protection Against Radiation Hazards in Space*, Book 2, TID-7652, United States Atomic Energy Commission, pp. 433-522.
- Bethe, H. A.; Korff, S. A.; and Placzek, G., 1940.: On the Interpretation of Neutron Measurements in Cosmic Radiation. *Phys. Review*, vol. 57, second ser., no. 7, pp. 573-587.
- Chatterjee, A.; Tobias, C. A.; and Lyman, J. T., 1976: Nuclear Fragmentation in Therapeutic and Diagnostic Studies With Heavy Ions. *Spallation Nuclear Reactions and Their Applications*, B. S. P. Shen and M. Merker, eds., D. Reidel Publ. Co., pp. 169-191.
- Cleghorn, T. F.; Freier, P. S.; and Waddington, C. J., 1968: The Energy Dependence of the Fragmentation Parameters and Mean Free Paths of Cosmic-Ray Nuclei With $Z \geq 10$. *Canadian J. Phys.*, vol. 46, no. 10, pp. S572-S577.
- Cocconi, G.; Cocconi-Tongiorgi, V.; and Greisen, K., 1948: Neutrons in the Penetrating Showers of the Cosmic Radiation. *Phys. Review*, vol. 74, second ser., no. 12, pp. 1867-1868.
- Cocconi, G.; Cocconi Tongiorgi, V.; and Widgoff, M., 1950: Cascades of Nuclear Disintegrations Induced by the Cosmic Radiation. *Phys. Review*, vol. 79, second ser., no. 5, pp. 768-780.
- Curtis, S. B.; Doherty, W. R.; and Wilkinson, M. C., 1969: *Study of Radiation Hazards to Man on Extended Near Earth Missions*. NASA CR-1469.
- Curtis, S. B.; and Wilkinson, M. C., 1972: The Heavy Particle Hazard—What Physical Data Are Needed? *Proceedings of the National Symposium on Natural and Manmade Radiation in Space*, E. A. Warman, ed., NASA TM X-2440, pp. 1007-1015.
- Davis, Leverett, Jr., 1960: On the Diffusion of Cosmic Rays in the Galaxy. *Proceedings of the Moscow Cosmic Ray Conference*, International Union of Pure and Applied Physics (Moscow), pp. 220-225.
- Dye, D. L.; and Noyes, J. C., 1960: Biological Shielding for Radiation Belt Particles. *J. Astronaut. Sci.*, vol. VII, no. 3, pp. 64-70.
- Dye, David L., 1962: Space Proton Doses at Points Within the Human Body. *Proceedings of the Symposium on the Protection Against Radiation Hazards in Space*, Book 2, TID-7652, United States Atomic Energy Commission, pp. 633-661.
- Feshbach, H.; and Huang, K., 1973: Fragmentation of Relativistic Heavy Ions. *Phys. Lett.*, vol. 47B, no. 4, pp. 300-302.
- Foelsche, T., 1959: Estimate of the Specific Ionization of Heavy Cosmic Ray Primaries in Tissue or Water. *J. Astronaut. Sci.*, vol. VI, no. 4, pp. 57-62.
- Freier, Phyllis; Lofgren, E. J.; Ney, E. P.; and Oppenheimer, F., 1948: The Heavy Component of Primary Cosmic Rays. *Phys. Review*, vol. 74, second ser., no. 12, pp. 1818-1827.
- Ganapol, Barry D.; Townsend, Lawrence W.; and Wilson, John W., 1989: *Benchmark Solutions for the Galactic Ion Transport Equations: Energy and Spatially Dependent Problems*. NASA TP-2878.

Transport Methods and Interactions for Space Radiations

- Ganapol, Barry D.; Townsend, Lawrence W.; Lamkin, Stanley L.; and Wilson, John W., 1991: *Benchmark Solutions for the Galactic Heavy-Ion Transport Equations With Energy and Spatial Coupling*. NASA TP-3112.
- Ginzburg, V. L.; and Syrovatskii, S. I. (H. S. H. Massey, transl., and D. Ter Haar, ed.), 1964: *The Origin of Cosmic Rays*. Macmillan Co.
- Gloeckler, G.; and Jokipii, J. R., 1969: Physical Basis of the Transport and Composition of Cosmic Rays in the Galaxy. *Phys. Review Lett.*, vol. 22, no. 26, pp. 1448-1453.
- Goldberger, M. L., 1948: The Interaction of High Energy Neutrons and Heavy Nuclei. *Phys. Review*, vol. 74, no. 10, pp. 1269-1277.
- Goldhaber, A. S., 1974: Statistical Models of Fragmentation Processes. *Phys. Lett.*, vol. 53B, no. 4, pp. 306-308.
- Heckman, H. H.; Greiner, D. E.; Lindstrom, P. J.; and Bieser, F. S., 1972: Fragmentation of ^{14}N Nuclei at 29 GeV: Inclusive Isotope Spectra at 0° . *Phys. Review Lett.*, vol. 28, no. 14, pp. 926-929.
- Heckman, H. H., 1975: *Heavy Ion Fragmentation Experiments at the Bevatron*. NASA CR-142589.
- Hess, Victor F.; and Eugster, Jakob, 1949: *Cosmic Radiation and Its Biological Effects*, Second ed., Revised and Augmented. Fordham Univ. Press.
- Janni, Joseph F., 1982a: Proton Range-Energy Tables, 1 keV-10 GeV—Energy Loss, Range, Path Length, Time-of-Flight, Straggling, Multiple Scattering, and Nuclear Interaction Probability. Part 1. For 63 Compounds. *At. Data & Nuclear Data Tables*, vol. 27, nos. 2/3, pp. 147-339.
- Janni, Joseph F., 1982b: Proton Range-Energy Tables, 1 keV-10 GeV—Energy Loss, Range, Path Length, Time-of-Flight, Straggling, Multiple Scattering, and Nuclear Interaction Probability. Part 2. For Elements $1 \leq Z \leq 92$. *At. Data & Nuclear Data Tables*, vol. 27, nos. 4/5, pp. 341-529.
- Lambiotte, Jules J., Jr.; Wilson, John W.; and Filippas, Tassos A., 1971: Proper-3C: *A Nucleon-Pion Transport Code*. NASA TM X-2158.
- Letaw, John; Tsao, C. H.; and Silberberg, R., 1983: Matrix Methods of Cosmic Ray Propagation. *Composition and Origin of Cosmic Rays*, Maurice M. Shapiro, ed., D. Reidel Publ. Co., pp. 337-342.
- Lezniak, J. A., 1979: The Extension of the Concept of the Cosmic-Ray Path-Length Distribution to Nonrelativistic Energies. *Astrophys. & Space Sci.*, vol. 63, no. 2, pp. 279-293.
- Metropolis, N.; Bivins, R.; Storm, M.; Turkevich, Anthony; Miller, J. M.; and Friedlander, G., 1958: Monte Carlo Calculations on Intranuclear Cascades. I. Low-Energy Studies. *Phys. Review*, vol. 110, second ser., no. 1, pp. 185-203.
- Peters, B., 1958: The Nature of Primary Cosmic Radiation. *Progress in Cosmic Ray Physics*, J. G. Wilson, ed., Interscience Publ., Inc., pp. 191-242.

- Raisbeck, G. M.; and Yiou, F., 1975: Production Cross Sections of Be Isotopes in C and O Targets Bombarded by 2.8 GeV α Particles: Implications for Factorization. *Phys. Review Lett.*, vol. 35, no. 3, pp. 155-159.
- Schaefer, Hermann J., 1959: *Radiation and Man in Space*. Volume 1 of *Advances in Space Science*, Frederick I. Ordway III, ed., Academic Press, Inc., pp. 267-339.
- Schimmerling, Walter; Rapkin, Marwin; Wong, Mervyn; and Howard, Jerry, 1986: The Propagation of Relativistic Heavy Ions in Multielement Beam Lines. *Med. Phys.*, vol. 13, no. 2, pp. 217-228.
- Townsend, L. W.; and Wilson, J. W., 1988: Nuclear Cross Sections for Hadronic Transport. *Trans. American Nuclear Soc.*, vol. 56, pp. 277-279.
- Wilson, John W.; and Lamkin, Stanley L., 1975: Perturbation Theory for Charged-Particle Transport in One Dimension. *Nuclear Sci. & Eng.*, vol. 57, no. 4, pp. 292-299.
- Wilson, John W., 1977a: *Analysis of the Theory of High-Energy Ion Transport*. NASA TN D-8381.
- Wilson, J. W., 1977b: Depth-Dose Relations for Heavy Ion Beams. *Virginia J. Sci.*, vol. 28, no. 3, pp. 136-138.
- Wilson, John W., 1983: *Heavy Ion Transport in the Straight Ahead Approximation*. NASA TP-2178.
- Wilson, John W.; Townsend, L. W.; Bidasaria, H. B.; Schimmerling, Walter; Wong, Mervyn; and Howard, Jerry, 1984: ^{20}Ne Depth-Dose Relations in Water. *Health Phys.*, vol. 46, no. 5, pp. 1101-1111.
- Wilson, John W.; and Badavi, F. F., 1986: Methods of Galactic Heavy Ion Transport. *Radiat. Res.*, vol. 108, pp. 231-237.
- Wilson, John W.; and Townsend, L. W., 1988: A Benchmark for Galactic Cosmic-Ray Transport Codes. *Radiat. Res.*, vol. 114, no. 2, pp. 201-206.
- Wilson, John W.; Lamkin, Stanley L.; Farhat, Hamidullah; Ganapol, Barry D.; and Townsend, Lawrence W., 1989a: *A Hierarchy of Transport Approximations for High Energy Heavy (HZE) Ions*. NASA TM-4118.
- Wilson, John W.; Townsend, Lawrence W.; Nealy, John E.; Chun, Sang Y.; Hong, B. S.; Buck, Warren W.; Lamkin, S. L.; Ganapol, Barry D.; Khan, Ferdous; and Cucinotta, Francis A., 1989b: BRYNTRN: *A Baryon Transport Model*. NASA TP-2887.

1
2
3
4
5
6
7
8
9
10
11
12
13
14
15
16
17
18
19
20
21
22
23
24
25
26
27
28
29
30
31
32
33
34
35
36
37
38
39
40
41
42
43
44
45
46
47
48
49
50
51
52
53
54
55
56
57
58
59
60
61
62
63
64
65
66
67
68
69
70
71
72
73
74
75
76
77
78
79
80
81
82
83
84
85
86
87
88
89
90
91
92
93
94
95
96
97
98
99
100

100

Chapter 7

Dose Approximation in Arbitrary Convex Geometry

7.1. Introduction

A convenient property of energetic heavy-charged particles, when passing through matter, is that the primaries and their secondary particles remain relatively confined to the primary beam axis. As a consequence, the particle beam in matter is not strongly affected by near boundaries, and the problem of calculating dose in a complicated geometric object is greatly simplified (Wilson and Khandelwal, 1974; Schimmerling et al., 1986). Furthermore, the small beam width is a useful expansion parameter to develop a series that converges rapidly for most practical dose calculations. The final result relates dose at any point in an arbitrary convex region to an integral over solutions to the straight ahead approximation of the Boltzmann equation for normal incidence on a semi-infinite slab.

Energetic massive-charged particles constitute much of the radiation environment that man is subjected to in space. An attendant problem for radiation shield design is the evolution of the resultant dose in complex geometric objects, such as the human body. Although simple calculations neglecting nuclear reactions are often made (Cucinotta and Wilson, 1985; Santoro et al., 1986; Seltzer, 1980), several researchers have demonstrated that nuclear reaction effects are generally important (Shen, 1963; Alsmiller, 1967; Armstrong and Bishop, 1971). Incorporation of nuclear reaction effects requires solution of the Boltzmann transport equation subject to appropriate boundary conditions (Alsmiller, 1967).

The imposition of complicated boundary conditions often limits one's ability to obtain solutions to the transport problem even in the restricted sense of numerical solution. Even for such general techniques as the Monte Carlo method, the complexity introduced by complicated boundaries leads to prohibitively long calculations on present-day computers so that typical calculations approximate complicated objects such as the human body by slabs (Armstrong and Bishop, 1971), cylinders, or spheres (Santoro et al., 1986) of uniform soft tissue. In fact, the extensive calculations of dose in tissue slabs constitute most of our understanding of radiation dose in humans, although the relations between dose rates in a slab and dose rates in a particular body organ are at best poorly understood (Neufeld and Wright, 1972; Langley and Billings, 1972).

There is an approximate form of transport theory in which the transport equation is solvable for complex boundaries. The use of the "straight ahead" approximation reduces consideration to one-dimensional transport or a sort of ray tracing. The principal simplification of the straight ahead approximation is that lateral boundaries do not enter the solution along a given ray. The disadvantages of the method are that the effects of lateral dispersion on the buildup of secondaries are neglected and the errors of the approximation are generally not known (Alsmiller, 1967).

In this chapter, we derive an expansion for the solution to the transport equation in two dimensions subject to boundary conditions given for an arbitrary convex region. The expansion parameter is taken as the lateral dispersion, which is so small that the lowest order expansion term is the dominant contribution. When the expansion is applied to the straight ahead theory, only the first term is nonzero because lateral dispersion is zero in this case. The advantages of using the first term of the expansion of the transport solution instead of the straight ahead theory are that the effects of lateral dispersion on the buildup of secondaries are taken into account and the errors associated with the approximation are known. On the basis of general principles, the present expansion always provides an overestimate of dose (conservative estimate), and in almost all circumstances this overestimate is small. The extension to three dimensions is conceptually the same but with more complicated algebra.

7.2. High-Energy Transport

The fields of type j particles are represented by the functions $\phi_j(\vec{x}, E, \vec{\Omega})$, which denote the particle fluence of energy E that crosses a plane normal to the direction of motion $\vec{\Omega}$ per unit solid angle as seen at a position \vec{x} . The fields satisfy the steady linear Boltzmann transport equation

$$\begin{aligned} & \left[\vec{\Omega} \cdot \vec{\nabla} + \sigma_j(E) - \frac{\partial}{\partial E} S_j(E) \right] \phi_j(\vec{x}, E, \vec{\Omega}) \\ & = \zeta_j(\vec{x}, E, \vec{\Omega}) + \sum_k \int d\Omega' \int dE' \sigma_{jk}(E, E', \vec{\Omega} \cdot \vec{\Omega}') \phi_k(\vec{x}, E', \vec{\Omega}') \end{aligned} \quad (7.1)$$

where $S_j(E)$ is the stopping power (energy loss per unit path length), $\sigma_j(E)$ is the total macroscopic cross section, $\zeta_j(\vec{x}, E, \vec{\Omega})$ is the source of type j particles, and the cross section for type j secondary particles of energy E produced by collisions of type k particles of energy E' with the medium is represented by $\sigma_{jk}(E, E', \vec{\Omega} \cdot \vec{\Omega}')$. The Boltzmann equation admits solution in a closed region for which the inward-directed flux is specified on the boundary $\vec{\Gamma}$. The boundary condition is that

$$\phi_j(\vec{\Gamma}, E, \vec{\Omega}) = \psi_j(\vec{\Gamma}, E, \vec{\Omega}) \quad (7.2a)$$

for all $\vec{\Omega}$ such that $\vec{n} \cdot \vec{\Omega} < 0$, where \vec{n} is the outward directed unit normal and $\psi_j(\vec{\Gamma}, E, \vec{\Omega})$ is a specified boundary function determined from exterior sources. Homogeneous boundary conditions can be used by including an equivalent boundary source on the right side of equation (7.1) given by

$$\xi_j(\vec{\Gamma}, E, \vec{\Omega}) = -\vec{n} \cdot \vec{\Omega} \psi_j(\vec{\Gamma}, E, \vec{\Omega}) \quad (7.2b)$$

A useful property of equation (7.1) is the linearity that allows superposition of solutions. Thus, the solution for a sum of sources is the sum of solutions for each source. As will be seen, there is a great advantage in considering the solution for an arbitrary source as a superposition of solutions for unidirectional monoenergetic point sources.

Presently, the energy absorbed per unit mass or dose is of interest. The dose at a point \vec{x} is taken as

$$D(\vec{x}) = \frac{1}{d} \sum_j \int d\vec{\Omega}' \int dE' \phi_j(\vec{x}, E', \vec{\Omega}') S_j(E') \quad (7.3)$$

where d is the mass density. Since the fields $\phi_j(\vec{x}, E', \vec{\Omega}')$ are linear functions of the source, we may rewrite equation (7.3) as

$$D(\vec{x}) = \sum_k \int_{\Gamma} dl \int d\vec{\Omega} \int dE R_k(\vec{x}, E, \vec{\Omega}, \vec{\Gamma}) \xi_k[\vec{\Gamma}(l), E, \vec{\Omega}] \quad (7.4)$$

when all sources lie on the boundary $\vec{\Gamma}$ and dl is the incremental boundary surface. From the linearity of equation (7.1), the relation between the fields and the source is

$$\phi_j(\vec{x}, E', \vec{\Omega}') = \sum_k \int dE \int d\vec{\Omega} \int dl G_{jk}(\vec{x}, \vec{\Gamma}, E', E, \vec{\Omega}', \vec{\Omega}) \zeta_k(\vec{\Gamma}, E, \vec{\Omega}) \quad (7.5)$$

where G_{jk} is Green's function. The dose response becomes

$$R_k(\vec{x}, E, \vec{\Omega}, \vec{\Gamma}) = \frac{1}{d} \int dE' \int d\vec{\Omega}' \sum_j G_{jk}(\vec{x}, \vec{\Gamma}, E', E, \vec{\Omega}', \vec{\Omega}) S_j(E') \quad (7.6)$$

The function $R_k(\vec{x}, E, \vec{\Omega}, \vec{\Gamma})$ is the dose at a point \vec{x} caused by a point source of type k particles of energy E located at the point $\vec{\Gamma}$ on the boundary and directed toward $\vec{\Omega}$. Note that R_k in equation (7.6) is a solution for homogeneous boundary conditions of equation (7.1) when taken with equation (7.4); R_k is a function of the geometric shape of the bounding surface.

We see that the boundaries enter the solution given by equation (7.4) in two essential ways:

1. The boundary enters the dose calculation by equation (7.4) as an integral over the equivalent boundary source.
2. The homogeneous boundary condition enters through the function R_k .

The properties of the function R_k are discussed in the next section, where it will be argued that although R_k depends on the boundaries, this dependence is weak and, therefore, negligible. Supportive evidence of this claim will be presented, and some numerical results will be discussed. Based on these properties, an approximate form of R_k will be derived that results in simplification of equation (7.4) by relating it to flux-to-dose-rate conversion factors for radiation incident normally on a slab.

7.3. Properties of the Dose Response Function

In this section we first discuss the dose response when all boundaries are far removed. A specific general form for the response is determined. The effects of

near boundaries are then discussed, especially in the context of calculating $D(\vec{x})$ given by equation (7.4). The discussion is limited primarily to response to proton sources, but some aspects of high-energy neutrons will also be discussed. The methods are even more appropriate for ions heavier than protons.

Protons of energy less than a few hundred MeV interact with dense matter predominantly through energy loss in collisions with electrons in the surrounding material. The probability of nuclear reaction before stopping is rather small, and relatively few secondaries are produced when reactions do occur. The paths of the primary particles are confined to a small cylinder about the initial direction, with the deviations in the paths resulting predominantly from multiple coulomb scattering through very small angles.

At several hundred MeV, nuclear reactions are important, and most primary particles will suffer nuclear reaction before stopping. The most energetic secondaries are confined in a narrow cone about the initial direction (this cone narrows with increasing primary energy as shown by Shen (1965)) and are closely confined to the initial beam axis over at least the first mean-free path (≈ 1 m in water). Low-energy secondary-charged particles are stopped near their point of production, and only the low-energy neutrons are able to migrate far from the beam axis. At large distances from the beam, only a net outward flux of low-energy neutrons is observed; this flux decreases exponentially because of absorptive processes in the medium. These processes are shown schematically in figure 7.1.

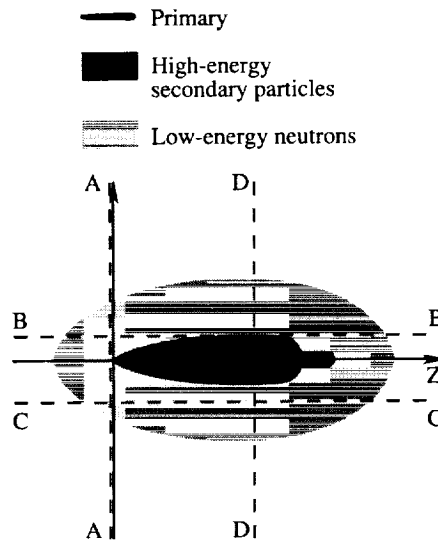


Figure 7.1. Schematic representation of the response to a point source of monoenergetic protons.

At very high energies, nuclear reactions tend to dominate, and the distinction between incident neutrons and protons all but disappears. A principal mode of transferring energy to the medium is through the multitude of secondary particles produced in nuclear reaction.

The dose response will now be parameterized in such a way to exhibit the above properties. We represent the dose response of a unidirectional point source of protons of energy E at the origin directed along the z -axis of an infinite medium as

$$R(z, E, r) = R_N(z, E) g[\delta(E, z), r] \quad (7.7)$$

where r is the radial coordinate normal to the z -axis. This is shown schematically in figure 7.1. The parameter $\delta(E, z)$ is the root-mean-square value of the beam width. The amount of shading in the figure illustrates the magnitude of the dose. The functions on the right side of equation (7.7) are chosen so that $g(\delta, r)$ gives the lateral profile of the beam with

$$\int_{-\infty}^{\infty} r^{2n} g(\delta, r) dr = C_{2n} \delta^{2n} \quad (7.8)$$

and $C_0 = 1$ so that $R_N(z, E)$ is the fluence-to-dose conversion factor for a uniform source incident normal to the $z = 0$ plane. We now consider the changes in the dose response if a boundary is moved to some position near the beam.

First, consider placing a void to the left of the $z = 0$ plane, which is boundary A in figure 7.1. This means that radiation will no longer backscatter from the material to the left of boundary A and the doses with and without the boundary are related by

$$R(E, z, r) = R^A(E, z, r) + \epsilon^A(z, r) \quad (7.9)$$

The fact that the dose with the boundary far removed is an overestimate of the dose with the boundary A is denoted by

$$\epsilon^A(0, r) \geq \epsilon^A(z, r) \geq 0 \quad (7.10)$$

If we use the approximation of R^A as

$$R^A(E, z, r) \approx R(E, z, r) \quad (7.11)$$

then the order of magnitude of the overestimate of dose is given by

$$\begin{aligned} & \int_{-\infty}^{\infty} [R(E, z, r) - R^A(E, z, r)] dr \\ &= [R_N(E, z) - R_N^A(E, z)] \\ &\leq [R_N(E, 0) - R_N^A(E, 0)] \\ &\approx 2 \times 10^{-3} R_N(E, 0) \end{aligned} \quad (7.12)$$

as estimated (actually overestimated) from the numerical results of Irving et al. (1965) and Alsmiller et al. (1965). The placement of a void to the right of boundary D parallel to A located downstream from the source would be expected to produce similar effects.

A more difficult question concerns the effects of lateral boundaries, shown as C or B in figure 7.1. Clearly, as long as the lateral boundaries are removed from

the heavily shaded areas, the effects are negligible. Thus, if the distance from the beam axis to the boundary is greater than the beam width δ , then the lateral boundaries will not greatly affect the interior solution.

Beam profiles for 400-MeV protons and neutrons have been calculated by Wright, Hamm, and Turner (1971) and are shown in figures 7.2 and 7.3; their results show that $\delta \leq 1$ cm in tissue. The purpose of the next section is to derive an approximate form for equation (7.4), which makes use of the beam width being small, that is applicable to the transport of protons, high-energy neutrons, and heavy ions.

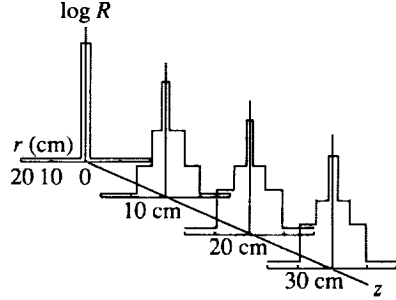


Figure 7.2. Beam profiles of a point source of 400-MeV protons calculated by Wright, Hamm, and Turner (1971).

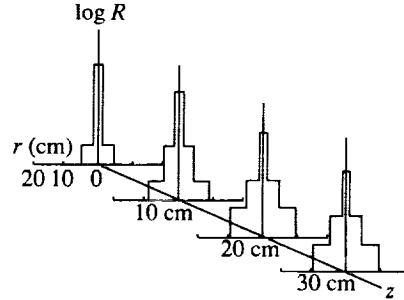


Figure 7.3. Beam profiles of a point source of 400-MeV neutrons calculated by Wright, Hamm, and Turner (1971).

7.4. Expansion for Two-Dimensional Transport

We consider the transport solution in a closed, convex, two-dimensional region. The boundary is defined by a vector function $\vec{\Gamma}(l)$, where l is the path length along the boundary curve. The unit tangent to the curve is

$$\vec{t}(l) = \frac{d\vec{\Gamma}(l)}{dl} \quad (7.13)$$

and points in the direction of increasing l . The outward-directed unit normal is

$$\vec{n}(l) = -\rho(l) \frac{d\vec{t}(l)}{dl} \quad (7.14)$$

where $\rho(l)$ is the radius of curvature. The dose Δ at an interior point \vec{x} caused by a boundary source $\zeta(\vec{\Gamma}, E, \vec{\Omega})$ is given by

$$\Delta(\vec{x}, E, \vec{\Omega}) = \int_{\Gamma} R^{\Gamma} [E, z(\vec{\Gamma}, \vec{x}, \vec{\Omega}), r(\vec{\Gamma}, \vec{x}, \vec{\Omega})] \zeta(\vec{\Gamma}, E, \vec{\Omega}) dl \quad (7.15)$$

where the arguments of R^{Γ} are

$$z(\vec{\Gamma}, \vec{x}, \vec{\Omega}) = \vec{\Omega} \cdot (\vec{\Gamma} - \vec{x}) \quad (7.16)$$

$$r(\vec{\Gamma}, \vec{x}, \vec{\Omega}) = \vec{\Omega}_{\perp} \cdot (\vec{\Gamma} - \vec{x}) \quad (7.17)$$

where $\vec{\Omega}_\perp$ is a unit vector perpendicular to $\vec{\Omega}$. We now seek means whereby the above integral can be approximated.

We recall that the effects of boundaries on $R^\Gamma(E, z, r)$ are expected to be small so that the replacement

$$R^\Gamma(E, z, r) \rightarrow R(E, z, r) \quad (7.18)$$

provides an overestimate of the dose and the error is negligible so that

$$\Delta(E, x, \Omega) \approx \int_\Gamma R[E, z(\vec{\Gamma}, \vec{x}, \vec{\Omega}), r(\vec{\Gamma}, \vec{x}, \vec{\Omega})] \zeta(\vec{\Gamma}, E, \vec{\Omega}) dl \quad (7.19)$$

Note that equation (7.19) is a considerable simplification over equation (7.15). The replacement of R^Γ by R means that the transport equation needs to be solved only once to determine the function R , which is then applicable to all problems through equation (7.19). Now we will make use of the property that $R(E, z, r)$ has a maximum at $r = 0$ and drops precipitously away from the maximum. To do this, we first make a translation along the bounding curve to the point where

$$r(\vec{\Gamma}, \vec{x}, \vec{\Omega}) = \vec{\Omega}_\perp \cdot (\vec{x} - \vec{\Gamma}) = 0 \quad (7.20)$$

label the point $l_x(\vec{\Omega})$, and define a new variable

$$s = l - l_x(\vec{\Omega}) \quad (7.21)$$

and the vector function

$$\vec{\gamma}(s) = \vec{\Gamma}(l) - \vec{\Gamma}[l_x(\vec{\Omega})] \quad (7.22)$$

We can then rewrite

$$z(\vec{\Gamma}, \vec{x}, \vec{\Omega}) = z_x(\vec{\Omega}) - \vec{\Omega} \cdot \vec{\gamma}(s) \quad (7.23)$$

$$r(\vec{\Gamma}, \vec{x}, \vec{\Omega}) = -\vec{\Omega}_\perp \cdot \vec{\gamma}(s) \quad (7.24)$$

and the integral as

$$\begin{aligned} \Delta(\vec{x}, E, \vec{\Omega}) &= \int_{-s_1(\vec{\Omega})}^{s_2(\vec{\Omega})} R[E, z_x(\vec{\Omega}) - \vec{\Omega} \cdot \vec{\gamma}(s), -\vec{\Omega}_\perp \cdot \vec{\gamma}(s)] \\ &\quad \times \zeta[\vec{\Gamma}_x + \vec{\gamma}(s), E, \vec{\Omega}] ds \end{aligned} \quad (7.25)$$

where the limits of integration are given by solutions of

$$\vec{t}(-s_1) \cdot \vec{\Omega} = -1 \quad (7.26)$$

$$\vec{t}(s_2) \cdot \vec{\Omega} = 1 \quad (7.27)$$

where $\vec{t}(s)$ is the unit tangent at s and is directed toward increasing s . We can further simplify equation (7.25) by transforming the integral over path length s to an integral over the lateral dimension r .

Consider the expansion

$$r = -\vec{\Omega}_\perp \cdot \vec{t}(0)s + \frac{1}{2\rho_o} \vec{\Omega}_\perp \cdot \vec{n}(0)s^2 + \dots \quad (7.28)$$

which, when inverted, reads $(\vec{n}_o \cdot \vec{\Omega} = \vec{\Omega}_\perp \cdot \vec{t}_o$ and where subscript o denotes evaluation at $r = s = 0$):

$$s = \frac{-r}{\vec{n}_o \cdot \vec{\Omega}} + \frac{1}{2\rho_o} \frac{\vec{\Omega} \cdot \vec{t}_o}{\vec{n}_o \cdot \vec{\Omega}} \frac{r^2}{(\vec{n}_o \cdot \vec{\Omega})^2} + \dots \quad (7.29)$$

so that

$$z(\vec{\Gamma}, \vec{x}, \vec{\Omega}) = z_x(\vec{\Omega}) + \left(\frac{\vec{\Omega} \cdot \vec{t}_o}{\vec{\Omega} \cdot \vec{n}_o} \right) r - \frac{1}{2\rho_o} \times \frac{(\vec{\Omega} \cdot \vec{t}_o)^2 - (\vec{\Omega} \cdot \vec{n}_o)^2}{(\vec{\Omega} \cdot \vec{n}_o)^4} r^2 + \dots \quad (7.30)$$

and

$$\vec{\gamma}(s) = -\vec{t}_o \left(\frac{r}{\vec{n}_o \cdot \vec{\Omega}} \right) + \frac{1}{2\rho_o} \left(\vec{t}_o \frac{\vec{\Omega} \cdot \vec{t}_o}{\vec{\Omega} \cdot \vec{n}_o} - \vec{n}_o \right) \left(\frac{r}{\vec{n}_o \cdot \vec{\Omega}} \right)^2 + \dots \quad (7.31)$$

With a change of variables,

$$\begin{aligned} \Delta(\vec{x}, E, \vec{\Omega}) &= \int_{-r_1(\vec{\Omega})}^{r_2(\vec{\Omega})} R \left[E, z_x + \left(\frac{\vec{\Omega} \cdot \vec{t}_o}{\vec{\Omega} \cdot \vec{n}_o} \right) r - \frac{1}{2\rho_o} \frac{(\vec{\Omega} \cdot \vec{t}_o)^2 - (\vec{\Omega} \cdot \vec{n}_o)^2}{(\vec{\Omega} \cdot \vec{n}_o)^2} r^2, r \right] \\ &\times \phi \left\{ \vec{\Gamma}_x - \vec{t}_o \left(\frac{r}{\vec{n}_o \cdot \vec{\Omega}} \right) + \frac{1}{2\rho_o} \left[\vec{t}_o \frac{\vec{\Omega} \cdot \vec{t}_o}{\vec{n}_o \cdot \vec{\Omega}} - \vec{n}_o \right] \left(\frac{r}{\vec{n}_o \cdot \vec{\Omega}} \right)^2 \right. \\ &\left. + \dots, \vec{\Omega}, E \right\} \left[1 - \frac{1}{\rho_o} \frac{\vec{\Omega} \cdot \vec{t}_o}{(\vec{\Omega} \cdot \vec{n}_o)^2} r + \dots \right] dr \end{aligned} \quad (7.32)$$

where $r_1(\vec{\Omega})$ and $r_2(\vec{\Omega})$ are the distances from \vec{x} to the boundary along the direction perpendicular to $\vec{\Omega}$. Expanding the integrand of equation (7.32) and using equations (7.7) and (7.8) give

$$\begin{aligned} \Delta(x, E, \Omega) &= \left[\int_{-\infty}^{\infty} - \int_{r_2(\vec{\Omega})}^{\infty} + \int_{-r_1(\vec{\Omega})}^{-\infty} \right] R_N [z_x(\vec{\Omega}), E] \phi(\vec{\Gamma}_x, \vec{\Omega}, E) g(\delta, r) \\ &\times \left[1 + \frac{R'_N}{R_N} \left(\frac{\vec{\Omega} \cdot \vec{t}_o}{(\vec{\Omega} \cdot \vec{n}_o)} \right) r + \frac{\vec{t}_o \cdot \vec{\nabla} \phi}{\vec{n}_o \cdot \vec{\Omega}} r + \frac{1}{\rho_o} \frac{\vec{t}_o \cdot \vec{\Omega}}{(\vec{\Omega} \cdot \vec{n}_o)^2} r + O(r^2) \right] dr \\ &\approx R_N [z_x(\vec{\Omega}), E] \phi(\vec{\Gamma}_x, \vec{\Omega}, E) [1 + O(\delta^2)] \\ &- \left(\int_{r_2}^{\infty} + \int_{-\infty}^{-r_1} \right) R_N [z_x(\vec{\Omega}), E] \phi(\vec{\Gamma}_x, \vec{\Omega}, E) g(\delta, r) dr \\ &\approx R_N [z_x(\vec{\Omega}), E] \phi(\vec{\Gamma}_x, \vec{\Omega}, E) \{ 1 + O(\delta^2) - \delta [g(\delta, r_1) + g(\delta, r_2)] \} \end{aligned} \quad (7.33)$$

where the last term in equation (7.33) is inferior to terms $O(\delta^2)$, i.e.,

$$O(\delta^2) \gg \delta g(\delta, r_i)$$

for $r_i \gg \delta$. The solution for all sources of different E and $\vec{\Omega}$ is then found from equation (7.33) as

$$D(\vec{x}) = \int_0^\infty \int_\Omega R_N[z_x(\vec{\Omega}), E] \phi(\vec{\Gamma}_x, \vec{\Omega}, E) [1 + O(\delta^2)] d\vec{\Omega} dE \quad (7.34)$$

which can be evaluated by using a simple approximate quadrature. The error terms in equation (7.34) contain the quantities

$$\frac{\delta}{\rho_0}, \frac{R'_N \delta}{R_N}, \frac{\vec{\nabla} \phi \cdot \vec{l}_0 \delta}{\phi}, \frac{R''_N \delta^2}{R_N}, \frac{\vec{\nabla}^2 \phi \delta^2}{\phi}$$

in the form of second-order products in δ .

Generally, δ is quite small. This is the basis for the straight ahead approximation; and in the limit as $\delta \rightarrow 0$, the first term in equation (7.34) is the sole surviving term when applied to the straight ahead theory. In the real situation, δ is nonzero and the first term in equation (7.34) will still give satisfactory results even when straight ahead theory is inadequate.

The greatest importance of equation (7.34) is that the fluence-to-dose conversion factors for normal incidence on a semi-infinite slab are all the information required to compute doses in any arbitrary convex object. These fluence-to-dose conversion factors are well-known for neutrons and protons of several energies for depths up to 30 cm in soft tissue. An interpolation to other energies and an extrapolation to large depths are given by Wilson and Khandelwal (1974 and 1976) and have been extended for tissue systems shielded by aluminum. (See chapter 8.)

Perhaps the main limitation in using equation (7.34) is the assumption that the lateral distance from the dose point to the boundary is large compared with the beam width; i.e., $r_i \leq \delta$ so that $\delta g(\delta, r_i) \gg O(\delta^2)$. This could always be corrected by a knowledge of the lateral profile of the beam where the expression

$$D(\vec{x}) = \int_0^\infty \int_\Omega \int_{-r_1(\vec{\Omega})}^{r_2(\vec{\Omega})} R_N[z_x(\vec{\Omega}), E] \phi(\vec{\Gamma}_x, \vec{\Omega}, E) g(\delta, r) dr d\vec{\Omega} dE + O(\delta^2) \quad (7.35)$$

is used in place of equation (7.34). The main limitation is that $g(\delta, r)$ is not sufficiently well-known in the literature. There is some question as to the importance of such terms, as has been shown by Wilson and Khandelwal (1974) with a numerical example. Note also that the result of equation (7.34) is always an overestimate to equation (7.35) and thus is always conservative. The conservativeness of equation (7.34) follows because the integrand of equation (7.35) is positive definite. Finally, we note that equation (7.34) or (7.35) is the desired approximate form for equation (7.4). The accuracy is associated with the beam width δ , and errors are sufficiently small in many applications to the transport

of protons, heavy ions, and high-energy neutrons. As a check on the formalism expressed by equation (7.34), we have calculated the fluence-to-dose conversion factors for isotropic protons on a 30-cm tissue slab and compared the results with "exact" Monte Carlo results. The comparison can be made from table 7.1. Equation (7.34) is seen to be accurate for dose points near the boundary ($x = 0$) as well as at great depths. The condition under which equation (7.35) provides a more accurate result is not yet clear. The calculation of the function $R_N(x, E)$ for protons and heavy ions and their validation is the main topic of the rest of this report.

Table 7.1. Comparison of Isotropic Incident Proton Conversion Factors^a for a 30-cm Tissue Slab

[Present approximations compared with "exact" Monte Carlo results]

x , cm	Exact	Approximate	Error, percent
$E = 100$ MeV			
1	2.78	2.65	-4.7
3	2.92	2.45	-16
5	2.15	1.92	11
7	0.56	.90	60
8	≈ 0.01	0	
$E = 200$ MeV			
1	1.66	1.70	2.4
5	1.72	1.62	-6.0
10	1.48	1.41	-4.6
15	1.14	1.16	1.7
20	.81	.79	-2.5
$E = 300$ MeV			
1	1.29	1.29	0
5	1.34	1.35	.8
10	1.28	1.26	-1.6
15	1.18	1.14	-3.4
20	1.03	1.01	-1.9
25	.89	.88	-1.1
$E = 400$ MeV			
1	1.16	1.17	0.9
5	1.20	1.27	5.9
10	1.14	1.22	7.0
15	1.17	1.13	-4.1
20	1.10	1.04	-5.5
25	1.01	.94	-6.9

^aUnits are chosen as 10^{-10} Gy/(proton cm^{-2}).

7.5. References

- Alsmiller, R. G., Jr.; Irving, D. C.; Kinney, W. E.; and Moran, H. S., 1965: The Validity of the Straightahead Approximation in Space Vehicle Shielding Studies, *Second Symposium on Protection Against Radiations in Space*, Arthur Reetz, Jr., ed., NASA SP-71, pp. 177-181.
- Alsmiller, R. G., Jr., 1967: High-Energy Nucleon Transport and Space Vehicle Shielding. *Nuclear Sci. & Eng.*, vol. 27, no. 2, pp. 158-189.
- Armstrong, T. W.; and Bishop, B. L., 1971: Calculation of the Absorbed Dose and Dose Equivalent Induced by Medium-Energy Neutrons and Protons and Comparison With Experiment. *Radiat. Res.*, vol. 47, no. 3, pp. 581-588.
- Cucinotta, Francis A.; and Wilson, John W., 1985: *Computer Subroutines For Estimation of Human Exposure to Radiation in Low Earth Orbit*. NASA TM-86324.
- Irving, D. C.; Alsmiller, R. G., Jr.; Kinney, W. E.; and Moran, H. S., 1965: The Secondary-Particle Contribution to the Dose From Monoenergetic Proton Beams and the Validity of Current-to-Dose Conversion Factors. *Second Symposium on Protection Against Radiations in Space*, Arthur Reetz, Jr., ed., NASA SP-71, pp. 173-176.
- Langley, R. W.; and Billings, M. P., 1972: A New Model For Estimating Space Proton Dose to Body Organs. *Nuclear Technol.*, vol. 15, no. 1, pp. 68-74.
- Neufeld, Jacob; and Wright, Harvel, 1972: Radiation Levels and Fluence Conversion Factors. *Health Phys.*, vol. 23, no. 2, pp. 183-186.
- Santoro, R. T.; Alsmiller, R. G., Jr.; Barnes, J. M.; and Corbin, J. M., 1986: *Shielding of Manned Space Stations Against Van Allen Belt Protons: A Preliminary Scoping Study*. ORNL/TM-10040 (Contract No. IDOD3070-0000), Oak Ridge National Lab.
- Schimmerling, Walter; Rapkin Marwin; Wong, Mervyn; and Howard, Jerry, 1986: The Propagation of Relativistic Heavy Ions in Multielement Beam Lines. *Med. Phys.*, vol. 13, no. 2, pp. 217-228.
- Seltzer, Stephen, 1980: SHIELDOSE: A Computer Code for Space-Shielding Radiation Dose Calculations. NBS Tech. Note 1116, U.S. Dep. of Commerce.
- Shen, S. P., 1963: Nuclear Problems in Radiation Shielding in Space. *Astronaut. Acta*, vol. IX, Fasc. 4, pp. 211-274.
- Shen, B. S. P., 1965: Some Experimental Data on the Nuclear Cascade in Thick Absorbers. *Second Symposium on Protection Against Radiations in Space*, Arthur Reetz, Jr., ed., NASA SP-71, pp. 357-362.
- Wilson, John W.; and Khandelwal, G. S., 1974: Proton Dose Approximation in Arbitrary Convex Geometry. *Nuclear Technol.*, vol. 23, no. 3, pp. 298-305.
- Wilson, John W.; and Khandelwal, Govind S., 1976: Proton-Tissue Dose Buildup Factors. *Health Phys.*, vol. 31, no. 2, pp. 115-118.

Transport Methods and Interactions for Space Radiations

Wright, H. A.; Hamm, R. N.; and Turner, J. E., 1971: Effect of Lateral Scattering on Absorbed Dose From 400 MeV Neutrons and Protons. *International Congress on Protection Against Accelerator and Space Radiation*, J. Baarli and J. Dutrannois, eds., CERN 71-16, Volume 1, European Organization for Nuclear Research, pp. 207-219.

Chapter 8

Nucleon Transport Methods

8.1. Introduction

Understanding the interaction of energetic charged particles with bulk matter is important for determining shield quality (Shen, 1963; Alsmiller, 1967), dosimeter design (Khandelwal and Wilson, 1973), and radiology (Armstrong, 1972; Armstrong and Bishop, 1971), as well as for astrophysics (Murzin and Sarycheva, 1970; Shen 1967), and solar system studies (Reedy and Arnold, 1972). Detailed studies of charged-particle transport with regeneration have been hampered by terms arising from energy loss caused by atomic ionization and excitation (Haffner, 1967). Generally, charged-particle transport calculations are made by using Monte Carlo methods (Alsmiller, 1967), where errors of the procedure are difficult to evaluate and a degree of insight is lost in the handling of large amounts of numerical data. Clearly, an approximation procedure that allows an error test that is both easily mechanized and related directly to the particle fields is desirable.

Analytical methods have been developed to represent solutions to the Boltzmann equation for charged-particle transport. These results are obtained by using an approximate Boltzmann equation for which analytical solution is possible. For example, approximations ignoring energy loss through ionization have been used in studying the high-energy nucleonic cascade development in the Earth's atmosphere (Cocconi, Cocconi Tongiorgi, and Widgoff, 1950). Energy loss caused by ionization is generally important, and only the high-energy secondaries are adequately treated. The so-called Passow approximations have found utility in recent studies (O'Brien, 1971). The restrictions on the Passow approximations are that all secondaries are produced in the forward direction (straight ahead approximation), energy loss caused by ionization is neglected, and the secondary-particle-production spectra must be proportional to E_s^α , where α is constant.

The solution of the Boltzmann equation including ionization energy loss has been inadequately treated. Alsmiller (1967) has given approximate expressions without estimates of their validity, but with a note of caution that the result is adequate only over very small distances compared with one mean-free path. Neither has a general treatment of the solution been given nor have questions of convergence been answered.

In the present chapter, we consider the solution of the Boltzmann equation for charged-particle transport and answer questions on the convergence of the solution technique (Wilson and Lamkin, 1975). For the present, we assume one-dimensional transport (which is a reasonable approximation for nucleon transport, see Alsmiller (1967) and Wright et al. (1969)) in which production of neutral secondaries is ignored. The equations are otherwise realistic and, as we will see, provide a good first approximation to proton transport. Herein we solve the charged-particle Boltzmann equation as coupled perturbation equations (in the context of slowing-down theory). The inverse of the Boltzmann operator is derived and the original Boltzmann equation is replaced by a set of quadratures. The implementation is discussed and convergence of the perturbation series is examined. The final results are compared with those obtained by Monte Carlo

methods (Wright et al., 1969). Implications on the interaction of high-energy protons with tissue are then discussed.

8.2. Charged-Particle Transport

8.2.1. Energy-independent cross sections. The Boltzmann equation for proton transport (neglecting coupling to other particle fields) in the straight ahead approximation is given as

$$\left(\frac{\partial}{\partial x} - \frac{\partial}{\partial E} S(E) + \sigma \right) \phi(x, E) = \int_E^\infty f(E, E') \phi(x, E') dE' \quad (8.1)$$

where $S(E)$ is the proton stopping power, σ is the macroscopic proton cross section that we take as energy independent, and $f(E, E')$ is the secondary-particle-production cross section. The production cross section satisfies

$$\int_0^{E'} f(E, E') dE = m\sigma \quad (8.2)$$

where m is the average number of protons produced per event.

The differential operator of equation (8.1) can be simplified by making a nonlinear transformation on E as

$$r = \int_0^E \frac{dE'}{S(E')} \quad (8.3)$$

which follows from the method of characteristics in partial differential equations theory (Wilson and Lamkin, 1975). By further mapping the particle field $\phi(x, E)$ and production cross section as

$$\psi(x, r) = S(E) \phi(x, E) \quad (8.4)$$

$$\bar{f}(r, r') = S(E) f(E, E') \quad (8.5)$$

we may rewrite equation (8.1) as

$$\left[\frac{\partial}{\partial x} - \frac{\partial}{\partial r} + \sigma \right] \psi(x, r) = \int_r^\infty \bar{f}(r, r') \psi(x, r') dr' \quad (8.6)$$

The characteristic coordinate along which the solution propagates is simply $x - r$, and the solution may be written as a line integral along this coordinate. The result may be written as

$$\begin{aligned} \psi(x, r) = & \exp(-\sigma x) \psi(0, x + r) \\ & + \int_0^x dz \exp(-\sigma z) \int_{r+z}^\infty dr' \bar{f}(r + z, r') \psi(x - z, r') \end{aligned} \quad (8.7)$$

where the boundary condition is

$$\psi(0, r) = S(E) \phi(0, E) \quad (8.8)$$

Solution to equation (8.7) may be written in terms of quadratures as follows

$$\psi_0(x, r) = \exp(-\sigma x) \psi(0, r + x) \quad (8.9)$$

$$\psi_n(x, r) = \int_0^x dz \exp(-\sigma z) \int_{r+z}^{\infty} dr' \bar{f}(r + z, r') \psi_{n-1}(x - z, r') \quad (8.10)$$

with

$$\psi(x, r) = \sum_{i=0}^{\infty} \psi_i(x, r) \quad (8.11)$$

which is recognized as the Neumann series.

The secondary source spectra were discussed in chapter 5 and are of the form

$$\bar{f}(r, r') \approx a \exp(-\alpha r) + c \exp[\gamma(r - r')] \quad (8.12)$$

where the coefficients α and γ are slowly varying functions of r' .

The first term corresponds to knockout nucleons and evaporation particles so that

$$\alpha r' \gg 1 \quad (8.13)$$

The second term corresponds to the quasi-elastic scattered primary such that

$$\gamma r' \ll 1 \quad (8.14)$$

Typically, $\alpha \approx 1 \rightarrow 10 \text{ cm}^2/\text{g}$ while $\gamma \approx 10^{-3} \rightarrow 10^{-2} \text{ cm}^2/\text{g}$. As a result of linearity of equation (8.7), we will solve for each term of equation (8.12) separately and evaluate the cross term last.

8.2.2. Discrete spectrum. The solution for a discrete spectrum at the boundary is developed as follows. The first term is given as

$$\psi_0(x, r) = \exp(-\sigma x) \delta(r_o - r - x) \quad (8.15)$$

where r_o corresponds to the energy at the boundary. The quasi-elastic transported particles may be solved directly (Wilson et al., 1988 and 1989) as

$$\psi_{c_1}(x, r) = x \exp(-\sigma x) c \exp[\gamma(r_o - r - x)] \quad (8.16)$$

with

$$\psi_{c_n}(x, r) = \frac{1}{n!} x^n \exp(-\sigma x) \frac{c^n}{(n-1)!} (r_o - r - x)^{n-1} \exp[-\gamma(r_o - r - x)] \quad (8.17)$$

It is easily shown that

$$\begin{aligned}\psi_c(x, r) &= \sum_{n=1}^{\infty} \psi_{c_n}(x, r) \\ &= \exp[-\sigma x - \gamma(r_o - r - x)] \sqrt{\frac{cx}{r_o - r - x}} \\ &\quad \times I_1 \left[2\sqrt{cx(r_o - r - x)} \right]\end{aligned}\quad (8.18)$$

where $I_1(Z)$ is a modified Bessel function of first order (Wilson et al., 1988). Equation (8.18) can also be derived by using Laplace transforms (Ganapol et al., 1991). The total flux is found for each term as

$$\Phi_{c_n}(x) = \int_0^{r_o - x} \psi_n(x, r) dr \quad (8.19)$$

so that

$$\Phi_0(x) = \exp(-\sigma x) \quad (8.20)$$

as expected, and

$$\Phi_{c_1}(x) = \frac{c}{\gamma} x \exp(-\sigma x) \{1 - \exp[-\gamma(r_o - x)]\} \quad (8.21)$$

$$\Phi_{c_2}(x) = \frac{1}{2} \frac{c^2}{\gamma^2} x^2 \exp(-\sigma x) \{1 - [1 + \gamma(r_o - x)] \exp[-\gamma(r_o - x)]\} \quad (8.22)$$

At very high energies ($r_o \rightarrow \infty$), the total flux values become

$$\Phi_{c_n}(x) = \frac{1}{n!} \left(\frac{c}{\gamma} x\right)^n \exp(-\sigma x) \quad (8.23)$$

as expected because $c \approx m_Q \sigma \gamma$, where m_Q is the quasi-elastic multiplicity (Wilson et al., 1989).

The low-energy term of the secondary spectrum can likewise be treated. The first term is

$$\begin{aligned}\psi_{a_1}(x, r) &= \frac{a}{\alpha} \exp(-\sigma x) \left\{ \exp(-\alpha r) - \exp[-\alpha(r + x)] \right\} U(r_o - x - r) \\ &= \frac{a}{\alpha} \exp(-\sigma x) [F_a(r + x) - F_a(r)]\end{aligned}\quad (8.24)$$

where $F_a(r)$ is the cumulative spectrum. The total fluence contribution is

$$\Phi_{a_1}(x) = \frac{a}{\alpha^2} \exp(-\sigma x) \left\{ 1 + \exp(-\alpha r_o) - \exp(-\alpha x) - \exp[-\alpha(r_o - x)] \right\} \quad (8.25)$$

which shows initial linear growth for small x to some maximum value limited by the $\exp(-\sigma x)$ factor if αr_o is large or by $1 - \exp[-\alpha(r_o - x)]$ if αr_o is small compared with σr_o . If αr_o is large, the secondary particle fluence rises quickly to equilibrium with the primary beam for $x \gg \alpha^{-1}$ and slowly declines as the primary beam attenuates according to

$$\Phi_{a_1}(x) \approx \frac{a}{\alpha^2} \exp(-\sigma x) \quad (8.26)$$

The next secondary spectral term is

$$\begin{aligned} \psi_{a_2}(x, r) = & \frac{a^2}{2\alpha^3} \exp(-\sigma x) \exp(-\alpha r) [1 + \exp(-2\alpha x) - 2 \exp(-\alpha x)] \\ & \times \left\{ \exp(-\alpha r) - \exp[-\alpha(r_o - x)] \right\} \end{aligned} \quad (8.27)$$

The fluence grows for small x as

$$\psi_{a_2}(x, r) \approx \frac{3}{4} \frac{a^2}{\alpha} x^2 \exp(-\sigma x) \exp(-2\alpha r) \quad (8.28)$$

and approaches a value given by

$$\psi_{a_2}(x, r) \approx \frac{a^2}{2\alpha^3} \exp(-\sigma x) \exp(-2\alpha r) \quad (8.29)$$

where equilibrium with the primary beam is established. The total flux is

$$\begin{aligned} \Phi_{a_2}(x) = & \frac{a^2}{4\alpha^4} \exp(-\sigma x) [1 + \exp(-2\alpha x) - 2 \exp(-\alpha x)] \left\{ 1 + \exp[-2\alpha(r_o - x)] \right. \\ & \left. - 2 \exp[-\alpha(r_o - x)] \right\} \end{aligned} \quad (8.30)$$

The equilibrium flux is

$$\Phi_{a_2}(x) \approx \frac{a^2}{4\alpha^4} \exp(-\sigma x) \quad (8.31)$$

and can be compared with the first perturbation term for which

$$\frac{\Phi_{a_2}(x)}{\Phi_{a_1}(x)} \leq 10^{-2} \quad (8.32)$$

for most materials. The series for the $\psi_a(x, r)$ converges very rapidly so that

$$\psi_a(x, r) \approx \psi_{a_1}(x, r) + \psi_{a_2}(x, r) \quad (8.33)$$

to better than 1 percent accuracy, and neglecting the second term gives results within 1 percent.

We now evaluate the cross terms of the series. The low-energy secondary particle flux produced by quasi-elastic secondaries is given by

$$\begin{aligned} \psi_{ac}(x, r) = & \frac{a}{\alpha^2} \frac{c}{\gamma} \exp(-\sigma x) \exp(-\alpha r) \left[(\alpha x - 1) + \exp(-\alpha x) \right] \\ & \times \left\{ 1 - \exp[-\gamma(r_o - x - r)] \right\} \end{aligned} \quad (8.34)$$

for which the total integrated flux is

$$\begin{aligned} \Phi_{ac}(x) = & \frac{a}{\alpha^2} \frac{c}{\gamma \alpha (\alpha - \gamma)} \exp(-\sigma x) \left[(\alpha x - 1) + \exp(-\alpha x) \right] \\ & \times \left((\alpha - \gamma) \{ 1 - \exp[-\alpha(r_o - x)] \} \right. \\ & \left. - \alpha \exp[-\gamma(r_o - x)] \{ 1 - \exp[-(\alpha - \gamma)(r_o - x)] \} \right) \end{aligned} \quad (8.35)$$

Because $\alpha \gg \gamma$, we find that for high-energy primaries (i.e., $r_o \rightarrow \infty$) the total flux rises quadratically from the boundary and rapidly approaches equilibrium with the quasi-elastic secondaries (eq. (8.21)) as seen in

$$\Phi_{ac}(x) \approx \frac{a}{\alpha^2} \frac{c}{\gamma} x \exp(-\sigma x) \quad (8.36)$$

Similar results can be found for the higher order quasi-elastic secondary terms. The quasi-elastic scattering of low-energy secondaries is similarly derived as

$$\begin{aligned} \psi_{ca}(x, r) = & \frac{a}{\alpha} \frac{c}{\alpha + \gamma} \exp(-\sigma x) \left\{ \frac{1 - \exp[-(\alpha - \gamma)x]}{\alpha - \gamma} - \frac{1}{\gamma} [1 - \exp(-\gamma x)] \right\} \\ & \times \left\{ \exp(-\alpha r) - \exp[-\alpha(r_o - x)] \exp[-\gamma(r_o - x - r)] \right\} \end{aligned} \quad (8.37)$$

The total integrated flux is

$$\begin{aligned} \Phi_{ca}(x) = & \frac{a}{\alpha} \frac{c}{\alpha + \gamma} \exp(-\sigma x) \left\{ \frac{1 - \exp(-\alpha - \gamma)x}{\alpha - \gamma} - \frac{1}{\gamma} [1 - \exp(-\gamma x)] \right\} \\ & \times \left(\frac{1}{\alpha} \{ 1 - \exp[-\alpha(r_o - x)] \} \right. \\ & \left. - \frac{1}{\gamma} \{ \exp[-\alpha(r_o - x)] - \exp[-(\alpha + \gamma)(r_o - x)] \} \right) \end{aligned} \quad (8.38)$$

For high energy and $x \gg \alpha^{-1}$,

$$\Phi_{ca}(x) \approx \frac{a}{\alpha^2} \frac{c}{\alpha^2} \exp(-\sigma x) \quad (8.39)$$

It is clear that equilibrium is established with the primary beam caused by the short range of the first-generation, low-energy secondary particles (i.e., $\alpha \gg \gamma$). Note that $\Phi_{ca}(x)$ is inferior to $\Phi_{ac}(x)$ once equilibrium is established ($x \gg \alpha^{-1}$) and is therefore small as $x \rightarrow 0$, thus making the cross term of equation (8.36) the main contribution.

8.2.3. Continuous spectrum. We consider a continuous energy spectrum at the boundary given by an exponential so that

$$\psi_0(x, r) = \exp(-\sigma x) \exp[-\beta(r + x)] \quad (8.40)$$

where typical values of β are $\alpha \gg \beta \gg \gamma$. The next terms of the quasi-elastic series are given by

$$\psi_{c_n}(x, r) = \frac{1}{n!} x^n \exp(-\sigma x) \left(\frac{c}{\gamma + \beta} \right)^n \exp[-\beta(x + r)] \quad (8.41)$$

Clearly, the quasi-elastic series may be summed as

$$\sum_{n=0}^{\infty} \psi_{c_n}(x, r) = \exp[cx/(\gamma + \beta)] \exp(-\sigma x) \exp[-\beta(x + r)] \quad (8.42)$$

The total flux associated with each term is

$$\Phi_n(x) = \frac{1}{n!} \left(\frac{cx}{\gamma + \beta} \right)^n \frac{1}{\beta} \exp(-\sigma x - \beta x) \quad (8.43)$$

The total flux

$$\Phi_c(x) = \frac{1}{\beta} \exp[cx/(\beta + \gamma)] \exp(-\sigma x) \exp(-\beta x) \quad (8.44)$$

converges by virtue of $\beta \gg \gamma$.

The low-energy secondaries may likewise be evaluated to give

$$\psi_{a_1}(x, r) = \frac{a}{\alpha} \exp(-\sigma x) \exp[-\beta(x + r)] \left\{ \exp(-\alpha r) - \exp[-\alpha(r + x)] \right\} \quad (8.45)$$

The total flux is given as

$$\Phi_{a_1}(x) = \frac{a}{\alpha} \frac{1}{\alpha + \beta} \exp(-\sigma x) \exp(-\beta x) [1 - \exp(-\alpha x)] \quad (8.46)$$

The flux grows linearly at small $x \ll \alpha^{-1}$ and approaches equilibrium with the primary beam for $x \gg \alpha^{-1}$. The equilibrium value is

$$\Phi_{a_1}(x) \approx \frac{a}{\alpha} \frac{1}{\alpha + \beta} \exp(-\sigma x) \exp(-\beta x) \quad (8.47)$$

The next term is given as

$$\begin{aligned} \psi_{a_2}(x, r) = & \frac{a}{\alpha} \frac{a}{\alpha + \beta} \exp(-\sigma x) \exp[-\beta(x + r)] \\ & \times \left\{ \frac{1}{2\alpha} \exp(-2\alpha r) [1 - \exp(-2\alpha x)] \right. \\ & \left. - \frac{1}{\beta} \exp(-\alpha x - 2\alpha r) [1 - \exp(-\beta x)] \right\} \end{aligned} \quad (8.48)$$

for which the corresponding integrated flux is

$$\begin{aligned} \Phi_{a_2}(x) = & \frac{a}{\alpha} \frac{a}{\alpha + \beta} \frac{1}{2\alpha + \beta} \exp(-\sigma x) \exp(-\beta x) \\ & \times \left\{ \frac{1}{2\alpha} [1 - \exp(-2\alpha x)] - \frac{1}{\beta} [1 - \exp(-\beta x)] \exp(-\alpha x) \right\} \end{aligned} \quad (8.49)$$

The flux again approaches equilibrium for $x \gg \alpha^{-1}$ as

$$\Phi_{a_2}(x) \approx \frac{1}{2} \frac{a^2}{\alpha^2} \frac{\beta}{\alpha + 2\beta} \frac{1}{\beta} \exp(-\sigma x) \exp(-\beta x) \quad (8.50)$$

As in the discrete spectrum case,

$$\frac{\Phi_{a_2}(x)}{\Phi_{a_1}(x)} < 0.01 \quad (8.51)$$

The cross term representing the low-energy secondaries produced by the quasi-elastic scatter particles is

$$\begin{aligned} \psi_{ac}(x, r) = & \frac{a}{\beta} \frac{c}{\gamma + \beta} \exp(-\sigma x - \alpha r - \beta x) \\ & \times \left\{ \frac{\alpha x - \beta x - 1 + \exp[-(\alpha - \beta)x]}{(\alpha - \beta)^2} \right. \\ & \left. - \frac{\exp(-\beta r) [\alpha x - 1 + \exp(-\alpha x)]}{\alpha^2} \right\} \end{aligned} \quad (8.52)$$

The corresponding total flux is

$$\begin{aligned} \Phi_{ac}(x) = & \frac{a}{\alpha\beta} \frac{c}{\gamma + \beta} \exp(-\sigma x - \beta x) \\ & \times \left\{ \frac{\alpha x - \beta x - 1 + \exp[-(\alpha - \beta)x]}{(\alpha - \beta)^2} - \frac{\alpha x - 1 + \exp(-\alpha x)}{\alpha(\alpha + \beta)} \right\} \end{aligned} \quad (8.53)$$

The flux rises quadratically for small x to an equilibrium value for $x \gg \alpha^{-1}$ as

$$\Phi_{ac}(x) \approx \frac{a}{\alpha + \beta} \frac{c}{\gamma + \beta} \frac{x}{(\alpha - \beta)^2} \exp(-\sigma x - \beta x) \quad (8.54)$$

and remains in equilibrium with the $\psi_{c_1}(x, r)$ term throughout the rest of the median. The cross term representing the quasi-elastic scattering of the first-generation, low-energy flux is

$$\begin{aligned} \psi_{ca}(x, r) = & \frac{a}{\alpha^2} \frac{c}{\gamma + \beta + \alpha} \exp(-\sigma x) \exp(-\beta x) \exp[-(\alpha + \beta)r] \\ & \times [1 - (\alpha x - 1) \exp(-\alpha x)] \end{aligned} \quad (8.55)$$

The corresponding integrated flux is

$$\Phi_{ca}(x) = \frac{a}{\alpha^2} \frac{c}{\gamma + \alpha + \beta} \frac{\exp(-\sigma x - \beta x)}{\alpha + \beta} [1 - (\alpha x - 1) \exp(-\alpha x)] \quad (8.56)$$

The flux rises quadratically at small x and approaches an equilibrium value for $x \gg \alpha^{-1}$ as

$$\Phi_{ca}(x) \approx \frac{a}{\alpha^2} \frac{c}{\gamma + \beta + \alpha} \frac{\exp(-\sigma x - \beta x)}{\alpha + \beta} \quad (8.57)$$

and remains in equilibrium with the surviving flux of primary particles. Clearly, the Φ_{ca} flux is inferior to the Φ_{ac} flux at all values of x .

These results are useful in developing an understanding of the role of various contributions in the particle-production terms of equations (8.10) or (8.6). They likewise serve as a means of developing numerical procedures and testing those procedures for error propagation. We will further discuss this role in a latter section. The fact that the lower energy solutions converge quickly and remain in equilibrium with the primary beam has played an important role in the study of target-induced reaction and nuclear recoil effects in biological materials (Wilson, Townsend, and Buck, 1986; Wilson, Townsend, and Khan, 1989; Wilson, Shinn, and Townsend, 1990; Shinn, Wilson, and Ngo, 1990) and electronic materials (Ngo et al., 1989; Wilson, Stith, and Stock, 1983; Wilson, Walker, and Outlaw, 1984).

8.3. Buildup Factors

In passing through tissue, energetic protons interact mostly through ionization of atomic constituents by transferring small amounts of momentum to orbital electrons. Although nuclear reactions are far less numerous, their effects are magnified because of the large momentum transferred to the nuclear particles and the struck nucleus itself. Unlike the secondary electrons formed through atomic ionization by interaction with the primary protons, the radiations resulting from nuclear reactions are mostly heavily ionizing and generally have large biological effectiveness. Many of the secondary particles of nuclear reactions are sufficiently energetic to promote similar nuclear reactions and thus cause a buildup of secondary radiations. The description of such processes requires a solution of the transport equation. The approximate solutions for transporting protons in 30-cm-thick slabs of soft tissue for fixed incident energies have been found (Armstrong and Bishop, 1971; Wright et al., 1969; Alsmiller, Armstrong, and Coleman, 1970; Armstrong and Chandler, 1970; Snyder et al., 1969; Turner et al., 1964; Wright, Hamm, and Turner, 1971; Zerby and Kinney, 1965). The results of such calculations are dose conversion factors for relating the primary

monoenergetic proton fluence to dose or dose equivalent as a function of position in a tissue slab.

Whenever the radiation is spatially uniform, the dose at any point x in a convex object may be calculated by (Wilson and Khandelwal, 1974)

$$D(\vec{x}) = \int_0^\infty \int_\Omega R_n[z_x(\vec{\Omega}), E] \phi(\vec{\Omega}, E) d\vec{\Omega} dE \quad (8.58)$$

where $R_n(z, E)$ is the dose at depth z for normal incident protons of energy E on a tissue slab; $\phi(\vec{\Omega}, E)$ is the differential proton fluence along direction $\vec{\Omega}$; and $z_x(\vec{\Omega})$ is the distance from the boundary along $\vec{\Omega}$ to the point \vec{x} . It has been shown that equation (8.58) always overestimates the dose but is an accurate estimate when the ratio of the proton beam divergence (caused by nuclear reaction) to the radius of curvature of the body is small. Equation (8.58) is a practical prescription for introducing nuclear reaction effects into calculations of dose in geometrically complex objects, such as a human body. The main requirement is that the dose conversion factors for a tissue slab be adequately known for a broad range of energies and depths. Such a description is obtained through the use of buildup factors.

8.3.1. Simplified theory of proton buildup factors. The Boltzmann equation for proton transport in straight ahead approximation is given as

$$\left[\frac{\partial}{\partial x} - \frac{\partial}{\partial E} S(E) + \sigma \right] \phi(x, E) = \int_E^\infty f(E, E') \phi(x, E') dE' \quad (8.59)$$

where $S(E)$ is the proton stopping power, σ is the macroscopic interaction cross section which we presently take as energy independent, and $f(E, E')$ is the production cross section for secondary protons. Using the definitions

$$r = \int_0^E \frac{dE'}{S(E')} \quad (8.60)$$

$$\psi(x, r) = S(E) \phi(x, E) \quad (8.61)$$

$$\bar{f}(r, r') = S(E) f(E, E') \quad (8.62)$$

allows equation (8.59) to be rewritten as

$$\begin{aligned} \psi(x, r) = & \exp(-\sigma x) \psi(0, x+r) \\ & + \int_0^x dz \exp(-\sigma z) \int_{r+z}^\infty dr' \bar{f}(r+z, r') \psi(x-z, r') \end{aligned} \quad (8.63)$$

where the boundary condition is

$$\psi(0, r) = S(E) \phi(0, E) \quad (8.64)$$

The secondary-particle-production cross section is normalized as

$$\int_0^{E'} f(E, E') dE = m\sigma \quad (8.65)$$

where m is the average number of protons produced per nuclear event. Although m and σ are, in reality, functions of E' , our current interest is in monoenergetic boundary conditions as

$$\phi(0, E) = \delta(E - E_0) \quad (8.66)$$

and we take m and σ evaluated at the beam energy E_0 . The corresponding boundary condition on ψ is

$$\psi(0, r) = \delta(r - r_0) \quad (8.67)$$

The high-energy-production cross section is an exponential function of $E' - E$ and is used to approximate equation (8.62) as

$$f(r, r') \approx b \exp[-\gamma(r' - r)] \quad (8.68)$$

The normalization in equation (8.65) requires

$$b = \frac{m\sigma\gamma}{1 - \exp(-\gamma r_0)} \quad (8.69)$$

and $\gamma \approx 0.01 \text{ cm}^2/\text{g}$. Equation (8.63) may be solved by perturbation theory to obtain

$$\psi(x, r) = \sum_{i=0}^{\infty} \psi_i(x, r) \quad (8.70)$$

where

$$\psi_0(x, r) = \exp(-\sigma x) \delta(r + x - r_0) \quad (8.71)$$

$$\psi_1(x, r) = \exp(-\sigma x) \int_0^x \bar{f}(r + z, r_0 - x + z) dz \quad (8.72)$$

$$\psi_{n+1}(x, r) = \int_0^x dz \exp(-\sigma z) \int_{r+z}^{\infty} dr' \bar{f}(r + z, r') \psi_n(x - z, r') \quad (8.73)$$

which may be reduced using equation (8.69). For example,

$$\psi_1(x, r) = x \exp(-\sigma x) \bar{f}(r, r_0 - x) \quad (8.74)$$

$$\psi_2(x, r) = \frac{1}{2} x^2 \exp(-\sigma x) b(r_0 - x - r) \bar{f}(r, r_0 - x) \quad (8.75)$$

The successive contributions to dose may now be calculated

$$D_0(x) = \int_0^\infty \exp(-\sigma x) \delta(r+x-r_0) dE = S[\varepsilon(r_0-x)] \exp(-\sigma x) \quad (8.76)$$

$$D_1(x) = \bar{S}_1[\varepsilon(r_0-x)] m\sigma x \exp(-\sigma x) \quad (8.77)$$

$$D_2(x) = \bar{S}_2[\varepsilon(r_0-x)] m^2 \frac{\sigma^2 x^2}{2} \exp(-\sigma x) \quad (8.78)$$

where \bar{S}_1 and \bar{S}_2 are spectral averages of stopping power in which $\bar{S}_1(\varepsilon) = O(\varepsilon)$ and $\bar{S}_2(\varepsilon) = O(\varepsilon^2)$ for small ε . The total dose is then

$$D(x) = S[\varepsilon(r_0-x)] \exp(-\sigma x) + \sum_{i=1}^{\infty} \frac{1}{i!} (m\sigma x)^i \exp(-\sigma x) \bar{S}_i[\varepsilon(r_0-x)] \quad (8.79)$$

The dose buildup factor is then defined as

$$B(x, E_0) = 1 + \frac{\sum_{i=1}^{\infty} \frac{1}{i!} (m\sigma x)^i \bar{S}_i[\varepsilon(r_0-x)]}{S[\varepsilon(r_0-x)]} \quad (8.80)$$

With the property that

$$\lim_{x \rightarrow r_0} B(x, E_0) = 1 \quad (8.81)$$

which follows here from the neglect of the coupling between the proton and neutron fields.

Wilson and Khandelwal (1974) assumed that the buildup factor had the following form

$$B(x, E_0) = (A_1 + A_2 x + A_3 x^2) \exp(-A_4 x) \quad (8.82)$$

where A_4 was chosen to satisfy equation (8.81). It is seen that the choice of A_4 is not governed by the nuclear cross section but rather by the result that $\bar{S}_i(\varepsilon) \approx O(\varepsilon^i)$ for small ε . The presence of neutron production in the medium modifies the conclusion that equation (8.81) is valid.

8.3.2. Buildup in an external shield. We now consider the problem of buildup in an external shield. We assume that an equivalent distance in the shield can be defined so that the stopping power in equivalent distance units of the shield and exposed media are equal. Consequently, the Boltzmann equations of the two media differ only in their nuclear cross sections as

$$\left[\frac{\partial}{\partial x} - \frac{\partial}{\partial E} S(E) + \sigma_s \right] \phi(x, E) = \int_E^\infty f_s(E, E') \phi(x, E') dE' \quad (8.83)$$

$$\left[\frac{\partial}{\partial x} - \frac{\partial}{\partial E} S(E) + \sigma \right] \phi(x, E) = \int_E^\infty f(E, E') \phi(x, E') dE' \quad (8.84)$$

For a monoenergetic beam on the boundary of the shield, the solution is given as

$$\psi_0(x, r) = \exp(-\sigma_s x) \delta(r_o - x - r) \quad (8.85)$$

$$\psi_1(x, r) = x \exp(-\sigma_s x) \bar{f}_s(r, r_o - x) \quad (8.86)$$

The particles appearing at the media interface provide the boundary condition of the exposed medium; thus,

$$\psi_0(0, r) = \exp(-\sigma_s t_s) \delta(r_o - t_s - r) + t_s \exp(-\sigma_s t_s) \bar{f}_s(r, r_o - t_s) + \dots \quad (8.87)$$

where t_s is the shield thickness. To evaluate the proton field in the exposed media we may use equation (8.63) and the above boundary value in equation (8.87) to obtain

$$\begin{aligned} \psi(x, r) = & \exp(-\sigma x) \exp(-\sigma_s t_s) \delta(r_o - t_s - x - r) \\ & + \exp(-\sigma x) t_s \exp(-\sigma_s t_s) \bar{f}_s(r + x, r_o - t_s) \\ & + \exp(-\sigma_s t_s) x \exp(-\sigma x) \bar{f}(r, r_o - t_s - x) + \dots \end{aligned} \quad (8.88)$$

Using equation (8.68), we may rewrite equation (8.88) as

$$\begin{aligned} \psi(x, r) = & \exp(-\sigma_s t_s - \sigma x) \delta(r_o - t_s - x - r) + [t_s \bar{f}_s(r, r_o - t_s - x) \\ & + x \bar{f}(r, r_o - t_s - x)] \exp(-\sigma_s t_s - \sigma x) + \dots \end{aligned} \quad (8.89)$$

Similar to equation (8.79), we have

$$\begin{aligned} D_s(t_s, x, E_o) = & \exp(-\sigma_s t_s - \sigma x) S[\varepsilon(r_o - t_s - x)] \\ & + \left\{ m_s \sigma_s t_s \bar{S}_{s1}[\varepsilon(r_o - t_s - x)] \right. \\ & \left. + m \sigma x \bar{S}_1[\varepsilon(r_o - t_s - x)] \right\} \exp(-\sigma_s t_s - \sigma x) + \dots \end{aligned} \quad (8.90)$$

It is clear that equation (8.90) may be written as

$$\begin{aligned} D_s(t_s, x, E_o) = & D(t_s + x, E_o) + [\exp(-\sigma_s t_s) - \exp(-\sigma t_s)] D(x, E_s) \\ & + t_s \exp(-\sigma x) \left\{ m_s \sigma_s \bar{S}_{s1}[\varepsilon(r_o - t_s - x)] \exp(-\sigma_s t_s) \right. \\ & \left. - m \sigma \bar{S}_1[\varepsilon(r_o - t_s - x)] \exp(-\sigma t_s) \right\} \\ \approx & D(t_s + x, E_o) + t_s \left\{ (\sigma - \sigma_s) D(x, E_s) \right. \\ & \left. + \exp(-\sigma x) (m_s \sigma_s - m \sigma) \bar{S}_1[\varepsilon(r_o - t_s - x)] \right\} + \dots \end{aligned} \quad (8.91)$$

where $E_s = \varepsilon(r_o - t_s)$. One may define the shield buildup factor relative to the exposed media as

$$D_s(t_s, x, E_o) = \left\{ \frac{1 + t_s [(\sigma - \sigma_s)D(x, E_s) + \exp(-\sigma x)(m_s \sigma_s - m\sigma) \bar{S}_1]}{D(t_s + x, E_o)} + \dots \right\} \times D(t_s + x, E_o) \quad (8.92)$$

Clearly, the coefficient of t_s in equation (8.92) is reduced if $\sigma \approx \sigma_s$, and furthermore it is reduced to a small contribution as $m \rightarrow m_s$. This occurs because the spectral distribution functions have $\gamma \approx \gamma_s$ for all materials since γ is largely determined from the proton-proton scattering amplitude.

8.3.3. Tissue buildup factors. We now consider the implementation of the above ideas into a practical formulation of proton buildup factors in tissue. Available information on conversion factors is for discrete energies from 100 MeV to 1 TeV in rather broad energy steps for depths from 0 to 30 cm in semi-infinite slabs of tissue (Alsmiller, Armstrong, and Coleman, 1970; Armstrong and Chandler, 1970; Turner et al., 1964; Zerby and Kinney, 1965). The nuclear reaction data used for high-energy nucleons are usually based on Monte Carlo estimates (Bertini, 1963 and 1969; Bertini and Guthrie, 1971) with low-energy neutron reaction data taken from experimental observation. The quality factor as defined by ICRP 26 (Anon., 1977) is used for protons. The quality factor for heavier fragments and the recoiling nuclei is arbitrarily set to 20 which is considered conservative (Wilson, Shinn, and Townsend, 1990), but the average quality factor obtained by calculation is comparable with estimates obtained through observations made in nuclear emulsion (Schaefer and Sullivan, 1970).

To fully use equation (8.58), a parameterization of the conversion factor was introduced by Wilson and Khandelwal (1974) that allowed reliable interpolation and extrapolation from known values. A refinement and an extension of that work are now discussed.

The conversion factor $R_n(z, E)$ is composed of two terms representing the dose caused by the primary beam protons and the dose caused by secondary particles produced in nuclear reactions. Thus,

$$R_n(z, E) = R_p(z, E) + R_s(z, E) \quad (8.93)$$

where the conversion factor of the primary dose equivalent is

$$R_p(z, E) = \frac{P(E) Q_F[S(E_r)] S(E_r)}{P(E_r)} \quad (8.94)$$

with the reduced energy given by

$$E_r = \varepsilon[R(E) - z] \quad (8.95)$$

and with the usual quality factor Q_F defined as a function of linear energy transfer (LET), with LET denoted here by the symbol S , and total nuclear survival

probability for a proton of energy E given by

$$P(E) = \exp \left[- \int_0^E \frac{\sigma(E') dE'}{S(E')} \right] \quad (8.96)$$

where macroscopic cross section $\sigma(E)$ for tissue as calculated by Bertini is given by Alsmiller et al. (1972). The $R(E)$ is the usual range-energy relation for protons in tissue, and $\varepsilon(x)$ is the inverse of $R(E)$. The proton total optical thickness given by

$$\tau(E) = \int_0^E \frac{\sigma(E') dE'}{S(E')} \quad (8.97)$$

is given in table 8.1 for purposes of numerical interpolation. In the case of conversion factors for absorbed dose, $R_p(z, E)$ is taken as

$$R_p(z, E) = \frac{P(E) S(E_r)}{P(E_r)} \quad (8.98)$$

The representation of the conversion factors is simplified by rewriting equation (8.93) as

$$R_n(z, E) = \left[1 + \frac{R_s(z, E)}{R_p(z, E)} \right] R_p(z, E) \equiv B(z, E) R_p(z, E) \quad (8.99)$$

where $B(z, E)$ is recognized as the dose buildup factor. The main advantage of introducing the buildup factor into equation (8.99) is that unlike $R_n(z, E)$, the buildup factor is a smoothly varying function of energy at all depths in the slab and can be approximated by the simple function

$$B(z, E) = (A_1 + A_2 z + A_3 z^2) \exp(-A_4 z) \quad (8.100)$$

where the parameters A_i are understood to be energy dependent. The parameters A_i are found by fitting equation (8.100) to the values of the buildup factors as estimated from the Monte Carlo calculations of proton conversion factors. The resulting coefficients are shown in table 8.2. The coefficients for 100-, 200-, and 300-MeV protons were obtained with the Monte Carlo data of Turner et al. (1964). The values at 400, 730, 1500, and 3000 MeV were obtained from the results of Alsmiller, Armstrong, and Coleman (1970). The 10-GeV entry was obtained from the calculations of Armstrong and Chandler (1970). Some values noted in table 8.2 were obtained by interpolating between data points or smoothly extrapolating to unit buildup factor at proton energies near the coulomb barrier for tissue nuclei (≈ 12 MeV). The coefficients are found for all energies to 10 GeV by using second-order Lagrange interpolation between the values shown in table 8.2. The resulting buildup factors are shown in figures 8.1 and 8.2 in comparison with the Monte Carlo results, where the error bars were determined by drawing smooth limiting curves so as to bracket the Monte Carlo values and to follow the general functional dependence. The uncertainty limits should, therefore, be interpreted as approximately 2σ limits, rather than 1σ ranges generally used in expressing uncertainty limits.

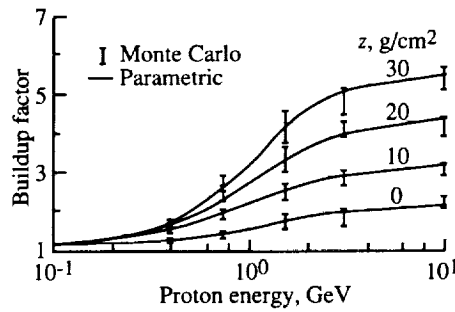


Figure 8.1. Dose buildup factor for several depths in tissue as function of incident proton energy.

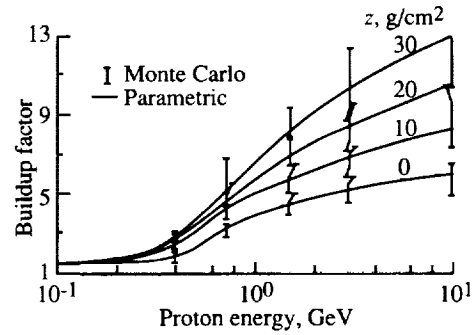


Figure 8.2. Dose equivalent buildup factor for several depths in tissue as function of incident proton energy.

Table 8.1. Total Tissue Optical Thickness for Protons

E , GeV	$\tau(E)$	E , GeV	$\tau(E)$
0	0	1.3	6.57
.01	.0033	1.5	8.03
.025	.0171	1.7	9.52
.05	.0510	2.0	11.76
.1	.135	2.2	13.27
.15	.239	2.4	14.78
.2	.362	2.6	16.29
.25	.501	2.8	17.79
.3	.655	3.0	19.29
.35	.822	4.0	26.62
.4	1.004	5.0	38.81
.5	1.429	6.0	40.84
.7	2.471	7.0	47.75
.9	3.743	8.5	57.91
1.1	5.143	10.0	67.85

In figure 8.3 the dose as a function of depth is shown in comparison to measurements of Baarli and Goebel at CERN (Switzerland) (Properties of High-Energy Beams From a 600-MeV Synchrocyclotron. Presented at XI International Congress of Radiology (Rome), Sept. 1965). Also shown are the Monte Carlo values interpolated between 400 and 730 MeV. The uncollided primary proton contribution is shown separately. The dose equivalent is likewise shown in figure 8.4. The extreme importance of secondary radiation is clearly shown.

Within the space program, one has shield material that is mostly aluminum. We are therefore interested in attenuating space radiation by the appropriate

Table 8.2. Buildup-Factor Parameters

E , GeV	Dose equivalent				Dose			
	A_1	A_2	A_3	A_4	A_1	A_2	A_3	A_4
^a 0.03	1.00	0	0	0	1.00	0	0	0
^a .06	1.20	0	0	.0300	1.07	.010	0	.010
.10	1.40	.020	0	.0300	1.10	.040	0	.026
^a .15	1.50	.070	0	.0385	1.12	.060	0	.031
.20	1.60	.090	0	.0400	1.15	.062	0	.032
.30	1.70	.110	0	.0330	1.20	.068	0	.026
.40	1.90	.130	0	.0228	1.24	.071	0	.0228
.73	3.40	.156	.00035	.0150	1.40	.090	.0001	.0150
^a 1.2	4.32	.167	.00145	.0130	1.67	.094	.0008	.0122

^aDenotes interpolated values.

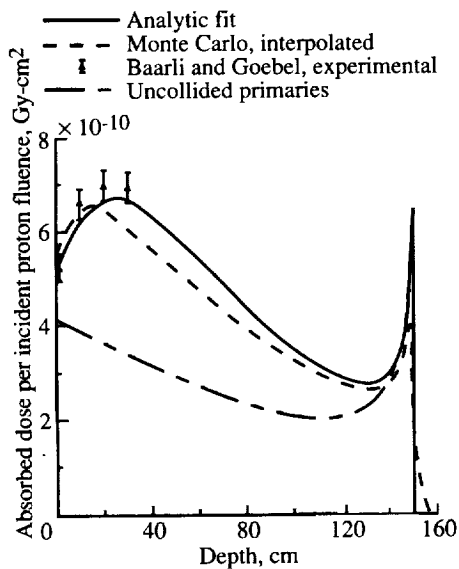


Figure 8.3. Proton depth-dose relation: analytic fit (nuclear effects), Monte Carlo, experiments, and primary protons for 592-MeV protons.

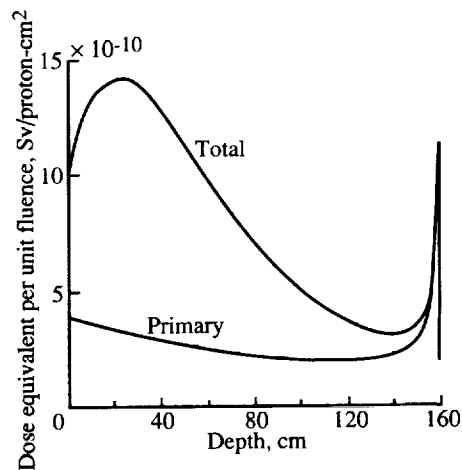


Figure 8.4. Proton depth-dose equivalent relation including nuclear effects for 600-MeV protons.

amount of aluminum before the radiation enters the astronaut's body. As a first step, we replace the appropriate aluminum thickness z_s (given in g/cm^2) by a range of equivalent thickness of tissue \hat{z}_s for 50-MeV protons as has been the custom in space-radiation protection as

$$\hat{z}_s = \frac{R_{\text{tiss}}(50)}{R_{\text{Al}}(50)} z_s \equiv \rho z_s \quad (8.101)$$

For definiteness we note that $\rho \approx 0.787$. The conversion factor of the primary dose equivalent is then

$$R_p(z + \hat{z}_s, E) = \exp \left[- \left(\rho^{-1} \sigma_{\text{Al}} - \sigma_{\text{tiss}} \right) \hat{z}_s \right] \times \frac{P(E) Q_F[S(E_r)] S(E_r)}{P(E_r)} \quad (8.102)$$

where the reduced energy is

$$E_r = \varepsilon [R(E) - z - \hat{z}_s] \quad (8.103)$$

and the exponential factor corrects $P(E)$ by the appropriate aluminum-tissue-combined attenuation factor. The primary absorbed dose is identical in form to equation (8.102) except that $Q_F(S)$ is equal to unity. Note that σ_{Al} and σ_{tiss} are taken presently as the asymptotic macroscopic cross sections where energy dependence is negligible. The complete conversion factors are

$$R_n(z + \hat{z}_s, E) = R_p(z + \hat{z}_s, E) + R_s(z + \hat{z}_s, E) \quad (8.104)$$

where $R_s(z + \hat{z}_s, E)$ is the contribution including secondary particles. We rewrite equation (8.104) as

$$R_n(\hat{z}_s + z, E) = B_{\Delta}(\hat{z}_s, E) R_{\text{tiss}}(z + \hat{z}_s, E) \quad (8.105)$$

where $B_{\Delta}(\hat{z}_s, E)$ is an aluminum buildup factor relative to tissue which is unity for $\hat{z}_s = 0$ and $E \ll 100$ MeV. The aluminum factor has been found (units for E are GeV and for \hat{z}_s are g/cm^2) to be reasonably approximated by

$$B_{\Delta}(\hat{z}_s, E) = 1 + \frac{0.02\hat{z}_s E}{(1 + E)} \exp(-0.022\hat{z}_s) \quad (8.106)$$

for the dose equivalent and by

$$B_{\Delta}(\hat{z}_s, E) = 1 + \frac{0.02\hat{z}_s E}{6(1 + E)} \exp(-0.01\hat{z}_s) \quad (8.107)$$

for the absorbed dose. Equation (8.56) is rewritten as

$$D(\vec{x}) = \int_0^{\infty} \int_{\Omega} R_n[\hat{z}_s(\vec{\Omega}), z(\vec{\Omega}), E] \phi(\vec{\Omega}, E) d\vec{\Omega} dE \quad (8.108)$$

where $\hat{z}_s(\vec{\Omega})$ is the aluminum thickness distribution (Atwell et al., 1989) about the dose point \vec{x} and $z(\vec{\Omega})$ is the astronaut self-shielding distribution about the dose point (Billings and Yucker, 1973). This method has proven very useful in estimating space proton exposures.

8.4. Numerical Methods

In the rest of this chapter, we consider numerical methods for estimating solutions to the Boltzmann equation. We first consider the numerical solution of the

charged-particle transport equation with energy-independent nuclear parameters as a test bed for numerical methods. We then propose a general method for fully coupled, neutron-proton transport in the straight ahead approximation using the nuclear data bases of chapters 4 and 5 which resulted in the code system (Wilson et al., 1989) known as the BRYNTRN (baryon transport code.) The numerical convergence and the comparison with Monte Carlo derived results are studied.

8.4.1. Energy-independent proton model. The Boltzmann equation for proton transport in the straight ahead approximation is given as

$$\left[\frac{\partial}{\partial x} - \frac{\partial}{\partial E} S(E) + \sigma \right] \phi(x, E) = \int_E^\infty f(E, E') \phi(x, E') dE' \quad (8.109)$$

where $S(E)$ is the proton stopping power, σ is the macroscopic interaction cross section that we presently take as energy independent, and $f(E, E')$ is the production secondary-particle spectrum. Using the definitions

$$r = \int_0^E \frac{dE'}{S(E')} \quad (8.110)$$

$$\psi(x, r) = S(E) \phi(x, E) \quad (8.111)$$

and

$$\bar{f}(r, r') = S(E) f(E, E') \quad (8.112)$$

allows equation (8.109) to be written as

$$\left[\frac{\partial}{\partial x} - \frac{\partial}{\partial r} + \sigma \right] \psi(x, r) = \int_r^\infty \bar{f}(r, r') \psi(x, r') dr' \quad (8.113)$$

The advantage of equation (8.113) over equation (8.109) is that derivatives of $\phi(x, E)$ with respect to E display large variations at low energy and are difficult to approximate numerically, whereas $\psi(x, r)$ is well behaved at all values of r and approaches a constant at small values of r .

8.4.2. First-order explicit methods. The boundary condition is specified at $x = 0$ and first-order explicit methods imply a forward difference formula in x to propagate the solution from the boundary. We assume an x -grid denoted by x_i separated by distance h and an r -grid denoted by r_j separated by distance Δ . A backward difference along the boundary yields

$$\frac{1}{h} (\psi_{i+1,j} - \psi_{i,j}) - \frac{1}{\Delta} (\psi_{i,j} - \psi_{i,j-1}) + \sigma \psi_{i,j} = \zeta_{ij} \quad (8.114)$$

where $\psi_{i,j}$ is taken as zero for $j < 0$ corresponding to a negative residual range.

This explicit procedure yields

$$\psi_{i+1,j} = \left(1 + \frac{h}{\Delta} - \sigma h \right) \psi_{i,j} - \frac{h}{\Delta} \psi_{i,j-1} + h \zeta_{ij} \quad (8.115)$$

Clearly, a stable method must propagate the boundary as an energy shifted and attenuated beam of particles. Note that the lowest energy point may be solved as

$$\psi_{i+1,0} = \left(1 + \frac{h}{\Delta} - \sigma h\right)^{i+1} \psi_{0,0} \quad (8.116)$$

when the secondary source terms are set to zero. A stable solution requires

$$1 > \sigma h > \frac{h}{\Delta} \quad (8.117)$$

for which Δ must be chosen greater than the nuclear mean-free path. Such a requirement ($\Delta > \sigma^{-1}$) resulting in poor energy resolution will not allow an adequate representation of typical boundary conditions resulting in large numerical errors.

A second explicit method uses a forward difference along the boundary as

$$\frac{1}{h} (\psi_{i+1,j} - \psi_{i,j}) - \frac{1}{\Delta} (\psi_{i,j+1} - \psi_{i,j}) + \sigma \psi_{i,j} = \zeta_{ij} \quad (8.118)$$

and is represented in a stepping procedure as

$$\psi_{i+1,j} = \left(1 - \frac{h}{\Delta} - h\sigma\right) \psi_{i,j} + \frac{h}{\Delta} \psi_{i,j+1} + \zeta_{ij} h \quad (8.119)$$

It is clear that for some values of J the values of $\psi_{0,j}$ are zero for $j > J$ and the boundary propagation of $\psi_{i,J}$ is

$$\psi_{i,J} = \left(1 - \frac{h}{\Delta} - h\sigma\right)^i \psi_{0,J} \quad (8.120)$$

which converges if $\frac{h}{\Delta} + h\sigma < 1$. For numerical accuracy, $h \ll \Delta$ and $h \ll \sigma^{-1}$ are also required. The first condition is particularly hard to meet because Δ becomes rapidly small at low energies which makes the low-energy spectrum difficult to calculate without special procedures.

8.4.3. "Linearized" methods. A method was proposed and received considerable use in which the stopping-power term was "linearized" in such a way that analytical methods could be applied and numerical stability issues circumvented. This requires an assumed form for the flux as

$$\phi(x, E) \approx \frac{c}{E^\alpha} \quad (8.121)$$

and stopping power as

$$S(E) = nk \left(\frac{k}{E}\right)^{\frac{1}{n}-1} \quad (8.122)$$

The energy derivative in equation (8.109) is then approximated as

$$\frac{\partial}{\partial E}[S(E)\phi(x, E)] \approx -\frac{n\alpha - n + 1}{r(E)}\phi(x, E) \quad (8.123)$$

after which equation (8.109) is written as

$$\left[\frac{\partial}{\partial x} + \frac{n\alpha - n + 1}{r(E)} + \sigma\right]\phi(x, E) = \int_E^\infty f(E, E')\phi(x, E')dE' \quad (8.124)$$

which may be solved analytically because E enters only as a parameter. Note that the range-energy relations enter as an effective attenuation similar to the finite-difference approximation (eq. (8.120)). Although equation (8.124) contains no instability, there are large inherent errors as discussed elsewhere (Wilson and Badavi, 1986).

8.4.4. Unconditionally stable numerical methods. The differential operator of equation (8.113) may be inverted to yield

$$\psi(x, r) = \exp(-\sigma x)\psi(0, r+x) + \int_0^x dz \exp(-\sigma z) \int_{r+z}^\infty dr' \bar{f}(r+z, r')\psi(x-z, r') \quad (8.125)$$

where the boundary condition is

$$\psi(0, r) = S(E)\phi(0, E) \quad (8.126)$$

A numerical algorithm for equation (8.125) is found by noting that

$$\begin{aligned} \psi(x+h, r) &= \exp(-\sigma h)\psi(x, r+h) \\ &+ \int_0^h dz \exp(-\sigma z) \int_r^\infty dr' \bar{f}(r+z, r'+z) \\ &\times \psi(x+h-z, r'+z) \end{aligned} \quad (8.127)$$

which can be simplified by using

$$\psi(x+h-z, r) \approx \exp[-\sigma(h-z)]\psi(x, r+h-z) + O(h) \quad (8.128)$$

which yields

$$\begin{aligned} \psi(x+h, r) &\approx \exp(-\sigma h)\psi(x, r+h) \\ &+ \exp(-\sigma h) \int_0^h dz \int_r^\infty dr' \bar{f}(r+z, r'+z)\psi(x, r'+h) \end{aligned} \quad (8.129)$$

with the order of h^2 , where h is the step size. Equation (8.129) is accurate for distances such that $\sigma h \ll 1$ and may be used to relate the spectrum at some point x to the spectrum at $x+h$. Therefore, one may begin at the boundary ($x=0$) and propagate the solution to any arbitrary interior point using equation (8.129).

Several advantages are seen in the above method. First, the range-energy relations enter the solution exactly. Second, the method introduces no extraneous unstable roots that arose in earlier methods by not treating the range-energy relation accurately. The inherent stability will tend to dampen any errors committed at the boundary or generated in the interior. Truncation errors enter the solution of equation (8.129), and their generation and propagation will now be considered.

8.5. Error Analysis of Unconditionally Stable Methods

There are two immediate questions regarding the use of equation (8.129) in the solution of charged-particle transport: (1) What are the relative errors in numerical implementation, and (2) how do these errors propagate into the solution domain? Although these two questions cannot be dealt with entirely independently, we first consider relative errors and then study their propagation.

8.5.1. Local relative error. Numerical interpolation in BRYNTRN was motivated by the observation that the high-energy spectrum for most space radiation varies as $E^{-\alpha}$ as noted in equation (8.121). Similarly, for $r_i \leq r \leq r_{i+1}$ we used

$$\psi(x, r) \approx a_i (r_i/r)^{\alpha_i} \quad (8.130)$$

where

$$a_i = \psi(x, r_i) \quad (8.131)$$

$$\alpha_i = \frac{\ln \left[\frac{\psi(x, r_{i+1})}{\psi(x, r_i)} \right]}{\ln(r_i/r_{i+1})} \quad (8.132)$$

and we define $\Delta = r_2 - r_1$. We evaluate the relative error for equation (8.130) for typical space spectra.

The galactic cosmic-ray spectrum is given approximately as

$$\psi_{\text{GCR}}(r) \approx \frac{1}{1 + r^2} \quad (8.133)$$

for which (with $i = 1$)

$$a_1 = (1 + r_1^2)^{-1} \quad (8.134)$$

$$\alpha_1 = \frac{\ln \left\{ 1 + \left[2r_1 \Delta + \Delta^2 \right] / (1 + r_1^2) \right\}}{\ln [1 + (\Delta/r_1)]} \quad (8.135)$$

and we assume that $\Delta \ll 1$. We evaluate the spectrum at the midpoint $r_m = r_1 + \frac{1}{2}\Delta$ and compare. First, note that

$$\ln [\psi_{\text{GCR}}(r_m)] = -\ln \left(1 + r_1^2 + \Delta r_1 + \frac{1}{4}\Delta^2 \right) \quad (8.136)$$

is the exact value compared with

$$\ln \left[a_1 \left(\frac{r_1}{r_m} \right)^{\alpha_1} \right] = -\ln(1+r_1^2) - \frac{\ln \left(1 + \frac{2r_1\Delta + \Delta^2}{1+r_1^2} \right) \ln \left(1 + \frac{1}{2} \frac{\Delta}{r_1} \right)}{\ln \left(1 + \frac{\Delta}{r_1} \right)} \quad (8.137)$$

The error ε is examined in the following three limits:

For $r_i \gg 1$,

$$\varepsilon \approx +\frac{1}{4} \frac{\Delta^2}{r_1^2} \quad (8.138)$$

for $\Delta \ll r_i \ll 1$,

$$\varepsilon \approx \frac{1}{4} \Delta^2 \quad (8.139)$$

and for $\Delta \approx r_1 \ll 1$,

$$\varepsilon \approx 0.17r_1\Delta \quad (8.140)$$

It is clear from these limits that accuracy is easy to maintain for large values of r_1 , but errors are progressively greater for lower values of r_1 . One obvious problem with equation (8.130) is its concave shape between grid values leading to discontinuous derivatives.

Many solar-flare particle events are exponential rigidity spectra as

$$\phi \approx \exp \left[\frac{-P(E)}{P_o} \right] \quad (8.141)$$

where the momentum is

$$P(E) = \sqrt{E(E + 2Mc^2)} \quad (8.142)$$

with Mc^2 denoting the rest energy. In analogy we consider a trial spectrum

$$\phi = \exp \left\{ \frac{-[r(r+1)]^{1/2}}{r_o} \right\} \quad (8.143)$$

and the interpolating function of equation (8.130).

Consequently,

$$a_1 = \exp \left\{ \frac{-[r(r+1)]^{1/2}}{r_o} \right\} \quad (8.144)$$

$$\alpha_1 = \frac{\sqrt{(r_1 + \Delta)(r_1 + 1 + \Delta)} - \sqrt{r_1(r_1 + 1)}}{r_o \ln[1 + (\Delta/r_1)]} \quad (8.145)$$

and assume that $\Delta \ll 1$. At the midpoint we have

$$\ln \phi = \frac{- \left[\left(r_1 + \frac{\Delta}{2} \right) \left(1 + r_1 + \frac{\Delta}{2} \right) \right]^{1/2}}{r_o} \quad (8.146)$$

which is the exact value to be compared with

$$\ln \left[a_1 \left(\frac{r}{r_m} \right)^{\alpha_1} \right] = \frac{- [(r_1 + \Delta)(1 + r_1 + \Delta)]^{1/2}}{r_o} - \frac{\left[\sqrt{(r_1 + \Delta)(1 + r_1 + \Delta)} - \sqrt{r_1(r_1 + 1)} \right] \ln \left(1 + \frac{\Delta}{2r_1} \right)}{r_o \ln \left(1 + \frac{\Delta}{r_1} \right)} \quad (8.147)$$

The error ϵ is examined in the limits as before:

For $r_1 \gg 1$,

$$\epsilon \approx -\frac{3 \Delta}{2 r_o} \quad (8.148)$$

and for $\Delta \leq r_1 \ll 1$,

$$\epsilon \approx -\frac{3}{4} \frac{\Delta}{r_o \sqrt{r_1}} \quad (8.149)$$

Clearly, one requirement for high accuracy is $\Delta \ll r_o$, but the error still increases as r_1 becomes small.

An alternate choice for an interpolating function is

$$\psi(r) = a_i \exp[-b_i(r - r_i)] \quad (r_i \leq r \leq r_{i+1}) \quad (8.150)$$

This function has the qualitative feature of being convex as are most space spectra. As before,

$$a_i = \psi(r_i) \quad (8.151)$$

with b_i given as

$$b_i = \frac{-\ln [\psi(r_2)/\psi(r_1)]}{r_2 - r_1} \quad (8.152)$$

Analysis shows that the assumed GCR spectrum is always correct to $O(\Delta^2)$ which is taken to be small. For the rigidity spectrum, the error is

$$\epsilon \approx \frac{\Delta}{r_o} \quad (r_1 \gg 1 \gg \Delta) \quad (8.153)$$

$$\varepsilon \approx \frac{\sqrt{r_1}}{2r_o} \Delta \quad (1 \gg r_1 \gg \Delta) \quad (8.154)$$

$$\varepsilon = \frac{\Delta}{2\sqrt{r_1}r_o} \quad (1 \gg r_1 \approx \Delta) \quad (8.155)$$

The errors for the interpolating function (8.150) are on the same order as the earlier interpolating function (8.130), except that their coefficient is a factor of 2 to 3 smaller and the error is now an overestimate.

8.5.2. Error propagation. In consideration of how errors are propagated in the use of equation (8.129), the error is introduced locally by calculating $\psi(x, r+h)$ over the range (energy) grid over which it was defined as

$$\psi(x+h, r_i) = \exp(-\sigma h) \psi(x, r_i+h) \quad (8.156)$$

We denote the truncation error introduced into equation (8.156) as

$$\psi(x, r_i+h) = \psi_{\text{int}}(x, r_i+h) + \varepsilon_i(h) \quad (8.157)$$

After the k th step from the boundary, the numerical solution is

$$\psi(kh, r_i) = \exp(-\sigma kh) \psi_{\text{int}}[(k-1)h, r_i+h] + \sum_{\ell=0}^{k-1} \exp[-\sigma(k-\ell)h] \varepsilon_{\ell}(h) \quad (8.158)$$

Suppose that $0 \leq \varepsilon_{\ell}(h) \leq \varepsilon(h)$ for all values of ℓ , then the propagated error is bound by

$$\varepsilon_{\text{prp}}(h) = \sum_{\ell=0}^{k-1} \exp[-\sigma(k-\ell)h] \varepsilon_{\ell}(h) \leq \varepsilon(h) \sum_{\ell=0}^{k-1} \exp[-\sigma(k-\ell)h] \quad (8.159)$$

We note that

$$\sum_{\ell=0}^{k-1} \exp(-\sigma kh) \exp(\sigma h \ell) \approx \frac{1}{h\sigma} [1 - \exp(-\sigma kh)] \quad (8.160)$$

Clearly, the propagated error on the k th step is bound by

$$\varepsilon_{\text{prp}}(h) < \frac{\varepsilon(h)}{h\sigma} [1 - \exp(-\sigma kh)] \quad (8.161)$$

where $\varepsilon(h)$ is the maximum error per step. The propagated error grows each step to a maximum value of $\varepsilon(h)/h\sigma$ and would require $\varepsilon(h)$ to be on the order of $O(h^2)$ for good convergence. The asymptotic bound for the propagated error is

$$\varepsilon_{\text{prp}} \leq \varepsilon(h) \sum_{\ell=0}^{\infty} \exp(-\sigma \ell h) = \varepsilon(h) \frac{\exp(-\sigma h)}{1 - \exp(-\sigma h)} \quad (8.162)$$

emphasizing again the need to control the error as $h\sigma \rightarrow 0$. It is clear that the higher order techniques are required to control error propagation as found in recent studies (Shinn et al., 1991).

8.5.3. Numerical procedure. We now consider numerical methods for the integral portion of equation (8.127). We will make use of the form of the interaction given by equation (8.12) for which an analytic solution has already been obtained. As shown in connection with equation (8.129), equation (8.127) may be rewritten as

$$\begin{aligned} \psi(x+h, r) = & \exp(-\sigma h) \psi(x, r+h) \\ & + \exp(-\sigma h) \int_0^h dz \int_r^\infty dt a \exp[-\alpha(r+z)] \psi(x, t+h) \\ & + \exp(-\sigma h) \int_0^h dz \int_r^\infty dt c \exp[\gamma(r-t-Q)] \psi(x, t+h) \\ & + O(h^2) \end{aligned} \quad (8.163)$$

where Q represents the average energy shift of the projectile producing the secondary particles across the interval x to $x+h$. In principle, a, α, c , and γ are dependent on projectile energy as well and would be evaluated using the same value of Q (Wilson et al., 1989). With the analytic forms in equation (8.163), we may perform the integrals as

$$\begin{aligned} \psi(x+h, r) = & \exp(-\sigma h) \psi(x, r+h) \\ & + \exp(-\sigma h) \int_r^\infty dt \frac{a}{\alpha} \left[\exp(-\alpha r) - \exp[-\alpha(r+h)] \right] \psi(x, t+h) \\ & + \exp(-\sigma h) \int_r^\infty dt hc \exp[\gamma(r-t)] \psi(x, t+h) + O(h^2) \end{aligned} \quad (8.164)$$

The integral terms of equation (8.164) can be written in terms of the cumulative secondary spectra denoted as

$$F_a(r, t) = \int_0^r a \exp(-\alpha z) dz \quad (8.165)$$

and

$$F_c(r, t) = \int_0^r c \exp[\gamma(z-t)] dz \quad (8.166)$$

In particular,

$$\frac{a}{\alpha} \left\{ \exp(-\alpha r) - \exp[-\alpha(r+h)] \right\} = F_a(r+h, t+Q) - F_a(r, t+Q) \quad (8.167)$$

$$\begin{aligned}
ch \exp[\gamma(r-t-Q)] &= [F_c(r+h, t+Q) - F_c(r, t+Q)] \\
&\times \left[1 - \frac{1}{2}\gamma(h-2Q) + O(h^2) \right] \quad (8.168)
\end{aligned}$$

which may now be substituted into equation (8.164) to obtain

$$\begin{aligned}
\psi(x+h, r) &= \exp(-\sigma h) \psi(x, r+h) \\
&+ \exp(-\sigma h) \int_r^\infty dt [F_a(r+h, t+Q) - F_a(r, t+Q)] \psi(x, t+h) \\
&+ \exp(-\sigma h) \int_r^\infty dt [F_c(r+h, t+Q) - F_c(r, t+Q)] \psi(x, t+h) \\
&+ O(h-2Q) + O(h^2) \quad (8.169)
\end{aligned}$$

The second-order accuracy is maintained only if Q is chosen at the midpoint of the interval (i.e., $Q = \frac{1}{2}h$). Additional details of this analysis can be found in Wilson et al. (1989). The propagation equation is implemented as

$$\begin{aligned}
\psi(x+h, r) &= \exp(-\sigma h) \psi(x, r+h) \\
&+ \int_r^\infty dt \bar{F} \left(h, r, t + \frac{h}{2} \right) \psi(x, t+h) \quad (8.170)
\end{aligned}$$

where

$$\begin{aligned}
\bar{F}(h, r, t) &= \int_0^h \bar{f}(r+z, t) dz \\
&\equiv F(r+h, t) - F(r, t) \quad (8.171)
\end{aligned}$$

and is related to the cumulative energy spectrum by

$$F(r, t) = \int_0^{\varepsilon(r)} f(E, E') dE \quad (8.172)$$

where $\varepsilon(r)$ is the energy associated with the residual range r and $E' = \varepsilon(t)$.

8.6. Coupled Baryon Transport Methods

The coupled baryon transport equations are of the form

$$\left[\frac{\partial}{\partial x} - \nu_j \frac{\partial}{\partial E} S(E) + \sigma_j(E) \right] \phi_j(x, E) = \sum_k \int_0^\infty f_{jk}(E, E') \phi_k(x, E') dE' \quad (8.173)$$

where ν_j is the range scaling parameter, $S(E)$ is the stopping power of the protons, $\sigma_j(E)$ is the total cross section, $\phi_j(x, E)$ is the differential flux spectrum of type j

baryons, and $f_{jk}(E, E')$ is a differential energy cross section for redistribution of particle type and energy. Utilizing the definitions

$$\tau = \int_0^E \frac{dE'}{S(E')} \quad (8.174)$$

$$\psi_j(x, r) = S(E) \phi_j(x, E) \quad (8.175)$$

and

$$\bar{f}_{jk}(r, r') = S(E) f_{jk}(E, E') \quad (8.176)$$

allows equation (8.173) to be written as

$$\left[\frac{\partial}{\partial x} - \nu_j \frac{\partial}{\partial r} + \sigma_j(r) \right] \psi_j(x, r) = \sum_k \int_r^\infty \bar{f}_{jk}(r, r') \psi_k(x, r') dr' \quad (8.177)$$

which may be rewritten as (Wilson and Lamkin, 1975; Wilson and Badavi, 1986)

$$\begin{aligned} \psi_j(x, r) = & \exp[-\zeta_j(r, x) \psi_j(0, r + \nu_j x)] \\ & + \sum_k \int_0^x \int_r^\infty \exp[-\zeta_j(r, z)] \bar{f}_{jk}(r + \nu_j z, r') \\ & \times \psi_k(x - t, r') dr' dz \end{aligned} \quad (8.178)$$

where the exponential is the integrating factor with

$$\zeta_j(r, t) = \int_0^t \sigma_j(r + \nu_j t') dt' \quad (8.179)$$

If the interactions are such that

$$\bar{f}_{jk}(r, r') = \delta_{jk} g(r - r') \quad (8.180)$$

where g denotes the appropriate spectral function, then the solutions to equation (8.177) are of the form

$$\psi_j(x, r) = \chi(x, r + \nu_j x) \quad (8.181)$$

To demonstrate how remarkable equation (8.181) is, we note that if $\chi(x, r)$ is the solution to the neutron transport equation ($\nu_n = 0$), then $\chi(x, r + \nu_p x)$ is the solution to the proton transport problem independent of the functional form chosen for the stopping power.

Rather simple numerical procedures follow from equation (8.179). Noting that the first-order nature of equation (8.173) allows $\psi_j(x, r)$ to be taken as a boundary condition for propagation to larger values of x , one may approximate equation (8.179) as

$$\begin{aligned}
\psi_j(x+h, r) &= \exp[-\zeta_j(r, h)] \psi_j(x, r + \nu_j h) \\
&+ \sum_k \int_0^h \int_r^\infty \exp[-\zeta_j(r, z)] \bar{f}_{jk}(r + \nu_j z, r') \\
&\times \psi_k(x+h-z, r') dz dr' \tag{8.182}
\end{aligned}$$

which may be used to develop a numerical stepping procedure. Equation (8.182) has provided the basis for a number of new transport codes for baryons of mass number greater than or equal to 1. (See Wilson and Lamkin (1975); Wilson and Badavi (1986); Wilson et al. (1989); Shinn et al. (1990).) These codes are now being extended to couple with the meson fields and with the negative baryon number fields.

If h is sufficiently small such that

$$\sigma_j(r') h \ll 1 \tag{8.183}$$

then, according to perturbation theory (Wilson and Lamkin, 1975)

$$\psi_k(x+h-z, r') \approx \exp[-\zeta_k(r, h-z)] \psi_k[x, r' + \nu_k(h-z)] \tag{8.184}$$

which may be used to approximate the above integral of equation (8.182).

For many cases of practical interest (e.g., accelerator studies), monoenergetic particle beams are used, and separation of the singular terms from the solution becomes convenient. The initial beam of type J particles of energy E_0 (where $\tau_0 = R(E_0)$) is taken as

$$\psi_j(0, r) = \delta_{jJ} \delta(\tau_0 - r) \tag{8.185}$$

and the solution is written by the replacement

$$\psi_j(x, r) \Rightarrow \psi_{j0}(x, r) + \psi_j(x, r) \tag{8.186}$$

The corresponding singular terms are

$$\psi_{k0}(x, r) = \exp[-\zeta_k(r, x)] \delta(\tau_0 - r - \nu_k x) \delta_{kj} \tag{8.187}$$

The regular terms of equation (8.182) for $k = p$ may be written as

$$\begin{aligned}
\psi_p(x+h, r) &= \exp[-\zeta_p(r, h)] \psi_p(x, r+h) \\
&+ \int_0^h dz \exp[-\zeta_p(r, z)] \sum_j \int_{r+z}^\infty \bar{f}_{pj}(r+z, r') \\
&\times [\psi_{j0}(x+h-z, r') + \psi_j(x+h-z, r')] dr' \tag{8.188}
\end{aligned}$$

and the regular terms for $k = n$ are

$$\begin{aligned} \psi_n(x+h, r) &= \exp[-\sigma_n(r)h] \psi_n(x, r) \\ &+ \int_0^h dz \exp[-\sigma_n(r)z] \sum_j \int_r^\infty \bar{f}_{nj}(r, r') \\ &\times [\psi_{j0}(x+h-z, r') + \psi_j(x+h-z, r')] dr' \end{aligned} \quad (8.189)$$

The singular contribution under the integrals of equations (8.188) and (8.189) can be evaluated with equation (8.187), and the approximations in equations (8.183) and (8.184) can be applied to find

$$\begin{aligned} \psi_p(x+h, r) &= \exp[-\sigma_p(r)h] \psi_p(x, r+h) \\ &+ \exp\left\{-\left[\sigma_p(r) + \sigma_p(r'_o)\right] \frac{h}{2}\right\} \bar{F}_{pp}(h, r, r'_o) \delta_{pj} \exp[-\zeta_p(r'_o, x)] \\ &+ \exp\left\{-\left[\sigma_p(r) + \sigma_n(r_o)\right] \frac{h}{2}\right\} \bar{F}_{pn}(h, r, r_o) \delta_{nj} \exp[-\sigma_n(r_o)x] \\ &+ \int_r^\infty \exp\left\{-\left[\sigma_p(r) + \sigma_p\left(r' + \frac{h}{2}\right)\right] \frac{h}{2}\right\} \\ &\times \bar{F}_{pp}\left(h, r, r' + \frac{h}{2}\right) \psi_p(x, r' + h) dr' \\ &+ \int_r^\infty \exp\left\{-\left[\sigma_p(r) + \sigma_n\left(r' + \frac{h}{2}\right)\right] \frac{h}{2}\right\} \\ &\times \bar{F}_{pn}\left(h, r, r' + \frac{h}{2}\right) \psi_n\left(x, r' + \frac{h}{2}\right) dr' \end{aligned} \quad (8.190)$$

and

$$\begin{aligned} \psi_n(x+h, r) &= \exp[-\sigma_n(r)h] \psi_n(x, r) \\ &+ h \bar{f}_{np}(r, r'_o) \exp\left\{-\left[\sigma_n(r) + \sigma_p(r'_o)\right] \frac{h}{2}\right\} \delta_{pj} \exp[-\zeta_p(r'_o, x)] \\ &+ h \bar{f}_{nn}(r, r'_o) \exp\left\{-\left[\sigma_n(r) + \sigma_n(r_o)\right] \frac{h}{2}\right\} \delta_{nj} \exp[-\sigma_n(r_o)x] \\ &+ h \int_r^\infty \exp\left\{-\left[\sigma_n(r) + \sigma_p(r')\right] \frac{h}{2}\right\} \bar{f}_{np}(r, r') \psi_p\left(x, r' + \frac{h}{2}\right) dr' \\ &+ h \int_r^\infty \exp\left\{-\left[\sigma_n(r) + \sigma_n(r')\right] \frac{h}{2}\right\} \bar{f}_{nn}(r, r') \psi_n(x, r') dr' \end{aligned} \quad (8.191)$$

where $r'_o = r_o - x - \frac{h}{2}$ and \bar{F} is related to the cumulative spectrum F as given by

$$\bar{F}_{ij}(h, r, r') = \int_0^h \bar{f}_{ij}(r+z, r') dz$$

with

$$F_{ij}(r, r') = \int_0^{\varepsilon(r)} f_{ij}(E, E') dE \quad (8.193)$$

$\varepsilon(r)$ is the energy associated with residual range r , and $E' = \varepsilon(r')$. Equations (8.190) and (8.191) are evaluated by establishing an x -grid at which $\psi_j(x_m, r)$ is evaluated, where h is the distance between each successive evaluation. The integral over r' is accomplished by establishing an r -grid (and the corresponding E -grid) and using

$$\int_{r_n}^{\infty} g(r_n, r') \psi_j(x_m, r') dr' \approx \sum_{\ell=n}^{\infty} g_n(r_n, \bar{r}_\ell) \int_{r_\ell}^{r_{\ell+1}} \psi_j(x_m, r) dr' \quad (8.194)$$

where $\bar{r}_\ell = (r_\ell + r_{\ell+1})/2$, and the series terminates at the highest value of ℓ in the r -grid. There is a spatially dependent discontinuity in the proton flux spectrum that requires right- and left-hand interpolation and integration. These discontinuities have been treated in the computational procedures.

8.7. Results and Discussion

Because the buildup factors are functions of both energy and thickness, the first step in verifying such a method is to compare the result at various fixed (discrete) energies. Comparisons were made (Wilson et al., 1989) between BRYNTRN and Monte Carlo results for monoenergetic protons at various energies and were in reasonable agreement considering the numerical difficulty involved in discrete energy calculations with BRYNTRN. For the buildup-factor method, comparisons made with Monte Carlo are shown in figures 8.5 and 8.6 and with experiment in figure 8.7.

The dose and dose equivalent calculated as functions of depth in tissue with and without aluminum shield are shown in figures 8.5 and 8.6 for normal incident protons at discrete energies of 400, 660, 730, 1500, and 3000 MeV. The limited Monte Carlo results with 0 g/cm² shielding are obtained from Alsmiller, Armstrong, and Coleman (1970). The calculated values with the buildup-factor method are seen to be in reasonable agreement despite the crudeness in the buildup parameters chosen. Although there are no Monte Carlo data available with shielding at discrete energy, the doses calculated with 30 g/cm² of aluminum shield by the buildup-factor method are also presented in the figures for qualitative comparison. In general, the dose is increased because of the presence of the shield (transition effect discussed in chapter 1). The increase in dose over those with no shielding results from neutrons produced in aluminum, especially in the first few centimeters of the tissue. For protons at the lowest energy (400 MeV), the Bragg peak appears at 55 cm in depth as the protons approach their limiting range as they travel through the shield and tissue.

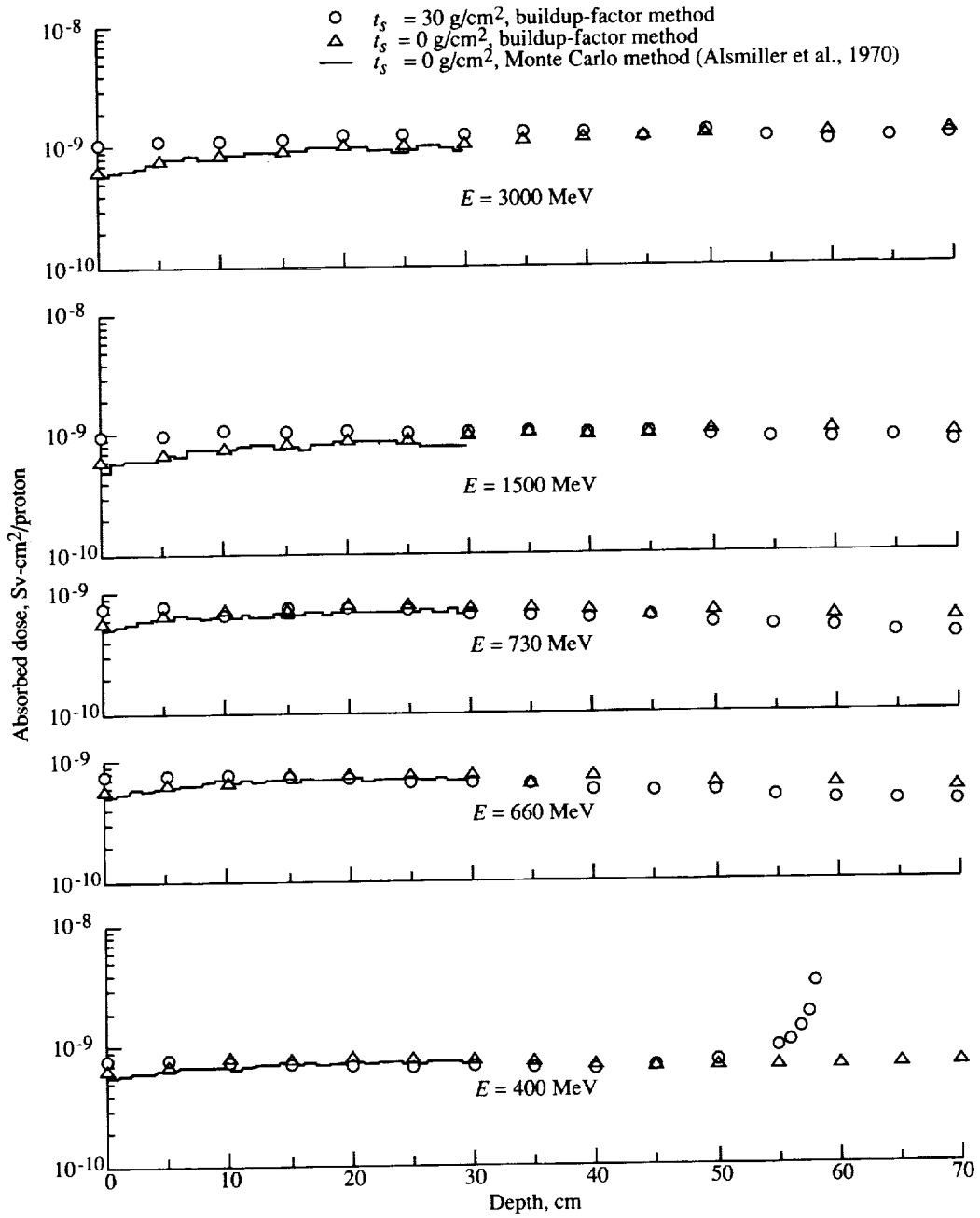


Figure 8.5. Dose in tissue (with or without aluminum shield) exposed to normal incident protons at various discrete energies.

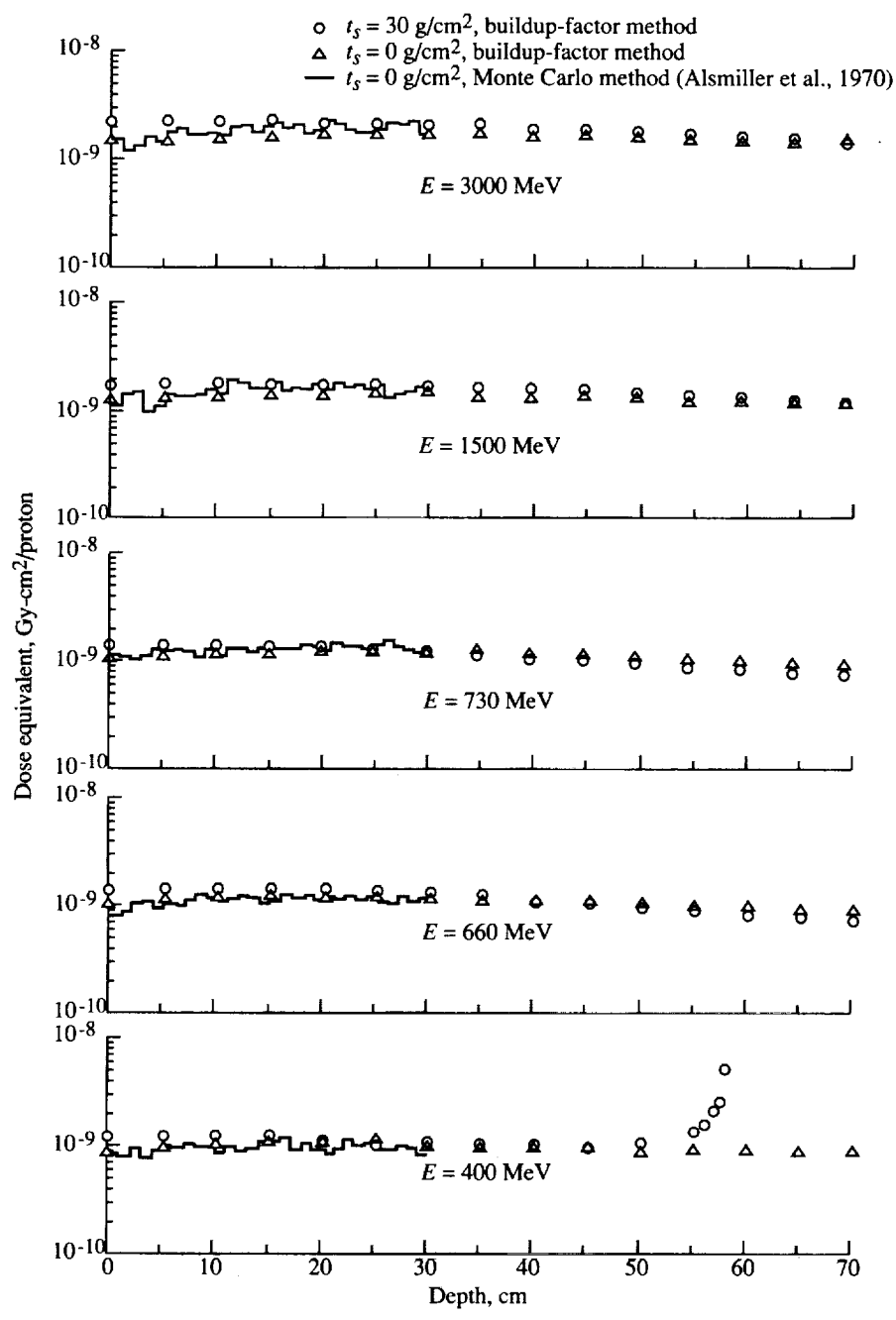


Figure 8.6. Dose equivalent in tissue (with or without aluminum shield) exposed to normal incident protons at various discrete energies.

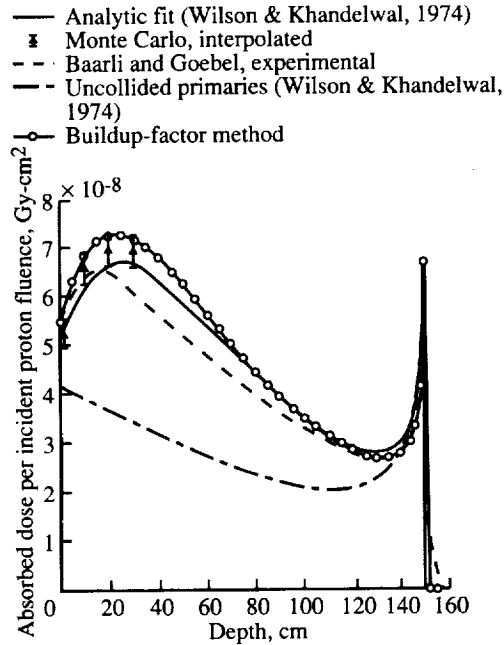


Figure 8.7. Comparison of predicted dose in tissue with experimental data for normal incident protons at 592 MeV.

Figure 8.7 shows a comparison of the experimental data of Baarli and Goebel at CERN, the buildup-factor method, and the interpolated Monte Carlo result (Alsmiller, Armstrong, and Coleman, 1970; Turner et al., 1964; Wright, Hamm, and Turner, 1971) for the absorbed dose in tissue that is exposed to a proton beam of 592 MeV. Also shown are the earlier buildup-factor calculations (Wilson and Khandelwal, 1974) for uncollided primary and total absorbed doses. Observe that the dose from the buildup, which is the difference between the total and uncollided primary, is substantial. The usual Bragg peak is also obvious for both the analytical and experimental results. The buildup-factor calculations are approximately within the uncertainties of interpolated Monte Carlo values and are in reasonable agreement with the experimental data.

To verify both BRYNTRN and the buildup-factor method in case of a continuous energy spectrum of incident protons, dose calculations were made (figs. 8.8 and 8.9) for shielded tissue being exposed to a typical solar-flare spectrum for which Monte Carlo results were available (Scott and Alsmiller, 1967 and 1968). The flare spectrum taken from Scott and Alsmiller (1967) is of the Webber (1966) form and is exponential in rigidity with characteristic rigidity $P_0 = 100$ MV and normalized to 10^9 protons/cm² with energy greater than 30 MeV. Only the portion of the spectrum between 50 and 400 MeV was considered for the Monte Carlo calculation (Scott and Alsmiller, 1967 and 1968). Nevertheless, for the current calculations, the high-energy cutoff at 400 MeV was ignored, and very small differences of a few percent were found (figs. 8.8(a) and 8.9(a)) because the

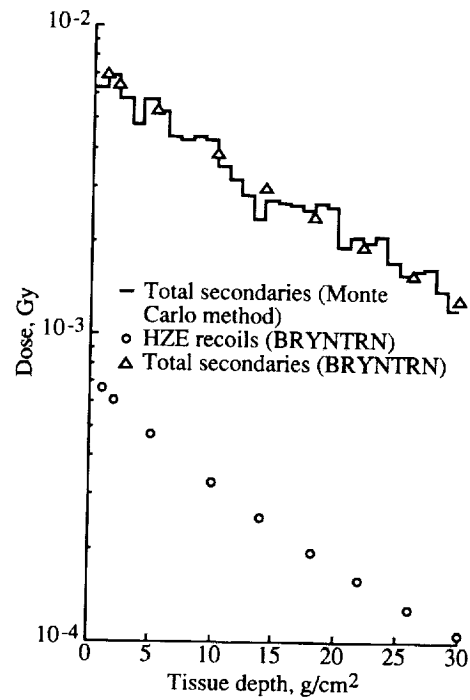
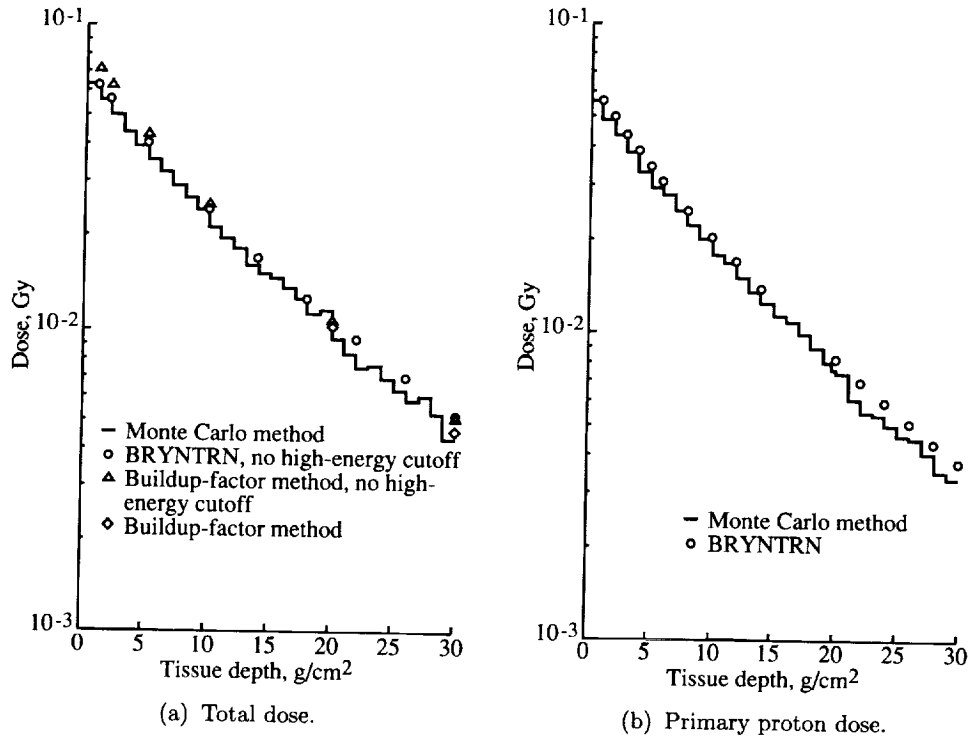


Figure 8.8. Various quantities of doses in tissue behind 20 g/cm² of aluminum shield to normal incidence of a solar-flare proton spectrum of Webber form with rigidity equal to 100 MV.

spectrum contains very few highly penetrating energetic protons, which may become significant only at depths beyond current interest. The tissue had an aluminum shield thickness of 20 g/cm^2 (fig. 8.8) and an iron shield thickness of 20 g/cm^2 (fig. 8.9).

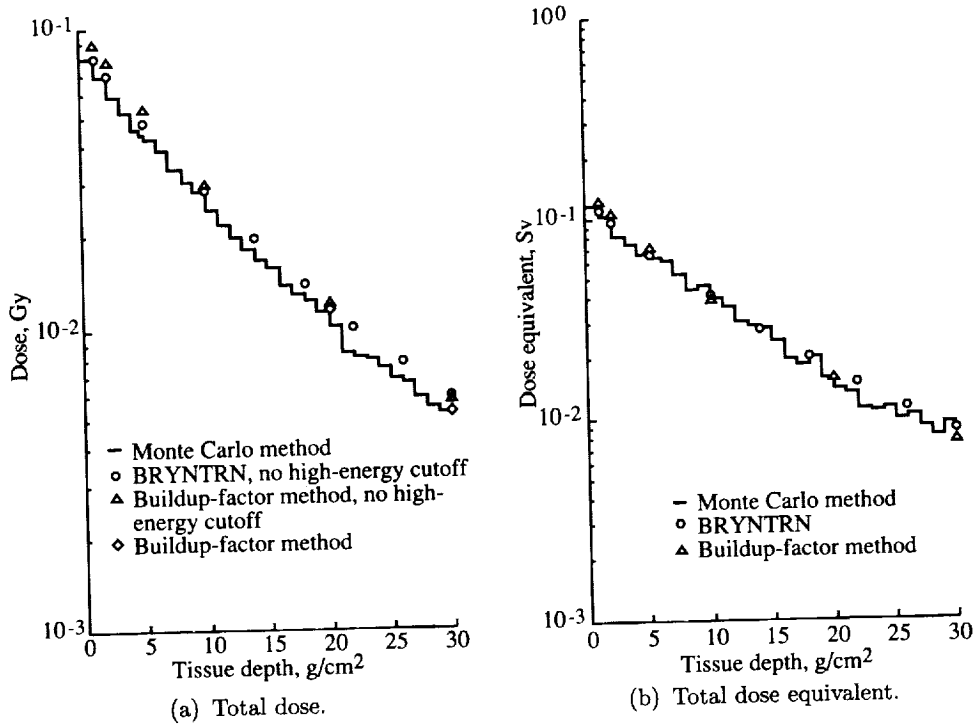
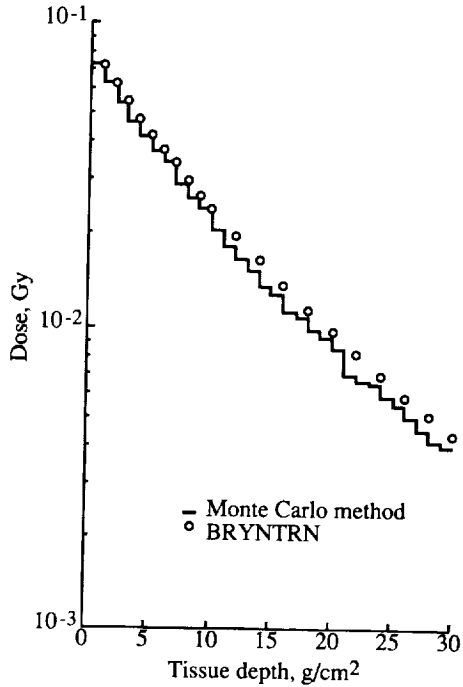
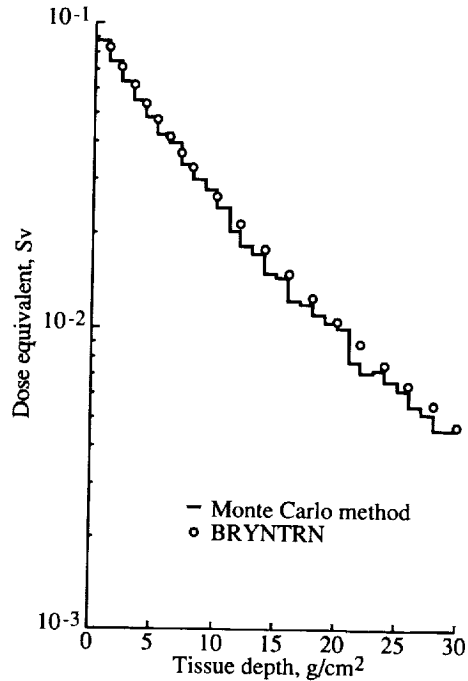


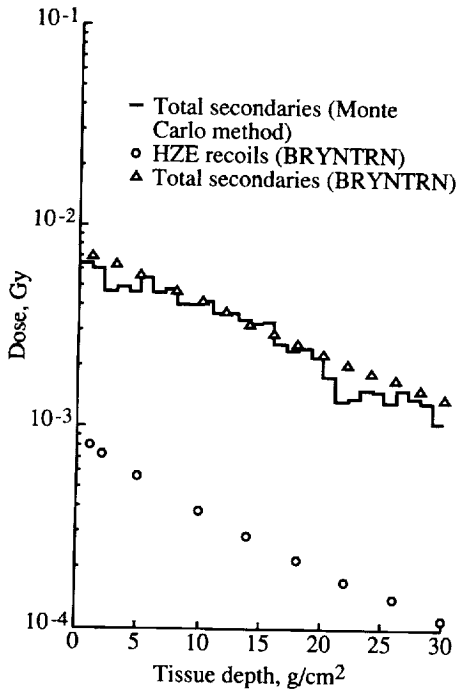
Figure 8.9. Various quantities of doses in tissues behind 20 g/cm^2 of iron shield to normal incidence of a solar-flare spectrum of Webber form with rigidity equal to 100 MV.



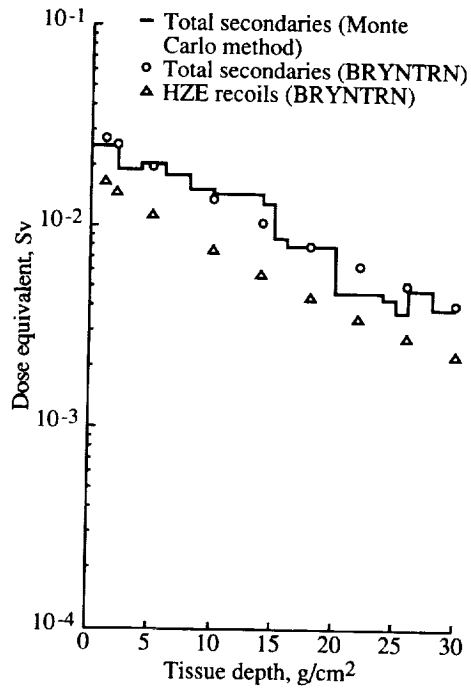
(c) Primary dose.



(d) Primary dose equivalent.



(e) Total secondary and heavy ion recoil doses.



(f) Total secondary and heavy ion recoil dose equivalents.

Figure 8.9. Concluded.

The buildup-factor results presented for iron, however, were obtained with the same values of buildup parameters chosen for aluminum. This is allowable because the nuclear reaction cross sections are roughly the same for both materials at the energies of interest (below 400 MeV). The total doses by the buildup-factor method are seen to be in good agreement (within 5–10 percent) with both Monte Carlo and BRYNTRN results. (See figs. 8.8(a) and 8.9(e)–(f).) (Note that the total secondary dose is the sum of the secondary proton and secondary neutron dose of Scott and Alsmiller (1967 and 1968).) The heavy ion recoil dose and dose equivalent of BRYNTRN show that the actual physical dose from heavy recoils may not be important, but their contribution to the dose equivalent can be significant because of the large quality factor.

Dose calculations are also made for a continuous spectrum that contains more high-energy protons. Because no Monte Carlo results are available in the high-energy range, the February 1956 solar-flare event is chosen for comparison between BRYNTRN and the buildup-factor method. The solar-flare spectrum given as the integral fluence form in protons/cm² is

$$\phi_P(> E) = 1.5 \times 10^9 \exp\left(-\frac{E-10}{25}\right) + 3 \times 10^8 \exp\left(-\frac{E-100}{320}\right) \quad (8.195)$$

where E is the energy in MeV. The results shown in figure 8.10 are for the dose and dose equivalent in tissue with 0, 10, and 30 g/cm² of aluminum shielding. The agreement between these two deterministic methods is seen to be reasonably good. With the future improvement to include neutron coupling, the buildup-factor method, which is gaining in computational efficiency for flare-dose analysis, would probably be favored in parametric studies of spacecraft shield design.

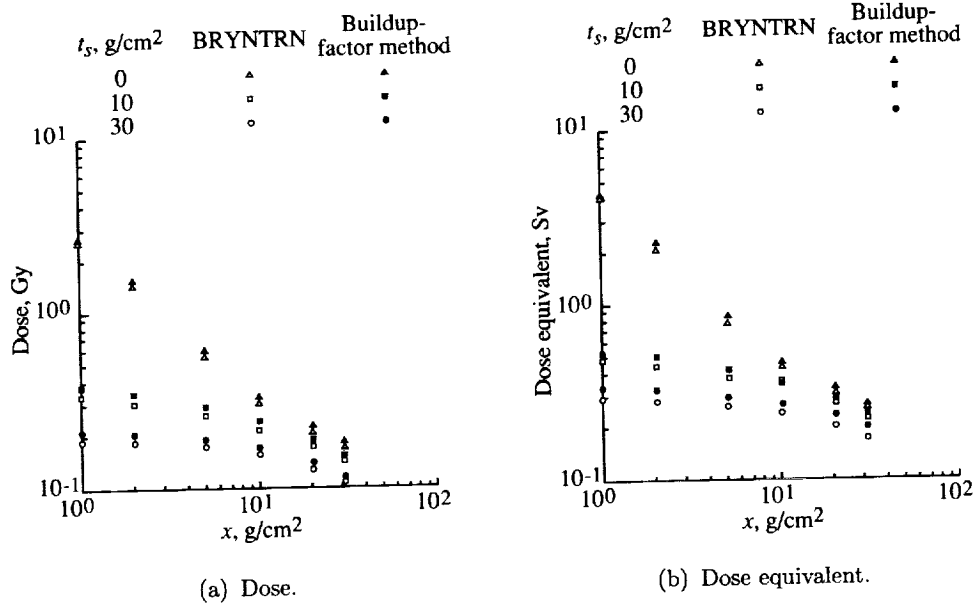


Figure 8.10. Dose in tissue behind various thicknesses of aluminum shield to normal incidence of the February 1956 solar-flare event.

8.8. Concluding Remarks

A comparison has been made of the calculated doses in tissue behind various thicknesses of shielding with exposure to various proton spectra for the buildup-factor method, BRYNTRN, and the Monte Carlo method. The results are found to be in reasonable agreement (within 5–10 percent), but with some overestimation by the buildup factors when the effect of neutron production in the shield is significant. Future improvement to include neutron coupling in the buildup-factor theory should alleviate this shortcoming. Impressive agreement for various components of doses is obtained between BRYNTRN and the Monte Carlo calculation. This is not surprising in the sense that both use some form of the Bertini cross-section data, but it does reflect on the contributions from corrections for the straight ahead approximation since the Monte Carlo calculation is a fully three-dimensional code. The straight ahead errors are, as expected, reasonably small. (See chapter 7.)

8.9. References

- Alsmiller, R. G., Jr., 1967: High-Energy Nucleon Transport and Space Vehicle Shielding. *Nuclear Sci. & Eng.*, vol. 27, no. 2, pp. 158–189.
- Alsmiller, R. G., Jr.; Armstrong, T. W.; and Coleman, W. A., 1970: The Absorbed Dose and Dose Equivalent From Neutrons in the Energy Range 60 to 3000 MeV and Protons in the Energy Range 400 to 3000 MeV. *Nuclear Sci. & Eng.*, vol. 42, no. 3, pp. 367–381.
- Alsmiller, R. G., Jr.; Santoro, R. T.; Barish, J.; and Claiborne, H. C., 1972: *Shielding of Manned Space Vehicles Against Protons and Alpha Particles*. ORNL-RSIC-35, U.S. Atomic Energy Commission.
- Anon., 1977: *Recommendations of the International Commission on Radiological Protection*. ICRP Publ. 26, Pergamon Press.
- Armstrong, T. W.; and Chandler, K. C., 1970: *Calculation of the Absorbed Dose and Dose Equivalent From Neutrons and Protons in the Energy Range From 3.5 GeV to 1.0 TeV*. ORNL-TM-3758, U.S. Atomic Energy Commission.
- Armstrong, T. W.; and Bishop, B. L., 1971: Calculation of the Absorbed Dose and Dose Equivalent Induced by Medium-Energy Neutrons and Protons and Comparison With Experiment. *Radiat. Res.*, vol. 47, no. 3, pp. 581–588.
- Armstrong, T. W., 1972: *Radiation Transport Codes for Potential Applications Related to Radiobiology and Radiotherapy Using Protons, Neutrons, and Negatively Charged Pions*. ORNL-TM-3816 (NASA Order H-38280A), Oak Ridge National Lab.
- Atwell, William; Beever, E. Ralph; Hardy, Alva C.; and Cash, Bernard L., 1989: A Radiation Shielding Model of the Space Shuttle for Space Radiation Dose Exposure Estimations. *Advances in Nuclear Engineering Computation and Radiation Shielding*, Volume 1, Michael L. Hall, ed., American Nuclear Soc., Inc., pp. 11:1–11:12.
- Bertini, Hugo W., 1963: Low-Energy Intranuclear Cascade Calculation. *Phys. Review*, vol. 131, second ser., no. 4, pp. 1801–1821.

Transport Methods and Interactions for Space Radiations

- Bertini, Hugo W., 1969: Intranuclear-Cascade Calculation of the Secondary Nucleon Spectra From Nucleon-Nucleus Interactions in the Energy Range 340 to 2900 MeV and Comparisons With Experiment. *Phys. Review*, vol. 188, second ser., no. 4, pp. 1711-1730.
- Bertini, Hugo W.; and Guthrie, Miriam P., 1971: News Item—Results From Medium-Energy Intranuclear-Cascade Calculation. *Nuclear Phys.*, vol. A169, no. 3, pp. 670-672.
- Billings, M. P.; and Yucker, W. R., 1973: *The Computerized Anatomical Man (CAM) Model*. NASA CR-134043.
- Cocconi, G.; Cocconi Tongiorgi, V.; and Widgoff, M., 1950: Cascades of Nuclear Disintegrations Induced by the Cosmic Radiation. *Phys. Review*, vol. 79, second ser., no. 5, pp. 768-780.
- Ganapol, Barry D.; Townsend, Lawrence W.; Lamkin, Stanley L.; and Wilson, John W., 1991: *Benchmark Solutions for the Galactic Heavy-Ion Transport Equations With Energy and Spatial Coupling*. NASA TP-3112.
- Haffner, James W., 1967: *Radiation and Shielding in Space*. Academic Press, Inc.
- Khandelwal, G. S.; and Wilson, J. W., 1973: Proton Dosimeter Design for Distributed Body Organs. *Nuclear Technol.*, vol. 20, no. 1, pp. 64-67.
- Murzin, V. S.; and Sarycheva, L. I., 1970: *Cosmic Rays and Their Interactions*. NASA TT F-594.
- Ngo, Duc M.; Wilson, John W.; Buck, Warren W.; and Fogarty, Thomas N., 1989: *Nuclear-Fragmentation Studies for Microelectronic Applications*. NASA TM-4143.
- O'Brien, K., 1971: Cosmic-Ray Propagation in the Atmosphere. *Nuovo Cimento*, vol. 3A, no. 3, pp. 521-547.
- Reedy, R. C.; and Arnold, J. R., 1972: Interaction of Solar and Galactic Cosmic-Ray Particles With the Moon. *J. Geophys. Res.*, vol. 77, no. 4, pp. 537-555.
- Schaefer, Hermann J.; and Sullivan, Jeremiah J., 1970: *Nuclear Emulsion Recordings of the Astronauts' Radiation Exposure on the First Lunar Landing Mission Apollo XI*. NASA CR-115804.
- Scott, W. Wayne; and Alsmiller, R. G., Jr., 1967: *Comparisons of Results Obtained With Several Proton Penetration Codes*. ORNL-RSIC-17 (Contract No. W-7405-eng-26, NASA Order R-104(10)), Oak Ridge National Lab.
- Scott, W. Wayne; and Alsmiller, R. G., Jr., 1968: *Comparisons of Results Obtained With Several Proton Penetration Codes—Part II*. ORNL-RSIC-22 (Contract No. W-7405-eng-26, NASA Order R-104(10)), Oak Ridge National Lab.
- Shen, S. P., 1963: Nuclear Problems in Radiation Shielding in Space. *Astronaut. Acta*, vol. IX, Fasc. 4, pp. 211-274.
- Shen, B. S. P., ed., 1967: *High-Energy Nuclear Reactions in Astrophysics—A Collection of Articles*. W. A. Benjamin, Inc.

- Shinn, Judy L.; Wilson, John W.; Nealy, John E.; and Cucinotta, Francis A., 1990: *Comparison of Dose Estimates Using the Buildup-Factor Method and a Baryon Transport Code (BRYNTRN) With Monte Carlo Results*. NASA TP-3021.
- Shinn, J. L.; Wilson, J. W.; and Ngo, D. M., 1990: Risk Assessment Methodologies for Target Fragments Produced in High-Energy Nucleon Reactions. *Health Phys.*, vol. 59, no. 1, pp. 141-143.
- Shinn, Judy L.; Wilson, John W.; Weyland, Mark; and Cucinotta, Francis A., 1991: *Improvements in Computational Accuracy of BRYNTRN (A Baryon Transport Code)*. NASA TP-3093.
- Snyder, W. S.; Wright, H. A.; Turner, J. E.; and Neufeld, Jacob, 1969: Calculations of Depth-Dose Curves for High-Energy Neutrons and Protons and Their Interpretation for Radiation Protection. *Nuclear Appl.*, vol. 6, no. 4, pp. 336-343.
- Turner, J. E.; Zerby, C. D.; Woodyard, R. L.; Wright, H. A.; Kinney, W. E.; Snyder, W. S.; and Neufeld, J., 1964: Calculation of Radiation Dose From Protons to 400 MeV. *Health Phys.*, vol. 10, no. 11, pp. 783-808.
- Webber, William R., 1966: *An Evaluation of Solar-Cosmic-Ray Events During Solar Minimum*. D2-84274-1, Boeing Co.
- Wilson, John W.; and Khandelwal, G. S., 1974: Proton Dose Approximation in Arbitrary Convex Geometry. *Nuclear Technol.*, vol. 23, no. 3, pp. 298-305.
- Wilson, John W.; and Lamkin, Stanley L., 1975: Perturbation Theory for Charged-Particle Transport in One Dimension. *Nuclear Sci. & Eng.*, vol. 57, no. 4, pp. 292-299.
- Wilson, John W.; Stith, John J.; and Stock, L. V., 1983: *A Simple Model of Space Radiation Damage in GaAs Solar Cells*. NASA TP-2242.
- Wilson, John W.; Walker, Gilbert H.; and Outlaw, R. A., 1984: Proton Damage in GaAs Solar Cells. *IEEE Trans. Electron Devices*, vol. ED-31, no. 4, pp. 421-422.
- Wilson, John W.; and Badavi, F. F., 1986: Methods of Galactic Heavy Ion Transport. *Radiat. Res.*, vol. 108, pp. 231-237.
- Wilson, John W.; Townsend, Lawrence W.; and Buck, Warren W., 1986: On the Biological Hazard of Galactic Antinuclei. *Health Phys.*, vol. 50, no. 5, pp. 666-667.
- Wilson, John W.; Townsend, Lawrence W.; Ganapol, Barry D.; and Lamkin, Stanley L., 1988: Methods for High Energy Hadronic Beam Transport. *Trans American Nuclear Soc.*, vol. 56, pp. 271-272.
- Wilson, John W.; Townsend, Lawrence W.; and Khan, Ferdous, 1989: Evaluation of Highly Ionizing Components in High-Energy Nucleon Radiation Fields. *Health Phys.*, vol. 57, no. 5, pp. 717-724.
- Wilson, John W.; Townsend, Lawrence W.; Nealy, John E.; Chun, Sang Y.; Hong, B. S.; Buck, Warren W.; Lamkin, S. L.; Ganapol, Barry D.; Khan, Ferdous; and Cucinotta, Francis A., 1989: BRYNTRN: *A Baryon Transport Model*. NASA TP-2887.

Transport Methods and Interactions for Space Radiations

Wilson, John W.; Shinn, Judy L.; and Townsend, Lawrence W., 1990: Nuclear Reaction Effects in Conventional Risk Assessment for Energetic Ion Exposure. *Health Phys.*, vol. 58, no. 6, pp. 749-752.

Wright, Harvel A.; Anderson, V. E.; Turner, J. E.; Neufeld, Jacob; and Snyder, W. S., 1969: Calculation of Radiation Dose Due to Protons and Neutrons With Energies From 0.4 to 2.4 GeV. *Health Phys.*, vol. 16, no. 1, pp. 13-31.

Wright, H. A.; Hamm, R. N.; and Turner, J. E., 1971: Effect of Lateral Scattering on Absorbed Dose From 400 MeV Neutrons and Protons. *International Congress on Protection Against Accelerator and Space Radiation*, J. Baarli and J. Dutrannois, eds., CERN 71-16, Volume 1, European Organization for Nuclear Research, pp. 207-219.

Zerby, C. D.; and Kinney, W. E., 1965: Calculated Tissue Current-to-Dose Conversion Factors For Nucleons Below 400 MeV. *Nuclear Instrum. & Methods*, vol. 36, no. 1, pp. 125-140.

Chapter 9

High Charge and Energy (HZE) Transport

9.1. Introduction

Propagation of galactic ions through matter has been studied for the past 40 years as a means of determining the origin of these ions. Peters (1958) used the one-dimensional equilibrium solution ignoring ionization energy loss and radioactive decay to show that the light ions have their origin in the breakup of heavy particles. Davis (1960) showed that one-dimensional propagation is simplistic and that leakage at the galactic boundary must be taken into account. Ginzburg and Syrovatskii (1964) argued that the leakage can be approximated as a superposition of nonequilibrium one-dimensional solutions. The "solution" to the steady-state equations is given as a Volterra equation by Gloeckler and Jokipii (1969), which is solved to first order in the fragmentation cross sections by ignoring energy loss. They provide an approximation to the first-order solution with ionization energy loss included that is only valid at relativistic energies. Lezniak (1979) gives an overview of cosmic-ray propagation and derives a Volterra equation including the ionization energy loss which he refers to as a solution "only in the iterative sense" and evaluates only the unperturbed term. No attempt is made to evaluate either the first-order perturbation term or higher order terms. The main interest among cosmic-ray physicists has been in first-order solutions in the fragmentation cross sections, since path lengths in interstellar space are on the order of 3–4 g/cm². Clearly, higher order terms cannot be ignored in accelerator or space shielding transport problems (Wilson, 1977a, 1977b, and 1983; Wilson et al., 1984). Aside from this simplification, the cosmic-ray studies discussed above have neglected the complicated three-dimensional nature of the fragmentation process.

Several approaches to the solution of high-energy heavy ion propagation including the ionization energy loss have been developed (Wilson, 1977a, 1977b, and 1983; Wilson et al., 1984, 1989a, and 1987b; Wilson and Badavi, 1986; Wilson and Townsend, 1988; Curtis, Doherty, and Wilkinson, 1969; Allkofer and Heinrich, 1974; Chatterjee, Tobias, and Lyman, 1976; Letaw, Tsao, and Silberberg, 1983; Ganapol, Townsend, and Wilson, 1989; Townsend, Ganapol, and Wilson, 1989) over the last 20 years. All but one (Wilson, 1977a) have assumed the straight ahead approximation and velocity conserving fragmentation interactions. Only two (Wilson, 1977a; Wilson, et al., 1984) have incorporated energy-dependent nuclear cross sections. The approach by Curtis, Doherty, and Wilkinson (1969) for a primary ion beam represented the first-generation secondary fragments as a quadrature over the collision density of the primary beam. Allkofer and Heinrich (1974) used an energy multigroup method in which an energy-independent fragmentation transport approximation was applied within each energy group after which the energy group boundaries were moved according to continuous slowing down theory ($-dE/dx$). Chatterjee, Tobias, and Lyman (1976) solved the energy-independent fragment transport equation with primary collision density as a source and neglected higher order fragmentation. The primary source term extended only to the primary ion range from the boundary. The energy-independent transport solution was modified to account for the finite range of the secondary fragment ions.

Wilson (1977b) derived an expression for the ion transport problem to first order (first collision term) and gave an analytic solution for the depth-dose relation. Wilson (1977a) examined the more common approximations used in solving the heavy ion transport problem. The effects of conservation of velocity on fragmentation and the straight ahead approximation are found to be negligible for cosmic-ray applications. Solution methods for representing the energy-dependent nuclear cross sections are developed (Wilson, 1977a). Letaw, Tsao, and Silberberg (1983) approximate the energy loss term and ion spectra by simple forms for which energy derivatives are evaluated explicitly (even if approximately). The resulting ordinary differential equations in position are solved analytically similar to the method of Allkofer and Heinrich (1974). This approximation results in a decoupling of motion in space and a change in energy. In Letaw's formalism, the energy shift is replaced by an effective attenuation factor. Wilson adds the next higher order (second collision) term (Wilson, 1983). This term was found to be very important in describing ^{20}Ne beams at 670 MeV/nucleon. The three-term expansion of (Wilson, 1983) was modified to include the effects of energy variation of the nuclear cross sections (Wilson et al., 1984). The integral form of the transport equation (Wilson 1977a) was further used to derive a numerical marching procedure to solve the cosmic-ray transport problem (Wilson and Badavi, 1986). This method can easily include the energy-dependent nuclear cross sections within the numerical procedure. Comparison of the numerical procedure (Wilson and Badavi, 1986) with an analytic solution to a simplified problem (Wilson and Townsend, 1988) validates the solution technique to about 1 percent accuracy. Several solution techniques and analytic methods have been developed for testing future numerical solutions to the transport equation (Ganapol, Townsend, and Wilson, 1989; Townsend, Ganapol, and Wilson, 1989). More recently, an analytic solution for the laboratory ion beam transport problem has been derived assuming a straight ahead approximation, velocity conservation at the interaction site, and energy-independent nuclear cross sections (Wilson et al., 1989a).

In the previous overview of past developments, the applications split into two separate categories according to a single ion species with a single energy at the boundary versus a broad host of elemental types with a broad, continuous energy spectrum. Techniques requiring a representation of the spectrum over an array of energy values require vast computer storage and computation speed for the laboratory beam problem to maintain sufficient energy resolution. On the other hand, analytic methods (Wilson, 1977a and 1977b; Wilson and Badavi, 1986) are probably best applied in a marching procedure (Wilson and Badavi, 1986), which again has within it a similar energy resolution problem. This is a serious limitation because we require a final High Charge and Energy (HZE) Code for cosmic-ray shielding that has been validated by laboratory experiments.

In this chapter, we begin with the most simplified assumptions for which the problem may be solved completely. Solutions to a more complete theory may then be compared with prior results as limiting cases. In this way, the more complete but approximate analysis will have some basis for evaluating the accuracy of the solution method. The lowest order approximation will be totally energy independent. The next most complicated solution to be considered herein will have energy-independent nuclear cross sections but will treat the energy-dependent

atomic/molecular processes and the energy spread of the primary beam. A fully energy-dependent theory must await further development, although some terms are discussed.

9.2. Energy-Independent Flux

If the ion beam is of sufficiently high energy that the energy shift caused by atomic/molecular collisions brings none of the particles to rest in the region of interest, then

$$\left[\frac{\partial}{\partial x} + \sigma_j \right] \phi_j(x) = \sum_k m_{jk} \sigma_k \phi_k(x) \quad (9.1)$$

where $\phi_j(x)$ is the flux of type j ions, σ_j is the nuclear absorption cross section, and m_{jk} is the fragmentation parameter for producing type j ions from type k . The solution for a given incident ion type J is given in terms of a set of g -functions as follows:

$$g(j_1) = \exp(-\sigma_{j_1} x) \quad (9.2)$$

$$g(j_1, j_2, \dots, j_n, j_{n+1}) = \frac{g(j_1, j_2, \dots, j_{n-1}, j_n) - g(j_1, j_2, \dots, j_{n-1}, j_{n+1})}{\sigma_{j_{n+1}} - \sigma_{j_n}} \quad (9.3)$$

for which the solution for the type j ion flux is written as

$$\phi_j^{(0)}(x) = \delta_{jJ} g(j) \quad (9.4)$$

$$\phi_j^{(1)}(x) = m_{jJ} \sigma_J g(j, J) = m_{jJ} \sigma_J \frac{\exp(-\sigma_j x) - \exp(-\sigma_J x)}{\sigma_J - \sigma_j} \quad (9.5)$$

$$\phi_j^{(2)}(x) = \sum_k m_{jk} \sigma_k m_{kJ} \sigma_J g(j, k, J) \quad (9.6)$$

$$\phi_j^{(3)}(x) = \sum_{k,l} m_{jk} \sigma_k m_{kl} \sigma_l m_{lJ} \sigma_J g(j, k, l, J) \quad (9.7)$$

with

$$\phi_j(x) = \sum_i \phi_j^{(i)}(x) \quad (9.8)$$

This solution is equivalent to that derived by Ganapol, Townsend, and Wilson (1989). We now consider some applications of this formalism. The cross-section data base is discussed by Townsend, Wilson, and Bidasaria (1983a and 1983b).

9.2.1. Neon beam transport. We first note that for ^{20}Ne incident on water, ^{19}Ne and ^{19}F have only one contributing term in equation (9.8). This is shown in figure 9.1. Also shown in figure 9.1 are the fluxes of various isotopes of secondary ion fragments. The effect of successive terms of equation (9.8) is shown in table 9.1 for the ^{15}O flux. It is clear from the table that the fourth and higher order collision terms are completely negligible and that third collision terms are a rather minor

contribution. Hence, a three-term expansion as we have used in the past (Wilson, 1977a and 1983; Wilson et al., 1984) appears justified. The relative magnitude of the terms contributing to the ${}^7\text{Li}$ flux generated by the ${}^{20}\text{Ne}$ beam is presented in table 9.2. The fourth collision term is negligible at small penetration distances and small, but not negligible, at distances greater than 30 cm. The greater penetrating power of the lighter mass fragments is demonstrated in figure 9.2. Also note the difference in solution character caused by the importance of the higher order term.

9.2.2. Iron beam transport. We first note that for ${}^{56}\text{Fe}$ incident on water, ${}^{55}\text{Fe}$ and ${}^{55}\text{Mn}$ have only one contributing term in equation (9.8). The ${}^{54}\text{Mn}$ has two terms, and the slight difference in solution character can be seen in figure 9.3. Results for ${}^{52}\text{V}$ are also shown. The convergence rate of equation (9.8) is demonstrated in table 9.3. Again, the fourth collision term is negligible, whereas the three-term expansion we have used before seems quite accurate at these depths for these ions. Distinguished from prior results, the ${}^{16}\text{O}$ flux has significant contributions from higher order terms for depths beyond 20 cm, as seen in table 9.4. Clearly, a more complete theory with higher order terms is required than the one previously used for ion beams of particles heavier than ${}^{20}\text{Ne}$. The different solution character of the lighter mass fragments is clearly demonstrated in figure 9.4.

9.3. Monoenergetic Ion Beams

When moving through extended matter, heavy ions lose energy through interaction with atomic electrons along their trajectories. On occasion, they interact violently with nuclei of the matter and produce ion fragments moving in the forward direction and low-energy fragments of the struck target nucleus. The transport equations for the short range target fragments can be solved in closed form in terms of collision density (Wilson, 1977a; Wilson et al., 1984). Hence, the projectile fragment transport is the interesting unsolved problem. In previous work, the projectile ion fragments were treated as if all went straightforward (Wilson, 1977b and 1983; Wilson et al., 1984 and 1989a; Wilson and Badavi, 1986; Wilson and Townsend, 1988; Curtis, Doherty, and Wilkinson, 1969; Allkofer and Heinrich, 1974; Chatterjee, Tobias, and Lyman, 1976; Letaw, Tsao, and Silberberg, 1983; Ganapol, Townsend, and Wilson, 1989; Townsend, Ganapol, and Wilson, 1989). We continue with this assumption herein, noting that an extension of the beam fragmentation model to three dimensions is being developed (Shavers, 1988; Schimmerling et al., 1986).

With the straight ahead approximation and the target secondary fragments neglected (Wilson, 1977a and 1977b; Wilson, 1983; Wilson et al., 1984), the transport equation may be written as

$$\left[\frac{\partial}{\partial x} - \frac{\partial}{\partial E} \tilde{S}_j(E) + \sigma_j \right] \phi_j(x, E) = \sum_{k>j} m_{jk} \sigma_k \phi_k(x, E) \quad (9.9)$$

where $\phi_j(x, E)$ is the flux of ions of type j with atomic mass A_j at x moving along the x -axis at energy E in units of MeV/nucleon, σ_j is the corresponding macroscopic nuclear absorption cross section, $\tilde{S}_j(E)$ is the change in E per unit

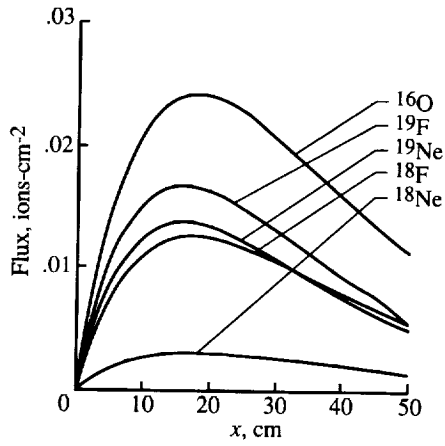


Figure 9.1. Ion fragment flux of various isotopes as function of depth in water for ^{20}Ne incident beam.

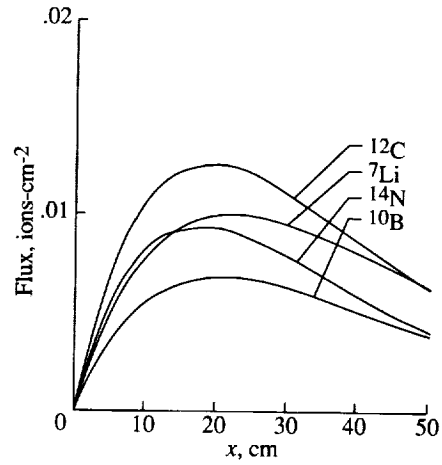


Figure 9.2. Flux of light ion fragments as function of depth in water for ^{20}Ne incident beam.

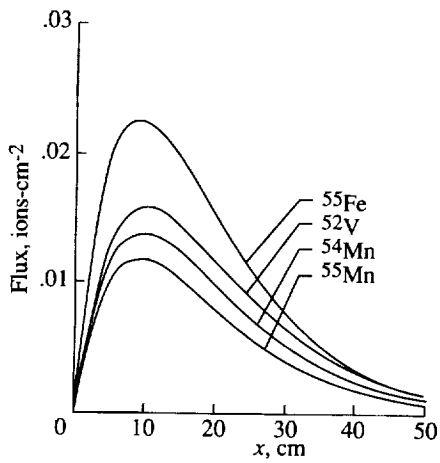


Figure 9.3. Ion fragment flux of various isotopes as function of depth in water for ^{56}Fe incident beam.

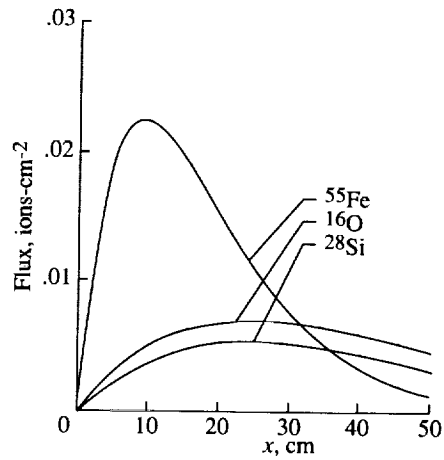


Figure 9.4. Flux of light ion fragments as function of depth in water for ^{56}Fe incident beam.

Transport Methods and Interactions for Space Radiations

Table 9.1. Normalized Contributions to ^{15}O Flux From Successive Collision Terms for ^{20}Ne Transport in Water

Fragment term	^{15}O flux at x of—				
	10 cm	20 cm	30 cm	40 cm	50 cm
$\phi^{(1)}$	1.00E0	1.00E0	1.00E0	1.00E0	1.00E0
$\phi^{(2)}$	1.01E-1	2.01E-1	3.02E-1	4.03E-1	5.04E-1
$\phi^{(3)}$	2.63E-3	1.05E-2	2.36E-2	4.18E-2	6.52E-2
$\phi^{(4)}$	3.31E-5	2.52E-4	8.58E-4	2.03E-3	3.95E-3

Table 9.2. Normalized Contributions to ^7Li Flux From Successive Collision Terms for ^{20}Ne Transport in Water

Fragment term	^7Li flux at x of—				
	10 cm	20 cm	30 cm	40 cm	50 cm
$\phi^{(1)}$	1.00E0	1.00E0	1.00E0	1.00E0	1.00E0
$\phi^{(2)}$	1.62E-1	3.20E-1	4.72E-1	6.18E-1	7.58E-1
$\phi^{(3)}$	1.15E-2	4.53E-2	9.98E-2	1.73E-1	2.63E-1
$\phi^{(4)}$	4.02E-4	3.16E-3	1.04E-2	2.39E-2	4.53E-2

Table 9.3. Normalized Contributions to ^{52}V Flux From Successive Collision Terms for ^{56}Fe Transport in Water

Fragment term	^{52}V flux at x of—				
	10 cm	20 cm	30 cm	40 cm	50 cm
$\phi^{(1)}$	1.00E0	1.00E0	1.00E0	1.00E0	1.00E0
$\phi^{(2)}$	7.91E-2	1.52E-1	2.37E-1	3.15E-1	3.94E-1
$\phi^{(3)}$	2.37E-3	9.48E-3	2.13E-2	3.79E-2	5.91E-2
$\phi^{(4)}$	2.24E-5	1.73E-4	5.93E-4	1.41E-3	2.75E-3

Table 9.4. Normalized Contributions to ^{16}O Flux From Successive Collision Terms for ^{56}Fe Transport in Water

Fragment term	^{16}O flux at x of—				
	10 cm	20 cm	30 cm	40 cm	50 cm
$\phi^{(1)}$	1.00E0	1.00E0	1.00E0	1.00E0	1.00E0
$\phi^{(2)}$	5.87E-1	1.12E0	1.59E0	2.00E0	2.36E0
$\phi^{(3)}$	1.86E-1	7.08E-1	1.49E0	2.46E0	3.56E0
$\phi^{(4)}$	3.06E-2	2.63E-1	9.44E-1	2.33E0	4.72E0

distance, and m_{jk} is the fragmentation parameter for ion j produced in collision by ion k . The range of the ion is given as

$$R_j(E) = \int_0^E \frac{dE'}{\tilde{S}_j(E')} \quad (9.10)$$

The solution to equation (9.9) is found subject to boundary specification at $x = 0$ and arbitrary E as

$$\phi_j(0, E) = F_j(E) \quad (9.11)$$

Usually, $F_j(E)$ is called the incident beam spectrum.

It follows from Bethe's theory that

$$\tilde{S}_j(E) = \frac{A_p Z_j^2}{A_j Z_p^2} \tilde{S}_p(E) \quad (9.12)$$

for which

$$\frac{Z_j^2}{A_j} R_j(E) = \frac{Z_p^2}{A_p} R_p(E) \quad (9.13)$$

The subscript p refers to proton. Equation (9.12) is quite accurate at high energy and only approximately true at low energy. At low energy, equation (9.12) is modified by electron capture by the ion which effectively reduces its charge, higher order Born corrections to Bethe's theory, and nuclear stopping at the lowest energies. Herein, the parameter ν_j is defined as

$$\nu_j = \frac{Z_j^2}{A_j} \quad (9.14)$$

so that

$$\nu_j R_j(E) = \nu_k R_k(E) \quad (9.15)$$

Equations (9.14) and (9.15) are used in the subsequent development, and the energy variation in ν_j is neglected. The limits of assumed constant ν_j hold only for $E > 10$ MeV/nucleon (Schimmerling et al., 1986). The inverse function of $R_j(E)$ is defined as

$$E = R_j^{-1} [R_j(E)] \quad (9.16)$$

and subsequently plays a fundamental role. For the purpose of solving equation (9.9), define the coordinate transformation (Wilson, 1977a and 1983),

$$\left. \begin{aligned} \eta_j &\equiv x - R_j(E) \\ \xi_j &\equiv x + R_j(E) \end{aligned} \right\} \quad (9.17)$$

and new functions

$$\left. \begin{aligned} \chi_j(\eta_j, \xi_j) &\equiv \tilde{S}_j(E) \phi_j(x, E) \\ \bar{\chi}_k(\eta_j, \xi_j) &\equiv \chi_k(\eta_k, \xi_k) \end{aligned} \right\} \quad (9.18)$$

where

$$\left. \begin{aligned} \xi_j + \eta_j &= \xi_k + \eta_k \\ \eta_j - \xi_j &= \frac{\nu_k}{\nu_j}(\eta_k - \xi_k) \end{aligned} \right\} \quad (9.19)$$

for which equation (9.9) becomes

$$\left(2 \frac{\partial}{\partial \eta_j} + \sigma_j\right) \chi_j(\eta_j, \xi_j) = \sum_k m_{jk} \sigma_k \frac{\nu_j}{\nu_k} \bar{\chi}_k(\eta_j, \xi_j) \quad (9.20)$$

where the σ_j is assumed to be energy independent. Solving equation (9.20) by using line integration with the integrating factor,

$$\mu_j(\eta_j, \xi_j) = \exp\left[\frac{1}{2}\sigma_j(\xi_j + \eta_j)\right] \quad (9.21)$$

results in

$$\begin{aligned} \chi_j(\eta_j, \xi_j) &= \exp\left[-\frac{1}{2}\sigma_j(\xi_j + \eta_j)\right] \chi_j(-\xi_j, \xi_j) \\ &+ \frac{1}{2} \int_{-\xi_j}^{\eta_j} \exp\left[\frac{1}{2}\sigma_j(\eta' - \eta_j)\right] \sum_k m_{jk} \sigma_k \frac{\nu_j}{\nu_k} \chi_k(\eta'_k, \xi'_k) d\eta' \end{aligned} \quad (9.22)$$

where

$$\left. \begin{aligned} \eta'_k &= \frac{\nu_k + \nu_j}{2\nu_k} \eta' + \frac{\nu_k - \nu_j}{2\nu_k} \xi_j \\ \xi'_k &= \frac{\nu_k - \nu_j}{2\nu_k} \eta' + \frac{\nu_k + \nu_j}{2\nu_k} \xi_j \end{aligned} \right\} \quad (9.23)$$

and the boundary condition (eq. (9.11)) is written as

$$\chi_j(-\xi_j, \xi_j) = \tilde{S}_j[R_j^{-1}(\xi_j)] F_j[R_j^{-1}(\xi_j)]$$

Consider a Neumann series for equation (9.22) for which the first term is

$$\chi_j^{(0)}(\eta_j, \xi_j) = \exp\left[-\frac{1}{2}\sigma_j(\eta_j + \xi_j)\right] \tilde{S}_j[R_j^{-1}(\xi_j)] F_j[R_j^{-1}(\xi_j)] \quad (9.24)$$

and the second term is

$$\begin{aligned} \chi_j^{(1)}(\eta_j, \xi_j) &= \frac{1}{2} \int_{-\xi_j}^{\eta_j} \exp\left[\frac{1}{2}\sigma_j(\eta' - \eta_j)\right] \sum_k m_{jk} \sigma_k \frac{\nu_j}{\nu_k} \exp\left[-\frac{1}{2}\sigma_k(\eta'_k - \xi'_k)\right] \\ &\times \tilde{S}_k[R_k^{-1}(\xi'_k)] F_k[R_k^{-1}(\xi'_k)] d\eta' \end{aligned} \quad (9.25)$$

An expression for $\chi_j^{(2)}(\eta_j, \xi_j)$ is derived once equation (9.25) is reduced, and higher order terms can be found by continued iteration of equation (9.22). These expressions (eqs. (9.24) and (9.25)) are now simplified for a monoenergetic beam of type M ions.

The boundary condition is now taken as

$$F_j(E) = \delta_{jM} \delta(E - E_o) \quad (9.26)$$

where δ_{jM} is the Kronecker delta, $\delta(\)$ is the Dirac delta, and E_o is the incident beam energy. Thus,

$$\chi_j(-\xi_j, \xi_j) = \tilde{S}_j [R_j^{-1}(\xi_j)] \delta_{jM} \delta[R_j^{-1}(\xi_j) - E_o] = \delta_{jM} \delta[\xi_j - R_j(E_o)] \quad (9.27)$$

for which $\chi_j^{(0)}$ becomes

$$\chi_j^{(0)}(\eta_j, \xi_j) = \delta_{jM} \exp\left[-\frac{1}{2}\sigma_j(\eta_j + \xi_j)\right] \delta[\xi_j - R_j(E_o)] \quad (9.28)$$

and $\chi_j^{(1)}$ becomes

$$\begin{aligned} \chi_j^{(1)}(\eta_j, \xi_j) &= \frac{1}{2} \int_{-\xi_j}^{\eta_j} m_{jM} \sigma_M \frac{\nu_j}{\nu_M} \exp\left[\frac{1}{2}\sigma_j(\eta' - \eta_j) - \frac{1}{2}\sigma_M(\eta'_M + \xi'_M)\right] \\ &\quad \times \delta[\xi'_M - R_M(E_o)] d\eta' \end{aligned} \quad (9.29)$$

where ξ'_M is given by equations (9.23) for $k = M$. The contribution to the integral (eq. (9.29)) occurs at

$$\eta' = \frac{2\nu_M}{\nu_M - \nu_j} R_M(E_o) - \frac{\nu_M + \nu_j}{\nu_M - \nu_j} \xi_j \quad (9.30)$$

provided that η' lies on the interval $-\xi_j < \eta' < \eta_j$ so that

$$\chi_j^{(1)}(\eta_j, \xi_j) = \frac{m_{jM} \sigma_M \nu_j}{|\nu_M - \nu_j|} \exp\left[-\frac{1}{2}\sigma_M(\xi_j + \eta') - \frac{1}{2}\sigma_j(\eta_j - \eta')\right] \quad (9.31)$$

The simplified form in equation (9.31) may now be used to calculate the next iteration of equation (9.22):

$$\begin{aligned} \chi_j^{(2)}(\eta_j, \xi_j) &= \frac{1}{2} \sum_k m_{jk} \sigma_k m_{kM} \sigma_M \frac{\nu_j}{|\nu_M - \nu_k|} \int_{-\xi_j}^{\eta_j} \exp\left[-\frac{1}{2}\sigma_M(\xi_k'' + \tilde{\eta}) \right. \\ &\quad \left. - \frac{1}{2}\sigma_k(\eta_k'' - \tilde{\eta}) - \frac{1}{2}\sigma_j(\eta_j - \eta'')\right] d\eta'' \end{aligned} \quad (9.32)$$

where

$$\left. \begin{aligned} \eta_k'' &= \frac{\nu_k + \nu_j}{2\nu_k} \eta'' + \frac{\nu_k - \nu_j}{2\nu_k} \xi_j \\ \xi_k'' &= \frac{\nu_k - \nu_j}{2\nu_k} \eta'' + \frac{\nu_k + \nu_j}{2\nu_k} \xi_j \end{aligned} \right\} \quad (9.33)$$

and

$$\tilde{\eta} = \frac{2\nu_M}{\nu_M - \nu_k} R_M(E_0) - \frac{\nu_M + \nu_k}{\nu_M - \nu_k} \xi_k'' \quad (9.34)$$

with the requirement that $-\xi_k'' < \tilde{\eta} < \eta_k''$. The inverse of the transformation is now applied to obtain from equation (9.28)

$$\phi_j^{(0)}(x, E) = \frac{1}{\tilde{S}_j(E)} \exp(-\sigma_j x) \delta_{jM} \delta[x + R_j(E) - R_M(E_0)] \quad (9.35)$$

and from equation (9.31)

$$\begin{aligned} \phi_j^{(1)}(x, E) &= \frac{1}{\tilde{S}_j(E)} m_{jM} \sigma_M \frac{\nu_j}{|\nu_M - \nu_j|} \exp\left\{-\frac{1}{2}\sigma_j [x - R_j(E) - \eta']\right. \\ &\quad \left.-\frac{1}{2}\sigma_M [x + R_j(E) + \eta']\right\} \end{aligned} \quad (9.36)$$

so long as

$$\frac{\nu_M}{\nu_j} [R_M(E_0) - x] < R_j(E) < \frac{\nu_M}{\nu_j} R_M(E_0) - x \quad (9.37)$$

Otherwise, $\phi_j^{(1)}(x, E)$ is zero. After a complicated but straightforward manipulation, a similar result may be obtained from equation (9.32) for $\phi_j^{(2)}(x, E)$.

In reducing equation (9.32), it is useful to define

$$x_M = \frac{1}{2} (\xi_k'' + \tilde{\eta}) \quad (9.38)$$

$$x_k = \frac{1}{2} (\eta_k'' - \tilde{\eta}) \quad (9.39)$$

$$x_j = \frac{1}{2} (\eta_j - \eta'') \quad (9.40)$$

and make a change in variables as

$$\begin{aligned} \phi_j^{(2)}(x, E) &= \frac{1}{\tilde{S}_j(E)} \sum_k m_{jk} \sigma_k m_{kM} \sigma_M \frac{\nu_j}{|\nu_M - \nu_k|} \\ &\quad \times \int_{x_{jl}}^{x_{ju}} \exp(-\sigma_M x_M - \sigma_k x_k - \sigma_j x_j) dx_j \end{aligned} \quad (9.41)$$

where the integral is understood to be nonzero only in the physically allowed regions as presently explained. One may easily demonstrate

$$x_M + x_k + x_j = x \quad (9.42)$$

and

$$\nu_M x_M + \nu_k x_k + \nu_j x_j = \nu_M R_M(E_0) - \nu_k R_k(E) \quad (9.43)$$

for which the parametric solution is given as

$$x_M = \frac{\nu_M R_M(E_0) - \nu_k [R_k(E) + x] + (\nu_k - \nu_j)x_j}{\nu_M - \nu_k} \quad (9.44)$$

$$x_k = \frac{\nu_M [R_M(E) + x] - \nu_M R_M(E_0) - (\nu_M - \nu_j)x_j}{\nu_M - \nu_k} \quad (9.45)$$

The requirement that x_M and x_k be bounded by the interval 0 to $x - x_j$ yields

$$\left\{ \begin{array}{c} 0 \\ \frac{\nu_k [R_k(E) + x] - \nu_M R_M(E_0)}{\nu_k - \nu_j} \end{array} \right\} \leq x_j \leq \left\{ \begin{array}{c} x \\ \frac{\nu_M [R_M(E) + x] - \nu_M R_M(E_0)}{\nu_M - \nu_j} \end{array} \right\} \quad (9.46)$$

as the appropriate limits for the integral in equation (9.41) when $\nu_M > \nu_k > \nu_j$. In the braces in equation (9.46), we always choose the most restrictive value for the limit. The requirement of equation (9.46) also implies the result that

$$R_M^{-1} [R_M(E_0) - x] \leq E \leq R_k^{-1} \left[\frac{\nu_M R_M(E_0) - \nu_j x}{\nu_k} \right] \quad (9.47)$$

as the range over which the result of equation (9.41) is not zero. If $\nu_k > \nu_M > \nu_j$, then

$$\left\{ \begin{array}{c} 0 \\ \frac{\nu_M [R_M(E) + x] - \nu_M R_M(E_0)}{\nu_M - \nu_j} \end{array} \right\} \leq x_j \leq \left\{ \begin{array}{c} x \\ \frac{\nu_k [R_k(E) + x] - \nu_M R_M(E_0)}{\nu_k - \nu_j} \end{array} \right\} \quad (9.48)$$

As a result of equation (9.48),

$$R_k^{-1} \left[\frac{\nu_M}{\nu_k} R_M(E_0) - x \right] \leq E \leq R_M^{-1} \left[R_M(E_0) - \frac{\nu_j}{\nu_M} x \right] \quad (9.49)$$

If $\nu_M > \nu_j > \nu_k$, it follows that

$$0 \leq x_j \leq \left\{ \begin{array}{c} x \\ \frac{\nu_M [R_M(E) + x - R_M(E_o)]}{\nu_M - \nu_j} \\ \frac{\nu_M R_M(E_o) - \nu_k R_k(E) - \nu_k x}{\nu_j - \nu_k} \end{array} \right\} \quad (9.50)$$

where the lesser of the three values in the braces is used as the upper limit of x_j for which the integral of equation (9.32) is not zero. As a result of equation (9.50),

$$R_M^{-1} [R_M(E_o) - x] \leq E \leq R_k^{-1} \left[\frac{\nu_M}{\nu_k} R_M(E_o) - x \right] \quad (9.51)$$

The integral in equation (9.41) may now be evaluated as

$$\begin{aligned} \phi_j^{(2)}(x, E) = \sum_k \frac{\sigma_{jk} \sigma_{kM} \nu_j}{\tilde{S}_j(E) |\nu_M - \nu_k| \Delta_{jkM}} & [\exp(-\sigma_M x_{Ml} - \sigma_k x_{kl} - \sigma_j x_{jl}) \\ & - \exp(-\sigma_M x_{Mu} - \sigma_k x_{ku} - \sigma_j x_{ju})] \end{aligned} \quad (9.52)$$

where x_{Mu} , x_{ku} , x_{Ml} , and x_{kl} are the values of equations (9.44) and (9.45) evaluated at the corresponding upper and lower limits of x_j and

$$\Delta_{jkM} = \sigma_j + \left[\frac{(\nu_k - \nu_j)}{(\nu_M - \nu_k)} \sigma_M - \frac{(\nu_M - \nu_j)}{(\nu_M - \nu_k)} \sigma_k \right] \quad (9.53)$$

Higher order terms are similarly derived.

The total integral flux associated with each term may be evaluated as

$$\Phi_j^{(1)}(x) = \int_0^\infty \phi_j^{(1)}(x, E) dE \quad (9.54)$$

One may easily show that

$$\int_0^\infty \phi_j^{(1)}(x, E) dE = \frac{\sigma_{jM} [\exp(-\sigma_j x) - \exp(-\sigma_M x)]}{\sigma_M - \sigma_j} \quad (9.55)$$

in agreement with equation (9.5). Furthermore,

$$\begin{aligned} \int_0^\infty \phi_j^{(2)}(x, E) dE = \sum_k \frac{\sigma_{jk} \sigma_{kM}}{|\nu_M - \nu_k| \Delta_{jkM}} & \left\{ \left(\frac{\nu_k - \nu_j}{\sigma_k - \sigma_j} \right) \right. \\ & \times [\exp(-\sigma_j x) - \exp(-\sigma_k x)] \\ & \left. - \left(\frac{\nu_M - \nu_j}{\sigma_M - \sigma_j} \right) [\exp(-\sigma_j x) - \exp(-\sigma_M x)] \right\} \end{aligned} \quad (9.56)$$

which agrees with equation (9.6) as $\nu_k \rightarrow \nu_M$. This relation of equation (9.56) and equation (9.6) has been used previously (Wilson, 1983).

9.3.1. Total flux comparisons. The results of equations (9.36) and (9.52) are integrated numerically over their entire energy spectrum and given along with values from corresponding energy-independent solutions in table 9.5. The primary beam was taken as ^{20}Ne at 1380 MeV/nucleon. Clearly, the energy-dependent solutions appear quite accurate.

Table 9.5. Total Flux From Energy-Independent Solution and Numerically Integrated Differential Spectrum

[Values in parentheses are from energy-independent solution]

Fragment	Term	Flux, cm^{-2} , at water depth x of—	
		5 cm	20 cm
^{18}F	$\phi^{(1)}$	0.00727 (0.00717)	0.01148 (0.01140)
	$\phi^{(2)}$	0.00018 (0.00018)	0.00114 (0.00114)
^{17}O	$\phi^{(1)}$	0.00729 (0.00729)	0.01173 (0.01174)
	$\phi^{(2)}$	0.00017 (0.00017)	0.00112 (0.00112)
^{16}O	$\phi^{(1)}$	0.01350 (0.01349)	0.02193 (0.02202)
	$\phi^{(2)}$	0.00029 (0.00029)	0.00191 (0.00190)
^{15}N	$\phi^{(1)}$	0.00470 (0.00481)	0.00796 (0.00796)
	$\phi^{(2)}$	0.00032 (0.00033)	0.00220 (0.00220)
^{13}C	$\phi^{(1)}$	0.00511 (0.00521)	0.00894 (0.00887)
	$\phi^{(2)}$	0.00032 (0.00033)	0.00224 (0.00224)
^{12}C	$\phi^{(1)}$	0.00668 (0.00682)	0.01173 (0.01178)
	$\phi^{(2)}$	0.00056 (0.00056)	0.00398 (0.00398)
^{11}B	$\phi^{(1)}$	0.00417 (0.00417)	0.00735 (0.00732)
	$\phi^{(2)}$	0.00036 (0.00036)	0.00259 (0.00259)

9.3.2. Monoenergetic beam results. The fluorine spectral flux at various depths in a water column is shown in figure 9.5. The primary beam was ^{20}Ne ions at 600 MeV/nucleon corresponding to a range of 30 cm. There is a clear structure caused by the fluorine isotopes shown in the spectrum. The most energetic ions are ^{19}F . The ^{18}F and ^{17}F spectral components are clearly resolved. Only the ^{19}F is able to penetrate to the largest depth represented in figure 9.5 (35 cm). A similar, but more complicated, isotopic structure is seen in the oxygen spectra of figure 9.6. The greater number of oxygen isotopes contributing has a smoothing effect on the resultant spectrum. This effect is even more clearly seen in figure 9.7 for the nitrogen isotopes. Some of the smoothness results from the higher order term $\phi^{(2)}$ in the perturbation expansion. The boron flux of figure 9.8 shows very little isotopic structure. Qualitatively, similar results are obtained for an iron beam of the same range (30 cm) as shown in figures 9.9 to 9.13.

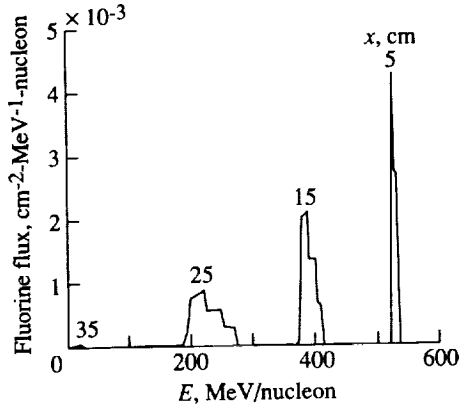


Figure 9.5. Fluorine flux spectrum produced by ^{20}Ne beam at 600 MeV/nucleon in water column at various depths.

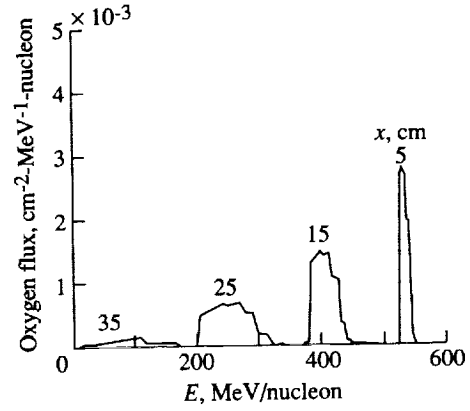


Figure 9.6. Oxygen flux spectrum produced by ^{20}Ne beam at 600 MeV/nucleon in water column at various depths.

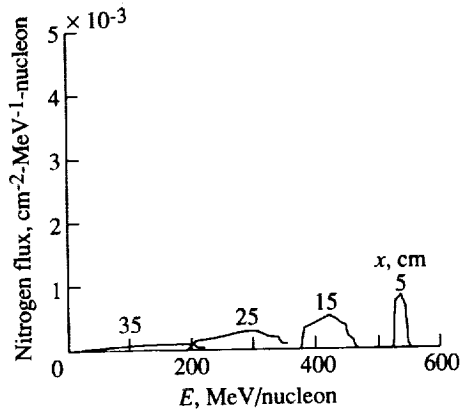


Figure 9.7. Nitrogen flux spectrum produced by ^{20}Ne beam at 600 MeV/nucleon in water column at various depths.

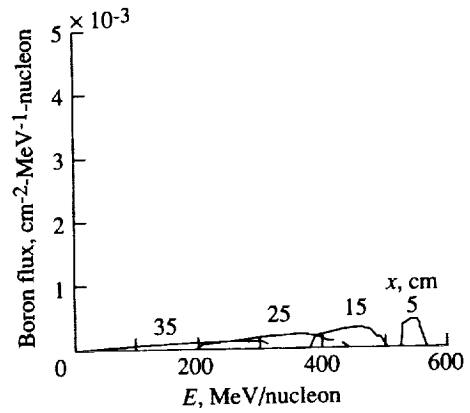


Figure 9.8. Boron flux spectrum produced by ^{20}Ne beam at 600 MeV/nucleon in water column at various depths.

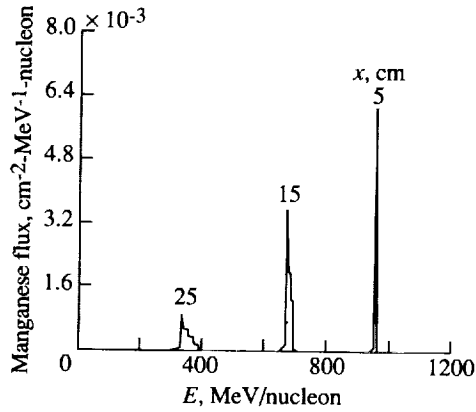


Figure 9.9. Manganese flux spectrum produced by ^{56}Fe beam at 1090 MeV/nucleon in water column at various depths.

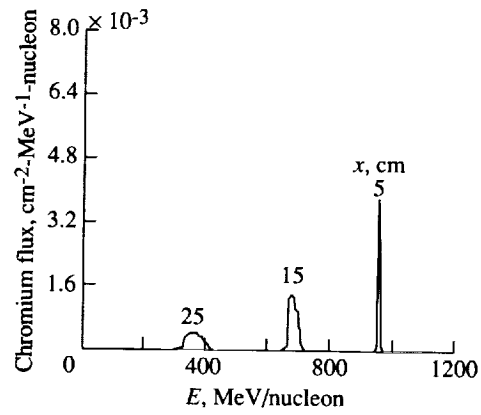


Figure 9.10. Chromium flux spectrum produced by ^{56}Fe beam at 1090 MeV/nucleon in water column at various depths.

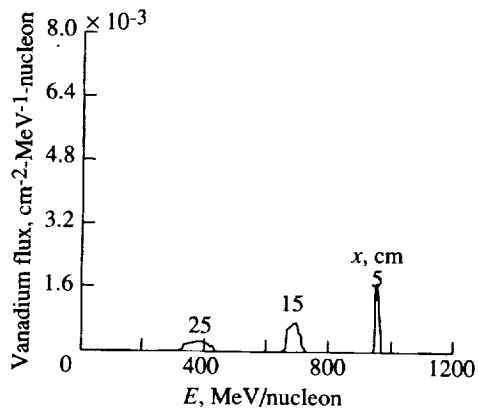


Figure 9.11. Vanadium flux spectrum produced by ^{56}Fe beam at 1090 MeV/nucleon in water column at various depths.

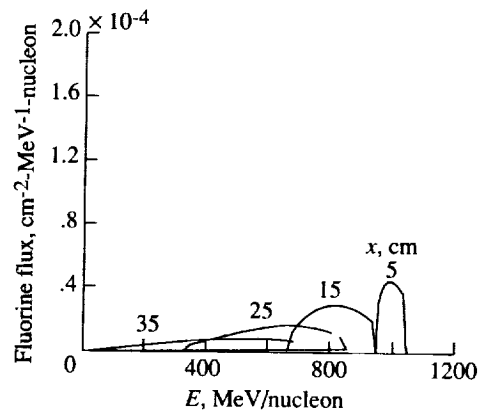


Figure 9.12. Fluorine flux spectrum produced by ^{56}Fe beam at 1090 MeV/nucleon in water column at various depths.

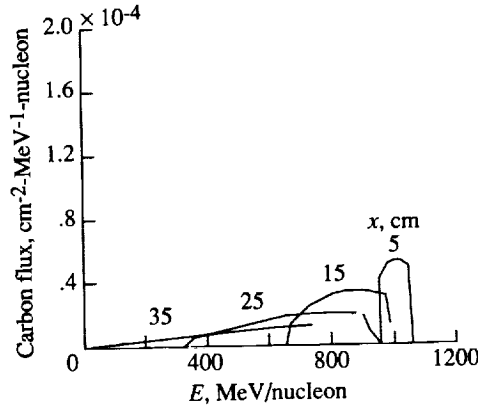


Figure 9.13. Carbon flux spectrum produced by ^{56}Fe beam at 1090 MeV/nucleon in water column at various depths.

9.4. Realistic Ion Beams

In section 9.3, we assumed that a monoenergetic beam was present at the boundary. We now take the incident ion beam flux to be

$$\phi_j(0, E) = \frac{1}{\sqrt{2\pi}\Delta} \exp\left[-\frac{(E - E_o)^2}{2\Delta^2}\right] \quad (9.57)$$

where E_o is the nominal beam energy and Δ is related to the half-width at half-maximum. The full solution is then found as a superposition of results from section 9.3. The uncollided flux is found to be

$$\phi_M^{(0)}(x, E) = \frac{\tilde{S}_M(E_m)}{\tilde{S}_M(E)} \exp(-\sigma_M x) \frac{1}{\sqrt{2\pi}\Delta} \exp\left[\frac{(E_o - E_m)^2}{2\Delta^2}\right] \quad (9.58)$$

where $R_M(E_m) = R_M(E) + x$. One similarly arrives at

$$\begin{aligned} \phi_j^{(1)}(x, E) = & \frac{\sigma_j M \nu_j}{\tilde{S}_j(E) |\nu_M - \nu_j|} \exp\left\{-\frac{1}{2}\sigma_j [x - R_j(E) - \eta'_o] - \frac{1}{2}\sigma_M [x + R_j(E) + \eta'_o]\right\} \\ & \times \frac{1}{2} \left[\operatorname{erf}\left(\frac{E_u - E_o}{\sqrt{2}\Delta}\right) - \operatorname{erf}\left(\frac{E_l - E_o}{\sqrt{2}\Delta}\right) \right] \end{aligned} \quad (9.59)$$

where

$$E_l = R_M^{-1} \left\{ \frac{\nu_j}{\nu_M} [R_j(E) + x] \right\} \quad (9.60)$$

$$E_u = R_M^{-1} \left\{ \frac{\nu_j}{\nu_M} R_j(E) + x \right\} \quad (9.61)$$

$$\eta'_o = \frac{2\nu_M}{\nu_M - \nu_j} R_M(E_o) - \frac{\nu_M + \nu_j}{\nu_M - \nu_j} [R_j(E) + x] \quad (9.62)$$

The second collision contribution to the ion energy spectrum is similar:

$$\begin{aligned} \phi_j^{(2)}(x, E) = & \sum_k \frac{\sigma_{jk}\sigma_{kM}\nu_j}{\tilde{S}_j(E) |\nu_M - \nu_k| \Delta_{jkM}} [\exp(-\sigma_M x_{Ml} - \sigma_k x_{kl} - \sigma_j x_{jl}) \\ & - \exp(-\sigma_M x_{Mu} - \sigma_k x_{ku} - \sigma_j x_{ju})] \\ & \times \frac{1}{2} \left[\operatorname{erf} \left(\frac{E_u - E_o}{\sqrt{2}\Delta} \right) - \operatorname{erf} \left(\frac{E_l - E_o}{\sqrt{2}\Delta} \right) \right] \end{aligned} \quad (9.63)$$

where

$$E_l = \left\{ \begin{array}{ll} R_M^{-1} \left[\frac{\nu_k R_k(E) + \nu_j x}{\nu_M} \right] & (\nu_M > \nu_k > \nu_j) \\ R_M^{-1} \left[R_M(E) + \frac{\nu_j x}{\nu_M} \right] & (\nu_k > \nu_M > \nu_j) \\ R_M^{-1} \left[\frac{\nu_k (R_k(E) + x)}{\nu_M} \right] & (\nu_M > \nu_j > \nu_k) \end{array} \right\} \quad (9.64)$$

$$E_u = \left\{ \begin{array}{ll} R_M^{-1} [R_M(E) + x] & (\nu_M > \nu_k > \nu_j) \\ R_M^{-1} \left[\frac{\nu_k (R_k(E) + x)}{\nu_M} \right] & (\nu_k > \nu_M > \nu_j) \\ R_M^{-1} [R_M(E) + x] & (\nu_M > \nu_j > \nu_k) \end{array} \right\} \quad (9.65)$$

and x_M and x_k evaluated at the upper and lower limit values of x_j are obtained from equations (9.44) and (9.45).

The elemental flux spectra were recalculated for ^{20}Ne ions at 600 MeV/nucleon with a 0.2-percent energy spread assumed for the primary beam. The resulting fluorine flux is shown in figure 9.14. Although the spectral results are quite similar to the monoenergetic beam case, there is a considerable smoothing of the total spectrum. Similar results are obtained for the oxygen flux as well in figure 9.15. In distinction, the nitrogen and carbon spectra show only slight isotopic structure as seen in figures 9.16 and 9.17. Qualitatively similar results are obtained for the ^{56}Fe realistic beam as shown in figures 9.18 through 9.22.

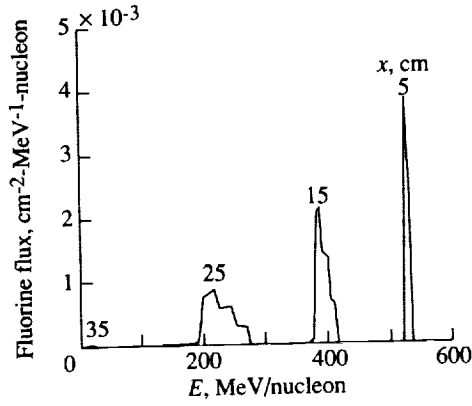


Figure 9.14. Fluorine flux spectrum produced by ^{20}Ne beam at 600 MeV/nucleon with 0.2-percent energy spread in water column at various depths.

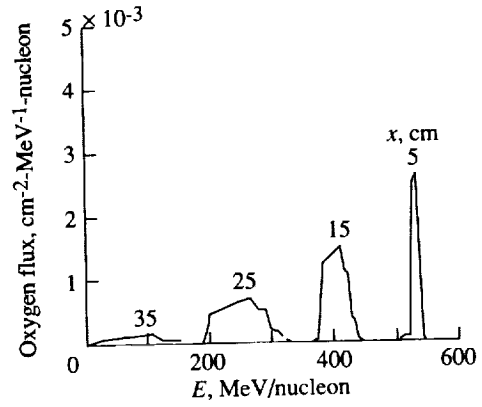


Figure 9.15. Oxygen flux spectrum produced by ^{20}Ne beam at 600 MeV/nucleon with 0.2-percent energy spread in water column at various depths.

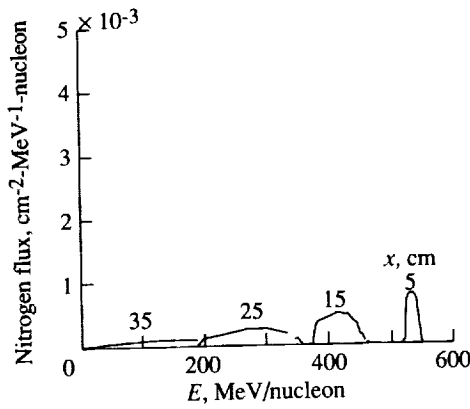


Figure 9.16. Nitrogen flux spectrum produced by ^{20}Ne beam at 600 MeV/nucleon with 0.2-percent energy spread in water column at various depths.

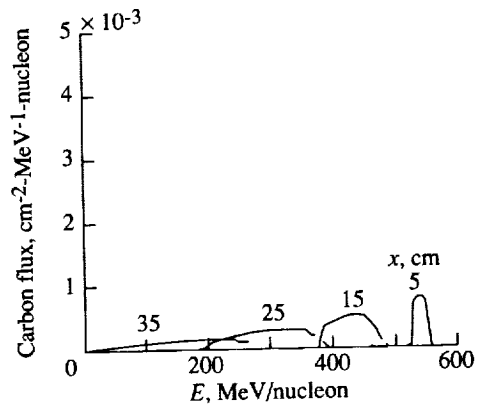


Figure 9.17. Carbon flux spectrum produced by ^{20}Ne beam at 600 MeV/nucleon with 0.2-percent energy spread in water column at various depths.

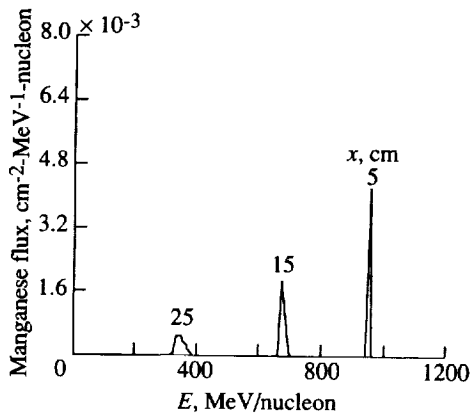


Figure 9.18. Manganese flux spectrum produced by ^{56}Fe beam at 1090 MeV/nucleon with 0.2-percent energy spread in water column at various depths.

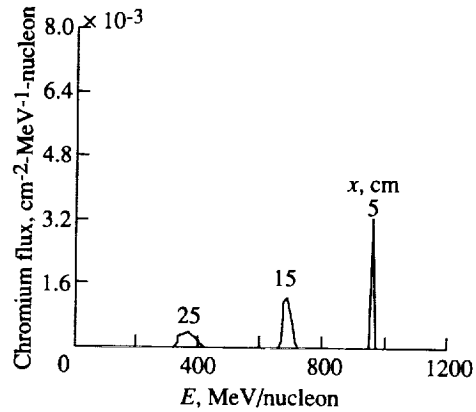


Figure 9.19. Chromium flux spectrum produced by ^{56}Fe beam at 1090 MeV/nucleon with 0.2-percent energy spread in water column at various depths.

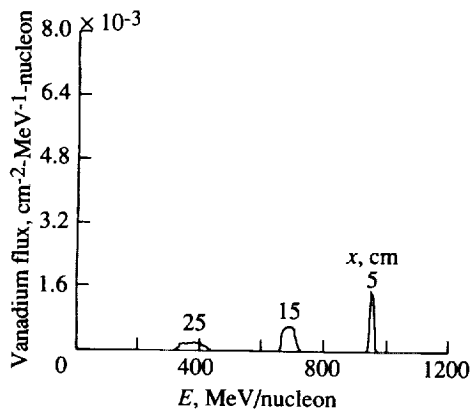


Figure 9.20. Vanadium flux spectrum produced by ^{56}Fe beam at 1090 MeV/nucleon with 0.2-percent energy spread in water column at various depths.

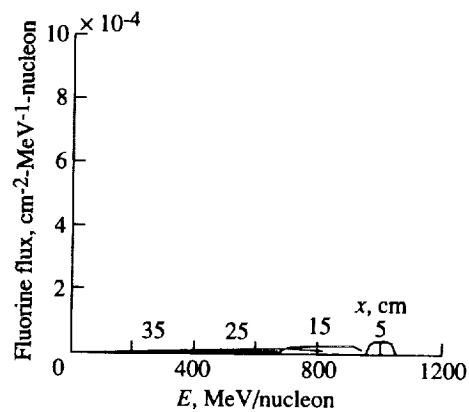


Figure 9.21. Fluorine flux spectrum produced by ^{56}Fe beam at 1090 MeV/nucleon with 0.2-percent energy spread in water column at various depths.

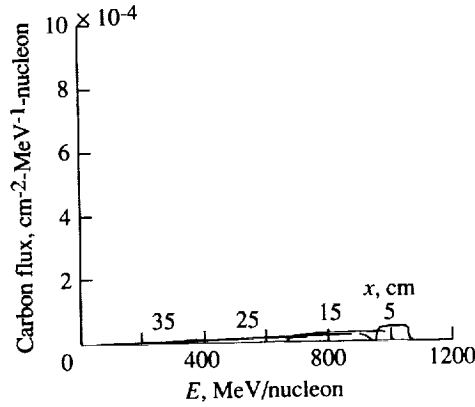


Figure 9.22. Carbon flux spectrum produced by ^{56}Fe beam at 1090 MeV/nucleon with 0.2-percent energy spread in water column at various depths.

9.5. Approximate Spectral Solutions

In sections 9.3 and 9.4, the spectral solutions of the secondary ion flux were derived to second-order collision terms. Such a three-term expansion is not always an adequate representation of the transport solution. In this section, we derive approximate expressions for the perturbation series. Clearly, the more accurate results would be used to the order to which they are known, and the higher order terms would be taken to the approximate expressions of this section.

9.5.1. Approximate monoenergetic beams. The uncollided beam solution is taken as

$$\phi_j^{(0)}(x, E) = \phi_j^{(0)}(x) \frac{1}{\bar{S}_j(E)} \delta[x + R_j(E) - R_j(E_0)] \quad (9.66)$$

which is equal to the result in equation (9.35). The first-order collision term is approximated by noting that the energy dependence of the exponent of equation (9.36) is slowly varying in energy resulting in (Wilson, 1977a, 1977b, and 1983; Wilson et al., 1984)

$$\phi_j^{(1)}(x, E) \approx \frac{\phi_j^{(1)}(x)}{E_{ju} - E_{jl}} \quad (9.67)$$

where

$$E_{jl} = R_j^{-1} \left\{ \frac{\nu_M}{\nu_j} [R_M(E_0) - x] \right\} \quad (9.68)$$

$$E_{ju} = R_j^{-1} \left\{ \frac{\nu_M}{\nu_j} R_M(E_0) - x \right\} \quad (9.69)$$

Similarly,

$$\phi_j^{(2)}(x, E) = \sum_k \frac{\sigma_{jk} \sigma_{kM} g(j, k, M)}{E_{ju} - E_{jl}} \quad (9.70)$$

where

$$E_{jl} = \left\{ \begin{array}{ll} R_M^{-1} \{R_M(E_o) - x\} & (\nu_M > \nu_k > \nu_j) \\ R_k^{-1} \left\{ \frac{\nu_M}{\nu_k} R_M(E_o) - x \right\} & (\nu_k > \nu_M > \nu_j) \\ R_M^{-1} \{R_M(E_o) - x\} & (\nu_M > \nu_j > \nu_k) \end{array} \right\} \quad (9.71)$$

and

$$E_{ju} = \left\{ \begin{array}{ll} R_k^{-1} \left\{ \frac{\nu_M R_M(E_o) - \nu_j x}{\nu_k} \right\} & (\nu_M > \nu_k > \nu_j) \\ R_M^{-1} \left\{ R_M(E_o) - \frac{\nu_j x}{\nu_M} \right\} & (\nu_k > \nu_M > \nu_j) \\ R_k^{-1} \left\{ \frac{\nu_M}{\nu_k} R_M(E_o) - x \right\} & (\nu_M > \nu_j > \nu_k) \end{array} \right\} \quad (9.72)$$

Higher order terms ($n > 2$) are taken as

$$\phi_j^n(x, E) \approx \frac{\phi_j^{(n)}(x)}{E_{ju} - E_{jl}} \quad (9.73)$$

where E_{ju} and E_{jl} are given by equations (9.71) and (9.72). In all the expressions for $\phi_j^{(n)}$ given by equations (9.67), (9.70), and (9.73), the flux values are taken as zero unless

$$E_{jl} \leq E \leq E_{ju} \quad (9.74)$$

The approximate monoenergetic beam solutions are given in figures 9.23 through 9.26 and should be compared with the solutions found in section 9.3. The ^{17}O flux at 20 cm of water is shown in figure 9.23 as contributed by the first collision term. The trapezoidal (solid) curve is the exact solution for the first collision term derived in section 9.3. The rectangular (dashed) curve is the approximate first collision term of equation (9.67). Terms for other fragment spectra are similar to those shown in figure 9.23. The solution for the second collision contribution to the ^{17}O flux at 20 cm of water is shown in figure 9.24. The nearly rectangular solution (dashed curve) is the approximation given by equation (9.70). A triangular spectral function of the same energy interval could yield improved results. The spectra of fragments which are much lighter than the primary beam are more accurately represented by the approximate solutions as seen in figures 9.25 and 9.26. This improvement results from the greater number of terms in the summation of equation (9.52). This leads us to believe that the higher order terms in the perturbation series can be adequately represented by the approximation in equation (9.73). This is especially true because higher order terms in many applications are only small corrections.

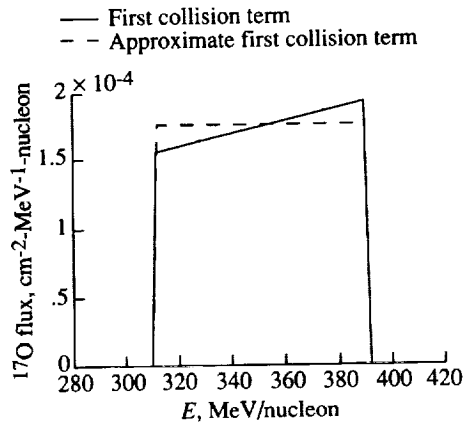


Figure 9.23. ^{17}O flux spectral term according to first collision term and approximate first collision term.

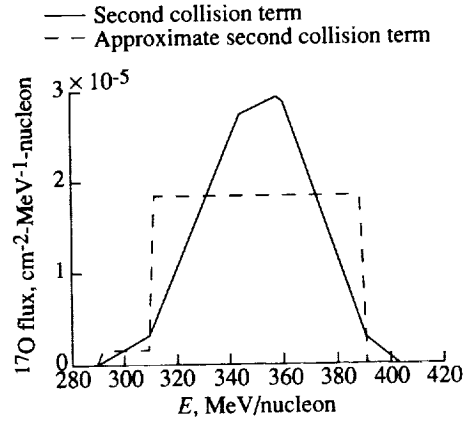


Figure 9.24. ^{17}O flux spectral term according to second collision term and approximate second collision term.

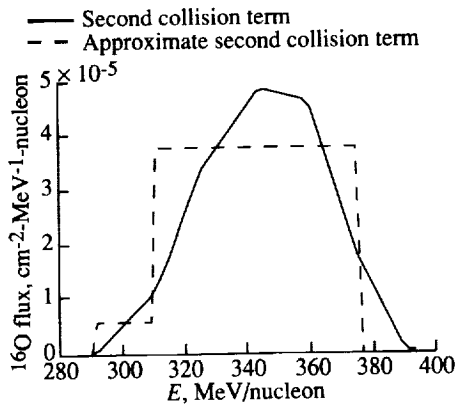


Figure 9.25. ^{16}O flux spectral term according to second collision term and approximate second collision term.

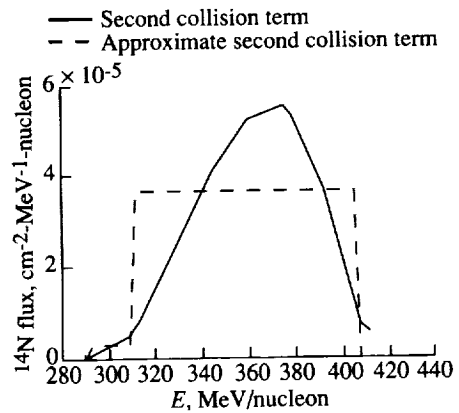


Figure 9.26. ^{14}N flux spectral term according to second collision term and approximate second collision term.

9.5.2. Approximate realistic beams. Approximate solutions for realistic ion beams may be found by using a superposition of the approximate monoenergetic beam solutions. The incident ion beam is taken as

$$\phi_j(0, E) = \frac{1}{\sqrt{2\pi}\Delta} \exp\left[-\frac{(E - E_o)^2}{2\Delta^2}\right] \delta_{jM} \quad (9.75)$$

where E_o is the nominal beam energy and Δ is related to the half-width at half-maximum. The first term is then, as before,

$$\phi_M^{(0)}(x, E) = \frac{\tilde{S}_M(E_m)}{\tilde{S}_M(E)} \exp(-\sigma_M x) \frac{1}{\sqrt{2\pi}\Delta} \exp\left[-\frac{(E_o - E_m)^2}{2\Delta^2}\right] \quad (9.76)$$

where $R_M(E_m) = R_M(E) + x$. One similarly arrives at

$$\phi_j^{(1)}(x, E) = \phi_j^{(1)}(x) \frac{1}{2} \left[\operatorname{erf}\left(\frac{E_u - E_o}{\sqrt{2}\Delta}\right) - \operatorname{erf}\left(\frac{E_l - E_o}{\sqrt{2}\Delta}\right) \right] (E_{ju} - E_{jl})^{-1} \quad (9.77)$$

where

$$E_u = R_M^{-1} \left\{ \frac{\nu_j}{\nu_M} R_j(E) + x \right\} \quad (9.78)$$

$$E_l = R_M^{-1} \left\{ \frac{\nu_j}{\nu_M} [R_j(E) + x] \right\} \quad (9.79)$$

and E_{ju} and E_{jl} are given by equations (9.68) and (9.69). Additional computation yields

$$\begin{aligned} \phi_j^{(2)}(x, E) &= \sum_k \sigma_{jk} \sigma_{kM} g(j, k, M) \frac{1}{2} \left[\operatorname{erf}\left(\frac{E_u - E_o}{\sqrt{2}\Delta}\right) - \operatorname{erf}\left(\frac{E_l - E_o}{\sqrt{2}\Delta}\right) \right] \\ &\times (E_{ju} - E_{jl})^{-1} \end{aligned} \quad (9.80)$$

where E_{ju} and E_{jl} are given by equations (9.71) and (9.72), and E_l and E_u are given in equations (9.64) and (9.65). The remaining higher order terms are taken as

$$\begin{aligned} \phi_j^{(n)}(x, E) &= \sum_{j_1, \dots, j_{n-1}} \sigma_{jj_{n-1}, \dots, j_1, M} g(j, j_{n-1}, \dots, j_1, M) \frac{1}{2} \left[\operatorname{erf}\left(\frac{E_u - E_o}{\sqrt{2}\Delta}\right) - \operatorname{erf}\left(\frac{E_l - E_o}{\sqrt{2}\Delta}\right) \right] \\ &\times (E_{ju} - E_{jl})^{-1} \end{aligned} \quad (9.81)$$

where E_{jl} and E_{ju} are given by equations (9.68) and (9.69), and E_u and E_l are given by equations (9.78) and (9.79).

These approximate equations for realistic ion beams are given in figures 9.27 to 9.30 and should be compared with the more exact formulas given in section 9.4.

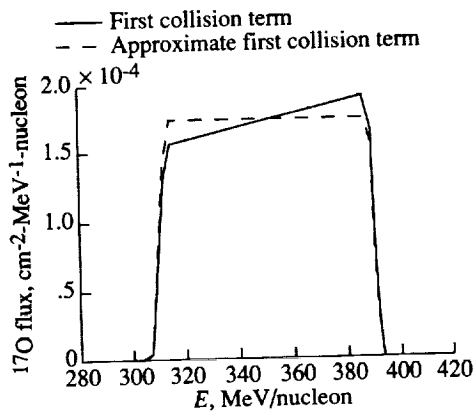


Figure 9.27. ^{17}O flux spectral term for energy spread ^{20}Ne beam according to first collision term and approximate first collision term.

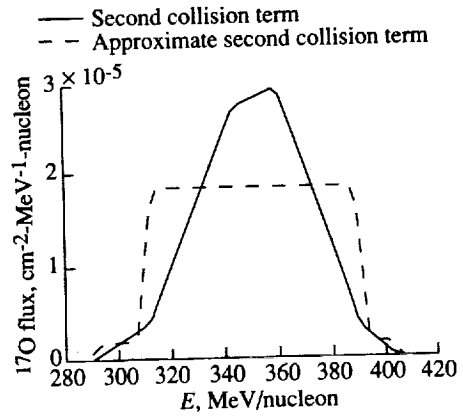


Figure 9.28. ^{17}O flux spectral term for energy spread ^{20}Ne beam according to second collision term and approximate second collision term.

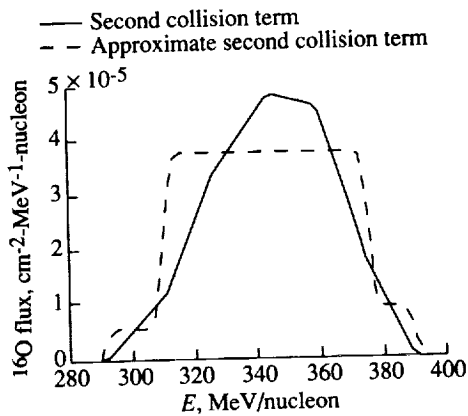


Figure 9.29. ^{16}O flux spectral term for energy spread ^{20}Ne beam according to second collision term and approximate second collision term.

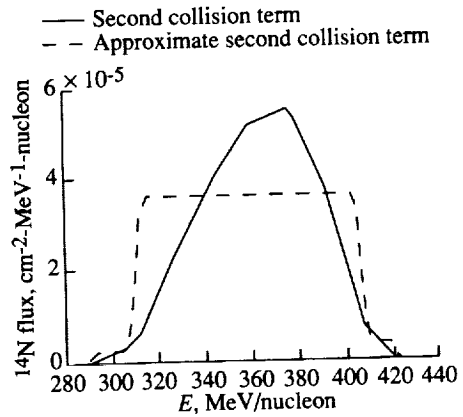


Figure 9.30. ^{14}N flux spectral term for energy spread ^{20}Ne beam according to second collision term and approximate second collision term.

The primary ion beam is taken as ^{20}Ne at 600 MeV/nucleon with a 0.2-percent energy spread. The ^{17}O flux first collision term is shown in figure 9.27 for the two formalisms. The effect of the beam energy spread is seen as a rounding of the spectrum at the edges compared with the monoenergetic case in figure 9.23. The second collision term is shown in figure 9.28. The approximate second collision term improves for the lighter fragments as seen in figures 9.29 and 9.30. Higher order collision terms are expected to be more accurate because of the large number of combinations of contributing ion terms.

9.6. Recommended Methods

An energy-independent theory has been used to show that the perturbation expansion up to the double collision term is adequate for all fragments whose mass is near that of the projectile. This is why the three-term expansion was able to explain the Bragg curve data for ^{20}Ne beams in water with reasonable accuracy (Wilson et al., 1984). As a starting point for the calculation of the transition of heavy ion beams in materials, the use of the three-term expansion can be further corrected by use of the approximate higher order terms given in section 9.5. As an example of such a procedure, we give results for ^{20}Ne beams at 600 MeV/nucleon in water. The results are shown in figures 9.31 to 9.36 as successive partial sums of the perturbation series. The solid line is the first collision term. The dashed curve includes the double collision terms. The long-dash-short-dash curve includes the triple collision term and can hardly be distinguished from the long-dash-double-short-dash curve which includes the quadruple collision terms. The results for penetration to 20 cm of water are shown in figures 9.31 to 9.36. The monoenergetic beam results for ^{17}O , ^{16}O , and ^{12}C are given in figures 9.31 to 9.33, respectively. The double collision term is seen to be always an important contribution. The triple collision term shows some importance for ^{12}C , whereas higher order terms are negligible. Similar results are shown in figures 9.34 to 9.36 for an energy spread of 0.2 percent.

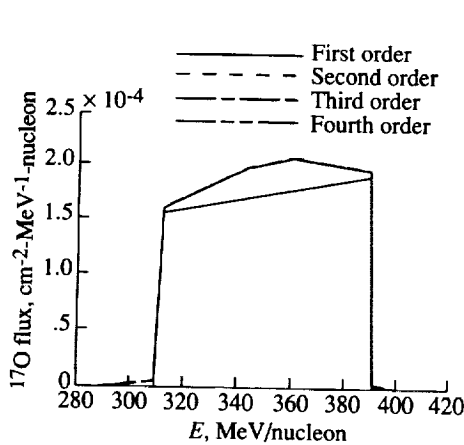


Figure 9.31. Sequence of approximations of ^{17}O flux spectrum after 20 cm of water for first-, second-, third-, and fourth-order theories.

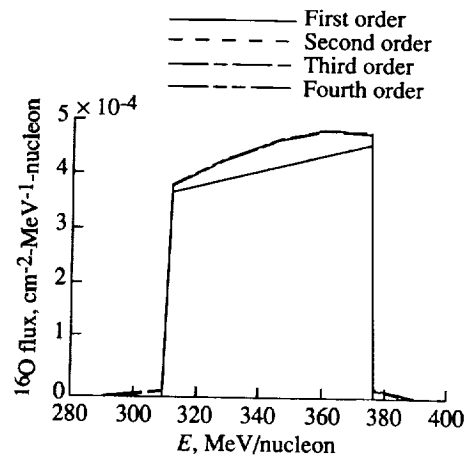


Figure 9.32. Sequence of approximations of ^{16}O flux spectrum after 20 cm of water for first-, second-, third-, and fourth-order theories.

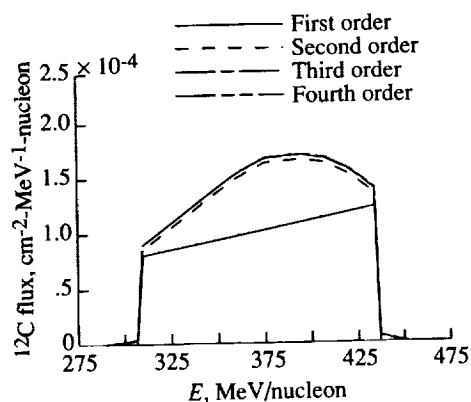


Figure 9.33. Sequence of approximations of ^{12}C flux spectrum after 20 cm of water for first-, second-, third-, and fourth-order theories.

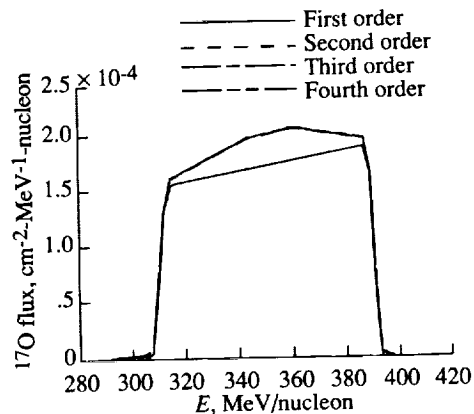


Figure 9.34. Sequence of approximations for energy spread solution of ^{17}O flux spectrum after 20 cm of water for first-, second-, third-, and fourth-order theories.

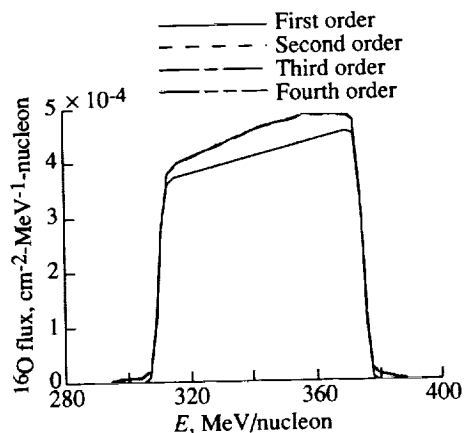


Figure 9.35. Sequence of approximations for energy spread solution of ^{16}O flux spectrum after 20 cm of water for first-, second-, third-, and fourth-order theories.

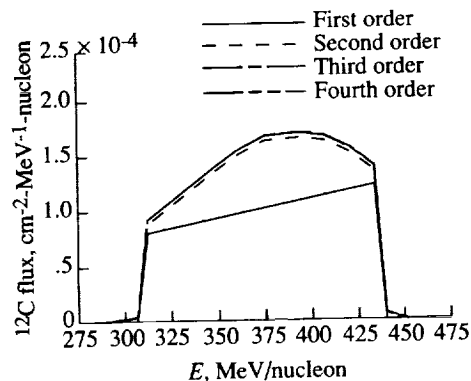


Figure 9.36. Sequence of approximations for energy spread solution of ^{12}C flux spectrum after 20 cm of water for first-, second-, third-, and fourth-order theories.

9.7. Impulse Response

One form of Green's function is the impulse response corresponding to a δ -like source term at the boundary. We therefore seek a solution of

$$\left[\frac{\partial}{\partial x} - \frac{\partial}{\partial E} \tilde{S}_j(E) + \sigma_j \right] G_{jM}(x, E; E') = \sum_k m_{jk} \sigma_k G_{kM}(x, E; E') \quad (9.82)$$

where the boundary condition is

$$G_{jM}(0, E; E') = \delta_{jM} \delta(E - E') \quad (9.83)$$

for which any arbitrary transport solution may be written as

$$\phi_j(x, E) = \sum_M \int_0^\infty G_{jM}(x, E; E') F_M(E') dE' \quad (9.84)$$

where $F_M(E')$ is the flux at the boundary. The solution to equations (9.82) and (9.83) is straightforward, even if tedious (Wilson, 1977a, 1977b, and 1983; Wilson et al., 1989a) and is arrived at by using the method of characteristics (Wilson and Lamkin, 1975). The solution is expressed as a series as

$$G_{jM}(x, E; E') = \sum_i G_{jM}^{(i)}(x, E; E') \quad (9.85)$$

where

$$G_{jM}^{(0)}(x, E; E') = \frac{1}{\tilde{S}_j(E)} \exp(-\sigma_j x) \delta_{jM} \delta[x + R_j(E) - R_M(E')] \quad (9.86)$$

and

$$G_{jM}^{(1)}(x, E; E') = \frac{1}{\tilde{S}_j(E)} m_{jM} \sigma_M \frac{\nu_j}{|\nu_M - \nu_j|} \exp \left\{ -\frac{1}{2} \sigma_j [x - R_j(E) - \eta'] - \frac{1}{2} \sigma_M [x + R_j(E) + \eta'] \right\} \quad (9.87)$$

so long as

$$\frac{\nu_M}{\nu_j} [R_M(E') - x] < R_j(E) < \frac{\nu_M}{\nu_j} R_M(E') - x \quad (9.88)$$

where

$$\eta' = \frac{2\nu_M}{\nu_M - \nu_j} R_M(E') - \frac{\nu_M + \nu_j}{\nu_M - \nu_j} [R_j(E) + x] \quad (9.89)$$

otherwise, $G_{jM}^{(1)}(x, E; E')$ is zero. After a complicated but straightforward manipulation, a similar result may be obtained for $G_{jM}^{(2)}(x, E; E')$ as

$$G_{jM}^{(2)}(x, E; E') = \sum_k \frac{\sigma_{jk}\sigma_{kM}\nu_j}{\bar{S}_j(E)|\nu_M - \nu_k|\Delta_{jkM}} [\exp(-\sigma_M x_{Ml} - \sigma_k x_{kl} - \sigma_j x_{jl}) - \exp(-\sigma_M x_{Mu} - \sigma_k x_{ku} - \sigma_j x_{ju})] \quad (9.90)$$

where

$$\Delta_{jkM} = \sigma_j + \left(\frac{\nu_k - \nu_j}{\nu_M - \nu_j} \sigma_M - \frac{\nu_M - \nu_j}{\nu_M - \nu_k} \sigma_k \right) \quad (9.91)$$

and x_{Mu} , x_{ku} , x_{Ml} , and x_{kl} are values of x_M and x_k evaluated at the corresponding upper and lower limits of x_j and

$$x_M = \frac{\nu_M R_M(E') - \nu_k [R_k(E) + x] + (\nu_k - \nu_j)x_j}{\nu_M - \nu_k} \quad (9.92)$$

$$x_k = \frac{\nu_M [R_M(E) + x] - \nu_M R_M(E') - (\nu_M - \nu_k)x_j}{\nu_M - \nu_k} \quad (9.93)$$

The requirements that x_M and x_k be bounded by the interval 0 to $x - x_j$ yields

$$\left\{ \begin{array}{c} 0 \\ \frac{\nu_k [R_k(E) + x] - \nu_M R_M(E')}{\nu_k - \nu_j} \end{array} \right\} \leq x_j \leq \left\{ \begin{array}{c} x \\ \frac{\nu_M [R_M(E) + x] - \nu_M R_M(E')}{\nu_M - \nu_j} \end{array} \right\} \quad (9.94)$$

as the appropriate limiting values in equation (9.90) when $\nu_M > \nu_k > \nu_j$. In the braces, we always choose the most restrictive value for the limit. The requirement of equation (9.94) also implies the result that

$$R_M^{-1} [R_M(E') - x] \leq E \leq R_k^{-1} \left[\frac{\nu_M R_M(E') - \nu_j x}{\nu_k} \right] \quad (9.95)$$

as the range over which the result of equation (9.90) is not zero. In the event that $\nu_k > \nu_M > \nu_j$, then

$$\left\{ \begin{array}{c} 0 \\ \frac{\nu_M [R_M(E) + x] - \nu_M R_M(E')}{\nu_M - \nu_j} \end{array} \right\} \leq x_j \leq \left\{ \begin{array}{c} x \\ \frac{\nu_k [R_k(E) + x] - \nu_M R_M(E')}{\nu_k - \nu_j} \end{array} \right\} \quad (9.96)$$

As a result of equation (9.96),

$$R_k^{-1} \left[\frac{\nu_M R_M(E') - x}{\nu_k} \right] \leq E \leq R_M^{-1} \left[R_M(E') - \frac{\nu_j}{\nu_M} x \right] \quad (9.97)$$

In the event that $\nu_M > \nu_j > \nu_k$, it follows that

$$0 \leq x_j \leq \left\{ \begin{array}{l} x \\ \frac{\nu_M [R_M(E) + x - R_M(E')]}{\nu_M - \nu_j} \\ \frac{\nu_M R_M(E') - \nu_k R_k(E) - \nu_k x}{\nu_j - \nu_k} \end{array} \right\} \quad (9.98)$$

where the lesser of the three values in the braces is used as the upper limit of x_j for which $G^{(2)}$ of equation (9.90) is not zero. As a result of equation (9.98),

$$R_M^{-1} [R_M(E') - x] \leq E \leq R_k^{-1} \left[\frac{\nu_M}{\nu_k} R_M(E') - x \right] \quad (9.99)$$

Higher order terms are similarly derived. Approximate expressions have been obtained (Wilson et al., 1988) as

$$G_{jM}^{(n)}(x, E; E') = \sum_{k, j_1, \dots, j_{n-1}} \sigma_{jk} \frac{\sigma_{kj_1} \cdots \sigma_{j_{n-2}M} g(j, k, j_1, \dots, j_{n-2}, M)}{E_{uj} - E_{lj}} \quad (9.100)$$

where

$$E_{jl} = \left\{ \begin{array}{ll} R_M^{-1} \{R_M(E') - x\} & (\nu_M > \nu_k > \nu_j) \\ R_k^{-1} \left\{ \frac{\nu_M}{\nu_k} R_M(E') - x \right\} & (\nu_k > \nu_M > \nu_j) \\ R_M^{-1} \{R_M(E') - x\} & (\nu_M > \nu_j > \nu_k) \end{array} \right\} \quad (9.101)$$

and

$$E_{ju} = \left\{ \begin{array}{ll} R_k^{-1} \left\{ [\nu_M R_M(E') - \nu_j x] \nu_k^{-1} \right\} & (\nu_M > \nu_k > \nu_j) \\ R_M^{-1} \left\{ R_M(E') - \frac{\nu_j x}{\nu_M} \right\} & (\nu_k > \nu_M > \nu_j) \\ R_k^{-1} \left\{ \frac{\nu_M}{\nu_k} R_M(E') - x \right\} & (\nu_M > \nu_j > \nu_k) \end{array} \right\} \quad (9.102)$$

and the g functions of $n + 1$ arguments are defined as

$$g(j_1) = \exp(-\sigma_{j_1} x) \quad (9.103)$$

$$g(j_1, j_2, \dots, j_n, j_{n+1}) = \frac{g(j_1, j_2, \dots, j_{n-1}, j_n) - g(j_1, j_2, \dots, j_{n-1}, j_{n+1})}{\sigma_{j_{n+1}} - \sigma_{j_n}} \quad (9.104)$$

The expression for $G_{jM}^{(n)}$ given by equation (9.100) is taken as zero unless

$$E_{jl} \leq E \leq E_{ju} \quad (9.105)$$

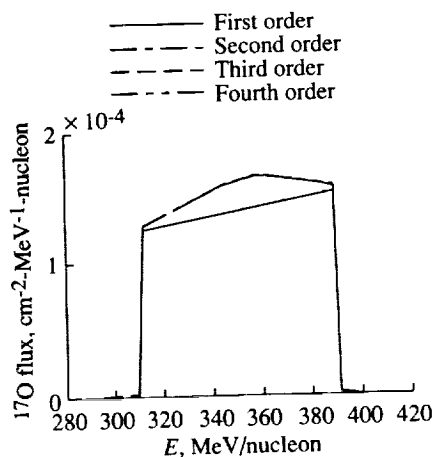


Figure 9.37. Sequence of approximations of ^{17}O flux spectrum after 20 cm of water for first-, second-, third-, and fourth-order (which cannot be distinguished) theories.

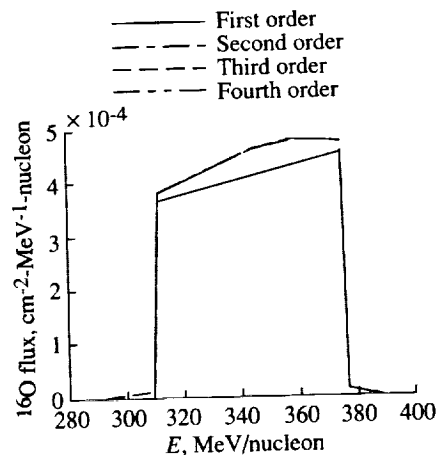


Figure 9.38. Sequence of approximations of ^{16}O flux spectrum after 20 cm of water for first-, second-, third-, and fourth-order (which cannot be distinguished) theories.

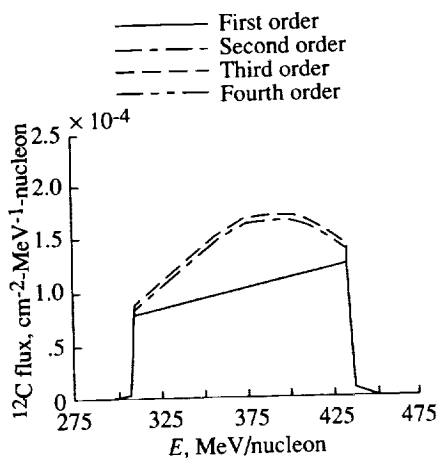


Figure 9.39. Sequence of approximations of ^{12}C flux spectrum after 20 cm of water for first-, second-, third-, and fourth-order (which cannot be distinguished) theories.

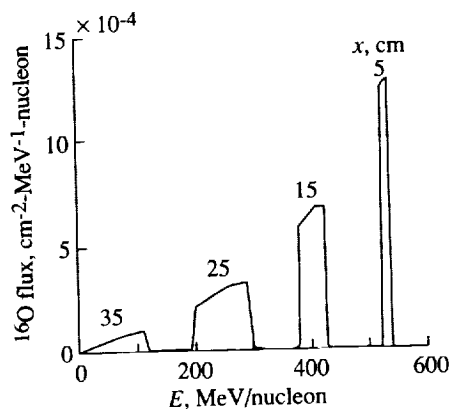


Figure 9.40. Green's function for ^{16}O flux spectrum response to 600-MeV/nucleon ^{20}Ne flux at boundary.

Portions of the Green's function are shown for incident ^{20}Ne beams at $E' = 600$ MeV/nucleon at $x = 20$ cm in figures 9.37 to 9.39. The contribution from $G^{(1)}$ is shown as the solid curve, $G^{(1)} + G^{(2)}$ is shown as the long-dash-short-dash curve, and $G^{(1)} + G^{(2)} + G^{(3)}$ is shown as the dashed curve. The long-dash-double-short-dash curve representing the inclusion of $G^{(4)}$ in the sum cannot be distinguished signifying convergence to a high degree of accuracy. A fuller presentation of the Green's function for ^{16}O fragments is given in figure 9.40, and a presentation of the Green's function for ^{12}C is given in figure 9.41. The results in figures 9.40 and 9.41

are found by summing the terms to $G^{(4)}$. From the present result, the solution for any arbitrary boundary condition may be found by using equation (9.84).

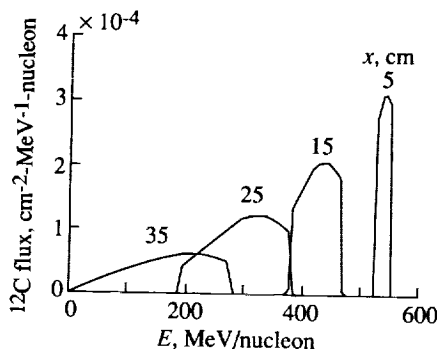


Figure 9.41. Green's function for ^{12}C flux spectrum response to a 600-MeV/nucleon ^{20}Ne flux at boundary.

Although the present formalism presents a closed-form solution for the more common form of the HZE propagation problem, many tasks remain before it is adequately solved. The inclusion of energy-dependent nuclear cross sections is known to be very important in obtaining accurate solutions to some problems (Townsend and Wilson, 1988a). Treating the momentum spread of the fragments is more complicated for the higher-order terms. The inclusion of the light fragment spectra is a difficult challenge (Wilson et al., 1989b). Finally, the three-dimensional aspects of the problem have only partially been treated (Shavers, 1988; Schimmerling et al., 1986). Even these shortcomings of the HZE propagation problem remain without the mention of uncertainties in nuclear cross sections (Townsend and Wilson, 1988a and 1988b) or atomic/molecular cross sections. Clearly much work remains.

9.8. Galactic Ion Transport

In the present section, we expand on the methods developed earlier for nucleon transport (Wilson and Lamkin, 1975) by combining analytic and numerical tools. The galactic cosmic-ray ion transport problem is transformed to an integral along the characteristic curve of that particular ion. As a result of the conservation of velocity in fragmentation, the perturbation series (Wilson and Lamkin, 1975) is replaced by a simple numerical procedure. The resulting method reduces the difficulty associated with the low-energy discretization and the restriction to a definite form for the stopping power. The resulting numerical computation is simple and nondemanding from computer requirements and yet gives superior results compared with other methods.

In the present work, we use the straight ahead approximation and neglect the target secondary fragments (Wilson, 1977a and 1983). The transport equation may be written as

$$\left[\frac{\partial}{\partial x} - \frac{\partial}{\partial E} \tilde{S}_j(E) + \sigma_j \right] \phi_j(x, E) = \sum_{k>j} m_{jk} \sigma_k \phi_k(x, E) \quad (9.106)$$

where $\phi_j(x, E)$ is the flux of ions of type j with atomic mass A_j at x moving along the x axis at energy E in units of MeV/nucleon; σ_j is the corresponding macroscopic nuclear absorption cross section; $\tilde{S}_j(E)$ is the change in E per unit distance; and m_{jk} is the multiplicity of ion j produced in collision by ion k . We recall the result of equation (9.22) as

$$\begin{aligned} \chi_j(\eta_j, \xi_j) = & \exp\left[-\frac{1}{2}\sigma_j(\xi_j + \eta_j)\right] \chi_j(-\xi_j, \xi_j) \\ & + \frac{1}{2} \int_{-\xi_j}^{\eta_j} \exp\left[\frac{1}{2}\sigma_j(\eta' - \eta_j)\right] \sum_k m_{jk} \sigma_k \frac{\nu_j}{\nu_k} \chi_k(\eta'_k, \xi'_k) d\eta' \end{aligned} \quad (9.107)$$

where

$$\eta'_k = \frac{\nu_k + \nu_j}{2\nu_k} \eta' + \frac{\nu_k - \nu_j}{2\nu_k} \xi_j$$

and

$$\xi'_k = \frac{\nu_k - \nu_j}{2\nu_k} \eta' + \frac{\nu_k + \nu_j}{2\nu_k} \xi_j$$

Defining

$$\psi_j(x, r_j) = \chi_j(\eta_j, \xi_j) \quad (9.108)$$

one may show

$$\begin{aligned} \psi_j(x, r_j) = & \exp(-\sigma_j x) \psi_j(0, r_j + x) \\ & + \int_0^x dz \exp(-\sigma_j z) \sum_k m_{jk} \sigma_k \frac{\nu_j}{\nu_k} \psi_k\left(x - z, r_k + \frac{\nu_j}{\nu_k} z\right) \end{aligned} \quad (9.109)$$

Furthermore, it is easy to show that

$$\begin{aligned} \psi_j(x + h, r_j) = & \exp(-\sigma_j h) \psi_j(x, r_j + h) \\ & + \int_0^h dz \exp(-\sigma_j z) \sum_k m_{jk} \sigma_k \frac{\nu_j}{\nu_k} \psi_k\left(x + h - z, r_k + \frac{\nu_j}{\nu_k} z\right) \end{aligned} \quad (9.110)$$

It is clear from equation (9.109) that

$$\psi_k(x + h - z, r_k) = \exp[-\sigma_k(h - z)] \psi_k(x, r_k + h) + O(h - z) \quad (9.111)$$

which upon substitution into equation (9.110) yields

$$\begin{aligned} \psi_j(x + h, r_j) = & \exp(-\sigma_j h) \psi_j(x, r_j + h) \\ & + \int_0^h dz \exp(-\sigma_j z) \sum_k m_{jk} \sigma_k \frac{\nu_j}{\nu_k} \\ & \times \exp[-\sigma_k(h - z)] \psi_k\left(x, r_k + \frac{\nu_j}{\nu_k} z + h - z\right) \end{aligned} \quad (9.112)$$

which is correct to order h^2 . This expression may be further approximated by

$$\begin{aligned} \psi_j(x+h, r_j) &= \exp(-\sigma_j h) \psi_j(x, r_j + h) \\ &+ \sum_k m_{jk} \sigma_k \frac{\nu_j}{\nu_k} \left[\frac{\exp(-\sigma_j h) - \exp(-\sigma_k h)}{\sigma_k - \sigma_j} \right] \psi_k \left(x, r_k + \frac{\nu_j}{\nu_k} h \right) \end{aligned} \quad (9.113)$$

which is accurate to $O[(\nu_k - \nu_j) \nu_j^{-1} h]$. Equation (9.113) is the basis of the Galactic Cosmic-Ray (GCR) Transport Code, HZETRN (Wilson and Badavi, 1986; Wilson et al., 1988; Wilson, Townsend, and Badavi, 1987a).

There are several quantities of interest that are now given. The integral fluence is given as

$$\phi_j(x, >E) = \int_{R_j(E)}^{\infty} \psi_j(x, r) dr \quad (9.114)$$

The energy absorption per gram is

$$D_j(x, >E) = \int_E^{\infty} A_j \psi_j[x, R_j(E)] dE \quad (9.115)$$

with the dose equivalent given as

$$H_j(x, >E) = A_j \int_E^{\infty} Q_F \psi_j[x, R_j(E)] dE \quad (9.116)$$

These quantities are used in shield design studies for protection against galactic cosmic rays.

9.8.1. Galactic cosmic-ray propagation. The semiempirical fragmentation cross sections (Wilson, Townsend, and Badavi, 1987b) for iron nuclei colliding with atmospheric nuclei are presented along with values obtained by the original model of Bowman, Swiatecki, and Tsang (1973), the results of the parameterization by Silberberg, Tsao, and Letaw (1983), and the experiments (for carbon targets) of Westfall et al. (1979) in figure 9.42. Quite reasonable values are obtained for these elemental fragmentation cross sections although considerable uncertainty exists in the neutron removal cross section. The light fragment production cross sections for the three models are shown in table 9.6. Clearly, vast differences in estimates of light fragment production exist between the three models. Unfortunately, there are no experimental data to resolve these differences.

The galactic cosmic-ray propagation in the Earth's atmosphere was calculated according to the present propagation model and shown with the fluence measurements of Webber and Ormes (1967) in figure 9.43. The differential spectrum of each species was taken as $1/(1000 + E)^{2.5}$ and elemental distributions according to Adams, Silberberg, and Tsao (1981) and Silberberg, Tsao, and Letaw (1983). These data (table 1 of Tsao et al., 1983) were renormalized within the usual categories of L ($3 < Z < 5$), M ($6 < Z < 9$), LH ($10 < Z < 14$), and H ($20 < Z < 28$) at the top of the atmosphere with extrapolations of the data of Webber and Ormes

(1967). The renormalized incident flux was used to calculate the results shown in figure 9.43.

Table 9.6. Light Fragment Production From Iron Nuclei Cross Sections

Element	Iron nuclei cross sections, mb, from—		
	Bowman, Swiatecki, and Tsang, 1973	Silberberg, Tsao, and Shapiro, 1976	Present
Li	10.6	130	19.2
Be	40.3	107	6.9
B	46.0	81	20.2
C	20.8	72	22.0

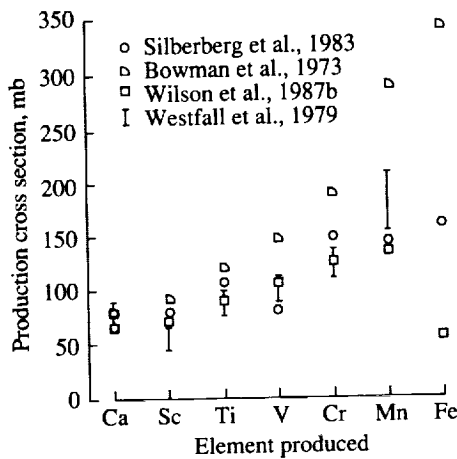


Figure 9.42. Fragment production cross sections of three models and experiments of Westfall et al. (1979).

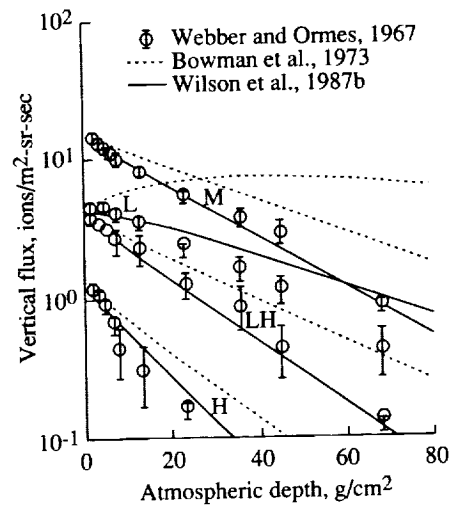


Figure 9.43. Cosmic-ray transition curves for ion energies above 360 MeV/nucleon at high latitudes for two fragmentation models and experiments of Webber and Ormes (1967). Input flux (Wilson et al., 1987b) was renormalized at top of atmosphere.

9.8.2. Discussion of results. It is clear that the original fragmentation model of Bowman, Swiatecki, and Tsang (1973) is oversimplified, a fact of which they have been fully aware. It appears that the present corrections to their model will allow “reasonable” results in the propagation of these broad categories. It is difficult to say as to what accuracy the calculations are performed because various compensating errors can be committed without changing the present result. This is especially important in view of the uncertainty in the neutron removal cross section as noted by comparing the three values of iron fragmentation cross sections in figure 9.42. Such an error in removal cross section could be hidden in the measurements of Webber and Ormes by either a change in total absorption or

various charge changing processes, which cannot be observed in the data of Webber and Ormes (1967).

The linear energy-transfer (LET) spectra of normal incident galactic ions are derived from equation (9.114) with

$$\phi_j(x, >S) = \phi_j(x, >E_{m_j}) - \phi_j(x, >E_{S_j}) \quad (9.117)$$

where E_{m_j} corresponds to the energy when $S_j(E)$ is maximum and E_{S_j} is the energy when $S_j(E_{S_j}) = S$. The LET spectra are calculated for the present Langley Research Center nuclear model (NUCFRAG) and are shown in figure 9.44 for several atmospheric depths and geomagnetic cutoff of 1.48 GeV/c. The nearly discontinuous steps in the LET spectra are located at the highest LET for each ion type and are located according to the ion charge squared. There is an observable steepening of the LET spectra as a function of atmospheric depth associated with the breakup of highly ionizing heavy nuclei into smaller nuclear fragments. The flux with LET greater than 200 MeV-cm²/g is reduced by 1 order of magnitude in penetrating to 60 g/cm² (approximately 63 000 ft), the highest cruise altitude of present day commercial aircraft. Similar results are shown for the fragmentation cross sections of the model of Bowman, Swiatecki, and Tsang (1973) in figure 9.45. It is clear in comparing results from the two models that considerable disagreement remains between them. It is further observed that considerable disagreement is expected in the midrange of the LET spectra for the cross sections of Silberberg, Tsao, and Shapiro (1976) in table 9.6. Clearly, a full solution to the problem of the LET spectra in the Earth's atmosphere must await the solution of the nuclear fragmentation problem. Meanwhile, the nuclear fragmentation model of the Langley Research Center presented in chapter 5 and used herein contains the principal physical mechanisms involved and is shown to give fair agreement with the data of Webber and Ormes (1967) as well as the fragmentation cross sections measured for iron beams on carbon targets by Westfall et al. (1979). For further comparison of this model with experiment, see Wilson, Townsend, and Badavi (1987a).

9.9. Analytic Benchmarks

In the present section, we address the question of GCR transport code validation. Ideally, validation should be accomplished with detailed transport data obtained from carefully planned and controlled experiments; unfortunately, there exists a paucity of such data. Although useful for comparison purposes, the atmospheric propagation measurements used previously (Wilson, Townsend, and Badavi, 1987a) are clearly not definitive because they consist of integral fluences of as many as 10 different nuclear species combined into a single datum. Although limited quantities of HZE dosimetry measurements from manned space missions (e.g., Skylab) are also available (Benton, Henke, and Peterson, 1977), numerous assumptions concerning the relationships between dosimeter locations and spacecraft shield thicknesses and geometry must be made to estimate astronaut doses using GCR codes. Because many of these assumptions may involve inherently large uncertainties (a factor of 2 or greater), it becomes difficult to attribute any differences to particular assumptions or approximations that may have been used in the analyses. Without definitive GCR transport measurements with which to

compare code predictions, other methods of validation must be considered. As noted by Wilson (1983) and Wilson et al. (1989a), there are several different versions of HZE transport codes available. When used with the same input spectra, interaction parameters, and boundary conditions, all should yield comparable results. The history of transport code development, however, suggests otherwise. For this reason, a realistic, nontrivial exact analytic solution to the simplified Boltzmann equation used to describe HZE transport has been formulated as an absolute standard for code comparison purposes.

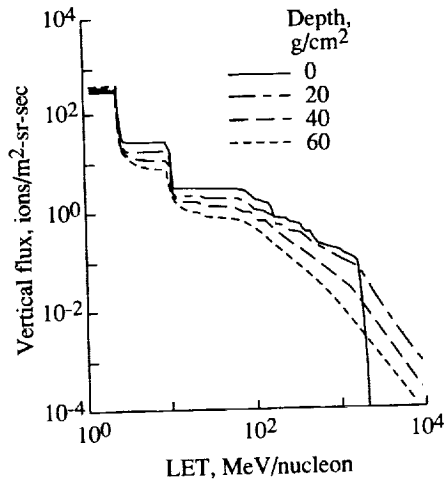


Figure 9.44. Cosmic-ray LET spectra at rigidity cutoff of 1.48 GV/c according to LaRC fragmentation model.

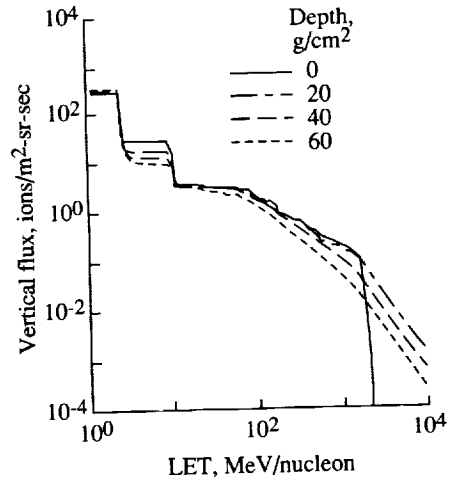


Figure 9.45. Cosmic-ray LET spectra at rigidity cutoff of 1.48 GV/c according to fragmentation model of Bowman, Swiatecki, and Tsang (1973).

For the benchmark problem, the incident spectrum is limited to a single ion type ($j = J$). Because the GCR spectrum for a typical ion is of the form

$$F(E) \sim E^{-\alpha} \quad (9.118)$$

where $\alpha \approx 2.5$, we choose the energy spectrum to be of similar functional form as

$$F_j(E) = \frac{\delta_{jJ}}{[R_J(E)]^2 \tilde{S}_j(E)} \quad (9.119)$$

Defining the characteristic variables as

$$\eta_j = x - R_j(E) \quad (9.120)$$

and

$$\xi_j = x + R_j(E) \quad (9.121)$$

equation (9.106) can be solved by the method of characteristics (Wilson, 1977a; Wilson and Townsend, 1988) to give

$$\psi_J(x, E) = \frac{\exp(-\hat{\sigma}_J x)}{[\nu_J x + R_J(E)]^2} \quad (9.122)$$

where

$$\psi_J(x, E) \equiv \tilde{S}_j(E) \phi_J(x, E) \quad (9.123)$$

and

$$\hat{\sigma}_J = \sigma_J(1 - m_{JJ}) \quad (9.124)$$

This is the trivial solution for the incident beam species. For $j < J$ (secondary fragments), it can be shown that

$$\psi_j(x, E) = \sigma_J m_{jJ} \frac{\nu_j}{\nu_J} I_j(x, E) \exp\left[\frac{-(\hat{\sigma}_j \eta_j + \hat{\sigma}_J \xi_j)}{2}\right] \quad (9.125)$$

where in terms of the exponential integral function $E_2(x)$ (see Abramowitz and Stegun, 1964),

$$I_j(x, E) = \frac{\exp[-b(\nu_J + \nu_j)\xi_j/2]}{\nu_J - \nu_j} \left[\frac{E_2(b\nu_j\xi_j)}{\nu_j\xi_j} - \frac{E_2(b\nu_J\xi_J)}{\nu_J\xi_J} \right] \quad (9.126)$$

for $j = J - 1$ and

$$b = \frac{\hat{\sigma}_J - \hat{\sigma}_j}{\nu_J - \nu_j} \quad (9.127)$$

Clearly, equations (9.126) and (9.127) are true for all values of j if $m_{kj} = 0$ for all values of $j < J$ (i.e., if the secondary fragments do not further fragment).

9.9.1. Benchmark results. The benchmark solution was calculated for an incident iron beam ($J = 26$) in an aluminum target, for which the input parameters are $\hat{\sigma}_{26} = 0.04568 \text{ cm}^2/\text{g}$, $\hat{\sigma}_{25} = 0.04260 \text{ cm}^2/\text{g}$, and $m_{25,26}\sigma_{26} = 0.00403 \text{ cm}^2/\text{g}$. Results of the GCR transport code simulation of this benchmark for the propagating incident iron beam and secondary manganese ($j = 25$) ions and the exact analytic predictions obtained from equations (9.122) and (9.125) are given in tables 9.7 and 9.8, respectively. It is clear from these tabulated results that the numerical solution methods developed previously (Wilson and Badavi, 1986; Wilson, Townsend, and Badavi, 1987a) are accurate in solving equation (9.106) for GCR transport to within about 1 percent. This indicates that any limitations to solving GCR transport problems accurately must focus upon the simplifying approximations used to obtain equation (9.106) as well as upon unresolved issues concerning the need to include the effects of multiple coulomb scattering, fragment momentum dispersion and, perhaps most importantly, the nature and quality of the input cross-section data bases. To illustrate this point, we are aware of only one heavy ion transport code (Wilson et al., 1984) which uses energy-dependent cross sections. Recent studies, however, suggest that fully energy-dependent cross

sections may be important for some transport code applications (Townsend and Wilson, 1988a).

Table 9.7. Benchmark Numerical Simulation and Analytic Solution for Iron Ions as Function of Ion Depth^a and Energy Into Aluminum Absorber

E, MeV/nucleon	$\psi_{\text{Fe}}(0, E)$		$\psi_{\text{Fe}}(10, E)$		$\psi_{\text{Fe}}(20, E)$	
	Numerical	Analytic	Numerical	Analytic	Numerical	Analytic
0.0198	1.394E5	1.394E5	4.334E-5	4.382E-5	6.942E-6	7.044E-6
0.1147	1.692E4	1.692E4	4.334E-5	4.381E-5	6.942E-6	7.044E-6
1.090	9.217E2	9.217E2	4.333E-5	4.379E-5	6.942E-6	7.043E-6
10.07	1.062E1	1.062E1	4.321E-5	4.360E-5	6.932E-6	7.027E-6
100.1	9.310E-3	9.310E-3	3.699E-5	3.718E-5	6.400E-6	6.478E-6
1 059	5.089E-6	5.089E-6	2.014E-6	2.019E-6	8.741E-7	8.799E-7
10 490	2.970E-8	2.970E-8	1.833E-8	1.833E-8	1.132E-8	1.132E-8

^aDepth is given in g/cm².

Table 9.8. Benchmark Numerical Simulation and Analytic Solution for Secondary Manganese Ions as Function of Ion Depth^a and Energy Into Aluminum Absorber

E, MeV/nucleon	$\psi_{\text{Mn}}(10, E)$		$\psi_{\text{Mn}}(20, E)$	
	Numerical	Analytic	Numerical	Analytic
0.0198	1.772E-6	1.780E-6	5.704E-7	5.768E-7
0.1147	1.772E-6	1.780E-6	5.704E-7	5.768E-7
1.090	1.772E-6	1.779E-6	5.704E-7	5.767E-7
10.07	1.767E-6	1.771E-6	5.696E-7	5.753E-7
100.1	1.504E-6	1.503E-6	5.242E-7	5.291E-7
1 059	7.797E-8	7.806E-8	6.880E-8	6.918E-8
10 490	7.004E-10	7.004E-10	8.728E-10	8.728E-10

^aDepth is given in g/cm².

9.9.2. Remarks. The need to develop suitable benchmarks for use in validating and comparing existing galactic cosmic-ray transport codes has been described and an exact nontrivial analytic benchmark solution presented. This benchmark solution was then used to establish computational accuracy for a previously published cosmic-ray transport code to within 1 percent. Finally, remaining unresolved issues in GCR transport were briefly described.

9.10. Methods for Energy-Dependent Cross Sections

The HZE transport methods presented herein are an extension of those presented elsewhere (Wilson, 1977a, 1977b, and 1983) and are based upon an analytical solution to the transport equation. In principle, these methods allow

for the calculations of absorbed dose caused by fragments of any species in each interaction generation for any arbitrary sequence of absorber layers. The present theory makes several approximations. In particular, projectile fragmentation parameters are obtained from semiempirical formulas (Silberberg, Tsao, and Shapiro, 1976; Silberberg, Tsao, and Letaw, 1983). Target fragmentation is neglected, and the energy loss of charged particles is accounted for by using the continuous slowing down approximation. The present calculations are one-dimensional; however, an extension to three dimensions is planned. Concurrently, an extensive experimental program is in progress at the Lawrence Berkeley Laboratory, BEVALAC, to measure the radiation fields of relativistic nuclei (Schimmerling, Curtis, and Vosburgh, 1977; Schimmerling et al., 1986 and 1989).

In this section, we compare our results with a Bragg ionization curve, obtained at the Lawrence Berkeley Laboratory, BEVALAC, for a neon beam at 670 MeV/nucleon. This example is used to present basic transport data in water. It also illustrates the need for obtaining a more accurate description of basic fragmentation parameters. In addition to the interests of the manned space program, the results are of importance to the radiation safety of high altitude aircraft (Wilson, 1981) and for radiation therapy using heavy ion beams (Schimmerling et al., 1986).

9.10.1. Depth-dose relations. The transport equation in the straight ahead approximation and neglecting target secondary fragments (Wilson, 1977a, 1977b, and 1983) may be written as

$$\left[\frac{\partial}{\partial x} - \frac{\partial}{\partial E} \tilde{S}_j(E) + \sigma_j(E) \right] \phi_j(x, E) = \sum_{k>j} m_{jk}(E) \sigma_k(E) \phi_k(x, E) \quad (9.128)$$

where $\phi_j(x, E)$ is the flux of ions of type j with atomic mass A_j at x with motion along the x axis and energy E in units of MeV/nucleon, $\sigma_j(E)$ is the corresponding macroscopic nuclear absorption cross section, $\tilde{S}_j(E)$ is the change in E per unit distance, and $m_{jk}(E)$ is the fragmentation parameter of ion j produced in collision by ion k . The form of the operator on the left-hand side of equation (9.128) is derived in chapter 6 (Wilson and Lamkin, 1975). Note that two terms arise from the energy differential operator. The first term arises from the scattering of particles to lower energy when traversing a distance Δx . The second term arises from contraction of the energy interval caused by the nonlinear relation between space and energy. The solution to equation (9.128) is to be found subject to boundary specification at $x = 0$ and arbitrary E as

$$\phi_j(0, E) = F_j(E) \quad (9.129)$$

and is usually called the incident beam spectrum.

The transport equation (9.128) is solved by the method of characteristics by using an iterative procedure (Wilson, 1983). The resultant series is used to

evaluate the dose given by

$$D(x) = \sum_j \int_0^\infty dE S_j(E) \phi_j(x, E) \quad (9.130)$$

which is evaluated for a monoenergetic beam of energy E_o . The stopping power is $S_j = A_j \tilde{S}_j$. The solution of the homogeneous equation resulting from setting the right-hand side of equation (9.128) to zero yields

$$D^{(0)}(x) = \frac{S_J(E_x) P_J(E_o)}{P_J(E_x)} \quad (9.131)$$

where

$$E_x = R_J^{-1}[R_J(E_o) - x] \quad (9.132)$$

is the residual energy and the P_j factors account for nuclear attenuation of the primary beam with

$$P_j(E) = \exp \left[- \int_0^E \frac{\sigma_j(e) de}{\tilde{S}_j(e)} \right] \quad (9.133)$$

The first perturbation to the homogeneous solution yields an additional contribution

$$D^{(1)}(x) \approx \sum_j A_j \nu_j (E_{u_j} - E_{l_j}) \left[\frac{m_{jJ}(E_o) \sigma_J(E_o) P_J(E_o)}{P_J(E_{l_j})} - \frac{m_{jJ}(E_{l_j}) \sigma_J(E_{l_j}) P_J(E_o)}{P_J(E_{l_j})} \right] \{[\sigma_j(E_o) - \sigma_j(E_o)]x\}^{-1} \quad (9.134)$$

where the energy spanned by these secondary ions is given by the "lower limit,"

$$E_{l_j} = R_j^{-1} \left\{ \frac{\nu_J}{\nu_j} [R_J(E_o) - x] \right\} \quad (9.135)$$

and "upper limit,"

$$E_{u_j} = R_j^{-1} \left[\frac{\nu_J}{\nu_j} R_J(E_o) - x \right] \quad (9.136)$$

A second perturbation of the homogeneous solution yields an additional contribution to the dose given by

$$D^{(2)}(x) \approx \sum_{jk} m_{jk} \sigma_k m_{kJ} \sigma_J \frac{A_j \nu_j (E'_{u_j} - E'_{l_j})}{(\nu_j - \nu_k)(\sigma_J - \sigma_k)x} \times \left[\frac{\exp(-\sigma_j x) - \exp(-\sigma_J x)}{\sigma_J - \sigma_j} - \frac{\exp(-\sigma_j x) - \exp(-\sigma_k x)}{\sigma_k - \sigma_j} \right] \quad (9.137)$$

where the energy range spanned by these tertiary ions is given by the upper limit,

$$E'_{u_j} = R_j^{-1} \left[\frac{\nu_J}{\nu_j} R_J(E_o) - x \right] \quad (9.138)$$

and the corresponding lower limit,

$$E'_{l_j} = R_j^{-1} \left\{ \frac{\nu_J}{\nu_j} [R_J(E_o) - x] \right\} \quad (9.139)$$

where m and σ of equation (9.137) are evaluated at E_o . The results of equations (9.138) and (9.139) are understood to be zero whenever the right-hand sides are negative. Equations (9.131) through (9.139) can be applied to various shield materials of uniform composition. Each specific application requires knowledge of the appropriate transport coefficients $S_j(E)$, σ_j , and m_{jk} .

9.10.2. Nuclear absorption. The nuclear absorption cross section σ_k is calculated from a quantum mechanical model of the heavy ion reaction (Wilson, 1975; Wilson and Costner, 1975). Appropriate solutions of the coupled-channel equations for high-energy composite particle scattering are used to calculate the elastic scattered amplitude from which total and absorption cross sections are derived (Wilson and Townsend, 1981; Townsend, Wilson, and Bidasaria, 1983a and 1983b).

The proton cross sections are shown in figures 9.46 and 9.47 for the oxygen constituent of water. The cross sections of ^{12}C projectiles at 2.1 GeV/nucleon onto various targets are shown in figure 9.48 with corresponding results for ^{16}O projectiles in figure 9.49. Additional values for ^{12}C projectiles (Townsend, 1982) are shown in table 9.9 along with experimental values from Jaros et al. (1978), Heckman et al. (1978), Cheshire et al. (1974), and Skrzypczak (1980). It is clear from the present results (Townsend, Wilson, and Bidasaria, 1983a and 1983b) that these cross sections are quite superior to our previous calculations (Wilson and Costner, 1975) and are in good agreement with the limited experimental data. Most nuclear cross sections appear better than 5 percent accurate regarding absorption mean-free paths, except for carbon nuclei where differences may be as large as 10 percent. Although little data are yet available on neon beams, the single datum ($A_T = 20$) in table 9.9 lends confidence that the cross-section data set presented in table 9.10, for light and medium mass ion mean-free paths in water, is quite accurate. Clearly, a great deal more experimental data are required for a complete evaluation. For convenience, we define a fundamental parameter associated with the absorption of a given ion in coming to rest. The average extinction coefficient is defined as

$$O_j(E) = \frac{\int_0^E \sigma_j(e) de / \tilde{S}_j(e)}{R_j(E)} \quad (9.140)$$

so that the survival probability is

$$P_J(E) = \exp [-O_j(E) R_j(E)] \quad (9.141)$$

The average extinction coefficients for several projectiles in water are shown in table 9.11. Values at intermediate projectile mass numbers can be found by numerical interpolation.

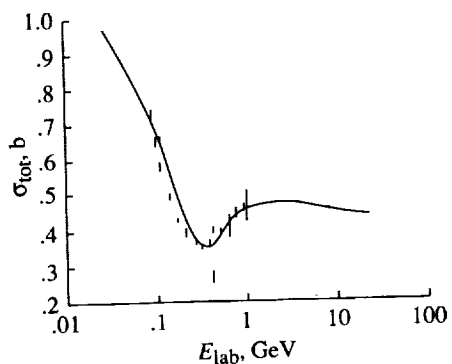


Figure 9.46. Total nuclear cross section for nucleons on oxygen targets.

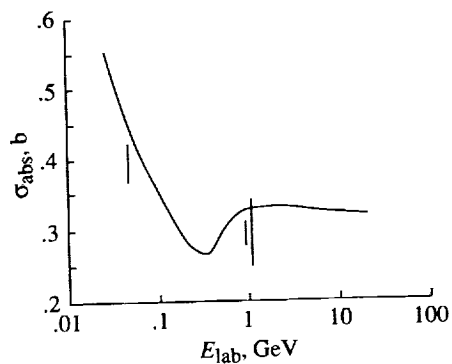


Figure 9.47. Absorption nuclear cross sections for nucleons on oxygen targets.

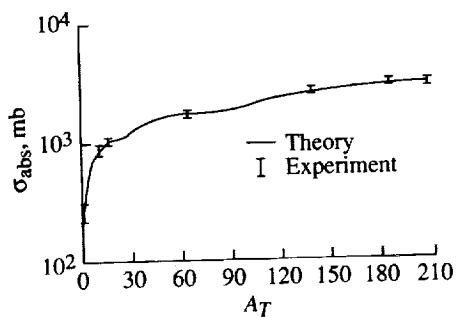


Figure 9.48. Absorption cross sections for ^{12}C projectiles at 2.1 GeV/nucleons onto various targets.

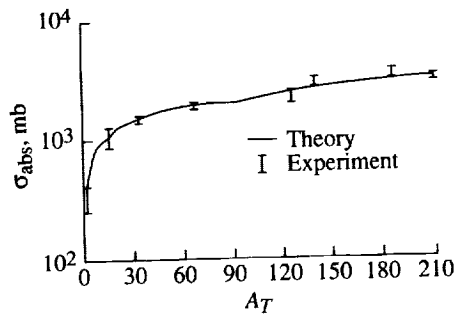


Figure 9.49. Absorption cross sections for ^{16}O projectiles at 2.1 GeV/nucleons onto various targets.

Table 9.9. Absorption Cross Sections for ^{12}C Projectiles Colliding With Various Target Nuclei

A_T	$\sigma_{\text{abs}}, \text{mb}$		$\sigma_{\text{exp}}, \text{mb}$
	Townsend, 1982	Wilson and Badavi, 1986	
0.87 GeV/nucleon			
12	819	763	^a 939 \pm 49
2.1 GeV/nucleon			
1	237	246	^a 269 \pm 14 ^b 258 \pm 21
12	839	781	^a 888 \pm 50 ^b 826 \pm 23
16	990	820	^b 1022 \pm 25
64	1727	1656	^b 1730 \pm 36
138	2519	2447	^c 2600 \pm 100
184	2924		^c 3000 \pm 100
208	3047	2969	^b 2960 \pm 65
3.6 GeV/nucleon			
12	836	779	^d 780 \pm 30
20	1059	902	^d 1040 \pm 60
64	1723	1653	^d 1700 \pm 90

^aJaros et al., 1978.^bHeckman et al., 1978.^cCheshire et al., 1974.^dSkrzypczak, 1980.

Table 9.10. Macroscopic Nuclear Absorption Cross Sections in Water

$E,$ MeV/nucleon	$\sigma_{\text{abs}}, m^{-1}$										
	^1H	^4He	^7Li	^9Be	^{12}C	^{16}O	^{20}Ne	^{27}Al	^{40}A	^{56}Fe	^{64}Cu
25	2.57	4.18	6.72	7.41	7.35	8.80	9.57	9.93	13.33	15.10	15.60
50	1.84	3.66	5.35	5.98	6.10	7.33	7.99	8.50	11.32	13.00	13.60
75	1.53	3.01	4.76	5.36	5.54	6.67	7.30	7.87	10.46	12.10	12.70
100	1.34	2.73	4.30	4.87	5.10	6.16	6.77	7.36	9.79	1.140	1.200
200	1.12	2.35	3.66	4.19	4.48	5.43	6.00	6.64	8.81	1.040	1.100
300	1.06	2.25	3.48	4.00	4.31	5.23	5.79	6.43	8.53	10.10	10.70
400	1.09	2.28	3.52	4.04	4.36	5.28	5.84	6.48	8.59	10.20	10.80
600	1.30	2.52	3.87	4.42	4.74	5.72	6.31	6.93	9.16	10.80	11.40
1000	1.43	2.67	4.10	4.68	4.98	6.01	6.61	7.22	9.52	1.115	1.180
2000	1.43	2.72	4.17	4.75	5.05	6.09	6.70	7.31	9.64	11.30	11.90
4000	1.39	2.70	4.12	4.69	5.01	6.03	6.64	7.27	9.57	11.20	11.80
10000	1.37	2.68	4.07	4.64	4.97	5.97	6.58	7.21	9.49	11.10	11.74

9.10.3. Nuclear fragmentation parameters. The basic fragmentation parameters for ions onto hydrogen targets are those of Silberberg, Tsao, and Shapiro (1976). These have been augmented by light fragment production cross sections of Bertini (Anon., 1968). The extension of the fragmentation on hydrogen targets to an arbitrary target nucleus is by a multiplicative scale factor (Silberberg, Tsao, and Shapiro, 1976) determined from the measured carbon fragmentation data at 1.05 GeV/nucleon (Lindstrom, et al., 1975) on various target nuclei. Silberberg, Tsao, and Shapiro suggested that the appropriate energy for evaluation of the hydrogen target fragmentation parameters is the total kinetic energy of the target ion as seen in the projectile rest frame. A second procedure was used herein in which the relative target velocity, rather than total kinetic energy, was assumed to be the appropriate parameter for evaluation of the hydrogen fragmentation cross sections (Schimmerling, Curtis, and Vosburgh, 1977), after which renormalization was used to ensure mass and charge conservation (velocity renormalized, VR). It is seen from figure 9.50 that reasonable estimates of the Bragg curve are obtained from these three terms provided by the present theory when the velocity-scaled renormalized parameters are used. Values for these fragmentation parameters (m_{ij} of equation (9.128)) are listed in table 9.12.

Contributions of the homogeneous term and the first and second perturbations with the velocity-scaled renormalized parameters are shown separately in figure 9.50 and show the rapid convergence of the series for the first 20 cm. The generally greater penetrability of successive generations of ion fragments indicates the need to consider the third perturbation term for depths beyond 30 cm.

Table 9.11. Average Extinction Coefficients for Ions in Water

E , MeV/nucleon	Extinction coefficient, m^{-1}										
	1H	4He	7Li	9Be	^{12}C	^{16}O	^{20}Ne	^{30}Si	^{40}Ar	^{50}V	^{60}Ni
25	2.57	4.18	6.72	7.41	7.34	8.79	9.56	10.42	13.30	14.55	15.35
50	2.24	4.00	6.11	6.77	6.79	8.15	8.87	9.79	12.46	13.67	14.52
75	1.94	3.62	5.55	6.19	6.28	7.54	8.22	9.19	11.65	12.82	13.69
100	1.73	3.31	5.13	5.75	5.89	7.08	7.74	8.73	11.04	12.19	13.05
200	1.35	2.72	4.25	4.81	5.04	6.09	6.70	7.72	9.71	10.81	11.67
300	1.21	2.50	3.89	4.44	4.70	5.69	6.28	7.31	9.17	10.24	11.09
400	1.16	2.41	3.74	4.27	4.56	5.52	6.10	7.13	8.93	10.00	10.85
600	1.18	2.40	3.72	4.25	4.55	5.51	6.08	7.11	8.90	9.98	10.83
1000	1.28	2.52	3.88	4.43	4.74	5.73	6.32	7.34	9.17	10.26	11.12
2000	1.38	2.64	4.06	4.63	4.93	5.95	6.55	7.57	9.46	10.55	11.42
4000	1.40	2.68	4.11	4.69	4.99	6.02	6.63	7.66	9.55	10.65	11.51
10000	1.38	2.69	4.10	4.67	4.99	6.00	6.61	7.65	9.53	10.62	11.48

Table 9.12. ^{20}Ne Fragmentation Parameters in Water for Velocity Scaling and Total Fragment Charge \bar{Z}_F

\bar{Z}_F	^{20}Ne fragmentation parameter at E , MeV/nucleon, of—				
	10	31.6	100	316	1000
0	1.313	0.968	0.962	1.289	2.160
1	3.141	2.176	1.975	2.377	3.181
2	0.971	0.713	0.587	0.525	0.652
3	0.035	0.023	0.031	0.046	0.082
4	0.042	0.026	0.037	0.050	0.079
5	0.003	0.013	0.035	0.061	0.074
6	0.005	0.026	0.080	0.121	0.111
7	0.020	0.048	0.090	0.106	0.083
8	0.193	0.225	0.289	0.267	0.183
9	0.303	0.268	0.217	0.195	0.158
10	0.008	0.158	0.122	0.077	0.060
11	0.043	0.009	0.002	0.000	0.000
$\bar{Z}_F \dots$	10.4	10.2	10.2	10.2	10.2

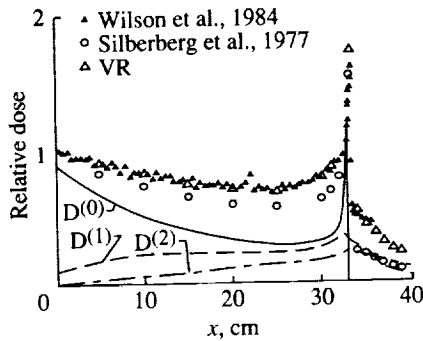


Figure 9.50. Energy deposition in water by ^{20}Ne ions at 670 MeV/nucleon.

It should be emphasized that the Bragg curve does not provide adequate information for radiation protection because of the probable large relative biological effectiveness (RBE) differences of the secondary components. The Bragg curve, however, is a readily accessible experimental quantity and any meaningful theory must reliably produce it. Since any variation from the Bragg curve may have important biological consequences caused by differences in RBE factors, a full evaluation requires more complete sets of experimental data. Clearly, evaluation of the next perturbation term is important, but an adequate knowledge of the specific fragmentation parameters is ultimately required to reduce the remaining error. This point is discussed further in section 9.11.

9.11. Laboratory Validation

Concurrent with the development of heavy ion transport codes and associated nuclear and atomic data bases are laboratory experiments with detailed measurements of ion type and energy within absorber layers of various materials. A detailed description of the experimental setup is given by Schimmerling et al. (1989) along with a description of experimental results for ^{20}Ne beams in water. The results were compared with a first collision transport code (HZESEC) developed by Curtis, Doherty, and Wilkinson (1969) and further improved by Schimmerling, Curtis, and Vosburgh (1977) by using the analysis code described by Shavers (1988) and Shavers et al. (1990). Generally, the transport calculations were found to be accurate to within 30 percent for depths less than ≈ 15 cm, and the effects of tertiary particles (not included in HZESEC) become significant at greater depths with differences up to a factor of 2. This is consistent with our earlier results (Wilson et al., 1984) in figure 9.50. The theory (HZESEC) based on the fragmentation cross sections of Silberberg, Tsao, and Shapiro generally underestimate the fragment fluence which is again consistent with our earlier conclusions (Wilson et al., 1984). A later version of this fragmentation shows a significant increase in the production of C, O, and F, whereas the production of N was reduced 7 percent.

The experimental methods and the corresponding elements of the theoretical model are depicted in figure 9.51. The experiment shown in the top view has the beam incident from the right passing through a multiwire proportional counter (B2WC2) before scattering on a lead foil which spreads the beam. The beam is bent with a bending magnet (B2M1) to align with the experiment axis where it first passes through a beam-monitoring scintillation counter (J). The beam focus

is monitored by a second multiwire proportional counter (MWPC) before passing through the monitoring ion chamber (IC1). The variable water column is the transport media being studied. The Bragg curve behind the water column is determined by using the ion chamber (IC2) for various water thicknesses. The time of flight column (TOF1 and TOF2) is enclosed by a vacuum chamber to minimize scattering losses in the detector system. The T_1 detector begins the timing clock which is stopped by a signal from T_2 . The differential energy detector (D_1 - D_3) responses are proportional to the particle charge squared. A second time of flight measurement is made with T_2 , T_3 , and T_4 for the most energetic particles. The theoretical model is represented by two parts. The nuclear fragmentation is represented by a one-dimensional transport code as depicted in the lower part of figure 9.51. Because of the large dimension of the experimental arrangement (several meters), even a small scattering is magnified in the large distances involved. The angular scattering is represented as a multiple-scattering acceptance model defining a solid angle of acceptance for the various (geometry-defining) detectors of the apparatus.

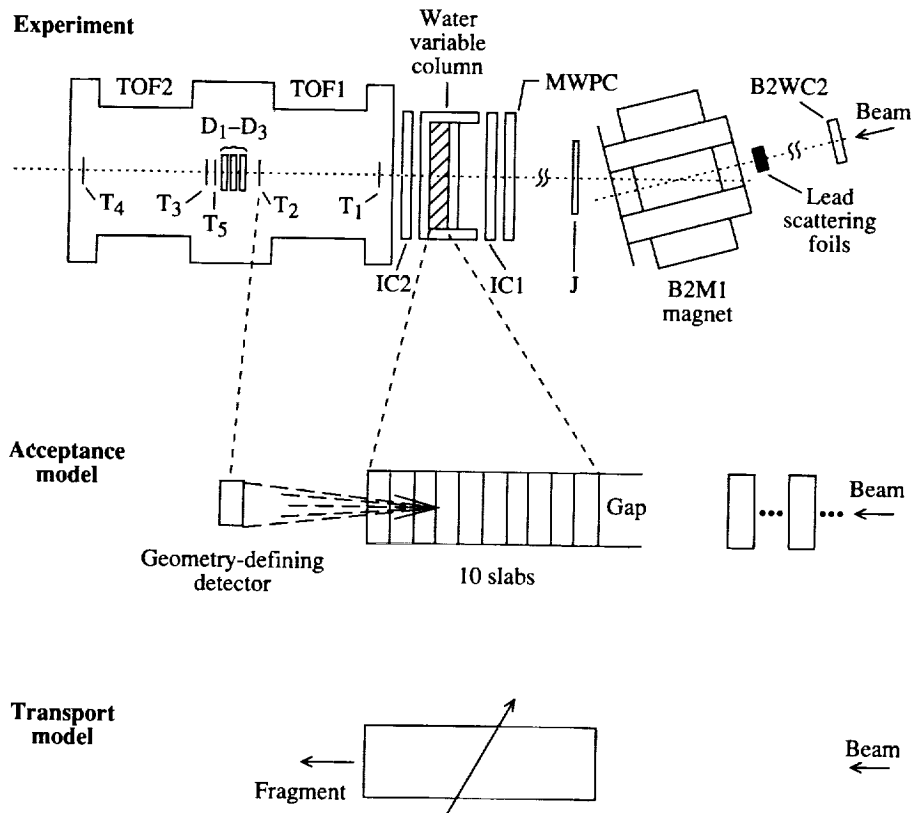


Figure 9.51. The fragmentation of ^{20}Ne at 670 MeV/nucleon as function of depth in water (from Shavers et al., 1990).

The acceptance functions for the experimental arrangement which accounts for the three-dimensional aspects of the transport (in part) were evaluated by the PROPAGATE code developed by Schimmerling et al. (1986) and is based

on their fundamental studies in multiple scattering (Wong et al., 1990). The analysis of the experimental data (Schimmerling et al., 1989; Schimmerling, 1990) was accomplished with the code (Shavers, 1988; Shavers et al., 1990) and equations (9.58), (9.59), (9.63), and (9.81) for the transport of an incident primary beam with a narrow Gaussian energy spread. A post-1984 version of the fragmentation model of Silberberg, Tsao, and Shapiro was used as opposed to an older version used in HZESEC (circa 1973).

The measured neon fluence spectra are shown with the calculated values in figure 9.52. The theoretical result multiplied by the acceptance of the detector at each value of LET is plotted as a histogram. In the plateau region of the Bragg curve, the agreement is within 1 percent of the maximum value. The differences at high LET are caused by neon isotopes which were not evaluated. The nuclear mean free path for the experiment was 16.5 g/cm^2 compared with the LBLBEAM value of 16.0 g/cm^2 . Figure 9.53 shows the first generation term for carbon fragments (dashed curve) and experimental data. Each isotope of carbon had applied its own acceptance. The fluence predictions are within 30 percent at water thicknesses up to 30 g/cm^2 . For increasing water depths and decreasing fragment mass, the number of possible reaction channels and higher-order interactions become more likely. The tertiary fluence contribution (solid curve) is included in figure 9.53, with the acceptance factor of the first generation term for each isotope being assumed. The integral fluence is shown in figure 9.54. Also shown are the results of HZESEC used in a previous analysis of the data (Shavers et al., 1990). The circles denote the experimental data, the solid line is the result of HZESEC (Shavers et al., 1990), the short-dashed line is the first generation term of LBLBEAM, and the long-dashed line is LBLBEAM including tertiary particles.

The threshold effect of the detector can be seen in the plots for the Be and B data, where the measured number of Be fragments falls significantly below all predictions for absorber thicknesses less than 25 g/cm^2 ; B seems to deposit signals above threshold at thicknesses greater than approximately 15 g/cm^2 .

The predictions of HZESEC are systematically lower than those of LBLBEAM, even for the lighter fragments, where differences in stopping-power calculations are not significant. One way in which such behavior could arise is if one of the models did not properly account for the lower mass isotopes. Such an effect may be a consequence of the fragmentation cross sections used by LBLBEAM, obtained from the latest semiempirical fits of Silberberg, Tsao, and Shapiro, which are larger than the older values used by HZESEC.

The difference between the first generation and the second generation predictions of LBLBEAM shows the expected effect of tertiary particles, which increases for lighter particles and thicker absorbers; however, the tertiary prediction of LBLBEAM is systematically greater than the data. One likely reason for this behavior must lie with the angular distribution of the fragments, which is not taken into account in the straight ahead approximation used by the present version of the transport code. Two effects contribute to the angular distribution of fragments. One effect is the compounding of the angular distributions of fragments emitted in nuclear interactions, which results in fewer fragments emitted into the narrow solid angle of the detector. The other effect is that the velocity

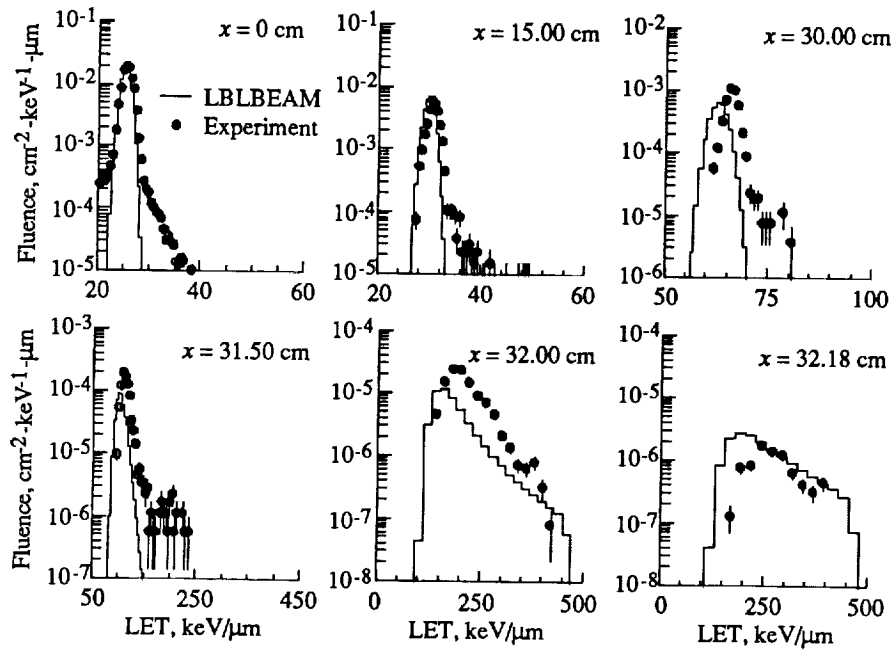


Figure 9.52. Differential fluence for neon nuclei incident on various thicknesses of water.

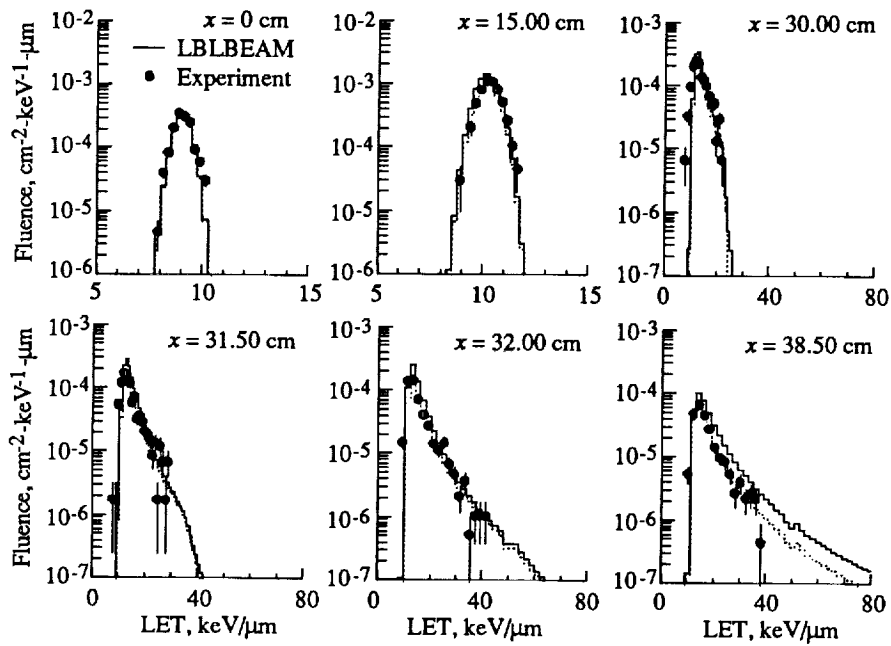


Figure 9.53. Differential fluence for carbon nuclei produced by neon nuclei incident on various thicknesses of water.

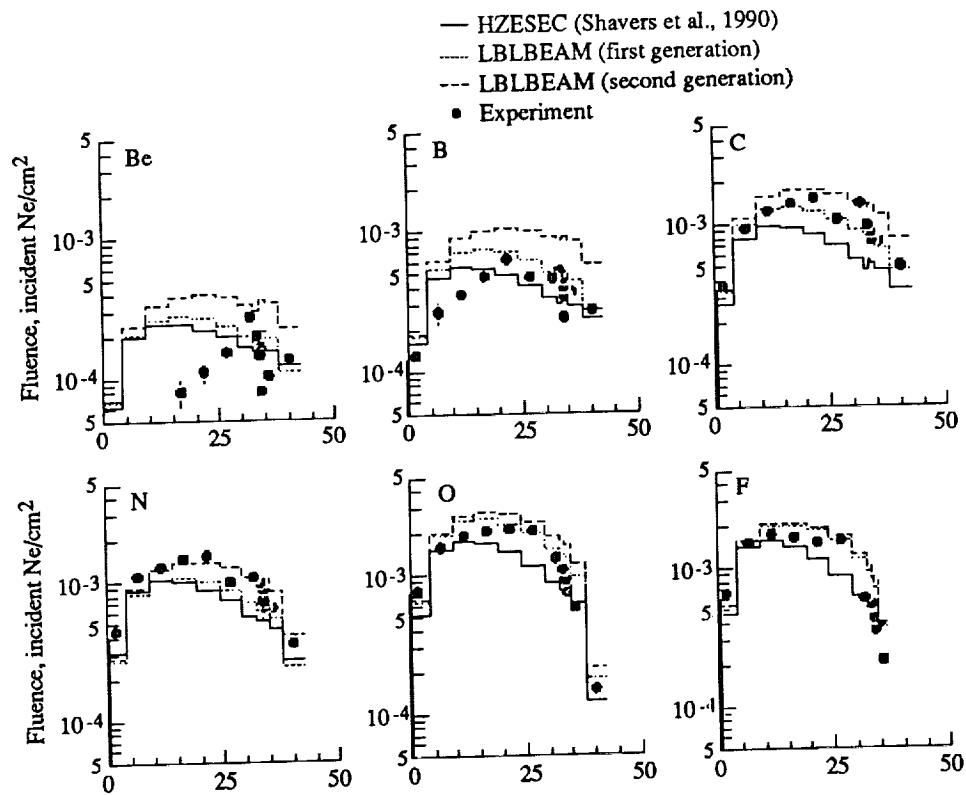


Figure 9.54. Integral fluence for all fragments produced by neon nuclei incident on various thicknesses of water as function of water column thickness.

of tertiary particles emerging from the absorber is no longer uniquely tied to the position at which it is produced and, therefore, the scattering calculation used for the acceptance is based on an erroneous amount of scattering material.

It is not immediately apparent that the more recent values of the cross sections are more accurate than the older values. The first-generation predictions of LBLBEAM may also be too large, if the geometric effects discussed do not result in significant differences between predicted secondary and tertiary particles. If this is the case, then the predictions of LBLBEAM would be expected to be below the measured data by an amount equivalent to the added contribution of tertiary particles, which is approximately the difference seen by HZESEC.

9.12. References

- Abramowitz, Milton; and Stegun, Irene A., eds., 1964: *Handbook of Mathematical Functions With Formulas, Graphs, and Mathematical Tables*. John Wiley & Sons, Inc. (Reprinted with corrections Dec. 1972.)
- Adams, J. H., Jr.; Silberberg, R.; and Tsao, C. H., 1981: *Cosmic Ray Effects on Microelectronics, Part I—The Near-Earth Particle Environment*. NRL Memo. Rep. 4506-Pt. I, U.S. Navy. (Available from DTIC as AD A103 897.)
- Allkofer, O. C.; and Heinrich, W., 1974: Attenuation of Cosmic Ray Heavy Nuclei Fluxes in the Upper Atmosphere by Fragmentation. *Nuclear Phys. B*, vol. B71, no. 3, pp. 429-438.
- Anon., 1968: *MECC-7 Intranuclear Cascade Code, 500-MeV Protons on O-16*. I4C Analysis Codes (Programmed for H. W. Bertini). Available from Radiation Shielding Information Center, Oak Ridge National Lab.
- Benton, E. V.; Henke, R. P.; and Peterson, D. D., 1977: Plastic Nuclear Track Detector Measurements of High-LET Particle Radiation on Apollo, Skylab, and ASTP Space Missions. *Nuclear Track Detect.*, vol. 1, no. 1, pp. 27-32.
- Bowman, J. D.; Swiatecki, W. J.; and Tsang, C. F., 1973: *Abrasion and Ablation of Heavy Ions*. LBL-2908, Lawrence Berkeley Lab., Univ. of California.
- Chatterjee, A.; Tobias, C. A.; and Lyman, J. T., 1976: Nuclear Fragmentation in Therapeutic and Diagnostic Studies With Heavy Ions. *Spallation Nuclear Reactions and Their Applications*, B. S. P. Shen and M. Merker, eds., D. Reidel Publ. Co., pp. 169-191.
- Cheshire, D. L.; Huggett, R. W.; Johnson, D. P.; Jones, W. V.; Rountree, S. P.; Verma, S. D.; Schmidt, W. K. H.; Kurz, R. J.; Bowen, T.; and Krider, E. P., 1974: Fragmentation Cross Sections of 2.1-GeV/Nucleon ^{12}C and ^{16}O Ions. *Phys. Review*, vol. 10, ser. D, no. 1, pp. 25-31.
- Curtis, S. B.; Doherty, W. R.; and Wilkinson, M. C., 1969: *Study of Radiation Hazards to Man on Extended Near Earth Missions*. NASA CR-1469.
- Davis, Leverett, Jr., 1960: On the Diffusion of Cosmic Rays in the Galaxy. *Proceedings of the Moscow Cosmic Ray Conference*, International Union of Pure and Applied Physics (Moscow), pp. 220-225.
- Ganapol, Barry D.; Townsend, Lawrence W.; and Wilson, John W., 1989: *Benchmark Solutions for the Galactic Ion Transport Equations: Energy and Spatially Dependent Problems*. NASA TP-2878.
- Ginzburg, V. L.; and Syrovatskii, S. I. (H. S. H. Massey, transl., and D. Ter Haar, ed.), 1964: *The Origin of Cosmic Rays*. Macmillan Co.
- Gloeckler, G.; and Jokipii, J. R., 1969: Physical Basis of the Transport and Composition of Cosmic Rays in the Galaxy. *Phys. Review Lett.*, vol. 22, no. 26, pp. 1448-1453.
- Heckman, H. H.; Greiner, D. E.; Lindstrom, P. J.; and Shwe, H., 1978: Fragmentation of ^4He , ^{12}C , ^{14}N and ^{16}O Nuclei in Nuclear Emulsion at 2.1 GeV/Nucleon," *Phys. Review*, vol. 17, ser. C, no. 5, pp. 1735-1747.

Transport Methods and Interactions for Space Radiations

- Jaros, J.; Wagner, A.; Anderson, L.; Chamberlain, O.; Fuzesy, R. Z.; Gallup, J.; Gorn, W.; Schroeder, L.; Shannon, S.; Shapiro, G.; and Steiner, H., 1978: Nucleus-Nucleus Total Cross Sections for Light Nuclei at 1.55 and 2.89 GeV/c per Nucleon. *Phys. Review*, vol. 18, ser. C, no. 5, pp. 2273-2292.
- Letaw, John; Tsao, C. H.; and Silberberg, R., 1983: Matrix Methods of Cosmic Ray Propagation. *Composition and Origin of Cosmic Rays*, Maurice M. Shapiro, ed., D. Reidel Publ. Co., pp. 337-342.
- Lezniak, J. A., 1979: The Extension of the Concept of the Cosmic-Ray Path-Length Distribution to Nonrelativistic Energies. *Astrophys. & Space Sci.*, vol. 63, no. 2, pp. 279-293.
- Lindstrom, P. J.; Greiner, D. E.; Heckman, H. H.; Cork, Bruce; and Bieser, F. S., 1975: *Isotope Production Cross Sections From the Fragmentation of ^{16}O and ^{12}C at Relativistic Energies*. LBL-3650 (NGR-05-003-513), Lawrence Berkeley Lab., Univ. of California.
- Peters, B., 1958: The Nature of Primary Cosmic Radiation. *Progress in Cosmic Ray Physics*, J. G. Wilson, ed., Interscience Publ., Inc., pp. 191-242.
- Schimmerling, Walter; Curtis, Stanley B.; and Vosburgh, Kirby G., 1977: Velocity Spectrometry of 3.5-GeV Nitrogen Ions. *Radiat. Res.*, vol. 72, no. 1, pp. 1-17.
- Schimmerling, Walter; Rapkin, Marwin; Wong, Mervyn; and Howard, Jerry, 1986: The Propagation of Relativistic Heavy Ions in Multielement Beam Lines. *Med. Phys.*, vol. 13, no. 2, pp. 217-228.
- Schimmerling, Walter; Miller, Jack; Wong, Mervyn; Rapkin, Marwin; Howard, Jerry; Spieler, Helmut G.; and Jarret, Blair V., 1989: The Fragmentation of 670A MeV Neon-20 as a Function of Depth in Water. *Radiat. Res.*, vol. 120, pp. 36-71.
- Schimmerling, Walter, 1990: Ground-Based Measurements of Galactic Cosmic Ray Fragmentation in Shielding. Paper presented at the 28th Plenary Meeting of COSPAR (The Hague, The Netherlands).
- Shavers, Mark R., 1988: Heavy-Ion Transport Code Calculations and Comparison With Experiment for a 670A MeV Accelerated Neon Beam Interacting With Water. M. E. Thesis, Univ. of Florida.
- Shavers, Mark R.; Curtis, Stanley B.; Miller, Jack; and Schimmerling, Walter, 1990: The Fragmentation of 670A MeV Neon-20 as a Function of Depth in Water. II. One-Generation Transport Theory. *Radiat. Res.*, vol. 124, pp. 117-130.
- Silberberg, R.; Tsao, C. H.; and Shapiro, M. M., 1976: Semiempirical Cross Sections, and Applications to Nuclear Interactions of Cosmic Rays. *Spallation Nuclear Reactions and Their Applications*, B. S. P. Shen and M. Merker, eds., D. Reidel Publ. Co., pp. 49-81.
- Silberberg, R.; Tsao, C. H.; and Letaw, John R., 1983: Improvement of Calculations of Cross Sections and Cosmic-Ray Propagation. *Composition and Origin of Cosmic Rays*, Maurice M. Shapiro, ed., D. Reidel Publ. Co., pp. 321-336.

- Skrzypczak, E., 1980: Cross-Sections for Inelastic ^4He and ^{12}C -Nucleus Collisions at 4.5 GeV/c/N Incident Momentum. *Proceedings of the International Conference on Nuclear Physics, Volume 1, Abstracts*, LBL-11118, (Contract No. W-7405-ENG-48), Lawrence Berkeley Lab., Univ. of California, p. 575.
- Townsend, Lawrence W., 1982: *Harmonic Well Matter Densities and Pauli Correlation Effects in Heavy Ion Collisions*. NASA TP-2003.
- Townsend, Lawrence W.; Wilson, John W.; and Bidasaria, Hari B.; 1983a: *Heavy-Ion Total and Absorption Cross Sections Above 25 MeV/Nucleon*. NASA TP-2138.
- Townsend, Lawrence W.; Wilson, John W.; and Bidasaria, Hari B., 1983b: *Nucleon and Deuteron Scattering Cross Sections From 25 MeV/Nucleon to 22.5 GeV/Nucleon*. NASA TM-84636.
- Townsend, L. W.; and Wilson, J. W., 1988a: An Evaluation of Energy-Independent Heavy Ion Transport Coefficient Approximations. *Health Phys.*, vol. 54, no. 4, pp. 409-412.
- Townsend, L. W.; and Wilson, J. W., 1988b: Nuclear Cross Sections for Hadronic Transport. *Trans. American Nuclear Soc.*, vol. 56, pp. 277-279.
- Townsend, Lawrence W.; Ganapol, Barry D.; and Wilson, John W., 1989: Benchmark Solutions for Heavy Ion Transport Code Validation. *Abstracts of Papers for the Thirty-Seventh Annual Meeting of the Radiation Research Society and Ninth Annual Meeting of the North American Hyperthermia Group*, Radiation Research Soc., p. 126.
- Tsao, C. H.; Silberberg, R.; Adams, J. H., Jr.; and Letaw, J. R., 1983: Cosmic Ray Transport in the Atmosphere—Dose and LET-Distributions in Materials. *IEEE Trans. Nuclear Sci.*, vol. NS-30, pp. 4398-4404.
- Webber, W. R.; and Ormes, J. F., 1967: Cerénkov-Scintillation Counter Measurements of Nuclei Heavier Than Helium in the Primary Cosmic Radiation. 1. Charge Composition and Energy Spectra Between 200 MeV/Nucleon and 5 beV/Nucleon. *J. Geophys. Res.—Space Phys.*, vol. 72, no. 23, pp. 5957-5976.
- Westfall, G. D.; Wilson, Lance W.; Lindstrom, P. J.; Crawford, H. J.; Greiner, D. E.; and Heckman, H. H., 1979: Fragmentation of Relativistic ^{56}Fe . *Phys. Review*, vol. 19, ser. C, no. 4, pp. 1309-1323.
- Wilson, John W., 1975: Composite Particle Reaction Theory. Ph.D. Diss., College of William and Mary in Virginia.
- Wilson, John W.; and Costner, Christopher M., 1975: *Nucleon and Heavy-Ion Total and Absorption Cross Section for Selected Nuclei*. NASA TN D-8107.
- Wilson, John W.; and Lamkin, Stanley L., 1975: Perturbation Theory for Charged-Particle Transport in One Dimension. *Nuclear Sci. & Eng.*, vol. 57, no. 4, pp. 292-299.
- Wilson, John W., 1977a: *Analysis of the Theory of High-Energy Ion Transport*. NASA TN D-8381.
- Wilson, J. W., 1977b: Depth-Dose Relations for Heavy Ion Beams. *Virginia J. Sci.*, vol. 28, no. 3, pp. 136-138.

Transport Methods and Interactions for Space Radiations

- Wilson, J. W., 1981: Solar Radiation Monitoring for High Altitude Aircraft. *Health Phys.*, vol. 41, no. 4, pp. 607-617.
- Wilson, J. W.; and Townsend, L. W., 1981: An Optical Model for Composite Nuclear Scattering. *Canadian J. Phys.*, vol. 59, no. 11, pp. 1569-1576.
- Wilson, John W., 1983: *Heavy Ion Transport in the Straight Ahead Approximation*. NASA TP-2178.
- Wilson, John W.; Townsend, L. W.; Bidasaria, H. B.; Schimmerling, Walter; Wong, Mervyn; and Howard, Jerry, 1984: ^{20}Ne Depth-Dose Relations in Water. *Health Phys.*, vol. 46, no. 5, pp. 1101-1111.
- Wilson, John W.; and Badavi, F. F., 1986: Methods of Galactic Heavy Ion Transport. *Radiat. Res.*, vol. 108, 1986, pp. 231-237.
- Wilson, J. W.; Townsend, L. W.; and Badavi, F. F., 1987a: Galactic HZE Propagation Through the Earth's Atmosphere. *Radiat. Res.*, vol. 109, no. 2, pp. 173-183.
- Wilson, John W.; Townsend, Lawrence W.; and Badavi, F. F., 1987b: A Semiempirical Nuclear Fragmentation Model. *Nuclear Instrum. & Methods Phys. Res.*, vol. B18, no. 3, pp. 225-231.
- Wilson, John W.; and Townsend, L. W., 1988: A Benchmark for Galactic Cosmic-Ray Transport Codes. *Radiat. Res.*, vol. 114, no. 2, pp. 201-206.
- Wilson, John W.; Townsend, Lawrence W.; Ganapol, Barry D.; and Lamkin, Stanley L., 1988: Methods for High-Energy Hadronic Beam Transport. *Trans. American Nuclear Soc.*, vol. 56, pp. 271-272.
- Wilson, John W.; Lamkin, Stanley L.; Farhat, Hamidullah; Ganapol, Barry D.; and Townsend, Lawrence W., 1989a: *A Hierarchy of Transport Approximations for High Energy Heavy (HZE) Ions*. NASA TM-4118.
- Wilson, John W.; Townsend, Lawrence W.; Nealy, John E.; Chun, Sang Y.; Hong, B. S.; Buck, Warren W.; Lamkin, S. L.; Ganapol, Barry D.; Khan, Ferdous; and Cucinotta, Francis A., 1989b: BRYNTRN: *A Baryon Transport Model*. NASA TP-2887.
- Wong, Mervyn; Schimmerling, Walter; Phillips, Mark H.; Ludewigt, Bernhard A.; Landis, Donald A.; Walton, John T.; and Curtis, Stanley B., 1990: The Multiple Coulomb Scattering of Very Heavy Charged Particles. *Med. Phys.*, vol. 17, no. 2, pp. 163-171.

Chapter 10

Target Fragment and Nuclear Recoil Transport

10.1. Introduction

The interaction of energetic charged particles with matter encompasses a broad host of physical processes of both atomic and nuclear origins. For biological systems, the patterns of local-event distributions are of essential concern because biological response is dominated by physical/chemical changes in localized sensitive volumes (Rossi, 1959). In principle, one can specify the fields within the material from which specific-event rates at the sensitive sites can be evaluated. Lacking from such a description are spatially and temporally correlated events which may bear some importance in some sensitive systems. In practice, however, the field quantities are never specified completely, thus leading to questions about the adequacy of such a reduced expression.

In most field calculations stopping power is customarily used without regard to how the energy lost to the medium is actually mediated. Inherent in such a description is that the details concerning the track structure formed by the passage of the particles is unimportant to system response. A suggestion long ago by Schaefer (1952) and experimental evidence now testify to the importance of track structure to biological consequences (Katz et al., 1971; Watt, 1989). The field of microdosimetric techniques has developed in response to the need to quantify the track structure of field quantities (Rossi, 1959). The importance of track structure is dependent on site size (Chatterjee, Maccabee, and Tobias, 1973) and is most effective for sites that are less than $1 \mu\text{m}$.

As an energetic charged particle passes through a region of material, it will suffer many atomic/molecular interactions to which only small amounts of energy are given to ionization/excitation at each interaction site. Secondary electrons and photons propagate the energy from the initial loss site and cause a broadening of the particle track (Katz et al., 1971; Chatterjee, Maccabee, and Tobias, 1973; Kellerer and Chmelevsky, 1975; Paretzke, 1988). In this way, the passing particle can affect a localized volume, even though the path is remote to the localized volume itself. Occasionally, the passing energetic particle undergoes a nuclear reaction in which a large amount of its kinetic energy is given to the nucleus of the struck atom. Often, several nuclear disintegration fragments (nuclear stars) are produced of sufficient energy to form well-defined tracks emanating from the interaction site. These fragments may also affect localized volumes remote to the initial trajectory of the particle.

In the past it was assumed that the radiobiological effectiveness (RBE) was related to the linear energy transfer (LET). Thus, risk assessment used LET-dependent quality factors (QF's) evaluated directly from field quantities. However, if biological response is governed by the energy deposit in small localized volumes, then biological risk is related to energy deposits within such volumes (Watt, 1989). The local energy deposited is related to lineal energy transfer, and RBE is not LET-dependent but rather depends on the lineal energy (energy absorbed by a small volume divided by the average chord of the volume). Indeed, recommended

QF's in the future (e.g., ICRU 40 (Anon., 1986)) may well be assumed to be a function of lineal energy and not LET. Thus, a current need is then to understand more fully the relationship between field quantities and microdosimetric quantities. If microdosimetry is the way of the future, such an understanding will be essential to the future assessment of radiation risk in such a complex radiation field as the space environment.

In the present work, we endeavor to evaluate the field quantities for the nuclear disintegration products formed in nuclear reactions in tissue. We consider explicitly the localized energy deposit associated with microdosimetric measurement. Effects of secondary electron fields are not considered herein but will be considered separately. The effect of secondary electrons was considered by Kellerer and Chmelevsky (1975), who showed that α -particles below 10 MeV and ^{16}O less than 12 MeV have negligible δ -ray contributions for site sizes 1 μm and larger. It is clear from their analysis that application to target fragmentation products in tissue limits the site size of the present work to the order of 1 μm or larger. We also address several related issues of target recoil and fragmentation effects on biological systems (Wilson, Townsend, and Badavi, 1987).

10.2. Target Fragment Transport

In chapter 6 we derived an expression for ion fluence in a region bounded by a surface $\vec{\Gamma}$ as (Wilson, 1977)

$$\begin{aligned} \phi_j(\vec{x}, \vec{\Omega}, E) &= \frac{S_j(E_\gamma) P_j(E_\gamma)}{S_j(E) P_j(E)} \phi_j(\vec{\Gamma}_{\Omega, x}, \vec{\Omega}, E_\gamma) \\ &+ \sum_k \int_E^{E_\gamma} dE' \frac{A_j P_j(E')}{S_j(E) P_j(E)} \int_{E'}^\infty dE'' \int d\vec{\Omega}' r_{jk}(E', E'', \vec{\Omega}, \vec{\Omega}') \\ &\times \phi_k \left\{ \vec{x} + [R_j(E) - R_j(E')] \vec{\Omega}, \vec{\Omega}', E'' \right\} \end{aligned} \quad (10.1)$$

where $E_\gamma = R_j^{-1}[\rho - d + R_j(E)]$, $\rho = \vec{\Omega} \cdot \vec{x}$, and $d = \vec{\Omega} \cdot \vec{\Gamma}_{\Omega, x}$. The integral over E' is a summation over the collisional source distribution from the boundary ($E' = E_\gamma$) to the point \vec{x} ($E' = E$). We approximate equation (10.1) in a perturbation series by taking

$$\phi_k(\vec{x}', \vec{\Omega}', E'') \approx \frac{S_k(E''_\gamma) P_k(E''_\gamma)}{S_k(E'') P_k(E'')} \phi_k(\vec{\Gamma}_{\Omega', x'}, \vec{\Omega}', E''_\gamma) \quad (10.2)$$

where

$$\vec{x}' = \vec{x} + [R_j(E) - R_j(E')] \vec{\Omega}$$

$$\rho' = \vec{\Omega}' \cdot \vec{x}'$$

$$d' = \vec{\Omega}' \cdot \vec{\Gamma}_{\Omega', x'}$$

$$E''_\gamma = R_k^{-1}[\rho' - d' + R_k(E'')]$$

We specialize to a unidirectional monoenergetic beam at the boundary as

$$\phi_k(\vec{\Gamma}, \vec{\Omega}, E) = \delta_{sM} \delta(E - E_p) \delta(\vec{\Omega} - \vec{\Omega}_p) \quad (10.3)$$

for which equation (10.1) may be simplified to

$$\begin{aligned} \phi_j(\vec{x}, \vec{\Omega}, E) = & \exp[-\sigma_j(\rho - d)] \frac{S_j(E_\gamma)}{S_j(E)} \delta_{jM} \delta(E_\gamma - E_p) \delta(\vec{\Omega} - \vec{\Omega}_p) \\ & + \int_E^{E_\gamma} dE' \frac{A_j}{S_j(E)} \exp\{-\sigma_j[R_j(E') - R_j(E)]\} \\ & \times \exp[-\sigma_m(\rho' - d')] \sigma_{jM}(E', E_p'', \vec{\Omega}, \vec{\Omega}_p) \end{aligned} \quad (10.4)$$

where $E_p'' = R_k^{-1}[R_k(E_p) - \rho' - d']$. If we restrict ourselves to a small volume of material ($\sigma_j(\rho - d) < 0.01$), then

$$\begin{aligned} \phi_j(\vec{x}, \vec{\Omega}, E) = & \frac{S_j(E_\gamma)}{S_j(E)} \delta_{jM} \delta(E_\gamma - E_p) \delta(\vec{\Omega} - \vec{\Omega}_p) \\ & + \int_E^{E_\gamma} dE' \frac{A_j}{S_j(E)} [\sigma_{jM}^P(E', E_p'', \vec{\Omega}, \vec{\Omega}_p) + \sigma_{jM}^T(E', E_p'', \vec{\Omega}, \vec{\Omega}_p)] \end{aligned} \quad (10.5)$$

where the projectile and target fragment terms are shown separately. The projectile term has a contribution only at energies near E_p'' whereas the target term has a contribution only for $E \ll E_p''$. At high energy we have

$$E_\gamma \approx E + \frac{1}{A_j} S_j(E) (\rho - d) \quad (10.6)$$

in which case

$$\begin{aligned} \phi_j(\vec{x}, \vec{\Omega}, E) \approx & \delta_{jM} \delta(E - E_p) \delta(\vec{\Omega} - \vec{\Omega}_p) \\ & + \sigma_{jM}^P(E, E_p, \vec{\Omega}, \vec{\Omega}_p) (\rho - d) \\ & + \int_E^{E_\gamma} dE' \frac{A_j}{S_j(E)} \sigma_{jM}^T(E', E_p, \vec{\Omega}, \vec{\Omega}_p) \end{aligned} \quad (10.7)$$

The absorbed-energy density is then

$$\begin{aligned} D(\vec{x}) = & \sum_j \int_0^\infty dE \int d\vec{\Omega} S_j(E) \phi_j(\vec{x}, \vec{\Omega}, E) \\ = & S_M(E_p) + \sum_j S_j(E_p) m_{jM}^P \sigma_m(\rho - d) \\ & + \sum_j \int_0^\infty A_j dE \int_E^{E_\gamma} dE' \sigma_{jM}^T(E', E_p, \vec{\Omega}, \vec{\Omega}_p) \end{aligned} \quad (10.8)$$

The first term clearly dominates the second. The fact that the third term is nonnegligible results from the large stopping power of the low-energy fragments represented by the third term compared with $S_M(E_p)$, which also results in all their energy being deposited locally. It is clear on this basis that equation (10.7) may be reduced to

$$\phi_j(\vec{x}, \vec{\Omega}, E) \approx \delta_{jM} \delta(E - E_p) \delta(\vec{\Omega} - \vec{\Omega}_p) + \int_E^{E_\gamma} dE' \frac{A_j}{S_j(E')} \sigma_{jM}^T(E', E_p, \vec{\Omega}, \vec{\Omega}_p) \quad (10.9)$$

Accordingly, the high-energy beam exposure of a small object can be treated by evaluating the direct ionization of the primary particles and the transport of low-energy fragments produced uniformly throughout the volume. This is represented in equation (10.9). We now consider some applications of target fragment transport.

10.3. Neutron KERMA

An interesting quantity concerning nuclear recoil and fragments is the neutron KERMA. The KERMA is a physically meaningful quantity at low-neutron energies where the kinetic energies of the produced charged particles are sufficiently low that they come to rest near their production site. Thus, equilibrium is easily established and the dose and KERMA are almost numerically equal. The kinetic energies of protons produced in tissue by high-energy neutrons are deposited far from the production site, and equilibrium is difficult to establish for high-neutron energies so that KERMA is numerically greater than dose. The KERMA is shown for various tissue constituents in figures 10.1 to 10.4 with an explanatory key for these figures given in chart A. Also shown are results from others (MacFarlane et al., 1978; Dimbylow, 1982; Caswell and Coyne in Anon., 1977a; Herling et al., 1981; Wells, 1979; Brenner, 1983; Alsmiller and Barish, 1976). Clearly, the KERMA from our data base is reasonable and reflects on the veracity of our charged-particle data base, which is based on the same models.

Chart A. Key to figures 1-4

Symbol	Source
┌─┐	MacFarlane et al., 1978
□	Dimbylow, 1982
○	Caswell and Coyne in Anon., 1977a
▽	Herling et al., 1981
★	Wells, 1979
⊙	Brenner, 1983
△	Alsmiller and Barish, 1976
●	Present data

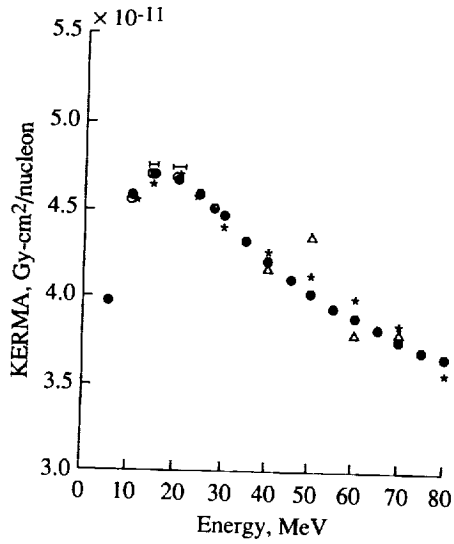


Figure 10.1. Neutron KERMA in hydrogen. See key given in chart A.

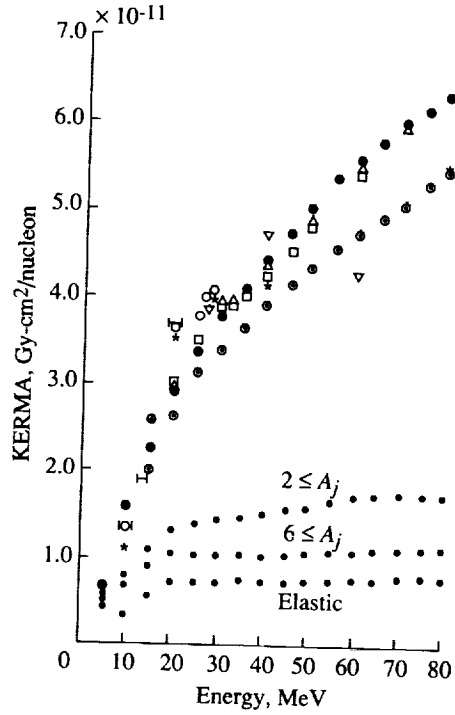


Figure 10.2. Neutron KERMA in carbon. See key given in chart A.

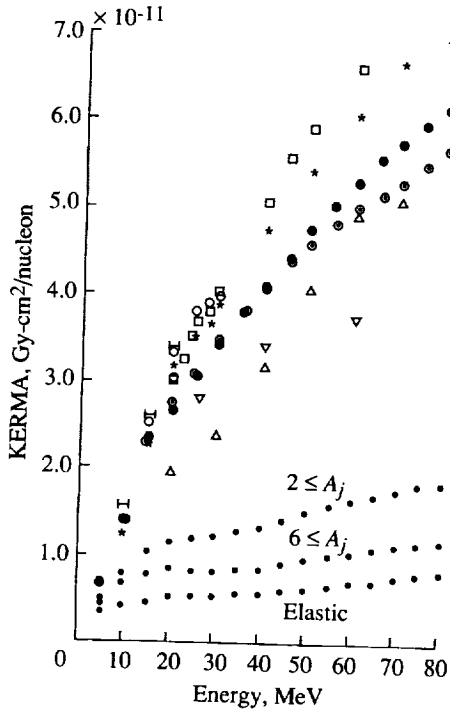


Figure 10.3. Neutron KERMA in nitrogen. See key given in chart A.

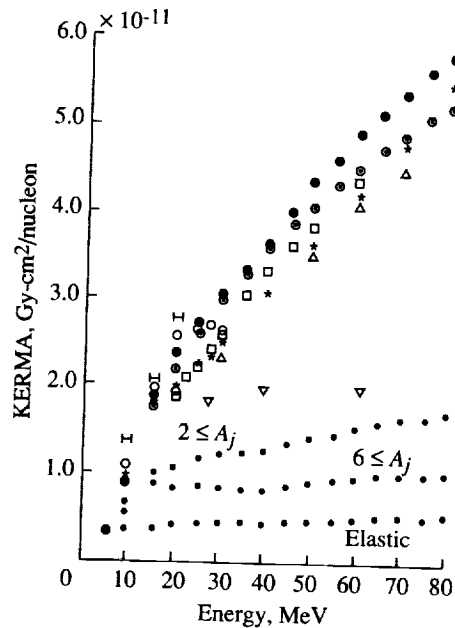


Figure 10.4. Neutron KERMA in oxygen. See key given in chart A.

10.4. Effects in Conventional Risk Assessment

Biological risks are related to the local energy deposited by the passage of energetic ions. The ionization energy loss is on the order of $0.2Z^2$ keV/ μ for a passing relativistic ion of charge Z . Some ions produce nuclear reactions in which 10 to 100 MeV are released (per event) locally as secondary nuclear fragments. The average energy transfer rate is $0.05A^{2/3}$ keV/ μ , where A is the ion atomic weight. Because the quality factor of the fragments is usually taken as 20, the risk associated with direct atomic ionization is on the order of the risk associated with the nuclear events for incident low-charge ions ($Z < 5$), although the risk is dominated by the direct ionization for high charge ($Z \gg 5$). At a sufficiently low energy, the direct ionization always dominates the biological risk independent of the ion charge and mass. In this chapter, we quantify these various contributions to biological risk using quality factors presently in force (ICRP 26 (Anon., 1977b)) and evaluate the effects of newly proposed quality factors (ICRU 40 (Anon., 1986)).

10.4.1. Theoretical considerations. We consider a volume of tissue through which a monoenergetic ion fluence $\phi_z(E_p)$ of energy E_p has passed and then evaluate the energy absorbed by the media in the passage. There are several processes by which the ion gives up energy to the media: electronic excitation/ionization, nuclear coulomb elastic scattering, nuclear elastic scattering, and nuclear reaction. The electronic excitation/ionization is contained in the stopping power that is evaluated by methods discussed in relation to equation (10.8) (Wilson et al., 1984). The nuclear coulomb elastic scattering is highly peaked at low momentum transfer, and the energy transfers per event of a few hundred electron volts or less are typical (Wilson, Stith, and Stock, 1983). The nuclear elastic scattering energy transfer is on the order of 1 MeV or less and can be neglected in comparison with reactive processes. A model for proton-induced reactions in tissue constituents has been given elsewhere (Wilson, Townsend, and Khan, 1989) and will provide the basis for the present evaluation.

The secondary-particle radiation fields $\phi_j(E)$ are given as

$$\phi_j(E) = \frac{1}{S_j(E)} \int_E^\infty \zeta_j(E') dE' \quad (10.10)$$

where $S_j(E)$ is the stopping power and $\zeta_j(E')$ denotes the particle source energy distributions given as

$$\zeta_j(E') = \rho \sigma_j(E_p) f_j(E') \phi_z(E_p) \quad (10.11)$$

where ρ is the nuclear density, $\sigma_j(E_p)$ is the fragmentation cross section, and $f_j(E)$ is the fragment spectrum as discussed elsewhere (Wilson, Townsend, and Khan, 1989). The total absorbed energy is approximately

$$D_Z(E_p) = S_Z(E_p) \phi_Z(E_p) + \sum_j \int_0^\infty S_j(E) \phi_j(E) dE \quad (10.12)$$

Equation (10.12) may be written as

$$D_Z(E_p) = S_Z(E_p) \phi_Z(E_p) + \sum_j E_j \sigma_j(E_p) \rho \phi_Z(E_Z) \quad (10.13)$$

where E_j is the average energy associated with each spectral distribution $f_j(E)$. Similarly, the dose equivalent is

$$H_Z(E_p) = Q_Z(E_p) S_Z(E_p) \phi_Z(E_p) + \sum_j \bar{Q}_{F_j} E_j \sigma_j(E_p) \rho \phi_Z(E_p) \quad (10.14)$$

where \bar{Q}_{F_j} is the spectral-averaged quality factor of the j th secondary particle (Shinn, Wilson, and Ngo, 1990). The sum over j will include the usual "evaporation" products, including the low-energy protons.

We now evaluate equation (10.13) for the conventional LET-dependent quality factor $Q(L)$ (ICRP 26 (Anon., 1977b)) and the lineal-energy-dependent (y) quality factor $Q(y)$ recently proposed (ICRU 40 (Anon., 1986)). To implement the $Q(y)$, we used appendix B of ICRU 40 (Anon., 1986), in which the lineal-energy distributions are assumed to be linearly dependent on y at a fixed LET. Some of the problems of this assumption have been discussed by Townsend, Wilson, and Cucinotta (1987), which we circumvent herein by assuming Q to be greater than or equal to 1. The spectral-averaged quality factors of the conventional method (ICRP 26 (Anon., 1977b)) and proposed method (ICRU 40 (Anon., 1986)) are shown in table 10.1 for the various isotopes produced in ^{16}O reactions. The proposed values are generally greater than the conventional values, except for the heavier fragments where the proposed values are substantially smaller. The conventional average quality factors show, generally, a weak isotope dependence, whereas the proposed average quality factors show a strong isotope dependence, with neutron-rich isotopes being the most biologically damaging.

10.4.2. Results and discussion. The dose equivalent per unit fluence of incident ions of charge Z and energy per nucleon E_p are shown in figures 10.5 and 10.6. Figure 10.5 is based on current quality factors (ICRP 26 (Anon., 1977b)), and figure 10.6 is based on newly proposed quality factors (ICRU 40 (Anon., 1986)). The proton-induced fragmentation cross sections are taken from chapters 4 and 5. The proton cross sections are velocity scaled according to the proposed factorization model of Lindstrom et al. (1975), as modified by Silberberg, Tsao, and Shapiro (1976). The limitations of this model, as discussed elsewhere (Wilson et al., 1984), do not concern us here because the ^{16}O and ^{12}C data were used in the original derivation by Lindstrom et al. (1975), retained in subsequent modifications of Silberberg, Tsao, and Shapiro (1976), and adequately represent the ^{16}O and ^{12}C data. The problems with this scaling model arise for nuclear fragmentation predictions far removed from projectile-target combinations used in fitting the model parameters. For example, there are no light fragment data for iron fragmentation for which the model could be fit (Wilson, Townsend, and Badavi, 1987); such experiments are currently in progress. The 50-percent increase we proposed for the ^{20}Ne data is within the uncertainty generally regarded for the Silberberg, Tsao, and Letaw (1983) parameterization. (Also see Mathews (1983).)

Table 10.1. Spectral-Averaged Quality Factor for Individual Isotopes Produced in 1-GeV, Proton-Induced Reactions in ^{16}O

Z_j	A_j	E_j , MeV	\bar{Q}_{Fj}	
			ICRP 26 (a)	ICRU 40 (b)
1	1	8.69	2.73	3.71
1	2	10.70	4.09	5.87
1	3	10.40	5.20	7.72
2	3	11.20	12.38	19.52
2	4	12.30	13.90	21.88
3	6	6.85	19.25	23.19
3	7	6.16	19.50	22.38
4	9	4.79	19.77	15.14
4	10	4.11	19.73	14.95
5	9	4.79	19.81	11.47
5	10	4.11	19.78	11.54
5	11	3.71	19.75	11.88
5	12	2.74	19.70	12.58
6	11	3.71	19.79	9.96
6	12	2.74	19.75	10.71
6	13	2.05	19.68	11.96
6	14	1.34	19.56	14.11
6	15	0.69	19.17	18.30
7	13	2.05	19.74	10.53
7	14	1.37	19.64	12.61
7	15	0.69	19.35	16.73
8	15	0.69	19.45	15.50

^aICRP 26 (Anon., 1977b).

^bICRU 40 (Anon., 1986).

The nuclear contribution to the dose equivalent increases rapidly at the lowest energies as new channel thresholds are passed with increasing energy opening new reaction mechanisms. The small variation seen between 20 MeV per nucleon and 300 MeV per nucleon is related to nuclear transparency (Townsend, Wilson, and Bidasaria, 1982). The new inelastic channels open above the pion production threshold cause a rapid rise in dose equivalent above 300 MeV per nucleon. The fractional contribution of nuclear reaction to the total dose equivalent is shown in table 10.2 for the two quality factors and ion types shown in figures 10.5 and 10.6 at 10 GeV per nucleon. The nuclear contribution to dose equivalent for ^{12}C and heavier ions is less than 5 percent. Nuclear contributions for lighter ions can be substantial and as high as 70 percent.

Table 10.2. Fractional Contribution of Nuclear Reactions to the Total Dose Equivalent at 10 GeV/nucleon for the ICRP 26 and ICRU 40 Quality Factors

Report (a)	Projectile						
	^1H	^4He	^3Li	^9Be	^{12}C	^{28}Si	^{56}Fe
ICRP 26	0.59	0.43	0.27	0.17	4.2×10^{-2}	2.5×10^{-3}	3.8×10^{-4}
ICRU 40	.70	.51	.34	.21	4.7×10^{-2}	2.1×10^{-3}	3.5×10^{-4}

^aICRP 26 (Anon., 1977b); ICRU 40 (Anon., 1986).

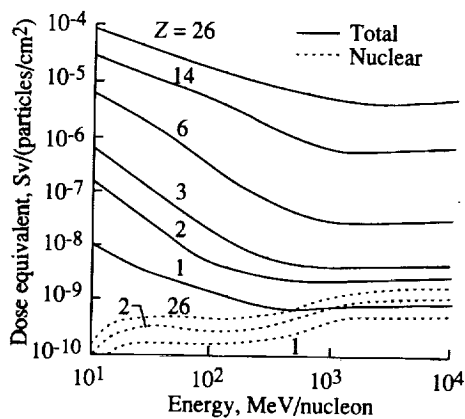


Figure 10.5. Dose equivalent of various ion types including nuclear reactions for the ICRP 26 quality factor (Anon., 1977b).

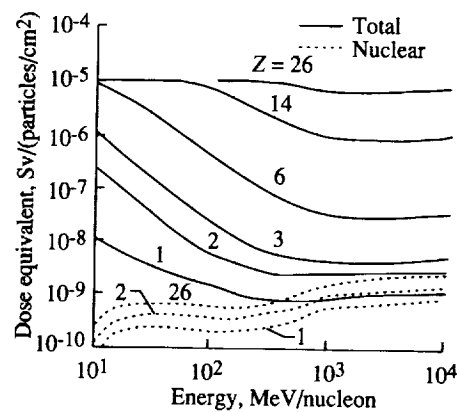


Figure 10.6. Dose equivalent of various ion types including nuclear reactions for the ICRU 40 quality factor (Anon., 1986).

The average quality factors including nuclear reaction effects are shown in figures 10.7 and 10.8. The nuclear effects are clearly seen as the rise in average quality factor at high energies, especially for the light ions. The increase in average quality factors for high-energy protons of ICRU 40 (Anon., 1986) compared with the value obtained for ICRP 26 (Anon., 1977b) is only 25 percent. Consequently, the earlier estimates of Alsmiller, Armstrong, and Coleman (1970), in which the quality factor of 20 for all nuclear fragments of mass greater than 1 nucleon was used, are expected to remain slightly conservative with respect to biological risk, even if the quality factor for ICRU 40 (Anon., 1986) is enforced. One interesting note with respect to figures 10.7 and 10.8 is that the average quality factor for high-energy protons is on the order of that for high-energy carbon ions.

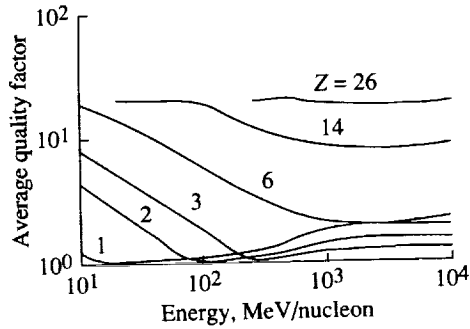


Figure 10.7. Average quality factor of various ion types including nuclear reactions for the ICRP 26 quality factor (Anon., 1977b).

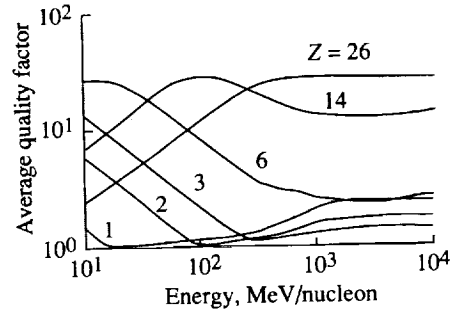


Figure 10.8. Average quality factor of various ion types including nuclear reactions for the ICRU 40 quality factor (Anon., 1986).

10.5. Bone-Tissue Interface Effects

The transport of high-energy nuclei through biological media is greatly affected by nuclear fragmentation events that produce both high- and low-energy sources of nuclear fragmentation product ions, depending on the mechanisms of projectile or target fragmentation, respectively. Fragmentation channels dominate the nuclear cross section at high energies causing broad distributions in ion mass and energy. For high-energy nucleons, the direct ionization is small and the high LET tissue fragments are expected to contribute significantly to their biological effectiveness. The low-energy target fragments with energies of a few MeV are more localized and simpler to treat because of the reduced importance of delta rays and energy-loss straggling (Kellerer and Chmelevsky, 1975). Although energy distributions for charged secondaries in tissue have been studied previously (Wilson, Townsend, and Khan, 1989), the importance of interface effects on the distribution of ions (Cucinotta, Hajnal, and Wilson, 1990) has not been considered in the past. The energy deposition in tissue from fragmentation products produced in bone may be of importance for determining carcinogenic risk because, for example, the epithelium cells near this interface within trabecular cavities are the relevant tissue for induction of bone tumors (Spiers, 1969; ICRP 11 (Anon., 1968b)).

Tissue sites within bone are randomly distributed throughout the calcified matrix, with typical marrow cavities (Beddoe, Darley, and Spiers, 1976) in trabecular bone having dimensions between 50 and 500 μm . Particle ranges for high Z recoils are much smaller than the cavity dimensions, with average energies of heavy target fragments being on the order of several MeV (Greiner et al., 1975). The interface geometry may have an important effect for the more penetrating proton recoils produced in the fragmentation event.

In this section we present solutions for fragment transport in the interface region within a plane geometry model for an incident beam of high-energy nucleons. The model presented is general and may be used to consider other interface effects, e.g., near the connective tissues located in bone. Fragment source spectra are modeled using the high-energy fragmentation model (Wilson, Townsend, and

Khan, 1989) and numerical results given for bidirectional transport. The effects of the interface geometry will be considered in future work.

10.5.1. Fragment transport. We consider the transport of nuclear fragments with charge Z in the vicinity of an interface of two distinct regions denoted by subscripts 1 and 2. We assume that a high-energy flux density of nucleons ϕ passes through the region inducing nuclear reactions. We assume the region to be of limited extent compared with the range of the incident particle, such that the change in ϕ over the region of interest is negligible. The fragment sources ζ_{1j} and ζ_{2j} within the regions are defined by Wilson (1977) as

$$\zeta_{1j}(E) = \frac{d\sigma_{1j}}{dE} \rho_1 \phi \quad (10.15)$$

$$\zeta_{2j}(E) = \frac{d\sigma_{2j}}{dE} \rho_2 \phi \quad (10.16)$$

where the subscript j labels the nuclear fragments; $d\sigma_{1j}/dE$ and $d\sigma_{2j}/dE$ are the fragmentation energy distributions for the two regions; and ρ_1 and ρ_2 are the densities of the two media. Constituent densities for tissue and bone found by Santoro, Alsmiller, and Chandler (1974) are given in table 10.3. The source terms are used in the Boltzmann equation for fragment transport in the two media, which is solved using the method of characteristics with the appropriate boundary condition at the interface. The flux density in medium 1 along a ray passing through the interface is then found as

$$\begin{aligned} \phi_{1j}(x, E) = & \frac{1}{S_{1j}(E)} \frac{S_{1j}(E_{1jb})}{S_{2j}(E_{1jb})} \int_{E_{1jb}}^{E_{2jab}} \zeta_{2j}(E') dE' \\ & + \frac{1}{S_{1j}(E)} \int_E^{E_{1jb}} \zeta_{1j}(E') dE' \end{aligned} \quad (10.17)$$

where x is a point in region 1 through which the ray passes, b is the distance in medium 1 along the ray, a is the chord of region 2 along the ray, and S_{1j} and S_{2j} are the fragment stopping powers in the two regions. The energy limits in equation (10.17) are given by

$$E_{1jb} = R_{1j}^{-1} [R_{1j}(E) + b] \quad (10.18)$$

and

$$E_{2jab} = R_{2j}^{-1} [R_{2j}(E_{1jb}) + a] \quad (10.19)$$

where the functions $R_{1j}(E)$ and $R_{2j}(E)$ are the range relations for fragments j , and R_{1j}^{-1} and R_{2j}^{-1} are the energies associated with the range r in each region defined by Wilson (1977) as

$$E = R_{1j}^{-1} [R_{1j}(E)] \quad (10.20)$$

The dose at depth x is given by

$$D_{1j}(x) = \int_0^\infty S_{1j}(E) \phi_{1j}(x, E) dE \quad (10.21)$$

which is evaluated numerically using the modified stopping powers (Wilson et al., 1984) of the Ziegler (1980) handbook.

Table 10.3. Densities for Tissue and Bone

Element	ρ_1 , tissue, cm^{-3} (a)	ρ_2 , bone, cm^{-3} (b)
H	6.265×10^{22}	7.074×10^{22}
C	9.398×10^{21}	2.851×10^{22}
N	1.342×10^{21}	2.148×10^{21}
O	2.551×10^{22}	2.855×10^{22}
P		2.518×10^{21}
Ca		4.086×10^{21}

^a ρ_1 , tissue = 1.0 g/cm.

^b ρ_2 , bone = 1.85 g/cm.

The spectral distribution for the production of a target fragment j is parameterized as

$$\frac{d\sigma_{1j}}{dE} = \frac{\sigma_{1j}}{(2\pi E_{01j}^3)^{1/2}} \sqrt{E} \exp\left(\frac{-E}{2E_{01j}}\right) \quad (10.22)$$

where σ_{1j} is the total fragmentation cross section for the production of j , and the energy parameter E_{01j} is related to the average energy of the fragment \bar{E}_{01j} by

$$E_{01j} = \frac{1}{3} \bar{E}_{01j} \quad (10.23)$$

The fragmentation cross sections used here are taken from the empirical parameterizations of Silberberg, Tsao, and Shapiro (1976) for $Z > 2$ ions and from the MECC-7 computer code for $Z = 1, 2$ ions in Anon. (1968a). The average energy of the fragmentation products is related to the momentum width measured in high-energy-ion fragmentation experiments (Greiner et al., 1975) that are fitted by an empirical model by Wilson, Townsend, and Khan (1989). These models for the fragmentation cross sections and average energies were applied to 1-GeV proton collisions on ^{12}C , ^{14}N , ^{16}O , ^{31}P , and ^{40}Ca , with results for ^{12}C , ^{14}N , and ^{40}Ca listed in table 10.4. Numerical values for ^{16}O were given in Wilson, Townsend, and Khan (1989).

We now pursue an analytic reduction of equation (10.21). Over a limited energy interval, the range of a fragment, which is fully ionized, can be approximated by a simple power relation

$$R_{1j}(E) = \alpha E^{pj} \quad (10.24)$$

Values for the parameter p_j are determined by considering the energy dependence for the ion ranges over the region of interest, corresponding to the spectral distributions, and α is fixed by the range energy relations. The distinct composition of the two media results in a host of nuclear fragments (the recoil ions) with varied energy spectra at x in such a way that distinct values of p_j , denoted p_{1j} and p_{2j} , should be used. Some modifications were made to improve the agreement with the numerical results of equation (10.21), with the resulting values shown in table 10.5. Listed in parentheses in table 10.5 are parameters for hydrogen and helium ions used to calculate the tissue contribution for the absorbed dose in bone. With the approximation of equation (10.24), the integral in equation (10.21) may be reduced to

$$\begin{aligned}
 D_{1j}(x) = & \phi \sigma_{1j} \rho \left\{ 3E_{01j} - E_{01j} \left[3 + \frac{\nu_b}{2E_{01j}} \right] \exp \left(\frac{-\nu_b}{2E_{01j}} \right) \right. \\
 & \left. + \frac{2\sqrt{2} p_{1j} b E_{01j}}{R_{1j}(E_{01j})} \left[\sqrt{\pi} \operatorname{erfc} \left(\sqrt{\frac{\nu_b}{2E_{01j}}} \right) + \frac{1}{2} \Gamma \left(\frac{3}{2}, \frac{\nu_b}{2E_{01j}} \right) \right] \right\} \\
 & + \phi \sigma_{2j} \rho \frac{R_{2j}(E_{02j})}{R_{1j}(E_{02j})} \left\{ E_{02j} \left(3 + \frac{\nu_b}{2E_{02j}} \right) \exp \left(\frac{-\nu_b}{2E_{02j}} \right) \right. \\
 & - \frac{2\sqrt{2} p_{2j} b E_{02j}}{R_{1j}(E_{02j})} \left[\sqrt{\pi} \operatorname{erfc} \left(\sqrt{\frac{\nu_b}{2E_{02j}}} \right) + \frac{1}{2} \Gamma \left(\frac{3}{2}, \frac{\nu_b}{2E_{01j}} \right) \right] \\
 & - E_{02j} \left(3 + \frac{\nu_{ab}}{2E_{02j}} \right) \exp \left(\frac{-\nu_{ab}}{2E_{02j}} \right) \\
 & \left. + \frac{2\sqrt{2} p_{2j} (b + a_1) E_{02j}}{R_{1j}(E_{02j})} \left[\sqrt{\pi} \operatorname{erfc} \left(\sqrt{\frac{\nu_{ab}}{2E_{02j}}} \right) + \frac{1}{2} \Gamma \left(\frac{3}{2}, \frac{\nu_{ab}}{2E_{02j}} \right) \right] \right\} \quad (10.25)
 \end{aligned}$$

where $\nu_b = R_{1j}^{-1}(b)$ and $a_1 = R_{2j}^{-1}(a)$. The ambiguity in expressing equation (10.25) was resolved by requiring the first term to vanish linearly as $b \rightarrow 0$ and the second term to vanish linearly as $a_1 \rightarrow 0$. This analytical reduction of the dose contribution for charged secondaries is expected to be extremely useful when the angular dependence is considered, where a similar form is obtained. Results for bidirectional transport along a single ray are given in the next section.

10.5.2. Results and discussion. The fragment transport model is now applied for the case of bidirectional transport for 1-GeV incident protons at the bone-tissue interface. We consider the interface at $x = 0$ and assume that $a \gg x$ such that $E_{2jab} \rightarrow \infty$. The source term is then divided into forward and backward contributions with

$$\zeta_{1j}^+(E) = \zeta_{1j}^-(E) = \frac{1}{2} \zeta_{1j}(E) \quad (10.26)$$

and similarly for ζ_{2j}^+ . We assume a unit incident fluence of protons. The source term moving to the left in tissue from tissue fragments is assumed to contribute

Table 10.4. Fragmentation Cross Sections and Fragment Average Energies for p -Nucleus Scattering at 1 GeV

Z_j	A_j	σ , mb	E_j , MeV
$A_T = 12; Z_T = 6$			
1	1	490.1	8.5
1	2	42.5	7.6
1	3	4.5	7.4
2	3	7.7	8.0
2	4	118.5	8.8
3	5	10.9	8.9
3	6	12.2	7.6
3	7	8.3	6.3
4	6	4.3	7.6
4	7	11.9	6.3
4	8	21.9	5.1
4	9	2.6	3.8
5	8	3.6	5.1
5	9	12.1	3.8
5	10	17.2	2.5
5	11	41.5	1.3
6	10	3.9	2.5
6	11	27.5	1.3
$A_T = 14; Z_T = 7$			
1	1	559.4	8.6
1	2	56.8	9.2
1	3	6.0	8.9
2	3	10.3	9.6
2	4	153.2	10.5
3	5	10.2	9.6
3	6	11.5	8.6
3	7	7.8	7.5
4	6	4.1	8.6
4	7	11.1	7.5
4	8	11.4	6.4
4	9	2.4	5.4
5	8	3.2	6.4
5	9	10.8	5.4
5	10	15.3	4.3
5	11	10.2	3.2
6	10	3.3	4.3
6	11	13.0	3.2
6	12	40.3	2.1
6	13	13.8	1.1
7	12	2.6	2.1
7	13	10.9	1.1

Table 10.4. Continued

Z_j	A_j	σ , mb	E_j , MeV
$A_T = 16; Z_T = 8$			
1	1	630.4	8.7
1	2	72.9	10.7
1	3	7.7	10.4
2	3	13.2	11.2
2	4	203.0	12.3
3	5	9.6	10.2
3	6	10.8	9.3
3	7	7.3	8.4
4	6	3.8	9.3
4	7	10.5	8.4
4	8	10.7	7.4
4	9	2.3	6.5
5	8	2.9	7.4
5	9	9.6	6.5
5	10	7.6	5.6
5	11	9.1	4.6
6	10	2.8	5.6
6	11	11.0	4.6
6	12	34.3	3.7
6	13	14.4	2.8
6	14	2.1	1.9
7	12	2.2	3.7
7	13	3.9	2.8
7	14	28.0	1.9
7	15	41.5	.9
8	14	3.5	1.9
8	15	28.5	.9
$A_T = 31; Z_T = 15$			
1	1	1150.6	9.0
1	2	140.9	11.3
1	3	26.9	11.2
2	3	36.1	13.2
2	4	265.5	10.1
3	5	5.7	12.1
3	6	6.9	11.6
3	7	5.2	11.1
4	6	2.1	11.6
4	7	6.2	11.1
4	8	7.0	10.7
4	9	1.7	10.2
5	8	1.1	10.7
5	9	3.9	10.2
5	10	3.5	9.7
5	11	4.8	9.3

Table 10.4. Continued

Z_j	A_j	σ , mb	E_j , MeV
$A_T = 40; Z_T = 20$			
1	1	1396.0	9.1
1	2	186.8	11.4
1	3	34.6	11.3
2	3	40.8	14.0
2	4	271.6	11.0
3	5	4.9	12.5
3	6	5.9	12.1
3	7	3.7	11.8
4	6	1.9	12.1
4	7	5.3	11.8
4	8	5.0	11.4
4	9	1.1	11.1
5	8	.7	11.4
5	9	2.3	11.1
5	10	2.2	10.7
5	11	1.7	10.4
6	10	.4	10.7
6	11	1.2	10.4
6	12	3.4	10.0
6	13	1.8	9.6
6	14	.9	9.3
7	12	.3	10.0
7	13	.6	9.6
7	14	2.8	9.3
7	15	2.6	8.9
7	16	.8	8.6
8	14	.5	9.3
8	15	1.6	8.9
8	16	4.9	8.6
8	17	2.9	8.2
8	18	1.5	7.9
9	17	2.0	8.2
9	18	4.0	7.9
9	19	4.2	7.5
9	20	1.4	7.1
9	20	2.0	7.5
10	19	2.0	7.1
10	20	6.9	7.1
10	21	5.1	6.8
10	22	2.9	6.4
11	21	2.6	6.8
11	22	5.8	6.4
11	23	7.2	6.1
11	24	2.6	5.7

Table 10.4. Concluded

Z_j	A_j	σ , mb	E_j , MeV
$A_T = 40; Z_T = 20$			
12	23	2.6	6.1
12	24	9.9	5.7
12	25	8.2	5.4
12	26	5.2	5.0
13	25	3.1	5.4
13	26	7.8	5.0
13	27	11.7	4.6
13	28	4.8	4.3
13	29	1.5	3.9
14	27	3.0	4.6
14	28	13.0	4.3
14	29	13.3	3.9
14	30	9.6	3.6
14	31	1.9	3.2
15	29	3.5	3.9
15	30	9.9	3.6
15	31	18.4	3.2
15	32	8.7	2.9
15	33	3.0	2.5
16	31	3.2	3.2
16	32	15.5	2.9
16	33	19.9	2.5
16	34	15.9	2.1
16	35	3.6	1.8
17	33	3.4	2.5
17	34	10.5	2.1
17	35	24.5	1.8
17	36	14.3	1.4
17	37	5.7	1.1
18	35	2.8	1.8
18	36	15.9	1.4
18	37	25.1	1.1
18	38	23.7	.7
19	37	18.0	1.1
19	38	21.3	.7
19	39	40.1	.4
20	39	18.9	.4

Table 10.5. Range-Energy Parameters

Z	p_1	p_2 (a)
1	0.10	0.1 (0.06)
2	.20	.2 (0.13)
3,4	0	.1
5,6	.15	0
>6	.25	0

^aValues in parentheses denote absorbed dose in bone.

one-half the equilibrium value of the absorbed dose, which is given by

$$D_{1j}^-(x) \approx \bar{E}_{01j} \sigma_{1j} \rho_1 \quad (10.27)$$

with a similar contribution for the absorbed dose in bone. Thus, each medium is assumed to be semi-infinite in extent.

The differential flux density at several depths in tissue is shown in figure 10.9 for low Z fragment components ($Z = 1, 2$) and in figure 10.10 for the high Z components ($Z > 2$), with the dashed lines showing the bone contribution to the flux, the dotted lines showing the tissue term, and the solid lines showing the total flux. From figure 10.9, the low Z fragments from bone entering tissue are seen to be appreciable for at least 1000 μm of tissue with a significant contribution from high-energy recoil and fragmentation particles ($E > 25$ MeV). In figure 10.10, the high Z fragments from bone are seen to contribute only over a small spatial region ($< 20 \mu\text{m}$) but they dominate the low- and high-energy portions of the spectra nearer to the interface.

In figures 10.11 and 10.12, the absorbed doses are shown in the region of the interface for the low Z and high Z fragments, respectively. The dotted line denotes the tissue contribution; the dashed line, the bone contribution; the solid line, the total absorbed dose. Both figures 10.11 and 10.12 show contributions to the absorbed dose from fragmentation events in adjacent media near the interface. There is also a buildup in dose close to the interface in tissue that is not present in bone. For the low Z ions, this buildup can be attributed to the higher production multiplicities for light ions produced from potassium and calcium present in bone; and for the high Z ions, this buildup is caused by $Z > 8$ ions produced from fragmentation on phosphorous and calcium. In tissue the interface effect on the absorbed dose is appreciable for only a few tens of a micrometer for high Z ions, and it is substantial to about 1000 μm for low Z ions. Conversion of the depth-dose curves to distribution in linear energy transfer (LET) will give a better indication of the importance of the high Z ions near the interface.

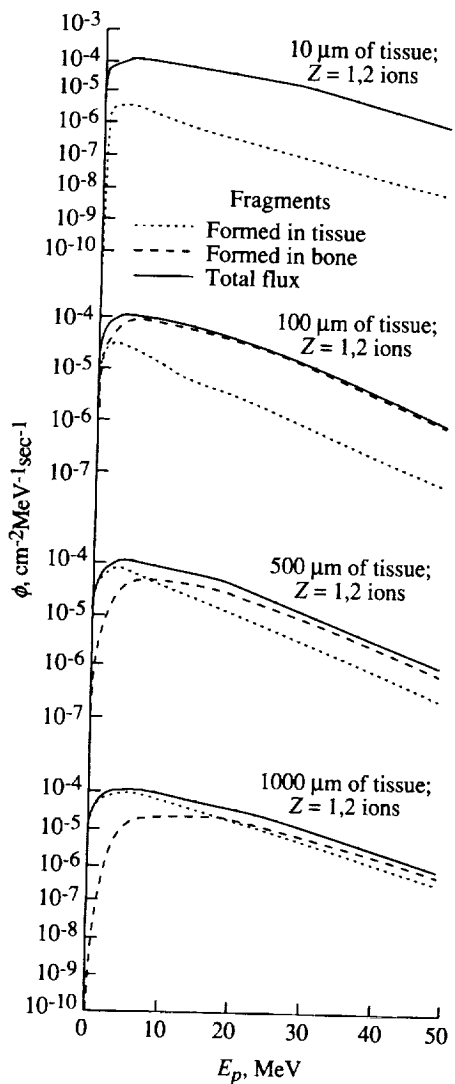


Figure 10.9. Differential flux for $Z = 1,2$ ion fragments at several depths in tissue.

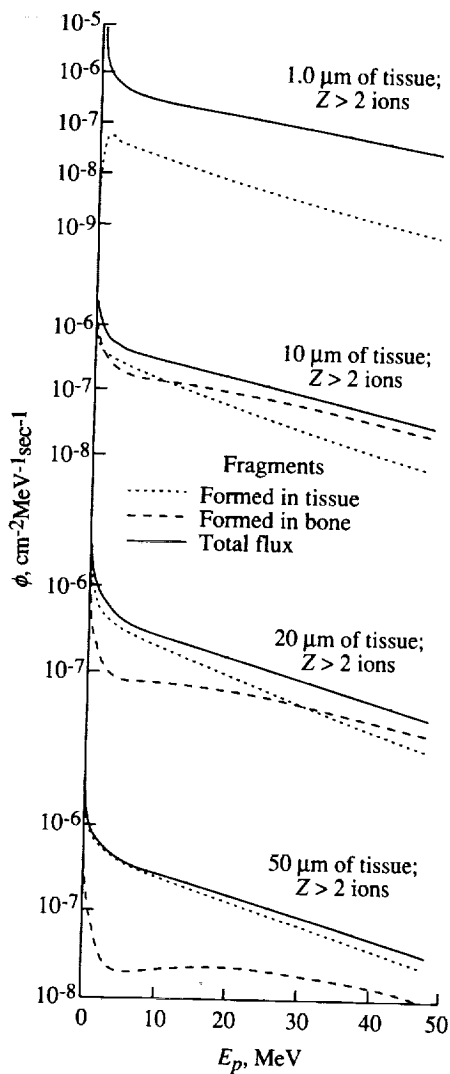


Figure 10.10. Differential flux for all fragments with $Z > 2$ at several depths in tissue.

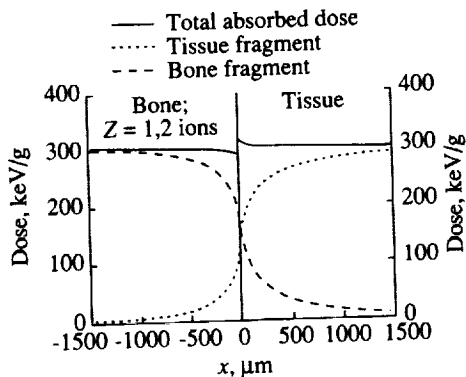


Figure 10.11. Absorbed depth dose in the region of the bone-tissue interface for $Z = 1,2$ fragments.

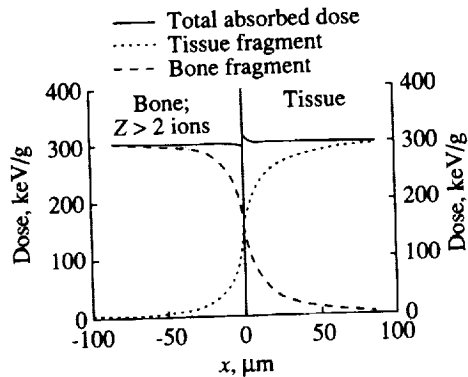


Figure 10.12. Absorbed depth dose in the region of the bone-tissue interface for all fragments with $Z > 2$.

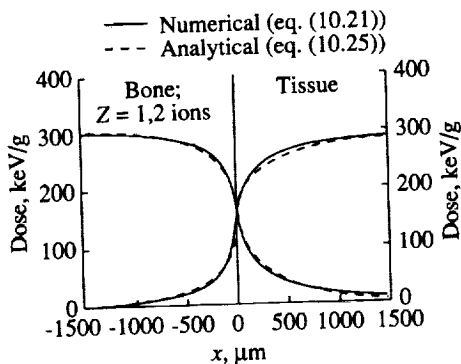


Figure 10.13. Comparison between numerical and analytical results for absorbed depth dose for $Z = 1,2$ fragments.

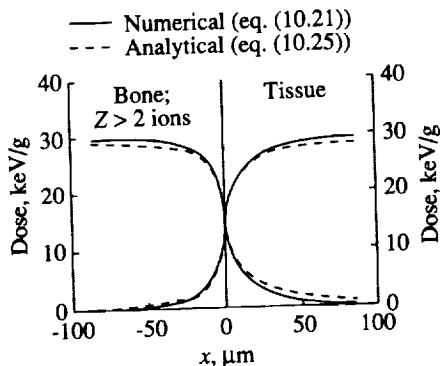


Figure 10.14. Comparison between numerical and analytical results for absorbed depth dose for $Z > 2$ fragments.

In figures 10.13 and 10.14, the analytic approximation of equation (10.25) to the absorbed dose (shown by dashed lines) is shown in comparison with the result obtained from numerical integration of equation (10.21) (shown by solid lines). The analytic results are seen to be quite accurate, converging to the equilibrium values slightly slower than the numerical result. The differences seen are within the accuracy of the fragmentation cross-section model used. The values for p_{1j} and p_{2j} listed in table 10.5 should show a slight dependence on the energy of the incident nucleon.

10.5.3. Conclusions. Solutions for the transport of fragmented target recoils produced by high-energy nucleons are found in the region of the interface between two distinct media. The differential flux and absorbed dose of the nuclear fragments are considered. A simple analytic formula for the absorbed dose is found in an approximate range-energy model. Interface effects were found to be important at the tissue-bone interface in a simple bidirectional transport model, showing a large enhancement in energy deposition from fragments formed

in adjacent media. The bone-tissue interface geometry should not be important for high Z fragments based on the results of past work; however, this geometry may become important for the more penetrating low Z fragments and should be a topic of future study. The evaluation of LET distributions near this interface should also be considered to assess the biological effectiveness of the individual fragment contributions.

10.6. Effects on Harderian Tumorigenesis

A quantitative understanding of the contributions of nuclear fragments to biological injury is required for an unambiguous interpretation of the relationship between relative biological effectiveness (RBE) and energy deposition as measured by linear energy transfer (LET). In the study of biological response, concomitant with exposure by particles from projectile fragmentation, there are contributions to biological injury by low-energy, target-nuclear fragments produced within the biological medium.

The effects of target fragmentation on the dose delivered by charged particles along their range can be regarded as small relative to those of projectile fragmentation for heavy-ion beams because fragments of high-energy projectiles are also of high energy in the target rest frame and dissipate this energy over their entire range. This is not true for protons that have no "projectile" fragments below the π -production thresholds. Although these facts have been known for a long time, there has not been a quantitative evaluation of the target fragment contributions to the exposure of biological systems. This section presents such an evaluation.

Biological injury is related to the local energy deposited by the passage of energetic ions. As noted in section 10.4, the ionization energy loss is on the order of $0.2Z^2$ keV/ μm for a traversing (i.e., not stopping) high-energy ion of charge Z . The average nuclear energy-transfer rate is $0.05A^{2/3}$ keV/ μm , where A is the ion atomic mass (i.e., the number of nucleons). Because the RBE factor of the fragments may be 20 or more, the biological response associated with direct atomic ionization is on the order of that associated with the nuclear events for incident low-charge ions ($Z < 5$) while the response is dominated by direct ionization for particles of high charge ($Z \gg 5$). In the present section, we quantify these various contributions by using, as an illustrative example, the dependence of RBE on LET obtained by Fry et al. (1985) for the induction of tumors in the Harderian gland of mice. This method is similar to that used by Schimmerling et al. (1987) for spermatogonial cell survival.

10.6.1. Radiation response of Harderian gland. The dose response of Harderian tumorigenesis has been measured for ^{60}Co γ and several ions (Fry et al., 1985; Fry, 1986). The approximate response is given as

$$P = 2.5 + 50 \left[1 - \exp\left(\frac{-D}{D_0}\right) \right] \quad (10.28)$$

where the percentage of tumor prevalence P at 600 days is given in terms of a radiosensitivity parameter D_o and the dose D . Tumor prevalence was scored by Fry et al. (1985) at 600 days after exposure as opposed to incident rates scored on postmortem. The D_o of equation (10.28) gives the exponential slope of the nonincidence curve of the at-risk population. The spontaneous tumor rate is the leading coefficient representing 2.5 percent. Note that only one-half the animals appear susceptible to tumor induction, or else the radiation has inactivated pretumorous cells before expression (Fry, 1986). The value of D_o depends on the ion type through which the RBE is found as ratios to the reference radiation value of D_o . The radiation types, their LET's, RBE, and radiosensitivity D_o are given in table 10.6. The measurements of Fry et al. (1985) are all given on a common equivalent dose basis in figure 10.15. It can be seen in figure 10.15 that the dose response curve of equation (10.28) represents the data to within 25 percent. It is easily shown that a small increase in RBE for ^{20}Ne and a small decrease in RBE for ^{12}C would bring all the data points to within 18 percent of equation (10.28).

Table 10.6. Harderian Gland Radiosensitivity Parameters

Radiation type	LET, keV/ μ	RBE	D_o , cGy
$^{60}\text{Co } \gamma$	0.2	1	769.5
^4He	18	5	153.9
^{12}C	80	11.2	68.7
^{20}Ne (distal)	190	28.5	27
^{40}Ar	6540	28.7	26.8

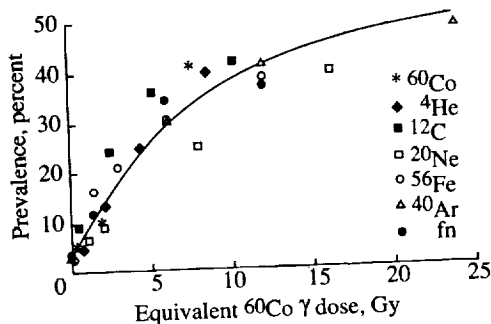


Figure 10.15. Dose response relationship for Harderian gland tumor from various radiations on an equivalent dose scale. The symbol fn refers to fission neutrons.

Equation (10.28) provides a basis for additivity. The probability of radiation-induced tumors within the population at risk is

$$P_r = 1 - \exp\left(\frac{-D}{D_o}\right) \quad (10.29)$$

for which the probability of being among the unaffected population is

$$Q = 1 - P_r = \exp\left(\frac{-D}{D_o}\right) \quad (10.30)$$

Consider two exposures with two different ion types. The probability of being unaffected by the first ion type is

$$Q_1 = \exp\left(\frac{-D_1}{D_{o1}}\right) \quad (10.31)$$

the probability that the unaffected population after exposure D_1 is unaffected by exposure D_2 is then

$$Q_2 = \exp\left(\frac{-D_2}{D_{o2}}\right) \quad (10.32)$$

so that the total unaffected population from the two exposures is

$$Q_{12} = Q_1 Q_2 = \exp\left[-\left(\frac{D_1}{D_{o1}} + \frac{D_2}{D_{o2}}\right)\right] \quad (10.33)$$

Therefore, the total radiation-induced prevalence is

$$P_{r12} = 1 - Q_{12} = 1 - \exp\left[-\left(\frac{D_1}{D_{o1}} + \frac{D_2}{D_{o2}}\right)\right] = 1 - \exp\left(\frac{-M}{D_{o1}}\right) \quad (10.34)$$

where

$$M = D_1 + \frac{D_{o1}}{D_{o2}} D_2 \quad (10.35)$$

is the effective dose for the two types of radiation. The RBE with exposure 1 taken as reference radiation is

$$\text{RBE} = \frac{D_{o1}}{D_{o2}} \quad (10.36)$$

and the effective dose is

$$M = \sum_i \text{RBE}_i D_i \quad (10.37)$$

The values of D_{oi} and RBE_i found by Fry et al. (1985) are given in table 10.6 with estimates of corresponding LET values. Note that we have used the LET estimates of Fry et al. (1985) and Fry (1986) except for ${}^4\text{He}$, where the LET of the most energetic ${}^4\text{He}$ ion at the exposure point is used.

For the fluence ϕ_i of monoenergetic particles of type i and energy E_p , the dose is approximated by $\phi_i(E_p) S_i(E_p)$, where $S_i(E_p)$ is the stopping power. For a distribution of particles with a spectrum of energies, the generalized effective dose M is given by

$$M = \sum_i \int \text{RBE}[L_i(E_p)] S_i(E_p) \phi_i(E_p) dE_p \quad (10.38)$$

after which the prevalence can be determined from equation (10.28) with $D_o = 770$ cGy for $^{60}\text{Co } \gamma$.

There are two approaches to understanding the RBE relation to LET. The first starts with the observation that biological response is related to the absorbed energy (for example, as Fry et al. (1985) have found for the Harderian gland). As the density of ionization at the sites of energy deposit increases, the ionization becomes more effective in producing biological response, and RBE rises with increasing LET. At some value of LET, the energy deposition reaches a maximum efficiency after which RBE remains constant as shown in figure 10.16. (The dashed line indicates ionization density enhancement saturation (IDES).) Such a view is suggested by the ^{56}Fe and ^{40}Ar data of Fry et al. (1985) which show the same RBE, but this is not necessarily conclusive. The second view is that biological response is a function of particle fluence and that a cross section can be defined which relates biological response to fluence level. This second view can also be justified using the data of Fry et al. (1985), where the cross section depends on particle type. If biological response is fluence related, then RBE decreases with increasing LET. Experimentally, fluence-based limited response is observed only at high LET, which we refer to as the fluence-based limit (FBL). The fluence-based limit RBE is shown in figure 10.16 as the full curve above 190 keV/ μm . Katz incorporates these two views into his track-structure model (Katz et al., 1971). For the present, we assume with Katz that low-LET radiation response is dose dependent (gamma-kill mode) and that the high-LET asymptotic RBE is proportional to the inverse LET (ion-kill mode).

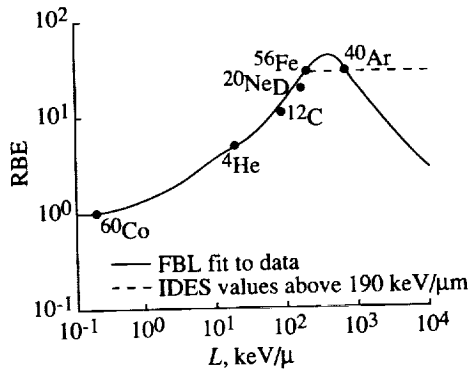


Figure 10.16. RBE measured by Fry et al. (1985) for various radiations.

The relation between RBE and LET for the various ions is shown in figure 10.16. The assumed functional form for the fluence-based limit (FBL) case is

$$\text{RBE} = 0.95 + \frac{a_1}{L} \left[1 + 2 \exp\left(\frac{-L}{14}\right) \right] \left[1 + \exp\left(-a_2 L^2 - a_3 L^3\right) \right] \quad (10.39)$$

where

$$\left. \begin{aligned} a_1 &= 18720 \\ a_2 &= 7.43 \times 10^{-6} \\ a_3 &= 1.14 \times 10^{-8} \end{aligned} \right\} \quad (10.40)$$

and L denotes LET in units of $\text{keV}/\mu\text{m}$. At high LET, the exponential terms become negligible and the response becomes fluence dependent above $500 \text{ keV}/\mu\text{m}$. For LET in the range above $190 \text{ keV}/\mu\text{m}$ for the high-ionization density results in enhancement saturation (IDES), and the RBE remains constant as shown by the dashed line in figure 10.16.

10.6.2. Ion reactions in tissue. Again we consider a volume of tissue through which a monoenergetic ion fluence $\phi_Z(E_p)$ of energy E_p has passed and endeavor to evaluate the energy absorbed by the media in the passage. There are several processes by which the ions give up energy to the media: electronic excitation/ionization, nuclear coulomb scattering, nuclear elastic scattering, and nuclear reaction. The electronic excitation/ionization is contained in the stopping power, which is evaluated by the methods discussed elsewhere (Wilson et al., 1984). The nuclear coulomb elastic scattering is highly peaked at low momentum transfer, and energy transfers per event of a few hundred electron volts or less are typical. (See, for example, Wilson, Stith, and Stock (1983).) The nuclear elastic scattering energy transfer is on the order of 1 MeV or less and can be neglected in comparison with reactive processes in the energy range of interest here. A model for proton-induced reactions in tissue constituents, given elsewhere (Wilson, Townsend, and Khan, 1989), will be used here as well.

The secondary particle radiation field $\phi_j(E)$ is given by Wilson (1977) as

$$\phi_j(E) = \frac{1}{S_j(E)} \int_E^\infty \zeta_j(E') dE' \quad (10.41)$$

where $S_j(E)$ is the stopping power and $\zeta_j(E')$ denotes the particle source energy distributions

$$\zeta_j(E) = \rho \sigma_j(E_p) f_j(E) \phi_Z(E_p) \quad (10.42)$$

where ρ is the nuclear density, $\sigma_j(E_p)$ is the fragmentation cross section, and $f_j(E)$ is the fragment spectrum as discussed elsewhere (Wilson, Townsend, and Khan, (1989)). The total absorbed energy is approximately

$$D_Z(E_p) = S_Z(E_p) \phi_Z(E_p) + \sum_j \int_0^\infty S_j(E) \phi_j(E) dE \quad (10.43)$$

Equation (10.43) may be written as

$$D_Z(E_p) = S_Z(E_p) \phi_Z(E_p) + \bar{E}_j \sigma_j(E_p) \rho \phi_p(E_p) \quad (10.44)$$

where \bar{E}_j is the average energy associated with each spectral distribution $f_j(E)$,

$$\bar{E}_j = \int_0^\infty E f_j(E) dE \quad (10.45)$$

Similarly, the equivalent ^{60}Co γ dose is

$$M_Z(E_p) = \text{RBE}_Z(E_p) S_Z(E_p) \phi_Z(E_p) + \sum_j \overline{\text{RBE}}_{Fj} \bar{E}_j \sigma_j(E_p) \rho \phi_Z(E_p) \quad (10.46)$$

where $\overline{\text{RBE}}_{F_j}$ is the spectral average RBE factor of the j th-type secondary-fragment particle. The sum over j will include the usual "evaporation" products including the low-energy protons. We now evaluate equation (10.46) for the LET-dependent RBE factor found by Fry et al. (1985) and extrapolated by equation (10.39) for both the FBL model and the IDES model. The spectral-averaged RBE factors are shown in table 10.7 for the various isotopes produced in ^{16}O reactions.

Table 10.7 Average RBE Factors for Individual Isotopes Produced in 1-GeV Proton-Induced Reactions in ^{16}O

Z_j	A_j	E_j , MeV	$\overline{\text{RBE}}_{F_j}$	
			IDES	FBL
1	1	8.69	3.67	3.67
1	2	10.70	4.83	4.83
1	3	10.40	5.73	5.73
2	3	11.20	14.09	14.37
2	4	12.30	16.39	16.79
3	6	6.85	27.45	32.89
3	7	6.16	28.22	34.60
4	9	4.79	29.22	37.82
4	10	4.11	29.12	37.45
5	9	4.79	29.32	32.54
5	10	4.11	29.25	32.06
5	11	3.71	29.18	31.88
5	12	2.74	29.03	32.07
6	11	3.71	29.26	27.52
6	12	2.74	29.18	28.32
6	13	2.05	29.00	29.69
6	14	1.34	28.67	31.70
6	15	.69	27.70	33.22
7	13	2.05	29.15	27.17
7	14	1.37	28.89	29.86
7	15	.69	28.16	33.01
8	15	.69	28.42	32.43

10.6.3. Results. The equivalent ^{60}Co γ dose per unit fluence of incident ions of charge Z and energy per nucleon E_p is shown in figures 10.17 and 10.18. Figure 10.17 is based on the RBE factor of the IDES model shown as the dashed line in figure 10.16. Figure 10.18 is based on the FBL model. The proton-induced fragmentation cross sections are taken from Wilson, Townsend, and Khan (1989). The proton cross sections are velocity scaled according to the proposed factorization model of Lindstrom et al. (1975) as modified by Silberberg, Tsao, and Shapiro (1976). The limitations of this model, as discussed elsewhere (Wilson, et al., 1984; Wilson, Townsend, and Badavi, 1987), do not concern us here because

the ^{16}O and ^{12}C data, which were used in the original derivation by Lindstrom et al. (1975) and were retained in subsequent modifications of Silberberg, Tsao, and Shapiro (1976), adequately represent the scaling for ^{16}O and ^{12}C data. The problems with this scaling model arise for nuclear fragmentation predictions far removed from projectile-target combinations used in fitting the model parameters. For example, there are no light fragment data ($A_j < 28$) for iron fragmentation to which the model could be fit. Such experiments are currently in progress. The 50-percent increase that we proposed for the ^{20}Ne data (Wilson et al., 1984) is within the uncertainty generally regarded for the Silberberg, Tsao, and Shapiro (1976) parameterization (for example, Mathews, 1983; Silberberg, Tsao, and Letaw, 1983).

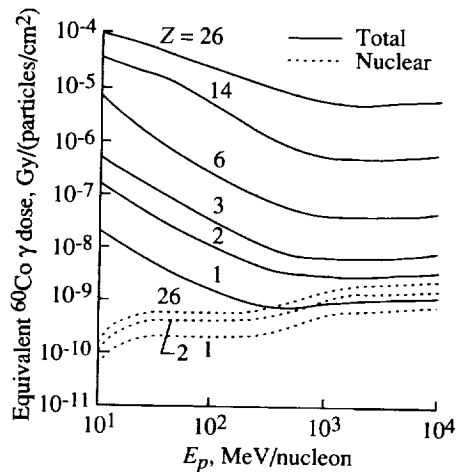


Figure 10.17. Equivalent ^{60}Co γ dose for various ion types including nuclear reaction effects with IDES.

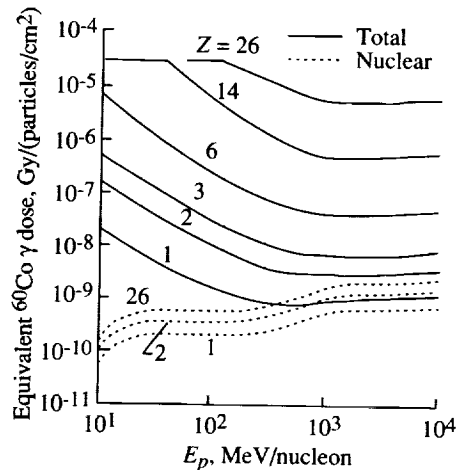


Figure 10.18. Equivalent ^{60}Co γ dose for various ion types including nuclear reaction effects for FBL.

The nuclear contribution to the equivalent ^{60}Co γ initially increases rapidly with increasing energy as new reaction-mechanism thresholds are passed. Only a small variation is seen between 30 MeV/nucleon and 300 MeV/nucleon and this is related to the nuclear transparency (Townsend, Wilson, and Bidasaria, 1982). New inelastic channels open above the pion production threshold and cause a rapid rise in the equivalent dose above 300 MeV/nucleon. Similar results for the fluence-based limit model are shown in figure 10.18. The fractional contribution of nuclear reaction effects for either RBE factor of figure 10.16 differs by a few percent, and representative values are shown in table 10.8 at 0.1, 1.0, 3.0, and 10.0 GeV/nucleon. The nuclear contribution to equivalent ^{60}Co γ doses for carbon and heavier ions is less than 5 percent. Nuclear contributions for lighter ions can be substantial and as high as 69 percent.

The average RBE factors including nuclear reaction effects are shown in figures 10.19 and 10.20. The nuclear effects are clearly seen as the rise in average RBE factor at high energies, especially for the light ions. The present results can now be used to better determine the relation of the ions between RBE and LET in future experiments.

Table 10.8. Fractional Contribution of Nuclear Reactions to the Total Dose Equivalent at Typical Energies

E, GeV/ nucleon	Projectile ion						
	¹ H	⁴ He	³ Li	⁹ Be	¹² C	²⁸ Si	⁵⁶ Fe
0.1	0.12	0.03	0.01	4.90×10^{-3}	1.50×10^{-3}	8.75×10^{-5}	1.80×10^{-5}
1.0	.59	.35	.17	8.10×10^{-2}	2.50×10^{-2}	2.40×10^{-3}	2.70×10^{-4}
3.0	.67	.43	.22	.11	3.50×10^{-2}	3.50×10^{-3}	4.0×10^{-4}
10.0	.69	.44	.23	.11	3.60×10^{-2}	3.60×10^{-3}	4.0×10^{-4}

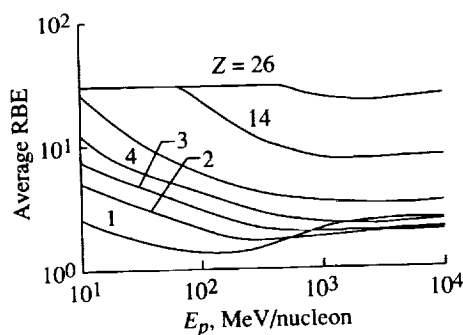


Figure 10.19. Average RBE of various ion types including contributions from nuclear reactions for the IDES model.

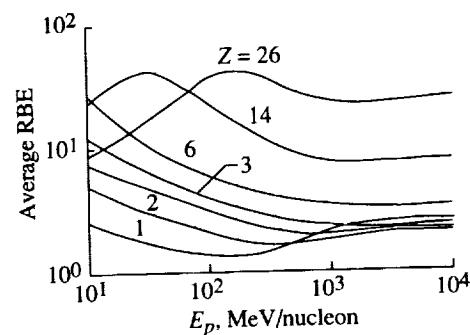


Figure 10.20. Average RBE of various ion types including contributions from nuclear reactions for the FBL model.

10.7. Effects on Cellular Track Models

The cellular track model of Katz has been described extensively (Katz et al., 1971; Katz, Sharma, and Homayoonfar, 1972; Katz, 1986). Here we outline its basic concepts and consider the extension to the mixed radiation field seen in space. The biological damage from passing ions is caused by delta-ray production. Cell damage is separated into a grain-count regime where damage occurs randomly along the ion path and the track-width regime, in which the damage is distributed like a "hairy rope." The response of the cells is described by four cellular parameters, two of which (m , the number of targets per cell, and D_o , the characteristic X-ray dose) are extracted from the response of the cellular system to X-ray or γ -ray irradiation. The other two (Σ_o , interpreted as the cross-sectional area of the cell nucleus within which the damage sites are located, and κ , a measure of size of the damage site) are found from survival measurements with track segment irradiations by energetic charged particles. The transition from the grain-count regime to the track-width regime takes place at $Z^{*2}/\kappa\beta^2$ on the order of 4, where Z^* is the effective charge and β , the velocity. The grain-count regime is at the lower values of $Z^{*2}/\kappa\beta^2$ and the track-width regime is at the higher values.

To accommodate for the capacity of cells to accumulate sublethal damage, two modes of inactivation are identified: ion kill (intratrack) and gamma kill (intertrack). For cells damaged by the passage of a single ion, the ion-kill mode occurs. The fraction of cells damaged in the ion-kill mode is taken as $P = \Sigma/\Sigma_o$, where Σ is the single-particle inactivation cross section and P is the probability of the damage in the ion-kill mode. Cells not damaged in the ion-kill mode can be sublethally damaged by the delta rays from the passing ion and then inactivated in the gamma-kill mode, by the cumulative addition of sublethal damage caused by delta rays from other passing ions. The surviving fraction of a cellular population N , whose response parameters are m , D_o , Σ_o , and κ , after irradiation by a fluence of particles F , is written as (Katz et al., 1971)

$$\frac{N}{N_o} = \pi_i \times \pi_\gamma \quad (10.47)$$

where the ion-kill survivability is

$$\pi_i = \exp(-\Sigma F) \quad (10.48)$$

and the gamma-kill survivability is

$$\pi_\gamma = 1 - \left[1 - \exp\left(\frac{-D_\gamma}{D_o}\right) \right]^m \quad (10.49)$$

The gamma-kill dose fraction is

$$D_\gamma = (1 - P)D \quad (10.50)$$

where D is the absorbed dose. The single-particle inactivation cross section is given by

$$\Sigma = \Sigma_o \left[1 - \exp\left(\frac{-Z^{*2}}{\kappa\beta^2}\right) \right]^m \quad (10.51)$$

where the effective charge number is

$$Z^* = Z \left[1 - \exp\left(\frac{-125\beta}{Z^{2/3}}\right) \right] \quad (10.52)$$

In the track-width regime where $P > 0.98$, we take $P = 1$.

For cell transformation, the fraction of transformed cells per surviving cell is

$$T = 1 - \frac{N'}{N'_o} \quad (10.53)$$

where N'/N'_o is the fraction of nontransformed cells, and a set of cellular response parameters for transformations m' , D'_o , Σ'_o , and κ' is used. The RBE at a given survival level is given by

$$\text{RBE} = \frac{D_X}{D} \quad (10.54)$$

where

$$D_X = -D_o \ln \left[1 - \left(1 - \frac{N}{N_o} \right)^{1/m} \right] \quad (10.55)$$

is the X-ray dose at which this level is obtained. Equations (10.47) through (10.55) represent the cellular track model for monoenergetic particles. Mixed radiation fields have been considered previously in the Katz model. (See, for example, Katz, Sharma, and Homayoonfar, 1972.) Next, we consider placing the model in terms of the particle fields described previously.

10.7.1. Katz model and target fragments. The target fragmentation fields are found in closed form in terms of the collision density (Wilson, 1977) because these ions are of relatively low energy. Away from any interfaces, the target fields are in a local equilibrium and may be written as

$$\phi_\alpha(x, E_\alpha; E_j) = \frac{1}{S_\alpha(E_\alpha)} \int_{E_\alpha}^{\infty} \frac{d\sigma_{\alpha j}(E', E_j)}{dE'} \phi_j(x, E_j) dE' \quad (10.56)$$

where the subscript α denotes the target fragment type, $S_\alpha(E)$ denotes the stopping power, and E_α and E_j are in units of MeV.

The particle fields of the projectiles and target fragments determine the level and type of radiological damage at the endpoint of interest. The relationship between the fields and the cellular response is now considered within the Katz cellular track model.

The ion-kill term now contains a projectile term as well as a target fragment term as

$$(\Sigma F) = \Sigma_j(E_j) \phi_j(x, E_j) + \sum_\alpha \int_0^\infty dE_\alpha \phi_\alpha(x, E_\alpha; E_j) \Sigma_\alpha(E_\alpha) \quad (10.57)$$

while the corresponding gamma-kill dose becomes

$$D_\gamma = [1 - P_j(E_j)] S_j(E_j) \phi_j(x, E_j) + \sum_\alpha \int_0^\infty dE_\alpha [1 - P_\alpha(E_\alpha)] S_\alpha(E_\alpha) \phi_\alpha(x, E_\alpha; E_j) \quad (10.58)$$

Use of equations (10.56) and (10.57) allows one to define an effective cross section as

$$\Sigma_j^*(E_j) = \Sigma_j(E_j) + \sum_\alpha \int_0^\infty dE_\alpha \frac{\Sigma_\alpha(E_\alpha)}{S_\alpha(E_\alpha)} \int_{E_\alpha}^{\infty} dE' \frac{d\sigma_{\alpha j}(E', E_j)}{dE'} \quad (10.59)$$

The first term of equation (10.59) is caused by the direct ionization of the media by the passing ion of type j . The second term results from the target fragment produced in the media.

10.7.2. Results and discussion. Katz (Waligorski, Sinclair, and Katz, 1987) has obtained cellular parameters for survival and neoplastic transformations of C3H10T1/2 from the experiments of Yang et al. (1985) as given in table 10.9. We note the large uncertainties in the transformation data of Yang, which should lead to a similar uncertainty in the transformation parameters. Parameter sets were found from data for instantaneous and delayed plating of the cells after the irradiation. Here, only the delayed plating case is considered. General agreement with the measured RBE values (Waligorski, Sinclair, and Katz, 1987) was found using these parameter sets. The single-particle inactivation cross section neglecting target fragmentation of equation (10.59) is shown in figures 10.21 and 10.22 for cell death and transformation, respectively, as a function of the energy (given in MeV/nucleon) of the passing ion. The target fragmentation contribution (the second term in eq. (10.59)) for protons has been evaluated as shown in figures 10.23 and 10.24 and is shown as the dashed curve. The second term of equation (10.59) dominates over the proton direct ionization (dotted line) at high energy. For high-LET particles (low energy), the direct ionization dominates and target fragmentation effects become negligible. A simple scaling by $\sqrt{A_j}$ relates the proton target fragment term to ions of mass A_j . The resulting effective action cross sections for cell death and transformation are plotted in figures 10.25 and 10.26, respectively. We note that the low-energy ^{56}Fe component of the GCR spectra extends into the track width regime where $\Sigma > \Sigma_o$ and is not represented in the present calculation. The error introduced by the present calculation is small.

Table 10.9. Cellular Response Parameters for C3H10T1/2 Cells

Cell-damage type	m	D_o , cGy	Σ_o , cm^2	κ
Death	3	280	5.0×10^{-7}	750
Transformation	2	26 000	1.15×10^{-10}	750

10.8. Effects on Fluence-Related Risk Coefficients

The idea underlying the risk per unit fluence concept was introduced by Curtis, Dye, and Sheldon (1965). The fluence-related risk coefficient F_j was defined by S. B. Curtis¹ et al. as the probability of a given endpoint of interest (e.g., cancer) per unit fluence of type j particles passing through the organ. A first estimate of $F_j(L_j)$ can be found from the RBE values of Fry et al. (1985) and Fry (1986) as approximated by equation (10.39) using the aforementioned definition of Curtis et al.¹

$$F_j(L_j) = \frac{\text{RBE}(L_j) L_j}{12.5D_o} \quad (10.60)$$

¹ Curtis, S. B.; Townsend, L. W.; Wilson, J. W.; Powers-Risius, P.; Alpen, E. L.; and Fry, R. J. M.: Fluence-Related Risk Coefficients Using the Harderian Gland Data as an Example. Paper presented at the 28th Plenary Meeting of COSPAR (The Hague, The Netherlands), June 25–July 6, 1990.

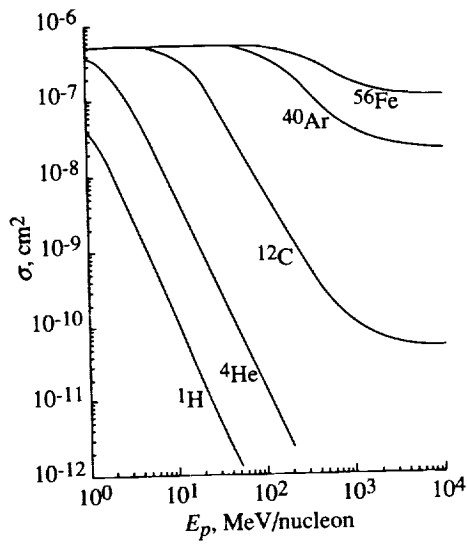


Figure 10.21. Cell-death cross sections for several ions in C3H10T1/2 cells according to the Katz model for direct ionization effects only.

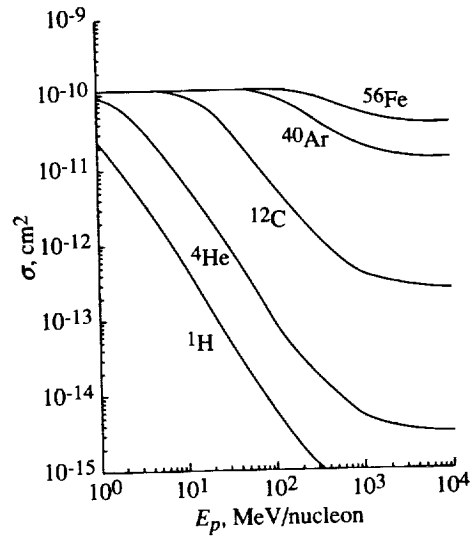


Figure 10.22. Cell-transformation cross sections for several ions in C3H10T1/2 cells according to the Katz model for direct ionization effects only.

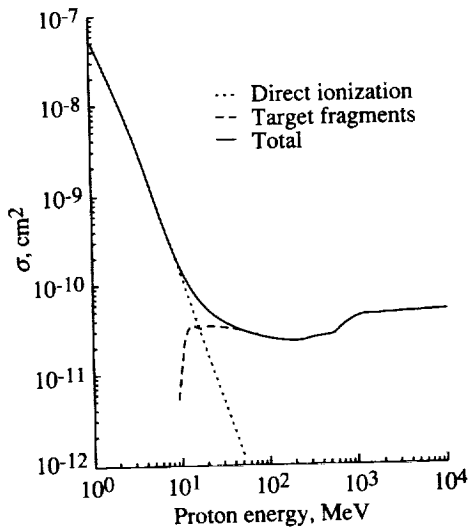


Figure 10.23. Cell-death cross sections including effects of nuclear reactions for protons in C3H10T1/2 cells according to the Katz model.

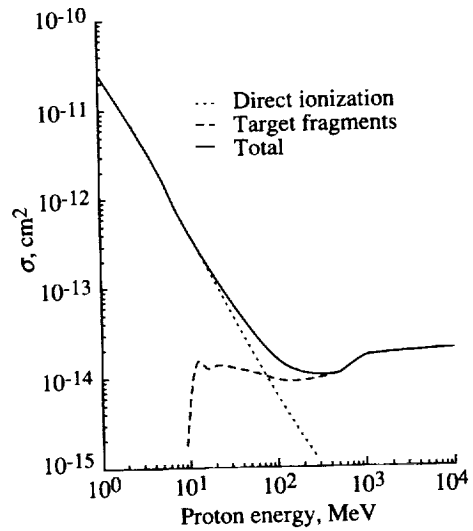


Figure 10.24. Cell-transformation cross sections including nuclear reaction effects for protons in C3H10T1/2 cells according to the Katz model.

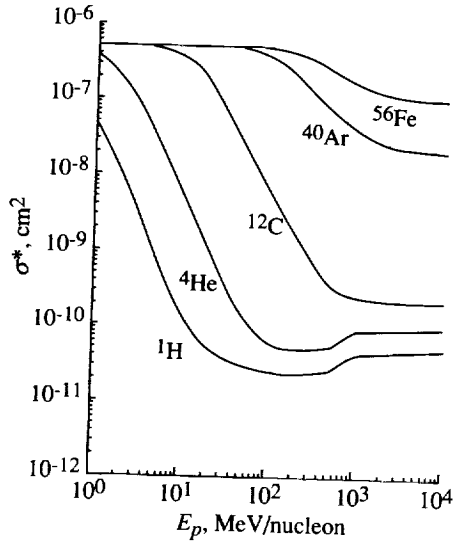


Figure 10.25. Effective cell-death cross sections including nuclear reaction effects for various ions in C3H10T1/2 cells.

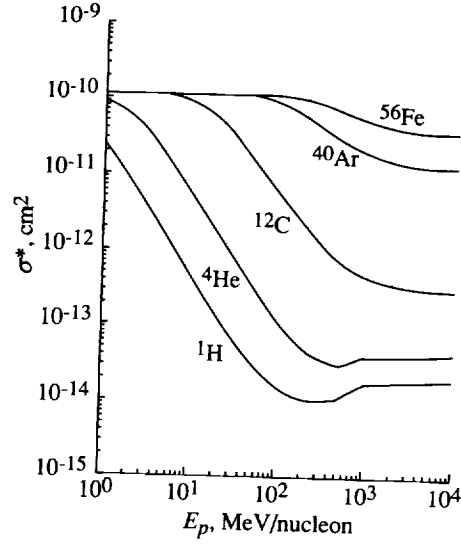


Figure 10.26. Cell-transformation cross sections including nuclear reaction effects for various ions in C3H10T1/2 cells.

and represents the risk coefficient for direct ionization only because RBE was taken as unity for ^{60}Co γ rays. In addition to the ionization caused directly by primary and high-energy secondary nuclei from fragmentation of the primary ions, the nuclei constituting biological tissue (i.e., the "target" nuclei) will break up into lower energy and, in some cases, very highly ionizing target fragments. Target fragment fluences $\phi_j(E_j)$, produced by a passing energetic ion of energy E_j , are given by

$$\phi_j(E_j) = \frac{1}{L_j(E_j)} \int_{E_j}^{\infty} \sigma_j(E_i) f_j(E'_j, E_i) \phi_i(E_i) dE'_j \quad (10.61)$$

where $\sigma_j(E_i)$ is the macroscopic fragmentation cross section, $f_j(E'_j, E_i)$ is the energy distribution of the j th fragment, and $\phi_i(E_i)$ is the fluence of passing ions of energy E_i . The total prevalence is given in terms of F_i as

$$P = F_i(L_i) \phi_i(E_i) + \sum_j \int_0^{\infty} F_j[(L_j(E_j))] \phi_j(E_j) dE_j \quad (10.62)$$

It is useful to define an effective $F_i^*(L_i)$ using equation (10.62) as

$$F_i^*(L_i) = F_i(L_i) + \sum_j \int_0^{\infty} dE_j \frac{F_j[L_j(E_j)]}{L_j(E_j)} \int_{E_j}^{\infty} dE'_j \sigma_j(E_i) f_j(E'_j, E_i) \quad (10.63)$$

The effective F_i^* are shown in figure 10.27 as a function of particle energy for representative charge components with the target fragment contributions shown separately.

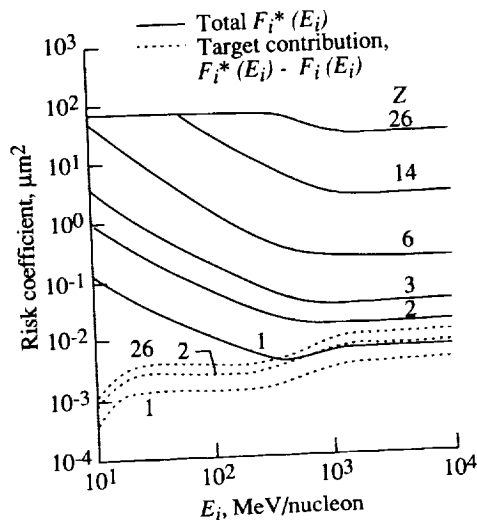


Figure 10.27. Fluence-related risk coefficients as a function of particle energy per nucleon for the total (ionization plus target fragmentation) contribution.

10.9. Effects on Hit-Size Effectiveness Spectrum

A somewhat different fluence-related concept has been introduced to overcome the problem of relating the absorbed dose to the dose equivalent (Bond et al., 1985). This method requires the measurement of the hit-size spectra within an appropriate sensitive volume size. The risk is estimated as a weighted average over the hit-size spectra. The measurement device is a gas proportional counter simulating a small tissue volume, and the weight function is found from radiobiological experimental data. Because we use continuous slowing down theory without regard to the transport of secondary electrons, we are limited to site sizes greater than 1 μm .

10.9.1. Microdosimetric quantities. Consider a convex region of tissue bounded by a surface Γ through which passes a flux of energetic nuclear particles displayed as dashed lines in figure 10.28. We currently examine the nuclear fragments they produce within the tissue volume denoted by starlike events in figure 10.28 and ignore the direct effects of the primary particles that we have treated elsewhere. The appropriate continuity equation is given as

$$\left[\vec{\Omega} \cdot \vec{\nabla} - \frac{\partial}{\partial E} S_Z(E) \right] \phi_Z(\vec{x}, \vec{\Omega}, E) = \zeta_Z(E) \quad (10.64)$$

where $S_Z(E)$ is the stopping power, $\phi_Z(\vec{x}, \vec{\Omega}, E)$ is the ion flux at \vec{x} moving in direction $\vec{\Omega}$ with energy E (in MeV), and the volumetric ion source $\zeta_Z(E)$ is formed by the collision density of the passing energetic particles and is herein assumed to be uniform and isotropic. We assume the inward-directed flux of ions Z to be zero on the boundary. We note that the solution to equation (10.64) is related to the cumulative spectrum of ion fragments produced by the nuclear collision. This spectrum is readily related to the LET spectrum in tissue as has been derived

elsewhere (Wilson et al., 1988). We now consider the more complicated problem of microdosimetry.

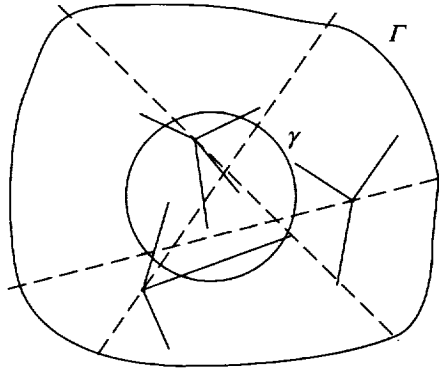


Figure 10.28. Nuclear-star events in a tissue region Γ in which a sensitive site is bound by γ .

The microdosimetric problem is to simply evaluate the energy fluctuations in a small specific region caused by the interaction of a tissue system with a radiation field. We will follow custom and assume the sensitive volume bound by a surface $\bar{\gamma}$ to be a small sphere of tissue of radius a embedded in a larger tissue matrix, as represented in figure 10.28. We represent the sensitive site boundary by the surface $\bar{\gamma}$ and consider the solution of equation (10.64) subject to the boundary condition

$$\phi_Z(\bar{\gamma}, \bar{\Omega}, E) = \frac{1}{S_Z(E)} \int_E^{E_b} \zeta_Z(E') dE' \quad (10.65)$$

for values of $\bar{\Omega}$ such that $\bar{n} \cdot \bar{\Omega} < 0$, where \bar{n} is the outward-directed normal to $\bar{\gamma}$. We assume that the boundary $\bar{\Gamma}$ is sufficiently removed that $E_b \rightarrow \infty$ for simplicity. Note that this is usually true because such limits are normally achieved over distances of a few hundred micrometers. For example, the average energy of the ${}^7\text{Li}$ fragments in tissue (Wilson, Townsend, and Khan, 1989) is 6.1 MeV. The field solution to equation (10.64) subject to the boundary condition in equation (10.65) is

$$\phi_Z(\bar{x}, \bar{\Omega}, E) = \frac{S_Z(E_a)}{S_Z(E)} \phi_Z(\bar{\gamma}, \bar{\Omega}, E_a) + \frac{1}{S_Z(E)} \int_E^{E_a} \zeta_Z(E') dE' \quad (10.66)$$

which is the fragment field due to the surrounding tissue environment and ion sources within the sensitive volume itself.

Although the fields within the region $\bar{\gamma}$ may be evaluated directly by equations (10.65) and (10.66), it is not clear how this field quantity is related to the fluctuation of absorbed energy within the volume bound by $\bar{\gamma}$. Caswell (1966) solved the problem of absorbed-energy fluctuation for nuclear recoils from low-energy neutron elastic scattering assuming isotropic scattering. The ICRU 40 report (Anon., 1986) suggests a relation that assumes constant stopping powers across the region. We derive herein a general solution to the energy fluctuation

problem by using equations (10.65) and (10.66) for a monoenergetic source for which any arbitrary spectral source may be found by superposition.

10.9.2. Response to an internal volumetric source. We first consider the term with internal sources. The particles produced within the sphere have a spectrum given by $\zeta_Z(E)$, and as the particles leave the volume, the spectrum is modified to

$$\phi_Z(\vec{\gamma}, \vec{\Omega}, E) = \frac{1}{S_Z(E)} \int_E^{E_a} \zeta_Z(E') dE' \quad (10.67)$$

This spectral modification is related to the spectrum of energy absorbed (neglecting the diffusive role of the secondary electrons). We consider here a monoenergetic spectral source that can be modified for any arbitrary source spectrum by superposition. The source spectrum is taken as

$$\zeta_Z(E) = \frac{\rho\sigma}{4\pi} \phi \delta(E - E_p) \quad (10.68)$$

where σ is the nuclear production cross section, assumed herein to be energy independent, and ρ is the nuclear density. The solution is

$$\phi_Z(\vec{\gamma}, \vec{\Omega}, E) = \begin{cases} \frac{\rho\sigma\phi}{4\pi S_Z(E)} & (E \leq E_p \leq E_a) \\ 0 & (\text{Otherwise}) \end{cases} \quad (10.69)$$

where ϕ is the flux of energetic initiating particles and

$$E_a = R_Z^{-1} [R_Z(E) + 2a \cos \theta] \quad (10.70)$$

with θ being the colatitude at the local normal to $\vec{\gamma}$. The differential energy spectrum of particles leaving the surface $\vec{\gamma}$ is

$$\frac{df_{vi}}{dE} = 2\pi A \int_{\mu_0}^1 \phi_Z(\vec{\gamma}, \vec{\Omega}, E) \mu d\mu = \frac{A\rho\sigma\phi}{4 S_Z(E)} (1 - \mu_0^2) \quad (10.71)$$

where μ_0 is the lower range of $\mu = \cos \theta$ subject to

$$\mu_0 = \begin{cases} \frac{R_Z(E_p) - R_Z(E)}{2a} & (E < R_Z^{-1}([R_Z(E_p) - 2a])) \\ 1 & (\text{Otherwise}) \end{cases} \quad (10.72)$$

and A is the surface area of the sphere. The total number of fragments produced is

$$N_{\text{tot}} = 4\pi \int_0^\infty \int_{\vec{\gamma}} \zeta_Z(E) r^2 dr d\vec{\Omega} dE = \frac{4}{3} \pi a^3 \rho\sigma\phi \quad (10.73)$$

with which we may write for the normalized spectrum

$$\frac{dF_{vi}}{dE} = \frac{1}{N_{\text{tot}}} \frac{df_{vi}}{dE} = \frac{3}{4a S_Z(E)} \left\{ 1 - \left[\frac{R_Z(E_p) - R_Z(E)}{2a} \right]^2 \right\} \quad (10.74)$$

The spectrum extends over the range

$$R_Z^{-1} [R_Z(E_p) - 2a] \leq E \leq E_p \quad (10.75)$$

where the lower limit extends to zero if $R_Z(E_p)$ is less than $2a$ for which some particles will come to rest inside the volume. The spectral distributions of emitted ${}^7\text{Li}$ ions are indicated in figures 10.29 and 10.30 for several values of a between 1 and 20 μm .

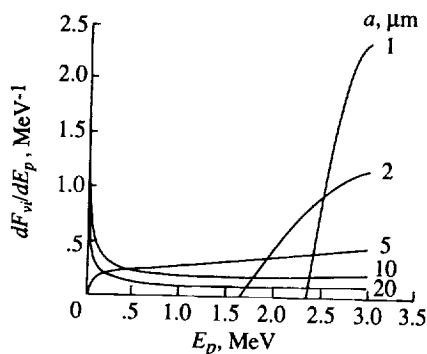


Figure 10.29. Exit spectrum of ${}^7\text{Li}$ due to internal 3-MeV sources in tissue spheres of radii between 1 and 20 μm .

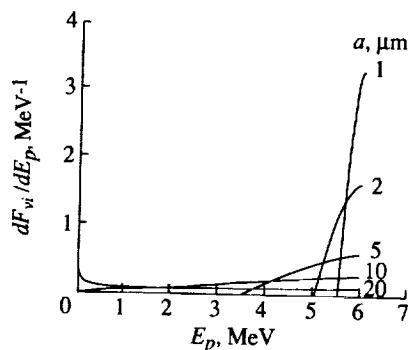


Figure 10.30. Exit spectrum of ${}^7\text{Li}$ due to internal 6-MeV sources in tissue spheres of radii between 1 and 20 μm .

The spectrum of ${}^7\text{Li}$ ions emitted from the surface of the tissue spheres for a 3-MeV source energy is shown in figure 10.29. The results for the 1- μm sphere show minimal degradations of the source energy spectrum. The escaping energy spectrum for the larger spheres is beginning to approach the shape of the equilibrium spectrum of the ion flux spectrum of the surrounding tissue. Indeed, very little effect on the escaping spectrum is seen from the increased leakage in reducing the radius from 20 to 10 μm . The ${}^7\text{Li}$ range on the order of the sphere diameter and the spectrum is probably an equilibrium spectrum. Note that the spectrum in figure 10.29 is only from the escaping ions corresponding to the ion sources within 10 μm of the surface. Figure 10.30 shows similar results for 6-MeV ${}^7\text{Li}$ ions. Note that the 20- μm spectrum is still near equilibrium because the ion range (22 μm) is on the order of the sphere radius.

The integrated spectral function represents the fraction of escaping particles

$$\int_0^{E_p} \frac{dF_{vi}}{dE} dE = \frac{3}{4a} \int_{R_Z(E_p)-2a}^{R_Z(E_p)} \left\{ 1 - \left[\frac{R_Z(E_p) - R}{2a} \right]^2 \right\} dR$$

$$= \begin{cases} 1 & R_Z(E_p) > 2a \\ \frac{3}{4a} R_Z(E_p) \left[1 - \frac{R_Z(E_p)^2}{12a^2} \right] & (R_Z(E_p) \leq 2a) \end{cases} \quad (10.76)$$

The energy loss spectrum is made up of two components: those generated with energy E_p that escape with energy E and those that do not escape. The energy losses ε and E are related as

$$\varepsilon = E_p - E \quad (10.77)$$

with the result that the distribution of ε and E is related as

$$\frac{dF_{va}}{d\varepsilon} = \frac{dF_{vi}}{dE} \quad (10.78)$$

so that

$$\frac{dF_{va}}{d\varepsilon} = \frac{3}{4a S_Z(E_p - \varepsilon)} \left\{ 1 - \left[\frac{R_Z(E_p) - R_Z(E_p - \varepsilon)}{2A} \right]^2 \right\} \quad (10.79)$$

thus giving the energy loss spectrum of escaping ions. The energy loss spectrum for ${}^7\text{Li}$ ions escaping the sphere is shown for three sphere radii in figures 10.31 to 10.33. A second contribution comes from ions that stop within the volume, giving the total energy loss spectrum as

$$\frac{dF_{ai}}{d\varepsilon} = \frac{dF_{va}}{d\varepsilon} + \left\{ 1 - \frac{3}{4a} R_Z(E_p) \left[1 - \frac{R_Z(E_p)^2}{12a^2} \right] \right\} \delta(\varepsilon - E_p) \quad (10.80)$$

Equation (10.80) is useful for calculating the absorption spectrum for an isolated sphere. The energy loss spectrum is related to the lineal energy spectrum by multiplying equation (10.80) by the average chord of the sensitive site. One may show with little effort that the terms in equation (10.80) are equivalent to Caswell's starter and insider results for recoil proton spectra, respectively. Indeed, Caswell's results are easily derived using equation (10.80). The energy loss spectrum of ${}^7\text{Li}$ ions produced externally to the surface $\bar{\gamma}$ is now considered.

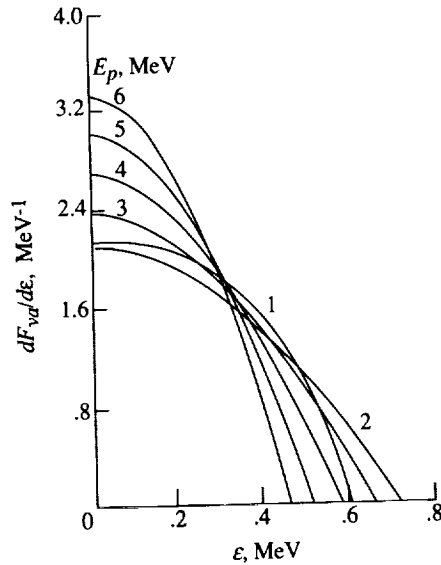


Figure 10.31. Energy loss spectrum of ${}^7\text{Li}$ ions in a $1\text{-}\mu\text{m}$ tissue sphere for internal source energies between 1 and 6 MeV.

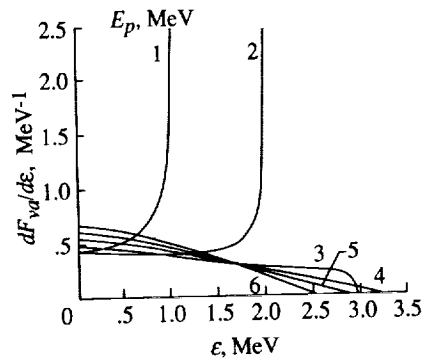


Figure 10.32. Energy loss spectrum of ${}^7\text{Li}$ ions in a $5\text{-}\mu\text{m}$ tissue sphere for internal source energies between 1 and 6 MeV.

10.9.3. Response to a surface source. To evaluate the surface terms, we first consider the response to a monoenergetic source term by taking the boundary function as

$$\phi_Z(\vec{\gamma}, \vec{\Omega}, E) = \frac{1}{2\pi} \delta(E - E') \quad (10.81)$$

for which the solution for surface sources is

$$\phi_Z(\vec{x}, \vec{\Omega}, E) = \frac{S_Z(E_a)}{2\pi S_Z(E)} \delta(E_a - E') \quad (10.82)$$

We evaluate equation (10.82) on the surface of the sphere (i.e., $\vec{x} = \vec{\gamma}$) and calculate the total spectrum of exiting particles as

$$\begin{aligned} \frac{df_s}{dE} &= 2\pi A \int_0^1 \mu \phi_Z(\vec{\gamma}, \vec{\Omega}, E) d\mu \\ &= \frac{A}{4a^2 S_Z(E)} \left\{ \begin{array}{l} R_Z(E') - R_Z(E) \quad (R_Z^{-1}[R_Z(E') - 2a] \leq E \leq E') \\ 0 \quad \text{(Otherwise)} \end{array} \right\} \end{aligned} \quad (10.83)$$

The total number of escaping ions is

$$N_{\text{tot}} = \int_0^\infty \frac{df_s}{dE} dE = \left\{ \begin{array}{l} \frac{A}{2} \quad (R_Z(E') \geq 2a) \\ \frac{A}{2} \frac{[R_Z(E')]^2}{2a} \quad (R_Z(E') < 2a) \end{array} \right\} \quad (10.84)$$

We may now find the energy loss spectrum from this source. The total number of particles crossing into the volume is $A/2$ with individual energies of E' . For $R_Z(E') < 2a$, the number of stopping ions is

$$N_s = \frac{A}{2} \left\{ 1 - \left[\frac{R_Z(E')}{2a} \right]^2 \right\} \quad (10.85)$$

and the corresponding ion energy loss spectrum is

$$\frac{df_s}{d\varepsilon} = N_s \delta(E' - \varepsilon) \quad (10.86)$$

Note that there are no stopping ions if $R_Z(E') > 2a$. The total energy loss spectrum is

$$\frac{df_{sa}}{d\varepsilon} = \left. \frac{df_s}{dE} \right|_{E=E'-\varepsilon} + N_s \delta(E' - \varepsilon) \quad (10.87)$$

similar to our earlier result in equation (10.80).

10.9.4. Response to an external volumetric source. We now apply equation (10.87) to determine the response to external volumetric source terms present at the boundary of the sphere as given by equation (10.66). First, by using equations (10.83) and (10.87) we consider the energy loss spectrum for

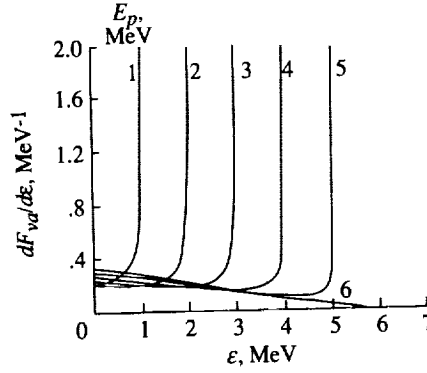


Figure 10.33. Energy loss spectrum of ${}^7\text{Li}$ ions in a $10\text{-}\mu\text{m}$ tissue sphere for internal source energies between 1 and 6 MeV.

the surface ion source term for ions that are able to escape the sphere. The energy loss spectrum is

$$\begin{aligned} \frac{df_{ve}}{d\varepsilon} &= \frac{2\pi A}{4a^2} \int_{\varepsilon}^{E_p} \frac{R_Z(E') - R_Z(E' - \varepsilon)}{S_Z(E' - \varepsilon)} \frac{\rho\sigma\phi}{4\pi S_Z(E')} dE' \\ &= \frac{A}{2} \frac{\rho\sigma\phi}{4a^2} \int_{R_Z(\varepsilon)}^{R_Z(E_p)} \frac{R_Z(E') - R_Z(E' - \varepsilon)}{S_Z(E' - \varepsilon)} d[R_Z(E')] \end{aligned} \quad (10.88)$$

One can easily show that equation (10.88) produces Caswell's results for crossers produced by neutron collisions with hydrogen. The integral in equation (10.88) cannot be further reduced without assuming some functional form for $S_Z(E)$. Because the ions are of relatively low energy, we assume that $S_Z(E)$ is proportional to velocity as predicted by Fermi and Teller (1947) and Lindhard (1954). We find that

$$\frac{df_{ve}}{d\varepsilon} = \frac{A}{2} \frac{\rho\sigma\phi}{4a^2} \frac{R_Z(E_p - \varepsilon)}{S_Z(E_p - \varepsilon)} \{2 R_Z(E_p - \varepsilon) - [R_Z(E_p) - R_Z(\varepsilon)]\} \quad (10.89)$$

The contribution to the energy loss spectrum from stoppers ions is

$$\begin{aligned} \frac{df_{ve}}{d\varepsilon} &= 2\pi \int_{\varepsilon}^{E_p} N_s(E') \delta(E' - \varepsilon) \frac{\rho\sigma\phi}{4\pi S_Z(E')} dE' \\ &= \frac{A}{4} \frac{\rho\sigma\phi}{S_Z(\varepsilon)} \left\{ 1 - \left[\frac{R_Z(\varepsilon)}{2a} \right]^2 \right\} \end{aligned} \quad (10.90)$$

for which the total energy loss spectrum from external volume sources is given by summing equations (10.89) and (10.90). It can be shown that equation (10.90) produces Caswell's results for the stoppers produced by low-energy neutron collisions with hydrogen.

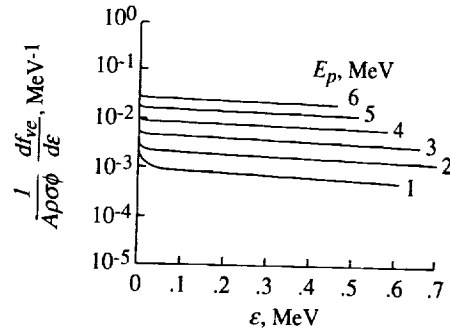


Figure 10.34. Energy loss spectrum of ${}^7\text{Li}$ ions in a $1\text{-}\mu\text{m}$ tissue sphere for external source energies between 1 and 6 MeV.

The energy loss spectrum in a $1\text{-}\mu\text{m}$ sphere caused by external volumetric sources in the tissue matrix is shown in figure 10.34. The maximum energy loss is indicative of the energy-dependent stopping power. Otherwise, the energy loss spectrum is nearly uniform in energy. A rather strong energy dependence is seen in the energy loss spectrum for the $5\text{-}\mu\text{m}$ and $10\text{-}\mu\text{m}$ spheres shown in figures 10.35 and 10.36, respectively. The low-energy spectrum is dominated by the low-energy particles entering the boundary $\bar{\gamma}$ and has insufficient energy to escape, as given by equation (10.90). The high-energy shoulder seen most clearly for the 2-MeV curve in figure 10.36 is caused by passing entirely through the region and escaping $\bar{\gamma}$ with a portion of the low-energy particles as given by equation (10.89).

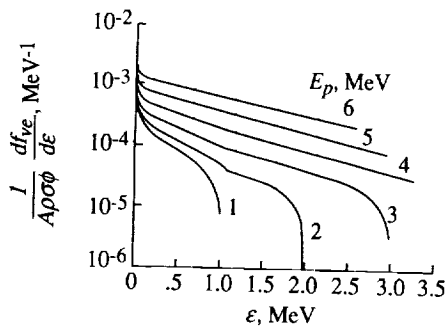


Figure 10.35. Energy loss spectrum of ${}^7\text{Li}$ ions in a $5\text{-}\mu\text{m}$ tissue sphere for external source energies between 1 and 6 MeV.

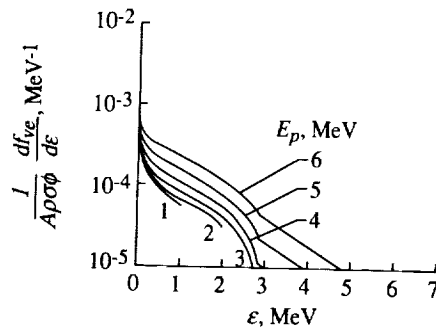


Figure 10.36. Energy loss spectrum of ${}^7\text{Li}$ ions in a $10\text{-}\mu\text{m}$ tissue sphere for external source energies between 1 and 6 MeV.

10.9.5. Remarks. A general method is found by which the energy absorption spectrum in a small spherical cavity is related to the source spectrum of the nuclear fragmentation event. The energy absorption spectrum may be found for arbitrary reaction source spectra. The current method can be used for evaluating the lineal energy distribution of the important $1\text{-}\mu\text{m}$ spherical dosimeter, which directly relates to the proposed quality factors (ICRU 40 (Anon., 1986)). The results of Caswell for the proton spectra from isotropic neutron scattering are easily derived

from the present formalism. The current method can be easily applied to other geometries for any arbitrary source spectra. For example, the same methods are being used to analyze fragmentation events in thin surface barrier detectors.

The hit spectrum in electronic devices is related to the single-event upset problem. Application of these methods to electronic-related problems is given elsewhere (Ngo et al., 1989).

10.10. References

- Alsmiller, R. G., Jr.; Armstrong, T. W.; and Coleman, W. A., 1970: *The Absorbed Dose and Dose Equivalent From Neutrons in the Energy Range 60 to 3000 MeV and Protons in the Energy Range 400 to 3000 MeV*. ORNL TM-2924, U.S. Atomic Energy Commission.
- Alsmiller, R. G., Jr.; and Barish, J., 1976: *Neutron Kerma Factors for H, C, N, and O and Tissue in the Energy Range 20 to 70 MeV*. ORNL/TM-5702 (Contract No. W-7405-eng-26), Oak Ridge National Lab.
- Anon., 1968a: *MECC-7 Intranuclear Cascade Code, 500-MeV Protons on O-16. I4C Analysis Codes* (Programmed for H. W. Bertini). Available from Radiation Shielding Information Center, Oak Ridge National Lab.
- Anon., 1968b: *A Review of the Radiosensitivity of the Tissues in Bone*. ICRP Publ. 11, Pergamon Press.
- Anon., 1977a: *Neutron Dosimetry for Biology and Medicine*. ICRU Rep. 26, International Commission on Radiation Units and Measurements.
- Anon., 1977b: *Recommendations of the International Commission on Radiological Protection*. ICRP Publ. 26, Pergamon Press.
- Anon., 1986: *The Quality Factor in Radiation Protection*. ICRU Rep. 40, International Commission on Radiation Units and Measurements.
- Beddoe, A. H.; Darley, P. J.; and Spiers, F. W., 1976: Measurements of Trabecular Bone Structure in Man. *Phys. Med. & Biol.*, vol. 21, no. 4, pp. 589-607.
- Bond, V. P.; Varma, M. N.; Sondhaus, C. A.; and Feinendegen, L. E., 1985: An Alternative to Absorbed Dose, Quality, and RBE at Low Exposures. *Radiat. Res.*, suppl. 8, vol. 104, pp. S-52-S-57.
- Brenner, D. J., 1983: Neutron Kerma Values Above 15 MeV Calculated With a Nuclear Model Applicable to Light Nuclei. *Phys. Med. & Biol.*, vol. 29, no. 4, pp. 437-441.
- Caswell, Randall S., 1966: Deposition of Energy by Neutrons in Spherical Cavities. *Radiat. Res.*, vol. 27, pp. 92-107.
- Chatterjee, A.; Maccabee, H. D.; and Tobias, C. A., 1973: Radial Cutoff LET and Radical Cutoff Dose Calculations for Heavy Charged Particles in Water. *Radiat. Res.*, vol. 54, pp. 479-494.

- Cucinotta, Francis A.; Hajnal, Ferenc; and Wilson, John W., 1990: Energy Deposition at the Bone-Tissue Interface From Nuclear Fragments Produced by High-Energy Nucleons. *Health Phys.*, vol. 59, no. 6, pp. 819-825.
- Curtis, S. B.; Dye, D. L.; and Sheldon, W. R., 1965: Fractional Cell Lethality Approach to Space Radiation Hazards. *Second Symposium on Protection Against Radiations in Space*, Arthur Reetz, Jr., ed., NASA SP-71, pp. 219-223.
- Dimbylow, P. J., 1982: Neutron Cross-Section and Kerma Value Calculations for C, N, O, Mg, Al, P, S, Ar and Ca From 20 to 50 MeV. *Phys. Med. & Biol.*, vol. 27, no. 8, pp. 989-1001.
- Fermi, E.; and Teller, E., 1947: The Capture of Negative Mesotrons in Matter. *Phys. Review*, vol. 72, no. 5, pp. 399-408.
- Fry, R. J. M.; Powers-Risius, P.; Alpen, E. L.; and Ainsworth, E. J., 1985: High-LET Radiation Carcinogenesis. *Radiat. Res.*, vol. 104, pp. S-188-S-195.
- Fry, R. J. M., 1986: Radiation Effects in Space. *Adv. Space Res.*, vol. 6, no. 11, pp. 261-268.
- Greiner, D. E.; Lindstrom, P. J.; Heckman, H. H.; Cork, Bruce; and Bieser, F. S., 1975: Momentum Distributions of Isotopes Produced by Fragmentation of Relativistic ^{12}C and ^{16}O Projectiles. *Phys. Review Lett.*, vol. 35, no. 3, pp. 152-155.
- Herling, G. H.; Bassel, R. H.; Adams, J. H.; and Fraser, W. A., 1981: *Neutron-Induced Reactions in Tissue-Resident Elements*. NRL Rep. 8441, U.S. Navy. (Available from DTIC as AD A101 519.)
- Katz, R.; Ackerson, B.; Homayoonfar, M.; and Sharma, S. C., 1971: Inactivation of Cells by Heavy Ion Bombardment. *Radiat. Res.*, vol. 47, pp. 402-425.
- Katz, Robert; Sharma, S. C.; and Homayoonfar, M., 1972: The Structure of Particle Tracks. *Topics in Radiation Dosimetry, Supplement 1*, F. H. Attix, ed., Academic Press, Inc., pp. 317-383.
- Katz, Robert, 1986: Biological Effects of Heavy Ions From the Standpoint of Target Theory. *Adv. Space Res.*, vol. 6, no. 11, pp. 191-198.
- Kellerer, A. M.; and Chmelevsky, D., 1975: Criteria for the Applicability of LET. *Radiat. Res.*, vol. 63, pp. 226-234.
- Lindhard, J., 1954: On the Properties of a Gas of Charged Particles. *Mat.-Fys. Medd.—K. Dan. Vidensk. Selsk.*, vol. 28, no. 8, pp. 1-58.
- Lindstrom, P. J.; Greiner, D. E.; Heckman, H. H.; Cork, Bruce; and Bieser, F. S., 1975: *Isotope Production Cross Sections From the Fragmentation of ^{16}O and ^{12}C at Relativistic Energies*. LBL-3650 (NGR-05-003-513), Lawrence Berkeley Lab., Univ. of California.
- MacFarlane, R. E.; Barrett, R. J.; Muir, D. W.; and Boicourt, R. M., 1978: *The NJOY Nuclear Data Processing System: User's Manual*. LA-7584-M (ENDF-272) (Contract W-7405-ENG. 34), Los Alamos Scientific Lab.

Transport Methods and Interactions for Space Radiations

- Mathews, G. J., 1983: Complete Fragment Yields From Spallation Reactions Via a Combined Time-of-Flight and $\Delta E-E$ Technique. *Composition and Origin of Cosmic Rays*, Maurice M. Shapiro, ed., D. Riedel Publ. Co., pp. 317-320.
- Ngo, Duc M.; Wilson, John W.; Buck, Warren W.; and Fogarty, Thomas N., 1989: *Nuclear-Fragmentation Studies in Microelectronic Applications*. NASA TM-4143.
- Paretzke, Herwig G., 1988: Problems in Theoretical Track Structure Research for Heavy Charged Particles. *Quantitative Mathematical Models in Radiation Biology*, Jürgen Kiefer, ed., Springer-Verlag, pp. 49-56.
- Rossi, Harald H., 1959: Specification of Radiation Quality. *Radiat. Res.*, vol. 10, pp. 522-531.
- Santoro, R. T.; Alsmiller, R. G., Jr.; and Chandler, K. C., 1974: *The Effects of Bone in the Use of Negatively Charged Pions in Cancer Radiotherapy*. ORNL-TM-4407 (Order NSF/RANN AG-399), Oak Ridge National Lab.
- Schaefer, Hermann J., 1952: Exposure Hazards From Cosmic Radiation Beyond the Stratosphere and in Free Space. *J. Aviation Med.*, vol. 23, no. 4, pp. 334-344.
- Schimmerling, Walter; Alpen, Edward L.; Powers-Risius, Patricia; Wong, Mervyn; DeGuzman, Randy J.; and Rapkin, Marwin, 1987: The Relative Biological Effectiveness of 670 MeV/A Neon as a Function of Depth in Water for a Tissue Model. *Radiat. Res.*, vol. 112, no. 3, pp. 436-448.
- Shinn, J. L.; Wilson, J. W.; and Ngo, D. M., 1990: Risk Assessment Methodologies for Target Fragments Produced in High-Energy Nucleon Reactions. *Health Phys.*, vol. 59, no. 1, pp. 141-143.
- Silberberg, R.; Tsao, C. H.; and Shapiro, M. M., 1976: Semiempirical Cross Sections, and Applications to Nuclear Interactions of Cosmic Rays. *Spallation Nuclear Reactions and Their Applications*, B. S. P. Shen and M. Merker, eds., D. Reidel Publ. Co., pp. 49-81.
- Silberberg, R.; Tsao, C. H.; and Letaw, John R., 1983: Improvement of Calculations of Cross Sections and Cosmic-Ray Propagation. *Composition and Origin of Cosmic Rays*, Maurice M. Shapiro, ed., D. Reidel Publ. Co., pp. 321-336.
- Spiers, F. W., 1969: Transition-Zone Dosimetry. *Radiation Dosimetry, Second ed.*, Volume III, Frank H. Attix and Eugene Tochilin, eds., Academic Press, pp. 809-867.
- Townsend, L. W.; Wilson, J. W.; and Bidasaria, H. B., 1982: On the Geometric Nature of High-Energy Nucleus-Nucleus Reaction Cross Sections. *Canadian J. Phys.*, vol. 60, no. 10, pp. 1514-1518.
- Townsend, Lawrence W.; Wilson, John; and Cucinotta, Francis A., 1987: A Simple Parameterization for Quality Factor as a Function of Linear Energy Transfer. *Health Phys.*, vol. 53, no. 5, pp. 531-532.
- Waligorski, M. P. R.; Sinclair, G. L.; and Katz, R., 1987: Radiosensitivity Parameters for Neoplastic Transformations in C3H10T1/2 Cells. *Radiation Res.*, vol. 111, pp. 424-437.
- Watt, D. E., 1989: On Absolute Biological Effectiveness and Unified Dosimetry. *J. Radiol. Prot.*, vol. 9, no. 1, pp. 33-49.

- Wells, Alan H., 1979: A Consistent Set of KERMA Values for H, C, N, and O for Neutrons of Energies From 10 to 80 MeV. *Radiat. Res.*, vol. 80, pp. 1-9.
- Wilson, John W., 1977: *Analysis of the Theory of High-Energy Ion Transport*. NASA TN D-8381.
- Wilson, John W.; Stith, John J.; and Stock, L. V., 1983: *A Simple Model of Space Radiation Damage in GaAs Solar Cells*. NASA TP-2242.
- Wilson, John W.; Townsend, L. W.; Bidasaria, H. B.; Schimmerling, Walter; Wong, Mervyn; and Howard, Jerry, 1984: ^{20}Ne Depth-Dose Relations in Water. *Health Phys.*, vol. 46, no. 5, pp. 1101-1111.
- Wilson, J. W.; Townsend, L. W.; Badavi, F. F., 1987: Galactic HZE Propagation Through the Earth's Atmosphere. *Radiat. Res.*, vol. 109, no. 2, pp. 173-183.
- Wilson, John W.; Chun, S. Y.; Buck, W. W.; and Townsend, L. W., 1988: High Energy Nucleon Data Bases. *Health Phys.*, vol. 55, no. 5, pp. 817-819.
- Wilson, John W.; Townsend, Lawrence W.; Khan, Ferdous, 1989: Evaluation of Highly Ionizing Components in High-Energy Nucleon Radiation Fields. *Health Phys.*, vol. 57, no. 5, pp. 717-724.
- Yang, Tracy Chui-Hsu; Craise, Laurie M.; Mei, Man-Tong; and Tobias, Cornelius A., 1985: Neoplastic Cell Transformation by Heavy Charged Particles. *Radiation Res.*, vol. 104, pp. S-177-S-187.
- Ziegler, J. F., 1980: *Handbook of Stopping Cross-Sections for Energetic Ions in All Elements*. Volume 5 of *The Stopping and Ranges of Ions in Matter*, J. F. Ziegler, ed., Pergamon Press Inc.

1
2
3
4
5
6
7
8
9
10
11
12
13
14
15
16
17
18
19
20
21
22
23
24
25
26
27
28
29
30
31
32
33
34
35
36
37
38
39
40
41
42
43
44
45
46
47
48
49
50
51
52
53
54
55
56
57
58
59
60
61
62
63
64
65
66
67
68
69
70
71
72
73
74
75
76
77
78
79
80
81
82
83
84
85
86
87
88
89
90
91
92
93
94
95
96
97
98
99
100

101
102
103
104
105
106
107
108
109
110
111
112
113
114
115
116
117
118
119
120
121
122
123
124
125
126
127
128
129
130
131
132
133
134
135
136
137
138
139
140
141
142
143
144
145
146
147
148
149
150
151
152
153
154
155
156
157
158
159
160
161
162
163
164
165
166
167
168
169
170
171
172
173
174
175
176
177
178
179
180
181
182
183
184
185
186
187
188
189
190
191
192
193
194
195
196
197
198
199
200

Chapter 11

Space-Radiation Exposure Issues

11.1. Introduction

Most of the work presented in previous chapters has been of a more fundamental nature rather than strictly space related exposure issues. That is, the main body of issues covered is as fundamental to radiobiology and radiation therapy as to space radiation. There are clear gaps in the presented methodologies and data bases. There is also a need to improve the atomic/molecular description in our work to include, first of all, improved stopping powers and to treat the fluctuation phenomena associated with slowing down as well as multiple scattering. The light fragment ($Z \leq 2$) production and transport need to treat the full energy spectra as well as the angular dependence. This is especially true not only for the laboratory related work but also for the angular scatter of neutrons in space computations. A heavy ion code for the laboratory analysis with energy-dependent nuclear cross sections has been developed (Wilson et al., 1984; Townsend and Wilson, 1988) but space-radiation codes have ignored the energy-dependent HZE cross sections. A laboratory code that includes light fragments in any realistic way does not exist. Greater knowledge of nuclear fragmentation processes and a corresponding transport theory are required.

In addition to these physical factors, there are unresolved biological issues. The differences in the radiosensitivity of various tissues within an individual as well as individual differences are generally assumed to result from repair mechanisms (Curtis, 1986; Fritz-Niggli, 1988). The work of Swenberg, Holwitt, and Speicher (1990) suggests these differences may result from the structural state of the DNA as well. Repair also affects the dose response for protracted exposure. Current radiation-protection guidelines use quality factors that are independent of dose rate (no time-modifying factors), which may be of unusual importance in the small dose rate exposures often experienced in space (NCRP 98, (Anon., 1989)). Clearly, well understood dose-rate-dependent models are needed (Scott and Ainsworth, 1980; Curtis, 1986; Anon., 1989). Furthermore, exposure received on a Lunar or Mars mission will involve heavy ion exposure for which many issues concerning appropriate relative biological effectiveness (RBE) factors (hence, quality factors) are yet unknown. The accumulated heavy ion exposure levels will be large and unprecedented in human experience. Although these issues may be studied in ground-based exposures with model biological systems, extrapolating to human exposure is difficult at best, and space stress factors such as microgravity are unknown possible modifying factors in radiobiological response.

In addition to radiobiological response issues is the need to evaluate dose nonuniformity caused by body self-shielding and dose gradients within the shielding structure. For example, tumor prevalence in the female breast is site specific even for relative uniform exposure (NCRP 85 (Anon., 1986a)). We are led to believe that the exposure of only sensitive sites may be effective in tumor formation. Conversely, exposure of insensitive sites is assumed to be noneffective, and nonuniformity of exposure is a critical issue. In this chapter, we make some

preliminary assessments concerning these issues and examine a limited number of shielding strategies to mitigate these radiation effects.

11.2. Galactic Cosmic-Ray Exposure

The incident galactic cosmic-ray spectrum (Adams, 1987) for free space is propagated through the target material by using the accurate analytical/numerical solutions to the transport equation described in chapter 10. These solution methods have been verified (to within 2 percent accuracy) by comparison with exact, analytical benchmark solutions to the ion transport equation (Wilson and Townsend, 1988; Wilson et al., 1988).

These transport calculations include

1. Linear energy-transfer (LET) dependent quality factors from ICRP 26 (Anon., 1977)
2. Dose contributions from propagating neutrons, protons, α -particles, and heavy ions (high-energy, high-charge (HZE) particles)
3. Dose contributions that result from target nuclear fragments produced by all neutrons and primary protons and their secondaries
4. Dose contributions due to nuclear recoil in tissue

Major shortcomings of the calculations are as follows:

1. Except for tissue targets, mass number 2 and 3 fragment contributions are neglected
2. Target fragmentation contributions from HZE particles and their charged secondaries are neglected (although they are included for nucleons)
3. All secondary particles from HZE interactions are presently assumed to be produced with a velocity equal to that of the incident particle; for neutrons produced in HZE particle fragmentations, this is conservative
4. A quality factor of 20 is assigned to all multiple charged target fragments from the incident protons; to improve this approximation, one must calculate target fragment spectra correctly
5. Meson contributions to the propagating radiation fields are neglected
6. Nucleus-nucleus cross sections are not fully energy dependent (nucleon-nucleus cross sections are fully energy dependent)

For these shortcomings, items 3 and 4 are conservative; the remaining items, however, are not and alone probably result in a 15- to 30-percent underestimate of the exposure. As discussed elsewhere (Townsend, Wilson, and Nealy, 1989), the main sources of uncertainty are the input nuclear fragmentation model and the

incident galactic cosmic-ray (GCR) spectrum. Taken together, they could easily impose a factor of 2 or more uncertainty in the exposure predictions.

11.2.1. Results. In the present results we use the ICRP 26 (Anon., 1977) quality factors, which are currently in force within the U.S. space program. Figure 11.1 displays dose equivalent (in units of sieverts per year) as a function of water shield thickness (in units of areal density, g/cm^2 , or thickness, cm). Curves are displayed for solar minimum and solar maximum periods. The numerical values used in this figure are listed in table 11.1. Also listed in this table are values for the absorbed dose in centigrays per year as a function of water shield thickness. For all thicknesses considered, the dose and dose equivalent during solar maximum are less than half the dose equivalent during solar minimum, at least according to the current estimates derived from the CREME environmental model of Adams (1987). Figure 11.2 displays results for dose and dose equivalent behind an aluminum shield. Also shown are measurements with argon filled ion chambers at two shielded locations on the Prognoz satellite (Kovalev, Muratova, and Petrov, 1989). The results for the $1 \text{ g}/\text{cm}^2$ location are the most clear by experimental design. The mass distribution for the deeply shielded counter was poorly defined (Kovalev, Muratova, and Petrov, 1989); this uncertainty is denoted in the figure by parentheses around the data points. The solar maximum model predicted by CREME is clearly an underestimate. The solar minimum model appears in reasonable agreement with the Prognoz data. Therefore, we will restrict the present analysis to solar minimum periods, which are the most limiting for GCR exposures. This is

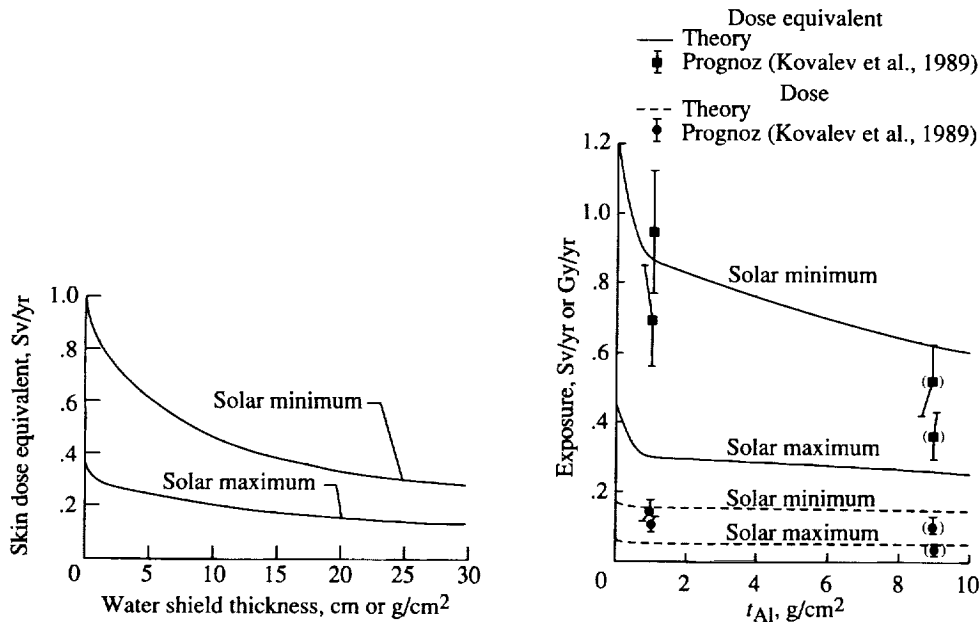


Figure 11.1. Dose equivalent resulting from galactic cosmic rays as function of water shield thickness.

Figure 11.2. Deep space exposure behind aluminum shield. Parentheses denote depth of interior of Prognoz spacecraft.

Table 11.1. Galactic Cosmic-Ray Dose and Dose Equivalent in Tissue for Various Water Shield Thicknesses

[All values are rounded to nearest 0.1]

Thickness, cm or g/cm ²	Solar maximum		Solar minimum	
	Dose, cGy/yr	Dose equivalent, cSv/yr	Dose, cGy/yr	Dose equivalent, cSv/yr
0	6.4	45.1	17.1	120.6
1	5.4	29.0	14.9	82.6
2	5.4	27.6	14.6	76.1
3	5.4	26.3	14.4	70.3
4	5.4	25.1	14.2	65.4
5	5.4	24.0	14.0	61.1
6	5.4	23.0	13.8	57.4
7	5.3	22.0	13.7	54.1
8	5.3	21.2	13.5	51.1
9	5.3	20.4	13.4	48.6
10	5.3	19.6	13.3	46.3
11	5.3	19.0	13.2	44.2
12	5.3	18.4	13.1	42.4
13	5.3	17.8	13.0	40.7
14	5.2	17.3	12.9	39.3
15	5.2	16.8	12.8	37.9
16	5.2	16.3	12.7	36.7
17	5.2	15.9	12.6	35.6
18	5.2	15.6	12.6	34.6
19	5.2	15.2	12.5	33.7
20	5.2	14.9	12.4	32.8
25	5.1	13.6	12.1	29.6
30	5.1	12.7	11.9	27.3
40	5.0	11.6	11.4	24.6
50	4.9	11.0	10.9	22.9

not meant to imply, however, that exposures during solar maximum periods are not important. On the contrary, the cumulative exposures that result from combined GCR and increased solar flare activity during solar maximum could potentially be significant. Analyses of these hazards are reported in chapter 12.

The actual compositions of the calculated radiation fields are displayed in tables 11.2 through 11.4; values for dose equivalent, dose, and particle flux are listed by particle type (neutrons, protons, etc.) and as a function of water thickness. The target fragment dose and dose equivalent contributions for incident protons and their secondaries, computed with BRYNTRN (Wilson et al., 1989), are displayed separately in these tables. The quality factor of target fragments ($A > 1$) is assumed to be 20.

Estimates of the thicknesses of water shielding required to protect astronauts from GCR particles can be obtained from table 11.1 or figure 11.1. At present, there are no recommended exposure limits for deep space exploratory missions. Therefore, we will use the currently proposed annual limits for Space Station *Freedom* as guidelines as recommended by NCRP 98 (Anon., 1989). The annual limits are 3 Sv to the skin (0.01 cm depth), 2 Sv to the ocular lens (0.3 cm depth), and 0.5 Sv to the blood-forming organs (5 cm depth). Clearly, from table 11.1, none of these limits are exceeded during periods of

Table 11.2. Solar Minimum Galactic Cosmic-Ray Dose Equivalent in Tissue for Various Particle Types and Water Shield Thicknesses

[All values are rounded to nearest 0.1]

Thickness, cm or g/cm ²	Dose equivalent, cSv/yr, from—					
	Neutrons	Protons	Target fragments	α -particles	HZE	Total
0	0	9.7	0	7.0	102.5	119.2
1	0.3	6.6	5.9	3.4	66.4	82.6
2	0.6	7.0	5.9	3.2	59.3	76.0
3	0.9	7.4	5.8	3.1	53.1	70.3
4	1.2	7.7	5.8	3.0	47.7	65.4
5	1.4	8.0	5.8	2.9	43.0	61.1
6	1.7	8.2	5.8	2.8	38.9	57.4
8	2.1	8.6	5.7	2.6	32.1	51.1
10	2.6	9.0	5.6	2.4	26.7	46.3
15	3.5	9.6	5.4	2.0	17.4	37.9
20	4.3	10.0	5.2	1.6	11.7	32.8
25	4.9	10.2	5.0	1.3	8.0	29.4
30	5.4	10.4	4.8	1.0	5.2	26.8
40	6.2	10.4	4.4	0.7	2.8	24.5
50	6.6	10.2	4.0	0.5	1.4	22.7

Transport Methods and Interactions for Space Radiations

Table 11.3 Solar Minimum Galactic Cosmic-Ray Dose in Tissue for Various Particle Types and Water Shield Thicknesses

[All values are rounded to nearest 0.1]

Thickness, cm or g/cm ²	Dose, cGy/yr, from—					
	Neutrons	Protons	Target fragments	α-particles	HZE	Total
0	0	6.2	0	3.0	7.8	17.0
1	0.1	6.0	0.3	2.7	5.8	14.9
2	0.1	6.4	0.3	2.6	5.3	14.7
3	0.2	6.6	0.3	2.5	4.9	14.5
4	0.2	6.8	0.3	2.4	4.5	14.2
5	0.3	7.1	0.3	2.3	4.1	14.1
6	0.4	7.2	0.3	2.2	3.8	13.9
8	0.5	7.5	0.3	2.0	3.2	13.5
10	0.5	7.8	0.3	1.9	2.8	13.3
15	0.7	8.3	0.3	1.6	1.9	12.8
20	0.9	8.6	0.3	1.3	1.4	12.5
25	1.1	8.7	0.3	1.1	1.0	12.2
30	1.2	8.8	0.2	0.9	0.8	11.9
40	1.3	8.8	0.2	0.6	0.4	11.3
50	1.4	8.6	0.2	0.4	0.2	10.8

Table 11.4. Solar Minimum Galactic Cosmic-Ray Flux for Various Particle Types and Water Shield Thicknesses

[All values are rounded to nearest 0.1]

Thickness, cm or g/cm ²	Flux, particles/cm ² /yr, from—			
	Neutrons	Protons	α-particles	HZE
0	0E7	1.3E8	1.2E7	1.4E6
1	0.4E7	1.3E8	1.2E7	1.3E6
2	0.8E7	1.3E8	1.2E7	1.2E6
3	1.2E7	1.3E8	1.1E7	1.2E6
4	1.6E7	1.4E8	1.1E7	1.1E6
5	1.9E7	1.4E8	1.0E7	1.1E6
6	2.2E7	1.4E8	1.0E7	1.0E6
8	2.9E7	1.4E8	0.9E7	0.9E6
10	3.5E7	1.4E8	0.9E7	0.8E6
15	4.7E7	1.4E8	0.7E7	0.6E6
20	5.8E7	1.4E8	0.6E7	0.5E6
25	6.7E7	1.4E8	0.5E7	0.4E6
30	7.4E7	1.4E8	0.4E7	0.3E6
40	8.4E7	1.3E8	0.3E7	0.2E6
50	9.0E7	1.3E8	0.2E7	0.1E6

solar maximum activity, as the unshielded (0 cm depth) dose equivalent is estimated to be less than 0.5 Sv. Similarly, during solar minimum periods, the estimated unshielded dose equivalent of 1.2 Sv does not exceed either exposure limits for the skin or the ocular lens. The dose equivalent at 5 cm depth, which yields an estimate of the exposure to the unshielded blood-forming organs (BFO), is 0.61 Sv, which exceeds the 0.5-Sv limit by 22 percent. To reduce this estimated exposure below 0.5 Sv requires about 3.5 g/cm² (3.5 cm) of water shielding in addition to the body self-shielding of 5 g/cm² (5 cm).

For comparison purposes, calculations of skin (0 cm depth) and BFO (5 cm depth) exposures behind various thicknesses of aluminum and liquid hydrogen shielding were made. The results are presented in tables 11.5 through 11.12. For aluminum, 6.5 g/cm² (2.4 cm) of shielding thickness is required to reduce the BFO dose equivalent below the annual limit. (See table 11.7.) For liquid hydrogen, 1 g/cm² (14 cm) of shielding is required. For relative comparison purposes, the BFO dose equivalent as a function of shield thickness (areal density) is plotted in figure 11.3 for these three materials. Clearly, shielding effectiveness per unit mass increases as the composition of the shield changes from heavier to lighter mass elements. For liquid hydrogen, an added advantage is the reduced neutron fluence that is caused by the absence of neutrons in the target composition and by the lack of target fragment contributions because of the elementary nature of hydrogen. From these results, for an allowed BFO exposure of 0.25 Sv/year, which corresponds to an uncertainty factor of 2 in a 0.5 Sv/year estimate, the mass ratios for the shielding are about 1:5:11 for LH₂:H₂O:Al. Obviously, for GCR shielding, the materials of choice are those composed of low atomic mass number constituents with significant hydrogen content.

Table 11.5. Solar Minimum Galactic Cosmic-Ray Dose Equivalent at 0 cm Deep in Tissue for Various Particle Types and Aluminum Shield Thicknesses

[All values are rounded to nearest 0.1]

Thickness, ^a g/cm ²	Dose equivalent, cSv/yr, from--					
	Neutrons	Protons	Target fragments	α-particles	HZE	Total dose equivalent
1	0.4	7.5	5.9	3.5	69.4	86.8
2	0.8	8.2	5.9	3.4	64.5	82.8
3	1.2	8.6	5.9	3.3	59.9	79.0
4	1.6	9.0	5.9	3.2	55.7	75.4
5	2.0	9.4	5.9	3.2	51.9	72.2
6	2.4	9.7	5.8	3.1	48.4	69.4
8	3.1	10.2	5.8	2.9	42.4	64.4
10	3.8	10.6	5.8	2.8	37.4	60.3
15	5.3	11.5	5.7	2.4	27.9	52.7
20	6.6	12.0	5.5	2.1	21.3	47.6
30	8.7	12.7	5.3	1.6	13.1	41.3

^a1 g/cm² of aluminum is equivalent to 0.37 cm thickness.

Transport Methods and Interactions for Space Radiations

Table 11.6. Solar Minimum Galactic Cosmic-Ray Dose at 0 cm Deep in Tissue for Various Particle Types and Aluminum Shield Thicknesses

[All values are rounded to nearest 0.1]

Thickness, ^a g/cm ²	Dose, cGy/yr, from—					
	Neutrons	Protons	Target fragments	α-particles	HZE	Total dose
1	0.1	6.3	0.3	2.7	6.1	15.5
2	0.2	6.8	0.3	2.6	5.7	15.5
3	0.2	7.1	0.3	2.6	5.3	15.5
4	0.3	7.4	0.3	2.5	5.0	15.5
5	0.4	7.6	0.3	2.4	4.9	15.5
6	0.5	7.8	0.3	2.4	4.5	15.4
8	0.6	8.2	0.3	2.3	4.0	15.4
10	0.7	8.5	0.3	2.2	3.6	15.3
15	1.0	9.1	0.3	1.9	2.8	15.1
20	1.3	9.5	0.3	1.7	2.3	15.0
30	1.7	10.0	0.3	1.3	1.5	14.7

^a1 g/cm² of aluminum is equivalent to 0.37 cm thickness.

Table 11.7. Solar Minimum Galactic Cosmic-Ray Dose Equivalent at 5 cm Deep in Tissue for Various Particle Types and Aluminum Shield Thicknesses

[All values are rounded to nearest 0.1]

Thickness, ^a g/cm ²	Dose equivalent, cSv/yr, from—					
	Neutrons	Protons	Target fragments	α-particles	HZE	Total dose equivalent
1	1.7	8.2	5.8	2.8	40.3	58.8
2	2.1	8.5	5.8	2.8	37.7	56.8
3	2.4	8.7	5.8	2.7	35.4	54.9
4	2.7	8.9	5.7	2.6	33.3	53.3
5	3.0	9.1	5.7	2.5	31.4	51.7
6	3.3	9.3	5.7	2.5	29.6	50.3
8	3.9	9.6	5.7	2.3	26.4	47.8
10	4.4	9.9	5.6	2.2	23.6	45.7
15	5.6	10.5	5.5	1.9	18.1	41.7
20	6.6	10.9	5.4	1.7	14.1	38.8
30	8.3	11.4	5.3	1.3	8.9	35.2
50	10.4	11.6	4.3	0.8	3.8	30.9

^a1 g/cm² of aluminum is equivalent to 0.37 cm thickness.

Table 11.8. Solar Minimum Galactic Cosmic-Ray Dose at 5 cm Deep in Tissue for Various Particle Types and Aluminum Shield Thicknesses

[All values are rounded to nearest 0.1]

Thickness, ^a g/cm ²	Dose, cGy/yr, from—					
	Neutrons	Protons	Target fragments	α -particles	HZE	Total dose
1	0.4	7.2	0.3	2.2	3.8	14.0
2	0.4	7.4	0.3	2.2	3.7	14.0
3	0.5	7.6	0.3	2.1	3.5	13.9
4	0.6	7.7	0.3	2.1	3.3	13.9
5	0.6	7.8	0.3	2.0	3.1	13.9
6	0.7	8.0	0.3	2.0	3.0	13.9
8	0.8	8.2	0.3	1.9	2.7	13.8
10	0.9	8.4	0.3	1.8	2.5	13.8
15	1.3	8.7	0.3	1.6	2.0	13.8
20	1.3	9.0	0.3	1.4	1.6	13.6
30	1.7	9.3	0.3	1.1	1.1	13.3
50	2.1	9.3	0.2	0.7	0.5	12.7

^a1 g/cm² of aluminum is equivalent to 0.37 cm thickness.

Table 11.9. Solar Minimum Galactic Cosmic-Ray Flux for Various Particle Types and Aluminum Shield Thicknesses

[All values are rounded to nearest 0.1]

Thickness, ^a g/cm ²	Flux, particles/cm ² /yr, from—			
	Neutrons	Protons	α -particles	HZE
0	0E7	1.3E8	1.2E7	1.4E6
1	0.6E7	1.3E8	1.2E7	1.3E6
2	1.2E7	1.3E8	1.2E7	1.3E6
3	1.8E7	1.3E8	1.2E7	1.3E6
4	2.4E7	1.4E8	1.2E7	1.2E6
5	2.9E7	1.4E8	1.1E7	1.2E6
6	3.4E7	1.4E8	1.1E7	1.1E6
8	4.4E7	1.4E8	1.0E7	1.1E6
10	5.4E7	1.4E8	1.0E7	1.0E6
15	7.6E7	1.4E8	1.0E7	1.0E6
20	9.5E7	1.4E8	0.9E7	0.8E6
30	12.5E7	1.4E8	0.8E7	0.7E6
50	16.3E7	1.4E8	0.6E7	0.5E6
			0.4E7	0.3E6

^a1 g/cm² of aluminum is equivalent to 0.37 cm thickness.

Table 11.10. Solar Minimum Galactic Cosmic-Ray Depth Dose Equivalent in Tissue for Various Particle Types and Liquid Hydrogen Shield Thicknesses

[All values are rounded to nearest 0.1]

Thickness, ^a g/cm ²	Dose equivalent, cSv/yr, from—				Total dose equivalent
	Neutrons	Protons	α -particles	HZE	
Skin dose equivalent (0 cm depth)					
0	0	9.4	6.7	101.6	117.7
3	0.2	6.6	2.7	31.8	41.3
10	0.6	7.8	1.5	6.31	6.2
25	0.8	8.1	0.4	0.4	9.7
50	0.7	6.6	0.1	<0.1	7.4
75	0.6	4.8	<0.1	<0.1	5.4
100	0.4	3.3	<0.1	<0.1	3.8
BFO dose equivalent (5 cm depth)					
0	1.4	8.0	2.9	43.0	61.1
3	1.8	8.8	2.2	21.2	34.1
10	1.9	9.6	1.2	4.6	17.2
25	1.7	9.4	0.4	0.3	11.7
50	1.3	7.4	<0.1	<0.1	8.7
75	0.9	5.3	<0.1	<0.1	6.2
100	0.7	3.6	<0.1	<0.1	4.3

^a1 g/cm² of LH₂ is equivalent to 14 cm thickness.

Table 11.11. Solar Minimum Galactic Cosmic-Ray Depth Dose in Tissue for Various Particle Types and Liquid Hydrogen Shield Thicknesses

[All values are rounded to nearest 0.1]

Thickness, ^a g/cm ²	Dose, cGy/yr, from—				
	Neutrons	Protons	α -particles	HZE	Total dose
Skin dose equivalent (0 cm depth)					
0	0	6.2	3.0	7.8	17.0
3	0.1	6.4	2.2	3.2	11.9
10	0.1	7.5	1.2	0.9	9.7
25	0.2	7.7	0.4	0.1	8.4
50	0.2	6.2	<0.1	<0.1	6.5
75	0.1	4.5	<0.1	<0.1	4.7
100	0.1	3.1	<0.1	<0.1	3.2
BFO dose (5 cm depth)					
0	0.3	7.1	2.3	4.1	14.0
3	0.4	7.8	1.8	2.3	12.3
10	0.4	8.5	1.0	0.7	10.6
25	0.4	8.3	0.3	0.1	9.0
50	0.3	6.5	<0.1	<0.1	6.8
75	0.2	4.7	<0.1	<0.1	4.9
100	0.1	3.2	<0.1	<0.1	3.3

^a1 g/cm² of LH₂ is equivalent to 14 cm thickness.

Table 11.12. Solar Minimum Galactic Cosmic-Ray Flux for Various Particle Types and Liquid Shield Thicknesses

[All values are rounded to nearest 0.1]

Thickness, ^a cm or g/cm ²	Flux, particles/cm ² /yr, from—			
	Neutrons	Protons	α -particles	HZE
0	0E6	1.3E8	1.2E6	138.9E6
3	2.8E6	1.4E8	9.9E6	94.9E6
10	6.8E6	1.4E8	5.8E6	42.4E6
25	9.6E6	1.3E8	1.8E6	8.1E6
50	8.9E6	1.0E8	0.3E6	0.5E6
75	7.0E6	0.7E8	0.4E5	0.3E5
100	5.3E6	0.5E8	0.6E4	0.2E4

^a1 g/cm² of LH₂ is equivalent to 14 cm thickness.

11.2.2. Discussion. Although the calculations are useful for estimating relative shield effectiveness to compare different materials, quantitatively the calculations should be considered preliminary estimates of actual shield mass requirements. Aside from the previously mentioned shortcomings related to neglecting meson production and target fragment contributions from interactions of HZE particles and the target medium, figure 11.3 shows that the dose equivalent is a slowly decreasing function of shield thickness. This is a result of secondary particle production processes whereby the heavier GCR nuclei are broken into nucleons and lighter nuclear fragments by nuclear and coulombic interactions with the shield material. This slow decrease in dose equivalent with increasing shield thickness means that relatively small uncertainties in predicted doses that arise from nuclear fragmentation model inaccuracies may yield large uncertainties in estimated shield thicknesses. A preliminary analysis of the nonlinear relationship between exposure uncertainty was presented by Townsend, Wilson, and Nealy (1989). The most startling finding was that a factor of 2 uncertainty in exposure amplified into an order of magnitude uncertainty in shield mass requirements. To further illustrate this, water shield mass increase (in percent) as a function of BFO exposure uncertainty (in percent) is listed in table 11.13. For the latter quantity, the calculated exposure is assumed to be smaller than the actual exposure by the percentage indicated; that is, the exposure is underestimated.

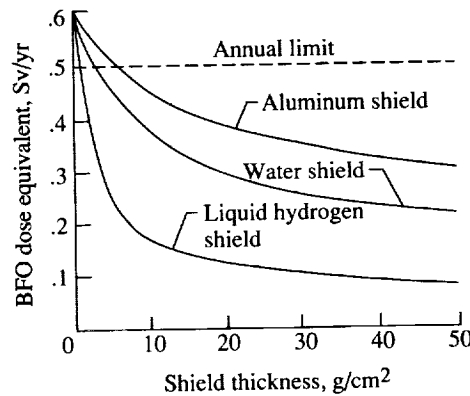


Figure 11.3. Dose equivalent in BFO as function of shield type and thickness.

Again we note that if the exposure is underestimated by a factor of 2 (the 50-percent entry), then the resultant shield mass must be increased by an order of magnitude (1000 percent). To account for the ≈ 15 -percent uncertainty that results from the neglect of meson production and the incomplete treatment of target fragmentation, the shield mass must be doubled (increased by 100 percent). Similarly, possible inaccuracies in the input fragmentation cross sections could underestimate the exposures by as much as 20 to 30 percent (Townsend and Wilson, 1988) and result in potential shield mass increases by up to a factor of 4 (over a 400 percent increase). Clearly the *complete* development of an accurate and comprehensive transport code is needed, and uncertainties in the actual GCR environmental model and in the input nuclear fragmentation models need to be resolved through additional theoretical and experimental research as has been emphasized at Langley for many years. (See chapter 1.). Finally, we note that radiation exposure is cumulative and therefore requires consideration

of contributions from all sources, including onboard nuclear power sources, solar particle events, and GCR's. Exposure to onboard sources reduces the allowed exposures from solar flares and cosmic rays and thereby increases the required shield thicknesses that are necessary to stay below the exposure limits.

Table 11.13. Increase in Water Shield Mass for Various Exposure Uncertainties

BFO exposure uncertainty, ^a percent	Increase in water shield mass, percent
10	43
15	100
20	129
30	414
40	614
50	1000

^aExposures assumed to be *underestimated* by the indicated percent.

11.3. GCR Component Breakdown

Although GCR's probably include every natural element, not all are important for space-radiation-protection purposes. For example, the elemental abundances for species heavier than iron (charge number, $Z > 26$) are typically 2 to 4 orders of magnitude smaller than iron (Adams, Silberberg, and Tsao, 1981), and therefore are of negligible importance in this regard. For elements lighter than iron, species with an odd charge number are significantly less abundant than their neighboring species with even charge numbers. This is readily seen in figure 11.4, which displays abundances (normalized to silicon = 100) for ions from helium ($Z = 2$) to iron. The data were taken from Simpson (1983). From this figure, the most abundant elements that are heavier than helium are carbon ($Z = 6$), oxygen ($Z = 8$), magnesium ($Z = 12$), silicon ($Z = 14$), and iron ($Z = 26$). Although neon ($Z = 10$) is about equal in abundance to iron, its much lower charge number suggests that its contribution to the total dose (nearly proportional to Z^2) should be much lower than that for iron. Therefore, we did not include neon in this analysis. Instead, we estimated component contributions to dose and dose equivalent for seven elemental GCR constituents: protons, helium, carbon, oxygen, magnesium, silicon, and iron.

The component analysis is performed by separately transporting each of the seven ion species (solar minimum abundances) through the aluminum shield. At each shield thickness (0, 2, and 10 g/cm²), the dose and dose equivalent are computed for the incident ion species and all subsequent-generation collision products. The latter are categorized as HZE (all secondary ions having $Z > 2$), alpha particles ($Z = 2$), protons ($Z = 1$), and neutrons. The results are presented in tables 11.14 and 11.15. The entries labeled 0 g/cm² aluminum shield represent unshielded exposures and consist only of primary ion contributions. From these tables, we note that these seven ions constitute over 80 percent of the unshielded GCR dose and nearly 70 percent of the unshielded GCR dose equivalent. Although

protons (hydrogen) account for nearly 90 percent of the incident flux, they only account for 36 percent of the unshielded total GCR dose and less than 10 percent of the total dose equivalent. Helium nuclei, which comprise nearly 10 percent of the incident flux, account for 18 percent of the total unshielded dose and only 6 percent of the unshielded total dose equivalent. The entire heavy ion component of the spectrum, which comprises about 2 percent of the incident GCR flux, accounts for nearly half of the unshielded dose (46 percent) and over 85 percent of the unshielded total dose equivalent. The largest single contribution to the heavy ion component is iron, which accounts for 9 percent of the total unshielded GCR dose and 26 percent of the total dose equivalent.

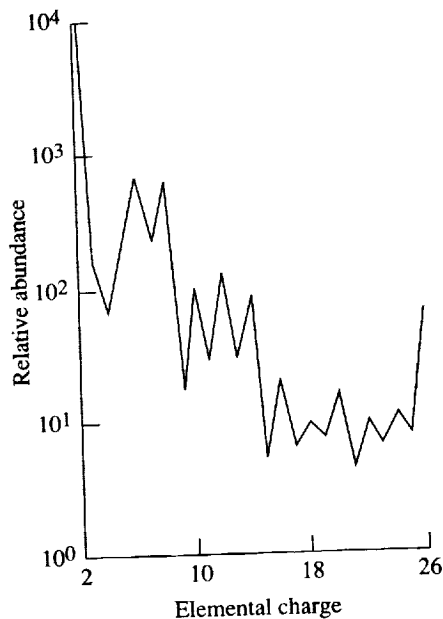


Figure 11.4. Elemental abundances.

Behind 2 g/cm² of aluminum shielding (a thin spacecraft), the main contributions to the dose equivalent (table 11.15) come from the incident ions. The total contribution from all secondaries is less than 2 percent of the primary contribution from incident protons and their secondaries. The HZE contribution to the secondary total dose equivalent (0.67 cSv) is nearly equal to the secondary neutron contribution (0.81 cSv). In these tables, no separate entry for secondary protons produced by primary protons is made because of the difficulty in extracting this information from the current version of the GCR transport code. Instead, the values listed for primary dose and dose equivalent represent the sum of primary and secondary proton contributions.

At 10 g/cm² aluminum shielding, the largest single contributor to GCR total dose and dose equivalent is hydrogen (protons) and its secondaries, which account for 58 percent of the dose and 24 percent of the dose equivalent. Surprisingly, the second largest contributor is iron and its secondaries, which accounts for 18 percent of the total GCR dose equivalent. Again from table 11.15, we note that the HZE

Table 11.14. Dose in Water by GCR Component for Several Aluminum Shield Thicknesses

Incident ion species	Primary ion dose, cGy	Dose from secondary particles, cGy				Ion total, cGy	Percent of total GCR
		HZE	α -particles	Protons	Neutrons		
Aluminum shield 0 g/cm ² thick							
<i>p</i>	6.21				0	6.21	36
α	3.02			0	0	3.02	18
C	0.83	0	0	0	0	0.83	5
O	1.37	0	0	0	0	1.37	8
Mg	0.66	0	0	0	0	0.66	4
Si	0.69	0	0	0	0	0.69	4
Fe	1.56	0	0	0	0	1.56	9
Total	14.34	0	0	0	0	14.34	84
Aluminum shield 2 g/cm ² thick							
<i>p</i>	6.70				0.12	6.82	45
α	2.62			0.03	0.03	2.68	18
C	0.69	<0.01	<0.01	<0.01	<0.01	0.69	5
O	1.13	0.01	<0.01	0.01	<0.01	1.15	8
Mg	0.53	0.01	<0.01	<0.01	<0.01	0.54	4
Si	0.54	0.01	<0.01	<0.01	<0.01	0.55	4
Fe	0.86	0.03	<0.01	<0.01	<0.01	0.89	6
Total	13.07	0.06	<0.01	<0.04	0.15	13.32	90
Aluminum shield 10 g/cm ² thick							
<i>p</i>	8.17				0.55	8.72	58
α	2.13			0.21	0.13	2.47	16
C	0.48	0.01	<0.01	0.03	0.01	0.53	4
O	0.73	0.03	<0.01	0.03	0.01	0.80	5
Mg	0.31	0.02	<0.01	0.01	<0.01	0.34	2
Si	0.30	0.03	<0.01	0.01	<0.01	0.34	2
Fe	0.44	0.07	<0.01	0.01	0.01	0.53	4
Total	12.56	0.16	<0.01	0.30	0.71	13.73	91

Table 11.15. Dose Equivalent in Water by GCR Component for Several Aluminum Shield Thicknesses

Incident ion species	Primary Ion dose equivalent, cSv	Dose from secondary particles, cSv				Ion total, cSv	Percent of total GCR
		HZE	α -particles	Protons	Neutrons		
Aluminum shield 0 g/cm ² thick							
p	9.73				0	9.73	8
α	6.96			0	0	6.96	6
C	4.94	0	0	0	0	4.94	4
O	11.11	0	0	0	0	11.11	9
Mg	8.01	0	0	0	0	8.01	7
Si	9.63	0	0	0	0	9.63	8
Fe	30.90	0	0	0	0	30.90	26
Total	81.28	0	0	0	0	81.28	68
Aluminum shield 2 g/cm ² thick							
p	8.09				0.68	8.77	11
α	3.38			0.04	0.11	3.53	5
C	3.25	0.01	<0.01	0.01	0.01	3.28	4
O	7.85	0.05	<0.01	<0.01	<0.01	7.92	10
Mg	5.91	0.06	<0.01	<0.01	<0.01	5.97	8
Si	7.10	0.09	<0.01	<0.01	<0.01	7.19	9
Fe	17.04	0.46	<0.01	<0.01	<0.01	17.50	23
Total	52.62	0.67	<0.01	0.06	0.81	54.16	70
Aluminum shield 10 g/cm ² thick							
p	10.15				2.99	13.14	24
α	2.75			0.30	0.54	3.59	7
C	2.12	0.04	<0.01	0.03	0.04	2.23	4
O	4.76	0.16	<0.01	0.04	0.05	5.01	9
Mg	3.23	0.18	<0.01	0.01	0.02	3.44	6
Si	3.71	0.24	<0.01	0.01	0.01	3.97	7
Fe	8.68	1.25	<0.01	0.02	0.02	9.97	18
Total	35.40	1.87	<0.01	0.41	3.67	41.35	75

contribution to the secondary total dose equivalent (1.87 cSv) is comparable with that which results from secondary neutrons (3.67 cSv).

Several other comments on the results displayed in tables 11.14 and 11.15 are appropriate. First, the secondary neutron and proton dose-equivalent contributions that arise from heavy ion fragmentations, although nearly equal, appear to be relatively small compared with the secondary HZE contribution. Second, the secondary alpha production from all sources appears negligible. Both of these findings may be in error because of the relatively simple treatment of light ion production used by the semiempirical nuclear fragmentation model (Wilson, Townsend, and Badavi, 1987) in the GCR transport code and the paucity of relevant experimental data needed to improve that treatment. Since the fragmentation model used does conserve charge and mass, the dose-equivalent contributions from these ions will probably not change enough to alter the major conclusions. For example, increasing secondary proton and alpha production from heavy ions by an order of magnitude would only increase the dose-equivalent contribution from secondary protons by 1.26 cSv and from alpha particles by less than 0.1 cSv. Finally, the results presented in the tables neglect target-fragment contributions. For heavy ions, the target-fragment contributions (Shinn, Wilson, and Nealy, 1990) to the total dose equivalent is small (less than 5 percent of the heavy ion total dose equivalent for ions heavier than carbon) and of no consequence for this study. For protons, the target-fragment contribution is about 5 cSv, which will increase the relative contribution from protons to the total dose and dose equivalent but will not alter the major conclusions of this chapter.

11.4. Quality Factors

The quality factor (QF) as defined in International Commission on Radiological Protection publication no. 26 (Anon., 1977) or proposed in the International Commission on Radiological Units and Measurements report no. 40 (Anon., 1986b) is not expected to be a valid method for assessing biological risk for deep space missions in which the HZE particles of the GCR are of major concern. No human data for cancer induction from HZE particles exist, and information on biological effectiveness is expected to be taken from experiments with animals and cultured cells (Sinclair, 1985). Experiments with cultured cells (Yang et al., 1985; Thacker, Stretch, and Stephens, 1979; Wulf et al., 1985) indicate that the relative biological effectiveness of HZE particles is dependent on particle type, energy, and level of fluence. Use of a single parameter, such as LET or lineal energy (Katz and Cucinotta, 1991), to determine radiation quality will therefore represent an extreme oversimplification for GCR risk assessment.

Katz has presented a theoretical model that predicts the correct RBE behavior as observed in recent experimental studies by using track segment irradiations with heavy ions on cultured mammalian cells (Katz et al., 1971; Katz, Sharma, and Homayoonfar, 1972; Waligorski, Sinclair, and Katz, 1987). Cells at risk in deep space will be subject to a complicated mixture of particles varying in composition with the amount and type of shielding surrounding them. The fluence levels in space are such that a single cell will probably be exposed to only a few ion encounters over an extended period. Katz has developed a model for the ion-kill mode of cell death or neoplastic transformation that corresponds to low-fluence

exposures. The delta-ray (energetic electrons produced in ion collisions) radial dose distribution that surrounds the ion track is assumed to initiate the biological damage, and the cell response to the radiation field is parameterized by using target theory and results from gamma-ray and track segment irradiations. The level of damage for a mixed radiation field is determined by the cellular response parameters and the local flux of particles. The deterministic transport code for calculating the differential flux of ions behind natural and protective radiation shielding exposed to the GCR spectrum is used to calculate the biological damage to mammalian cell cultures expected for 1 year in deep space at solar minimum behind various depths of aluminum shielding by using the Katz cellular damage model. Cell death and neoplastic transformations for C3H10T1/2 cells (cultured mouse cells) are considered for typical levels of spacecraft shielding. The Katz parameters are given in table 11.16. The results of this study must be considered preliminary in that the transport code is in an early stage of development as discussed in section 11.2.

Table 11.16. Cellular Response Parameters for C3H10T1/2 Cells

Damage type	m	D_o , cGy	Σ_o , cm ²	κ
Killing	3	280	5.0E-7	750
Transformation	2	26 000	1.15E-10	750

11.4.1. Katz model. The surviving fraction of a cellular population N , whose response parameters are m , D_o , Σ_o , and κ , after irradiation by a fluence of particles F is written as

$$\frac{N}{N_o} = \pi_i \times \pi_\gamma \quad (11.1)$$

where the ion-kill survivability is

$$\pi_i = \exp(-\Sigma F) \quad (11.2)$$

and the gamma-kill survivability is

$$\pi_\gamma = 1 - \left[1 - \exp\left(\frac{-D_\gamma}{D_o}\right) \right]^m \quad (11.3)$$

The gamma-kill dose fraction is

$$D_\gamma = (1 - P)D \quad (11.4)$$

where D is the absorbed dose. The single-particle inactivation cross section is given by

$$\Sigma = \Sigma_o \left\{ 1 - \exp\left[\frac{-(Z^*)^2}{\kappa\beta^2}\right] \right\}^m \quad (11.5)$$

where the effective charge number is

$$Z^* = Z \left[1 - \exp \left(\frac{-125\beta}{Z^{2/3}} \right) \right] \quad (11.6)$$

In the track-width regime, where $P > 0.98$, we take $P = 1$.

For neoplastic cell transformation, the fraction of transformed cells per surviving cell is

$$T = 1 - \frac{N'}{N'_0} \quad (11.7)$$

where N'/N'_0 is the fraction of nontransformed cells and a set of cellular response parameters for transformations m' , D'_0 , Σ'_0 , and κ' is used. The RBE at a given survival level is given by

$$\text{RBE} = \frac{D_X}{D} \quad (11.8)$$

where

$$D_X = -D_0 \ln \left[1 - \left(1 - \frac{N}{N_0} \right)^{1/m} \right] \quad (11.9)$$

is the X-ray dose at which this level is obtained. Equations (11.1) through (11.9) represent the cellular track model for monoenergetic particles. Mixed radiation fields have been considered previously in the Katz (1986) model.

The cellular track model was applied to predict the fraction of C3H10T1/2 cells killed or transformed for 1 year in deep space at solar minimum for typical spacecraft shielding. The GCR environment was taken from the Naval Research Laboratory code (Adams, Silberberg, and Tsao, 1981). Aluminum shielding was considered with a local region of tissue for the cell cultures. Tables 11.17 and 11.18 contain individual particle fluences and absorbed doses, respectively, for the protons, α -particles, $Z = 3$ to 9 ions, and $Z = 10$ to 28 ions as determined by the Langley GCR code. Results for the fraction of C3H10T1/2 cells killed and transformed for 1 year at solar minimum are listed in tables 11.19 and 11.20, respectively. The gamma-kill mode was of negligible importance in the calculations, which indicates that biological damage in deep space from GCR particles at the cellular level will indeed result from the action of single particles. The importance of the target terms in biological effects for low-LET protons and α -particles is apparent. The results also indicate that the HZE component of the GCR spectrum is most damaging for small shielding depths. At large depths, the HZE components undergo many fragmentations; this causes proton buildup with increasing shield depth. At large depths, the protons (and neutrons) dominate the biological effects. In comparing individual charge components, we see that the particles with high Z have a reduced effectiveness for the transformation endpoint.

Also listed in tables 11.19 and 11.20 are the RBE versus depth values for the two endpoints. Table 11.21 presents the current RBE values beside the average QF's taken from Townsend et al. (1990a) with the same transport code. That the RBE and QF are nearly equal at small depths is coincidental. We note that the QF is independent of the fluence level, which is not true for the Katz model.

Table 11.17. Flux Year at Solar Minimum Behind Aluminum Shielding

x , g/cm ²	Flux, particles/cm ² /yr, from—			
	Protons	α -particles	Low Z (a)	High Z (b)
0	1.29E8	1.24E7	1.09E6	3.0E5
1	1.31E8	1.21E7	1.05E6	2.8E5
2	1.33E8	1.18E7	1.01E6	2.7E5
3	1.34E8	1.15E7	0.98E6	2.5E5
5	1.36E8	1.10E7	0.91E6	2.2E5
10	1.40E8	0.97E7	0.77E6	1.7E5
20	1.43E8	0.77E7	0.57E6	1.1E5

^a $Z = 3$ to 9 ions.

^b $Z = 10$ to 28 ions.

Table 11.18. Dose for Solar Minimum Behind Aluminum Shielding

x , g/cm ²	Dose, cGy/yr, from—				
	Protons	α -particles	Low Z (a)	High Z (b)	Total
0	6.2	3.0	2.8	5.0	17.1
1	6.3	2.7	2.5	3.6	15.1
2	6.8	2.6	2.4	3.3	15.1
3	7.1	2.6	2.3	3.1	15.0
5	7.6	2.4	2.1	2.7	14.8
10	8.5	2.1	1.7	2.0	14.3
20	9.5	1.7	1.1	1.1	13.4

^a $Z = 3$ to 9 ions.

^b $Z = 10$ to 28 ions.

Table 11.19. Fraction of C3H10T1/2 Cells Killed in Deep Space for 1 Year at Solar Minimum Behind Aluminum Shielding

$x, \text{g/cm}^2$	Fraction of cells killed by—					
	Protons	α -particles	Low Z (a)	High Z (b)	Total	RBE
Including Target Fragments						
0	1.35E-2	0.46E-2	0.57E-2	2.08E-2	4.46E-2	7.1
1	0.76E-2	0.15E-2	0.43E-2	1.84E-2	3.18E-2	7.0
2	0.80E-2	0.14E-2	0.41E-2	1.69E-2	3.04E-2	6.9
3	0.83E-2	0.14E-2	0.38E-2	1.55E-2	2.90E-2	6.8
5	0.88E-2	0.14E-2	0.34E-2	1.32E-2	2.68E-2	6.7
10	0.95E-2	0.12E-2	0.25E-2	0.91E-2	2.22E-2	6.5
20	1.02E-2	0.09E-2	0.15E-2	0.49E-2	1.74E-2	6.2
Without target fragments						
0	0.84E-2	0.37E-2	0.55E-2	2.08E-2	3.79E-2	6.7
1	0.24E-2	0.06E-2	0.41E-2	1.83E-2	2.54E-2	6.5
2	0.28E-2	0.06E-2	0.39E-2	1.68E-2	2.41E-2	6.3
3	0.31E-2	0.06E-2	0.37E-2	1.55E-2	2.27E-2	6.2
5	0.35E-2	0.06E-2	0.33E-2	1.31E-2	2.04E-2	6.1
10	0.42E-2	0.05E-2	0.24E-2	0.91E-2	1.61E-2	5.7
20	0.49E-2	0.04E-2	0.14E-2	0.48E-2	1.15E-2	5.3

^a $Z = 3$ to 9 ions.^b $Z = 10$ to 28 ions.

Table 11.20. Fraction of C3H10T1/2 Cells Transformed in Deep Space for 1 Year at Solar Minimum Behind Aluminum Shielding

$x, \text{g/cm}^2$	Fraction of cells transformed by—					
	Protons	α -particles	Low Z (a)	High Z (b)	Total	RBE
Including target fragments						
0	5.2E-6	2.0E-6	3.1E-6	7.5E-6	1.78E-5	6.4
1	3.5E-6	1.0E-6	2.7E-6	6.7E-6	1.39E-5	6.4
2	3.7E-6	1.0E-6	2.6E-6	6.2E-6	1.35E-5	6.3
3	3.9E-6	0.9E-6	2.4E-6	5.7E-6	1.29E-5	6.3
5	4.2E-6	0.9E-6	2.2E-6	4.9E-6	1.22E-5	6.2
10	4.7E-6	0.8E-6	1.7E-6	3.5E-6	1.06E-5	6.0
20	5.2E-6	0.6E-6	1.1E-6	2.0E-6	.88E-5	5.7
Without target fragments						
0	3.2E-6	1.6E-6	3.1E-6	7.5E-6	1.53E-5	6.0
1	1.4E-6	0.6E-6	2.7E-6	6.7E-6	1.13E-5	5.8
2	1.6E-6	0.6E-6	2.5E-6	6.2E-6	1.09E-5	5.7
3	1.8E-6	0.6E-6	2.4E-6	5.7E-6	1.05E-5	5.6
5	2.1E-6	0.5E-6	2.1E-6	4.9E-6	0.97E-5	5.4
10	2.5E-6	0.5E-6	1.6E-6	3.5E-6	0.82E-5	5.2
20	3.0E-6	0.4E-6	1.0E-6	2.0E-6	0.64E-5	4.9

^a $Z = 3$ to 9 ions.^b $Z = 10$ to 28 ions.

Table 11.21. Quality Factors and RBE for Cell Death and Transformation
 [1 Year in deep space at solar minimum for aluminum shielding]

$x, \text{g/cm}^2$	Quality factor (a)	RBE (cell kill)	RBE (transformation)
0	7.1	7.1	6.4
1	5.6	7.0	6.4
2	5.3	6.9	6.3
3	5.1	6.8	6.3
5	4.7	6.7	6.2
10	3.9	6.5	6.0
20	3.2	6.2	5.7

^aICRP 26 (Anon., 1977).

The Katz model indicates a substantial increase in risk relative to the ICRP 26 (Anon., 1977) quality factors for greater amounts of shielding (Cucinotta et al., 1991). The RBE's show a simple scaling with exposure time for the GCR particles as shown in equations (11.8), (11.9), and (11.2) in which ion kill dominates. Here we find for

$$\frac{N}{N_0} \approx 1 \quad (11.10)$$

with

$$\Sigma F \ll 1 \quad (11.11)$$

that

$$\text{RBE} = \frac{D_0}{LET} \sigma^{1/m} F^{(-1+1/m)} \quad (11.12)$$

Then scaling the RBE as a function of duration in deep space to the 1-year value RBE_1 , we find for a duration period of τ with $F = n\tau$ that

$$\text{RBE}(\tau) = \left(\frac{\tau}{\tau_1}\right)^{(-1+1/m)} \text{RBE}_1 \quad (11.13)$$

such that a one-hit ($m = 1$) system RBE becomes fluence independent

$$\text{RBE}(\tau) = \text{RBE}_1 \quad (11.14)$$

for a two-hit system ($m = 2$)

$$\text{RBE}(\tau) = \frac{\text{RBE}_1}{\sqrt{\tau/\tau_1}} \quad (11.15)$$

and for a three-hit system ($m = 3$)

$$\text{RBE}(\tau) = \frac{\text{RBE}_1}{(\tau/\tau_1)^{2/3}} \quad (11.16)$$

Results of this scaling approximation agree with calculations that use equations (11.1) through (11.10), as shown in table 11.22, whereby values obtained with the approximations of equation (11.13) are shown in parentheses as scaled from the 1-year RBE values taken from table 11.21; results of calculations are shown without parentheses. The extremely large RBE values that would be obtained for small values of τ are caused by the choice of energetic photons as the reference radiation.

Table 11.22. RBE for Cell Death and Cell Transformations of C3H10T1/2 Cells for GCR Spectrum at Solar Minimum Behind Aluminum Shielding

[Values in parentheses scaled from 1 year value by using eq. (11.16)]

$x, \text{g/cm}^2$	1 month	1 year	2 years
0	33.2 (37.0)	7.1	4.8 (4.6)
1	33.2 (36.1)	7.0	4.7 (4.5)
3	32.4 (35.1)	6.8	4.5 (4.3)

$x, \text{g/cm}^2$	1 month	1 year	2 years
0	22.3 (22.2)	6.4	4.6 (4.5)
1	22.0 (22.2)	6.4	4.5 (4.5)
3	21.6 (21.8)	6.3	4.4 (4.4)

11.4.2. Remarks. A track structure model has been used with a deterministic GCR transport code to predict the fractions of cell death and neoplastic transformations for C3H10T1/2 cells in deep space behind typical spacecraft shielding. Results indicate that the level of damage from the GCR particles does not attenuate appreciably for large amounts of spacecraft shielding and that single particles acting in the ion-kill mode dominate the effects. The contribution from target fragments was important in assessing the biological effect of protons and alpha particles. The RBE values obtained in this fluence-dependent model were more severe than the ICRP 26 quality factors. A simple scaling law with the duration time in space accounted for the change in RBE with fluence for the uniform GCR background.

The resulting average RBE of our calculations for both cell killing and transformation are remarkably close, when we consider the large difference in radiosensitivity parameters for these endpoints and the huge difference in the fraction of affected cells. About 1000 times as many cells are killed as are transformed. Nevertheless, 90 percent of the cells survive the conditions calculated here, and of these about 1 or 2 in 100 000 are transformed. Yet this is not an

insignificant fraction when we consider the number of cells per cubic centimeter in tissue and speculate about the number of cells transformed by radiation that might lead to cancer.

The cell population in tissue, about $10^9/\text{cm}^3$, suggests that after 1 year of exposure to GCR at solar minimum there would be about 10^4 transformed cells/ cm^3 in tissue if in vitro and in vivo transformation parameters were equal. Additionally, we do not know the minimum number of transformed cells that can be injected into a mouse to induce a cancer. Clearly, priority must be assigned to the investigation of these questions. If one or two transformed cells per cm^3 were to lead to cancer, as in leukemia, we could not tolerate an exposure in which the transformation fraction exceeded 10^{-9} .

11.5. Other Biological Effect Modifications

The rising RBE at low GCR dose results from the multitarget assumption in Katz theory that leads to the sigmoid behavior in the survival curve of low-LET radiation as opposed to the exponential behavior is observed by Todd and Tobias (1974) to occur at 150 to 200 $\text{keV}/\mu\text{m}$ for mammalian cells. Many also believe that the sigmoid behavior is related to repair mechanisms. This view is promoted by single-exposure and split-exposure experiments with a delay of 2.5 or 23 hours between fractions using V79 hamster cells as shown in figure 11.5 (Elkind and Sutton, 1960). Repair is indicated by the sigmoid response of the second exposure after either the 2.5-hour repair period or especially the 23-hour

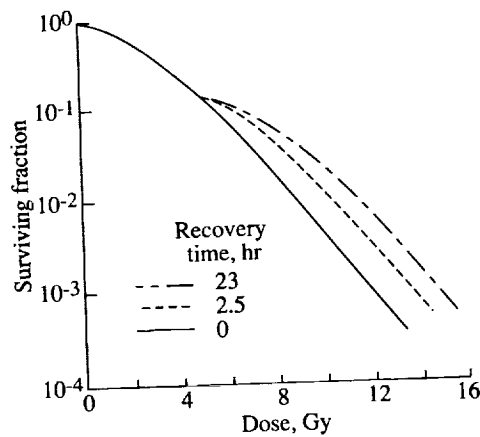


Figure 11.5. Fractional survival of cultured Chinese hamster cells for single exposure and exposure in two fractions (Elkind and Sutton, 1960).

repair period. Obviously, the RBE based on such a photon exposure protocol depends on the history of the radiation induced damage. Similar survival studies with confluent C3H10T1/2 mouse cells (G1) indicate no repair for this endpoint for high-LET radiations (Yang et al., 1986). As a result of operative repair mechanisms (sparing) for low-LET exposure (fig. 11.6) and the lack of repair for high-LET exposure (fig. 11.7), the corresponding RBE is dose rate dependent (Yang et al., 1986) as shown in figure 11.8. Also shown in figure 11.8 are the RBE values for neoplastic transformations. (Note, great liberty has been taken in connecting the data points). The increase in RBE at low dose rate is in part indicative of repair of the damage for low-LET radiation (fig. 11.9) but additional enhancement of high-LET exposure at low dose rate (presumably some misrepair mechanism) also contributes to cell transformations (fig. 11.10). If misrepair/repair plays a role, then this role should be observed in the delayed plating experiments of Yang et al. (1989) as shown in figure 11.11. Instead the delayed plating experiments show no transformation misrepair, but repair appears in cell survival data in distinction to the earlier low dose rate experiments with the same cell system.

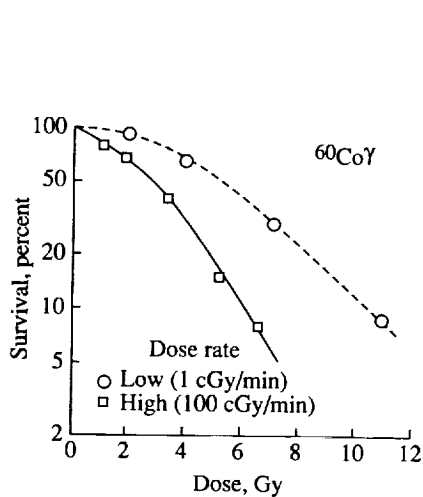


Figure 11.6. Survival fraction of confluent mouse cells at two dose rates displaying sparing at low dose rate (Yang, et al., 1986).

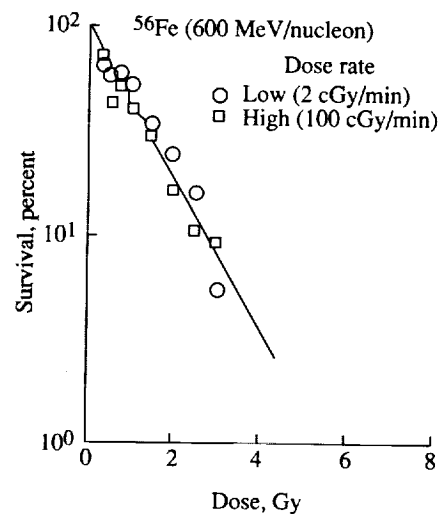


Figure 11.7. Dose rate effects on confluent mouse cell survival for high-LET exposure (Yang et al., 1986).

Similar dose rate enhancement effects are observed in asynchronous cell cultures by Hill et al. (1982 and 1985, fig. 11.12) and whole animal exposures as observed by Thomson et al. (1981a and 1981b), Thomson, Williamson, and Grahn (1983, 1985a, 1985b, and 1986), and Thomson and Grahn (1988 and 1989) (fig. 11.13). These effects are considered the result of cell cycle phenomena (Rossi and Kellerer, 1986; Brenner and Hall, 1990). The basic model assumes that some phases of the cell cycle are more affected by radiation exposure. This is clearly seen in the cell synchronous experiments which are shown in figure 11.14 (Sinclair, 1968). The model of dose rate enhancement assumes only one cell phase is effective in injury of only that fraction in the sensitive phase. At a later time, a different

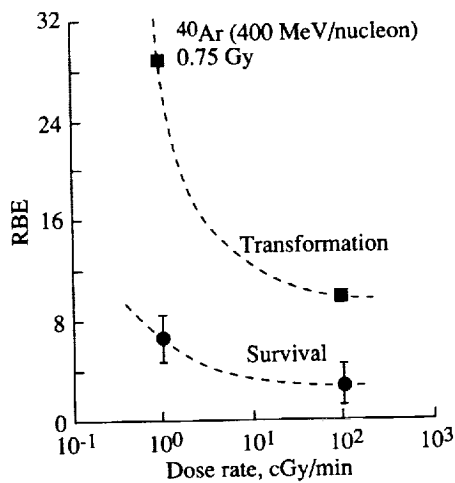


Figure 11.8. RBE as function of dose rate. The curves are to guide eye.

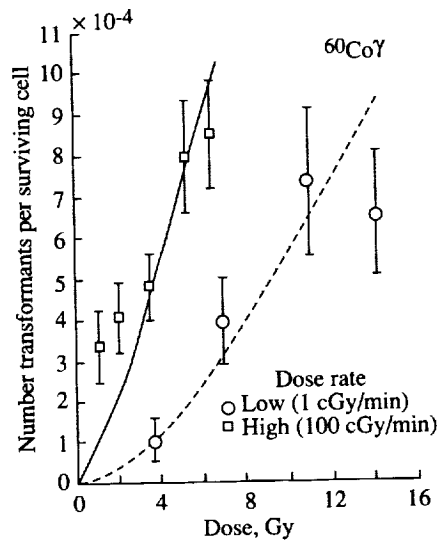


Figure 11.9. Repair processes for confluent mouse cell cultures exposed to γ -rays at low LET.

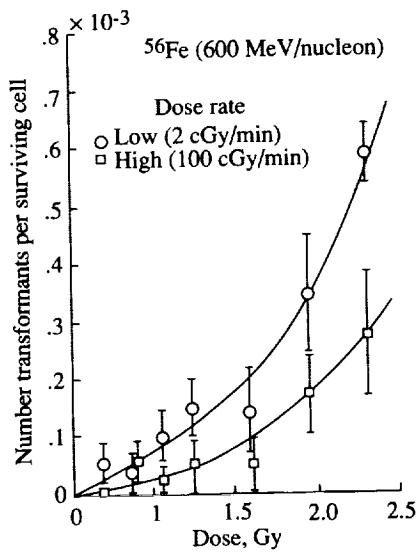


Figure 11.10. Cell transformation rate enhanced at low dose rate for high LET exposure with possible misrepair mechanism indicated.

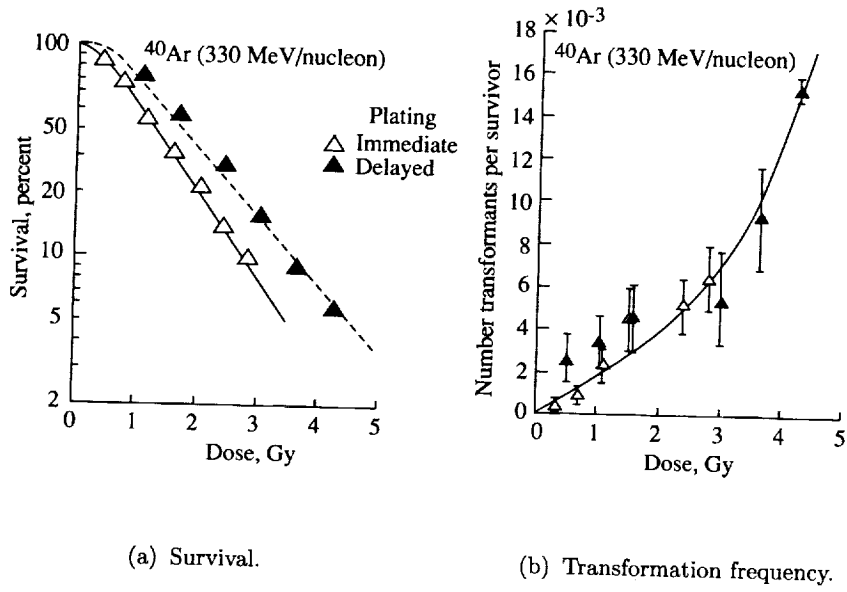


Figure 11.11. C3H10T1/2 cells irradiated by 330 MeV/u argon ions (Yang et al., 1986).

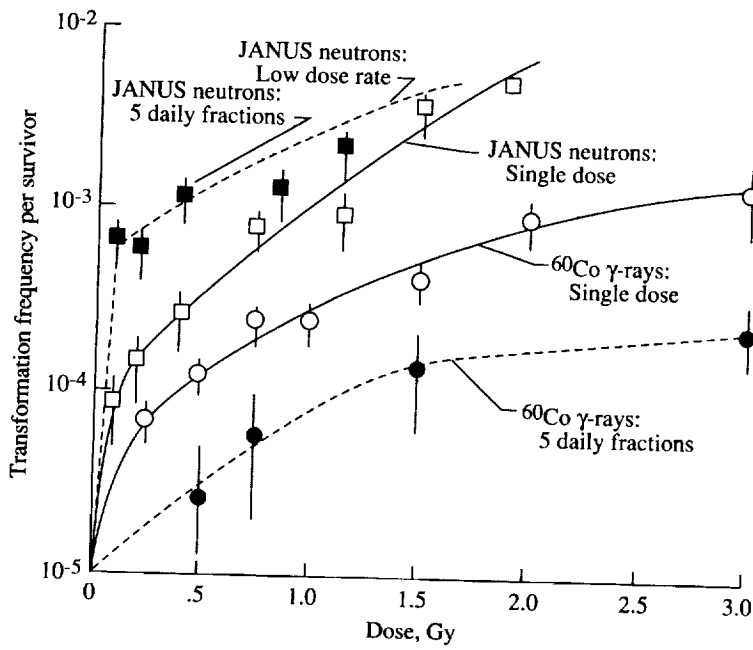


Figure 11.12. Transformation frequencies in C3H10T1/2 cells (Hill et al., 1982 and 1985).

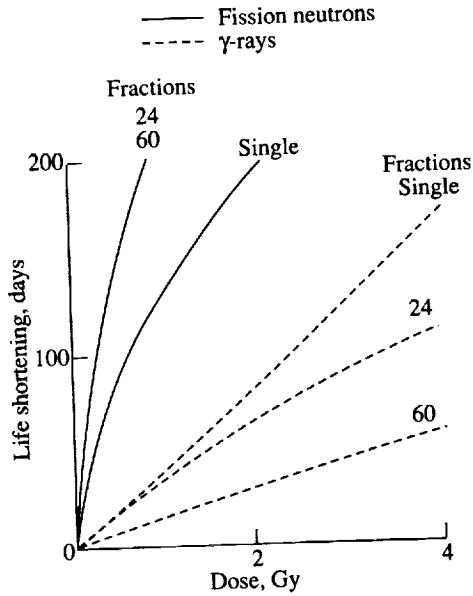


Figure 11.13. Life shortening in mice after single, 24, or 60 fractions of neutrons and after single, 24, or 60 fractions of γ -rays. Curves are fit to data of Thomson et al.

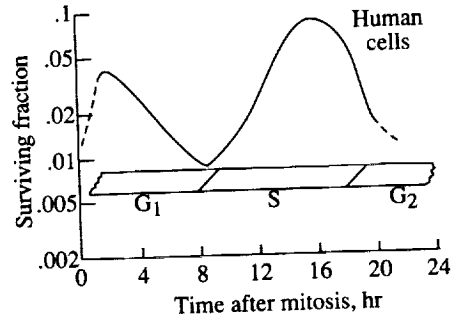


Figure 11.14. Survival of synchronized human cells exposed to 500 rads of 200 kV X-rays.

fraction of cells is in the appropriate phase thus providing two exposed groups of cells and an apparent enhancement. Such a model was exploited in the work of Brenner and Hall (1990). This explanation fails to explain the enhancement effects observed by Yang et al. (1986) in cell transformation in stationary phase (G1) confluent C3H10T1/2.

Clearly the risk to long-term GCR/SCR exposure will be difficult to evaluate because of the low dose rate, fractionated components, and the complex mixture of low- and high-LET radiations in space. Operative repair and cycle enhanced effects will require at least an intimate knowledge of the LET distributions at affected tissues or possibly more comprehensive track structure data.

11.6. Nuclear Models, Materials, and LET Spectra

As is clear from the previous discussion, the distribution of exposure components over LET is a primary indicator of biological response. For example, low-LET components allow certain biological repairs at low dose rates and a low RBE value, and high-LET components can show enhanced biological effects at low dose rates and generally high RBE values. There is clear evidence that the relative contributions to exposure from various LET components can be altered through the choice of shield material. The transmitted LET spectrum for an aluminum shield is shown in figure 11.15 with the transmitted LET spectrum for a liquid hydrogen shield in figure 11.16. Although a rather large shift in LET can be accomplished by choice of shield composition, an exact evaluation must await improved nuclear fragmentation cross sections since uncertainty in cross sections cause LET shifts of the same order of magnitude. These shifts can be seen by comparing LET

spectra in the Earth's atmosphere by using the Bowman, Swiatecki, and Tsang (1973) fragmentation model shown in figure 11.17 with the LaRC fragmentation model (see chapter 5) shown in figure 11.18.

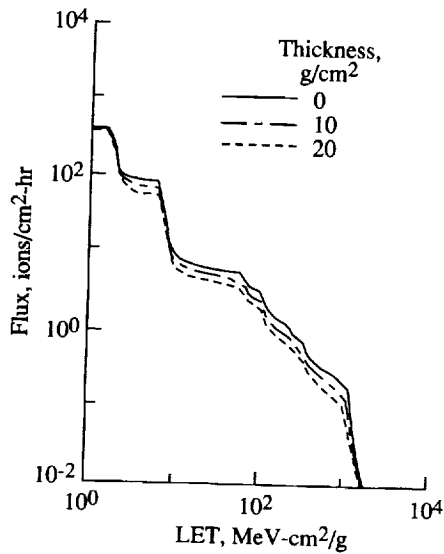


Figure 11.15. GCR integral LET spectra in aluminum for 30° orbit at altitude of 400 km.

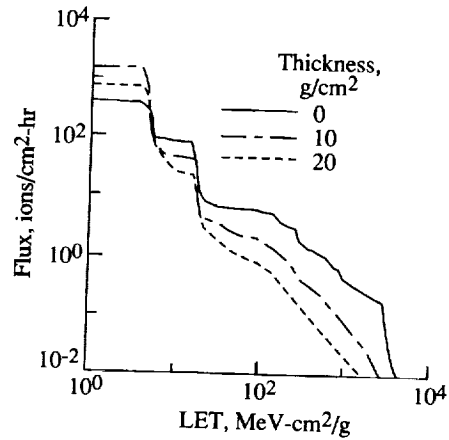


Figure 11.16. GCR integral LET spectra in hydrogen for 30° orbit at altitude of 400 km.

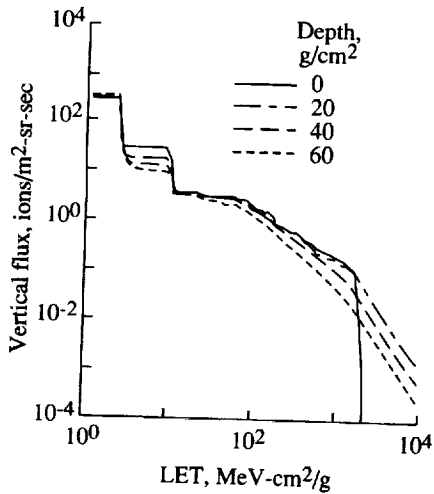


Figure 11.17. GCR integral LET spectra in Earth's atmosphere for fragmentation parameters of Bowman, Swiatecki, and Tsang, 1973.

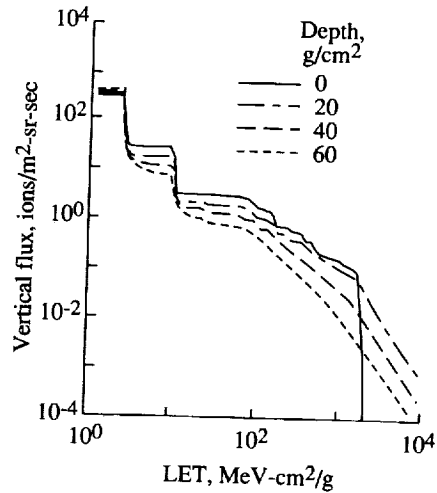


Figure 11.18. GCR integral LET spectra in Earth's atmosphere for fragmentation parameters of LaRC.

11.7. Human Geometry Factors

The significance of improving the accuracy (Shinn, Wilson, and Nealy, 1990) for predicting the dose and dose equivalent that astronauts will incur during future NASA missions has been demonstrated in several studies (Khandelwal and Wilson, 1974; Wilson and Denn, 1976; Townsend, Wilson, and Nealy, 1988; Nealy, Wilson, and Townsend, 1989). For example, Townsend, Wilson, and Nealy (1988) indicate that an increase of 20 percent in predicted BFO dose equivalent due to GCR's equates to a tripling of the required shield mass from 5 g/cm² to 16 g/cm² of water to meet the recommended annual BFO limit of 0.5 Sv. Large uncertainties are associated with the current dose estimate analysis, and every possible effort is needed to improve the accuracy to accomplish these missions in the most economical way without compromising the well-being of the astronauts.

One of the customary estimation practices that has been considered to be fairly reliable in the past is the use of the equivalent sphere model to obtain dose or dose equivalent to BFO. Langley and Billings (1972b) examined the feasibility of using a set of dosimetry spheres to monitor real-time organ doses received by astronauts under various space-radiation and vehicle conditions. They made comparisons between the doses calculated for the spheres and the detailed body geometry under a range of solar proton energy spectrum characteristics and also under various vehicle radiation-shielding thicknesses. The spectra were characterized by an assumed form described by Webber (1963). The optimal radii were determined for those spheres with the corresponding correlation constants that best represented the averaged organ doses under those assumed conditions. Although a moderate error of 18 percent for the correlation was found, one might question whether the accuracy will hold under less idealized particle spectral conditions.

11.7.1. Equivalent sphere model. This section reexamines the accuracy of the equivalent sphere model in approximating the BFO doses for more realistic conditions. The calculation made in a separate study (Simonsen et al., 1990) for the radiation transport through the atmosphere of Mars for the three largest solar flares observed in the last half century is extended here to include detailed BFO geometry. Comparisons are made for the dose equivalent to the various distributed BFO with the reported values based on the equivalent sphere model.

The Langley Research Center nucleon transport code BRYNTRN (Wilson et al., 1989) was used by Simonsen et al. (1990) to obtain dose and dose equivalent on the surface of Mars caused by large solar flares. The transport code was based on the straight ahead approximation, which reduces consideration to one-dimensional transport; the merits of this approximation have been discussed elsewhere (Alsmiller et al., 1965; Alsmiller, Irving, and Moran, 1968). An asymptotic expansion for the solution to the transport equation in two dimensions, subject to boundary conditions given for an arbitrary convex region, was derived by Wilson and Khandelwal (1974). The first term of the expansion was an accurate approximation of the dose and for the case of an isotropic proton fluence spectrum given by

$$D(\vec{x}) = 4\pi \int_0^\infty \phi(E) \int_0^\infty R(t, E) f_x(t) dt dE \quad (11.17)$$

with

$$\int_0^{\infty} f_x(t) dt = 1 \quad (11.18)$$

where $R(t, E)$ is the fluence-to-dose conversion factor at the depth t for normal incidence protons on a slab and $f_x(t)$ is the areal density distribution function for the point \vec{x} . The quantity $f_x(t) dt$ is the fraction of the solid angle for which the distance to the surface from the point \vec{x} lies between t and $t + dt$.

To simplify the computational task (that is, without making any change to the BRYNTRN code), equation (11.17) is rewritten as

$$D(\vec{x}) = 4\pi \int_0^{\infty} f_x(t) D_x(t) dt \quad (11.19)$$

with

$$D_x(t) = \int_0^{\infty} \phi(E) R(t, E) dE \quad (11.20)$$

where $D_x(t)$ is the dose or dose equivalent at depth t for normal incidence protons on a slab of tissue. With the areal density distribution function for BFO's given by the detailed geometry work described by Langley and Billings (1972a) and Billings and Yucker (1973), equation (11.19) can be calculated.

11.7.2. Results. The three solar flare spectra used for this study are those of February 1956, November 1960, and August 1972; however, Langley and Billings used a Webber (1963) form of integral spectra given by the inverse exponential of proton magnetic rigidity with a range of rigidity parameter P_0 from 50 to 200 MV. Figure 11.19 shows these three flare spectra and the best fit to the earlier two events with the Webber form. The actual spectra, especially the high-energy range of the February 1956 event (Foelsche et al., 1974) are different from the analytical form of Webber.

The average dose equivalents at the surface of Mars caused by these three solar flare events are shown in figure 11.20 as a function of slab (water) thickness for the low density Mars atmosphere model ($16 \text{ g/cm}^2 \text{ CO}_2$ vertically) used in Simonsen et al. (1990). These average values of dose equivalent are obtained by summing the directional (anisotropic) dose equivalent over the solid angle and are used as $D_x(t)$ in this section. The calculated results from equation (11.19) are presented in table 11.23 for the five distributed compartments of the blood-forming organ. Also shown for comparison are the average BFO and 5-cm (water) depth dose equivalents.

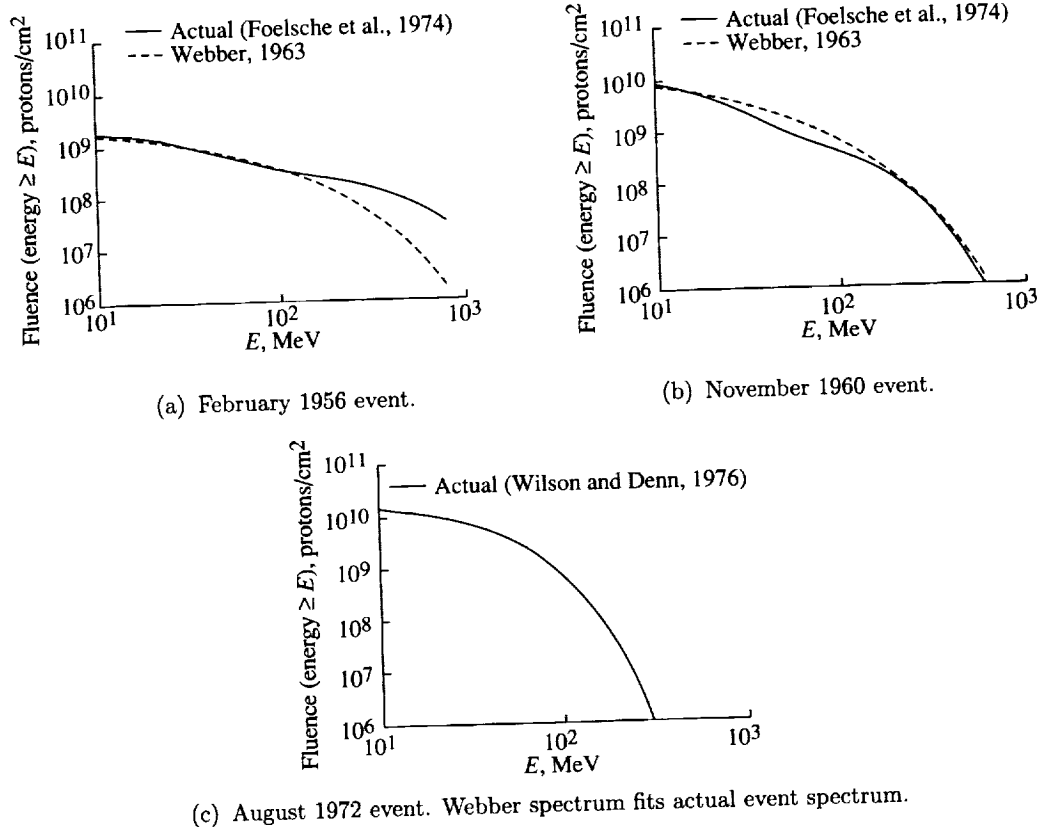


Figure 11.19. Fluence spectra for three major solar particle events.

It is customary (Space Science Board, 1970; Beck, Stokes, and Lushbaugh, 1972) to represent the average BFO exposure (dose or dose equivalent) with the 5-cm sphere based on the recommendation of the Space Science Board (1970). Conversely, the average BFO dose was found to be about half the 5-cm sphere dose in several analytical findings, such as the one from Langley and Billings (1972b). For the August 1972 event, the average BFO value for the detailed geometry (table 11.23) is fairly close (within 10 percent) to half of the value for a 5-cm sphere. However, the differences are larger for the other two flares, with 30 and 41 percent for November 1960 and February 1956 spectra, respectively. This wide discrepancy among these three events probably occurs because the two earlier flares contain more penetrating high-energy protons (fig. 11.19) and the actual spectra do not conform to the simple analytical form that Langley and Billings (1972b) used. Also, the 5-cm sphere dose is conservative for these three events.

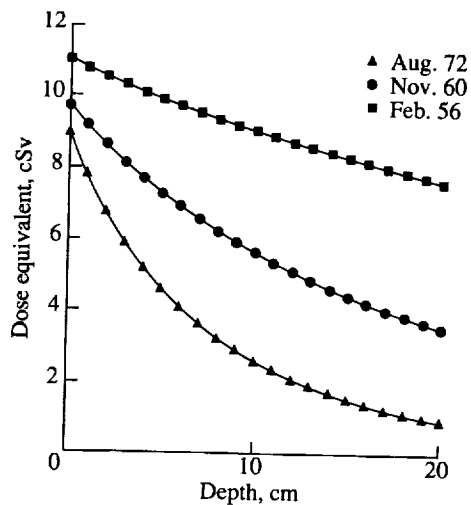


Figure 11.20. Dose equivalent at Mars surface as function of slab (water) thickness for low-density Mars atmosphere model.

Table 11.23. BFO Dose Equivalent on Mars Surface-Low Density Atmosphere Model

Solar flare event	Dose equivalents, cSv, for—						
	Arms	Legs	High trunk	Low trunk	Skull	Average BFO value	5-cm sphere
Feb. 1956	8.74	8.60	8.32	7.98	8.91	8.45	9.94
Nov. 1960	5.66	5.34	4.95	4.32	5.75	5.21	7.31
Aug. 1972	3.20	2.73	2.42	1.76	3.09	2.56	4.61

The equivalent sphere model of Billings and Langley is not accurate enough for precise, quantitative estimates of body doses and vehicle-shielding requirements in connection with future NASA mission studies. Furthermore, the 5-cm sphere dose recommended by the Space Science Board is always an overestimate and could lead to serious shielding penalties. This statement is based on the comparison made with the detailed body geometry calculation for BFO with actual solar flare spectra. The 5-cm equivalent sphere model of the BFO is shown to break down for more realistic spectra than the simple mathematical forms used in previous studies. Future works that involve actual exposure estimates or shield mass requirements should be extended to include all body geometries, including other critical organs, such as eyes, skin, and active BFO (Shinn, Wilson, and Nealy, 1990).

11.8. August 1972 Solar Particle Event Risk Assessment

At present no radiation exposure limits for astronauts on interplanetary missions have been established. However, it has been suggested that the dose

Transport Methods and Interactions for Space Radiations

equivalent limits recently recommended by the National Council on Radiation Protection and Measurements in their report 98 (Anon., 1989) be used as guidelines for planning purposes. These limits are listed in table 11.24.

Table 11.24. Ionizing Radiation Exposure Limits

[From NCRP 98 (Anon., 1989)]

Exposure interval	Dose equivalent, Sv, for—		
	Skin	Ocular lens	BFO
30 Days	1.5	1	0.25
Annual	3	2	0.50
Career	6	4	^a 1-4

^aVaries with gender and age at initial exposure.

To assess the risk to astronauts on a mission outside the Earth's magnetosphere from the August 1972 solar particle event (SPE), the cumulative doses and dose equivalents as a function of time during the event were computed for the skin, ocular lens, and bone marrow. This event was chosen for analysis because it is one of the largest known SPE's and is the standard to which other events are compared. The integral proton fluence spectra as a function of energy and time are displayed in figure 11.21. These data, obtained from Interplanetary Monitoring Platform (IMP) satellite measurements during the SPE, were taken from figure 6 of Wilson and Denn (1976).

For purposes of analysis, two shielding thicknesses are considered: (1) a "nominal" spacecraft thickness of 2 g/cm² of aluminum and (2) a storm shelter shielded by 20 g/cm² of aluminum. The resultant skin doses and dose equivalents as a function of time are displayed in figure 11.22. The cumulative doses/dose equivalents for all organs are listed in table 11.25. For the nominal spacecraft, all limits in table 11.24, including the career limit, are exceeded by a substantial amount. For a total dose of about 11 Sv (1100 rem), skin erythema, and epilation (hair loss) are probable (Wilson and Denn, 1976). These are acute responses to the high exposure. If a storm shelter is provided, the skin dose equivalents are well below the recommended 30-day limit of 1.5 Sv and should pose no hazard to the crew.

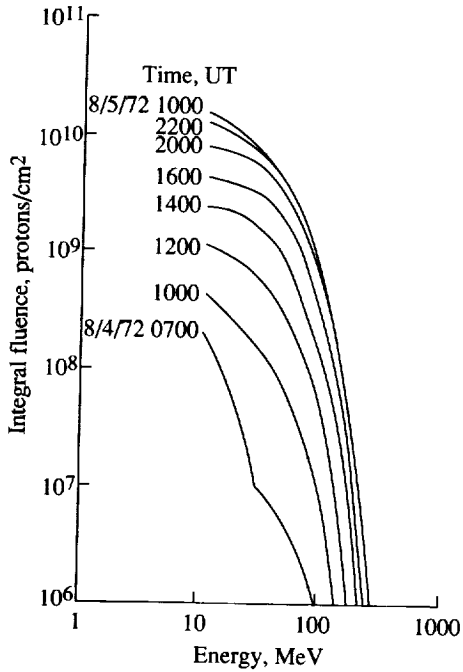


Figure 11.21. August 1972 solar particle event fluence as function of energy and time.

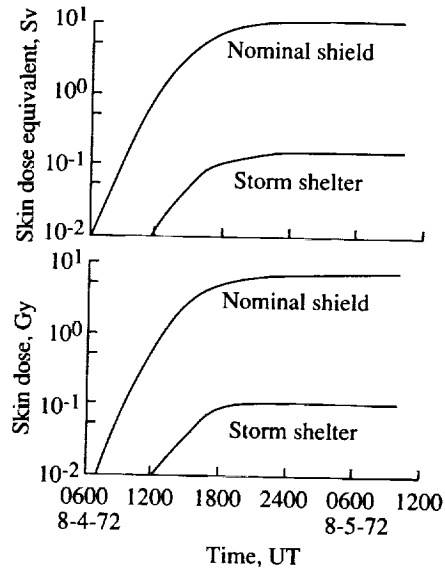


Figure 11.22. Skin dose and dose equivalent as function of time for August 1972 solar particle event. Results are displayed for nominal (2 g/cm² aluminum) and storm shelter (20 g/cm² aluminum) shielding configurations.

Table 11.25. Cumulative Doses and Dose Equivalents for the August 1972 Solar Particle Event

Al shield thickness, g/cm ²	Dose, Gy	Dose equivalent, Sv
Skin		
2	7.61	11.30
20	0.12	0.18
Ocular lens		
2	6.35	9.09
20	0.12	0.17
BFO		
2	0.92	1.24
20	0.04	0.07

Figure 11.23 displays the doses and dose equivalents to the ocular lens as a function of time. Again, for the nominal spacecraft, all limits in table 11.24 are significantly exceeded. Responses to an estimated dose equivalent to the eye in excess of 9 Sv include early erythema to the lid skin and an increased probability of cataract formation (Townsend et al., 1990a; Wilson and Denn, 1976). For the storm shelter configuration, the eye dose equivalent is well below the 30-day limit of 1.0 Sv.

Next, the doses and dose equivalents to the bone marrow, as a function of time, are displayed in figure 11.24. For the nominal spacecraft, the estimated dose equivalent of nearly 1.3 Sv is clinically significant. Blood-count changes will be detectable. Nausea and vomiting would be possible from damage to the intestinal lining (Wilson and Denn, 1976). For the storm shelter, the estimated dose equivalents are small (<70 mSv) and appear to pose no threat to the immediate health of the crew since they are well within the recommended 30-day limit.

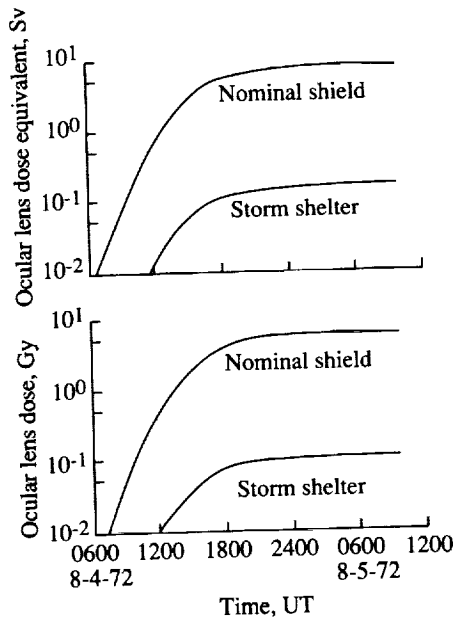


Figure 11.23. Ocular lens dose and dose equivalent as function of time for August 1972 solar particle event. Results are displayed for nominal (2 g/cm^2 aluminum) and storm shelter (20 g/cm^2 aluminum) shielding configurations.

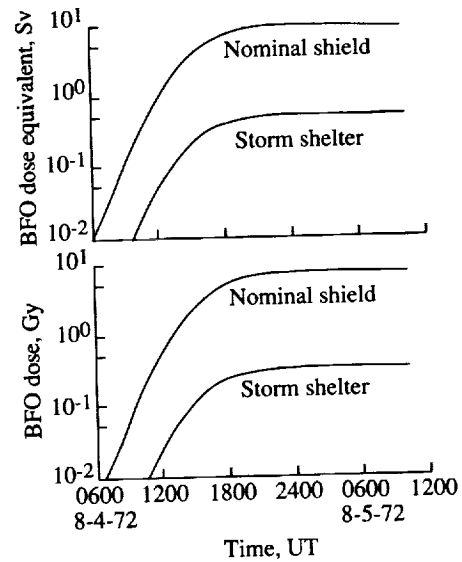


Figure 11.24. Bone marrow dose and dose equivalent as function of time for August 1972 solar particle event. Results are displayed for nominal (2 g/cm^2 aluminum) and storm shelter (20 g/cm^2 aluminum) shielding configurations.

Finally, mission directors need to recognize the critical nature of an SPE emergency and implement timely, appropriate, protective measures to ensure crew safety and health. To illustrate the rapidity with which such decisions may be required, table 11.26 presents an approximate time sequence of events beginning with the optical flare observation at 0621 UT on August 4, 1972. Radiation exposure references are to the nominal (2 g/cm² Al) configuration. Astronauts on extravehicular activity (EVA), who are essentially unshielded, would have considerably less time to seek shelter. During the peak intensity period (1400 UT to 1600 UT), the average dose equivalent rates were ≈ 1.5 Sv/hr (skin), ≈ 1.25 Sv/hr (eye), and ≈ 170 mSv/hr (bone marrow) behind nominal spacecraft shielding.

These dose equivalent rates are considerably lower than the usual rates used in radiotherapy of around 1 Gy/min. Repair processes in cells and tissues are known to have characteristic repair times of 30 to 120 minutes. Because the dose from this event will be received over a time period of about 12 to 18 hours, some damage that occurs early in the period will be repaired during the exposure period itself. Such a situation is known to decrease the resulting biological effect. Various theoretical approaches (Kellerer and Rossi, 1972; Thames, 1985; Curtis, 1986) have been developed to handle such a situation. A more extensive analysis, however, is beyond the scope of this section. For present purposes, and to be on the conservative side, we assume that the dose is acute (i.e., received fast enough so that repair during the exposure can be neglected).

Table 11.26. August 4, 1972, Event Sequence

Approximate time, UT	Event (Al shielding 2 g/cm ² thick assumed)
0621	Optical flare observed
1300	30-day limit exceeded for skin and ocular lens
1400	30-day limit exceeded for BFO; annual limit exceeded for ocular lens
1500	Annual limit exceeded for skin
1600	Annual limit exceeded for BFO; career limit exceeded for ocular lens
1700	Career limit exceeded for skin

11.9. Hypothetical, Worst-Case SPE Scenario Results

Although the August 1972 SPE was the largest in terms of particle fluence, the overall spectrum was fairly soft (the fluence decreased rapidly with increasing particle energy) and therefore easily shielded. For more energetic events (with harder spectra), greater thicknesses of shielding are needed to achieve a significant percentage reduction in dose/dose equivalent. The SPE with the hardest spectrum to date was probably the February 1956 event. Fortunately, it had only one tenth the fluence of the August 1972 event and therefore probably would not have been mission or life threatening. Because the August 1972 SPE actually involved a series of large events over a period of several days (Wilson and Denn, 1976), it

is interesting to hypothesize a possible combined August 1972 and February 1956 SPE scenario—with one of the events in the 1972 sequence having the hardness and fluence of the 1956 event (Townsend et al., 1990b). This combined spectrum is displayed in figure 11.25. The resultant doses and dose equivalents are listed in table 11.27. Acute effects expected with only nominal shielding include skin erythema, epilation, increased cataract formation in the lens, blood-count changes, nausea, and perhaps vomiting (NCRP 98 (Anon., 1989)). Again, quickly taking refuge in a storm shelter should provide adequate protection, although the 30-day limit for BFO exposure is exceeded.

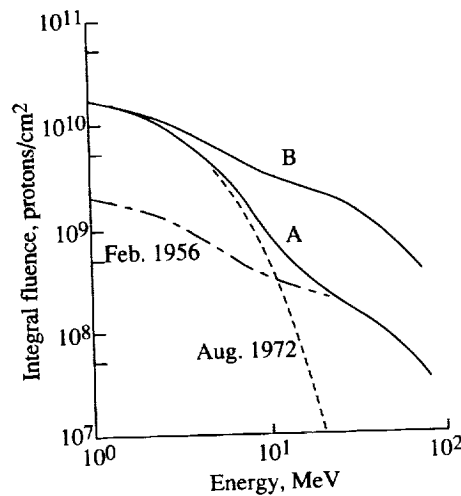


Figure 11.25. Fluence spectra for hypothetical worst-case solar particle events compared with February 1956 and August 1972 cases. Case A is combined August 1972 and February 1956 events. Case B is August 1972 event with February 1956 energy spectrum.

Another possible worst-case scenario would involve an event similar to the August 1972 event with the spectral hardness of the February 1956 event. The event fluence spectrum for this scenario is also depicted in figure 11.25. The resultant doses/dose equivalents for the nominal and storm shelter shielding chosen for this study are listed in table 11.28. For a nominal spacecraft, the effective whole body dose equivalent could be lethal. Even within a storm shelter, acute effects, such as skin erythema, vomiting, blood changes, and possibly even death, could occur since the bone marrow would receive over 2.6 Sv. However, such an event, or anything closely resembling it, has never been observed.

Table 11.27. Doses and Dose Equivalents for Combined August 1972 and February 1956 Solar Particle Event

Al shield thickness, g/cm ²	Dose, Gy	Dose equivalent, Sv
Skin		
2	9.47	14.2
20	0.28	0.43
Ocular lens		
2	7.83	11.3
20	0.28	0.43
BFO		
2	1.18	1.64
20	0.20	0.31

Table 11.28. Doses and Dose Equivalents for 1972 Solar Particle Event Fluence with a 1956 Solar Particle Event Spectral Hardness

Al shield thickness, g/cm ²	Dose, Gy	Dose equivalent, Sv
Skin		
2	0.3	15.5
20	1.99	3.02
Ocular lens		
2	8.95	13.0
20	2.00	3.04
BFO		
2	3.04	4.40
20	1.71	2.62

Using the coupled neutron-proton deterministic transport code, BRYNTRN, and the CAM model for the human geometry (Billings and Yucker, 1973), we have computed detailed exposure estimates for the bone marrow, ocular lens, and skin of astronauts on manned missions beyond the Earth's magnetosphere. Calculations were performed for crews protected by nominal (2 g/cm² aluminum) and heavily shielded (20 g/cm² aluminum) thicknesses of shielding for the August 1972 solar particle event, the largest ever recorded. We found that all current exposure limits, including career limits, would be exceeded for the ocular lens and skin if only nominal shielding is provided. For the bone marrow, 30-day and annual limits would also be exceeded. If the crew quickly sought refuge in

a heavily shielded storm shelter, potential exposures could be maintained within current guidelines. Decisions to seek shelter must be made quickly, however, because limits are initially exceeded within 6 to 7 hours after the optical flare is observed on the solar disk. All exposure limits, except career BFO limits, would be exceeded within about 10 hours. Health effects from such exposures include skin erythema, epilation, blood changes, and cataract formation in the lens.

Two hypothetical worst-case SPE scenarios were also analyzed. The first scenario assumed a February 1956 event as a part of the sequence of flares that comprised the August 1972 event. For nominal spacecraft shielding, all exposure limits, including career BFO limits, would be exceeded. Acute health effects are identical to those previously mentioned for the August 1972 event. If a flare shelter is quickly used by the crew, only the 30-day limit for BFO would be exceeded. The time required to reach the shelter for such a high-energy event could be as short as 20 minutes after the optical flare is observed (Foelsche et al., 1974). The second scenario assumed the highly unlikely prospect that an SPE possessing the August 1972 fluence with the February 1956 spectral hardness could occur. For this hypothetical event, which has never been even approximately observed, the estimated crew exposures would be severe and possibly life threatening, even within a 20 g/cm² aluminum storm shelter.

11.10. Exposure of Female Breast

No regulatory dose limits are specifically assigned for the radiation exposure of female breasts during manned space flight. However, the relatively high radiosensitivity of the glandular tissue of the breasts and its potential exposure to solar-flare protons on short- and long-term missions mandate a priori estimation of the associated risks. In this section, a model for estimation of dose equivalent within the breast is developed to assess important exposure factors for future NASA missions.

The female breast and torso geometry is represented by a simple interim model. The proton dose-buildup factor procedure discussed in a previous chapter is used to estimate doses. A computer code has been developed that considers geomagnetic shielding, magnetic-storm conditions, spacecraft shielding, and body self-shielding. Inputs to the code include proton energy spectra, spacecraft orbital parameters, STS orbiter-shielding distribution at a given position, and a single parameter that allows for variation in breast size.

Virtually all breast cancers arise from the 15 to 20 glandular tissue lobes that exist within the connective tissue stroma. The stroma lies beneath a thin outer layer of skin and a subdermal layer of adipose tissue that is several millimeters to about 1 cm thick. Most breast cancers occur centrally and laterally in proportion to the amounts of glandular tissue in these volumes (NCRP 85 (Anon., 1986a)). The masses of the various types of tissue in the breast vary widely between individuals and with age.

11.10.1. Simplified breast geometry. We take as an interim geometry, a tissue-equivalent truncated sphere placed on a finite-tissue-equivalent slab (Shavers et al., 1991). The slab dimensions are taken as the mean dimensions of

the trunk, and the dimensions for the truncated spheres are to be in accordance with individual geometry. Herein we consider small, medium, and large breast sizes by taking the sphere radius a to be taken as a parameter 7, 10, and 13 cm, respectively, with a base after truncation of 13.4, 19.6, and 25 cm, respectively; the $0g$ height ($a-d$) is then 5, 8, and 11 cm. The sensitive sites are assumed distributed and average exposure calculated along the axis of symmetry as a mean dose at depths of 0.5, 2, 4, and 7 cm. For convenience, we establish a spherical coordinate system centered at each dose point (t_o) and zenith outward along the axis of symmetry. The general geometry in any meridional plane is shown in figure 11.26. The length l is a function of the azimuthal angle, ϕ . We neglect the shielding provided by the second breast. The chord length in the breast tissue is

$$\Delta_1(\theta) = \left[(a - t_o)^2 \cos^2 \theta + t_o(2a - t_o) \right]^{\frac{1}{2}} - (a - t_o) \cos \theta \quad (11.21)$$

and the total chord length is

$$t(\theta) = \Delta_1(\theta) \quad (0 \leq \theta \leq \frac{\pi}{2} + \varepsilon_1) \quad (11.22)$$

where

$$\tan \varepsilon_1 = \frac{a - t_o - d}{l}$$

and θ is the polar angle. With the definition $\varepsilon = \theta - \frac{\pi}{2}$, the trunk chord length may be written in terms of the following function:

$$z = l \tan \varepsilon - (a - d - t_o) \quad (11.23)$$

as

$$\Delta_2(\theta) = \begin{cases} 0 & (z \leq 0) \\ \frac{z}{\sin \varepsilon} & (0 \leq z \leq t) \\ \frac{t}{\sin \varepsilon} & (\text{Otherwise}) \end{cases} \quad (11.24)$$

The total thickness function is then

$$t(\theta) = \Delta_1(\theta) + \Delta_2(\theta) \quad (0 \leq \theta \leq \frac{\pi}{2} + \varepsilon_2) \quad (11.25)$$

where

$$\tan \varepsilon_2 = \frac{a - t_o - d}{\sqrt{a^2 - d^2}}$$

For larger values of θ ,

$$t(\theta) = \begin{cases} \frac{z + a - d - t_o}{\sin \varepsilon} & (0 \leq z \leq t) \\ \frac{t + a - d - t_o}{\sin \varepsilon} & (t \leq z) \end{cases} \quad (11.26)$$

The azimuthal values of l will have local minima at $\phi = 0, \pi, \frac{\pi}{2}$, and $\frac{3}{2}\pi$ corresponding to l_1, l_2, l_3 , and l_4 . There are four boundaries in ϕ separating the local minima and related through

$$\frac{l_1}{\cos \phi_1} = \frac{l_2}{\cos(\frac{\pi}{2} - \phi_1)} \quad (11.27)$$

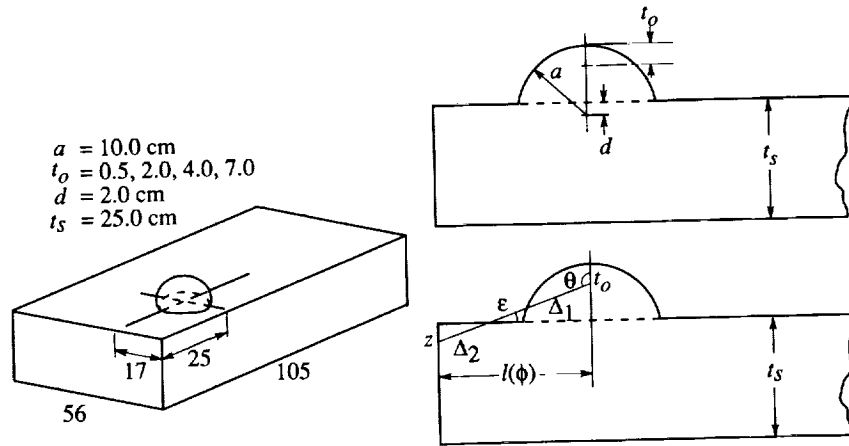


Figure 11.26. Breast geometry in meridional plane showing basic variables.

$a = 10.0$ cm
 $t_o = 0.5, 2.0, 4.0, 7.0$
 $d = 2.0$ cm
 $t_s = 25.0$ cm

$$\frac{l_2}{\cos(\phi_2 - \frac{\pi}{2})} = \frac{l_3}{\cos(\pi - \phi_2)} \quad (11.28)$$

$$\frac{l_3}{\cos(\phi_3 - \pi)} = \frac{l_4}{\cos(\frac{3}{2}\pi - \phi_3)} \quad (11.29)$$

$$\frac{l_4}{\cos(\phi_4 - \frac{3}{2}\pi)} = \frac{l_1}{\cos(2\pi - \phi_4)} \quad (11.30)$$

Then l as a function of azimuth is

$$l(\phi) = l_i / \cos[\phi - (i-1)\frac{\pi}{2}] \quad (\phi_{i-1} \leq \phi \leq \phi_1) \quad (11.31)$$

where $\phi_o \equiv \phi_4 - 2\pi$. The total chord length is then given by $t(\theta, \phi)$ or $t(\Omega)$, where numerical values are given by equations (11.21) through (11.31). Approximate values of l_i are 17, 80, 39, and 25 cm for which

$$\phi_1 \rightarrow \phi_4 = \{78^\circ, 116^\circ, 212.7^\circ, 304.2^\circ\}$$

The thickness t_s is taken as 25 cm. The dose response is given as usual by

$$R_B(E) = \int d\Omega R[E, t(\Omega)] \quad (11.32)$$

The present method has been incorporated into a computer code written for the Shuttle geometry (Wilson et al., 1990) for use in future mission analyses.

11.10.2. Results. The solar event of February 1956 was a large, high-energy event in which energetic particles up to several GeV were observed. As a relativistic particle event, the ground-level neutron monitor onset started about 20 minutes after the optical flare and peaked 20 minutes after onset as shown in

figure 11.27. The intensities decayed in 2 to 3 hours after the event. In contrast, the event of August 1972 was a relatively soft spectrum but of high intensity. Onset was 4 hours with peak intensities reached a few hours after onset followed by slow decay over the next dozen hours (table 11.26). In terms of high-energy intensity and total proton fluence, these two events bracket most other large events.

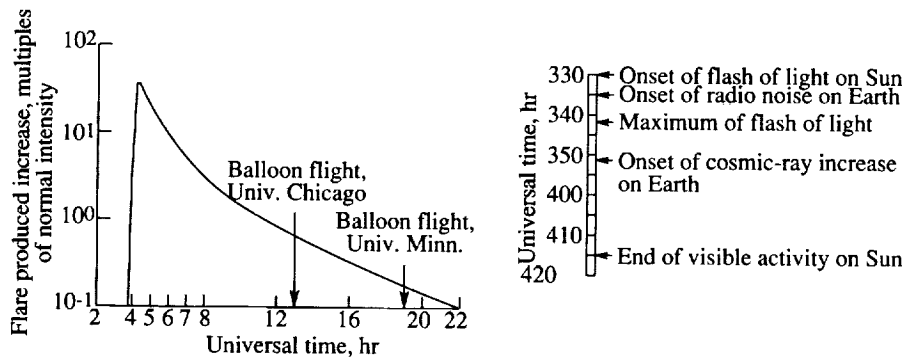


Figure 11.27. Cosmic-ray neutron surge at sea level during large solar event of Feb. 23, 1956.

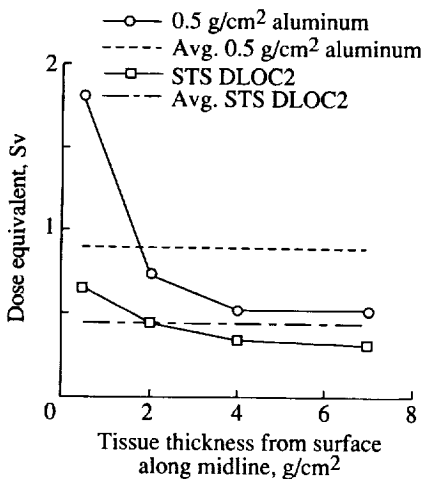


Figure 11.28. Dose equivalent exposure along breast centerline for Feb. 23, 1956.

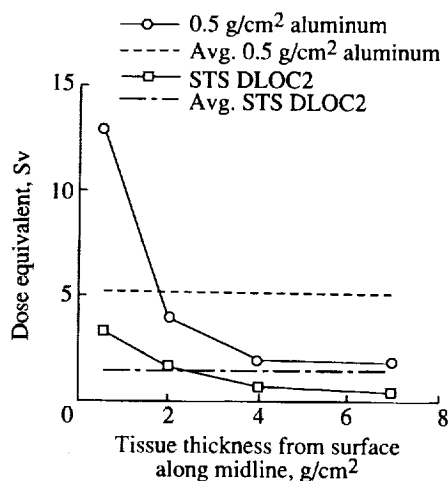


Figure 11.29. Dose equivalent exposure along breast centerline for Aug. 4, 1972.

A dose for a medium-size breast was calculated for these two events with two standard shield configurations. The first shield was an aluminum shield 0.5 g/cm^2 thick, which is representative of a hardened spacesuit, and the second was the least shielded region in the STS, which is representative of typical spacecraft shielding without the use of a storm shelter. The concern here is not so much the overall exposure, which varies greatly from event to event, but rather the dose distribution which may be important in assessing the exposure. Results are shown in figures 11.28 and 11.29. These results clearly show that the large variations in exposure occur over a large volume of breast tissue for either event for the aluminum shield 0.5 g/cm^2 thick. Even for a typical spacecraft configuration, large dose gradients exist within the breast tissues for the softer solar flare spectra.

The exposure is expected to be fairly uniform within a spacecraft for a high-energy spectrum that resembles the spectrum of the February 1956 event.

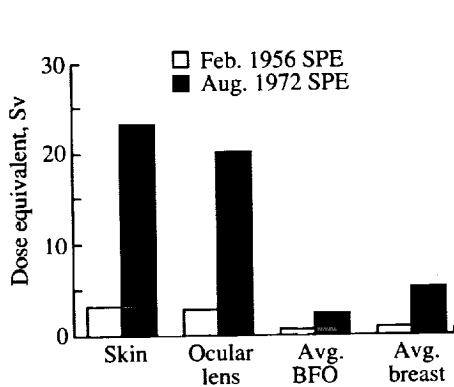


Figure 11.30. Organ dose equivalent for hardened space suit for two solar events.

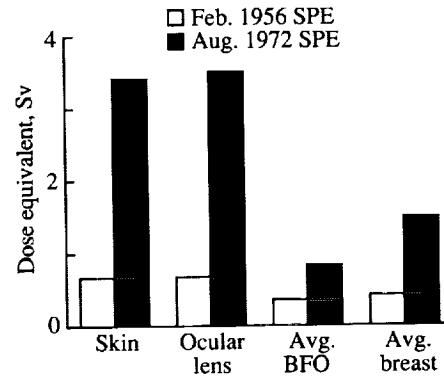


Figure 11.31. Organ dose equivalent for typical space vehicle for two solar events.

The average breast exposure and exposure values for other critical organs are presented in figures 11.30 and 11.31. A comparison of figures 11.30 and 11.31 clearly shows that the average breast exposure may be twice the exposure of the blood-forming organs, especially for low-energy, solar particle event spectra. This is a potentially important factor in the overall exposure budget.

Qualitatively, no great differences were observed in the dose gradient along the axis of symmetry for the three breast sizes; therefore average doses for the three breast sizes will be within 10 percent of the average among the sizes. This result occurs because dose distribution depends on the radius of curvature (Wilson and Khandelwal, 1974), which varies slowly with breast size. This result greatly simplifies the monitoring of individual exposure because the 10-cm radius model should provide adequate values for all. This is especially true if the astronauts are located inside the vehicle where breast-size effects are entirely negligible. However, even for extravehicular activity in heavy space suits (0.5 g/cm^2), this is a reasonably accurate approximation.

Exposure estimates for the female breast in future space missions can be made on the basis of a fixed, typical breast size ($a = 10 \text{ cm}$). One should remember that dose variations within the sensitive volume can be large (a factor of 2 to 3), although breast size does not appear to be a sensitive factor. Further work in assessing the importance of this large dose variation should be made.

11.11. References

- Adams, J. H., Jr.; Silberberg, R.; and Tsao, C. H., 1981: *Cosmic Ray Effects on Microelectronics. Part I—The Near-Earth Particle Environment*. NRL Memo. Rep. 4506-Pt. I, U.S. Navy. (Available from DTIC as AD A103 897.)
- Adams, James H., Jr., 1987: *Cosmic Ray Effects on Microelectronics*, Part IV. NRL Memo. Rep. 5901 (Revised), Naval Research Lab.

- Alsmiller, R. G., Jr.; Irving, D. C.; Kinney, W. E.; and Moran, H. S., 1965: The Validity of the Straightahead Approximation in Space Vehicle Shielding Studies. *Second Symposium on Protection Against Radiations in Space*, Arthur Reetz, Jr., ed., NASA SP-71, pp. 177-181.
- Alsmiller, R. G., Jr.; Irving, D. C.; and Moran, H. S., 1968: Validity of the Straightahead Approximation in Space-Vehicle Shielding Studies, Part II. *Nuclear Sci. & Eng.*, vol. 32, no. 1, pp. 56-61.
- Anon., 1977: *Recommendations of the International Commission on Radiological Protection*. ICRP Publ. 26, Pergamon Press.
- Anon., 1986a: *Mammography—A User's Guide, Recommendations of the National Council on Radiation Protection and Measurements*. NCRP Rep. No. 85.
- Anon., 1986b: *The Quality Factor in Radiation Protection*. ICRU Rep. 40, International Commission on Radiation Units and Measurements.
- Anon., 1989: *Guidance on Radiation Received in Space Activities*. NCRP Rep. No. 98, National Council on Radiation Protection and Measurements.
- Beck, W. L.; Stokes, T. R.; and Lushbaugh, C. C., 1972: Dosimetry for Radiobiological Studies of the Human Hematopoietic System. *Proceedings of the National Symposium on Natural and Manmade Radiation in Space*, E. A. Warman, ed., NASA TM X-2440, pp. 974-981.
- Billings, M. P.; and Yucker, W. R., 1973: *The Computerized Anatomical Man (CAM) Model*. NASA CR-134043.
- Bowman, J. D.; Swiatecki, W. J.; and Tsang, C. F., 1973: *Abrasion and Ablation of Heavy Ions*. LBL-2908, Lawrence Berkeley Lab., Univ. of California.
- Brenner, D. J.; and Hall, E. J., 1990: The Inverse Dose-Rate Effect for Oncogenic Transformation by Neutrons and Charged Particles: A Plausible Interpretation Consistent With Published Data. *Int. J. Radiat. & Biol.* vol. 58, no. 5, pp. 745-758.
- Cucinotta, Francis A.; Katz, Robert; Wilson, John W.; Townsend, Lawrence W.; Nealy, John E.; Shinn, Judy L., 1991: *Cellular Track Model of Biological Damage to Mammalian Cell Cultures From Galactic Cosmic Rays*. NASA TP-3055.
- Curtis, Stanley B., 1986: Lethal and Potentially Lethal Lesions Induced by Radiation—A Unified Repair Model. *Radiat. Res.*, vol. 106, pp. 252-270.
- Elkind, M. M.; and Sutton, Harriet, 1960: Radiation Response of Mammalian Cells Grown in Culture. I. Repair of X-Ray Damage in Surviving Chinese Hamster Cells. *Radiat. Res.*, vol. 13, nos. 1-6, pp. 556-593.
- Foelsche, Trutz; Mendell, Rosalind, B.; Wilson, John W.; and Adams, Richard R., 1974: *Measured and Calculated Neutron Spectra and Dose Equivalent Rates at High Altitudes; Relevance to SST Operations and Space Research*. NASA TN D-7715.
- Fritz-Niggli, Hedi, 1988: The Role of Repair Processes in Cellular and Genetical Response to Radiation. *Terrestrial Space Radiation and Its Biological Effects*, Percival D. McCormack, Charles E. Swenberg, and Horst Bückner, eds., Plenum Press, pp. 213-235.

Transport Methods and Interactions for Space Radiations

- Hill, C. K.; Buonaguro, F. M.; Myers, C. P.; Han, A.; and Elkind, M. M., 1982: Fission-Spectrum Neutrons at Reduced Dose Rates Enhance Neoplastic Transformation. *Nature*, vol. 298, pp. 67-69.
- Hill, C. K.; Carnes, B. A.; Han, A.; and Elkind, M. M., 1985: Neoplastic Transformation Is Enhanced by Multiple Low Doses of Fission-Spectrum Neutrons. *Radiat. Res.*, vol. 102, pp. 404-410.
- Katz, R.; Ackerson, R.; Homayoonfar, M.; and Sharma, S. C., 1971: Inactivation of Cells by Heavy Ion Bombardment. *Radiat. Res.*, vol. 47, pp. 402-425.
- Katz, Robert; Sharma, S. C.; and Homayoonfar, M., 1972: The Structure of Particle Tracks. *Topics in Radiation Dosimetry*, Supplement 1, F. H Attix, ed., Academic Press, Inc., pp. 317-383.
- Katz, Robert, 1986: Biological Effects of Heavy Ions From the Standpoint of Target Theory. *Adv. Space Res.*, vol. 6, no. 11, pp. 191-198.
- Katz, Robert; and Cucinotta, F. A., 1991: RBE vs. Dose for Low Doses of High-LET Radiations. *Health Phys.*, vol. 60, no. 5, pp. 717-718.
- Kellerer, Albrecht M.; and Rossi, Harald H., 1972: The Theory of Dual Radiation Action. *Current Top. Radiat. Res. Q.*, vol. 8, no. 2, pp. 85-158.
- Kovalev, E. E.; Muratova, I. A.; and Petrov, V. M., 1989: Studies of the Radiation Environment Aboard Prognoz Satellites. *Nuclear Tracks & Radiat. Meas.*, vol. 16, no. 1, pp. 45-48.
- Khandelwal, G. S.; and Wilson, John W., 1974: *Proton Tissue Dose for the Blood Forming Organ in Human Geometry: Isotropic Radiation*. NASA TM X-3089.
- Langley, R. W.; and Billings, M. P., 1972a: Methods of Space Radiation Dose Analysis With Applications to Manned Space Systems. *Proceedings of the National Symposium on Natural and Manmade Radiation in Space*, E. A. Warman, ed., NASA TM X-2440, pp. 108-116.
- Langley, R. W.; and Billings, M. P., 1972b: A New Model for Estimating Space Proton Dose to Body Organs. *Nuclear Technol.*, vol. 15, no. 1, pp. 68-74.
- Nealy, John E.; Wilson, John W.; and Townsend, Lawrence W., 1989: Preliminary Analyses of Space Radiation Protection for Lunar Base Surface Systems. SAE Tech. Paper Ser. 891487.
- Rossi, H. H.; and Kellerer, A. M., 1986: The Dose Rate Dependence of Oncogenic Transformation by Neutrons May Be Due to Variation of Response During the Cell Cycle. *Int. J. Radiat. & Biol.*, vol. 50, no. 2, pp. 353-361.
- Scott, B. R.; and Ainsworth, E. J., 1980: State-Vector Model for Life Shortening in Mice After Brief Exposures to Low Doses of Ionizing Radiation. *Math. Biosci.*, vol. 49, pp. 185-205.
- Shavers, Mark; Poston, John W.; Atwell, William; Hardy, Alva C.; and Wilson, John W., 1991: *Preliminary Calculation of Solar Cosmic Ray Dose to the Female Breast in Space Missions*. NASA TM-4235.
- Shinn, Judy L.; Wilson, John W.; and Nealy, John E., 1990: *Reliability of Equivalent Sphere Model in Blood-Forming Organ Dose Estimation*. NASA TM-4178.

- Simonsen, Lisa C.; Nealy, John E.; Townsend, Lawrence W.; and Wilson, John, W., 1990: *Radiation Exposure for Manned Mars Surface Missions*. NASA TP-2979.
- Simpson, J. A., 1983: Elemental and Isotopic Composition of the Galactic Cosmic Rays. *Annual Review of Nuclear and Particle Science*, Volume 33, J. D. Jackson, Harry E. Gove, and Roy F. Schwitters, eds., Annual Reviews Inc., pp. 323-381.
- Sinclair, Warren K., 1968: Cyclic X-Ray Responses in Mammalian Cells In Vitro. *Radiat. Res.*, vol. 33, pp. 620-643.
- Sinclair, W. K., 1985: Experimental RBE Values of High LET Radiations at Low Doses and the Implications for Quality Factor Assignment. *Radiat. Prot. Dosim.*, vol. 13, no. 1-4, pp. 319-326.
- Space Science Board, 1970: *Radiation Protection Guides and Constraints for Space-Mission and Vehicle-Design Studies Involving Nuclear Systems*. National Academy of Sciences, National Research Council.
- Swenberg, Charles E.; Holwitt, Eric A.; and Speicher, James M., 1990: Superhelicity and DNA Radiation Sensitivity. SAE Tech. Paper Ser. 901349.
- Thacker, John; Stretch, Albert; and Stephens, Miriam A., 1979: Mutation and Inactivation of Cultured Mammalian Cells Exposed to Beams of Accelerated Heavy Ions. II. Chinese Hamster V79 Cells. *Int. J. Biol.*, vol. 36, no. 2, pp. 137-148.
- Thames, Howard D., 1985: 'An Incomplete-Repair' Model for Survival After Fractionated and Continuous Irradiations, *Int. J. Radiat. & Biol.*, vol. 47, pp. 317-339.
- Thomson, John F.; Williamson, Frank S.; Grahn, Douglas; and Ainsworth, E. John, 1981a: Life Shortening in Mice Exposed to Fission Neutrons and γ Rays. I. Single and Short-Term Fractionated Exposures. *Radiat. Res.*, vol. 86, pp. 559-572.
- Thomson, John F.; Williamson, Frank S.; Grahn, Douglas; and Ainsworth, E. John, 1981b: Life Shortening in Mice Exposed to Fission Neutrons and γ Rays. II. Duration-of-Life and Long-Term Fractionated Exposures. *Radiat. Res.*, vol. 86, pp. 573-579.
- Thomson, John F.; Williamson, Frank S.; and Grahn, D., 1983: Life Shortening in Mice Exposed to Fission Neutrons and γ Rays. III. Neutron Exposures of 5 and 10 Rad. *Radiat. Res.*, vol. 93, pp. 205-209.
- Thomson, John F.; Williamson, Frank S.; and Grahn, Douglas, 1985a: Life Shortening in Mice Exposed to Fission Neutrons and γ Rays. IV. Further Studies With Fractionated Neutron Exposures. *Radiat. Res.*, vol. 103, pp. 77-88.
- Thomson, John F.; Williamson, Frank S.; and Grahn, Douglas, 1985b: Life Shortening in Mice Exposed to Fission Neutrons and γ Rays. V. Further Studies With Single Low Doses. *Radiat. Res.*, vol. 104, pp. 420-428.
- Thomson, John F.; Williamson, Frank S.; and Grahn, Douglas, 1986: Life Shortening in Mice Exposed to Fission Neutrons and γ Rays. VI. Studies With the White-Footed Mouse, *Peromyscus Leucopus*. *Radiat. Res.*, vol. 108, pp. 176-188.

Transport Methods and Interactions for Space Radiations

- Thomson, John F.; and Grahn, Douglas, 1988: Life Shortening in Mice Exposed to Fission Neutrons and γ Rays. VII. Effects of 60 Once-Weekly Exposures. *Radiat. Res.*, vol. 115, pp. 347-360.
- Thomson, John F.; and Grahn, Douglas, 1989: Life Shortening in Mice Exposed to Fission Neutrons and γ Rays. VIII. Exposures to Continuous γ Radiation. *Radiat. Res.*, vol. 118, pp. 151-160.
- Todd, Paul; and Tobias, Cornelius A., 1974: Cellular Radiation Biology. *Space Radiation Biology and Related Topics*, Cornelius A. Tobias and Paul Todd, eds., Academic Press, Inc., pp. 141-196.
- Townsend, L. W.; and Wilson, J. W., 1988: An Evaluation of Energy-Independent Heavy Ion Transport Coefficient Approximations. *Health Phys.*, vol. 54, no. 4, pp. 409-412.
- Townsend, Lawrence W.; Wilson, John W.; and Nealy, John E., 1988: *Preliminary Estimates of Galactic Ray Shielding Requirements for Manned Interplanetary Missions*. NASA TM-101516.
- Townsend, Lawrence W.; Wilson, John W.; and Nealy, John E., 1989: Space Radiation Shielding Strategies and Requirements for Deep Space Missions. SAE Tech. Paper Ser. 891433.
- Townsend, Lawrence W.; Nealy, John E.; Wilson, John W.; and Simonsen, Lisa C., 1990a: *Estimates of Galactic Cosmic Ray Shielding Requirements During Solar Minimum*. NASA TM-4167.
- Townsend, L. W.; Wilson, J. W.; Shinn, J. L.; and Curtis, S. B., 1990b: Human Exposure to Large Solar Particle Events in Space. Paper presented at the 28th Plenary Meeting of COSPAR (The Hague, The Netherlands).
- Waligorski, M. P. R.; Sinclair, G. L.; and Katz, R., 1987: Radiosensitivity Parameters for Neoplastic Transformations in C3HT10T1/2 Cells. *Radiation Res.*, vol. 111, pp. 424-437.
- Webber, W. R., 1963: *An Evaluation of the Radiation Hazard Due to Solar-Particle Events*. D2-90469, Aero-Space Div., Boeing Co.
- Wilson, John W.; and Khandelwal, G. S., 1974: Proton Dose Approximation in Arbitrary Convex Geometry. *Nuclear Technol.*, vol. 23, no. 3, pp. 298-305.
- Wilson, John W.; and Denn, Fred M., 1976: *Preliminary Analysis of the Implications of Natural Radiations on Geostationary Operations*. NASA TN D-8290.
- Wilson, John W.; Townsend, L. W.; Bidasaria, H. B.; Schimmerling, Walter; Wong, Mervyn; and Howard, Jerry, 1984: ^{20}Ne Depth-Dose Relations in Water. *Health Phys.*, vol. 46, no. 5, pp. 1101-1111.
- Wilson, John W.; Townsend, Lawrence W.; and Badavi, F. F., 1987: A Semiempirical Nuclear Fragmentation Model. *Nuclear Instrum. & Methods Phys. Res.*, vol. B18, no. 3, pp. 225-231.
- Wilson, John W.; and Townsend, L. W., 1988: A Benchmark for Galactic Cosmic-Ray Transport Codes. *Radiat. Res.*, vol. 114, no. 2, pp. 201-206.

- Wilson, John W.; and Townsend, Lawrence W.; Ganapol, Barry; Chun, Sang Y.; and Buck, Warren W., 1988: Charged-Particle Transport in One Dimension. *Nuclear Sci. & Eng.*, vol. 99, no. 3, pp. 285-287.
- Wilson, John W.; Townsend, Lawrence W.; Nealy, John E.; Chun, Sang Y.; Hong, B. S.; Buck, Warren W.; Lamkin, S. L.; Ganapol, Barry D.; Khan, Ferdous; and Cucinotta, Francis A., 1989: BRYNTRN: *A Baryon Transport Model*. NASA TP-2887.
- Wilson, John, W.; Khandelwal, Govind S.; Shinn, Judy L.; Nealy, John E.; Townsend, Lawrence W.; and Cucinotta, Francis A., 1990: *Simplified Model for Solar Cosmic Ray Exposure in Manned Earth Orbital Flights*. NASA TM-4182.
- Wulf, H.; Kraft-Weyrather, W.; Miltenburger, H. G.; Blakely, E. A.; Tobias, C. A.; and Kraft, G., 1985: Heavy-Ion Effects on Mammalian Cells: Inactivation Measurements With Different Cell Lines. *Radiat. Res.*, vol. 104, suppl. 8, pp. S-122-S-134.
- Yang, Tracy Chui-Hsu; Craise, Laurie M.; Mei, Man-Tong; and Tobias, Cornelius A., 1985: Neoplastic Cell Transformation by Heavy Charged Particles. *Radiat. Res.*, vol. 104, pp. S-177-S-187.
- Yang, Tracy Chui-Hsu; Craise, Laurie M.; Mei, Man-Tong; and Tobias, Cornelius A., 1986: Dose Protection Studies With Low- and High-LET Radiations on Neoplastic Cell Transformation In Vitro. *Adv. Space Res.*, vol. 6, no. 11, pp. 137-147.
- Yang, Tracy Chui-Hsu; Craise, Laurie M.; Mei, Man-Tong; and Tobias, Cornelius A., 1989: Neoplastic Cell Transformation by High-LET Radiation: Molecular Mechanisms. *Adv. Space Res.*, vol. 9, no. 10, pp. (10)131-(10)140.

100

100

100

100

100

100

100

100

Chapter 12

Application to Space Exploration

12.1. Introduction

The next major space endeavor after Space Station *Freedom* will be the human exploration of the Moon and Mars (The 90-Day Study (Anon., 1989b)). A critical aspect of these missions is the safety and health of the crew. One of the major health concerns is the damaging effects of ionizing space radiation (Parker and West, 1973). Once the crew leaves the Earth's protective environment, they will be bombarded by radiations of varying energies and ranges of intensity. The most harmful components of these radiations are trapped electrons and protons in the Van Allen belts, solar flare protons, and galactic cosmic rays. Adequate shielding will be required to protect the crew from this environment.

Astronaut doses incurred from the Van Allen belts are highly dependent on the time spent in the high flux regions of the belt and the state of fields at the time of exposure (Burrell, Wright, and Watts, 1968; Wilson and Cucinotta, 1984; Cucinotta and Wilson, 1985). Large temporal variations are observed in the outer zone for which dose incurred over a short time period may increase by an order of magnitude and more (Wilson and Denn, 1976 and 1977; Wilson, 1978). The nature of the energy spectrum is such that crew members in a typical shielded spacecraft can incur very large doses. However, moderate shielding (approximately 2 g/cm^2) and a single pass through the belts usually result in relatively small delivered doses ($<1 \text{ cSv}$) under normal field conditions. These doses are of most concern for low Earth to geostationary orbit operations (Wilson and Denn, 1977; Wilson, 1978) and for spiraling trajectories through the belts. In either case, the large scale fluctuations are of great importance in determining shield requirements. Although galactic cosmic rays (GCR) are ever present, the low-energy GCR are deflected by the geomagnetic field (Wilson, 1978).

Outside the influence of the Earth's magnetic field, the astronauts will be constantly bombarded by galactic cosmic rays. The constant bombardment of these particles delivers a steady although low-level dose rate. The intensity of the GCR flux varies over the approximately 11-year solar cycle due to the interplanetary plasma resulting from the expanding solar corona. The maximum dose received occurs at solar minimum due to the lower solar plasma output. For the long-duration missions, this dose can become career limiting. Thus, the amount of shielding required to protect the astronauts will depend on the time within the solar cycle and duration of the mission.

Anomalously large solar proton events are relatively rare with one or two events per solar cycle. The largest flares observed in cycles 18 and 19 are the November 1948, February 1956, the May to July 1959 events series, and the November 1960 series. It was generally believed that the unusually large solar turbulence experienced in cycles 18 and 19 resulted in the largest events to be observed. However, the rather uneventful cycle 20 at the close of its activity produced an event on August 4, 1972, completely out of proportion to all expectations (Wilson and Denn, 1976; Wilson, 1978). Solar cycle 21 (1975-1986) proved relatively quiet with no unusually large events. However, with the onset of cycle 22, old concerns

are confirmed with several large events occurring in the latter half of 1989. A solar flare event can be very dangerous if a spacecraft is inadequately shielded because flares can deliver a very high dose in a short period of time as was first made clear by the August 1972 event (Wilson and Denn, 1976). For relatively short-duration missions (2-3 months), the most important radiation hazard is the possibility of an unusually large solar proton event. The amount of shielding required for protection will depend on the nature of the energy spectrum and intensity of the flare. The means of setting shield requirements for such events are uncertain because there is no way yet of predicting either event size or spectrum.

Shielding must be provided to maintain crew doses to an acceptable level. Currently there are no limits established for exploratory class missions; however, it is recommended by NCRP 98 (Anon., 1989a, p. 163) that limits established for operations in low Earth orbit be used as *guidelines* for mission studies. The Space Station *Freedom* (SSF) limits are established (table 12.1) by the National Council on Radiation Protection and Measurement (NCRP 98 (Anon., 1989a)) and include dose equivalent limits for the blood-forming organ (BFO), ocular lens, and skin. For high-energy radiation from galactic cosmic rays and solar flare protons, the dose delivered to the BFO is the most important because of latent carcinogenic effects. Although other organs of the individual are at risk to cancer, only the blood-forming organ (BFO), ocular lens, and skin have been specifically limited (NCRP 98 (Anon., 1989a)). It is generally regarded that the BFO dose is a good indicator of whole-body exposure. Such notions are founded on ground level experience and need not apply to space radiation where large dose gradients are known to exist and have important consequences on risk assessment (Shinn, Wilson, and Nealy, 1990; Shavers et al., 1991). When detailed body geometry is not considered, the BFO dose is usually computed as the dose incurred at a depth of 5 cm in tissue as recommended by the Space Science Board (1970). Dose equivalent rate limits are established for short-term exposures (30 days), annual exposures, and total career exposure. These values are given in table 12.1. Note that dose equivalent is used for all limits although the quality factor mainly applies to carcinogenesis and mutagenesis (NCRP 98 (Anon., 1989a)). Short-term exposures are important when considering solar flare events because of their high dose rate (Committee on the Biological Effects of Ionizing Radiations, 1990 (BEIR V)). Doses received from GCR on long-duration missions are especially

Table 12.1. Dose Equivalent Limits Recommended for U.S. Astronauts in Low Earth Orbit

Exposure time	Dose equivalent recommended limit, Sv, for —		
	BFO	Ocular lens	Skin
Career	^a 1-4	4	6
Annual	0.5	2	3
30 days	0.25	1	1.5

^aVaries with age and gender.

important to total career limits, which are determined by the age and gender of the individual. For instance, career limits for typical male and female astronauts who are 30 years old at the time of their first exposure are 2 Sv and 1.4 Sv, respectively. The limit on whole-body exposure for a 3-year Mars mission would be 1.5 Sv using the BFO limit for SSF compared with the limit used in the Soviet Union space program of 4 Sv (Yablontsev, 1990). The appropriateness of the use of quality factors for GCR exposures is unknown (NCRP 98 (Anon., 1989a)).

Current mission scenarios for the Nation's Space Exploration Initiative are described in The 90-Day Study (Anon., 1989b). The final goal of the Initiative is to establish two permanent operational outposts on both the Moon and Mars. After a 3-day trip from Earth to the Moon, crew rotation times on the surface are described as starting with a 30-day stay, to a 6-month stay, to a 12-month stay, and finally growing to a 600-day stay. The flight time to Mars is estimated to take from 7 months to over a year each way. Crew rotations on the martian surface are described as starting with a 30-day stay, to a 90-day stay, up to a 600-day stay. Thus, an entire Mars mission is estimated to take anywhere from 500 to 1000 days round trip. Different shielding strategies will exist for each phase of each lunar and martian mission. Deep space shielding requirements for lunar transfer vehicles will differ greatly from those selected for the Mars vehicles because of the large differences in travel time. Likewise, planetary habitation shielding strategies utilizing local resources will differ greatly from the transfer vehicles. Habitation shielding on the lunar surface versus that on the martian surface will also differ greatly because of the differences in the environment and the protection provided by the martian atmosphere.

12.2. Space-Radiation Environment

The types of particle radiations that occur in space are summarized in figure 12.1. There are both temporal as well as spatial variations. For example, trapped particles exist only in the geomagnetic field where mirror points lie well above the atmosphere, the solar wind can only be seen outside the Earth's magnetosphere, the auroral electrons are trapped particles with mirror points in the atmosphere and are seen only in polar regions during geomagnetic disturbances, solar cosmic rays are rare transient events associated with solar flares, and so on. (See Wilson (1978) for more details.) The radiations with energies below 100 keV and the protons below 10 MeV are mainly important only from a material point of view—for example, thermal control coatings—and are considered biologically unimportant. The radiations of immediate importance for biological consideration are the trapped protons in the inner zone, the trapped electrons in both the inner and the outer zones, and solar flare protons. Galactic cosmic rays are also biologically important. They are of low intensity but many questions surround them because of their particular composition, and their biological action is potentially hazardous and not well understood experimentally. Data used in constructing figure 12.1 are taken from Noll and McElroy (Anon., 1975a), Foelsche (1963), McDonald (1963), Divine (Anon., 1975b), and Johnson (1965).

The impact of radiation on Earth orbital operations is shown in table 12.2 (Wilson, 1978). We see that imposed limits are very restrictive in some regions of space. Within the inner zone below 400 n.mi. are mostly protons and electrons.

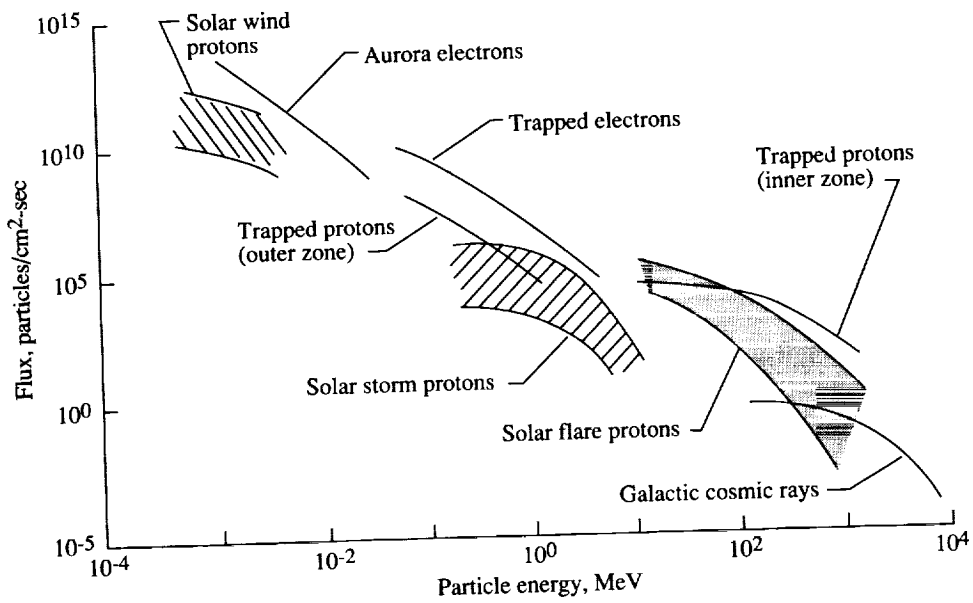


Figure 12.1. Space-radiation environment (Wilson, 1978).

Table 12.2. Impact of Radiation on Operations in Earth Orbit

Source	Particles	Aluminum shielding, g/cm ²	Number of days ^a	Limiting factor
Inner zone ($h < 400$ n.mi)	Protons Electrons	2	22	Testes
Outer zone ($h > 19\,000$ n.mi)	Electrons	6.7 1.4	90 90	Testes ^b Skin, lens, BFO
Solar cosmic rays	Proton Alpha	5 10	0.25 0.5	Lens, testes, skin BFO, lens, testes
Galactic cosmic rays	Proton Alpha Carbon : Iron	?	?	Nonregenerative tissue with unique function?

^aNumber of days to reach quarterly exposure limit.

^bPersonal shielding is assumed for testes.

Behind a shield 2 g/cm^2 thick, only about 22 days are required to reach the quarterly exposure limit at this altitude. The limiting biological factor is the testes which could be protected by personal shielding. As for the outer zone, which is important to the space solar power satellites and interplanetary transportation, the radiation is primarily electrons, and a shield constructed from aluminum on the order of 6.7 g/cm^2 is required to reach the quarterly exposure limits in 90 days. The limiting biological factor is again the testes. If the bremsstrahlung is eliminated by putting a high Z material on the innerside of the wall, the shield could be reduced substantially. Then a shield thickness of only 1.4 g/cm^2 is required to meet the quarterly exposure limit in 90 days and the limiting factors are skin, ocular lens, and the blood-forming organs. This shield 1.4 g/cm^2 thick is, of course, an absolute minimum shield because there is no personal shielding that is practical for the organs involved. Interplanetary travel exposure is reduced by a rapid transit through this region but large short-term temporal variations need to be addressed (Wilson and Denn, 1977; Wilson, 1978). The solar cosmic rays consist mostly of protons and alphas with fewer other particles. Behind 5 g/cm^2 , only about 6 hours are required to reach exposure limits, and the limiting factors are listed in table 12.2. For a shield of 10 g/cm^2 , it takes about 0.5 day to reach exposure limits for the ocular lens and testes, which can be protected by using personal shielding. The galactic cosmic rays contain a little bit of everything, and the type of shielding required and the number of days to reach exposure limits are presently in question. Most probably the hazard will be associated with nonregenerative tissues which also have a unique function, carcinogenesis, and mutagenesis. Galactic heavy ions will probably be the ultimate limiting factor in space operations, but all these points are still open for debate since definitive biological data are still lacking (NCRP 98 (Anon., 1989a)). Conclusions are drawn from data taken from Burrell, Wright, and Watts (1968), Wilson and Denn (1976 and 1977), and Grahn (1973).

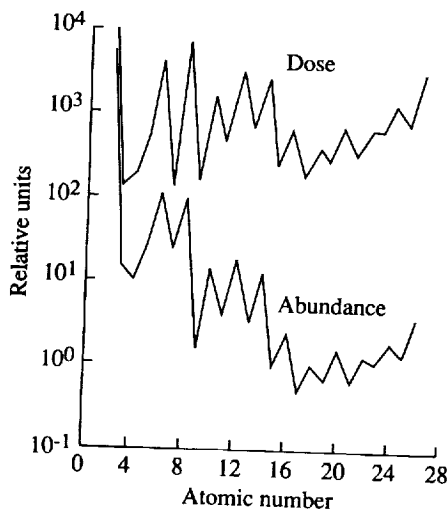


Figure 12.2. Galactic heavy ion intensities.

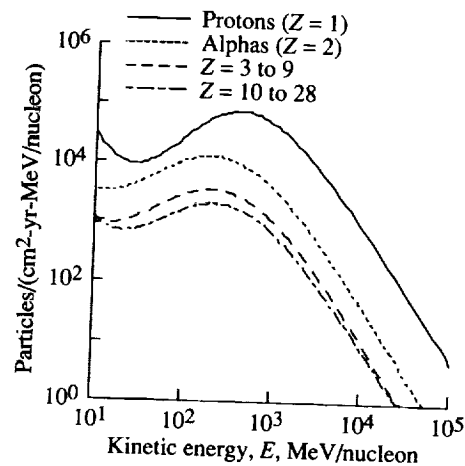


Figure 12.3. Galactic cosmic-ray ion spectra for solar minimum conditions (Adams, Silberberg, and Tsao, 1981).

12.2.1. Galactic cosmic rays. Figure 12.2 shows how the abundance of galactic cosmic rays falls off as the higher atomic numbers are reached (J. A. Simpson and M. Garcia-Munoz, University of Chicago).¹ The dose is proportional to the charge squared. The relative dose contribution is more nearly the same for different particle types; it doesn't follow that the less abundant types are necessarily negligible. The deep space differential spectra are shown in figure 12.3 for solar minimum conditions (Adams, Silberberg, and Tsao, 1981).

The galactic cosmic rays are affected by interaction with the Earth's magnetic field (fig. 12.4). Mainly the low rigidity particles are excluded from equatorial regions at low altitudes, whereas near the poles the particles may come in freely at all altitudes. Although the particles with low rigidity are seen at low altitude mainly near the polar region, the heavy ions are by far the most rigid particles (mass to charge ratio) of the galactic beam. Consequently, mostly protons are lost in the equatorial region having a greater proportion of heavy ions.

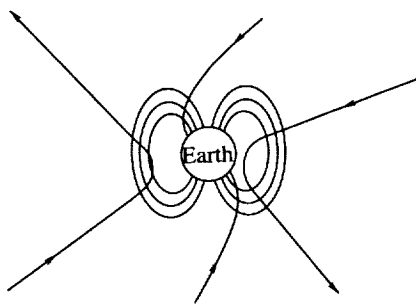


Figure 12.4. Galactic cosmic-ray interaction with geomagnetic field.

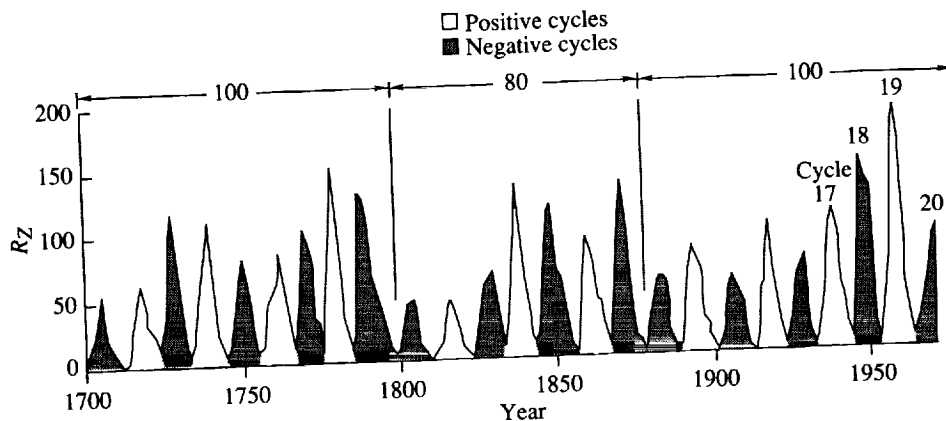


Figure 12.5. Annual smoothed sunspot numbers.

12.2.2. Solar activity. Most space radiations are affected by solar activity in one way or the other, either as their source or in some secondary effect. Figure 12.5 shows the annual smoothed sunspot numbers for the past few hundred years. The main feature is that the concept of a "typical" solar cycle is uncertain.

¹ Unpublished data measured aboard IMP-4 in 1970.

It is clearly illustrated that cycle 19 is one of the most extreme cycles in terms of sunspot numbers that we have ever seen (last full cycle at right). Cycle 20, shown in part just to the right of cycle 19, was pretty close to an average cycle and we should keep that in mind when we discuss solar cosmic rays later. These data were taken from Sleeper (1972).

One effect observed during solar activity was the fluctuation of the expanding solar corona. The galactic cosmic rays coming in from galactic space interact with this plasma and slow down. In figure 12.6 we show the amount of energy that the particles lose coming in from galactic space to Earth orbit represented as a potential function. It correlates reasonably well with sunspot number which is related to solar activity. These data were taken from O'Brien (1972). The effects of increased solar modulation during solar maximum are demonstrated in figure 12.7.

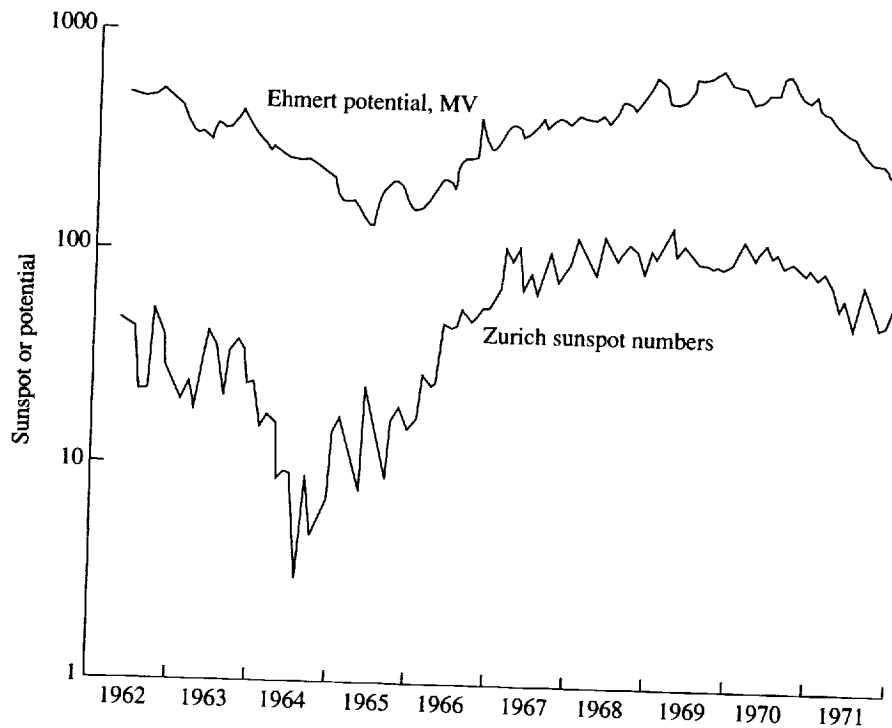


Figure 12.6. Galactic cosmic-ray modulation parameter and solar activity (O'Brien, 1972).

12.2.3. Solar cosmic rays. Occasional solar flares are associated with the Sun and solar activity. Plasma is ejected from a large number of optical flares, and this causes type IV radio bursts. During some of these flares (actually very few), there are particles that are ejected at high energy into interplanetary space. These high-energy particles are able to escape the solar magnetic fields only if the lines are open to the interplanetary region. The data shown in figure 12.8 were taken from Slutz et al. (1971), King (1974), and Blizard (1969). This figure shows the sunspot numbers during cycles 19 and 20 and plots of the proton fluence greater than 30 MeV. This is the total fluence of each individual particle event as

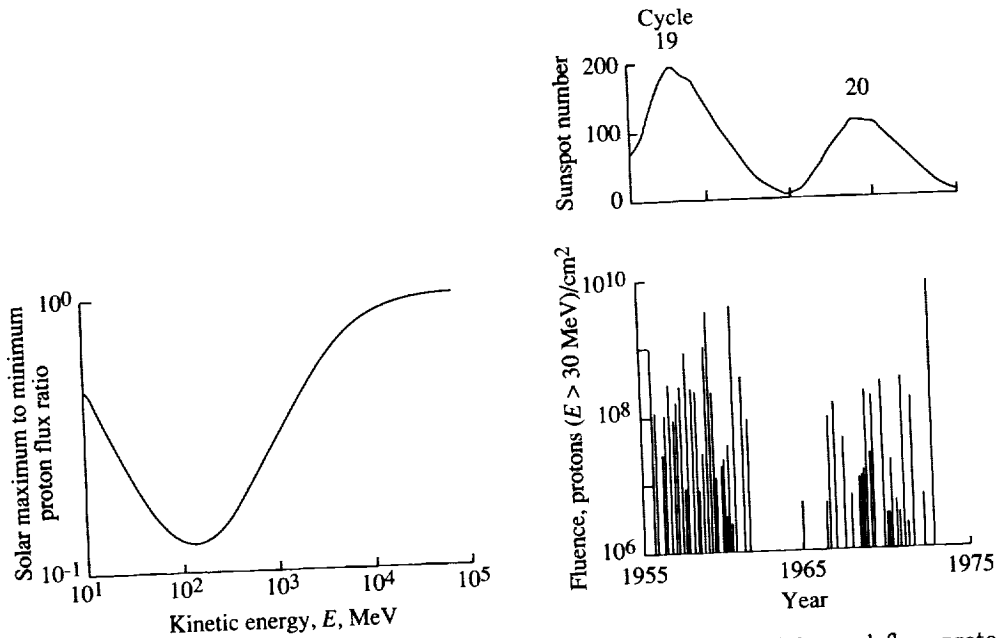


Figure 12.7. GCR proton flux reduction factors at solar maximum (Adams, Silberberg, and Tsao, 1981).

Figure 12.8. Solar activity and flare proton fluence.

a function of time of occurrence. There is a rough correlation between the number of particles and the degree of solar activity. Generally there are anywhere from one to perhaps five solar events which might be called major events during any particular cycle.

Some details of what happened during cycles 18, 19, and 20 can be found in figure 12.9. Here we show just the major events that occurred during these particular cycles; notice that, in general, the largest events are usually absent during the ascending or descending phase of the solar cycle. Major events are usually absent during solar maximum and, of course, also during solar minimum. The events denoted by dashes are of little significance to manned space flight. Data were taken from Blizard (1969) and King (1974).

There is a rough correlation between the solar activity and the particle fluences that are observed in any given year. Plotted in figure 12.10 are proton yearly fluences as a function of the average yearly sunspot number during cycle 19 for protons of energy greater than 1 MeV (upper curve), greater than 10 MeV (middle curve), and greater than 40 MeV (lower curve). There is some general dependence of the fluence of particles associated with sunspot number, although there are significant deviations. These correlations are made for predictive purposes. If the sunspot numbers in the next cycle can be predicted, a correlation between sunspot number and particle fluence can be made. Then it is possible to make an estimate of what sort of exposure might be expected in the coming solar cycle. Data were taken from Webber (1966) and Curtis, Doherty, and Wilkinson (1969).

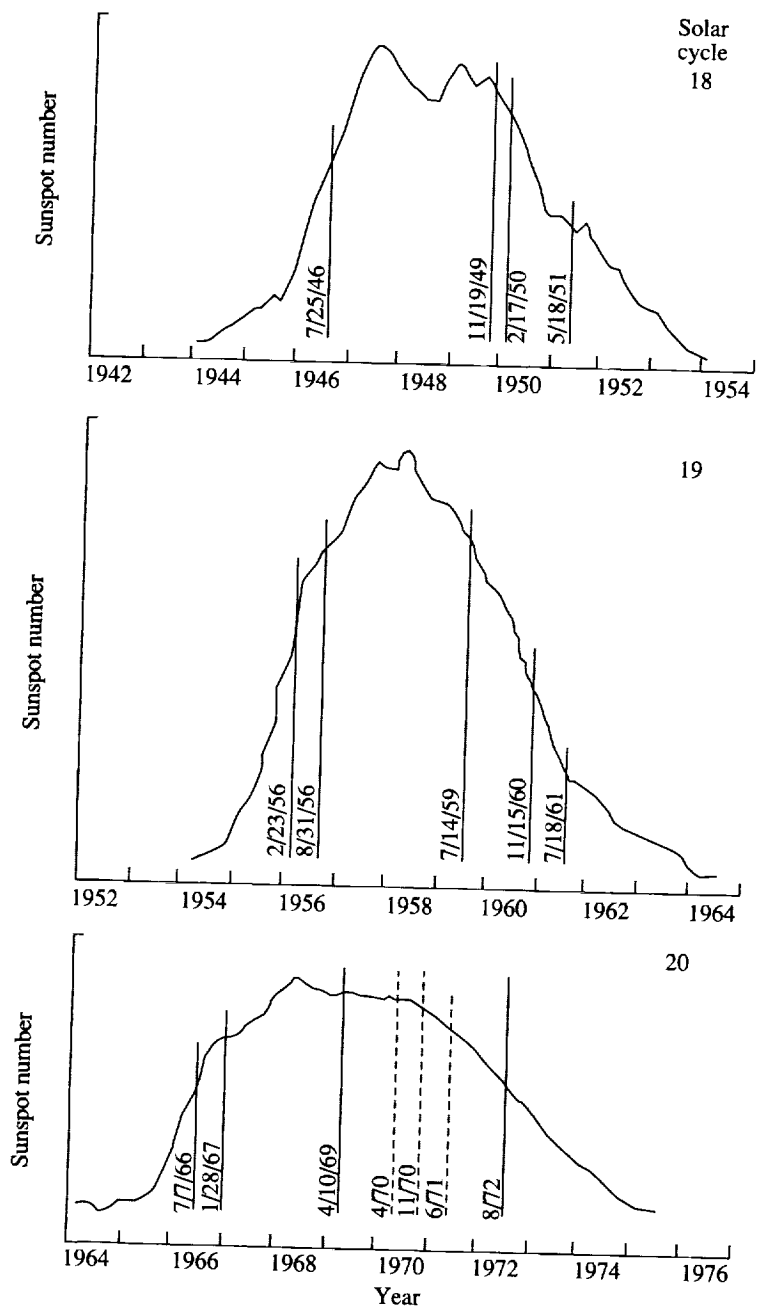


Figure 12.9. Major solar particle events of the last three solar cycles.

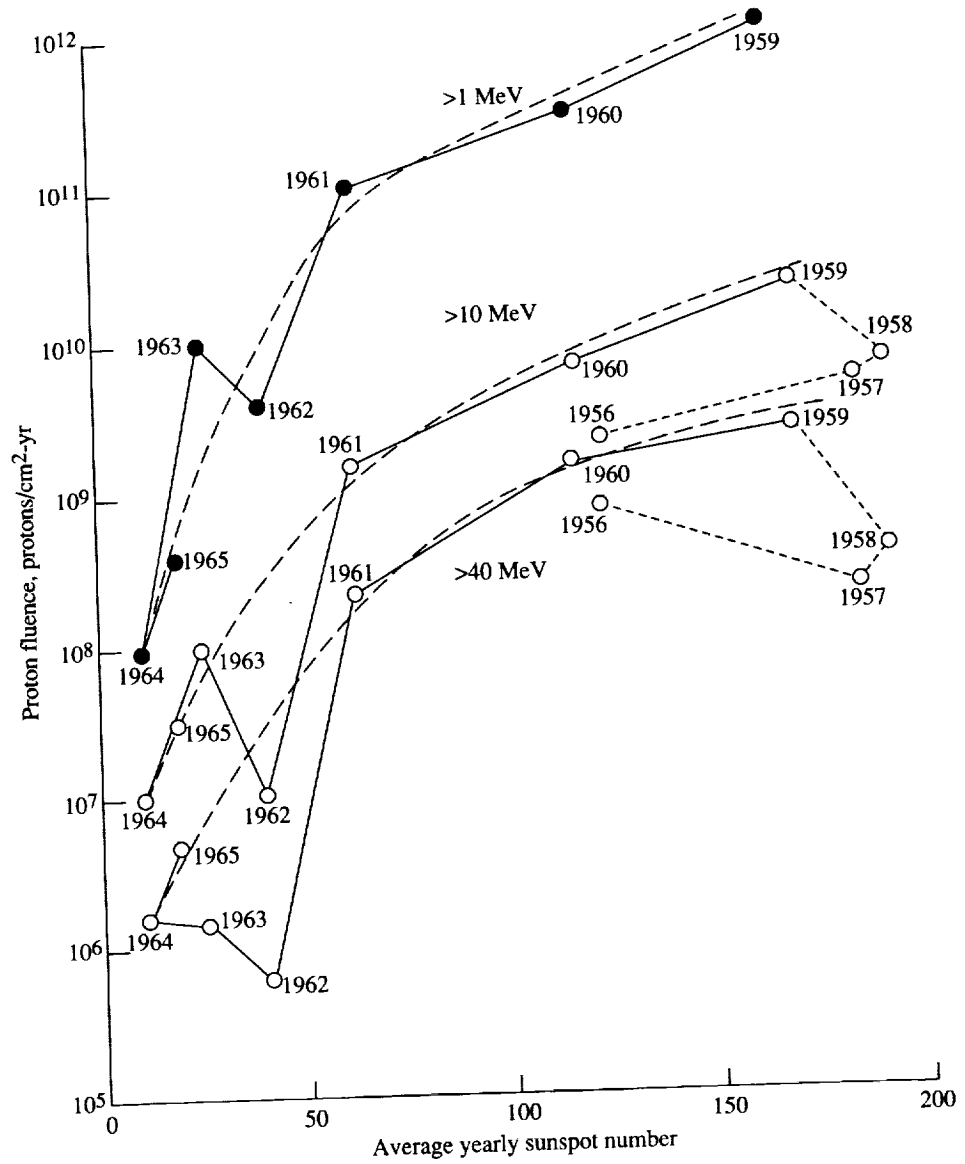


Figure 12.10. Solar cosmic-ray yearly fluence during cycle 19.

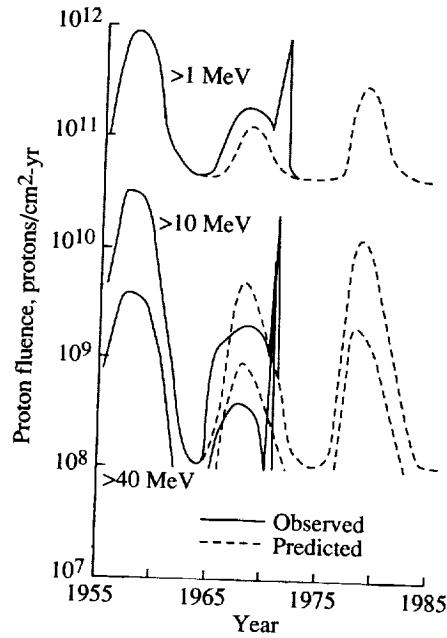


Figure 12.11. Yearly proton fluence at geostationary orbit.

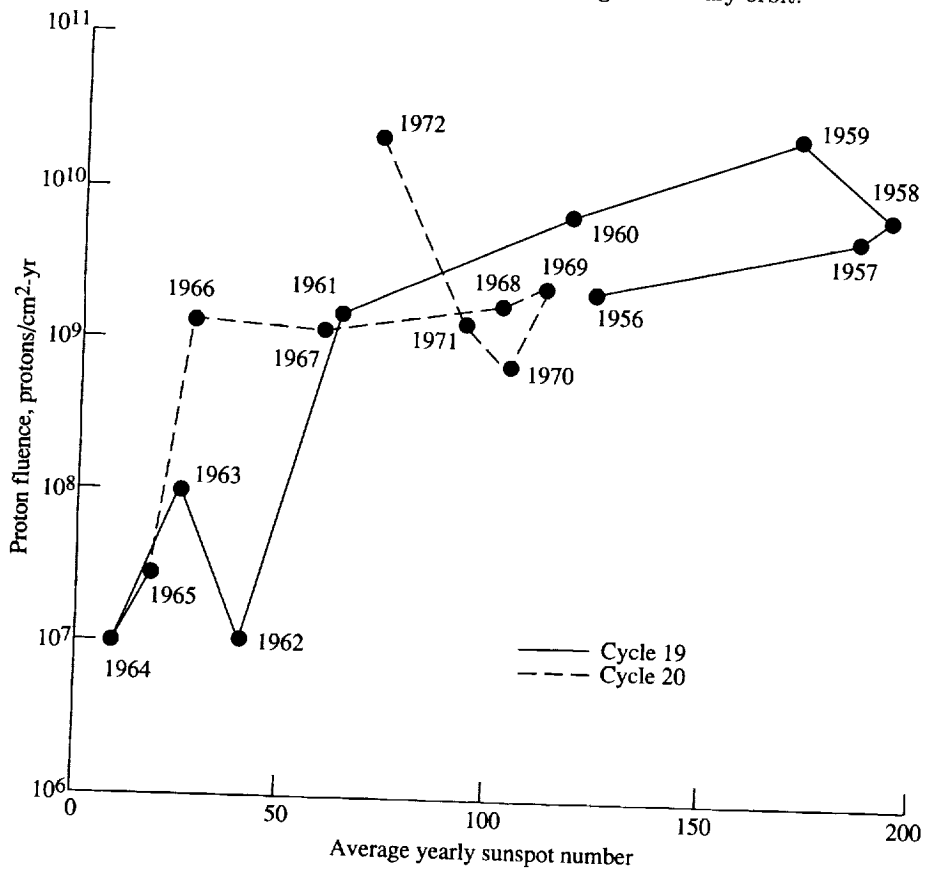


Figure 12.12. Solar cosmic-ray yearly fluence above 10 MeV.

A set of such predictions based on the correlations shown in figure 12.10 is shown in figure 12.11 for some predictive models on solar cycles. We plotted the calendar year as a function of the proton fluence and we show cycle 19 on which the correlations were based. The solid curves are the observed values going into cycle 20, and the dashed curves are the predicted values. The predictions were fairly accurate up to August 1972; after that there are rather large deviations from the predictive curve. In fact, while we thought that cycle 20 was going to be a rather mild cycle it turned out that the largest event, as far as space exposure is concerned, occurred during this rather ordinary cycle—consequently changing our thinking about the importance of solar flares (Wilson and Denn, 1976). We always thought solar flares were serious but we did not realize just how hazardous (potentially lethal) they were until August 1972. Data were taken from Curtis and Wilkinson (1971) and King (1974).

Figure 12.12 shows the data for energies above 10 MeV as a function of sunspot number from cycle 19 (figure 12.11) with the observation made during cycle 20 added to it. We see that the August 1972 event gives most of the contribution during that particular year. Keeping the correlation curve of figure 12.10 in mind and comparing the location of the 1962 event and 1972 event (or the 1962 year and the 1972 year), these correlations are accurate to within about a factor of 10 on the basis of the data we now have.

In particular, the event of November 1960 and the May–July event series of 1959 were previously thought to be the most serious events we had to design for in space operations. Now we find that the exposure from the August 1972 event is about three to four times greater than the two earlier events. Whether we will have a future event that will exceed the dose of the August 1972 event is an open question. Obviously, one would expect that an even larger event could occur with some smaller probability. How to assign the chance of occurrence is questionable.

The solar cosmic rays produced on the Sun must still travel to Earth. The transit time between the Sun and the Earth is typically 20 minutes for relativistic particles, but sometimes it takes up to a few hours depending on the spectrum and the interplanetary magnetic field configuration (fig. 12.13). The spectral distribution at Earth changes as a function of time because high-energy particles tend to arrive before lower energy particles. The angular distribution of the particles varies greatly from event to event. During some of the high-energy events, the particles tend to be directional early in the event and approach isotropy later as the lower energy particles arrive. Similar to galactic cosmic rays, the solar protons tend to be eliminated from equatorial regions of the Earth's magnetosphere. However, nearly all particles incident in polar regions are transmitted to low altitudes (fig. 12.13).

The integral fluence spectra of three major proton events observed during cycles 19 and 20 are shown in figure 12.14. It was previously thought that the November 1960 event was the most hazardous for space operations, and we were basing our designs on this limit. As the figure shows, the August 1972 event dominates at energies below 100 MeV, and it has changed our thinking about the limits for the most hazardous case. We originally considered the largest event observed in the cycle of greatest activity to be the worst-case event, i.e., November

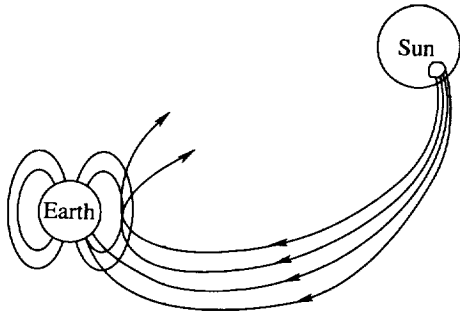


Figure 12.13. Solar cosmic-ray Earth interaction.

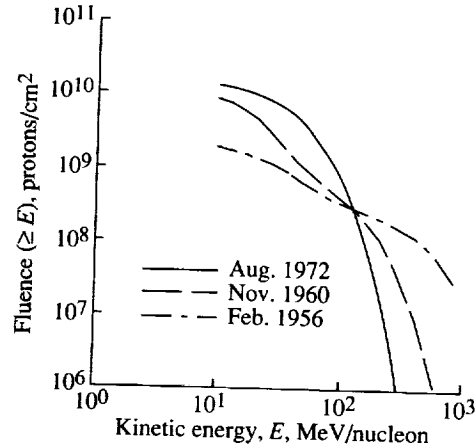


Figure 12.14. Proton fluence of three major solar events.

1960. Now a much larger event has occurred in a rather inactive cycle which destroys our logic. Someday the August 1972 event may well be overshadowed by some future event. These data were taken from Foelsche (1963) and King (1974).

The dose equivalent in the center of the sphere of radius r is shown in figure 12.15. Compare the August 1972 depth-dose relation to that of the February 1956 event. Clearly in the region about 1 to 20 g/cm^2 , which is the important region for spacecraft shielding, the August 1972 event is (in places) an order of magnitude more serious than the February 1956 event. The November 1960 event lies about halfway between these two curves.

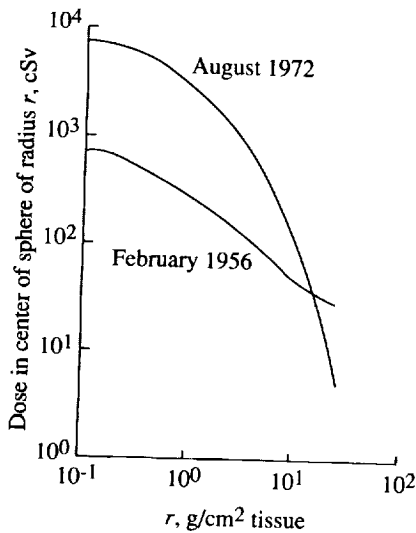


Figure 12.15. Dose equivalent from two major solar events (Wilson and Denn, 1976).

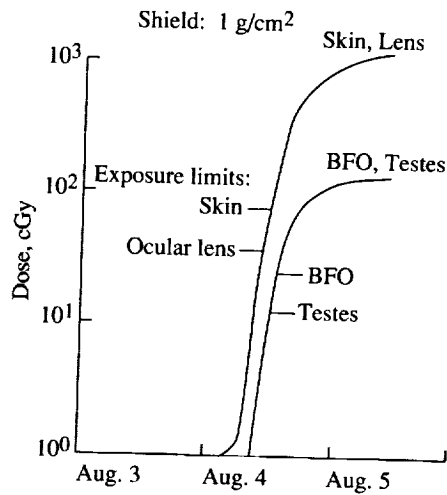


Figure 12.16. Dose from a major solar flare (Wilson and Denn, 1976).

Figure 12.16 presents the exposure limits and the dose behind a shield of 1 g/cm² during the August 1972 event. The dose limits were determined by calculating the effective average quality factor for the August 4, 1972 event. This average quality factor is about 1.3, and it is the value used in deriving this figure. Of course the average quality factor is spectrum dependent; 1.3 cannot be used for all events because it depends very much on the energy content of the event. For this particular quality factor the exposure limits are reached for the lens of the eye first and the skin later. Note that the dose greatly exceeds the allowed limits behind the shielding 1 g/cm² thick, which in the past has been a typical thickness for spacecraft shielding. These curves also take into account the body geometry (Khandelwal and Wilson, 1974; Billings and Yucker, 1973). Data were taken from Wilson and Denn (1976).

The 30-day exposure limits and also the time required to reach these exposure limits during the August 1972 event are shown in table 12.3. This is the time after the onset of particle emission—not the time after the optical flare is observed but rather the time after the particles are first seen arriving at Earth's orbit. Generally, if a person is very lightly shielded he still has about 2 to 4 hours to seek shelter. This is adequate time to move to a more protective region. At 10 g/cm² of tissue equivalent material, the dose limits to the BFO and skin are never reached. The limiting factors are the lens of the eye and the testes, and these can be taken care of by using personal shielding. Therefore, a shelter of about 10 g/cm² of a material like polyethylene (plus personal shielding) would be adequate protection from the August 1972 event. Data were taken from Wilson and Denn (1976).

Table 12.3. Time Required to Reach Exposure Limits for August 4, 1972 Event

Shield thickness, g/cm ²	BFO, hr	Skin, hr	Ocular lens, hr	Testes, ^a hr
0.2	6.0	3.0	1.9	4.4
0.4	6.1	3.5	2.4	4.9
1	6.3	4.7	3.6	5.2
5	8.9	8.0	6.5	7.3
10	∞	∞	11.7	12.7

^aValues are overestimated since the testes dose is taken to be the same as the BFO dose.

Solar cycle 21 (1975–1986) was relatively quiet with no flare events of these magnitudes recorded. The flares of cycle 21 may constitute the typical proton fluence within a solar cycle due to the more normally occurring smaller and medium size events. The proton fluxes due to flare events were measured by particle monitors onboard the Interplanetary Monitoring Platform satellites, IMP-7 and IMP-8. Fifty-five flares within solar cycle 21 had integral fluences greater than 10⁷ protons/cm² for energies greater than 10 MeV. The other flares of lower fluence and energy would contribute negligibly to dose calculations.

Figure 12.17(a) shows the integral fluences of the 55 flares as they are distributed in time throughout the cycle, and figure 12.17(b) shows the fluence spectra for each of these flares (Goswami et al., 1988).

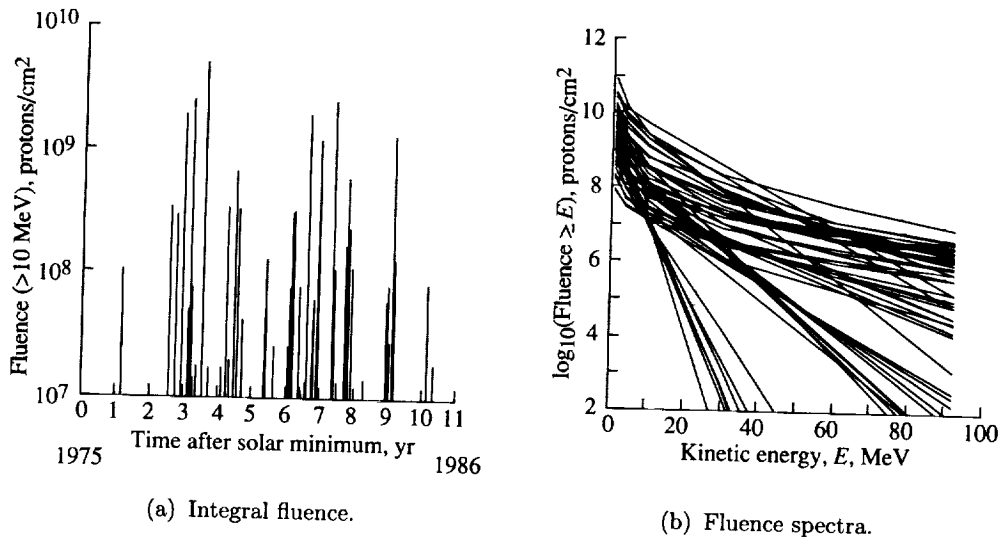


Figure 12.17. Solar proton flares during solar cycle 21 (1975–1986) (Goswami et al., 1988).

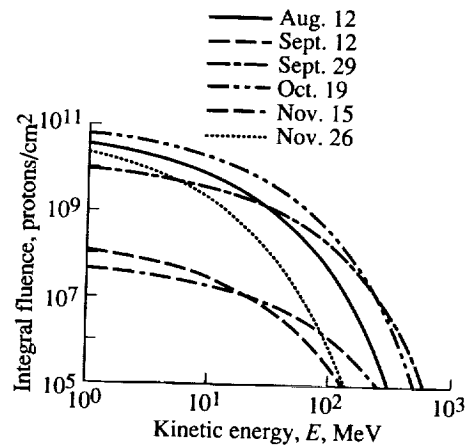


Figure 12.18. Six large solar flare integral fluences based on 1989 GOES-7 data (Sauer, Zwickl, and Ness, 1990).

With the onset of solar cycle 22 (1986–1997), several flares larger than any recorded in cycle 21 have already occurred in the months of August through December 1989. Six flares occurring in this time frame have been recorded by the GOES-7 satellite. Figure 12.18 shows the proton fluence energy spectra based on rigidity functions reported by Sauer, Zwickl, and Ness (1990). The magnitude of the October 1989 event is on the order of that of the August 1972 event and has heightened concern over flare shielding strategies. The addition of these six flares can provide a fairly realistic estimate of a flare environment that may

be encountered during missions taking place in the 5 or 6 years of active Sun conditions.

12.2.4. Geomagnetic effects on orbital environment. Charged particles arriving at some location within the geomagnetosphere are deflected by the Lorentz force $e\vec{v} \times \vec{B}$ which prevents penetration for some directions of incidence and some energies. Such phenomena were extensively studied by Störmer (1930) for a dipole magnetic field which provides the basis for classifying the orbital trajectories of charged particles arriving at some location within the field. As a part of Störmer's theory, allowed trajectories with no connection to asymptotic trajectories exist; these are now recognized as trapping regions associated with Van Allen radiation. Numerical solutions to the charged particle equations of motion in a more realistic geomagnetic field model were introduced by McCracken (1962a, 1962b, and 1962c) and further advanced by Smart and Shea (1983), Shea and Smart (1983), and Shea, Smart, and Gentile (1983). Our purpose here is not to supplant the vastly detailed numerical work but to seek a simple analytic form to reasonably approximate the more general numerical solutions. The numerical work of Smart and Shea is indispensable.

The geomagnetic field can be reasonably approximated by a tilted dipole with moment $M = r_e^3 31\,500$ nT displaced from the Earth's center by 430 km or $0.068r_e$, where $r_e = 6378$ km. The tilt angle is 11.7° at 69° W longitude. The magnetic quadrupole contributions are then about 10 percent at the surface and decrease to 5 percent at $2r_e$. Higher order moments are even smaller. The motion of charged particles in the geomagnetic field was studied extensively by Störmer. We outline his methods herein. In spherical coordinates, Störmer showed that the azimuth angle ϕ is an ignorable coordinate possessing an integral for the particles trajectories such that

$$\cos \omega = \frac{\gamma}{mvr \sin \theta} - \left(\frac{ZeM}{mvc} \right) \frac{\sin \theta}{r^2} \quad (12.1)$$

where m is the mass of the particle, Ze is the charge, v is the velocity, c is the velocity of light, r is radial distance from the center of the field, θ is colatitude, γ is an integration constant, and ω is the angle between the velocity vector and the azimuthal direction. The allowed Störmer regions consist of the space for which

$$|\cos \omega| \equiv \left| \frac{\gamma}{mvr \sin \theta} - \left(\frac{ZeM}{mvc} \right) \frac{\sin \theta}{r^2} \right| \leq 1 \quad (12.2)$$

Further analysis of the condition in equation (12.2) shows stable trapping regions as well as the Störmer main cone of transmission given for $\gamma = 2mv(ZeM/mvc)^{1/2}$. The Störmer main cone is given (Kuhn, Schwamb, and Payne, 1965) by the solid angle element

$$\Omega = 2\pi(1 + \cos \omega) \quad (12.3)$$

which contains the allowed directions of arrival for particles of rigidity R (momentum per unit charge) given by

$$R = \frac{M}{c} \frac{\sin^4 \theta}{r^2 [1 + (1 - \sin^3 \theta \cos \omega)^{1/2}]^2} \quad (12.4)$$

Henceforth we replace the colatitude θ by the magnetic latitude λ_m and note that Ω varies from 0 to 4π reaching its half-value at $\omega = \pi/2$ including angles up to the vertical direction. The vertical cutoff model is expressed as

$$\Omega \approx 4\pi U [R - R_C(\lambda_m)] \quad (12.5)$$

where the vertical cutoff rigidity from equation (12.4) is

$$R_C(\lambda_m) = \frac{M}{4cr^2} \cos^4 \lambda_m \quad (12.6)$$

and $U(x)$ is the unit step function.

Not included in the above formalism are those trajectories which are cut off by the shadow cast by the solid Earth. The fraction of the solid angle covered by the shadow of the Earth is estimated with the assumption that the curvature of the local trajectories is large compared with the radius of the Earth (Kuhn, Schwamb, and Payne, 1965). Then the solid angle fraction is

$$\frac{\Omega_{\text{sh}}}{4\pi} = \frac{1}{2} \left[1 + \cos \left(\sin^{-1} \frac{1}{r} \right) \right] \quad (12.7)$$

The corrected solid angle for the vertical cutoff model is then

$$\Omega = \Omega_{\text{sh}} U [R - R_C(\lambda_m)] \quad (12.8)$$

which leaves the local solid angle open to transmission of charged particles of rigidity R at altitude r and geomagnetic latitude λ_m .

Spacecraft in low Earth orbit (LEO) are typically in circular orbits; this simplifies the analysis. The orbit plane is inclined with respect to the equatorial plane. Since the angular momentum (spin) of the Earth and the orbital angular momentum of the spacecraft are conserved, the angle between them is fixed and equal to the inclination angle i . The magnetic axis rotates with the Earth and therefore precesses about the rotational axis within a 24-hour period. The geographic location of the ascending node likewise moves around the geographic equator every 24 hours. The inclination of the orbit plane relative to the magnetic axis i_m likewise is periodic. If η is the geographic coordinate of the ascending node line, then

$$\cos i_m = \cos i \cos \theta_m + \sin i \sin \theta_m \cos (\eta - \phi_m - 90^\circ) \quad (12.9)$$

where θ_m and ϕ_m are the magnetic north pole colatitude and longitude. The average transmission factor around this orbit \bar{F} is then

$$\bar{F}(R, i, \eta) = \frac{\Omega_{\text{sh}}}{i_m} \int_0^{i_m} U[R - R_C(\lambda)] d\lambda = \frac{i_m - \lambda_m}{i_m} \Omega_{\text{sh}} \quad (12.10)$$

where λ_m is the magnetic latitude with cutoff at R as given by

$$R_C(\lambda_m) = R \quad (12.11)$$

We note that i_m goes through a maximum and minimum orbit corresponding to $\eta_{\text{max}} = \phi_m - 90^\circ$ and $\eta_{\text{min}} = \phi_m + 90^\circ$ for which $i_m = i + \theta_m$ and $i_m = |i - \theta_m|$, respectively, as we have shown elsewhere (Wilson et al., 1990).

We may also calculate the long-term average over many days of orbits by averaging equation (12.10) over the node angle η as

$$\bar{F}(R, i) = \frac{1}{\pi} \int_0^\pi \Omega_{\text{sh}} \frac{i_m - \lambda_m}{i_m} d\eta = \frac{1}{\pi} \int_{\phi_\lambda}^\pi \Omega_{\text{sh}} \frac{i_m - \lambda_m}{i_m} d\phi \quad (12.12)$$

where

$$\cos i_m = \cos i \cos \theta_m + \sin i \sin \theta_m \cos \phi \quad (12.13)$$

and

$$\phi_\lambda = \begin{cases} 0 & (\lambda_m \leq |i - \theta_m|) \\ \cos^{-1} \left[\frac{\cos \lambda_m - \cos i \cos \theta_m}{\sin i \sin \theta_m} \right] & (|i - \theta_m| \leq \lambda_m \leq i + \theta_m) \\ \pi & (\lambda_m > i + \theta_m) \end{cases} \quad (12.14)$$

Equation (12.12) may be rewritten as

$$\bar{F}(R, i) = \Omega_{\text{sh}} \left[\left(1 - \frac{\phi_\lambda}{\pi} \right) - \frac{1}{\pi} \int_{\phi_\lambda}^\pi \frac{\lambda_m}{i_m} d\phi \right] \quad (12.15)$$

where the last integral is approximated by a numerical quadrature. The results of equation (12.15) are compared with the numerical calculations of Smart and Shea (1983) for 400-km (216-n.mi.) orbits at several inclinations in figure 12.19 for this centered dipole field model with $\theta_m = 11.7^\circ$ (tilt angle) and longitude $\phi_m = -69^\circ$ (69° W).

An important correction to the centered dipole field is the displacement of the geomagnetic dipole 430 km (232 n.mi.) from the Earth's center. Unfortunately, the formalism is very complicated, since the distance r from the dipole center is no longer constant even for a circular orbit. The offset dipole decreases the cutoffs in the Atlantic hemisphere defined by the meridional plane normal to the tilt direction and increases the cutoffs in the remaining hemisphere over the Pacific. We define two cutoff functions for centered dipole fields as

$$R_j(\lambda_m) = \frac{14.9}{(r + \delta_j)^2} \cos^4 \lambda_m \quad (12.16)$$

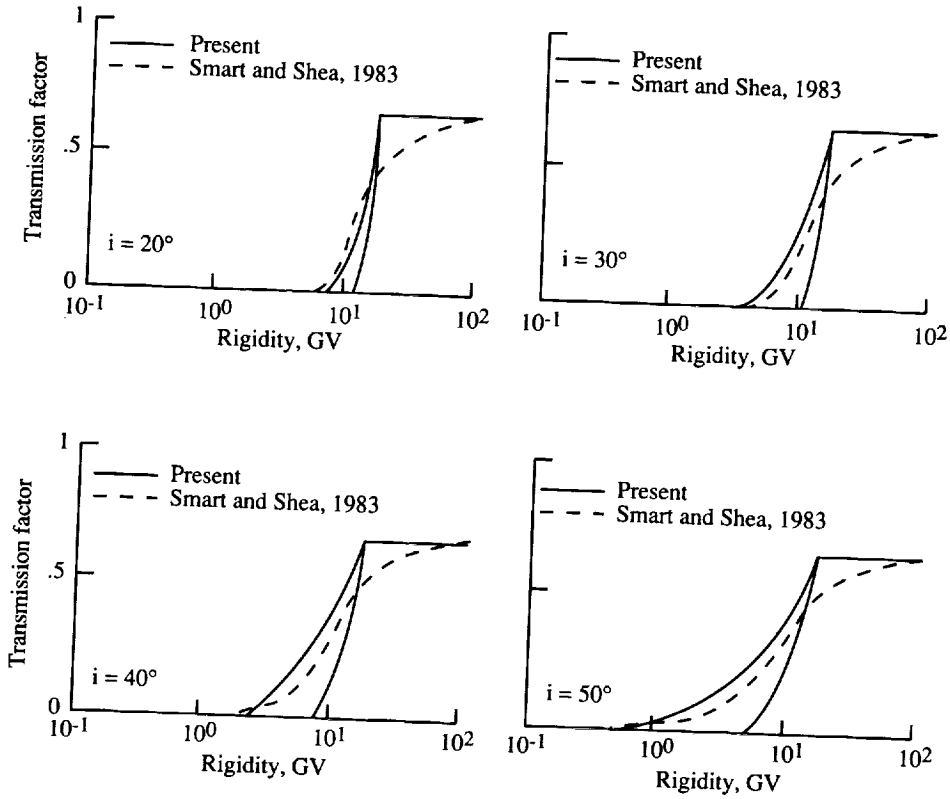


Figure 12.19. Dipole maximum and minimum cutoff model and numerical simulation of exact geomagnetic field model.

where $j = A$, $\delta_A = 593$ km (320 n.mi.) for the Atlantic hemisphere; $j = P$, $\delta_P = -504$ km (-272 n.mi.) for the Pacific; λ_m is the usual magnetic latitude which depends on the hemisphere; and τ is the geocentric radius of the orbit. The value 14.9 GV is found from the value of the dipole moment of $r_e^3 31\,500$ nT, and values of δ_j were chosen to match the minimum equatorial cutoff in the Atlantic region of Shea and Smart (1983) and the maximum cutoff in the Pacific. The calculation of the orbit average transmission factor is as before except that the two hemispheres are considered separately as

$$\bar{F}(R, i, \eta) = \frac{1}{2} \Omega_{\text{sh}} \left[\frac{i_m - \lambda_A}{i_m} + \frac{i_m - \lambda_P}{i_m} \right] \quad (12.17)$$

where

$$R_A(\lambda_A) = R \quad (12.18)$$

and

$$R_P(\lambda_P) = R \quad (12.19)$$

Similarly, the long-term average of equation (12.12) is extended to each hemisphere as

$$\bar{F}(R, i) = \frac{\Omega_{\text{sh}}}{2\pi} \left[\int_{\phi_A}^{\pi} \left(\frac{i_m - \lambda_A}{i_m} \right) d\phi + \int_{\phi_P}^{\pi} \left(\frac{i_m - \lambda_P}{i_m} \right) d\phi \right] \quad (12.20)$$

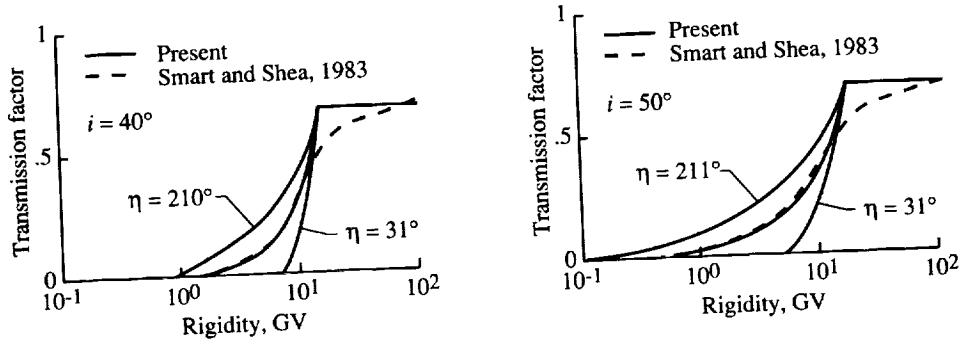


Figure 12.20. Offset dipole model average transmission factors with detailed calculations of Smart and Shea (1983) and maximum and minimum transmission factors.

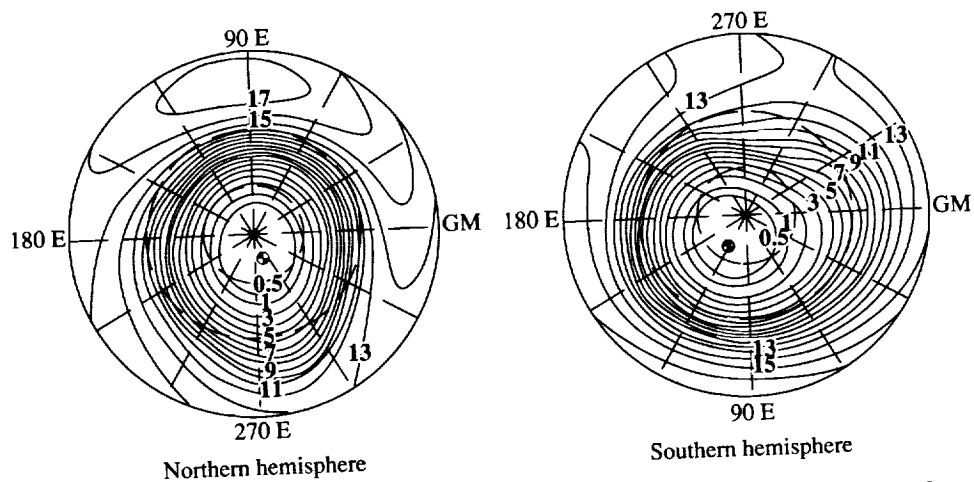


Figure 12.21. Vertical cutoff contours showing location of corresponding magnetic poles.

Table 12.4. Geographic Locations of Offset Poles in Present Calculations

Magnetic pole	Longitude, ϕ_m , deg	Tilt, θ_m , deg
North	-69	16
South	121	22

where the integrals are evaluated as described for equation (12.15). The average transmission factors of equation (12.20) are compared with the numerical calculations of Smart and Shea (1983) in figure 12.20. The tilt angles of the poles (Johnson, 1965) are given in table 12.4 along with suitably chosen longitudes and are shown in relation to the vertical cutoff rigidities of Shea and Smart in figure 12.21.

During times of intense solar activity, the solar plasma emitted in solar flares and subflares advances outward and arrives at 1 AU from the Sun. If the Earth is locally present, the plasma interacts with the geomagnetic field in which the plasma pressure performs work on the local geomagnetic field. The initial impact produces hydromagnetic waves causing a general increase in geomagnetic intensity. As plasma flow is established, it generates large electric ring currents and a corresponding impressed magnetic storm field. In the initial phase (hydromagnetic wave), the storm field is parallel to the equatorial field after which the storm field reverses in the main phase of the storm caused by ring currents within the magnetopause and opposes the quiet field, causing a net decrease of the field strength. The main phase is followed by slow recovery to the quiet field conditions (Johnson, 1965).

The magnetic storm model used here assumes a uniform magnetic field impressed on the normal quiet field (Kuhn, Schwamb, and Payne, 1965). The storm field strength can be found from the change in the horizontal field component around the geomagnetic equator. We represent this field by H_{st} . Typical values of H_{st} in the main phase range from substorm values -10 nT to severe storms with -500 nT. On rare occasions, for very intense storms, the storm field exceeds -1000 nT.

Magnetic disturbances have been observed for many years, and various classification schemes for such disturbances have been proposed. The planetary magnetic index K_p is based on magnetometer measurements of 12 stations worldwide. The K_p index is related to a derived planetary index a_p and storm field strength by Bartels (Johnson, 1965) given in table 12.5.

Table 12.5. Relation of Magnetic Indices to Magnetic Storm Field Strength

K_p	a_p	$ H_{st} , \text{ nT}$
0	0	0
1	4	8
2	7	14
3	15	30
4	27	54
5	48	96
6	80	160
7	132	264
8	207	414
9	400	800

The vertical cutoff rigidity as given by equation (12.16) is further modified to approximate the effects of geomagnetic disturbances. It was shown by Kuhn, Schwamb, and Payne (1965) that the appropriate equation is

$$R_C(\lambda_m) = \frac{14.9}{r^2} \cos^4 \lambda_m \left[1 + \frac{H_{st} r^3}{M} \left(\frac{4}{\cos^6 \lambda_m} - 1 \right) \right] \quad (12.21)$$

for the centered dipole field. In the context of our approximation of the offset-tilted dipole field, we get

$$R_j(\lambda_m) = \frac{14.9}{(r + \delta_j)^2} \cos^4 \lambda_m \left[1 + \frac{H_{st} (r + \delta_j)^3}{M} \left(\frac{4}{\cos^6 \lambda_m} - 1 \right) \right] \quad (12.22)$$

This vertical cutoff replaces equation (12.16) and applies to storm conditions. Note that the cutoff is zero whenever the result of equation (12.22) is negative. The corresponding transmission factor on the worst-case orbit ($\eta \approx 211^\circ$) is shown in relation to the quiet field average transmission factors of Smart and Shea (1983) in figure 12.22.

12.2.5. Dose estimation. In passing through tissue, energetic protons interact mostly through ionization of atomic constituents by the transfer of small amounts of momentum to orbital electrons. Although the nuclear reactions are far less numerous, their effects are magnified because of the large momentum transferred to the nuclear particles and the struck nucleus itself. Unlike the secondary electrons formed through atomic ionization by interaction with the primary protons, the radiations resulting from nuclear reactions are mostly heavy ionizing and generally have large biological effectiveness. Many of the secondary particles of nuclear reactions are sufficiently energetic to promote similar nuclear reactions and thus cause a buildup of secondary radiations. The description of such processes requires solution of the transport equation. The approximate solutions for the transition of protons in 30-cm-thick slabs of soft tissue for fixed incident energies have been made (Wilson and Khandelwal, 1976). The results of such calculations are dose conversion factors for relating the primary monoenergetic proton fluence to dose or dose equivalent as a function of position in a tissue slab.

Whenever the radiation is spatially uniform, the dose at any point x in a convex object may be calculated (Wilson and Khandelwal, 1974) by

$$D(\vec{x}) = \int_0^\infty \int_\Omega R_n [z_x(\vec{\Omega}), E] \phi(\vec{\Omega}, E) d\vec{\Omega} dE \quad (12.23)$$

where $R_n(z, E)$ is the dose at depth z for normal incident protons of energy E on a tissue slab, $\phi(\vec{\Omega}, E)$ is the local differential proton fluence along direction $\vec{\Omega}$, and $z_x(\vec{\Omega})$ is the distance from the boundary along $\vec{\Omega}$ to point \vec{x} . It has been shown that equation (12.23) always overestimates the dose but is an accurate estimate when the ratio of the proton beam divergence due to nuclear reaction to the radius of curvature of the body is small (Wilson and Khandelwal, 1974). Equation (12.23) is a practical prescription for introducing nuclear reaction effects into calculations

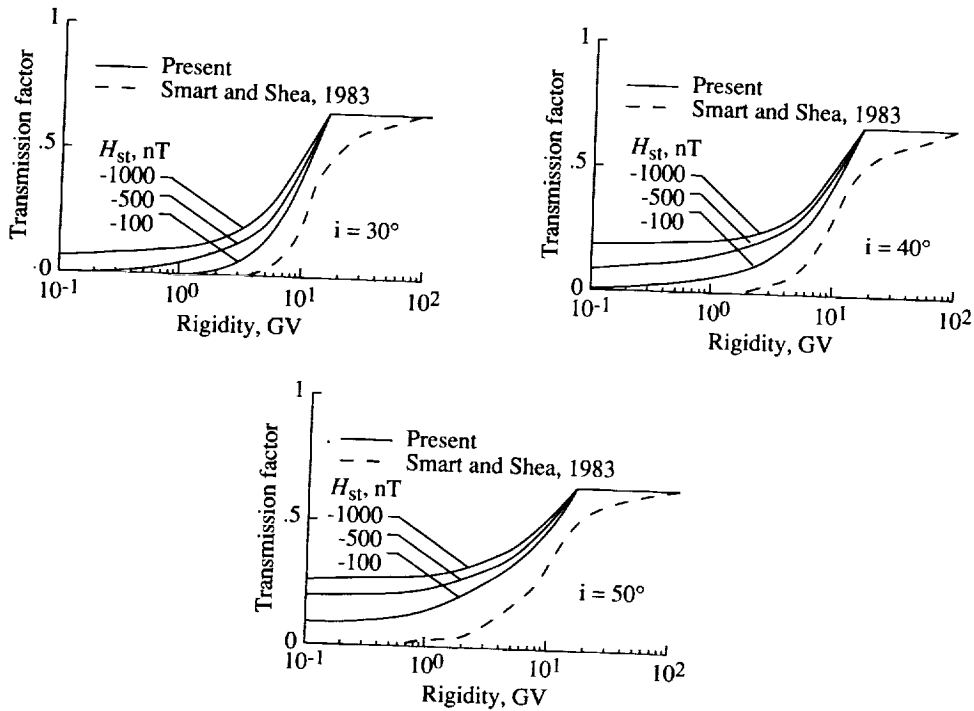


Figure 12.22. Maximum transmission factor for various storm fields and quiet time average transmission of Smart and Shea (1983). $\eta = 211^\circ$.

of dose in geometrically complex objects such as the human body. The main requirement is that the dose conversion factors for a tissue slab be adequately known for a broad range of energies and depths. The dose conversion factors for tissue were derived by Wilson and Khandelwal (1976), and a correction for an aluminum shield is found in chapter 8. The spacecraft geometry is taken as an aluminum sphere of large radius.

12.2.6. Method for Shuttle geometry. In section 12.2.5, the calculation of astronaut (convex object) exposure in the center of a large aluminum sphere of arbitrary thickness was derived for a specific orbit with either the quiet geomagnetic field or with a geomagnetic disturbance. We denote that result by $D_{sph}(t_s)$, and it has a different value for each critical organ for which exposure within the aluminum sphere of thickness t_s is evaluated. Within the context of assumed isotropic radiation, the exposure at some location within the Shuttle (taken as a typical spacecraft geometry) is

$$D = \int_0^\infty D_{sph}(t_s) f(t_s) dt_s \quad (12.24)$$

where $f(t_s)$ describes the mass distribution of the Shuttle structure assumed to be aluminum about that particular location. Physically, $f(t_s) dt_s$ is the solid angle

fraction for which the areal density to the Shuttle surface lies between t_s and $t_s + dt_s$. The cumulative distribution of areal density is given by

$$F_C(t_s) = \int_0^{t_s} f(t_s) dt_s \quad (12.25)$$

and is shown for two locations in the Shuttle (Atwell et al., 1989) in figure 12.23. Also shown in figure 12.23 are the following approximate functions:

$$f_1(t_s) = \left\{ \begin{array}{ll} \frac{0.176}{t_s} & (1 \leq t_s \leq 2) \\ \frac{0.113}{t_s} & (2 \leq t_s \leq 20) \\ \frac{0.353}{t_s} & (20 \leq t_s \leq 120) \end{array} \right\} \quad (12.26)$$

and

$$f_2(t_s) = \left\{ \begin{array}{ll} \frac{0.303}{t_s} & (1 \leq t_s \leq 6) \\ \frac{0.147}{t_s} & (6 \leq t_s \leq 132) \end{array} \right\} \quad (12.27)$$

where the functions are understood to be zero outside specified ranges. Formulas (12.24), (12.26), and (12.27) are used in conjunction with the methods described in sections 12.2.4 and 12.2.5 to estimate Shuttle exposure in the two locations, referred to by Atwell et al. (1989) as dosimeter locations 1 and 2, which are the most and the least shielded locations in the Shuttle crew compartment, respectively. The method can be easily expanded to include more astronaut organs and other Shuttle locations.

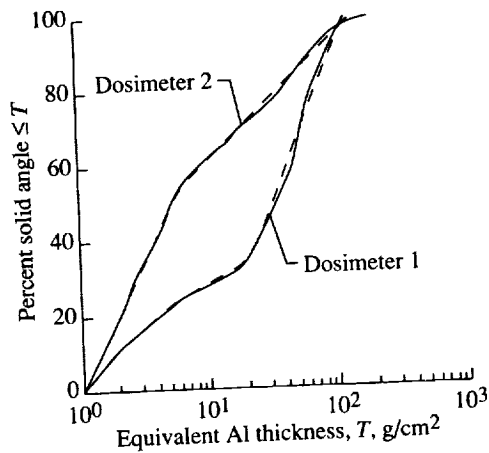


Figure 12.23. Mass distribution of two locations on Shuttle flight deck (Atwell et al., 1989).

12.2.7. Results. The maximum exposure limits in force for the Space Station *Freedom* are shown in table 12.1. The dose and dose equivalent to critical body organs for an aluminum shield 1 g/cm² thick are shown in tables 12.6 through 12.9 for various storm conditions (H_{st}). The exposures are shown for a worst exposed orbit ($\eta = 211^\circ$) and the average over all η . The average is shown, since average transmission factors are calculated by several groups, and one may

be tempted to use the transmission factor appropriate for the galactic cosmic-ray background (Curtis, Doherty, and Wilkinson, 1969; Adams, 1987). It is clear from the results in tables 12.6 through 12.9 that such use of average cutoffs provides exposure estimates which could be too small by a factor of 2 to 10. Such an underestimate is clearly unacceptable. Furthermore, if the current dose estimates are compared with values for transmission factors derived for a tilted concentric dipole field (Wilson et al., 1990), the dose values of the current field model are a factor of 3 to 5 higher. The eccentric field has two effects which lower the cutoffs. The offset displaces the South magnetic pole to lower latitudes and lowers the geomagnetic cutoff values over the Atlantic. The methods derived herein allow evaluating exposures as a function of the location of the line of nodes and should provide acceptable estimates of exposure.

Table 12.6. Skin Dose Behind Aluminum Shield 1 g/cm² Thick During February 25, 1956, November 12-13, 1960, and August 4, 1972, Events With Various Storm Fields

Orbit inclination, deg	Skin dose, cGy, during—								
	Feb. 1956 for H_{st} , nT, of—			Nov. 1960 for H_{st} , nT, of—			Aug. 1972 for H_{st} , nT, of—		
	-100	-500	-900	-100	-500	-900	-100	-500	-900
30, max	< 0.1	2.2	12.0	0	4.9	34.0	0	15.0	100.0
30, avg	< 0.1	0.3	2.6	0	0.5	7.1	0	1.6	22.0
40, max	2.9	19.0	28.0	6.3	53.0	79.0	19.0	170.0	240.0
40, avg	0.4	5.4	9.8	0.8	15.0	28.0	2.3	47.0	86.0
50, max	17.0	31.0	39.0	47.0	89.0	111.0	140.0	280.0	340.0
50, avg	4.8	13.0	18.0	13.0	36.0	51.0	39.0	110.0	160.0

Table 12.7. Skin Dose Equivalent Behind Aluminum Shield 1 g/cm² Thick During February 25, 1956, November 12-13, 1960, and August 4, 1972, Events With Various Storm Fields

Orbit inclination, deg	Skin dose equivalent, cSv, during—								
	Feb. 1956 for H_{st} , nT, of—			Nov. 1960 for H_{st} , nT, of—			Aug. 1972 for H_{st} , nT, of—		
	-100	-500	-900	-100	-500	-900	-100	-500	-900
30, max	< 0.1	3.3	17.0	0	7.0	49.0	0	20.0	140.0
30, avg	< 0.1	0.4	3.7	0	0.7	10.0	0	2.1	30.0
40, max	4.3	27.0	39.0	8.9	78.0	110.0	25.0	230.0	333.0
40, avg	0.7	7.7	14.0	1.1	22.0	40.0	3.1	63.0	120.0
50, max	24.0	44.0	54.0	68.0	130.0	160.0	200.0	380.0	470.0
50, avg	6.8	18.0	25.0	18.0	52.0	74.0	53.0	150.0	220.0

Table 12.8. BFO Dose Behind Aluminum Shield 1 g/cm² Thick During February 25, 1956, November 12-13, 1960, and August 4, 1972, Events With Various Storm Fields

Orbit inclination, deg	BFO dose, cGy, during—								
	Feb. 1956 for H_{st} , nT, of—			Nov. 1960 for H_{st} , nT, of—			Aug. 1972 for H_{st} , nT, of—		
	-100	-500	-900	-100	-500	-900	-100	-500	-900
30, max	< 0.1	1.0	3.3	0	0.9	4.4	0	1.8	10.0
30, avg	< 0.1	0.2	0.8	0	0.1	1.0	0	0.2	2.3
40, max	1.4	4.9	6.8	1.3	6.7	9.5	2.5	16.0	24.0
40, avg	0.3	1.5	2.5	0.2	2.0	3.4	0.4	4.7	8.8
50, max	4.6	7.6	9.3	6.2	11.0	13.0	15.0	27.0	33.0
50, avg	1.5	3.2	4.4	1.8	4.4	6.2	4.2	11.0	16.0

Table 12.9. BFO Dose Equivalent Behind Aluminum Shield 1 g/cm² Thick During February 25, 1956, November 12-13, 1960, and August 4, 1972, Events With Various Storm Fields

Orbit inclination, deg	BFO dose equivalent, cSv, during—								
	Feb. 1956 for H_{st} , nT, of—			Nov. 1960 for H_{st} , nT, of—			Aug. 1972 for H_{st} , nT, of—		
	-100	-500	-900	-100	-500	-900	-100	-500	-900
30, max	< 0.1	1.7	5.1	0	1.3	6.1	0	2.6	15.0
30, avg	< 0.1	0.3	1.2	0	0.2	1.3	0	0.3	3.3
40, max	2.3	7.6	10.0	1.8	9.2	13.0	3.6	23.0	34.0
40, avg	0.5	2.3	3.9	0.3	2.7	4.7	0.5	6.7	12.0
50, max	7.3	12.0	14.0	8.5	15.0	18.0	21.0	38.0	48.0
50, avg	2.3	5.0	6.9	2.5	6.1	8.6	6.0	15.0	22.0

From observing the levels of exposure in low inclination orbits ($i \approx 30^\circ$), a significant exposure could clearly occur if particle arrivals coincided with a large magnitude ($K_p \approx 9$) magnetic disturbance. On the basis of the present analysis, a more in-depth study of potential solar flare exposure of the Space Station *Freedom* seems warranted. Such a study should include a review of the history of major geomagnetic disturbances in proximity to solar particle events, a review of alternate geomagnetic storm models, and a review of the specific Space Station *Freedom* shield geometry.

The exposure for Shuttle flight in a 400-km (216-n.mi.) orbit with a 50° inclination is shown in table 12.10 for the February 23, 1956, solar event spectrum as compiled by Foelsche et al. (1974). A magnetic storm was assumed to be in

progress with an impressed field of -100 nT. The results shown in table 12.10 are for the long-term, average geomagnetic cutoffs, since these are directly comparable with the work of other geomagnetic models (Curtis, Doherty, and Wilkinson, 1969; Adams, 1987). We note, however, that actual exposure could be greatly different depending on the location of the line of nodes at the time of arrival of the high-energy flare particles.

Table 12.10. Human Exposure at Two Locations in Shuttle Crew Compartment for February 23, 1956, Event With $H_{st} = -100$ nT at 400 km and Orbit Inclination of 50°

Location	Exposure in—					
	BFO		Skin		Lens	
	cGy	cSv	cGy	cSv	cGy	cSv
1	2.6	4.9	4.0	6.8	4.1	7.6
2	3.4	5.9	6.0	9.4	6.0	10.0

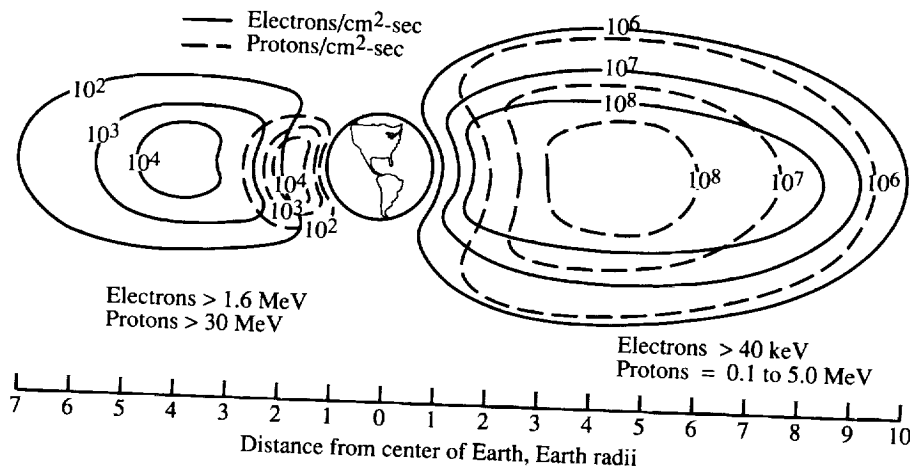


Figure 12.24. Near-Earth trapped radiation and solar proton environment (Parker and West, 1973).

12.2.8. Geomagnetically trapped radiations. The trapped radiation, illustrated in figure 12.24, follows a helical path along the magnetic field lines between the mirror points. The location of the mirror points along the field line depends on the pitch angle at the magnetic equator and the energy of the particle. The greater the energy or the higher the pitch angle, the deeper the mirror points lie in the magnetic field. If the particle energy and pitch angle are sufficiently large, the mirror point is so deep that the particle interacts with the atmosphere and is lost from the particle population. For the inner zone it appears at least for the protons that the particle source is primarily neutrons which are produced in atmosphere by solar and galactic cosmic rays. The outer zones appear to be

something like a pipe line with strong sources and strong sinks. The particles flow rapidly through these regions, and on the average they maintain a fairly high population density although the residence time is short. (See Singley and Vette, 1972.)

The Earth's magnetic field is not centered at the Earth's geographic center. Also, the main dipole moment, along the principal axis of the magnetic field, is tilted with respect to the Earth's rotational axis so that the geomagnetic field is not symmetrical with respect to geographic coordinates. The exposure as a function of altitude is expressed as maximum stay time before reaching the exposure limit (Wilson, 1978) in figure 12.25.

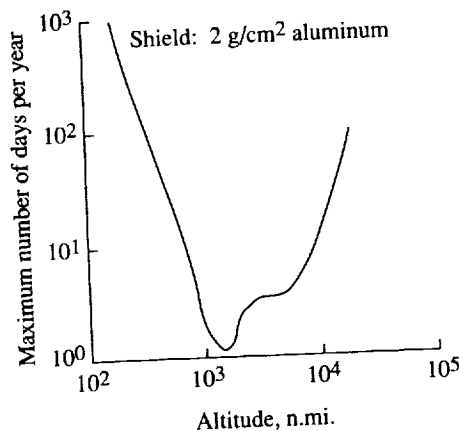


Figure 12.25. Limits imposed by trapped radiations on space operations within a 2 g/cm² aluminum shield.

12.3. Analysis for Deep Space Missions

The analyses presented here focus on the shielding requirements for GCR and different flare scenarios (Simonsen and Nealy, 1991). Shielding thicknesses selected for these missions should also reduce doses incurred from the Van Allen belts to a negligible amount providing long times are not spent in the belts.

12.3.1. Transport codes. The NASA Langley Research Center nucleon and heavy ion transport computer code HZETRN (Wilson et al., 1991) is used to predict the propagation and interactions of the deep space nucleons and heavy ions through various media. For large solar flare radiation, the baryon transport code BRYNTRN (Wilson et al., 1989) is used. For the galactic cosmic rays, an existing heavy ion transport code is integrated with the BRYNTRN code to include the transport of high-energy heavy ions up to atomic number 28 (Wilson and Badavi, 1986; Wilson, Townsend, and Badavi, 1987; Wilson et al., 1991). Both codes solve the fundamental Boltzmann transport equation in the one-dimensional, or straight ahead, approximation form:

$$\left[\frac{\partial}{\partial x} - \frac{\partial}{\partial E} S_j(E) + \sigma_j(E) \right] \phi_j(x, E) = \sum_{k>j} \int_E^{\infty} \sigma_{jk}(E, E') \phi_k(x, E') dE' \quad (12.28)$$

where the quantity to be evaluated, $\phi_j(x, E)$, is the flux of particles of type j having energy E at spatial location x . The solution methodology of this integrodifferential equation may be described as a combined analytical-numerical technique (Wilson, 1977). The accuracy of this numerical method has been determined to be within approximately 1 percent of exact benchmark solutions (Wilson and Townsend, 1988). The data required for solution consist of the stopping power S_j in various media, the macroscopic total nuclear cross sections σ_j , and the differential nuclear interaction cross sections σ_{jk} . The differential cross sections describe the production of type j particles with energy E by type k particles of energies $E' > E$. Detailed information on these data base compilations is described in chapters 4 and 5.

In addition to benchmark solution checks on the numerical precision of the code, comparisons with standard Monte Carlo type calculations have been made (Shinn et al., 1990). Samples of BRYNTRN results and results from the statistical Nucleon Transport Code (NTC) (Scott and Alsmiller, 1968) are shown in figure 12.26, where the dose values are given for a 30-cm tissue layer behind an aluminum shield of 20 g/cm². The input spectrum used is expressed analytically with the integral fluence F as a function of proton rigidity R :

$$F(>E) = C_o \exp \left[\frac{-R(E)}{R_o} \right] \quad (12.29)$$

with R_o equal to 100 MV and C_o chosen so that $F(30 \text{ MV})$ equals 10^9 protons/cm². Such a function is representative of a large proton event, and the BRYNTRN results show excellent agreement with the Monte Carlo calculations.

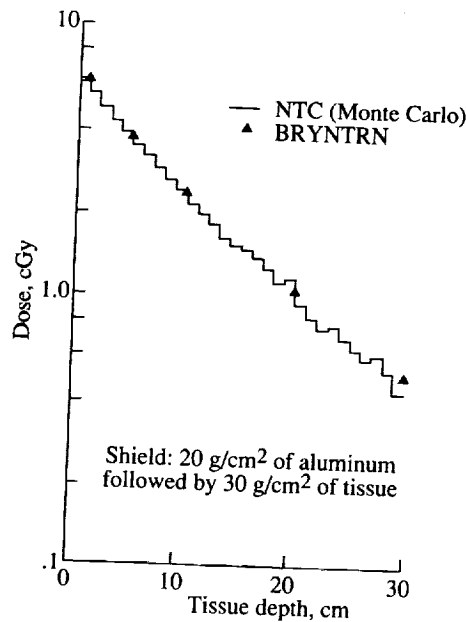


Figure 12.26. Comparison of results from BRYNTRN with equivalent Monte Carlo calculations (Shinn et al., 1990).

The present GCR code formulation is considered to be an interim version, since some features of the transport interaction phenomena have yet to be incorporated. These include improvements and additions to the existing nucleus-nucleus cross sections and their energy dependence and provisions for pion and muon contributions. Further improvements in target fragmentation treatment and computational efficiency are to be incorporated (Shinn and Wilson, 1991) even though computational execution times are already faster than counterpart statistical (Monte Carlo) calculations. These improvements should not greatly alter the current results, and the present interim version of the GCR code should provide a reasonable description of cosmic-ray particle fluxes and the corresponding dose predictions. The results included herein are preliminary and should be considered as current state-of-the-art "best estimates."

The absorbed dose D due to energy deposition at a given location x by all particles is calculated according to

$$D(x) = \sum_j \int_0^\infty S_j(E) \Phi_j(x, E) dE \quad (12.30)$$

The degree to which biological systems undergo damage by ionizing radiation is not simply proportional to this absorbed dose for all particle types. For human exposure, the dose equivalent is defined by introducing the quality factor Q which relates the biological damage incurred because of any ionizing radiation to the damage produced by soft X-rays. (See limitations on Q discussed in chapter 11.) In general, Q is a function of linear energy transfer, which in turn is a function of both particle type and energy. For the present calculations, the quality factors used are those defined by the International Commission on Radiological Protection (ICRP 26 (Anon., 1977)). The values of dose equivalent H are computed as

$$H(x) = \sum_j \int_0^\infty Q_j(E) S_j(E) \Phi_j(x, E) dE \quad (12.31)$$

These values are used to specify radiation exposure limits. (See table 12.1.) Strictly speaking, the limits in table 12.1 apply to low Earth orbit operations but are used as guidelines in the current analysis as suggested by NCRP 98 (Anon., 1989a).

12.3.2. Propagation data. The BRYNTRN code and the combined nucleon/heavy ion transport code are easily applied to various media. The GCR and solar flare energy distributions (figs. 12.3, 12.14, 12.17(b), and 12.18) are input for the code as the initial particle fluxes at the media boundaries. Results include slab calculations of the particle-flux energy distributions at various absorber amounts from which slab dose estimates as a function of absorber amount are determined. The slab calculations correspond to a monodirectional beam of particles normally incident on a planar layer of shield material. The dose at a specific slab-shield depth with normal incident radiation is equivalent to the dose in the center of a spherical shield of the same thickness in a field of isotropic radiation. (See chapter 7 for limitations.) This is depicted in figure 12.27. This relation was shown formally by Wilson and Khandelwal (1974).

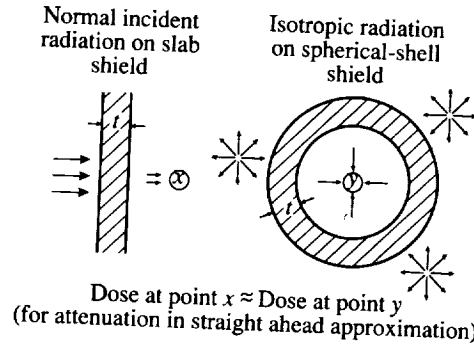


Figure 12.27. Calculation equivalence of slab shield and spherical-shell shield.

Basic propagation data have been generated for a variety of materials for both the GCR spectrum and different flare spectra. The propagation results are displayed as dose versus absorber amounts (g/cm^2) which can be converted to a linear thickness by dividing by density. Displaying results in this manner is helpful in comparing the shield effectiveness of various materials because equal absorber amounts for a given shielded volume will yield equal shield masses even though their linear thicknesses may differ.

For incident solar flare protons, the variation of dose with shield amount is sensitive to the energy characteristics (differential flux spectra). Figure 12.28 illustrates the BFO dose as a function of depth in aluminum followed by a 5-cm tissue layer for the three flares whose spectra are shown in figure 12.14. For these flares, the proton fluences have an approximate coincidence close to 100 MeV. Consequently, this behavior is reflected in a corresponding crossover of the dose-depth curves of figure 12.28, where the coincidence occurs at approximately $15 \text{ g}/\text{cm}^2$ of aluminum.

The combined fluences of the solar proton events occurring in the latter part of 1989 (fig. 12.18) have spectral characteristics similar to the August 1972 event. The BFO dose as a function of depth for several shield materials is shown in figure 12.29 for this flare scenario. On a per-unit-mass basis, water and lithium hydride have almost identical shield effectiveness properties for all shield thicknesses. Such similarities apply as well to media of low atomic weight and high hydrogen content (e.g., hydrocarbon polymers) which may be used as bulk shields. The curves for aluminum and lead are indicative of the decreasing relative effectiveness of higher atomic weight media. This effect can be attributed to the differences in proton stopping powers of the materials and to the greater numbers of secondary nucleons generated in the heavier materials. This effect is further exemplified by the results shown in figure 12.30, which shows the BFO dose-depth functions for the GCR spectra at solar minimum conditions. In addition to water and aluminum, results for liquid hydrogen (which may be used in an application to propellant tank structures) show the dramatic superiority of this material as a shield. This is largely caused by the greatly reduced generation of reaction products (nucleons and fragments) created by the GCR heavy ions traversing the hydrogen medium. For the very energetic GCR spectrum, most of the reduction in dose for all the materials shown occurs in the first 20 to $30 \text{ g}/\text{cm}^2$, with the magnitude of the dose gradient decreasing at larger thicknesses.

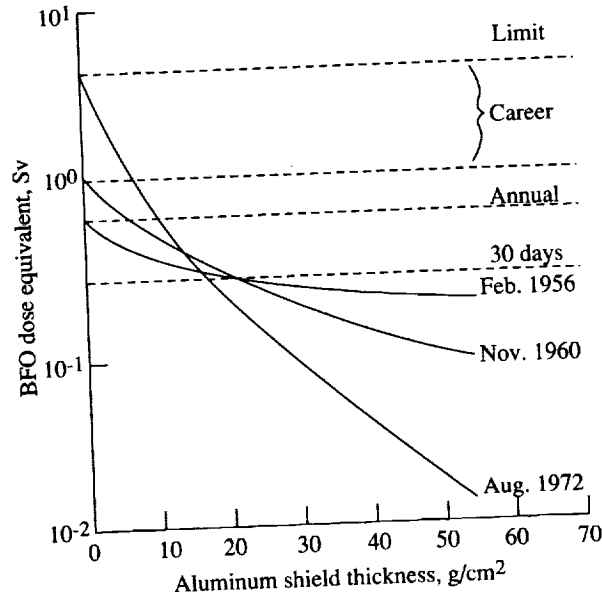


Figure 12.28. BFO dose equivalent as function of aluminum shield thickness for three large solar flare events (Townsend et al., 1989).

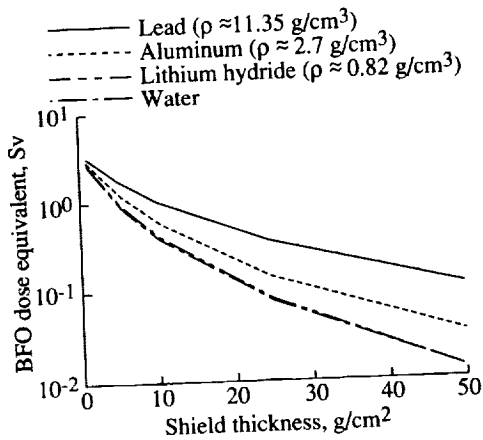


Figure 12.29. BFO dose equivalent versus depth functions for sum of 1989 flare fluences for four materials.

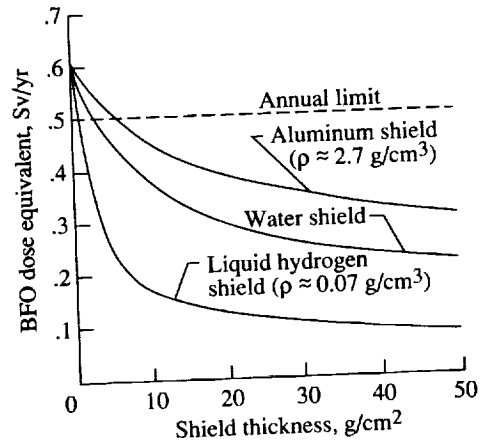


Figure 12.30. BFO dose equivalent as function of shield type and thickness resulting from galactic cosmic rays at solar minimum (Townsend et al., 1990a).

The differences between the GCR at solar minimum and maximum with respect to water shield thicknesses are shown in figure 12.31 (Townsend et al., 1990a). The incurred dose equivalents between these two extremes are seen to differ by about a factor of 2 for shield amounts up to 30 g/cm². These results were computed for the GCR spectra at solar minimum and maximum as specified by the NRL CREME model. However, recent measurements (Kovalev, Muratova, and

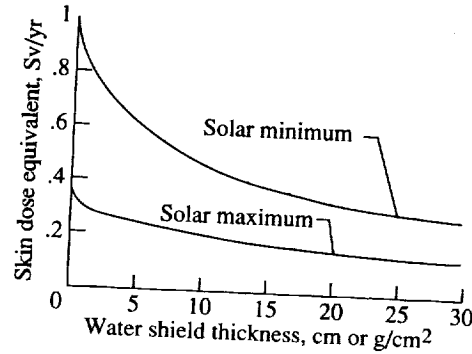


Figure 12.31. Dose equivalent as function of water shield thickness resulting from galactic cosmic rays at solar minimum (Townsend et al., 1990a).

Petrov, 1989) made during the last solar cycle imply that the GCR intensity during solar maximum may actually be greater than that prescribed in the NRL model. (See chapter 11.)

We have dealt with the transport results for some of the more common materials which may be fabricated and/or supplied as shield media. For habitats on the Moon and Mars surfaces, the regolith (or soil) of a particular locale is a convenient candidate for bulk shielding. In the analyses presented herein, the regolith composition is modeled with the mass normalized concentrations of the five most abundant elements found in the soil. The lunar model composition is based on Apollo return samples (Dalton and Hohmann, 1972), and the martian model composition is based on Viking lander data (Smith and West, 1983). The normalized compositions used in the regolith shielding studies are given in table 12.11 (Nealy, Wilson, and Townsend, 1988; Simonsen et al., 1990b). Moderate changes in composition are found to have negligible effects on the overall shielding properties (Nealy, Wilson, and Townsend, 1988 and 1989). As might be expected from the similarity of the Mars and Moon constituents, the regolith shielding characteristics are comparable.

Table 12.11. Composition of Lunar and Martian Regoliths

Regolith	Composition, percent of normalized mass	Density, g/cm ³
Lunar	52.6 SiO ₂ 19.8 FeO 17.5 Al ₂ O ₃ 10.0 MgO	0.8-2.15
Martian	58.2 SiO ₂ 23.7 Fe ₂ O ₃ 10.8 MgO 7.3 CaO	1.0-1.8

The results of BFO dose versus depth in lunar regolith are given for the three large flares of solar cycles 19 and 20 in figure 12.32. The regolith results are very similar to those for aluminum (fig. 12.28); this is not surprising, since the mean molecular weight of the lunar regolith is comparable with the atomic weight of aluminum. Figure 12.33 shows the calculated propagation data for the GCR at solar minimum conditions, with the contributions to the dose by neutrons, protons, α -particles, and two groups of heavier ions shown individually. For very thin layers, the heaviest ion group ($10 \leq Z \leq 28$) contributes over half the dose. For increasing thicknesses, the heavier ions fragment and react with target nuclei to produce particles of lower mass (ultimately nucleons) which then deliver the greater percentage of the dose. For the lunar soil, approximately 90 percent of the dose is estimated to result from nucleons (mostly secondaries) for shield layers greater than approximately 20 g/cm².

The exposures on Mars differ considerably from those on the moon because of the carbon dioxide atmosphere on Mars. Consequently, dose-depth functions are generated in carbon dioxide for the flare spectra of figure 12.14. These results are shown in figure 12.34. The shielding effectiveness per unit mass of carbon dioxide is greater than the effectiveness of either aluminum or regolith results as shown previously (figs. 12.28 and 12.32). This is particularly the case for shield amounts exceeding 25 to 30 g/cm² of material. A similar observation may be made for the GCR results for carbon dioxide (fig. 12.35) compared with the corresponding calculations for aluminum and lunar regolith (figs. 12.30 and 12.33). The basic carbon dioxide propagation data may be applied to the martian atmosphere when gas density as a function of altitude is specified.

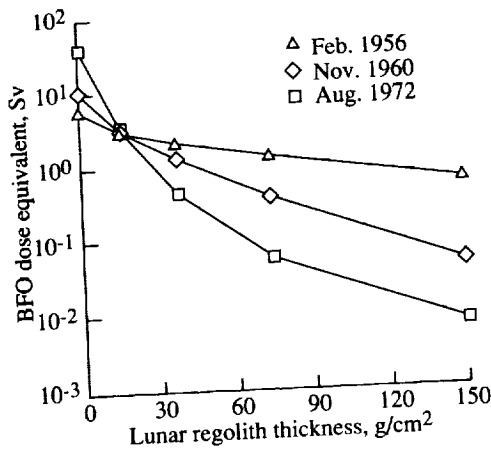


Figure 12.32. Predicted BFO dose equivalent for slab thickness between 0 and 150 g/cm² in simulated lunar regolith for three solar flare events (Nealy, Wilson, and Townsend, 1988).

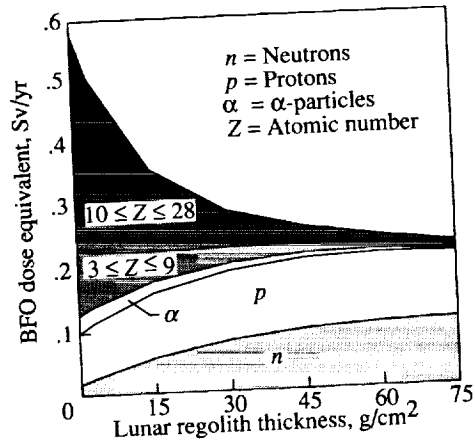


Figure 12.33. Annual BFO dose equivalent contribution from specified particle constituents as function of lunar regolith thickness for GCR at solar minimum (Nealy, Wilson, and Townsend, 1989).

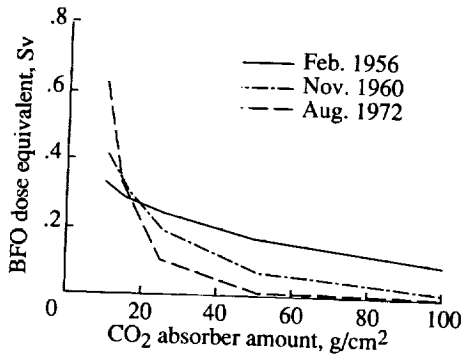


Figure 12.34. BFO dose equivalent as function of carbon dioxide absorber amounts for three solar flare events (Simonsen et al., 1990a).

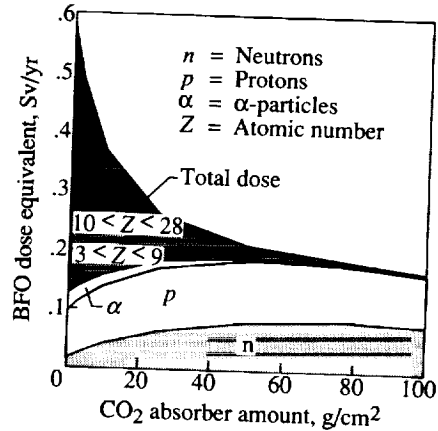


Figure 12.35. Annual BFO dose equivalent contributions from specified particle constituents as function of carbon dioxide absorber amount for GCR at solar minimum (Simonsen et al., 1990a).

When martian regolith is considered as a protective shield medium, the transport calculations must be made for the atmosphere-regolith thicknesses combined. In this case, the detailed flux-energy spectra emergent from a specified carbon dioxide amount must be used as input for the subsequent regolith calculation. Sample BFO dose results for such a procedure are given in figure 12.36, where fixed carbon dioxide amounts are used in conjunction with regolith layers. Two GCR cases and the energetic 1956 solar flare are included in the analysis. For moderate carbon dioxide absorber amounts, the dose reductions from additional regolith layers are small compared with the dose reduction occurring in the first few g/cm^2 of atmosphere (figs. 12.34 and 12.35).

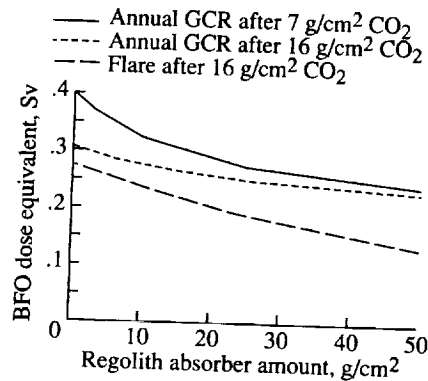


Figure 12.36. BFO dose equivalent as function of regolith absorber amount after transport through martian atmosphere in vertical direction (Simonsen et al., 1990b).

12.4. Description of Shield Assessment Results

When the computed propagation data for the GCR and solar flare protons in different materials are applied to specific shield geometries, the dose at a specific target point can be evaluated. To evaluate the dose at a particular point, the radiation from all directions must be determined. In deep space, radiation will surround the crew from the full 4π sr. However, on a planetary surface, only a solid angle of 2π is considered because the mass of the planet protects the crew from half the deep space radiation. The dose contribution attributed to particles arriving from a given direction is determined by the shield thickness encountered along its straight-line path to a specified target point. For shield assessments in these analyses, the absorber amounts and the corresponding dosimetric quantities are evaluated for zenith angles between 0° and 90° in 5° increments, and for azimuth angles of 0° to 360° also in 5° increments. The directional dose is then numerically integrated over the solid angle (4π for deep space, 2π for planetary applications) about a target point to determine the total dose at that point. For deep space calculations when a spherical shielded volume is considered, the slab dose calculations can be used directly. (See fig. 12.27). The dose estimates presented here conservatively estimate the skin dose as the dose at 0 cm depth and the BFO dose as the dose at 5 cm depth. When detailed body geometry is considered, for example, incorporating the thickness distributions of the Computerized Anatomical Man Model (Billings and Yucker, 1973), the estimated doses will generally be lower, with the amount of reduction being dependent on the energetic particle environment spectrum (Shinn, Wilson, and Nealy, 1990). Dose estimates using the propagation data for various materials are determined for the following shielded volumes: (1) interplanetary transportation vehicles, (2) lunar habitats, and (3) martian habitats.

12.4.1. Transportation vehicles. Unshielded BFO dose equivalents in deep space are substantial and could be lethal if an unusually large flare occurred. From galactic cosmic radiation at solar minimum, the unshielded astronaut would receive approximately 0.6 Sv/yr. The three large flare events of August 1972, November 1960, and February 1956 would have delivered unshielded doses of approximately 4.11, 1.10, and 0.62 Sv, respectively. The GCR dose is over the annual limit of 0.5 Sv/yr and the flare doses are significantly greater than the 30-day limit of 0.25 Sv. Clearly, both lunar and martian transportation vehicles must offer adequate protection. The protection for the short lunar travel time will most likely emphasize flare protection, whereas the protection required for the longer travel time required for Mars must consider both the GCR and the flares combined. The following analyses consider radiation protection for transportation vehicles required for various flare scenarios and for galactic cosmic radiation.

The normal-incidence slab calculations, presented in section 12.3, can be used to estimate the doses inside nearly spherical structures in an assumed isotropic radiation field. Results of such an application are presented in table 12.12 for the three large solar flare events (Townsend et al., 1989). The aluminum wall thicknesses required to reduce the incurred dose from large flares to the astronaut 30-day limits for ocular lens, skin, and blood-forming organs are estimated. Even though the individual flare spectra exhibit marked differences (fig. 12.14), the

Table 12.12. Aluminum Shield Thickness Required for Solar Flare Protection to Remain Below the 30-Day Limit

[Data from Townsend et al., 1989]

Organ	Aluminum shield thickness for solar flare event in—					
	February 1956		November 1960		August 1972	
	g/cm ²	cm	g/cm ²	cm	g/cm ²	cm
Skin	1.3	0.5	2.5	1.0	7.5	2.8
Ocular lens	1.5	0.6	3.5	1.3	9.5	3.5
BFO	24.0	8.9	22.0	8.1	18.0	6.7

required shielding thicknesses range from approximately 18 to 24 g/cm² (7 to 9 cm) of aluminum. The shielding mass required can be reduced by approximately 15 to 30 percent using water as shielding with thicknesses of only 15 to 20 g/cm² required (Townsend et al., 1989). These shielding estimates include only a flare contribution and represent a minimum acceptable wall thickness. Rather than shielding an entire spacecraft with these wall thicknesses, the crew can be provided with a heavily shielded “shelter” for protection during a large flare event. More recent solar flare analyses have been done by Nealy et al. (1990a), Simonsen et al. (1991), and Townsend, Shinn, and Wilson (1991).

For long-duration missions, contributions from the GCR and the more numerous smaller flares should be considered. Dose evaluations throughout a complete solar cycle are made with the flare data (fig. 12.17) measured during solar cycle 21 between 1975 and 1986 (Nealy et al., 1990b). The GCR contribution is assumed to vary sinusoidally from peak values at solar minimum to the smallest dose rate at solar maximum. Normal-incidence slab calculations for the dose evaluations are made with effective water shield thicknesses. Water, both potable and waste, may be a likely shield material for long-duration missions since it will probably be available in large quantities. Water calculations can be used to simulate results for other media with low atomic weight and high hydrogen content. Consequently, reasonable shield mass requirements may be estimated on the basis of water transport results.

Figures 12.37 and 12.38 show sample BFO dose estimates from this study as a function of time within the solar cycle. In figure 12.37, the dose equivalent incurred for an effective water shield of 5 g/cm² is given for mission durations of 3, 12, and 36 months. The figure shows the dose integrated over mission duration time, with the flare contribution (according to solar cycle 21 distribution) appearing as deviations above the smooth sinusoidal curve, which would be seen for the GCR contribution alone. The results indicate that the flare contribution is not conspicuous in comparison with the more regularly varying GCR component. Note, however, that there were no unusually large events in cycle 21 as has been observed in cycles 18, 19, 20, and 22. For missions of duration longer than 1 year in cycle 21, the dose contributions due to the normally occurring solar flares may not be significant in comparison with the GCR (for shield amounts greater than

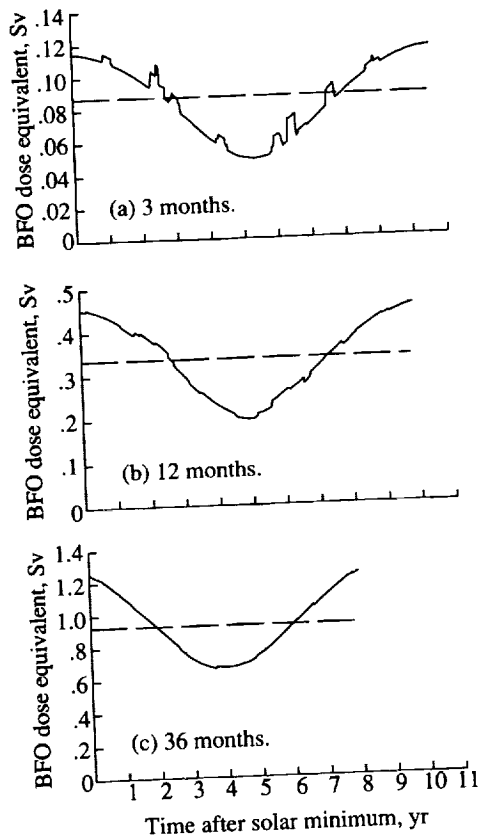


Figure 12.37. Free-space BFO dose equivalent incurred for water-slab shields 5 g/cm^2 thick for three mission lengths as function of time in cycle after solar minimum. Dashed lines indicate cycle average values (Nealy et al., 1990b).

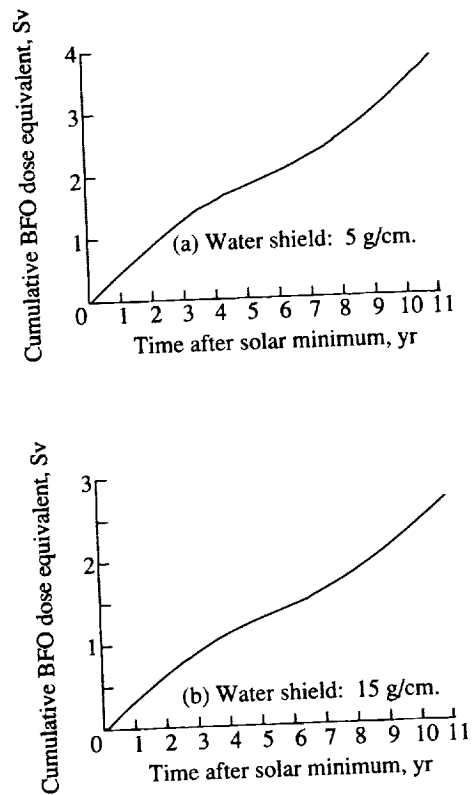


Figure 12.38. Cumulative total BFO dose equivalent incurred throughout the 11-year solar cycle for water slab shields (Nealy et al., 1990b).

5 g/cm^2). If this is true, the cumulative dose is approximately proportional to the mission duration time.

The BFO dose received by crew members on a 3-month, 12-month, or 36-month mission starting in any portion of solar cycle 21 may be predicted from figure 12.37. For example, the final dose value on figure 12.37(c) of about 1.25 Sv represents the dose incurred for a mission beginning 8 years after solar minimum and lasting over the next 3 years. This plot (fig. 12.37(c)) also indicates that a 36-month mission beginning 4 years after solar minimum would result in a total incurred dose approximately 45 percent lower than would be received on a mission beginning at solar minimum.

Figure 12.38 illustrates the variation of the cumulative incurred dose equivalent throughout the entire solar cycle 21 for water shields 5 and 15 g/cm^2 thick. This type of representation is useful in estimating incurred dose for long-duration

missions (2 years or more) which begin and end at arbitrary times within solar cycle 21. For example, from figure 12.38(a), the total BFO dose for a 5-year mission beginning at solar minimum is predicted to be approximately 1.80 Sv for shielding 5 g/cm² thick. However, if the 5-year mission begins 3 years after solar minimum, the total incurred dose is estimated to be approximately 1.35 Sv (2.6 Sv at year 8 minus 1.25 Sv at year 3).

The preceding results from the solar cycle 21 analysis do not include contributions from a rarely occurring giant solar proton event (e.g., the events of 1956, 1960, 1972, 1989), and such an event must be accounted for separately as circumstances warrant. For example, for a 1- or 2-year mission spanning the solar minimum, a large proton event would be highly unlikely, whereas during active Sun conditions, a larger (but still relatively small) probability exists that incurred doses would be considerably increased because of large flare episodes.

The results of the solar cycle 21 study indicate that a reasonably conservative radiation environment for exposure analysis may be derived from the solar minimum GCR flux with the inclusion of one large proton event. The BFO dose depth variation for such an environment consisting of the fluence of the 1972 large proton event in combination with the annual GCR contribution is given in figure 12.39. The BFO dose equivalent of 0.5 Sv is exceeded for water shield thicknesses less than about 18 g/cm². For shields thicker than 25 or 30 g/cm², the flare dose is insignificant. These propagation data can be used to estimate shield masses of various manned habitation modules.

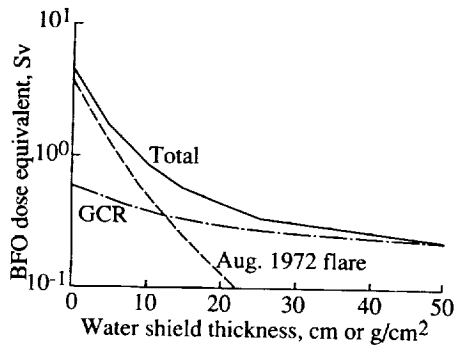


Figure 12.39. BFO dose equivalent as a function of water shield thickness for August 1972 flare and GCR at solar minimum (Simonsen and Nealy, 1991).

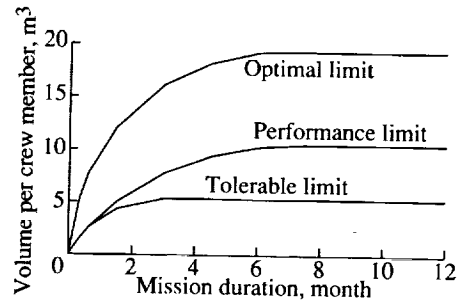


Figure 12.40. Guidelines for the determination of total habitable volume required per person in space module (NASA-STD-3000 (Anon., 1987)).

Guidelines for manned module volume requirements are graphically depicted in figure 12.40 (Anon., 1987). According to these guidelines, long-duration missions would require at least 10 m³ per crew member as a performance limit and approximately 19 m³ as an optimal limit. (Here, the tolerance limit volume is not considered to be applicable for normal operations on extended missions.) A four person crew is recommended for a manned Mars mission (The 90-Day Study (Anon., 1989b)) which implies a minimum habitable volume of approximately 42 m³. If a cylindrical module is assumed, with diameter equal to length, the shield mass of the configuration may then be found as a function of dose delivered

near the center of the module. Figure 12.41 shows the annual delivered dose due to GCR and the August 1972 flare as a function of cylinder wall mass. Again, equivalent water shield thicknesses are used in these estimates (fig. 12.39). If one considers an acceptable design criteria to be 50 to 70 percent of the maximum allowable dose, then shield masses on the order of 20 to 30 metric tons are required for the volume of 42 m³. Estimates of shield mass will be greater if aluminum is assumed to be the shielding material because of the poorer shielding characteristics of aluminum. In some cases, the shield mass can be a significant fraction of the total mass of the candidate concepts of the Mars transportation vehicle (The 90-Day Study (Anon., 1989b)). However, the bulk shielding mass is not necessarily extra mass that must be provided but the total shielding required which can include the pressure vessel walls, water tanks, fuel tanks, and other components of the spacecraft.

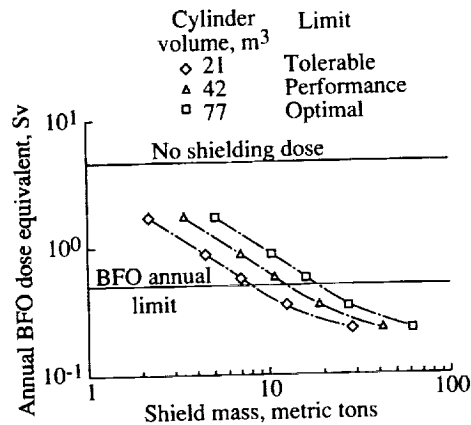


Figure 12.41. BFO dose equivalent incurred from the August 1972 flare and GCR (fig. 12.39) versus shield mass for cylindrical modules (Length/Diameter = 1.0) of various volumes based on the requirements of figure 12.40 for a four man crew (Simonsen and Nealy, 1991).

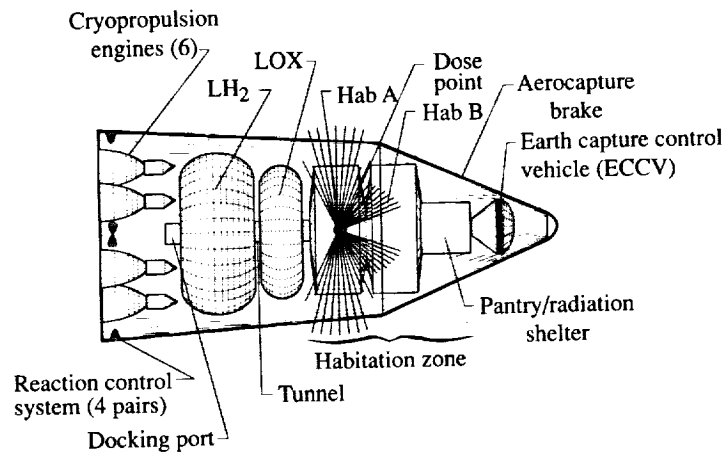


Figure 12.42. Configuration of martian piloted vehicle with sample directional dose patterns for a point inside of Hab A module (Simonsen and Nealy, 1991).

The basic propagation data generated in the form of slab dose estimates can also be used for more detailed dose analyses of specific shielded configurations. One such configuration, depicted in figure 12.42, is a concept of a manned Mars transfer vehicle developed by the Martin Marietta Corporation. This concept contains two cylindrical habitation modules (diameter of 7.6 m, length of 2.7 m). For the present calculation, the combination of components and bulk shielding for each habitat module is assumed to be equivalent to an effective water shield thickness of 5 g/cm². Also contributing to the shielding are the ECCV, pantry, and fuel tanks.

The directional dose due to GCR (at solar minimum) was calculated for an interior point in the center habitat modules. Figure 12.42 shows the axisymmetric directional dose pattern superimposed on the vehicle configuration outline. This pattern consists of vectors emanating from a target point with their lengths proportional to the annual GCR dose per unit solid angle. Although the radiation field outside the spacecraft is assumed to be isotropic, geometry effects cause the internal field to be highly anisotropic. In particular, very little radiation penetrates from solid angles subtending the fuel tanks, which in the illustrative calculation are assumed to be full. By numerically integrating the directional dose, the BFO dose in the center of Hab A is estimated to be 0.29 Sv/yr.

Total BFO dose estimates are also predicted for a variety of points within each module from which contours of the dose variation are obtained. Figure 12.43 shows the variation of the BFO dose within the habitation modules. The influence of the fuel tank is evident in the lower overall doses of the module closest to the fuel supply (Hab A). The large dose gradient evident at the top of Hab B is because of the thick walls of the adjacent flare shelter. Analyses such as these are expected to be of importance in the design stages of deep space modules with regard to such things as crew-quarters layout, placement of equipment, storage of consumables, and waste.

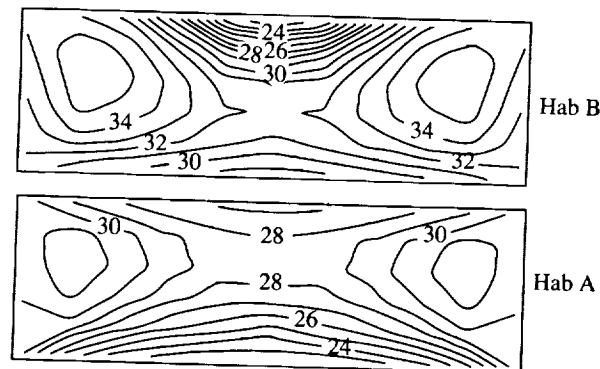


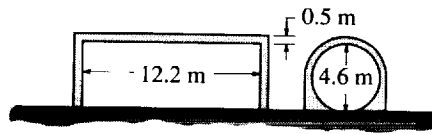
Figure 12.43. Variation in annual BFO dose equivalent for cylindrical habitation modules for galactic cosmic rays. (Simonsen and Nealy, 1991). Contour increments are 1 cSv/yr.

12.4.2. Lunar surface habitation. Once on the lunar surface, the radiation hazards of deep space will be less severe. Unshielded BFO dose estimates for the flare events of August 1972, November 1960, and February 1956 are approximately half those of deep space: 2.05 Sv, 0.55 Sv, and 0.31 Sv, respectively. These dose estimates are significantly higher than the 30-day limit of 0.25 Sv. The BFO dose incurred from the GCR at solar minimum is estimated to be approximately 0.3 Sv/yr, which is below the annual limit of 0.5 Sv/yr. However, the GCR dose in conjunction with medium to large flare event doses may reach the annual limit and become career limiting for long-duration missions. These values clearly show the need for radiation protection while on the lunar surface. Local resources, such as lunar regolith, will be available for use as protective shielding to cover habitats. In this section, several habitat configurations are considered with different regolith shielding thicknesses for protection.

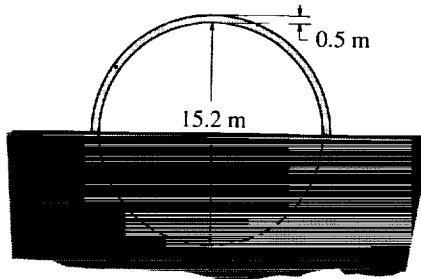
Dose calculations inside candidate habitats are predicted with the computed propagation data for solar flares and the GCR shown in figures 12.32 and 12.33. A conservative estimate of the deep space environment is to assume the combination of GCR at solar minimum and one large proton event. From figures 12.32 and 12.33, the regolith slab dose estimates imply that a thickness of 50 cm (75 g/cm^2 with regolith density assumed to be 1.5 g/cm^3) will reduce the BFO dose equivalent to approximately 0.4 Sv for the sum of the GCR and one large flare (February 1956). With the 2π -sr shielding on the lunar surface, it is expected that, with a regolith layer of 50 cm, the annual dose for this environment is reduced to approximately 0.2 Sv. Thus, a shield thickness of 50 cm is selected for analysis to reduce dose levels to slightly less than one half the annual limit (or a design safety factor of approximately 2). Shield thicknesses of 75 cm and 100 cm are also selected for analysis to determine the extent to which additional shielding will further reduce annual doses.

Early lunar habitats are described as a Space Station *Freedom* derived module and an inflatable/constructible sphere (Alred et al., 1988). The Space Station *Freedom* module is assumed to be 4.6 m in diameter and 12.2 m in length as shown in figure 12.44(a). The module is assumed to be lengthwise on the lunar surface covered with either 50 cm (or 75 g/cm^2 with regolith density assumed to be 1.5 g/cm^3) or 100 cm of lunar regolith overhead. Along the sides, the regolith material is filled in around the cylinder to form a vertical wall up to the central horizontal plane. For the 50-cm layer, the shield thickness will vary from 230 cm to 50 cm from ground level up to this plane. The spherical habitat is 15.2 m in diameter and is modeled as a half-buried sphere with the portion above ground level shielded with a regolith layer of either 50 cm, 75 cm, or 100 cm (fig. 12.44(b)).

The integrated BFO dose estimates which would have been incurred from the three flare events with shield thicknesses of 75 g/cm^2 and 150 g/cm^2 are shown in table 12.13 (Nealy, Wilson, and Townsend, 1988). The values in the table represent the dose in the center of the habitat for each flare event. The dose distribution was also calculated throughout each habitat. For the cylindrical module, the general dose levels show little change for heights above and below the center plane. The radiation field maxima occur at about two thirds the distance between the center and end wall. For the spherical habitat the field maximum occurs above the center point at positions closer to the top, whereas doses in



(a) Cylindrical module (side and end views).



(b) Spherical module.

Figure 12.44. Modeled shielded configurations of candidate lunar habitation modules (Nealy, Wilson, and Townsend, 1989).

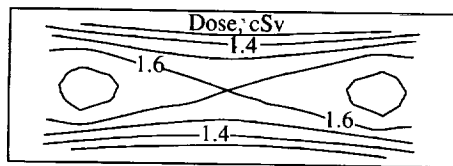


Figure 12.45. Variation in BFO dose equivalent from November 1960 solar flare within cylinder shielded overhead with regolith 75 g/cm^2 thick for central horizontal plane (Nealy, Wilson, and Townsend, 1988).

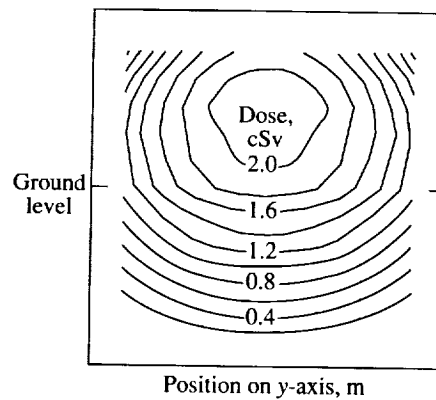


Figure 12.46. Variation in BFO dose equivalent from November 1960 flare event within a half-buried sphere shielded overhead with regolith 75 g/cm^2 thick (Nealy, Wilson, and Townsend, 1988).

Table 12.13. BFO Dose Comparisons for Three Large Solar Flares for Lunar Habitats

[Data from Nealy, Wilson, and Townsend, 1988]

Flare data	Regolith thickness, cm	Predicted dose, cSv	
		Cylinder (center)	Sphere (center)
Feb. 1956	50	7.48	7.04
	100	2.70	2.94
Nov. 1960	50	1.60	1.90
	100	0.16	0.23
Aug. 1972	50	0.25	0.30
	100	0.03	0.04

the buried half are significantly reduced. The BFO dose variations within these habitats for the November 1960 flare event are shown in figures 12.45 and 12.46.

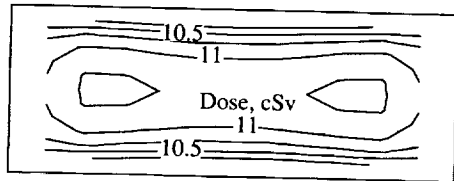
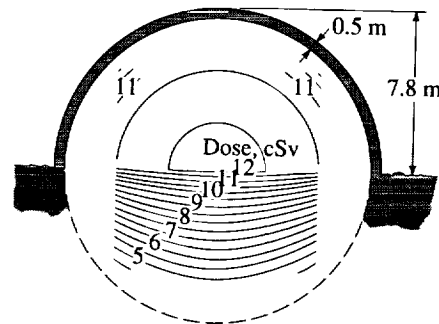
Dose predictions are also included for the GCR at solar minimum conditions. The maximum integrated BFO doses estimated in each habitat for various shield thicknesses are shown in table 12.14 (Nealy, Wilson, and Townsend, 1989). For the cylindrical habitat configuration, the dose variation throughout the configuration is relatively small (fig. 12.47). For the portion of the spherical habitat above ground level, the dose variation is also relatively small with a broad maximum dose rate observed directly above the center point of the sphere (approximately 0.11 to 0.12 Sv/yr). Below ground level, a large gradient in dose rate is shown in the downward direction, with values in the lower section decreasing to less than 5 cSv/yr (fig. 12.48). With overhead shielding of 112.5 g/cm², the dose rate maximum is reduced to 0.08 to 0.1 Sv/yr throughout the upper half of the sphere. This increased shielding is of even less significance in the regions below the ground where predicted doses approach the same low values as seen in the calculation for 75 g/cm². Relatively little reduction in dose (less than 20 percent) occurs for a 50-percent increase in layer thickness; this indicates that further substantial dose reductions would require very thick layers of material.

To make a conservative yearly estimate of dose, the crew is assumed to receive the dose delivered from the GCR and from one large flare (the February 1956 flare since it delivers the largest dose in the shielded module). If 75 g/cm² of regolith is selected for coverage, such a BFO dose in the cylindrical habitat is approximately 0.195 Sv/yr. Estimating the dose estimate in the spherical habitat is more complicated because of the large variation in dose throughout the habitat; however, the maximum dose estimated is approximately 0.19 Sv/yr. These dose estimates are well below the established guidelines for U.S. astronauts of 0.5 Sv/yr. The 30-day limits, with regard to the flares, remain below the 0.25 Sv limit. The skin doses, not presented in this analysis, are also well below the established 30-day and annual limits. These estimates have not taken into account the added shielding provided by the pressure vessel wall, supporting structures, or the placement of equipment in and around the module.

Table 12.14. GCR Integrated BFO Results for Lunar Habitats

[Data from Nealy, Wilson, and Townsend, 1989]

Habitat geometry	Regolith thickness		BFO dose equivalent Sv/yr
	cm	g/cm ² (a)	
Cylindrical	50	75	0.12
Spherical	50	75	0.12
	75	112.5	0.10

^aRegolith density of 1.5 g/cm³ is assumed.Figure 12.47. Variation in annual BFO dose equivalent from GCR variation within a cylinder shielded overhead with regolith 75 g/cm² thick for the central horizontal plane (Nealy, Wilson, and Townsend, 1989).Figure 12.48. Variation in annual BFO dose equivalent from GCR within a half-buried sphere shielded overhead with regolith 75 g/cm² thick (Nealy, Wilson, and Townsend, 1989).

Shielding from solar flare events is essential on the lunar surface whether in the form of heavily shielded areas (i.e., flare shelters) or overall habitat protection for any mission duration. For longer stay times on the surface, the shielding from GCR becomes necessary to reduce the overall career exposure of the crew. A regolith shield thickness of 50 cm is estimated to provide adequate flare and GCR protection. However, before an optimum thickness and shielding strategy is selected, the complete mission scenario (including the lunar transport vehicle) needs to be studied in detail.

12.4.3. Martian surface habitation. The radiation environment on the martian surface is less severe than that found on the lunar surface. Although Mars is devoid of an intrinsic magnetic field strong enough to deflect charged particles, it does have a carbon dioxide atmosphere which will help protect surface crews from deep space radiative fluxes. Estimating the unshielded doses anticipated for crew members on the surface of Mars is more difficult than estimates made for

the Moon in which deep space estimates are simply divided in half. On Mars, the protection provided by the atmosphere must be considered.

The amount of protection provided by the Mars atmosphere depends on the composition and structure of the atmosphere and altitude of the crew. In this analysis, the composition of the atmosphere is assumed to be 100 percent carbon dioxide. The Committee on Space Research has developed warm high- and cool low-density models of the atmospheric structure (Smith and West, 1983). The low-density model and the high-density model use surface pressures of 5.9 mbars and 7.8 mbars, respectively. The amount of protection provided by the atmosphere, in the vertical direction, at various altitudes is shown in table 12.15 (Simonsen et al., 1990a). In these calculations, a spherically concentric atmosphere is assumed such that the amount of protection provided increases with increasing zenith angle. Dose predictions at altitudes up to 12 km are included in the analysis because of the great deal of topographical relief present on the Mars surface.

Table 12.15. Martian CO₂ Atmospheric Protection in Vertical Direction

[Data from Simonsen et al., 1990a]

Altitude, km	Low-density model, g/cm ²	High-density model, g/cm ²
0	16	22
4	11	16
8	7	11
12	5	8

Dose estimates are predicted for the galactic cosmic radiation for the minimum of the solar activity cycle (fig. 12.3). The fluence spectra at 1 AU are used for the three large flares of August 1972, November 1960, and February 1956 (fig. 12.14). In the vicinity of Mars (approximately 1.5 AU), the fluence from these flares is expected to be less; however, there is still much discussion on the dependence of the radial dispersion of the flare with distance. Therefore, for the flare calculations in this analysis, the deep space fluence energy spectra at 1 AU have been conservatively applied to Mars. The surface doses at various altitudes in the atmosphere are determined from the computed propagation data for the GCR and the solar flare protons through carbon dioxide as shown in figures 12.34 and 12.35.

Integrated dose equivalent calculations were made for both the high-density and the low-density atmosphere models at altitudes of 0, 4, 8, and 12 km. The corresponding skin and BFO dose estimates are shown in tables 12.16 and 12.17 (Simonsen et al., 1990a). A total yearly skin and BFO dose may be conservatively estimated as the sum of the annual GCR dose and the dose due to one large flare. At the surface, such an estimated skin dose equivalent is 0.21 to 0.24 Sv/yr and an estimated BFO dose equivalent is 0.19 to 0.22 Sv/yr (GCR plus Feb. 1956 event).

Table 12.16. Integrated Skin Dose Equivalents for Martian Atmospheric Models

[Data from Simonsen et al., 1990a]

Condition		Integrated skin dose equivalent, Sv, at altitude of—			
		0 km	4 km	8 km	12 km
Galactic cosmic ray (annual)	High-density	0.113	0.134	0.158	0.186
	Low-density	0.132	0.159	0.189	0.224
Aug. 1972 solar flare event	High-density	0.039	0.095	0.211	0.428
	Low-density	0.09	0.219	0.462	0.826
Nov. 1960 solar flare event	High-density	0.064	0.10	0.148	0.211
	Low-density	0.097	0.151	0.219	0.296
Feb. 1956 solar flare event	High-density	0.092	0.111	0.133	0.159
	Low-density	0.11	0.134	0.162	0.191

Table 12.17. Integrated BFO Dose Equivalents for Martian Atmospheric Models

[Data from Simonsen et al., 1990a]

Condition		Integrated BFO dose equivalent, Sv, at altitude of—			
		0 km	4 km	8 km	12 km
Galactic cosmic ray (annual)	High-density	0.105	0.12	0.137	0.156
	Low-density	0.119	0.138	0.158	0.18
Aug. 1972 solar flare event	High-density	0.022	0.048	0.095	0.174
	Low-density	0.046	0.099	0.185	0.303
Nov. 1960 solar flare event	High-density	0.050	0.075	0.106	0.144
	Low-density	0.073	0.108	0.148	0.191
Feb. 1956 solar flare event	High-density	0.085	0.10	0.117	0.134
	Low-density	0.099	0.118	0.136	0.153

Transport Methods and Interactions for Space Radiations

At an altitude of 12 km, an estimated skin dose equivalent is 0.61 to 1.05 Sv/yr and an estimated BFO dose equivalent is 0.33 to 0.48 Sv/yr (GCR plus Aug. 1972 event). These dose predictions imply that the atmosphere of Mars may provide shielding sufficient to maintain the annual skin and BFO dose levels below the current U.S. astronaut limits of 3 and 0.5 Sv/yr, respectively.

The 30-day limits are important when considering the doses incurred from a solar flare event. The only 30-day limit exceeded is the BFO limit of 0.25 Sv for the August 1972 event at an altitude of 12 km. However, as seen in figure 12.34, the August 1972 flare is rapidly attenuated by matter, and a few g/cm^2 of additional shielding should reduce the anticipated dose below this limit. These dose predictions imply that the atmosphere of Mars may also provide sufficient shielding to maintain 30-day dose levels for the skin and BFO below the current U.S. astronaut limits of 1.5 and 0.25 Sv, respectively.

Mars exploration crews are likely to incur a substantial dose while in transit to Mars and perhaps from other radiation sources (e.g., nuclear reactors) which will reduce the allowable dose that can be received while on the surface. Therefore, additional shielding may be necessary to maintain short-term dose levels below limits or to help maintain career dose levels as low as possible. By utilizing local resources, such as martian regolith, shielding materials can be provided without excessive launch weight requirements from Earth.

The GCR particle flux and solar flare particle flux spectra obtained during the atmosphere calculations at altitudes of 0 and 8 km are now used as input conditions for regolith shield calculations. For a representative large solar flare contribution, the very penetrating spectrum of the February 1956 event is selected for further analysis. This event has the greatest flux of high-energy particles which results in the highest dose at the martian surface. The subsequently calculated particle flux versus energy distributions in the regolith can then be used to determine the dose at specified locations in the shield media. The dose contribution attributed to particles arriving from a given direction is now determined by the amount of CO_2 traversed and then the shield thickness encountered along its straight-line path to a specified target point. An example of some of the basic propagation data required is shown in figure 12.36.

One early martian habitat is described as a Space Station *Freedom* derived module, which is 8.2 m in length and 4.45 m in diameter (The 90-Day Study (Anon., 1989b)). The cylindrical module is assumed to be lengthwise on the martian surface with various thicknesses of martian regolith surrounding it. Another configuration assumes that the module is situated 2 m from a cliff 10-m high. (See fig. 12.49.)

A series of calculations are performed for various regolith thicknesses covering the module. Again, no consideration is given to the added shielding provided by the pressure vessel and internal equipment. The largest integrated dose equivalent in a vertical plane through the center of the cylinder is plotted versus an effective regolith thickness in figure 12.50 (Simonsen et al., 1990b). As shown in the figure, the regolith does not provide much additional protection from the GCR or the flare event than that already provided by the carbon dioxide atmosphere. The slope of

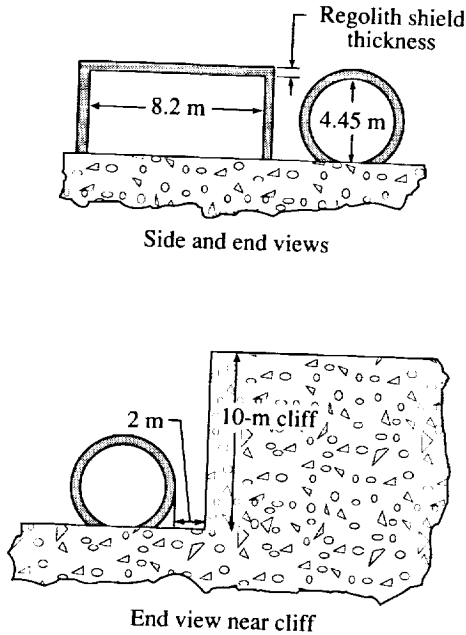


Figure 12.49. Cylindrical habitat module with regolith shielding for Mars (Simonsen et al., 1990b).

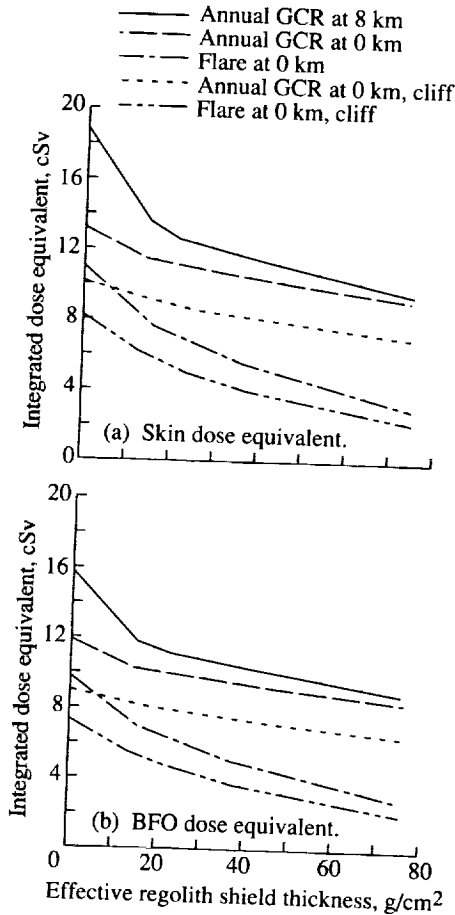


Figure 12.50. Maximum dose equivalent in central cross-sectional plane of module as function of effective regolith shield thickness (Simonsen et al., 1990b).

each curve is relatively flat after 20 g/cm², with most of the dose reductions for the skin and BFO occurring in the first 20 g/cm². For 20 g/cm² of regolith protection, the annual BFO dose equivalent due to GCR is reduced from 0.119 to 0.1 Sv/yr at 0 km, and from 0.158 to 0.112 Sv/yr at 8 km. The annual skin dose equivalent is reduced from 0.132 to 0.11 Sv/yr at 0 km and from 0.189 to 0.126 Sv/yr at 8 km. For 20 g/cm² of regolith protection, the BFO dose equivalent due to the solar flare is reduced from 0.099 to 0.063 Sv/event at 0 km. The skin dose equivalent is reduced from 0.11 to 0.069 Sv/event.

For the GCR, the dose variation within the module in the radial direction is not large, approximately 5 to 20 percent for 15 to 50 cm of shielding, respectively. For the February 1956 solar flare event, the variation in dose equivalent is approximately 25 to 40 percent for 15 to 50 cm of shielding, respectively. In the axial direction, the dose estimates for both the GCR and the flare showed a

variation of less than 1 percent; this suggests that the doses incurred in cylindrical habitats of other lengths would be comparable in magnitude.

A possible way to further reduce the dose equivalent received on the martian surface would be to locate the habitat next to a cliff. As shown in figure 12.50(b), the cliff further reduces the BFO dose equivalent by approximately 0.02 to 0.03 Sv/yr for the GCR at 0 km and by approximately 0.01 to 0.015 Sv/event for the February 1956 flare at 0 km. Similar decreases are also obtained for the skin dose (fig. 12.50(a)). The shielding provided by the cliff and atmosphere alone results in a BFO dose equivalent of 0.091 Sv/yr for the GCR and 0.074 Sv/event for the February 1956 event.

From this analysis, it is concluded that moderate thicknesses of martian regolith do not provide substantial additional protection to that already provided by the carbon dioxide atmosphere. If regolith is used as shielding material, the largest reduction in dose equivalent occurs in the first 20 g/cm² (or approximately 15 cm if a regolith density of 1.5 g/cm³ is assumed). Thus, if additional protection using martian regolith is desired, a shield thickness on the order of 15 to 20 cm is recommended. If additional protection using 15 cm of martian regolith is provided at an altitude of 0 km, the annual skin and BFO dose equivalent will be reduced from 0.24 to 0.18 Sv/yr and from 0.22 to 0.16 Sv/yr, respectively (Simonsen et al., 1990b).

For radiation protection provided by regolith on the surface of Mars, mission planners and medical personnel must decide if the radiation doses anticipated warrant the added equipment and time required for crew members to "bury" themselves. For the shorter stay times of 30 to 90 days, the additional requirements placed on a Mars mission to cover a module may be unnecessary, especially if a flare shelter is provided. A logical alternative to massive shielding efforts is to take advantage of local terrain features found on the surface of Mars. Regolith shielding may become more attractive for the longer stay times of 600 days or for futuristic permanent habitation.

12.5. Issues and Concerns

Estimates and predictions of radiation exposure and incurred doses for space exploration missions usually require complex analysis techniques and involve uncertainties that are presently difficult to quantify. Some issues and concerns regarding radiation exposure estimates and shielding requirements are discussed in the following subsections.

12.5.1. Environment. Confidence in the estimates of incurred dose for lunar and martian missions is directly related to the accuracy and development of the current space-radiation environmental models. With regard to the charged-particle environmental models, only in some cases do enough data exist for estimates of uncertainties and natural variabilities. At the present time, no particular flare model has been established as a practical standard. However, a likely future candidate is the statistical model developed at the Jet Propulsion Laboratory (Feynman and Gabriel, 1990). The continued development, endorsement, and

implementation of standard environmental models are important aspects of mission scenario analyses and shield design studies.

12.5.2. Transport codes. The accuracy of transport codes used to describe the propagation of particles through matter is another concern. Monte Carlo techniques are generally regarded as most faithfully representing the details of the complex processes involving high-energy radiation transport. In many cases, simpler and faster codes, which are far less costly and time consuming to implement, may be used to adequately describe the transport. The precision of such codes may be evaluated by comparisons with equivalent Monte Carlo calculations, or with exact benchmark solutions (when they can be found). Once the mathematical precision of a particular code is established, the ultimate accuracy of its prediction will depend on the interaction cross-section data base used as input for calculations. Presently, nucleon (neutrons and protons) interaction cross sections are relatively well-known for wide ranges of energy and target materials. However, data are very limited for interaction cross sections for the 20 to 25 heavy ion nuclei of importance for GCR exposure. Inevitably, data extrapolations and extensions by complex theoretical techniques are implemented in order to provide a comprehensive cross-section data base (Norbury and Townsend, 1986; Townsend and Wilson, 1985; Wilson and Badavi, 1986). This creates uncertainties in the transport calculations which are very difficult to quantify. (See chapter 11 for further discussion.)

12.5.3. Radiobiology. Standard dosimetric techniques used to evaluate health risks due to radiation exposures are presently being challenged, particularly with regard to latent effects due to the high-energy, low dose-rate exposure from the GCR heavy ions. Current methods for evaluating dose equivalents resulting from heavy ion exposure utilize biological effectiveness quality factors (Q) which are specified as functions of linear energy transfer (LET) of the projectile particles to the biological system being traversed (ICRP 26 (Anon., 1977)). Predictions of dose equivalent incurred in deep space from the GCR with the standard methods indicate that substantial shielding (20–50 g/cm²) is required to reduce dose levels to an annual dose of 0.25 to 0.3 Sv (Townsend et al., 1990a). Such shield amounts are very massive when large habitation modules are involved. Thus, efforts are in progress toward better definition of risk assessment for GCR exposures. Newly proposed quality factors have been based on recent biological effects data (ICRU 40 (Anon., 1986)). Preliminary calculations with the latest Q values indicate that previous evaluations may have been somewhat, but not dramatically, conservative (Wilson, Shinn, and Townsend, 1990). Other recent studies have suggested abandoning the Q value/LET system (Katz, 1986) and formulating more detailed models of cell destruction and transformation using radiosensitivity parameters derived from biological experiments (Cucinotta et al., 1991). The current limitation of such models is the lack of methods to extrapolate from cell damage to expression at the organismic level, lack of comprehensive cell repair model, and the physiological factors. It is expected that such direct biophysical models would be a distinct improvement. However, evolution of such models is directly coupled to the available data bases for radiobiological effects, which are very limited for GCR-type radiations. Clearly, the relationship between heavy ion

exposure and health risk is in need of better definition. For further discussion, see chapter 11.

12.5.4. Dosimetric measurement. The preceding discussion naturally leads to additional questions concerning measurement and monitoring of incurred radiation doses. Present space flight dosimetry instrumentation includes dosimeters of both thermo-luminescent and proportional counter types, and they have been shown to be reliable and accurate for the Space Transportation System (STS) mission (Atwell, 1990). In general, STS dose rates are fairly low. For the 28.5° inclination orbits at altitudes between 250 and 350 km, the average dose rate is observed to be approximately 0.01 cGy/day (or 0.036 Gy/yr). Steady dose rates in deep space, even with thick shields, are expected to be substantially higher (factors of 5 to 10), with intermittent (solar flare) dose rates higher still. Further advancement in dosimetric instrumentation and techniques will be required to monitor the astronaut deep space exposures, with emphasis on active, as opposed to passive, dosimeters. In particular, since the GCR interactions with thick shields may produce a high yield of neutrons and precision in neutron dosimetry is currently considered to be rather poor (Paić, 1988), improvements are currently needed in this case.

12.5.5. Flare prediction. The forecasting of large solar proton events is of vital importance for missions of long duration. Practically continuous monitoring of various aspects of solar activity (i.e., X-rays, radio emissions, sunspot number) during solar cycle 21 (1975-1986) and up to the present time has provided a valuable data base for flare-forecasting statistics. The approach to flare forecasting used at the NOAA Space Environment Laboratory during recent years is to examine the intensities of X-rays and radio emissions as they relate to the release of energetic particles from the solar surface. Estimates of the peak proton flux may also be made from these observations. For flare predictions during solar cycle 21, the number of events which occurred without prediction was about 10 percent of the total. This resulted primarily because the initial X-ray and radio bursts were not on the visible portion of the Sun (Heckman et al., 1984). The false-alarm rate was approximately 50 percent; therefore, further work in this area is needed. Other techniques combine high-resolution observations of sunspot group patterns and magnetic field configurations in conjunction with H_{α} -line emission. The prediction of occurrence with the use of these techniques is claimed to be up to several days in advance (Zirin and Liggett, 1987). This method appears to show promise, but more observations are required to demonstrate the practicality of its implementation on a routine basis. For missions of long duration, additional onboard instruments for active proton detection should also be available to indicate when the use of a well-shielded storm shelter is warranted.

12.5.6. Alternate shielding concepts. Other topics of concern in the area of space-radiation shielding include the effectiveness of material types (or combination of material types) and alternate approaches to bulk shielding (e.g., magnetic and electromagnetic field deflection methods). As previously discussed in section 2.3.2, recent results indicate that hydrogenous materials of low atomic weight are substantially superior to heavy metals for energetic ion shielding. However, little has been done in the study of the behavior of combinations,

for example, alternating layers of light and heavy materials. Further studies should also address structural details of shields: in particular, corrugatedlike panels and/or shadow shielding techniques may offer advantages over simple wall structures. One recent study has indicated that magnetic shielding is of little use for protection from GCR (Townsend et al., 1990b). However, the Townsend study also showed that for representative large proton flares, great reductions in exposure can be achieved; thus, the potential use of such a technique for flare protection may still be viable.

12.6. Concluding Remarks

Before astronaut dose estimates and subsequent shielding requirements can be determined for advanced missions to the Moon and Mars, many details of the missions must be specified. For instance, many items must be defined in order to determine specific shielding requirements: the transfer vehicle configuration, the habitat configuration, the length of time required to shield habitats with regolith, the career limits of the crew, the year of the mission (solar minimum or maximum conditions), the duration of the mission. Mars mission planning includes particular concerns such as whether any nuclear powered propulsion is envisioned, the location of the habitat on the martian surface, whether the crew will be spiraled through the Van Allen belts. Estimates must also be made as to where the Mars crew will spend their time en route to Mars; that is, how much of their time is anticipated to be spent in the more heavily shielded areas of the spacecraft as opposed to the less heavily shield areas. Even with the specific details of the mission defined, the final shield design must consider the many uncertainties associated with current state-of-the-art transport analysis.

Steps toward quantifying some of the issues involved with radiation protection for advanced manned missions to the Moon and Mars have been presented in this chapter. After the definition of the galactic cosmic-ray environment and the selection of various flare environment scenarios, deterministic transport codes were used to determine the transport and attenuation of the deep space radiative fluxes through different media. From these basic propagation data, conservative dose estimates and shielding requirements are determined for simple-geometry transfer vehicles and for possible lunar and martian habitat configurations. The results that have been presented are just part of the information required to determine radiation-protection requirements for each phase of a complete mission scenario. However, all this must await an improved understanding of biological response to heavy ion exposure and identification of important biological consequences which must be mitigated.

12.7. References

- Adams, J. H., Jr.; Silberberg, R.; and Tsao, C. H., 1981: *Cosmic Ray Effects on Microelectronics. Part I—The Near-Earth Particle Environment*. NRL Memo. Rep. 4506-Pt. I, U.S. Navy. (Available from DTIC as AD A103 897.)
- Adams, James H., Jr., 1987: *Cosmic Ray Effects on Microelectronics, Part IV*. NRL Memo. Rep. 5901 (Revised), Naval Research Lab.

Transport Methods and Interactions for Space Radiations

- Alred, J.; Bufkin, A.; Graf, J.; Kennedy, K.; Patterson, J.; Petro, A.; Roberts, M.; Stecklein, J.; and Sturm, J., 1988: Development of a Lunar Outpost: Year 2000-2005. *Lunar Bases & Space Activities in the 21st Century*, NASA, AIAA, Lunar & Planetary Inst., American Geophysical Union, American Nuclear Soc., American Soc. of Civil Engineers, Space Studies Inst., and National Space Soc., Paper No. LBS-88-240.
- Anon., 1975a: *The Earth's Trapped Radiation Belts*. NASA Space Vehicle Design Criteria (Environment). NASA SP-8116.
- Anon., 1975b: *Interplanetary Charged Particles*. NASA Space Vehicle Design Criteria (Environment). NASA SP-8118.
- Anon., 1977: *Recommendations of the International Commission on Radiological Protection*. ICRP Publ. 26, Pergamon Press.
- Anon., 1986: *The Quality Factor in Radiation Protection*. ICRU Rep. 40, International Commission on Radiation Units and Measurements.
- Anon., 1987: *Man-Systems Integration Standards—Volume 1*. NASA CR-185625-VOL. 1.
- Anon., 1989a: *Guidance on Radiation Received in Space Activities*. NCRP Rep. No. 98, National Council on Radiation Protection and Measurements.
- Anon., 1989b: *Report of the 90-Day Study on Human Exploration of the Moon and Mars*. NASA Johnson Space Center.
- Atwell, William; Beever, E. Ralph; Hardy, Alva C.; and Cash, Bernard L., 1989: A Radiation Shielding Model of the Space Shuttle for Space Radiation Dose Exposure Estimations. *Advances in Nuclear Engineering Computation and Radiation Shielding*, Volume 1, Michael L. Hall, ed., American Nuclear Soc., Inc., pp. 11:1-11:12.
- Atwell, William, 1990: Astronaut Exposure to Space Radiation: Space Shuttle Experience. SAE Tech. Paper Ser. 901342.
- Blizard, J. B., 1969: *Long Range Solar Flare Prediction*. NASA CR-61316.
- Billings, M. P.; and Yucker, W. R., 1973: *The Computerized Anatomical Man (CAM) Model*. NASA CR-134043.
- Burrell, M. O.; Wright, J. J.; and Watts, J. W., 1968: *An Analysis of Energetic Space Radiation and Dose Rates*. NASA TN D-4404.
- Committee on the Biological Effects of Ionizing Radiations, 1990: *Health Effects of Exposure to Low Levels of Ionizing Radiation*. BEIR V, National Academy Press.
- Cucinotta, Francis A.; and Wilson, John W., 1985: *Computer Subroutines for Estimation of Human Exposure to Radiation in Low Earth Orbit*. NASA TM-86324.
- Cucinotta, Francis A.; Katz, Robert; Wilson, John W.; Townsend, Lawrence W.; Nealy, John E.; and Shinn, Judy L., 1991: *Cellular Track Model of Biological Damage to Mammalian Cell Cultures From Galactic Cosmic Rays*. NASA TP-3055.

- Curtis, S. B.; Doherty, W. R.; and Wilkinson, M. C., 1969: *Study of Radiation Hazards to Man on Extended Near Earth Missions*. NASA CR-1469.
- Curtis, S. B.; and Wilkinson, M. C., 1971: *Radiation Hazards to Man*. NASA CR-125592.
- Dalton, Charles; and Hohmann, Edward, eds., 1972: *Conceptual Design of a Lunar Colony*. NASA CR-129164.
- Feynman, Joan; and Gabriel, Stephen B., 1990: A New Model for Calculation and Prediction of Solar Proton Fluences. AIAA-90-0292.
- Foelsche, T., 1963: Specific Solar Flare Events and Associated Radiation Doses. *Space Radiation Effects*, ASTM Special Tech. Publ. No. 363, American Soc. for Testing & Materials, pp. 1-13.
- Foelsche, Trutz; Mendell, Rosalind B.; Wilson, John W.; and Adams, Richard R., 1974: *Measured and Calculated Neutron Spectra and Dose Equivalent Rates at High Altitudes; Relevance to SST Operations and Space Research*. NASA TN D-7715.
- Grahn, Douglas, ed., 1973: *HZE-Particle Effects in Manned Spaceflight*. Space Science Board, National Research Council, National Academy of Sciences.
- Goswami, J. N.; McGuire, R. E.; Reedy, R. C.; Lal, D.; and Jha, R., 1988: Solar Flare Protons and Alpha Particles During the Last Three Solar Cycles. *J. Geophys. Res.*, vol. 93, no. A7, pp. 7195-7205.
- Heckman, G.; Hirman, J.; Kunches, J.; and Balch, C., 1984: The Monitoring and Prediction of Solar Particle Events—An Experience Report. *Adv. Space Res.*, vol. 4, no. 10, pp. 165-172.
- Johnson, Francis S., ed., 1965: *Satellite Environment Handbook*, Second ed. Stanford Univ. Press.
- Khandelwal, G. S.; and Wilson, John W., 1974: *Proton Tissue Dose for the Blood Forming Organ in Human Geometry: Isotropic Radiation*. NASA TM X-3089.
- Katz, Robert, 1986: Biological Effects of Heavy Ions From the Standpoint of Target Theory. *Adv. Space Res.*, vol. 6, no. 11, pp. 191-198.
- King, Joseph H., 1974: Solar Proton Fluences for 1977-1983 Space Missions. *J. Spacecr. & Rockets*, vol. 11, no. 6, pp. 401-408.
- Kovalev, E. E.; Muratova, I. A.; and Petrov, V. M., 1989: Studies of the Radiation Environment Aboard Prognoz Satellites. *Nuclear Tracks & Radiat. Meas.*, vol. 16, no. 1, pp. 45-48.
- Kuhn, E.; Schwamb, F. E.; and Payne, W. T., 1965: Solar Flare Hazard to Earth-Orbiting Vehicles. *Second Symposium on Protection Against Radiations in Space*, Arthur Reetz, Jr., ed., NASA SP-71, pp. 429-434.
- McCracken, K. G., 1962a: The Cosmic-Ray Flare Effect. 1. Some New Methods of Analysis. *J. Geophys. Res.*, vol. 67, no. 2, pp. 423-434.
- McCracken, K. G., 1962b: The Cosmic-Ray Flare Effect. 2. The Flare Effects of May 4, November 12, and November 15, 1960. *J. Geophys. Res.*, vol. 67, no. 2, pp. 435-446.

Transport Methods and Interactions for Space Radiations

- McCracken, K. G., 1962c: The Cosmic-Ray Flare Effect. 3. Deductions Regarding the Interplanetary Magnetic Field. *J. Geophys. Res.*, vol. 67, no. 2, pp. 447-458.
- McDonald, Frank B., ed., 1963: *Solar Proton Manual*. NASA TR R-169.
- Nealy, John E.; Wilson, John W.; and Townsend, Lawrence W., 1988: *Solar-Flare Shielding With Regolith at a Lunar-Base Site*. NASA TP-2869.
- Nealy, John E.; Wilson, John W.; and Townsend, Lawrence W., 1989: Preliminary Analyses of Space Radiation Protection for Lunar Base Surface Systems. SAE Tech. Paper Ser. 891487.
- Nealy, John E.; Simonsen, Lisa C.; Sauer, Herbert H.; Wilson, John W.; and Townsend, Lawrence W., 1990a: *Space Radiation Dose Analysis for Solar Flare of August 1989*. NASA TM-4229.
- Nealy, John E.; Simonsen, Lisa C.; Townsend, Lawrence W.; and Wilson, John W., 1990b: Deep Space Radiation Exposure Analysis for Solar Cycle XXI (1975-1986). SAE Tech. Paper Ser. 901347.
- Norbury, John W.; and Townsend, Lawrence W., 1986: *Electromagnetic Dissociation Effects in Galactic Heavy-Ion Fragmentation*. NASA TP-2527.
- O'Brien, Keran, 1972: The Cosmic Ray Field at Ground Level. Paper presented at the Second International Symposium on the Natural Radiation Environment (Houston, Texas).
- Paić, Guy, ed., 1988: *Ionizing Radiation: Protection and Dosimetry*. CRC Press, Inc.
- Parker, James F., Jr.; and West, Vita R., eds., 1973: *Bioastronautics Data Book*, Second ed. NASA SP-3006.
- Sauer, Herbert H.; Zwickl, Ronald D.; and Ness, Martha J., 1990: *Summary Data for the Solar Energetic Particle Events of August Through December 1989*. Space Environment Lab., National Oceanic and Atmospheric Adm.
- Scott, W. Wayne; and Alsmiller, R. G., Jr., 1968: *Comparisons of Results Obtained With Several Proton Penetration Codes—Part II*. ORNL-RSIC-22 (Contract No. W-7405-eng-26, NASA Order R-104(10)), Oak Ridge National Lab.
- Shavers, Mark; Poston, John W.; Atwell, William; Hardy, Alva C.; and Wilson, John W., 1991: *Preliminary Calculation of Solar Cosmic Ray Dose to the Female Breast in Space Missions*. NASA TM-4235.
- Shea, M. A.; and Smart, D. F., 1983: A World Grid of Calculated Cosmic Ray Vertical Cutoff Rigidities for 1980.0. *18th International Cosmic Ray Conference—Conference Papers*, MG Sessions, Volume 3, Tata Inst. of Fundamental Research (Colaba, Bombay), pp. 415-418.
- Shea, M. A.; Smart, D. F.; and Gentile, L. C., 1983: The Cosmic Ray Equator Determined Using the International Geomagnetic Reference Field for 1980.0. *18th International Cosmic Ray Conference—Conference Papers*, MG Sessions, Volume 3, Tata Inst. of Fundamental Research (Colaba, Bombay), pp. 423-426.
- Shinn, Judy L.; Wilson, John W.; and Nealy, John E., 1990: *Reliability of Equivalent Sphere Model in Blood-Forming Organ Dose Estimation*. NASA TM-4178.

- Shinn, Judy L.; Wilson, John W.; Nealy, John E.; and Cucinotta, Francis A., 1990: *Comparison of Dose Estimates Using the Buildup-Factor Method and a Baryon Transport Code (BRYNTRN) With Monte Carlo Results*. NASA TP-3021.
- Shinn, Judy L.; and Wilson, John W., 1992: *An Efficient Heavy Ion Transport Code: HZETRN*. NASA TP-3147.
- Simonsen, Lisa C.; Nealy, John E.; Townsend, Lawrence W.; and Wilson, John W., 1990a: *Radiation Exposure for Manned Mars Surface Missions*. NASA TP-2979.
- Simonsen, Lisa C.; Nealy, John E.; Townsend, Lawrence W.; and Wilson, John W., 1990b: *Space Radiation Shielding for a Martian Habitat*. SAE Tech. Paper Ser. 901346.
- Simonsen, Lisa C.; and Nealy, John E., 1991: *Radiation Protection for Human Missions to the Moon and Mars*. NASA TP-3079.
- Simonsen, Lisa C.; Nealy, John E.; Sauer, Herbert H.; and Townsend, Lawrence W., 1991: *Solar Flare Protection for Manned Lunar Missions: Analysis of the October 1989 Proton Flare Event*. SAE Tech. Paper Ser. 911351.
- Singley, G. W.; and Vette, J. I., 1972: *A Model Environment for Outer Zone Electrons*. NASA TM X-69989.
- Sleeper, H. P., Jr., 1972: *Planetary Resonances, Bi-Stable Oscillation Modes, and Solar Activity Cycles*. NASA CR-2035.
- Slutz, Ralph J.; Gray, Thomas B.; West, Marie L.; Stewart, Frank G.; and Leftin, Margo, 1971: *Solar Activity Prediction*. NASA CR-1939.
- Smart, D. F.; and Shea, M. A., 1983: *Geomagnetic Transmission Functions for a 400 km Altitude Satellite*. *18th International Cosmic Ray Conference—Conference Papers*, MG Sessions, Volume 3, Tata Inst. of Fundamental Research (Colaba, Bombay), pp. 419–422.
- Smith, Robert E.; and West, George S., compilers, 1983: *Space and Planetary Environment Criteria Guidelines for Use in Space Vehicle Development*, 1982 Revision (Volume 1). NASA TM-82478.
- Space Science Board, 1970: *Radiation Protection Guides and Constraints for Space-Mission and Vehicle-Design Studies Involving Nuclear Systems*. National Academy of Sciences, National Research Council.
- Störmer, Carl, 1930: *Periodische Elektronenbahnen im Felde eines Elementarmagneten und ihre Anwendung auf Brüches Modellversuche und auf Eschenhagens Elementarwellen des Erdmagnetismus*. *Z. Astrophys.*, Bd. 1, pp. 237–274.
- Townsend, Lawrence W.; and Wilson, John W., 1985: *Tables of Nuclear Cross Sections for Galactic Cosmic Rays—Absorption Cross Sections*. NASA RP-1134.
- Townsend, Lawrence W.; Nealy, John E.; Wilson, John W.; and Atwell, William, 1989: *Large Solar Flare Radiation Shielding Requirements for Manned Interplanetary Mission*. *J. Spacecr. & Rockets*, vol. 26, no. 2, pp. 126–128.

Transport Methods and Interactions for Space Radiations

- Townsend, Lawrence W.; Nealy, John E.; Wilson, John W.; and Simonsen, Lisa C., 1990a: *Estimates of Galactic Cosmic Ray Shielding Requirements During Solar Minimum*. NASA TM-4167.
- Townsend, L. W.; Wilson, J. W.; Shinn, J. L.; Nealy, J. E.; and Simonsen, L. C., 1990b: Radiation Protection Effectiveness of a Proposed Magnetic Shielding Concept for Manned Mars Missions. SAE Tech. Paper Ser. 901343.
- Townsend, Lawrence W.; Shinn, Judy L.; and Wilson, John W., 1991: Interplanetary Crew Exposure Estimates for the August 1972 and October 1989 Solar Particle Events. *Radiat. Res.*, vol. 126, pp. 108-110.
- Webber, William R., 1966: *An Evaluation of Solar-Cosmic-Ray Events During Solar Minimum*. D2-84274-1, Boeing Co.
- Wilson, John W.; and Khandelwal, G. S., 1974: Proton Dose Approximation in Arbitrary Convex Geometry. *Nuclear Technol.*, vol. 23, no. 3, pp. 298-305.
- Wilson, John W.; and Denn, Fred M., 1976: *Preliminary Analysis of the Implications of Natural Radiations on Geostationary Operations*. NASA TN D-8290.
- Wilson, John W.; and Khandelwal, Govind S., 1976: Proton-Tissue Dose Buildup Factors. *Health Phys.*, vol. 31, no. 2, 1976, pp. 115-118.
- Wilson, John W., 1977: *Analysis of the Theory of High-Energy Ion Transport*. NASA TN D-8381.
- Wilson, John W.; and Denn, Fred M., 1977: *Implications of Outer-Zone Radiations on Operations in the Geostationary Region Utilizing the AE4 Environmental Model*. NASA TN D-8416.
- Wilson, John W., 1978: Environmental Geophysics and SPS Shielding. *Workshop on the Radiation Environment of the Satellite Power System*, Walter Schimmerling and Stanley B. Curtis, eds., LBL-8581, UC-41 (Contract W-7405-ENG-48), Univ. of California, pp. 33-116.
- Wilson, John W.; and Cucinotta, Frank, 1984: *Human Exposure in Low Earth Orbit*. NASA TP-2344.
- Wilson, John W.; and Badavi, F. F., 1986: Methods of Galactic Heavy Ion Transport. *Radiat. Res.*, vol. 108, pp. 231-237.
- Wilson, J. W.; Townsend, L. W.; and Badavi, F. F., 1987: Galactic HZE Propagation Through the Earth's Atmosphere. *Radiat. Res.*, vol. 109, no. 2, pp. 173-183.
- Wilson, John W.; and Townsend, L. W., 1988: A Benchmark for Galactic Cosmic-Ray Transport Codes. *Radiat. Res.*, vol. 114, no. 2, pp. 201-206.
- Wilson, John W.; Townsend, Lawrence W.; Nealy, John E.; Chun, Sang Y.; Hong, B. S.; Buck, Warren W.; Lamkin, S. L.; Ganapol, Barry D.; Khan, Ferdous; and Cucinotta Francis A., 1989: BRYNTRN: A Baryon Transport Model. NASA TP-2887.

- Wilson, John W.; Shinn, Judy L.; and Townsend, Lawrence W., 1990: Nuclear Reaction Effects in Conventional Risk Assessment for Energetic Ion Exposure. *Health Phys.*, vol. 58, no. 6, pp. 749-752.
- Wilson, John W.; Khandelwal, Govind S.; Shinn, Judy L.; Nealy, John E.; Townsend, Lawrence W.; and Cucinotta, Francis A., 1990: *Simplified Model for Solar Cosmic Ray Exposure in Manned Earth Orbital Flights*. NASA TM-4182.
- Wilson, John W.; Chun, Sang Y.; Badavi, Forooz F.; Townsend, Lawrence W.; and Lamkin, Stanley L., 1991: HZETRN: A Heavy Ion/Nucleon Transport Code for Space Radiations. NASA TP-3146.
- Yablontsev, N. N., 1990: Documents Setting Standards for Radiation Safety for Space Flight. *Kosm. Biol. Aviakosmicheskaya Meditsina*, vol. 24, no. 1, p. 55.
- Zirin, Harold; and Liggett, Margaret A., 1987: Delta Spots and Great Flares. *Sol. Phys.*, vol. 113, nos. 1 & 2, pp. 267-283.

11

12

13

14

15

16

17

18

19

Chapter 13

Radiation Safety in the Earth's Atmosphere

13.1. Introduction

When the possibility of high-altitude supersonic commercial aviation was first seriously proposed, Foelsche (1962) brought to light a number of concerns with respect to atmospheric radiation. Subsequently, a detailed study of the atmospheric radiation components at high altitudes was conducted from 1965 to 1971 at the Langley Research Center (LaRC) by Foelsche et al. (1974). In that study the major role of atmospheric neutrons in radiation exposure was uncovered. These studies utilized an instrument package consisting of tissue equivalent ion chambers, organic scintillator neutron spectrometers, and nuclear emulsion. A theoretical program to predict atmospheric radiation levels and to specifically extend the neutron spectrum into the range outside that measured by the scintillation spectrometer was also developed (Wilson et al., 1970). It was found that the neutron spectrum due to galactic cosmic rays was nearly independent of solar modulation. However, the neutron spectrum produced by solar cosmic rays was found to vary from event to event. An overview of that program is given by Foelsche (1977). The conclusion of this previous work was that high-altitude commercial aviation required special considerations for radiation protection (Wilson, 1981), whereas the worst-case flights for pre-1980 subsonic airlines were well within the exposure limits of the general population (Foelsche et al., 1974; Friedberg and Neas (in Anon., 1980)).

Three factors have changed since those studies: (1) increases in quality factors seem imminent (ICRU 40 (Anon., 1986); Sinclair¹); (2) reduced exposure limits are being proposed; and (3) flight crews are logging greatly increased hours at altitude (Bramlitt, 1985; Wilson and Townsend, 1988 and 1989; Friedberg et al., 1989; Busick, 1989; Barish, 1990). At present, the Langley data base on biologically important components appears to be the most complete and comprehensive available, but updating with new quality factors and providing for easy use by the health physics community is required. Furthermore, concerns on atmospheric radiation exposure remain for such NASA-related aircraft as the National Aero-Space Plane, the Advanced Supersonic Transport, and the Hypersonic Transport.

A computer program called GREP (Galactic Radiation Exposure Program) was written by S. B. Curtis of the Boeing Company over 20 years ago. The dose was estimated using the ion chamber data of Neher (1961) and Neher and Anderson (1962) and the neutron data of Hess, Canfield, and Lingenfelter (1961). The code was modified for various aircraft trajectories between city pairs by Wallace and Sondhaus (1978). The inadequacy of the data base used was reviewed by Foelsche (1962) and Friedberg and Neas (in Anon., 1980). A similar code was written later using the theoretical model of O'Brien and McLaughlin (1972) for atmospheric radiation. In this later code (Friedberg et al., 1989) the O'Brien-McLaughlin theoretical model was used with neutron, proton, and pion dose equivalents increased by a factor of 2 in accordance with the recommendations

¹ Sinclair, W. K.: Recent Developments in Estimates of Cancer Risk From Ionizing Radiation. Paper presented at the 20th SAE International Conference on Environmental Systems (Williamsburg, VA), July 9-12, 1990.

of NCRP 91 (Anon., 1987). On the basis of analysis of the high-latitude data of Foelsche et al. (1974) using the newly proposed quality factors of ICRU 40 (Anon., 1986), the increase of quality factor by a factor of 2 does not seem fully justified (Wilson and Townsend, 1988; Shinn, Wilson, and Ngo, 1990) and should be substantially conservative in exposure estimates. In the present chapter we undertake a reanalysis of the quality factor increase using measured field quantities. Furthermore, the use of measured data within the Earth's atmosphere is not governed by the uncertainty associated with the galactic cosmic ray (GCR) spectrum and charge distribution (Wilson, Shinn, and Townsend, 1990) and the uncertainty in their propagation in the atmosphere (Wilson, Townsend, and Badavi, 1987). Indeed, the measured data are the primary sources of information on the atmospheric exposure levels and their meaning in terms of biological risk.

In the present chapter we use currently known data to generate radiation field values within the Earth's atmosphere as a function of time. These are compared where possible with values obtained by other methods. The data base will ultimately provide a test bed for the transport codes discussed in previous chapters. In addition, the newly developed codes will provide information on high linear energy-transfer (LET) components in the uppermost atmosphere of importance to future NASA missions such as the National Aero-Space Plane (NASP).

13.2. Solar Effects on Atmospheric Radiations

Very little ionizing radiation would be found in the Earth's atmosphere were it not for the presence of extraterrestrial energetic particulate radiation. These extraterrestrial particles have two primary sources. The first discovered source is the diffuse component originating from remote regions of our galaxy (galactic cosmic rays or GCR), and the second source is a more local and more directed source from our local star, Sol (solar cosmic rays or SCR). Both sources contain particles consisting mainly of protons and smaller amounts of heavier particles as elements stripped of their electrons. Both show time variations correlated with the natural solar cyclic processes most easily observed as magnetic disturbances in the solar surface called sunspots. The area of the solar disk covered by sunspots varies in cycles lasting from 10.5 to 13 years. Detailed records exist on solar observations for 21 complete cycles, and we are currently near the maximum of cycle 22. A more fragmentary record exists for several hundred years. The solar cycle affects the extraterrestrial particulate environment in two ways.

The solar plasma output (solar wind) increases during years of high solar activity associated with the expanding solar corona. The expanding plasma field entraps the local solar magnetic field at the time of ejection and transports it outward into the solar system. The GCR are denied access to the solar system according to the status of the interplanetary plasma, and they are modulated by the solar cycle. The modulation must wait for the plasma to fill a certain region of space (out to several astronomical units (AU)). The time delay depends on the solar wind velocity, and the time to reach equilibrium with the sunspot number depends on the rate of rise in solar activity. Because of these delays, the GCR intensity in relation to sunspot number shows a typical hysteresis effect. Such a curve using neutron monitor data (Freier and Waddington, 1965) is shown in figure 13.1

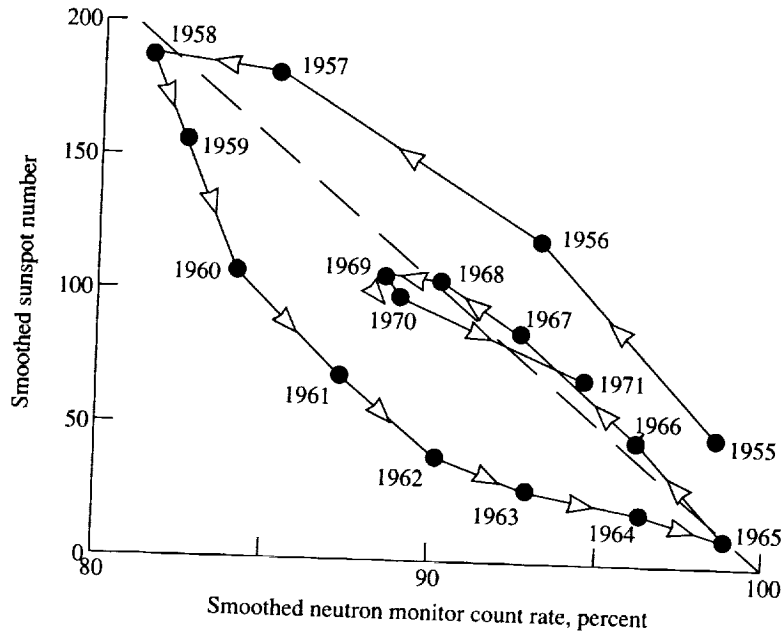


Figure 13.1. Regression plot between smoothed sunspot numbers and smoothed neutron monitor count rates of Mount Washington in New Hampshire and the Deep River neutron monitor (DRNM) in Canada.

for cycle 19 for 1955 to 1965. (A neutron monitor is a ground level device sensitive to neutrons produced in a lead converter by nuclear particles and has been in use for 50 years to observe cosmic-ray intensities.) If we imagine that the time delays are removed, we conjecture that all the data would lie on the correlation curve given as the dashed line. Note that the more slowly rising cycle 20 shown as 1965 to 1971 appears nearly in equilibrium with the modulation effects and closely approximates the correlation curve.

The magnetic irregularities observed as sunspots are responsible for the acceleration of the plasma of the solar surface. This occurs especially when magnetic regions coalesce into plages and their individual magnetic fields annihilate, thus generating large electric fields that accelerate the local plasma (solar flare) to very high energies (sometimes more than 15 GeV). Such particles escape the solar surface and propagate outward along the sectorized magnetic field lines into interplanetary space. Such particles are sometimes seen arriving at the Earth. The events are most likely to cause local cosmic ray increases on the Earth if the solar flare occurred on the western limb. SCR arriving at Earth vary by orders of magnitude in intensity and spectral content and very few events are of importance to present-day commercial aircraft operation (operating below 50 000 ft).

13.3. Background Radiation Data Base

13.3.1. Radiation levels at high latitude. The low-level background radiation in the Earth's atmosphere is generated by the impact of the GCR on the top of the atmospheric layer. The incident GCR intensity varies in time

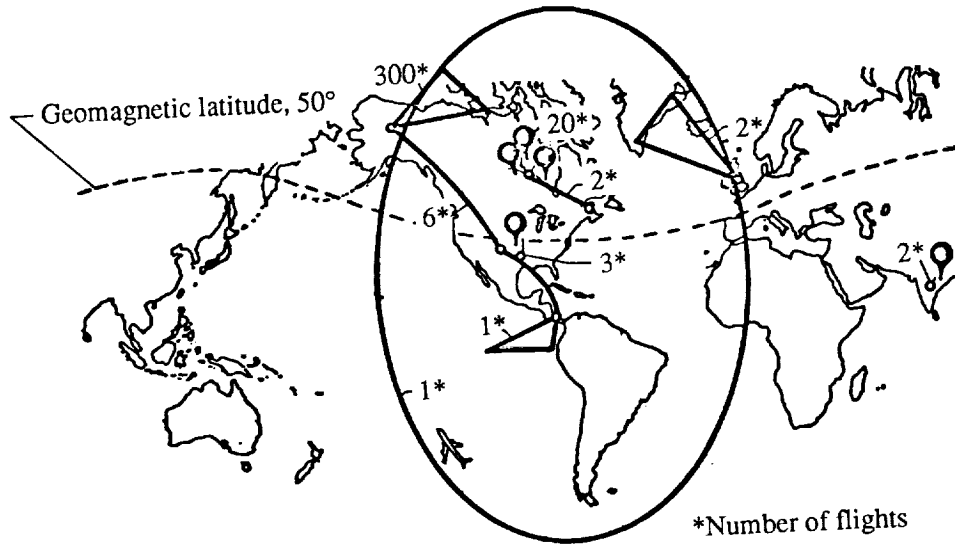


Figure 13.2. High-altitude radiation measurements made between 1965 and 1971.

because of solar modulation and over the surface because of exclusion of the lower energy particles as one approaches the equator by a deflection in the Earth's magnetic field. The representation of the time variations will be accomplished through keying the background to the high-latitude neutron monitor count rates (percent of maximum), and the geomagnetic effects are handled by expressing the environment in terms of the local geomagnetic vertical cutoff rigidity. (Rigidity is related to the radius of curvature of a charged particle in moving through a magnetic field.)

The NASA study is indicated in figure 13.2. The experimental package consisted of encapsulated NE-222 liquid scintillators for neutron spectral measurements throughout the fast neutron region and above, tissue equivalent ion chambers, and nuclear emulsion. The tissue equivalent ion chamber measures the overall radiation dose, and the neutron spectrometer and nuclear emulsion allow an assessment of the high LET components. There were 25 high-altitude balloon flights at various times in cycle 20 and at different latitudes. The balloon flights provide the best altitude survey of environmental quantities. There were over 300 airplane flights using General Dynamics/Martin RB-57F, Lockheed U-2, and Boeing 707 airplanes. The airplanes provided detailed latitude surveys, balloon calibration rendezvous flights, and flights during solar flare events. Because of limited funds, it is unfortunate that not all the data could be finally reduced and that we could not continue the flight program through August 1972 when an extremely large solar event occurred. A more detailed description of the experiment is given by Foelsche et al. (1974) and Korff et al. (1979).

Figure 13.3 shows the measurements made on a high-altitude balloon flight during galactic cosmic ray maximum at 69° N geomagnetic latitude. The instruments for this flight were only lightly shielded (less than 1 g/cm² of fiber glass and foam for thermal insulation). The features to be noted in figure 13.3 are the

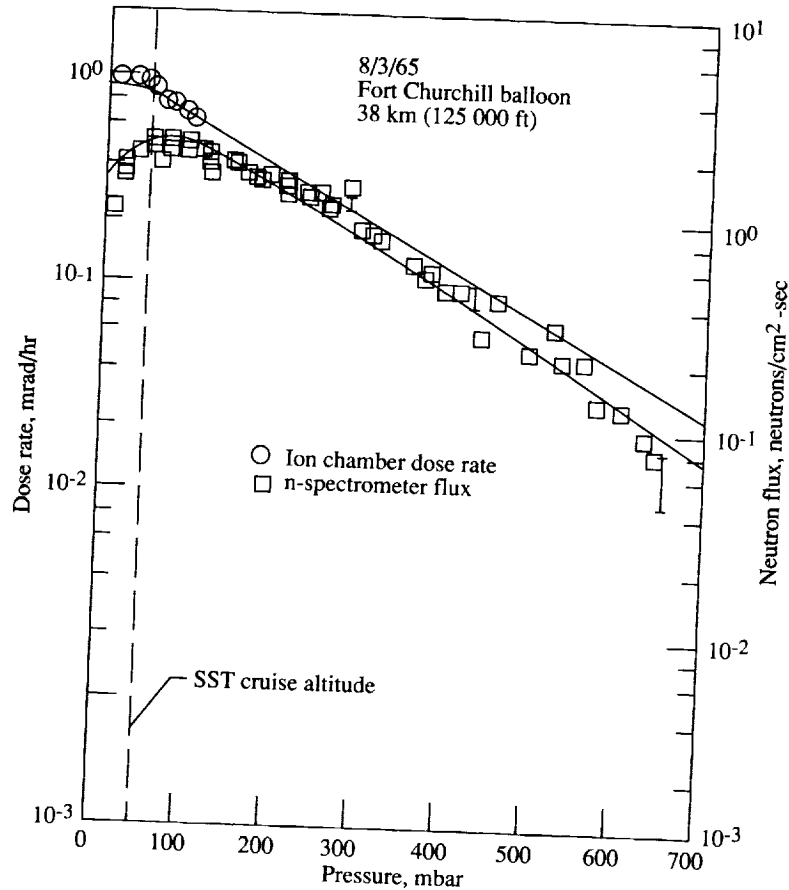


Figure 13.3. Galactic cosmic-ray maximum (August 3, 1965; 1 year after sunspot minimum; Fort Churchill, Canada; geomagnetic latitude $\approx 69^\circ$). Neutron flux from 1 to 10 MeV (right scale), and ion chamber dose rate (left scale) is a function of altitude.

broad maximum in the neutron flux, with peak at 60 to 70 millibars (mbar) and the leveling off of the ion chamber dose rate above 50 mbar ($1 \text{ mbar} \approx 1 \text{ g/cm}^2$). Also shown is the present neutron model environment to be discussed and the model dose rate in tissue to be compared with ion chamber data.

Figure 13.4 shows data from a low-altitude balloon flight during galactic cosmic-ray maximum (1 month after the flight shown in figure 13.3) at 55° N geomagnetic latitude. Note that although the ionization dose rate is considerably reduced, the neutron flux has changed very little. These reductions are due to the increase in geomagnetic cutoff energies when going to lower latitudes. The proton cutoff at Fort Churchill, Canada, caused by solar modulation may have been on the order of a few hundred MeV because of the residual atmosphere (geomagnetic cutoff of 2 MeV), and the geomagnetic proton cutoff at St. Paul, Minnesota, during the magnetically quiet period at the beginning of September 1965 was approximately 800 MeV. The present neutron model environment and tissue dose rate agree well with the data.

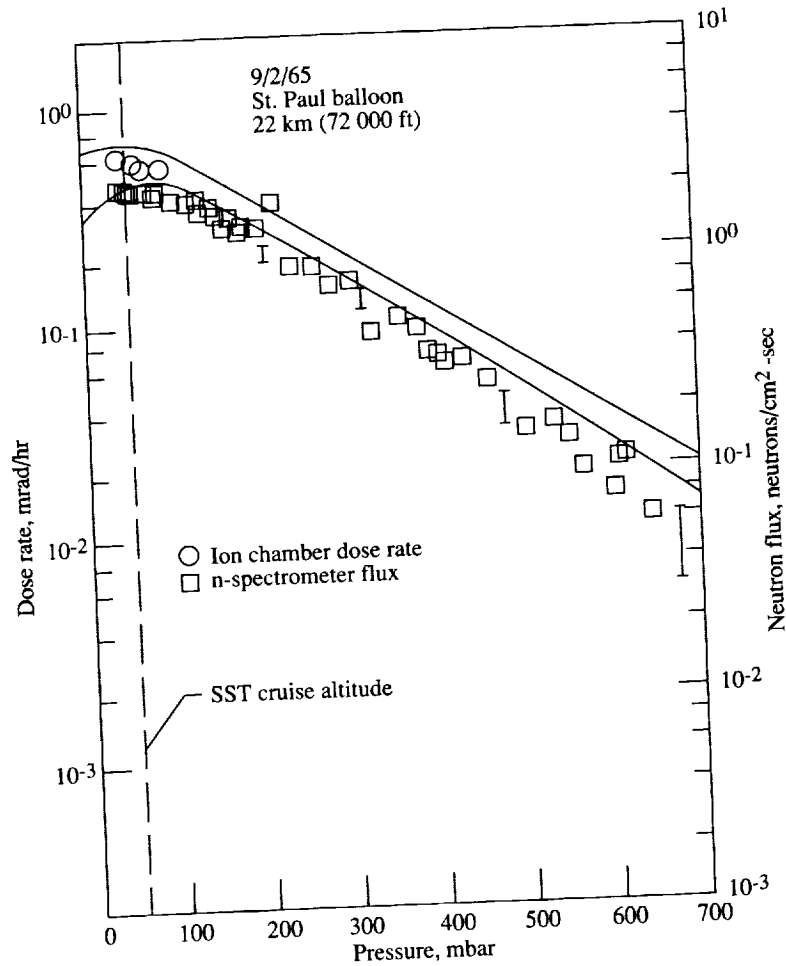


Figure 13.4. Galactic cosmic-ray maximum (September 2, 1965; St. Paul, Minnesota; geomagnetic latitude $\approx 55^\circ$). Neutron flux from 1 to 10 MeV (right scale), and ion chamber dose rate (left scale) is a function of altitude. Compare with data in figure 13.3 at higher latitude.

Shown in figure 13.5 are data from a second flight above Minnesota. This flight differs from the one shown in figure 13.4 in that the ion chamber and neutron spectrometer were placed in a spherical shell of tissue equivalent material (phantom) 15 cm or 15 g/cm² thick. The ion chamber dose rate is not appreciably changed from the earlier flight. (See fig. 13.4.) The neutron flux has decreased significantly, and the neutron energy spectrum was found to be flatter in the range from 1 to 10 MeV. This reduction is due to the relatively large moderation of neutrons of energies below about 10 MeV by the hydrogen in the phantom, which outweighs the production of new neutrons by the calcium, carbon, and nitrogen in the phantom.

In figure 13.6 data are plotted for a flight from Fort Churchill, Canada, in a period of increased solar activity, which is typical for about 2 years after galactic

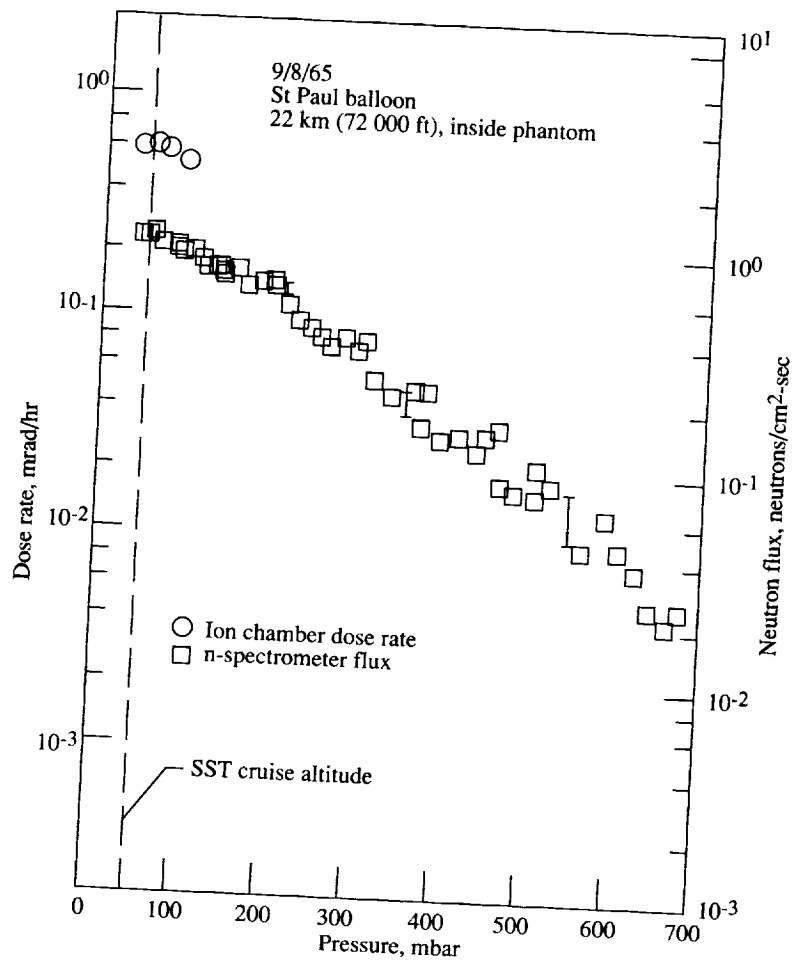


Figure 13.5. Galactic cosmic-ray maximum (September 8, 1965; St. Paul, Minnesota; geomagnetic latitude $\approx 55^\circ$). In flights of figures 13.3 and 13.4, the sensors were lightly shielded (less than 1 g/cm^2 of fiber glass and foam). In this flight, the sensors were surrounded by tissue equivalent material, including calcium, of about 15 g/cm^2 thickness to obtain an approximate measurement of the neutron fluxes and ion chamber dose rates in the center of the human body.

cosmic-ray maximum. The ion chamber dose rate and the neutron flux decreased by about the same percentage during the 2 years. These decreases are due to a corresponding increase in the scattering power of the interplanetary magnetic fields. The solid line between 0 and 300 g/cm^2 in figure 13.6 is the altitude profile of neutron intensities 1 to 10 MeV as obtained from the theoretical nucleon cascade calculations described by Wilson et al. (1970). The neutron flux and tissue dose rate of the present model environment are also shown.

Table 13.1 contains neutron fluxes and spectral indices in the range from 1 to 10 MeV for flights during 1965 to 1968 at high latitudes at an atmospheric depth

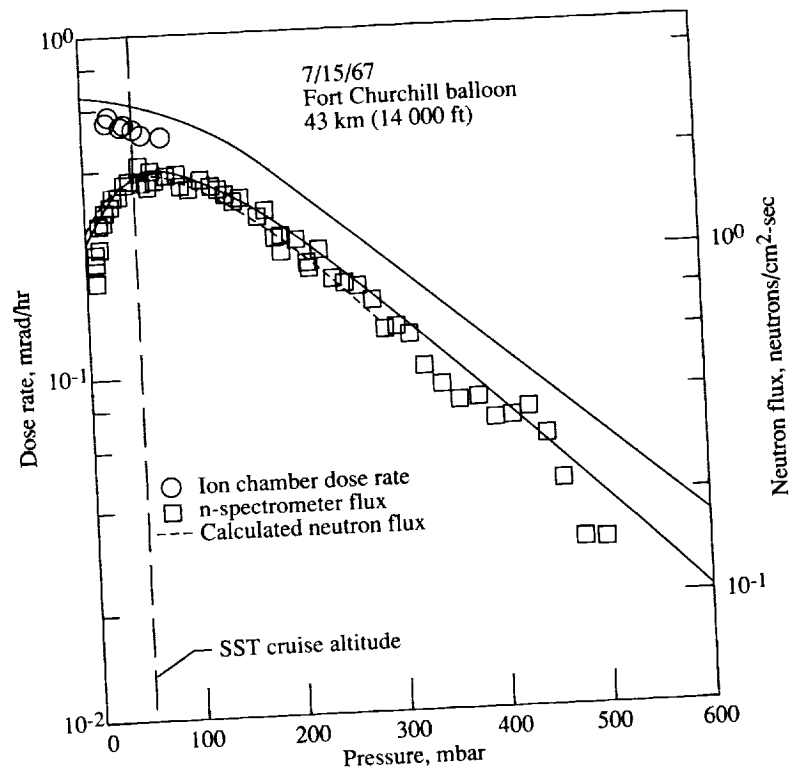


Figure 13.6. Galactic cosmic rays 2 years after galactic cosmic-ray maximum (July 15, 1967; Fort Churchill, Canada; geomagnetic latitude $\approx 69^\circ$). Compare with figure 13.3 for a flight at galactic cosmic-ray maximum. The neutron flux and ion chamber dose rate have both decreased about 25 to 30 percent at SST altitudes (solar modulation). The solid line is the altitude dependence obtained by theory.

Table 13.1. Neutron Flux (Integral Flux in Range From 1 to 10 MeV) and Spectral Index (Differential Energy Spectrum $\approx AE^{-x}$) at SST Altitude

Date	Location ^a	Shielding ^b	Flux, neutrons/cm ² -sec	Spectral index, x	DRNM
8/3/65 ^c	Ft. Churchill	Air	2.46	1.26	7038
9/2/65	St. Paul	Air	2.16	1.29	6999
7/15/67 ^c	Ft. Churchill	Air	1.81	1.23	6644
7/18/68 ^c	Ft. Churchill	Air	1.52	1.16	6389
8/9/65 ^c	Ft. Churchill	Air + phantom	1.35	.96	7004
9/8/65	St. Paul	Air + phantom	1.08	.86	7018

^aLocations: Ft. Churchill, Canada, and St. Paul, Minnesota.

^bPhantom denotes tissue equivalent material.

^cUsed in dose calculations.

of approximately 60 g/cm^2 or an altitude of 20 km (65 000 ft). These data were supplemented by theoretical extrapolations of the neutron spectra (see Wilson, Lambiotte, and Foelsche, 1969; Wilson et al., 1970; Wilson, 1972) in the range from 0.1 to 1 MeV according to the spectral shape calculated by Newkirk (1963) and in the range from 10 to 500 MeV according to the flat spectral slope ($E^{-1.2}$), first found by J. W. Wilson using Monte Carlo nucleon transport calculations on the basis of neutron production cross sections for incident protons up to 2 GeV energy of Bertini (1967) and semiempirical extrapolation to 10 GeV.

In figure 13.7, as an example for the neutron dose determinations, the neutron spectrum from galactic cosmic rays measured from 1 to 10 MeV at supersonic transport (SST) altitude on August 3, 1965, above Fort Churchill is extrapolated by the preceding method to lower energies (0.01 MeV) and higher energies (500 MeV); the results of the Monte Carlo calculations are shown by the horizontal dashes representing the neutron fluxes compiled in the corresponding energy bins. From this spectrum the dose and dose equivalent rates for hands and feet due to neutrons are obtained by summing the dose rates resulting from multiplying the flux in each energy interval by the corresponding flux-to-dose rate conversion factor for the extremities. The resulting dose rate is $1.23 \mu\text{Gy/hr}$ (0.123 mrad/hr), and the corresponding dose equivalent rate is $7.72 \mu\text{Sv/hr}$ (0.772 mrem/hr). In addition to the spectrum, the separate contributions in the different energy ranges to the dose and dose equivalent rates are indicated in figure 13.7 (linear scale). The neutrons of energies greater than 10 MeV are found to contribute (through recoil protons and stars) 35 percent to the total dose equivalent rate of neutrons. The neutrons of energy from 0.1 to 1 MeV, assumed to have an energy spectrum similar to that given by Newkirk, contribute about 27 percent. The unmeasured part of the spectrum thus contributes about 70 percent to the neutron dose equivalent rate in extremities.

The main results of these measurements on galactic cosmic rays are the determination of both the absolute values of the energetic secondary neutron fluxes (1 to 10 MeV) and the dose as measured with tissue equivalent ion chambers. The neutron spectrum, which was in doubt before the present experiments, especially for high latitudes and altitudes, was found to be of a flatter spectrum. The tissue equivalent ion chamber yielded the contributions of neutrons (via recoil protons) to the absorbed dose in tissue, which is not obtained in conventional metal-walled ion chambers. In addition, the actual measurements of neutron spectra and tissue dose rates inside a spherical body phantom experimentally relate the dose equivalents in thin tissue equivalent samples (corresponding to the extremities) to the depth dose equivalents in the human body, and thus confirm theoretical calculations (Foelsche et al., 1974).

The theoretical spectra have as yet to be normalized by adjusting the absolute intensities to the measured neutron spectra in the range from 1 to 10 MeV. The theoretical spectra are based on calculations for proton primaries and do not accurately take into account the α -particles and heavier nuclei that are present in galactic and solar cosmic rays because the secondary production cross sections in reactions with air have not been satisfactorily determined either theoretically or

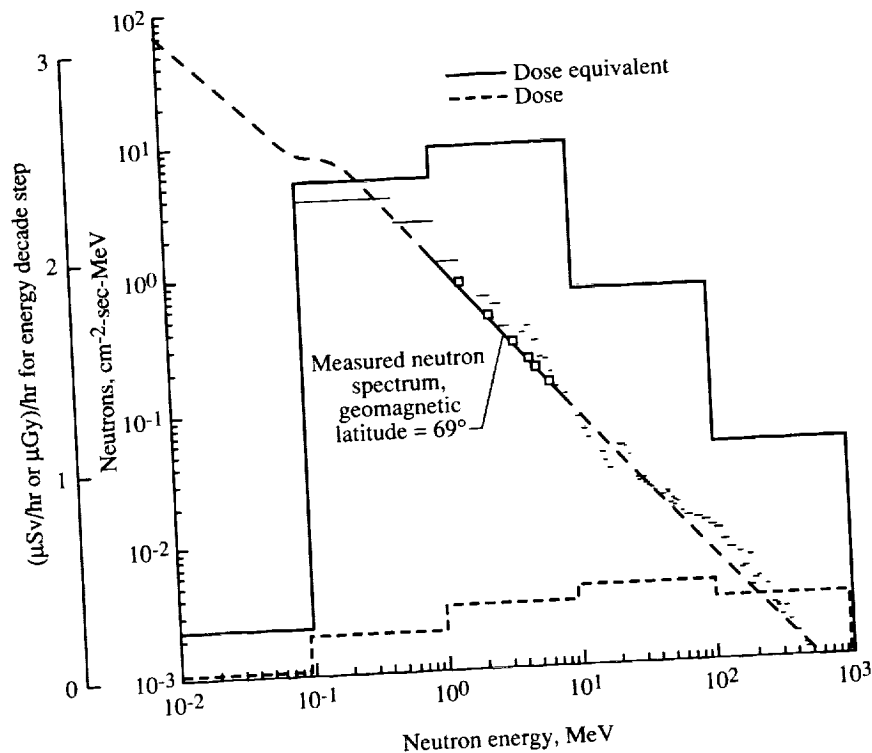


Figure 13.7. High-latitude (geomagnetic latitude $\approx 69^\circ$) neutron spectrum measured at SST altitudes ($\approx 50 \text{ g/cm}^2$) on August 3, 1965 (heavy solid line between 1 and 10 MeV), by Mendell in Korff et al. (1979) with its extension to lower and higher energies (heavy dashed curve) compared with the shape of the Monte Carlo spectrum (histogram, horizontal dashes). The linear scale is for the dose rates in extremities calculated from the NASA spectrum (Sv—heavy step curve; Gy—dashed step curve).

experimentally. For the present purposes, it is considered satisfactory to assume that only the intensity, and not the shape, of the neutron spectra at subsonic and supersonic jet altitudes is substantially changed by the heavier primaries.

The various contributions to the total dose equivalent rate as measured in high latitudes for the initial phases of the present solar cycle (1965 to 1968) are shown in figure 13.8. The different contributions in the figure correspond to the types of instrumentation with which the measurements were made. The tissue equivalent ion chamber measures only the energy deposited in a thin tissue sample (that is, the absorbed dose rate) by all radiation components. This measurement, however, does not provide the biologically equivalent dose rate since much of the dose equivalent rate is due to components with a quality factor Q_F greater than unity, such as proton recoils and heavily ionizing star prongs in tissue from neutron and charged-particle reactions with tissue nuclei. These contributions to the excess of the total dose equivalent over the corresponding absorbed dose given by the tissue equivalent ion chamber (Sv minus Gy) are referred to as the $Q_F - 1$ increments. They are derived by an analysis of the neutron spectrometer

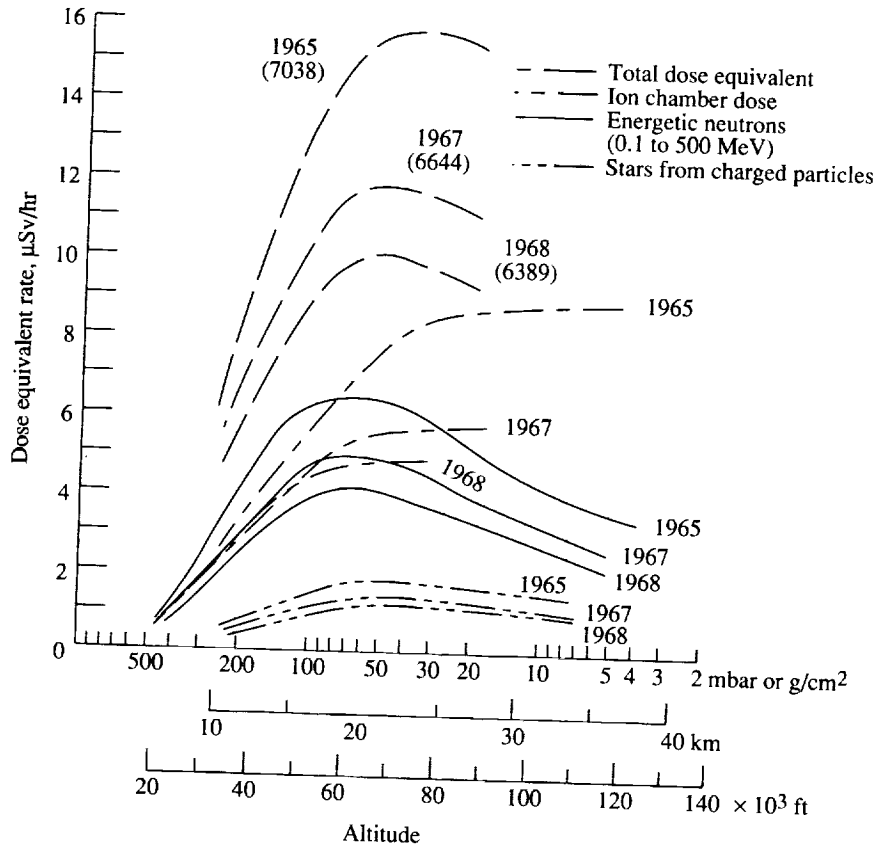


Figure 13.8. Galactic cosmic-ray dose equivalent rates for extremities (hands and feet) and approximately for eyes as a function of altitude at different phases of the solar cycle for high latitudes.

and tissue equivalent nuclear emulsion data. (The nuclear emulsion data from the British Royal Aerospace Establishment (R.A.E.) were used, as explained subsequently.) The components of the total dose equivalent rate, derived from measurements and shown in figure 13.8, are as follows:

(1) The tissue absorbed dose rate from all radiation components, that is, from charged primaries and secondaries, including mesons, gamma rays, neutrons (via recoil protons, heavy recoils, and neutron-produced stars), and stars produced by energetic charged particles, all of which are measured in the tissue equivalent ion chamber. As explained before, some of these components have, because of their large linear energy transfer, a quality factor greater than unity. This excess constitutes parts (2) and (3).

(2) The $Q_F - 1$ increment rate produced in tissue by energetic neutrons (0.1 to 500 MeV) via recoils and stars.

(3) The $Q_F - 1$ increment rate caused by stars in tissue produced by primary and secondary charged particles.

Component (2), the neutron $Q_F - 1$ increment rate, is found from the measured neutron fluxes in the range from 1 to 10 MeV extended to lower and higher energies as explained in a previous paragraph (see fig. 13.7) by subtracting the inferred dose rate from the inferred neutron dose equivalent rate. The neutron $Q_F - 1$ increment rate on August 3, 1965, at SST altitude is thus found, for example, for the extremities as $6.5 \mu\text{Sv/hr}$ (i.e., $7.72 - 1.23$, see fig. 13.7).

Component (3), the dose equivalent rate due to stars produced by charged particles, was derived from measurements at different altitudes in tissue equivalent emulsions by P. J. N. Davison of the British R.A.E., where the increment is referred to as "star damage energy." The total star $Q_F - 1$ increment derived by Davison included the contribution of neutron-produced stars already taken into account in (2); the star contribution from charged particles is approximately one-half of the total star $Q_F - 1$ increment at high altitudes (20 km (65 000 ft) to 34 km (100 000 ft)) and one-third of the total star $Q_F - 1$ increment at subsonic altitudes (11 km (37 000 ft)), as theoretical calculations indicate. This part is plotted in figure 13.8. The total dose equivalent rate is obtained by summing parts (1), (2), and (3).

The total extremity dose equivalent rate in figure 13.8 in high latitudes as a function of altitude exhibits a maximum at about 35 g/cm^2 (22 km or 75 000 ft) during galactic cosmic-ray maximum (approximately 1 to 2 years after sunspot minimum). The maximum decreases in magnitude and appears to move deeper into the atmosphere as the galactic cosmic-ray minimum is approached. This peak is mainly due to the broad maximum in the neutron fluxes at these altitudes. (See the neutron data in figs. 13.3 and 13.6 and the neutron contribution in fig. 13.8.) The absorbed energy measured in the ion chamber does not exhibit this peak. It may furthermore be noted that the neutron dose equivalent rate contributes about 50 percent to the total dose equivalent rate at these altitudes.

13.3.2. Radiation levels within the geomagnetic field. The latitude surveys were made mostly by airplanes so that the relation between airplane count rates and balloon count rates needs to be established (the effect of neutron production and moderation by the airplane structure). The airplane count rates are found to be 10 percent higher in balloon rendezvous flights with identical instruments as well as within the solar cycle for the same instrument (Korff et al., 1979) as shown in figure 13.9. The latitude surveys by balloons and airplanes are shown in figure 13.10 at the transition maximum and at 250 g/cm^2 for different phases of solar cycle 20. The curves in the figure are our approximation to the data given by

$$\begin{aligned} \phi_{1-10}(x_m, R, C) = & 0.23 \\ & + [1.1 + 0.167(C - 100)] \exp\left(\frac{-R^2}{81}\right) + \left[0.991 + 0.0501(C - 100)\right. \\ & \left. + 0.4 \exp\left(\frac{(C - 100)}{3.73}\right)\right] \exp\left(\frac{-R^2}{12.96}\right) \end{aligned} \quad (13.1)$$

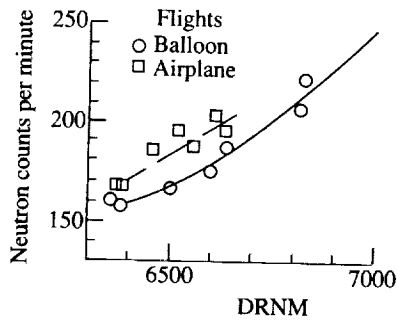


Figure 13.9. Count rates of neutron channels 2-7 in balloon flights and airplane flights. Effect of airplane material on neutron count rates is illustrated.

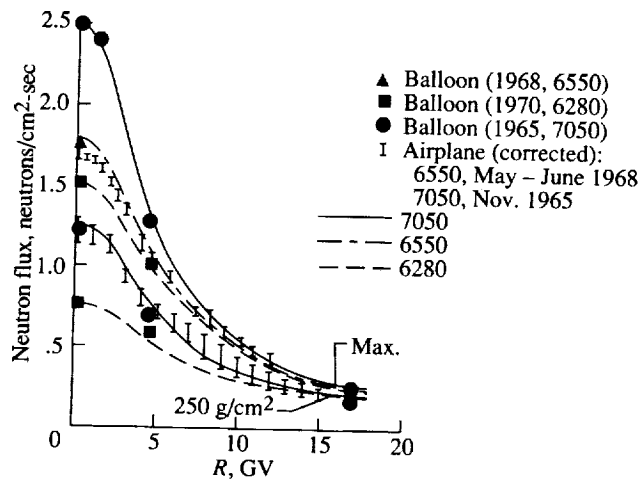


Figure 13.10. Fast neutron flux (in range from 1 to 10 MeV) at the transition maximum and at 250-g/cm² depth as a function of vertical cutoff rigidity R for various times in the solar cycle and DRNM count rates.

at the transition maximum and

$$\begin{aligned} \phi_{1-10}(250, R, C) = & 0.17 \\ & + [0.787 + 0.035(C - 100)] \exp\left(\frac{-R^2}{25}\right) \\ & + \left[-0.107 - 0.0265(C - 100) \right. \\ & \left. + 0.612 \exp\left(\frac{(C - 100)}{3.73}\right) \right] \exp\left(\frac{-R^2}{139.2}\right) \end{aligned} \quad (13.2)$$

at depths of 250 g/cm² in the atmosphere where R is local cutoff rigidity (in units of GV) and C is the high-latitude neutron monitor count rate in percent of maximum. At depths below 250 g/cm², the neutrons attenuate with attenuation length (g/cm²) given by

$$\lambda = 165 + 2R \quad (13.3)$$

The flux at all altitudes is approximated as

$$\phi_{1-10}(x, R, C) = f(R, C) \exp\left(\frac{-x}{\lambda}\right) - F(R, C) \exp\left(\frac{-x}{\Lambda}\right) \quad (13.4)$$

where

$$f(R, C) = \exp\left(\frac{250}{\lambda}\right) \phi_{1-10}(250, R, C) \quad (13.5)$$

$$\Lambda = \lambda \left[1 - \frac{\phi_{1-10}(x_m, R, C) \exp\left(\frac{x_m}{\lambda}\right)}{f(R, C)} \right] \quad (13.6)$$

and

$$F(R, C) = \frac{\Lambda}{\lambda} f(R, C) \exp\left(\frac{x_m}{\Lambda} - \frac{x_m}{\lambda}\right) \quad (13.7)$$

where the transition maximum altitude corresponds to

$$x_m = 50 + \ln \left\{ 2000 + \exp[-2(C - 100)] \right\} \quad (13.8)$$

The neutron environment model given by equations (13.1) to (13.8) is shown in figures 13.3, 13.4, and 13.6 in comparison with the experimental data. The flux from 1 to 10 MeV is converted to dose equivalent and dose using 3.14 $\mu\text{Sv-cm}^2\text{-sec/hr}$ (0.314 mrem-cm²-sec/hr) and 0.5 $\mu\text{Gy-cm}^2\text{-sec/hr}$ (0.05 mrad-cm²-sec/hr), respectively. The accepted quality factor within the U.S. is the one in ICRP 26 (Anon., 1977) and is used in the current estimates.

Unfortunately, not all ion chamber data or all nuclear emulsion data were reduced. For our present purpose we will use the argon-filled ion chamber data to represent the altitude, latitude, and solar cycle dependence and use the available tissue equivalent ion chamber data as a guide. The ion chamber data of GREP

Table 13.2. Ionization Rates in Air Measured by Argon-Filled Chambers^a
at Solar Minimum ($C = 98.3$ in 1965)

R, GV	Ion pairs, $\text{cm}^{-3}\text{-sec}^{-1}$, for air depths, g/cm^2 , of—													
	30	40	50	60	70	80	90	100	120	140	200	245	300	1034
0	445.0	430.0	414.0	399.0	383.0	366.0	349.0	332.0	298.0	266.0	181.0	136.0	95.0	1034
.01	445.0	430.0	414.0	399.0	383.0	366.0	349.0	332.0	298.0	266.0	181.0	136.0	95.0	11.4
.16	444.0	430.0	414.0	399.0	383.0	366.0	349.0	332.0	298.0	266.0	181.0	136.0	95.0	11.4
.49	411.8	404.3	394.4	382.0	369.0	354.8	339.4	325.0	292.3	264.5	181.0	136.0	95.0	11.4
1.97	325.0	333.0	340.0	335.0	330.0	312.5	308.0	300.0	285.0	264.0	181.0	134.0	95.0	11.4
2.56	300.0	305.0	310.0	305.0	300.0	290.0	285.0	280.0	255.0	230.0	173.0	126.0	95.0	11.4
5.17	185.0	195.0	208.0	208.0	208.0	208.0	208.0	208.0	195.0	185.0	135.0	103.0	75.0	10.6
8.44	127.6	137.0	145.0	150.2	153.8	155.8	156.0	154.6	149.7	142.2	111.3	87.0	66.6	10.4
11.70	85.0	92.0	98.0	100.0	102.0	105.0	107.0	110.0	108.0	105.0	80.0	77.0	60.0	10.0
14.11	70.0	75.0	82.0	85.0	89.0	93.6	95.0	100.0	98.0	95.0	78.0	68.8	50.0	10.0
17.00	66.3	73.8	80.0	84.8	88.5	91.1	92.6	93.5	93.4	90.5	75.0	62.3	48.0	10.0

^aExperimental data extrapolated to provide estimates of ionization rates over a wide range of altitudes and geomagnetic cutoffs.

Table 13.3. Ionization Rates in Air Measured by Argon-Filled Chambers^a
at Solar Maximum ($C = 80$ in 1958)

R, GV	Ion pairs, $\text{cm}^{-3}\text{-sec}^{-1}$, for air depths, g/cm^2 , of—													
	30	40	50	60	70	80	90	100	120	140	200	245	300	1034
0	264.6	267.5	267.0	265.0	258.0	252.0	243.0	235.0	216.3	197.0	145.0	109.2	78.8	11.4
.01	264.6	267.8	267.0	265.0	258.0	251.0	243.0	235.0	216.3	197.0	145.0	109.2	78.8	11.4
.16	264.0	264.9	265.0	264.0	257.0	250.0	243.0	233.0	215.0	197.0	145.0	109.2	78.8	11.4
.49	264.0	264.9	265.0	262.0	256.0	249.0	242.0	231.0	213.2	197.0	145.0	109.2	78.8	11.4
1.97	264.0	265.0	265.0	262.0	252.0	245.0	241.0	231.0	212.5	197.0	145.0	107.8	78.8	11.4
2.56	235.0	237.5	240.0	240.0	239.0	238.0	237.0	230.0	209.0	197.0	145.0	101.6	78.8	11.4
5.17	162.5	168.0	179.0	182.0	178.0	175.2	174.0	173.8	170.0	160.0	159.0	88.3	65.0	10.6
8.44	95.0	103.5	112.0	118.0	118.0	119.0	120.0	122.0	118.0	117.0	100.6	78.7	60.2	10.4
11.70	78.2	85.0	90.7	92.7	94.8	98.0	100.0	103.1	101.2	98.4	75.0	72.2	56.2	10.0
14.11	65.7	70.7	77.5	80.5	84.3	89.0	90.5	95.3	93.5	90.9	74.0	65.9	47.9	10.0
17.0	63.0	70.3	76.4	81.1	84.8	87.5	89.1	90.2	90.1	87.4	72.6	60.3	46.5	10.0

^a Experimental data extrapolated to provide estimates of ionization rates over a wide range of altitudes and geomagnetic cutoffs.

is shown in table 13.2 for solar minimum ($C = 98.3$ in 1965) and in table 13.3 for solar maximum ($C = 80$ in 1958) as obtained for cycle 19. We note that the low-energy GCR had not fully recovered in the summer of 1965 with the result that the high-latitude ionization at high altitude is about 10 percent lower than that in 1954. Furthermore, the 1958 measurements near solar maximum covered only mid to high latitudes, and the low-latitude data in table 13.3 are likely to be about 10 percent too high at high altitudes. The ionization rates in tables 13.2 and 13.3 are the rates in air per atmosphere of pressure. They are directly converted to exposure units and absorbed dose in tissue. The comparison with the tissue equivalent ion chamber requires the addition of the neutron absorbed dose rates as shown in figures 13.3, 13.4, and 13.6 where good consistency between the two methods is demonstrated. Dose equivalent estimates require an estimate of the high LET components associated with charged particles and are found from the measurements in nuclear emulsion as shown in figure 13.8. The corresponding average quality factor for proton-produced stars is found from Davison's emulsion data as

$$Q_F = 1 + 0.35 \exp\left(\frac{-x}{416}\right) - 0.194 \exp\left(\frac{-x}{65}\right) \quad (13.9)$$

This average quality factor will be applied to ion chamber dose rate data.

13.3.3. Comparison with other methods. This first comparison is with the dose equivalent rate meter of the Brookhaven National Laboratory (BNL). The BNL instrument is a tissue equivalent spherical proportional counter of 22-cm radius filled at 10 torr with tissue equivalent gas (corresponds to a 3- μm tissue site). The LET spectra are derived using the triangular relation to lineal energy which assumes that the chamber size is small compared with the range of the particles being detected. The ICRP 26 quality factor (Anon., 1977) is used to calculate dose equivalent rates. Because of the large chamber size at the chosen pressures, the high LET events are greatly distorted by the triangular assumption. For example, a 100-keV/ μm proton moving along the diameter would register only a 75-keV pulse instead of the 300-keV pulse expected using the triangular distribution. The instrument-assigned quality factor would be 10 instead of the correct value of 20. Such distortions are worse for multiple charged ions. Therefore, the BNL instrument could significantly underestimate the average quality factor. With this limitation in mind, in table 13.4 we give the BNL measurements made in 1971 and 1972 along with results of the present model. Approximate neutron monitor count rates used in evaluating the present model are given for the Deep River neutron monitor (DRNM) in Canada. The dose rates are in very good agreement, but the quality factors of the present model are substantially larger than the values measured by the BNL instrument. The present results are shown in table 13.5 with the results of the British Aerospace/Aerospatiale Concorde dosimeter and the HARIS instrument. The Concorde dosimeter consists of three shielded Geiger counters and a BF_3 proportional counter for neutron detection. The HARIS instrument consists of a gas-filled tissue equivalent proportional counter and tissue equivalent ion chamber. It has some of the same limitations as the BNL instrument.

Transport Methods and Interactions for Space Radiations

Table 13.4. Radiation Measurements of the BNL Instrument Compared With Those of Present Model (Values in Parentheses)

Geomagnetic latitude, °N	Date	Altitude, km	Areal density, g/cm ²	Absorbed dose rate, μGy/hr	Dose equivalent rate, μSv/hr
36.7	Aug. 29, 1972: DRNM ≈6950	3.0	694	0.18 (0.18)	0.25 (0.30)
		6.1	460	.58 (0.57)	1.00 (1.12)
		9.1	303	1.38 (1.21)	2.50 (2.55)
		12.2	188	2.80 (2.32)	4.75 (4.82)
41.7	Aug. 30, 1972: DRNM ≈6950	3.0	694	0.20 (0.19)	0.25 (0.36)
		6.1	460	.63 (0.59)	0.88 (1.29)
		9.1	303	1.50 (1.28)	2.45 (2.99)
		12.2	188	3.10 (2.57)	5.25 (5.76)
50.0	June 17, 1972: DRNM ≈6950	3.0	694	0.22 (0.20)	0.35 (0.43)
		6.1	460	.61 (0.69)	1.05 (1.63)
		9.1	303	1.68 (1.59)	2.75 (3.95)
		12.2	188	3.45 (3.14)	5.80 (7.61)
58.0	July 18, 1972: DRNM ≈6950	3.0	694	0.19 (0.20)	0.42 (0.45)
		6.1	460	.63 (0.69)	1.21 (1.72)
		9.1	303	1.70 (1.59)	2.90 (4.25)
		12.2	188	3.90 (3.35)	7.00 (8.52)
69.4 69.6 68.4 67.3	June 29, 1971: DRNM ≈6850	9.1	303	1.59 (1.57)	2.34 (4.09)
		11.6	204	2.88 (2.97)	4.89 (7.53)
		15.2	116	4.89 (4.97)	7.93 (12.09)
		18.3	71	6.03 (6.14)	10.39 (14.24)

Table 13.5. Present Results and Radiation Measurements Made With the Concorde Instrument and the HARIS at 18.3 km and High Geomagnetic Latitude

Geomagnetic latitude, °N	Date (1969)	DRNM	Dose equivalent rates, μSv/hr, for—		
			Concorde	HARIS	Present
65-70	Nov. 3	6369	9	10.7	11.7-11.5
67	Nov. 17	6429	7-9	7.8	11.9
70	Nov. 19	6442	5-7	6.3	12.0
70	Nov. 21	6510	7-9	6.9	12.4
70	Nov. 21	6537	7-9	6.5	12.5

The present model is compared with several sources in table 13.6. Of particular note is the result of Schaefer's measurements with nuclear emulsion (Friedberg and Neas in Anon., 1980). In particular, the ionization tracks of all particles other than nuclear stars lead to 5.8 μGy/hr and 10.5 μSv/hr, which is in good agreement with the values from the BNL instrument of 6.0 μGy/hr and 10.4 μSv/hr as given in tables 13.4 and 13.6. The nuclear-star contributions from Schaefer's

Table 13.6. Present Results Compared With Other Estimates of Galactic Radiation

Source of data	Dose equivalent rate, $\mu\text{Sv/hr}$, for altitude (areal density) of—	
	11.0 km (255 g/cm ²)	18.3 km (71 g/cm ²)
At or near 55°N, solar average (DRNM = 6660)		
Present	5.9	12.1
O'Brien and McLaughlin (1972)	4.1	13.2
LaRC: Extremities	6.2	12.5
42°N, 43°N, at or near solar maximum (DRNM = 6950)		
Present	4.8	8.6
O'Brien and McLaughlin (1972)	3.3	9.8
BNL	3.9	
67°N–70°N, at or near solar maximum (DRNM = 6850)		
Present	6.7	14.2
BNL	4.1	10.4
Concorde		8.0
HARIS		9.0
Schaefer in Anon. (1980)		15.0

nuclear emulsion data give final values of 6.5 $\mu\text{Gy/hr}$ and 15.0 $\mu\text{Sv/hr}$ in excellent agreement with those of the present model of 6.1 $\mu\text{Gy/hr}$ and 14.2 $\mu\text{Sv/hr}$, respectively. The importance of the nuclear-star contribution has also been noted by Friedberg and Neas in Anon. (1980). The present model appears to be in excellent agreement with measurements, which include the high LET components associated with nuclear-star contributions.

13.4. Global Dose Rate Estimates

The dose rate evaluation methods described herein are directly applicable to predictions, or estimates, of global dose rate patterns. The requirements for such an analysis include the geographic distribution of magnetic cutoff values and the global pressure fields at the altitudes of interest. The vertical magnetic cutoff values are taken here as the 1980.0 epoch data of Smart and Shea (1983) and are shown in figure 13.11. The atmospheric climatological data have been extracted from the Langley Research Center General Circulation Model (LaRC-GCM) of the Earth's atmosphere (Grose et al., 1987; Blackshear, Grose, and Turner, 1987), with enhanced resolution for vertical structure as given by R. S. Eckman et al. in presently unpublished work. For purposes of computations presented herein, the original latitude-longitude grid has been reduced to 10° increments by appropriate interpolation of the LaRC-GCM data; i.e., the latitude grid points are -90° S to +90° N and the longitudes progress from -180° W to +180° E in 10°

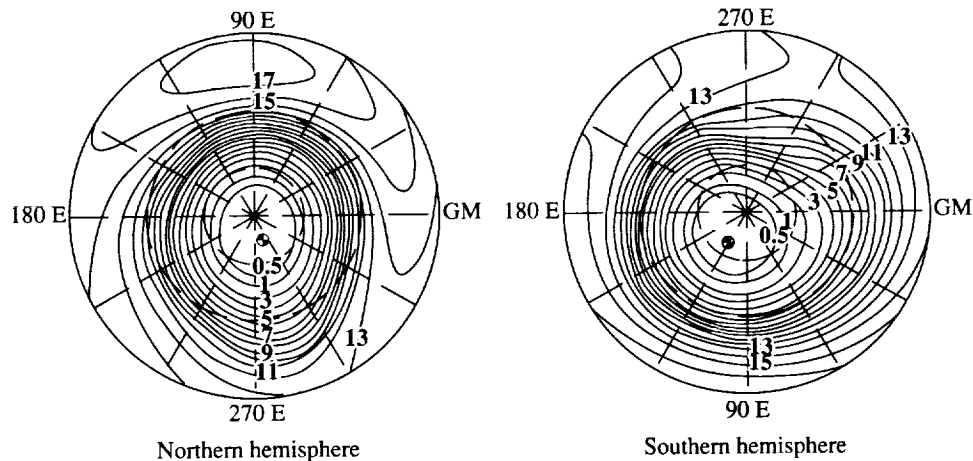


Figure 13.11. Contour of vertical geomagnetic cutoff values from data of Smart and Shea (1983). Contour increments are 1 GV except for the lowest (0.5 GV) contour. Magnetic pole locations are indicated.

steps. Of course, any desired pressure altitude distribution may be substituted; for example, the widely used NASA/Marshall Space Flight Center Global Reference Atmospheric Model (Justus et al., 1980) or other real-time meteorological fields can be used. The principal reasons for utilization of the LaRC-GCM data in the present calculations relate to the fact that both seasonal and north-south hemisphere asymmetries appear to be well represented in the upper troposphere and stratosphere (Grose et al., 1989), with the influence of surface topography taken into account.

The global dose rate analysis has been performed for three altitudes: 10, 14, and 18 km (approximately 33 000, 46 000, and 60 000 ft, respectively). Pressure distributions at these altitudes are shown in figures 13.12, 13.13, and 13.14, respectively. In these figures, the pressure distributions are shown in polar stereographic projection for both hemispheres and for both solstice conditions. The northern hemisphere winter solstice (the southern hemisphere summer) has been modeled as an average of pressure for the first 10 days in January as given by the LaRC-GCM. The corresponding opposite solstice conditions are represented by an average of the data for the first 10 days in July. Pressure contours are given in millibars (mbar). (Note that for the Earth's atmosphere, pressure in millibars is numerically within 2 percent of the overhead absorber amount in units of g/cm^2 .) Some general salient features of the pressure distributions may be noted; for example, the equator-to-pole latitudinal gradient is much larger for each hemisphere in winter than in summer. As a consequence, a substantial seasonal variation in dose rates may result, particularly for high-latitude flights in the northern hemisphere.

13.4.1. ICRP 26 quality factors. Contour maps of the dose rates at solar minimum corresponding to the three altitude levels are presented in figures 13.15, 13.16, and 13.17. Dose rate values for the contours are expressed in units of $\text{cSv}/1000 \text{ hr}$ (equivalent to mrem/hr). For altitudes of 10 and 14 km, dose rates

increase from low latitudes by approximately a factor of 3 as polar regions are approached. At the 18-km altitude ($\approx 60\,000$ ft), the equator-to-pole increase is on the order of a factor of 5, largely because of the increasing influence of the geomagnetic cutoffs relative to the atmospheric attenuation. Note that even for the 14-km altitude, dose rates at high latitudes in the polar winter are greater than 1 cSv/1000 hr. Such regions of the globe in the northern hemisphere encompass several common international flight paths. Two such routes (N.Y.-London and N.Y.-Tokyo), which are indicated in figure 13.18, have been overlaid on satellite-view projections of the globe showing contour maps of the northern hemisphere winter dose rate at the 18-km level. The orientations of the projections are such that the pertinent great circle routes appear as straight lines on the figures.

Figure 13.19 shows the winter dose rate contours at the 10-km altitude for the contiguous United States. (Note the change in scale from previous figures; dose rates in fig. 13.19 are given in mSv/1000 hr.) The U.S. dose rate differs by approximately a factor of 2 within the latitude belt of the nation. Dose rates for many of the northern states exceed 0.6 cSv/1000 hr (0.6 mrem/hr).

During the summer months at solar minimum, the dose rates for the northernmost flights in the contiguous U.S. drop to about 0.47 cSv/1000 hr. Crew members operating 1000 hr or more on northern U.S. routes at 10 km or more obviously exceed the allowable exposure for the general population. The dose rates at solar minimum at 14 km are greater by nearly a factor of 2 and represent a substantial fraction of the dose allowed a radiation worker (50 mSv/year) for a 1000 hr/year exposure. A more detailed analysis of commercial airplane operations is clearly needed. This is especially true if newly proposed increases in quality factors are enforced (ICRU 40 (Anon., 1986)).

13.4.2. Revised quality factors. All previous results were based on the quality factors of ICRP 26 (Anon., 1977). Average neutron quality factors have been derived using the proposed ICRU 40 quality factors in Anon. (1986) and will be used here to estimate expected future upward revisions. The contributions to neutron dose equivalent rates in neutron energy subintervals as presented in figure 13.7 are shown in the first three columns of table 13.7. The corresponding previous average quality factors for each subinterval are shown in column four. The newly proposed quality factors (ICRU 40 (Anon., 1986)) are averaged over each subinterval according to the neutron spectrum produced by GCR and then are applied to obtain new estimates of the neutron dose equivalent rates, as shown in columns five and six. The results change the dose equivalent by 60 percent. We do not increase the charged-particle star contribution since the assumed quality factor of 20 is a generous overestimate of nuclear-star contributions to dose equivalent (Wilson, Shinn, and Townsend, 1990).

The revised dose equivalent rates at solar minimum for 10-, 14-, and 18-km altitudes are shown for winter solstice and summer solstice in figures 13.20, 13.21, and 13.22, respectively. During solar minimum years, flight crews who spend over 1000 hr at altitudes in excess of 10 km (33 000 ft) in the northern polar region can receive up to 1 cSv per year in excess of that allowed for the general population.

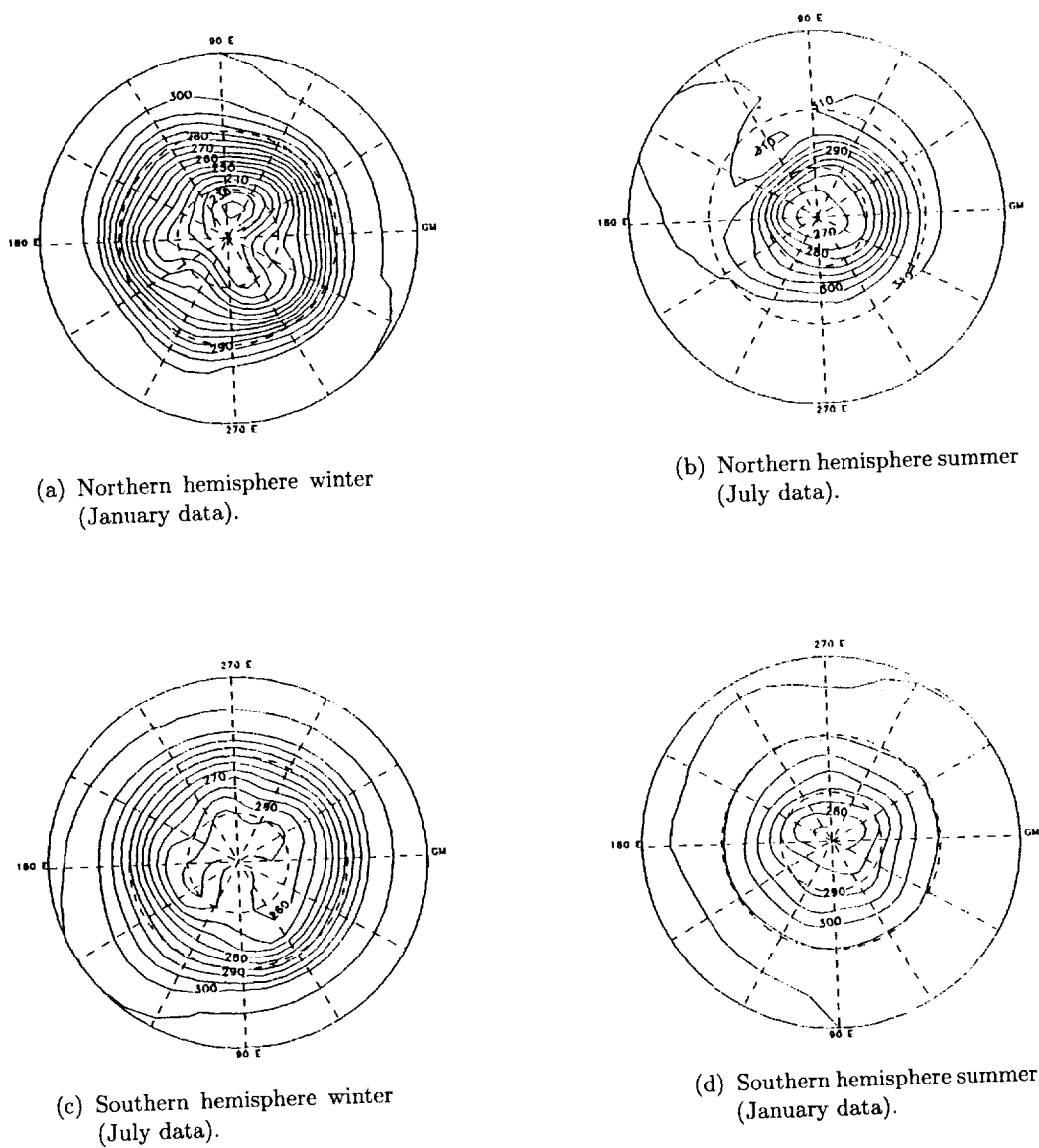
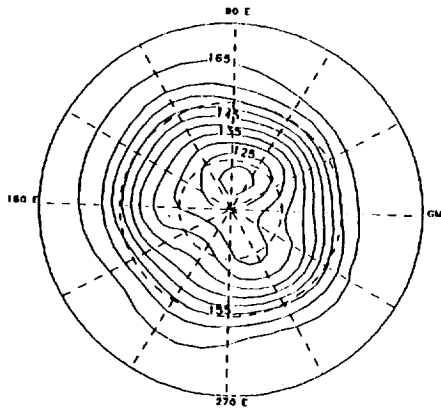
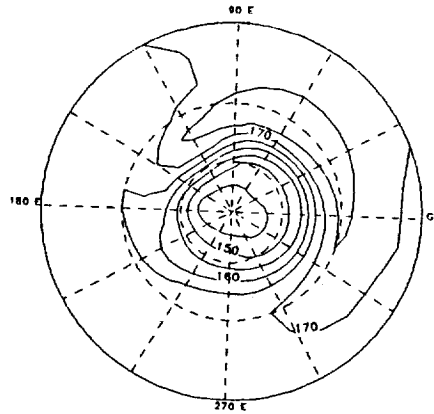


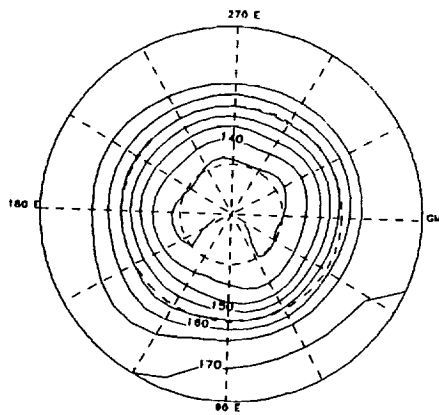
Figure 13.12. Global pressure distribution for solstice conditions at 10-km altitude (approximately 33 000 ft). Contour increment is 5 mbar.



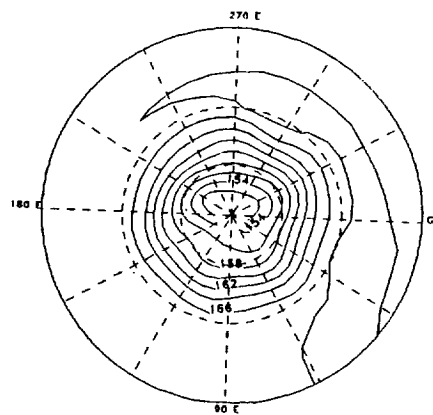
(a) Northern hemisphere winter (January data).



(b) Northern hemisphere summer (July data).



(c) Southern hemisphere winter (July data).



(d) Southern hemisphere summer (January data).

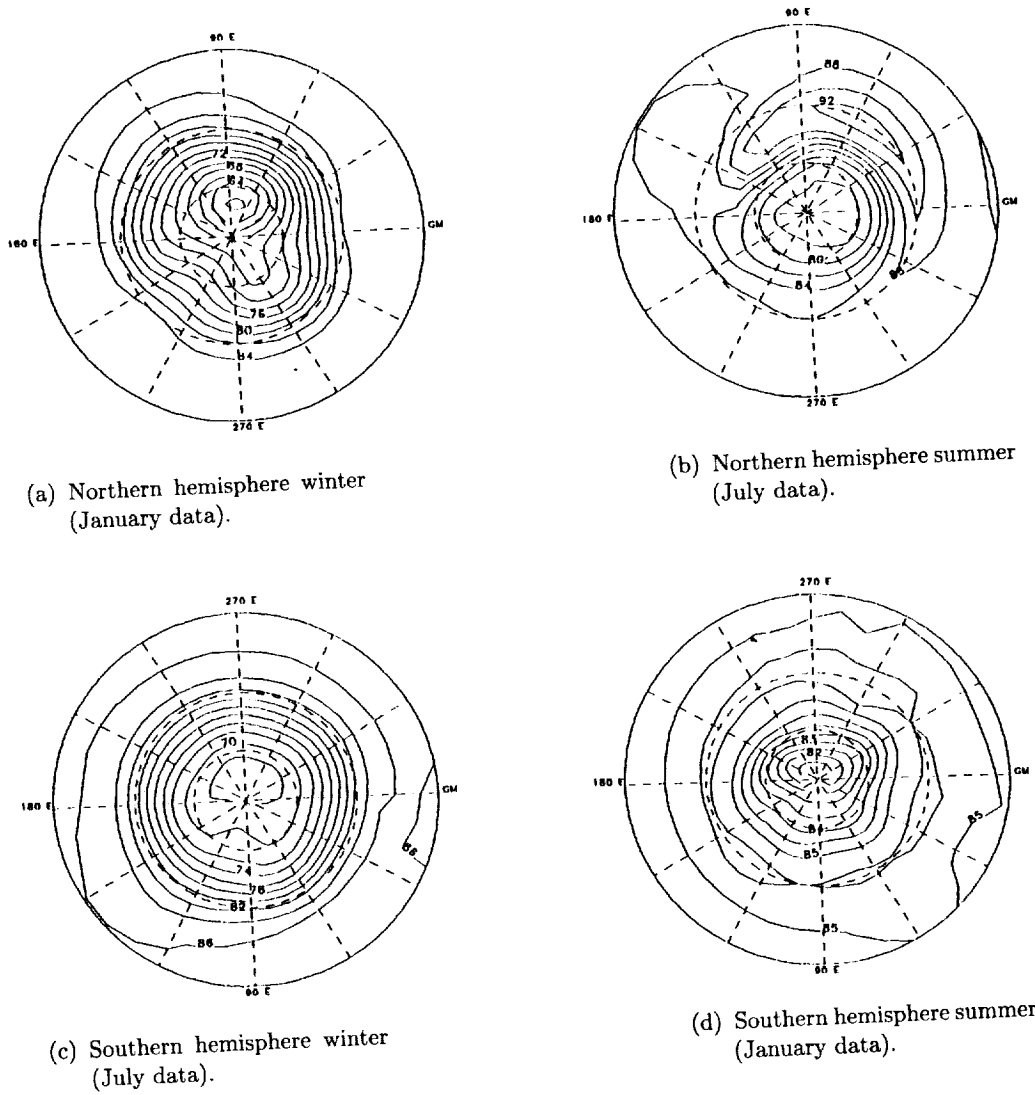
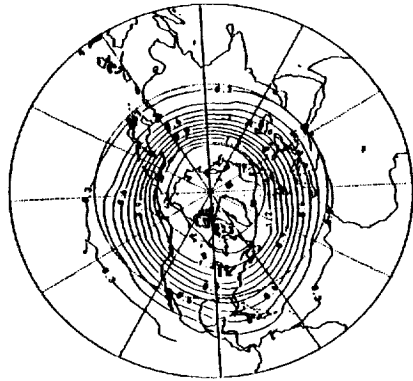
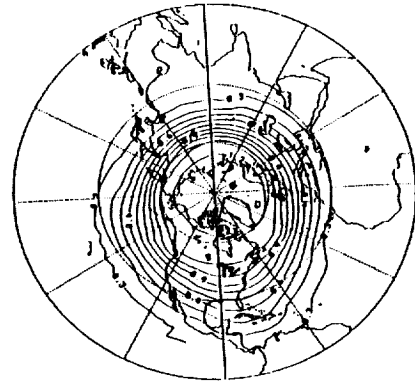


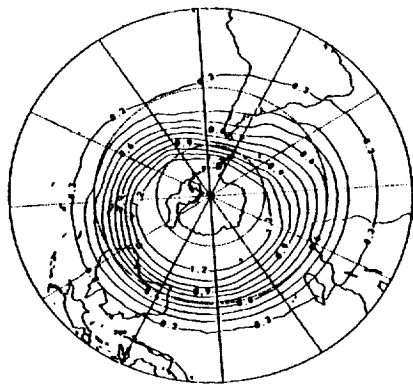
Figure 13.14. Global pressure distribution for solstice conditions at 18-km altitude (approximately 60 000 ft). Contour increment is 2 mbar.



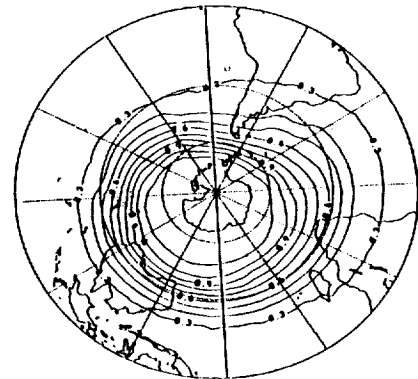
(a) Northern hemisphere winter
(January data).



(b) Northern hemisphere summer
(July data).

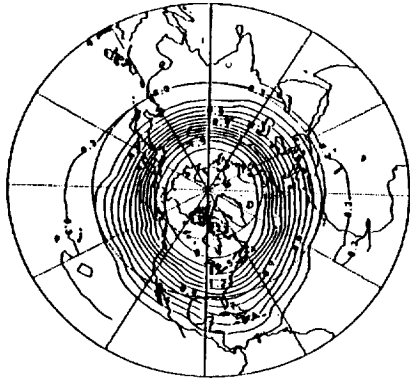


(c) Southern hemisphere winter
(July data).

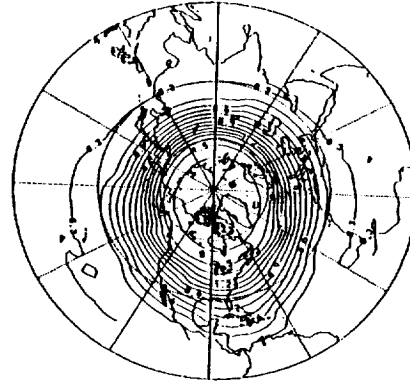


(d) Southern hemisphere summer
(January data).

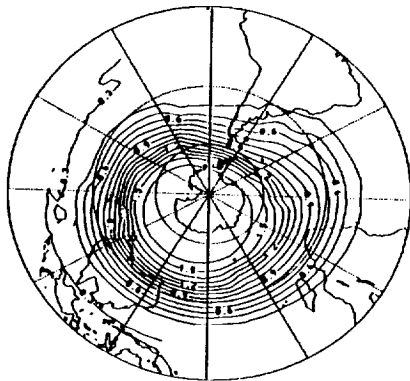
Figure 13.16. Contours of dose rate during solstice conditions at 14-km altitude (approximately 46 000 ft). Contour increment is 0.1 cSv/1000 hr.



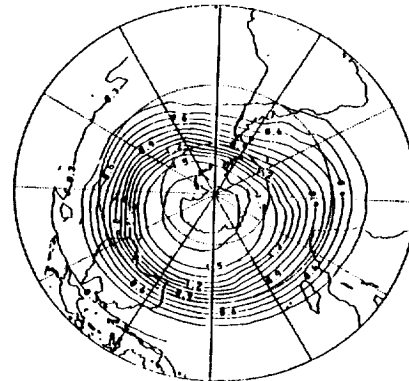
(a) Northern hemisphere winter (January data).



(b) Northern hemisphere summer (July data).

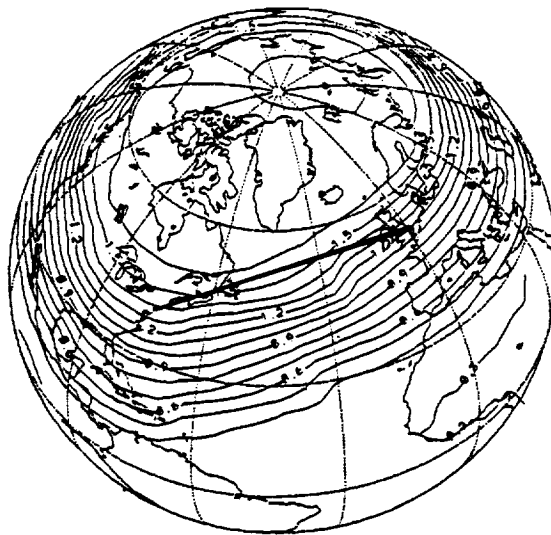


(c) Southern hemisphere winter (July data).

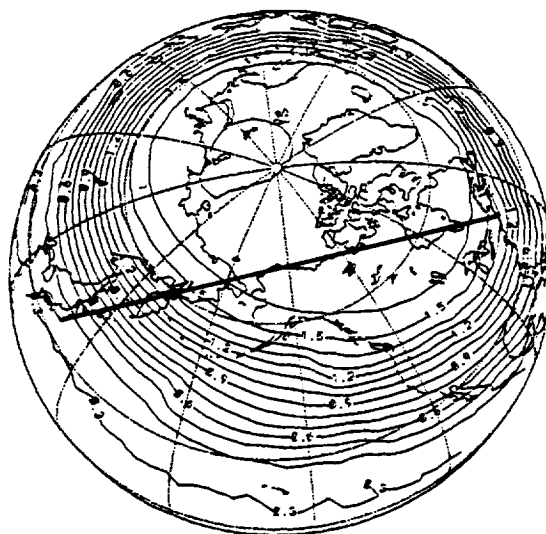


(d) Southern hemisphere summer (January data).

Figure 13.17. Contours of dose rate during solstice conditions at 18-km altitude (approximately 60 000 ft). Contour increment is 0.1 cSv/1000 hr.



(a) New York-London.



(b) New York-Tokyo.

Figure 13.18. International great circle routes for northern hemisphere winter at 18-km altitude.
Dose rate contour increment is 0.1 cSv/1000 hr.

The exposure nearly doubles if the cruise altitudes are near 14 km (46 000 ft), and this increase represents a substantial fraction of the exposure allowed a radiation worker.

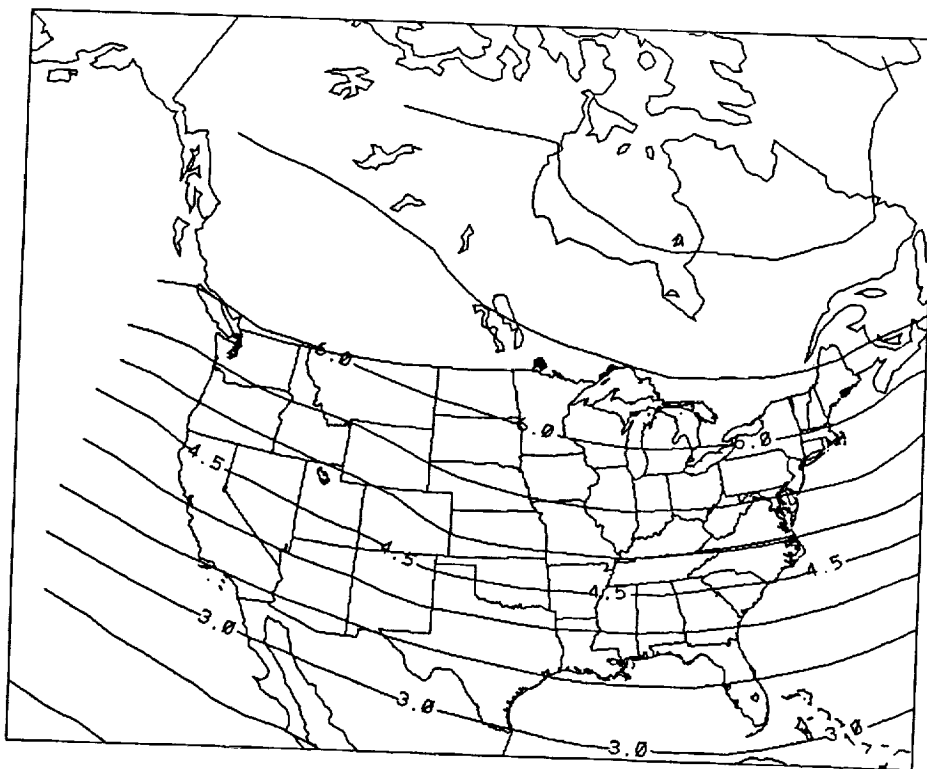


Figure 13.19. Winter solstice dose rate contours for continental United States at 10-km altitude (approximately 33 000 ft). Contour increment is 0.5 mSv/1000 hr.

Table 13.7. Dose and Dose Equivalent Rates in Neutron Energy Intervals With the ICRP 26^a and Proposed ICRU 40^b Quality Factors

[ΔE : neutron energy interval, MeV; ΔD : dose, $\mu\text{Gy/hr}$;
 ΔH : dose equivalent, $\mu\text{Sv/hr}$; Q : quality factor]

ΔE	ΔD	ΔH_{ICRP}	Q_{ICRP}	Q_{ICRU}	ΔH_{ICRU}
0.1-1	0.20	2.34	11.7	19.4	3.88
1-10	.32	2.52	7.9	17.6	5.63
10-100	.39	1.81	7.0	7.0	1.81
100-1000	.31	1.04	3.4	3.4	1.04
0.1-1000	1.22	7.71	6.3	10.1	12.36

^aICRP 26 (Anon., 1977).

^bICRU 40 (Anon., 1986).

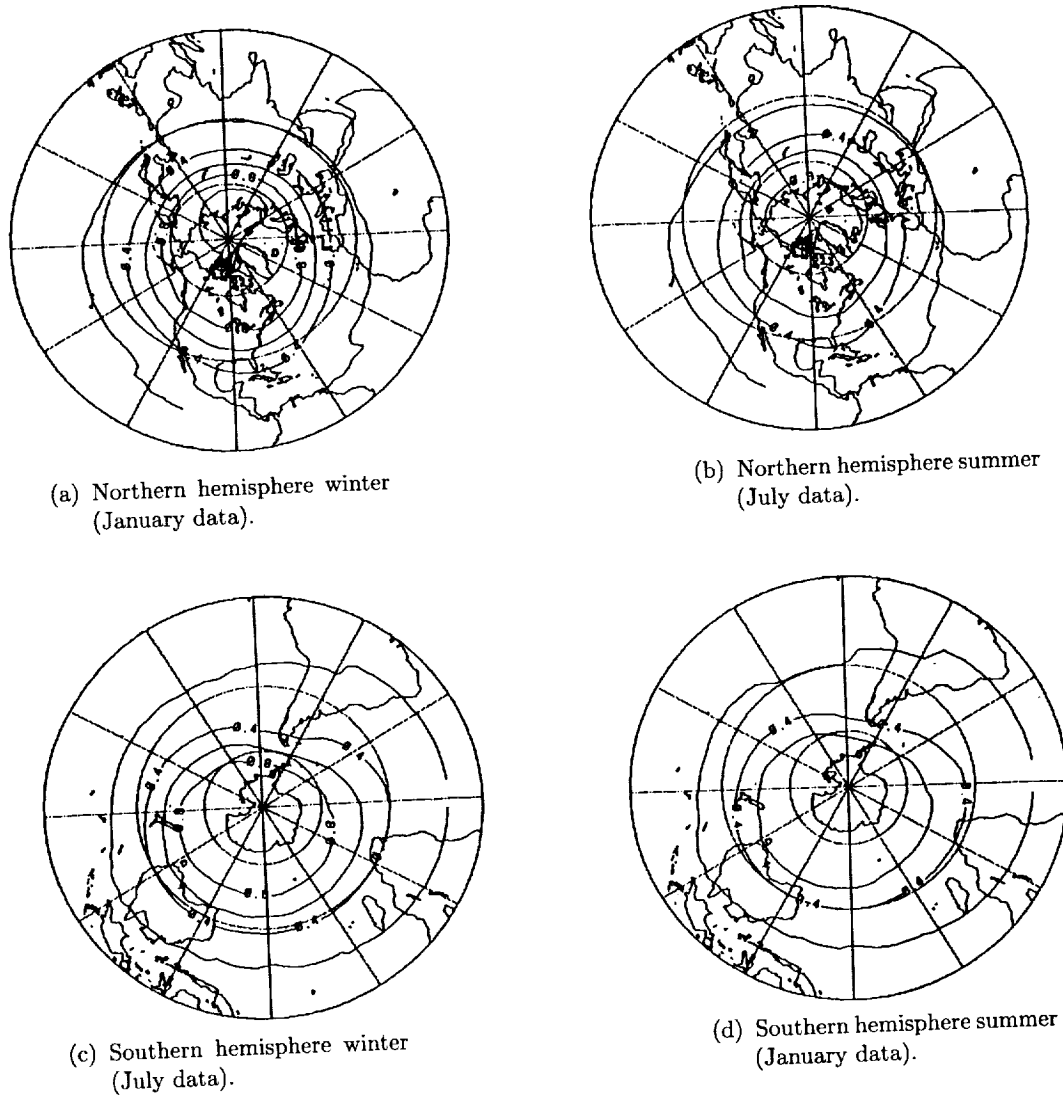


Figure 13.20. Contours of dose rate during solstice conditions at 10-km altitude (approximately 33 000 ft) computed with ICRU 40 quality factors (Anon., 1986). Contour increment is 0.2 cSv/1000 hr.

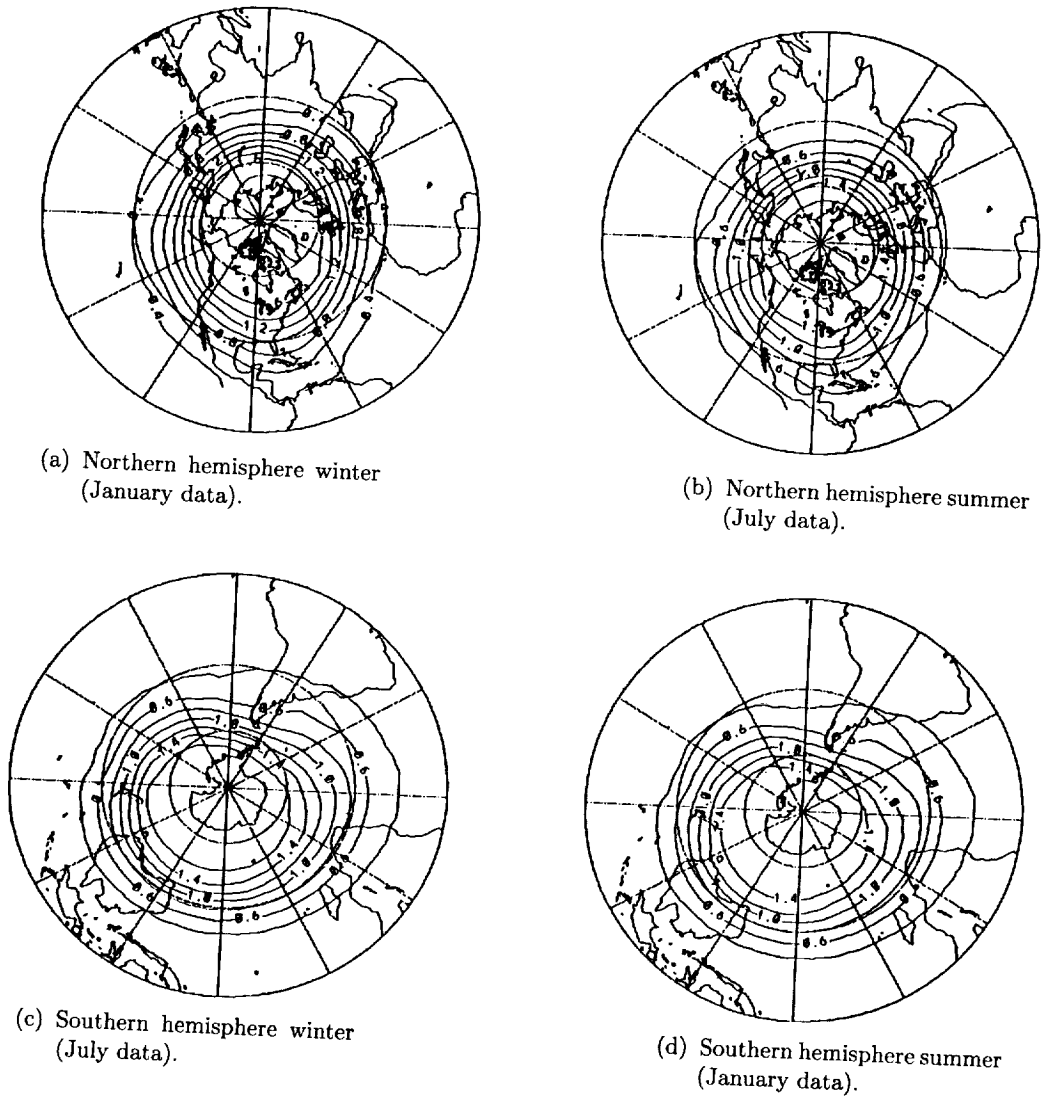
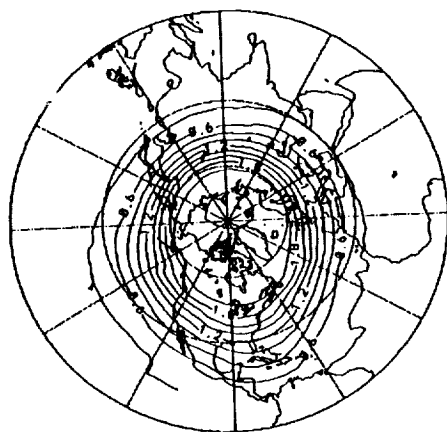
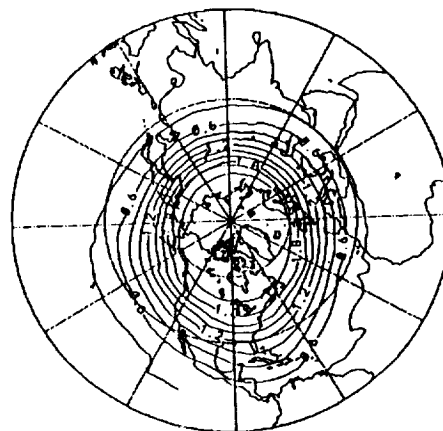


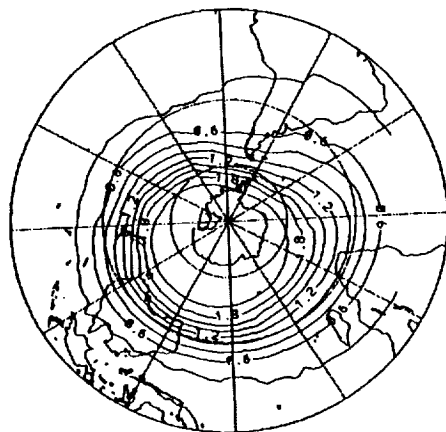
Figure 13.21. Contours of dose rate during solstice conditions at 14-km altitude (approximately 46 000 ft) computed with ICRU 40 quality factors (Anon., 1986). Contour increment is 0.2 cSv/1000 hr.



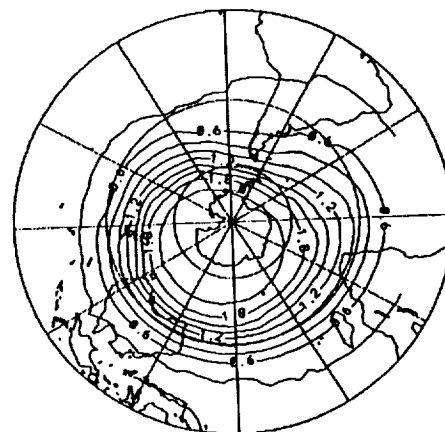
(a) Northern hemisphere winter
(January data).



(b) Northern hemisphere summer
(July data).



(c) Southern hemisphere winter
(July data).

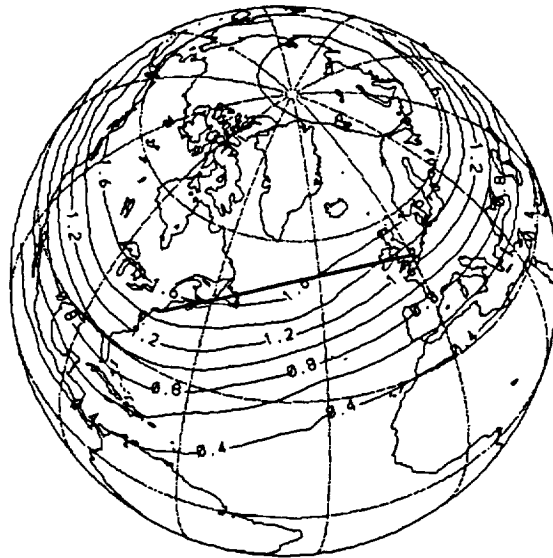


(d) Southern hemisphere summer
(January data).

Figure 13.22. Contours of dose rate during solstice conditions at 18-km altitude (approximately 60 000 ft) computed with ICRU 40 quality factors (Anon., 1986). Contour increment is 0.2 cSv/1000 hr.



(a) New York-London.



(b) New York-Tokyo.

Figure 13.23. International great circle routes for northern hemisphere at 14-km altitude. Dose rate contours are computed with ICRU 40 quality factors (Anon., 1986) and are in increments of 0.2 cSv/1000 hr.

International flights for New York-London and New York-Tokyo are shown in figure 13.23 at solar minimum during winter solstice for 14-km altitudes. Such

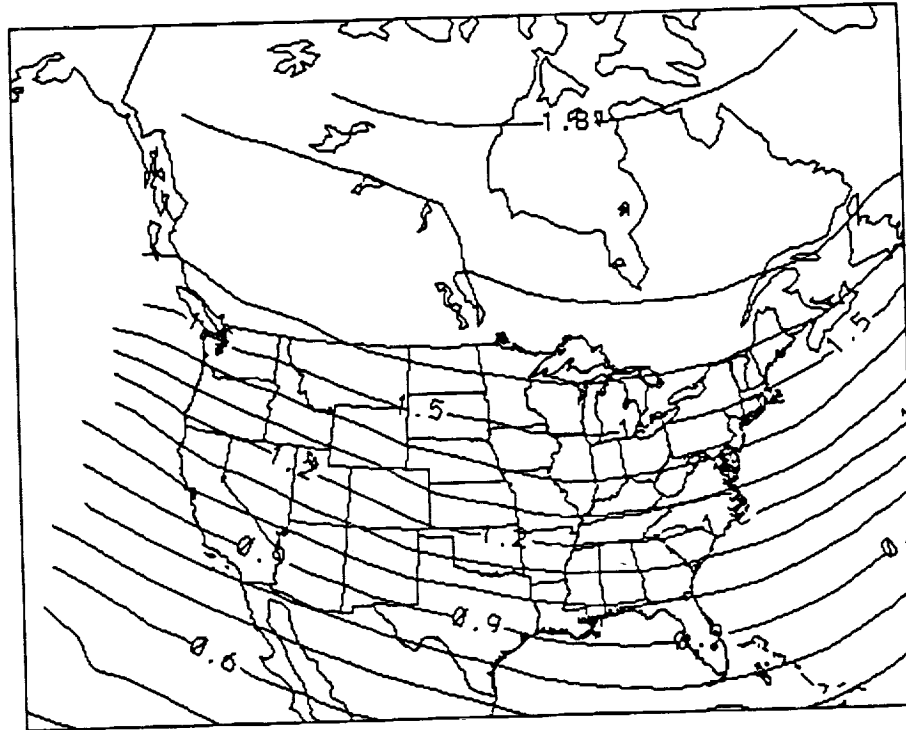


Figure 13.24. Winter solstice dose rate contours for contiguous United States at 14-km altitude (approximately 46 000 ft) using ICRU 40 quality factors (Anon., 1986). Contour increment is 0.1 cSV/1000 hr.

flights will accumulate more than 1.5 cSV/1000 hr. Clearly, high exposures relative to the general public are indicated and some thought to possible crew rotation (especially for potentially pregnant crew members) seems advisable. The winter dose rates at 14-km altitude during solar minimum can be quite high over the contiguous U.S. as shown in figure 13.24. Some counseling will be in order if the newly proposed quality factors are, in fact, adopted.

The revised Q_F dose equivalent rates are shown in figure 13.25 for solar maximum (in 1969) at the 14-km altitude. The dose rates decreased by 20 to 40 percent in reaching solar maximum in cycle 20. The decrease for cycle 19 (in 1958) would have been substantially greater.

13.5. Analysis for Selected Flight Paths

The environmental model described previously is used in conjunction with the background radiation data base to estimate incurred dose equivalent rates for several intercontinental and domestic routes at three altitudes (12, 14, and 17 km, corresponding approximately to 40 000, 46 000, and 56 000 ft, respectively). Several tables of results have been prepared (tables 13.8-13.12) in which the predicted average dose rates are presented for the selected flight paths as various input parameters are altered. The routes are specified as minimum distance (great circle) routes at constant altitude. Tables 13.8 and 13.9 give results computed

for solar-minimum, northern hemisphere winter conditions, and they illustrate the effect of the proposed ICRU 40 quality factors (Anon., 1986) quality factors (table 13.8) as opposed to the generally lower ICRP 26 quantities (Anon., 1977) (table 13.9). The ICRU 40 quality factors result in dose equivalent values that are higher by 25 to 33 percent, with largest increases for the higher latitude routes. In order to examine the effect of active Sun conditions, tables 13.10 and 13.11 have been generated for solar maxima of cycles 19 and 20, respectively, in which the relative solar activity is shown to have an inverse relationship to the Deep River neutron monitor count in figure 13.1. It is seen that the decrease in dose rate during solar maximum may be quite large, especially at high latitudes. For example, the average rates at all altitudes considered for the New York-Tokyo route are reduced to almost half the predicted quiet Sun values (table 13.10 compared with table 13.8). A comparison of tables 13.10 and 13.11 for different solar maxima indicates the effects of variabilities between different cycles.

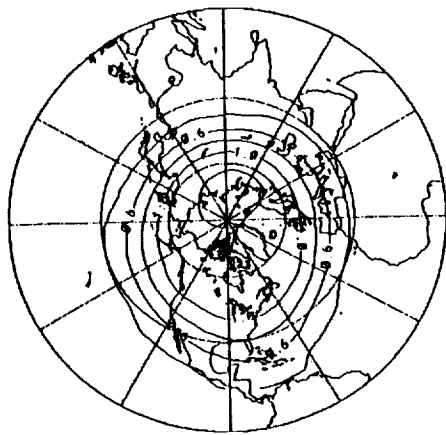
Finally, table 13.12 presents corresponding results for northern hemisphere summer solstice conditions, for which the pressure at a given altitude is usually

Table 13.8. Dose Equivalent Rate in January at Solar Cycle Minimum (DRNM = 7157) for ICRU 40 Quality Factors (Anon., 1986)

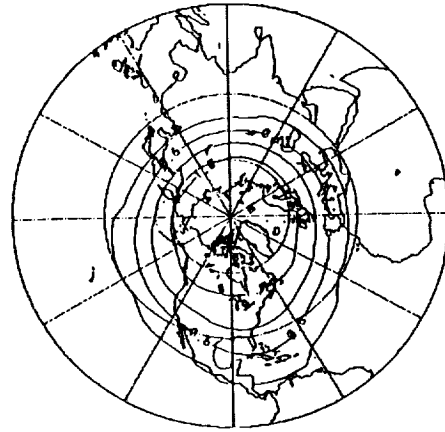
City pairs	Dose equivalent rate, cSv/1000 hr, at altitude of—		
	12 km (39 370 ft)	14 km (45 932 ft)	17 km (55 774 ft)
N.Y.-Tokyo	1.09	1.37	1.62
N.Y.-London	1.22	1.55	1.82
N.Y.-Seattle	1.20	1.56	1.86
Paris-Rio	.39	.49	.57
Paris-D.C.	1.17	1.49	1.74
Atlanta-L.A.	.79	1.02	1.22
Atlanta-N.Y.	1.00	1.29	1.56
Atlanta-S.F.	.85	1.10	1.31

Table 13.9. Dose Equivalent Rate in January at Solar Cycle Minimum (DRNM = 7157) for ICRP 26 Quality Factors (Anon., 1977)

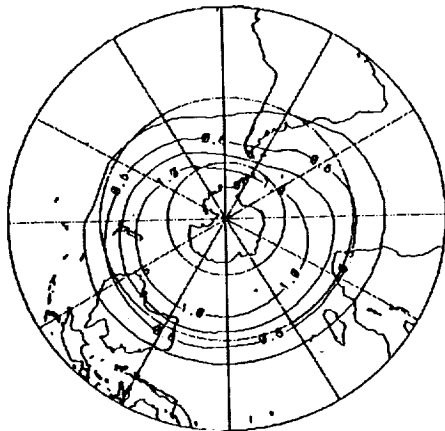
City pairs	Dose equivalent rate, cSv/1000 hr, at altitude of—		
	12 km (39 370 ft)	14 km (45 932 ft)	17 km (55 774 ft)
N.Y.-Tokyo	0.82	1.04	1.24
N.Y.-London	.92	1.18	1.39
N.Y.-Seattle	.90	1.18	1.42
Paris-Rio	.31	.39	.46
Paris-D.C.	.88	1.13	1.33
Atlanta-L.A.	.60	.79	.94
Atlanta-N.Y.	.75	.98	1.19
Atlanta-S.F.	.64	.84	1.01



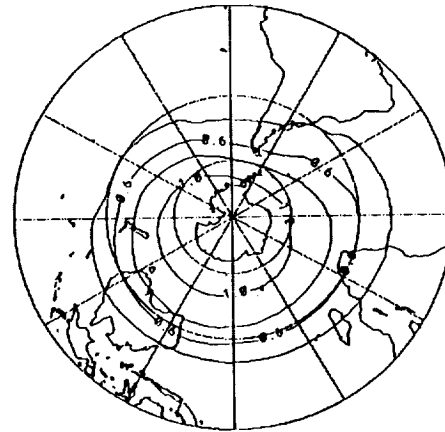
(a) Northern hemisphere winter
(January data).



(b) Northern hemisphere summer
(July data).



(c) Southern hemisphere winter
(July data).



(d) Southern hemisphere summer
(January data).

Figure 13.25. Contours of dose rate during solstice conditions at solar maximum activity for 14-km altitude computed with ICRU 40 quality factors (Anon., 1986). Contour increment is 0.2 cSV/1000 hr.

Table 13.10. Dose Equivalent Rate in January at Solar Cycle Maximum
(DRNM = 5700; cycle 19) for ICRU 40 Quality Factors (Anon., 1986)

City pairs	Dose equivalent rate, cSv/1000 hr, at altitude of—		
	12 km (39 370 ft)	14 km (45 932 ft)	17 km (55 774 ft)
N.Y.-Tokyo	0.63	0.77	0.86
N.Y.-London	.69	.85	.97
N.Y.-Seattle	.67	.84	.97
Paris-Rio	.35	.41	.46
Paris-D.C.	.68	.84	.95
Atlanta-L.A.	.59	.73	.82
Atlanta-N.Y.	.63	.80	.92
Atlanta-S.F.	.61	.76	.85

Table 13.11. Dose Equivalent Rate in January at Solar Cycle Maximum
(DRNM = 6280; cycle 20) for ICRU 40 Quality Factors (Anon., 1986)

City pairs	Dose equivalent rate, cSv/1000 hr, at altitude of—		
	12 km (39 370 ft)	14 km (45 932 ft)	17 km (55 774 ft)
N.Y.-Tokyo	0.75	0.96	1.12
N.Y.-London	.84	1.07	1.26
N.Y.-Seattle	.81	1.06	1.27
Paris-Rio	.35	.43	.50
Paris-D.C.	.81	1.04	1.22
Atlanta-L.A.	.62	.80	.96
Atlanta-N.Y.	.72	.94	1.14
Atlanta-S.F.	.66	.85	1.01

Table 13.12. Dose Equivalent Rate in July at Solar Cycle Minimum (DRNM = 7157)
for ICRU 40 Quality Factors (Anon., 1986)

City pairs	Dose equivalent rate, cSv/1000 hr, at altitude of—		
	12 km (39 370 ft)	14 km (45 932 ft)	17 km (55 774 ft)
N.Y.-Tokyo	0.92	1.24	1.57
N.Y.-London	1.04	1.41	1.77
N.Y.-Seattle	1.02	1.41	1.82
Paris-Rio	.37	.47	.56
Paris-D.C.	.99	1.35	1.70
Atlanta-L.A.	.70	.94	1.20
Atlanta-N.Y.	.86	1.18	1.52
Atlanta-S.F.	.75	1.02	1.29

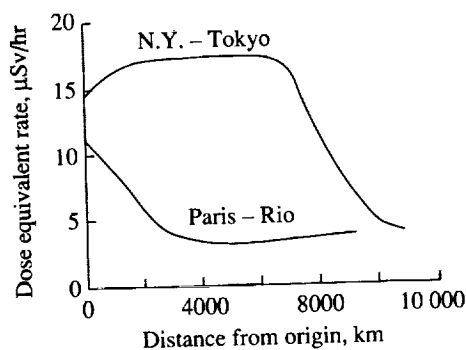


Figure 13.26. Dose equivalent rate profile along aircraft intercontinental flight trajectories at 17 km (56 000 ft).

higher than in winter. Consequently, dose equivalent rates are somewhat lower than those for the corresponding wintertime values, as may be seen by comparing tables 13.12 and 13.8. In addition, the seasonal variation is less for routes at low latitudes since annual pressure changes are not as pronounced.

As a final illustration of the range of dose rate variation along particular flight paths, the calculated dose equivalent rates at 14-km altitude for New York-Tokyo and for Paris-Rio de Janeiro are shown as a function of distance traveled in figure 13.26. The dose rate for New York-Tokyo is in excess of 1.5 cSv/1000 hr since much of the route is at high latitudes ($>50^{\circ}$ N). In contrast, the Paris-Rio calculation, for which most time is spent at tropical and subtropical latitudes, shows much lower dose rates. The average dose rate for the more northern route exceeds that of the low-latitude route by more than 2-1/2 times.

In the preceding discussion, dose equivalent rates have been expressed in cSv/1000 hr, or mrem/hr. If one assumes that crew members spend 1000 hr per year at altitude, the tabular results convert directly to annual incurred dose. When such a conversion is made, it is noteworthy that only the flight path at equatorial latitudes (Paris-Rio) is determined to be within the 0.5-cSv annual limit for the general populace. The more northern routes, especially at high altitudes, are often in excess of this limit by factors of 2 and sometimes 3.

13.6. References

- Anon., 1977: *Recommendations of the International Commission on Radiological Protection*. ICRP Publ. 26, Pergamon Press.
- Anon., 1980: *Cosmic Radiation Exposure During Air Travel*. FAA-AM-80-2, FAA Advisory Committee on Radiation Biology Aspects of the Supersonic Transport, U.S. Dep. of Transportation.

- Anon., 1986: *The Quality Factor in Radiation Protection*. ICRU Rep. 40, International Commission on Radiation Units and Measurements.
- Anon., 1987: *Recommendations on Limits for Exposure to Ionizing Radiation*. NCRP Rep. No. 91, National Council on Radiation Protection and Measurements.
- Barish, R. J., 1990: Health Physics Concerns in Commercial Aviation. *Health Phys.*, vol. 59, no. 2, pp. 199-204.
- Bertini, Hugo W., 1967: *Preliminary Data From Intranuclear-Cascade Calculations of 0.75-, 1-, and 2-GeV Protons on Oxygen, Aluminum, and Lead, and 1-rm GeV Neutrons on the Same Elements*. ORNL-TM-1996, U.S. Atomic Energy Commission.
- Blackshear, W. T.; Grose, W. L.; and Turner, R. E., 1987: Simulated Sudden Stratospheric Warming; Synoptic Evolution. *Q. J. Royal Meteorol. Soc.*, vol. 113, no. 477, pp. 815-846.
- Bramlitt, Edward T., 1985: Commercial Aviation Crewmember Radiation Doses. *Health Phys.*, vol. 49, no. 5, pp. 945-948.
- Busick, D. D., 1989: Should Airline Crews Be Monitored for Radiation Exposure? Paper presented at Health Physics Society 34th Annual Meeting (Albuquerque, New Mexico).
- Foelsche, Trutz, 1962: *Radiation Exposure in Supersonic Transports*. NASA TN D-1383.
- Foelsche, Trutz; Mendell, Rosalind B.; Wilson, John W.; and Adams, Richard R., 1974: *Measured and Calculated Neutron Spectra and Dose Equivalent Rates at High Altitudes; Relevance to SST Operations and Space Research*. NASA TN D-7715.
- Foelsche, Trutz, 1977: Radiation Safety in High-Altitude Air Traffic. *J. Aircr.*, vol. 14, no. 12, pp. 1226-1233.
- Freier, P. S.; and Waddington, C. J., 1965: The Helium Nuclei of the Primary Cosmic Radiation as Studied Over a Solar Cycle of Activity, Interpreted in Terms of Electric Field Modulation. *Space Sci. Reviews*, vol. IV, no. 3, pp. 313-372.
- Friedberg, W.; Faulkner, D. N.; Snyder, L.; Darden, E. B., Jr.; and O'Brien, K., 1989: Galactic Cosmic Radiation Exposure and Associated Health Risks for Air Carrier Crewmembers. *Aviation, Space, & Environ. Med.*, vol. 60, no. 11, pp. 1104-1108.
- Grose, W. L.; Nealy, J. E.; Turner, R. E.; and Blackshear, W. T., 1987: Modeling the Transport of Chemically Active Constituents in the Stratosphere. *Transport Processes in the Middle Atmosphere*, G. Visconti and R. Garcia, eds., D. Reidel Publ. Co., pp. 229-250.
- Grose, W. L.; Eckman, R. S.; Turner, R. E.; and Blackshear, W. T., 1989: Global Modeling of Ozone and Trace Gases. *Atmospheric Ozone Research and Its Policy Implications*, T. Schneider et al., eds., Elsevier, pp. 1021-1035.

Transport Methods and Interactions for Space Radiations

- Hess, W. N.; Canfield, E. H.; and Lingenfelter, R. E., 1961: Cosmic-Ray Neutron Demography. *J. Geophys. Res.*, vol. 66, no. 3, pp. 665-677.
- Justus, C. G.; Fletcher, G. R.; Gramling, F. E.; and Pace, W. B., 1980: *The NASA/MSFC Global Reference Atmospheric Model—MOD 3 (With Spherical Harmonic Wind Model)*. NASA CR-3256.
- Korff, Serge A.; Mendell, Rosalind B.; Merker, Milton; Light, Edward S.; Verschell, Howard J.; and Sandie, William S., 1979: *Atmospheric Neutrons*. NASA CR-3126.
- Neher, H. V., 1961: Cosmic-Ray Knee in 1958. *J. Geophys. Res.*, vol. 66, no. 12, pp. 4007-4012.
- Neher, H. V.; and Anderson, Hugh R., 1962: Cosmic Rays at Balloon Altitudes and the Solar Cycle. *J. Geophys. Res.*, vol. 67, no. 4, pp. 1309-1315.
- Newkirk, L. L., 1963: Calculation of Low-Energy Neutron Flux in the Atmosphere by the S_n Method. *J. Geophys. Res.*, vol. 68, no. 7, pp. 1825-1833.
- O'Brien, Keran; and McLaughlin, James E., 1972: The Radiation Dose to Man From Galactic Cosmic Rays. *Health Phys.*, vol. 22, no. 3, pp. 225-232.
- Shinn, J. L.; Wilson, J. W.; and Ngo, D. M., 1990: Risk Assessment Methodologies for Target Fragments Produced in High-Energy Nucleon Reactions. *Health Phys.*, vol. 59, no. 1, pp. 141-143.
- Smart, D. F.; and Shea, M. A., 1983: Geomagnetic Transmission Functions for a 400 km Altitude Satellite. *18th International Cosmic Ray Conference—Conference Papers*, MG Sessions, Volume 3, Tata Inst. of Fundamental Research (Colaba, Bombay), pp. 419-422.
- Wallace, Roger W.; and Sondhaus, C. A., 1978: Cosmic Radiation Exposure in Subsonic Air Transport. *Aviation, Space, & Environ. Med.*, vol. 49, no. 4, pp. 610-623.
- Wilson, John W.; Lambiotte, Jules J.; and Foelsche, T., 1969: Structure in the Fast Spectra of Atmospheric Neutrons. *J. Geophys. Res.*, vol. 74, no. 26, pp. 6494-6496.
- Wilson, John W.; Lambiotte, Jules J., Jr.; Foelsche, Trutz; and Filippas, Tassos A., 1970: *Dose Response Functions in the Atmosphere Due to Incident High-Energy Protons With Application to Solar Proton Events*. NASA TN D-6010.
- Wilson, J. W., 1972: Production and Propagation of Atmospheric Neutrons. *Trans. American Nuclear Soc.*, vol. 15, no. 2, pp. 969-970.
- Wilson, J. W., 1981: Solar Radiation Monitoring for High Altitude Aircraft. *Health Phys.*, vol. 41, no. 4, pp. 607-617.

- Wilson, J. W.; Townsend, L. W.; and Badavi, F. F., 1987: Galactic HZE Propagation Through the Earth's Atmosphere. *Radiat. Res.*, vol. 109, no. 2, pp. 173-183.
- Wilson, John W.; and Townsend, Lawrence W., 1988: Radiation Safety in Commercial Air Traffic: A Need for Further Study. *Health Phys.*, vol. 55, no. 6, pp. 1001-1003.
- Wilson, J. W.; and Townsend, L. W., 1989: Errata—Radiation Safety in Commercial Air Traffic: A Need for Further Study. *Health Phys.*, vol. 56, no. 6, pp. 973-974.
- Wilson, John W.; Shinn, Judy L.; and Townsend, Lawrence W., 1990: Nuclear Reaction Effects in Conventional Risk Assessment for Energetic Ion Exposure. *Health Phys.*, vol. 58, no. 6, pp. 749-752.

-

-

·

|

|

|

·

·

|||||

Chapter 14

Radiation Effects in Electronic Materials

14.1. Introduction

The physical processes by which particles interact with electronic materials are the same as for any other material, namely, interaction with orbital electrons, elastic scattering with atomic nuclei of the material, and nonelastic reactions. It is the specific properties of these materials and the interaction in circuits which make the study of electronic materials of special interest. The interaction with orbital electrons raises the conductivity of the media until the charge released is collected or recombines with hole states or traps in the media. Such processes depend on external connections to the media. Elastic scattering with media nuclei depends on the binding potential of the surrounding medium, and a dislocation or series of dislocations can occur if the energy transfer is above the binding threshold. Such dislocations provide traps for the conduction electrons and holes. The nonelastic processes provide a release of kinetic energy as nuclear fragments produced by the reaction. The kinetic energy is given over to orbital electrons and elastic scattering with nuclei in the medium. The energy released in these nuclear reactions is given to orbital electrons and causes a temporary large increase in the conductivity. In the present chapter we will quantify these aspects of the interactions and treat two diverse applications of interest to the space program.

14.2. Gallium Arsenide Solar Cells

Gallium arsenide (GaAs) solar cells have received considerable attention because of their potential usefulness in high-power space-energy systems as well as special space-probe applications where high operating temperature is a limiting factor for silicon solar cells (Anon., 1977). However, space-radiation damage to the GaAs cells may be a limiting factor in Earth orbit above 2000 km and on interplanetary missions unless sufficient shielding is provided to keep damage levels within acceptable limits (Wilson, Stith, and Stock, 1983). Consequently, radiation damage studies have been made (Walker and Conway, 1978a and 1978b; Heinbockel, Conway, and Walker, 1980; Conway, Walker, and Heinbockel, 1981; Li et al., 1981; Loo, Knechtli, and Kamath, 1981; Kamath, 1981; Wilson et al., 1982; and Wilson, Stith, and Walker, 1982) on the effects of proton and electron irradiation, including defect characterization and annealing. Since damage effects are not generally additive, the combined effects of electron and proton exposure, as well as angular and spectral factors, are not known from the available experimental data base (Walker and Conway, 1978b; Loo, Knechtli, and Kamath, 1981; Kamath, 1981). To determine design parameters for a specific space environment, extensive laboratory testing or a model of the effects of the specific radiation components on the cell performance is required. Within the context of a detailed model, the question of additivity of specific radiation components can be adequately understood, and the cell performance can be evaluated under appropriate space environment conditions.

Earlier models for electron radiation damage assumed the defects to be produced uniformly throughout the cell volume and modeled the cell performance in terms of cell-averaged diffusion lengths of the minority carriers (Walker and

Conway, 1978a and 1978b; Heinbockel, Conway, and Walker, 1980). However, for low-energy protons, defects are not produced uniformly throughout the cell volume. Thus, there is a specific dependence of cell efficiency on proton energy. Consequently, the present report treats the geometric distribution of the displacement damage in detail, and cell performance is evaluated in terms of the cell-averaged minority-carrier recombination probability in diffusion to the cell junction. The average of the minority recombination probability over the cell active region weighted according to the solar-averaged photoabsorption rate is used to estimate the decrement in the short-circuit current.

14.2.1. Proton defect formation. Atomic displacements caused by proton impact with atomic nuclei result in crystal defects as illustrated in figure 14.1. The formation rate of these defects is related to Rutherford's cross section (Dienes and Vineyard, 1957):

$$\sigma_D(E) = \frac{4\pi a_0^2 E_R^2 Z_2^2}{M_2 E} \left(\frac{1}{T_D} - \frac{1}{T_m} \right) \quad (14.1)$$

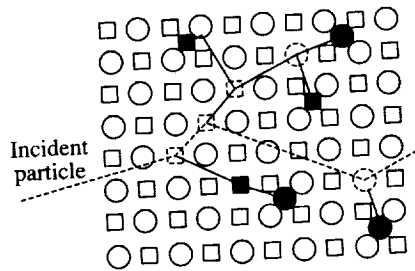


Figure 14.1. Defect formation by particulate radiation in a binary crystal. Defects shown are replacements, vacancies, and interstitials.

where a_0 is Bohr's radius, E_R is Rydberg's constant, Z_2 is the atomic number of the struck nucleus, M_2 is the corresponding nuclear mass number, E is the proton kinetic energy, T_D is the energy required to displace the nucleus from its lattice site, and T_m is the maximum energy transfer in the collision; T_m is given by

$$T_m = \frac{4M_2}{(1 + M_2)^2} E \quad (14.2)$$

The displacement cross section and average energy transfer for protons in GaAs with $Z_2 \approx 32$ and $M_2 \approx 72.5$ are shown in figures 14.2 and 14.3. The threshold for displacement requires that $T_m > T_D$. The fact that $T_D \approx 9.5$ eV (Bauerlein, 1963) ensures that only close collisions result in displacement, so that screening corrections to the Rutherford formula are unimportant. If the atomic recoil energy is sufficiently large ($T \gg T_D$), additional displacements can be produced by the recoiling nucleus before it comes to rest at an interstitial site. The average number

of recoil displacements produced by one initiating proton collision event is given as a function of the maximum energy transfer by

$$\bar{\nu}_D(E) = \begin{cases} 1 + \frac{T_m}{2(T_m - T_D)} \log\left(\frac{T_m}{T_D}\right) & (T_m > 2T_D) \\ 1.0 & (2T_D > T_m > T_D) \end{cases} \quad (14.3)$$

with the assumption that half the recoil energy produces further displacements and the other half is dissipated in other processes. These quantities allow the calculation of the number of displacements produced per unit distance traveled by a proton of fixed energy.

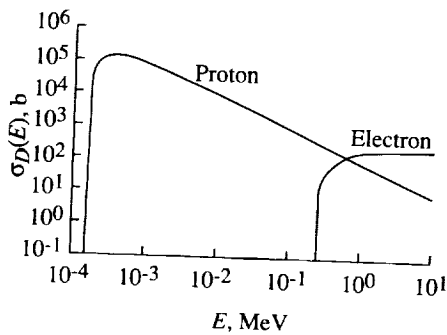


Figure 14.2. Displacement cross section for energetic protons and electrons.
 $1 \text{ barn} = 1 \times 10^{-28} \text{ m}^2$.

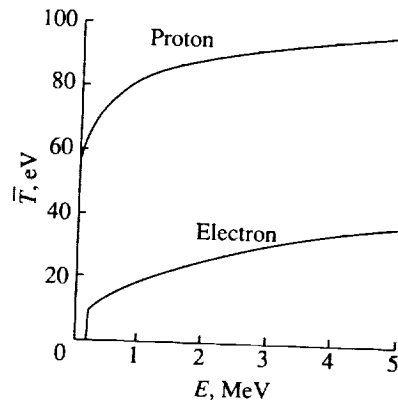


Figure 14.3. Average energy transferred to recoiling nucleus.

In passing through a crystal, most of the energy of a proton is transferred to orbital electrons (Andersen and Ziegler, 1977). The path length traveled in coming to rest is found by fitting the data of Andersen and Ziegler (1977) as

$$P(E) = 0.077E^{0.5} + 1.125 \times 10^{-4}E^{1.64} \quad (14.4)$$

where E is in keV and $P(E)$ is in μm . As derived from the slowing-down theory, a unique value of kinetic energy can be associated with each position along the trajectory of a proton. The proton energy as a function of the distance p yet to be traveled before coming to rest is given by

$$E = \frac{209.6p^{2.08}}{1 + 1.055p^{1.43}} \quad (14.5)$$

as determined by integrating the stopping-power data of Andersen and Ziegler (1977). In the process of coming to rest, the proton undergoes multiple scatterings from atomic nuclei, of which a few result in displacements. This process alters ever so slightly the direction of motion of the proton. The depth of penetration

$R(E)$ and path length $P(E)$ are approximately related by

$$P(E)^{-1}R(E) = \left[1 - \exp\left(-0.084E^{0.55}\right)\right] \quad (14.6)$$

This ratio is related to the average deviation in the direction of motion and is most important at low energies. The average depth of penetration and initial energy as related through equations (14.4) and (14.6) can be approximated by

$$R(E) = 0.0062E + 2.92 \times 10^{-5}E^{1.77} \quad (14.7)$$

There is no unique energy associated with a given depth of penetration because of multiple scattering. However, the average energy of protons which penetrate and stop at a depth x is

$$E = \frac{593x^{1.5}}{x + 3.71x^{0.5}} \quad (14.8)$$

The preceding quantities were used to determine the displacement density within a GaAs crystal.

A proton of energy E_o incident on the face of the crystal travels a distance

$$P_o = P(E_o) \quad (14.9)$$

before coming to rest. After traveling a distance p the energy will be reduced to

$$E = \frac{209.6(P_o - p)^{2.08}}{1 + 1.055(P_o - p)^{1.43}} \quad (14.10)$$

At this position p , the displacement mean-free path is

$$\ell_D(E) = \frac{1}{n\sigma_D(E)} \quad (14.11)$$

where n is the density of scattering centers in the crystal ($4.42 \times 10^{10}/\mu\text{m}^3$), and $\sigma_D(E)$ is the displacement cross section averaged for GaAs ($M_2 = 72.5$ and $Z_2 = 32$). The average number of displacements per unit path length is

$$\xi_D(E) = \frac{\bar{\nu}_D(E)}{\ell_D(E)} \quad (14.12)$$

The use of equations (14.10) and (14.12) allows appropriate partitioning of the proton energy into electronic excitation and displacements everywhere along its path.

The number of displacements along the proton path is related to the displacement damage in the crystal. For a normally incident proton of energy E_o on the face of a crystal, the number of displacements along its path is given by equations (14.10) and (14.12). However, by the time its energy is reduced to E , it has penetrated to an average depth x given by

$$x = R(E_o) - R(E) \quad (14.13)$$

The path length and penetration depth are related to the average direction cosine (Janni, 1966) and are approximated here by solving the equation $\bar{\mu}(E) = dP(E)/dR(E)$ using equations (14.4) and (14.6). In terms of $\bar{\mu}(E)$, the average number of displacements per unit depth is

$$\frac{dD(E)}{dx} = \bar{\mu}(E) \xi_D(E) \quad (14.14)$$

where x is found from equation (14.13). The effects of multiple scattering are demonstrated in figure 14.4. The results of equation (14.14) for the average proton path due to multiple scattering (solid line) are compared with calculations neglecting multiple scattering (dashed line) according to equation (14.12). The difference between the two curves is a measure of the fluctuations caused by multiple scattering.

The total number of displacements formed along the path of a proton with initial energy E_o is

$$D(E_o) = \int_0^{E_o} \xi_D(E) \frac{dP(E)}{dE} dE \quad (14.15)$$

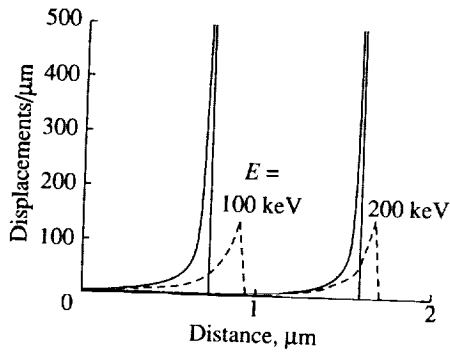


Figure 14.4. Displacement density for a single proton path.

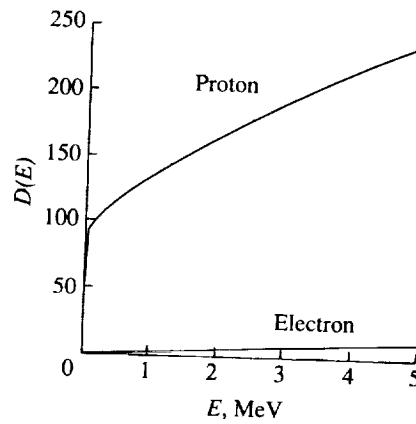


Figure 14.5. Total number of displacements formed in bringing a particle to rest in GaAs crystal.

The numerical evaluation of equation (14.15) as shown in figure 14.5 is approximated by (E_o in units of keV)

$$D(E_o) = \left\{ \begin{array}{ll} 0 & (E_o < 0.64) \\ 12.4 + 350.4 (1 - 0.8236 E_o^{0.016}) \log_{10}(E_o) & (0.64 < E_o < 20) \\ 47.83 + 20.48 (1 + 3.246 \times 10^{-3} E_o^{0.721}) \log_{10}(E_o) & (20 < E_o) \end{array} \right\} \quad (14.16)$$

where the effective threshold displacement energy for the proton is 0.64 keV. Equation (14.13) was also evaluated using the displacement theory of Lindhard, Scharff, and Schiott (LSS) (1963) as discussed by Peterson and Harkness (1976). The numerical values of the LSS theory and the present results are in good agreement. (See Wilson et al., 1982.)

14.2.2. Electron defect formation. One of the significant differences between proton and electron interaction is that relativistic effects must be included in the electron interaction. The Mott-McKinley-Feshbach (McKinley and Feshbach, 1948; see also Vook, 1968) relativistic electron scattering cross section leads to the expression

$$d\sigma = \pi r_c^2 Z_2^2 \left(\frac{1 - \beta^2}{\beta^4} \right) \left(\frac{T_m}{T^2} - \frac{\beta^2}{T} + \frac{\pi\alpha\beta}{T_m} \left(\frac{T_m}{T} \right)^{\frac{3}{2}} - \frac{\pi\alpha\beta}{T} \right) dT \quad (14.17)$$

where r_c is the classical electron radius, Z_2 is the atomic number of the target atom, β is the ratio of the electron velocity to the speed of light, T is the energy transferred in the collision, and α equals $Z_2/137$. Integration yields the displacement cross section shown in figure 14.2 and given by

$$\sigma_D(E) = \pi Z_2^2 r_c^2 \left(\frac{1 - \beta^2}{\beta^4} \right) \times \left[\frac{T_m}{T_D} - 1 - \beta^2 \log \left(\frac{T_m}{T_D} \right) + 2\pi\alpha\beta \left(\sqrt{\frac{T_m}{T_D}} - 1 \right) - \pi\alpha\beta \log \left(\frac{T_m}{T_D} \right) \right] \quad (14.18)$$

where T_D is the displacement threshold, the maximum energy transfer T_m is

$$T_m = \frac{2E}{M_2 c^2} (E + 2mc^2) \quad (14.19)$$

M_2 is the mass of the atom, m is the mass of the electron, and c is the velocity of light. In a collision between an electron of energy E and an atom, the atom acquires an energy in excess of T_D for cross section $\sigma_D(E)$.

A requirement for displacement of a nucleus is that $T > T_D$. The value of T_D used in deriving this model is 9.5 eV. The average energy transfer during a collision is

$$\bar{T}(E) = \frac{1}{\sigma_D(E)} \int_{T_D}^{T_m} T \frac{d\sigma_D(E)}{dT} dT = \frac{T_m \log \left(\frac{T_m}{T_D} \right) - \beta^2 (T_m - T_D) + 2\pi\alpha\beta (T_m - \sqrt{T_m T_D}) - \pi\alpha\beta (T_m - T_D)}{\frac{T_m}{T_D} - 1 - \beta^2 \log \left(\frac{T_m}{T_D} \right) + 2\pi\alpha\beta \left(\sqrt{\frac{T_m}{T_D}} - 1 \right) - \pi\alpha\beta \log \left(\frac{T_m}{T_D} \right)} \quad (14.20)$$

Figure 14.3 illustrates the dependence on electron energy of the average energy transfer between an electron of initial energy E and a gallium or arsenic atom. If the energy transfer $T(E) \gg T_D$, additional atomic displacements can be

produced by the initial recoiling nucleus before it comes to rest at an interstitial or replacement site. The average number of recoils caused by one electron colliding with an atom is given as a function of the average energy transfer by

$$\bar{\nu}_D(E) = \begin{cases} 1 & (T_D < \bar{T}(E) < 2T_D) \\ 1 + \frac{\bar{T}(E)}{2T_D} & (\bar{T}(E) > 2T_D) \end{cases} \quad (14.21)$$

assuming half the recoil energy produces further displacements and assuming the other half is dissipated in other processes.

The displacement mean-free path is

$$\ell_D(E) = \frac{1}{n \sigma_D(E)} \quad (14.22)$$

where n is the density of scattering centers in the crystal ($4.42 \times 10^{22}/\text{cm}^3$) and $\sigma_D(E)$ is the displacement cross section average for GaAs ($M_2 = 72.5$ and $Z_2 = 32$). The average number of displacements per unit path length produced by an electron of initial energy E is

$$\begin{aligned} \xi_D(E) &= \frac{\bar{\nu}_D(E)}{\ell_D(E)} = n \bar{\nu}_D(E) \sigma_D(E) \\ &= \begin{cases} n \sigma_D(E) & (T_D < \bar{T}(E) < 2T_D) \\ n \sigma_D(E) + \frac{n}{2T_D} \sigma_D(E) \bar{T}(E) & (\bar{T}(E) > 2T_D) \end{cases} \end{aligned} \quad (14.23)$$

The total number of displacements produced along the path of an electron of initial energy E_0 is

$$D(E_0) = \int_0^{E_0} \frac{\xi_D(E)}{S(E)} dE = n \int_0^{E_0} \frac{\bar{\nu}(E) T_D(E)}{S(E)} dE \quad (14.24)$$

where

$$S(E) = \begin{cases} 0.381 E^{0.084} & (260 < E < 1000 \text{ keV}) \\ 0.623 + 4.25 \times 10^{-5} E & (1000 < E < 10\,000 \text{ keV}) \end{cases} \quad (14.25)$$

is the stopping-power formula ($\text{keV}/\mu\text{m}$) determined from data of Pages et al. (1972). Numerical evaluation of the displacement integral can be approximated by

$$D(E) = \begin{cases} 0 & (E < 260 \text{ keV}) \\ -3.6 + 3.32 \times 10^{-3} E + 3.58 \exp(-1.094 \times 10^{-3} E) & (260 < E < 10\,000 \text{ keV}) \end{cases} \quad (14.26)$$

Figure 14.5 illustrates the dependence of atomic displacements in GaAs on initial electron energy as found from evaluation of equation (14.24).

In passing through the crystal, the electron is slowed down as it interacts with orbital electrons and atomic nuclei. Using data from Pages et al. (1972), the range of the electron in GaAs as a function of initial electron energy E is given by

$$R(E) = 0.4027E^{1.16} - 5.95 \times 10^{-5}E^2 \quad (14.27)$$

where $R(E)$ is in μm and E is in keV. The effects of multiple scattering are neglected in this formula for $R(E)$ because multiple scattering of electrons is relatively unimportant in the thin GaAs cells treated herein.

From the same data used in determining the range formula, a formula for the average energy of an electron that penetrates to a depth R and stops is

$$E = 2.217R^{0.86} + (2.25 \times 10^{-5}) R^2 \quad (14.28)$$

After penetrating to a depth of x within the crystal, the electron energy is given by

$$E_o(x) = 2.217(R_o - x)^{0.86} + 2.25 \times 10^{-5}(R_o - x)^2 \quad (14.29)$$

The effect of these radiation-induced defects on cell performance is discussed in the section 14.2.3.

14.2.3. Minority-carrier recombination. It is assumed that these radiation-induced displacements within the crystal form recombination centers for the minority carriers of the electron-hole pairs produced by photon absorption. A minority carrier, once formed, undergoes thermal diffusion (Hovel, 1975) until it is trapped and recombines or is separated at the junction. The root-mean-square distance traveled in moving to a position a distance L away from the source point is (Liverhant, 1960)

$$\bar{r} = \sqrt{6} L \quad (14.30)$$

If σ_r is the recombination cross section and L is the distance along an arbitrary straight line path to the junction, the fractional loss of pairs due to recombination in reaching the junction along a fixed direction is

$$f(\mu) = \left\{ \begin{array}{l} \left\{ 1 - \exp \left[- \int_{x_j}^x \sigma_r D_v(x) \sqrt{6} \frac{dx}{\mu} \right] \right\} \quad (x > x_j) \\ \left\{ 1 - \exp \left[- \int_x^{x_j} \sigma_r D_v(x) \sqrt{6} \frac{dx}{\mu} \right] \right\} \quad (x < x_j) \end{array} \right\} \quad (14.31)$$

where μ is the cosine of the direction to the junction, and $D_v(x)$ is the displacement density. Averaging the fractional loss over all directions toward the junction

$$F(x) = \int_0^1 f(\mu) d\mu \quad (14.32)$$

results in

$$F(x) = 1 - E_2 \left(\sqrt{6} \sigma_r \left| \int_x^{x_j} D_v(x) dx \right| \right) \quad (14.33)$$

where summations over all spectral and angular components are implied. Note that $E_2(z)$ is the exponential integral of order 2.

The photoabsorption rate density at a depth x within the cell for the solar spectrum is

$$\rho(x) = K\gamma \exp(-\gamma x) \quad (14.34)$$

where K is the integrated flux in the absorption band and γ is the photoabsorption coefficient averaged over the solar spectrum ($\gamma \approx 1.4 \mu\text{m}^{-1}$). The rate at which the photocurrent is collected under short-circuit conditions is

$$I_{sc,0} = \int_0^t \eta_c(x) \rho(x) dx \quad (14.35)$$

where $\eta_c(x)$ is the normal or preirradiated collection efficiency and t is the depth of the active region. The normal collection efficiency is known in terms of diffusion lengths, lifetimes, and surface recombination rates of the minority carriers; electric fields; and cell dimensions (Loo et al., 1978).

To derive a simple expression for the short-circuit current in an irradiated cell, the following simplifying assumptions are made. First, it is assumed that the radiation-induced defects do not greatly alter the internal-cell electric fields. It is further assumed that the radiation defects mainly alter the cell operation through change in the minority-carrier lifetime in the bulk. Surface recombination plays only a secondary role for heteroface cells. (See Walker and Conway, 1978a and 1978b.) Viewing $\eta_c(x)$ as a probability of current collection of an electron-hole pair produced at x , it is further assumed that the normal collection efficiency and the recombination probability with radiation defects are statistically independent. This independence, which allows the postirradiation short-circuit current to be written as

$$I_{sc} = \int_0^t \eta_c(x) [1 - F(x)] \rho(x) dx \quad (14.36)$$

for which the fractional remaining current is

$$I_{sc}/I_{sc,0} = 1 - \left[\frac{\int_0^t \eta_c(x) F(x) \rho(x) dx}{\int_0^t \eta_c(x) \rho(x) dx} \right] \quad (14.37)$$

For a well-designed high-collection-efficiency solar cell, $\eta_c(x)$ is nearly spatially independent over the cell active volume, so that further simplification results in

$$I_{sc}/I_{sc,0} \approx 1 - \left[\frac{\int_0^t F(x) \rho(x) dx}{\int_0^t \rho(x) dx} \right] \quad (14.38)$$

which is used throughout the remainder of the present work.

14.2.4. Evaluation of defect spatial distribution. Central to the calculation of radiation effects as outlined in the preceding section is evaluation of the integral of the defect volume density. This integral is related to a cumulative defect function by

$$D_c(x) = \int_0^x D_v(x') dx' \quad (14.39)$$

This quantity may be evaluated for a fluence $\phi(E_o)$ of normally incident particles of energy E_o . This is accomplished by simply calculating the particle residual energy $E_o(x)$ after the particle penetrates to a depth x and noting that

$$D_c(x) = \{D(E_o) - D[E_o(x)]\} \phi(E_o) \quad (14.40)$$

Since $E_o(x)$ is the residual-energy function for normal incidence, the corresponding result for oblique incidence is

$$D_c(x) = \left\{ D(E_o) - D \left[E_o \left(\frac{x}{\cos \theta} \right) \right] \right\} \phi(E_o) \quad (14.41)$$

where θ is the angle of incidence to the normal of the surface. Generalizing for a spectrum of particles and isotropic incidence,

$$D_c(x) = 2\pi \int_0^\infty dE_o \int_0^1 d(\cos \theta) \left\{ D(E_o) - D \left[E_o \left(\frac{x}{\cos \theta} \right) \right] \right\} \phi(E_o) \quad (14.42)$$

where $4\pi \phi(E_o)$ is the omnidirectional differential fluence spectrum.

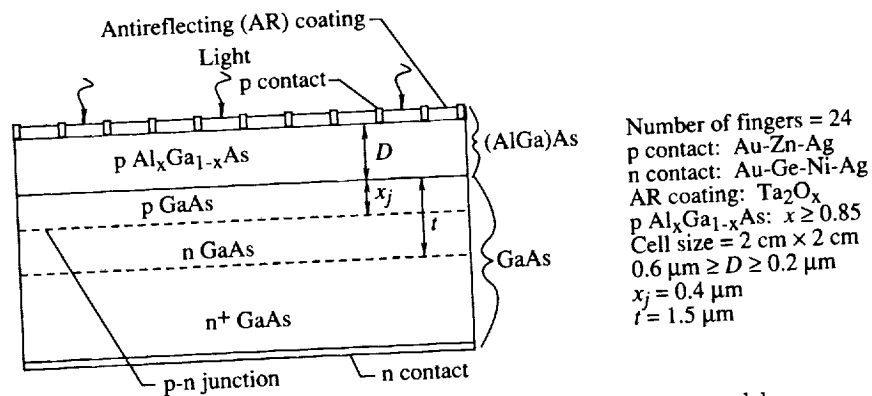


Figure 14.6. GaAs solar cell structure used in present model.

14.2.5. Comparison with experiment. The geometry of the solar cells used in experimental tests (Loo, Knechtli, and Kamath, 1981; Kamath, 1981) is shown in figure 14.6. The changes in the cell current collection efficiency as given by equation (14.38) were evaluated numerically and are shown in figure 14.7 for the solar cell parameters shown in figure 14.6. Since the protons follow neither the trajectory of the average proton nor the trajectory in which multiple-scattering is neglected (fig. 14.4), improvements were made by including the effects of multiple scattering. These effects were estimated by averaging with equal weight the cell damage for the two functions shown in figure 14.4, in which some effects

of deviations about the average trajectory are included. It is clear that an understanding of the low-energy experimental data requires detailed modeling of multiple-scattering effects. The window thickness parameters which varied from cell to cell in experimental tests (Li et al., 1981; Kamath, 1981) were assumed to be governed by a uniform distribution in the present calculations. The model results averaged over the window thickness are compared with short-circuit current measurements (Loo, Knechtli, and Kamath, 1981; Kamath, 1981) of irradiated cells shown in figure 14.7. The best value of recombination cross section, in cm^2 , for proton induced defects is

$$\sigma_r \approx 6 \times 10^{-14} \quad (14.43)$$

which is in fair agreement with the estimated average cross section ($\sigma_r \approx 1.06 \times 10^{-13} \text{ cm}^2$) determined from deep-level transient spectroscopy (Li et al., 1981).

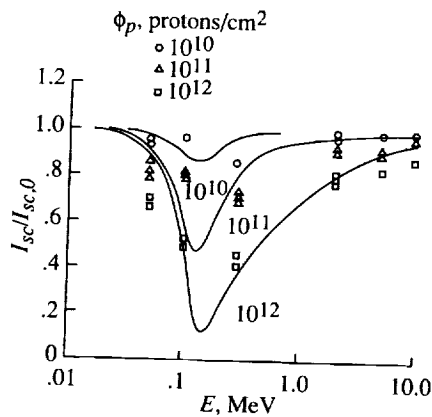


Figure 14.7. Reduced short-circuit efficiency for monoenergetic proton exposure at three fluence levels.

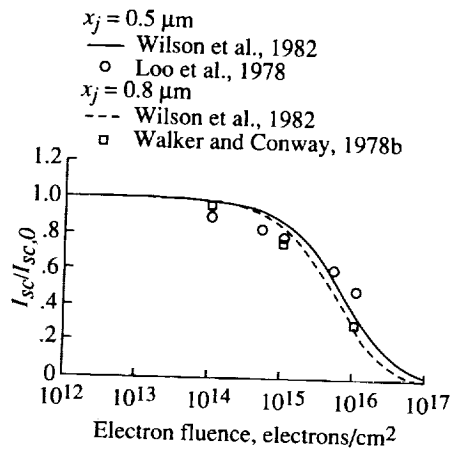


Figure 14.8. Reduced short-circuit current after 1 MeV of electron exposure for two junction depths.

The fractional short-circuit current remaining after 1 MeV of electron irradiation is shown as a function of electron fluence in figure 14.8. The recombination cross section, in cm^2 , is

$$\sigma_r \approx 4 \times 10^{-14} \quad (14.44)$$

and calculations were made for two junction depths, namely $0.5 \mu\text{m}$ and $0.8 \mu\text{m}$. Also shown in figure 14.8 are corresponding experimental data of Walker and Conway (1978b) and Loo et al. (1978). The reasonable consistency of the theory for vastly different particle types is gratifying.

14.2.6. Equivalent electron-fluence concept. It is customary in protection from mixed-radiation environments to develop concepts under which effects of radiations of different quality may be combined to ascertain the total effect on device performance. From an electronic device standpoint, the equivalent electron fluence is usually employed as the combinational rule. The equivalent electron fluence is defined as that fluence of electrons of fixed energy (usually 1 MeV) which

produces the same effect on the device performance as a particle fluence of a particular type, energy, and fluence level. The fluence of electrons ϕ_e equivalent to a fluence of protons $\phi_p(E_p)$ of energy E_p is given by

$$R_p[\phi_p(E_p)] = R_e(\phi_e) \quad (14.45)$$

where R_p and R_e are the device response functions for proton and electron damage (Tada and Carter, 1977). If equation (14.45) is satisfied, the equivalent-fluence ratio may be defined as

$$\tau_f(E_p) = \frac{\phi_e}{\phi_p(E_p)} \quad (14.46)$$

and the main usefulness of the concept requires that $\tau_f(E_p)$ not depend on the magnitude of $\phi_p(E_p)$. The equivalence for solar cells is usually related through the minority-carrier diffusion length for which the equivalent-fluence ratio is expressed as the ratio of the damage coefficients (Wilson, Stith, and Walker, 1982; Tada and Carter, 1977). The combined effects of electron and proton exposure are then

$$R_{tot}[\phi_p(E_p), \phi_e] = R_e[\phi_e + \tau_f(E_p)\phi_p(E_p)] \quad (14.47)$$

where ϕ_e and $\phi_p(E_p)$ are the mixed environmental components. The strong energy dependence of the response to protons arising from spatial nonuniformity in cell damage brings into question the usefulness of the concept of equivalent electron fluence (Wilson, Stith, and Walker, 1982; Tada and Carter, 1977).

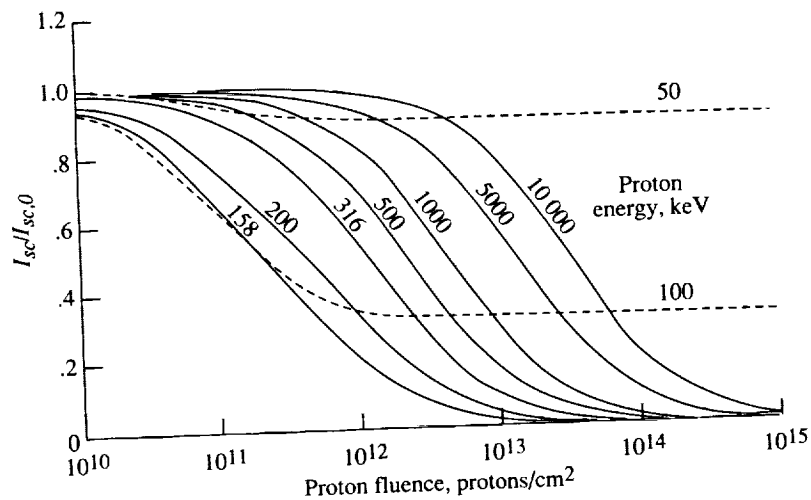


Figure 14.9. Reduced short-circuit current for monoenergetic proton exposure for 0.5- μm junction cells.

The remaining short-circuit current for 0.4- μm window cells and 0.5- μm junction cells as a function of proton energy and fluence is shown in figure 14.9. The equivalent-fluence ratio was calculated using equations (14.45) and (14.46) for 1-MeV electron-fluence levels $\phi_e = 1.7 \times 10^{15}$ electrons/cm², 6.8×10^{15} electrons/cm², and 2.3×10^{16} electrons/cm² at $I_{sc}/I_{sc,0} = 0.8, 0.5,$ and 0.2 (as

shown in fig. 14.8 for the 0.5- μm junction cell). The resulting values of $r_f(E_p)$ are shown in figure 14.10 for each of the three fluence levels. For the equivalent-fluence concept to be useful, the three curves must coincide at all proton energies as they do above 500 keV. However, in the proton energy range 50 to 500 keV, where the cell is extremely sensitive, the usefulness of equivalent electron fluence is generally limited by the strong dependence of the equivalent-fluence ratio on the damage level. This has important consequences in terms of radiation testing, since the mixed environment generally must be simulated to ensure a valid test unless the bivariate equivalent-fluence ratio is adequately known. On the other hand, for a given (fixed) environment, test procedures could be established through the use of the present model, for a given cell type. Thus, an "equivalent" electron fluence could be established in the restricted sense of fixed environmental components.

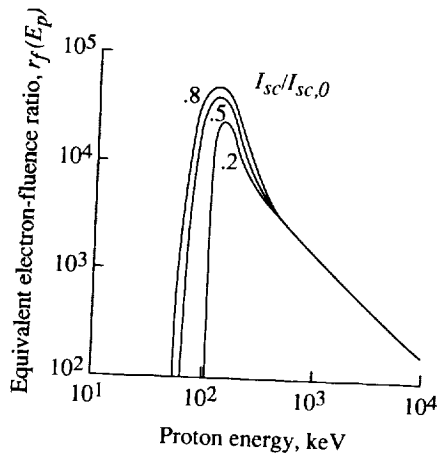


Figure 14.10. Equivalent electron-fluence ratio for a cell with 0.5- μm junction depth and a 0.4- μm $\text{Al}_x\text{Ga}_{1-x}\text{As}$ window.

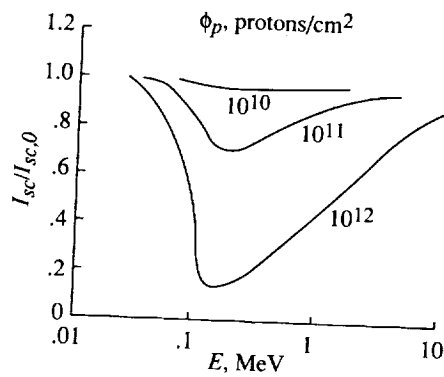


Figure 14.11. Reduced short-circuit current for isotropic incident protons at three fluence levels.

14.2.7. Angular isotropy effects. The radiation in space can, for most practical purposes, be considered isotropic, and most radiation models present data as the omnidirectional fluence. Such angular factors generally have great importance in radiation protection problems (Wilson, Stith, and Walker, 1982), and such effects within the context of this simple model are evaluated here. The relationship between defect density distribution within the cell and cell performance having been established, the defect density is now evaluated for isotropic-incidence monoenergetic protons by replacing $\phi(E_o)$ in equation (14.42) with a δ -function. Results are shown in figure 14.11. Clearly, angular isotropy effects show no major differences in cell sensitivity at all energies and fluence levels, although a general increase in radiation resistance at the lowest fluence levels is apparent. However, at the high fluence levels, the sensitivity is increased in the 200-keV to 1-MeV region. At higher energies ($E \gg 1$ MeV), angular factors are relatively less important because of the high penetrating power of the protons.

In general, the angular factors are helpful if fluence levels are sufficiently low that the reduced penetration of low-energy protons at oblique angles of incidence serves to provide the cell with added protection. At high fluence levels and

fixed energy, the minority-carrier recombination rates near the end of the proton trajectories tend to saturate for normal incidence, whereas isotropic incidence tends to distribute these defects more uniformly over the cell. This uniform distribution increases their effectiveness for cell damage, which in turn accounts for the increased cell sensitivity for $E > 200$ keV (as shown in fig. 14.11 for $\phi_p = 10^{12}$ protons/cm²). The spectral characteristics for performance evaluation in space applications must still be considered in the protection against space radiation.

Solar cell performance is likewise evaluated for isotropically incident 1-MeV electrons. The results are shown in figure 14.12 as a function of omnidirectional fluence level (0.5- μ m junction depth and infinite backing is assumed). Comparison of figure 14.12 with figure 14.8 for normal incidence shows that an isotropically incident electron is equivalent to four normally incident electrons. Clearly, isotropic incidence is a most important factor for space-radiation testing.

14.2.8. Effects of space-radiation environment. Space missions to the fringes of the geomagnetic field and interplanetary missions experience the yearly solar-particle fluence during highly solar-active years (Foelsche, 1963) on the order of

$$\phi_p(E_p) \approx \frac{5 \times 10^{14}}{E_p} \quad (14.48)$$

where E_p is in keV and ϕ_p is in protons/cm². The remaining short-circuit current calculated from equations (14.38) and (14.48) as a function of cover glass thickness is shown in figure 14.13. It is clear that an unshielded cell would not survive a major solar event and requires a cover glass of about 25 μ m to ensure performance levels to within 90 percent of their initial value.

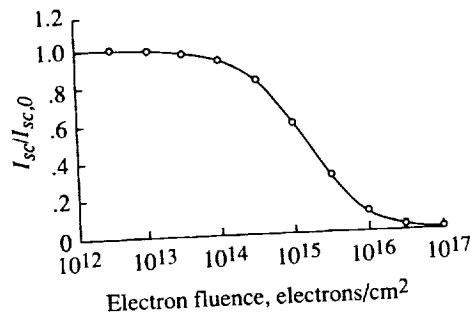


Figure 14.12. Reduced short-circuit current for isotropically incident 1-MeV electrons as a function of omnidirectional fluence.

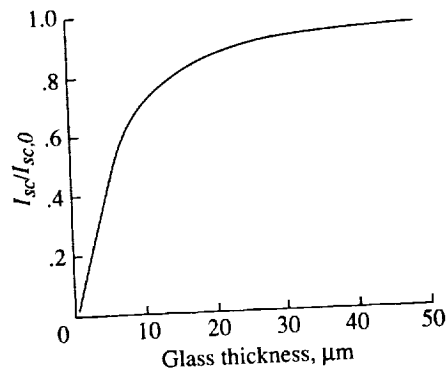


Figure 14.13. Reduced short-circuit current due to a large solar event of a cell with a 0.5- μ m junction depth and a 0.5- μ m Al_{1-x}Ga_xAs window as a function of cover glass thickness.

The protons trapped at geosynchronous altitude ($L = 6.6$ Earth radii) are well approximated (Sawyer and Vette, 1976) by

$$\phi_p(E_p) = 2.5 \times 10^{14} \exp \left[-1.27 - 0.0072E_p + \frac{230}{E_p} \right] \quad (14.49)$$

where ϕ_p is in protons/cm²-yr. The corresponding yearly electron fluence (Singly and Vette, 1972) is

$$\phi_e(E_e) = 4.5 \times 10^{14} \exp \left(-2.832 \times 10^{-3} E_e \right) \quad (14.50)$$

in electrons/cm²-yr. The short-circuit current ratio is calculated for equivalent 1-, 5-, and 10-yr missions in the trapped environment with results shown in figure 14.14 as a function of cover glass thickness. Equations (14.48) to (14.50) are integrated flux and must be differentiated for use in equation (14.42). A 15- μm glass cover is required to stop the geosynchronous trapped protons. Cover glass thickness beyond 15 μm is ineffective for protection against the electron environment. The effects of the geosynchronous trapped environment are combined with a single large solar event in figure 14.15 for 1-, 5-, and 10-yr missions. Little improvement in cell protection is obtained by having a cover glass thickness in excess of about 30 μm . For a complete evaluation of solar cell performance, one needs to consider the production of color centers in the cover glass and their effect on cell performance.

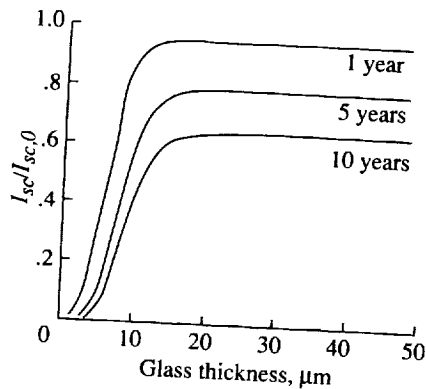


Figure 14.14. Reduced short-circuit current of a cell with 0.5- μm junction depth and a 0.5- μm $\text{Al}_{1-x}\text{Ga}_x\text{As}$ window as a function of cover glass thickness in geosynchronous environment.

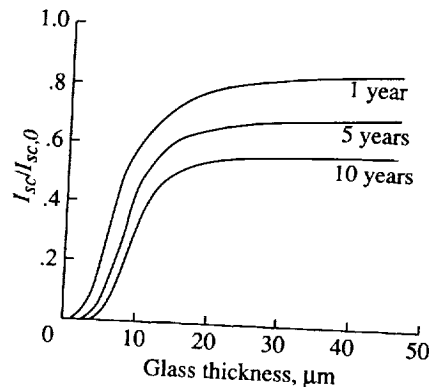


Figure 14.15. Reduced short-circuit current of a cell with a 0.5- μm junction depth and a 0.5- μm $\text{Al}_{1-x}\text{Ga}_x\text{As}$ window as a function of cover glass thickness in combined geosynchronous and solar cosmic-ray environment.

14.3. Microscopic Defect Structures and Equivalent Electron-Fluence Concepts

The problem of additivity of exposure due to protons and electrons rests on the concept that proton damage and electron damage are in some sense equivalent.

When equivalence is valid then for any proton fluence causing damage in a cell, there is an equivalent electron fluence (usually 1 MeV) which causes the same damage level. In this way electron and proton damage can be added for total damage effect. In section 14.2.6 the issue of equivalent electron density of defects examined from the point of view of the macroscopic spatial density of defects produced in a GaAs shallow junction solar cell (Wilson and Stock, 1984). The calculations utilized a simple model of short-circuit current for the cell by Wilson, Walker, and Outlaw (1984) which has achieved considerable success in predicting experimental results (Wilson et al., 1982; Wilson, Stith, and Walker, 1982). More recently, further experiments have fully justified damage level for protons in the energy range below about 0.5 MeV (Anspaugh and Downing, 1984). Although it is not clear from these published experimental results as to what "high" and "low" damage levels were actually used in the experiment and that they measured the power decrement rather than the short-circuit current decrement, the comparison between theory and experiment shown in figure 14.16 is quite encouraging.

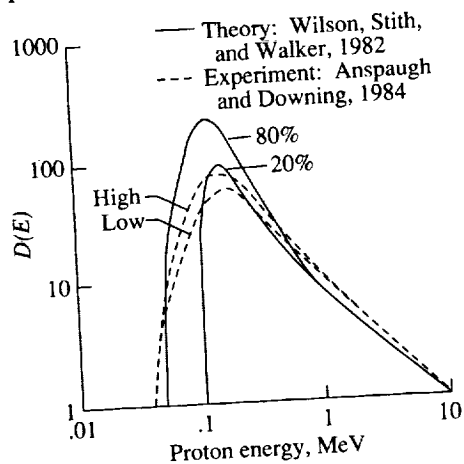


Figure 14.16. Proton damage coefficient.

In addition to the equivalent fluence for test exposure, one must take account of exposure time and temperature since a degree of self-healing of the cell is normally present. In this respect one may call to mind the experience with GaAs cells on NTS-2 for which annealing in flight is suspected (Walker, Statler, and Lambert, 1978). When such factors are fully considered, a reexamination of electron equivalency must be made since evidence exists which indicates that defect structures produced by proton exposure do not readily anneal (Anspaugh and Downing, 1981). Further study of space-radiation damage in which the chemistry of specific defects are included is clearly needed.

In the present section we will examine the question of equivalence in terms of the microscopic defect structures. The equivalent electron fluence concept is then said to hold only if the macroscopic and microscopic defect densities are reasonably represented under simplified test conditions. Implications as to minimum test requirements will be discussed.

14.3.1. Theory. Atomic displacements caused by particle impact with atomic nuclei result in crystal defects. The formation of the defects is related to the energy-transfer cross section, which is obtained from Rutherford's cross section for protons and Mott's cross section for electrons. The maximum energy transfer for protons is $T_m = 4M E_p / (1 + M)^2$ where M is the atomic weight of the struck nucleus and E_p is the proton energy. The maximum energy transfer for an electron of energy E_e is similarly $T_m = 2E_e (E_e + 2m_e c^2) / M_c^2$ where $m_e c^2$ is the electron rest energy.

The minimum energy transfer to produce one displacement is $T_D \approx 9.5$ eV. At least one displacement is produced whenever $T \geq T_D$. When the recoil energy exceeds T_D , the nucleus is proficient in producing further recoils with half its energy and the remaining half is lost in electronic excitation. Hence, the total number of recoils is

$$\nu \approx 1 + \frac{T}{2T_D} \quad (T \geq 2T_D) \quad (14.51)$$

One may be tempted to take the integer part of ν , but this would be incorrect since ν as written is to be interpreted as a mean for many such events. We now introduce the cross section for producing ν or more defects as

$$\sigma_\nu(E) = \int_{T_\nu}^{T_m} \frac{d\sigma}{dT} dT \quad (14.52)$$

where $T_\nu = 2(\nu - 1)T_D$. The probability that more than ν defects are produced in a given collision is then

$$P_\nu = \frac{\sigma_\nu(E)}{\sigma_D(E)} \quad (14.53)$$

where $\sigma_D(E)$ is the total displacement cross section. Values for P_ν are shown in figure 14.17 as a function of proton energy for values of ν from 2 to 10. It is seen that an asymptotic value for P_ν is reached rather quickly ($E_p \approx 23$ keV).

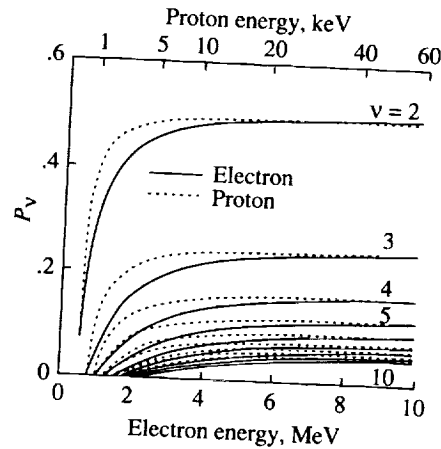


Figure 14.17 Defect number probabilities.

Values of P_ν are also shown in figure 14.17 as a function of electron energy and values of ν from 2 to 10. Note we have the relation between maximum energy transfer of the proton and electron (i.e., T_m (proton) = T_m (electron)) so that

$$E_p = \frac{(1 + M)^2 E_e (E_e + 2m_e c^2)}{2M^2 c^2} \quad (14.54)$$

Clearly the defect structures produced by protons and electrons are quite different for electron energies below 10 MeV. This is shown more clearly in table 14.1 where values of P_ν for protons and electrons of various energies are compared. The number of defects at a recoil site is nearly independent of proton energy, as shown in table 14.1. In distinction, the 1-MeV electron produced defects are vastly different. The number of defects at the recoil site of electrons approaches the proton values only as the electron energy exceeds 10 MeV.

Table 14.1. Defect Probabilities for Protons and Electrons

ν	Probability of forming ν defects—						
	For protons with energies E_p , MeV, of—				For electrons with energies E_e , MeV, of—		
	0.02	0.05	0.1	1	1	5	10
2	0.496	0.498	0.499	0.500	0.314	0.489	0.501
3	.243	.247	.249	.250	.046	.232	.249
4	.159	.164	.165	.167	.001	.145	.164
5	.117	.122	.123	.125		.103	.122
7	.075	.080	.082	.083		.060	.079
10	.047	.052	.054	.055		.033	.050

It is clear from the data presented that 1-MeV electron-induced defects appear as isolated events of two or three displacements. In distinction, proton-induced defects show a broad range of defect structures with appreciable numbers having more than five displacement sequences. It is believed that this is the main source of difference in annealing properties between proton and 1-MeV electron irradiation damage.

In order to provide a better understanding of the process of defect formation and kinetics, a binary-collision simulation code MARLOWE is employed (Robinson and Torrens, 1974). The GaAs unit cell is shown in figure 14.18. The primary recoil atom energy was taken as 20 eV corresponding to the average energy transferred by a 1-MeV electron and 90 eV representing the average energy transferred by the collision of a proton of a few MeV (see figure 14.3). This work is continuing at Virginia State University (John J. Stith).

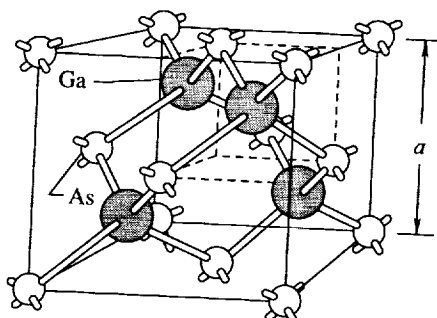


Figure 14.18. A unit cell of the GaAs crystal showing the corresponding lattice parameters.

The results from the computer simulations yielded information on the spatial distribution of the defect pairs (close pairs, near pairs, and distant pairs), as well as details on possible clusters of defects, such as multiple vacancies. Close pairs are vacancy-interstitial pairs that are separated by distances that are less than nearest neighbors separation; near pairs are vacancy-interstitial pairs that are separated by distances greater than nearest neighbors separation but less than the distance between second-nearest neighbors; and distant pairs are interstitial-vacancy pairs that are separated by distances greater than the distance between second-nearest neighbors. Information is also generated on improper replacements which are produced in irradiated binary crystals, such as gallium arsenide. These are a form of stable defect produced in the damaged crystal.

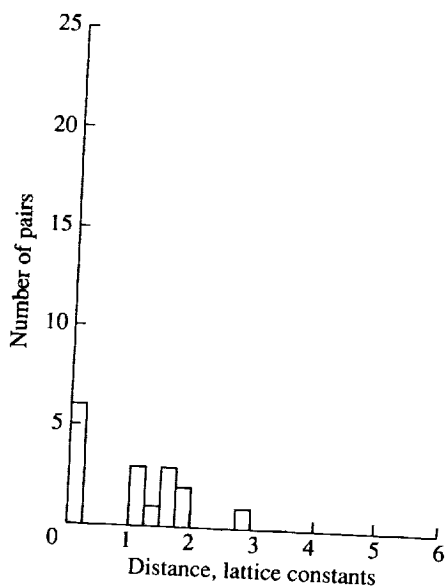


Figure 14.19. Distribution of interstitial-vacancy pairs for a 20 eV primary recoil atom.

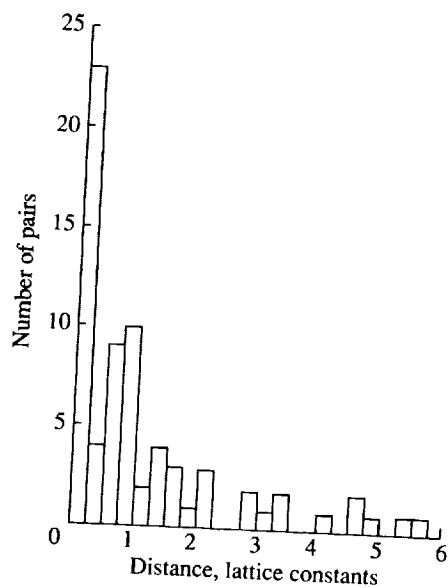


Figure 14.20. Distribution of interstitial-vacancy pairs for a 90 eV primary recoil atom.

The graphs in figures 14.19 and 14.20 show the distribution of the separations of the pairs for the 20- and 90-eV recoil energies, respectively. These distributions include close, near, and distant pairs. When the distributions on the two

graphs are compared, it is clear that there are more interstitial-vacancy pairs for the higher-energy cascades than for the lower-energy cascades. This is to be expected. The results from two different cascades are displayed in figures 14.21 through 14.26. Figures 14.21 and 14.22 show the relative positions of the interstitials and the vacancies produced in the crystal. Close, near, and distant pairs are displayed. The circle represents a vacancy and the square represents an interstitial. In figures 14.23 and 14.24 the close pairs are not included since it is a good probability that the vacancies and interstitials that form the close pairs will combine (self-anneal). The triangle is used to represent defects caused by improper replacements that occur in the crystal. Figures 14.25 and 14.26 display improper replacements and the distant pairs. The distant pairs may still exist after annealing of the crystal and would represent, along with the improper replacements, stable defects within the crystal. When a proper pair combines, two defects are eliminated; but when an improper pair combines, two defects are reduced to one defect which is different from either of the two original defects. There is a sizable difference between the number of distant pairs for the high-energy primary recoil atoms over the number of distant pairs for the low-energy primary recoil atoms. It should also be noted that the high-energy primary recoil atom generates several subcascades, giving rise to more extensive damage structures within the crystal. This is qualitatively similar to the experimental results that demonstrated a high degree of difficulty in annealing proton radiation damage as compared with annealing electron radiation damage in gallium arsenide. Future work will concentrate on developing a defect kinetic model and correlation with deep level electron spectroscopic analysis of radiation produced defects.

14.3.2. Conclusions. The macroscopic defect density variation effects on equivalent electron fluence being well-established, the effect of microscopic defect structures reveals an additional requirement on the equivalent electron-fluence concept. It has been shown the 1-MeV electrons can never reproduce proton irradiation damage on the microscopic scale. This is the probable difference in annealing between electron and proton damaged cells observed by Anspaugh and Downing (1981). A full explanation must await further study on the chemical kinetics of defect structures. In any case, a minimum requirement will be the use of 10-MeV electrons to assure equivalence on the microscopic level of defect formation.

14.4. GaAs Model Refinements

The original model for GaAs solar cells was admittedly simplified (Wilson, Walker, and Outlaw, 1984) but still explained the main features of the proton-induced radiation damage response curves and the annealing characteristics of the cells (Stith and Wilson, 1985). Several modifications of the basic concepts were accomplished by various researchers.

The photon absorption coefficient exhibits strong wavelength dependence and has been used as a probe for study of the internal workings of GaAs photovoltaic systems. J. Y. Yaung (1984) incorporated photoabsorption properties into the short-circuit model to provide the spectral dependence of radiation damage. The resulting spectral response is shown in figure 14.27. When the spectral attenuation coefficient properly accounts for the depth dependence of the minority carrier

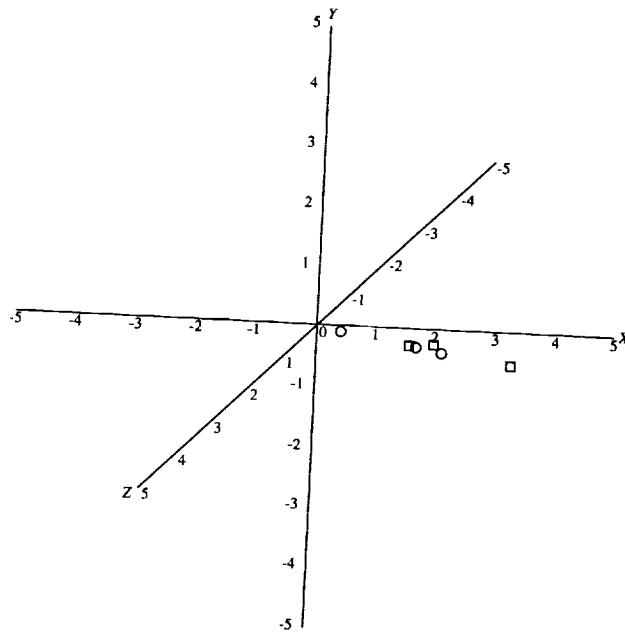


Figure 14.21. Vacancy and interstitial sites for a typical 20 eV primary atom recoil event. Coordinates in lattice constants. All pairs.

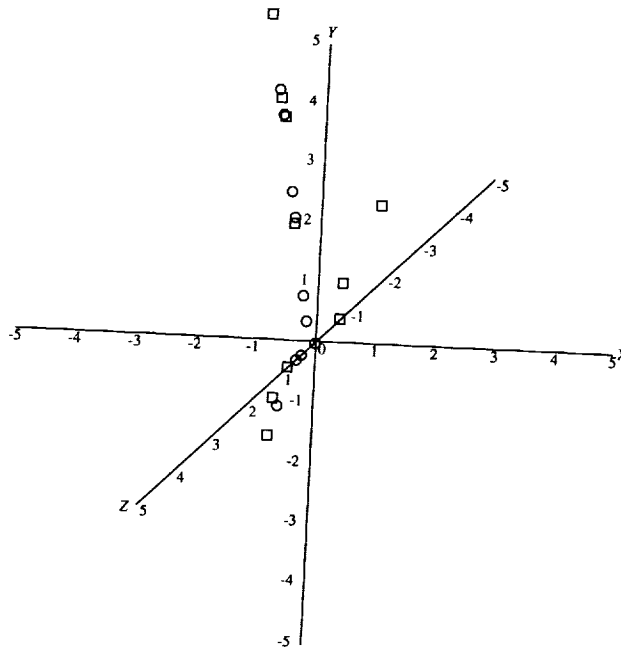


Figure 14.22. Vacancy and interstitial sites for a typical 90 eV primary atom recoil event. Coordinates in lattice constants. All pairs.

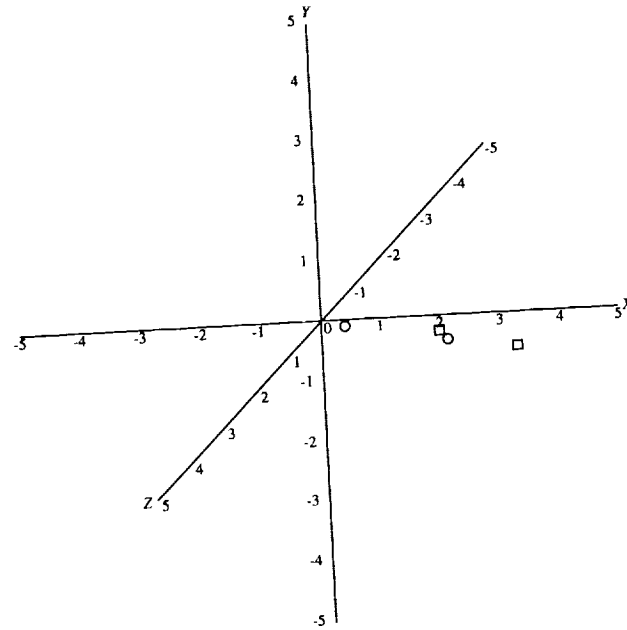


Figure 14.23. Vacancy and interstitial sites remaining after annealing of close pairs caused by 20 eV primary recoil atom. Coordinates in lattice constants. No close pairs.

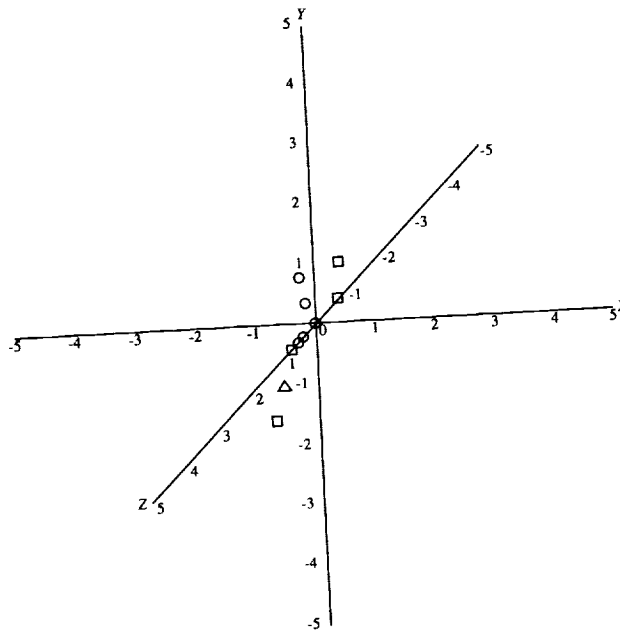


Figure 14.24. Vacancy and interstitial sites remaining after annealing of close pairs caused by 90 eV primary recoil atom. Coordinates in lattice constants. No close pairs.

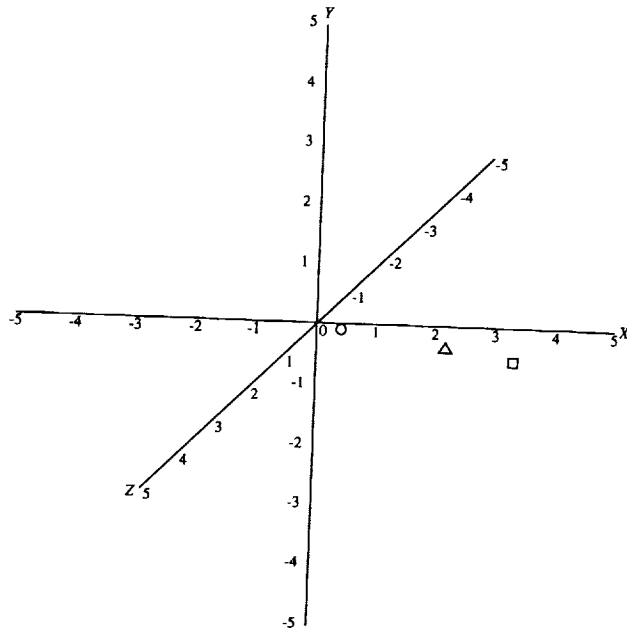


Figure 14.25. Improper replacements and distant pairs from 20 eV primary recoil event. Coordinates in lattice constants. No close pairs or near pairs.

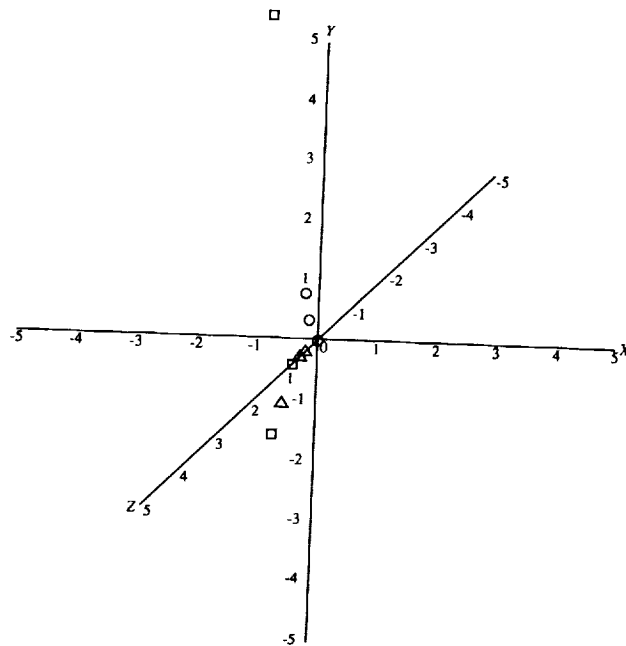


Figure 14.26. Improper replacements and distant pairs from 90 eV primary recoil event. Coordinates in lattice constants. No close pairs or near pairs.

source, the average damage response to low-energy protons is somewhat improved, as shown in figure 14.28. The spectral averaged model shows similar success in application to silicon solar cells, as seen in figures 14.29 and 14.30. In addition to the spectral dependence, Yeh, Li, and Loo (1985) added the recombination differences of the *p*- and *n*-material and find excellent agreement with their experimental data. (See fig. 14.31.)

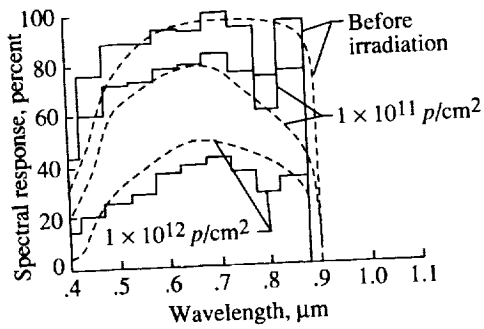


Figure 14.27. Experimental and simulated spectral responses for (AlGa)As-GaAs solar cell before and after proton irradiation (Proton energy = 290 keV).

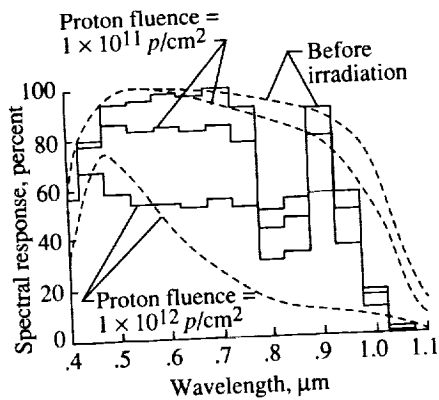


Figure 14.29. Experimental and Yang's simulated spectral responses for silicon solar cell before and after proton irradiation (Proton energy = 290 keV).

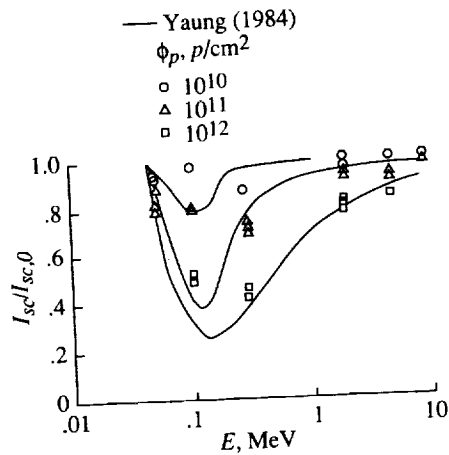


Figure 14.28. Final results of predicting I_{sc} damage on GaAs solar cell.

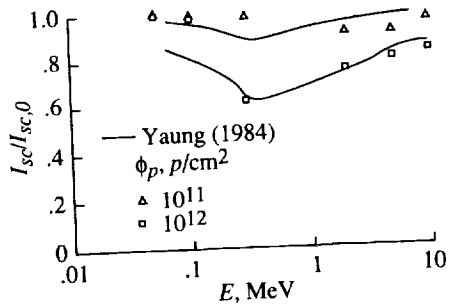


Figure 14.30. Final results of predicting I_{sc} damage on silicon solar cell.

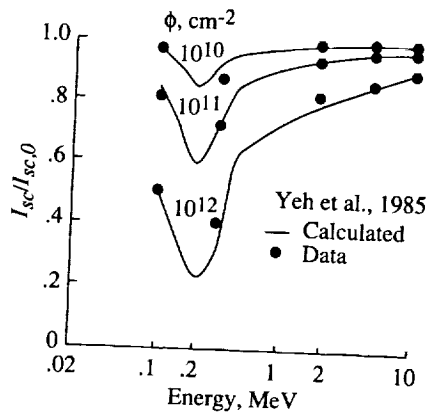


Figure 14.31. The calculated I_{sc} degradation ratio in the $\text{Al}_{0.85}\text{Ga}_{0.15}\text{As-GaAs}$ p - n junction solar cell. The thickness of the window layer is $0.34 \mu\text{m}$, and the junction depth is $0.5 \mu\text{m}$.

14.5. Microelectronic Applications

The early suggestion that some spacecraft anomalies may result from the passage of the galactic ions through microelectronic circuits (Binder, Smith, and Holman, 1975) has now been well-established. Although the direct ionization by protons appears as an unlikely candidate, the recoil energy of nuclear-reaction products is suspected as a source of single-event upset (SEU) phenomena (Wyatt et al., 1979; Guenzer et al., 1980; Petersen, 1980). As a result, a number of fundamental experimental and theoretical studies were undertaken to better understand the phenomena. McNulty and coworkers examined the energy deposition of proton reaction products in Si by using surface-barrier detectors of various thicknesses for 2.5 to $200 \mu\text{m}$ (McNulty et al., 1980). They also developed a Monte Carlo code for theoretical evaluation of energy deposition for such products. (See McNulty et al., 1980; McNulty, Farrell, and Tucker, 1981.) A comparison of McNulty's work with the well-established medium energy cascade code (MECC-7) developed by Bertini and coworkers at the Oak Ridge National Laboratory showed some differences in predicted reaction products and even greater differences in energy spectral contribution. (See Hamm et al., 1981.) An evaluation of Si reaction products was likewise made by Petersen (1980), and, although no direct comparison was made with McNulty's experiments, an estimate of SEU rates in the trapped-proton environment was made.

Following these fundamental studies, more-detailed applications to specific-device geometries and parameters were made. Bradford evolved an energy deposition formalism (Bradford, 1982) using the cross sections of Hamm et al. (1981). McNulty et al. (1980) applied their Monte Carlo model to dynamic random access memory (DRAM) devices with reasonable success and discussed the implications of heavy ion SEU phenomena on proton-induced SEU events through secondary reaction processes (Bisgrove et al., 1986). The fundamental consideration is the evaluation of the energy deposited within the sensitive volume (depletion region) of the device in question as the result of a passing proton. The ionization due to the proton itself makes only a small contribution to the critical charge. Nuclear-reaction events usually produce several reaction products (a

heavy fragment and several lighter particles, although a few heavy fragments may be produced simultaneously on some occasions), and all the resultant products can make important contributions to the deposited energy. Such nuclear-event products are, of course, correlated in both time and space.

There are three distinct approaches to a fundamental description of the energy deposition events. McNulty and coworkers developed a Monte Carlo code in which multiparticle events are calculated explicitly, including spatial and specific-event (temporal) correlation effects. Although this is the most straightforward way of treating the full detail, it is a complex computational task. A second class of methods begins with the volumetric source of collision events and calculates the SEU probability by using the chord-length distribution. (See Bradford, 1982; Fernald and Kerns, 1988.) Although in principle the correlation effects could be so incorporated, they appear to be ignored in both the cited references. A third approach in which linear energy-transfer (LET) distributions and chord-length distributions are used seems most appropriate for external sources. (See Petersen et al., 1982; Tsao et al., 1983.) This last approach applies if the LET distribution from external sources is constant over the sensitive volume, but its applicability to volumetric sources is questionable. At the very least, this approach ignores correlation effects.

Nuclear data bases for biological systems were examined by Wilson et al. (1988). The MECC-7 results underestimated by nearly a factor of 2 the energy-transfer cross section for multiple-charged ion products. In an analysis with greater detail, (Wilson et al., 1989), the Silberberg-Tsao (Tsao et al., 1983) fragmentation parameters were found to be superior to the MECC-7 results. The primary differences appear for the lighter of the multiple-charged fragments. Further comparison with experiments on Al targets shows both Monte Carlo nuclear models (McNulty's code OMNI as well as MECC-7) to underestimate production cross sections for products lighter than fluorine in proton-induced reactions. Although these intranuclear-cascade models are capable of representing multiparticle correlation, the inherent inaccuracies in predicting cross sections is a serious limitation.

In the present section, the effects of nuclear recoil on electronic devices are examined and the development of a formalism for application to specific-device parameters is begun. As a test of our methods as they develop, the results are compared with the experimental measurements of McNulty et al. (1980).

14.5.1. Microelectronic upsets. An electronic device is sensitive to the sudden introduction of charge into the active elements of its circuits. The amount of such charge that is sufficient to change the state of a logic circuit is called the critical charge. As shown in figure 14.32, there is a rough relationship between the critical charge Q_c and the device feature size L (Petersen et al., 1982). This relationship is as follows:

$$Q_c \approx 0.0156L^2 \quad (14.55)$$

where Q_c is measured in pC and L is measured in μm . Upsets in a device are then dependent on the charge produced in comparison to the critical charge.

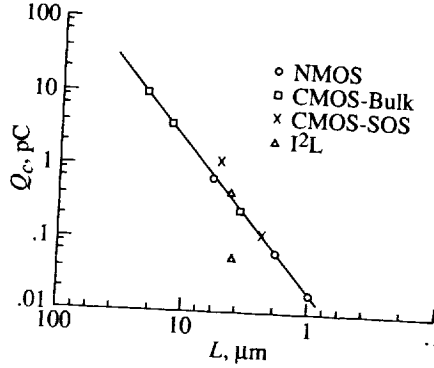


Figure 14.32. Critical charge as a function of feature size in several device types.

The charge released ΔQ in a material because of the passage of an energetic ion is related to the kinetic energy lost ΔE during the passage and is given by

$$\Delta Q = \frac{\Delta E}{22.5} \quad (14.56)$$

where ΔQ has units pC and ΔE has units MeV. The energy lost by an ion in passing through a region is related to its stopping power ($-\frac{dE}{dx} = S_z(E')$) in the medium. The distance traveled before coming to rest is

$$R_Z(E) = \int_0^E \frac{dE'}{S_z(E')} \quad (14.57)$$

If an ion is known to come to rest in distance x , then its energy is found through the inverse of relation (14.57) as

$$E = R_Z^{-1}(x) \quad (14.58)$$

Equation (14.58) is used to calculate energy loss. The energy loss by an ion of charge Z and energy E in passing through the active region of a device with collection length L_c is given by

$$\Delta E = E - R_Z^{-1}[R_Z(E) - L_c] \quad (14.59)$$

where

$$L_c = W_{\text{epi}} + W_n \quad (14.60)$$

In equation (14.60), W_{epi} is the epitaxial layer thickness and W_n is the width of the depletion region (Chern, Seitchik, and Yang, 1986). The energy loss depends on the particle isotope (i.e., ion mass) and angle of incidence. The range-energy relations described by Wilson et al. (1989) are utilized. As a practical matter to reduce numerical error inherent to numerical interpolation,

$$\Delta E = R_Z^{-1}[R_Z(E)] - R_Z^{-1}[R_Z(E) - L_c] \quad (14.61)$$

is used in place of equation (14.59). The result of equation (14.59) depends on the global error (fixed at 1 percent) in the computer code, while equation (14.61)

depends only on the local relative error (quite small). The charge introduced into the feature is given by equations (14.56) and (14.61). An example for a particular collection length of $2 \mu\text{m}$ is shown in figure 14.33 for each ion type. A simplified geometry is assumed in which the channel length and width and the collection length (fig. 14.34) are taken as equal to the feature size. The E, Z plane can be divided into regions for which

$$\Delta Q(E) \geq Q_c \tag{14.62}$$

The value of $\Delta Q(E)$ depends on the feature size L . (See eq. (14.55).) The ion mass for each value of Z was taken as the natural mass in arriving at the contour of constant ΔQ shown in figure 14.35. The average recoil energies from the fragmentation of ^{16}O and ^{28}Si produced by collision with high-energy protons (Wilson et al., 1989) are also shown in figure 14.35. The importance of a given fragment type for a given feature size for the device may be judged from the average recoil energies from the fragmentation of ^{16}O and ^{28}Si .

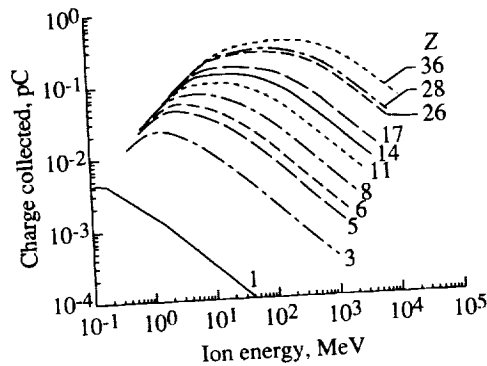


Figure 14.33. Charge collected as a function of ion energy with a collection length of $2 \mu\text{m}$.

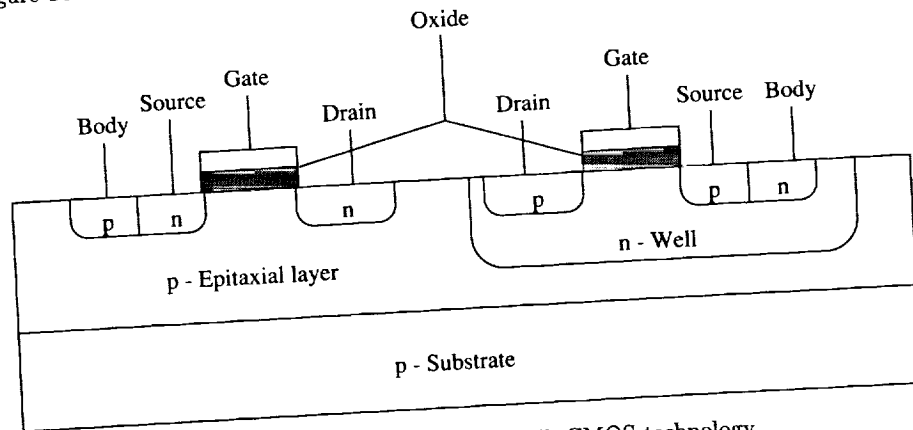


Figure 14.34. Cross section of bulk CMOS technology.

It is doubtful that any of the fragments produce upsets in the $4\text{-}\mu\text{m}$ and larger devices (note that simplified geometries have been used). Also, the lighter fragments of Li, He, and H are not suspected for SEU's in this simple geometry and figure 14.35 is applicable to incident cosmic-ray ions.

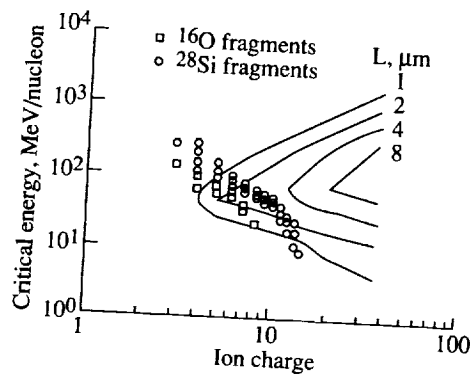


Figure 14.35. Critical energy as a function of ion charge for several feature sizes. Average recoil energies of fragments of silicon and oxygen are superimposed.

14.5.2 Nuclear-fragmentation cross sections. Although nuclear fragmentation has been under study for nearly 50 years, the absolute cross sections still stir some controversy. The experimental problem is that the main-reaction products could be directly observed only in recent years and even now only in rather sophisticated experiments. Rudstam (1966) studied the systematics of nuclear fragmentation and supposed the fragment isotopes to be in a bell-shaped distribution about the nuclear stability line. Silberberg and Tsao (Tsao et al., 1983) continued the Rudstam parametric approach and added many correction factors as new experimental evidence became available.

Concurrently, Monte Carlo simulation of the Serber model (1947) and final decay through compound nuclear models showed some success (Hamm et al., 1981; Bertini, 1969). Even so, Monte Carlo simulation shows little success in predicting fragments whose mass is small compared with the original target nuclear mass (Wilson et al., 1988; Kwiatkowski et al., 1983). Of the various models for nucleon-induced fragmentation in ^{28}Si , the model of Silberberg and Tsao is probably the most reliable. The main limitation of their model is that only inclusive cross sections are predicted; particle correlations could prove important in predicting SEU.

Measurements of ^{27}Al fragmentation in proton beams have been made by Kwiatkowski et al. (1983). These experiments are compared in figure 14.36 with the Monte Carlo results of OMNI and MECC-7. Also shown are the results from Silberberg and Tsao (Tsao et al., 1983); generally, these results appear to be within a factor of 2 of the experiment. The model of Silberberg and Tsao (Tsao et al., 1983) is the only model which predicts significant contributions in the important range below the mass of carbon $A_F = 12$.

The spectrum of average recoil energy is calculated using the formalism of Wilson et al. (1989) and the Silberberg-Tsao cross sections and is shown for comparison with the spectrum according to the Bertini cross sections in figure 14.37. The Bertini cross sections are greatly underestimated above 24 MeV and greatly overestimated below 9 MeV. The Bertini results are typical for currently available intranuclear-cascade models. Experimental evidence indicates

that even the Silberberg-Tsao values are too small above 6 MeV (Kwiatkowski et al., 1983).

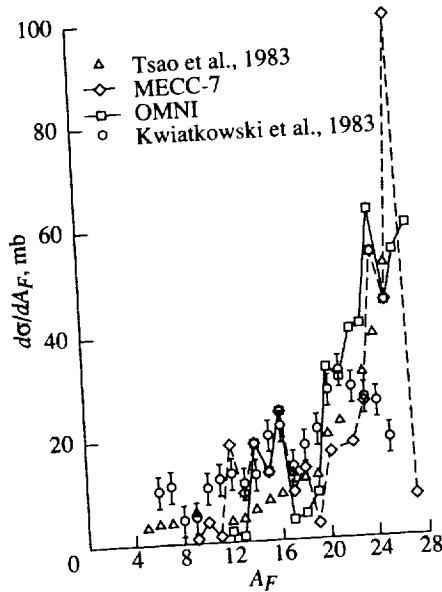


Figure 14.36. Fragmentation cross section for 180-MeV protons on Al targets calculated by various models compared with experimental measurements.

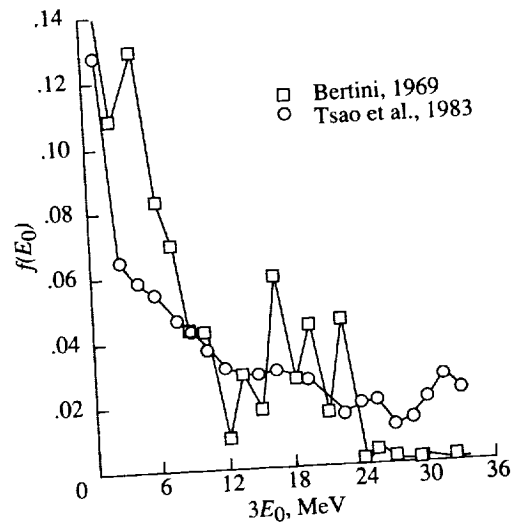


Figure 14.37. Spectrum of average energy predicted by Silberberg and Tsao cross sections compared with Bertini cross sections.

14.5.3. Nuclear recoil transport. The transport of the recoil fragments is described as follows:

$$\left[\vec{\Omega} \cdot \nabla - \frac{\partial}{\partial E} S_z(E) \right] \phi_z(\vec{x}, \vec{\Omega}, E) = \zeta_z(E) \quad (14.63)$$

where $\phi_z(\vec{x}, \vec{\Omega}, E)$ is the ion flux at \vec{x} moving in direction $\vec{\Omega}$ with energy E and where $\zeta_z(E)$ is the ion-source density assumed to be isotropic and uniformly distributed through the media. The solution to equation (14.63) is in a closed region bounded by the surface $\vec{\Gamma}$ subject to the boundary condition

$$\phi_z(\vec{\Gamma}, \vec{\Omega}, E) = \psi_z(\vec{\Omega}, E) \quad (\vec{n} \cdot \vec{\Omega} < 0) \quad (14.64)$$

where \vec{n} is the outward-directed normal of the surface $\vec{\Gamma}$. The solution is found by using the method of characteristics (Wilson and Lamkin, 1975; Wilson, 1977) as

$$\phi_z(\vec{x}, \vec{\Omega}, E) = \frac{S_z(E_b)}{S_z(E)} \phi_z(\vec{\Gamma}, \vec{\Omega}, E_b) + \frac{1}{S_z(E)} \int_E^{E_b} \zeta_z(E') dE' \quad (14.65)$$

where $\vec{\Gamma}$ is the point on the boundary determined by projecting \vec{x} along the direction $\vec{\Omega}$ and

$$E_b = R_Z^{-1} [R_Z(E) + b] \quad (14.66)$$

where

$$b = \vec{\Omega} \cdot (\vec{x} - \vec{\Gamma}) \quad (14.67)$$

Equation (14.65) may be used to evaluate the spectrum of particles leaving the region that can be related to the spectrum of energy deposited in the media. An isolated sheet of silicon of thickness a , which is obviously similar to the McNulty surface-barrier detectors, is considered. The inward-directed flux at the boundary is then zero. We first consider a monoenergetic ion source

$$\zeta_z(E) = \frac{\sigma_z \phi}{4\pi} \delta(E - E') \quad (14.68)$$

for which

$$\phi_z(\vec{x}, \vec{\Omega}, E) = \frac{\sigma_z \phi}{4\pi S_z(E)} \begin{cases} 1 & (E \leq E' \leq E_b) \\ 0 & (\text{Otherwise}) \end{cases} \quad (14.69)$$

where σ_z is the silicon-fragmentation cross section and ϕ is the flux of initiating energetic particles. The spectrum of ions leaving the sheet (ignoring edge effects) is

$$\begin{aligned} \frac{df_z}{dE} &= 4\pi A \int_0^1 \mu \phi_z(\vec{\Gamma}, \vec{\Omega}, E) d\mu \\ &= \frac{A\sigma_z \phi}{2S_z(E)} \begin{cases} \frac{a^2}{[R_Z(E') - R_Z(E)]^2} & (0 \leq E \leq R_Z^{-1}[R_Z(E') - a]) \\ 1 & (R_Z^{-1}[R_Z(E') - a] \leq E \leq E') \\ 0 & (E' < E) \end{cases} \quad (14.70) \end{aligned}$$

where A is the area of the sheet and μ is the cosine of the colatitude with respect to the local surface normal. The total number of escaping particles is found by integrating the spectrum given by equation (14.70) and is

$$N_e = Aa\sigma_z \phi \begin{cases} \left[1 - \frac{a}{2R_Z(E')} \right] & (a \leq R_Z(E')) \\ \frac{R_Z(E')}{2a} & (a > R_Z(E')) \end{cases} \quad (14.71)$$

From equation (14.71), the total number of ions which stop in the sheet is

$$N_S = Aa\sigma_z \phi \begin{cases} \left[\frac{a}{2R_Z(E')} \right] & (a \leq R_Z(E')) \\ \left[1 - \frac{R_Z(E')}{2a} \right] & (a > R_Z(E')) \end{cases} \quad (14.72)$$

Obviously, an ion produced with energy E' which leaves the sheet with energy E suffered an energy loss ε to the sheet given by

$$\varepsilon = E' - E \quad (14.73)$$

which we use to find the energy-loss spectrum as

$$\frac{df_{z\delta}}{d\varepsilon} = \left. \frac{df_z}{dE} \right|_{E=E'-\varepsilon} + N_S \delta(E' - \varepsilon) \quad (14.74)$$

Considering that equation (14.74) is the energy deposition in a sheet of area A and thickness a as the result of a monoenergetic volumetric source, the response to any arbitrary spectral source can be found by superposition.

14.5.4. Fragmentation energy-loss spectra. The fragmentation-source energy distribution (normalized to unity) is given as

$$\rho(E') = \sqrt{\frac{E'}{2\pi E_0^3}} \exp\left(\frac{-E'}{2E_0}\right) \quad (14.75)$$

where $3E_0$ is the mean-fragment energy and is given by Wilson et al. (1989) based on previous work by Goldhaber (1974)

The energy-loss spectrum is found by using equations (14.74) and (14.75) as

$$\begin{aligned} \frac{dF}{d\varepsilon} &= \int_{\varepsilon}^{\infty} \left. \frac{df_{z\delta}}{d\varepsilon} \right|_{E=E'-\varepsilon} \rho(E') dE' \\ &= \int_0^{\infty} \left. \frac{df_{z\delta}}{d\varepsilon} \right|_{E=E'+\varepsilon} \rho(E + \varepsilon) dE \end{aligned} \quad (14.76)$$

The contribution from stopping ions is readily evaluated to give

$$\frac{dF}{d\varepsilon} = N_S(\varepsilon) \rho(\varepsilon) + \int_0^{\infty} \left. \frac{df_{z\delta}}{d\varepsilon} \right|_{E'=E+\varepsilon} \rho(E + \varepsilon) dE \quad (14.77)$$

where the second term of equation (14.77) requires more attention.

The energy-degradation function in the integral of equation (14.77) is given by equation (14.74). It is not clear how the integral in equation (14.77) is to be evaluated. As an approximate evaluation, the energy-degradation function is approximated by two or three line segments as given in equations (14.78) and (14.81).

If $R_Z(\varepsilon) > 2a$, then

$$\left. \frac{df_z}{dE} \Big|_{E'=E+\varepsilon} = \frac{A\sigma_z\phi}{2S_z(E)} \begin{cases} \frac{a^2}{R_Z^2(\varepsilon)} + \left[\frac{1}{4} - \frac{a^2}{R_Z^2(\varepsilon)} \right] \frac{R_Z(E)}{R_Z(E_2)} & (0 \leq E \leq E_2) \\ \frac{1}{4} + \frac{3[R_Z(E) - R_Z(E_2)]}{4[R_Z(E_1) - R_Z(E_2)]} & (E_2 \leq E \leq E_1) \\ 1 & (E_1 \leq E \leq \infty) \end{cases} \right\} \quad (14.78)$$

where E_2 is the solution of

$$R_Z(E_2) = R_Z(E_2 + \varepsilon) - 2a \quad (14.79)$$

and E_1 is the solution of

$$R_Z(E_1) = R_Z(E_1 + \varepsilon) - a \quad (14.80)$$

In the event that $R_Z(\varepsilon) < 2a$, then

$$\left. \frac{df_z}{dE} \Big|_{E'=E+\varepsilon} = \frac{A\sigma_z\phi}{2S_z(E)} \begin{cases} \frac{a^2}{R_Z^2(\varepsilon)} + \left[1 - \frac{a^2}{R_Z^2(\varepsilon)} \right] \frac{R_Z(E)}{R_Z(E_1)} & (0 \leq E \leq E_1) \\ 1 & (E_1 + E \leq \infty) \end{cases} \right\} \quad (14.81)$$

with the understanding that E_1 is zero if $R_Z(\varepsilon) < a$. The second term of equation (14.77) is divided into three subintervals as follows:

$$I_1(\varepsilon) = \int_0^{E_2} \frac{df_z}{d\varepsilon} \Big|_{E'=E+\varepsilon} \rho(E + \varepsilon) dE \quad (14.82)$$

$$I_2(\varepsilon) = \int_{E_2}^{E_1} \frac{df_z}{d\varepsilon} \Big|_{E'=E+\varepsilon} \rho(E + \varepsilon) dE \quad (14.83)$$

$$I_3(\varepsilon) = \int_{E_1}^{\infty} \frac{df_z}{d\varepsilon} \Big|_{E'=E+\varepsilon} \rho(E + \varepsilon) dE \quad (14.84)$$

First, $I_1(\varepsilon)$ is zero unless $R_Z(\varepsilon) > 2a$, for which

$$I_1(\varepsilon) = \frac{A\sigma_z\phi}{2} \left\{ \frac{a^2}{R_Z^2(\varepsilon)} P(E_2, \varepsilon) + \left[\frac{1}{4} - \frac{a^2}{R_Z^2(\varepsilon)} \right] \frac{Q(E_2, \varepsilon)}{R_Z(E_2)} \right\} \quad (14.85)$$

$$I_2(\varepsilon) = \frac{A\sigma_z\phi}{2} \left\{ \frac{1}{4} - \frac{3}{4} \frac{R_Z(E_2)}{[R_Z(E_1) - R_Z(E_2)]} \right\} [P(E_1, \varepsilon) - P(E_2, \varepsilon)] \\ + \frac{A\sigma_z\phi}{2} \frac{3}{4} \frac{Q(E_1, \varepsilon) - Q(E_2, \varepsilon)}{[R_Z(E_1) - R_Z(E_2)]} \quad (14.86)$$

$$I_3(\varepsilon) = \frac{A\sigma_z\phi}{2} \int_{E_1}^{\infty} \frac{\rho(E + \varepsilon)}{S_z(E)} dE \quad (14.87)$$

If $a \leq R_Z(\varepsilon) \leq 2a$, then E_2 and $I_1(\varepsilon)$ are zero and

$$I_2(\varepsilon) = \frac{A\sigma_z\phi}{2} \left\{ \frac{a^2}{R_Z^2(\varepsilon)} P(E_1, \varepsilon) + \left[1 - \frac{a^2}{R_Z^2(\varepsilon)} \right] \frac{Q(E_1, \varepsilon)}{R_Z(E_1)} \right\} \quad (14.88)$$

When $R_Z(\varepsilon) \leq a$, then $E_1 = E_2 = 0$, so that $I_1(\varepsilon)$ and $I_2(\varepsilon)$ both vanish and

$$I_3(\varepsilon) = \frac{A\sigma_z\phi}{2} \int_0^{\infty} \frac{\rho(E + \varepsilon)}{S_z(E)} dE \quad (14.89)$$

In equations (14.85), (14.86), and (14.88), P and Q are given by

$$P(E_i, \varepsilon) = \int_0^{E_i} \frac{\rho(E + \varepsilon)}{S_z(E)} dE \quad (14.90)$$

$$Q(E_i, \varepsilon) = \int_0^{E_i} \frac{R_Z(E) \rho(E + \varepsilon)}{S_z(E)} dE \quad (14.91)$$

The integral of equation (14.90) may be approximated for values of $E_i \leq \frac{1}{4}\varepsilon$ by

$$P(E_i, \varepsilon) \approx \frac{R_Z(E_0)}{\sqrt{2}} \rho(\varepsilon) \gamma\left(\frac{1}{2}, \frac{E_i}{2E_0}\right) \quad (14.92)$$

where γ is an incomplete gamma function. For larger values of E_i ($\frac{1}{4}\varepsilon \leq E_i \leq 4\varepsilon$), the integral may be taken as

$$P(E_i, \varepsilon) \approx \frac{R_Z(E_0)}{\sqrt{2}} \rho(\varepsilon) \left[\frac{1}{2} \gamma\left(\frac{1}{2}, \frac{\varepsilon}{8E_0}\right) + \frac{1}{2} \gamma\left(\frac{1}{2}, \frac{E_i}{2E_0}\right) \right. \\ \left. + \sqrt{\frac{2E_0}{\varepsilon}} \gamma\left(1, \frac{E_i}{2E_0}\right) - \sqrt{\frac{2E_0}{\varepsilon}} \gamma\left(1, \frac{\varepsilon}{8E_0}\right) \right] \quad (14.93)$$

Whenever $E_i > 4\epsilon$, the integral is approximately

$$P(E_i, \epsilon) \approx \frac{R_Z(E_0)}{\sqrt{2}} \rho(\epsilon) \left[\frac{1}{2} \gamma \left(\frac{1}{2}, \frac{\epsilon}{8E_0} \right) + \frac{1}{2} \gamma \left(\frac{1}{2}, \frac{4\epsilon}{2E_0} \right) + \sqrt{\frac{2E_0}{\epsilon}} \gamma \left(1, \frac{E_i}{2E_0} \right) - \sqrt{\frac{2E_0}{\epsilon}} \gamma \left(1, \frac{\epsilon}{8E_0} \right) \right] \quad (14.94)$$

The integral in equation (14.91) may be approximated by

$$Q(E_i, \epsilon) \approx \frac{R_Z^2(E_0)}{2E_0} [C(E_i + \epsilon) - C(\epsilon)] \quad (14.95)$$

where $C(\epsilon)$ is the integral spectrum as follows:

$$C(E) = \int_0^E \rho(E') dE' \quad (14.96)$$

A useful check on the approximations involved is the strict requirement

$$I_1(\epsilon) + I_2(\epsilon) + I_3(\epsilon) \leq \frac{A\sigma_z\phi}{2} \int_0^\infty \frac{\rho(E + \epsilon)}{S_z(E)} dE \quad (14.97)$$

The total absorption spectrum is then

$$\frac{dF}{d\epsilon} = N_S(\epsilon) \rho(\epsilon) + I_1(\epsilon) + I_2(\epsilon) + I_3(\epsilon) \quad (14.98)$$

and is shown in figure 14.38 for detector thicknesses of 1 to 5 μm with $E_0 = 3.5$ MeV. Similar results are shown in figure 14.39 for detector thicknesses of 50 to 200 μm . In comparing figures 14.39 and 14.40, it is shown that the energy-loss spectrum is approaching the fragment-production spectrum as a becomes larger. The normalization is always

$$\int_0^\infty \frac{dF}{d\epsilon} = 1 \quad (14.99)$$

which is satisfied by numerical evaluation to within 2 percent.

14.5.5. Results. Typical fragmentation cross sections calculated using the Silberberg-Tsao model are shown in table 14.2 for 125-MeV protons. The values of E_0 are taken from Wilson et al. (1989). The calculated response of the 2.5- μm detector is shown in figure 14.41; these values should be compared with the experiments of McNulty, Farrell, and Tucker (1981) and the values according to the Monte Carlo code of the McNulty group, which are also shown in figure 14.41. The peak value at zero energy is fixed by the total reaction cross section and total proton flux. It appears that the total reaction cross section of the McNulty code is too small. Otherwise, the present theory and the Monte Carlo code show nearly equivalent agreement with the experiments. Similar comments apply to the 4.2- μm detector response (fig. 14.42) with one exception. The energetic events above 20 MeV observed in experiments are well represented by the present theory

but, as expected, not by the Monte Carlo code (see fig. 14.37). This high-energy agreement between theory and experiment is observed for the 24.1- μm detector, but the Monte Carlo code again fails to predict the high-energy events, as shown in figure 14.43. The improved model of the present work is again clearly displayed for the 158-MeV experiments of McNulty et al. (1981), as shown in figures 14.44 and 14.45.

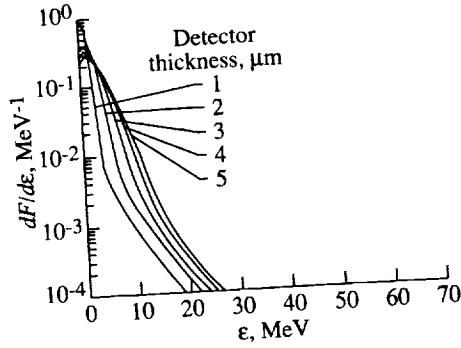


Figure 14.38. Total absorption spectrum for surface-barrier detector of 1 to 5 μm and $E_0 = 3.5$ MeV.

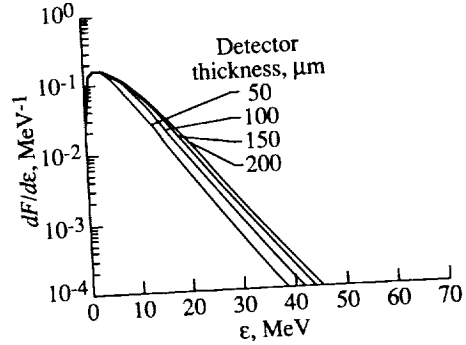


Figure 14.39. Total absorption spectrum for surface-barrier detector of 50 to 200 μm and $E_0 = 3.5$ MeV.

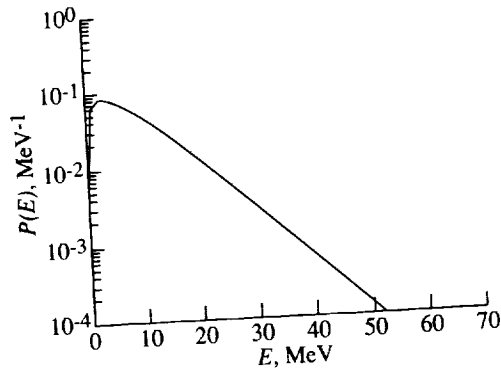


Figure 14.40. Energy-loss spectrum for $E_0 = 3.5$ MeV.

+ Theory: Ngo et al., 1989
 — Monte Carlo code, McNulty et al., 1981
 - - Experiment, McNulty et al., 1981

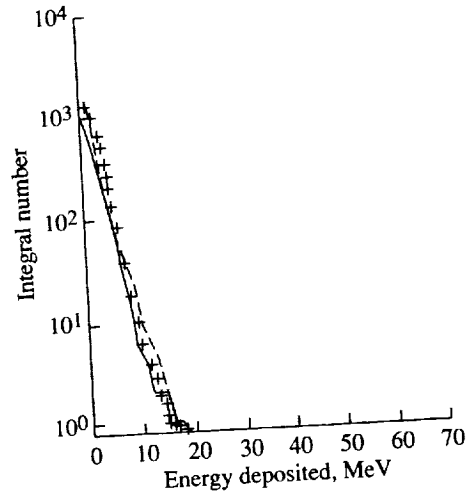


Figure 14.41. Response of a 2.5- μm surface-barrier detector to 125-MeV protons (2.14×10^8 protons).

Table 14.2. Cross-Section Parameters for Fragmentation of ^{28}Si by 125-MeV Protons

A_F	σ_F , mb	E_0 , MeV
27	67.7	0.17
26	50.8	.34
25	44.5	.50
24	37.7	.67
23	24.7	.84
22	24.5	1.01
21	14.7	1.17
20	15.3	1.34
19	8.1	1.51
18	7.3	1.68
17	6.4	1.85
16	6.1	2.01
15	4.2	2.18
14	2.9	2.35
13	1.9	2.52
12	2.3	2.68
11	1.5	2.85
10	1.0	3.02
9	1.1	3.19
8	1.7	3.35
7	1.9	3.52
6	1.5	3.69
5	1.2	3.86
4	145.9	2.08
3	29.1	2.92
2	70.7	2.06
1	710.5	2.06

The inability of the Monte Carlo code to predict the most energetic fragments could be a serious limitation in predicting SEU in some devices. Although the Silberberg-Tsao cross sections for proton-induced reactions are not in complete agreement with some recent cross-section measurements, they still provide improved ability over Monte Carlo models. The methods of analysis used herein will be applied to specific-device geometries in the near future.

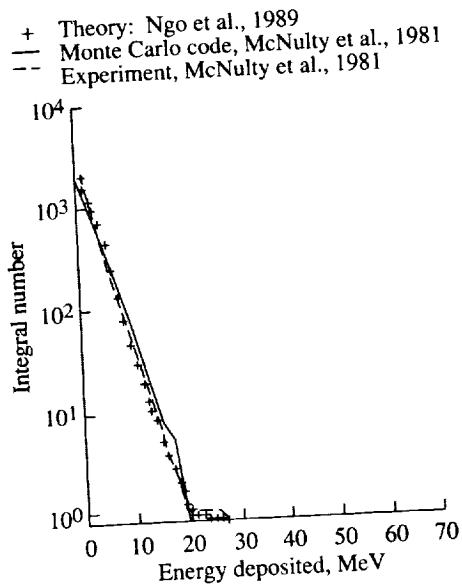


Figure 14.42. Response of a 4.2- μm surface-barrier detector to 125-MeV protons (2.14×10^8 protons).

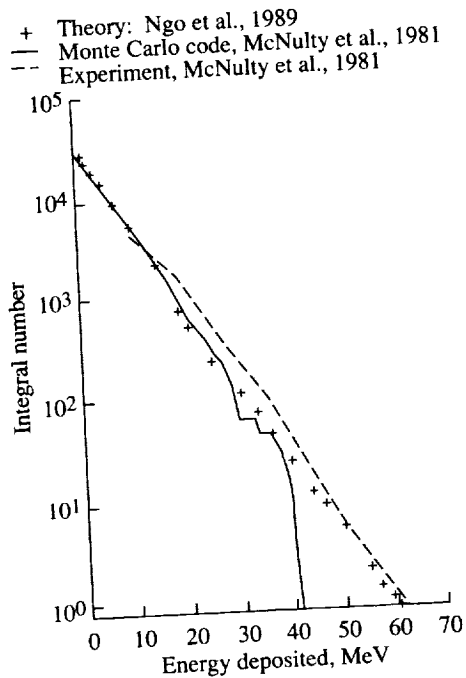


Figure 14.43. Response of a 24.1- μm surface-barrier detector to 125-MeV protons (6.42×10^8 protons).

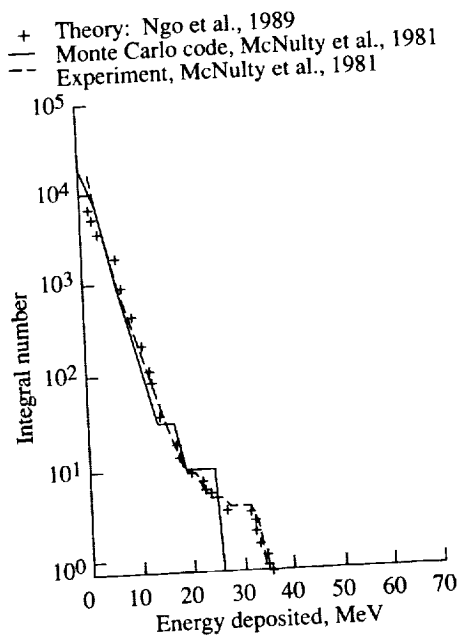


Figure 14.44. Response of a 2.5- μm surface-barrier detector to 158-MeV protons (3.9×10^9 protons).

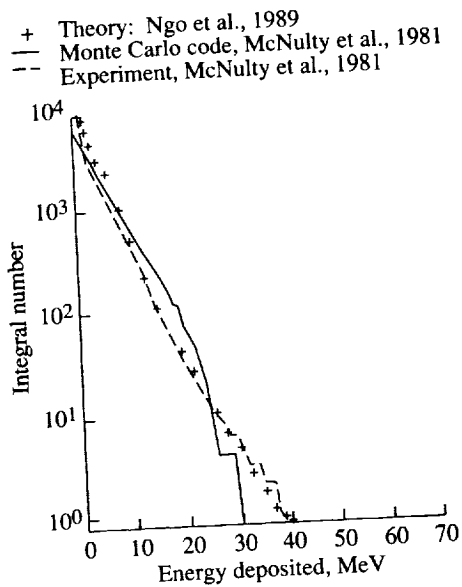


Figure 14.45. Response of an 8.7- μm surface-barrier detector to 158-MeV protons (3.9×10^8 protons).

14.6. References

- Andersen, H. H.; and Ziegler, J. F., 1977: *Hydrogen—Stopping Powers and Ranges in All Elements. Volume 3 of The Stopping and Ranges of Ions in Matter*, J. F. Ziegler, organizer, Pergamon Press, Inc.
- Anon., 1977: *Solar Power Satellite Concept Evaluation, Activities Report—July 1976 to June 1977. Volume I—Summary*. NASA TM-74820.
- Anspaugh, B. E.; and Downing, R. G., 1981: Damage Coefficients and Thermal Annealing of Irradiated Silicon and GaAs Solar Cells. *The Conference Record of the Fifteenth IEEE Photovoltaic Specialists Conference—1981*, Inst. of Electrical and Electronics Engineers, Inc., pp. 499–505.
- Anspaugh, B. E.; and Downing, R. G., 1984: *Radiation Effects in Silicon and Gallium Arsenide Solar Cells Using Isotropic and Normally Incident Radiation*. NASA CR-174007.
- Bauerlein, R., 1963: Messung der Energie zur Verlagerung eines Gitteratoms durch Elektronenstoss in $A^{III}B^V$ -Verbindungen. *Z. Phys.*, vol. 176, no. 4, pp. 498–509.
- Bertini, Hugo W., 1969: Intranuclear-Cascade Calculation of the Secondary Nucleon Spectra From Nucleon-Nucleus Interactions in the Energy Range 340 to 2900 MeV and Comparisons With Experiment. *Phys. Review*, vol. 188, second ser., no. 4, pp. 1711–1730.
- Binder, D.; Smith, E. C.; and Holman, A. B., 1975: Satellite Anomalies From Galactic Cosmic Rays. *IEEE Trans. Nuclear Sci.*, vol. NS-22, no. 6, pp. 2675–2680.
- Bisgrove, J. M.; Lynch, J. E.; McNulty, P. J.; Abdel-Kader, W. G.; Kletnieks, V.; and Kolasinski, W. A., 1986: Comparison of Soft Errors Induced by Heavy Ions and Protons. *IEEE Trans. Nuclear Sci.*, vol. NS-33, no. 6, pp. 1571–1576.
- Bradford, John N., 1982: Microvolume Energy Deposition From High Energy Proton-Silicon Reactions. *IEEE Trans. Nuclear Sci.*, vol. NS-29, no. 6, pp. 2085–2089.
- Chern, J. H.; Seitchik, J. A.; and Yang, P., 1986: Single Event Charge Collection Modeling in CMOS Multi-junctions Structure. *1986 International Electron Devices Meeting—Technical Digest*, IEEE Catalog No. 86CH2381-2, Inst. of Electrical and Electronics Engineers, Inc., pp. 538–541.
- Conway, E. J.; Walker, G. H.; and Heinbockel, J. H., 1981: A Thermochemical Model of Radiation Damage and Annealing Applied to GaAs Solar Cells. *The Conference Record of the Fifteenth IEEE Photovoltaic Specialists Conference—1981*, IEEE Catalog No. 81CH1644-4, Inst. of Electrical and Electronics Engineers, Inc., pp. 38–44.
- Dienes, G. J.; and Vineyard, G. H., 1957: *Radiation Effects in Solids*. Interscience Publ., Inc.
- Fernald, Kenneth W.; and Kerns, Sherra E., 1988: Simulation of Proton-Induced Energy Deposition in Integrated Circuits. *IEEE Trans. Nuclear Sci.*, vol. 35, no. 1, pp. 981–986.
- Foelsche, T., 1963: Specific Solar Flare Events and Associated Radiation Doses. *Space Radiation Effects*, ASTM Special Tech. Publ. No. 363, American Soc. for Testing & Materials, pp. 1–13.

Transport Methods and Interactions for Space Radiations

- Goldhaber, A. S., 1974: Statistical Models of Fragmentation Processes. *Phys. Lett.*, vol. 53B, no. 4, pp. 306-308.
- Guenzer, C. S.; Allen, R. G.; Campbell, A. B.; Kidd, J. M.; Petersen, E. L.; Seeman, N.; and Wolicki, E. A., 1980: Single Event Upsets in RAMs Induced by Protons at 4.2 GeV and Protons and Neutrons Below 100 MeV. *IEEE Trans. Nuclear Sci.*, vol. NS-27, no. 6 pp. 1485-1489.
- Hamm, R. N.; Rustgi, M. L.; Wright, H. A.; and Turner, J. E., 1981: Energy Spectra of Heavy Fragments From the Interaction of Protons With Communications Materials. *IEEE Trans. Nuclear Sci.*, vol. NS-28, no. 6, pp. 4004-4006.
- Heinbockel, J. H.; Conway, E. J.; and Walker, G. H., 1980: Simultaneous Radiation Damage and Annealing of GaAs Solar Cells. *Fourteenth IEEE Photovoltaic Specialists Conference—1980*, Inst. of Electrical and Electronics Engineers, Inc., pp. 1085-1089.
- Hovel, Harold J., 1975: *Semiconductors and Semimetals. Volume 11—Solar Cells*. Academic Press, Inc.
- Janni, Joseph, F., 1966: *Calculations of Energy Loss, Range, Pathlength, Straggling, Multiple Scattering, and the Probability of Inelastic Nuclear Collisions for 0.1- to 1000-MeV Protons*. AFWL-TR-65-150, U.S. Air Force. (Available from DTIC as AD 643 837.)
- Kamath, G. S., 1981: GaAs Solar Cells for Space Application. *Proceedings of the 16th Intersociety Energy Conversion Engineering Conference. Volume I—Technologies for the Transition*, American Soc. of Mechanical Engineers, pp. 416-421.
- Kwiatkowski, K.; Zhou, S. H.; Ward, T. E.; Viola, V. E., Jr.; Brever, H.; Mathews, G. J.; Gökmen, A.; and Mignerey, A. C., 1983: Energy Deposition in Intermediate-Energy Nucleon-Nucleus Collisions. *Phys. Review Lett.*, vol. 50, no. 21, pp. 1648-1651.
- Li, S. S.; Chiu, T. T.; Schoenfeld, D. W.; and Loo, R. Y., 1981: Defect Characterization and Thermal Annealing Study of 200 KeV Proton Irradiated n-GaAs LPE Layers. *Defects and Radiation Effects in Semiconductors, 1980*, R. R. Hasiguti, ed., Inst. of Physics, pp. 335-340.
- Lindhard, J.; Scharff, M.; and Schiott, H. E., 1963: Range Concepts and Heavy Ion Ranges (Notes on Atomic Collisions, II). *Mat.-Fys. Medd.—K. Dan. Vidensk. Selsk.*, vol. 33, no. 14, pp. 1-42.
- Liverhant, S. E., 1960: *Nuclear Reactor Physics*. John Wiley & Sons, Inc.
- Loo, R.; Goldhammer, L.; Anspaugh, B.; Knechtli, R. C.; and Kamath, G. S., 1978: Electron and Proton Degradation in (AlGa)As-GaAs Solar Cells. *Thirteenth IEEE Photovoltaic Specialists Conference—1978*, Inst. of Electrical and Electronics Engineers, Inc., pp. 562-570.
- Loo, R.; Knechtli, R. C.; and Kamath, G. S., 1981: Enhanced Annealing of GaAs Solar Cell Radiation Damage. *The Conference Record of the Fifteenth IEEE Photovoltaic Specialists Conference—1981*, IEEE Catalog No. 81-CH1644-04, Inst. of Electrical and Electronics Engineers, Inc., pp. 33-37.
- McKinley, William A., Jr.; and Feshbach, Herman, 1948: The Coulomb Scattering of Relativistic Electrons by Nuclei. *Phys. Review*, vol. 74, second ser., no. 12, pp. 1759-1763.

- McNulty, Peter J.; Farrell, Gary E.; and Tucker, William P., 1981: Proton-Induced Nuclear Reactions in Silicon. *IEEE Trans. Nuclear Sci.*, vol. NS-28, no. 6, pp. 4007-4012.
- McNulty, P. J.; Farrell, G. E.; Wyatt, R. C.; Rothwell, P. L.; Filz, R. C.; and Bradford, J. N., 1980: Upset Phenomena Induced by Energetic Protons and Electrons. *IEEE Trans. Nuclear Sci.*, vol. NS-27, no. 6, pp. 1516-1522.
- Ngo, Duc M.; Wilson, John W.; Buck, Warren W.; and Fogarty, Thomas N., 1989: *Nuclear-Fragmentation Studies for Microelectronic Applications*. NASA TM-4143.
- Pages, Lucien; Bertel, Evelyne; Joffre, Henri; and Sklavenitis, Laodamas, 1972: Energy Loss, Range, and Bremsstrahlung Yield for 10-keV to 100-MeV Electrons in Various Elements and Chemical Compounds. *At. Data*, vol. 4, no. 1, pp. 1-127.
- Petersen, E. L., 1980: Nuclear Reactions in Semiconductors. *IEEE Trans. Nuclear Sci.*, vol. NS-27, no. 6, pp. 1494-1499.
- Petersen, E. L.; Shapiro, P.; Adams, J. H., Jr.; and Burke, E. A., 1982: Calculation of Cosmic-Ray Induced Soft Upsets and Scaling of VLSI Devices. *IEEE Trans. Nuclear Sci.*, vol. NS-29, no. 6, pp. 2055-2063.
- Peterson, N. L.; and Harkness, S. D., eds., 1976: *Radiation Damage in Metals*. American Soc. for Metals.
- Robinson, Mark T.; and Torrens, Ian M., 1974: Computer Simulation of Atomic-Displacement Cascades in Solids in the Binary-Collision Approximation. *Phys. Review B*, vol. 9, no. 12, pp. 5008-5024.
- Rudstam, G., 1966: Systematics of Spallation Yields. *Zeitschrift fur Naturforschung*, vol. 21a, no. 7, pp. 1027-1041.
- Sawyer, Donald M.; and Vette, James I., 1976: *AP-8 Trapped Proton Environment for Solar Maximum and Solar Minimum*. NASA TM X-72605.
- Serber, R., 1947: Nuclear Reactions at High Energies. *Phys. Review*, vol. 72, no. 11, pp. 1114-1115.
- Singley, G. Wayne; and Vette, James I., 1972: *The AE-4 Model of the Outer Radiation Zone Electron Environment*. NSSDC 72-06, NASA Goddard Space Flight Center.
- Stith, John J.; and Wilson, John W., 1985: Microscopic Defect Structures and Equivalent Electron Fluence Concepts. *Eighteenth IEEE Photovoltaic Specialists Conference—1985*, IEEE Catalog No. 85CH2208-7, Inst. of Electrical and Electronics Engineers, Inc., pp. 1716-1717.
- Tada, H. Y.; and Carter, J. R., Jr., 1977: *Solar Cell Radiation Handbook*. JPL Publ. 77-56 (Contract NAS7-100), California Inst. of Technology. (Available as NASA CR-155554.)
- Tsao, C. H.; Silberberg, R.; Adams, J. H., Jr.; and Letaw, J. R., 1983: Cosmic Ray Transport in the Atmosphere—Dose and LET-Distributions in Materials. *IEEE Trans. Nuclear Sci.*, vol. NS-30, pp. 4398-4404.
- Vook, Frederick L., ed., 1968: *Radiation Effects in Semiconductors*. Plenum Press.

Transport Methods and Interactions for Space Radiations

- Walker, D. H.; Statler, R. L.; and Lambert, R. J., 1978: Solar Cell Experiments on the NTS-2 Satellite. *The Conference Record of the Thirteenth IEEE Photovoltaic Specialists Conference—1978*, IEEE Catalog No. 78CH1319-3, Inst. of Electrical and Electronics Engineers, Inc., pp. 100-106.
- Walker, Gilbert H.; and Conway, Edmund J., 1978a: Recovery of Shallow Junction GaAs Solar Cells Damaged by Electron Irradiation. *J. Electrochem. Soc.*, vol. 125, no. 10, pp. 1726-1727.
- Walker, Gilbert H.; and Conway, Edmund J., 1978b: Short Circuit Current Changes in Electron Irradiated GaAs/GaAs Solar Cells. *The Conference Record of the Thirteenth IEEE Photovoltaic Specialists Conference—1978*, Inst. of Electrical and Electronics Engineers, Inc., pp. 575-579.
- Wilson, John W., 1977: *Analysis of the Theory of High-Energy Ion Transport*. NASA TN D-8381.
- Wilson, John W.; and Lamkin, Stanley L., 1975: Perturbation Theory for Charged-Particle Transport in One Dimension. *Nuclear Sci. & Eng.*, vol. 57, no. 4, pp. 292-299.
- Wilson, John W.; Stith, John J.; and Stock, L. V., 1983: *A Simple Model of Space Radiation Damage in GaAs Solar Cells*. NASA TP-2242.
- Wilson, John W.; Stith, John J.; and Walker, Gilbert H., 1982: On the Validity of Equivalent Electron Fluence for GaAs Solar Cells. *Sixteenth IEEE Photovoltaic Specialists Conference—1982*, Inst. of Electrical and Electronics Engineers, Inc., pp. 1439-1440.
- Wilson, John W.; and Stock, L. V., 1984: Equivalent Electron Fluence for Space Qualification of Shallow Junction Heteroface GaAs Solar Cells. *IEEE Trans. Electron Devices*, vol. ED-31, no. 5, pp. 622-625.
- Wilson, John W.; Townsend, L. W.; Chun, S. Y.; and Buck, W. W., 1988: High Energy Nucleon Data Bases. *Health Phys.*, vol. 55, no. 5, pp. 817-819.
- Wilson, John W.; Townsend, Lawrence W.; Nealy, John E.; Chun, Sang Y.; Hong, B. S.; Buck, Warren W.; Lamkin, S. L.; Ganapol, Barry D.; Khan, Ferdous; and Cucinotta, Francis A., 1989: BRYNTRN: *A Baryon Transport Model*. NASA TP-2887.
- Wilson, John W.; Walker, Gilbert H.; and Outlaw, R. A., 1984: Proton Damage in GaAs Solar Cells. *IEEE Trans. Electron Devices*, vol. ED-31, no. 4, pp. 421-422.
- Wilson, John W.; and Walker, Gilbert H.; Outlaw, R. A.; and Stock, L. V., 1982: A Model for Proton-Irradiated GaAs Solar Cells. *Sixteenth IEEE Photovoltaic Specialists Conference—1982*, Inst. of Electrical and Electronics Engineers, Inc., pp. 1441-1442.
- Wyatt, R. C.; McNulty, P. J.; Toumbas, P.; Rothwell, P. L.; and Filz, R. C., 1979: Soft Errors Induced by Energetic Protons. *IEEE Trans. Nuclear Sci.*, vol. NS-26, no. 26, pp. 4905-4910.
- Yaung, J. Y., 1984: Model of Solar Cell Proton Damage. *Space Photovoltaic Research and Technology—1983, High Efficiency, Radiation Damage, and Blanket Technology*, NASA CP-2314, pp. 56-62.

Yeh, C. S.; Li, S. S.; and Loo, R. Y., 1985: A Simple Model for Calculating the Displacement Damage in Electron and Proton Irradiated AlGaAs/GaAs/InGaAs (or Ge) Multijunction Solar Cells. *Eighteenth IEEE Photovoltaic Specialists Conference—1985*, IEEE Catalog No. 85CH2208-7, Inst. of Electrical and Electronics Engineers, Inc., pp. 657-662.

Chapter 15

Concluding Remarks

15.1. Current Status

The final goal of the present research program is to provide the design engineer with analysis tools to adequately design future NASA space structures and to assure that acceptable risks are not exceeded. To validate code accuracy, we require these analysis tools to be compared with well-controlled experiments. Although we have made great progress toward this goal, still many difficult tasks remain before this goal is achieved.

The first step in progressing toward this goal is the development of transport codes and data bases for HZE and nucleonic components in the straight ahead approximation. An even more restrictive assumption than the straight ahead approximation is applied to the HZE fragments by assuming that the velocity is conserved in the interaction. The current code versions either apply in space (HZETRN, BRYNTRN) or in the laboratory (LABTRN, LBLTRN) exclusively. Hence, a code for space which can be validated in laboratory experiments is beyond our present capability. Even then the HZE cross sections are assumed to be energy independent for the space code HZETRN and the most general laboratory code LBLTRN. Although the laboratory code LABTRN does treat energy-dependent cross sections, it only allows evaluation of the absorbed dose within an absorber. Three generalizations of these codes are required: (1) the straight ahead approximation should be replaced with a two-stream approximation, (2) the full energy dependence of the nuclear cross sections should be added, and (3) the spectral components of the HZE fragmentation should be introduced. Even these additions to the current codes will not provide a complete description of the transport process. Such a complete description requires the introduction of mesons, antibaryons, and their decay, and reaction products, especially the electromagnetic cascades. The incompleteness of the present codes results in part from the data bases utilized. The generation of such a data base is in progress and our next immediate goal is to have a complete set of one-dimensional codes.

15.2. Future Goals

The first goal beyond the present work is to develop a complete set of one-dimensional codes that are able to evaluate biological response in an arbitrary shield geometry for engineering applications. After this initial goal has been accomplished, we will move onward toward fully three-dimensional codes by first generating a new data base for atomic/molecular collisions as well as a more complete nuclear data base. Such three-dimensional codes are particularly important for validation in laboratory experiments. These validated three-dimensional codes will provide the codes for future space engineering design.

NASA Langley Research Center
Hampton, VA 23665-5225
September 20, 1991

Acknowledgments

First I want to thank my wife, Delores Gelino Wilson, and son, John-Paul Wilson, for their patience during those periods when much of this work was being done at home and during the writing of the report. Also, I want to pay tribute to my mentor, teacher, and friend, Dr. Trutz Foelsche (deceased). The Langley Management deserves credit for encouraging this work both "in season" and "out of season." Special credit goes to Frank Hohl (deceased) and George P. Wood who rescued it; to Edmund J. Conway who encouraged it, even out of season; and to William M. Piland who helped restart it. Their foresight has at long last been vindicated. Thanks to the many friends and students who contributed to the work over these many years and are too numerous to mention, but whose names appear on many references cited herein, especially S. L. Lamkin, F. F. Badavi, C. M. Costner, D. M. Ngo, L. V. Stock, and S. Y. Chun. A special thank you to Professor Carl Carlson at the College of William and Mary in Virginia, Williamsburg, Virginia, for encouragement during a very difficult period of this research. Many thanks to the staff of the Langley Technical Editing Branch and the Langley Publications Section for their heroic efforts to complete this document for its intended use at the NATO Advanced Study Institute held in Amerção de Pera, Portugal. We acknowledge Dr. Frank Sultzman of the Life Sciences Division, NASA Office of Space Science and Applications, for his constant support of this effort. This work has been supported by the Life Sciences Division, NASA Office of Space Science and Applications; NASA Office of Aeronautics and Space Technology; Air Surgeon Generals Office, Federal Aviation Administration; the National Cancer Institute; and the Physics Department, Old Dominion University, Norfolk, Virginia.

REPORT DOCUMENTATION PAGE			Form Approved OMB No. 0704-0188	
Public reporting burden for this collection of information is estimated to average 1 hour per response, including the time for reviewing instructions, searching existing data sources, gathering and maintaining the data needed, and completing and reviewing the collection of information. Send comments regarding this burden estimate or any other aspect of this collection of information, including suggestions for reducing this burden, to Washington Headquarters Services, Directorate for Information Operations and Reports, 1215 Jefferson Davis Highway, Suite 1204, Arlington, VA 22202-4302, and to the Office of Management and Budget, Paperwork Reduction Project (0704-0188), Washington, DC 20503				
1. AGENCY USE ONLY (Leave blank)	2. REPORT DATE December 1991	3. REPORT TYPE AND DATES COVERED Reference Publication		
4. TITLE AND SUBTITLE Transport Methods and Interactions for Space Radiations			5. FUNDING NUMBERS WU 199-04-16-11	
6. AUTHOR(S) John W. Wilson, Lawrence W. Townsend, Walter Schimmerling, Govind S. Khandelwal, Ferdous Khan, John E. Nealy, Francis A. Cucinotta, Lisa C. Simonsen, Judy L. Shinn, and John W. Norbury				
7. PERFORMING ORGANIZATION NAME(S) AND ADDRESS(ES) NASA Langley Research Center Hampton, VA 23665-5225			8. PERFORMING ORGANIZATION REPORT NUMBER L-16882	
9. SPONSORING/MONITORING AGENCY NAME(S) AND ADDRESS(ES) National Aeronautics and Space Administration Washington, DC 20546-0001			10. SPONSORING/MONITORING AGENCY REPORT NUMBER NASA RP-1257	
11. SUPPLEMENTARY NOTES Wilson, Townsend, Nealy, Cucinotta, Simonsen, and Shinn: Langley Research Center, Hampton, VA; Schimmerling: Lawrence Berkeley Laboratory, University of California, Berkeley, CA; Khandelwal and Khan: Old Dominion University, Norfolk, VA; Norbury: Rider College, Lawrenceville, NJ				
12a. DISTRIBUTION/AVAILABILITY STATEMENT Unclassified Unlimited Subject Category 93			12b. DISTRIBUTION CODE	
13. ABSTRACT (Maximum 200 words) A review of the program in space-radiation protection at the Langley Research Center is given. The relevant Boltzmann equations are given with a discussion of approximation procedures for space applications. The interaction coefficients are related to the solution of the many-body Schrödinger equation with nuclear and electromagnetic forces. Various solution techniques are discussed to obtain relevant interaction cross sections with extensive comparison with experiments. Solution techniques for the Boltzmann equations are discussed in detail. Transport computer code validation is discussed through analytical benchmarking, comparison with other codes, comparison with laboratory experiments, and measurements in space. Applications to missions to the Moon and Mars are discussed.				
14. SUBJECT TERMS Nuclear interactions; Radiation transport; Lunar; Mars			15. NUMBER OF PAGES 616	
			16. PRICE CODE A99	
17. SECURITY CLASSIFICATION OF REPORT Unclassified	18. SECURITY CLASSIFICATION OF THIS PAGE Unclassified	19. SECURITY CLASSIFICATION OF ABSTRACT	20. LIMITATION OF ABSTRACT	

NSN 7540-01-280-5500

Standard Form 298 (Rev. 2-89)
Prescribed by ANSI Std. Z39-18
298-102

